SET 2024
SHANGHAI

21st International Conference on Sustainable Energy Technologies

12 to 14th August 2024, Shanghai, China

Sustainable Energy Technologies 2024
Conference Proceedings: Volume 3

WSSET

World Society of Sustainable Energy Technologies

Proceedings of the 21st International Conference on Sustainable Energy Technologies

SET2024

12 – 14th August 2024, Shanghai, China

Edited by
Professor Saffa Riffat

Supported by SET2024 Conference Organising Committee:

Chair: Professor Saffa Riffat
Co-Chair: Professor Zhongzhu Qiu
Editors: Dr Ziwei Chen
Dr Tianhong Zheng
Dr Yanan Zhang
Dr Yi Fan
Ms Zeny Amante-Roberts

Reference to a conference paper:
To cite a paper published in these conference proceedings, please substitute the highlighted sections of the reference below with the details of the article you are referring to:
Author(s) Surname, Author(s) Initial(s), 2024. 'Title of paper'. In: Riffat, Su. ed., **Sustainable Energy Technologies**: Proceedings of the 21st International Conference on Sustainable Energy Technologies, 12-14th August 2024, Shanghai, China. University of Nottingham: Buildings, Energy & Environment Research Group. Pp XX-XX. Available from: nottingham-repository.worktribe.com/ [Last access date].

ISBN-13 978-0-85358-356-1
Version: 01.12.2024

Foreword

The 21st International Conference on Sustainable Energy Technologies (SET2024) held in Shanghai, China, from August 12–14, 2024, represented a significant milestone in the field of sustainable energy, uniting experts, researchers, and industry leaders from around the world. Organised through a collaborative effort between the World Society of Sustainable Energy Technologies (WSSET) and the Shanghai University of Electric Power, SET2024 served as a premier platform for the exchange of the latest technical innovations, presentation of cutting-edge research, and discussion of critical issues poised to shape the global energy landscape. This year's focus encompassed not only the research and development of sustainable energy technologies but also their applications, emphasizing the urgent need for energy security and the role of AI in achieving these goals.

The conference drew distinguished experts, scholars, and industry representatives who shared insights and recent advancements, fostering robust discussions and facilitating the practical application of scientific discoveries. This event also catalysed collaboration among universities, industries, and governments, reinforcing the essential link between research, policy, and industry practice.

The proceedings address core themes reflecting the multifaceted nature of sustainable energy development in Renewable Energy Technologies, Energy Storage and Conversion, Low Carbon Buildings and Sustainable Architecture, Sustainable Urban Development and Cities and Policies And Management. These topics highlight the interdisciplinary approaches and systemic shifts needed to support sustainable growth in energy sectors worldwide.

With participation from over 320 delegates and nearly 550 abstracts received, SET2024 provided an invaluable forum for exchanging both academic research and practical applications. We extend our sincere gratitude to all contributing authors for their commitment and invaluable contributions to both the conference and this publication. Special recognition goes to our international scientific committee for their guidance and thorough review of submissions, as well as to the organising committee, volunteers, and other contributors who made SET2024 a success. Our deep appreciation also goes to our sponsors PCM Products Ltd., Terry Payne, and UK EDU Ltd. for their generous support.

Thank you all for your commitment to advancing sustainable energy technologies and contributing to a shared future of innovation, sustainability, and collaboration.

Professor Saffa Riffat
Chair in Sustainable Energy Technologies
President of the World Society of Sustainable Energy Technologies
SET2024 Chair

Contents

#261: Design and performance analysis on a heat pipe solar PV/T collector

Lanhua DAI[1*], Hongbo ZHU[1], Yuting YANG[1], Xiaolong LI[2]

[1] Changzhou institute of technology, China, * dailh@czu.cn
[2] Changzhou university, China

Abstract: A three-dimensional unsteady model is established to study the cooling performance for a heat pipe photovoltaic/thermal (HP-PV/T) collector. The numerical models are experimentally verified using the published research results. The fin groups (circle, rectangle) which combined with the condenser section of heat pipe with different quantities are designed to identify the optimal finned condenser type for the HP-PV/T collector. The influence of fin shape and number of condensing sections of heat pipe on equivalent efficiency performance of PV/T collector is analyzed. The results indicate that the circle fin groups with the number of four showed the highest thermal conductivity and the best thermal stability compared to the rectangular one. Furthermore, the impact of the mass flow rate of water, inlet temperature and material of the fin groups on the thermal and electricity performance of the HP-PV/T collector are investigated. When the fin groups are being operated simultaneously, the total energy production of the HP-CPV/T collector using copper is higher than that using steel. The thermal and electricity efficiencies of the HP-CPV/T collector using the cooper fin groups are observed with the value of 64.3% and 64.8%, respectively.

Keywords: ANSYS Simulation; PV/T Collector; Heat Pipe; Fin Groups; Equivalent Efficiency

1. INTRODUCTION

Solar energy is a primary source of energy for the development of human agriculture and industry. CuInGaSe2 (CIGS) photovoltaic (PV) module is a representative of renewable energy in the industry that has significantly reduced the PV Wattage cost from 2.3 $ in 2015 to less than 0.5$ in 2020 and increased their electrical efficiency to over 23.4% in 2021 compared to 17% in 2005[Nanayakkara, 2017].

Concentrating Photovoltaic (CPV) systems employ inexpensive optics, like mini mirrors, to concentrate sunlight 200-1000 times for improved efficiency. Yet, PV cell output drops 0.5% per 1℃ rises in temperature, reducing efficiency. High module surface temperatures exacerbate this issue. To counteract, heat transfer fluids like water or air are used to cool the PV module, lowering cell temperatures and boosting electricity conversion efficiency. Conventional heat exchangers typically utilize aluminum panels, which may provide insufficient contact area between the PV cells and the circulating working fluids. To address the insufficient contact area issue, the recent study adopted a heat pipe, which is a highly efficient thermal conductor, as a feasible solution. Solar radiation continuously heats up PV modules, causing heat loss to the surroundings. Photovoltaic/thermal (PV/T) technology addresses this by efficiently producing both heat and electricity, optimizing dual output and enhancing overall efficiency [Wang, 2019, Joshi, 2018]. Researchers globally have extensively studied PV/T collectors to improve their electric and thermal efficiency, categorizing them into air-, liquid-, and heat pipe-based systems based on cooling methods. Air-based systems prove more cost-efficient for PV cell cooling, albeit with a lower heat transfer rate [Boutina, 2018]. In contrast, liquid-based systems are deemed more practical due to their higher thermal conductivity and more efficient heat transfer compared to air [Tiwari, 2006, Othman, 2016]. However, these systems have the disadvantage of being susceptible to freezing and leakage, which can result in higher maintenance costs [Chen, 2015, Fang, 2012].

To address the drawbacks associated with air-based and liquid-based PV/T modules, heat pipes have been integrated into the PV/T system. Heat pipe-based PV/T modules offer significant advantages, including minimal heat loss, high outlet temperatures, and sustained high efficiency even under adverse conditions. Recent theses have provided only a basic introduction to heat pipe photovoltaic/thermal (PV/T) modules. In pursuit of performance enhancement, researchers have endeavored to incorporate various heat transfer designs into heat pipe PV/T systems [Esfe, 2020, Preet, 2018, Ju, 2017, George, 2019].

To boost heat transfer, a copper fin is welded onto the heat pipe's condenser, as shown in Figure 1. Two matching fin groups flank the condenser, enhancing heat dispersion. Each fin is made from 1 mm thick copper, 10 mm long, and 2 mm wide.

This paper introduces mathematical and CFD models for analyzing finned and non-finned PV/T systems. It conducts simulations to evaluate a novel cooling structure's thermal performance and compares the thermal, electrical, and overall efficiency of a finned heat pipe PV/T collector to a standard non-finned version.

2. COLLECTOR DESIGN

The present system integrates a standard CuInGaSe2 (CIGS) PV panel (Table 1) with a parallel compound parabolic concentrator that involves a light compensation mirror. A single heat pipe is placed at the PV panel base, as depicted in Figure 1.

Table 1: Specification of the PV module

Cell Type	CuInGaSe2 Cell
Open circuit voltage	25.2V
Short circuit current	7.35A
Maximum power piont	6.41A&19.50V
PV efficiency	20.13%
temperature coefficient	0.017

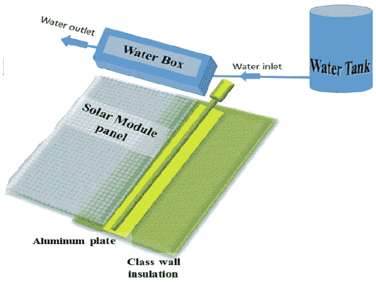

Figure 1: Heat pipe PV/T collector without concentrating optics

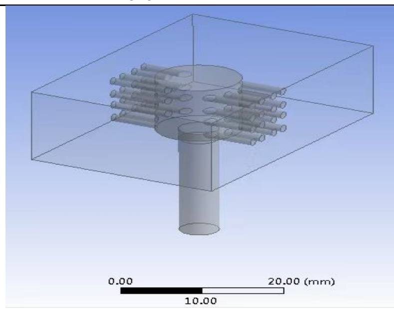

Figure 2: Condenser section of a single finned heat pipe

A schematic diagram of condenser section of finned heat pipe place in the water box is presented in Figure 2. The collector is designed to facilitate natural circulation of water through the condenser within the water duct. This design enhances heat dissipation through the outer finned surface of the condenser, thereby increasing the heat transfer rate as water flows. This approach is aimed at harnessing excess heat. The heat pipe is directly affixed to the rear surface of the aluminum panel situated beneath the photovoltaic (PV) cell. This configuration increases the rate of heat transfer from the PV module surface to the circulating fluid. Consequently, it significantly augments the heat transfer interactions among the various components within the back panel of the PV/T collector, serving to reduce thermal resistance.

The proposed model of the concentrating finned heat pipe photovoltaic/thermal (HP-CPV/T) collector has been developed through modifications to the heat pipe PV/T model previously reported by Pei [Pei, 2011] and the low concentrating PV/T model reported by Stylianos Stylianou [Stylianou, 2016]. Therefore, when developing the relevant mathematical models for assessing thermal, electrical, and overall performance efficiency, the conclusions derived from the aforementioned models can be effectively applied to the present photovoltaic/thermal (PV/T) collector.

The parameters utilized for the simulation are detailed in Table 2. Generally, key parameters to consider include the average temperature on the PV panel and the outlet temperature of the water box. These parameters necessitate the application of CFD fluid mechanics software for a detailed analysis of the heat sink at the condenser section of the heat pipe to draw accurate conclusions. Given the parallel arrangement of the PV/T model, it is assumed that the fluid flow rate is uniform within the water box. The material properties and physical dimensions of the components, including the PV plate, working fluid, copper heat pipe, back aluminum panel, and fin group, are assumed to be consistent [Zhang, 2020].

In the concentrating finned heat pipe photovoltaic/thermal (HP-CPV/T) collector, the overall efficiency is attributed to the effectiveness of the photovoltaic (PV) and photothermal components. Consequently, the overall efficiency of the collector can be determined by calculating the efficiencies of the photovoltaic and photothermal sides respectively.

Table 2: Data for the simulation.

PV module	Length & width	1188mm*140mm
	Temperature coefficient (%/°C)	0.017
	Reference average PV panel temperature(°C)	55
	Density (kg/ m^3)	0.00058
	Thickness (mm)	2.25
Back panel	Material	Aluminum
	Thickness (mm)	1.2
	Density (kg/ m^3)	2700
	Specific heat capacity (J/Kg·K)	930
	Thermal conductivity (W/m·K)	205
Heat pipe	Material	Copper
	No. of heat pipes	1
	Heat pipe spacing(mm)	1540
	Effective thermal conductivity (W/m.K)	86000
Working fluid used	Material	Water:
	Mass flow(kg/s/m^2)	0.081
	Inlet temperature (°C)	25
Fin group	Material	Copper
	Fin shape	Circle Rectangle
	Fin length(mm)	10
	Fin spacing(mm)	Circle:1.5 Rectangle:1.25

3. CFD MODEL

In order to analyze the performance of a finned heat pipe PV/T collector, the temperature distribution on the condenser of heat pipe was predicted using the model built in ANSYS FLUENT software [Stylianou,2016]. Accurate and precise predictions of the temperature profile across the condenser section of a heat pipe are crucial for the development of a prototype for complex solar energy systems, such as a heat pipe photovoltaic/thermal (PV/T) collector [Renno, 2013]. In this paper, special attention was given to the selection of boundary conditions and discretization schemes, which are critical for the accuracy of the model. The modeling process and subsequent numerical analysis were conducted in three distinct stages. The initial stage involved the development of a finned condenser model. This was followed by the validation of the model using experimental data. The final stage was an assessment of the overall performance of the collector, specifically examining the impact of various fin configurations on the condenser of the heat pipe.

A CFD solver based on the finite volume method (FVM) was used to discretize the continuous governing equations into algebraic counterparts [Misha, 2020]. Numerical solving of algebraic equations yields the solution field. Convergence in continuity, momentum, and energy equations is set by specific criteria, with residuals dropping to 10^{-3} for continuity and momentum, and10^{-6} for the energy equation to signal convergence. Constant inlet temp and flow rate in the water box are assumed.

3.1. Physical model

A typical heat pipe photovoltaic/thermal (HP-PV/T) collector comprises photovoltaic (PV) cells, heat pipe, back panel, and working fluid. Given the high photothermal conversion rate of the HP-PV/T collector, a heat transfer analysis has been conducted. The specific steps are as follows: (1) Part of the sunlight was directly projected on the surface of the PV cell, and another part of the sunlight is reflected to the surface of the photovoltaic cell through the composite concentrator; (2) Solar radiation heats the photovoltaic cell, and most of the radiant energy absorbed by it is converted into heat energy; (3) The heat energy on the back of the PV cell was transferred to the heat-absorbing aluminum plate through the insulating layer and the adhesive layer, and the heat can be calculated as the internal heat source of the HP-PV/T collector; (4) The heat in the aluminum plate was absorbed by the working fluid inside the heat pipe, and was transferred from the evaporation section of the heat pipe to the condensation section of the heat pipe by evaporation-condensation; (5) The heat reaches the condensation section of the heat pipe and dissipates heat to the water through the fins on the condensation section.

In particular, to expedite the CFD simulation, a quarter of the fin group may be utilized, which is determined to have a heat exchange efficiency equivalent to 86.3% of the heat transfer efficiency of the full fin assembly.

3.2. Mathematical model

Having created the finned condenser model, the subsequent step involves setting up the case for simulation. This phase is critical, as it requires consideration of all parameters that impact the collector's performance. These include meteorological data (ambient temperature, irradiance), specific design (mirrors, PV cells, receiver), and operational variables (mass flow rate, inlet water temperature, type of fin group). For the steady-state mathematical model of this PV/T collector, the following parameters must also be taken into account: concentration factor, concentrated intensity, actual PV efficiency, effective absorption factor, and cooling load.

Concentration factor

Starting with the concentration factor, it is defined as the ratio between the aperture area of the mirrors and the illuminated area of the PV cells. The aperture area of this system is 0.323 m2 while the illuminated PV area of the PV cells equals 0.1664 m2. Therefore the concentration factor equals C=1.94.

Equation 1: Concentration factor of PV/T collector.

$$C = \frac{Aperture\ Area\ of\ Mirrors}{Illuminated\ PV\ Area}$$

Concentrated Intensity

Having calculated the concentration factor, the next step is to determine the concentrated intensity. This term stands for the direct irradiance G (W/m2) falling on the mirrors multiplied with concentration factor C.

Equation 2: Concentration Intensity of PV/T collector.

$$Concentrated\ Intensity\ = C \cdot G$$

Actual PV efficiency

First, the efficiency of the PV cells has to be calculated by Table 1. As mentioned in section 1.1, the PV cells efficiency is affected by the temperature of the cells. The actual PV efficiency ηPV is affected by the PV efficiency at the maximum power point, the temperature coefficient α (%/ºC) and the mean PV cells temperature Tm (ºC).

Equation 3: Actual PV efficiency of PV/T collector.

$$\eta_{PV} = \eta[1 - a(T_m - 25)]$$

Effective absorption factor

To proceed with the model, the cooling load calculation accounts for Aeff, the effective absorption factor reflecting solar power conversion to heat. With Tm, the PV cells' mean temperature, initially estimated using meteorological and operational data like mass flow rate and inlet fluid temperature, alongside PV cell specs for max efficiency and temperature coefficient α from the datasheet, the next step is determining Aeff. This factor, depicted in Figure 3, involves assumptions considering mirror and PV cell impacts within the collector, illustrating energy loss distribution in its diagram.

Equation 4: Effective absorption factor of PV/T collector.

$$A_{eff} = 0.757 - (\eta_{PV} \times 77.3\%)$$

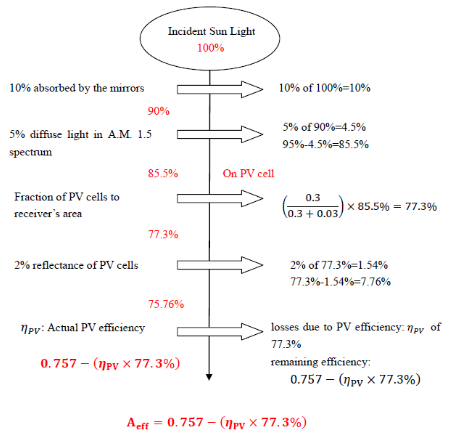

Figure 3: A series of assumptions in mathematical model

Cooling load

Equation (4) demonstrates how the effective absorption factor is ascertained relative to the efficiency of the PV cells. Utilizing this factor, one can then compute the cooling load, which represents the proportion of incident irradiance that is converted into heat within the system. This parameter is subsequently transformed into a volumetric load measured in watts per cubic meter

(W/m³) and is employed as a consistent energy input for the PV component. Indeed, this approach constitutes the method by which solar radiation is integrated into the model.

Equation 5: Cooling load of PV/T collector. $$CCooling\ load = A_{eff} \times Concentrated\ Intensity(W/m^2)$$

Actual PT efficiency

Equation 6: Actual PT efficiency of PV/T collector. $$C\eta_{th} = \frac{\dot{m} \cdot C_p \cdot \Delta T}{G \cdot C \cdot A}$$

where:

$\dot{m}$=mass flow rate (kg/s)

- Cp=the specific heat capacity of the fluid (J/kg/°C)
- ΔT=the temperature difference of fluid between the outlet in the inlet (°C)
- G=the solar irradiance (W/m[2])
- C=optical concentration factor (-)
- A=the illuminated PV area (m[2])

To assess the heat flow through fluid-solid interactions, a conjugate heat transfer mechanism was considered. For this purpose, the entire model is divided into two domains based on their physical properties: the finned condenser constitutes the solid domain, while the water represents the fluid domain. The domains are distinguished by different colors, as depicted in Figure 4.

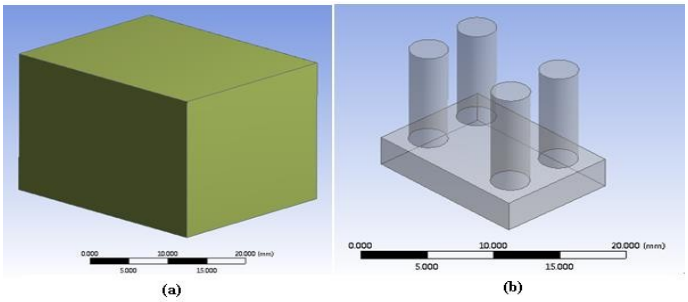

Figure 4: Area divided in calculation:(a) fluid domain (b) solid domain

The k − ε two-transport-equation model, enhanced with advanced wall treatment, was selected to solve and analyze turbulence within the water box. The governing equations, which define the velocity, pressure, and temperature in the fluid domain, are as follows:

Continuity equation:

Equation 7: Continuity equation of fluid domain. $$\frac{\partial u}{\partial x} + \frac{\partial v}{\partial y} + \frac{\partial w}{\partial z} = 0$$

Momentum equation:

Equation 8: Momentum equation of fluid domain.
$$\left(u\frac{\partial u}{\partial x} + v\frac{\partial u}{\partial y} + w\frac{\partial u}{\partial z}\right) = -\frac{1}{\rho}\frac{\partial p}{\partial x} + \mu\left\{\frac{\partial^2 u}{\partial x^2} + \frac{\partial^2 u}{\partial y^2} + \frac{\partial^2 u}{\partial z^2}\right\}$$
$$\left(u\frac{\partial v}{\partial x} + v\frac{\partial v}{\partial y} + w\frac{\partial v}{\partial z}\right) = -\frac{1}{\rho}\frac{\partial p}{\partial y} + \mu\left\{\frac{\partial^2 v}{\partial x^2} + \frac{\partial^2 v}{\partial y^2} + \frac{\partial^2 v}{\partial z^2}\right\}$$
$$\left(u\frac{\partial z}{\partial x} + v\frac{\partial z}{\partial y} + w\frac{\partial z}{\partial z}\right) = -\frac{1}{\rho}\frac{\partial p}{\partial z} + \mu\left\{\frac{\partial^2 w}{\partial x^2} + \frac{\partial^2 w}{\partial y^2} + \frac{\partial^2 w}{\partial z^2}\right\}$$

Energy equation:

Equation 9: Energy equation of fluid domain. $$u\frac{\partial T}{\partial x} + v\frac{\partial T}{\partial y} + w\frac{\partial T}{\partial z} = \alpha\left\{\frac{\partial^2 T}{\partial x^2} + \frac{\partial^2 T}{\partial y^2} + \frac{\partial^2 T}{\partial z^2}\right\}$$

Where: u_i is velocity field u, v, w along x, y, z.

3.3. Boundary Conditions and Grid Study

Meanwhile, a mass flow rate boundary condition was implemented at the water box inlet. A pressure-outlet boundary condition was applied to the outlet section of the working water fluid. For the analysis, an ambient air temperature of 30°C was assumed, and an incident solar radiation of 840 W/m² was considered for the location in Nanjing. Owing to the opaque back aluminum panel of the PV/T collector, a fixed heat flux was applied as a thermal boundary condition. This approach was taken in lieu of employing a solar ray tracing algorithm, as the solar load model's ray tracing feature within FLUENT does not account for the internals.

For the proper meshing of the condenser section integrated with fins, an automatic mesh generation method was employed, specifically alternating between the tetrahedron and patch conforming algorithms. A denser mesh was applied to critical areas of heat transfer, such as the fins on the condenser of the heat pipe. To ensure the accuracy of the desired solution, a grid independence test was conducted, particularly focusing on problems involving heat transfer fluid dynamics. In this study, different grid sizes were evaluated based on the temperature of the finned condenser. The aim of this step is to validate that the predicted performance of the photovoltaic/thermal (PV/T) condenser remains consistent irrespective of grid size variations. This process of identifying the optimal mesh size is also known as a grid independence study. For the given finned heat pipe PV/T collector, three grid sizes, comprising 186,382, 216,542, and 263,421 elements, were tested, as presented in Table 3. The optimal mesh size, suitable for both independent and simultaneous fluid modes, was determined to be 186,382 elements.

Table 3: A grid independency test

Case	Number of Elements	Simulation time [s]	Outlet temperature of water[°C]
Case 1	186382	100	36.21
Case 2	216542	100	36.15
Case 3	263421	100	36.29

The model of the condenser section of the heat pipe, featuring both circular and rectangular fin groups, has been validated independently. The validation of the model was conducted by comparing the predicted outlet water temperatures from a non-finned condenser with the experimental data obtained for a novel heat pipe photovoltaic/thermal (PV/T) system, as presented by Pei [Pei, 2011], as shown in Figure 5. For the purpose of this comparison, similar geometric and operational parameters were utilized, as reported in the reference [Pei, 2011], The discrepancy between simulated and experimental data lessens over time during constant input parameter tests, particularly after an initial disparity due to varying solar irradiance. The model's performance improves, aligning more closely with measurements as operations continue.

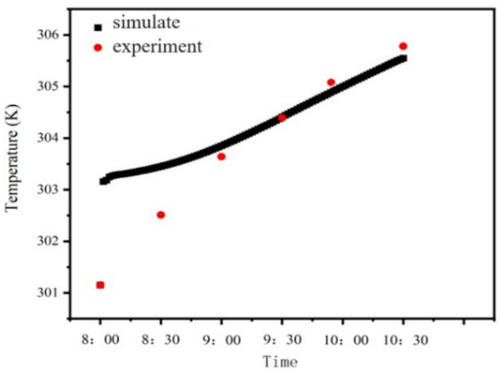

Figure 5: Comparison of the simulation value of the outlet water temperature with the experimental data

4. RESULTS AND DISCUSSION

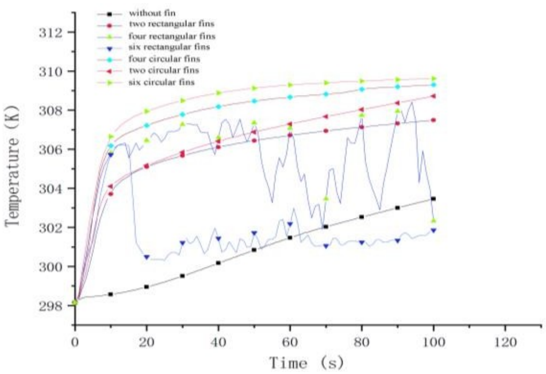

Figure 6: The variations of the outlet temperature for different fins

Figure 6 illustrates the variations in the fin group under identical fluid flow rates and inlet temperatures. The influence of the fin groups' shape (Circle and Rectangle) and quantity (2,4,6) for outlet temperature are discussed here in comparison. The results indicate that for circular fins, an increase in the number of fins leads to a more pronounced heating effect. Conversely, in the case of square fins, an increase in the number of fins results in less effective heating performance. Upon investigation, it was observed that water may encounter square fins in the header, causing the flow to transition from laminar to turbulent. This change can lead to a backflow at the outlet and thorough mixing of cold and hot water. As shown in Figures 7 and 8, the instantaneous outlet temperature and the temperature differential between inlet and outlet both decreases.

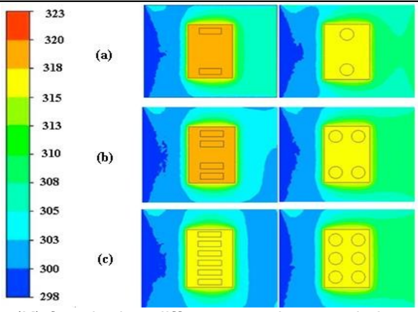

Figure 7: The temperature horizontal distribution(K) for placing different numbers and shapes of fins: (a) two rectangles and twocircles(b) four rectangles and four circles (c) six rectangles and six circles

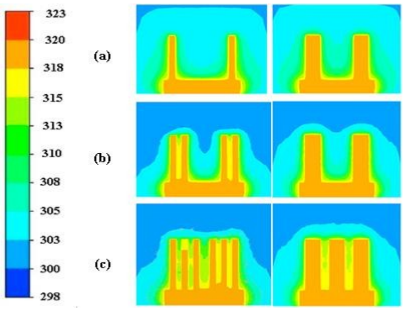

Figures 8: The temperature vertical distribution (K) for placing different numbers and shapes of fins:(a) two rectangles and twocircles (b) four rectangles and four circles (c) six rectangles andsix circles

It can be inferred from Figures 6, 7, and 8 that when four circular fins are installed, the resulting effect surpasses that of other parameters. A uniform temperature distribution is observed at the outlet, indicative of effective heat dissipation. The circular fins positioned on the condensation section of the heat pipe can significantly enhance the temperature gradient between the inlet and outlet. This enhancement subsequently improves the thermal and electrical efficiency of the heat pipe photovoltaic/thermal (PV/T) collector. Furthermore, in the case of the reference photovoltaic (PV) module cooled by a heat pipe without fins [Al Hasnawi, 2021], the electrical efficiency was found to be 7.8%. The lower efficiency (7.8%) in reference design, attributed to a single, air-exposed heat pipe, led to the adoption of a finned heat pipe in the present study. This modification yielded an improved electrical efficiency of 19.72% under steady-state conditions by expanding the heat transfer surface area and optimizing heat extraction from PV cells. The integration of circular fin groups, leveraging their advanced thermo-physical properties, further amplifies efficiency per unit area. Consequently, combining circular fin groups with a heat pipe in PV/T collectors emerges as a promising strategy, surpassing the performance of conventional heat pipe-based collectors.

Table 4: Various parameters affecting collector efficiency

Parameters								
Mass flow rate of water (kg/s)			Inlet temperature（K）			Material of fin		
Case A	Case B	Case C	Case D	Case E	Case F	Case G	Case H	Case I
0.08	0.09	0.10	298.15	301.15	304.15	Steel	Copper	Aluminum

It is worthwhile investigating the thermal performance of individual parameters within a heat pipe photovoltaic/thermal (HP-PV/T) collector when circular fin groups are operated simultaneously, as detailed in Table 4. Notably, the combination of water mass flow rate, inlet temperature, and fin material as three parameters that can be optimized is particularly appealing when applied to the circular fin groups on the heat pipe condenser. This preference is due to the superior thermo- physical properties of these parameters in the context of heat pipe PV/T collector research. Given the simultaneous operation, the thermal performance of each parameter is closely linked to its counterpart, such as the thermal and electrical efficiency of the collector. Hence, it is important to recognize the contribution of the water mass flow rate, inlet temperature, and fin material to the overall performance of the heat pipe PV/T collector.

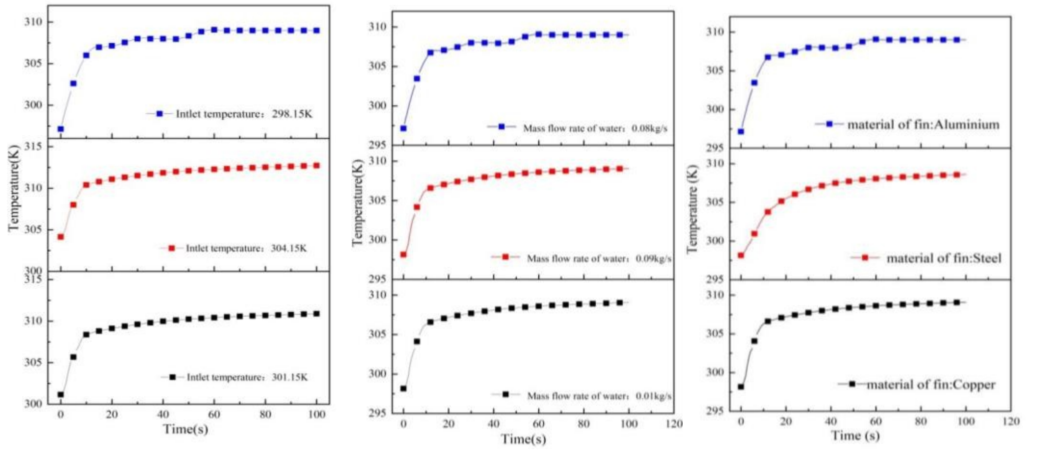

Figure 9: The variations of the outlet temperature for different parameters

As depicted in Figures 9 and 10, in a scenario where the mass flow rate of water is increased while all other parameters are held constant in the simulation, the fluid with an increased flow rate extracts additional heat. Consequently, the temperature difference between the inlet and outlet of the water tank is enhanced. When the inlet temperature rises, the outlet temperature exhibits only a minor change, resulting in a relatively small temperature difference that remains a limitation to improving efficiency. The material of the fin, when altered at constant parameters, significantly influences the amount of heat extracted by the water. Notably, copper, aluminum, and steel are observed to have a substantial impact. Therefore, the total accumulated heat extracted by the fin material and an increased mass flow rate is greater than that achieved by merely boosting the inlet temperature when employing circular fin groups.

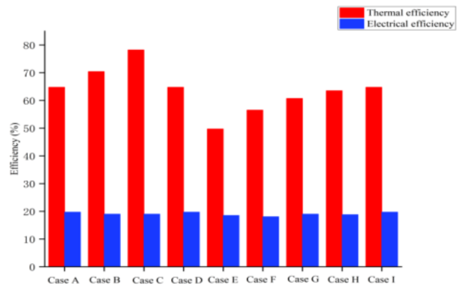

Figure 10: A performance comparison of the current parameter with previously reported PV/T collector

5. CONCLUSION

Transient CFD models for a concentrating finned heat pipe photovoltaic/thermal (HP-CPV/T) collector were developed in this study. To ascertain the optimal fin group configuration for the HP-CPV/T collector, the impact of fins of varying shapes on the condenser was assessed. The findings indicated that the circular finned design yielded more promising results compared to the rectangular fin. Simultaneous operation showed the HP-CPV/T collector with copper fin groups produced more total energy than those with steel fin groups. The steel fins reached a max total equivalent efficiency of 64.3%, which climbed to 64.8% with increased mass flow rate.

In summary, the study proved that the fin group's heat transfer efficiency in the HP-CPV/T collector's condenser relies heavily on material and design. It enhances heat extraction from PV modules to the heat pipe at high temps, outperforming traditional designs. Future research will prioritize outdoor experiments to refine and maximize the collector's performance.

6. REFERENCES

Al Hasnawi A G T, Judran H K, Ibrahim A K. Experimental investigation of cooling solar photovoltaic (PV) cells by using heat pipe approach[J]. Journal of Chemical Technology and Metallurgy, 2021, 56(4): 815-818.

Boutina L., Khelifa A., Touafek K., Lebbi M., Baissi M.T., Improvement of PVT air-cooling by the integration of a chimney tower (CT/PVT). Applied Thermal Engineering, 2018, 129: 1181–1188.

Chen J.F., Dai Y.J., Building componentized solar photovoltaic/thermal (PV/T) devices and their applications in construction. Construction Science and Technology, 2015, 8: 53–55, 60.

Esfe M.H., Kamyab M.H., Valadkhani M., Application of nanofluids and fluids in photovoltaic thermal system: An updated review. Solar Energy, 2020, 199: 796–818.

Fang J., Liu Y.S., Yang J.J., Fang W.J., Gao T., Yang Z.L., Peng L., Gu M.A., The study of building-integrated photovoltaic/thermal solar system. East China Electric Power, 2012, 40: 108–111.

George M., Pandey A.K., Rahim N.A., Tyagi V.V., Shahabuddin S., Saidur R., Concentrated photovoltaic thermal systems: A component-by-component view on the developments in the design, heat transfer medium and applications. Energy Conversion and Management, 2019, 186: 15–41.

Joshi S.S., Dhoble A.S., Photovoltaic-Thermal systems (PVT): Technology review and future trends. Renewable and Sustainable Energy Reviews, 2018, 92: 848–882.

Ju X., Xu C., Liao Z.R, Du X.Z., Wei G.S., Wang Z.F., Yang Y.P., A review of concentrated photovoltaic- thermal (CPVT) hybrid solar systems with waste heat recovery (WHR). Science Bulletin, 2017, 62: 1388–1426.

Misha S, Abdullah A L, Tamaldin N, et al. Simulation CFD and experimental investigation of PVT water system under natural Malaysian weather conditions[J]. Energy Reports, 2020, 6: 28-44.

Nanayakkara S U, Horowitz K, Kanevce A, et al. Evaluating the economic viability of CdTe/CIS and CIGS/CIS tandem photovoltaic modules[J]. Progress in Photovoltaics: Research and Applications, 2017, 25(4): 271-279.

Othman M.Y., Hamid S.A., Tabook M.A.S., Sopian K., Roslan M.H., Ibrahim Z., Performance analysis of PV/T Combine with water and air heating system: An experimental study. Renewable Energy, 2016, 86: 716–722.

Preet S., Water and phase change material based photovoltaic thermal management systems: A review. Renewable and Sustainable Energy Reviews, 2018, 82: 791–807.

Pei G. Fu H.D. Zhang T., et al. A numerical and experimental study on a heat pipe PV/T system[J]. Solar energy, 2011, 85(5): 911-921.

Renno C, Petito F. Design and modeling of a concentrating photovoltaic thermal (CPV/T) system for a domestic application[J]. Energy and buildings, 2013, 62: 392-402.

Siecker J, Kusakana K, Numbi B P. A review of solar photovoltaic systems cooling technologies[J]. Renewable and Sustainable Energy Reviews, 2017, 79: 192-203.

Stylianou, Stylianos. "Thermal Simulation of Low Concentration PV/Thermal System Using a Computational Fluid Dynamics Software." (2016).

Tiwari A., Sodha M.S., Performance evaluation of hybrid PV/thermal water/air heating system: A parametric study. Renewable Energy, 2006, 31: 2460–2474.

Wang Y C, Wu T T, Chueh Y L. A critical review on flexible Cu (In, Ga) Se2 (CIGS) solar cells[J]. Materials Chemistry and Physics, 2019, 234: 329-344.

Zhang, Chunxiao, et al. "A review on recent development of cooling technologies for photovoltaic modules." Journal of Thermal Science 29 (2020): 1410-1430.

#262: A simulation comparison of side cooling plate and immersion cooling battery thermal management systems

Zekun JIANG[1]; Ruixin MA[1]; Yang XU[1]; Weicheng XUAN[1]; Binbin YU[1,2]*; Junye SHI[1,2]; Jiangping CHEN[1,3]

[1] Institute of Refrigeration and Cryogenics, Shanghai Jiao Tong University, Shanghai 200240, China
[2] Shanghai Jiao Tong University ZhongGuanCun Research Institute, Liyang 213300, China
[3] Shanghai Engineering Research Center of High Efficient Cooling System, Shanghai, 200240, China
Corresponding Author E-mail addresses: ybbedc@sjtu.edu.cn

Abstract: Immersion cooling technology is regarded as the optimal choice to meet the stringent thermal management requirements of future high-energy density battery packs. In this study, a module composed of 48 high-nickel ternary lithium-ion batteries, each with a capacity of 175 Ah, totaling 30.7kWh, was selected as the research subject. The total heat generation during 3C charging was 8.64kW. The high-performance side cooling plate BTMS was chosen as the benchmark, which, under severe conditions of an initialtemperature of 40°C and an inlet flow rate of 4.45L/min, nearly met the cooling demands during 3C fast charging, with a safe operating time of 694 seconds. Due to the significantly lower density, specific heat capacity, and thermal conductivity of the dielectric fluid used for immersion cooling compared to the water-glycol used for the side cooling plate, the basic immersion cooling BTMS, which has aflow structure similar to that of the side cooling plate BTMS, actually reduced cooling performance under the same conditions, decreasing the safe operating time by approximately 26.22%. Assuming 3C CC charging lasts for 20 minutes, the maximum temperature and temperature difference at the end of charging for the module using basic immersion cooling increased by 20.34% and 220.45%, respectively. The only advantage of the basic immersion cooling BTMS is its significantly lower pressure drop of 0.32 kPa, compared to the side cooling plate BTMS's pressure drop of 6.25 kPa. Further research is required to enhance the thermal management performance of immersion cooling in large module applications.

Keywords: Immersion Cooling, High-Nickel Ternary Lithium-Ion Battery, Side Cooling Plate, Battery Thermal Management System

1. INTRODUCTION

Electricity is a clean, efficient, and renewable secondary energy source. When used as a power source for automobiles, it can alleviate the energy crisis and significantly reduce environmental pollution. In response to the transportation sector's call to reduce carbon footprints, automakers are rapidly developing electric vehicles (EVs). In 2021, global EV sales were three times those of 2019, reaching 6.6 million units (Hwang et al., 2024). EVs are gradually replacing conventional internal combustion engine vehicles(ICEVs).

Lithium-ion batteries (LIB) have become the preferred power source for EVs due to their high energy density, high power density, and long lifespan (Lu et al., 2020). The performance and lifespan of lithium-ion batteries (LIB) are closely related to their operating temperature, with the optimal operating temperature range being 15-35 °C (Chen et al., 2016). To ensure consistent performance and lifespan of the batteries within a pack, it is recommended to maintain a temperature difference of less than 5°C within the battery pack (Patil et al., 2020). BTMSs are gaining increasing attention, and numerous experimental and numerical studies have been conducted on various BTMSs under different cooling conditions, such as air cooling, liquid cooling, and phase-change material (PCM) cooling. Air cooling BTMS is structurally simple and relatively low-cost compared to other BTMSs. However, due to the poor heat transfer properties of air, this BTMS is only suitable for small battery packs with low heat generation (Zhang et al., 2021). In PCM BTMS, phase-change materials (PCM) can absorb a significant amount of heat within a specific phase change temperature range, thereby maintaining better temperature uniformity in the battery pack. However, PCM BTMS is a passive system and cannot be used alone (Murali et al., 2021). Liquid cooling BTMSs are classified into direct and indirect liquid cooling BTMSs. Indirect liquid cooling directs the coolant to the battery using a cooling device to absorb heat while preventing the coolant from directly contacting the battery, thus avoiding short circuits. Common indirect liquid cooling systems typically use cooling plates to dissipate the battery's heat. Indirect liquid cooling offers superior performance due to the better cooling capabilities of its heat transfer medium. However, it also significantly increases system complexity, and the thermal resistance between the cooling plate and the battery reduces cooling efficiency. Additionally, there is a risk of leakage (Kharabati and Saedodin, 2024). Direct liquid cooling BTMSs, also known as immersion cooling, use high dielectric constant insulating fluids to directly cool the batteries, offering higher cooling efficiency compared to other BTMSs. Therefore, it is considered a potential BTMS solution to meet the extreme thermal management demandsof future high-energy density battery packs.

Due to these advantages, immersion cooling BTMS is considered the ultimate BTMS choice for the future, attracting the attention of many researchers. However, in most studies, the comparison for immersion cooling BTMS is primarily with air cooling BTMS, with only a few using traditional bottom cooling plate BTMS as a benchmark. This limited comparison does not conclusively demonstrate that immersion BTMS is the most superior BTMS. Therefore, in this study, the research subject is a large module composed of 48 high-nickel ternary lithium-ion prismatic cells, each with a capacity of 175Ah. This module contains about one-fourth of the battery cells of a 140kWh pure electric vehicle battery pack from a certain brand. Compared to cylindrical or pouch cells, high-energy-density prismatic cells generate more heat during operation and have a smaller heat dissipation surface area, posing more stringent requirements for the BTMS. The chosen comparison benchmark is the BTMS of the pure electric vehicle battery pack, specifically the high-performance side cooling plate BTMS, which was recognized by Time Magazine as one of the Best Inventions of 2022.

2. RESEARCH APPROACH

2.1. Design concept

The Side cooling plate BTMS (as illustrated in Figure 1(a)) is an innovative indirect cooling BTMS that combines excellent coolingperformance with good engineering feasibility. Compared to the traditional bottom cooling plate BTMS, the side cooling plate BTMSsignificantly enhances the heat dissipation area. For example, in the battery module selected for this study, implementing the side cooling plate BTMS increased the heat dissipation area by 500% compared to the traditional bottom cooling plate BTMS. Although it increases production complexity and battery pack assembly difficulty, its superior cooling performance meets the cooling demands of higher energy density battery packs under extreme conditions using higher current rates (C-rate). Currently, the industry has already achieved mass production and sales of pure electric vehicles equipped with side cooling plate BTMS. C-rate represents theunit of the speed for the battery to be charged or discharged from 0 to 100% or vice versa. For example, charging under 3C and discharging under 0.5C for 180Ah battery means the battery is charged in 1/3 h with 540 A of current and discharged in 2 h with 90A of current. A cooling plate contains 10 channels, divided into 3 circuits. This design reduces the temperature rise of the coolant within each circuit, thereby decreasing the temperature gradient along the flow direction in the battery module and enhancing the temperature uniformity of the module. The cross-sectional views of the cooling plate and the side cooling plate BTMS module are shown in Figure 1 (b)-(c). To initially compare the cooling performance of the two systems directly, this study designed an immersion cooling BTMS based on the structure of the side cooling plate BTMS (as illustrated in Figure 1(e)). Keeping the battery module arrangement and spacing unchanged, the battery module was placed in an immersion cooling enclosure, using dielectric fluid to cool the batteries. The enlarged front view and cross-sectional view of the immersion cooling BTMS are shown in Figure 1 (f)-(g).

The batteries used in this study are high-nickel ternary (NCM) prismatic lithium-ion batteries (CATL). The main specifications are listed in Table 1. In actual electric vehicles, batteries are used at the battery pack level, with the battery cooling system arranged in parallel. Analysis and predictions at the module level and battery pack level will show similar results. Therefore, in this study, the cooling target is set at the module level, which significantly reduces computational costs compared to battery pack-level analysis. The selection of the research subject was based on a pure electric vehicle equipped with a side cooling plate BTMS. This vehicle features a battery pack composed of 216 cells, with a total energy capacity of approximately 140kWh, providing over 800km of pure electric range. Therefore, this study selected a module containing 48 cells as the research subject, with the number of cells being about one-fourth of the actual battery pack. The module's energy capacity is approximately

30.7kWh, as shown in Figure 1. To improve the cooling efficiency and structural strength of the BTMS while reducing vehicle weight, aluminum is used as the primary material for the side cooling plate. Aluminum is also used for baffles. To reduce the contact thermal resistance between the cooling plate and the battery cells, thermal grease is utilized. The properties of these materials are listed in Table 2. The coolant in the side cooling plate is a 50% by mass water-ethylene glycol solution, which has a freezing point below -30°C, ensuring the BTMSoperates normally in cold environments. The dielectric fluid in the immersion cooling BTMS is an organic mixture from Lubrizol, with a dielectric strength greater than 27kV/mm, ensuring the safe operation of the BTMS. Their properties are listed in Table 3. The properties of the water-glycol solution were referenced from the ASHRAE Handbook (ASHRAE and Engineers, 2005). Additionally,the boiling point of the water-glycol is 105°C, while the boiling point of the dielectric fluid is greater than 150°C. In all 3C charging simulations, the liquid temperature did not exceed its boiling point.

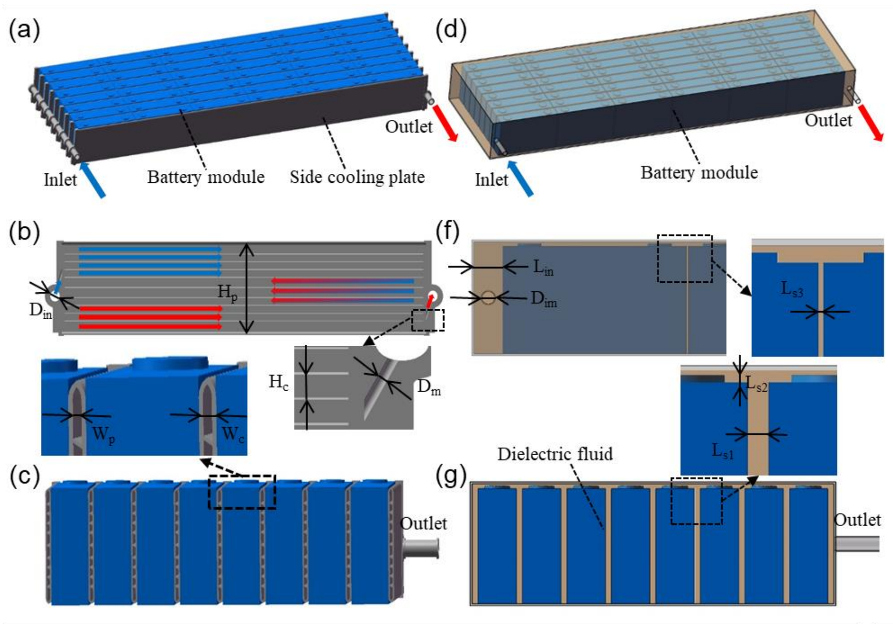

Figure 1： (a)-(c)Schematic for the side cooling plate BTMS battery module, (a)the 3D view of the side cooling plate BTMS battery module, (b) frontal cross-sectional view of the side cooling plate, (c)lateral cross-sectional view of the side cooling plate BTMS battery module; (e)-(g)Schematicfor the immersion cooling BTMS battery module, (e)the 3D view of the immersion cooling BTMS battery module, (f)magnified frontal view of the immersion cooling BTMS battery module, (g) lateral cross-sectional view of the immersion cooling BTMS battery module

Table 1: Prismatic battery cell and module specifications.

Parameter	Value
Battery	
Nominal capacity (Ah)	175
Nominal energy (Wh)	640.5
Nominal voltage (V)	3.66
Voltage operating rang (V)	2.7-4.2
Thickness (mm)	39
Length (mm)	203
Height (mm)	122
Density ($kg{\cdot}m^{-3}$)	2331
Specific heat ($J{\cdot}kg^{-1}{\cdot}K^{-1}$)	1000
Thermal conductivity ($W{\cdot}m^{-1}{\cdot}K^{-1}$)	12(length)/10(height)/1(thickness)
Cathode material	NMC(LiNi0.88Mn0.01Co0.09Al0.02O2)
Anode material	Graphite and Si particles

Table 2: Properties of material used in CFD model.

Material	Density (kg・m-3)	Specific heat (J・kg-1・K-1)	Thermal conductivity (W・m-1・K-1)
Aluminum	2719	870	202
Thermal grease	1000	1100	1

Table 3: Properties of water-glycol mixture and dielectric fluid used in CFD model

Property	Value
Water-glycol	
Density ($kg{\cdot}m^{-3}$)	$993.1+0.9841\times T[K]-2.42\times10^{-3}\times T^2[K]$
Specific heat ($J{\cdot}kg^{-1}{\cdot}K^{-1}$)	$2148+3.863\times T[K]$
Thermal conductivity ($W{\cdot}m^{-1}{\cdot}K^{-1}$)	$-0.1658+2.98\times10^{-3}\times T[K]-3.80\times10^{-6}\times T^2[K]$
Viscosity($kg{\cdot}m^{-1}{\cdot}s^{-1}$)	$3.11\times10^6\times\exp(-7.57\times10^{-2}\times T[K])+1.371\times\exp(-2.07\times10^{-2}\times T[K])$
Dielectric fluid	
Density ($kg{\cdot}m^{-3}$)	$989.5-0.6677\times T[K]$
Specific heat ($J{\cdot}kg^{-1}{\cdot}K^{-1}$)	$1099+3.488\times T[K]$
Thermal conductivity ($W{\cdot}m^{-1}{\cdot}K^{-1}$)	$0.1969-2.05\times10^{-4}\times T[K]$
Viscosity ($kg{\cdot}m^{-1}{\cdot}s^{-1}$)	$1.837\times107\times\exp(-7.9\times10^{-2}\times T[K])+2.458\times\exp(-2.06\times10^{-2}\times T[K])$

2.2. Computational domain and boundary conditions

This study will investigate and compare the side cooling plate BTMS and immersion cooling BTMS at the module level. In the side cooling plate BTMS, the coolant enters through the inlet and is distributed to the parallel-arranged side cooling plates via a distribution manifold. The 10 channels in the cooling plate are divided into three circuits, where the coolant flows in an S-shaped path within the cooling plate, exchanging heat with the plate to indirectly cool the batteries. The coolant existing the cooling plate converges in the collection manifold and flows out through the outlet. This design of the cooling plate enhances the coolant flow speed within the channels, thereby improving heat transfer. It also reduces the temperature rise of the coolant in each circuit, thus decreasing the temperature gradient along the flow direction of the battery module. The performance of the immersion cooling BTMS will be evaluated against the benchmark set by the side cooling plate BTMS. Therefore, all geometric parameters in the side cooling plate BTMS are fixed, such as the inlet diameter of the side cooling plate D_{in} (the outlet diameter is the same as the inlet diameter), the width of the channels within the side cooling plate W_c, the width of the side cooling plates W_p.

Correspondingly, the structure of the basic immersion cooling BTMS is similar to that of the side cooling plate BTMS. The arrangement and spacing of the battery module, the diameter of the inlets and outlets, and the position of the inlets and outlets relative to the module remain unchanged. The battery module is fully immersed in dielectric fluid. The gaps between the batte ries form the flow channels for the coolant, which flow through these channels and directly exchange heat with the batteries to cool them. After comparing the performance of the two BTMSs, this study focuses on the parameters that significantly impact the cooling performance of the immersion cooling BTMS, such as the spacing between staggered batteries L_{s1}, the number of baffles, and the number of inlets and outlets. The geometrical parameters of the side cooling plate BTMS and the initial design point parameters of the immersion cooling BTMS are shown in Table 4.

Table 4: Geometrical parameters of the side cooling BTMS and immersion cooling BTMS

Variable	Parameter	Value (mm)
D_{in}	Diameter of side cooling plate inlet	14
H_p	Height of side cooling plate	116
W_p	Width of side cooling plate	6
W_c	Width of channel within side cooling plate	3
H_c	Height of channel within side cooling plate	8
D_m	Diameter of side cooling plate microchannel	3
L_{in}	Length of spacing between battery and side wall	32
D_{im}	Diameter of immersion cooling inlet	14
L_{s1}	Length of spacing between staggered batteries	6
L_{s2}	Length of spacing between battery and top wall	5
L_{s3}	Length of spacing batteries in the same line	2

The coolant inlet temperature for both the side cooling plate and immersion cooling BTMS is set at 20°C, with an initial inlet velocityof 0.48 m/s (typically, the coolant inlet flow rate for a vehicle-level BTMS is 20L/min; therefore, the inlet flow rate for the module in this study is approximately 2/9 of that value, about 4.45L/min). This study focuses on comparing the cooling performance of the twoBTMSs during fast charging at high temperatures; hence, the initial temperature of all computational domains is set to 40°C. In the side cooling plate BTMS model, the battery surfaces are not in contact with the cold plate and the cold plate surfaces are not in contact with the batteries are adiabatic. In the immersion cooling BTMS model, the outer surface of the fluid domain is adiabatic.

2.3. Numerical solutions and governing equations

Certain assumptions were applied for numerical computations with the ANSYS Fluent software, as follows.

- The numerical calculation model considers the influence of gravity.
- The transient-state condition changes over time and turbulent conditions exist for the fluid flow.
- All materials will not undergo any phase change process.
- The heat generated within the battery is uniform.
- All of the properties without the water-glycol and dielectric fluid are calculated at 25℃.

- The battery geometry in the numerical calculation model only considers the active region.
- A thermal resistance was set on the coupling surface between the cooling plate and the battery surface, equivalent toapplying a 2mm layer of thermal grease in the contact area between the battery and the cooling plate.
- Battery can be fully charged with a 3C constant-current (CC) mode from a 0% state-of-charge (SOC). The heat generationrate of the battery remains constant during the charging process.

Lithium-ion batteries generate heat during charging and discharging, which arises from the Joule heating effect and the reversible heat generation effect of solid and electrolyte phases during charge transfer. The heat generation rate Q_{gen} can be express as Equation 1 (Xun et al., 2013):

Equation1: Heat generation of battery.

$$Q_{gen} = I(OCV - U) - IT_{bat}\frac{dOCV}{dT_{bat}}$$

Where:

- Q_{gen} = heat generation of battery (J)
- I =battery current (A)
- OCV = open-circuit voltage (V)
- U = battery voltage (V)
- T_{bat} = temperature of battery (K)
- $\frac{dOCV}{dT_{bat}}$ = entropic coefficient (V/K)

The heat generated by the battery is defined as a constant heat generation source and calculated by Eq 1**.** The Accelerating Rate Calorimeter (ARC) is a typical thermal analysis instrument used to evaluate the thermal decomposition characteristics and hazards of substances. It is currently widely employed to assess the thermal behavior of lithium- ion batteries, including heat generation during charging and discharging, the onset temperature of thermal runaway, and the maximum temperature rise rate during thermal runaway. The main structure of the ARC includes an adiabatic furnace, a control system, and a temperature testing system. During operation, the system continuously monitors the temperature of the sample and uses the control system to maintain the furnace temperature equal to the sample temperature, thereby ensuring that the sample remains in an approximately adiabatic state. This study uses the ARC to test the heat generation of the battery during 3C charging at an initial temperature of 40°C. The setup and test results for measuring the heat generation of the battery during 3C charging areshown in Figure 2. As shown in Table 5, the average heat generation rates of the batteries will be utilized for subsequent simulation comparisons and structural optimization.

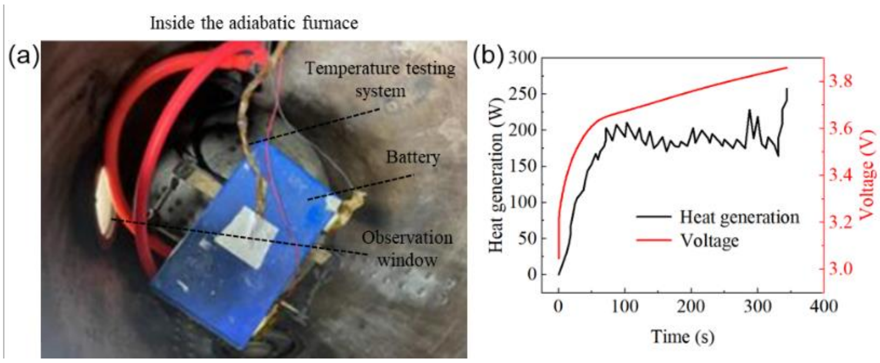

Figure 2: (a) The setup for measuring the heat generation of the battery during 3C charging using the ARC, (b) the test results

Table 5: Average heat generation of the battery at an initial temperature of 40°C

Charge rate	Heat generation density/cell (W/m3)	Heat generation rate/cell (W)	Heat generation rate/module (kW)	Heat generation rate/pack (kW)
3C	183850.91	180	8.64	38.88

The energy equation for the battery can be expressed as Equation 2(Choi et al., 2023):

Equation 2: Energy equation for the battery.

$$mc_p\frac{dT}{dt} = \lambda_x\frac{\partial^2 T}{\partial x^2} + \lambda_y\frac{\partial^2 T}{\partial y^2} + \lambda_z\frac{\partial^2 T}{\partial z^2} + Q_{gen}$$

Where:

- m = mass of battery (kg)
- c_p = specific heat of battery (J/kg • K)
- T = temperature of battery (K)
- λ = thermal conductivities of battery (W/㎣K)

The simulation is conducted in ANSYS Fluent. The fluid flow is in the laminar, semi-turbulence, and fully turbulent state when Re <
1000， 1000 < Re < 3000, and Re > 3000, respectively. Where Reynolds number Re is calculated by Equation 3:

Equation 3: Reynolds number.

$$Re = \frac{\rho_l v D_h}{\mu}$$

Where:

- Re = Reynolds number
- ρ_l = density of fluid (kg/m^3)
- v = velocity of fluid (m/s)
- D_h = hydraulic diameter (m)
- μ = dynamic viscosity (Pa • s)

In the side cooling plate BTMS model, the flow inside the cold plate is in a laminar state with Re less than 300. In the manifold pipes connecting the inlet and outlet, as well as in the microchannels, the flow transitions to or is in a turbulent state, with the maximum Re greater than 3900. Therefore, the standard k-e turbulence model is used for calculations. In all immersion cooling BTMS models, the flow is in a laminar state because the Re is less than 800. The convergence criterion for the momentum equation is 10 $^{-5}$, and the energy equation is 10^{-8} for transient calculation.

2.4. Model verification

The ANSYS Fluent software was used for 3D numerical simulation to compare the performance of side cooling plate BTMS and basic immersion cooling BTMS, followed by structural optimization of the immersion cooling BTMS. The geometric model was developed with the ANSYS Design Modeler in the ANSYS Workbench, as shown in Figure 3 (a). The mesh was generated using a tetrahedral meshing strategy and the capture proximity options for more accurate computations with the ANSYS Fluent Meshing. Finally, the generated mesh was converted to a polyhedron considering the convergence and computational cost, as shown in Figure 3 (b). For the transient calculation of side cooling plate BTMS, the time step of 2 s, 1 s, 0.5 s, 0.1 s were selected for independenceverifications, as shown in Figure 3 (c).It can be seen that the curves of maximum temperature and pressure drop for 0.5 s and 0.1 sintervals have minimized deviations, as thus the 0.5 s time step is used for calculation. Generating finer meshes can improve the accuracy of the CFD model, but additional meshes will significantly increase computational costs. Therefore, a mesh independencestudy is necessary to select an appropriate number of mesh elements that balance accuracy and time costs, as shown in Figure 3(c). The T_{max} of grid number of 21,655,585 and 25,680,293 are almost the same, which differs by 0.04%. Hence, the grid number of21,655,585 is enough to ensure the calculation accuracy. Time step and grid independence study results of immersion cooling BTMS battery module model is shown in Figure 3 (d). Similarly, a time step of 0.5 s and a grid number of 6,566,610 are chosen for the CFD model calculations of the immersion cooling BTMS

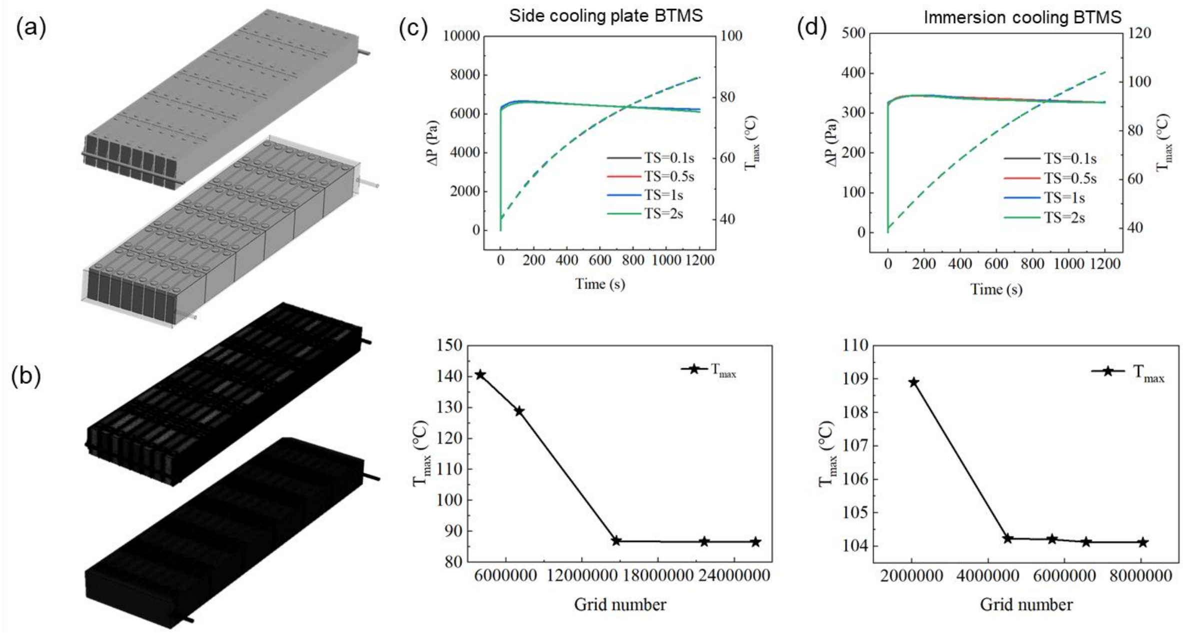

Figure 3: (a) Geometry of the side cooling plate BTMS battery module and immersion cooling BTMS battery module, (b) computational fluid dynamics (CFD) model with mesh interface, (c) time step and grid independence study result of side cooling plate BTMS battery module model, (d)time step and grid independence study result of immersion cooling BTMS battery module model

2.5. Evaluating indicators

In addition to the maximum temperature T_{max} and pressure drop ΔP, the maximum temperature difference between batteries within the module dT is also used to evaluate the cooling performance of the BTMS. This study selects the center temperature of each battery to calculate the maximum temperature difference. Where dT is calculated by Equation 4:

Equation 4: Maximum temperature difference.

$$dT = T_{max} - T_{min}$$

Where:

- dT = maximum temperature difference between batteries within the module (℃)
- T_{max} = center temperatures of the hottest batteries within the module (℃)
- T_{min} = center temperatures of the coldest batteries within the module (℃)

Cooling capacity is a key indicator of BTMS performance, while excessive pressure drop leading to increased pump power reducesBTMS efficiency. Therefore, many studies have introduced a cooling performance factor ε to measure the efficiency, as expressedin Equation 5 as follow (Huang et al., 2022):

Equation 5: Cooling capacity.

$$Q_{cool} = \dot{m}\,(c_{pl,out}T_{out} - c_{pl,in}T_{in})$$

Where:

- Q_{cool} = cooling capacity (W)
- $\dot{m}$ = inlet mass flow rate (kg/s)
- T_{out} = outlet temperature of the fluid (K)
- T_{in} = inlet temperature of the fluid (K)
- $c_{pl,out}$ = outlet specific heat of the fluid (J/kg・K)
- $c_{pl,in}$ = inlet specific heat of the fluid (J/kg・K)

3. RESULTS

The simulations were conducted under 3C charging conditions, with an initial temperature of 40°C. Experimental testing of the battery selected for this study showed that it could only charge from 0% SOC to 65% SOC in 3C constant current (CC) mode, which takes 13 minutes. Upon reaching the cutoff voltage, charging switches to constant voltage (CV) mode, where the charging voltage is maintained at the cutoff voltage, and the charging current continuously decreases. When the charging current drops to the cutoff current, the battery reaches 100% SOC, marking the end of charging. In CV mode, since the charging current continuously decreases, the heat generated by the battery also decreases, reducing the thermal load on the BTMS accordingly. To study the extreme performance of the BTMS and facilitate the comparative simulation of the side cooling plate and immersion cooling BTMSs, as well as the subsequent structural optimization of immersion cooling, the simulation assumes that the battery can be charged from 0% SOC to full charge in 3C CC mode, lasting for 20 minutes. Under this assumption, the battery generates high heat throughout the charging process, presenting a significant challenge to the BTMS performance. The performance is evaluated by comparing the maximum temperature T_{max} and the maximum temperature difference dT at the end of charging, the BTMS pressure drop ΔP, and cooling capacity Q_{cool}. When the key parameters （T_{max}和dT） of the compared systems are similar, additional evaluations are conducted by measuring the center temperatures of the battery's main surface (the surface in contact with the cooling plate) and the top surface (the surface with the tabs) to calculate the maximum temperature difference, further aiding in performance assessment. Additionally, the transient values of key parameters over time were monitored to evaluate the BTMS performance from an engineering perspective. For example, the target temperature during fast charging is set to 75°C. Charging is stopped when the maximum temperature within the battery module exceeds this value to extend battery life and prevent thermal runaway. In this scenario, the performance of the BTMS can be assessed by comparing the time taken for the module's maximum temperature to reach 75°C, referred to as the safe operating time (t_{safe}). Improving the cooling performance of the BTMS increases t_{safe}, allowing the battery module to remain within a safe temperature range for a longer period during fast charging.

3.1. Performance comparison of side cooling plate and basic immersion cooling BTMSs

The performance of the side cooling plate BTMS and the basic immersion cooling BTMS was compared through simulations, the results are shown in Figure 5. The simulations were conducted under 3C charging conditions with an initial temperature of 40°C. The inlet temperature and inlet flow rate for both cooling fluids were set to 20°C and 4.45L/min, respectively. This section does not compare performance under the same mass flow rate because, at 20°C, the density of the water-glycol solution is 1.35 times that of the dielectric fluid. Thus, the same mass flow rate would result in a much higher volumetric flow rate for the dielectric fluid. Although the pressure drops (which is related to pump power consumption) of the side cooling plate BTMS would still be much greater than that of the immersion cooling BTMS in this scenario, the BTMS pressure drop constitutes only a small portion of the total system pressure drop in the entire vehicle system. Other components, such as the chiller and valves, have significant pressure drops . Increasing the flow rate would substantially increase the pressure drop across these components, thereby significantly raising the overall system pressure drop. Therefore, conditions with the same volumetric flow rate were initially chosen to compare the performance of the BTMSs and conduct subsequent structural optimizations.

The transient temperature results during 3C charging and the comparison of various indicators at the end of charging of the two BTMSs are shown in Figure 5. Setting the target temperature for fast charging at 75°C, the t_{safe} for the side cooling plate BTMS is 694 seconds. This allows the module's SOC to increase from 0% to 57.83%, closely matching the experimental test resul t, which indicates the battery's maximum 3C CC charging duration is 780 seconds. At this point, the module's maximum temperature difference is 5.26°C, essentially meeting the safe operational temperature difference for the module. In contrast, the safe operating time for the immersion cooling BTMS during 3C fast charging is 512 seconds, allowing the module's SOC to increase from 0% to 42.67%. The t_{safe} is reduced by 26.22% compared to the side cooling plate BTMS. At this point, the module's maximum temperaturedifference is 12.48°C, which represents a relative increase of 137.26%. Operating the module with a large temperature difference can lead to deterioration in lifespan and performance. If a target temperature difference is set during fast charging, the safe fast charging duration for the immersion cooling BTMS module would be further significantly reduced. At the end of charging, the maximum temperature and maximum temperature difference for the side cooling BTMS module are 86.58°C and 8.85°C, respectively. For the immersion cooling BTMS module, these values are 104.19°C and 28.36°C, respectively. Compared to the side cooling BTMS module, the immersion cooling BTMS module's maximum temperature and maximum temperature difference increased by 20.34% and 220.45%, respectively. The cooling capacities of the side cooling plate BTMS and the immersion cooling BTMS are 7.49kW and 6.24kW, respectively. Compared to the side cooling plate BTMS, the cooling capacity of the immersion cooling BTMS decreased by 16.69%. The results indicate that the side cooling plate BTMS performs exceptionally well, nearly meeting the cooling demands of the battery module during fast charging under harsh conditions. In contrast, the basic immersion cooling BTMSshows significant shortcomings in temperature control (especially in maintaining temperature uniformity within the module) and cooling capacity. A series of optimizations will be conducted to improve its performance. The pressure drop of the immersion cooling BTMS is 0.32kPa, which is significantly lower than the 6.25kPa pressure drop of the side cooling plate BTMS. This is due to the larger internal flow area in the immersion cooling system, resulting in a relatively lower flow velocity of the dielectric fluid, with the flow being in a laminar state. However, this also leads to a decrease in its heat transfer capability.

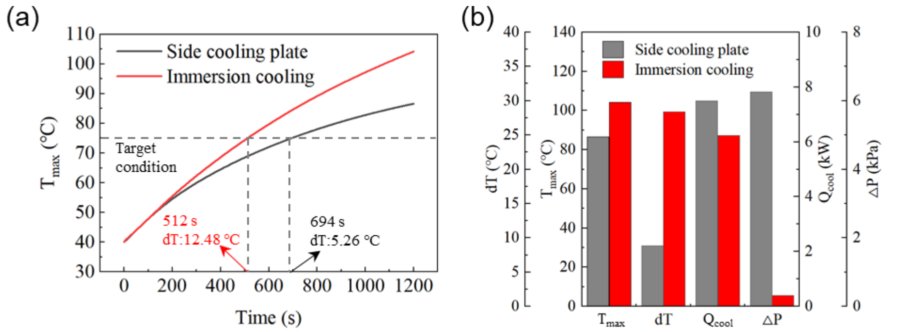

Figure 4： (a) Transient maximum temperature, (b) comparison of maximum temperature, temperature difference, cooling capacity and pressuredrop at the end of charging between the side cooling plate and immersion cooling BTMSs

3.2. Comparison of the temperature contour and streamline diagrams

Typically, in traditional BTMS, such as air cooling or bottom cooling plate systems, the lowest temperature region is near the fluid inlet, and the highest temperature region is near the fluid outlet. This results in a steady temperature increase from the inlet area to the outlet area. In the side cooling plate BTMS, the individual battery cells exhibit a sandwich-like temperature distribution, with lower temperatures on the main surfaces and higher temperatures at the center. The highest temperature within the module is found in the battery cells near the outlet area, as shown in Figure 5 (a). From the streamline diagram, it can be observed that due to thepresence of microchannel distribution holes, the coolant is approximately evenly distributed across all cooling plates, ensuring goodtemperature uniformity within the module. The temperature distribution trend within the module is determined by the coolant flow pattern and the inlet-outlet temperature difference. In the absence of dead zones (where all batteries within the module are effectively cooled) and with uniform fluid distribution, the temperature difference between the coolant at the inlet and outlet often determines the maximum temperature difference within the module. Batteries near the inlet exchange heat with cooler fluid, while batteries near the outlet exchange heat with warmer fluid, making the temperature difference between hot and cold fluid positively correlated with the overall temperature difference within the module. Although the coolant exit temperature is 48.32°C, resulting in an inlet-outlet temperature difference of 28.32°C, the division of the flow paths within the cooling plate distributes this large temperature difference across multiple flow paths, thereby significantly reducing the overall temperature difference. The flow channel of the side cooling plate is divided into three circuits, with an average temperature rise of 9.44°C per circuit. At this point, the maximum temperature difference is 8.85°C, further demonstrating the correlation between the module temperature difference and the inlet-outlet temperature difference. This also confirms that dividing the flow paths effectively enhances cooling performance.

Since the density and specific heat capacity of the dielectric fluid are both lower than those of the water-glycol solution (for instance, at 20°C , the density and specific heat capacity of the dielectric fluid are 783 kg·m-3 and 2121 $J{\cdot}kg^{-1}{\cdot}K^{-1}$, respectively, whereas the values for water-glycol are 1073 $kg{\cdot}m^{-3}$ and 3281 $J{\cdot}kg^{-1}{\cdot}K^{-1}$), the temperature difference of the fluid during heat exchange is proportional to the product of density and specific heat capacity for the same amount of heat transfer. The product of density and specific heat capacity for water-glycol is 2.09 times that of the dielectric fluid. Due to differences in thermal conductivity and convective heat transfer intensity, the heat transfer capacity of the dielectric fluid is lower than that of water-glycol. Therefore, its inlet-outlet temperature difference is approximately 1.72 times that of water-glycol, resulting in a temperature difference of 48.83°C. Such a large inlet-outlet temperature difference results in poor temperature uniformity and a relatively higher maximum temperature for the immersion cooling BTMS. Figure 5 (b) shows its temperature distribution. It can be clearly observed that the temperature near the outlet area is significantly higher than that near the inlet area, with the highest temperature point appearing at the upper part of the batteries close to the outlet. This is because the denser cold fluid tends to sink, and the outlet is positioned level with the middle of the battery, causing the incoming cold fluid to flow more readily in the lower half of the BTMS, leaving the upper part of the module insufficiently cooled. In the area farther from the inlet, a concentrated streamline region appears, with more fluid flowing into the gaps between the batteries farther from the inlet. This uneven flow distribution further deteriorates heat transfer. The flow rate in the gaps between the batteries near the inlet is relatively low, resulting in the hottest region appearing in the upper corner of the module near the outlet. Compared to the side cooling plate BTMS, the differences in fluid properties and flow distribution uniformity prevent the immersion cooling BTMS from effectively controlling the module's maximum temperature and temperature difference within the optimal range during 3C charging.

When studying single cells or small modules, immersion cooling often demonstrates superior cooling performance. However, this conclusion is challenged at the large module level. The aforementioned research indicates that, despite having a larger heat exchange area and lower thermal resistance, the overall performance of basic immersion cooling BTMS in large modules is significantly inferior to that of side cooling plate BTMS. Further research, such as optimizing flow channels and improving dielectric fluids, is necessary to fully unlock the potential of immersion cooling.

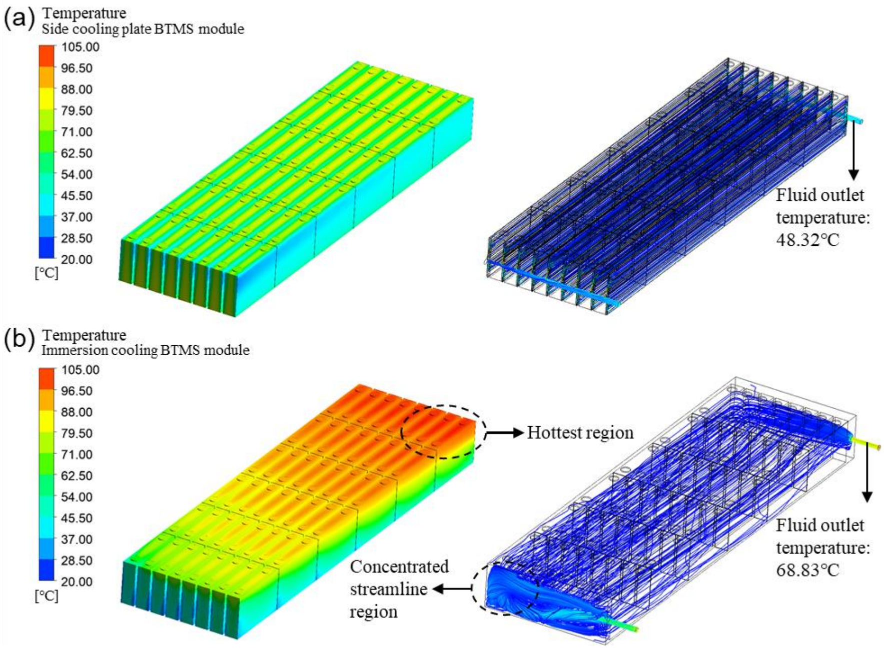

Figure 5: (a) Temperature contour and streamline results of the side cooling plate BTMS module, (b) Temperature contour and streamline results ofthe immersion cooling BTMS module

4. CONCLUSION

This study conducted a comprehensive comparison between immersion cooling BTMS and side cooling plate BTMS through simulations. The main conclusions are summarized as follows:

- The side cooling plate BTMS exhibits excellent cooling performance. Under harsh conditions, it almost meets the cooling demands of the module during 3 C fast charging. The safe operating time is 694 s, with a temperature difference of 5.26 °C.
- The basic immersion cooling BTMS, which maintains a flow structure similar to the side cooling plate, performs worse. The safe operating time is 512 s, a decrease of approximately 26.22 %, with a temperature difference of 12.48 °C. Assuming 3C CC charging can last for 20 minutes, at the end of charging, the maximum temperature and temperature difference for the immersion cooling BTMS are 104.19 °C and 28.36 °C, respectively. This represents increases of 20.34 % and 220.45 % compared to the side cooling plate BTMS, which has values of 86.58 °C and 8.85 °C, respectively.

This paper presents a comparative simulation study of BTMS at the large module level, revealing that the performance of basic immersion cooling falls significantly short of that of the side cooling plate. The limitation of this study lies in its inability to simulate the actual heat generation characteristics of the battery during fast charging. Instead, the comparison and optimization were based on the assumption of constant heat generation throughout.

5. REFERENCES

ASHRAE, A. J. R. & ENGINEERS, A.-C. 2005. handbook–Fundamentals, chapter 8. Atlanta: American Society of Heating.

CHEN, D. F., JIANG, J. C., KIM, G. H., YANG, C. B. & PESARAN, A. 2016. Comparison of different cooling methods for lithium ionbattery cells. Applied Thermal Engineering, 94, 846-854.

CHOI, H., LEE, H., KIM, J. & LEE, H. S. 2023b. Hybrid single-phase immersion cooling structure for battery thermal managementunder fast-charging conditions. Energy Conversion and Management, 287.

HUANG, Y., WEI, C. & FANG, Y. 2022. Numerical investigation on optimal design of battery cooling plate for uneven heat generation conditions in electric vehicles. Applied Thermal Engineering, 211**,** 118476.

HWANG, F. S., CONFREY, T., REIDY, C., PICOVICI, D., CALLAGHAN, D., CULLITON, D. & NOLAN, C. 2024. Review of battery
thermal management systems in electric vehicles. Renewable & Sustainable Energy Reviews, 192.

KHARABATI, S. & SAEDODIN, S. 2024. A systematic review of thermal management techniques for electric vehicle batteries. Journal of Energy Storage, 75.

LU, M. Y., ZHANG, X. L., JI, J., XU, X. F. & ZHANG, Y. Y. C. 2020. Research progress on power battery cooling technology for electric vehicles. Journal of Energy Storage, 27.

MURALI, G., SRAVYA, G. S. N., JAYA, J. & VAMSI, V. N. 2021. A review on hybrid thermal management of battery packs and it's cooling performance by enhanced PCM. Renewable & Sustainable Energy Reviews, 150.

PATIL, M. S., SEO, J. H., PANCHAL, S., JEE, S. W. & LEE, M. Y. 2020. Investigation on thermal performance of water-cooled Li- ion pouch cell and pack at high discharge rate with U-turn type microchannel cold plate. International Journal of Heat and Mass Transfer, 155.

XUN, J. Z., LIU, R. & JIAO, K. 2013. Numerical and analytical modeling of lithium ion battery thermal behaviors with different coolingdesigns. Journal of Power Sources, 233**,** 47-61.

ZHANG, J. J., WU, X. L., CHEN, K., ZHOU, D. & SONG, M. X. 2021. Experimental and numerical studies on an efficient transient heat transfer model for air-cooled battery thermal management systems. Journal of Power Sources, 490.

#272: Enhanced heat transfer performance of concentrated photovoltaic system through liquid spray cooling

Haifei CHEN[1], Yongsheng CUI[1], Yanglong ZHAO[1], Yunjie WANG[2], Mingguo PENG[1], Jie YANG[1], HuihanYANG[3], Linqi FU[1]

[1] Changzhou University, Changzhou, Jiangsu Province, China, chfs@cczu.edu.cn
[2] Nanjing University of Science and Technology, Nanjing, Jiangsu Province, China, wyj15106123753@163.com
[3] Department of Chemical Engineering, University College London, London WC1E 6BT, United Kingdom,zczqhy1@ucl.ac.uk

Abstract: The Fresnel concentrated photovoltaic system uses Fresnel lenses to focus large areas of sunlight onto small areas of high-efficiency photovoltaic cells, thereby improving the photoelectric conversion efficiency. However, the high heat flux density generated by the system can easily cause component damage and place higher demands on cooling technology. Among various cooling methods, spray cooling technology stands out as one of the most promising and efficient heat dissipation techniques. This study aims to enhance heat transfer by combining spray cooling technology with enhanced surface techniques. The heat transfer mechanisms of spray cooling under both groove-type and upright-type enhanced surfaces are investigated. An experimental systemwas built to study the heat transfer capability of spray cooling at high heat flux. Under a high concentration ratio, temperatures can becontrolled below 35°C, reflecting a 14% reduction compared to the peak temperature. The fluidity of the working medium on the surface is inversely proportional to the structure height and directly proportional to the channel width. The addition of enhanced surfaces enhances heat transfer to a certain extent due to the increased heat transfer area, while it also suppresses heat transfer due to the reduced fluidity of the working medium on the heat exchange surface. To address this dual effect, a new dimensionless parameter, α, was introduced to characterize the interplay between these factors. A dimensionless analysis method was then applied to derive heat transfer correlations for spray-enhanced cooling, providing valuable insights for engineering applications.

Keywords: Solar Energy，Concentrating Photovoltaic, Spray Cooling, Enhanced Surface, Enhanced Heat Transfer

1. INTRODUCTION

With the growing global demand for clean energy, solar energy has garnered significant attention as a renewable energy source. The most common method of harnessing solar energy is through photovoltaic (PV) power generation. The core component of PV technology is the photovoltaic cell, which captures and stores energy to achieve power generation (Hosenuzzaman et al., 2015). Inrecent years, the efficiency of photovoltaic cells has steadily improved through the development of new cell materials and structures (Khokhar et al., 2022; Mahmoudi et al., 2018). However, as technology advances, traditional optimization methods are approachingthe efficiency limits of these cells. Concentrated photovoltaic (CPV) technology has been proposed to address this issue by providing a new solution (Tian et al., 2023). CPV systems, which focus sunlight on photovoltaic cells to enhance energy conversion efficiency, have become a hot topic in both research and application.

However, excessively high concentration ratios in CPV systems generate high heat flux densities, accompanied by significant heat,causing the operating temperature of the cells to rise rapidly. Without effective cooling, the performance of photovoltaic cells can decline or even result in thermal damage (Du et al., 2012). Therefore, efficient cooling methods are essential. Spray cooling, as a novel heat dissipation technology, offers advantages such as high heat transfer coefficients, good temperature uniformity, and low contact thermal resistance (Liang and Mudawar, 2017a, 2017b). It is considered one of the most effective ways to address cooling issues in high-power devices. Chen et al. (Chen et al., 2022) explored the potential of combining spray cooling technology with HCPV and established an experimental platform for a spray-cooled HCPV/T system. Analysis of the experimental data revealed that the spray-cooled HCPV/T system achieved over 45% thermal efficiency and over 27% electrical efficiency, with total exergy efficiency reaching 34%.

Currently, research on enhancing heat transfer in spray cooling primarily focuses on spray parameters, cooling media, and enhanced surfaces. In studies on factors influencing single-phase spray cooling, Wang et al. (Wang et al., 2010) analysed the effect of spray height. The research indicated that when the major axis of the elliptical spray impact zone precisely intersects with the square test surface at an inclined spray, the utilization rate of the working fluid is maximized, and heat transfer performance is optimal. Silk et al. (Silk et al., 2006) investigated the impact of nozzle inclination angles on the heat transfer performance of spray cooling systems. The experiments showed that compared to vertical incidence, when the spray inclination angle exceeds 0° (15°, 30°, 45°), inclined spray incidence helps eliminate stagnation zones on the heat sink surface, promoting the flow of the surface liquid film, thereby enhancing the heat transfer process.

Enhancing heat transfer performance by altering the cooling fluid is also an important method of heat transfer augmentation. Besides water, other media such as ethanol and nanofluids have been applied in spray cooling. These different media possess distinct physical and thermal properties, significantly affecting the enhanced heat transfer performance of spray cooling. Liu et al. (Liu et al., 2018) compared the thermal conductivity of pure water and various ethanol-water mixtures in spray cooling. The experimental results indicated that the addition of ethanol significantly increased the thermal conductivity of the mixture, though the enhancement was relatively small within the doping ratio range. Hsieh et al. (Hsieh et al., 2016, 2015) selected deionized water, pure silver-water, andmulti-walled carbon nanotube (MWCNT) nanofluids as working media to investigate the impact of nanoparticle concentration on surface heat flux. The results showed that the heat flux of pure silver-water nanofluid with a volume fraction of 0.0075% reached upto 274 W/cm², significantly higher than that of deionized water under the same conditions, by a factor of 2.4.

In the application of spray cooling for heat transfer, in addition to altering the cooling fluid, improving the structure of the heat dissipation surface has also become an important approach to enhance heat transfer performance. Zhang et al. (Zhang et al., 2015) explored the impact of coatings on the heat transfer characteristics of spray cooling using water as the working fluid. The results indicated that the critical heat flux density of nano-structured surfaces and surfaces coated with SiO_2 films was approximately 11.6% and 5.8% higher than that of smooth surfaces, respectively. Coursey et al. (Coursey et al., 2007) studied the effect of different groove heights on straight-channel surfaces and found that when the channel height was 3 mm, the spray cooling heat transfer effect was optimal, with a heat flux density of 124 W/cm². Chien et al. (Chien and Chang, 2011) used FC-72 as the cooling medium to investigate the heat transfer surfaces with straight-channel and square-shaped structures. The results showed that as the wetted area increased, the heat transfer effect of spray cooling significantly improved. Zhang et al. (Zhang et al., 2024) conducted numerical simulations ofspray cooling on various grooved surfaces using deionized water as the working fluid. The results showed that compared to smooth surfaces, the heat transfer performance of straight-grooved surfaces improved by 8.50% but was lower than the 25.55% achieved by radial-grooved surfaces. Among them, inclined-grooved surfaces achieved the strongest cooling capability due to gravity- accelerated liquid film flow.

However, among the aforementioned enhanced heat transfer methods, nanofluid spray cooling faces issues of poor nanofluid stability. Additionally, long-term use of nanofluid spray cooling can lead to the deposition of nanoparticles on the heat transfer surface, increasing thermal resistance and deteriorating heat transfer performance. Furthermore, altering the heat transfer surface structurehas a direct impact on the cooling and heat transfer performance of spray systems. However, this approach is primarily used in traditional cooling methods, such as air cooling and water cooling, with relatively few studies on its application in conjunction with spray systems. This study integrates enhanced surfaces with spray cooling and applies it to the thermal management of concentrating photovoltaics (CPV). Through experiments and simulations, the effects of different structures on the temperature and electrical properties of the cell were studied, and dimensionless parameters were fitted to characterize the interactions between the influencing factors. This research provides insights into cooling methods for solar cells in the CPV field.

2. PHYSICAL MODEL AND EXPERIMENTAL SET

2.1. physical model

Fresnel concentrated photovoltaic systems use Fresnel lenses to concentrate sunlight onto a small area of photovoltaic cells. The system is usually equipped with a sunlight tracking device to ensure that the light is always focused on the cell, thereby achieving efficient photoelectric conversion. Since the concentration makes the battery generate high temperature, efficient cooling means areneeded to dissipate the heat, a Fresnel high-power concentration spray cooling system is proposed. As shown in Figure 1, the nozzle atomizes the cooling medium into numerous small droplets under high pressure. These droplets are sprayed onto the object to be cooled at a fixed angle. By means of heat exchange and phase change evaporation between the cooling medium and the heat exchange surface, the heat from the area to be cooled is forcibly removed, thus cooling the heat exchange interface. The computational domain is a rectangular region measuring 22 mm × 40 mm × 40 mm, with the cooling area being a 2 mm × 20 mm × 20 mm solar cell. The solar cell is located in the centre and fixed on a vertical axis.

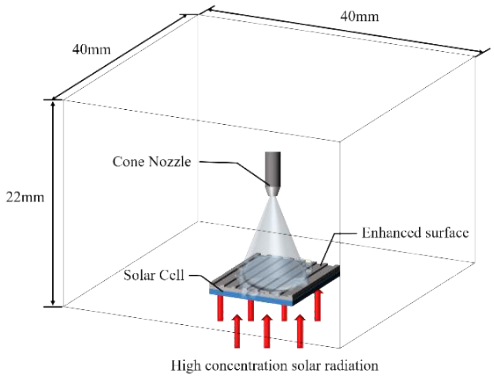

Figure 1: Schematic diagram of spray cooling model based on solar cell

In the simulation, air in the computational domain is treated as the continuous phase using the Eulerian method, while liquid droplets are considered the discrete phase using the Lagrangian method. In spray cooling, interactions between the continuous and discrete phases—where motion trajectories and heat exchange affect each other—are crucial. Solving the governing equations of both phases alternately is necessary to accurately model the process.

Equation 1: Momentum coupling equation.

$$F_x = \left[\frac{3\mu C_d \mathrm{Re}}{4\rho_d d_p^2}(u_x - u_{d,x}) + \frac{g_x(\rho_d-\rho)}{\rho_d} - D_{T,P}\frac{1}{m_d T}\frac{\partial T}{\partial x}\right]\dot{m}_d \Delta t$$
$$F_y = \left[\frac{3\mu C_d \mathrm{Re}}{4\rho_d d_p^2}(u_y - u_{d,y}) + \frac{g_y(\rho_d-\rho)}{\rho_d} - D_{T,P}\frac{1}{m_d T}\frac{\partial T}{\partial y}\right]\dot{m}_d \Delta t$$
$$F_z = \left[\frac{3\mu C_d \mathrm{Re}}{4\rho_d d_p^2}(u_z - u_{d,z}) + \frac{g_z(\rho_d-\rho)}{\rho_d} - D_{T,P}\frac{1}{m_d T}\frac{\partial T}{\partial z}\right]\dot{m}_d \Delta t$$

Equation 2: Mass coupling equation.

$$S_m = \frac{\Delta m_d}{m_{d,0}} m_{d,0}$$

Equation 3: Energy coupling equation.

$$S_h = \left[\frac{\bar{m}_d}{m_{d,0}} c_p \Delta T_d + \frac{\Delta m_d}{m_{d,0}}\left(-h_{fg} + \int_{T_{ref}}^{T_d} c_{p,H_2O}\, dT\right)\right]\dot{m}_{d,0}$$

Where:

- $\dot{m}_d$ = the mass flow rate of the discrete phase particles (kg/s)
- Δt = the time step (s)
- $m_{d,0}$ = the initial mass of the particles (kg)
- $\bar{m}_d$ = the average mass of particles in the control body (kg)
- h_{fg} = the latent heat of vaporization (J/kg)
- T_d = the temperature of the particle when it leaves the control volume (K)
- T_{ref} = the reference temperature corresponding to the enthalpy (K)

In the process of simulating the spray cooling system for concentrated photovoltaic (CPV), the concentrated solar cell can be simplified as a heat source with uniform solar irradiance for calculation, ignoring the heat generated by its own operation and other environmental factors. One sun concentration is calculated as 1000 W/m². The electrical energy output of the solar cell is influenced by solar radiation concentrated by the concentrator onto the surface and the electrical efficiency of the solar cell. The electrical efficiency of the solar cell can be calculated by the following equation (Chen et al., 2021):

Equation 4: Electrical efficiency of the solar cell.

$$\eta_{PV} = \eta_s \cdot \left[1 - \beta_r \cdot \left(T_w - T_{ref}\right)\right]$$

Where:

- η_s = the photoelectric conversion efficiency of the solar cell under reference conditions
- β_r = the temperature coefficient for the output current and voltage of the solar cell
- T_w = the wall temperature (K)

2.2. Experimental setup

The experimental setup for the spray cooling system, shown in Figure 2, consists of three main systems: the spray cooling liquid supply circulation system, the simulated heat source power control system, and the data acquisition system. The spray cooling liquid supply system includes components such as a low-temperature constant temperature bath, filter, hydraulic pump, flow control valve, adjustment rod, nozzle, connecting pipes, and valves. The simulated heat source system features a conductive copper block, electric heater, power adjustment device, and electrical connections. The data acquisition system comprises a thermometer, pressure gauge, glass rotor flowmeter, K-type thermocouple, data acquisition instrument, and computer.

During operation, the cooling medium stored in the low-temperature constant temperature bath is pressurized by the hydraulic pump and circulated through the system. It splits into two branches, with one branch directed to the spray nozzle and the other returning to the bath. The cooling medium, atomized into tiny droplets, rapidly contacts the heated surface, facilitating efficient heat removal through various mechanisms. The heated medium is then collected, cooled, and recirculated through the system, completing the spray cooling cycle. The experiment maintained consistent operating conditions with the working fluid inlet temperature set at 15°C,an ambient temperature at 20°C, and a concentration ratio of 500.

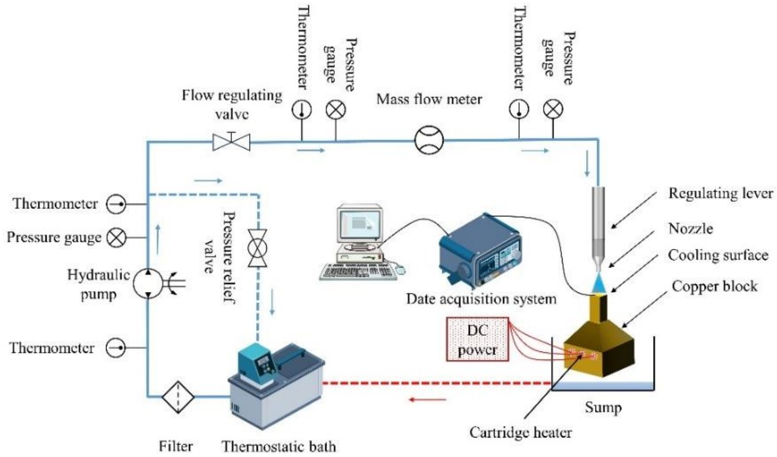

Figure 2: Experimental system schematic diagram

The heated copper block is enveloped in a high-efficiency insulation material, allowing the heat transfer process to be modelled as one-dimensional axial heat conduction. By simplifying Fourier’s law, the formula for the calculated heat flow density is derived as follows:

Equation 5: Fourier’s law.

$$q = \lambda \frac{(T_i - T_j)}{\Delta\delta}$$

Where:

- q = the heat flow density (W/m^2)
- λ = the thermal conductivity of copper block, taken as 298.15 W/m·K
- T_i = the temperatures of the temperature measurement points of the i-th layer (℃)
- T_j = the temperatures of the temperature measurement points of the j-th layer (℃)
- $\Delta\delta$ = the two distance between layers (mm)

Given that the copper block conducts heat axially in one dimension, the surface temperature of the copper block is expressed as:

Equation 6: the surface temperature of the copper block.

$$T_{suf} = T_1 - (T_i - T_j)\frac{\delta_1}{\Delta\delta}$$

Where:

- T_{suf} = the surface temperature (℃)
- T_1 = the temperature of the temperature measurement points closest to the surface (℃)

- δ_1 = the difference between the heat exchange surface and the first the distance between layers (mm)

Consequently, the formula for calculating the heat transfer coefficient on the surface of the heated copper block is given by:

Equation 7: the surface temperature of the copper block.

$$h = \frac{q}{\Delta t}$$

Where:

- h = the heat transfer coefficient (W/m²·K)
- Δt = the difference between the surface temperature and the cooling fluid inlet temperature (℃)

Due to the experimental apparatus's precision limitations, errors in outcomes are inevitable. Primary sources of error include ±0.1 mm distance measurement error between temperature points, ±0.5 °C K-type thermocouple accuracy, and ±0.15 mL/s flow meter accuracy. The error can be computed using the following formula.

Equation 8: errors analysis.

$$\partial_z = \sqrt{\sum_{i=0}^{n} \left(\frac{df}{dy_i}\right)^2 \partial_{y_i}^2}$$

Consequently, the errors in surface temperature, heat flux density, heat transfer coefficient, and electrical efficiency are ±1.8%, ±1.6%, ±3.4%, and ±1.7% respectively.

2.3. Model validation

Figure 3 shows the variation of the average surface temperature with the number of grids and its comparison with experimental results. It can be observed that when the number of grids exceeds 100,000, the change in the surface average temperature is minimal. This indicates that increasing the number of grids does not significantly affect the calculation results. Furthermore, when compared to experimental results under the same conditions, the temperature difference gradually decreases and stabilizes. Considering both accuracy and computation speed, this study chooses to use 120,000 grids for subsequent simulations.

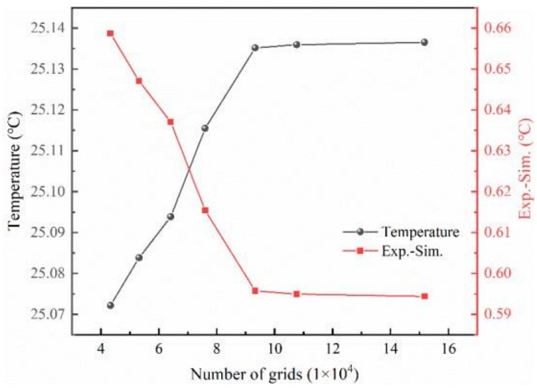

Figure 3: Diagram of thermocouple arrangement

3. RESULTS AND DISCUSSION

3.1. Performance analysis of solar cells under different structures

To investigate the thermoelectric performance of concentrated photovoltaics under spray cooling, an experiment investigated the thermoelectric performance of concentrated photovoltaics under spray cooling using water. The study maintained a concentration ratio of 500 and a nozzle inlet temperature of 15°C. Figure 4 shows trends in cell surface temperature, surface heat transfer coefficient, and system electrical efficiency at varying mass flow rates. Increasing the spray flow rate gradually lowers the cell surface temperature and enhances both the surface heat transfer coefficient and electrical efficiency. This improvement results from better atomized droplet impact and disturbance on the liquid film, improving heat exchange and electrical output.

When the spray flow rate increased from 1.2 L/min to 1.4 L/min, the surface temperature only decreased by 0.2°C, which is not significant; the increase in the surface heat transfer coefficient also decreased, only improving by 9.3%; the electrical efficiency increased by 19.71%, reaching 29.85% at a flow rate of 1.4 L/min. This is because, as the mass flow rate continues to increase, excess droplets thicken the liquid film formed on the heat source surface, slowing down the increase in the heat transfer coefficient and thus worsening heat transfer. Therefore, adopting an appropriate mass flow rate is crucial for improving system efficiency during spray cooling. Additionally, enhancing the surface structure can further improve heat transfer performance.

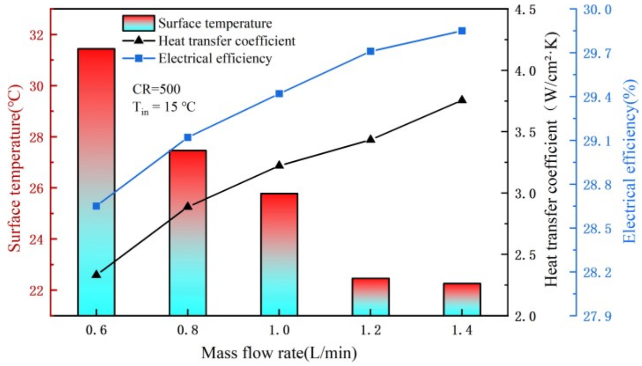

Figure 4: Comparison of solar cell performance under different mass flow rates

Figure 5 compares the temperature and performance of solar cells with different structures. Under various concentration ratios, solar cells with enhanced surfaces consistently exhibit better cooling effects than those without enhanced surfaces. As the concentration ratio increases, the temperature differences between solar cells with different backplate structures become more pronounced. Evenunder a 500-fold concentration, the surface temperature of the solar cells can be maintained below 40°C, which further affects the electrical efficiency of the solar cells. The efficiency of solar cells with enhanced surfaces consistently remains above 29%, higher than those without enhanced surfaces.

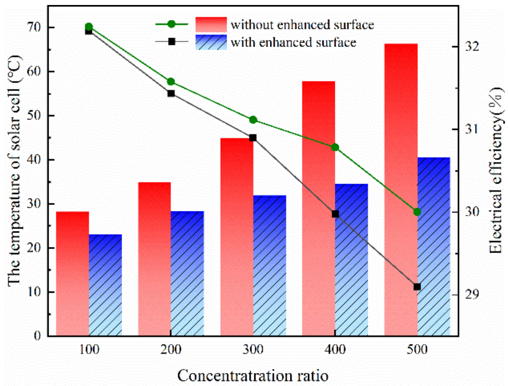

Figure 5: Comparison of solar cell performance under different concentration ratios

3.2. Effect of structural parameters on heat transfer performance of spray cooling

This study selected straight-groove and vertical structures as research objects to investigate the effects of structure height and channel width on spray cooling heat transfer. Different structural parameters influence heat transfer in two aspects: changes in heattransfer area and the flow state of the working fluid on the surface. Among these, channel area is the primary influencing factor; themore complex the structure, the poorer the fluidity of the working fluid on the heat transfer surface, thereby affecting the heat transfer effect. In different structures, the surface temperature distribution varies significantly. Figure 6 illustrates the temperature and liquid film thickness contour maps for solar cells with different surface structures. The average thickness of liquid film in straight fins and cubic pin fins is 0.137 mm and 0.127 mm, respectively. The cubic pin fins are more conducive to the flow of liquid film, and the thickness of liquid film is reduced by 7.3%. Because the liquid film distribution is more uniform, the cubic pin fins show better temperature uniformity.

With a fixed channel width, the selected structure heights in this study are: 0.2 mm, 0.4 mm, 0.6 mm, 0.8 mm, and 1 mm. The temperature, Reynolds number (Re), and Weber number (We) distributions of the heat exchange surface at different heights are shown in Figure 7. The temperature variation trends for the straight groove surface structure and the vertical surface structure are consistent: as the height increases, the temperature of the heat exchange surface first decreases rapidly and then increases slowly. The minimum temperatures for the straight groove and vertical structures are 36.1°C and 33.6°C, respectively. Overall, the heat exchange effect of the enhanced vertical surface is superior to that of the straight groove surface. The addition of surface structures inhibits the flow state of the working fluid to a certain extent, and with increasing height, the Re distribution for both structures decreases. On the other hand, increasing the height also increases the heat exchange area. Therefore, the change in heat exchange effect is influenced by the combined effects of the flow state of the working fluid on the heat exchange surface and changes in the heat exchange area. The We variation trends for both the straight groove and vertical surface structures are consistent: We increases and then decreases with height, reaching a maximum at a height of 0.6 mm for both structures. The We variation trend is opposite to that of the temperature. The heat exchange area details are shown in Table 1. Before a height of 0.6 mm, the increased heat exchange area enhances the heat exchange effect more than the structure inhibits the working fluid flow. However, beyond 0.6 mm, the weakening of the working fluid flow more significantly affects the heat exchange effect.

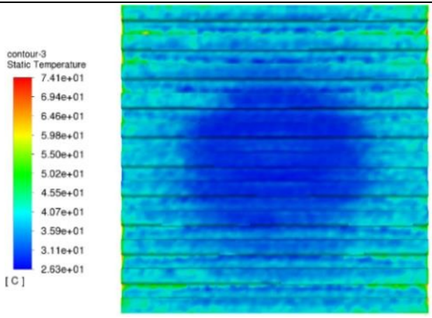

(a) Temperature distribution - Straight fins

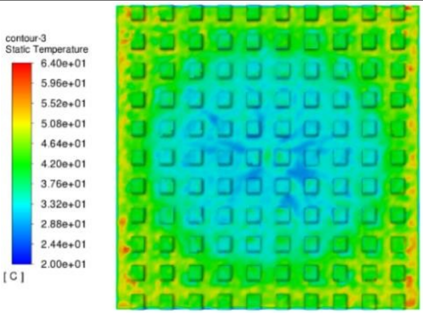

(b) Temperature distribution - Cubic pin fins

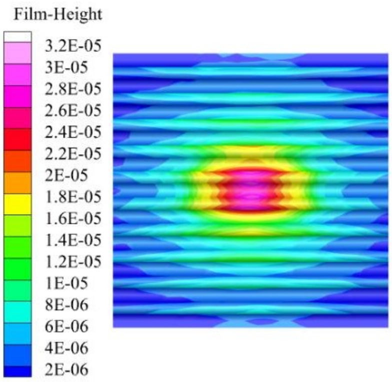

(c) Liquid film distribution - Straight fins

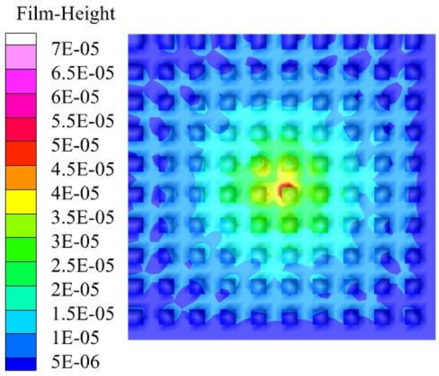

(d) Liquid film distribution - Cubic pin fins

Figure 6: Temperature distribution and liquid film distribution under different structures

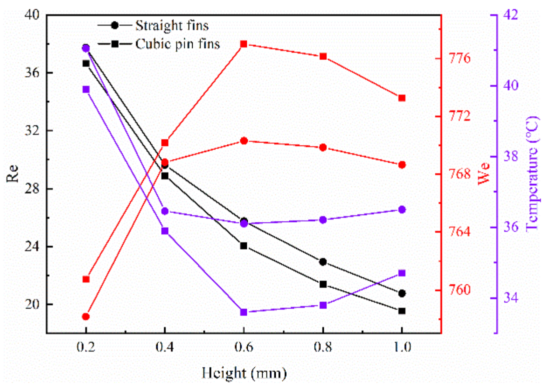

Figure 7: The temperature, Reynolds number and Weber number of the heat exchange surface at different heights

Table 1: Heat transfer area at different structural heights

Heat exchange surface structure	Height/mm	Heat exchange surface area /mm^2	Heat exchange surface increase /mm^2	Flow channel area /mm^2
Straight fins	0.2	480	80	180
	0.4	560	160	
	0.6	640	240	
	0.8	720	320	
	1	800	400	
Cubic pin fins	0.2	484	84	301
	0.4	568	168	
	0.6	652	252	
	0.8	736	336	
	1	820	420	

Based on the aforementioned optimal height of 0.6 mm, the channel width is varied. The temperature, Re, and We distributions of the heat exchange surface at different channel widths are shown in Figure 8. As the height increases, the Re distribution for both structures also increase, indicating that the increase in channel width promotes the flow of the working fluid over the heat exchange surface, enhancing heat transfer. However, the increase in heat exchange area decreases, resulting in an eventual increase in temperature instead of a decrease. The We distribution for both structures increase first and then decreases, with

We reaching a maximum at a channel width of 0.6 mm, opposite to the temperature trend. The heat exchange area for different channel widths is detailed in Table 2. Increasing the channel width reduces the structural features on the heat exchange surface, thereby reducing the increase in heat exchange area while increasing the channel area. Therefore, the change in heat exchange effect is influenced by the combined effects of the flow state of the working fluid on the heat exchange surface and the change in channel area. Before a channel width of 0.6 mm, the promotion of working fluid flow by the increased channel area strengthens heat exchange more than the reduction in heat exchange rea weakens it. However, beyond 0.6 mm, the reduction in heat exchange area more significantly affects the heat exchange effect.

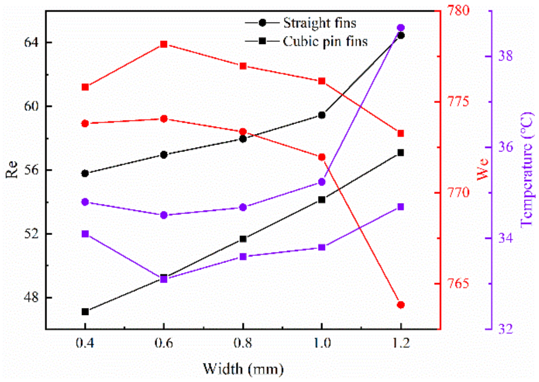

Figure 8: The temperature, Reynolds number and Weber number of the heat exchange surface at different width

Table 2: Heat transfer area at different channel width

Heat exchange surface structure	Height/mm	Heat exchange surface area /mm^2	Heat exchange surface increase /mm^2	Flow channel area /mm^2
Straight fins	0.4	616	216	120
	0.6	584	184	160
	0.8	568	168	180
	1	552	152	200
	1.2	536	136	220
Cubic pin fins	0.4	839.32	439.3	204
	0.6	738.4	338.4	256
	0.8	683.8	283.8	279
	1	628	228	300
	1.2	585.64	185.6	317.2

3.3. Effect of the ratio α of the flow channel area to the increased area on the heat transfer performance ofspray cooling

Considering that changes in the structure will cause variations in the channel area and the increase in area, while the increase in heat transfer area enhances heat transfer, the reduced channel area on the other hand hinders the flow of the working fluid, thereby weakening heat transfer. Therefore, it is necessary to comprehensively consider the influence of both parameters. This paper defines an area influence factor α, which is defined as follows:

Equation 9: Area influence factor.

$$\alpha = \frac{S_{add}}{S_{channel}}$$

Where:

- S_{add} = the increase in the heat transfer area
- $S_{channel}$ = the channel area

Figure 9 shows the variation trends of temperature, Re, and We for different area influence factors α in both straight-groove and vertical structures. The variation trends of these parameters in both structures exhibit similarities. The size of α indirectly reflects the fluidity of the working fluid on the heat transfer surface; the larger the α, the less favorable it is for the fluid flow on the heat transfer surface, which is shown in the figure as a decrease in the Re number. For both straight-groove and vertical structures, the temperature trend first decreases and then increases, with the lowest temperature occurring around α equal to 1. This indicates that neither the channel area nor the increase in heat transfer area should be excessively large; instead, there should be a balance between the two. We trend for both structures are exactly opposite to the temperature trend, also showing a maximum value around α equal to 1.

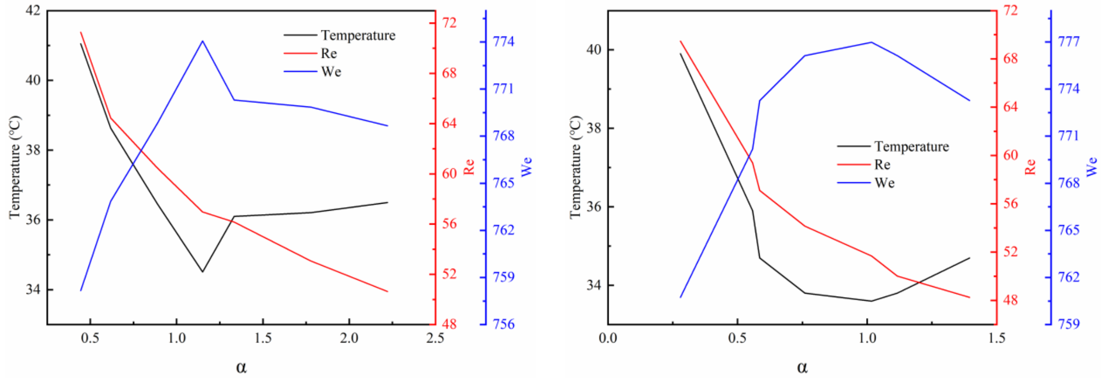

(a) straight fins (b) cubic pin fins

Figure 9: The variation trend of temperature, Re and We under the different α of the straight fins

3.4. Enhanced dimensionless correlation fitting of heat transfer surface

In spray cooling heat transfer based on enhanced surfaces, the parameters of the surface structure and the nozzle parameters affect dimensionless numbers such as the Re number, Pr number, and We number. The Re number characterizes the influence of inertial forces in the flow field; after adding surface structures, the disturbance of the liquid film on the heat transfer surface is enhanced, thereby improving heat transfer. The Pr number represents the ratio of the fluid's momentum transfer capability to its heat transfer capability. The We number characterizes the scale of droplet deformation and breakup. Using these dimensionless numbers and the area influence factor α, a dimensionless correlation for enhanced heat transfer surfaces can be derived.

In this study, changes in the structure cause variations in the channel area and increase in area. Although an increase in heat transfer area enhances heat transfer, the reduced channel area, on the other hand, hinders the flow of the working fluid, thereby weakening heat transfer. Therefore, it is necessary to comprehensively consider their impacts.

Equation 10: Dimensionless correlation (straight fins). $$Nu_{straight} = e^{97.0706}Re^{1.0165}Pr^{4.4025}We^{-15.513}\alpha^{0.0844}$$

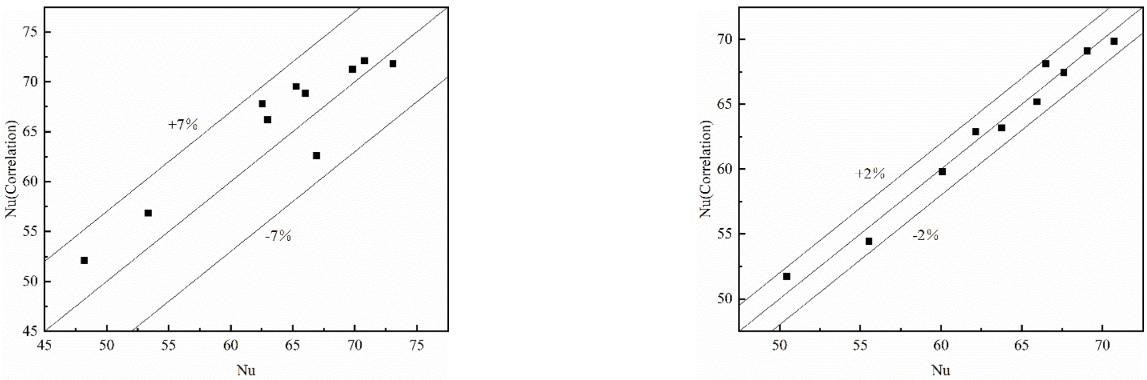

(a) straight fins (b) cubic pin fins

Figure 10: Consider the dimensionless correlation between Re, Pr, We and α to predict and compare the simulated values

When the enhanced surface is of the straight-groove type, the comparison between the predicted values from the dimensionless correlation involving Re, Pr, We, and α and the simulated values is shown in Figure 10. The fitted Nu is more accurate, with all datapoints falling within a deviation of the fitted line. This formula provides a better description of spray cooling based on straight-groove enhanced surfaces under low flow rates.

Similarly, the dimensionless correlation for the vertical type can be obtained as follows:

Equation 11: Dimensionless correlation (cubic pin fins). $$Nu_{cubic} = e^{10.3642}Re^{1.212}Pr^{3.5478}We^{-2.3559}\alpha^{0.1233}$$

4. CONCLUSION

Spray cooling coupled with enhanced surfaces effectively dissipates heat in concentrated photovoltaic (CPV) systems. Using this cooling method in Fresnel-type CPV systems through experiments and simulations, the effects of the addition of enhanced structures on the performance of the cells were investigated, and the reasons for these changes were analysed.

1.The addition of enhanced surfaces significantly improves cell performance. As the concentration ratio increases, the difference brought about by the addition of enhanced surfaces becomes more pronounced. Even under 500 times concentration, the addition of enhanced surfaces can keep the solar cell surface temperature below 40°C, with efficiency always remaining above 29%.

2.The impact of enhanced surfaces includes both positive and negative effects. The height and channel width of the two studied structures enhance heat transfer within a certain range, but beyond this range, heat transfer deteriorates. The addition of enhanced surface made the liquid film thinner. The average thickness of the liquid film in straight pins and cubic pin fins was 0.137 mm and 0.127 mm, respectively. The cubic pin fins were more conducive to the flow of the liquid film, and the thickness of the liquid film was reduced by 7.3%. On the other hand, the change of structural parameters will affect the change of the flow channel area and the increase value of heat transfer area, and both will affect the heat transfer.

3.Furthermore, considering the combined effect of the increase in heat transfer area and the channel area influenced by the structural parameters, the dimensionless parameter α was proposed. The best heat transfer effect is achieved when α is close to 1, indicatingthat the increase in heat transfer area and the channel area are approximately equal, achieving optimal heat transfer. Considering the effects of Reynolds number, Prandtl number, Weber number, and α, a dimensionless correlation for heat transfer was derived.

5. REFERENCES

Hosenuzzaman, M., Rahim, N.A., Selvaraj, J., et al, 2015. Global prospects, progress, policies, and environmental impact of solar photovoltaic power generation. Renewable and Sustainable Energy Reviews, 41, 284–297.

Mahmoudi, T., Wang, Y., Hahn, Y.-B., 2018. Graphene and its derivatives for solar cells application. Nano Energy, 47, 51–65.

Khokhar, M.Q., Hussain, S.Q., Chowdhury, S., et al, 2022. High-efficiency hybrid solar cell with a nano-crystalline silicon oxide layer as an electron-selective contact. Energy Conversion and Management, 252, 115033.

Tian, J., Zhou, S., Wang, Y., 2023. Assessing the technical and economic potential of wind and solar energy in China—A provincial- scale analysis. Environmental Impact Assessment Review, 102, 107161.

Du, B., Hu, E., Kolhe, M., 2012. Performance analysis of water cooled concentrated photovoltaic (CPV) system. Renewable and Sustainable Energy Reviews, 16, 6732–6736.

Liang, G., Mudawar, I., 2017a. Review of spray cooling – Part 1: Single-phase and nucleate boiling regimes, and critical heat flux. International Journal of Heat and Mass Transfer, 115, 1174–1205.

Liang, G., Mudawar, I., 2017b. Review of spray cooling – Part 2: High temperature boiling regimes and quenching applications. International Journal of Heat and Mass Transfer, 115, 1206–1222.

Chen, H., Wang, Y., Yang, H., et al, 2022. Experimental investigation and exergy analysis of a high concentrating photovoltaic system integrated with spray cooling. Energy Conversion and Management, 268, 115957.

Wang, Y., Liu, M., Liu, D., et al, 2010. Experimental study on the effects of spray inclination on water spray cooling performance in non-boiling regime. Experimental Thermal and Fluid Science, 34, 933–942.

Silk, E.A., Kim, J., Kiger, K., 2006. Spray cooling of enhanced surfaces: Impact of structured surface geometry and spray axis inclination. International Journal of Heat and Mass Transfer, 49, 4910–4920.

Liu, H., Cai, C., Yin, H., et al, 2018. Experimental investigation on heat transfer of spray cooling with the mixture of ethanol and water. International Journal of Thermal Sciences, 133, 62–68.

Hsieh, S.-S., Leu, H.-Y., Liu, H.-H., 2015. Spray cooling characteristics of nanofluids for electronic power devices. Nanoscale Res Lett, 10, 139.

Hsieh, S.-S., Liu, H.-H., Yeh, Y.-F., 2016. Nanofluids spray heat transfer enhancement. International Journal of Heat and Mass Transfer, 94, 104–118.

Zhang, Z., Jiang, P., Christopher, D., et al, 2015 Experimental investigation of spray cooling on micro-, nano- and hybrid-structuredsurfaces. International Journal of Heat and Mass Transfer, 80, 26-37.

Coursey, J.S., Kim, J., Kiger, K.T., 2007. Spray Cooling of High Aspect Ratio Open Microchannels. Journal of Heat Transfer, 129, 1052–1059.

Chien, L.-H., Chang, C.-Y., 2011. An experimental study of two-phase multiple jet cooling on finned surfaces using a dielectric fluid. Applied Thermal Engineering, 31, 1983–1993.

Zhang, W., Liu, C., Yang, T., et al, 2024. Numerical investigation on heat transfer enhancement of spray cooling by surface structure optimization. International Journal of Heat and Mass Transfer, 223, 125220.

Chen, H., Li, G., Zhong, Y., et al, 2021. Exergy analysis of a high concentration photovoltaic and thermal system for comprehensive use of heat and electricity. Energy, 225, 120300.

#273: Heat transfer numerical analysis and performance evaluation of coaxial geothermal heat exchanger under soil freezing conditions

Ruijia LIU [1], Wenshuo ZHANG[2], Shaoqing HAN[3] Ping CUI*

[1] Shandongjianzhu university, liurj1536@163.com
[2] Shandongjianzhu university, 9861801585@163.com
[3] Shandongjianzhu university, 3068183210@qq.com
* Shandongjianzhu university, sdcuiping@sdjzu.edu.cn

Abstract: Seasonal thermal energy storage can significantly contribute to district heating and cooling systems based on sustainableenergy whenever there is a seasonal imbalance between energy generation and utilization. To enhance the heat storage capacity, the soil temperature can be reduced to below 0℃in winter, and the time and intensity of direct water supply by using low-temperature soil can be increased in summer. It is necessary to consider the effect of phase change on geothermal heat exchange operation. The water in the soil releases latent heat after freezing, which can improve the heat performance of the ground heat exchanger. An innovative numerical heat transfer model inside a coaxial geothermal heat exchanger (CGHE) is presented, considering the freezing of ground moisture. The finite difference method is adopted to solve the temperature distribution, and the model's accuracy is validated with experimental data. Based on the theoretical analysis to study the thermodynamic parameters influence of antifreeze and soil on the freezing heat transfer performance of CGHE, compare the heat transfer model with frozen and unfrozen heat transfer to analyze the calculated errors. The results show that glycerin is most suitable for CGHE as a heat transfer medium. The release of latent heat during freezing augments the heat extraction rate, and the error range is 11.8%, so the relevant conclusions in this study can provide a reference for the design of CGHE under freezing heat transfer conditions.

Keywords: Coaxial Heat Exchanger, Numerical Simulations, Phase Change Heat Transfer, Heat Transfer Performance

1. INTRODUCTION

In recent years, the quest for sustainable and energy-efficient heating and cooling solutions has intensified, spurred by environmental concerns and the drive for cost-effective alternatives. Among these solutions, the geothermal heat exchanger (GHE) technology can significantly reduce energy savings and carbon emissions. In 2023, the International Geothermal Association (IGA) released the latest advancements (*Global Geothermal Update 2023*, 2023) in direct geothermal uses. The global installed capacity of geothermal heating and cooling has reached 173,303 MW, and the global annual use of geothermal heating and cooling has reached 1,476,312 TJ, as shown in Figure 1. This vital data underscores geothermal energy's critical role in the growing contribution to sustainable global energy initiatives.

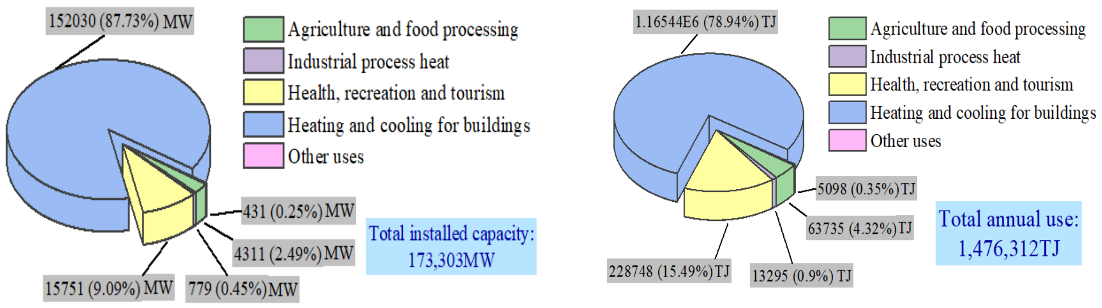

(a) 2023 Global installed capacity of geothermal heating and cooling (MW.)

(b) 2023 Global annual use of geothermal heating and cooling (T.J.)

Figure 1: Global geothermal heating and cooling production released by IGA

Among them is a simple installation procedure and small local thermal resistance compared to U-shaped GHE (Li et al., 2020). This study aims to propose an innovative mathematical heat transfer model of CGHE in a 2D column coordinate system, considering thefreezing of soil moisture. The numerical implementation of the model based on the Finite Difference Method (FDM) makes it possible to investigate the effect of soil freezing on the temperature distribution inside the CGHE and its thermal performance. It is essential to highlight that, in deep CGHEs, only pure water (without antifreeze) with positive inlet temperature is permitted to avoid contaminating deep groundwater resources (Cai et al., 2022). Consequently, this study focuses on a shallow vertical CGHE with a negative inlet temperature of circulating fluid. The findings of this study can further enhance the adoption of CGHE for seasonal energy storage and extend the utilization of geothermal energy in cold regions.

2. METHODOLOGY

2.1. Model assumptions

To improve calculation efficiency while maintaining prediction accuracy, the following assumptions are adopted:

1. The thermal properties of ground, pipe, water, and backfilling materials depend on their specific temperatures, and the propertiesof the ground are homogeneous in each ground layer.

2. The soil is regarded as a porous medium model, filling the pores with saturated water.

3. The lateral and bottom boundaries of the borehole model are set to be temperature constant.

4. The soil heat transfer along the radius direction is analyzed without considering the temperature change along the depth direction of the CGHE.

5. Ignoring the volume expansion of water in soil after freezing, the density of water before and after freezing is considered unchanged.

2.2. Heat transfer governing equation

Heat transfer equation of the soil surrounding the CGHE

(1) Heat transfer governing equation

Based on the above assumptions, the heat transfer governing equations of the CGHE are described as follows. Since each groundlayer is axially symmetric, the heat transfer process of each ground layer can be regarded as a 2D unsteady heat transfer model in the cylindrical coordinate (Fang et al., 2018).

*Equation 2 : H*eat transfer governing equations of the CGHE $\rho c\frac{\partial T}{\partial \tau}=\frac{1}{r}\frac{\partial}{\partial r}(r\lambda\frac{\partial T}{\partial r})+\frac{\partial}{\partial z}(\lambda\frac{\partial T}{\partial z})$

During heat extraction, the heat flux exchanged between the CGHE, and the ground is highest at the borehole wall and diminishes as it moves outward radially. To account for the heat transfer characteristics in the ground, variable spatial steps in the radial direction are used to enhance computational efficiency. Thus, a new radial coordinate is adopted, which can be described as (Fanget al., 2018),

Equation 2: New radial coordinate of *v*ariable spatial steps in the radial direction $\sigma=ln\left(\frac{r}{r_0}\right),\frac{r_{i+1}}{r_i}=\frac{r_1}{r_0}=exp\ (\Delta\sigma)=\beta$

Applied the new radial coordinate in the control Equation, it can be rewritten as

Equation 3: New radial coordinate in the control Equation $\rho c\frac{\partial T}{\partial \tau}=\lambda(\frac{1}{r^2}\frac{\partial^2 T}{\partial \sigma^2}+\frac{\partial^2 T}{\partial z^2})$

Where:

- ρ = density of soil (kg/m^3)
- c = heat capacity of soil (J/(kg·K))
- λ = thermal conductivity (W/(m·K))
- T = temperature (℃)
- z = numerical direction coordinates (m)
- r = radial coordinates (m)

(2) Initial and boundary conditions

The soil temperature at any depth in the stratum can be calculated by equation (2)

Equation 4: Soil temperature at any depth in the stratum

$$t(r,z,\tau)=t_a+\frac{q_g}{h_a}+\sum_{j=1}^{m-1}\frac{q_g}{k_j}(H_j-H_{j-1})+\frac{q_g}{k_m}(z-H_{m-1})$$

$$\tau=0, H_{m-1}\le z\le H_m, r_b\le r\le r_{bnd}$$

Where:

- t_a = ambient air temperature (℃)
- h_a= convective heat transfer coefficient at the ground surface (W/(m^2·K))
- H_j = bottom coordinate of the j-layer
- q_g = geothermal heat flux (W/m^2)
- k = ground thermal conductivity (W/(m·K))

The bottom boundary of the whole calculation region is set far below the bottom of the borehole, with an extra distance of 200 m beneath the borehole bottom. The temperature remains constant as no thermal interference occurred at this bottom boundary.

The heat convection boundary condition is set at the ground surface, which can be expressed by equation (5).

Equation 5: The heat convection boundary condition

$$k\frac{\partial t}{\partial z}=h_a(t-t_a), z=0, r_b\le r\le r_{bnd}, \tau\ge 0$$

(3) Numerical discretization

The alternative direction finite difference method (ADFDM) combines the forward and backward FDM and uses them alternatively in adjacent time steps. This approach ensures that no more than three unknowns need to be solved for each numerical node, which significantly improves the calculation efficiency. Based on the geometric characteristics of the CGHE, the FDM is utilized to establish the computational grid division for the efficient simulation model. The grid division is shown in Figure 2.

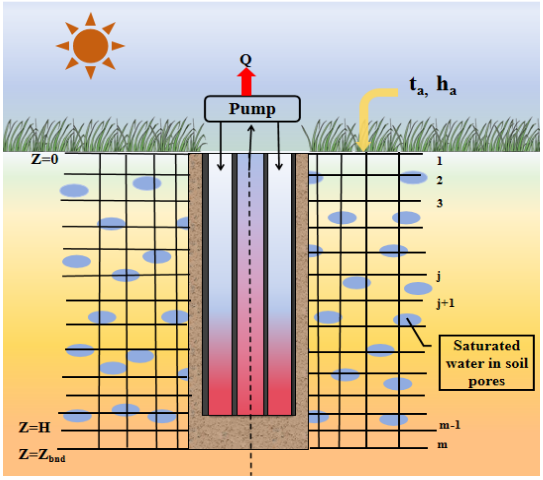

Figure 2: Numerical discretization of the CGHE

Equation 6: The numerical equations of the ground interior

$$-B_r t_{i-1,j}^{p+1} + (1+2B_r)t_{i+1,j}^{p+1} - B_r t_{i+1,j}^{p+1} = B_z t_{i,j-1}^{p} + (1-2B_z)t_{i,j}^{p} + B_z t_{i,j+1}^{p}$$
$$-B_z t_{i,j-1}^{p+1} + (1+2B_z)t_{i,j}^{p+1} - B_z t_{i,j+1}^{p+1} = B_r t_{i-1,j}^{p} + (1-2B_r)t_{i,j}^{p} + B_r t_{i+1,j}^{p}$$

where, $B_r = \frac{\lambda\Delta\tau}{\rho c\ (r\Delta\sigma)^2}$, $B_z = \frac{\lambda\Delta\tau}{\rho c\ (\Delta z)^2}$.

Equation 7: The numerical equations of the ground surface

$$-2B_z t_{i,j+1}^{p+1} + (1+2B_z+B_h)t_{i,j}^{p+1} - B_h t_a = B_r t_{i-1,j}^{p} + (1-2B_r)t_{i,j}^{p} + B_r t_{i+1,j}^{p}$$
$$(1+2B_r)t_{i,j}^{p+1} - B_r t_{i-1,j}^{p+1} + B_r t_{i+1,j}^{p+1} = 2B_z t_{i,j+1}^{p} + (1-2B_z-2B_h)t_{i,j}^{p} + B_h t_a$$

where, $B_h = \frac{2h\Delta\tau}{\rho c\Delta z}$

Equation 8: The numerical equations of the soil interface

$$-B_{r12} t_{i-1,j}^{p+1} + (1+2B_{r12})t_{i,j}^{p+1} - B_{r12} t_{i+1,j}^{p+1} = B_{z1} t_{i,j-1}^{p} + (1-B_{z1}-B_{z2})t_{i,j}^{p} + B_{z2} t_{i,j+1}^{p}$$
$$-B_{z1} t_{i,j-1}^{p+1} + (1+2B_{z1}+B_{z2})t_{i,j}^{p+1} - B_{z2} t_{i,j+1}^{p+1} = B_{r12}(t_{i-1,j}^{p} + t_{i+1,j}^{p}) + (1-2B_{r12})t_{i,j}^{p}$$

where, $B_{r12} = \frac{(k_{jj}+k_{jj+1})\Delta\tau}{(\rho c_{jj}+\rho c_{jj+1})\ (r\Delta\sigma)^2}$, $B_{z1} = \frac{2k_{jj}\Delta\tau}{(\rho c_{jj}+\rho c_{jj+1})\ (\Delta z)^2}$, $B_{z2} = \frac{2k_{jj+1}\Delta\tau}{(\rho c_{jj}+\rho c_{jj+1})\ (\Delta z)^2}$

Equivalent heat capacity method

Since soil is a multi-component material, it is regarded as a porous medium model in this study, in which the pores are filled with saturated water. The phase transition occurs over a narrow temperature range. It expands as freezing time progresses, so the soil is divided into a frozen zone, unfrozen zone and solid-liquid two-phase zone according to temperature.

The phase change region of frozen soil is addressed using the equivalent heat capacity method, with temperature as the parameter to be determined. Based on the law of conservation of energy, the specific heat function is established within the phase transition range as follows:

Equation 9: Specific heat function within the phase transition

$$\int_{T_d-\delta}^{T_d+\delta} c(T)dT = \int_{T_d-\delta}^{T_d} c_{is}(T)dT + \int_{T_d}^{T_d+\delta} c_{ws}(T)dT + \Psi$$

Where:

- c = specific heat capacity of the two-phase region (J/(kg·K))
- c_{is} = specific heat capacity of the frozen region (J/(kg·K))
- c_{ws}= specific heat capacity of the unfrozen region (J/(kg·K))
- δ = variation range of soil freezing temperature (℃)
- T_d = freezing temperature of soil (℃)
- Ψ= latent heat of ice formation per unit volume (kJ/kg)

Assuming that the volume heat capacity of the frozen and unfrozen regions is constant, the region in the two-phase region can be obtained according to equation (9). The volume heat capacity is

Equation 10: Volume heat capacity within the phase transition

$$c(T) = \frac{c_{is} + c_{ws}}{2} + \frac{\Psi}{2\delta}$$

Similarly, for thermal conductivity, the values remain constant in both the frozen and unfrozen regions, while in the phase transition zone, they vary continuously. Thus, the thermal conductivity in the two-phase zone is considered to have a linear correlation with temperature in this study. The thermal conductivity equation in the phase transition zone can be expressed as follows:

Equation 11: Thermal conductivity equation in the phase transition zone

$$\lambda(T) = \lambda_{is} + \frac{\lambda_{ws} - \lambda_{is}}{2}[T - (T_d - \delta)]$$

Where:

- λ = thermal conductivity of the two-phase region (W/(m·K))
- λ_{is} = thermal conductivity of the frozen region (W/(m·K))
- λ_{ws}= thermal conductivity of the unfrozen region (W/(m·K))

Therefore, the function of thermal conductivity and volumetric heat capacity of each region is as follows:

Equation 12: Thermal conductivity function of each region

$$\lambda = \begin{cases} \lambda_{is} & T \le T_d - \delta \\ \lambda_{is} + \frac{\lambda_{ws} - \lambda_{is}}{2}[T - (T_d - \delta)] & T_d - \delta \le T \le T_d + \delta \\ \lambda_{ws} & T \ge T_d + \delta \end{cases}$$

Equation 13: Volumetric heat capacity of each region

$$\rho c = \begin{cases} \rho_{sp}\, c_s(1-\varepsilon) + \rho_w c_s \varepsilon & T \le T_d - \delta \\ \rho(\frac{c_{is} + c_{ws}}{2} + \frac{\varepsilon\Psi}{2\delta}) & T_d - \delta \le T \le T_d + \delta \\ \rho_{sp}\, c_s(1-\varepsilon) + \rho_w c_s \varepsilon & T \ge T_d + \delta \end{cases}$$

Where:

- ρ_w = density of water (kg/m^3)
- ρ_{sp} = density of dry soil (kg/m^3)
- ε = moisture content of the soil

Heat transfer equation of the fluid in CGHE

(1) Heat transfer governing equation
In CGHE, the heat-carrying fluid moves from top to bottom along the annular area between the pipes and rises to the inner pipe. The energy differential equation of the fluid in the inner tube is

Equation 14: The energy differential equation of the fluid in the inner tube

$$C_2 \frac{\partial t_{f2}}{\partial \tau} = \frac{t_{f2} - t_{f1}}{R_2} + \rho_f c_f \frac{\partial t_{f2}}{\partial z}$$

The energy differential equation for the fluid in the outer tube is

Equation 15: The energy differential equation of the fluid in the outer tube

$$C_1 \frac{\partial t_{f1}}{\partial \tau} = \frac{t_{f2} - t_{f1}}{R_2} + \frac{t_b - t_{f1}}{R_1} - \rho_f c_f \frac{\partial t_{f1}}{\partial z}$$

Where:

- C_1 = per-length heat capacity of the outer channel (J/m·K)
- C_2 = per-length heat capacity of the inner channel (J/m·K)

Considering the inner pipe and circulating water inside the inner pipe, the specific heat capacities should be calculated by

Equation 16: The energy differential equation of the fluid in the outer tube

$$C_1 = \frac{\pi}{4}(d_{1i}^2 - d_{2o}^2)\rho_f c_f + \frac{\pi}{4}(d_{10}^2 - d_{1i}^2)\rho_1 c_1 + \frac{\pi}{4}(d_b^2 - d_{1o}^2)\rho_g c_g$$

Equation 17: The energy differential equation of the fluid in the inner tube

$$C_2 = \frac{\pi}{4} d_{2i}^2 \rho_f c_f + \frac{\pi}{4}(d_{2o}^2 - d_{2i}^2)\rho_2 c_2$$

Where:

- ρ_f =density of the circulating fluid ($\mathrm{kg/m^3}$)
- c_f = specific heat capacity of the circulating fluid (J/(kg·K))
- ρ_1 =density of the outer pipe wall ($\mathrm{kg/m^3}$)
- c_1 = specific heat capacity of the outer pipe wall (J/(kg·K))
- ρ_2 =density of the inner pipe wall ($\mathrm{kg/m^3}$)
- c_2 = specific heat capacity of the inner pipe wall(J/(kg·K))
- ρ_g =density of the backfilling material ($\mathrm{kg/m^3}$)
- c_g = specific heat capacity of the backfilling material (J/(kg·K))

R_1((m·k)/W) is the thermal resistance between the circulating water in the outer pipe and the borehole wall, and R_2 is the thermal resistance between the circulating water in the inner and outer pipes, which can be calculated by

Where:

Equation 18: The thermal resistance between the circulating water in the outer pipe and the borehole wall R_1

$$R_1 = \frac{1}{\pi d_{1i} h_1} + \frac{1}{2\pi k_{p1}} ln\frac{d_{1o}}{d_{1i}} + \frac{1}{2\pi k_g} ln\frac{d_b}{d_{2i}}$$

Equation 19: Thermal resistance between the circulating water in the inner and outer pipe R_2

$$R_2 = \frac{1}{\pi d_{2i} h_2} + \frac{1}{2\pi k_{p2}} ln\frac{d_{2o}}{d_{2i}} + \frac{1}{\pi d_{2o} h_1}$$

- k_g = thermal conductivity of backfill material (W/(m·K))
- k_{p1} = thermal conductivity of outer pipe (W/(m·K))
- k_{p2} = thermal conductivity of inner pipe (W/(m·K))
- d_{1o} = outer pipe's outer diameter (m)
- d_{2o} = inner pipe's outer diameter (m)
- d_{1i} = outer pipe's inner diameter (m)
- d_{2i} = inner pipe's inner diameter (m)
- d_g = borehole diameter (m)

h_1 and h_2 are the convective heat transfer coefficients of the annular pipe and inner pipe, which can be calculated by

Equation 20 : The convective heat transfer coefficients

$$h = \frac{Nu \times k}{d}$$

Initial and boundary conditions

The boundary conditions of the flow direction of the pipe are

Equation 21 : boundary conditions of the flow direction of the pipe

$$\begin{cases} t_{f1} = t_{f2} - \frac{Q}{Mc}, & z = 0 \\ t_{f1} = t_{f2}, & z = H \end{cases}$$

Where:

- Q = total heat transfer rate of the CGHE (W)
- M = mass flow rate (kg/s)
- c = specific heat capacity of the circulating fluid (J/(kg·K)

Numerical discretization

The numerical equations of fluid in the inner pipe are:

Equation 22: The numerical equations of of fluid in the inner pipe

$$-B_2 t_{f1,j}^{p+1} + (1 + B_2) t_{f2,j}^{p+1} = B_5(t_{f2,j-1}^{p} - t_{f2,j+1}^{p}) + t_{f2,j}^{p}$$

$$-B_5 t_{f2,j-1}^{p+1} + t_{f2,j}^{p+1} + B_5 t_{f2,j+1}^{p+1} = B_2 t_{f1,j}^{p} + (1 - B_2) t_{f2,j}^{p}$$

where, $B_2 = \frac{\Delta\tau}{C_2 R_2}$, $B_5 = \frac{C\Delta\tau}{2C_z \Delta z}$.

2.3. Numerical model solving process

Incorporating the soil freezing model based on the equivalent heat capacity method, the calculation model of the CGHE differs fromtraditional models. The model proposed in this study requires assessing the frozen state of the soil at various temperatures and substituting different formulas for thermal conductivity and heat capacity, as illustrated in Figure 3.

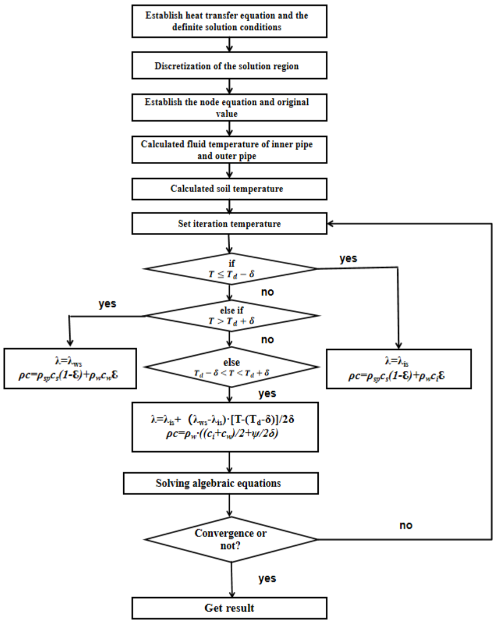

Figure 3: Flow chart to calculate the soil temperature of the CGHE considering the freezing of ground moisture

3. MODEL VALIDATION

This study selected another simulated data involving a soil freezing model from reference (Vasilyev et al., 2022b). In the referenced(Vasilyev et al., 2022b), the author used Matlab's ode15s solver to simulate the steady-state temperature variation of water along a100m-deep CGHE, with an inlet water temperature of -10℃and a flow rate of 0.3 kg/s. In this study, we set the same input parameters as the reference (Vasilyev et al., 2022b), including the inlet fluid temperature, mass flow rate, soil thermal capacity and heat conductivity coefficient. The comparison results among the numerical simulation results of this study and those of reference and the measured data are shown in Figure 4. It can be seen from Figure 4 that the proposed numerical result in this study follows a trend similar to both the measured data and the simulated data from the reference (Vasilyev et al., 2022b). The maximum error between the developed model and the referred model is found to be 5%. Therefore, the numerical model is considered reliable for further analysis of the performance of the CGHE.

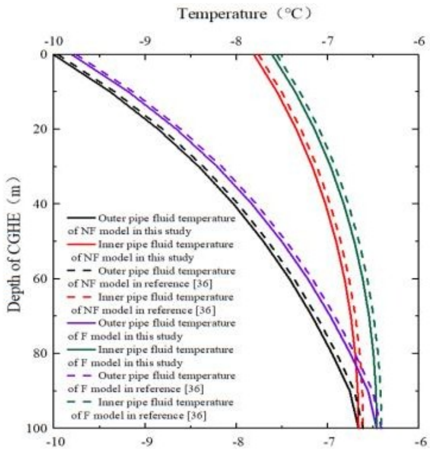

Figure 4: Comparison of simulated and measured outlet temperatures with the literature [36]

4. MODEL PARAMETER

To effectively showcase the model's capabilities through simulations, it becomes imperative to establish the parameters for the CGHE. The parameters associated with shallow ground heat exchangers often span a broad spectrum. In this study, we abstain from focusing on any specific heat exchanger type. Thus, for numerical simulations, we have opted for typical parameter values documented in existing literature (Shah et al., 2022). These specified values are outlined in Table 1.

Table 1: CGHE parameters in this study

	Description	Value
H	CGHE depth	100 m
d_{1o}	Outer diameter of outer pipe	0.160 m
d_{1i}	Inner diameter of outer pipe	0.148 m
d_{2o}	Outer diameter of inner pipe	0.086 m
d_{2i}	Inner diameter of inner pipe	0.080 m
d_b	Borehole diameter	0.200 m
k_g	Thermal conductivity of backfill material	1.5 W/(m·k)
k_{p1}	Thermal conductivity of outer pipe	40 W/(m·k)
k_{p2}	Thermal conductivity of inner pipe	0.4 W/(m·k)
$\rho_1 c_1$	Volumetric heat capacity of outer pipe	3.4×10^6 $(J/m^3 \cdot K)$ $\rho_2 c_2$
	Volumetric heat capacity of inner pipe	1.2×10^6 $(J/m^3 \cdot K)$ $\rho_g c_g$
Volumetric heat capacity of grout		5.0×10^6 $(J/m^3 \cdot K)$
M	Mass flow rate	1.2 kg/s
T_a	Atmospheric temperature	10 ℃
h_a	Convective heat transfer coefficient	15 W/(m2·k)

Zhang et al. (Zhang Yongcai, 2019) utilized a TCL thermal conductivity meter to measure frozen and unfrozen soil's thermal conductivity and volumetric heat capacity at varying moisture contents. He validated the mathematical model of heat transfer for soil freezing around U- GHE through sandbox experiments. In this study, we adopted soil parameters with different moisture content from the literature (Zhang Yongcai, 2019). Using formulas (14) and (15), we calculated the thermal conductivity of the two-phase zone, where T represents the temperature (K). The volumetric heat capacity of the two-phase zone was calculated based on the latent heat of the fusion of water, which is 334 kJ/kg. The measured data (Zhang Yongcai, 2019) and calculated results are shown in Table 2.

Table 1 Physical property parameters of soil under different moisture content

Moisture content (%)	Freezing temperature T_d (K)(variation range δ)	Thermal Conductivity W/(m·K)			Volumetric heat capacity $(kJ/m^3 \cdot K)$			Density (kg/m[3])
		Frozen zone	Two-phase zone	Unfrozen zone	Frozen zone	Two-phase zone	Unfrozen zone	
5	273.06 (2.0)	0.67	-0.14*T+38.84	0.53	1110.64	19808.98	1206.85	2228.09
10	273.04 (2.33)	1.04	-0.25*T+69.20	0.79	1170.13	36472.66	1363.72	2454.37
15	273.02 (2.54)	1.30	-0.27*T+74.92	1.03	1230.02	53136.21	1520.55	2624.25
20	273.00 (2.74)	1.56	-0.34*T+94.26	1.22	1290.98	69799.91	1677.42	2803.81

Soil influences the heat transfer of CGHE

Soil exhibits varied thermal physical properties at different moisture levels. The physical property parameters of soil at various moisture contents are detailed in Table 2. This section will configure the model parameters based on Table 2 and analyze the impact on CGHE heat transfer performance under soil moisture contents of 5%, 10%, 15%, and 20% over 100 hours of operation.

The F and NF models allow for the analysis of potential calculation discrepancies between the two models. In the NF model, which neglects moisture freezing, we assume that moisture behaves akin to antifreeze. Within model NF, ground parameters across strata are calculated by the equation (27) at any given temperature.

Equation 2: The *equation of* ground parameters $$p = (1 - \varepsilon)p_w + \varepsilon p_i$$

where p denotes ρc or λ, ε is the moisture content of soil.

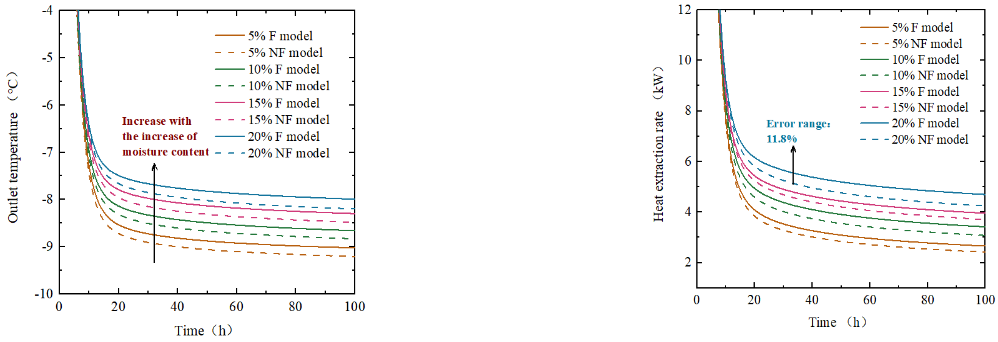

(a) Outlet temperature of F and NF model

(b) The heat extraction rate of F and NF model

Figure 8: Comparison of outlet temperature and heat extraction rate between model F and NF (Tin= -10℃, M=1.2 kg/s, Ta=15℃)

In our model, the freezing of ground moisture results in a rise in the soil's thermal conductivity, consequently leading to an increase in the heat extraction rate from the external soil to the CGHE. As depicted in Figure 8, irrespective of adding a soil freezing model, the CGHE outlet water temperature rises with increasing soil moisture content and decreases over time. Notably, when the moisture content is 20% under specified conditions, the fluid temperature at the CGHE outlet is -8.77 ℃ in the N.F. model and -8.49 ℃ in the F model. Within the considered parameters, a temperature discrepancy of 0.28 ℃ translates to a heat extraction rate difference of 817.44 W, representing an 11.8% increase in heat extraction rate compared to the N.F. model.

As shown in Figure 10(b), the borehole wall temperatures of the F model and N.F. model after 100 hours and 200 hours of operation are compared using the calculation model from this study. The calculation error between the F and NF models is 5.6%, and the temperature decreases by 0.38℃from 100 hours to 200 hours of operation. This discrepancy occurs because moisture in the soil releases latent heat during condensation, which slows down the rate of soil freezing. As a result, the borehole wall temperature is higher in soils with more incredible moisture content, and the soil temperature decreases as the moisture content decreases. It is essential to note the temperature discontinuities at the soil interfaces, which indicate a soil layer with significantly higher thermal conductivity than the adjacent layer. Consequently, the heat flux from the surrounding soil into this layer is more significant than in the adjacent layer, resulting in a higher soil temperature.

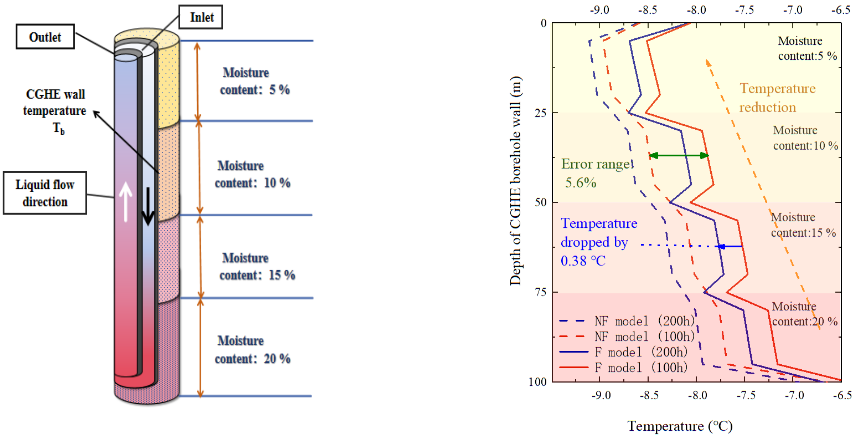

(a)The physical model consists of 4 types of soil. (b)Temperature variation of the borehole wall

Figure 10: Computational model and results of heterogeneous soil (Ta= -5 ℃, Tin= -10℃, M=1.2 kg/s)

5. CONCLUSION

The paper introduces a novel mathematical model for analyzing heat transfer within a shallow vertical CGHE and surrounding soil. This model considers soil heterogeneity and the geothermal gradient while also incorporating the freezing process of ground moisture at negative fluid temperatures. The water-ice phase transition is represented using the equivalent heat capacity method. Numerical implementation of the model is conducted using the finite difference method on a non-homogeneous spatial grid, assuming the axial symmetry of the problem. The model is implemented in a Visual environment on a personal computer, enhancing accessibility for abroad spectrum of specialists.

The influence of whether to add the soil freezing model on the calculation results was also analyzed in this study. After adding the soil freezing model, the outlet water temperature of CGHE increased by 0.28 ℃, and the heat extraction rate increased by 11.8% compared with the calculation model without the soil freezing model. The release of latent heat during freezing augments the heat extraction rate directed towards the CGHE, consequently elevating the outlet temperature of CGHE. In calculating heterogeneous soils with different water contents, the borehole wall temperature is higher in soils with more excellent moisture content, and the soil temperature decreases as the moisture content decreases. The temperature discontinuities at the soil interfaces indicate a soil layer with significantly higher thermal conductivity than the adjacent layer.

6. REFERENCES

Zhang, Y..Study on the freezing and heat transfer performance of the soil around the buried pipe heat exchanger in the cold climate area [D]. Donghua University, 2019.

Cai, W., Wang, F., Jiang, J., Wang, Z., Liu, J., & Chen, C. (2022). Long-term Performance Evaluation and Economic Analysis for Deep Borehole Heat Exchanger Heating System in Weihe Basin. Frontiers in Earth Science, 10, 806416. https://doi.org/10.3389/feart.2022.806416

Fang, L., Diao, N., Shao, Z., Zhu, K., & Fang, Z. (2018). A computationally efficient numerical model for heat transfer simulation of deep borehole heat exchangers. Energy and Buildings, 167, 79–88. https://doi.org/10.1016/j.enbuild.2018.02.013

Global Geothermal Update 2023: IGA unveils new key Geothermal Power & Direct Use data – International Geothermal Association.

Gnielinski, V. (2013). On heat transfer in tubes. International Journal of Heat and Mass Transfer, 63, 134–140. https://doi.org/10.1016/j.ijheatmasstransfer.2013.04.015

Li, P., Guan, P., Zheng, J., Dou, B., Tian, H., Duan, X., & Liu, H. (2020). Field Test and Numerical Simulation on Heat Transfer Performance of Coaxial Borehole Heat Exchanger. Energies, 13(20), 5471. https://doi.org/10.3390/en13205471

Shah, A., Krarti, M., & Huang, J. (2022). Energy Performance Evaluation of Shallow Ground Source Heat Pumps for Residential Buildings. Energies, 15(3), 1025. https://doi.org/10.3390/en15031025

Vasilyev, G., Peskov, N., & Lysak, T. (2022). Numerical Simulation of Heat Extraction by a Coaxial Ground Heat Exchanger Under Freezing Conditions. SSRN Electronic Journal. https://doi.org/10.2139/ssrn.4127025

#276：Fabrication of phase change thermal storage unit possesses water-proof and high mechanical strength

Hanze WEI[1], Ziao ZHENG[1], Chunyuan ZHENG[2], Bin LI[2], Bingchen ZHAO[2], Ziqing WEI[1], Xiaoqiang ZHAI[1]

[1] Institute of Refrigeration and Cryogenics, Shanghai Jiao Tong University, Shanghai, 200240, China
[2] Midea Group, Foshan, 528311, China

Abstract: Phase Change Material (PCM) has been brought to the fore by the blooming demands of large-scale energy storage. However, the PCM and Heat Transfer Fluid (HTF) are not supposed to contact each other directly due to the risk of leakage, which requires a heat exchanger to realize heat transfer. This may induce extra cost and lower overall heat storage efficiency. In this paper, a novel type of water-proof and high-strength Phase Change Thermal Storage Unit (PCTSU) is fabricated with the method of in-situ polymerization. The phase change material Polyethylene Glycol (PEG) is packaged and coated by Polymethyl Methacrylate (PMMA)/ Isobornyl Methacrylate (IBMA) co-polymer. The P(MMA-co-IBMA) structure renders the PCTSU with the ability to be leakage-free in a water environment and maintain macro shape at high temperatures. Thermal enhance filler Expanded Graphite (EG) is also added, for good measure, EG also plays a role as the second package structure to consolidate the shape-stable character. Mechanical strength and leakage test results validate that the fabricated PCTSU can keep the compression modulus of 5.83 MPa at 65 ℃. The PEG leakage is not detected under high-temperature water immersion environment, proving an ideal water-proof feature. Besides, the PCTSU possesses excellent thermal properties. The phase changes latent heat enthalpy can reach 132J/g, and the thermal conductivity can reach 1.499 W/(m·K), which renders the PCTSU with ideal heat storage capacity and power density. This new type of PCTSU may provide a high-efficiency solution for large-scale thermal storage equipment design.

Keywords: Shape-Stable Phase Change Material, Water-Proof, Mechanical Strength

1. INTRODUCTION

In the current context, the high-efficiency utilization of renewable energy is a scorching-hot issue with the depletion of traditional foilenergy. From the prospect of global energy supply chain decarbonization, the International Energy Agency (IEA) asserts that the share of renewable electricity generation will bounce beyond 30%.[1] Behind the stimulating data, it is unavoidable to notice that renewable energy possesses intrinsic defects such as intermittence and randomness, which impede the widespread application of renewable energy.[2,3,4] Effective energy storage technology is a promising way to remedy renewable energy's shortcomings in application. Among the available methods, the Latent Heat Thermal Energy Storage (LHTES) has been widely investigated and utilized in practice scenarios.[5] The innovative system stores and releases heat by phase change material (PCM), thereby contributing to the storage of heating/cooling energy with the merits of superior energy storage density compared with sensible heat thermal energy storage.[6] This feature endows LHTES with great application potential. Considering the phase change type, PCM can be categorized into solid-solid phase change, solid-liquid phase change, and liquid-gas phase change. [7,8] Among these, solid- liquid PCM is conspicuous for its wide-ranging phase change temperature and low volume change during the phase change process.[9] However, the intrinsic defects of low thermal conductivity and risk of leakage at melting state impede its further application. [10, 11]

Nowadays, PCM is not only screened by phase change enthalpy and phase change temperature but also considers more solutionsthat touch upon the practice application scenarios. To diminish the adverse effect brought about by such disadvantages, integratingPCM with heat exchangers is a plausible solution. [12,13] The integrated PCM heat exchanger usually places the PCM bulk in metal fin [14], shell [15], or tube [16] acting as the thermal conductivity enhancer and encapsulation structure simultaneously. Cui et al. [17] proposed a metal foam-fin hybrid structure phase change heat exchanger and a numerical analysis based on an artificial neural network was carried out to assess the heat transfer performance in an inclination container. At the inclination angle of 90°, the dimensionless time (Fo×Ste) reduced by 60.02 % compared with pure PCM, showing higher heat release efficiency. Shi et al. [18] evaluated the thermal performance of a heat changer filled with inorganic salt/expanded graphite as composite PCM and optimized by orthogonal experimental design. The simulation results elucidated that the comprehensive evaluation index of the longitudinally ribbed phase change heat exchanger is 1.91 and 0.78 for the heat storage and release process respectively, which is much higher than the finless heat exchanger. And the fin height makes the best contribution to the heat transfer performance by optimization results. Jia et al. [18] put forward a spherical phase change material capsule unit with a pin-fin structure, various configurations of pin-fin design are simulated to obtain the optimum pin-fin structure which has better heat transfer performance. Simulation results revealed that with the 6 fins inserted, the cold charging time was decreased by over 50 %. The optimized geometry configuration ofthe fin is that the ratio of length and diameter is 0.75 when the spherical phase change material capsule inner diameter is 20 mm. Ly et al. [20] manufacture the gyroid PCM heat exchanger based on the polymer 3D print method. The experiments of thermal performance were executed, and results showed that the charge and discharge time of the gyroid heat exchanger is 20% shorter compared with traditional shell-tube heat exchanger and the measured pressure drop was up to 44 % lower. It is worth noting that though the metal gyroid heat exchanger has much higher thermal conductivity, the polymer one still maintains the leading edge in unit mass heat transfer rate thanks to the low density. From the existing research on PCM heat exchangers, a thermally conductivestructure is essential to be inserted between PCM and HTF. This in-direct contact adds redundant thermal contact between PCM and HTF, which has an adverse effect on the improvement of overall heat transfer performance of heat exchanger. What's more, the metal structure or some complicated geometry is of high cost in production, which may impair the economic feasibility of large-scale applications. A solution to realize direct contact is indispensable and imperative.

To overcome the difficulties of direct contact between HTF and PCM, many efforts have been made. The solution can be categorized into material-orientation and structure-orientation. The material-orientation method focuses on the selection of PCM which is insoluble in water and separated by density difference. Khademi et al. [21] realized the direct contact between water and PCM by the unsolvable Oleic acid. Thanks to the density difference between Oleic acid in the melting state and solidification state, the PCM willsubmerge into water at the solidification state and float to the surface when melting, which creates a full contact pattern for PCM and water. Nomura et al. [22] designed a direct contact heat exchanger for PCM. In the research, erythritol was adopted as PCM, and oil was selected as HTF, which is insoluble with each other. Experimental test results indicated that the flow rate of HTF and the inlet temperature of HTF are the most important factors that have an impact on thermal storage performance. Fan et al. [23] raised the concept of an ejection PCM direct contact heat storage system, the sodium acetate trihydrate (SAT) was selected as thephase change material and ejected into the mineral oil by nozzle. The heat transfer process is completed during this process. For the structure-orientation method, the PCM is encapsulated or wrapped by a specific structure like a shell, coating film, or porous structure, which exerts physical isolation between PCM and HTF. Luo et al. [24] adopted polydopamine as a polymer-coated layer to facilitate rGO/PEG SSPCM composite with more competitive encapsulation and photothermal conversion properties. The experiment results indicated that the hydrophilicity of the PDA-coated surface was improved, and the thermal conversion efficiency lifted by 2.5%. Nevertheless, the entire water contact test is not being commenced, which may not reflect the actual water-proof ability. Suyitno et al. [25] preliminarily assessed a direct contact cascaded inorganic salty/HDPE PCM as moderate temperature heat storage material. Owing to the immiscible feature of the combination of inorganic salt and HDPE, the phase transition can occur solitarily, which omits the demand for buffering structure between two different PCMs. However, long-term stability is not validated in this research. For direct contact with the method of density difference and immiscibility. From a comparative view, the material- orientation solution achieves true direct contact, but the phase change process still happens macroscopically. This feature results in the multi-phase flow in the system which significantly increases the complexity of the system. What's more, the thermal conductivityof PCM is hard to modify due to its unorganized shape. As for the structure-orientation method, the shell and coating are the most common strategies adopted to actualize the goal. However, the solutions offered by existing researchers rarely examine the combination of protection structure and PCM, additionally, to ensure the leakage-proof property, the shell or coating film is thick which weakens the conception of direct contact.

Shape-stable phase change material (SSPCM) is an ideal solution to deal with the shape-stable issues during the phase change process, which is a promising way to fabricate phase change material heat storage unit.[26] SSPCM encapsulates PCM into a specific microstructure that can confine the PCM in a small space, preventing leakage. Considering the durability in long-term usage and ability to cope with extreme conditions. Mechanical property is a pivotal factor that should be considered in actual application. The heat storage unit ought to be intact under persistent high temperatures and pressure. Aimed at SSPCM, numerous methods have been proposed to optimize the mechanical properties of the material. Wang et al. [27] adopted porous fly ash ceramsite as the aggregate to confine paraffin by the method of vacuum impregnation. At the loading rate of 45.33 wt%, the paraffin leakage rate can be controlled under 3%, and the compressive strength of the sample can be over 3.5MPa. However, the tests were carried out at room temperature, for which the paraffin is in solid state. The results may not reflect the real strength of the material at melting state. Xiong et al. [28] fabricated carboxymethyl chitosan/boron nitride aerogel by sol-gel method and loaded with PEG as SSPCM. Experiment results showed that the compressive stress of SSPCM at 80% compressive strain can reach up to 12.18MPa with a PEG loading rate of 96%. The same problem occurred when the mechanical strength test did not involve the condition of PEG melting. What's more, the leakage-proof property needs further validation. Kastiukas et al. [29] selected expanded clay as lightweight aggregate (LWA) to impregnate the paraffin as the shape-stable phase change material. To endow the SSPCM with the feature of leakage-proof property, the polyester resin was coated to the surface of SSPCM, the test results reveal that the mass loss of PCM under 50℃3%. It's a pity that the thermal storage density is a little bit lower which is 57.93J/g. To develop the portable cold-chain food transfer bag, Tang et al. [30] synthesized water-based SSPCM using the conception of the EG-sodium polyacrylate (PAAS) network as the support material. The water was first soaked by EG's porous structure, then the in-situ polymerization was adopted to construct cross-link PAAS structure to enhance the mechanical properties of EG. Test results indicated that the thermal conductivity of the SSPCM has the potential to be over 5.60W/(m·K), while the phase change enthalpy reaches 263.1J/g. The maximum tensile stress at 10wt% PAAS is 0.351MPa, the maximum bending stress can reach 0.515MPa, which demonstrates a 142% and 390% improvement compared with the original EG based SSPCM. Yin et al. [31] used hot press method to fabricate PEG-based SSPCM which is supported and encapsulated by MXene framework. The thermal conductivity of the fabricated SSPCM reached 0.7013, and no visible leakage was observed at 70℃. The existing research on mechanical properties mainly focuses on SSPCM in the ambient temperature. However, once the temperature goes beyond the melting temperature, the liquid state will influence the overall mechanical property remarkably. The mechanical property urgently needs to be discussed in multi- temperature conditions which can reflect the shape-stable performance of SSPCM globally.

Different types of solutions had been investigated, which bring about crucial possibility to realize pragmatic direct contact PCM heatexchanger. However, most of them are confronted with quantities of barriers under the scenario of application orientation. The main obstacles retard the step can be summarized as follow:

(1) The SSPCM combines extraordinary mechanical property and high conductivity that needed to be developed in-depth.
(2) The anti-leakage when direct contact with HTF should be addressed in long-term use under the prerequisite of low system complexity.
(3) SSPCM should be easy and low-cost to be fabricated, which is compatible for large-scale production.

In this research, a novel type of spherical shape-stable Phase Change Thermal Storage Unit (PCTSU) that realizes direct contact with water meanwhile possesses exceptional mechanical properties offered by innovative encapsulation structure of P(MMA-co-IBMA) copolymer. What's more, taking advantage of the in-situ polymerization, the expanded graphite has the chance to be added as the thermal conducting filler. The characterization results show that the modulus of the fabricated shape-stable heat storage unit can reach 10.61 MPa at ambient temperature, and still maintain 5.83 MPa at the temperature of 65℃. The shape-stable heat storage unit is designed based on P(MMA-co-IBMA) co-polymer as the encapsulation structure which has much better mechanical properties compared with pure PMMA encapsulation structure. The co-polymer also can be used as a water-proof coating to endow the spherical PCTSU with the ability of water contacting, the long-term water submerge test with a high-low temperature cycle is executed, and results show no evidence leakage happend. Meanwhile, the thermal conductivity of the fabricated PCTSU can reach1.499 W/(m·K), which is over 6 times higher than the pure PEG, and the thermal conductivity has more potential to be improved with industry scale. The PCTSU is promising to be used in packed bed PCM heat exchangers, guiding the design and production of directcontact PCM heat exchangers.

2. METHODOLOGY

2.1 Materials

PEG with an average molecular weight of 6000 (PEG-6000) is supplied by Sinopharm Chemical Reagent Co., Ltd. Methyl methacrylate (MMA) is supplied by Shanghai Aladdin Biochemical Technology Co., Ltd. 2,2'-Azobis(2-methylpropionitrile) (AIBN) which is under recrystallization is provided by Shanghai Macklin Chemistry Co., Ltd. Isobornyl methacrylate (IBMA) is supplied by Shanghai Aladdin Biochemical Technology Co., Ltd. Besides, Expandable Graphite at a mean diameter of 75μm is supplied by Shanghai Aladdin Biochemical Technology Co., Ltd.

2.2 Preparation of expanded graphite

In this research, the high-temperature heating expanded method is selected to prepare the expanded graphite by expandable graphite. Expandable graphite is firstly dried in a drying oven at 60℃ for 8 hours. For the heating process, the dried expandable graphite is transferred to an iron crucible, and put into a muffle furnace, keeping for 40s at 950℃. After full expansion, the expanded graphite is obtained.

2.3 Fabrication of P (MMA-co-IBMA)/PEG/EG PCTSU.

The main method to fabricate the phase change heat storage unit is the in-situ polymerization, for which the PEG molecular can beencapsulated by P (MMA-co-IBMA) macromolecular during the continuous polymerization, and EG also has the chance to be added before the unit solidify completely. The preparation procedure is carried out as Fig. 1, whose details are as follows:

1) The PEG-6000 is heated to 80℃ with fully melted state and mixed with EG under the ultra-sonic treatment; 2) The mixture is putinto the vacuum drying oven configured with -1 bar and 80℃, and maintained for 8 hours ensures the completely absorption by layered structure of EG; 3) PMMA and IBMA are transferred to the three-neck flask with a mass ratio of 4:1, and the AIBN is also added as the polymerization initiator whose mass ratio is 3‰. The pre-polymerization commenced at 80℃ water baths along with 130 rpm stirring for 17 min; 4) The mixture of EG and PEG is injected into the polymer rapidly and stirred at the speed of 200rpm for 3 min; 5) Before the mixture become excessive viscous, it is poured into the spherical mold and put into the 65℃ drying oven for 8 h. 6) Remove the sphere-shape PCTSU from the mold. The PCTSU will be coated in the sequential procedure.

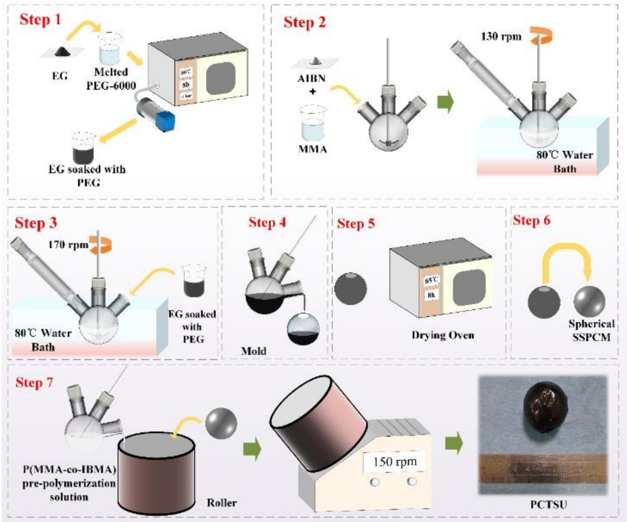

Figure 1: The fabrication procedure of PCTSU

2.4 Water-proof coating of spherical PCTSU

The water-proof coating is still based on the P(MMA-co-IBMA) polymer, which is adaptable for the fabricated PCTSU. The coating method is inspired by the fabrication of Chinese traditional food—rice dumpling, which can be referred to in Step 7 of Fig. 7. The co- polymer is coated uniformly on the surface of the heat storage unit during the continuous rolling. The operation process is presented below: 1) The pre-polymerization solution whose MMA and IBMA mass ratio is 4:1 is prepared with the same method which has been illustrated as step 2 in sub-chapter 2.5; 2) 3 wt% EG which has been grinded into small particle was added into the solution which can augment the thermal conductivity of coating film; 3) Pour the co-polymer into the roller loaded with pre-heated PCTSU, and rotate at the speed of 150 rpm for 3 min; 4) Fetch out the coated heat storage unit and put into the 80℃ drying oven for 8 hours for solidification. After the abovementioned steps, the PCTSUs with water-proof property are obtained.

2.5 Characterization

The Scanning electronic microscopic (SEM) (Rise-MAGNA, TESCAN) is used to obtain clear morphology image of samples. Before the measurement, the surface of samples is coated with carbon by surface carbon plating treatment in a vacuum evaporator (Q 150T ES, Quorum Technologies) for 15 s. The scanning is executed under vacuum conditions, the accelerating voltage is configured as 5 KeV. Water-proof property of the fabricated PCTSU is to avert PEG encapsulated in the unit to dissolve in water under the water immersion condition. The unit is put into a 100ml beaker filled with water. The beaker is placed in room temperature and 70℃ drying ovens in turns, and every temperature last for 24 hours. The unit is fetched out every 24 hours to be weighed. In the sameroutine, the remaining water is supposed to be dried up at 110℃'s drying oven, whose purpose is to check and quantify the PEG dissolved in water. The boiling point of PEG is around 250 ℃, which is well above the waters. The mechanical property is characterized by Dynamic Mechanic Analyzer (DMA), anticipating acquainting the strain-stress curve of the fabricated heat storage unit under compression condition. The test under room temperature is executed by Netsch Gambo and temperature above the melting temperature is tested by TA DMA Q850. The fabricated PCTSU is cut into the cube with the size of 7mm (Length)×7mm (Width)×5mm (Height), which is used as the test sample. The test model is selected as compression. For the room temperature test, the clamp adopted the 20mm disk-shape one while for the 65℃condition, the 10mm disk-shape clamp is applied. The curves are got under the strain ramp model, the strain ramp rate is chosen as 5 %/min, the maximum strain rate is 50%. The test terminates whenthe strain rate reaches the maximum or the mechanical failure is detected. The structure and chemical composition are detected byXRD (D8 Advance, Bruker) and FT-IR (Nicolet 6700, ThermoFisher) technologies. Phase change temperature range and latent heat enthalpy are measured by a Differential Scanning Calorimeter (DSC) (DSC8000, Perkin Elmer). The fabricated heat storage units are pre-treated to little bulk samples whose weight is in the range of 7-12mg. The prepared samples are placed in the aluminum crucibles and sealed by the solid compressor. The sealed crucible is put into the furnace, additionally, an empty crucible is also deployed in the furnace as the reference sample. Nitrogen is purged into the furnace at a flow rate of 20ml/min. The test step is as follow: 1) The furnace holds at the temperature of 10℃ for 1min. 2) When the heat flow is stable, the sample will go through a cooling process from 10℃to 70℃at a constant rate of 5℃/min. 3) The sample will keep 70℃for 1min. 4) A cooling process is carried out from 70℃to 10℃keeping the same temperature variation rate of 5℃/min. Thermal conductivity of the fabricated heat storage unit is characterized by Hot Disk method (TPS 2500, HotDisk). The test is carried out at room temperature, using the C5501 probe. The probe is sandwiched between two identical cylindrical shaped samples with the thickness of 13 mm and diameter of 39 mm. The thermal stability of SSPCMs is evaluated by Thermal Gravimetry Analyzer (TGA) (TGA5500, TA).

The heat storage and release test are carried out to depict the temperature-time curves. In this test, a micro thermal couple (TC-100, AIDIWEN Co,.Ltd) is placed in the center of the PCTSU during the fabrication procedure, tracking the temperature variation. The constant-temperature bath acts as the high-temperature source and a Dewar flask loaded with 50ml 10℃ water is applied as the low-temperature source. The unit is heated from 15℃ to 60℃, 62.5℃, 65℃, 67.5℃, and 70℃. Followed by an expeditious transferto dewar flask, the unit undergo a cooling process. The temperature of the unit's center and water in dewar flask are recorded by a data acquisition instrument (Keithley 2700, Tektronix).

3. RESULTS AND DISCUSSION

3.1. Morphology

The micro morphology scanned by SEM can be seen in Fig. 2. The layered structure of expanded graphite can be seen in Fig. 2 (a)- (b), for (a) shows the original EG and (b) reveal the EG soaked with PEG under the vacuum impregnation treatment. The image distinctively displays that the layered structure of EG is filled with PEG compared with the original one. No obvious vacant is observed in the vision. This feature gives substantial evidence that EG has the ability to load the PEG and cooperate with PMMA toform the double encapsulation structure. In Fig. 2 (b) and (c), the cross-linked structure is detected. Compared with the morphologyof PEG on the surface of EG, the cross-link structure is supposed to be regarded as PMMA polymer. The PMMA cross-link structure is avail of providing confinement for PEG and EG soaked with PEG, which fulfils the function of maintaining macro shape and being leakage-proof during the phase change process. The EG debris in the unit sample is presented in Fig. 2 (e) and (f). The EG are embedded in the composite and no visible gap or detachment is detected. The results prove excellent compatibility which guarantees the low contact thermal resistance between EG and PEG/PMMA.

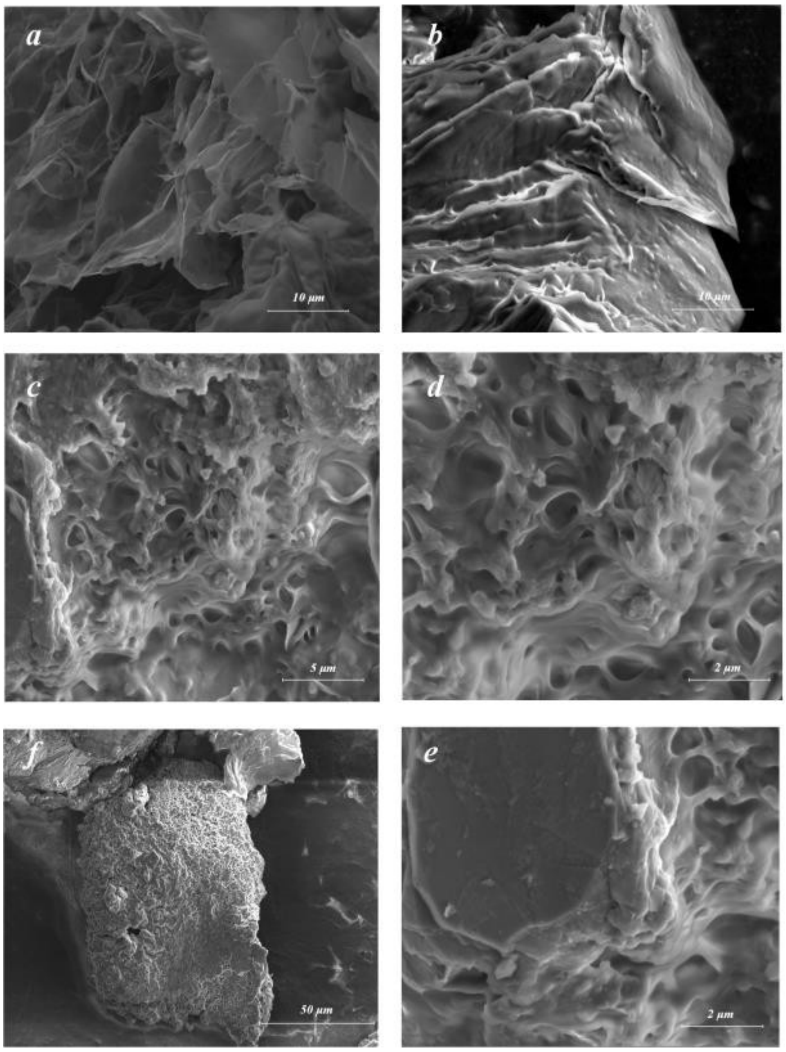

Figure 2: SEM images of samples (a) Layered structure of original EG (b) EG soaked with PEG (c) and (d) cross-link structure of PMMA (f) and (e)EG embedded in the PEG/PMMA composite

3.2. Water-proof property

In the water-proof property test, the spherical PCTSU contacts water directly with an alternative temperature environment. For each temperature lasting 24 hours, the ten-day test has validated the water-proof property of the fabricated PCTSU which detailed data is shown in Fig. 3 and Fig. 4. In Fig. 3, the leakage mass is evaluated followed by the method that has been introduced in the chapter
2.5. and the appearance of the sample during the test is exhibited either. The leakage mass data keeps stable at 0 which means there is no perceptible leakage occurred during the test, and no manifest macro change is observed. The test data is cogent to verify the waterproof property of the fabricated PCTSU. It is worth noting that the weight of the sample presents an upward trend, which can be expounded by the water absorption of P(MMA-co-IBMA). The macromolecular of P(MMA-co-IBMA) possessed the intrinsic property of swelling under the interaction of water. The water will go into the gap of the macro molecular which presents a weight increase from the macro view. During the test, the sample absorbs water mainly from day 3 to day 6 and eventually goes to a stable value. Though the water absorption existed, the water-proof performance is not weakened.

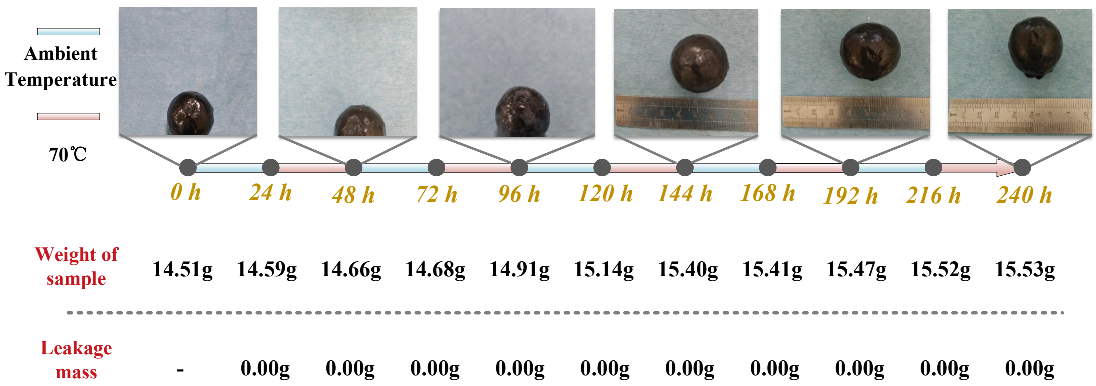

Figure 3: The leakage mass and change of appearance of the sample during the water-proof test

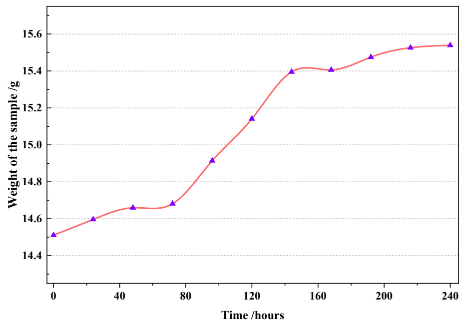

Figure 4: The variation trend of sample's weight during the water-proof test

3.3. Mechanical property

In the section on mechanical property, the strain-stress curve is the main property to be investigated, by which can derive the modulus of the material. Considering the application scenario of packed bed, the spherical PCTSU needs to be stacked layer by layer. So, the compression strength is a more important index. The compression strain-stress curves are present in Fig. 5. To assess the mechanical enhancement of the co-polymer, the unit encapsulated by PMMA is also tested. In Fig. 5 (a), the strain-stress curves of the PMMA encapsulation sample and P(MMA-co-IBMA) encapsulation sample under room temperature is displayed. Test results reveal that the overall curves are similar for the two encapsulation methods, nonetheless, the compression modulus of the P(MMA-co-IBMA) encapsulated one is much more conform with the linear form in the starting stage. The small discrepancy in overall modules is due to the high mass fraction of PEG. The PEG is in a solid state under room temperature which provides tremendous stiffness for the sample. The compression modulus of the PMMA encapsulation sample can reach 11.63 MPa while the 10.61 MPa for P(MMA-co-IBMA) encapsulation. However, as Fig. 5 (b) and (c) show, when the temperature comes to 65℃, assuring the PEG in a fully melting state. The strain-stress curves show many more differences Both of the two encapsulation methods possess the same curve shape, sequentially representing the elastic stage, plastic stage, and densified stage. But the modulus of P(MMA-co-IBMA) encapsulated one is much higher, which is over two magnitudes. Which still has a compression modulus of 5.83 MPa. The results prove the better mechanical property of co-polymer encapsulation owing to the higher rigidity of the co-polymer's molecules.

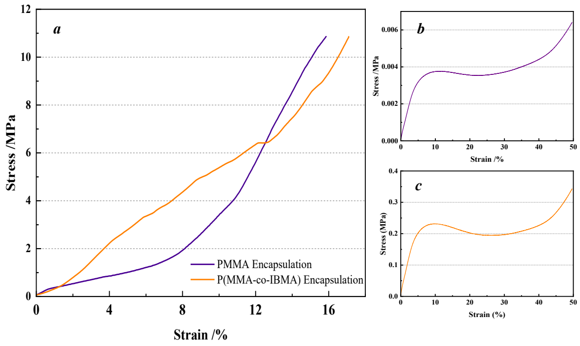

Figure 5: Strain-stress curves of PMMA and P(MMA-co-IBMA) encapsulation samples (a) Strain-stress curve under room temperature (b) Strain-stress curve of PMMA encapsulation sample under 65℃ (c) Strain-stress curve of P(MMA-co-IBMA) encapsulation sample under 65℃

3.4. Chemical composition and structure

The possible chemical interaction between the components in SSPCM can be investigated by the FT-IR method. Fig. 6 shows the FT-IR characteristic band of PMMA, PEG-6000, PCTSU sample without and with 6 wt% EG. According to Fig. 6, no new peak is observed in SSPCM's spectrum compared with pure components, which offers substantial evidence that there is no extra chemical reaction happening during the fabrication process.

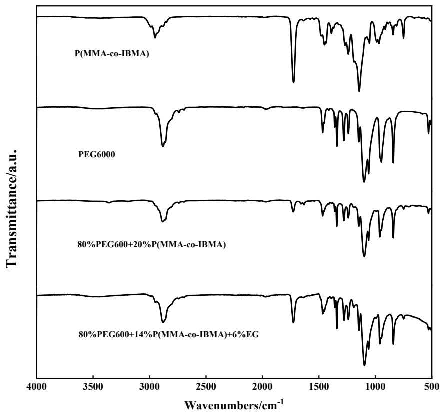

Figure 6: FT-IR spectrum of P(MMA-co-IBMA), PEG-6000, thermal storage sample without and with EG

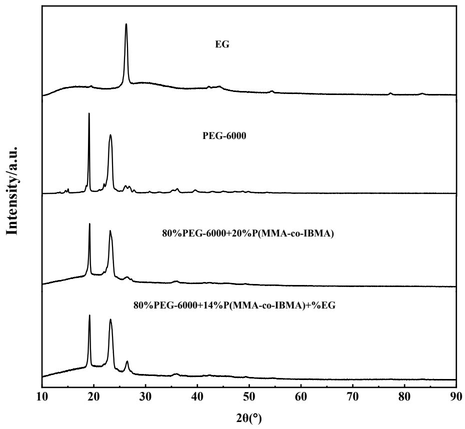

Figure 7: XRD spectrum of EG, PEG-800, PEG-6000, thermal storage sample without and with EG

Fig. 7 displays the XRD spectrum pattern of EG, PEG-800, and the fabricated unit with and without EG. The typical diffraction peaks of PEG-6000 are identical in those of fabricated samples, which confirms that the PEG-6000 exists crystalline state in the PCTSU. The intensity of the diffraction peak of PEG-6000 in fabricated samples is diluted owing to the reduction of mass fraction. In the sample with 6 wt% EG's spectrums, the PEG-6000 and EG's peaks are observed, no other peak is detected. The result suggests that P(MMA-co-IBMA) possesses amorphous properties.

3.5. Thermal property

The PCTSU's thermal properties are vital for the thermal storage function, which determines its performance. Thermal properties of the fabricated PCTSU comprise of phase change temperature, phase change enthalpy, thermal conductivity, and thermal stability. Fig. 8 shows the DSC curves of PEG-6000 and fabricated samples with different EG mass fractions, and the thermal conductivity data is shown in Fig. 9. The main thermal properties are also collected in Tab. 1. According to the DSC curves, the phase change temperature and enthalpy can be calculated. The peak phase change temperature for both melting and freezing of fabricated PCTSU are both slightly lower than the pure PEG-6000, this is the confinement effect of polymer, which can be explained by Gibbs-Thomson equation [32]. Under polymer encapsulation, the melting point variation is inversely proportional to the pore size. The cross-link structure of co-polymer stated in chapter 3.1 will split PEG bulk into small crystals and affect the melting point. In terms of phase change enthalpy, a decrease trend emerged after the encapsulation, significantly, the remaining phase change enthalpy compared with pure PEG-6000 is lower than the PEG, loading rate (80%). This phenomenon is also attributed to the confinement effect of polymer. For the thermal conductivity, the addition of EG can effectively improve the thermal conductivity of the PCTSU. When the mass fraction of EG reaches 6%, thermal conductivity of the unit gains the value of 1.499 W/(m • K), which is more than 6 times higher than the unit without EG addition, bringing a tremendous increase in the power of thermal storage and release.

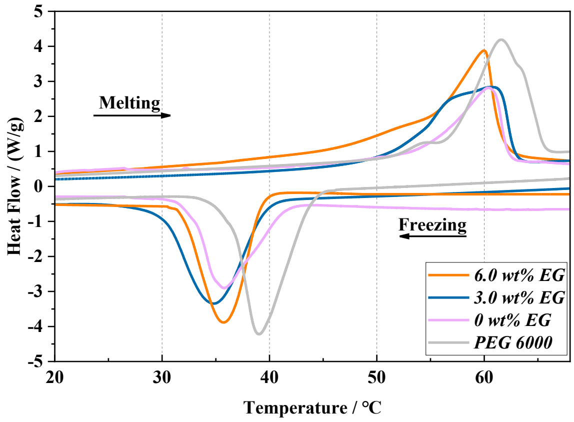

Figure 8: DSC curves

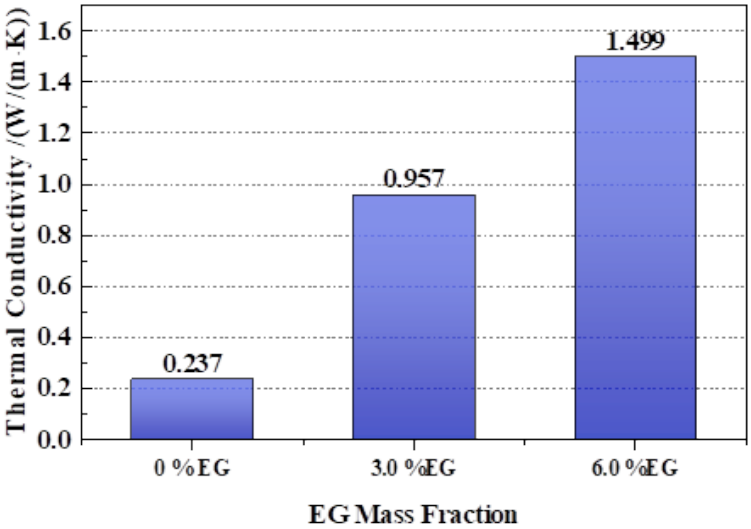

Figure 9: Thermal conductivity

Table 1: Main thermal properties summary of SSPCMs

	Melting Enthalpy	Peak Melting Phase Change Temperature	Freezing Enthalpy	Peak Freezing Phase Change Temperature	Thermal Conductivity
6.0 wt%EG	132.92 J/g	59.991 ℃	128.86 J/g	35.712 ℃	1.499 W/(m·K)
3.0 wt%EG	132.73 J/g	60.691 ℃	130.64 J/g	35.014 ℃	0.957 W/(m·K)
0 wt%EG	118.254 J/g	60.450 ℃	112.78 J/g	35.775 ℃	0.237 W/(m·K)
Pure PEG	191.713 J/g	61.589 ℃	187.921 J/g	39.242 ℃	-

The thermal stability of the fabricated unit is characterized by TG curves, referring to Fig. 10 and Tab. 2. For the fabricated

PCTSU, the curves give a clear one-stage degradation process, whose starting temperature is around 320℃ and finalize at around 470℃. The degradation temperature of the unit is much higher than the phase change temperature of PEG, confirming the thermal stability of the fabricated PCTSU. The remaining weight in the figure denote the EG whose melting temperature is over 1300℃. Compared with the pure P(MMA-co-IBMA), the fabricated PCTSU has a higher degradation temperature, suggesting that PEG has higher degradation temperature.

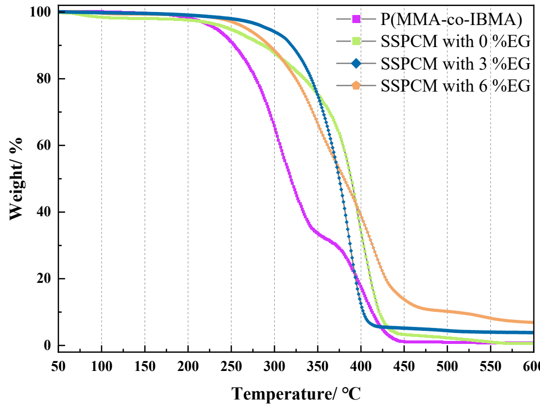

Figure 10: TG curves of P(MMA-co-IBMA) and unit with different EG mass fraction

Table 2: The results summary of SSPCMs' starting temperature of decomposition

EG mass fraction/ %	Starting temperature of Degradation/ ℃
P(MMA-co-IBMA)	276.37
0 %	346.22
3 %	348.92
6 %	328.93

The dynamic heat storage and release test is also carried out for different heat storage temperatures of 60℃, 62.5℃, 65.0℃, 67.5℃, 70℃, and the same release temperature of 15℃. Because of the difficulties in the fabrication of spherical shapes, the unit with 3 wt% EG is adopted in this test rather than the 6 wt% one. The heating and cooling curves are presented in Fig.11. In Fig. 11 (a), the heating process takes around 550s when the central temperature comes to a stable value. For the cooling process in Fig. 11 (b), the completion of release takes 550s either. However, both of the curves do not show an evident 'platform effect' caused by phase change latent heat. This may be due to the two following reasons: 1) The volume of the spherical PCTSU is too small that the phase change procedure is fast and hard to be detected in a curve; 2) The phase change temperature range of PEG-6000 is fairly large, which make the extra phase change enthalpy amortize into the wide range, causing the subtle 'platform effect'.

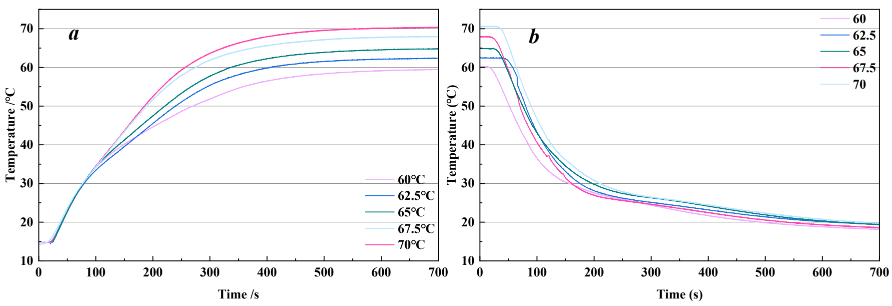

Figure 11: Dynamic heat storage and release curves of the single unit

4. CONCLUSION

In this paper, a novel type of PCTSU that can directly into contact with water is fabricated by P(MMA-co-IBMA) co-polymer encapsulation and coating method. The water-proof and mechanical properties are examined which guarantee the long-term use ofpacked bed phase change heat exchanger. Furthermore, the chemical structure and thermal properties are also characterized. Themain outcomes of this research are as follows:

1) A safe and easy method to fabricate the water-proof PCTSU is proposed. The P(MMA-co-IBMA) co-polymer play the role of supporting structure and water-proof coating layer simultaneously, which enable the PEG to contact directly with water and augment heat transfer efficiency. The water-proof test reveals that there is no visible leakage in long term water immersion with high-low temperature cycle.
2) The P(MMA-co-IBMA) and EG both act as the support structure to load PEG, which form the 'double encapsulation'. This method endows the PCTSU with high mechanical strength. The compression modulus at room temperature can reach

10.61 MPa. For 65℃, the co-polymer encapsulation sample still maintain the modulus of 5.83 MPa, which is two magnitudes higher than the PMMA encapsulation one.

3) The thermal properties are also investigated. After the encapsulation, the phase change enthalpy can still be over 130 J/g. With the addition of EG, the thermal conductivity of the PCTSU can reach 1.499 W/(m • K), which is 6 times higher than the sample without EG. The dynamic heat storage and release test further proves the high efficiency in heat transfer. TG test also validates the thermal stability, assures the durability in high temperature condition.

5. REFERENCES

[1] Kartal M, Pata U, Depre. O, et al, 2023. Effectiveness of nuclear and renewable electricity generation on CO2 emissions: Daily- based analysis for the major nuclear power generating countries. Journal of Cleaner Production 426, 139121.

[2] Chen L, Xie X., He J, et al, 2023. Wideband oscillation monitoring in power systems with high-penetration of renewable energy sources and power electronics: A review. Renewable and Sustainable Energy Reviews 175, 113148.

[3] Khalid M, Ahmed I, AlMuhaini M, et al, 2024. A novel computational paradigm for scheduling of hybrid energy networks considering renewable uncertainty limitations. Energy Reports, 11, 1959-1978.

[4] Ren F, Wei Z, and Zhai X, 2022. A review on the integration and optimization of distributed energy systems. Renewable and Sustainable Energy Reviews, 162, 112440.

[5] Liu K., Wu C., Gan H, et al, 2024. Latent heat thermal energy storage: Theory and practice in performance enhancement basedon heat pipes. Journal of Energy Storage, 97: 112844.

[6] Mukherjee S, Meshram H, Rakshit D, et al, 2023. A comparative study of sensible energy storage and hydrogen energy storageapropos to a concentrated solar thermal power plant. Journal of Energy Storage 61, 106629.

[7] Lopez-Morales J, Serrano A, Centeno-Pedrazo A, et al, 2024. Bis (dialkylammonium)-based hybrid organic–inorganic ionicmaterials as solid–solid phase change materials. Chemical Engineering Journal, 495, 153501.

[8] Wang C, Geng X, Chen J, et al, 2024. Multiple H‐Bonding Cross‐Linked Supramolecular Solid–Solid Phase Change Materialsfor Thermal Energy Storage and Management. Advanced Materials 36.11, 2309723.

[9] Lin L, Yang D, Luo Z, et al, 2023. Numerical study on melting and heat transfer characteristics of vertical cylindrical PCM with a focus on the solid-liquid interface heat transfer rate. Journal of Energy Storage 72, 108370.

[10] Yang W, Lin R, Li X, et al, 2023. High thermal conductive and anti-leakage composite phase change material with halloysitenanotube for battery thermal management system. Journal of Energy Storage 66, 107372.

[11] Tripathi B, Shukla S, and Rathore P, 2023. A comprehensive review on solar to thermal energy conversion and storage using phase change materials. Journal of Energy Storage 72, 108280.

[12] Herbinger F, and Dominic G, 2022. Experimental comparative analysis of finned-tube PCM-heat exchangers' performance. Applied Thermal Engineering, 211, 118532.

[13] Togun H, Sultan H, Mohammed H, et al, 2024. A critical review on phase change materials (PCM) based heat exchanger:different hybrid techniques for the enhancement. Journal of Energy Storage 79, 109840.

[14] Moradian A, Mohammad A, andSahand M, 2022. Melting expedition in horizontal triplex tube heat exchangers via radial and combined radial-axial fins. Journal of Energy Storage, 56, 106129.

[15] Li B, Zhai X, and Cheng X, 2019. Thermal performance analysis and optimization of multiple stage latent heat storage unit based on entransy theory. International Journal of Heat and Mass Transfer, 135, 149-157.

[16] Li B, Zhai X, and Cheng X, 2018. Experimental and numerical investigation of a solar collector/storage system with composite phase change materials. Solar Energy, 16, 65-76.

[17] Cui W, Si T, Li X, et al, 2022. Heat transfer analysis of phase change material composited with metal foam-fin hybrid structure in inclination container by numerical simulation and artificial neural network. Energy Reports, 8, 10203-10218.

[18] Shi J, Wang L, Chen S, et al, 2024. Thermal performance of phase change material based heat exchanger filled with inorganic salt/expanded graphite. Journal of Energy Storage, 87, 111240.

[19] Jia X, Zhai X, and Cheng X, 2019. Thermal performance analysis and optimization of a spherical PCM capsule with pin-fins for cold storage. Applied Thermal Engineering, 148, 929-938.

[20] Ly D, Kishi Y, Nakayama T, et al, 2024. Thermal performance of polymer gyroid heat exchangers combined with phase change materials as a latent heat thermal energy storage system: An experimental investigation. International Journal of Heat and Mass Transfer, 226, 125531.

[21] Khademi A, Darbandi M, Schneider G, et al, 2023. A comparative study of melting behavior of phase change material with direct fluid contact and container inclination. Energy Nexus, 10, 100196.

[22] Nomura T, Tsubota M, Oya T, et al, 2013. Heat release performance of direct-contact heat exchanger with erythritol as phase change material. Applied Thermal Engineering, 61.2, 28-35.

[23] Fan D, Zhao W, Tian Y, et al, 2021. Ejection and breakup behaviors of a novel direct contact thermal storage using ejection PCM. Journal of Energy Storage, 36, 102409.

[24] Luo W, Zou M, Luo L, et al, 2024. Efficient enhancement of photothermal conversion of polymer-coated phase change materials based on reduced graphene oxide and polyethylene glycol. Journal of Energy Storage, 78, 109950.

[25] Suyitno B, Pane E, Rahmalina D, et al, 2023. Preliminary characterization and thermal evaluation of a direct contact cascaded immiscible inorganic salt/high-density polyethylene as moderate temperature heat storage material. Results in Materials 19, 100443.

[26] Umair M, Zhang Y, Iqbal K, et al, 2019. Novel strategies and supporting materials applied to shape-stabilize organic phase change materials for thermal energy storage–A review. Applied energy, 235, 846-873.

[27] Wang X, Li W, Huang Y, et al, 2023. Study on shape-stabilised paraffin-ceramsite composites with stable strength as phase change material (PCM) for energy storage. Construction and Building Materials, 388, 131678.

[28] Xiong H, Gu L, Niu C, et al, 2024. Shape-stable phase change materials based on carboxymethyl chitosan/boron nitride nanosheets high-strength aerogel. Diamond and Related Materials, 145, 111126.

[29] Kastiukas G, Zhou X, and Castro-Gomes J, 2016. Development and optimisation of phase change material-impregnated lightweight aggregates for geopolymer composites made from aluminosilicate rich mud and milled glass powder." Construction and Building Materials, 110, 201-210.

[30] Tang L, Ling Z, Zhang Z, et al, 2024. Enhanced mechanical and thermal properties of expanded graphite/ice phase change materials through in-situ polymerization of sodium polyacrylate in cold chain logistics. Chemical Engineering Journal , 152869.

[31] Yin G, Lopez A, Collado I, et al, 2024. MXene multi-functionalization of polyrotaxane based PCMs and the applications in electronic devices thermal management. Nano Materials Science.

[32] Scalfi L, Coasne B, Rotenberg B, 2021. On the Gibbs–Thomson equation for the crystallization of confined fluids. The Journal of Chemical Physics, 154.11, 114711.

#278: Research on the flexible photovoltaic cell in different bending forms

Xinyi TIAN[1], Jun WANG[2], Jie JI[3]

[1] Department of Thermal Science and Energy Engineering, University of Science and Technology of China, Hefei, Anhui, China, txy0818@mail.ustc.edu.cn
[2] Department of Environmental and Energy Engineering, Anhui Jianzhu University, Hefei, Anhui, China, wj0412@mail.ustc.edu.cn
[3] Department of Thermal Science and Energy Engineering, University of Science and Technology of China, Hefei, Anhui, China, jijie@ustc.edu.cn

Abstract: Flexible photovoltaic cells maintain high photoelectric conversion efficiency whose superior flexibility indicates the huge potential to integrate with complex surfaces, such as curved building exterior envelopes, portable smart devices, nonplanar vehicle skins, etc. Different from the planar-type PV, the varied application scenarios and complicated system design lead to the non-uniform solar irradiance distributed among the flexible solar cell's total irradiance receiving region, which requires refined model establishment to describe and analyse the cell's photoelectric performance. In this paper, the utilization of flexible solar cells was reviewed. Then experimental study was conducted in a laboratory environment to research on the photoelectric performance by flexible CIGS cells under specific working conditions (bending the solar cell into different arc-shaped forms assisted by the 3-D printing bases). Simulation workflow for the photoelectric theoretical model of the flexible solar cell under non-uniform illumination distribution causedby different bending forms is proposed and verified using the experimental results. The combined optical-electrical model is based on the single-diode model of the solar cell and the current continuity equation. Finite element method is applied to investigate the emitter and the finger regions' voltage and current density respectively. Simplified method to predict the bended PV cell's photoelectric power is proposed and the calculation deviation with the two-dimensional mathematical model is compared. The electrical power output by the flexible cells in different bending forms (cylindrical, semi-elliptic, parabolic) is investigated simulativelyto provide guidance for designing curved surfaces.

Keywords: Flexible PV; Experimental Study; Model Validation; Parametric Analysis; Photoelectric Performance

1. INTRODUCTION

According to “Renewable energy capacity statics 2023” by IRENA (IRENA (2023)), renewable energy accounted for 40% of the installed global power capacity whose generation capacity expanded by 295 GW at the end of 2022. Solar photovoltaic power predominates the market of solar energy with an increase of solar PV of 191450 MW throughout 2022. PV effect could utilize the power from natural sunlight and convert solar energy into clean and useful electricity power, offering a sustainable solution to the energy dilemma. The traditional silicon solar cells, including polycrystalline and monocrystalline silicon cells, hold a dominant position in the commercial photovoltaics market, accounting for over 80% of the market share. Recently, with the in-depth study of the advanced solar cells’ materials and structure, new generations of solar cells like thin-film cells and perovskite cells are growing in leaps and bounds, whose main development direction is the enhancement of solar cells’ good physical characteristics and high photoelectric conversion efficiency (Boulmrharj*, et al.*, 2022).

Flexible photovoltaic technology has drawn widespread attention to satisfy the demands for device development with high flexibility, lightweight, and complex surface structures. The novel use cases include curved building-integrated photovoltaics, PV-powered wearable devices, vehicle-integrated photovoltaics, etc. Various advanced flexible PV cells are fabricated and manufactured commercially in China, such as large-sized flexible crystalline silicon cells (Sunman Energy Co,. Ltd) and flexible copper indium gallium selenide (CIGS) cells (Kaisheng New Energy Co,. Ltd). Liu et al. employed the edge-blunting technique to improve the silicon wafers’ flexibility and manufacture the large-scale high-flexible silicon module (efficiency over 24%) (Liu*, et al.*, 2023). Yin et al. first encapsulated the PV module with self-developed polymer composite materials instead of the conventional glass cover; the metal frame is replaced by the sol-gel technique to ensure the module’s lightweight and flexibility, leading directions for the new light PV roof installation (Yin*, et al.*, 2023).

Researchers are committed to using flexible PV’s easy-bending characteristics to develop new concepts and structures. A commercial flexible monocrystalline silicon solar panel was used by Wang et al. to fabricate a curved photovoltaic-thermal system (Wang*, et al.*, 2024). Serpentine composite channels were combined with the curved PV/T units to comprise the water-heating module and provide domestic hot water for building users. Compared with the simple PV module with the same geometrical shape,the curved PV/T unit enhances the electrical efficiency and thermal efficiency by 17.33% and 22.79% under the south façade installation. Wang et al. took inspiration from the renowned Hui-style building, characterised by its distinctive pitched roof adorned with black curving tiles (Wang*, et al.*, 2022). Flexible thin-film PV cells were pasted on the curved absorb plates to imitate the traditional architectural characteristics. Multi-functions were designed including electricity generation, domestic hot water supply, active air heating, and ventilation to meet the different needs of the building users. Cai et al. integrated the curved PV ventilated facade with the heat pump system which could run cooling mode and heating mode. In the experiment under cooling mode, the curved flexible PV module got electrical efficiency improvement by 34.43%; in the experiment under heating mode, the curved façade could raise the system’s COP by 5.23% (Cai*, et al.*, 2024).

As the literature review shows above, the flexible PV technology has gained a lot of attention and been applied to innovative complicated energy scenarios. To explore the flexible PV cell’s performance designed in the curved form, this study focuses on thedecoupling method of the photoelectric model of the curved flexible PV cell bent in different forms, which involves the non-uniform illumination distribution determination, the extraction of the five key parameters of the studied PV cell, and the two-dimensional current density & voltage distribution calculation using finite element method (FEM). Experimental setup is established to measure the current-voltage curves and power-voltage curves of a flexible CIGS cell in the arc-shaped forms (central angle: 60°, 90°, 120°) to verify the theoretical model. Photoelectric performance by the cell in several bending forms with different geometrical parametersare compared to investigating the changing tendency of power at maximum power point and the normalized performance conversionefficiency.

2. MATERIALS AND METHODOLOGY

In this section, the experimental setup for the photoelectric performance test of the flexible bended PV cell is presented; then the mathematical modelling is established, including the non-uniform illumination distribution, the five parameters extraction method, and the two-dimensional current density & voltage distribution determination. To evaluate the bended PV cell’s photoelectric conversionprocess, $NPCE$ (i.e., normalized performance conversion efficiency) is introduced.

2.1. Experimental setup

To investigate the photoelectric performance by the flexible PV cell bended in the specific shape, 3D printing technology is applied to make the curved base. Three arc-shaped resin bases are printed whose central angles are 60°, 90°, and 120° respectively shownin Figure 1. A flexible CIGS cell sample (97.50 mm length and 43.75 mm width) is adhered to the curved base to present the curved PV pattern. The specification of the PV sample under standard testing condition (STC) refers to Table 1. A solar simulator (Oriel AAA 94043a, equipped with a 450 W Xenon lamp and an AM 1.5 filter) emits a standard light source with an intensity of 1000 W/m^2 (light spot size: 100 mm × 100 mm). The bended flexible cell is linked with the standard source measure units (Keithley series 2400) andthe current-voltage curve is measured using the four-point probe method.

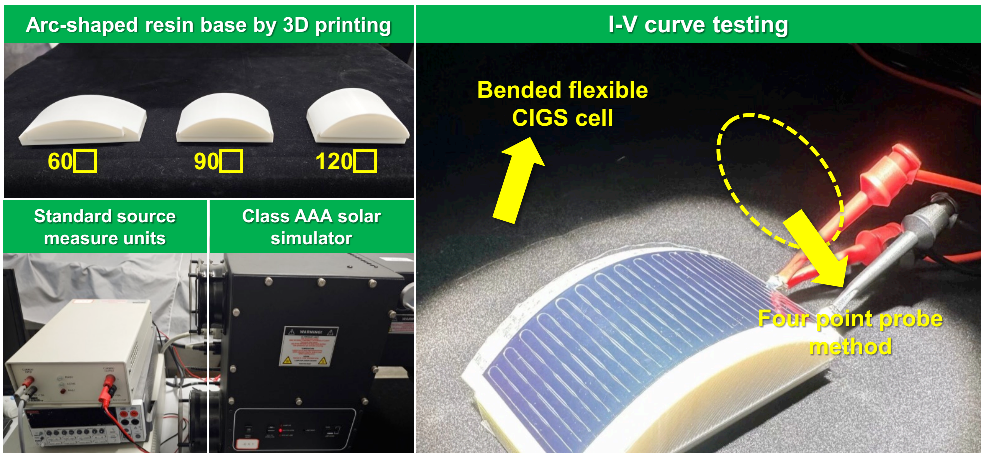

Figure 1: Actual photo of the experimental setup for the arc-shaped flexible PV cell with different central angles

Table 1: Specification of the PV sample used for the study (STC: 1000 W/m^2 AM 1.5, 25 °C)

Parameters	Value (unit)
Cell length	97.50 mm
Cell width	43.75 mm
Finger width	0.25 mm
Parallel finger space	3.00 mm
Film thickness	2.50 μm
Welding strip width	4.00 mm
Emitter (AZO) sheet resistance	25 Ω/□
Finger resistance per unit length	1.233 Ω/Ft
Short current under STC (I_{sc})	1.381 A
Open voltage under STC (V_{oc})	0.674 V
MPP current under STC (I_{mp})	1.242 A
MPP voltage under STC (V_{mp})	0.534 V
Short current temperature coefficient (α_{sc})	0.008%/K
Open voltage temperature coefficient (β_{oc})	-0.28%/K

The mathematical photoelectric modelling is decoupled and evaluated to describe the photoelectric performance of the bended flexible PV cell.

Non-uniform illumination distribution

To describe and simulate the stated non-uniformity quantitively, the optical design software *LightTools* is used to simulate the irradiance distribution among the nonplanar surface of the designed flexible PV device. The light source setting refers to the solar simulator used in the experiments. The 3D model file by *SolidWorks* (sldprt) is imported into *LightTools* and the nonplanar surface concerned is selected as the receiver. The numbers of the illuminance mesh of the curved surface are 100×100. The illumination simulation is conducted employing Monte-Carlo ray-tracing method, where the number of rays is set as 25 million.

Five parameters extraction methods

The single-diode model can describe the photoelectric performance of the photovoltaic cell, which requires five key parameters of the studied PV cell (Et-torabi, *et al.*, 2017) (photocurrent I_{ph}, diode reverse saturation current I_o, equivalent series resistance R_s, equivalent shunt resistance R_{sh}, diode ideal factor a). Shockley diode equation describes the single-diode model accurately, see Equation 1.

Equation 3: Single-diode model of the PV cell

$$I = I_{ph} - I_d - I_{sh} = I_{ph} - I_o\left[\exp\left(\frac{V + IR_s}{a}\right) - 1\right] - \frac{V + IR_s}{R_{sh}}$$

Where

– I_{ph} = Photocurrent (A)

- I_o = Diode reverse saturation current (A)
- R_s = Equivalent series resistance (Ω)
- R_{sh} = Equivalent shunt resistance (Ω)
- a = Diode ideal factor
- V = Voltage (V)
- I = Current (A)

There are several methods for the extraction of the five key parameters, such as iterative methods and analytical methods. In this study, the five parameters are extracted by the iterative method driven by Gauss-Seidel iterative algorithm, whose specific procedure refers to literature (Et-torabi, *et al.*, 2017). Based on the five parameters under standard testing conditions, the five parameters under real working conditions can be obtained according to the rules of conversion, see Equation 2.

Equation 4: PV cell's five parameters conversion rules

$$\begin{cases} a = a_{STC}T/T_{STC} \\ R_s = R_{s,STC}T/T_{STC}(1 - 0.217\ln(\frac{G}{G_{STC}})) \\ R_{sh} = R_{sh,STC}G_{STC}/G \\ I_o = I_{sc}(T)/\exp(V_{oc}(T)/a) \\ I_{ph} = G/G_{STC}I_{ph,STC}(1 + \alpha_{sc}(T - T_{STC})) \end{cases}$$

Where:

- $I_{sc} = I_{sc,STC}(1 + \alpha_{sc}(T - T_{STC}))$ = Short current under the real working condition (A)
- $V_{oc} = V_{oc,STC}(1 + \beta_{oc}(T - T_{STC}))$ = Open voltage under the real working condition (V)
- T = PV cell temperature under real working condition (K)
- T_{STC} = PV cell temperature under STC (K)
- G = solar irradiance under real working condition (W/m^2)
- G_{STC} = solar irradiance under STC (W/m^2)

Based on the five parameters extracted by the iterative method, the combined current-voltage relationship in Equation 1 could be decoupled by use of LambertW function (Appelbaum*, et al.*, 2014). Subsequently, it is able to draw the I-V curve under the real working condition and capture the maximum power point.

Two-dimensional current density & voltage distribution determination

The front surface of the flexible PV cell follows the two-dimensional current continuity equation, see Equation 3 (Lu*, et al.*, 2020).

Equation 3: Two-dimensional current continuity equation

$$-\nabla \cdot (\sigma \nabla V - J^e) = Q_j$$

Where:

- V = Electric potential (V)
- J^e = Current density (A/m^2)
- Q_j = Current source term (A/m^2)
- σ = Sheet conductivity of the material in the domain (Ω^{-1}m^{-1})

The conductivity of the emitter part σ_e equals to $\frac{1}{R_{sheet}t_e}$, where R_{sheet} is emitter sheet square resistance (Ω/m), t_e is emitter depth (m). The conductivity of the finger part σ_f equals to $\frac{1}{R_L W_f t_f}$, where R_L is finger resistance per unit length (Ω/m), W_f is finger width (m), t_f is finger depth (m). The generated current density of the lightened emitter part is $Q_{j,e} = (I_{ph} - I_d - I_{sh})/A$ while the current density of the dark part can be expressed as $Q_{j,f} = (-I_d - I_{sh})/A$.

The solving of two-dimensional current continuity equation is conducted by the finite element method (FEM), which can be executed on *COMSOL Multiphysics* (Mellor*, et al.*, 2009). Front side of the flexible PV cell is separated as emitter region and finger region, and meshed respectively. The boundary conditions include: 1) interface condition: applied to the entire simulation domain to ensurethe current continuity through the internal boundaries of different media; 2) electrical insulation: the outer boundary of the simulation domain is considered to be electrically insulated; 3) electrical potential for external load: the ends of the welding strip are connectedwith the external load and the electrical potential is equal to the working voltage of the PV cell.

Performance evaluation

To evaluate the bended flexible PV cell's photoelectric performance, the normalized power conversion efficiency ($NPCE$) is introduced in this study to characterise the cell's electrical power conversion efficiency as shown in Equation 4.

Equation 5: Normalized performance conversion efficiency ($NPCE$)

$$NPCE = \frac{P_{mp}}{GA_n} \times 100\%$$

Where:

- $NPCE$ = Normalized performance conversion efficiency (%)
- P_{mp} = Electrical power under the maximum power point (W)
- G = Solar irradiance intensity per area transmitted by the solar simulator (W/m^2)
- A_n = Normalized area of the PV cell (m^2)

2.3. Simulation workflow

Based on the afore-mentioned modelling establishment, the simulation workflow is conducted. The special bending form is designed in the 3D software. Then, the 3D model file is imported into the optical system modelling software *LightTools* to obtain the non- uniform illumination distribution data among the nonplanar PV cell lightened by the standard solar simulator. The photoelectric parameters of the PV cell under STC are input into the program for the PV five parameters extraction on *MATLAB* to calculate the current density of the illuminated and the dark areas. Next, the two-dimensional electric field model of the flexible PV cell is built and decoupled in *COMSOL Multiphysics* to output the 2D current density and voltage distribution of among the bended PV cells. The current-voltage curve is depicted, and the maximum power point is tracked.

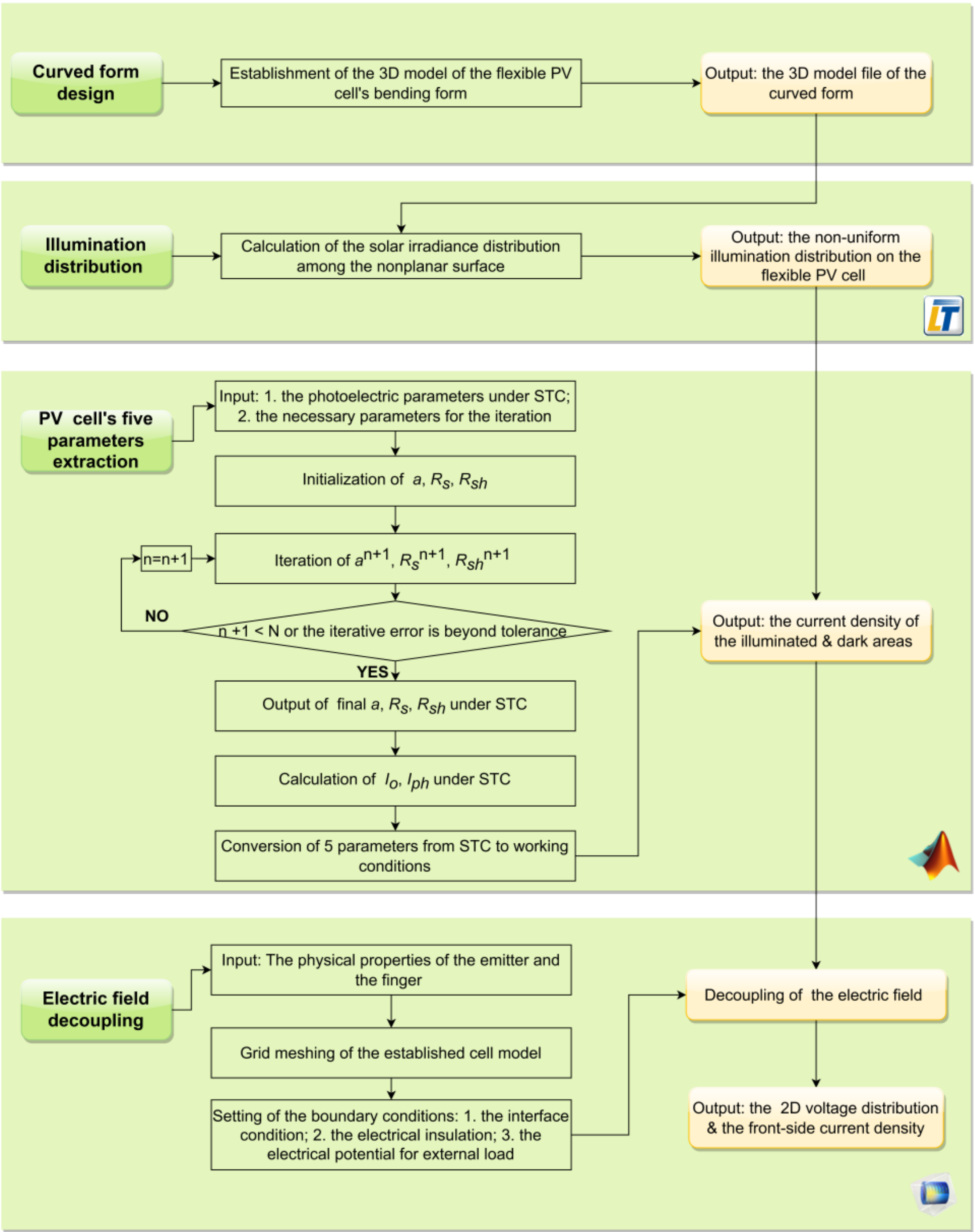

Figure 2: The flowchart of the simulation workflow for the photoelectric performance analysis of the bended flexible PV cell

3. RESULTS AND DISCUSSION

In this section, the theoretical modelling is verified by the experimental study; the two-dimensional front surface current density andthe voltage distribution is analysed; then, the parametric analysis is conducted to investigate the photoelectric performance by the flexible PV cell in different bending forms (cylindrical, semi-elliptic, parabolic).

3.1. Model validation

The theoretical model is validated by the experimental data collected under the laboratory conditions. The indoor temperature of the laboratory is set as 25 °C. The current-voltage curves and the power-voltage curves by the arc-shaped flexible PV cell with the central angle of 60°, 90°, and 120°. P_{mp} are 0.650 W, 0.564 W, and 0.534 W respectively; $NPCE$ are 15.946%, 14.654%, and 15.086% respectively. Figure 3 presents the comparison of the experimental and simulated results of the I-V curves and P-V curves (scatter graph: experimental results; line graph: simulated results). As shown in the figure, the simulation fits well with the measured data.

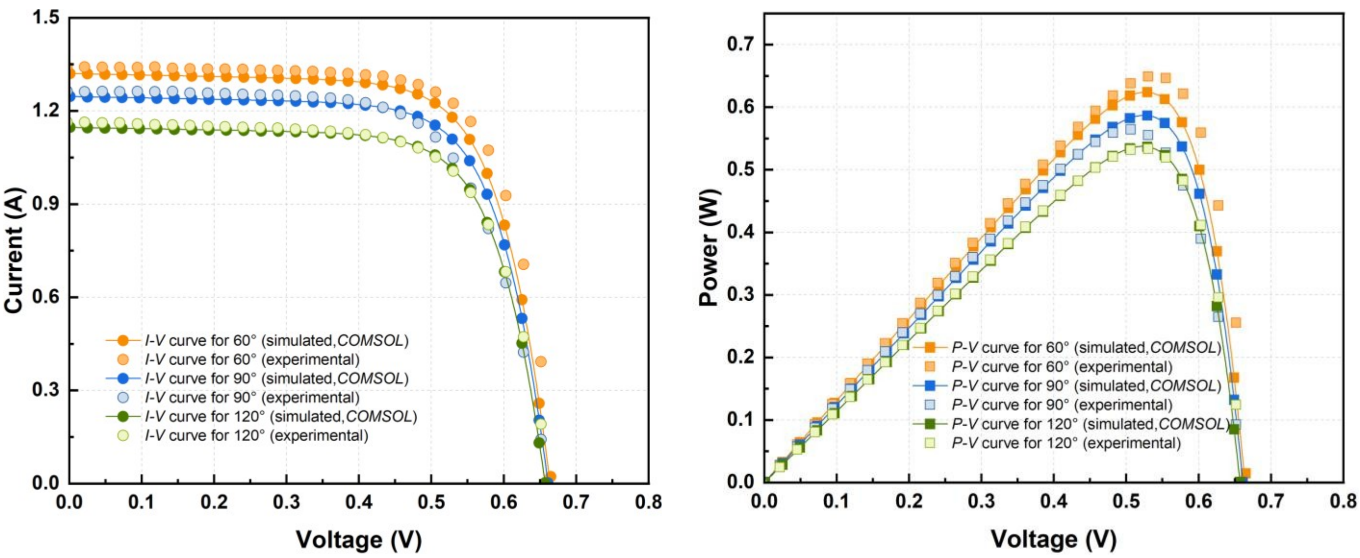

(a) (b)

Figure 3: The comparison of the experimental and simulated results of the I-V curves and P-V curves by the flexible PV cell with the central angle of60°, 90°, and 120°

The decoupling of the photoelectric model based on the finite element method takes account of the two-dimensional non-uniform solar irradiance distribution among the front-side of the flexible PV cell, but the decoupling process would take a lot of time and computing resources. To simplify the coupled photoelectric model, it is assumed that the solar irradiance is distributed on the bended flexible PV cell uniformly while the total solar irradiance intensity keeps the same as the actual non-homogeneous solar irradiance distribution. Based on this assumption, the equivalent solar irradiance could be imported into the single-diode model to obtain the five parameters under real working conditions and the *I-V* curve could be drawn to capture P_{mp}. The comparison of the experimental and the simulated results by two different methods is illustrated in Table 2. For the PV cell combined with three arc-shaped forms, the relative deviation between the experimental and the *COMSOL* simulated results are 4.0%, 4.08%, and 0.56% respectively, which is an acceptable range. The simulated results calculated by the simplified model have a 3.07%, 4.96%, 1.31% relative deviation. Therefore, it is reasonable to utilize the simplified model to conduct the P_{mp} prediction quickly and precisely.

Table 2: Comparison of flexible PV cell's photoelectric power at maximum power point (experimental & simulated)

Arc-shaped form type	Photoelectric power at maximum power point (W)		
	Experimental result	Simplified simulated result	*COMSOL* simulated result
60°	0.650	0.630	0.624
90°	0.564	0.592	0.587
120°	0.534	0.541	0.537

3.2. Front surface voltage distribution and current density

The two-dimensional electric field simulation is conducted by *COMSOL* and the related 2-D images are plotted. Take the bended flexible PV cell with the central angle of 120° for example. The irradiance distribution among the curved PV cell is symmetrical. Thehighest solar irradiance is 1000 W/m^2 located in the middle of the cell while the lowest irradiance appears at both ends of the cell (value: 519.54 W/m^2). Figure 4(a) presents the voltage distribution among the front side of the bended PV cell. It could be observedthat the lowest junction voltage is distributed in the left and right regions where is near the end of the welding strip (0.520 V, also V_{mpp} for the whole cell). In the red region located under the middle of the PV cell, the junction voltage comes to 0.552 V which is the highest value among the studied regions. There, the photogenerated current flow needs to overcome bigger resistance of the emitter film and finger due to the long distance to arrive the end of the welding strip.

Illuminated by the irradiance, the emitter region would generate current, and the coiled fingers would collect the photogenerated current, lead the current to the welding strip, and provide electrical power for the external load. Considering good electrical conductivity of the finger compared with the semi-conductor film, only the current density distributions among the emitter region arepainted in simulated diagrams for better visual effect. As demonstrated in Figure 4(b), the photogenerated current near the straight part of the fingers would be separated to the fingers on both sides while the photoelectric current generated near the coiledpart of the fingers would be merged near the bended fingers. Hence, there exists a high current density near the bended finger part. The generation of the internal current is positively related to the value of the arriving illumination on the PV cell. For the PV cell with the central angle of 120°, the received illumination near both ends is relatively smaller, which leads to comparatively lower current density on the emitter part.

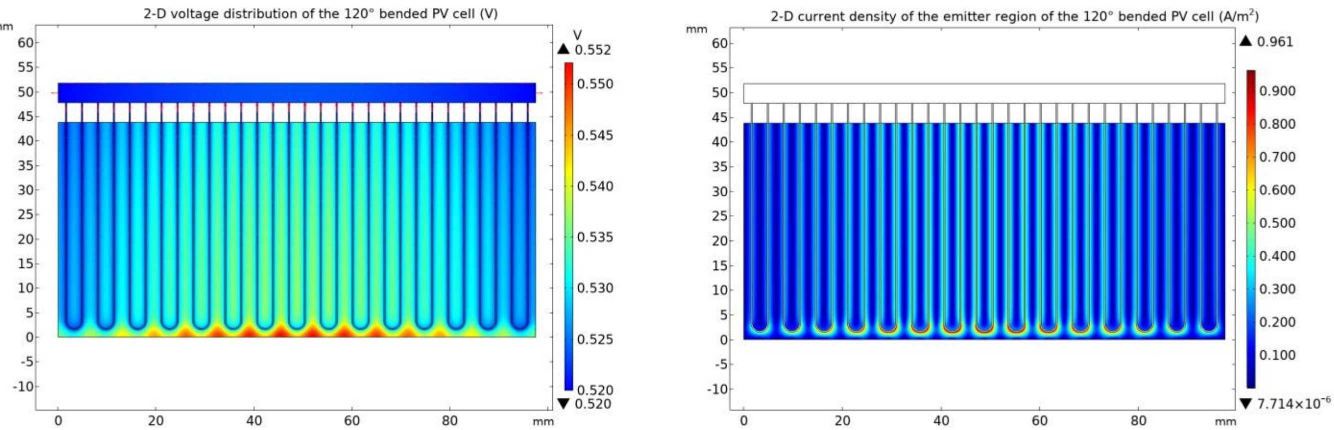

Figure 4: Simulated two-dimensional electric field of the bended flexible PV cell with the central angle of 120°. (a) front-side voltage distribution; (b)current density among the emitter regions

3.3. Parametric analysis

In consideration of the complex spatial structure of the flexible PV application, it is vital to compare the electrical performance by the flexible curved PV in typical different bending forms. Figure 5 presents the rendering figure of the studied nonplanar bases. The curved base is set as the cylindrical type, the semi-elliptic type, and the parabolic type. The central angle of the cylindrical base changes from 60° to 180° with the step of 20°. The eccentricity of the semi-elliptic base changes from 0.5 to 0.9 with the step of 0.1. The function of the parabola is defined as $y = kx^2$. The coefficient k is set as 0.01, 0.02, 0.03, 0.04, 0.05, 0.1, 0.2.

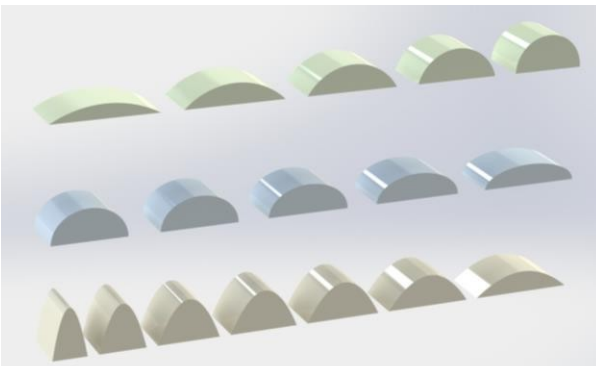

Figure 5: Rendering figure of the different curved bases (cylindrical, semi-elliptic, and parabolic)

The illumination distribution of the different curved bases is simulated and imported into the photoelectric model to draw the power-voltage curve and capture the maximum electrical power point. The maximum electrical power (P_{mp}) and the normalized performance conversion efficiency ($NPCE$) by each curved PV cell are plotted in Figure 6. As shown in Figure 6(a), with the increase of the central angle, the arriving irradiance intensity decreases so P_{mp} declines from 0.624 W to 0.410 W. $NPCE$ shows a similar trend with P_{mp}, falling from 15.308% to 14.946%. For the semi-elliptic type of cell, as the eccentricity expands, the semi-elliptic surface becomes more flattened and P_{mp} rises from 0.431 W to 0.517 W. $NPCE$ has an opposite tendency compared with P_{mp}, decreasing from 14.895% to13.743%. The coefficient of the parabola's controlling equation changes from 0.01 to 0.2 while the curve's opening becomes smaller.
P_{mp} declines from 0.589 W to 0.257 W while $NPCE$ rises from 15.372% to 19.483%. The concept of $NPCE$ demonstrates the generated photoelectric power per unit irradiance intensity. For cylindrical-type and semi-elliptic-type bending, $NPCE$ rises with the increase of the projection area of the bended cell while $NPCE$ by the parabolic-type cell shows a rising trend with the reduction of the projection area. Hence, for the parabolic PV cell with a smaller opening, although the amount of electrical yield is less, the smaller projection area would lead to a higher normalized photoelectric efficiency.

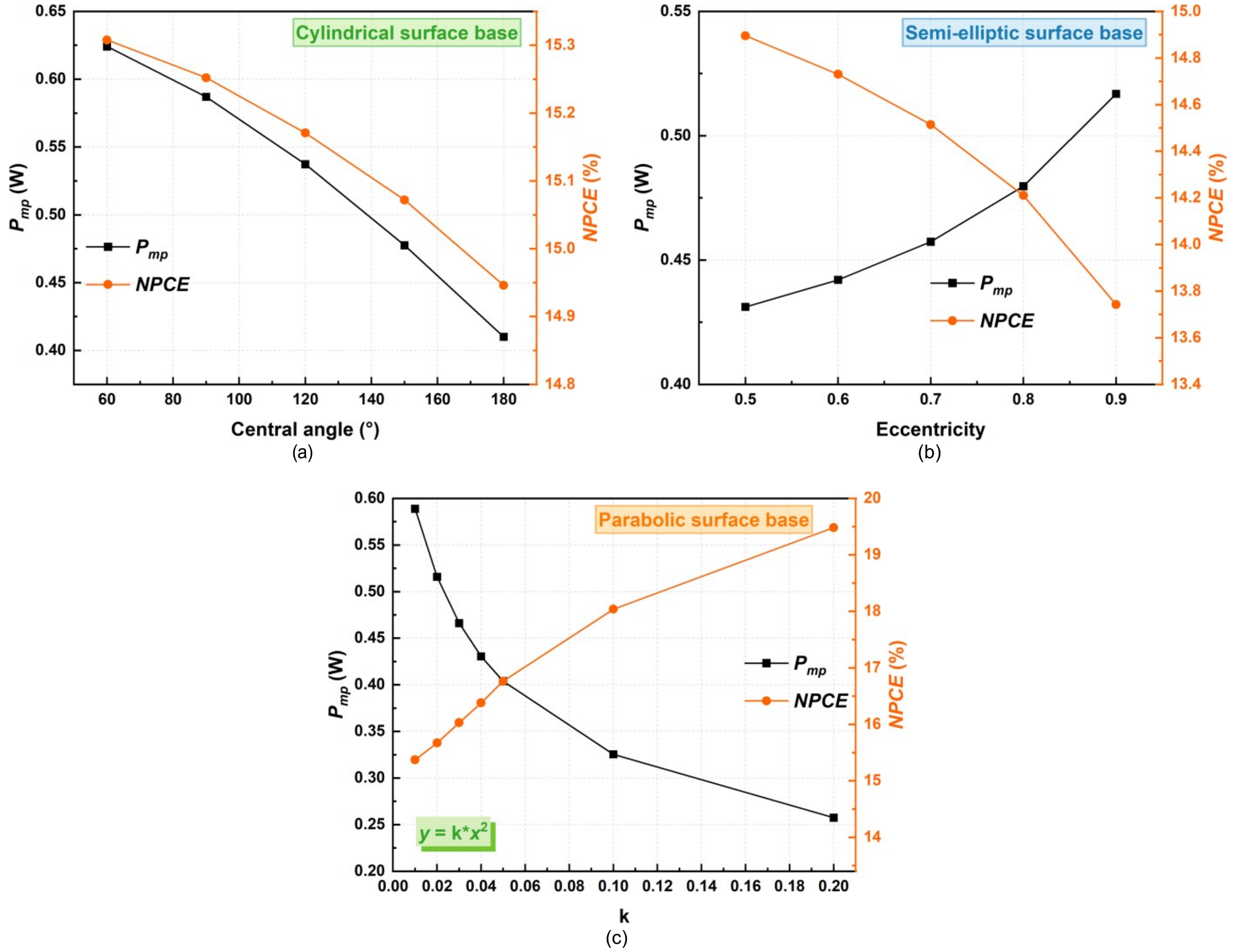

Figure 6: Photoelectric performance by the flexible photovoltaic cell in different bending forms. (a) cylindrical surface base; (b) semi-elliptic surface base; (c) parabolic surface base

4. CONCLUSION

This study focuses on the photoelectric performance by the flexible PV cell bended in different forms. Considering the PV cell under bended working conditions, the non-uniform illumination distribution among the PV cell's front side is simulated; the current density of the emitter part and the finger part is determined based on single-diode model; the two-dimensional voltage and the current density distribution on the front side of the PV cell is decoupled applying the finite element method. The experimental setup is built to collect the current-voltage data by the arc-shaped PV cell. The main conclusions are as follows:

- Illuminated by the standard solar simulator, the maximum electrical power output by the bended arc-shaped PV cell with the central angle of 60°, 90°, and 120° is 0.650 W, 0.564 W, and 0.534 W respectively; the normalized performance conversion efficiency ($NPCE$) is 15.946%, 14.654%, and 15.086%, respectively;
- The validity of the correlated two-dimensional photoelectric model is confirmed through the comparison of experimental data and simulated results, which exhibit a strong agreement;
- A simplified model is presented on the premise that the solar irradiance is uniformly distributed on the curved flexible PV cell, while maintaining the same total solar irradiance intensity as the real non-uniform solar irradiance distribution. The simplified simulated power at maximum power point has a 3.07%, 4.96%, 1.31% relative deviation compared with the measured values;
- The simulated two-dimensional voltage distribution and the current density of the bended flexible PV cell with the central angle of 120° are plotted and analysed. The electric field exhibits symmetry, and the current density in the emitter zone is positively correlated with the solar irradiation received;
- The parametric analysis of the flexible cell in different bending forms (cylindrical, semi-elliptic, parabolic) demonstrates that $NPCE$ of the cylindrical cell and semi-elliptic cell rises with the increase of the projection area of the bended cell while $NPCE$ by the parabolic-type cell shows a rising trend with the reduction of the projection area.

In the future, based on the coupled photoelectric model established in the article, performance of the novel flexible PV-powered device could be predicted accurately and efficiently; the architects could design complex curved BIPV envelopes based on the optimal generated electrical power and normalized performance conversion efficiency.

5. REFERENCES

[1] IRENA (2023) Renewable capacity statistics 2023, International Renewable Energy Agency, Abu Dhabi.

[2] Boulmrharj S (2022) Performance evaluation of grid-connected silicon-based PV systems integrated into institutional buildings: An experimental and simulation comparative study. Sustainable Energy Technologies and Assessments, 53, 102632. Available at:https://doi.org/10.1016/j.seta.2022.102632

[3] Liu W (2023) Flexible solar cells based on foldable silicon wafers with blunted edges. Nature, 617, 717-723. Available at:10.1038/s41586-023-05921-z

[4] Yin Z (2023) Investigation on the operating characteristics of a directly-attached light crystalline silicon PV roof. Solar Energy, 262, 111849. Available at:https://doi.org/10.1016/j.solener.2023.111849

[5] Wang J (2024) Design and experimental study of a novel flexible PV/T structure. Energy, 296, 131139. Available at:https://doi.org/10.1016/j.energy.2024.131139

[6] Wang J (2022) Field experimental investigation of a multifunctional curved CIGS photovoltaic/thermal (PV/T) roof system for traditional Chinese buildings. Energy Conversion and Management, 271, 116219. Available at:https://doi.org/10.1016/j.enconman.2022.116219

[7] Cai J (2024) Conceptual design and preliminary experimental study on curved PV ventilated facade assisted heat pump system (CPVF-HP). Energy Conversion and Management, 305, 118277. Available at:https://doi.org/10.1016/j.enconman.2024.118277

[8] Et-torabi K (2017) Parameters estimation of the single and double diode photovoltaic models using a Gauss–Seidel algorithm and analytical method: A comparative study. Energy Conversion and Management, 148, 1041-1054. Available at:https://doi.org/10.1016/j.enconman.2017.06.064

[9] Appelbaum J (2014) Parameters extraction of solar cells – A comparative examination of three methods. Solar Energy Materials and Solar Cells, 122, 164-173. Available at:https://doi.org/10.1016/j.solmat.2013.11.011

[10] Lu Y (2020) Effect of grid and optimization on improving the electrical performance of compound parabolic concentrator photovoltaic cells. Solar Energy, 196, 607-615. Available at:https://doi.org/10.1016/j.solener.2019.12.065

[11] Mellor A (2009) A two-dimensional finite element model of front surface current flow in cells under non-uniform, concentrated illumination. Solar Energy, 83, 1459-1465. Available at:https://doi.org/10.1016/j.solener.2009.03.016

#280: Performance analysis of a novel lightweight photovoltaic curtain wall components under different climatic conditions

Guofeng TAO[1], Qunzhi ZHU* [2], Yonggang CHEN[3], Xiaolong SHI[4], Jun GUAN[4]

[1] College of Energy and Mechanical Engineering, Shanghai University of Electric Power, Shanghai 201306, China, taoguofeng0523@163.com

[2] * College of Energy and Mechanical Engineering, Shanghai University of Electric Power, Shanghai 201306, China, zhuqunzhi@shiep.edu.cn

[3] China Huadian Group Co.LTD.Shanghai Branch.

[4] China State Construction International Holdings Limited.

Abstract: As the trend of global warming is getting severe, the need to use various clean energy sources is increasing. The use of clean energy sources in cities helps to reduce energy consumption, such as photovoltaic (PV) and photovoltaic thermal (PVT). Dueto limited roof area, PV has gradually been installed on other planes of the building. This paper investigates the practical application of lightweight PV curtain wall modules, including installation locations, positions, and orientations. First, we use EnergyPlus to build a base model of an office building and then fit PV curtain wall modules. The performance of the PV curtain wallmodules is analyzed in typical cities (Harbin, Beijing, Shanghai, Chengdu, Guangzhou) in five typical climate zones in China. Through simulation experiments, the power generation capacity of different cavity distances under different climatic conditions is derived. We compared the annual power generation data for each facade at the optimal cavity distance. We found that the capacityof PV curtain wall modules installed on the south facade is better than the east and west facades in Harbin, Beijing, and Shanghai, while the west facade is better than the south and east facades in Chengdu and Guangzhou. This paper also introduces semi- transparent PV modules and analyses the power generation of the building when normal glass and semi-transparent PV modules are installed. The impact on the indoor environment is also analyzed. After installation, the building's power generation capacity increased by at least 50% compared to installing glass, and the glare index setpoint exceeded time is reduced by at least 30.19%. It can also ensure that there is still more than 50% of daylight indexed time in the rooms in the north facade of Chengdu and other cities, which is much more friendly to the indoor environment than the time when the glass was installed. The results of this paper provide a useful reference for building installation of PV curtain wall modules and provide ideas for optimal installation.

Keywords: Lightweight PV Curtain Wall Modules, Building-Integrated Photovoltaic (BIPV), Building Energy Saving and Emission Reduction

1. INTRODUCTION

Renewable energy is the main source of clean energy generation, with urbanization continuing to speed up, the energy demand of the building also continues to rise. To meet energy saving and emission reduction targets, the building sector has been paying increasing attention to energy production from PV in various forms in buildings (Peng and Lu, 2013, Quesada et al., 2012). There isa large number of studies related to PV roofs. In 2003 M. Ciampi et al. (Ciampi et al., 2003) suggested that the use of ventilated facades in combination with roofs can help to reduce the heat load in summer, thus reducing the energy consumption of air conditioning systems. Mahmut Sami Buker et al. (Buker and Riffat, 2016) realized the cooling of rooftop PV collectors by designing polyethylene heat exchange loop units for waste heat utilization and indoor air cooling. Taher Maatallah et al. (Maatallah et al., 2019) analyzed the overall performance of PVT-PCM/water system under various outdoor conditions and found that there is an improvement of 17.33% in electrical efficiency over the conventional PV panels and the system was analyzed economically. In the same year, Nina Shao et al. (Shao et al., 2019) investigated the experimental performance of PV roofs and researched new types of roofs with simultaneous functions of the building's exterior surface, power generation, and evaporation from a heat pump systemthat provides electricity, domestic hot water, and heating for the building. Ahmed Bilal Awan et al. (Awan et al., 2018) analyzed solar radiation and PV system performance at 44 different locations in Saudi Arabia to guide the planning of the optimal location for PV power generation. Effrosyni Gkaniatsou et al. (Gkaniatsou et al., 2021) optimized the mounting structure so that heat is distributed in both directions between the PV panels and the building environment, enabling the alternation of dehumidification and PV cooling. Jun Wang et al. (Wang et al., 2022) investigated a curved copper indium gallium selenide (CIGS) PV/T roofing system that embodies the curved aesthetics of traditional Chinese architecture while taking into account the realization of the building's multifunctionality.

However, the roof area of a building is limited, it cannot cover the increasing energy consumption. People try to integrate PV panels more deeply with the rest of the building. In 2018 Ruobing Liang et al. (Liang et al., 2018) proposed an opaque ventilated PV curtain wall system using refrigerant pumps for forced circulation cooling, and the PV efficiency of the curtain wall system installed on the west facade could reach up to 16% under an average radiation intensity of 496 W/m^2 and the experimental outlet water temperature could reach up to 43.9℃. However, they did not study the effect on the other facades. Two years later, Liang et al. (Liang et al., 2020) proposed an active opaque solar curtain wall system by adding an active layer to form a double-layer ventilated curtain wall that reduces heat flux through the external envelope by 40% and preheats the fresh air while generating electricity. Meng Li et al. (Li et al., 2019) proposed that PV panels can be integrated into precast concrete to form a new building facade, suggesting a new idea for the method of combining PV and architecture. Lijie Xu (Xu et al., 2020) cooled the PV facade through a composite of air and water to provide the building with winter heating, which can reach an indoor temperature of 18.6℃, and domestic hot water during the rest of the season. Rabee M. Reffat et al. (Reffat and Ezzat, 2023) simulated 92 different application scenarios by introducing PV with different levels of application on different facades of a building and compared the renewable energy available for each of the scenarios.

In recent years, PV curtain wall modules have attracted the attention of many researchers. In addition to focusing on how to improve the power generation efficiency of PV curtain walls, people have gradually begun to pay attention to the lightweight PV curtain wall modules and the integration of the appearance of the building. The first-choice window of the building, Junchao Huang et al. (Huang et al., 2018) study explored the energy-saving potential and applicability of a new vacuum PV insulated glazing unit in high-rise commercial buildings in different climatic conditions and compared the thermal and power generation performances of the interior after installing vacuum PV curtain wall with other glazing materials available in the building industry through simulations. Changyu Qiu et al. (Qiu and Yang, 2020) studied and compared the lighting performance of translucent PV glass and ordinary glass in five different cities in China using the DAYSIM software and found that PV glass prevents daylight glare to a large extent but does not take into account the energy consumption of the building. Also, the walls of the building were well-utilized. Haitao Wang et al. (Wang et al., 2023) simulated the PV efficiency of PV curtain wall at different ground heights when installing PV curtain wall in a building inHefei and concluded that for a 12-meter-high public building, the temperature has the least effect on the power generation efficiency of the PV curtain wall when the height is 0.7 meters. Yijun Fu et al. (Fu et al., 2023) established a new thermoelectric coupling model that can estimate the thermoelectric performance under actual working conditions by analyzing and studying a real PV curtain wall system, analyzing its energy generation mode and quantifying the effect of thermoelectric coupling. Jiayi Zhu et al. (Zhu and He, 2019) used the DSF model to study heat transfer in cavities and found that the double skin provides better thermal insulation than single glazing. Muhammad Siddique et al. (Siddique et al., 2023) conducted an experimental study with two different PV curtain wall systems and found that the BIPV south facade produced 38.6% more electricity than the BIPV Trombe wall, however, they did not study the other facades. Yutong Tan et al. (Tan et al., 2023) designed a vacuum-integrated PV curtain wall that integrates power generation, glare avoidance, and outdoor landscaping, and simulated its energy consumption using EnergyPlus 9.2, but did not study the performance of the curtain wall under multiple climatic conditions.

In the context of advocating low-carbon green development, lightweight PV curtain walls have a wide range of application prospectsin office buildings. However, in reality, there is a disconnect between PV system design and building design as well as curtain wall design strategies that disregard climate variety. Especially in China, where relevant research and practice started late, and where the geographical area is vast and the climatic differences are huge, relevant research has been urgently needed. Because of this, two representative lightweight PV curtain wall modules at the present stage are selected for study in this paper, which are faux architectural material PV curtain wall modules and semi-transparent PV modules. In this study, we simulated the installation of faux architectural material PV curtain wall modules on the walls of buildings in different typical cities, and analyzed the effects of differentcities, building facades, and cavity distances on the power generation of the modules. A comparative analysis of the building's power generation when glass and semi-transparent PV modules are installed in the windows in each case was also carried out, and the impact on indoor comfort was analyzed. The findings of this paper can be used as a guide for stakeholders in designing buildings for energy efficiency in the early planning stages. Provides good advice for subsequent installation of lightweight PV curtain wall modules.

2. RESEARCH DESIGN AND METHODOLOGY

The methodological framework of this paper mainly involves the development of a modeling platform by combining different simulation tools, statistical analysis methods, and optimization algorithms. The PV curtain wall modules are first tested in the laboratory to obtain their relevant parameters and then combined with EnergyPlus to perform dynamic building performance modeling. The performance of the PV curtain wall modules is further combined with traditional passive building parameters to perform qualitative and quantitative sensitivity analyses, and based on the results, a holistic optimization analysis is performed, where the impact of different design variables on the energy yield of the building is presented and discussed in detail.

2.1. Simulation tools and weather conditions

EnergyPlus, the primary tool for evaluating building energy consumption and PV power generation, is a building energy simulation engine developed by the U.S. Department of Energy (DOE) and the Lawrence Berkeley National Laboratory (LBNL), that can be used to perform comprehensive energy simulation analyses and economic analyses of a building's geometric appearance, heating,cooling, lighting, ventilation, and other energy consumption. It is also possible to define the geographical location of the building and simulate the conditions associated with the building in different geographical areas in combination with imported weather files. It is widely recognized as a powerful building performance prediction tool, and its accuracy has been validated by several existing studies (Delgarm et al., 2016, Khoroshiltseva et al., 2016). Thermal zones, operating schedules, internal loads, lighting and HVAC systems, and generators in buildings are modeled through the interconnection submodule of EnergyPlus (EnergyPlus™).

This paper is based on the five climate zones in the Thermal Design Code for Civil Buildings GB50176-2016 (China, 2016). The selected cities and city latitudes are: Harbin, 45.75°N; Beijing, 39.90°N; Shanghai, 31.23°N; Guangzhou, 23.13°N; Chengdu, 30.67°N, which represent the severe cold region, the cold region, the hot summer and cold winter region, the hot summer and warm winter region, and the mild region. Typical weather data of each region are in China Standard Weather Data (CSWD) format, and the data are obtained by Meteonorm software. The main differences between the five climates are the outdoor dry bulb temperature and solar radiation, as shown in Figure 1. The main standard for dividing the five climate zones is the average temperature of the coldest and hottest months. Harbin and Beijing have significantly cooler outdoor temperatures from October to April, Shanghai and Guangzhou have significantly warmer temperatures from May to September, while Chengdu has a prolonged period of warmth with average coldest month temperatures ranging from 0-13℃ and average hottest month temperatures ranging from 18-27℃. Also, the intensity of solar irradiation in each city varies among different months, due to the different latitudes and weather conditions in each place.

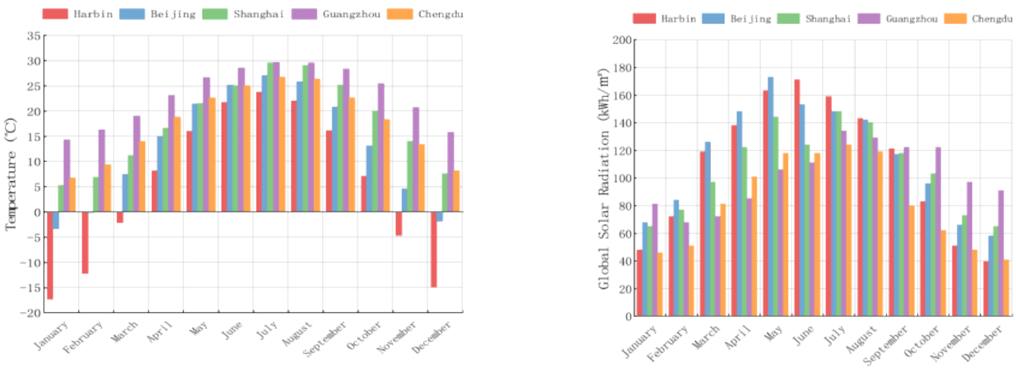

(a) Monthly dry bulb temperature (b) Monthly solar radiation

Figure 1: Weather conditions in five cities

2.2. Architectural modeling

The basic building model was developed from a simplified Chinese office building prototype. The original model setup is referenced to ANSI/ASHRAE/IES standard 90.1, while modified according to public building energy efficiency design standard GB50189-2015 (China, 2015) and green building evaluation standard GBT50378-2019 (China, 2019). The architectural model has a total floor area of 900㎡ on a single level with a floor height of 4 m and 12 floors, and the building is shown in Figure 1. Considering the light requirements of the office building, we have specified a window-to-wall ratio of 0.5 on all facades of the building, with windows located 0.9 m above the floor. We split each floor into five separate thermal zones, including four peripheral thermal zones facing different directions and one central thermal zone. Each peripheral thermal zone has an area of 200㎡ and a setpoint is set in the center for measuring changes in the internal environment of the zone, the height of the setpoint is 0.75 m from the ground, and the standard of daylight illuminance is set at 400 lux, and the standard of glare index is set at 20. The statistics include data from setpoints in the 1st, 6th, and 12th floors, representing the ground, middle, and top floors of the building. The design of other parameters within the building is shown in Table 1.

At the same time, we have simplified the boundary conditions of the building. The floors, walls, and ceilings of the zones in the building are considered to be adiabatic, with no heat being transmitted through them. Electrical equipment, energy and air-conditioning energy in the building are considered to be fixed. Ignore the effect of PV curtain wall modules installation on indoor temperatures.

Ignore office human program activities and human heat production. The building is relatively independent, ignoring the effect of building shadows on the PV curtain wall.

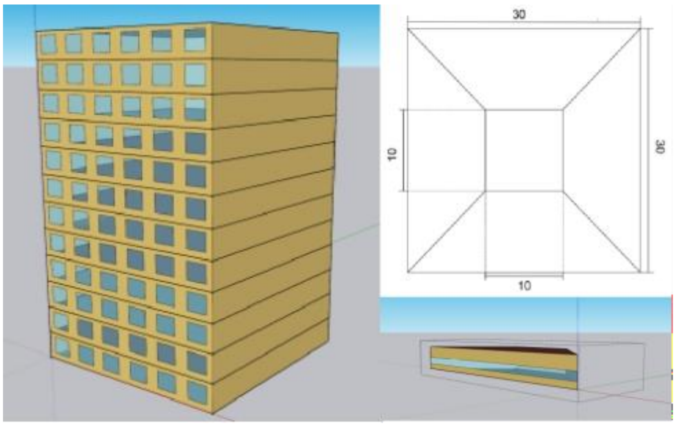

Figure 2: Exterior view of the building (left), single-storey floor plan of the building (top right), individual room displays (bottom right)

Table 1: Building internal parameters

Type	Data
Occupancy	14 Persons/100 ㎡
Lighting	10 W/㎡
Equipment	8 W/㎡
Occupancy schedule	Weekdays from 8 a.m. to 6 p.m. No occupancy or internal loads on weekends

3. PV CURTAIN WALL ANALYSIS

3.1. Simulation of PV curtain wall

We used an implantable generator model to predict the power generation of the PV curtain wall system and chose an equivalent diode model for the simulation, a simplified model that can quickly obtain the annual power generation of a single PV curtain wall modules. The relevant physical and electrical parameters of the two lightweight PV curtain wall modules used for the study are shown in Table 2(EnergyPlus™, EnergyPlus™, 2023, ASRE™).

Table 2: PV curtain wall modules related parameters

	Maximum Power（W）	Open-circuit Voltage（V）	Short-circuit Current(A)	Maximum Power Voltage (V)	Maximum Power Current(A)	Dimensions(mm)	Temperature Coefficients of Open-circuit Voltage(%/℃)	Temperature Coefficients of Short-circuit Current(%/℃)
Faux architectural material PV curtain wall modules	285.29	25.801	13.358	22.598	13.358	2000,1500,19	-0.321	0.06
Semi-transparent PV modules	270	116	3.59	86.37	3.15	1200,1800,34	-0.321	0.06

3.2. PV curtain wall operating temperature

Temperature plays a key role in the energy output productivity of PV modules. The output of the PV modules decreases as the temperature increases. Ambient air temperature and daytime temperature are not equal for solar cells. As solar cells are mostly dark in color, they absorb more solar energy, but this causes the cell temperature to rise. As a result, solar cells operate at temperaturesmuch higher than the ambient air temperature. Therefore, solar cells operate at much higher temperatures than the ambient air temperature. As the ambient temperature increases, the cell temperature increases further and the short-circuit current increases slightly but at the same time the open-circuit voltage, fill factor (FF), maximum power output, and efficiency decreases. The maximum output power of the PV modules decreases linearly with temperature (Chander et al., 2015). The power temperature coefficients of the modules selected for this study are all -0.214%/℃ (EnergyPlus™, 2023). The output power of the PV array is shown in Equation1 (Awan et al., 2018).

Equation 6: The output power of the PV array. $$P_{PV} = Y_{PV} f_{PV} \left(\frac{G_T}{G_{T,STC}}\right)\left[1 - \alpha_P\left(T_C - T_{C,STC}\right)\right]$$

Where:

- Y_{PV}: power output of PV array under standard testing conditions [kW]
- f_{PV}: PV derating factor [%]
- G_T: solar radiations incident on PV array in the current time step [kW/m^2]
- $G_{T,STC}$: incident radiations at standard test conditions [kW/m^2]
- α_P: temperature coefficient of power [%/℃]
- T_C: PV cell temperature in the current time step [℃]
- $T_{C,STC}$: PV cell temperature at standard test conditions [℃]

If we ignore the temperature effect on PV output, then the above equation of PV out will reduce as below

Equation 7: Simplified equation for the output power of the PV array. $$P_{PV} = Y_{PV} f_{PV} \left(\frac{G_T}{G_{T,STC}}\right)$$

To reduce the operating temperature of the PV curtain wall modules, this paper maintains a certain distance from the building facade to form a cavity when installing PV curtain wall modules and uses natural convection to cool the PV curtain wall modules. The distance of the cavity between the PV curtain wall modules and the building is not only an important factor affecting the heat transfer of PV but can also affect the building's thermal insulation performance. After literature research (Wang et al., 2023, Wu et al., 2019,Xiao, 2022, Yuqian, 2023), the cavity distance was determined to be in the range commonly used for practical installations, i.e. 0.04 m - 0.08 m. The installation dimensions for different urban conditions are set up and simulated through the EnergyPlus submodule. A comparative analysis of the optimal cavities is presented later.

4. RESULTS AND ANALYSES

In this paper, faux architectural material PV curtain wall modules are first installed on the building facade in the form of full coverage for power generation, to determine the basic power generation performance of each facade. Then, ordinary glass and semi- transparent PV modules are installed in the windows of the building. Faux architectural material PV curtain wall modules are installed in the walls of the facade to generate electricity jointly with the two. The optimal solution is determined step-by-step by changing a single variable at a time, and the effect of each variable is analyzed below.

4.1. Effect of cavities on power generation

Firstly, the power generation of four vertical facades in five typical cities was simulated with different cavity distances for the installation of faux architectural material PV curtain wall modules. The simulation results of the annual power generation of PV curtain wall modules are shown in Figure 3. From the results, when PV curtain wall modules were applied to office buildings in Harbin, Shanghai, and Chengdu in the four facing facades, east, south, west, and north, the annual power generation of the curtain walls decreased with the increase of the cavity spacing, with the maximum value obtained at a cavity distance of 0.04 m, and the minimum value at a distance of 0.08 m. The annual power generation of the curtain walls decreased with the increase of the cavity spacing, with the maximum value obtained at a distance of 0.04 m, and the minimum value obtained at a distance of 0.08 m. Significant changes in power generation were observed in both east and west facades installation, whereas changes in the south and north facades were significant only in specific areas, otherwise, the effect of the cavity on power generation was minimal.

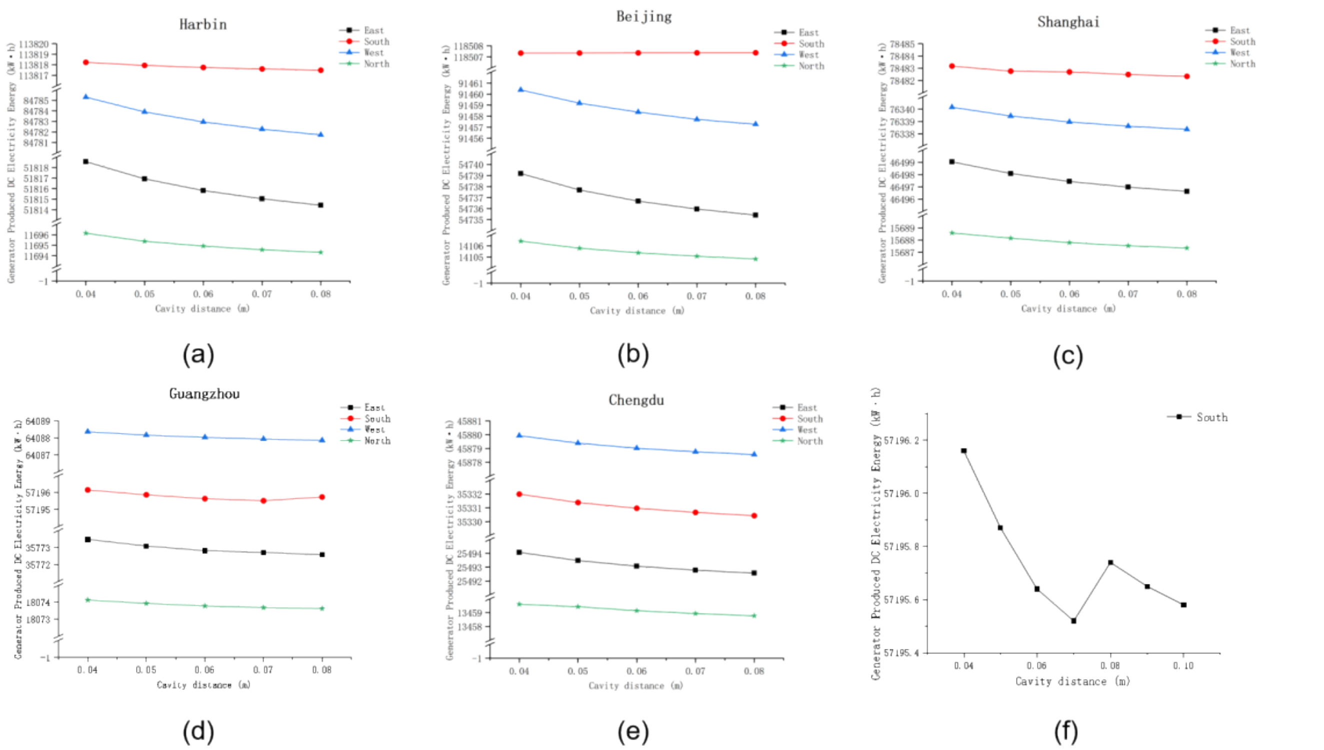

Figure 3: (a)-(e) Annual electricity generation at different cavity distances (m) in five city cities (f) Annual electricity generation study at different cavity distances on the south facade in Guangzhou

Particularly, the annual power generation of certain walls in some cities can appear differently. Based on Figure 2 (d) we found thatthe total annual power generation of the PV curtain wall modules on the south facade of the office building in Beijing has a slight increase with the increase of the cavity distance, and the maximum value is obtained at 0.08 m, which is 118,507.37 kW·h. According to the results in Figure 3 (e), when the PV curtain wall modules are installed on the south facade of Guangzhou in a range of the cavity distance from 0.04 to 0.07 m, the annual power generation has a slight increase with the cavity distance increases, a decrease in annual energy production occurs, but an increase in annual energy production occurs again at 0.08 m, which is a particular case in five cities. To further verify the relationship between cavity distance and annual electricity generation for this facade, we increased the cavity distance to 0.1 m. The simulation results are shown in Figure 3(f). The results show that the annual electricity generation reaches the maximum value at a cavity distance of 0.04 m and the extreme value of 57,195.74 kW·h at a cavity distance of 0.08 m. However, the difference between the extreme value and the maximum value is 0.00074%.

Meanwhile, we notice that the maximum value of the difference in annual electricity generation at different cavity distances for eachcity occurs in the north facade, and the highest value of the difference occurs in Shanghai with 0.079% and the lowest value occursin Guangzhou with 0.0028%. The highest minimum value of the difference in annual electricity generation for each city occurs in the west facade of Chengdu at 0.003% and the lowest in the south facade of Beijing at 0.00003%.

4.2. Power generation performance of different installation methods

Based on 4.1, we analyze the monthly power generation of the scheme of installing faux architectural material PV curtain wall modules with full coverage at the optimal installation cavity distance on the four facades of the building in five typical cities. The results of the simulation are shown in Figure 4.

The results show a decreasing trend in power generation on the south facade of buildings in the five cities from March to June, reaching a minimum in June. The power generation in summer was significantly lower than that in winter. Analyzed to climatic conditions, this is because of an increase in the number of rainy days from April to August, and ten or more days of precipitation in June, a period during which solar radiation increased but sunshine duration decreased. At the same time, the angle of solar incidence changes during the summer months, with the sun's altitude angle reaching its highest for the year on the summer solstice. At midday, the sun's rays are almost perpendicular to the ground, resulting in a very small angle of incidence of light on the PV curtain walls. And the increase in temperature at midday in summer resulted in a decrease in the power generation efficiency of the PV curtain walls, which had a significant impact on the power generation of the south facade.

We also notice that the west facade generation exceeds the south facade for all cities during the summer months. Generation in the west facade is significantly higher in the summer than in the winter and increases with the latitude at which the city is located. This is because summer days in the northern hemisphere are long and the length of day increases with latitude, especially in the high latitudes of China, such as Harbin, where the length of day on the summer solstice can be as long as 17 hours, so the west facade will be exposed to sunlight for a relatively longer period during the day. Before nightfall, when the temperature is lower than at midday, the efficiency of power generation is improved, and even if the light intensity is not as strong as at midday, more power generation will still be obtained.

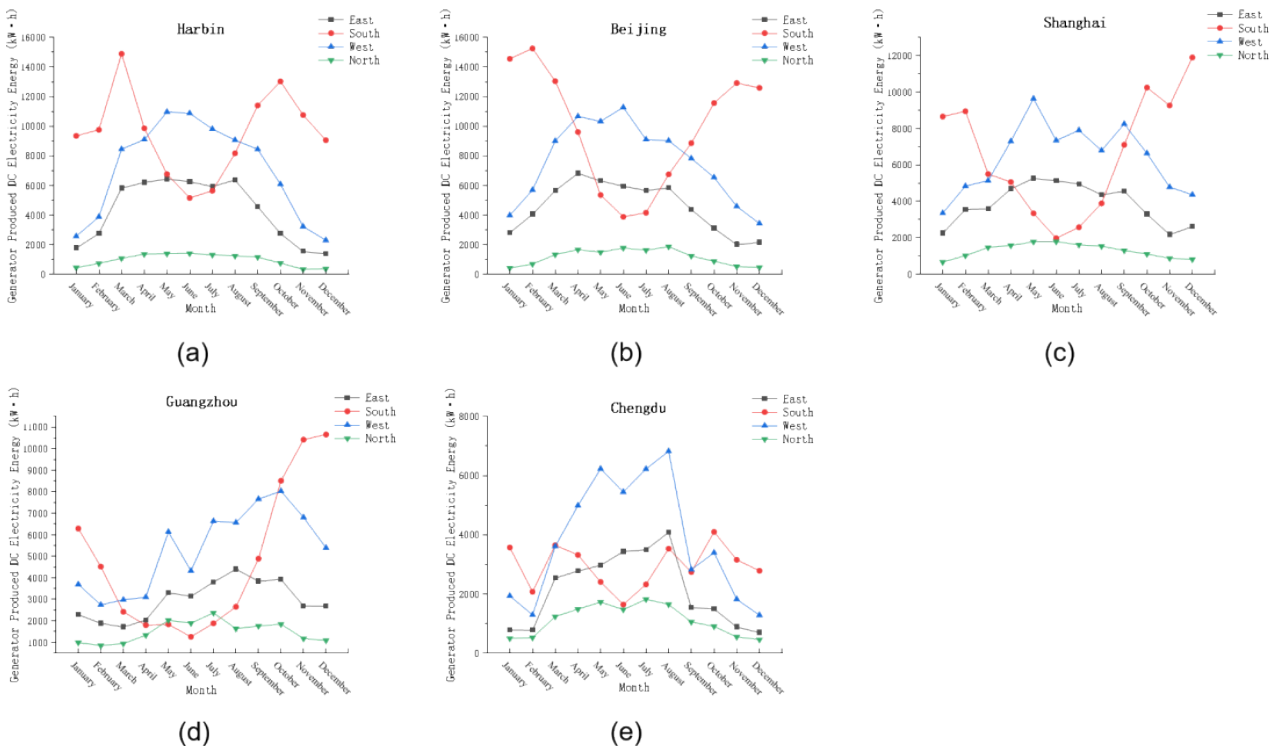

Figure 4: Full coverage of monthly electricity generation for each facade under five cities

After we summarize the annual power generation in these five cities, the statistical results are shown in Figure 5. We can see that the power generation when installing faux architectural material PV curtain wall modules on the east, south, and west facades of buildings in Harbin and Beijing is significantly better than that of the other three cities, which is attributed to the intensity of local solar radiation and the temperature. It is worth noting that the highest total annual power generation does not occur at the same facades in all five cities. We find the highest total annual power generation on the south facade of the building in Harbin, Beijing, and Shanghai. While in Guangzhou and Chengdu, the west facade has the highest total annual generation and the annual generation is 29.85% and 12.05% higher than that of the south facade, respectively. For the north facade, the annual electricity generation is at a lower level in all five cities. This is because the north facade of the northern hemisphere has a smaller angle of incidence of the sun, insufficient solar radiation intensity, and shorter hours of sunlight.

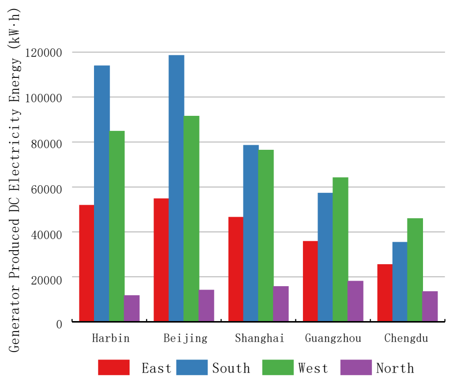

Figure 5: Full coverage of annual electricity generation for each facade under five cities

4.3. Semi-transparent PV modules power generation performance and impact on the indoor environment

On the basis of the above study, Figure 6 and Table 3 compared the annual energy production of glass and semi-transparent PV modules installed separately in windows when faux architectural material PV curtain wall modules are installed on the facade. We can see that the power generation trends on each facade in the five cities are the same as full coverage. At the same time, the building's power generation has been improved with an effect of 50.43%-70.56% when installed semi-transparent PV modules, compared with glass. In Shanghai, the growth across all facades reached more than 63.5%, which is the highest among all cities.

The power generation enhancement when installing semi-transparent PV modules on the north facade of each city is higher than the remaining three facades.

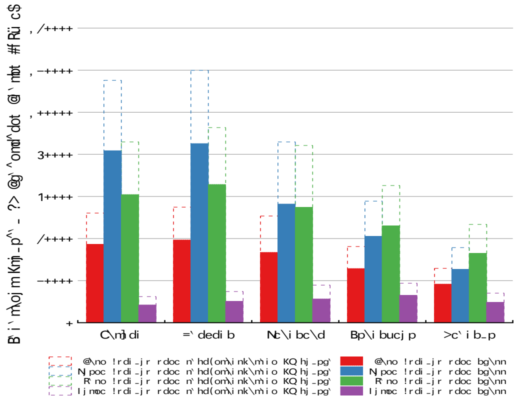

Figure 6: Annual electricity generation for each facade with semi-transparent PV modules and glass

Table 3: Installation of semi-transparent PV modules power generation growth rate

Location	Harbin	Beijing	Shanghai	Guangzhou	Chengdu
East	50.82%	50.43%	63.50%	51.72%	51.99%
South	51.81%	51.80%	64.18%	51.43%	51.48%
West	51.95%	52.02%	65.50%	52.58%	52.70%
North	58.71%	57.26%	70.56%	55.63%	56.29%

At the same time, we analyze the internal environment of the zones where ordinary glass and semi-transparent PV modules are installed. The simulations obtain daylight illuminance and glare index at the setpoint per hour. Daylight illuminance setpoint exceeded time and glare index setpoint exceeded time are analyzed in conjunction with the criteria, and the statistics of the results are shown in Figure Figure 1. We can see that the daylight illuminance setpoint exceeded time on the 6th floor is the longest, while the glare index setpoint exceeded time is the shortest. Daylight illuminance setpoint exceeded time are longest in the south of Chengdu, while the remaining four cities are longest in the east. We compared the data and found that the installation of semi-transparent PV modules on the 6th floor had the greatest reduction in glare index setpoint exceeded time and the least effect on daylight illuminance setpoint exceeded time, the result is shown in Figure 2. We found that the glare index setpoint exceeded time in the zone is reduced by at least 30.19% after the installation of semi-transparent PV modules. The best performance occurred on the north facade of Harbin, which is 82.57%, this greatly reduces the probability of glare in the zones. Chengdu's east, west, and south facades performed the best, with reductions of up to 56.56%. Because of the special characteristics of the material of the semi-transparent PV modules, the daylight illuminance setpoint exceeded time has decreased. The south facade of Beijing is at the highest level, with 2,839.25 hours reaching set standards. Reduced by 14.8% compared to normal glass hours, reaching 64.82% of the annual daytime hours (based on 12 hours each day). Unfortunately, Chengdu's facades and the north facades of other cities do not reach 50% of the annual daytime hours.

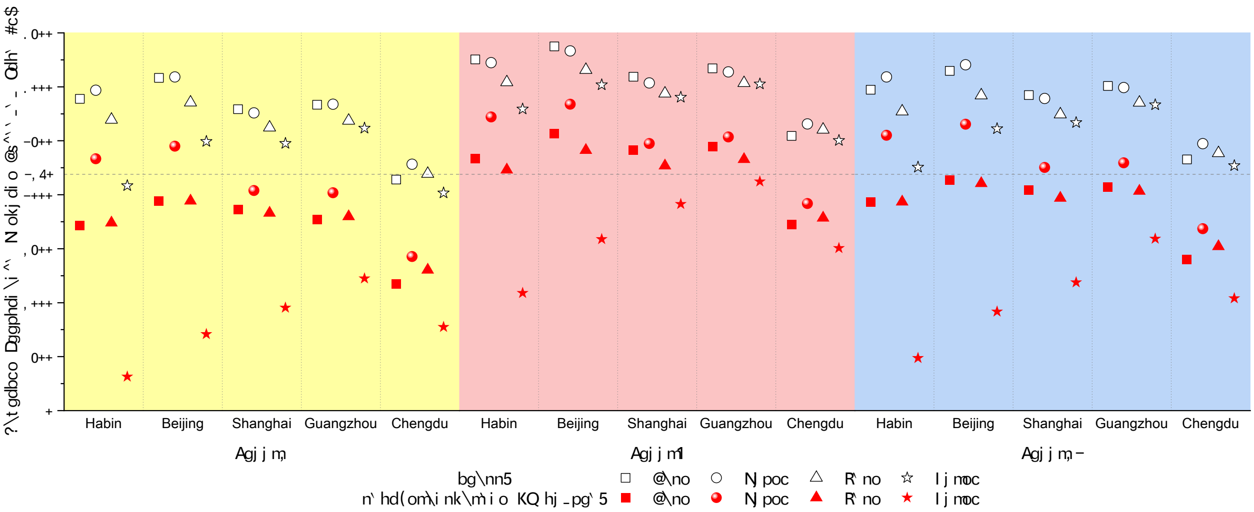

Figure 7: Comparison of daylight illuminance setpoint exceeded time

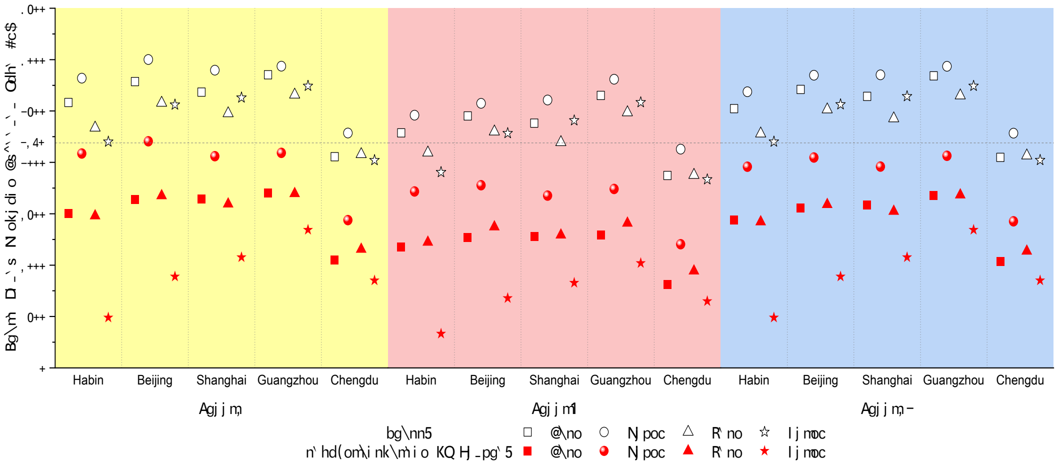

Figure 1: Comparison of glare index setpoint exceeded time

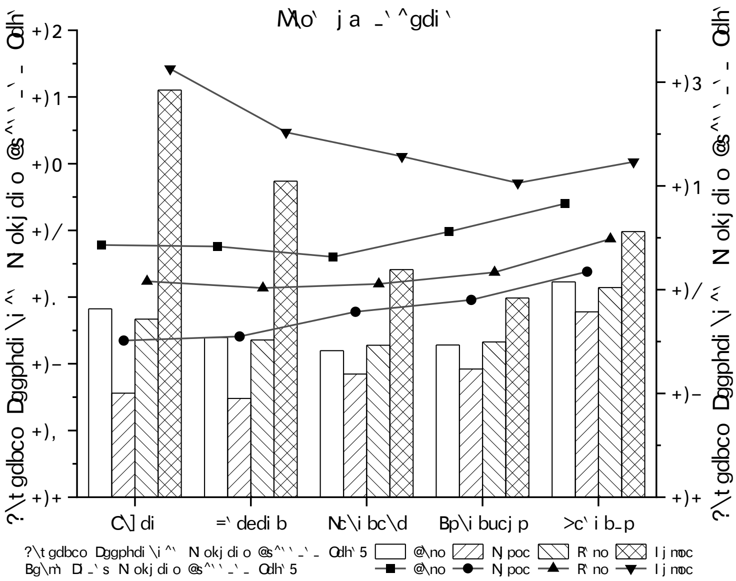

Figure 2: Rate of decline on the setpoint exceeded time on the 6th floor

5. CONCLUSION AND REFLECTIONS

This study investigated the energy-saving potential and applicability of new lightweight PV curtain wall modules in high-rise office buildings under different climatic conditions. Simulation experiments were conducted by selecting representative cities in five climate zones in China. The performance of power generation after installing PV curtain wall modules at different cavity distances and in different ways was compared. The data and analyses presented in this paper will provide some guidance for developing as well as planning the installation of PV curtain wall modules. The main conclusions are as follows:

a.By analyzing the power generation of lightweight PV curtain wall modules with individual full coverage and combined power generation, the east, south, and west facades of the buildings in each city have high power generation advantages, but the optimal power generation facades are different. The north facade has the lowest power generation in all cities due to insufficient solar irradiation intensity and duration. Although the semi-transparent PV modules installed on the north facade had the greatest reduction on glare index setpoint exceeded time, on balance, it is not suitable to install lightweight PV curtain wall modules on the north facade during actual installation.

b.About wall installed faux architectural material PV curtain wall modules, in the range of commonly used cavity distances, most cities can maximize the power generation of lightweight PV curtain wall modules by installing them at a cavity distance of 0.04m, except for the south facade of Beijing which is at 0.08 m. Among the five cities, Beijing has the highest potential to generate electricity by installing lightweight PV curtain wall modules, while Chengdu has the lowest potential.

c.The simulation results show that it is most suitable to install the lightweight PV curtain wall modules on the south facade for the actual installation in Harbin, Beijing, Shanghai. The combined power generation of the faux architectural material PV curtain wall modules and the semi-transparent PV modules can reach 115,193.75kW·h, 119,926.24kW·h, and 85,904.95kW·h, respectively, followed by the east and west facades. Guangzhou and Chengdu are more suitable to be installed on the west facade, with a combined generation capacity of 65,192.36kW·h and 46,707.13kW·h, with an increase by 29.85% and 12.05% over the south facade, respectively, followed by the south facade and the east facade.

d.To address the impact of installing semi-transparent PV modules on the indoor environment, comparing the changes in the indoor environment when the glass is installed. It is suggested to install semi-transparent PV modules on the east facade of each city, which can be effective in building interior glare index setpoint that exceed time and enhance the comfort of the office, followed by the west facade. The south facade performs the worst, but still reduces the glare index setpoint exceeded time by 30.19%-43.45%. Meanwhile, the middle floor on the east side of the office building performs best for optimization, reducing glare index setpoint exceeded time by 46.3%-56.56%.

However, there are some shortages in this paper. For example, the cities selected are not representative of all cities in the climate zone and further optimization for local conditions is still required for the actual installation. The window-to-wall ratio in this paper is a fixed value, the next step will be to study the effect of the window-to-wall ratio on power generation and the indoor environment under various climatic conditions.

6. REFERENCES

ASRE™. Available: http://www.advsolarpower.com/product/ [Accessed].

AWAN, A., ZUBAIR, M., P, P. & ABOKHALIL, A. 2018. Solar Energy Resource Analysis and Evaluation of Photovoltaic SystemPerformance in Various Regions of Saudi Arabia. Sustainability, 10.

BUKER, M. S. & RIFFAT, S. B. 2016. Performance Analysis of a Combined Building Integrated PV/T Collector with a Liquid Desiccant Enhanced Dew Point Cooler. Energy Procedia, 91**,** 717-727.

CHANDER, S., PUROHIT, A., SHARMA, A., NEHRA, S. P. & DHAKA, M. S. 2015. Impact of temperature on performance of seriesand parallel connected mono-crystalline silicon solar cells. Energy Reports, 1**,** 175-180.

CHINA, MOHURD. 2015. “National Standard of The People's Republic of China. Design standard for energy efficiency of public buildings, 50189–2015,” ed.

CHINA, MOHURD. 2016. “National Standard of The People's Republic of China. Code for thermal design of civil building, 50176- 2016,” ed.

CHINA, MOHURD. 2019. “National Standard of The People's Republic of China. Assessment standard for green building, 50378- 2019,” ed.

CIAMPI, M., LECCESE, F. & TUONI, G. 2003. Ventilated facades energy performance in summer cooling of buildings. Solar Energy, 75**,** 491-502.

DELGARM, N., SAJADI, B., KOWSARY, F. & DELGARM, S. 2016. Multi-oBeijingective optimization of the building energy performance: A simulation-based approach by means of particle swarm optimization (PSO). Applied Energy, 170**,** 293-303.

ENERGYPLUS™. Available: https://www.fareastglobal.com/category.aspx?NodeID=43&siteid=27546 [Accessed]. ENERGYPLUS™ 2023. EngineeringReference.

FU, Y., XU, W., WANG, Z., ZHANG, S., CHEN, X. & ZHANG, X. 2023. Experimental study on thermoelectric effect pattern analysisand novel thermoelectric coupling model of BIPV facade system. Renewable Energy, 217.

GKANIATSOU, E., MENG, B., CUI, F., LOONEN, R., NOUAR, F., SERRE, C. & HENSEN, J. 2021. Moisture-participating MOF thermal battery for heat reallocation between indoor environment and building-integrated photovoltaics. Nano Energy, 87.

HUANG, J., CHEN, X., YANG, H. & ZHANG, W. 2018. Numerical investigation of a novel vacuum photovoltaic curtain wall andintegrated optimization of photovoltaic envelope systems. Applied Energy, 229**,** 1048-1060.

KHOROSHILTSEVA, M., SLANZI, D. & POLI, I. 2016. A Pareto-based multi-oBeijingective optimization algorithm to design energy-efficient shading devices. Applied Energy, 184**,** 1400-1410.

LI, M., MA, T., LIU, J., LI, H., XU, Y., GU, W. & SHEN, L. 2019. Numerical and experimental investigation of precast concrete facadeintegrated with solar photovoltaic panels. Applied Energy, 253.

LIANG, R., PAN, Q., WANG, P. & ZHANG, J. 2018. Experiment research of solar PV/T cogeneration system on the building facadedriven by a refrigerant pump. Energy, 161**,** 744-752.

LIANG, R., WANG, P., ZHOU, C., PAN, Q., RIAZ, A. & ZHANG, J. 2020. Thermal performance study of an active solar buildingfacade with specific PV/T hybrid modules. Energy, 191.

MAATALLAH, T., ZACHARIAH, R. & AL-AMRI, F. G. 2019. Exergo-economic analysis of a serpentine flow type water basedphotovoltaic thermal system with phase change material (PVT-PCM/water). Solar Energy, 193, 195-204.

PENG, J. & LU, L. 2013. Investigation on the development potential of rooftop PV system in Hong Kong and its environmental benefits. Renewable and Sustainable Energy Reviews, 27, 149-162.

QIU, C. & YANG, H. 2020. Daylighting and overall energy performance of a novel semi-transparent photovoltaic vacuum glazing in different climate zones. Applied Energy, 276.

QUESADA, G., ROUSSE, D., DUTIL, Y., BADACHE, M. & HALLé, S. 2012. A comprehensive review of solar facades. Transparentand translucent solar facades. Renewable and Sustainable Energy Reviews, 16, 2643-2651.

REFFAT, R. M. & EZZAT, R. 2023. Impacts of design configurations and movements of PV attached to building facades on increasing generated renewable energy. Solar Energy, 252, 50-71.

SHAO, N., MA, L. & ZHANG, J. 2019. Experimental study on electrical and thermal performance and heat transfer characteristic of PV/T roof in summer. Applied Thermal Engineering, 162.

SIDDIQUE, M., SHAHZAD, N., UMAR, S., WAQAS, A., SHAKIR, S. & KASHIF JANJUA, A. 2023. Performance assessment of Trombe wall and south facade as applications of building integrated photovoltaic systems. Sustainable Energy Technologies and Assessments, 57.

TAN, Y., PENG, J., LUO, Z., LUO, Y., MA, T., JI, J., YANG, H., WANG, F. & ZHU, M. 2023. Multi-function partitioned design method for photovoltaic curtain wall integrated with vacuum glazing towards zero-energy buildings. Renewable Energy, 218.

WANG, H., WU, F., LU, N. & ZHAI, J. 2023. Comprehensive Research on the Near-Zero Energy Consumption of an Office Buildingin Hefei Based on a Photovoltaic Curtain Wall. Sustainability, 15.

WANG, J., TIAN, X., JI, J., ZHANG, C., KE, W. & YUAN, S. 2022. Field experimental investigation of a multifunctional curved CIGSphotovoltaic/thermal (PV/T) roof system for traditional Chinese buildings. Energy Conversion and Management, 271.

WU, S.-Y., WANG, T., XIAO, L. & SHEN, Z.-G. 2019. Effect of cooling channel position on heat transfer characteristics andthermoelectric performance of air-cooled PV/T system. Solar Energy, 180, 489-500.

XIAO, M. 2022. Effect of Natural Ventilation on Performance of semi-transparent Photovoltaic Double Skin Facade in Summer. Journal of BEE.

XU, L., LUO, K., JI, J., YU, B., LI, Z. & HUANG, S. 2020. Study of a hybrid BIPV/T solar wall system. Energy, 193.

YUQIAN, C. 2023. Heat Exchange Optimization of Photovoltaic Curtain Wall System in Near Zero Energy Building. Journal of Shenyang Jianzhu University (Natural Science).

ZHU, J. & HE, G. 2019. Heat transfer coefficients of double skin facade windows. Science and Technology for the Built Environment, 25, 1143-1151.

#283: Assessing urban building energy demand in future climate scenarios

A case study for the residential stock in Nottingham, UK

Athanasia APOSTOLOPOULOU[1], Carlos JIMENEZ-BESCOS[2], Carlos CALDERON[3], Robin WILSON[4], Doreen BOYD[5], Stefano CAVAZZI[6]

[1] University of Nottingham, Nottingham, United Kingdom, laxaa46@nottingham.ac.uk
[2] University of Westminster, London, United Kingdom, c.jimenezbescos@westminster.ac.uk
[3] Newcastle University, Newcastle, United Kingdom, carlos.calderon@ncl.ac.uk
[4] University of Nottingham, Nottingham, United Kingdom, robin.wilson@nottingham.ac.uk
[5] University of Nottingham, Nottingham, United Kingdom, doreen.boyd@nottingham.ac.uk
[6] Ordnance Survey, Southampton, United Kingdom, stefano.cavazzi@os.uk

Abstract: The most recent report on climate change from the IPCC (Intergovernmental Panel on Climate Change), in 2023, states that urgent action is needed to tackle global warming. The IPCC points out that by 2040, there is a greater than 50% risk that the temperature worldwide will approach or exceed 1.5 degrees Celsius (2.7 degrees Fahrenheit). On top of that, under high-emissionsscenarios, the global temperature could increase to that borderline even earlier, before 2037. Since building stock accounts for 40% of total global energy usage and 33% of greenhouse gas emissions each year, their continuous high demand for energy leads to the rapid growth of CO2 emissions. Accounting for that, the energy performance of buildings in urban scale under the future climate scenarios is a significant factor in immediately assisting with climate change mitigation. The purpose of this project was to estimate the influence of the climate change on the energy demand of two neighbourhoods in Nottingham, in United Kingdom, by comparingtheir current energy performance to the future. The methodology consists of the use of geospatial data for the building geometric parameters, in combination with energy-related data from the EPC (Energy Performance Certificate) dataset. The datasets were processed with Python programming language and the QGIS software, and the final dataset was imported to an energy model that was constructed with the use of Rhino and Grasshopper, with EnergyPlus simulations on the background. The model was run under9 different climate scenarios, namely under the present, under 2050s and 2080s for 4 different future scenarios each year. The results have shown that the absence of building stock renovation will lead to an accountable decrease in the heating demand of buildings, while the risk of overheating will be critically escalating.

Keywords: UBEM, OS Mastermap, EPC, Climate Change, Future Climate Scenarios

1. INTRODUCTION

In recent years deep research has been conducted regarding the complex system of climate worldwide, and its fluctuation through the time. Taking into consideration the pace that the climate has been changing in the past, it is evident that at present there is a rapid fluctuation in its variables, such as the temperature and the precipitation (Stagrum et al., 2020). This rapid change of weather conditions threatens the everyday life and well-being of people, and simultaneously influence the sustainability of the society's growth (Santamouris et al., 2020). In consequence, there is no doubt that the built environment will be drastically affected by the shift of the temperature, meaning that there will be an increase in the energy demand of buildings, in order to maintain human thermal comfort conditions internally. For that reason, climate change is one of the greatest concerns for humanity.

The relationship between the built environment and climate change is interdependent. According to the United Nations Environment Programme and their Global Status Report in 2022, it has been estimated that the energy demand of buildings, in 2021 has reached 4% increase compared to 2020 approximately, which is the highest in the last decade (United Nations Environment Programme, 2022). In addition to this, the same report points out that the CO_2 emissions from the building stock and all the relevant operations from people's everyday life, have reached the highest record to date, which is equal to 10 Gt CO_2 emissions. It is worth noting that the rise of CO2 emissions has been around 5% compared to year 2020. Therefore, the impact of the building stock to the future weather conditions is inevitable.

On the other hand, as it has been mentioned above, the building stock is affected by the climate change, and this is clear on the observed heating and cooling demand fluctuations (Ibrahim and Jimenez-Bescos, 2020; Wang and Lu, 2020). With a view to mitigating the climate change and adapting the current buildings to global warming, the refurbishment of the building stock is one way solution (Jimenez-Bescos and Oregi, 2019). Therefore, urgent action is needed to align the building sector with the environmental goals. City- planners and policymakers could have a better understanding of the significance of the situation, if research is done specifically for the energy performance of buildings in the future. As noted by Laktuka et al. in their research, persuading them to develop long-term policy is crucial, and for that energy performance evaluation under future climate scenarios is essential (Laktuka et al., 2021).

As regards retrofitting building stock and climate change, previous research study has been conducted for public buildings and their thermal performance in the future (Chow et al., 2013). The analysis has shown that by enhancing the insulation thickness of these buildings, the heating and cooling demand could be similar to the present up to 2080s. Nevertheless, Chow et al. stated that this is limited to public buildings and the particular region of China, where the climate is defined by hot summers and cold winters. Incontrast, another study from Rodrigues and Fernandes has shown that there will be no need for high insulated thermal envelopes upto 2050s for the Mediterranean residential stock (Rodrigues and Fernandes, 2020). In particular, their study recommends that thereis a high possibility that the decrease in the thermal transmittance (U-value) of the thermal envelope will be necessary, as their findings show a tiny drop in the heating demand and a considerable increase in the cooling demand. The findings of this analysis support the conclusions of Apostolopoulou et al., who suggested that the community should focus on the cooling demand since there will be a slight reduction in the heating demand in the 2050s and 2100s (Apostolopoulou et al., 2023). Finally, another research from Wang et al. for five different typical climate zones in China, predicted that the risk of overheating in buildings is extremely high, especially for the mild zone and the apartments that reach 3004.8% difference in the duration of heating season and 877.7% in the severity (Wang et al., 2022).

Nevertheless, the above research studies have been conducted at the individual building level, except of the research study f rom Apostolopoulou et al. which has implemented a physics-based bottom-up approach to estimate the urban building energy demand, but only for heating loads. Moreover, most of them have not considered a variety of archetypes, namely different building age and building types. Thus, it has been recognized that it is vital to carry out a district-scale research study that will take into account the demand for both heating and cooling under various future climate scenarios.

The aim of this research paper is to evaluate the annual residential heating (space heating and hot water) and cooling demand at city scale and under different climate conditions. In order to achieve this, climate analysis has been implemented for the present weather, and the weather in 2050s and 2080s, under different climate SSP models. In general, the SSPs describe possible global trends for the future that could make it more or less challenging to deal with climate change, mitigate it or adapt to it. Accordingto Armstrong, each SSP is a story about what might happen in the future (Armstrong, 2001; UNECE, n.d.). SSP1-2.6 is the "green" road, where city-planners are focused on sustainable development, SSP2-4.5 is the "middle" road, where society continues with the current policy patterns, SSP3-7.0 is the "rocky" road, where inequality and slow economic growth occurs, and SSP5-8.5 is the pathway where there is high consumption and fossil fuel development (ClimateData.ca, n.d.). Through the application of the developed methodology to these pathways, results for a broader sample of dwellings could be drawn, and policymakers could be provided an option for rapidly determining the most vulnerable areas to climate change.

2. METHODOLOGY

A bottom-up physics-based approach was used in order to develop an urban building energy model for the estimation of the energydemand, both heating (space heating and hot water) and cooling, of the residential building stock. The methodological approach was implemented for two neighbourhoods in Nottingham, UK at both individual building level and district level, and was run under the present weather and 8 different future climate scenarios.

The first step of the methodology was to create the energy model with the use of visual programming language. After that, the geospatial, geometric, and building data, vegetation data and terrain data were collected and processed via Python programming language and the QGIS platform, in order to turn the various datasets into a single dataset in the desired structure.

The next step was the choice of the case study areas, which was highly influenced by the data availability of each neighbourhood. The following step has been the creation of the future climate scenarios, by using the present weather data from Climate OneBuilding and feeding them to FutureWeatherGenerator_v1.2.2 tool. After having all the necessary data, both building and climate, these have been imported to the energy model, in order to make it run, and gather the energy demand results for each individual building. The results processing was the following step, which has been done with Python programming language, in order to acquire the district energy demand results for both case study areas. In sequence, climate analysis has been done for the comparison of the temperature over the year under the different climates. Finally, the visualization of the results was implemented with a variety of graphs that show the predicted trend of the building and district demand under different future climate scenarios. The methodological approach is briefly illustrated in Figure 1 below, and in the next subsections is described in more detail.

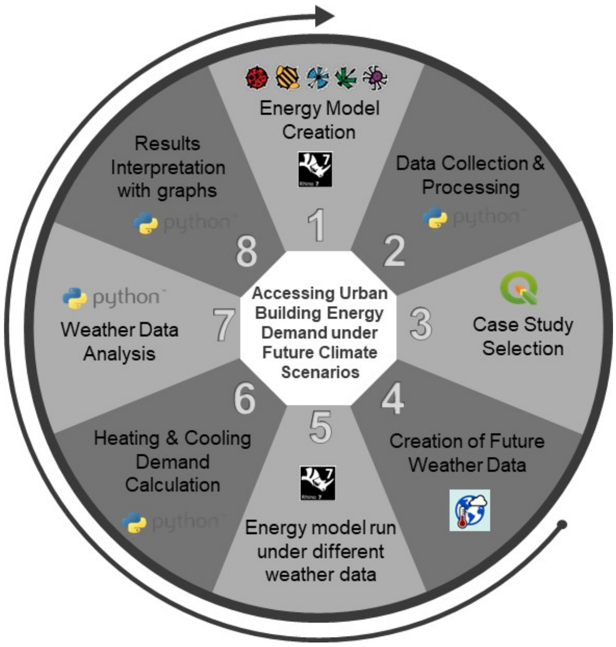

Figure 1: Methodological diagram

2.1. Energy Model Creation

Rhino7 and its addon Grasshopper have been used for the creation of the energy model. In more detail, Ladybug tools and URBANopt have been used in Grasshopper for the implementation of the energy balance calcula tions, as URBANopt uses EnergyPlus on the background, which is a validated software. In the energy model the first step is to import the shapefile with the geospatial and non-geospatial information of the under-test buildings. Then, each building is assigned to a specific archetype from the Grasshopper library, according to its building type and building age, in order to obtain data that were not available, such as some mechanical characteristics and construction materials. After that, other structures and buildings that exist in the case study area are included, in order to take into account, the influence of the shadow to the energy demand. The next step is the inclusion of the vegetation to the model from two different sources for better results regarding the shadow from surroundings. The following step is to include the terrain through Gismo addon, in order to project both buildings and trees to the right plane, which is the terrain height. After importing all these data, the climate data are inserted into the model, and then the URBANopt component in Grasshopper is set to run the EnergyPlus simulations for the estimation of the heating and cooling demand of all buildings.

2.2. Data Collection & Processing

The data that have been gathered for this project are geospatial, geometric, weather data, and come in various formats. Table 1 shows the datasets that have been gathered, their source and their format. More specifically, regarding the buildings, geospatial and geometric data were collected from Ordnance Survey, namely the OS MasterMap Topography layer and Building Height Attribute, which contain the building footprint, the building height, and the geometry polygons, which is the geospatial information for the location of each building (Digimap, n.d., n.d.). In addition, from Ordnance Survey, two more datasets have been used, the OS AddressBase Plus and the OS Boundary Line (Ordnance Survey, n.d.). The OS AddressBase Plus dataset was needed in order to connect the geospatial information of the buildings with the energy-related data that was acquired from Energy Performance Certificates (Open Data Communities, n.d.). Then, the datasets for the vegetation were gathered from both Nottingham City Council– Open Tree Dataset and Open Street Map – OSM Tree Dataset, for more precise and complete results (Nottingham City Council, 2023). Following the trees consideration as surroundings for the shadow calculations, it has been deemed essential to project all buildings and their surroundings to the actual terrain height. Therefore, the terrain dataset was gathered from Open Topography (Open Topography, n.d.). The last step has been to collect the present weather data from Climate OneBuilding in order to create thefuture data through FutureWeatherGenerator_v1.2.2 tool (Climate OneBuilding, n.d.).

After data acquisition, the datasets were imported in Jupyter notebook and Anaconda, in order to be processed with Python programming language. The datasets were cleaned from NaN values and outliers, merged with each other, and with a statistical approach and random mapping, the building age bands were imputed to buildings with unknown building age.

Table 4: Datasets

Dataset	Provider	Source	Format	Reference
OS MasterMap Topography layer	Ordnance Survey	Digimap, EDINA	GPKG	(Digimap, n.d.)
OS MasterMap Building Height attribute	Ordnance Survey	Digimap, EDINA	CSV	(Digimap, n.d.)
OS AddressBase Plus	Ordnance Survey	Ordnance Survey	CSV	(Ordnance Survey, n.d.)
OS Boundary Line	Ordnance Survey	Digimap, EDINA	SHP	(Digimap, n.d.)
Energy Performance Certificates	Open Data Communities	epc.opendatacommunities.org	CSV	(Open Data Communities, n.d.)
Open Tree Dataset	Nottingham City Council	https://www.opendatanottingham.org.uk/dataset.aspx?id=209	SHP	(Nottingham City Council, 2023)
OSM Tree Dataset	Open Street Map	Gismo component (Grasshopper)	-	-
Terrain Dataset	Open Topography	https://opentopography.org/search/node/	API key	(Open Topography, n.d.)
Climate OneBuilding	Climate OneBuilding	https://climate.onebuilding.org/	EPW	(Climate OneBuilding, n.d.)

2.3. Case Study Area Selection

For the case study area selection, the final dataset that has been created, was imported in QGIS platform, and with the building age as the main criterion, two different neighbourhoods in Nottingham, UK were selected. More specifically, the first case study area (CSA1) is located in Bestwood, Nottingham city, and contains older buildings. The second case study area (CSA2) is located in Bilborough, Nottingham city, and all of its are newer constructions. This selection has been chosen in order to investigate whether the climate change will affect in the same way different construction ages. Both case study areas consist of 300 dwellings each, approximately. Figure 2 illustrates the two neighbourhoods, through the Grasshopper and Rhino7 visualization.

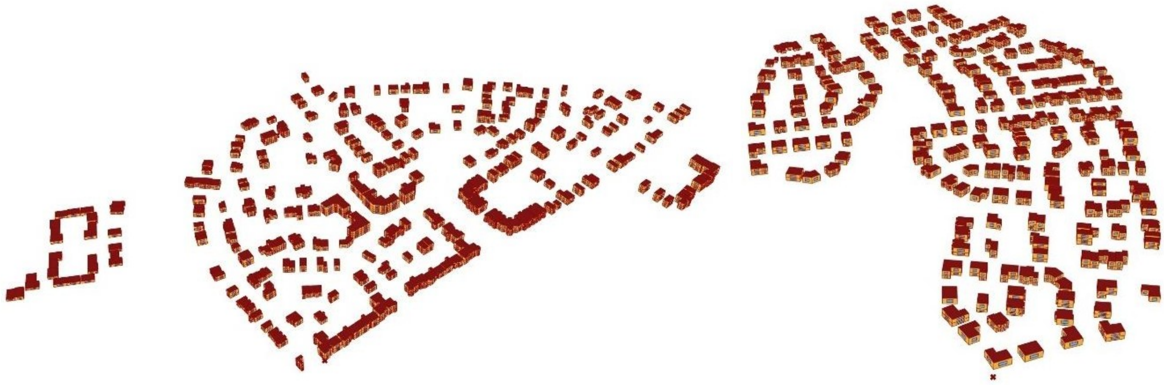

Figure 2: Case study area 1 (left-hand side) & Case study area 2 (right-hand side) – Honeybee model visualization in Rhino7.

2.4. Future Weather Data Creation

In order to run the energy model and obtain the energy demand of the buildings under the present climate and future climate, the FutureW eatherGenerator_v1.2.2 tool was used. More particularly, the Future Weather Generator is a free, open-source app, writtenin Java, which can be used to morph hourly weather data in EPW format, that align with the climate change scenarios ("Future Weather Generator – Morphs current weather for performance simulation of buildings in the future," n.d.). The climate change scenarios that are used are based on the Shared Socioeconomic Pathways (SSP), and more particularly SSP1-2.6, SSP2-4.5, SSP3-7.0, and SSP5-8.5. The timeframes that Future Weather Generator uses are 2050(2036-2065) and 2080(2066-2095). The initial dataset that has been used as the base climate for the weather predictions is the present weather data of the nearest weather station to the case study areas. Hence, after running the tool, the aforementioned pathways have been obtained in order to be fed into the energy model.

2.5. Energy Model Execution & Results Processing

After creating the energy model, and obtaining all the necessary datasets, the execution of the energy model has been done in order to obtain hourly energy demand for each individual building and each climate scenario. The energy model has been run 18 times, 9times for each case study area. The following step has been to process the results. The results have been obtained as CSV files for each dwelling, and in order to calculate the heating (space heating and hot water) and cooling demand at building and district level,32 Python scripts have been written, in order to extract the essential results and structure that needed for the interpretation and visualization. Finally, the present and future climate scenarios were processed through Python, in order to analyse the temperatureand enhance the understanding of the findings.

3. RESULTS & DISCUSSION

The purpose of this paper is to evaluate the influence of climate change in the building energy demand, and the significance for the establishment and implementation of the environmental policies. The results that have been obtained from the UBEM bottom-upphysics-based approach are presented in the following subsections.

3.1. Present Weather & Future Climate Scenarios

As has been mentioned above, it has been deemed essential to understand the way that the SSPs change over the two timeframes and the different socioeconomic pathways. For that reason, climate analysis has been implemented, and more particularly the average daily temperature has been calculated and plotted, in order to understand the level of temperature increasement due to global warming. As can be seen from Figure 3, there is an obvious upwards shift of the present weather temperature (red line graph) for the future climate scenarios, especially for the summer period. Moreover, it is clear that 2050 timeframe is characterized by lower temperatures than the 2080 timeframe, which is reasonable, as it is expected that the average daily temperature will be rising up due to climate change. Apart from the above, it can be seen that SSP5-8.5 is the future climate scenario with the highest increase in temperature. On the other hand, the rest three SSPs do not differentiate between them in that level as SSP5-8.5. In contrast, it can be seen that the reference SSP2 (middle road) indicates a lower temperature increase than SSP1 (sustainability). Nevertheless, Table 2 in combination with the graph in Figure 3 are helpful, in order to formulate some initial hypotheses for the results. According to the temperature change, it is expected that there will be an increase in the cooling demand, with a parallel decrease in the heating demand. However, the decrease in the heating demand should be lower, because as it is shown in Figure 3 in the winter season, and particularly in January and February, there is slight difference between the future climate scenarios and the present-historical weather data.

Table 2: Percentage difference in average daily temperature compared to present for future climate scenarios

Future Climate Scenarios	SSP1-2.6 2050	SSP1-2.6 2080	SSP2-4.5 2050	SSP2-4.5 2080	SSP3-7.0 2050	SSP3-7.0 2080	SSP5-8.5 2050	SSP5-8.5 2080
Percentage Difference from Present Weather	11.75%	16.74%	10.83%	22.36%	15.25%	30.85%	19.90%	39.77%

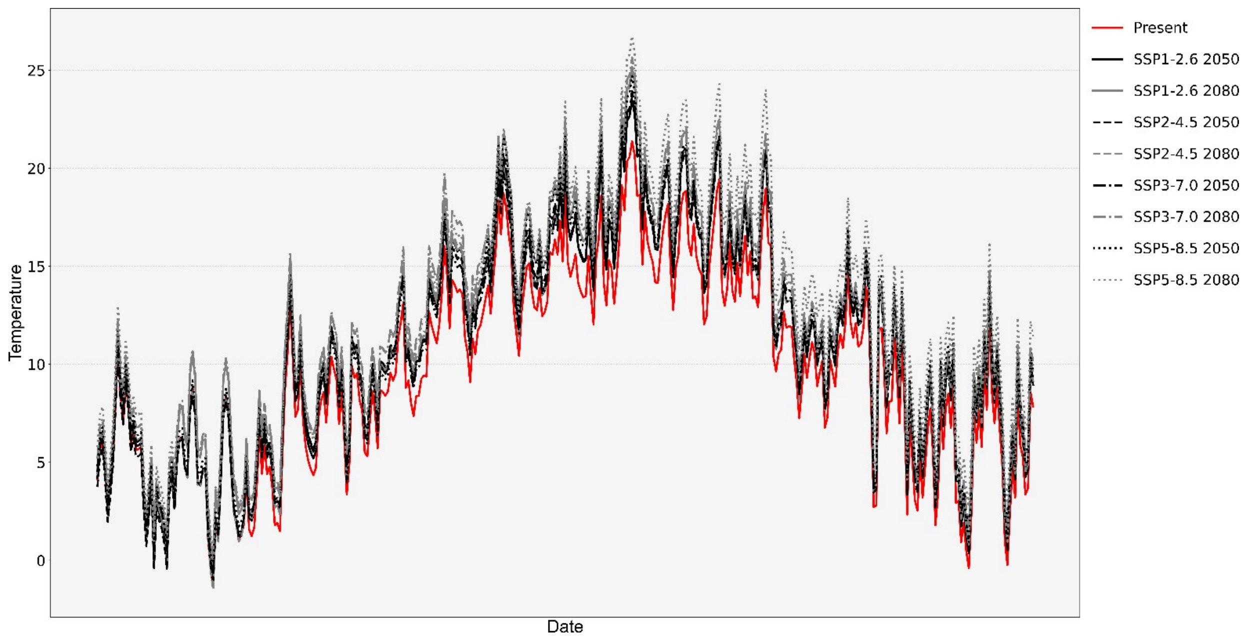

Figure 3: Average daily temperature under present weather and different future climate scenarios over the year

3.2. Annual Heating (Space Heating and Hot Water) & Cooling Demand at Building Level

After checking that the two CSAs have similar results, which means that the statistical approach and random mapping can be used for the imputation of building age for other areas, the combined actual results for the case study areas have been plotted. In Figure4, the annual building heating and cooling demand results are shown. In particular, it is clear that there is a decrease in the heating demand, and a higher increase in the cooling demand. As regards the line graphs of the two timeframes, which correspond to the average energy demand, for the heating demand the trend for Year 2050 is higher than the trend for Year 2080, and for the cooling demand the trend for Year 2050 is lower than the trend for Year 2080. These are the expected results from the climate analysis that has been done previously, as the increase in the temperature will shift the need for heating demand to higher need for cooling demand. Finally, the boxplots show that there is low distribution of the data, especially for the cooling demand, as the results are not very dispersed, and this means that there is a low uncertainty on the findings.

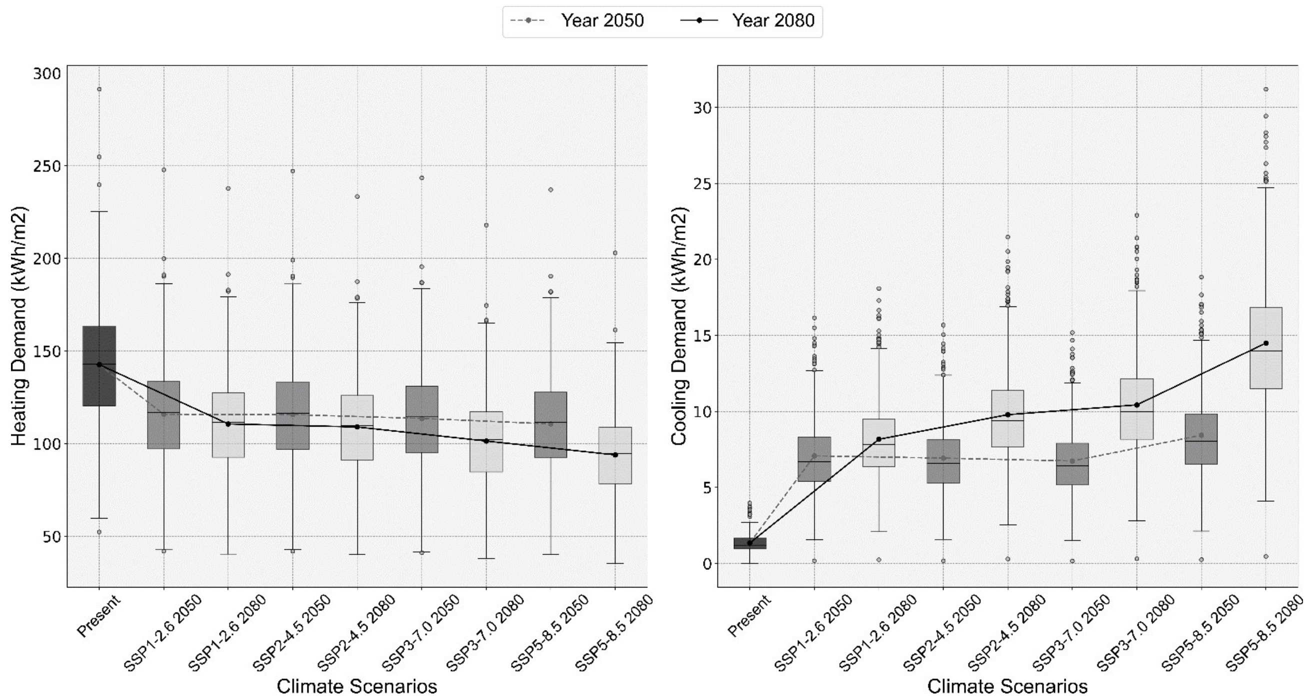

Figure 4: Annual building demand under different climate scenarios

3.3. Annual Heating (Space Heating and Hot Water) & Cooling Demand at District Level

The same process has been followed for the district level. Thus, after implementing the data processing and calculating the district energy demand out of the individual building demand, the graphs that are presented in the following figures have been plotted. More specifically, these graphs illustrate the heating (space heating and hot water) and cooling demand of the two neighbourhoods for every hour over the whole year, in Figure 5 and Figure 6, respectively.

Regarding the heating demand change from present weather to climate change scenarios, it is clear that no matter the pathway that society will follow in terms of economy, technology and environment, there will be a noticeable decrease in the heating demandof the two under-test neighbourhoods. The mean reduction between the present weather and all the future climate scenarios except of SSP5-8.5 for the year 2080, is approximately 0.01 kWh/m^2 per hour, which is equal to 25% average reduction. In addition, the highest reduction occurs for SSP5-8.5 for the year 2080, which is equal to around 50% mean reduction. This means that if there are no policy establishment for global warming and no environmental goals set, then the heating demand might decrease, but there is a high possibility of increased cooling loads.

Figure 6 illustrates the aforementioned hypothesis. There is no doubt that the cooling demand of urban areas will escalate, as hasbeen predicted from the climate analysis. In more detail, the below graph shows that at the moment, the cooling demand for UnitedKingdom, and especially for Nottingham is considerably low. On the other hand, it is evident that there is an extreme rise in the district cooling demand, which for the worst-case scenario (SSP5-8.5) and for the year 2080 heightens nearly to 0.08 kWh/m^2 from less than 0.01 kWh/m^2. Finally, in recent years cooling demand might seem insignificant for the UK, but in the future, it will be intensified, as the results show that the increase of the cooling demand is much higher than for heating demand, which is small compared to cooling demand change.

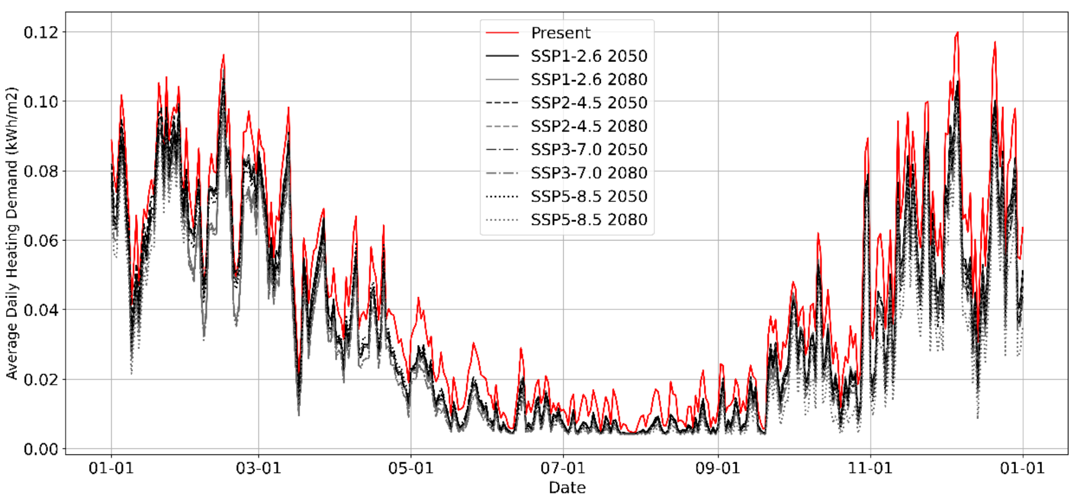

Figure 5: Average daily heating demand over the year at district scale

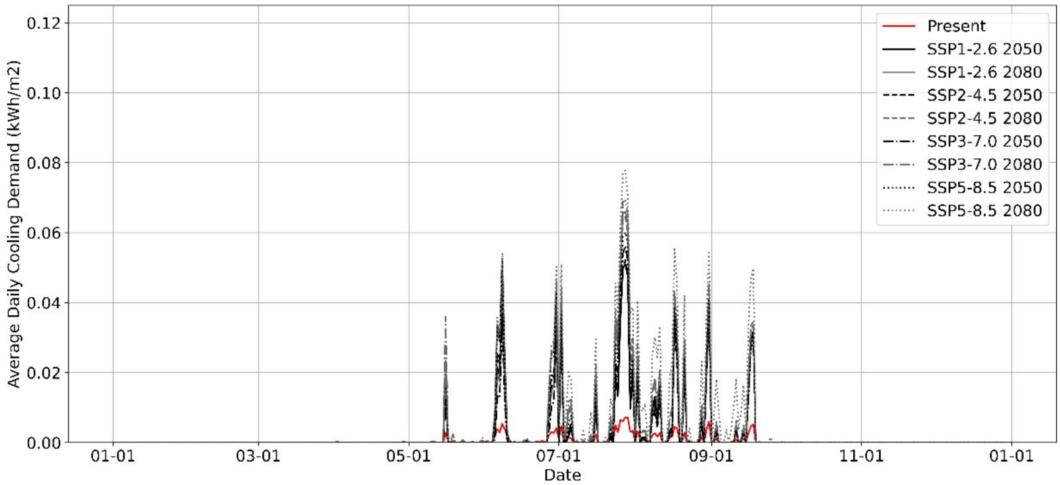

Figure 6: Average daily cooling demand over the year at district scale

4. CONCLUSION

The aim of this research study was the evaluation of the influence of climate change to the energy demand of the residential building stock as it is currently built. The present weather and 8 different climate scenarios were analysed, in order to evaluate the change in the average temperature throughout the years. More particularly, the future weather data that have been created based on the Shared Socioeconomic Pathways have been used, namely SSP1-2.6, SSP2-4.5, SSP3-7.0, and SSP5-8.5, for two different timeframes, year 2050 and year 2080.

The methodological approach has been constructed with Rhino7-Grasshopper and the Ladybug tools, and the energy simulations have run via URBANopt that implements EnergyPlus calculations on the background. The selected residential building stock is located in Nottingham, UK and consists of a variety of building types and building ages, in order to consider as many archetypes as possible. The findings have shown that for the SSP1-2.6, SSP2-4.5 and SSP3-7.0 scenarios, there will be a small drop in the heating demand, but an extremely high increasement in the cooling demand. On the other hand, for the worst-case scenario SSP5-8.5, there might be a higher decrease in the heating demand, but the cooling demand will explode, resulting in the risk of overheating in summer period, and the human thermal comfort loss inside the UK residential building stock.

The above leads to the conclusion that there should be a shift on the focus from the heating demand to the cooling demand of buildings. However, further investigation is required regarding the different building types and age, and the way each of them are affected by climate change. In this way, policy makers and urban planners will be able to make recommendations and establish new environmental goals, that will target the most vulnerable dwellings, and for the rapid assessment of this urban building energy modelling is the key.

5. AKNOWLEDGEMENT

To EPSRC Centre for Doctoral Training (CDT) in Geospatial Systems and to Ordnance Survey for funding this research and supporting it with geospatial data, with grant number EP/S023577/1.

6. NOMENCLATURE

CSA = Case Study Area

CSV = Comma-Separated Values

EPC = Energy Performance

CertificateOS = Ordnance Survey

SSP = Shared Socioeconomic Pathways

UBEM = Urban Building Energy Modelling

UK = United Kngdom

UNECE = United Nations Economic Commission for Europe

7. REFERENCES

Apostolopoulou, A., Jimenez-Bescos, C., Cavazzi, S., Boyd, D., 2023. Impact of Climate Change on the Heating Demand of Buildings. A District Level Approach. Environmental and Climate Technologies 27, 900–911. https://doi.org/10.2478/rtuect-2023-0066

Armstrong, J., 2001. The Forecasting Dictionary. Principles of Forecasting: A Handbook for Researchers and Practitioners.

Chow, D.H.C., Li, Z., Darkwa, J., 2013. The effectiveness of retrofitting existing public buildings in face of future climate change in the hot summer cold winter region of China. Energy and Buildings 57, 176 –186. https://doi.org/10.1016/j.enbuild.2012.11.012

Climate OneBuilding, n.d. Repository of free climate data for building performance simulation [WWW Document]. URL https://climate.onebuilding.org/ (accessed 11.17.23).

ClimateData.ca, n.d. Understanding Shared Socio-economic Pathways (SSPs). ClimateData.ca. URL https://climatedata.ca/resource/understanding-shared-socio-economic-pathways-ssps/ (accessed 5.28.24).

Digimap, n.d. OS MasterMap Topography Layer [WWW Document]. URL https://digimap.edina.ac.uk/webhelp/os/data_information/os_products/mastermap_topo.htm (accessed 6.20.22a).

Digimap, n.d. Building Height Attribute [WWW Document]. URL https://digimap.edina.ac.uk/help/gis/bha/ (accessed 11.16.23b).

Digimap, n.d. Ordnance Survey [WWW Document]. URL https://digimap.edina.ac.uk/os (accessed 6.26.21c).

Future Weather Generator – Morphs current weather for performance simulation of buildings in the future, n.d. URL https://future - weather-generator.adai.pt/ (accessed 5.26.24).

Ibrahim, A., Jimenez-Bescos, C., 2020. Assessing the Performance Gap of Climate Change on Buildings Design Analytical Stages Using Future Weather Projections. Environmental and Climate Technologies 24, 119–134. https://doi.org/10.2478/rtuect-2020-0091

Jimenez-Bescos, C., Oregi, X., 2019. Implementing User Behaviour on Dynamic Building Simulations for Energy Consumption. Environmental and Climate Technologies 23, 308–318. https://doi.org/10.2478/rtuect-2019-0097

Laktuka, K., Pakere, I., Lauka, D., Blumberga, D., Volkova, A., 2021. Long-Term Policy Recommendations for Improving the Efficiency of Heating and Cooling. Environmental and Climate Technologies 25, 382–391. https://doi.org/10.2478/rtuect- 2021-0029

Nottingham City Council, 2023. Trees (NCC Maintained).

Open Data Communities, n.d. Energy Performance of Buildings Data England and Wales [WWW Document]. URL https://epc.opendatacommunities.org/ (accessed 6.20.22).

Open Topography, n.d. High-Resolution Topography Data and Tools.

Ordnance Survey, n.d. AddressBase | OS Products [WWW Document]. URL https://www.ordnancesurvey. co.uk/business-government/products/addressbase (accessed 6.20.22).

Rodrigues, E., Fernandes, M.S., 2020. Overheating risk in Mediterranean residential buildings: Comparison of current and future climate scenarios. Applied Energy 259, 114110. https://doi.org/10.1016/j.apenergy.2019.114110

Santamouris, M., Paolini, R., Haddad, S., Synnefa, A., Garshasbi, S., Hatvani-Kovacs, G., Gobakis, K., Yenneti, K., Vasilakopoulou, K., Feng, J., Gao, K., Papangelis, G., Dandou, A., Methymaki, G., Portalakis, P., Tombrou, M., 2020. Heat mitigation technologies can improve sustainability in cities. An holistic experimental and numerical impact assessment of urban overheating and related heat mitigation strategies on energy consumption, indoor comfort, vulnerability and heat-related mortality and morbidity in cities. Energy and Buildings 217, 110002. https://doi.org/10.1016/j.enbuild.2020.110002

Stagrum, A.E., Andenæs, E., Kvande, T., Lohne, J., 2020. Climate Change Adaptation Measures for Buildings—A Scoping Review. Sustainability 12, 1721. https://doi.org/10.3390/su12051721UNECE, n.d. Shared Socioeconomic Pathways (SSPs).

United Nations Environment Programme, 2022. 2022 Global Status Report For Buildings and Construction: Towards a zero-emissions, efficient and resilient buildings and construction sector.

Wang, R., Lu, S., 2020. A novel method of building climate subdivision oriented by reducing building energy demand. Energy and Buildings 216, 109999. https://doi.org/10.1016/j.enbuild.2020.109999

Wang, R., Lu, S., Zhai, X., Feng, W., 2022. The energy performance and passive survivability of high thermal insulation buildings in future climate scenarios. Build. Simul. 15, 1209–1225. https://doi.org/10.1007/s12273-021-0818-3

#284: Heat storage and nano-encapsulation properties of modified core-shell paraffin@xFe/ZIF-67 composite phase change materials

Yan GAO[1,2,3,*], Yanteng LI[1], Jingchuan GUO[1], Xing RONG[3], Yong ZHOU[3], Guolan FAN[2], Ping CUI[1],
Guohong TIAN[4], Xudong ZHAO[5]

[1] Shandong Technology Innovation Center of Carbon Neutrality, School of Thermal Engineering, Shandong Jianzhu University, Jinan, China, 250013.
[2] Shandong Province Jinan Ecological and Environmental Monitoring Center, Jinan, China, 250101.
[3] Shandong Hi-speed Maintenance Group Engineering Technology Research Institute, Jinan, China, 250032.
[4] School of Mechanical Engineering Sciences, University of Surrey, Guildford, Surrey, UK, GU2 7XH.
[5] Energy and Environmental Institute, University of Hull, Hull, Yorkshire, UK, HU6 7RX.
* Correspondence: gaoyan18@sdjzu.edu.cn; Tel.: 008613864154887

Abstract: Phase change materials (PCMs) can reversibly store a large amount of energy, but there are many problems such as large volume change during the phase change process and easy leakage of materials, which demand to select an ideal shell material for effective encapsulation. The nano-encapsulation involves encapsulating PCMs at the nanoscale level, typically utilizing nanoparticles or nanostructured materials as carriers for PCMs. In this experiment, the modified Fe/ZIF-67 was synthesized by a solvothermal method and used as a shell. A composite PCMs of core-shell paraffin@Fe/ZIF-67 was prepared using the physical co-integration impregnation method. The characterization techniques, such as scanning electron microscopy (SEM), X-raydiffractometry (XRD), differential scanning calorimetry (DSC), and thermogravimetric analysis (TGA), were used to analyze the microscopic morphological structure, thermal properties, and other characteristics of the composite PCMs. The results showed thatthe modified ZIF-67 had an excellent protective effect on the paraffin core, the highest paraffin loading was 50% w/w, uniformly distributed in the pore channels of ZIF-67, and these two materials were only physically mixed without chemical reactions. Although the addition of Fe improved the thermal stability of the modified ZIF-67, the thermal stability and latent heat of paraffin@Fe/ZIF-67 as the composite PCMs were reduced by the influence of Fe doping. The 50% w/w paraffin@0Fe/ZIF-67 sample had the maximum stored energy of 67.85 J·g-1. The test results revealed that ZIF-67 material was a suitable shell for paraffin core, and the composite PCMs had more stable thermal properties, which exhibited excellent application prospects in energy storage.

Keywords: Modified ZIF-67; Paraffin; Core-Shell Structure; Composite Phase Change Materials; Latent Heat; Energy Storage

1. INTRODUCTION

Global energy consumption is still dominated by non-renewable fossil fuels, which not only generate severe environmental pollution but also make the energy crisis increasingly visible [1, 2]. At the same time, rapid technological developments have placed greater demands on the development of new energy sources and energy storage technologies. The researchers and stakeholders have been focusing on the development of clean and renewable energy sources and the improvement of energy conversion efficiency. Thermal Energy Storage (TES) uses sensible, latent, or thermochemical energy storage to reconcile the spatial and temporal mismatch of energy sources [3]. Latent thermal energy storage (LTES) is the most effective means of improving energy utilization, expanding thermal energy applications, and increasing the effectiveness of heat storage and discharge in a specific temperature range, compared to sensible thermal energy storage with low energy storage density and low controllable thermochemical energy storage [4, 5].

Phase change materials (PCMs) are advanced functional materials that are capable of storing and utilizing thermal energy by exploiting the latent heat in the phase change process. Most importantly, this utilization is reversible [6]. Latent thermal storage with the application of PCMs is one of the most excellent ways to store energy, being closest to isothermal and having the most preferred energy storage density during the heat storage and discharge process, enabling efficient storage and management of waste thermal energy or available thermal energy. PCMs for thermal energy storage can be classified into four major categories based on the phase state change: solid-solid, solid-liquid, solid-gas, and liquid-gas phase change materials [7]. The highest latent heat of melting values is found in solid-gas and liquid-gas phase change materials. However, they are not appropriate for practical applications due to the substantial volume changes during evolution due to the presence of gases and the requirement for specialized pressurized vessels. Solid-solid PCMs typically have high phase transition temperatures and low latent heat values [8]. Solid-liquid PCMs are used in various applications due to their high latent heat, intermediate phase transition temperatures, and minor volume changes (usually less than 10%) during the phase transition process [9].

Among many natural or composite solid-liquid PCMs, paraffin, as a saturated alkane, is one of the most preferred materials for application in LTES systems, mainly owing to its intermediate phase change enthalpy and wide melting temperature, its non-toxic and low cost, and its availability in the industry as a petroleum by-product with minimal negative environmental impact [10]. Despiteall these advantages, paraffin wax, like most single PCMs, suffers from low thermal conductivity and the tendency to leak during phase change, which are the main reasons that hinder the application of PCMs in heat storage and exothermic systems [11]. To solve such technical issues, scientists from numerous countries have conducted intensive analysis, such as introducing porous materials such as shell media victimization shell-shaped polymers to sequester the phase transition cores and developing shape-stablecomposite PCMs to boost the thermal conduction or thermal stability of the phase transition cores.

Tang et al. [12] synthesized mesoporous and macroporous Cr-MIL-101 hollow tubes by ligating Cr^{3+} with alkylated bridging ligands and encapsulated octadecane in hollow tube nanocontainers to produce composite PCMs. The results showed that composite PCMs had a thermal storage capacity of 187 $J \cdot g^{-1}$ and a maximum loading of 80%. Wang et al. [13] prepared composite PCMs by microencapsulating paraffin cores using a polymer shell and then expanded graphite particles were added. It was found that the thermal conductivity of the composites improved by 132%, the sensible specific heat was reduced by 28%, and the loading was up to 70%, which could effectively improve the heat transfer rate of heat exchangers. Qin et al. [14] used a degradable chitosan/gelatin co-emulsifier as a composite shell to solve the problem of low and irregular encapsulation efficiency of microencapsulated phase change materials, a degradable chitosan/gelatin co-emulsifier was used as a composite shell. N-tetradecane was encapsulated using glutaraldehyde for cross-linking. The results showed that the encapsulation efficiency of microcapsules and the latent heat value could reach 70.94% and 146.88 $J \cdot g^{-1}$, and the prepared microcapsules showed great thermal stability and thermal cycling reliability. The encapsulation or functionalized modification of PCMs has proven to be an effective way to improve the thermal performance of PCMs and prevent leakage.

Metal-Organic Frameworks (MOFs) are organic-inorganic hybrids with a multidimensional pore structure assembled from metal ions (ion clusters) and organic linkers, both of which are capable of ligand self-assembly [15, 16]. MOFs materials have beneficial chemical properties, such as adjustable pore size, large specific surface area, high porosity and directional tailoring and modification, which are widely used in multiphase catalysis [17], gas storage and separation [18] and pollutant adsorption [19]. Zeolitic Imidazolate Frameworks (ZIF-67) is a special type of MOFs material developed in recent years, which consists of organic bridging of tetrahedral square coordination of divalent transition Co^{2+} and heterocyclic imidazole ligands. Besides the properties of ordinary MOFs, ZIFs materials exhibited higher mechanical, chemical and thermal stability [20]. The metal sites of bimetallic organic frameworks are constituted by two different metal ions, which can generate synergistic effects between each other and intensify complexation with the organic ligands, providing a richer multi-metallic active site and more thermal stability than monometallic organic frameworks [21]. The use of MOFs as a shell with special characteristics can effectively compensate for the shortcomings of PCMs by preventing leakage and improving thermal properties.

This research used a solvothermal method to load Fe cooperating with Co into ZIF-67 as the linkage point for bimetallic modification, resulting in a favourable bimetallic synergistic effect between iron and cobalt. Using the modified ZIF-67 as the shell to encapsulate paraffin wax, the optimal loading capacity was studied to obtain the maximum energy storage and to solve the leakage problem during the phase change reaction of paraffin wax core. Meanwhile, the synergistic effects between iron and cobalton the material loaded paraffin wax core in the process of heat storage and discharge was also investigated.

2. RESEARCH METHODS

2.1. Experimental materials

Ferric nitrate nine-hydrate ($Fe(NO_3)_3 \cdot 9H_2O$,99.5%), cobalt nitrate hexahydrate ($Co(NO_3)_2 \cdot 6H_2O$,99.5%), 2-methylimidazole (99.5%), methanol (99%) and ethanol (99%) were all supplied by Shanghai Maclin Biochemical Technology Co., LTD., and No. 58 fully refined paraffin was supplied by Daqing Paraffin Sales Company. All the chemicals and materials were used without further purification.

2.2. Samples preparation

Preparation of modified MOFs

The modified ZIF-67 crystals were synthesized by solvothermal method [22]. $Fe(NO_3)_3 \cdot 9H_2O$ and $Co(NO_3)_2 \cdot 6H_2O$ were used as the bimetallic precursors at molar ratios of 0:2, 7:93, and 7:43 respectively. The mixed precursors were stirred into 10 ml of methanol. At the same time, 1025 mg of 2-methylimidazole was added into 20 ml of methanol. Subsequently, these two solutions were mixed and stirred for 30 min continually, and then stood at room temperature for 24 h. The resulting product was collected by centrifugation and washed thoroughly with deionized water and methanol. Finally, the purple solid was dried in an oven at 80 °C for24 h. The modified ZIF-67 samples with the molar ratios of Fe at 0%, 7%, and 14% respectively, were named as xFe/ZIF-67, where x referred to the percentage of Fe doping.

Preparation of composite PCMs

The preparation of composite PCMs was carried out by the physical co-impregnation method. The different qualities of paraffin were added to 100 ml anhydrous ethanol and stir at 60 °C until dissolved completely. Subsequently, 0.5g *x*Fe/ZIF-67 material was added to the mixture prepared above and stirred vigorously for 4h, and then cooled to room temperature and smashed to powder. To increase the uniformity of powder, the above operations were repeated 3 times. Finally, the powder was dried at 50 °C for 48 h until the anhydrous ethanol evaporated fully to obtain paraffin@*x*Fe/ZIF-67 composite PCMs. The prepared materials were named 30%@0Fe/ZIF-67, 50%@0Fe/ZIF-67, 70%@0Fe/ZIF-67 with different paraffin loadings of 30 wt%, 50 wt%, and 70 wt%,respectively. The main process preparation of the samples is shown in Figure 1.

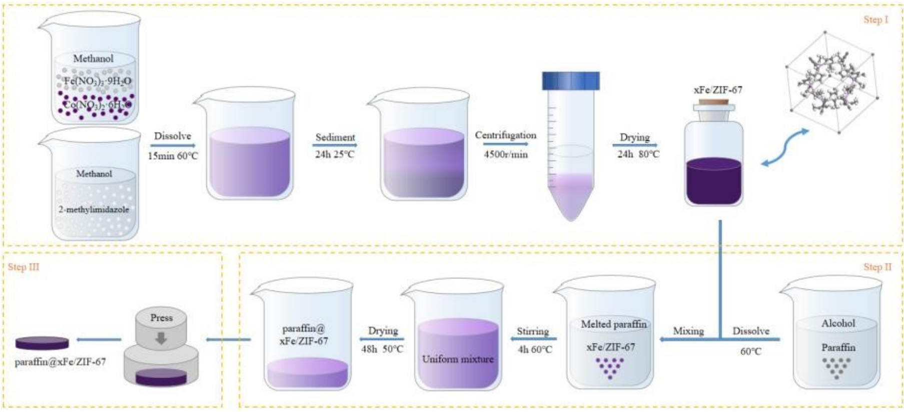

Figure 1: The main preparation process of paraffin@xFe/ZIF-67 composite PCMs

2.3. Characterization of physical and chemical properties

The microscopic morphology of the samples was examined using a SU8010 scanning electron microscope (Zeiss, German) with a resolution of 1 nm and an accelerating voltage of 0.1 - 30 kV. The crystal structures of the samples were analyzed at room temperature using an Smartlab 9 X-ray diffractometer (Rigaku, Japan) with a radiation source Co Ka, a scan speed of 20 deg·min^{-1}, a scan step of 0.01° and a scan range of 5° to 90°. The chemical structure of the combined PCMs samples was estimated by Tensor27 Fourier transform infrared spectroscopy (Bruker, German). The thermogravimetric results of the modified ZIF-67 material were determined using a comprehensive thermal analyzer TOLEDO TGA2 LF (Mettler, USA) with N_2 atmosphere protection, a fixed gas flow rate of 50 ml·min^{-1}, a temperature rise rate of 20°C·min^{-1}, and the mass change was measured from 50°C to 750°C.

The phase transition process of paraffin@*x*Fe/ZIF-67 composite PCMs was studied by TA Q20 Differential Scanning Calorimeter (Mettler Toledo, Switzerland), where the composites were heated and cooled at a rate of 10 K·min^{-1} between 30 °C and 90 °C in an N_2 atmosphere. The thermal stability of the materials was analyzed using a comprehensive STA 449 F5 thermal analyzer (Netzsch, German) in an N_2 atmosphere with a set temperature rise rate of 20 °C·min^{-1} and a gas flow rate of 50 ml·min^{-1}. The transient planar source technique was used to determine the heat transfer coefficient by tablets containing the same composite PCMs tested by TPS 2500S (HotDisk, Switzerland). Therefore, the tablets with the same diameter of 13 mm and the same mass of 300.0 mg of composite PCMs were prepared by a tablet press held at a pressure of 6.0 MPa for 3 min.

3. RESULTS AND DISCUSSION

3.1. Thermal stability analysis

Thermal stability analysis of modified xFe/ZIF-67

Since the measured samples were treated by vacuum and high-temperature activation before TGA testing, the removal of crystalline water and imidazole-like impurities was relatively complete, so the main reason for their weight loss was caused by the decomposition of the structure or molecules within the material. The weight loss curves can be broadly divided into two stages, the first stage was due to the removal of ligand water molecules bound in the center of the metal site, and the second stage was distributed to the collapse of the organic frameworks structure caused by high temperatures.

As shown in Figure 2(a), the decomposition of 0Fe/ZIF-67 started at 232°C with a small weight loss in the range of 232°C-502°C. The disintegration of the frameworks structure happened at about 502°C, and a rapid and significant weight loss occurred within 502°C-586°C, followed by a slowing down of the weight loss rate until the composite material was completely decomposed. The weight loss patterns of 7Fe/ZIF-67 and 14Fe/ZIF-67 were approximately the same as that of 0Fe/ZIF-67. However, it was obvious that with the increase of Fe doping, the decomposition temperature of the materials kept rising and the thermal stability increased significantly, by comparison the weight loss of different samples at the same temperature. Fe doping might increase the strength of the coordination bond between metal ions and ligands, thus making the material more resistant to thermal decomposition. Due to its superior heat stability, the Fe-modified ZIF-67 material was utilized for paraffin compounding tests.

The thermal stability assessment of PCMs was crucial in thermal energy storage applications. The thermogravimetric curves were shown in Figure 2(b). It can be clearly seen that the pure paraffin wax showed a one-step weight loss in the range of 204 -360 °C, and finally almost no weight remains, which indicated that the paraffin wax was completely volatilized after heating. Compared with pure paraffin, the paraffin@xFe/ZIF-67 composite samples all exhibited significant two-step degradations. The decomposition peaks appeared in the range of 220-505 ºC, corresponding to the evaporation of the ligand water molecules in paraffin and ZIFs. The decomposition peaks around 506-600ºC were mainly attributed to the collapse and decomposition of ZIFs structure.

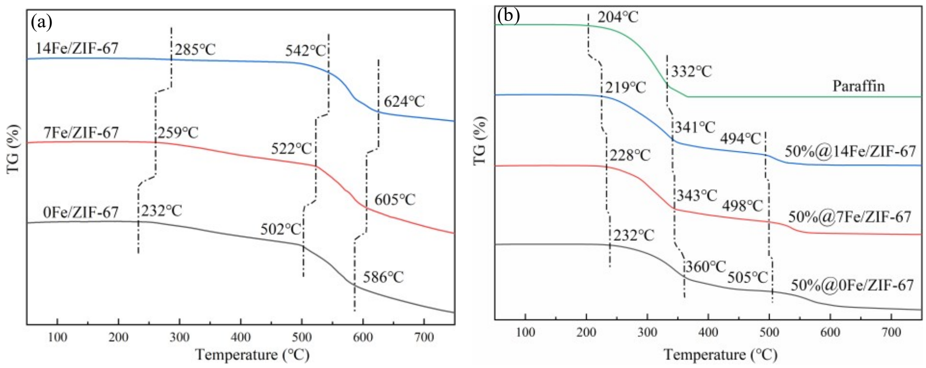

Figure 2: TGA pattern (a) modified bimetallic Fe/ZIF-67; (b) composite PCMs

3.2. Microscopic morphological analysis

Microscopic morphology analysis of modified xFe/ZIF-67

The microscopic morphology of the modified *x*Fe/ZIF-67 material was observed using a scanning electron microscopy (SEM). As shown in Figure 3(a), the 0Fe/ZIF-67 sample was spherical particles with rough surface and wrinkles. Figure 3(b) showed that the sample did not agglomerate, which was beneficial to the adsorption of paraffin by 0Fe/ZIF-67. Figure 3(c) indicated that the morphology of 7Fe/ZIF-67 was similar to that of 0Fe/ZIF-67 with a small increase in surface wrinkles. Due to Fe doping, as shown in Figure 3(d), the 7Fe/ZIF-67 sample began to generate a very small amount of impurity particles. With the further increase of Fe doping amount, as shown in Figure 3(e,f), the granular matter on the surface of the 14Fe/ZIF-67 sample increased significantly, thewrinkles became more obvious, and the ZIFs particle fragmentation and structural collapse appeared. It was not difficult to see from the comparison that with the increase of Fe doping amount, the surface of the sample was rougher, the wrinkles were more obvious, and there were granular or flaky substances attached. The higher amount of Fe doping caused this phenomenon more obvious.

Microscopic morphology analysis of composite PCMs

In order to more accurately observe the microscopic morphology of composite PCMs and judge the impact of paraffin loading on the morphology of paraffin@*x*Fe/ZIF-67, the simplest paraffin@0Fe/ZIF-67 sample was selected for comparative analysis. The results were shown in Figure 4. Compared with ZIF-67, the composite PCMs particles were plumper, meanwhile, the surface and edges were smoother. Due to the influence of paraffin viscosity, the original dodecahedral morphology of ZIFs samples was no longer obvious.

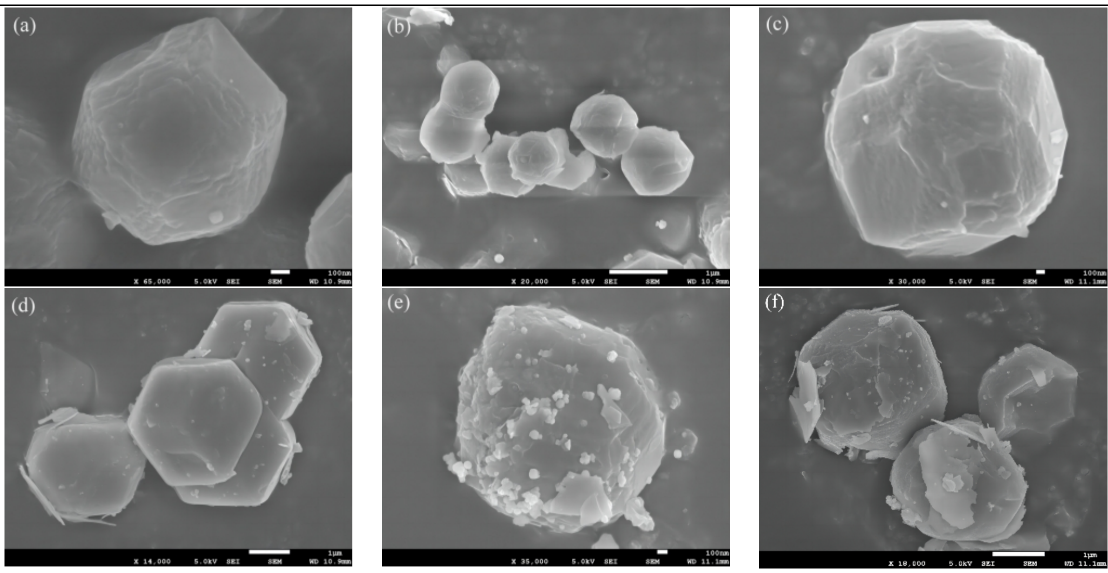

Figure 3: SEM images of modified xFe/ZIF-67 samples: (a, b) 0Fe/ZIF-67; (c, d) 7Fe/ZIF-67; (e, f) 14Fe/ZIF-67

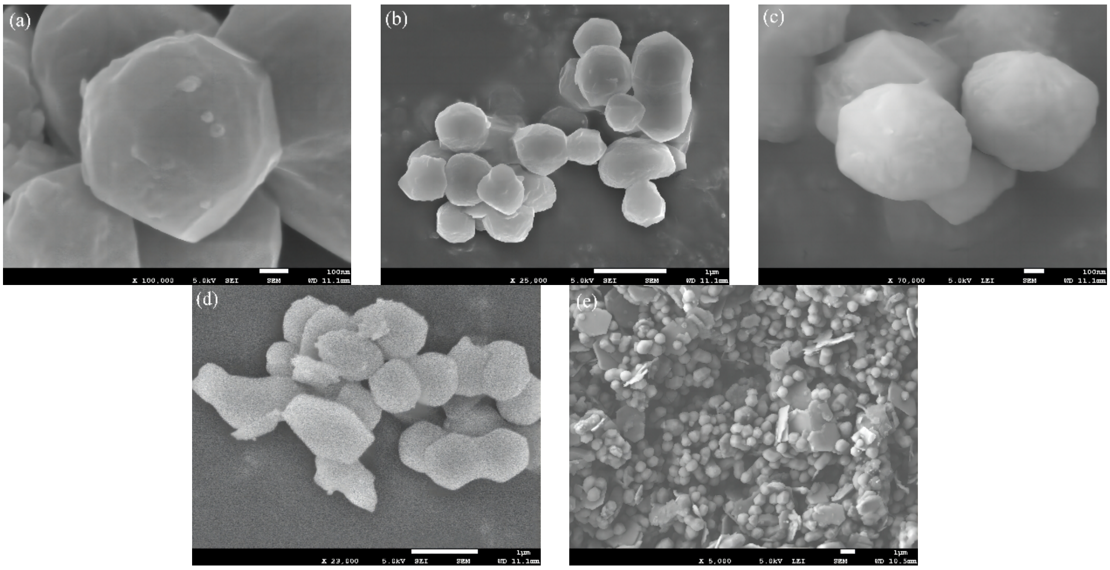

Figure 4: SEM images of composite PCMs samples: (a, b) 30%@0Fe/ZIF-67; (c,d) 50%@0Fe/ZIF-67; (e) 70%@0Fe/ZIF-67

The morphological difference between the composite PCMs was due to the different loading ratios of PCMs in the shell material. It could be clearly seen from Figure 5(a) and (b) that the morphology of the sample loaded with 30% paraffin wax was not much different from that of 0Fe/ZIF-67, but the surface smoothness increased, indicating that the paraffin wax was successfully impregnated into the modified ZIF-67 material through the pore capillary effect and surface tension. The morphology of the sample loaded with 50% paraffin wax became smooth and plump, as shown in Figure 5(c) and (d), indicating that the paraffin molecules were anchored in the frameworks through hydrogen bonding interactions with functional groups such as hydroxyl groups and uniformly distributed in the composite material. As the paraffin loading rose to 70%, some paraffin molecules were inevitably scattered on the surface of the shell material, and the leaked paraffin molecules were in the shape of smooth blocks, as shown in Figure 5(e), which indirectly confirmed that the optimal paraffin loading capacity of the modified ZIF-67 material.

3.3. X-ray diffraction analysis

X-ray diffraction analysis of modified xFe/ZIF-67

XRD analysis was performed to confirm the crystal structure of the modified bimetallic *x*Fe/ZIF-67, and the results were shown in Figure 5. It is obvious that the diffraction peaks presented in *x*Fe/ZIF-67 could all be successfully matched with the simulated standard card of ZIF-67, and the diffraction peaks were sharp and strong without significant shift, which indicated that the three-dimensional zeolite imidazole ester framework material of ZIF-67 was successfully prepared with excellent crystallinity. The modified bimetallic *x*Fe/ZIF-67 exhibited some more excellent properties, exhibiting major characteristic peaks in the lattice planes of (011), (002), (112) and (222) at around 2θ = 7.49°, 10.54°, 12.88° and 18.20°, and the intensity of these peaks was much higher than other peaks. When Fe doping amount was 0% and 7%, the lattice planes of (022), (013), (114), (233), and (134) were shownat 2θ=14.89°, 16.58°, 22.27°, 24.61° and 26.75°, but the peaks were weak, and the crystallinity was not obvious. When the Fe content increased to 14%, the intensity of the diffraction peaks enhanced, probably due to the Fe addition prompting the cross-linking effect between the original metal Co ions and the imidazole and accelerating the crystal growth.

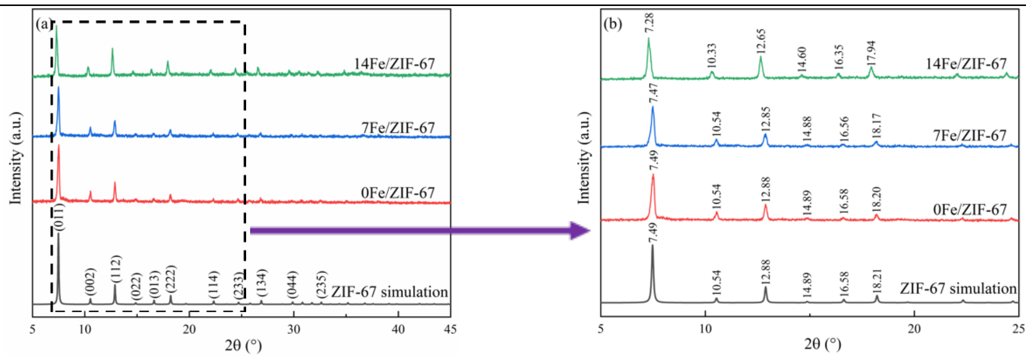

Figure 5: XRD pattern of modified bimetallic xFe/ZIF-67: (a) XRD pattern of 2θ from 5° to 45°; (b) Low diffraction angle shift analysis

In addition, as shown in Figure 5(b), the peak positions of the synthesized 0Fe/ZIF-67 were almost consistent with those of the simulated ZIF-67 crystal structure, which further proved the synthesis of a typical ZIF-67 structure. As Fe doping content increased to 7%, the diffraction peak position of 7Fe/ZIF-67 shifted slightly to the smaller angle. As Fe content continued to increase to 14%, the diffraction peak position of 14Fe/ZIF-67 shifted to the left more significantly, indicating that the crystal diffracted at smaller grazing angles. The reason for this phenomenon was the incorporation of heteroatom Fe with a larger atomic radius than the host Co, leading to the larger unit cell parameters and the increase of the crystal interplanar spacing.

X-ray diffraction analysis of composite PCMs

The XRD analysis of paraffin and composite PCMs was performed to confirm the crystal structure, and the results showed in Figure 6. The XRD pattern of solid paraffin showed two distinct peaks at 2θ = 21.43° and 23.85°, corresponding to the crystallographic planes of (110) and (200). For the composite PCMs with different paraffin loading ratios, the prominent characteristic peaks of paraffin were detected at 2θ = 21.43° and 23.85°, and other remarkable peaks at 2θ=7.49°, 10.54°, 12.88°, and 18.20° were attributed to ZIF-67 crystals. The above results indicated that the composite PCMs were successfully prepared and the crystal structure of modified bimetallic Fe/ZIF-67 could be kept unchanged after compounding with paraffin.

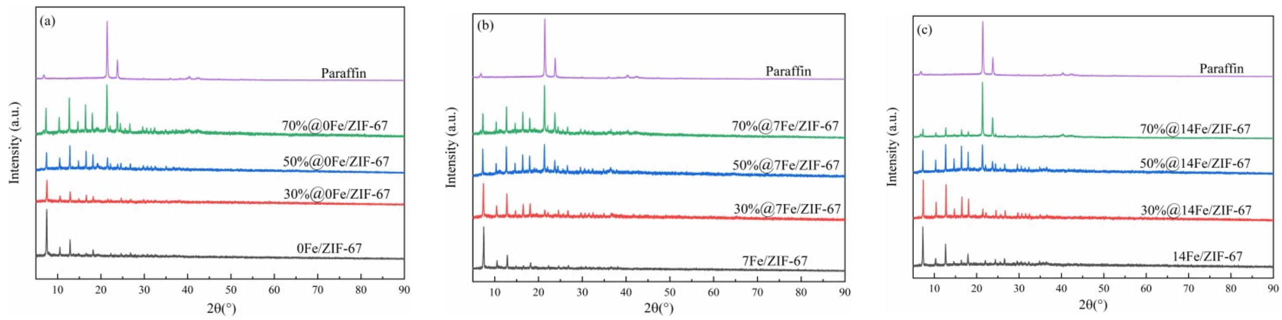

Figure 6: XRD patterns of composite phase change materials: (a) paraffin@0Fe/ZIF-67; (b) paraffin@7Fe/ZIF-67; (c) paraffin@14Fe/ZIF-67

By comparing the XRD curves, it was found that for three modified ZIF-67 materials with different Fe contents, when the paraffin content increased in the range of 0% to 50%, the characteristic peak intensity of paraffin improved slowly, and when the paraffin content continued to increase to 70%, the diffraction peak of paraffin enhanced significantly. The change of the characteristic peak intensity may be due to the fact that PCMs had reached the adsorption saturation state when the paraffin loading reached 50%, and the 70% paraffin loading made the composite PCMs partially leak. In addition, there were no new diffraction peaks appeared inthe XRD patterns of paraffin@*x*Fe/ZIF-67 with different paraffin loadings, which indicated that no chemical reaction occurred duringthe composite process of modified Fe/ZIF-67 with paraffin.

3.4. Fourier infrared spectral analysis

Figure 7 exhibited the FTIR spectra of single paraffin and different composite PCMs samples. In the single paraffin sample, the characteristic peaks at 719.42 cm^{-1}, 1377.12 cm^{-1}, and 2848.76 cm^{-1} were caused by the in-plane rocking vibration, deformation vibration, and symmetric stretching vibration of CH_2, respectively. In addition, the other two peaks at 1460 cm^{-1} and 2921 cm^{-1} wereattributed to the deformation vibration and symmetrical stretching vibration of CH_3. In composite PCMs samples, the characteristic peaks from bimetallic modified ZIF-67 (1423.41 cm^{-1}, 1305.76 cm^{-1}, 1141.82 cm^{-1} and 756.07 cm^{-1}) and paraffin (2921 cm^{-1}, 2848.76 cm^{-1}, 2853 cm^{-1}, 1460 cm^{-1} and 723 cm^{-1}) were observed simultaneously with sharp peak shapes and no significant shifts, indicating the paraffin@*x*Fe/ZIF-67 composites were successfully prepared. At the same time, no new characteristic peaks appeared in the FTIR pattern, which further proved that the composite of bimetallic modified ZIF-67 material and paraffin was only physically mixed without chemical reactions.

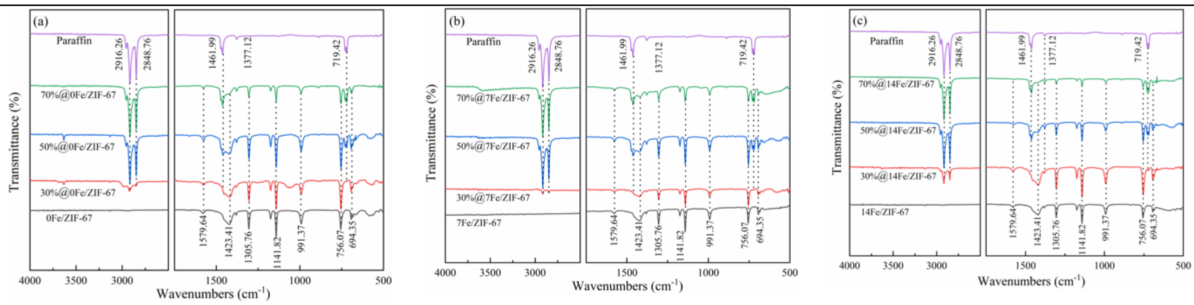

Figure 6: FTIR spectrum of composite phase change materials: (a) paraffin@0Fe/ZIF-67; (b) paraffin@7Fe/ZIF-67; (c) paraffin@14Fe/ZIF-67

The characteristic peaks attributed to paraffin in the composite PCMs samples kept increasing when the paraffin loading content varied from 0% to 50%. However, the paraffin peak intensity no longer changed when the paraffin content continued to increase from 50% to 70%. This phenomenon further confirmed that the PCMs were saturated with paraffin when the paraffin loading contentwas 50%, and the continued increase of paraffin loading would not promote the composite PCMs samples to absorb IR light at the corresponding wavelength. In addition, when the paraffin content was at 70%, the characteristic peaks attributed to the modified ZIF-67 were significantly reduced in 70%@*x*Fe/ZIF-67 compared to the PCMs samples with lower paraffin content (30%@*x*Fe/ZIF-67 and 50%@*x*Fe/ZIF-67).

3.5. Pore structure of modified xFe/ZIF-67

To evaluate the specific surface area and pore volume of the modified *x*Fe/ZIF-67 samples, N_2 adsorption-desorption experiments were performed. As shown in Figure 8(a), the N_2 adsorption-desorption isotherms of the modified *x*Fe/ZIF-67 belonged to type I isotherm according to the IUPAC classification, which revealed the presence of microporous structures in the material. In addition, the pore size distribution characteristics of the samples were investigated as shown in Figure 8(b). The micropores and mesopores in the sample were concentrated at about 0.8-2.0 nm and 2-10 nm, respectively, presenting a hierarchical pore structure with the coexistence of micropores and mesopores. The presence of micropores could generate a strong adsorption force on the phase change material and maintain the stability of composite materials, while the mesopores could provide a wider phase change space for paraffin wax and effectively improve heat storage efficiency. It was worth mentioning that if only micropores exist, the nano-constraining effect of micropores would inhibit the crystallization of the phase change material to a certain extent, which was not conducive to the release of latent heat.

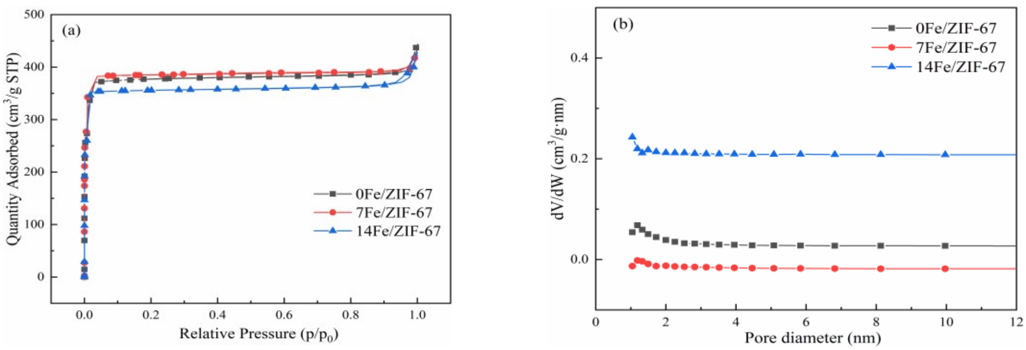

Figure 8: BET test of modified ZIF-67 material: (a) N_2 adsorption-desorption isotherm; (b) pore size distribution

3.6. Thermal conductivity of composite PCMs

The thermal conductivity was one of the most important indexes to evaluate the performance of composite PCMs samples. The larger the thermal conductivity was, the stronger the heat transfer capacity of composite PCMs sample, the higher the utilization efficiency in the heat storage and release process, and the faster the corresponding thermal response. Hot Disk detected the thermal conductivity of paraffin waxes with different composite PCMs samples, the trend of change was shown in Figure 9. The thermal conductivity of the pure paraffin sample was 0.282 $W \cdot m^{-1} \cdot K^{-1}$. However, the thermal conductivity of the composite PCMs samples was significantly diminished compared to pure paraffin, which was due to that the complex bridging pattern and high porosity of ZIF-67, as an inert support, leading to lower thermal conductivity and inhibiting the molecular interactions between the heat transfer media.

At the same time, the thermal conductivity of the composite PCMs samples increased significantly when the paraffin loading content increased from 30% to 50%. According to the previous characterization results, it had been confirmed that the paraffin loadwas saturated at 50%. So, when the paraffin content increased from 50% to 70%, it had little effect on the thermal conductivity of the PCMs samples. In addition, the Fe doping modification had no significant effects on the thermal conductivity, and the highest thermal conductivity of the different composite PCMs samples were all around 0.26 $W \cdot m^{-1} \cdot K^{-1}$, which was primarily determined by the inherent thermophysical properties of ZIF-67 and paraffin.

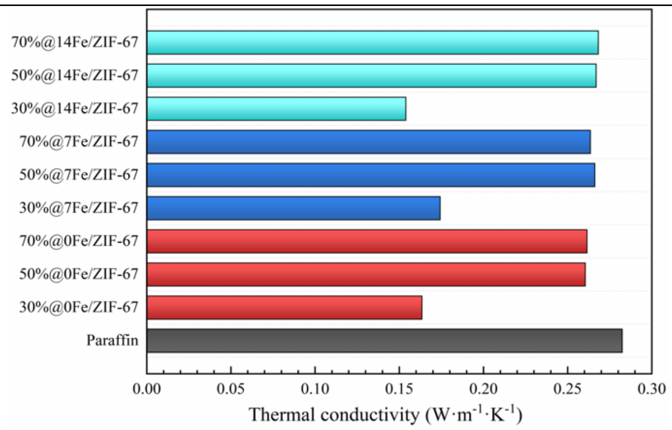

Figure 9: Thermal conductivity of composite PCMs samples

3.7. Thermal storage performance of composite PCMs

The phase transition behavior of paraffin@xFe/ZIF-67 composite PCMs samples was investigated using DSC analysis, and the results were shown in Figure 10. The single paraffin and composite PCMs samples exhibited similar heating/crystallization curves, even though there were significant differences in peak areas. The main peak with downward heat flow represented the endothermic melting process, corresponding to the solid-liquid transition of the sample. While the main peak with upward heat flow represented the exothermic crystallization process caused by the liquid-solid transition.

The data obtained by integrating the melting and crystallization intervals of the DSC curves are the enthalpy of melting (ΔH_m) and enthalpy of crystallization (ΔH_c) of different samples. T_m and T_c were the peak temperatures of the melting/crystallization process, respectively. The latent heat of melting and crystallization of single paraffin were 133.84 $J \cdot g^{-1}$ and 135.93 $J \cdot g^{-1}$, respectively, which was the source of heat storage and release performance of composite PCMs. Since the modified *x*Fe/ZIF-67 support was an inert material, it had no phase change in the scanning temperature range and its three-dimensional mesh structure formed inside limitedthe volume expansion of paraffin, which eventually reduced the latent heat of the composite PCMs sample without leading to changes in other physical properties.

The latent heat of melting and crystallization of the composite PCMs reached up to 67.85 $J \cdot g^{-1}$ and 69.23 $J \cdot g^{-1}$, respectively, with the melting temperature of 54.9°C and the crystallization temperature of 50.6°C, proving that the composite PCMs still had large enough phase change latent heat and relatively low phase change temperature, being suitable for application in the field of phase change heat storage materials.

In addition, the latent heat of the composite PCMs enlarged with increasing paraffin loading but showed a slight decrease when the paraffin loading rose from 50% to 70%. The reason for this phenomenon was that the paraffin wax had been adsorbed and saturated, and the loading continued to increase, which made the pressure in the pores of the modified *x*Fe/ZIF-67 increase continuously during the phase change process, hindering the thermal movement of paraffin molecules.

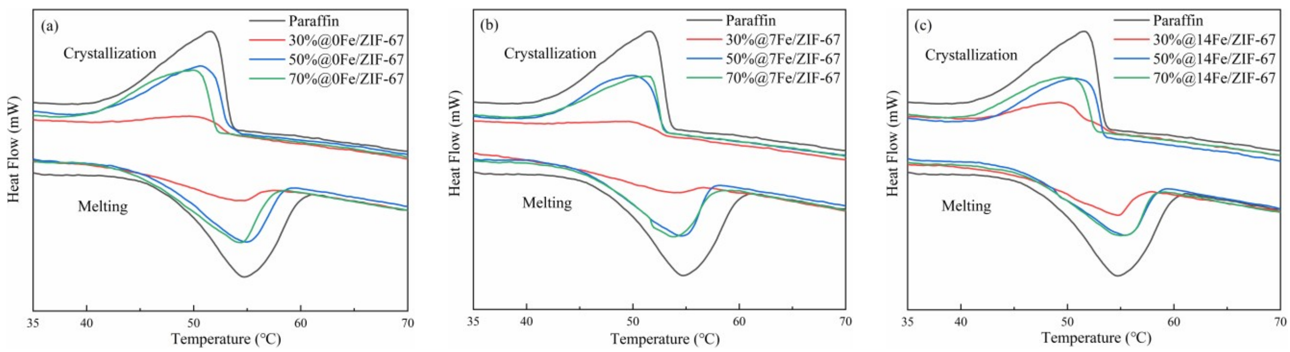

Figure 10: DSC analysis of composite PCMs: (a)paraffin@0Fe/ZIF-67; (b) paraffin@7Fe/ZIF-67; (c) paraffin@14Fe/ZIF-67

Since 50% paraffin was the optimal loading, 50%@0Fe/ZIF-67, 50%@7Fe/ZIF-67, and 50%@14Fe/ZIF-67 samples were selected to investigate the effect of Fe content on the latent heat of the composite phase change material. Figure 11 showed the impact trend of Fe doping on the heat storage and release capacity of the composite PCMs samples. The phase change enthalpy of the melting/crystallization process of the composite PCMs showed a decreasing trend with the increase of Fe content which inhibited the energy storage effect of the composite material.

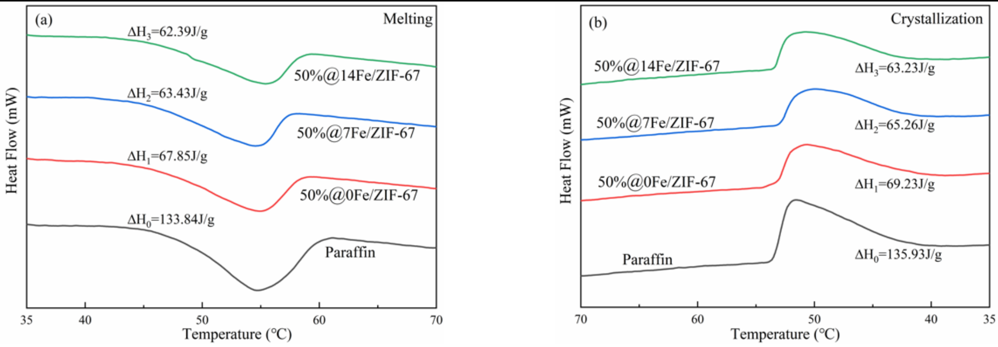

Figure 7: Melting/crystallization enthalpies of samples with different Fe contents (a) melting enthalpy; (b) crystallization enthalpy

3.8. Thermal cycle stability of composite PCMs

Based on the consideration that the 50%@0Fe/ZIF-67 sample has the best thermal properties and excellent sizing ability, the sample was subjected to 50 thermal cycles to test and analyze its stability. As shown in Figure 12(a) and (b), the XRD patterns andFTIR patterns of the samples did not change significantly before and after 50 thermal cycles, indicating that the phase composition remained unchanged. In summary, the 50%@0Fe/ZIF-67 sample exhibited an excellent thermal cycling stability. The DSC analysis and chemical structure analysis of 50%@0Fe/ZIF-67 after 50 thermal cycles were shown in Figure 12(c). The DSC curves of 50%@0Fe/ZIF-67 did not changed significantly after 50 thermal cycles, and the enthalpy of melting/crystallization decreased from until 67.85 $J \cdot g^{-1}$ and 69.23 $J \cdot g^{-1}$ to 66.93 $J \cdot g^{-1}$ and 68.56 $J \cdot g^{-1}$, with an enthalpy change of less than 1.4%.

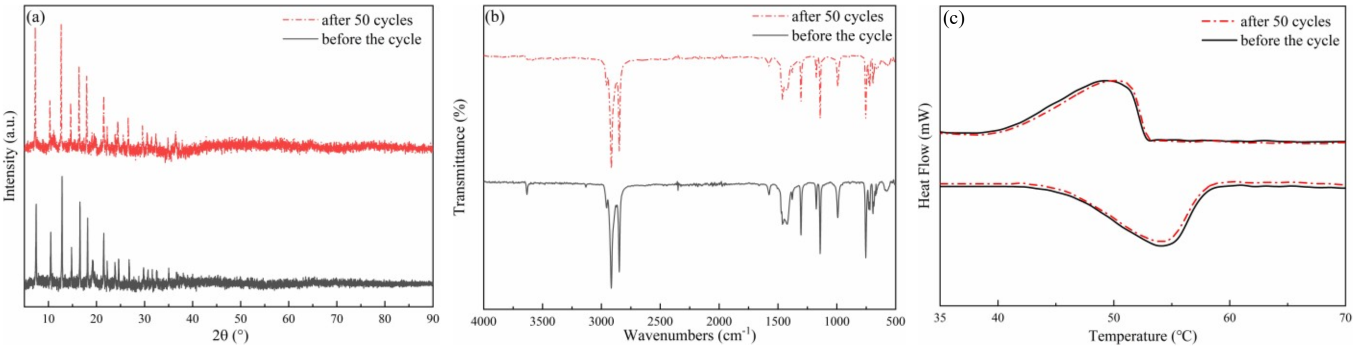

Figure 12: Thermal cycle stability of composite PCMs (a)XRD pattern; (b) FTIR pattern; (c) DSC patterns

4. CONCLUSION

In order to solve the problem that paraffin was easy to leak during the phase transition process, this study successfully constructed the composite PCMs of paraffin@*x*Fe/ZIF-67 using Fe-modified ZIF-67 as the shell and paraffin wax as the core, and analyzed the influence of Fe modification, the thermal conductivity and the variation trend of latent heat.

(1) The characterization results proved that the modification of ZIF-67 by Fe and the compounding of modified *x*Fe/ZIF-67 with paraffin only involved physical processes and no chemical changes occur. Combined with SEM and other characterization analysis, the composite was synthesized successfully and the composite PCMs had a maximum paraffin loading capacity of 50%, which effectively solved the problem of easy leakage during paraffin melting.

(2) For the modified *x*Fe/ZIF-67, the doping of Fe improved the thermal stability and the specific surface area of ZIF-67 to a certain extent. For the composite PCMs of paraffin@*x*Fe/ZIF-67, the doping of Fe caused a slight decrease in thermal stability and enthalpy, but PCMs still exhibited good loading and packaging capabilities.

(3) The modified *x*Fe/ZIF-67 was a thermally inert material, and the thermal conductivity of the formed composite PCMs decreased. The 50%@0Fe/ZIF-67 sample had the highest latent heat of phase change, the enthalpy of melting and crystallization reached 67.85 $J \cdot g^{-1}$ and 69.23 $J \cdot g^{-1}$, respectively, and the temperatures of melting and crystallization were 54.9 °C and 50.6 °C, correspondingly. Excellent thermal properties were still observed after 50 thermal cycles.

(4) At the optimal paraffin loading content of 50%, paraffin@xFe/ZIF-67 exhibited a decreasing trend in phase change enthalpy during melting and crystallization processes compared to pure ZIF-67, as the Fe content increased. This phenomenon indicated the introduction of Fe inhibited the latent heat storage capacity of the composite material.

5. ACKNOWLEDGEMENT

"Chunhui Plan" cooperative scientific research project of the Ministry of Education of China (HZKY20220498); China Postdoctoral Science Foundation (2020M671983); Postdoctoral Innovation Project of Shandong Province (202103077); China Scholarship

Council (202008370134); Shandong Province Housing and Urban-Rural Construction Science and Technology Project (2022-K7-11, 2021-K8-10, 2020-K2-10); National Natural Science Foundation of China (51976111).

6. REFERENCES

[1] Mishra, R.K.; Verma, K.; Mishra, V.; Chaudhary, B. 2022. A review on carbon-based phase change materials for thermal energy storage, Journal of Energy Storage, 50, 104166.

[2] Cunha, S.D.; Aguiar, J. 2020. Phase change materials and energy efficiency of buildings: A review of knowledge, Journal of Energy Storage, 27, 101083.

[3] Zhang, D.Y.; Li, C.C.; Lin, N.Z.; Xie, B.S.; Chen, J. 2022. Mica-stabilized polyethylene glycol composite phase change materials for thermal energy storage, International Journal of Minerals Metallurgy and Materials, 29, 168-176.

[4] Atinafu, D.G.; Chang, S.J.; Kim, K.H.; Dong, W.J.; Kim, S. 2020. A novel enhancement of shape/thermal stability and energy-storage capacity of phase change materials through the formation of composites with 3D porous (3,6)-connected metal- organic framework, Chemical Engineering Journal, 389, 124430

[5] Li, X.L.; Sheng, X.X.; Guo, Y.Q.; Lu, X.; Wu, H.; Chen, Y.; Zhang, L.; Gu, J.W. 2021. Multifunctional HDPE/CNTs/PW composite phase change materials with excellent thermal and electrical conductivities, Journal of Materials Science & Technology, 86, 171-179.

[6] Li, Y.Q.; Chen, Y.M.; Huang, X.B.; Jiang, S.H.; Wang, G. 2021. Anisotropy-functionalized cellulose-based phase change materials with reinforced solar-thermal energy conversion and storage capacity, Chemical Engineering Journal, 415, 129086.

[7] Chen, X.; Cheng, P.; Tang, Z.D.; Xu, X.L.; Gao, H.Y.; Wang, G. 2021. Carbon-Based Composite Phase Change Materials for Thermal Energy Storage, Transfer, and Conversion, Advanced Science, 8, 202001274.

[8] Wu, S.F.; Yan, T.; Kuai, Z.H.; Pan, W.G. 2020. Thermal conductivity enhancement on phase change materials for thermal energy storage: A review, Energy Storage Materials, 25, 251-295.

[9] Rathore, P.; Gupta, N.K.; Yadav, D.; Shukla, S.K.; Kaul, S. 2022. Thermal performance of the building envelope integrated with phase change material for thermal energy storage: an updated review, Sustainable Cities and Society, 79, 103690.

[10] Wang, L.Y.; Liu, Z.J.; Guo, Q.G.; Wang, H.Q.; Wang, X.L.; Dong, X.Z.; Tian, X.D.; Guo, X.H. 2022. Preparation and Thermal Characterization of Hollow Graphite Fibers/Paraffin Composite Phase Change Material, Coatings, 12, 12020160.

[11] Shoeibi, S.; Kargarsharifabad, H.; Mirjalily, S.; Sadi, M. 2022. A. Arabkoohsar, A comprehensive review of nano-enhanced phase change materials on solar energy applications, Journal of Energy Storage, 50, 104262.

[12] Tang, J.; Chen, X.Y.; Zhang, L.G.; Yang, M.; Wang, P.; Dong, W.J.; Wang, G.; Yu, F.; Tao, J.Z. 2018. Alkylated Meso-Macroporous Metal-Organic Framework Hollow Tubes as Nanocontainers of Octadecane for Energy Storage and Thermal Regulation, Small, 14, 201801970

[13] Wang, T.H.; Yang, T.F.; Kao, C.H.; Yan, W.M.; Ghalambaz, M. 2020. Paraffin core -polymer shell micro -encapsulated phase change materials and expanded graphite particles as an enhanced energy storage medium in heat exchangers, Advanced Powder Technology, 31, 2421-2429.

[14] Qin, S.Y.; Li, H.B.; Hu, C.Z. 2021. Thermal properties and morphology of chitosan/gelatin composite shell microcapsule via multi-emulsion, Materials Letters, 291, 129475.

[15] Liu, C.; Wang, J.; Wan, J.J.; Yu, C.Z. 2020. MOF-on-MOF hybrids: Synthesis and applications, Coordination Chemistry Reviews, 432, 213743.

[16] Liu, Y.; Huo, Y.Z.; Wang, X.X.; Yu, S.J.; Ai, Y.J.; Chen, Z.S.; Zhang, P.; Chen, L.; Song, G.; Alharbi, N.S.; Rabah, S.O.; Wang, X.K. 2021. Impact of metal ions and organic ligands on uranium removal properties by zeolitic imidazolate frameworkmaterials, Journal of Cleaner Production, 278, 123216.

[17] Rao, P.C.; Mandal, S. 2019. Potential Utilization of Metal-Organic Frameworks in Heterogeneous Catalysis: A Case Study of Hydrogen-Bond Donating and Single-Site Catalysis, Chemistry-An Asian Journal, 14, 4087-4102.

[18] Fan, W.D.; Zhang, X.R.; Kang, Z.X.; Liu, X.P.; Sun, D.F. 2021. Isoreticular chemistry within metal-organic frameworks for gas storage and separation, Coordination Chemistry Reviews, 443, 213968.

[19] Hang, C.; Akpinar, I.; Qin, Y.X.; Huang, L.P.; Wang, L.Y.; Li, W.Y.; Wu, J.H. 2021. A Review on Adsorption of Organic Pollutants from Water by UiO-67 and Its Derivatives, Journal of Nanoelectronics and Optoelectronics, 16, 1861-1873.

[20] Zhong, G.H.; Liu, D.X.; Zhang, J.Y. 2018. The application of ZIF-67 and its derivatives: adsorption, separation, electrochemistry and catalysts, Journal of Materials Chemistry A, 6, 1887-1899.

[21] Dong, Z.C.; Zhao, J.; Tian, Y.J.; Zhang, B.F.; Wu, Y. 2020. Preparation and Performances of ZIF-67-Derived FeCo Bimetallic Catalysts for CO2 Hydrogenation to Light Olefins, Catalysts, 10, 10040455.

[22] Jiao, C.W.; Wang, Z.M.; Zhao, X.X.; Wang, H.; Wang, J.; Yu, R.B.; Wang, D. 2019. Triple-Shelled Manganese-Cobalt Oxide Hollow Dodecahedra with Highly Enhanced Performance for Rechargeable Alkaline Batteries, Angewandte Chemie-International Edition, 58, 996-1001.

#285: A Comparative study on the applicability of the solar energy-powered embedded pipe envelope system in different envelope

Linfeng WANG[1,2], Chiu Chuen ONN[1,*], Bee Teng CHEW[3,*], Wuyan LI[4] and Yongcai LI[5]

[1] A Department of Civil Engineering, Faculty of Engineering, Universiti Malaya, Lembah Pantai, Kuala Lumpur 50603, Malaysia; linfengwang@outlook.com, onnchiuchuen@um.edu.my
[2] School of Civil Engineering, Sichuan University of Science and Engineering, Zigong 643000, China
[3] Department of Mechanical Engineering, Faculty of Engineering, Universiti Malaya, Lembah Pantai, Kuala Lumpur 50603, Malaysia; chewbeeteng@um.edu.my
[4] Yunnan Key Laboratory of Disaster Reduction in Civil Engineering, Faculty of Civil Engineering and Mechanics, Kunming University of Science and Technology, Kunming 650500, China; wuyanlee@foxmail.com
[5] School of Civil Engineering, Chongqing University, Chongqing 400045, China; yongcai85@163.com

Abstract: This study compares the heating efficiency of the Solar Energy-powered Embedded Pipe Envelope System (SEPES) in various building envelopes using a novel simulation model developed with TRNSYS. The evaluation includes indoor air temperature, inlet and outlet water temperatures in walls, internal surface temperatures of envelopes, and heating energy consumption across six different SEPES installations. Key findings include: 1) SEPES significantly improves indoor temperatures during cold winters in Harbin, with ceiling installations increasing temperatures by up to 8.4℃, and strategic placements optimizing warmth and energy efficiency; 2) Water temperature in SEPES pipes indicates heating capacity, with the highest temperatures in east and west wall installations; 3) Ceiling-embedded pipes perform best in blocking heat loss, with surface temperatures ranging from 7.42℃ to 11.59℃; 4) SEPES installations significantly reduce daily heat loads, with ceiling installations achieving the highest energy-saving rate of49.7%. Overall, ceiling installations are most effective, followed by the north wall, floor, south wall, east wall, and west wall.

Keywords: Solar Thermal Collector; Pipe Embedded Envelope; Building Envelope Applicability; Thermal Performance

1. INTRODUCTION

The Paris Agreement has established a global consensus on the necessity for energy-saving and low-carbon development. In order to further reduce energy consumption and carbon emissions, China has set itself the ambitious goal of striving to peak carbon dioxide emissions before 2030 and achieve carbon neutrality before 2060(Chen et al., 2020). In this context, the development of effective energy-saving methods and the improvement of energy utilization efficiency have important economic and environmental significance. Currently, building energy consumption accounts for a significant proportion of the total energy consumption in society. In 2018, China's annual building energy consumption reached 1.123 billion tons of standard coal, resulting in approximately 2.2 billion tons of CO_2 emissions (Guo et al., 2021). As living standards improve, there is a concomitant increase in the demand for indoor environmental quality in buildings. This has led to a rapid increase in the energy consumption of building HVAC systems. Studies have shown that in northern China, heating and air-conditioning energy consumption accounts for 50-60% of total building energy consumption (Yi, 2005). And in areas with hot summers and cold winters, this figure is as high as 65% (Yang, 2014). Therefore, reducing HVAC energy consumption in buildings is one of the most important ways to achieve building energy efficiency and reduce carbon emissions.

The building envelope is the interface between the indoor and outdoor environments, and heat transfer through the envelope is an important part of the building's cooling and heating load. In winter, the heat transfer loss of the enclosure structure is such that it exceeds 70% of the total heating load of the building (Li and Chen, 2019). Improving the thermal performance of a building plays an important role in reducing energy consumption associated with heating and air conditioning. Nevertheless, with the ongoing enhancement of the enclosure structure's performance, the potential for further enhancing its insulation and airtightness in reducingthe energy consumption of heating and air conditioning has become increasingly constrained. The construction of thick walls represents a significant investment in valuable building space, which in turn increases the overall costs of construction. Furthermore, the incorporation of thick walls into a building design introduces an increased risk of fire safety hazards (Yang et al., 2021, Shen et al., 2017). Conversely, the excessive insulation performance of the enclosure can result in an increased cooling load of the room during the transition season and summer, thereby increasing the energy consumption of air conditioning operation (D’Antoni and Saro, 2013). In this context, the exploration of active control methods for enclosure structures has attracted the attention of researchers.

Embedded pipe envelope represents a novel type of enclosure structure that incorporates a circulating pipeline system within itself and utilizes the hot/cool medium flow in the pipe to intercept the heat/cold loss through the building envelope (Xu et al., 2010, Xie etal., 2012). As one type of thermal active building system, embedded pipe envelope could be coupled with different cooling and heating sources (Krzaczek et al., 2019, Jobli et al., 2019, Sun et al., 2020, Jiang et al., 2020). The ground source heat pump is employed by Li to provide the heat required for winter heating to the embedded pipe wall (Shen et al., 2017, Shen and Li, 2017). The findings of the analysis indicate that the application of hot water at temperatures below room temperature can also be employed as an auxiliary heating source for residential buildings. During the heating season in Beijing, the system is capable of reducing the heat load by up to 84%, while the heat loss on the outer wall only increases by 18%. The energy-saving rate of the entire system is 44%, and the investment payback period is 2 years. Peizheng Ma (Ma et al., 2014) conducted a model of hydronic radiant cooling building using a parametric cooling tower in one summer in seven U.S. cities. They indicated that pipe-embedded envelope with cooling tower is possible only in locations of special meso-sale climatic condition such as Sacramento, CA. In other locations the use of the coupling system can only achieve homeostasis partially. Krzaczek et al. (Krzaczek and Kowalczuk, 2011) proposed a method of directly heating residential buildings using solar energy as a heat source. This method involves embedding polypropylene U-shaped pipes inside the exterior wall, allowing fluid to flow within the U-shaped pipe system with variable flow rates and inlet temperatures. The efficacy of this method in maintaining wall temperature stability during cold seasons has been demonstrated through empirical research. The intermittent and uncontrollable nature of solar radiation can be successfully integrated with a building structure that exhibits substantial thermal mass. This integration occurs simultaneously with the circulation of heat transfer mediums within solar collectors. This integration allows for the successful coupling of solar collectors with pipe-embedded envelopes, which exhibit a high response time. This integration is further supported by the fact that solar collectors can be coupled with pipe-embedded envelopes.

When coupled with a solar thermal collector, the pipe of the system can be embedded into different building envelopes, thereby contributing to the heating capacity of the indoor space, typically in the form of walls (Shen et al., 2022, He et al., 2022) (Yang and Chen, 2024), floors (Feng et al., 2016), or ceilings (Su et al., 2019, Ye et al., 2021). The specific geographical location and area of pipe embedded envelope has a considerable effect on the investment cost and thermal performance of the building. To avoid higher energy consumption caused by the unequal heat gain from the solar radiation in south and north walls, Junhao Shen etc. (Shen et al., 2022) put forth the concept of an active pipe embedded system with the objective of achieving heat redistribution between the north and south walls. The findings of their research indicate that the reduction in heating load during the heating season for the room utilizing this system in comparison to the control room is 12.8% in a climate characterized by hot summers and cold winters. For cold climate, the heating loads in January is reduced by 8.7%. Jinjuan (Feng et al., 2016) developed a new simplified method toimprove the design of radiant floors with solar radiation. They found that for cases with direct solar, the system capacity can increase up to 130-140W/m^2. Kan Xu (Xu et al., 2023) proposed a new roof with a pipe-embedded phase change material (PE-PCM) integrated with a solar collector. For fully utilize solar energy and improve building efficiency, the PE-PCM layer is attached to the inner side of the roof. The results of their study showed that the heating demand can be met by the novel structure. The total energy consumption for heating the room can be reduced by 54% compared to that of a conventional roof.

As mentioned previously, the solar energy-powered embedded pipe envelope system (SEPES) can be an efficient system that reduces indoor heating load and improve thermal comfort. The author's existing research (Wang et al., 2024) indicates that the SEPES cab elevate the indoor temperature by 14.5℃on the coldest heating day in a rural building in Beijing. Regional adaptability analysis also expounds that SEPES has good regional adaptability and is most suitable for climates characterized by both low temperaturesand abundant solar radiation. Regarding the aforementioned literature, SEPES can be coupled with different envelopes, such as floor, wall and ceiling. Due to the different orientations of the received solar radiation and the boundary conditions, the performance of building envelope structures coupled with SEPES varies. Hence, investigating the thermal performance of SEPES when activated in different envelopes is of significance. In this study, the thermal performance of SEPES coupled with six different envelopes was systematically evaluated, including indoor air temperature, Inlet and outlet water temperature in the wall, internal surface temperature of envelopes and heating energy consumption. The results of this research are expected to contribute to a comprehensive understanding of the practical applications of SEPES.

2. SYSTEM DESCRIPTION AND NUMERICAL MODEL

2.1. The Solar Energy-Powered Embedded Pipe Envelope System

The scheme of the solar energy-powered embedded pipe envelope system (SEPES) is shown in Figure 1. As shown, the system consists of a set of solar collectors, a water tank, and an embedded pipe in the exterior wall and the building. The exterior walls arecomposed of a brick layer. In the exterior wall, the water pipes are embedded in the middle position in a serpentine shape. The area of the embedded pipe structure on walls with different orientations is equal to the area of the solid wall. The embedded pipe areas for the east, west, north, and south walls are 11.25m^2, 13.5m^2, 26.28m^2, and 11.46m^2, respectively. The water inside the pipeline transfers heat sequentially to the various exterior walls of the building. The water pump provides power for the flow of water throughout the entire system.

There are two parts to the water circulation in the heat storage water tank. One of the loops is in the pipe-embedded wall, as previously indicated. In an additional circuit within the solar thermal collector, the heat generated by the photothermal effect is stored in a water tank, subsequently supplying the thermal energy to the building's envelope structure. The high-absorptance collector surface of the solar thermal collector, positioned atop the building, absorbs solar radiation to generate heat, thereby heating the circulating water in the system.

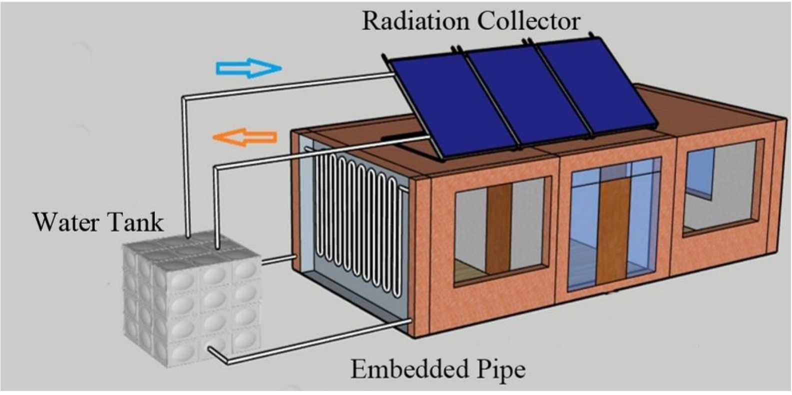

Figure 1: The solar energy-powered embedded pipe envelope system

2.2. Mathematical model of solar thermal collector and pipe-embedded wall

The mathematical model of a solar panel water heater is based on three fundamental equations: heat transfer, heat balance, and fluid dynamics. The heat balance equation considers the heat absorbed by the solar panel, the flow of fluid (usually water) through the panel, and the hot water flow rate in the water heater. It could be expressed as:

$$Q_u = IA_a - Q_{ol} - Q_{hl}$$

Where:

- Q_u = the energy absorbed by the heat transfer working fluid (W)
- I = the solar irradiance received by the surface of the collector (W/m^2)
- A_a = the effective area of the collector (m^2)
- Q_{ol} = the optical loss of the collector (W)
- Q_{hl} = the heat loss of the collector (W)

The mathematical model of embedded pipe walls is primarily comprised of heat transfer equations. The heat transfer equations mainly include the convective heat transfer between the fluid inside the pipeline and the wall, the thermal conductivity inside the wall, and the radiative and convective heat transfer on the wall surface. The control equations for these three heat transfer processes are as follows:

$$\begin{cases} k \cdot \left(\frac{\partial^2 T}{\partial^2 x} + \frac{\partial^2 T}{\partial^2 y}\right) = \rho_{wall} \cdot C_{p-wall} \cdot \frac{\partial T}{\partial t} \\ k \cdot \frac{\partial T}{\partial y}|_{y=\delta} = h_w \cdot (T_w - T) \\ k \cdot \frac{\partial T}{\partial y}|_{y=0} = h_a(T - T_a) - Q_{rad} \end{cases}$$

Where:

- k = the thermal conductivity coefficient of the wall ($W/m \cdot K$)
- ρ_{wall} = the density of the wall (kg/m^3)
- C_{p-wall} = the specific heat of the wall ($J/kg \cdot K$)
- h_w = the convective heat transfer coefficient between the internal surface of the pipe and the fluid ($W/m^2 \cdot K$)
- h_a = the convective heat transfer coefficient between the surface of the wall and the air ($W/m^2 \cdot K$)
- Q_{rad} = the radiation heat transfer between the wall surface and the environment (W)

The fluid dynamics equation describes the flow of fluid in the pipe. This involves the conservation of mass and momentum equations, which can be described using conventional equations of fluid flow:

$$\begin{cases} \frac{\partial_\rho}{\partial_t} + \nabla \cdot (\rho \mathbf{v}) = 0 \\ \rho \left(\frac{\partial_\mathbf{v}}{\partial_t} + (\mathbf{v} \cdot \nabla)\mathbf{v}\right) = -\nabla p + \mu \nabla^2 \mathbf{v} + \rho \mathrm{g} \\ \rho C_p \left(\frac{\partial_T}{\partial_t} + (\mathbf{v} \cdot \nabla) T\right) = k \nabla^2 T + \dot{Q} \end{cases}$$

Where:

- ρ = the fluid density (kg/m^3)
- t = time (s)
- $\mathbf{v}$ = the fluid velocity (m/s)
- ∇ = the gradient operator
- p = the fluid pressure (Pa)
- μ = the dynamic viscosity of the fluid
- g = the gravitational acceleration
- C_p = the specific heat capacity of the fluid ($Pa \cdot s$)
- T = the temperature of the fluid (K)
- k = the thermal conductivity coefficient of the fluid ($W/m \cdot K$)
- Q = the heat source (W)

2.3. Model Setting

The SEPES simulation model was developed using the module available in TRNSYS, as shown in Figure 2. Components and theirfunctions in the coupled simulation platform are shown in Table 1. Module type 73 was chosen to achieve the best functionality of the solar thermal collector. The Hottel–Whillier steady-state model is used for evaluating the thermal performance of the collector (Klein, 2018).

The solar energy-powered embedded pipe envelope system is more suitable for standalone buildings due to its structure. A typical rural building in Harbin in Northern China was chosen to be the study case in this research, shown in Figure 3. The thermal–physical characteristics of the building envelope structure are determined in accordance with the design specifications for China's cold region. Additionally, this is a typical rural building facing south. The personnel density within the building is designed at 0.05 person/m^2. Thewindows of all the houses were double-glazed with solar absorptance and emissivity of 0.6 and 0.9, respectively. The fundamental parameters of the SEPES are set forth in Table 2. Further information concerning the house is given in Table 3.

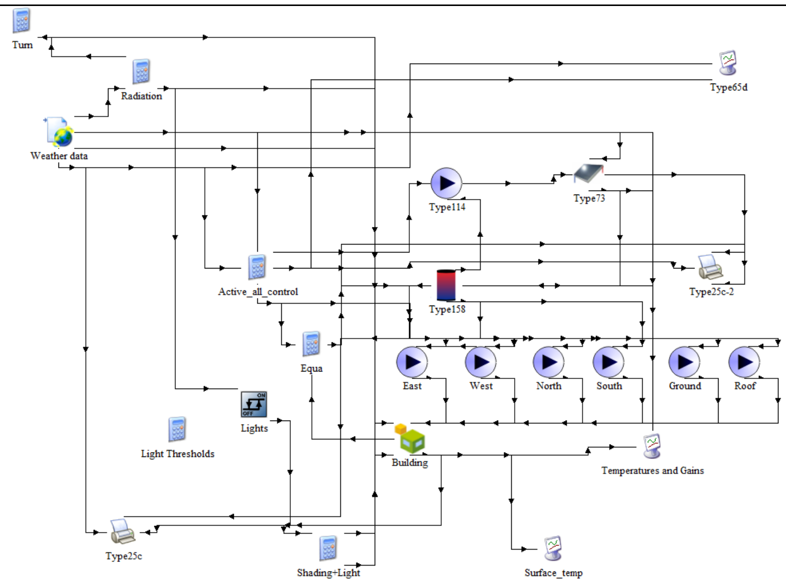

Figure 2: Scheme of the SEPES simulation model in TRNSYS

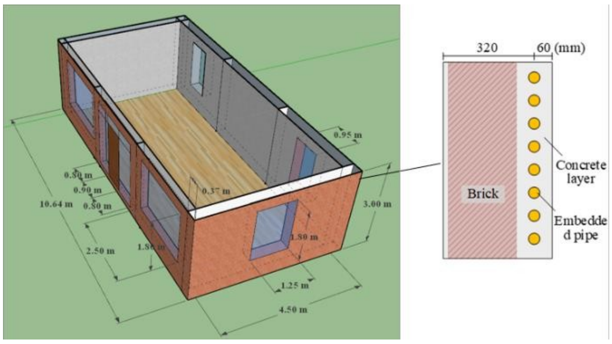

Figure 3: The layout of the typical building in this study

Table 1: Components and their functions in the coupled simulation platform.

Module Name	Calling Components	Function
Solar collector	Type 73	Models the thermal performance of a theoretical flat plate collector
Single-speed pump	Type 114	Models a single (constant) speed pump that is able to maintain a constant fluid outlet mass flow rate
Cylindrical Storage Tank	Type 158	Models a fluid-filled, constant volume storage tank
Weather data	Weather data	Provides outdoor temperature and humidity and calculates solar radiation
Outputs	Type 65d	Analysis the calculation results of each component
Printer	Type 25c	Output selected system variables at specified intervals of time
Differential Controller	Type 165	Generates a control function which can have a value of 1 or 0

Table 2: Designed parameters of the SEPES.

Design Parameter	Description Value	Design Parameter	Description Value
Solar collector		Water tank	
Number in series	1	Tank volume	10 m^3
Collector area	80 m^2	Loss coefficient of tank	3.4 $kJ/(h \cdot m^2 \cdot k)$
Fluid specific heat in SC	4.19 $kJ/(kg \cdot k)$	Pump of wall	
Absorptance of absorber plate	0.9	Number in series	6
Number of pumps	1	Rated power of pump	180 W
Rated power of pump	100 W	Rated flow rate	500 kg/hr

Table 3: Thermo-physical parameters of the building envelope.

	Material Layers		CHTC $(w/(m^2 \cdot k))$		U-Value $(w/(m^2 \cdot k))$
	Name	Thickness (mm)	Interior	Lateral	
External Wall	Plaster	2.5	3.06	17.78	0.6 (E, W, N) 0.65 (S)
	Brick	370 (E, W, N) 240 (S)			
	Insulation	48			
Floor and Interior walls	Insulation	30	3.06	3.06	1.0
	Concrete	120			

Roof	Insulation	80	3.06	17.78	0.45
	Concrete	240			
External window	Glass	4	3.06	17.78	3.2
	Air	3.2			
	Glass	4			

*CHTC means Convective Heat Transfer Coefficient.

3. RESULTS AND DISCUSSION

The northern regions of China have both centralized and non-centralized heating periods through the year. The central heating period in Harbin is from 20 October to 20 April of the following year, approximately 180 days, or half the year. The annual outdoor temperature and natural indoor temperature of a typical rural building in Harbin is shown in Figure 4. As shown in the figure, due to the attenuating and delaying effect of the building envelope structure on solar radiation and outdoor temperature changes, the indoor air temperature fluctuation is smoother than the outdoor temperature, and the average annual indoor air temperature is about 2.5℃ higher than the outdoor temperature. However, during the heating season, the natural indoor air temperature is generally below 10℃, with about half of the time below 0℃. As a result, the case building has a significant heating requirement during the heating season.

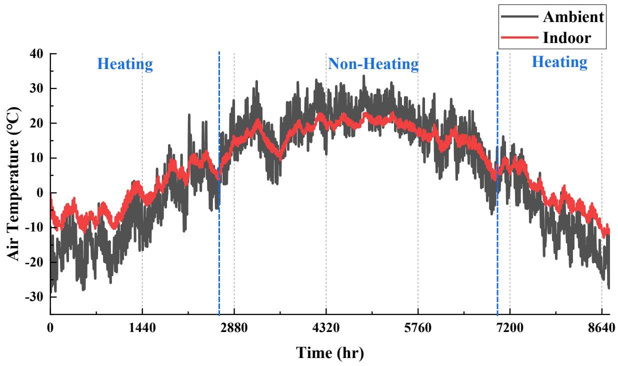

Figure 4: Annual ambient air temperature and natural indoor air temperature of the case building in Harbin

3.1. Thermal performance on a typical heating day

Indoor air temperature

The indoor air temperature of the buildings in this study is greatly affected by the outdoor low temperature environment during the heating season. Figure 5 illustrates the trend of indoor air temperature changes when pipes are embedded in different building envelopes. As shown in the Figure, for a typical heating day (2nd January) in Harbin, the outdoor air temperature variation range is -27℃to -12.3℃, with an average temperature of -20℃. For a raw building without SEPES, due to the barrier of the building envelope structure and the effect of indoor heat sources, the fluctuation range of indoor air temperature is relatively small, ranging from -8.6 ℃to -5.2 ℃. The sunshine duration in Harbin on January 2nd is about 8 hours. The application of the SEPES system in the building has a very positive effect on the thermal environment in the building. The embedding of pipes in any part of a building's enclosure structure can have the effect of raising the indoor air temperature for 24 hours. If the pipe is embedded in the floor, the maximum temperature of the air in the room can reach 1.8°C, which is 7°C higher than without the SEPES system. Here the SEPES system works in a similar way to a floor radiant system, which can transfer most of the heat provided by the sun to the indoor environment. Due to the presence of solar collectors, the ceiling is the least time exposed to direct sunlight. When SEPES works in the ceiling, the ceiling is the enclosure structure that offers the most resistance to heat loss. with the maximum increase being 8.4°C. Among the four walls, the north wall receives the least amount of direct sunlight and has the lowest wall temperature. Therefore, more heat is lost from the north wall the ambient. When SEPES is installed on the north wall, it can significantly increase in the indoor air temperature. On average, there is an increase of 6.1℃ per day, with a maximum increase of 6.2 ℃. SEPES installed on the south wall can increase the average air temperature in the room by 4.4°C, and SEPES installed on the east and west walls can increase the temperature by 3.2°C. The results of the analysis indicate that the installation of SEPES in the ceiling has a more pronounced effect on the improvement of the indoor air temperature, while the installation of SEPES on the west and east walls has a less significant impact. If SEPES is mainly installed in walls to isolate insulation loads, it is recommended to install it in the north wall. The heat storage tank can maintain the heating capacity of the system for 24 hours.

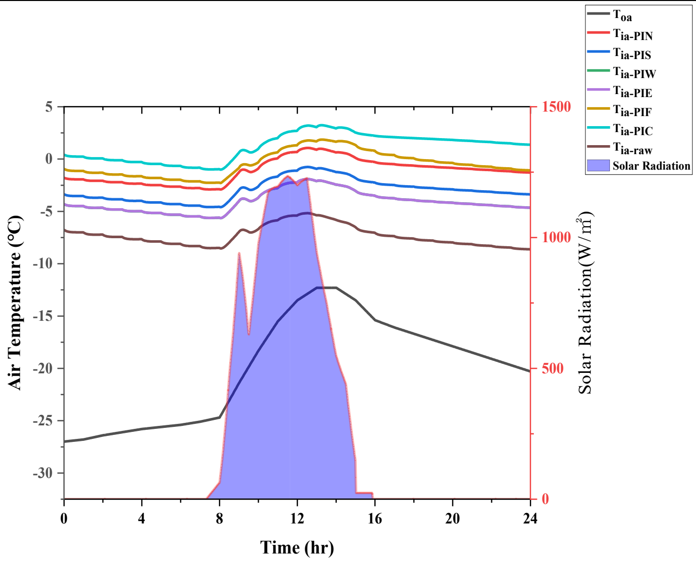

Figure 5: Trend of indoor air temperature changes when pipes are embedded in different building envelopes.

Inlet and outlet water temperature in the wall with the SEPES

The change in water temperature inside the pipe in the envelopes could reflect the SEPES system's heating capacity for the building and its ability to resist the heat load. The inlet and outlet water temperatures of SEPES installed in different envelopes are shown inFigure 6. The research building is in the northern hemisphere and faces south. The thermal performance of SEPES pipes installed on the east and west walls of the building is almost the same. As can be seen from the figure, the inlet water temperature of the SEPES pipes embedded in the east and west walls is the highest, with a daily variation range of 16.7℃~24.4 ℃and an average of 20.6 ℃. The outlet water temperature of the SEPES pipes embedded in the east and west walls is the highest, with a daily variation range of 13.2℃~19.4 ℃and an average of 16.5 ℃. The average temperature difference between the inlet and outlet of the pipeline is 4.1 ℃. The smaller area of the east and west walls relative to other envelopes results in less heat loss, which reduces the potential for indoor and outdoor heat dissipation. Additionally, the ceiling is obstructed by a solar collector, preventing the direct radiation of solar energy from the sun and the long-wave radiation from the sky to the collector, which results in a loss of heat. When the SEPES pipe is embedded in the ceiling and floor, the water temperature is relatively lower than when installed in the other 4 positions. The average temperature of inlet and outlet water is only 16.2 ℃ and 9.6 ℃ respectively, with a difference of 6.6℃. Moreover, a comparison of the water temperature at the embedded pipe inlet and outlet on the south wall of the SEPES-installed building with those on the corresponding north wall revealed that the south-wall inlet and outlet exhibited a higher temperature. The maximum values of the inlet and outlet water temperatures of the south wall are 22.7℃ and 16.2℃, respectively, while the corresponding temperatures of the north wall are 20.4℃and 11.5℃. Furthermore, there is a delay of about 3 hours between the fluctuation of water temperature in the SEPES storage tank and the fluctuation of solar radiation intensity. This is primarily a result of the heat storage capacity and thermal resistance of the building envelopes. To summarize, it can be stated that the water temperature in the pipe is the effective water temperature of SEPES. The effective water temperature variation of SEPES is mainly affected by direct solar radiation and the area of embedded pipe walls.

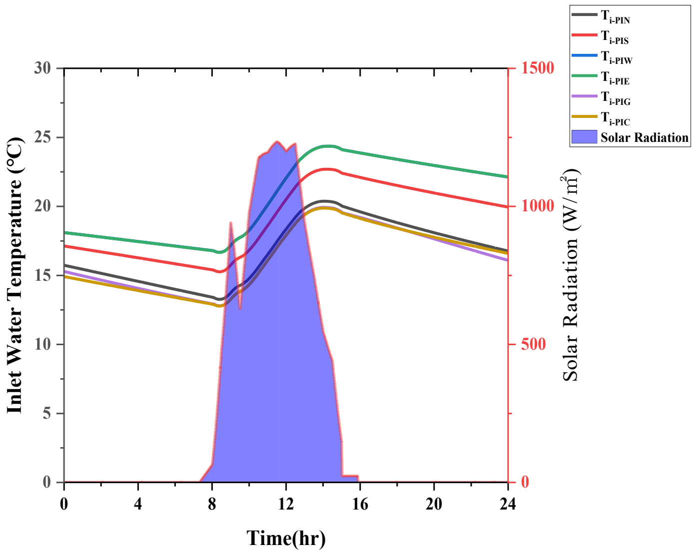

(a)

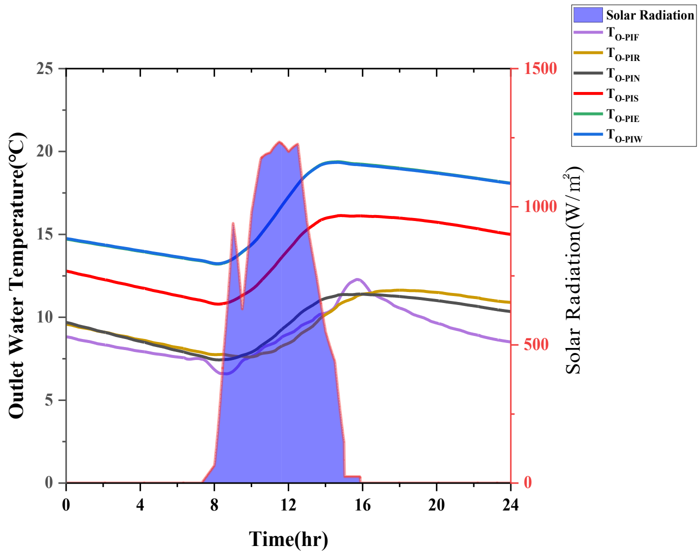

(b)

Figure 6: (a) Inlet water temperature in the wall with the SEPES; (b) Outlet water temperature in the wall with the SEPES

Internal surface temperature of the envelopes

The inner surface of the building envelope is subject to convective heat exchange with indoor air and radiative heat exchange with people and objects, which affects the thermal comfort of the indoor environment. The temperature of all walls, ceiling, and floor when SEPES pipes are embedded into different building envelope structures is presented in Figure 7. The internal surface temperature of the envelope, which contains embedded pipes, is demonstrably higher than that of other surfaces. As previously stated, the pipe embedded in the ceiling exhibits superior heat load blocking capability. Upon pipe integration into the ceiling, the temperature range of the inner surface of the ceiling exhibits fluctuations between 7.42 ℃and 11.59 ℃. The daily average temperature of the inner surface of the building envelopes is as high as 1.39℃. The absence of direct contact between the floor and outdoor air results in a reduction in heat loss. Even in the absence of solar radiation, the maximum internal surface temperature of floor can reach 11.3 ℃. In this instance, the mean daily temperature on the inner surface of the building envelopes is -0.12 ℃. Moreover, the mean temperature ofthe inner surface of the enclosure structure when the pipeline is embedded in the east, west, south, and north walls is -2.4 ℃, -2.4℃, -1.7 ℃, and -0.3 ℃, respectively. The preceding analysis demonstrates that the installation position of SEPES has a considerable influence on the overall heat loss of the building.

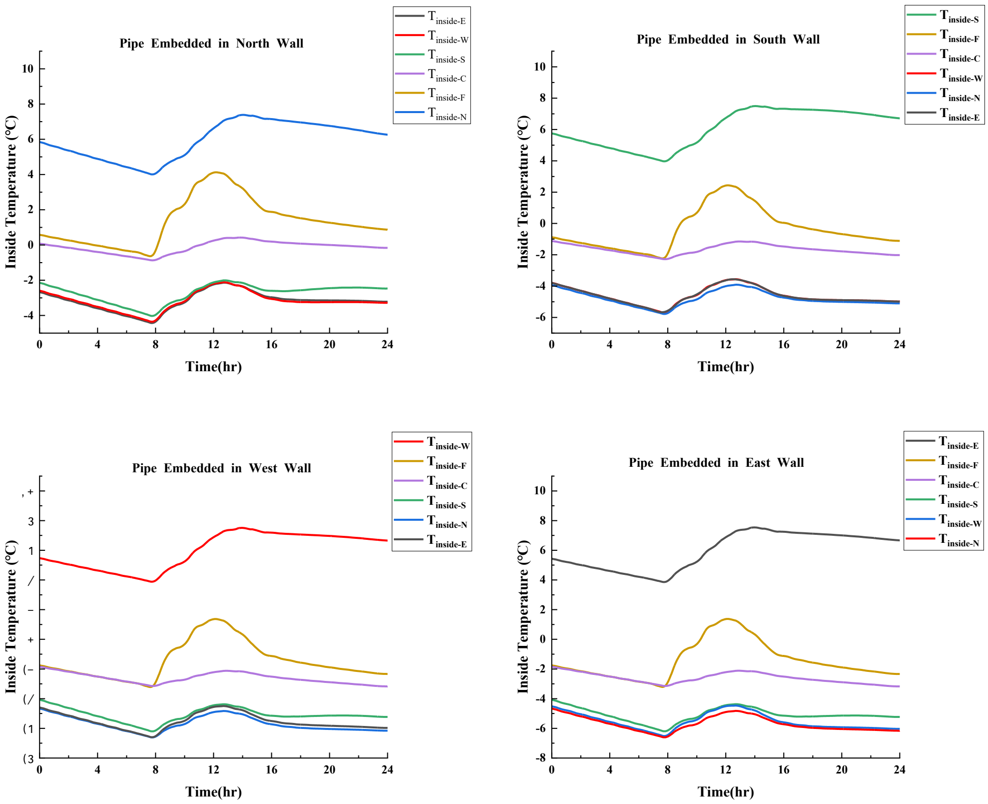

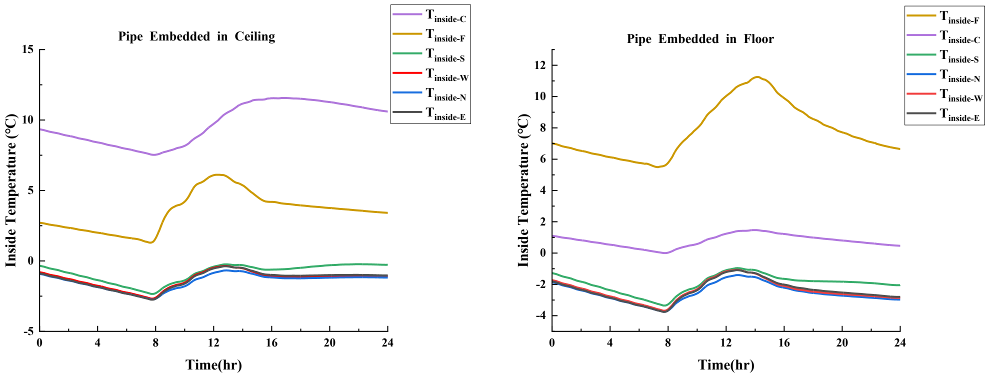

Figure 7: The internal surface temperature of the various pipe embedded building envelopes

3.2. Energy saving in heating period

As previously stated, the Solar Energy-powered Embedded Pipe Envelope System (SEPES), which is one of the thermal active building systems, has the capacity to reduce the heat load during the heating period of the building. In order to elucidate the energy- saving efficacy of SEPES installations in disparate enclosure structures for heating, the study conducted a comparative analysis of the daily heating loads between six installation positions. As demonstrated in Figure 8, following the activation of the SEPES system, the daily heat load of buildings during the heating season is reduced to varying degrees. When the SEPES is active in different envelopes, the average daily heat load through heating season ranges from 53.31KWh/D to 76.69KWh/D, while the average daily heat load of the case building is 103.8KWh/D without SEPES. With SEPES embedded in the ceiling, the total heating load for the heating season decreased from the initial 18897.06KWh to 9702.42KWh, yielding an energy-saving rate of 49.7%, indicating the most remarkably significant energy-saving effect. Moreover, as shown in Figure 8(f), during some periods in March and April, the heat load can even be completely compensated by SEPES. In addition, compared to the other three walls, the maximum heat load reduction is achieved when SEPES is installed on the north wall. The average daily heat load is 64.03KWh/D and energy-saving rate is 44% in this condition. Overall, the best thermal performance is achieved when the SEPES is installed in the ceiling. For other envelopes, the ability to reduce the consumption of heating energy is classified from the largest to the smallest as the north wall, the floor, the south wall, the east wall and the west wall.

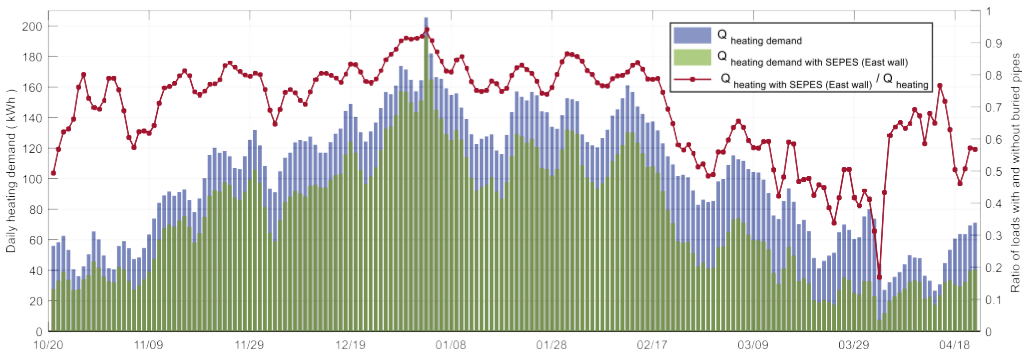

(a)

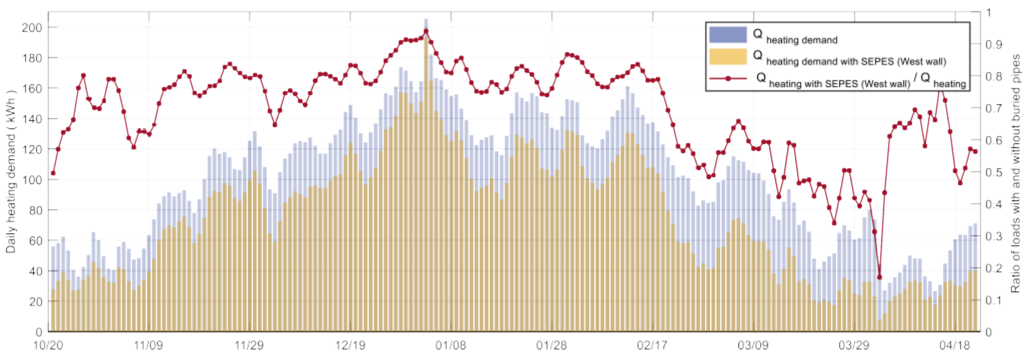

(b)

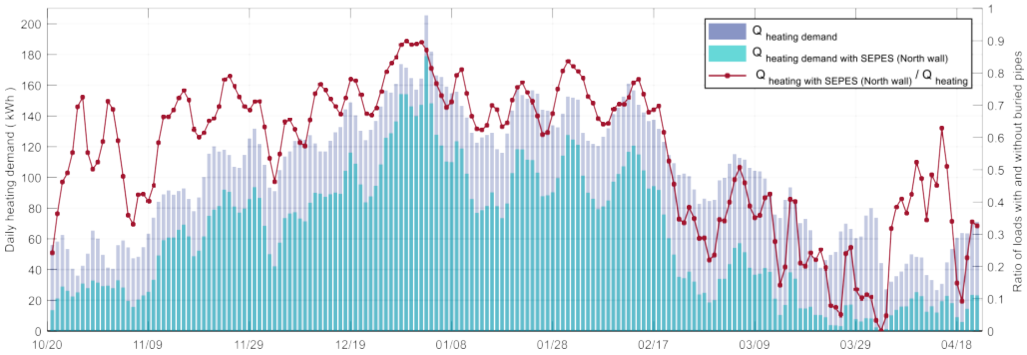

(c)

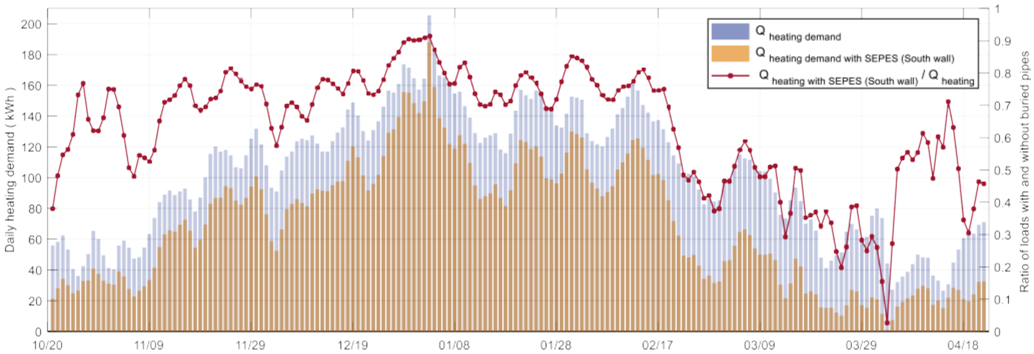

(d)

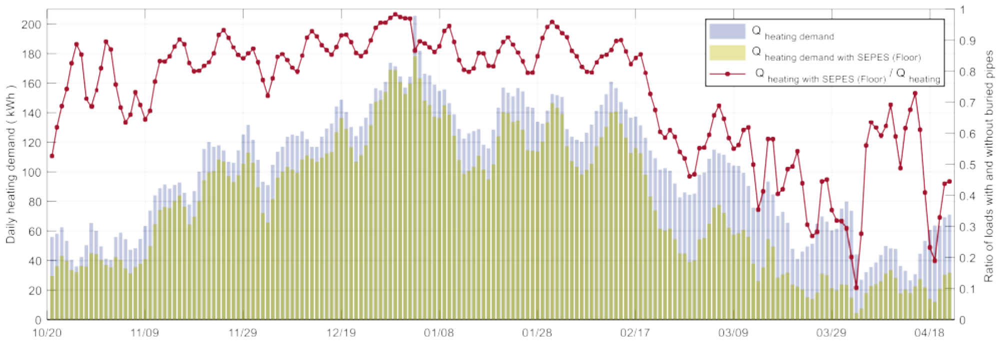

(e)

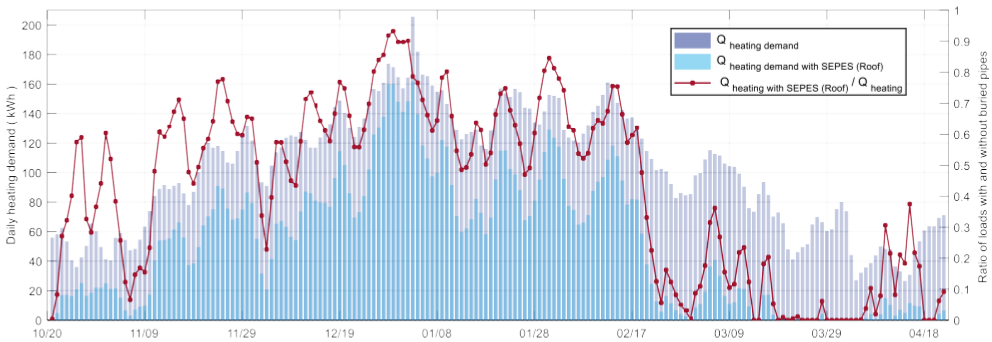

(f)

Figure 8. Heating energy consumption of SEPES when pipe is embedded in different envelopes:(a)East wall;(b)West wall;(c)North wall;(d)South wall;(e)Floor;(f)Ceiling

4. CONCLUSION

To compare the heating efficiency of the solar energy-powered embedded pipe envelope system in different building envelope, thisstudy developed a novel simulation model by coupled building with SEPES through TRNSYS. The indoor air temperature, Inlet andoutlet water temperature in the wall, internal surface temperature of envelopes and heating energy consumption of SEPES coupledwith six different envelopes was systematically evaluated. In summary, the conclusions can be drawn as follows:

1. The Solar Energy-powered Embedded pipe envelope System (SEPES) significantly improves indoor temperatures during cold winters in Harbin. Embedding SEPES in the ceiling is particularly effective, increasing indoor temperatures by up to 8.4℃, while installations on the walls also contribute but to a lesser extent. Strategic placement of SEPES, especially in the ceiling and north wall, optimizes indoor warmth and energy efficiency.

2. The study demonstrates that the water temperature in the SEPES pipes effectively indicates the system's heating capacity and resistance to heat load. The SEPES pipes located within the east and west walls exhibited the highest inlet and outlet water temperatures, with average values of 20.6°C and 16.5°C, respectively. This is attributed to the reduced heat loss from these smaller walls. Conversely, pipes located in the ceiling and floor exhibit lower temperatures, with an average of 16.2 °C at the inlet and 9.6
3. °C at the outlet. This is due to obstructions and reduced solar radiation. The south wall exhibits higher temperatures than the north wall, which highlights the impact of direct solar radiation and the area of embedded pipes on the efficiency of the SEPES system.

4. Ceiling-embedded pipes perform best, with temperatures ranging from 7.42℃ to 11.59℃, effectively blocking heat loss. Floors also retain heat well, reaching up to 11.3℃ even without solar radiation. The average inner surface temperatures for walls vary, with the north wall being the warmest at -0.3℃. These findings indicate that the position of SEPES installation greatly influences the building's overall heat loss and thermal performance.

5. Comparative analysis indicates that the installation of SEPES significantly reduces the daily heat loads, with average reductions ranging from 53.31 kWh/D to 76.69 kWh/D, in comparison to 103.8 kWh/D without SEPES. The ceiling installation of SEPES yielded the highest energy-saving rate of 49.7%, reducing the total heating load from 18,897.06 kWh to 9,702.42 kWh. The north wall installation also demonstrates a notable reduction in energy consumption, with a 44% decrease. In terms of overall thermal performance, the ceiling installation is the most effective, followed by the north wall, floor, south wall, east wall, and west wall, in descending order of efficacy.

5. ACKNOWLEDGEMENT

The authors are grateful for the financial support of the Research University (RU) Grant - Faculty Program (Grant No. GPF005A- 2023).

6. REFERENCES

CHEN, H., YANG, L. & CHEN, W. 2020. Modelling national, provincial and city-level low-carbon energy transformation pathways. Energy Policy, 137, 111096.

D'ANTONI, M. & SARO, O. 2013. Energy potential of a Massive Solar-Thermal Collector design in European climates. Solar energy, 93, 195-208.

FENG, J., SCHIAVON, S. & BAUMAN, F. 2016. New method for the design of radiant floor cooling systems with solar radiation. Energy and Buildings, 125, 9-18.

GUO, S., YAN, D., HU, S. & ZHANG, Y. 2021. Modelling building energy consumption in China under different future scenarios. Energy, 214, 119063.

HE, Y., ZHOU, H. & FAHIMI, F. 2022. Modeling and demand-based control of responsive building envelope with integrated thermalmass and active thermal insulations. Energy and Buildings, 276, 112495.

JIANG, S., LI, X., LYU, W., WANG, B. & SHI, W. 2020. Numerical investigation of the energy efficiency of a serial pipe-embeddedexternal wall system considering water temperature changes in the pipeline. Journal of Building Engineering, 31, 101435.

JOBLI, M. I., YAO, R., LUO, Z., SHAHRESTANI, M., LI, N. & LIU, H. 2019. Numerical and experimental studies of a Capillary-Tubeembedded PCM component for improving indoor thermal environment. Applied Thermal Engineering, 148, 466-477.

KLEIN, S. A. 2018. Calculation of Flat-Plate Collector Loss Coefficients, Renewable Energy.

KRZACZEK, M., FLORCZUK, J. & TEJCHMAN, J. 2019. Improved energy management technique in pipe-embedded wall heating/cooling system in residential buildings. Applied Energy, 254, 113711.

KRZACZEK, M. & KOWALCZUK, Z. 2011. Thermal Barrier as a technique of indirect heating and cooling for residential buildings. Energy and Buildings, 43, 823-837.

LI, N. & CHEN, Q. 2019. Experimental study on heat transfer characteristics of interior walls under partial-space heating mode in hot summer and cold winter zone in China. Applied Thermal Engineering, 162, 114264.

MA, P., WANG, L.-S. & GUO, N. 2014. Modeling of hydronic radiant cooling of a thermally homeostatic building using a parametric cooling tower. Applied energy, 127, 172-181.

SHEN, C. & LI, X. 2017. Energy saving potential of pipe-embedded building envelope utilizing low-temperature hot water in the heating season. Energy and Buildings, 138, 318-331.

SHEN, C., LI, X. & YAN, S. 2017. Numerical study on energy efficiency and economy of a pipe-embedded glass envelope directlyutilizing ground-source water for heating in diverse climates. Energy Conversion and Management, 150, 878-889.

SHEN, J., WANG, Z., LUO, Y., JIANG, X., ZHAO, H., CUI, D. E. & TIAN, Z. 2022. Performance evaluation of an active pipe-embeddedbuilding envelope system to transfer solar heat gain from the south to the north external wall. Journal of Building Engineering, 59, 105123.

SU, X., ZHANG, L., LIU, Z., LUO, Y., LIAN, J. & LUO, Y. 2019. A computational model of an improved cooling radiant ceiling panel system for optimization and design. Building and Environment, 163, 106312.

SUN, H., WU, Y., LIN, B., DUAN, M., LIN, Z. & LI, H. 2020. Experimental investigation on the thermal performance of a novel radiant heating and cooling terminal integrated with a flat heat pipe. Energy and Buildings, 208, 109646.

WANG, L., ONN, C. C., CHEW, B. T., LI, W. & LI, Y. 2024. Numerical Study of the Solar Energy-Powered Embedded Pipe EnvelopeSystem. Buildings, 14, 613.

XIE, J.-L., ZHU, Q.-Y. & XU, X.-H. 2012. An active pipe-embedded building envelope for utilizing low-grade energy sources. Journal of Central South University, 19, 1663-1667.

XU, K., XU, X. & YAN, T. 2023. Performance evaluation of a pipe-embedded phase change material (PE-PCM) roof integrated withsolar collector. Journal of Building Engineering, 71, 106582.

XU, X., WANG, S., WANG, J. & XIAO, F. 2010. Active pipe-embedded structures in buildings for utilizing low-grade energy sources: a review. Energy and buildings, 42, 1567-1581.

YANG, M. 2014. Energy consumption analysis and energy-saving air conditioning technology application of commercial complexesin hot summer and cold winter regions. Harbin Institute of Technology.

YANG, Y. & CHEN, S. 2024. Comprehensive thermal performances study on fin-enhanced thermo-activated building envelopes with anisotropic heat injection capacity. Energy Conversion and Management, 300, 117933.

YANG, Y., CHEN, S., CHANG, T., MA, J. & SUN, Y. 2021. Uncertainty and global sensitivity analysis on thermal performances ofpipe-embedded building envelope in the heating season. Energy Conversion and Management, 244, 114509.

YE, M., SERAGELDIN, A. A., RADWAN, A., SATO, H. & NAGANO, K. 2021. Thermal performance of ceiling radiant cooling panelwith a segmented and concave surface: Laboratory analysis. Applied Thermal Engineering, 196, 117280.

YI, J. 2005. Energy consumption status of buildings in China and effective energy-saving methods. Heating Ventilating & Air Conditioning, 35, 11.

#286: A two-stage energy management for plug-in hybrid tugboats based on MPC method

Qi YANG[1], Chao MENG[2], Wanyou LI[3, *], Xiqun LU[4]

[1] College of Power and Energy Engineering, Harbin Engineering University, Harbin, China, qiiyang@qq.com
[2] College of Energy, Xiamen University, Xiamen, China, meng@xmu.edu.cn
4 College of Power and Energy Engineering, Harbin Engineering University, Harbin, China, hrbeu_ripet_lwy@163.com
5 College of Power and Energy Engineering, Harbin Engineering University, Harbin, China, luxiqun@hrbeu.edu.cn

Abstract: Hybrid configuration for ships holds the potential to significantly enhance energy efficiency and reduce CO2 emissions which are already used on several ship types. This configuration presents an additional challenge in determining the optimal power distribution among multiple energy sources for more efficient, cost-effectiveness, and clean energy utilization. Currently, the rule-based strategy is widely used, which has poor flexibility. In order to further improve the performance, it is necessary to investigate better control strategies. In this work, a two-stage energy management strategy based on Mixed Integer Nonlinear Programming (MINLP) and Model Predictive Control (MPC) was proposed for plug-in hybrid tugboats equipped with diesel generators and energy storage devices, to achieve real-time optimal power distribution of multiple energy sources during voyages. Based on the actual operation data of the tugboat, a typical tugboat load curve was generated. Aiming at minimizing the equivalent fuel consumption, a mixed integer nonlinear optimization model was established, and the adjustable battery equivalent fuel factor and a series of constraints were considered. By solving the global optimal problem in the predicted time domain, the reference tracks of MPC were obtained, and finally the real-time optimal energy scheduling was realized. Simulation results demonstrate that the real-time optimization-based MPC (RT-MPC) energy management strategy can reach similar optimization effects compared with the global optimization-based MPC (G-MPC) energy management strategy, and the deviation is 0.726%. In addition, through the robustness verification, RT-MPC strategy can effectively deal with the load fluctuations and realize the real-time optimization of the system

Keywords: Energy Management; Hybrid Ship; Model Predictive Control; Mixed Integer Nonlinear Optimization; Energy Storage

1. INTRODUCTION

With the vigorous development of the marine economy, the number of ships continues to increase, leading to ship exhaust emissions becoming a significant source of air pollution (Chen, Fei and Wan, 2019). Consequently, the prevention and control of shipping pollution have become a focus issue (Wang, Yu and Xu, 2022). The International Maritime Organization (IMO) has proposed that greenhouse gas emissions from international shipping should peak as soon as possible and achieve net zero emissions around 2050 (IMO, 2023). Shipping emission reduction is urgent, green power including LNG, methanol, hydrogen and lithium batteries, etc, has gained widespread attention (Meng *et al.*, 2022). However, due to the limitation of technical maturity, it has not been widely used. Hybrid configurations can enhance the emission and economic performance and provide a feasible scheme for the transition of ships from traditional propulsion to green propulsion (Nivolianiti, Karnavas and Charpentier, 2024). Additionally, in the complex shipping environment, ships often experience frequent sudden changes, which can easily lead to stability problems (Dubey and Santoso, 2017). In order to realize the multi energy sources collaboration of hybrid system and improve the dynamic matching ability between source and load, finally realize more efficient, clean and safe energy utilization, the energy management of hybrid power system is the key issue of research.

The energy management strategy (EMS) of hybrid ship power system mainly includes rule-based strategy and optimization-based strategy. The rule-based methods include deterministic rules and fuzzy logic rules. Graf *et al.* (2022) set the maximum output powerof the battery as a fixed threshold and designed the output power of the fuel cell and the battery according to the demand power ofthe ship. Yuan *et al.* (2018) proposed an energy management strategy based on fuzzy logic for optimal allocation of multi-energy power, considering load demand and the randomness of solar energy. Khan, Faruque and Newaz (2017) introduced an EMS basedon fuzzy logic for power sharing among multiple energy storage systems. Rule-based energy management strategy is easy to implement, but it relies on experience and is less flexible and adaptable.

Optimization-based approaches can provide better solutions, encompassing global optimization and real-time optimization. Fang and Xu (2020) proposed a robust energy management method for all-electric marine microgrids with the aim of reducing fuel consumption (FC) and the energy efficiency operating index (EEOI). Ritari *et al.* (2020) developed a multi-period mixed integer linear programming (MILP) model to derive a globally optimal power management strategy for auxiliary engines and the battery which realizes economic improvement. Hou, Sun and Hofmann (2017) employed model predictive control (MPC) method to address the issue of power tracking and energy saving under various operational constraints in a hybrid power system consisting of battery and supercapacitor. While global optimization methods are adopted under specific routes and operating conditions and are mostly used for offline optimization. The real-time optimization algorithm can achieve real-time optimization with less computation but cannot guarantee global optimization. The combination of different energy management strategies will be the focus of future research and can be tailored according to the characteristics of research objects.

In this study, a two-stage energy management strategy combining global optimization and real-time optimization was proposed to address the energy management problem of diesel-electric hybrid power system of a tugboat. A mixed integer nonlinear programming (MINLP) model was constructed, aiming at minimum equivalent fuel consumption while considering a series of operational constraints. Based on the established MINLP model, global optimization was carried out in the prediction time domain considering the future effects caused by control action at each step. Subsequently, the model predictive control (MPC) method was used to obtain the optimal power allocation scheme in real time, using the global optimal solution as the reference trajectory. Finally, the superiority and robustness of the algorithm were verified by simulation. Due to the short prediction interval, the proposed two-stageenergy management strategy could not only retain the real-time response speed, but also achieve better optimization effect than the single-step real-time optimization.

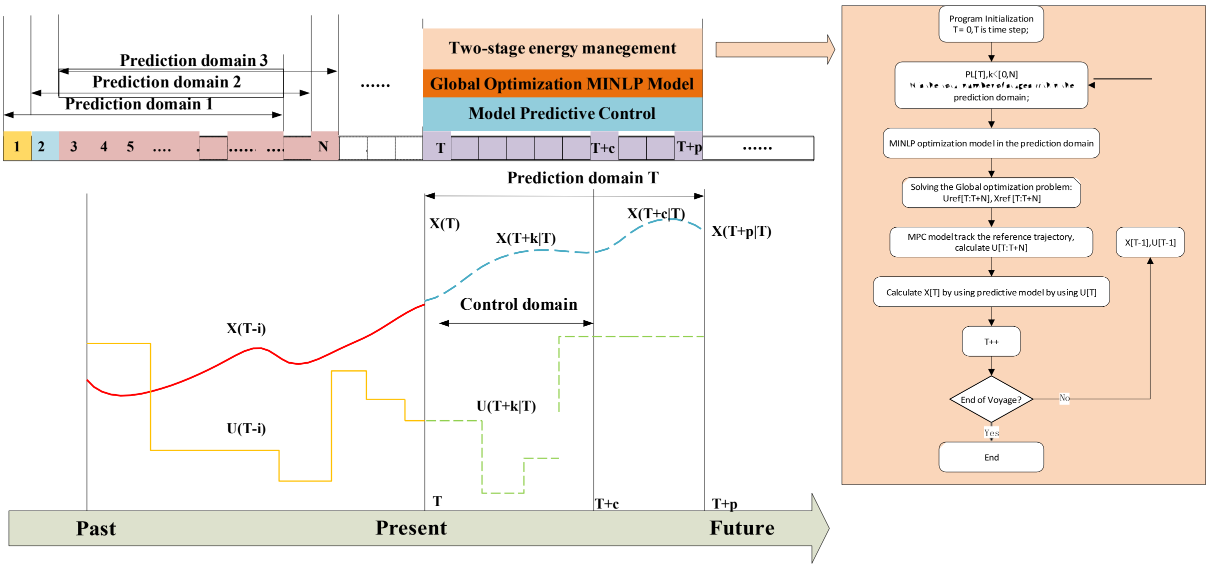

Figure 1: Schematic of the proposed two-stage energy management method

2. METHODOLOGY

In this work, a two-stage energy management strategy based on Model Predictive Control (MPC) and Mixed Integer Nonlinear Programming (MINLP) was proposed for hybrid tugboats equipped with diesel generators and energy storage devices, to achieve real-time optimal power distribution of multiple energy sources during voyages. The schematic of the proposed two-stage energy management method is shown in Figure 1.

2.1. Global optimization MINLP model

In this study, the collaborative optimization problem of power distribution among multiple energy sources in hybrid electric ships equipped with diesel generator sets and batteries was investigated. The constraints and objective functions involved in this model are analysed and designed below.

Objective Function

The objective function is to minimize the total equivalent fuel consumption, which contains generator fuel consumption, equivalent fuel consumption of battery and penalty consumption, as shown in Equations 1–5.

Equation 8:

$$min\,FC = \sum_t \sum_i FC_{i,t}^{gen} + \sum_t \sum_j FC_{j,t}^{bat} + p \sum_t \sum_i \varphi_{i,t}$$

Where:

- FC = equivalent fuel consumption of the hybrid system (g)
- $FC^{gen}_{i,t}$ = fuel consumption of the i-th generator set in the t-th period (g)
- $FC^{bat}_{i,t}$ = equivalent fuel consumption of the j-th battery pack in the t-th period (g)
- p = penalty coefficient of starting the generator
- $\varphi_{i,t}$ = the start variable of generator set, binary variable, 1 indicates the generator state switch from off to on

Equation 2:

$$FC_{i,t}^{gen} = \frac{P_{i,t}^{gen}}{\eta_{gen}} SFOC_{i,t}$$

Equation 3:

$$FC_{j,t}^{bat} = P_{j,t}^{bat} SFOC_{min}$$

Equation 4:

$$EF_{i,t}^{bat} = \begin{cases} k_{j,t}^{bat} \cdot \eta_{dis} \cdot \eta_{cha} / \eta_{gen}\ , & charge\ state \\ k_{j,t}^{bat} / (\eta_{dis} \cdot \eta_{cha} \cdot \eta_{gen})\ , & discharge\ state \end{cases}$$

Equation 5:

$$k_{j,t}^{bat} = 1 - \mu \frac{2 \cdot SOC_{j,t} - SOC_{mean}}{SOC_{mean}}$$

Where:

- $P^{gen}_{i,t}$ = output power of the i-th generator set in the t-th period (kW)
- $P^{bat}_{j,t}$ = output power of the j-th battery in the t-th period (kW)
- $SFOC^{gen}_{i,t}$ = specific fuel oil consumption(SFOC) of the i-th generator set in the t-th period (g/kWh)
- $SFOC_{min}$ = the minimum SFOC of the generator set (g/kWh)
- $EF^{bat}_{j,t}$ = equivalent factor of the j-th battery in the t-th period during charge and discharge mode
- $k^{bat}_{j,t}$ = the factor of the j-th battery in the t-th period, this value is set to bring the SOC of battery closer to the median value
- μ = a constant value
- SOC_{mean} = the mean SOC of battery
- $SOC_{j,t}$ = the SOC of the j-th battery in the t-th period
- η_{dis} = the efficient factor of battery during discharging mode
- η_{cha} = the efficient factor of battery during charging mode
- η_{gen} = the efficient factor of generator set

Constraint

Power Balance Constraint: The power balance constraint must be satisfied all the time during the operation of the system

Equation 6:

$$\sum_i P_{i,t}^{gen} + \sum_j P_{j,t}^{bat} = P_t^{load}$$

Where:

- P^{load}_t = the demand load power (kW)

Battery charging and discharging constraint: During the process of charging and discharging, it is necessary to meet the constraints of power limit, SOC limit and the depth of charging and discharging.

Equation 7: $$P_{j,t}^{bat} = P_{j,t}^{dis} - P_{j,t}^{cha}$$

Equation 8: $$0 \le P_{j,t}^{cha} \le \alpha_{j,t}^{cha} \cdot P_{max}^{cha}$$

Equation 9: $$0 \le P_{j,t}^{dis} \le \alpha_{j,t}^{dis} \cdot P_{max}^{dis}$$

Equation 10: $$\alpha_{j,t}^{cha} + \alpha_{j,t}^{dis} \le 1$$

Equation 11: $$SOC_{min} \le SOC_{j,t} \le SOC_{max}$$

Equation 12: $$SOC_{j,t} \equiv SOC_{j,t-1} + \frac{\eta_{cha} \cdot \alpha_{j,t-1}^{cha} \cdot P_{j,t-1}^{cha} \cdot \Delta T}{E_{cap}} - \frac{\alpha_{j,t-1}^{dis} \cdot P_{j,t-1}^{dis} \cdot \Delta T}{E_{cap} \cdot \eta_{dis}}$$

Where:

- $P^{dis}_{j,t}$ = discharging power of the j-th battery in the t-th period (kW)
- $P^{cha}_{j,t}$ = charging power of the j-th battery in the t-th period (kW)
- P^{dis}_{max} = the maximum discharging power (kW)
- P^{cha}_{max} = the maximum charging power (kW)
- E_{cap} = the capacity of battery (kWh)

Diesel generator set operation constraint: In order to accurately describe the actual response characteristics of the generator set and ensure that the generator works in the safe range, it is necessary to restrict the load and climb rate of the generator set.

Equation 13: $$P_{i,t}^{gen} = \eta_{gen} \cdot P_{i,t}^{die}$$

Equation 14: $$\alpha_{i,t}^{gen,on} \cdot P_{min}^{gen} \le P_{i,t}^{gen} \le \alpha_{i,t}^{gen,on} \cdot P_{max}^{gen}$$

Equation 15: $$\left| P_{i,t+1}^{gen} - P_{i,t}^{gen} \right| \le \varepsilon \cdot P_{max}^{gen}$$

Equation 16: $$\varphi_{i,t+1}^{gen} \ge \alpha_{i,t+1}^{gen,on} - \alpha_{i,t}^{gen,on}$$

Equation 17: $$\varphi_{i,t+1}^{gen} \le 1 - \alpha_{i,t}^{gen,on}$$

Equation 18: $$\varphi_{i,t+1}^{gen} \le \alpha_{i,t+1}^{gen,on}$$

Where:

- $P^{die}_{i,t}$ = output power of the j-th diesel engine in the t-th period (kW)
- $\alpha^{gen,on}_{i,t}$ = the start variable of generator set
- ε = the climb rate of generator set

2.2. MPC model

The MPC method mainly contains four parts: prediction model, rolling optimization, feedback correction and reference track, the MPC model in this study is described as follows.

Prediction Model

The prediction model is expressed in Equation 19

Equation 19: $$x = \begin{bmatrix} FC^{gen} \\ SOC \end{bmatrix}, u = \begin{bmatrix} P^{gen} \\ P^{bat} \end{bmatrix}, y = \begin{bmatrix} FC^{gen} \\ SOC \end{bmatrix}, v = P^{load}$$

Where:

- x = the state variable of the MPC system, contains the cumulative fuel consumption of generator set and the state of charge of battery.

- u = the control variable of the MPC system, contains the generator power and the battery power.
- v = the measured input, namely Pload in this case
- y = the output

The MPC control method is a phased rolling optimization method; thus, it is necessary to discretize the hybrid system model. The discretized MPC prediction model is established as follows

Equation 20: $$x(k+1) = Ax(k) + B_u u(k) + B_v$$

Equation 21: $$y(k) = Cx(k)$$

Equation 22: $$A = \begin{bmatrix} 1 & 0 \\ 0 & 1 \end{bmatrix}, B_u = \begin{bmatrix} a/\eta_{gen} & 0 \\ 0 & 1/E_{cap} \end{bmatrix}, B_v = \begin{bmatrix} b \\ 0 \end{bmatrix}, C = \begin{bmatrix} 1 & 0 \\ 0 & 1 \end{bmatrix}$$

Equation 23: $$\dot{FC} = a \cdot P^{die} + b$$

Where:

– A, B_u, B_v, C = coefficient matrices, and the matrix dimensions here are only indicative and should be modified according to the actual system.
– a, b = constant values, which are used to describe the fuel consumption of a generator set

Set the length of the prediction horizon to N, the future state of the system can be further derived as follows:

Equation 24: $$X(k) = \begin{bmatrix} x(k) \\ x(k+1|k) \\ x(k+2|k) \\ \vdots \\ x(k+N|k) \end{bmatrix}, U(k) = \begin{bmatrix} u(k) \\ u(k+1) \\ u(k+2) \\ \vdots \\ u(k+N-1) \end{bmatrix} Y(k) = \begin{bmatrix} y(k) \\ y(k+1|k) \\ y(k+2|k) \\ \vdots \\ y(k+N|k) \end{bmatrix}$$

Equation 25: $$M = \begin{bmatrix} I \\ A \\ A^2 \\ \vdots \\ A^N \end{bmatrix}, C_u = \begin{bmatrix} 0 & 0 & \cdots & 0 \\ B_u & 0 & \cdots & 0 \\ AB_u & B_u & \cdots & 0 \\ \vdots & \vdots & \cdots & \vdots \\ A^{N-1}B_u & A^{N-2}B_u & \cdots & B_u \end{bmatrix} V = \begin{bmatrix} 0 \\ B_v \\ AB_v + B_v \\ \vdots \\ A^{N-1}B_v + A^{N-2}B_v + \cdots B_v \end{bmatrix}$$

Equation 26: $$X(k) = Mx(k) + C_u U(k) + V$$

Equation 27: $$Y(k) = \begin{bmatrix} C & 0 & \cdots & 0 \\ 0 & C & \ddots & \vdots \\ 0 & \ddots & \ddots & 0 \\ 0 & 0 & 0 & C \end{bmatrix} X(k)$$

Rolling Optimization

The cost function J is defined as the sum of the difference between the measured output value of the process and the reference and the control input term, as expressed in Equation 28. The optimal control variable is obtained by minimizing the cost function.

Equation 28: $$J = \sum_{i=0}^{N-1} ((y(k+i|k) - ref(i))^T Q(y(k+i|k) - ref(i)) + u(k+i)^T Ru(k+i)) + (y(k+N|k) - ref)^T F(y(k+N|k) - ref(N))$$

Where:

– Q, R, F = the weight matrices.

Substituting the Equation 27 to 28 into the equation and ignoring the constant term, the cost function can be simplified as

Equation 29: $$J' = E^T U(k) + \frac{1}{2} U(k)^T HU(k)$$

Equation 30: $$E = 2{C_u}^T \bar{Q}(Mx(k) + V - ref)$$

Equation 31: $$H = 2{C_u}^T \bar{Q} C_u + \bar{R}$$

Equation 32: $$\begin{cases} A_{eq}U = b_{eq} \\ A_{ineq}U \leq b_{ineq} \end{cases}$$

Under the premise that the corresponding equality and inequality constraints are satisfied, the optimal control quantity of each step can be obtained by solving the above quadratic programming problem

Feedback Correction

At each stage, the new measured value is used as the initial condition of the prediction system, and the optimization problem is refreshed and solved.

Reference Track

To generate a reference curve for the MPC system, a mixed integer nonlinear optimization model is established with the aim of minimizing the equivalent fuel consumption, and the adjustable battery equivalent fuel factor and a series of constraints were considered, such as energy balance constraints, energy storage constraints, etc. By solving the global optimal problem in the predicted time domain, the reference tracks of MPC can be obtained, finally the real-time optimal energy scheduling can be realized. The MINLP model is expressed in 2.1

3. CASE STUDY AND RESULT

3.1. Case description

In this study, the hybrid tugboat named “Xia Gang Tuo 30” was used for the energy management strategy case study. The power system of the hybrid tugboat is composed of three diesel generator sets, two batteries, propulsion motors and the AC load. An overview of the hybrid electrical tugboat structure is shown in Figure 2. its basic parameters are given in Table 1.

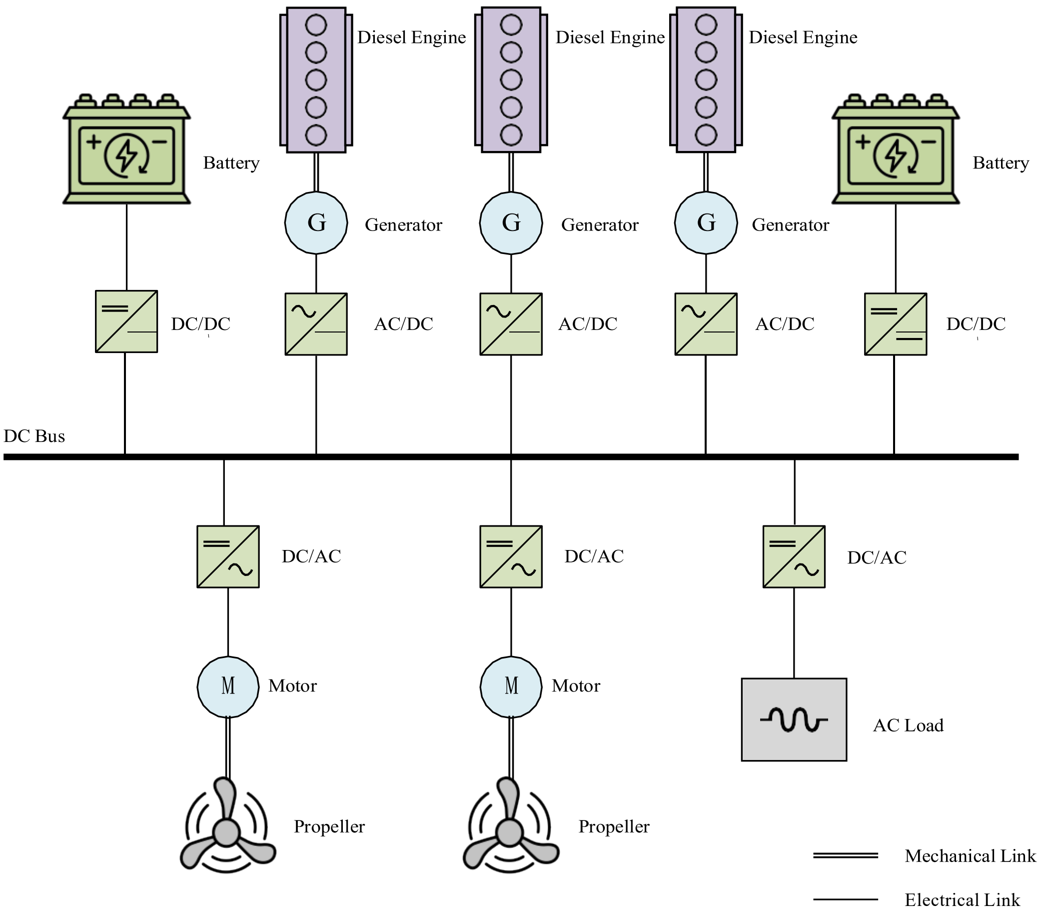

Figure 2: Schematic diagram of Architecture of the hybrid electrical tugboat

Based on actual 4-month operation data of the tugboat, the variation rule of the tugboat’s sailing load is analysed, as shown in Figure 3. Figure 4 shows the typical load curve used in the case study, as well as the actual load curve of the tugboat during an actual voyage. The SFOC curve and the fitting curve of fuel consumption per unit time are shown in Figure 5 and Figure 6, with the data having been standardized. As Figure 3-6 indicates that the tugboat operates under low load conditions for a long period during sailing, with less demand of high power, but there are sudden and large loading and unloading events. Therefore, employing appropriate energy management strategies and control measures to achieve the coordinated regulation of batteries and generator sets, while ensuring the diesel generator set works in the high-efficiency range, has a positive effect on the safety, stability, economy and emission performance of the ship power grid.

Table 1: Basic parameters of the hybrid power system

Devices	amount	Parameters	Values
Diesel engine	3	Rated power(kW)	1628
		Rated speed(rpm)	1800
Generator	3	Rated power(kW)	1400
Battery	2	Capacity(kWh)	980
		The maximum discharging power(kW)	784
		The maximum charging power(kW)	392
		Initial SOC	0.95, 0.90

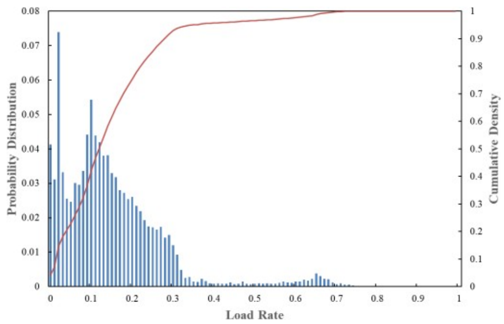

Figure 3: Tugboat load distribution curve

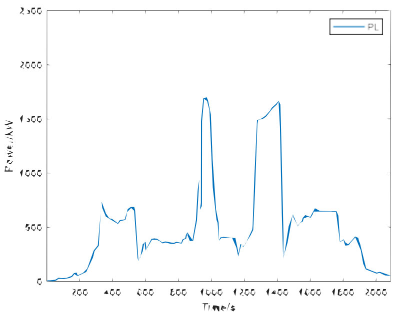

Figure 4: Typical tugboat load curve

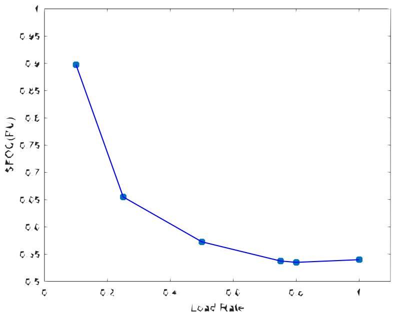

Figure 5: SFOC characteristic for diesel generator set

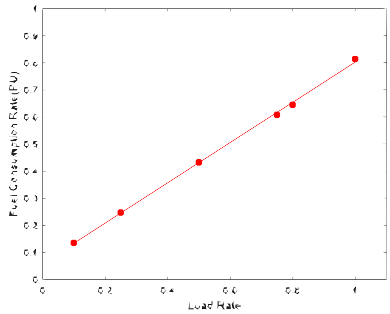

Figure 6: The fitting curve of fuel consumption per unit time

3.2. Results and analysis

According to the parameters and the typical load conditions set in Section 3.1, the proposed two-stage energy management strategy based on the combination of MPC and MINLP was validated. Taking the MPC energy management strategy based on global optimization (G-MPC) as the baseline, the optimization performance of MPC energy management strategy based on real-time optimization (RT-MPC) was evaluated. In addition, the implementation effect of the strategy under disturbed conditions was analysed to verify the robustness of the method. The simulation results are shown in Figure 7-14.

The reference output and actual output of diesel engine fuel consumption and battery SOC are shown in the Figure7 and Figure 8. It can be seen that the MPC control layer can track the optimization results of the upper layer well, ultimately achieving optimal control. The equivalent SFOC of each energy sources are shown in the Figure9 and the equivalent SFOC of batteries are specifically represented in Figure 10. As is shown in the figure, the diesel generator set should only be started if its fuel consumption rate is lower than the equivalent fuel consumption rate of the battery, that is, it always works in the high efficiency range, which is the embodiment of economic optimization in energy management strategy. In addition, due to the constraint of the climbing rate of the diesel generator set, the generator cannot directly load to the high efficiency zone or unload to zero when starting and stopping, so there are abnormal peaks in the SFOC curves of generator set. And it can be seen in conjunction with Figure 8 and Figure 10, due to the use of adjustable fuel consumption factor, MPC control well realizes the coordination of the two groups of batteries, which is manifested in that the equivalent fuel consumption of two batteries gradually tends to be consistent, and their SOC also converge.

The output power of each energy source is illustrated in Figure 11 ang Figure 12, it is observed that the starting time of the diesel generator set using the RT-MPC strategy is earlier than the G-MPC, and the output power is lower. but the diesel engine still operates within the high-efficiency range, with the load rate exceeding 70%. The implementation effects of the two strategies and their relative deviations are summarized in Table 2. The results demonstrate that, the voyage equivalent fuel consumption of the RT-MPC energy management strategy is 71.869kg, and the value of the G-MPC energy management strategy is 71.350kg, and the deviation is 0.726%%, which means the RT-MPC energy management strategy can achieve similar optimization effects compared with the G- MPC energy management strategy, thereby proving the superiority of the RT-MPC strategy.

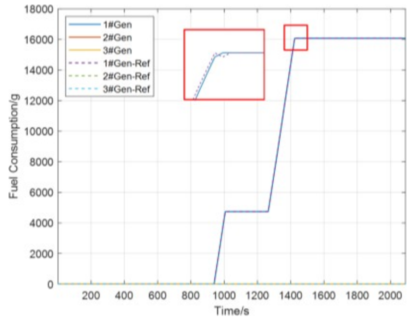

Figure 7: Fuel Consumption tracking condition

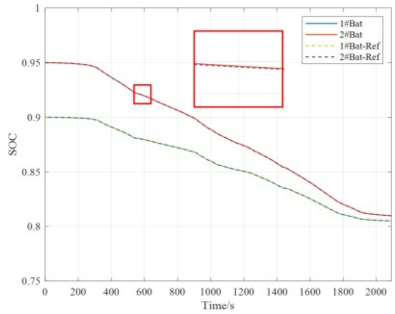

Figure 8: SOC tracking condition

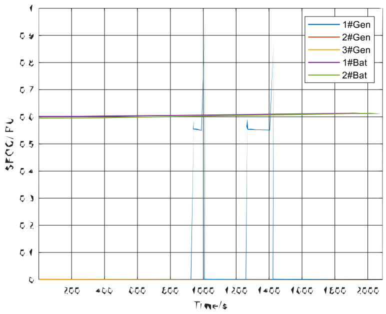

Figure 9: Equivalent SFOC of each energy sources

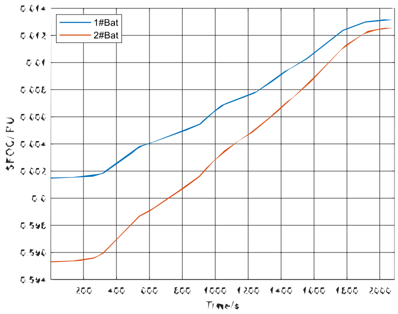

Figure 10: Equivalent SFOC of batteries

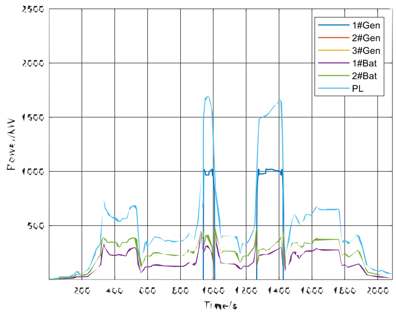

Figure 11: Output power on RT-MPC strategy

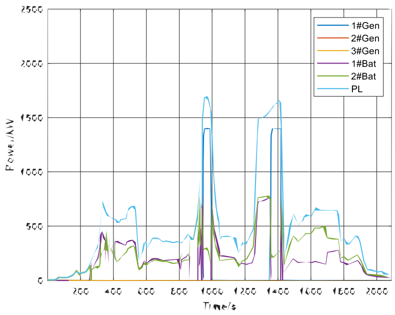

Figure12: Output power on G-MPC strategy

Table 2: Comparison of two energy management strategies

Item	Equivalent fuel consumption(kg)	Actual fuel consumption(kg)	SOC
G-MPC	71.350	10.805	0.790, 0.805
RT-MPC	71.869	16.074	0.805, 0.810
Relative deviation	0.726%	48.8%	1.25%

Figure 13 and Figure 14 show the RT-MPC simulation results under disturbed conditions (with 10% and 20% random noise). As can be seen from figures, the RT-MPC strategy can still maintain the generator's high-efficiency output under random disturbance conditions. The disturbances are mainly regulated by batteries, and generator power fluctuation does not exceed 88kw (8.8%). It demonstrates that the RT-MPC strategy can effectively smooth the generator power output and reduce shafting damage caused bysudden loading and unloading.

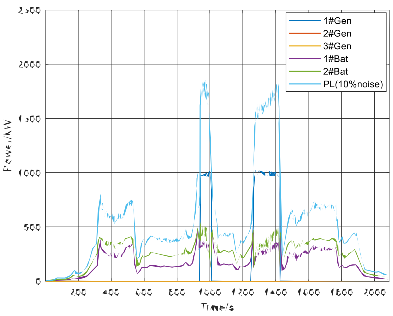

Figure 13: Output power on RT-MPC strategy with 10% noise

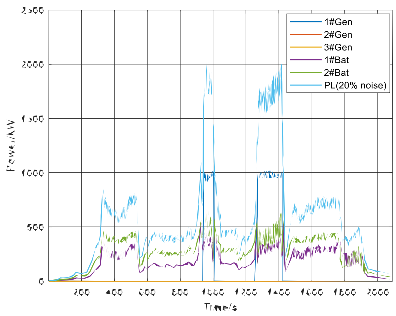

Figure 14: Output power on RT-MPC strategy with 20% noise

3. CONCLUSION

In this study, aiming at achieving real-time optimal allocation of multiple energy sources (diesel generator sets and batteries) duringthe voyage, a two-stage energy management strategy based on MINLP and MPC is proposed for a diesel-electric hybrid tugboat. G-MPC strategy is used as the benchmark to evaluate the implementation performance of RT-MPC strategy. The simulation results show that RT-MPC strategy can achieve a similar optimization effect compared with the G-MPC strategy, with a deviation of 0.726%. In addition, robustness is verified by the load disturbance condition, and the results show that the RT-MPC strategy can effectively deal with the load fluctuation and realize the real-time optimization of the system.

4. REFERENCES

Chen J, Fei Y, Wan Z. (2019) 'The relationship between the development of global maritime fleets and GHG emission from ship', Journal of environmental management, 242, pp. 31-39.

Wang C, Yu S, Xu L. (2022) 'Decisions on sailing frequency and ship type in liner ship with the consideration of carbon dioxide emissions', Regional Studies in Marine Science, 52, pp. 102371.

IMO. (2023) Marine environment protection committee (MEPC 80).

Meng L, Wang J, Yan W, et al. (2022) 'A differential game model for emission reduction decisions between ports and ship** enterprises considering environmental regulations', Ocean & Coastal Management, 225, pp. 106221.

Nivolianiti E, Karnavas Y L, Charpentier J F. (2024) 'Energy management of shipboard microgrids integrating energy storage systems: A review', Renewable and Sustainable Energy Reviews, 189, pp. 114012.

Dubey A and Santoso S. (2017) 'Availability-based distribution circuit design for shipboard power system', IEEE Transactions on Smart Grid， 8(4), pp. 1599–1608.

Graf T, Fonk R, Schröter J, et al. (2022) 'Investigation of a fuel cell hybrid system with a new modular test bench approach for all electric hybrid power train systems', Journal of Energy Storage, 56, pp. 105999.

Yuan Y, Zhang T, Shen B, et al. (2018) 'A fuzzy logic energy management strategy for a photovoltaic/diesel/battery hybrid ship based on experimental database', Energies, 11(9), pp. 2211.

Khan M M S, Faruque M O and Newaz A. (2017) 'Fuzzy logic based energy storage management system for MVDC power systemof all electric ship', IEEE Transactions on Energy Conversion, 32(2), pp. 798-809.

Fang S and Xu Y. (2020) 'Multi-objective robust energy management for all-electric shipboard microgrid under uncertain wind and wave', International Journal of Electrical Power & Energy Systems, 117, pp. 105600.

Ritari A, Huotari J, Halme J, et al. (2020) 'Hybrid electric topology for short sea ships with high auxiliary power availability requirement', Energy, 190, pp. 116359.

Hou J, Sun J and Hofmann H F. (2017) 'Mitigating power fluctuations in electric ship propulsion with hybrid energy storage system:Design and analysis'. IEEE Journal of Oceanic Engineering, 43(1), pp. 93-107.

#287: An experimental study for the effects of load resistances on small-scale ORC power systems performance

Qingxu Ma[1], Haiming Yu[2], Yuqi Wu[3], Yongchao Xu[4], Haohan Sha[5*]

[1] Qingdao University of Technology, China Qingdao, maqx0217@163.com
[2] Qingdao University of Technology, China Qingdao, yuhm0131@163.com
[3] Linyi Wisdom New Energy Technology Co., China Linyi, wyq@yantaibinglun.com
[4] Qingdao University of Technology, China Qingdao, xu1194903841@163.com
[5] Qingdao University of Technology, China Qingdao, haohansha@qut.edu.cn

Abstract: Organic Rankine Cycle (ORC) power systems convert low-temperature thermal energqy into electrical energy, which is a potential technology for waste heat recovery and renewable energy utilization. To improve the performance of small-scale ORC power systems, the relationship between system performance and load resistance in ORC should be further investigated. An ORC test-rig with a scroll expander directly connected to a generator was built. With a variable-temperature heat source, working fluid R141b and R245fa, and electrical load, the effects of the load resistance (50 Ω to 200 Ω) and the heat source temperature (75 °C to 95 °C) on the performance of the ORC system were investigated. The results show that the optimum value of load resistance existsfor the ORC system to maximize the output power or thermal efficiency, and this value varies with the heat source temperature andworking fluid. For R245fa, the optimal load resistance to achieve the maximum shaft output power changes from 100 Ω to 200 Ω when the heat source temperature reduces from 95 ℃ to 75 ℃. For R141b, the optimal load resistance to achieve the maximum shaft output power is fixed around 200 Ω. The analysis shows that the changes of load resistance affect the operating conditions ofthe scroll expander, which in turn affects the flow rate and heat transfer of the system. Therefore, the change of load resistances has a combined effect on system performance. This study highlights the importance of matching the load resistance, heat source temperature, and working fluid, and provides experimental data for optimizing ORC power systems.

Keywords: Organic Rankine Cycle; Low-Temperature Heat Source; Electronic Load; Scroll Expander; System Performance

1. INTRODUCTION

In recent years, the problem of energy shortage has become more and more serious. As a potential technology that can utilize low-temperature thermal energy such as solar and geothermal energy, Organic Rankine Cycle (ORC) has received increasing researchattention (Cao J, 2017, 139:206-21; Hu S, 2021, 14:6492). ORC power systems utilize organic working fluid with low boiling points to absorb low temperature heat and convert the working fluid into vapour with relatively high pressure to drive an expander to rotate. By connecting the expander to a generator, the mechanical energy will be converted to electrical energy. The basic structure of an ORC power system is shown in Fig. 1, which mainly consists of: a. expander, b. condenser, c. liquid receiver, d. pump, e. evaporator, and f. generator. Currently, most research of ORC power systems focus on the ORC structure (Yu ZT, 2022, 135: 97- 112) optimization method or devices optimization method, such as evaporator (Nematollahi, O, 2018; SHI L, 2024, 53(1): 115-123),condenser (MA X L, 2023, 44(1) :65-69), and expander (Wu LJ, 2021, 49 (12): 1778-1788; Yu HB, 2022). However, few studies focus on the effects of load resistance on ORC power systems performance, limiting the practical application of the technology.

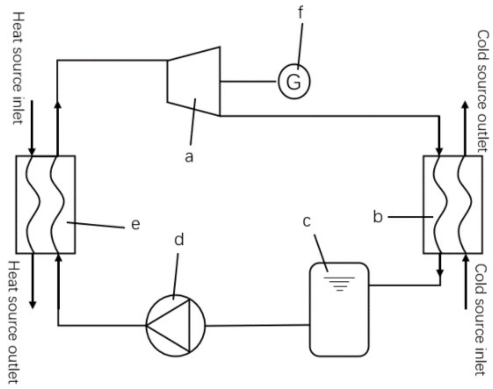

Figure 1: A simple ORC system

Previous studies usually focused only on the effect of load on the performance of ORC generation systems under a single operating condition (Cao L, 2018, 33(03):30-36; Jin YL, 2022, 246:123407; Tang L, 2014, 1268-1273). For example, Badescu et al. employed an electrical load for an ORC power system in order to investigate the effects of the system flow rate and load on the system efficiency (Badescu V, 2017, 139:206-21). The results revealed that the optimal mass flow rate that maximizes the net output power varies with the value of external load. Hou et al investigated the effects of the load resistance on the ORC system efficiency and output performance by building a free-piston expander-linear generator test bed (Hou XC, 2018, 212:1252-61). The results show that the efficiency of the free-piston expander gradually decreases with the increase of external load resistance, but the system peak voltage output increases when the external load resistance and the inlet pressure increase together. Cao et al employed a lamp array to explore the effects of load resistance on the system performance and found that an optimal matching relationship exists between rotational speed, load resistance and ORC thermal capacity (Cao S, 2019, 133 284-294). Zhao et al. designed a free-piston expander-linear generator test system in order to verify the effect of load resistance on the system performance (Zhao TL, 2020, 41(07): 237-243). The results show that the output power increases with the increase of load resistance and inlet pressure.

The impacts of load resistance on ORC power systems under various operating conditions remain to be explored. Based on an ORC test-rig, this study tested the effects of load resistance value from 50 Ω to 200 Ω on the system shaft power output and thermal efficiency when the temperature of the heat source ranges from 75 ℃ to 95 ℃ by using two types of organic working fluids respectively, R245fa and R141b. The reasons for the effect of load resistance on the system performance were further analysed byconsidering the factors such as expander inlet pressure, inlet temperature, rotational speed, torque and system flow rate.

2. RESEARCH TECHNIQUE

2.1. Experimental test rig

In this experiment, a small-scale ORC power system test-rig was built based on the research objectives, and its structure is shown in Figure. 2. The core of this test-rig consists of three major parts: the heat source part, the cold source part, and the ORC part. The information on the main components of each part has been listed in detail in Table 1. In ORC part, the expander generates electricity by driving a DC generator. A DC electronic load is connected to the generator, which can control the load resistance in the experiments and record the voltage and current.

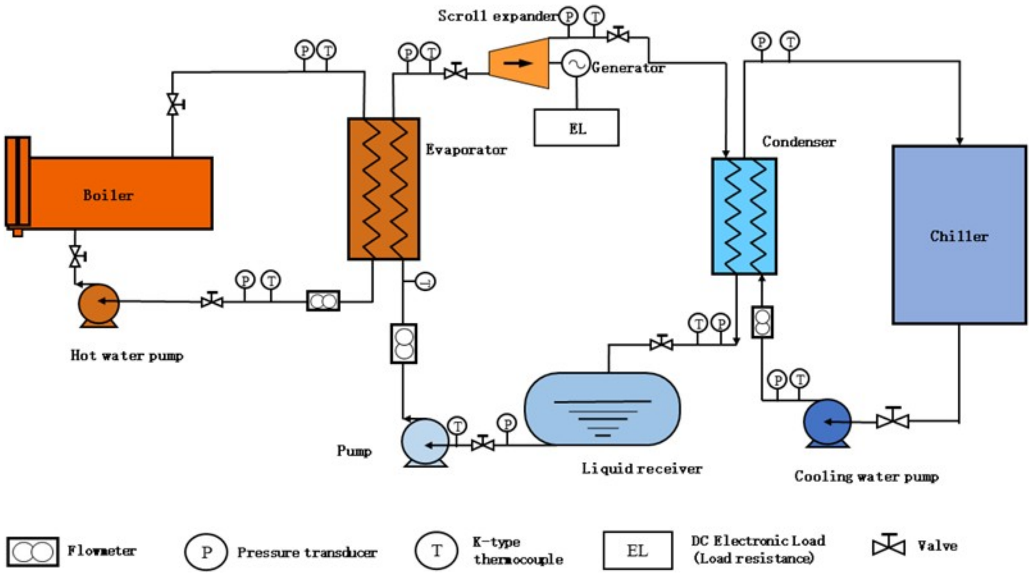

Figure 2: The ORC experimental platform schematic

To collect experimental data, different sensors were installed, including temperature, pressure, torque, rotational speed sensors, and etc. The parameters of these sensors are shown in Table 2, and their installation locations are marked in Figure 2. In addition, to minimize the potential impact of ambient temperature on the results, the 1.5-cm-thick thermal insulation was added to all equipment and pipe segments (except the diaphragm mass pump).

Table 1: Component parameters of the ORC test-rig

Components	Key information
Scroll expander	Manufacturer: Aotecar Type: ATC-085-C3
Evaporator/ Condenser	Plate heat exchanger Operation pressure: 3 Mpa Heat transfer area: 3.63 m^2
Pump	*Maximum flow rate 460L/h* *Pressure: 0.85 Mpa* *Power: 1.5 kW*
Electric boiler	*Heating capacity: 24 kW*
Chiller	*Cooling capacity: 6HP *2*
Generator	*Design output power: 800 W*

Table 2: The measuring instrument and external load of the ORC test-rig

Type	Range	Accuracy	Measuring point
K-thermocouple	0-1370 ℃	±0.5%	12
Pressure transducer	0-4 Mpa	0.25%	12
Turbine flowmeter	1.5-15 m^3/h	1.0%	1
Turbine flowmeter	1.5-15 m^3/h	1.0%	1
Ultrasonic flowmeter	>0.05 m^3/h	2.0%	1
Torque meter	0-20 N·m/0-10000r/min	0.3%	1
Electric power meter	0.5V-600V/0.01A-40A	0.1%	1
Generator	800W/48V	--	1
Resistive load	500V/100A/1200W	±5%	1

2.2. Exprimental scheme

In the experiment, two organic working fluid, five different heat source temperatures and four load resistances were set up. The organic working fluids are R141b and R245fa. The heat source temperatures are 75 ℃, 80 ℃, 85 ℃, 90 ℃, 95 ℃. The load resistances are 50 Ω, 100 Ω, 150 Ω, and 200 Ω. In total, there are 40 experimental cases. Each case was given sufficient time, easuring 30 minutes after the system data were stabilized, and the data of the last 10 minutes were taken for results analysis.

3. RESULT

Two indicators are selected to show the ORC power system performance: shaft output power and thermal efficiency, as shown in Figure 3 and Figure 4. For analysing the effects of load resistance, the operating parameters of the scroll expander, evaporator, and condenser are also presented in Figure 5-Figure 7.

Figure 3 presents the shaft output power under the different operating conditions. Results demonstrate that the load resistance cansignificantly affect the shaft power for all heat source temperatures and working fluids in the experiment, and an optimal load resistance may exist for maximizing the shaft power. For working fluid R245fa, the optimal load changes from around 100 Ω to 200 Ω when the heat source temperature reduces from 95 ℃ to 75 ℃. Under the heat source of 75 ℃, the shaft output power is more sensitive to the variation of load resistance, which increases by around 25% when the load resistance increases from 50 Ω to 200 Ω. For working fluid R141b, the optimal load resistances are 200 Ω for all heat source temperatures. Under the heat source of 95 ℃, the shaft output power is more sensitive to the variation of load resistance, which increases by around 50% when the load resistance increases from 50 Ω to 150 Ω.

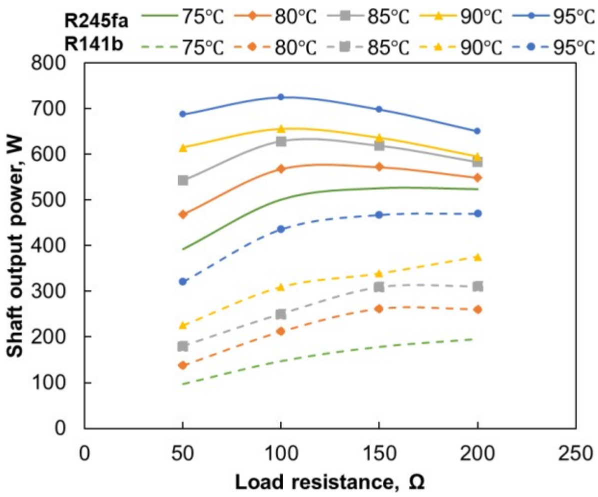

Figure 3: Variation of average output shaft work at different temperatures, working fluid, and load resistances in the experiments

Figure 4 presents the system thermal efficiency under experimental conditions. The tendency of the system thermal efficiency is similar as the tendency of the shaft output power, but the variation caused by the change of the load resistances is more remarkable. For example, by using R245fa and 95 ℃, the ORC system thermal efficiency reaches around 2.3% at 100 Ω, and reduces to around1.9% at 200 Ω. Also, the optimal load resistance to reach the maximum thermal efficiency is different from that to reach the maximum shaft output power. For example, by using R141b and heat source temperature 80 ℃, the shaft output power reaches the maximum value (262W) at 150 Ω, but the thermal efficiency reaches the maximum value (0.8%) at 200 Ω. The results of Figure 3 and Figure 4 remark that the ORC power system must match the heat source, working fluid, and load resistance to achieve the optimal performance.

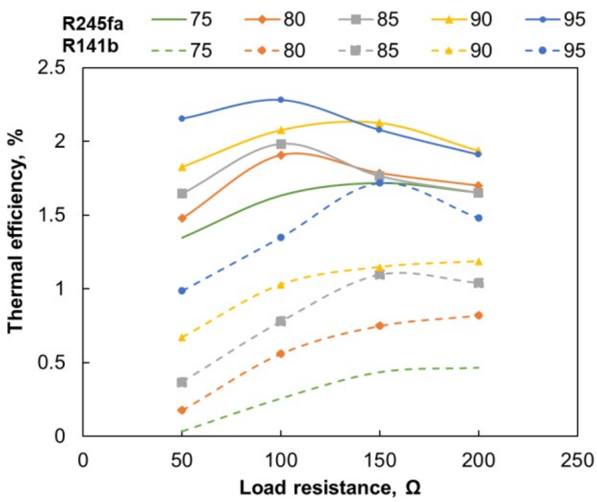

Figure 4: Variation of system thermal efficiency at different temperatures and load resistance in the experiments

Figure 5 presents the variations of the inlet/outlet temperature difference and pressure difference of the scroll expander (i.e., the evaporating pressure and condensing pressure difference) under the experimental conditions. The results show that for R245fa and R141b, a lower load resistance leads to a higher inlet/ outlet difference of temperature and pressure. For example, with the heat source temperature 95℃ and R245fa, the inlet/outlet pressure difference is 0.65 Mpa at 50 Ω, but is only 0.44 Mpa at 200 Ω. A larger temperature and pressure difference means that larger energy is consumed by the scroll expander.

The explanation of the variation of the inlet/outlet temperature and pressure difference caused by the load resistance is shown in Figure 6 which presents the scroll expander rotation and torque. A lower load resistance leads to a higher current in the electrical circuit, which means the generator requires a higher torque to drive and reduces the rotation speed of the scroll expander in turn to reach a balance. For example, for R245fa cases, the rotation speed and torque are around 1550~1735rpm and 3.2~3.6 N·m under a 200 Ω load resistance, but the rotation speed reduces to around 731~990 rpm and torque increases to around 5.1~6.6 N·m undera 50 Ω load resistance. This effect is also explained in reference (Wu LJ, 2021, 49 (12): 1778-1788).

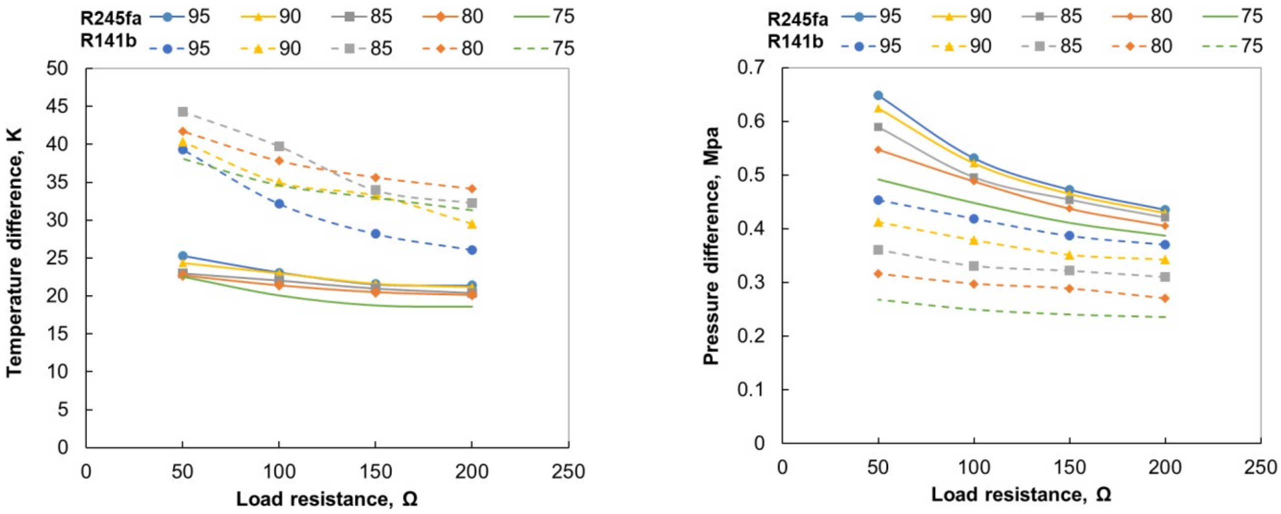

(a)Temperature difference (b) Pressure difference

Figure 5: Variation of inlet/outlet temperature and pressure difference of the scroll expander in the experiments

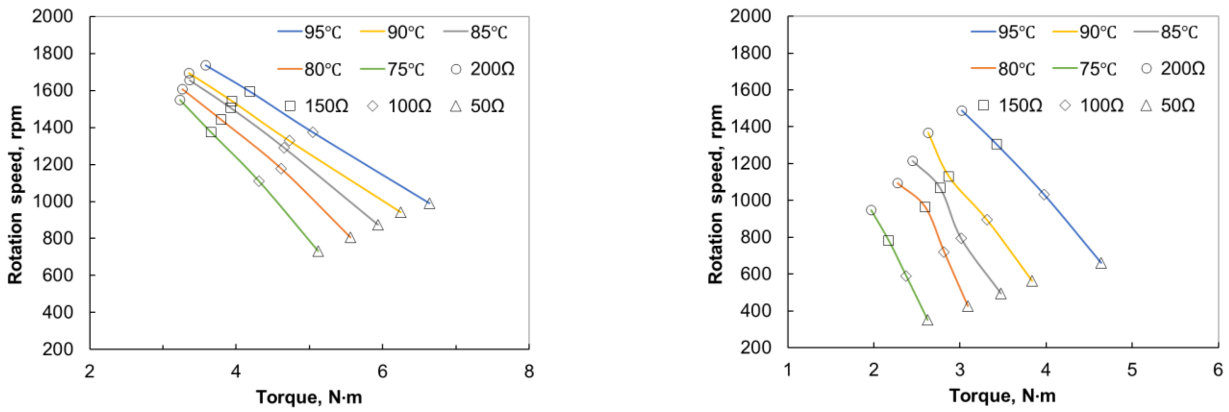

(a) R245fa (b) R141b

Figure 6: Variation of the expander rotation speed and torque in the experiments

Figure 7 presents the flow rate and heat transfer of the evaporator in the experiments with the heat source temperature 95℃ and R245fa (the highest power output and thermal efficiency). The results show that the variation of the load resistance changes the mass flow rate and thus the heat transfer rate. The average flow rate increases from 0.26 m^3/h at 50 Ω to 0.27 m^3/h at 200 Ω. The average heat transfer rate increases from 26.3 kW at 50 Ω to 27.3 kW at 200 Ω. The change of mass flow rate and the heat transfer are caused by the change of the expander rotation speed, which is also illustrated by the reference (Jin YL, 2022, 246:123407).

From the results, the load resistance firstly affects the operation of the generator and scroll ex-pander in the ORC power system, thereby influencing heat transfer, and ultimately affecting the performance of the entire system. When the load resistance changes,the voltage and current on it will change, leading the generator’s rotation speed and torque to reach a new balance. Due to their direct connection, the rotation speed and torque of the scroll expander vary with those of the generator. In the ORC power system, the scroll expander can be regarded as a throttling device. A change of the rotation speed and torque of the scroll expander means a change in the throttling process, which affects the flow rate and pressure difference between its inlet and out-let. Furthermore, these pressure differences and flow rate variations affect the heat transfer process in the evaporator and condenser. Since the heattransfer process and throttling process also can be affected by the heat source temperature and the type of working fluid, the whole system performance, i.e., the shaft output power and thermal efficiency, exhibits different optimal values under the combined conditions.

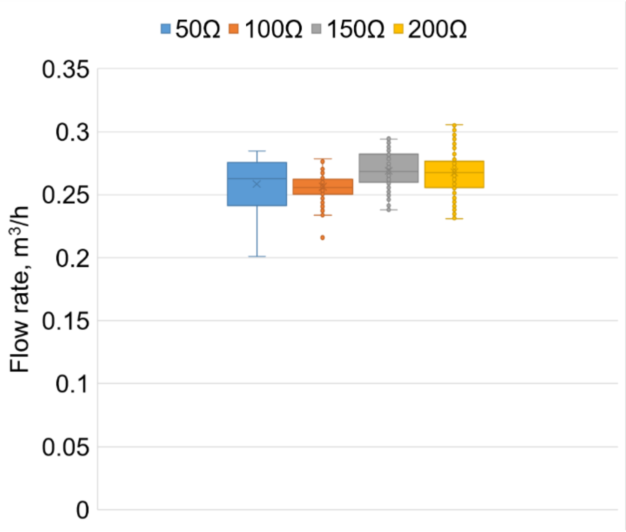

(a) Flow rate

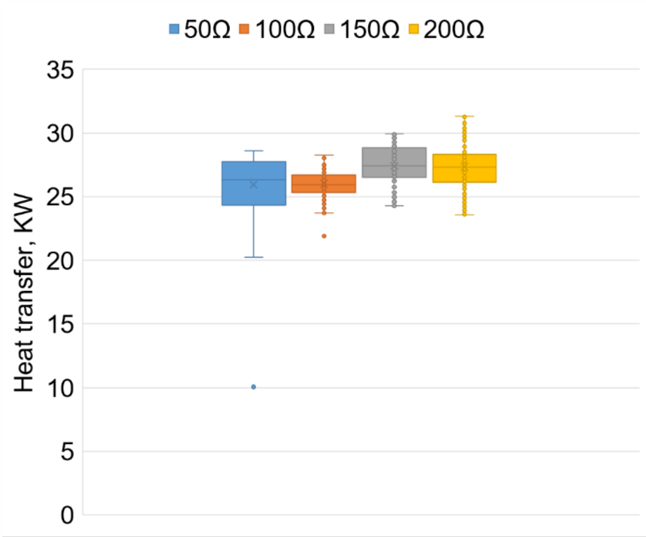

(b) Heat transfer

Figure 7: Variation of flow rate and evaporator heat transfer for case with R245fa and heat source temperature 95℃

4. CONCLUSION

The effects of load resistance variation on the ORC power system performance at different heat source temperatures and organic working fluid are experimentally investigated. Based on a small-scale ORC system test rig, the effects of four different load resistances on the output performance are clarified with five heat source temperatures and two working fluid R245fa/R141b. The results of the study show that:

1.Optimizing the performance to achieve maximum output work or thermal efficiency of an ORC power system requires that the working fluid, heat source temperature and load resistance are matched. For a given heat source temperature and working fluid, the optimum value of load resistance exists for the ORC system to maximize the output power or thermal efficiency, and this value varies with the heat source temperature and working fluid. For example, with R245fa, the optimal load resistance to achieve the maximumshaft output power changes from 100 Ω to 200 Ω when the heat source temperature reduces from 95 ℃ to 75 ℃. With R141b, the optimal load resistance to achieve the maximum shaft output power is fixed around 200 Ω.

2.The load resistance affects the operating conditions of the scroll expander, and further affects the whole ORC power system. The variation of the load resistance changes the rotation speed and torque required by generator and thus the scroll expander, which further changes the inlet/outlet temperature and pressure of the scroll expander. The rotation speed also changes the flow rate of the system and thus the heat transfer in the evaporator. For example, in R245fa cases, the rotation speed and torque are around 1550~1735 rpm and 3.2~3.6 N·m under a 200 Ω load resistance, but the rotation speed reduces to around 731~990 rpm and torque increases to around 5.1~6.6 N·m under a 50 Ω load resistance.

5. REFERENCES

Badescu V, Aboaltabooq MHK, Pop H, Apostol V, et al. 2017. Design and operational procedures for ORC-based systems coupledwith internal combustion engines driving electrical generators at full and partial load [J]. Energy Convers Manag, 139:206-21.

Cao J, Zheng L, Zheng Z, Peng J, Hu M, Wang Q, Leung M K H. 2023. Recent progress in organic Rankine cycle targeting utilisation of ultra-low-temperature heat towards carbon neutrality[J]. Applied Thermal Engineering, 231(September 2022): 120903.

Cao L, Zhang M, Liu XL. 2018. Dynamic Operating Characteristics of Organic Rankine Cycleunder Unsteady Heat Source [J]. Journal of Engineering for Thermal Energy and Power, 33(03):30-36.

Cao S ,Xu J ,Miao Z , et al. 2019. Steady and transient operation of an organic Rankine cycle power system [J]. Renewable Energy,133 284-294.

Hou XC, Zhang HG, Xu YH, Yu F, et al. 2018. External load resistance effect on the free piston expander-linear generator for organic Rankine cycle waste heat recovery system [J]. Appl Energy, 212:1252-61.

Hu S, Yang Z, Li J, Duan Y. 2021. A review of multi-objective optimization in organic rankine cycle (ORC) system design[J]. Energies, 14:6492.

Jin YL, Gao NP, Zhu T. 2022. Effect of resistive load characteristics on the performance of Organic Rankine cycle (ORC).

Energy,246:123407.

MA X L, WANG C, SHI W Q, et al. 2023. Numerical analysis and experimental investigation of the evaporator PPTD in ORC system[J] .Journal of Zhengzhou university (engineering science) , 44(1) :65-69.

Nematollahi, O; Abadi, G B; Kim, D Y; Kim, K C. 2018. Experimental study of the effect of brazed compact metal-foam evaporator in an organic Rankine cycle performance: Toward a compact ORC. Energy Conversion and Management, 173(), 37–45.

SHI L, ZHAO YL, PENG B. 2024. Based on the study of variable operating conditions and experimental verification of a small-scaleORC with a scroll expander[J]. Thermal Power Generation, 53(1): 115-123.

Tang L, Wang YP, Yang P, et al. 2014. Experimental study of optimal load characteristics of low temperature heat organic Ranine cycle power generation[J]. Journal of Shanghai Jiao Tong University, 48(09):1268-1273.

Wu LJ, Liang XY, Wei ZZ. 2021. Heat Transfer Characteristics Corrugated Plate Condenser in Organic Rankine Cycle for Blast Furnace Slag Flushing Water [J]. Journal of Tongji University (Natural Science), 49 (12): 1778-1788.

Yu HB. 2022. Investigations on Internal Generator Exhaust Cooling for Hermetic Expanders in Organic Rankine Cycles [D]. Beijing University of Technology.

Yu ZT, Feng CY, Bian FY, Wang DH. 2022. Investigation and optimization of a two-stage cascade ORC system for medium and low-grade waste heat recovery using liquefied natural gas cold energy [J]. International Journal of Refrigeration, 135: 97-112.

Zhao TL, Zhang HG, Hou XC. 2020. External Load Resistance Effect on Free Piston Expander-Linear Generator for Organic Rankine Cycle Waste Heat Recovery System [J]. Acta Energiae Solaris Sinica, 41 (07): 237-243.

#294: Experimental investigation on the photovoltaic-thermal comprehensive performance of swimming pool heating systems

Xinzhu CHEN[1], Chenglong LUO[2], Wenxin LI[3], Xiaoxiao SU[4], Qi LUO[5], Yanshun YU[6], Hua ZHANG[7], RuiliPENG[8]

[1] Nanjing University of Science and Technology, Nanjing, xzchen@njust.deu.cn
[2] Nanjing University of Science and Technology, Nanjing, xxlong@ustc.edu
[3] Xiamen University Malaysia, Kuala Lumpur, EGE2109312@xmu.edu.my
[4] Nanjing University of Science and Technology, Nanjing, xzchen@njust.deu.cn
[5] Ningbo University of Technology, Ningbo, ranyanhk@163.com
[6] Nanjing University of Science and Technology, Nanjing, yshunyu@njust.edu.cn
[7] Nanjing University of Science and Technology, Nanjing, zhua@njust.edu.cn
[8] Nanjing University of Science and Technology, Nanjing, 1403625742@qq.com

Abstract: Swimming pool systems typically consume a large amount of energy in terms of hot water supply and electricity supply. To prolong the swimming season and meet the energy demands of swimming pool facilities, this study establishes an outdoor PV/T simulation swimming pool heating system to investigate the photovoltaic-thermal performance and its impact on the thermal characteristics of the pool. The results show that the system exhibits good photovoltaic performance, with the all-day average PV efficiency of the two PV/T modules being approximately 19.5%. Additionally, the PV/T modules significantly heat the water, with theaverage temperature increase between the inlet and outlet being about 1.5°C and the average thermal efficiency of the modules reaching 20.63%. Under the heating effect of the PV/T modules, the pool water tank shows a significant thermal gain, with the all-day temperature of the tank increasing by around 10°C. The system's effective all-day power generation is 5.60 kWh, and the tank's cumulative heat gain is 2.00×10^4 kJ, with an average comprehensive efficiency η_c of 73.46%. demonstrating good economic and environmental benefits, thus providing an important reference for further optimization and promotion of PV/T swimming pool heating systems.

Keywords: Solar Energy; Outdoor Swimming Pool; PV/T System; Heat Losses

1. INTRODUCTION

In recent years, with the advancement of "dual carbon" goals, clean renewable energy has become a critical component of the energy market (Zhao et al., 2024). Among these, solar energy is distinguished as one of the cleanest, most efficient, inexhaustible, and economically viable options (Izam et al., 2022). However, traditional photovoltaic or solar thermal technologies each exhibit inherent limitations. Consequently, photovoltaic/thermal (PV/T) hybrid technology has been proposed (Sultan and Efzan, 2018). PV/T technology integrates photovoltaic and thermal conversion processes, enabling simultaneous electricity and heat generation, thereby significantly enhancing overall solar energy utilization efficiency (Hasan and Sumathy, 2010). This technology holds substantial market potential and is acknowledged as a pivotal developmental direction in the solar energy sector (Jia et al., 2019).

PV/T technology is typically classified into three main types based on its structure and operational principles: air-based (Choi et al., 2020), liquid-based (Daghigh et al., 2011), and hybrid (Daghigh and Khaledian, 2017), which integrates both air and liquid cooling methods. Numerous researchers have investigated various aspects of PV/T technology and its applications using innovative methodologies. Luo et al. (Luo et al., 2019) explored a PV-PCM-Trombe system that integrates PV-Trombe walls with phase change materials, demonstrating effective summer cooling of photovoltaic cells. Ji et al. (Ji et al., 2011) proposed a novel integrated solar collector for buildings capable of passive space and water heating modes, validating its dynamic numerical model through experimental data. Cai et al. (Cai et al., 2017) introduced a novel PV/T-air dual-source heat pump water heater (PV/T-AHPWH), combining parallel PV/T evaporators with air-source evaporators to efficiently recover energy, maintaining high efficiency even under low temperature and solar radiation conditions. These studies primarily focus on evaluating the thermal and electrical performance of different PV/T components and assessing the technology's suitability in various scenarios, such as building-integrated photovoltaic/thermal (BIPVT)systems and PV/T heat pump systems. PV/T technology has undergone preliminary validation across multiple domains and is gradually being integrated into practical applications.

Despite PV/T technology has been extensively studied (Chow, 2010), its application in swimming pool facilities lacks comprehensive analysis. Indoor and outdoor swimming pools typically consume significant energy for water heating, space heating, ventilation, andpump operation, ranging from hundreds to thousands of $kW{\cdot}h/m^2$ annually, depending on factors such as pool type, volume, area, operational hours, location, and climate conditions (Li et al., 2020; Trianti-Stourna et al., 1998). In the realm of liquid-based PV/T technology, addressing diverse thermal requirements requires a careful balance between meeting heating needs and optimizing the operational temperature of photovoltaic components. Specifically, for swimming pools (Sandnes and Rekstad, 2002; Tripanagnostopoulos et al., 2002) (typically maintained between 26°C and 28°C), low-temperature liquid-based PV/T heating technology emerges as an efficient energy-saving option. It effectively meets hot water demands while preserving photovoltaic electricity generation performance, offering distinct advantages in such specific applications.

Continuous and efficient energy supply is crucial for swimming pool systems, necessitating reliable models to describe their thermal requirements. Heat loss from swimming pools primarily includes convective heat loss, evaporative heat loss, and radiative heat loss (ASHRAE and air conditioning, 1995). Accurate modeling is essential for precise calculation of pool heat, prompting numerous scholars to develop models simulating energy and mass balances between swimming pools and their surroundings to predict pool temperatures under varying environmental conditions and validate their accuracy (Bai et al., 2004). Considering evaporation as a significant component of heat loss in outdoor swimming pools, Ruiz et al. (Ruiz and Martinez, 2010) compared different evaporation rate equation models and made model adjustments. However, there remains a lack of analysis of the electricity demand and supply dynamics in swimming pool facilities. Buonomano et al. (Buonomano et al., 2015) utilized TRNSYS software to analyze differences in indoor/outdoor pool thermal characteristics and related issues, conducting comprehensive dynamic analysis of thermal and electrical output and efficiency. Brottier et al. (Brottier and Bennacer, 2018) installed a 300 square meter PV/T collector in a 3000 m^3 outdoor swimming pool, meeting a daily demand of 8000 liters of hot water. From mid-May to mid-September, the thermal energy output reached 55 MWh, with an annual photovoltaic output of 52 MWh, surpassing expectations set by TRNSYS studies. The University Sport Centre (USC) of Bari [21] employed a PV/T S-CHP system covering 4000 m^2 of installation area, meeting 38.2% of the indoor swimming pool system's electricity demand, 23.7% of space heating demand, and 53.8% of swimming pool and hot water heating demand, showcasing significant carbon reduction potential.

These studies demonstrate the effectiveness of PV/T technology in various application scenarios and its immense potential in meeting both thermal and electrical demands. With the continuous development and maturation of PV/T technology, further research into its application in swimming pool heating systems is of paramount importance. To delve deeper into innovative applications of PV/T systems for swimming pool heating, this study conducts relevant experiments to investigate the comprehensive optoelectronic and thermal performance of the system, as well as the thermal characteristics of the pool. It analyzes the performance of PV/T modules under different conditions, evaluates the energy losses and gains of outdoor pools under environmental influences, and assesses the system's electrical requirements. The aim is to comprehensively evaluate the optoelectronic and thermal performance of PV/T swimming pool heating systems under varying conditions and provide a thorough analysis of their impact on pool thermal characteristics.

2. EXPERIMENTAL SYSTEM

2.1. PV/T Module Structure

The structure of the PV/T module is depicted in Figure 1, with dimensions of 2256mm×1133 mm and comprising 144 photovoltaic cells arranged in a 6×24 configuration, providing an effective area of 2.38 m^2. Detailed parameters are specified in Table 1. The water-cooling component consists of 6 thin copper tubes with an inner diameter of 9 mm and 2 manifold tubes of 22 mm diameter, insulated with 20 mm polystyrene material on the backside. Standard condition performance parameters for the PV/T module are outlined in Table 1.

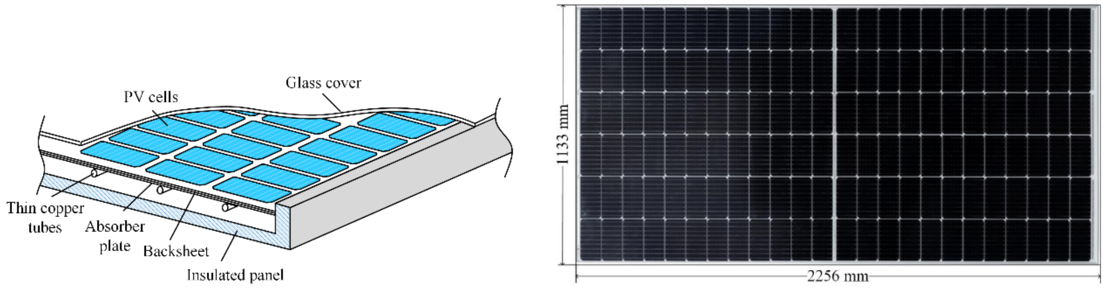

(a) (b)

Figure 1: Structure of the PV/T module (a) Schematic diagram (b) Physical diagram

2.2. Experimental setup

In order to investigate and analyze the photovoltaic -thermal performance and pool water temperature characteristics of a swimming pool heating system utilizing PV/T technology, an outdoor simulated PV/T heating system for the pool was constructed. The experimental platform is depicted in Figure 2. The simulated pool tank dimensions are 1100 mm × 800 mm × 600 mm, constructed from fiberglass reinforced plastic (FRP) with an additional 50 mm insulation layer to effectively reduce heat loss. The water circulation system setup is illustrated in Figure 4, incorporating a circulation pump, flow meter, and valves for regulating, recording water flow rates, and altering water circuit connections. The pump is adjustable with a flow range of 0-25 L/min and a maximum head of 15 m.

The experimental platform not only comprises functional structural components but also includes an experimental testing and data acquisition system. The experiment primarily measures temperatures, total solar irradiance, and the output voltage and current on the DC side of the PV/T modules. Temperature measurements utilize copper-constantan thermocouples at various points in the system, with a measurement accuracy of ±0.5°C. Each of the two PV/T modules is equipped with 12 thermocouples uniformly distributed along the vertical direction of the solar cells, and 5 thermocouples along the vertical direction of the thin copper tubes, with 1 measurement point at each end of the manifold tubes. Additionally, 6 temperature measurement points are placed along the water circuit pipes for measuring modules and swimming pool tank inlet and outlet water temperatures, while the pool temperature isdetermined by the average of 5 temperature points, as depicted in Figure 4. Outdoor air temperature measurements are also conducted. Solar irradiance is measured using a pyranometer installed on the same plane as the PV/T modules to capture the solar irradiance received by the module plane. The schematic diagram of the experimental system is shown in Figure 4. For current measurements, current sensors convert the output current on the PV modules' DC side into a voltage signal measurable by the data acquisition unit, while voltage is directly measured by the data acquisition unit. All data signals (including voltage and temperature) are collected and recorded using an Agilent 34970A data acquisition system. Parameters of each experimental measurement instrument are detailed in Table 2.

The experiments were conducted in Nanjing from early May to early June, corresponding to spring and early summer in Nanjing, with daytime temperatures reaching up to approximately 35°C. Conducting experiments during this period allow for a realistic reflection of the opto-thermal performance of PV/T pool heating systems during the spring-to-summer transition and early summerperiods.

Table 1: Standard condition performance parameters of PV/T module

Parameter	Value
Maximum Output Power	540 W
Photovoltaic Efficiency	21.12%
Rated Voltage	41.76 V
Rated Current	12.93 A
Open Circuit Voltage	49.70 V
Short Circuit Current	13.72 A
Heating Capacity	1397 W
Heat Exchange Area	2.54 m^2
Heat Exchange Volume	1.1 L

Table 2: Parameters of each measuring instrument.

Measurement	Parameter	Values
EL Tester	Model	PROVA 210
Micro-grid-connected inverter	Model	EZ1-M
	Maximum input power	800W
Current sensor	Model	SIN-DZI-20A
Pyranometer	Model	TBQ-2
	Measurement Range	0-2000 W/m^2
Flow meter	Model	FLC400
	Measurement Range	0.6~6m^3/h
Water Pump	Model	WS2415
	Maximum Flow Rate	25L/min
Data acquisition device	Model	Agilent 34970A
Copper-constantan thermocouples	Measurement error	±0.5° C

Figure 2: Experimental testing platform

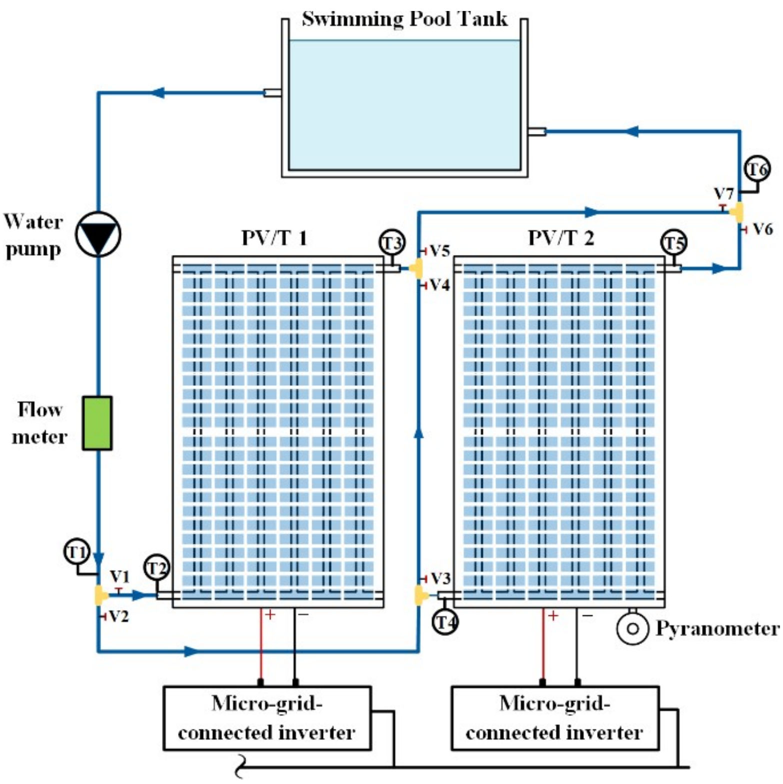

Figure 3: Schematic diagram of swimming pool tank measurement points

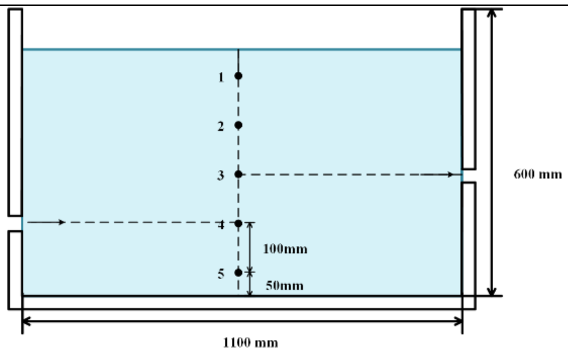

Figure 4: Schematic diagram of experimental system

2.3. Equations

Equation 9: Photovoltaic (PV) efficiency.

$$\eta_{PV} = \frac{P_m}{A_{PV} \cdot G} = \frac{I_m \cdot V_m}{A_{PV} \cdot G}$$

Where:

- P_m = maximum power output of the PV module (W)
- V_m = maximum voltage (V)
- I_m = maximum current (A)
- A_{PV} = surface area of the PV cells (m²)
- G = the solar irradiance on the module surface (W/m²)

Equation 2: Fill factor FF (ASHRAE and air conditioning).

$$FF = \frac{I_m \cdot V_m}{I_{sc} \cdot V_{oc}}$$

Where:

- V_{oc} = open-circuit voltage (V)
- I_{sc} = short-circuit current (A)

Equation 3: Photothermal efficiency.

$$\eta_{th} = \frac{\dot{Q}_m}{A_c \cdot G} = \frac{c_w \cdot \dot{m} \cdot (T_{out} - T_{in})}{A_c \cdot G}$$

Where:

- $\dot{Q}_m$ = heat gain (kJ)
- Ac = collector area (m²)
- cw = specific heat capacity of water (kJ/(kg·°C))
- $\dot{m}$ = mass flow rate (kg/s)
- Tout = outlet water temperature (°C)
- Tin = inlet water temperature (°C)

Equation 4: The overall thermal efficiency

$$\eta_t = \frac{c_w \cdot M \cdot (T_f - T_i)}{A_c \cdot G \cdot t}$$

Where:

- M = mass of water (kg)
- Tf = final water temperature (°C)
- Ti = initial water temperature (°C)
- t = operation time (s)

Equation 5: The total photovoltaic-thermal (PV/T) system efficiency η_{total}

$$\eta_{total} = \eta_{PV} + \eta_{th}$$

Considering that electrical energy is a higher-grade energy compared to thermal energy, the comprehensive performance evaluation index ηc of the PV/T module is defined as (Zhu et al., 2015):

Equation 6: the comprehensive performance evaluation index η_c

$$\eta_c = \eta_{th} + \frac{\eta_{PV}}{\eta_{power}}$$

Where:

– η_{power} = efficiency of traditional thermal power plants, typically taken as 37.26%.

3. RESULTS AND ANALYSIS

3.1. IV Testing

On May 7, 2024, the experimental system underwent IV testing under the operating condition with a water flow rate of 0.046 kg/s. Figure 5 illustrates the variations in solar irradiance and ambient temperature throughout the experimental day. Intermittent cloud cover led to significant fluctuations in irradiance. The irradiance ranged from 214.02 W/m^2 to 963.85 W/m^2, averaging 617.32 W/m^2. Irradiance commenced at its ascent around 8:00, peaking at 963.85 W/m^2 around noon. There were notable fluctuations in irradiance between 12:30 and 13:30. The mean ambient temperature for the day was 27.07°C, fluctuating between 20.80°C and 31.95°C.

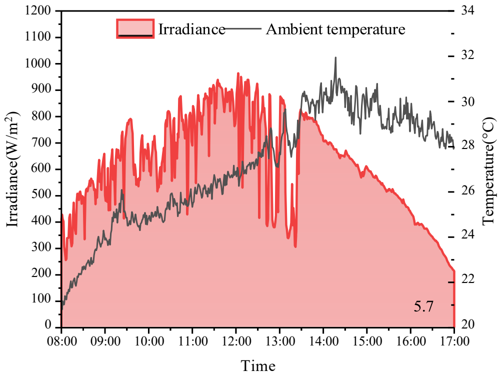

Figure 5: Experimental environmental parameters

Figure 6 shows the variation of maximum temperature, minimum temperature, temperature difference and average temperature of the solar cell of the PV/T module. For PV/T 1, the maximum temperature reaches 61.79°C at 12:00 and the minimum temperatureis 52.04°C, with a temperature difference of 9.75°C. The temperature of PV/T 2 is relatively high, but the maximum temperature difference is smaller compared with that of Module 1, and the average temperature difference for the whole day is 4.61°C. The average temperature of the solar cells of the two modules for the whole day is 48.02°C and 49.88°C, respectively.

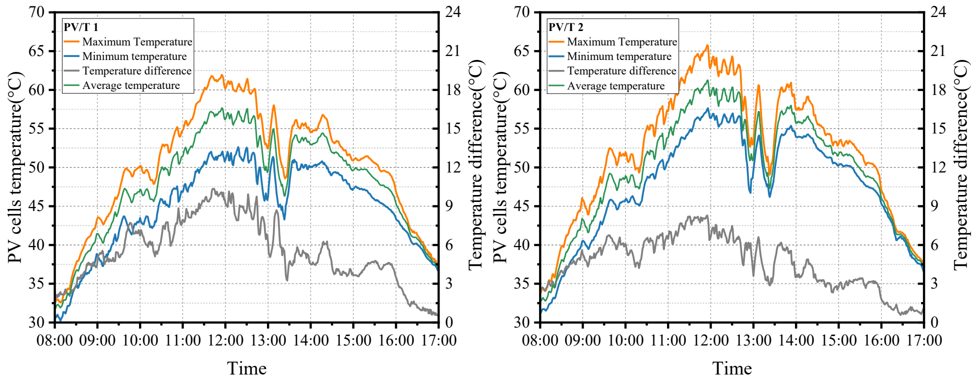

(a) *(b)*

Figure 6: Temperature variations of PV cell maximum temperature, minimum temperature, temperature difference and average temperature (a) PV/T 1 (b) PV/T 2

Under different environmental conditions, the electrical parameters and I-V, P-V curves of PV/T modules are analyzed. From Table3, it is evident that irradiance levels, cell temperatures, and photovoltaic performance parameters vary significantly at different times. Further analysis using the I-V and P-V curves in Figure 7 reveals that increasing irradiance leads to a significant increase in short circuit current and a slight increase in open circuit voltage. However, higher cell temperatures cause a decrease in open circuit voltage and fill factor, while slightly increasing short circuit current, partially offsetting performance improvements.

Table 3: Electrical performance parameters of PV/T modules under different environmental conditions

NO.	Time	G (W/m²)	T_{PV} (°C)	V_{oc} (V)	I_{sc} (A)	P_{max} (W)	FF (%)	η_{PV} (%)
1	8:02	411.73	32.07	45.77	5.24	193.6	80.8	17.69
2	8:38	537.85	37.78	45.32	7.07	251.9	78.5	17.49
3	10:02	600.23	46.86	44.15	8.62	295.4	77.6	21.81
4	10:08	726.51	47.05	44.54	10.21	349.1	76.7	18.67
5	11:02	828.36	52.16	44.00	11.78	408.6	78.7	20.16
6	11:51	894.52	57.17	43.33	12.93	424.7	75.8	18.60
7	12:15	879.47	56.19	43.58	12.89	421.4	75.0	19.36
8	13:57	731.79	53.37	43.89	11.27	374.1	75.5	21.31
9	14:27	652.00	52.55	43.72	9.907	330.9	76.4	21.33
10	15:09	570.34	49.67	44.02	8.357	280.6	76.9	20.72

11	15:45	490.20	47.46	43.98	6.569	223.9	77.5	19.57
12	16:15	393.07	42.82	44.29	4.83	168.2	78.6	18.32

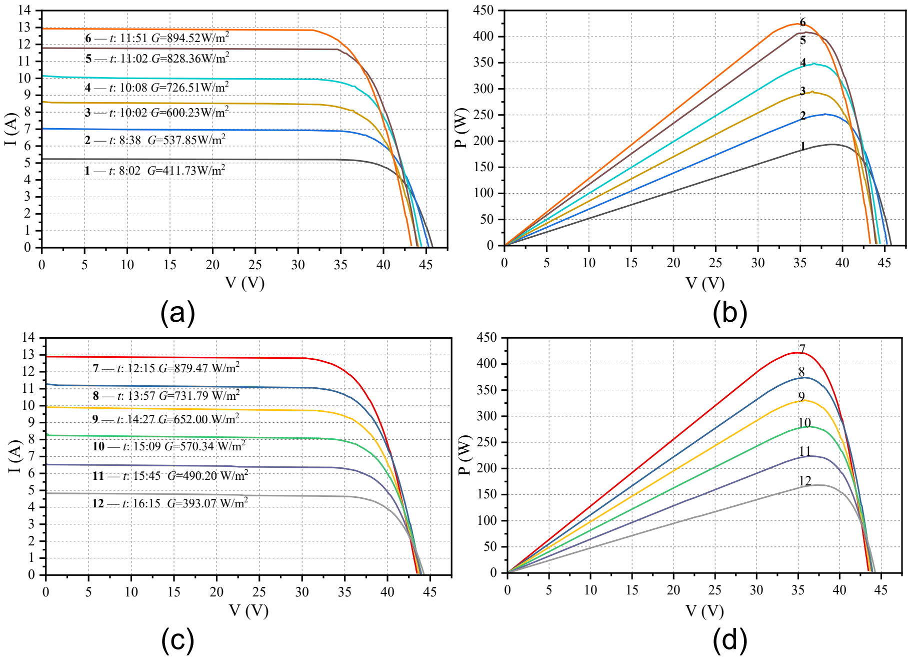

Figure 7: PV/T module under different environmental conditions (a) I-V Curve (Morning) (b) P-V Curve (Morning) (c) I-V Curve (Afternoon) (d) P-V Curve (Afternoon)

3.2. Grid connection operation

3.2.1 Photovoltaic performance

On June 8, 2024, a grid connection operation experiment was conducted. The solar irradiance and ambient temperature variations on the day of the experiment are shown in Figure 8. Irradiance peaked around 12:00 at 909.21 W/m², with an average irradiance of 598.86 W/m² throughout the day. There was significant fluctuation in irradiance between 12:30 and 16:30. The ambient temperature ranged approximately from 20.79°C to 34.48°C, averaging 29.91°C. The system water flow rate was 0.067 kg/s.

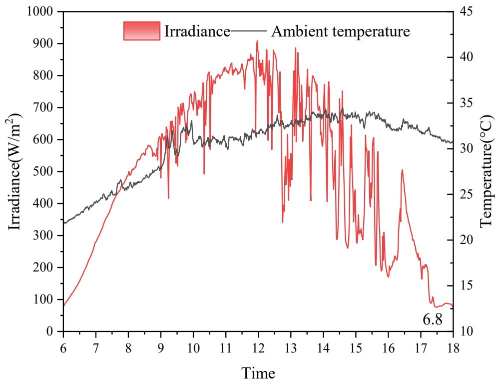

Figure 8: Experimental environmental parameters (June 8th)

Figure 9 shows the photovoltaic performance curves of PV/T modules. The trends in PV performance of both modules are generally consistent. Module 1 exhibits slightly higher power generation than Module 2 from 6:00 to 10:00, with peak power outputs around 10:30 at 394.15 W and 397.25 W, respectively. The photovoltaic conversion efficiency of both modules' peaks around 9:30, measuring 22.23% and 21.45%, respectively. Subsequently, as internal temperatures of the modules increase, efficiency slightly declines, reaching a low point around 12:00 at approximately 18%. The average daily photovoltaic efficiencies for the two modules are 19.45% and 19.52%, with power outputs of 237.31 W and 236.566 W, respectively, and energy outputs of 2.86 kWh and 2.85 kWh. The system's daily energy output totals 5.71 kWh.

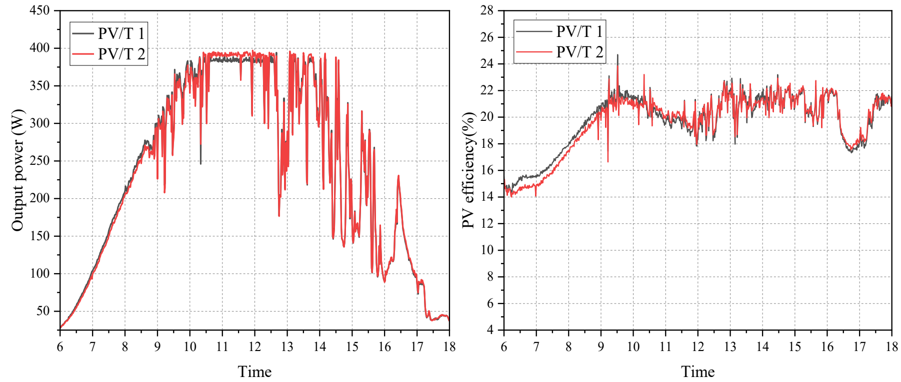

(a) (b)

Figure 9: PV/T module photovoltaic performance curves (a) Output power (b) PV efficiency (June 8th)

3.2.2 Photothermal Performance

In series mode, water first passes through PV/T 1, absorbing some heat before entering PV/T 2. This results in relatively higher temperatures in the cells of module 2. As shown in Figure 10, analyzing the temperature variations at different times and measurement points of the two modules. On PV/T 1, upper measurement points 2, middle points 6 and 7, and lower points 9, 10, and 11 exhibit localized high temperature regions, slightly warmer than other locations. The upper point 2 shows the most significant heat accumulation, reaching a peak temperature of 58.88°C at noon. PV/T module 2 shows high temperature regions at upper points 2, middle points 6, 7, 8, and lower point 12, with temperatures noticeably higher than PV/T 1 at noon, reaching a maximum of 61.37°C.

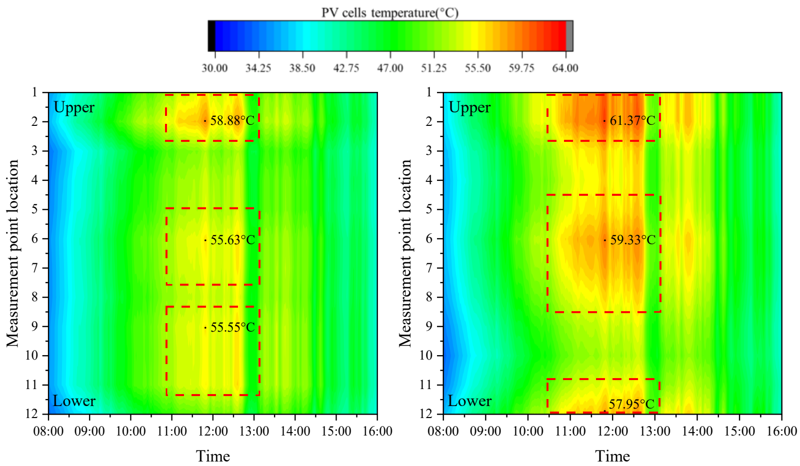

(a) (b)

Figure 10: Temperature distribution of PV cells in PV/T Modules at different time intervals (a) PV/T 1 (b) PV/T 2

Figure 11 illustrates the temperature variation and distribution of PV/T modules over time. Temperatures gradually rise from 6:00, peak around 12:30, and exhibit noticeable fluctuations around 13:00 due to solar radiation, followed by a general decline. Temperatures decrease gradually from top to bottom across all layers, forming distinct temperature gradients with consistent trends.

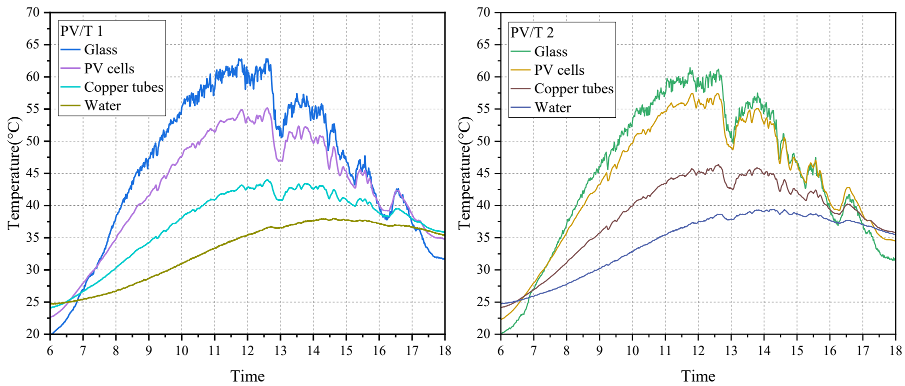

(a) (b)

Figure 11: Temperature variation and distribution of PV/T modules (a) PV/T 1 (b) PV/T 2 (June 8th)

Figure 12(a) shows the water temperature variation curves at the inlet and outlet of PV/T modules. Water passing sequentially through PV/T 1 and PV/T 2 for heating before returning to the tank. Temperature changes are monitored at various points, including the inlet and outlet water temperatures of PV/T 1 and PV/T 2. Starting from 6:00, water temperatures at all points gradually rise, reaching peak values between 14:00 and 14:30, followed by a slight decrease but remaining generally in the high-temperature range. During midday, influenced by solar radiation intensity and ambient temperature, the heating efficiency of the system peaks, resulting in the most significant temperature increase. PV/T modules demonstrate significant heating effects on water, with an average temperature rise of approximately 1.5°C, and an overall increase of about 3°C.

As solar radiation intensifies, the photothermal efficiency of PV/T modules gradually increases. As shown in Figure 12(b), module thermal efficiency reaches around 20% at 8:00, remains stable from 9:00 to 12:00, begins to decline from 12:00 to 16:00 with significant fluctuations influenced by solar radiation, and drops to about 15% around 17:00. The average daily thermal collection efficiencies of the two modules are 19.71% and 21.55% respectively. The total daily heat collection amounts to 1.25×104 kJ and 1.34×104 kJ respectively, with a combined total of 2.59×104 kJ.

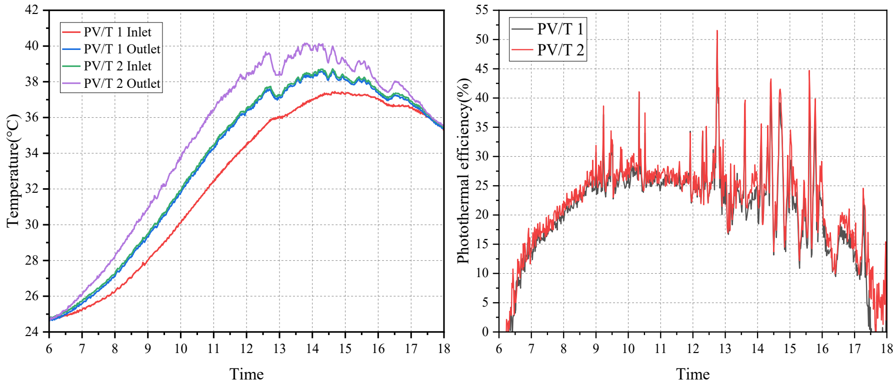

Figure 12: (a) Water temperature variation and (b) photothermal efficiency variation curve of PV/T modules

3.2.3 Thermal characteristics of the swimming pool tank

The swimming pool tank adopts a bottom inlet method, with an initial water temperature of 25.75°C. The temperature variation at different depths is shown in Figure 13. From 6:00 to 14:30, significant stratification of temperatures at different heights is observed. The temperature of 5 measurement points gradually close to the upper and middle temperatures at about 15:30, achieving a relatively uniform temperature distribution in the pool water. The average water temperature is 36.10°C, with a temperature rise of approximately 10°C throughout the day in the tank.

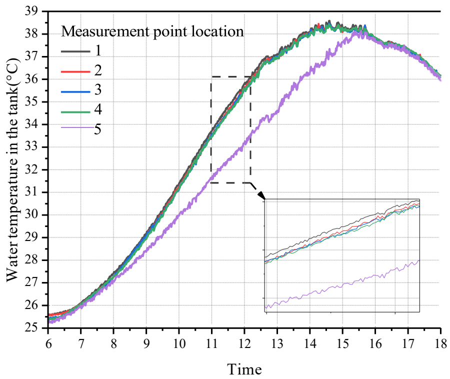

Figure 13: Temperature distribution and variation trends in the Tank

The heat gain of the open water tank not only depends on the heat transferred by the PV/T module. As shown in Figure 14(a), between 6:00 and 11:00, the heat gain of the water tank exceeds that collected by the PV/T module. Around 11:00, the heat gain of the water tank peaks, exceeding 1200W, and then begins to decrease. The heat collection by the PV/T module peaks around 12:00. As solar radiation intensity decreases and ambient temperature lowers, the heat gain of the water tank decreases significantly, with heat loss gradually increasing. Around 14:30, the heat gain of the water tank drops below zero, with heat dissipation from the tank exceeding the heating supply from the PV/T module. Regarding the overall thermal efficiency of the watertank, as shown in Figure 14(b), the total thermal efficiency increases rapidly in the morning, reaching a peak of about 45% around 7:00. The total thermal efficiency of the water tank decreased after 11:00, reaching zero by 15:00 and declining rapidly thereafter.

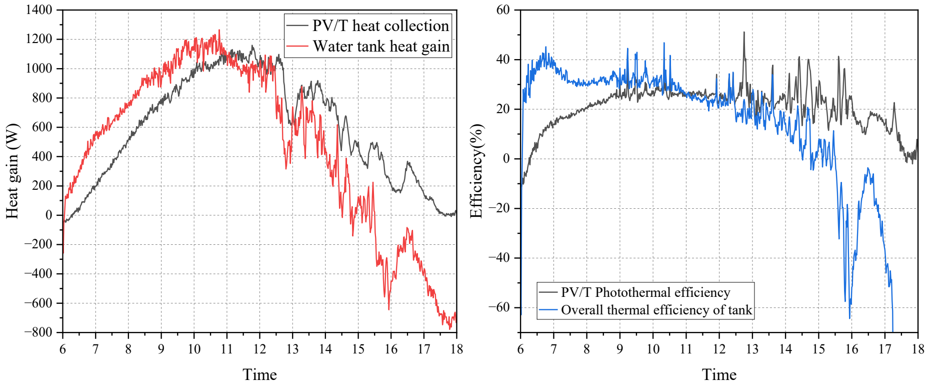

(a) (b)

Figure 14: Trends in water tank overall (a) Heat gain and (b) Thermal efficiency

3.2.4 Comprehensive Performance

As shown in Figure 15, From 10:00 to 14:00, both electricity generation and heat gain of the tank rapidly increase to high values. After 14:00, electricity generation growth slows down, and after 15:00, the heat gain of the tank starts to become negative, indicating significant heat losses in the system. The total electricity generated throughout the day is 5.71 kW·h. Considering the energy consumption of the water pump, which is 0.11 kW·h, the effective electricity generation of the system is 5.60 kW·h. The total heat gain of the swimming pool tank over the day amounts to 20086.97 kJ.

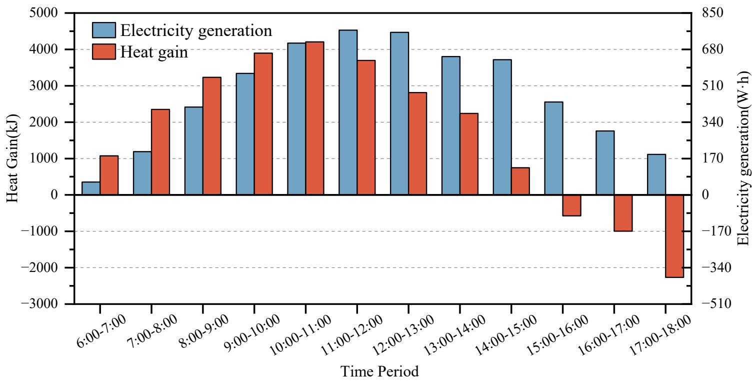

Figure 15: Variations in system electricity generation and heat gain over different time periods

The variation in overall efficiency is closely related to the changes in photovoltaic (PV) efficiency and thermal efficiency. As shown in Figure 16, The periods with higher overall efficiency (9:00-15:00) correspond to times when both PV efficiency and thermal efficiency are elevated. During midday when solar radiation intensity is high, both PV efficiency and thermal efficiency reach peak levels, maximizing overall efficiency. In the morning and evening, when solar radiation intensity is lower, both PV efficiency and thermal efficiency decrease, resulting in lower overall efficiency. The system's overall efficiency ηtotal and ηc average values are 40.38% and 73.46%, respectively.

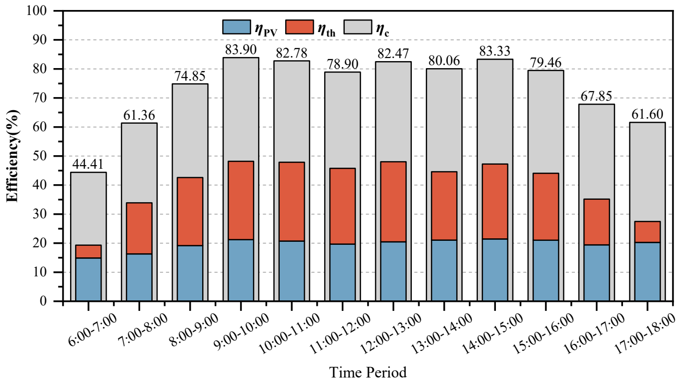

Figure 16: Variations in system overall efficiency ηtotal and ηc over different time periods

4. CONCLUSION

This paper provides an in-depth analysis of the comprehensive performance of the PV/T swimming pool heating system, yielding the following conclusions:

- PV/T 2 shows slightly higher temperatures than PV/T 1, with Module 1 demonstrating higher power generation and photovoltaic conversion efficiency, averaging 19.45% and 19.52% respectively throughout the day.
- The PV/T modules exhibit uneven cell temperature distribution during different time periods.
- The PV/T modules significantly heat water, achieving an average temperature increase of approximately 1.5°C at a water flow rate of 0.067 kg/s, peaking at 2°C during the morning hours.
- Over time, the heating effect on water shows a trend of increasing temperature difference followed by a decrease, with average heat collection efficiencies of 19.71% and 21.55% for the modules respectively.
- Under the heating from the PV/T modules, the swimming pool tank demonstrates notable heat gain effects, increasing the water temperature by approximately 10°C throughout the day.
- Unlike closed systems, the open nature of the swimming pool system results in significant influence from environmental factors. The tank temperature initially rises and then declines with increasing sunlight duration.
- The system achieves excellent comprehensive performance, with a total effective electricity generation of 5.60 kW·h, swimming pool tank accumulates a total heat gain of 2.00×10^4 kJ throughout the day. The system's average comprehensive efficiency η_c is 73.46%.

In summary, the PV/T modules exhibit good photovoltaic and thermal performance under various environmental conditions. The swimming pool tank, serving as a thermal storage and utilization system, shows significant heat gain effects under the heating action of the PV/T modules.

5. REFERENCES

ASHRAE T.E.S., air conditioning A.G., 1995. ASHRAE Handbook of applications, Storage American society of heating ventilation and air conditioning, Atlanta Georgia.

ASHRAE T.E.S.J.A.s.o.h.v., air conditioning A.G., 1995. ASHRAE Handbook of applications.

Bai X., Wu J., Wang R., 2004. Research on Application of Heat Pump Based on Heat Recovery in Dehumidification and Heating of Indoor Swimming Pool, Acta Energiae Solaris Sinica. 25, 838-844.

Brottier L., Bennacer R., Fachhochschule Ostschweiz, Hochschule Technik Rapperswil, Rapperswil, SWITZERLAND, 2018. Field test results of an innovative PV/T collector for an outdoor swimming pool. 12th International Conference on Solar Energy for Buildings and Industry (ISES EuroSun). https://doi.org/10.18086/eurosun2018.02.08.

Buonomano A., De Luca G., Figaj R.D., Vanoli L., 2015. Dynamic simulation and thermo-economic analysis of a PhotoVoltaic/Thermal collector heating system for an indoor–outdoor swimming pool, Energy Convers. Manage. 99, 176-192. https://doi.org/https://doi.org/10.1016/j.enconman.2015.04.022.

Cai J.Y., Ji J., Wang Y.Y., Zhou F., Yu B.D., 2017. A novel PV/T-air dual source heat pump water heater system: Dynamic simulation and performance characterization, Energy Convers. Manage. 148, 635-645. https://doi.org/10.1016/j.enconman.2017.06.036.

Choi H.U., Kim Y.B., Son C.H., Yoon J.I., Choi K.H., 2020. Experimental study on the performance of heat pump water heating system coupled with air type PV/T collector, Applied Thermal Engineering. 178. https://doi.org/10.1016/j.applthermaleng.2020.115427.

Chow T.T., 2010. A review on photovoltaic/thermal hybrid solar technology, Appl. Energy. 87,365-379. https://doi.org/10.1016/j.apenergy.2009.06.037.

Daghigh R., Khaledian Y., 2017. Design and fabrication of a bi-fluid type photovoltaic-thermal collector, Energy. 135, 112-127. https://doi.org/10.1016/j.energy.2017.06.108.

Daghigh R., Ruslan M.H., Sopian K., 2011. Advances in liquid based photovoltaic/thermal (PV/T) collectors, Renewable Sustainable Energy Rev. 15, 4156-4170. https://doi.org/10.1016/j.rser.2011.07.028.

Hasan M.A., Sumathy K., 2010. Photovoltaic thermal module concepts and their performance analysis: A review, Renewable Sustainable Energy Rev. 14, 1845-1859. https://doi.org/10.1016/j.rser.2010.03.011.

Izam N., Itam Z., Sing W.L., Syamsir A., 2022. Sustainable Development Perspectives of Solar Energy Technologies with Focus on Solar Photovoltaic-A Review, Energies. 15. https://doi.org/10.3390/en15082790.

Ji J., Luo C.L., Chow T.T., Sun W., He W., 2011. Modelling and validation of a building-integrated dual-function solar collector, Proceedings of the Institution of Mechanical Engineers Part a-Journal of Power and Energy. 225, 259-269. https://doi.org/10.1177/2041296710394243.

Jia Y.T., Alva G., Fang G.Y., 2019. Development and applications of photovoltaic-thermal systems: A review, Renewable & Sustainable Energy Reviews. 102, 249-265. https://doi.org/10.1016/j.rser.2018.12.030.

Li Y., Nord N., Huang G., Li X., 2020. Swimming pool heating technology: A state-of-the-art review, Build. Simul. 14, 421 - 440.

Lisco F., Bukhari F., Jones L.O., Law A.M., Walls J.M., Ballif C., 2023. ETFE and its Role in the Fabrication of Lightweight c-Si Solar Modules, IEEE J. Photovoltaics. 13, 349-354. https://doi.org/10.1109/jphotov.2023.3242212.

Luo C.L., Zou W., Sun D., Xu L.J., Ji J., Liao M.Y., 2019. Experimental Study of Thermal Effect of Lacquer Coating for PV-Trombe Wall System Combined with Phase Change Material in Summer, Int. J. Photoenergy. 2019. https://doi.org/10.1155/2019/7918782.

Ruiz E., Martinez P.J., 2010. Analysis of an open-air swimming pool solar heating system by using an experimentally validated TRNSYS model, Sol. Energy. 84, 116-123. https://doi.org/10.1016/j.solener.2009.10.015.

Sandnes B., Rekstad J., 2002. A photovoltaic/thermal (PV/T) collector with a polymer absorber plate. Experimental study and analytical model, Sol. Energy. 72, 63-73. https://doi.org/https://doi.org/10.1016/S0038-092X(01)00091-3.

Sultan S.M., Efzan M.N.E., 2018. Review on recent Photovoltaic/Thermal (PV/T) technology advances and applications, Sol. Energy. 173, 939-954. https://doi.org/10.1016/j.solener.2018.08.032.

Trianti-Stourna E., Spyropoulou K., Theofylaktos C., Droutsa K., Balaras C.A., Santamouris M., Asimakopoulos D.N., Lazaropoulou G., Papanikolaou N., 1998. Energy conservation strategies for sports centers: Part A. Sports halls, Energy Build. 27, 109-122. https://doi.org/https://doi.org/10.1016/S0378-7788(97)00040-6.

Tripanagnostopoulos Y., Nousia T., Souliotis M., Yianoulis P., 2002. Hybrid photovoltaic/thermal solar systems, Sol. Energy. 72, 217- 234. https://doi.org/https://doi.org/10.1016/S0038-092X(01)00096-2.

Zhao Y.Y., Li J.H., Tan Y.J., Zhu C.L., Chen Y.J., 2024. Recent progress in device designs and dual-functional photoactive materials for direct solar to electrochemical energy storage, Carbon Neutralization. 3, 32-63. https://doi.org/10.1002/cnl2.100.

Zhu T.-t., Diao Y.-h., Zhao Y.-h., Deng Y.-c., 2015. Experimental study on the thermal performance and pressure drop of a solar air collector based on flat micro-heat pipe arrays, Energy Convers. Manage. 94, 447-457. https://doi.org/https://doi.org/10.1016/j.enconman.2015.01.052.

#295: The Superiority of Low-Complexity Liquid Cooling Construction in Vehicle-Based Supercapacitors' Thermal Management Systems Compared to Air Cooling

Panchun TANG[1], Yuzhou FENG[2], Rong YAN[3], Ze SUN[4]

[1] East China University of Science and Technology, Shanghai 200237, China, 1498573694@qq.com
[2] East China University of Science and Technology, Shanghai 200237, China, 2638425210@qq.com
[3] Shanghai Aowei Technology Development Co., Ltd, Shanghai 201203, China, yr@aowei.com
[4] East China University of Science and Technology, Shanghai 200237, China, zsun@ecust.edu.cn

Abstract: The performance of air cooling and various liquid cooling systems in the thermal management of supercapacitors was investigated in this study. Effective thermal management is crucial for maintaining the performance and safety of supercapacitors, as excessive heat can lead to reduced efficiency, accelerated aging, and potential safety hazards. While air cooling is commonly used due to its simplicity and feasibility of implementation, it has limitations in high-power applications and environments with restricted airflow. In contrast, liquid cooling offers superior thermal conductivity and heat capacity. This research examined the effectiveness of two different liquid cooling structures—straight pipe and U-shaped channels—combined with downstream and counterflow patterns. Numerical simulation results revealed that all liquid cooling models significantly reduced the maximum temperature compared to air cooling: the maximum temperature of counterflow straight pipe channels decreased from 320.0 K to 300.0 K. Among the liquid cooling models, the straight pipe channels with counterflow pattern achieved the lowest temperature, which decreased from 315.0 K to just below 302.0 K; and stabilized the temperature difference around 1.0 K, indicating better temperature uniformity. The study also highlighted that while complex liquid cooling structures can bring marginal improvements, theoverall performance gains were limited relative to the increased complexity. The findings suggested that future designs of liquid cooling plates should balance the complexity with the achieved thermal optimization. This research provided valuable insights into optimizing thermal management solutions for supercapacitors, emphasizing the advantages of liquid cooling and the critical role of channel design in enhancing cooling performance.

Keywords: Supercapacitor, Thermal Management, Air Cooling, Liquid Cooling, Liquid Channel Design

1. INTRODUCTION

The transition to clean energy is essential for sustainable development and mitigating climate change (Demski et al., 2017; Kirat et al., 2024; Shang et al., 2024; Suman, 2021). Among various energy storage technologies, supercapacitors stand out due to their high-power density, long cycle life, and rapid charge/discharge capabilities, making them ideal for applications in electric vehicles, renewable energy systems, and industrial equipment (Gao et al., 2023; J. Zhang et al., 2023). However, effective thermal management is crucial for maintaining the performance and safety of supercapacitors, as excessive heat can lead to reduced efficiency, accelerated aging, and potential safety hazards (Gualous et al., 2009; Khan et al., 2024; Liu et al., 2022; Zhang et al., 2018).

Common thermal management techniques include passive and active cooling methods (Gharehghani et al., 2024). While heat pipes and phase change materials offer high thermal conductivity and efficient heat dissipation, their complexity often outweighs their benefits (Boldoo et al., 2024; Chu et al., 2024; Dubey and Arora, 2024; Luo et al., 2024; Yu et al., 2023). Considering the simplicity of structure and other practical factors, air cooling and liquid cooling are more commonly adopted for managing the thermal loads in supercapacitors (Azarifar et al., 2024; Habibi Khalaj and Halgamuge, 2017; Saha et al., 2024; Xu et al., 2023; G. Zhao et al., 2023).

Air cooling has been widely studied and implemented due to its simplicity and feasibility (K. Chen et al., 2024; Daniels and Prabhakar, 2023; Li et al., 2022; Maiorino et al., 2024; Ye et al., 2023). Various air-cooling structures, such as fin arrays and forced convection systems, have been explored to enhance heat dissipation (Liu et al., 2024; Xu et al., 2024). However, air cooling has limitations in high-power applications and environments with restricted airflow, leading to suboptimal thermal management performance (Habibi Khalaj and Halgamuge, 2017; Ye et al., 2023).

Liquid cooling, on the other hand, offers superior thermal conductivity and heat capacity (Saha et al., 2024; Wu et al., 2024; L. Zhaoet al., 2023). Research in liquid cooling encompasses several aspects, including the selection of cooling fluids and the design of cooling plates (Deng et al., 2018; Xie et al., 2023; F. Zhang et al., 2023; Zhao et al., 2024). The design of the cooling plate is particularly critical, as it directly impacts the efficiency of heat removal (Cao et al., 2019; Jiang et al., 2022; M. Li et al., 2023; R. Li etal., 2023; Ran et al., 2023; Sarvar-Ardeh et al., 2023). Despite the potential benefits, complex cooling plate designs often result in marginal performance improvements while significantly increasing manufacturing costs and system complexity.

Angani et al. proposed a hybrid liquid cooling plate, integrated Zig-Zag plates, for a 72V energy storage system and the results show that this liquid cooling system can offer proper operation conditions, ensuring uniform temperature distribution with 28% performance improvement (Angani et al., 2023). Jiahui Zhu et al. offered a novelty concept called a rib-grooved liquid-cooled plate, including grooves and ribs in the liquid cooling channels (Zhu et al., 2024). By adjusting the arrangement of accessories, the flows can be equalized with longitudinal swirl flows. However, the maximum temperature decreased by 0.74 K only, and the standard deviation of the surface temperature reduced by merely 0.18 K. In order to improve the uniformity of temperature distribution, Lei Sheng et al. novelly developed outlets and inlets doubled liquid cooling plates, which provide some inspiration from the mobility side (Sheng et al., 2019).

Zhang et al. designed a biomimetic fins structure from Limulus, reducing the average temperature by 1.69 K and the pressure difference declined by 6.81Pa, while the complex channels did not discuss in the relationship between bionic types of fins and optimization algorithm (Zhang et al., 2024a). Additionally, the suitable parameter configurations were not investigated. To increase the heat exchange area, Zhao et al. got inspiration from the beehive, designing a honeycomb liquid channel. In the best parameter configuration, the maximum temperature difference can only be reduced to a maximum of 4.0 K (D. Zhao et al., 2023). Fan et al. created a kind of bionic fishbone liquid cooling channel, which can be applied in a high-power charging-discharging process, reaching 6C (Fan et al., 2023). In this study, by orthogonal analysis, significant effect factors were explored, and the effect of reducing the maximum temperature was achieved by 0.84%. Objectively, the data did not indicate a significant improvement in cooling efficiency. Similarly, Liu et al. imitated leaf veins to structure a bionic branch liquid channel, sandwiched with a pouch battery (Liu et al., 2023). Although the maximum temperature can be controlled below 306.34 K, the difference in maximum temperature decreased by only 0.23 K between the leaf veins branch channel and the traditional parallel straight channel. Except for the fish bones and the leaf veins, the shape of the fish and blade has also been enquired into the channel design by Gao et al. (Gaoet al., 2024) and Zhang et al.(Zhang et al., 2024b), respectively. Despite the fact that anisotropic structures can bring about slight improvements, less than 1.0 K, the overall enhancement is disproportionately minimal compared to the substantial efforts and complexity involved in such designs. Chen et al. proposed a liquid cooling containing bionic spiral fins, which was wrapped by phase change material, analyzing the cooling performance by configuring characteristic structure parameters and matching an acceptablepreheating temperature. The addition of phase change materials and the implementation of complex fin structures substantially raise the costs, yet the enhancement in performance remains minimal (X. Chen et al., 2024).

The results from these innovative and complex structures show that although anisotropic structures may lead to marginal improvements in maximum temperature distribution, the overall performance gains are significantly modest in relation to the considerable complexity and resources required for these designs. Therefore, the design direction for liquid cooling plates should balance complexity and feasibility with the effectiveness of thermal optimization.

This study aims to compare the performance of air cooling and liquid cooling systems in the thermal management of supercapacitors. Specifically, we investigate two different liquid cooling structures and flow patterns to provide insights into their effectiveness and practical implementation. The findings of this study are expected to guide the future design of efficient liquid cooling solutions for supercapacitors.

2. METHOD

2.1. The method of calculating heat generation

The heat generation of the supercapacitor is a critical parameter in the design of the air-cooling system and liquid cooling channels.In this study, what was concerned was found proper thermal management technology and a better structure design by numericalsimulation. The heat generation measurement process has been accomplished in previous work, therefore, based on that, the heatgeneration was defined by the following equation as an input value (Zhang et al., 2022).

Equation 1: Heat Generation of The Supercapacitor. $$Q(t) = A_1t^6 + A_2t^5 + A_3t^4 + A_4t^3 + A_5t^2 + A_6t^1$$

Where:

- $Q(t)$ is the heat generation (W /m^3)
- A_1~A_2 are the specific parameters, shown in Table 1.
- t is the time (s)

Table 1: Heat generation parameters

parameter	A1	A2	A3	A4	A5	A6	A7
value	4.9132E-16	-3.7742E-12	1.0679E-8	-1.3417E-5	0.0076	-2.2208	17152

2.2. The methods of air cooling thermal management

Considering the complexity and feasibility of implementation, both air cooling and liquid cooling thermal management technologies were considered in this study with one air cooling model and four liquid cooling models, using different channel designs and flow patterns built.

An air cooling model was developed to provide a baseline for comparison with the liquid cooling models. Key parameters such as airflow rate, ambient temperature, and heat transfer media temperature in the inlet were defined based on typical operating conditions: 0.001m/s, 298.15 K, and 298.15 K, respectively. The designed structure of this air cooling system is shown in Figure 1 and the relative specifications are summarized in Table 2 and Table 3.

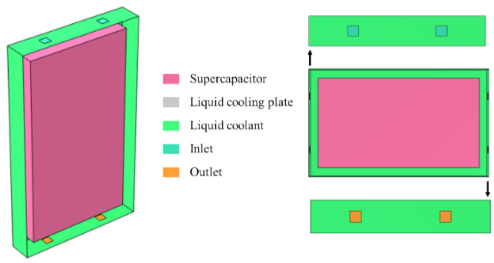

Figure 1: the structure diagram of an air cooling model

Table 2: Supercapacitor`s specifications

parameter	value	unit
Supercapacitor size	100*14*180	mm
Density	3000	kg/m³
Specific heat	1005.91	J/(kg·K)
Thermal conductivity	1.3	W/(m·K)
Rate capacity	2550	Ah

Table 3: Air cooling system`s specifications

parameter	value	unit
Flow channel size	120*22*200	mm
Inlet and outlet size	7.48*7.48	mm
Specific heat	4200	J/(kg·K)
Thermal conductivity	0.023	W/(m·K)
Density	1.29	kg/m³

2.3. The methods of liquid cooling thermal management

In contrast, four models of liquid cooling were considered: straight pipe channels and “U” shaped channels with two types of flow: downstream and counterflow. The structures for each design are described as follows. For the purpose of description, the liquid cooling model corresponding to these liquid-cooled plates and flow patterns will be referred to as the A~D model.

In the straight pipe channels, the coolant flows smoothly through eight parallel straight channels. The arrangement of the straight channels ensures uniform fluid distribution, and the simplistic structure design results in low flow resistance and pressure drop, enabling highly efficient heat transfer. The advantage of this design lies in its simplicity and efficiency, making it suitable for applications requiring high cooling efficiency.

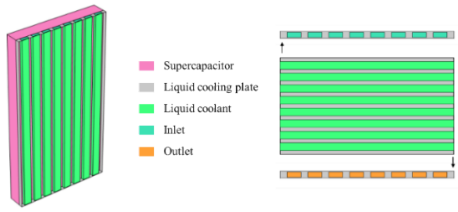

Figure 2: the structure diagram of A model: straight pipe channels with downstream flow pattern

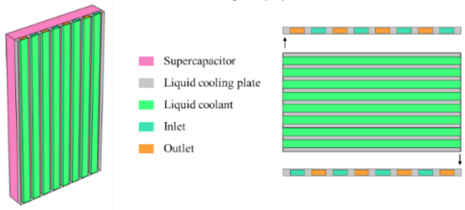

Figure 3: the structure diagram of B model: straight pipe channels with counterflow pattern

The structure of the U-shaped concurrent liquid cooling design consists of four U-shaped bend channels, where the coolant flows inthe same direction within each bend. The U-shaped design increases the contact area between the coolant and the channel walls, theoretically enhancing heat exchange efficiency. However, the added bends may cause higher flow resistance and pressure drop. With appropriate design and optimization, these issues can be mitigated to achieve better cooling performance.

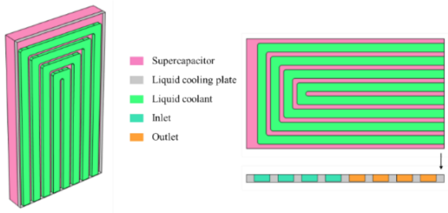

Figure 4: the structure diagram of C model: "U" shaped channels with downstream flow pattern

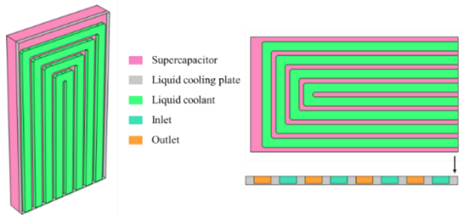

Figure 5: the structure diagram of D model: "U" shaped channels with counterflow pattern

In this study, water is used as the cooling medium for all liquid cooling designs. The properties of water are as follows: density of 1000 kg/m³, specific heat capacity of 4.18 kJ/kg·K, thermal conductivity of 0.6 W/m·K, and dynamic viscosity of 1.002 x 10^{-3} Pa·s. Water as a cooling medium has the advantages of high specific heat capacity and high thermal conductivity, allowing it to absorb and transfer a large amount of heat efficiently. Additionally, the stability and safety of water make it suitable for most operational conditions, being non-toxic and harmless, thus making it an ideal cooling medium. Moreover, considering the air cooling, the initial flow rate of liquid cooling is 0.001m/s, too.

By providing a detailed description of these three liquid cooling structures and the properties of the cooling medium, this study aimsto comprehensively compare their thermal management performance and try to guide future liquid cooling system designs.

2.4. The method of numerical simulation

In this study, computational fluid dynamics (CFD) simulations were conducted using COMSOL Multiphysics software to evaluate the thermal management performance of different cooling models. Four types of mesh numbers (200,000, 400,000, 800,000, and 1.6 million hexahedral elements, respectively) were considered. The largest difference in surface temperature between simulation and experiment data is less than 3% for a grid size of about 400,000. The heat transfer and fluid flow are coupled through the convection term $\rho_f C_p u \cdot \nabla T$, representing the transport of heat by the fluid motion. The simulations involved three main physical phenomena: solid heat transfer, fluid flow, and conjugate heat transfer (a coupled multi-physics field combining heat transfer and fluid flow). The governing equations for each physical field are described as follows.

Equation 2: Governing Equations of Solid Heat Transfer.

$$\rho_s C_p \frac{\partial T}{\partial t} = \nabla \cdot (k_s \nabla T) + Q_s$$

Where:

- ρ_s is the density of the solid material (kg/m^3)
- C_p is the specific heat capacity at constant pressure (J/kg • K)
- T is the temperature (K)
- k_s is the thermal conductivity of the solid material (W/m • K)
- Q_s the heat source term (W/m^3)

Equation 3: Governing Equations of Fluid Flow.

$$\rho_f \left(\frac{\partial u}{\partial t} + u \cdot \nabla u\right) = -\nabla p + \mu_f \nabla^2 u + F;\ \nabla \cdot u = 0$$

Where:

- ρ_f is the density of the fluid (kg/m^3)
- u is the fluid velocity vector (m/s)
- p is the pressure (Pa)
- μ_f is the dynamic viscosity of the fluid (Pa·s)
- F represents any external forces acting on the fluid (N/m^3)

Equation 4: Governing Equations of Conjugate Heat Transfer.

$$\rho_f C_p \frac{\partial T}{\partial t} + \rho_f C_p u \cdot \nabla T = \nabla \cdot \left(k_f \nabla T\right) + Q_f$$

Where:

- ρ_f is the density of the fluid (kg/m^3)
- C_p is the specific heat capacity at constant pressure (J/kg·K)
- T is the temperature (K)
- k_f is the thermal conductivity of the fluid (W/m·K)
- Q_f is the heat source term (W/m^3)
- u is the fluid velocity vector (m/s)

3. RESULTS AND DISCUSSION

3.1. Comparison of cooling methods

The performance of different cooling methods and channel designs was evaluated based on the maximum temperature and minimum temperature and the differential temperature between these two of the supercapacitors at various heat transfer medium flow rates. The results of air cooling models are shown in Figure 6.

As the results show, in the whole supercapacitor and thermal management system, the maximum temperature increases with the flow rate, stabilizing around 319.0 K at higher flow rates. Beyond that, the temperature difference increases almost linearly with the flow rate, reaching about 20.0 K at the highest flow rate tested. This indicates that air cooling is limited in achieving a uniform temperature distribution system, leading to a less effective thermal management system, potentially causing localized overheating and reduced overall efficiency of the supercapacitor. However, when just paying the focus on the cell, the maximum and minimum temperature follows a similar trend, stabilizing at approximately 319.0 K and 317.0 K respectively. Even the temperature difference decreases by 1.0 K only, which indicates a prominent temperature equalization within the supercapacitor.

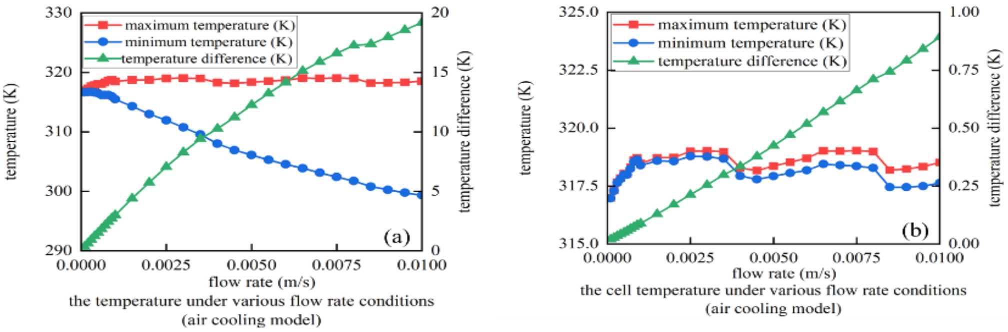

Figure 6: Results at different flow rates (in the air cooling model)

The temperature distribution and temperature differences across the supercapacitor and cooling plate configurations were analyzed for both A model and B model. The results are summarized in Figure 7. In contrast, the result of A model and B model demonstrates a significant reduction in maximum temperature compared to air cooling, with temperatures stabilizing around 303.0 K. The minimum temperature also decreases, stabilizing around 300.0 K. The temperature difference remains relatively low, demonstrating better temperature uniformity across the battery pack. This indicates that the eight parallel straight channels liquid cooling system is superior in reducing maximum temperature and improving temperature uniformity due to its simpler structure, which leads to lower flow resistance and more effective heat dissipation.

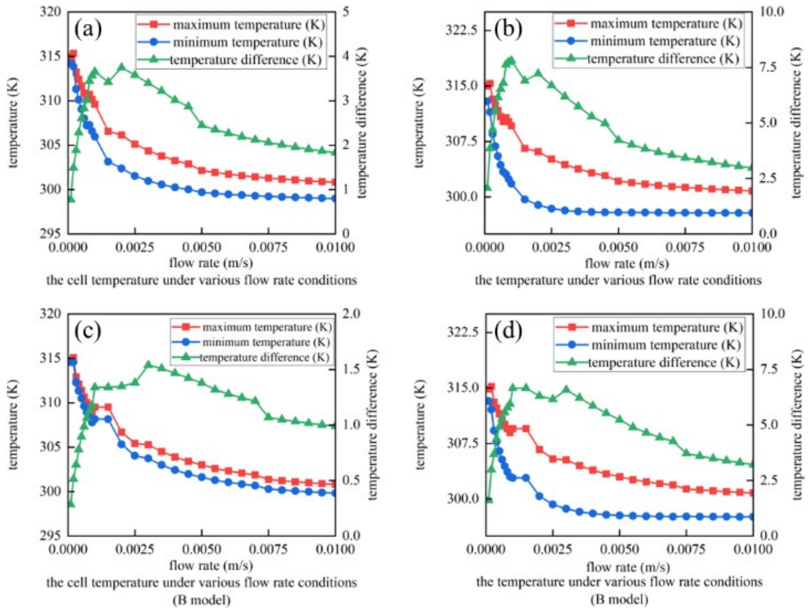

Figure 7: Results at different flow rates (in the A and B model)

In the A model, the maximum temperature decreases significantly with increasing heat transfer medium flow rates, from approximately 315.7 K at the lowest flow rate to about 302.5 K at the highest flow rate. The temperature difference shows an initial increase up to around 0.002 m/s and then decreases gradually, stabilizing around 3.0 K. When focusing on the supercapacitor cell, the maximum temperature similarly decreases, from around 315.5 K to 302.2 K, while the maximum temperature difference remains much lower than that of the entire system. In the result of B model, the cooling performance is improved. For the entire system, the maximum temperature decreases more quickly, and the temperature difference initially increases to about 7.0 K at a flow rate of 0.002 m/s and then stabilize around 3.0 K at higher flow rates. For the supercapacitor cell, the maximum temperature drops from approximately 315.4 K to 302.8 K, and the temperature difference also shows an initial peak and subsequent stabilization around 1.5 K and then a deduction to about 1.0 K.

These results highlight the superior cooling performance of the counterflow configuration compared to the downstream flow configuration. The counterflow design demonstrates a significant reduction in maximum temperature and improved temperature uniformity across the supercapacitor and cooling plate. The temperature distribution and differences across the supercapacitor andcooling plate configurations were also analyzed for both C model and D model. The results are summarized in Figure 8.

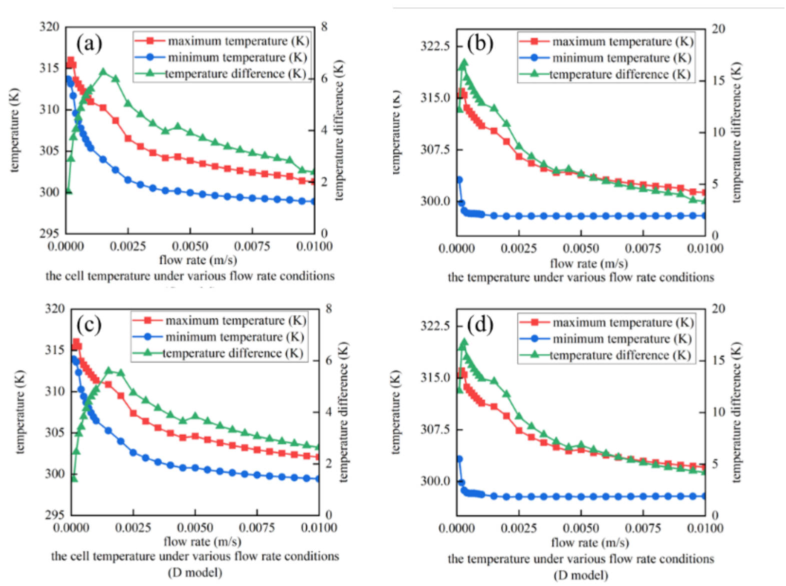

Figure 8: Results at different flow rates (in the A and B model)

In the C model, the maximum temperature decreases significantly with increasing heat transfer medium flow rates. For the entire system, the maximum temperature drops from approximately 315.5 K at the lowest flow rate to about 303.2 K at the highest flow rate, higher than the A model and B model but lower than air cooling model. The temperature difference gradually stabilized around 3.0 K. When focusing on the supercapacitor cells, the maximum temperature similarly decreases, from around 315.5 K to 303.0 K, while the temperature difference initially increases to about 6.0 K and then stabilizes around 2.5 K. While the C model provides better cooling than air cooling, it is less effective than the parallel straight channels due to higher flow resistance and less efficient heat transfer. In the D model, the cooling performance is further improved compared to the C model. For the entire system, the maximum temperature decreases more quickly, from approximately 315.4 K to about 302.8 K. The temperature difference stabilized around 4.5 K at higher flow rates. For the supercapacitor cells, the maximum temperature drops from approximately 315.4 K to 303.0 K, and the temperature difference stabilizes around 2.5 K.

Overall, the analysis clearly indicates that liquid cooling methods significantly outperform air cooling in both reducing the maximum temperature and improving temperature uniformity. Among the liquid cooling configurations, the eight parallel straight channels design and the U-shaped counterflow pattern design exhibit the best performance, with the latter achieving the lowest maximum temperature and most uniform temperature distribution. These findings underscore the importance of efficient cooling channel design in enhancing thermal management systems, thereby improving the performance and longer life spans of supercapacitors.

3.2. Comparison of liquid cooling designs

The performance of various liquid cooling designs was evaluated based on the maximum temperature and temperature difference across the supercapacitor at different heat transfer medium flow rates. The analyzed configurations include the simplest liquid cooling design (eight parallel straight channels), the optimized U-shaped downstream design, and the U-shaped counterflow pattern design. The results are presented in Figure 9.

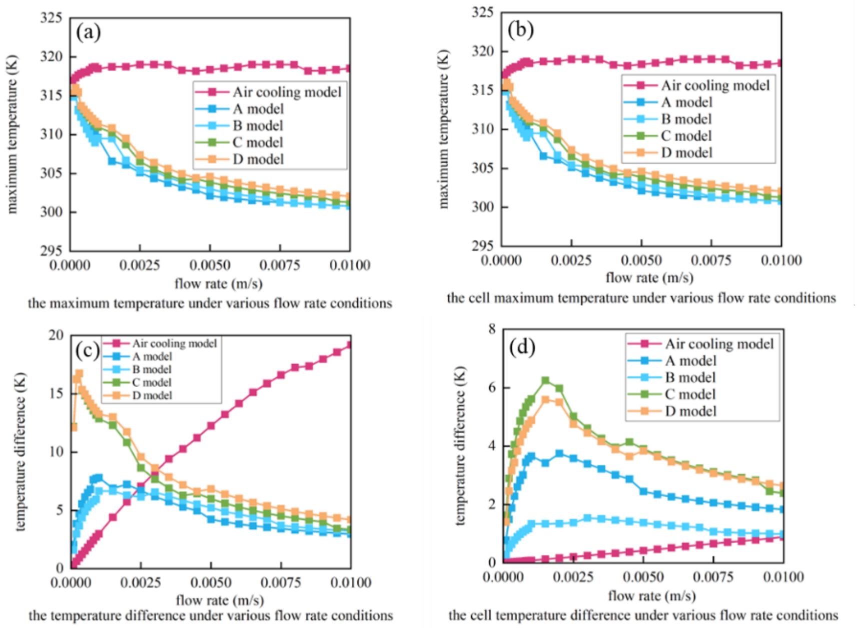

Figure 9: Comparisons of maximum temperature and temperature difference at different flow rates

From Figure 9(a) and Figure 9 (b), it can be illustrated that the maximum temperature of the supercapacitor for each liquid cooling design is a function of the heat transfer medium flow rate. The simplest liquid cooling design, represented by eight parallel straight channels, consistently shows the lowest maximum temperature across the whole flow rates domain. At the highest flow rate, this design achieves a maximum temperature of approximately 302.0 K. The optimized U-shaped concurrent design and the U-shaped counterflow pattern design exhibit higher maximum temperatures, stabilizing around 305.0 K and 307.0 K, respectively. This indicates that the simplest liquid cooling design is more effective in reducing the maximum temperature, primarily due to its straightforward flow path, which minimizes flow resistance and enhances heat transfer efficiency. From Figure 9(c) and Figure 9 (d), the lowest temperature difference is maintained across all flow rates, at higher flow rates, the B model remains around 1.0 K, indicating excellent temperature uniformity. In contrast, the optimized U-shaped downstream design and the U-shaped counterflow pattern design show higher temperature differences, peaking around 4.0 K and 5.0 K respectively, before gradually decreasing with increasing flow rates. These results suggest that the simplest design not only reduces the maximum temperature more effectively but also maintains better temperature uniformity across the battery pack.

Above all, the analysis demonstrates that the simplest liquid cooling design, featuring eight parallel straight channels, outperforms more complex configurations in both reducing maximum temperature and ensuring uniform temperature distribution. This highlightsthe efficiency and effectiveness of simple design solutions in thermal management systems, emphasizing that complex designs do not necessarily translate to better performance. The findings support the future trend towards simpler and more efficient liquid cooling structures for enhanced thermal management in battery systems.

4. CONCLUSION

This study comprehensively compared the thermal management performance of air cooling and various liquid cooling designs for battery packs. The findings demonstrate that liquid cooling significantly outperforms air cooling in reducing maximum temperature and improving temperature uniformity across the battery pack. Specifically, the simplest liquid cooling design, featuring eight parallel straight channels, achieved the best performance among the tested configurations. It consistently exhibited the lowest maximum temperature and the most uniform temperature distribution, highlighting its efficiency and effectiveness.

In contrast, more complex liquid cooling designs, such as the U-shaped downstream and counterflow configurations, resulted in higher maximum temperatures and greater temperature differences. These complex structures, while theoretically increasing the heat transfer surface area, introduced higher flow resistance and potential dead zones, thereby diminishing their overall cooling efficiency. Moreover, the increased complexity also leads to higher complexity and potential maintenance challenges. The results of this study underscore the importance of simplicity in liquid cooling design. Simple and efficient structures not only deliver superior cooling performance but also reduce complexity and minimize the risk of flow dead zones. Therefore, future trends in liquid cooling design should focus on optimizing straightforward solutions that ensure robust thermal management for high-power applications. These findings provide valuable insights into the development of next-generation cooling systems.

Overall, this research highlights the critical role of effective thermal management in enhancing the performance and longevity of battery systems. By demonstrating the advantages of simple liquid cooling designs, this study contributes to the ongoing efforts to develop more efficient and reliable cooling solutions for advanced energy storage.

5. REFERENCES

Angani, A., Kim, H.-W., Hwang, M.-H., Kim, E., Kim, K.-M., Cha, H.-R., 2023. A comparison between Zig-Zag plated hybrid parallel pipe and liquid cooling battery thermal management systems for Lithium-ion battery module. Applied Thermal Engineering219, 119599. https://doi.org/10.1016/j.applthermaleng.2022.119599

Azarifar, M., Arik, M., Chang, J.-Y., 2024. Liquid cooling of data centers: A necessity facing challenges. Applied Thermal Engineering 247, 123112. https://doi.org/10.1016/j.applthermaleng.2024.123112

Boldoo, T., Chinnasamy, V., Cho, H., 2024. Enhancing efficiency and sustainability: Utilizing high energy density paraffin-based various PCM emulsions for low-medium temperature applications. Energy 303, 131988. https://doi.org/10.1016/j.energy.2024.131988

Cao, W., Zhao, C., Wang, Y., Dong, T., Jiang, F., 2019. Thermal modeling of full-size-scale cylindrical battery pack cooled by channeled liquid flow. Int. J. Heat Mass Transfer 138, 1178–1187. https://doi.org/10.1016/j.ijheatmasstransfer.2019.04.137

Chen, K., Zhang, Z., Wu, B., Song, M., Wu, X., 2024. An air-cooled system with a control strategy for efficient battery thermal management. Appl. Therm. Eng. 236, 121578. https://doi.org/10.1016/j.applthermaleng.2023.121578

Chen, X., Shen, J., Xu, X., Wang, X., Su, Y., Qian, J., Zhou, F., 2024. Performance of thermal management system for cylindrical battery containing bionic spiral fin wrapped with phase change material and embedded in liquid cooling plate. Renewable Energy 223, 120087. https://doi.org/10.1016/j.renene.2024.120087

Chu, L., Zhao, X., Li, Z., Sun, Y., Xu, J., Wang, Z., Zhou, Z., 2024. Thermal hydraulic behavior of a large dimension hybrid heat pipe/oscillating heat pipe. Case Studies in Thermal Engineering 60, 104755. https://doi.org/10.1016/j.csite.2024.104755

Daniels, R.K., Prabhakar, A., 2023. Experimental and numerical investigation on the effect of cell arrangement on thermal runaway propagation in air cooled cylindrical Li-ion battery modules. Journal of Energy Storage 72, 108191. https://doi.org/10.1016/j.est.2023.108191

Demski, C., Capstick, S., Pidgeon, N., Sposato, R.G., Spence, A., 2017. Experience of extreme weather affects climate change mitigation and adaptation responses. Climatic Change 140, 149–164. https://doi.org/10.1007/s10584-016-1837-4

Deng, Y., Feng, C., E, J., Zhu, H., Chen, J., Wen, M., Yin, H., 2018. Effects of different coolants and cooling strategies on the cooling performance of the power lithium ion battery system: A review. Appl Therm Eng 142, 10–29. https://doi.org/10.1016/j.applthermaleng.2018.06.043

Dubey, A., Arora, A., 2024. Effect of various energy storage phase change materials (PCMs) and nano-enhanced PCMs on the performance of solar stills: A review. Journal of Energy Storage 97, 112938. https://doi.org/10.1016/j.est.2024.112938

Fan, X., Meng, C., Yang, Y., Lin, J., Li, W., Zhao, Y., Xie, S., Jiang, C., 2023. Numerical optimization of the cooling effect of a bionic fishbone channel liquid cooling plate for a large prismatic lithium-ion battery pack with high discharge rate. Journal of Energy Storage 72, 108239. https://doi.org/10.1016/j.est.2023.108239

Gao, D., Luo, Z., Liu, C., Fan, S., 2023. A survey of hybrid energy devices based on supercapacitors. Green Energy & Environment 8, 972–988. https://doi.org/10.1016/j.gee.2022.02.002

Gao, Q., Lei, Z., Huang, Y., Zhang, C., Chen, Y., 2024. Performance investigation of a liquid immersion cooling system with fish- shaped bionic structure for Lithium-ion battery pack. International Journal of Heat and Mass Transfer 222, 125156. https://doi.org/10.1016/j.ijheatmasstransfer.2023.125156

Gharehghani, A., Rabiei, M., Mehranfar, S., Saeedipour, S., Mahmoudzadeh Andwari, A., García, A., Reche, C.M., 2024. Progress in battery thermal management systems technologies for electric vehicles. Renewable and Sustainable Energy Reviews 202, 114654. https://doi.org/10.1016/j.rser.2024.114654

Gualous, H, Louahlia-Gualous, H, Gallay, R, Miraoui, A, 2009. Supercapacitor Thermal Modeling and Characterization in Transient State for Industrial Applications. IEEE Transactions on Industry Applications 45. https://doi.org/10.1109/TIA.2009.2018879

Habibi Khalaj, A., Halgamuge, S.K., 2017. A Review on efficient thermal management of air- and liquid-cooled data centers: From chip to the cooling system. Applied Energy 205, 1165–1188. https://doi.org/10.1016/j.apenergy.2017.08.037

Jiang, W., Zhao, J., Rao, Z., 2022. Thermal performance enhancement and prediction of narrow liquid cooling channel for battery thermal management. Int. J. Therm. Sci. 171, 107250. https://doi.org/10.1016/j.ijthermalsci.2021.107250

Khan, H.A., Tawalbeh, M., Aljawrneh, B., Abuwatfa, W., Al-Othman, A., Sadeghifar, H., Olabi, A.G., 2024. A comprehensive reviewon supercapacitors: Their promise to flexibility, high temperature, materials, design, and challenges. Energy 295, 131043. https://doi.org/10.1016/j.energy.2024.131043

Kirat, Y., Prodromou, T., Suardi, S., 2024. Unveiling the Nexus: Climate change, green innovation, and the pendulum of energy consumption and carbon emissions. Energy Economics 107727. https://doi.org/10.1016/j.eneco.2024.107727

Li, A., Yuen, A.C.Y., Wang, W., Weng, J., Yeoh, G.H., 2022. Numerical investigation on the thermal management of lithium-ion battery system and cooling effect optimization. Applied Thermal Engineering 215, 118966. https://doi.org/10.1016/j.applthermaleng.2022.118966

Li, M., Ma, S., Jin, H., Wang, R., Jiang, Y., 2023. Performance analysis of liquid cooling battery thermal management system in different cooling cases. Journal of Energy Storage 72, 108651. https://doi.org/10.1016/j.est.2023.108651

Li, R., Yang, Y., Liang, F., Liu, J., Chen, X., 2023. Investigation on Battery Thermal Management Based on Enhanced Heat Transfer Disturbance Structure within Mini-Channel Liquid Cooling Plate. Electronics 12, 832. https://doi.org/10.3390/electronics12040832

Liu, F., Chen, Y., Qin, W., Li, J., 2023. Optimal design of liquid cooling structure with bionic leaf vein branch channel for powerbattery. Applied Thermal Engineering 218, 119283. https://doi.org/10.1016/j.applthermaleng.2022.119283

Liu, H., Xie, J., Ma, X., 2024. Multi-objective optimization analysis of air-cooled heat dissipation coupled with thermoelectric coolingof battery pack based on orthogonal design. Applied Thermal Engineering 249, 123402. https://doi.org/10.1016/j.applthermaleng.2024.123402

Liu, W., Dong, C., Zhang, B., Cao, R., Qiao, Z., Tang, Y., Ye, C., Li, K., Ye, Y., 2022. Thermal characteristic and performance influence of a hybrid supercapacitor. Journal of Energy Storage 53, 105188. https://doi.org/10.1016/j.est.2022.105188

Luo, D., Yang, S., Yan, Y., Cao, J., Yang, X., Cao, B., 2024. Performance improvement of the automotive thermoelectric generator system with a novel heat pipe configuration. Energy 306, 132376. https://doi.org/10.1016/j.energy.2024.132376

Maiorino, A., Cilenti, C., Petruzziello, F., Aprea, C., 2024. A review on thermal management of battery packs for electric vehicles. Applied Thermal Engineering 238, 122035. https://doi.org/10.1016/j.applthermaleng.2023.122035

Ran, Y., Su, Y., Yan, K., Jiang, X., Zhao, Y., Shen, X., Liu, X., Yang, X., Chen, L., Wu, F., 2023. Electrical–thermal–fluidic coupling Li-ion battery pack consistency study. Journal of Energy Storage 70, 108031. https://doi.org/10.1016/j.est.2023.108031

Saha, S., Bose, B., Garg, A., Parthiv Chandra, K., Zhao, J., Panda, B., Gao, L., 2024. A topology optimization for design of double input-single output battery module liquid cooling plate with improved thermal performance. Journal of Energy Storage 97, 112750. https://doi.org/10.1016/j.est.2024.112750

Sarvar-Ardeh, S., Rafee, R., Rashidi, S., 2023. Enhancing the performance of liquid-based battery thermal management system byporous substrate minichannel. Journal of Energy Storage 71, 108142. https://doi.org/10.1016/j.est.2023.108142

Shang, Y., Sang, S., Tiwari, A.K., Khan, S., Zhao, X., 2024. Impacts of renewable energy on climate risk: A global perspective for energy transition in a climate adaptation framework. Applied Energy 362, 122994. https://doi.org/10.1016/j.apenergy.2024.122994

Sheng, L., Su, L., Zhang, H., Li, K., Fang, Yidong, Ye, W., Fang, Yu, 2019. Numerical investigation on a lithium ion battery thermal management utilizing a serpentine-channel liquid cooling plate exchanger. Int. J. Heat Mass Transfer 141, 658–668. https://doi.org/10.1016/j.ijheatmasstransfer.2019.07.033

Suman, A., 2021. Role of renewable energy technologies in climate change adaptation and mitigation: A brief review from Nepal. Renewable and Sustainable Energy Reviews 151, 111524. https://doi.org/10.1016/j.rser.2021.111524

Wu, X., Lu, Y., Ouyang, H., Ren, X., Yang, J., Guo, H., Han, X., Zhang, C., Wu, Y., 2024. Theoretical and experimental investigationson liquid immersion cooling battery packs for electric vehicles based on analysis of battery heat generation characteristics.Energy Convers. Manage. 310, 118478. https://doi.org/10.1016/j.enconman.2024.118478

Xie, J., Liu, X., Zhang, G., Yang, X., 2023. A novel strategy to optimize the liquid cooling plates for battery thermal management by precisely tailoring the internal structure of the flow channels. Int. J. Therm. Sci. 184, 107877. https://doi.org/10.1016/j.ijthermalsci.2022.107877

Xu, J., Guo, Z., Xu, Z., Zhou, X., Mei, X., 2023. A systematic review and comparison of liquid-based cooling system for lithium-ion batteries. eTransportation 17, 100242. https://doi.org/10.1016/j.etran.2023.100242

Xu, Y., Zhao, J., Chen, J., Zhang, H., Feng, Z., Yuan, J., 2024. Performance analyses on the air cooling battery thermal managementbased on artificial neural networks. Applied Thermal Engineering, 252, 123567. https://doi.org/10.1016/j.applthermaleng.2024.123567

Ye, J., Aldaher, A.Y.M., Tan, G., 2023. Thermal performance analysis of 18,650 battery thermal management system integrated with liquid cooling and air cooling. Journal of Energy Storage 72, 108766. https://doi.org/10.1016/j.est.2023.108766

Yu, Z., Zhang, J., Pan, W., 2023. A review of battery thermal management systems about heat pipe and phase change materials. Journal of Energy Storage 62, 106827. https://doi.org/10.1016/j.est.2023.106827

Zhang, F., He, Y., Wang, C., Liang, B., Zhu, Y., Gou, H., Xiao, K., Lu, F., 2023. A new type of liquid-cooled channel thermal characteristics analysis and optimization based on the optimal characteristics of 24 types of channels. Int. J. Heat Mass Transfer 202, 123734. https://doi.org/10.1016/j.ijheatmasstransfer.2022.123734

Zhang, F., Huang, Z., Li, S., Sun, S., Zhao, H., 2024a. Design and thermal performance analysis of a new micro-fin liquid coolingplate based on liquid cooling channel finning and bionic limulus-like fins. Appl. Therm. Eng. 237, 121597. https://doi.org/10.1016/j.applthermaleng.2023.121597

Zhang, F., Wang, F., Zhu, Y., He, Y., 2024b. Structural optimization of thermal management system for bionic liquid cold battery based on fuzzy grey correlation analysis. Applied Thermal Engineering 249, 123347. https://doi.org/10.1016/j.applthermaleng.2024.123347

Zhang, J., Gu, M., Chen, X., 2023. Supercapacitors for renewable energy applications: A review. Micro and Nano Engineering 21, 100229. https://doi.org/10.1016/j.mne.2023.100229

Zhang, L., Hu, X., Wang, Z., Sun, F., Dorrell, D.G., 2018. A review of supercapacitor modeling, estimation, and applications: A control/management perspective. RENEWABLE & SUSTAINABLE ENERGY REVIEWS 81, 1868–1878. https://doi.org/10.1016/j.rser.2017.05.283

Zhang, Z., Fu, L., Sheng, L., Ye, W., Sun, Y., 2022. Method of liquid-cooled thermal control for a large-scale pouch lithium-ion battery. Appl. Therm. Eng. 211, 118417. https://doi.org/10.1016/j.applthermaleng.2022.118417

Zhao, D., An, C., Jia, Z., Lei, Z., 2024. Structure optimization of liquid-cooled plate for electric vehicle lithium-ion power batteries. Int J Therm Sci 195, 108614. https://doi.org/10.1016/j.ijthermalsci.2023.108614

Zhao, D., Lei, Z., An, C., 2023. Research on battery thermal management system based on liquid cooling plate with honeycomb-like flow channel. Appl Therm Eng 218, 119324. https://doi.org/10.1016/j.applthermaleng.2022.119324

Zhao, G., Wang, X., Negnevitsky, M., Li, C., 2023. An up-to-date review on the design improvement and optimization of the liquid cooling battery thermal management system for electric vehicles. Appl. Therm. Eng. 219, 119626. https://doi.org/10.1016/j.applthermaleng.2022.119626

Zhao, L., Li, W., Wang, G., Cheng, W., Chen, M., 2023. A novel thermal management system for lithium-ion battery modules combining direct liquid cooling with forced air cooling. Appl Therm Eng 232,120992. https://doi.org/10.1016/j.applthermaleng.2023.120992

Zhu, J., Wang, J., Cheng, D., Mao, J., Zhang, K., 2024. Numerical investigation and parameter optimization on a rib-grooved liquid-cooled plate for lithium battery thermal management system. Journal of Energy Storage 85, 111085. https://doi.org/10.1016/j.est.2024.111085

#296: Coupling ventilated photovoltaic window with air-conditioning system: electrical, thermal, and daylight performance for different window-to-wall ratios

Yayun TANG[1], Jie JI[2], Chengyan ZHANG[3], Chuyao WANG[4]

[1] *Department of Thermal Science and Energy Engineering, University of Science and Technology of China, Hefei, Anhui, China. tangyayun@mail.ustc.edu.cn*
[2] *Department of Thermal Science and Energy Engineering, University of Science and Technology of China, Hefei, Anhui, China. jijie@ustc.edu.cn*
[3] *Department of Thermal Science and Energy Engineering, University of Science and Technology of China, Hefei, Anhui, China. zcy19013@mail.ustc.edu.cn, China.*
[4] *Department of Building Environment and Energy Engineering, The Hong Kong Polytechnic University, Hong Kong, China. chuyao.wang@polyu.edu.hk*

Abstract: Solar energy, owing to its emission-free properties and environmental sustainability, has been extensively explored for integration into buildings. Building-integrated photovoltaic (BIPV) technology contributes to energy conservation and emissions reduction by combining electricity generation with architectural design. However, conventional solar buildings face challenges related to single functionality, suboptimal photoelectric conversion, and a significant increase in space cooling load. In response, a semi- transparent BIPV window system combined with an air-conditioning system is proposed as a promising solution to improve comfort levels and reduce energy consumption. This study aims to provide valuable insights into optimizing system designs for achieving more energy-efficient buildings. The focus is on evaluating the energy and daylight performance of this combined system for various window-to-wall ratios (WWR). Electrical and thermal performance is simulated and assessed through solutions of the energy balance equations for each component of the system in the Matlab environment. Daylighting simulations are conducted using Design Builder software to analyze the distribution of natural light in indoor spaces and thus artificial lighting demand. Furthermore, the influence ofWWR on the energy benefits and consumption of a typical office integrated with this system is investigated for three typical cities inChina with hot-humid weather conditions. Results show that with a relatively large WWR (WWR ≥ 60%), the application of the system in the building offers better overall energy performance.

Keywords: PV Window, Power Generation, Air-Conditioning System, Lighting Energy, Building Energy Consumption

1. INTRODUCTION

As the world transitions towards sustainable energy technologies, integrating renewable energy sources into buildings becomes increasingly important. Semi-transparent photovoltaic windows (STPV-W) represent a promising technology that replaces conventional glass with STPV modules, providing both daylighting and clean electricity generation.

STPV has received extensive attention from scholars due to its potential benefits. Wang et al. (Wang et al., 2016) investigated the optical, electrical, and thermal performance of a ventilated STPV-W using a mathematical model developed with EnergyPlus software. Their findings revealed that replacing single-layer transparent glass with STPV insulating glass could save up to 25.3% ofenergy. Yadav et al. (Yadav and Hachem-Vermette, 2024) examined a STPV system composed of an air layer, glass panels, and curtains. Their study found that the system generated 361 Wh/m^2 of electricity daily, and it effectively reduced heating demand in cold weather while decreasing cooling energy consumption in hot climates. Tan et al. (Tan et al., 2023) developed a numerical model for vacuum PV glass units using Python, validating the model's accuracy with experimental test data. The units demonstrated excellent thermal insulation performance, with a U-value of less than 1.0 W/m^2·K. Additionally, a vacuum glass component with a 90% PV coverage ratio had an annual output of 24.77 kWh/m^2. PV coverage ratios exceeding 50% maintained good visual comfortfor occupants, with negligible discomfort glare. Qiu et al. (Qiu and Yang, 2022) combined STPV cells with vacuum glass, showing that the typical winter day heat flux density could reach approximately 250 W/m^2.

Despite these advancements, research on STPV modules has primarily focused on the thermal and electrical performance of the PV cells themselves. There has been less research that comprehensively considers the power generation performance of STPV-Wsystems and their impact on indoor air conditioning and daylighting, particularly with regard to the coupled operation of STPV-W and air conditioning systems under different window-to-wall ratios (WWR).

This study aims to address this gap by investigating the potential of coupling an air-conditioning system with a ventilated STPV-W in hot-humid weather conditions. The focus is on evaluating the electrical, thermal, and daylighting performance of this combined system for various WWRs.

2. METHODOLOGY

This section presents the system configuration and simulation methodology.

2.1 Structure of the STPV-W

Figure 1 illustrates a cross-section of a ventilated double-glazing STPV-W. The outdoor-facing PV glazing consists of a laminated PV film layer sandwiched between exterior and interior tempered glass, with a PV coverage ratio of 0.8. The interior side features common clear tempered glass, creating an air channel between it and the PV glazing.

In summer, when the air conditioning system is operational, supply air cooled to the dew-point state by an air handling unit (AHU) is introduced into the air channel of the STPV-W. The STPV-W converts solar irradiation into electrical energy while preheating the supply air at the dew point. An electric heating device then assists in raising the supply air temperature to an acceptable level of 18°C before being delivered into the indoor space. A more detailed description of the system's operating principle can be found in ourpreviously published paper (Tang et al., 2022).

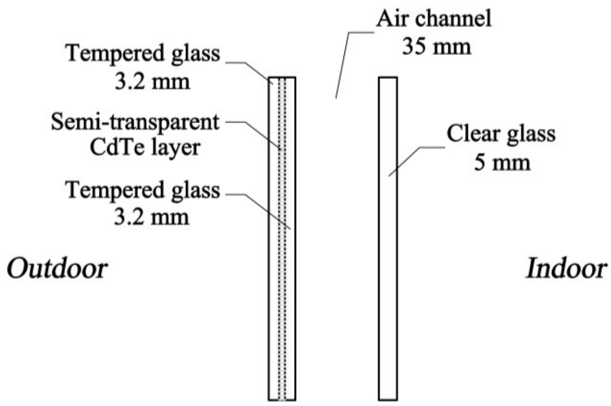

Figure 1: Cross section of the ventilated CdTe thin-film STPV-W

2.2 Performance evaluation model

The power output and electrical efficiency of the solar cells are calculated as

Equation 10: Electrical generation $$E_{PV} = \int_0^t A_{PV}\tau I\eta_e dt$$

Equation 2: Electrical efficiency $$\eta_e = \eta_0[1 - Br(T_{PV} - 298.15)]$$

Where:

- E = electrical energy (kWh)
- A_{PV} = area of PV cells (m^2)
- τ = transmittance
- I = incident solar radiation (W/m^2)
- η_0 = PV efficiency under standard testing conditions (Wang et al., 2021)
- Br = temperature coefficient of CdTe PV cells, K^{-1} (Skoplaki and Palyvos, 2009)
- T_{PV} = temperature of PV cells, K
- t = operating time, s

The heat recovered from the PV window is calculated by

Equation 3: Heat recovery $$Q_{rec,heat} = \int_0^t c_p\dot{m}_{ca}(T_{outlet} - T_{inlet})\,dt$$

Where:

- Q = thermal energy (kWh)
- c_p = specific heat of air (kJ/kg • °C)
- $\dot{m}_{ca}$ = mass flow rate of channel air (kg/s)
- T_{outlet} = temperature of channel outlet air, K
- T_{inlet} = temperature of channel inlet air, K

The fan energy is calculated by

Equation 4: Fan energy $$E_{fan} = \int_0^t \frac{\Delta P\dot{V}_{sa}}{\eta_{fan}} dt$$

Where:

- ΔP = fan pressure to overcome the flow resistances (Pa)
- V_{sa} = supply air volume flow rate (m^3/s)
- η_{fan} = fan efficiency

The energy benefits of the building incorporating this hybrid system are derived from two sources: the electricity generated by PV cells (E_{PV}) and the heat recovered from STPV-W ($Q_{rec,heat}$). On the other hand, the building's energy consumption encompasses the energy used by the air-conditioning system (E_{AHU}), the supply air fan (E_{fan}), and the artificial lighting (E_{lgt}). The net electricity consumption (NEC) of the building can be calculated using

Equation 5: Quantity of NEC $$\mathrm{NEC} = E_{AHU} + E_{fan} + E_{lgt} - E_{PV} - Q_{rec,heat}/COP$$

Where:

- COP = coefficient of performance of air-conditioning equipment, which is taken as 3.5(Tang et al., 2022)

2.3 Building characteristics for simulation

An office building was used for the case study, featuring the STPV-W integrated into the south-facing façade and connected to a primary return air-conditioning system. A three-dimensional schematic of the building is shown in Figure 2, with dimensions of 14 m(north-south) × 18 m (east-west) × 4.2 m in height. The building is occupied from 8:00 to 19:00.

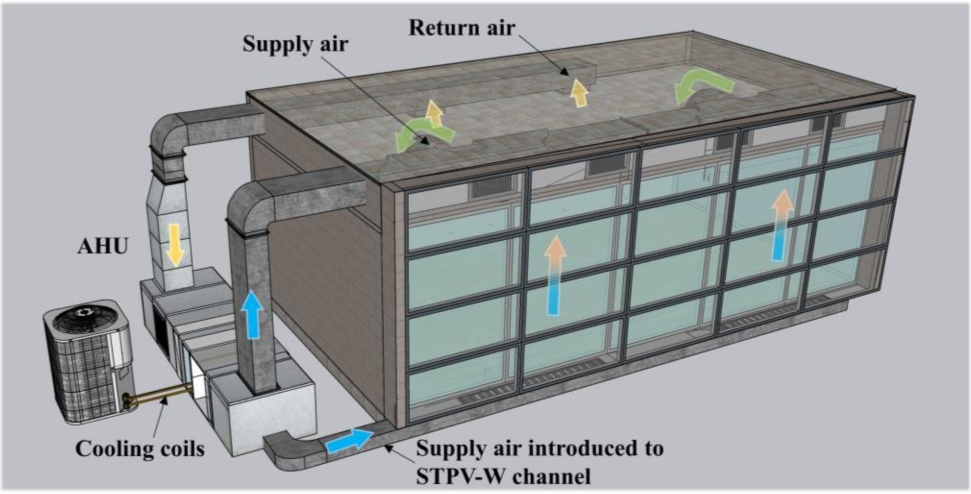

Figure 2: Building prototype integrated with the STPV-W coupled with an air-conditioning system

WWR, the proportion of a building's window area to its total façade area, is a key design factor influencing energy performance (Zhang et al., 2024). High WWR can lead to increased exposure to external weather conditions, affecting indoor environment control. Specifically, a large STPV-W area can make interiors more susceptible to temperature variations on the internal glazing surface. Furthermore, STPV glazing absorbs a portion of incoming solar radiation to generate electricity, while also producing heat and allowing daylight to penetrate. Enlarging the STPV-W area can enhance electricity generation, heat recovery, and natural daylight availability. However, the increased solar heat gain can raise cooling demand in summer by increasing heat gain due to higher solar heat penetration.

Therefore, exploring the optimal WWR is crucial for optimizing the STPV-W system in conjunction with the supply air handling. It involves balancing energy generation and consumption with indoor comfort. This balance ensures maximum energy efficiency by leveraging solar power benefits while minimizing additional energy consumption for room air conditioning and lighting, thus providing valuable design guidance.

In this study, the electrical, thermal, and daylight performance, as well as the net energy consumption (NEC), of the building with WWR of 20%, 40%, 60%, 80%, and 100%, were simulated. The façade design scenarios for different WWRs by changing the STPV- W height, are shown in Figure 3.

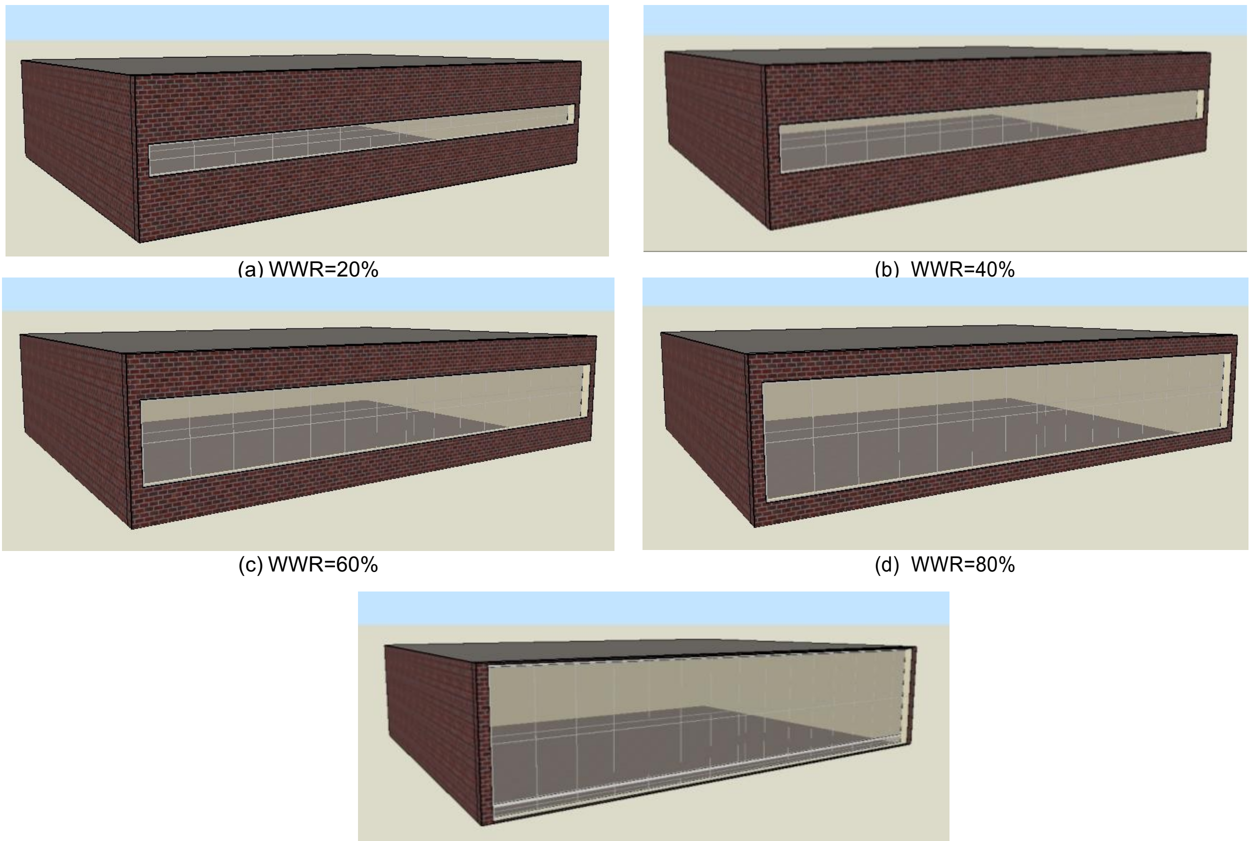

(a) WWR=20%

(b) WWR=40%

(c) WWR=60%

(d) WWR=80%

(e) WWR=100%

Figure 3: Facade design scenarios with varying WWR

2.4 Meteorological conditions for simulation

Locations in China are classified into five climatic zones based on different meteorological characteristics (Zhang et al., 2024). The studied system, designed for hot and humid weather conditions, specifically targets the building's cooling and dehumidification needs in summer. Therefore, the cooling seasons of the cold zone, hot summer and cold winter zone, and hot summer and warm winter zone are selected for the simulation study due to their hot and humid summers. Three cities, each representing one of these climatic regions, are selected as listed in Table 1. Using weather data from June 1 to August 31 of the Typical Meteorological Year (TMY) for these cities, the building performance evaluation was performed in 10 s time steps.

Table 1: Geographic and climatic information of 3 cities for the building simulation

	Climate zone	Latitude	Longitude	Summer avg. temp.	Summer avg. incident solar irradiance
Beijing	Cold	39.9° N	116.3° E	25.47 °C	189.77 kWh/m^2
Hefei	Hot summer and cold winter	31.5° N	117.2° E	26.87 °C	144.93 kWh/m^2
Guangzhou	Hot summer and warm winter	23.1° N	113.3° E	28.02 °C	119.37 kWh/m^2

2.5 Simulation methods and conditions

Electrical and thermal energy simulation

Based on the photoelectric properties of CdTe PV modules and the principles of thermodynamics, we have developed an unsteadycoupled model of the optical-electrical-thermal behavior of the double-glazing window system under forced convection. The output power of the PV module depends on the solar radiation intensity, the PV cell area, and its temperature.

Using the heat balance method, the temperature distribution for each envelope was derived, and the thermal processes affecting the indoor air were analyzed. Initially, the time- and space-dependent energy conservation equations were listed, and the initial and boundary conditions based on weather conditions were mathematically described. The grid nodes for the region defined by these equations were then divided. By discretizing the partial differential equations describing the flow and heat transfer processes using the finite volume method, they were transformed into a set of algebraic equations at each node. These equations were solved through iterative computation using Matlab programming.

In this simulation, the internal equipment and lighting loads are 20 W/m^2 and 11 W/m^2, respectively, and the indoor occupant density is 2.5 m^2/person. The indoor design set point is a temperature of 26 °C and a relative humidity of 60% in summer (Yount, 2017).

Daylight simulation

The annual daylighting performance of the building was modeled and simulated using DesignBuilder software. First, a three-dimensional geometric model of the building was created in DesignBuilder. Then, the optical properties—such as reflectance, transmittance, and absorptance—of each surface in the building model were defined. Subsequently, the sky model, geographic location, simulation time, and weather conditions were configured. The ray-tracing method was employed to analyze the travel of light through the components of each layer of the STPV-W and to model the distribution of natural light within the building's interior (Tang et al., 2022). The working plane was set at a height of 0.75 m above ground, with a target illuminance of 300 lux.

3. RESULT AND DISCUSSION

Figure 4 presents the simulation results for the impact of different WWRs on the performance parameters of the case buildings throughout the summer. Figure 5 illustrates the variations in energy benefits and consumption, and NEC, as the WWR increases.

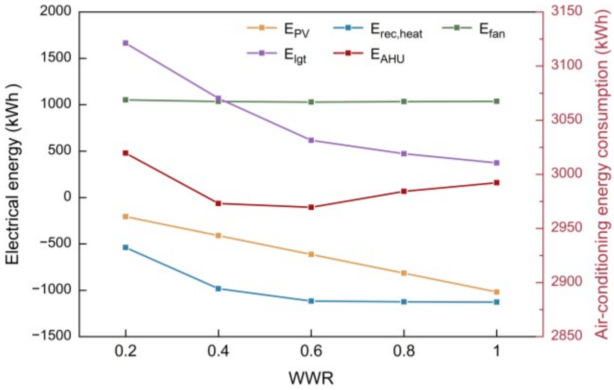

(a) Beijing

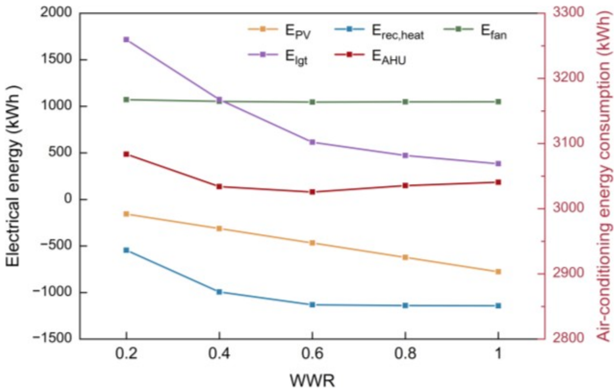

(b) Hefei

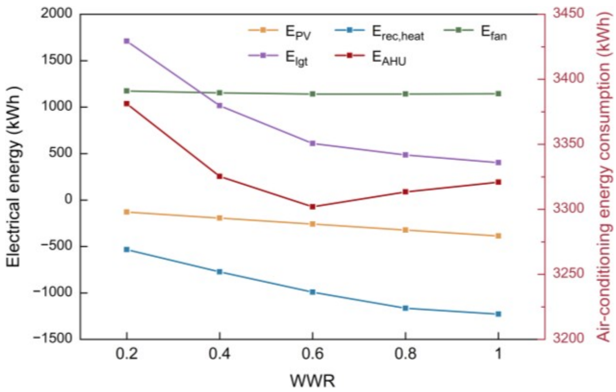

(c) Guangzhou

Figure 4: Variations in power generation, heat recovery, air-conditioning energy consumption, fan energy, and lighting demand for different WWRsthroughout the summer.

3.1 Impact of WWR on electricity generation

The amount of solar radiation received by the CdTe thin-film cells is a crucial factor influencing photovoltaic (PV) output. As the WWR increases, the PV glass area expands, allowing more solar irradiation to be incident on the PV glass surface, which is then converted into electrical and thermal energy. As shown in Figure 4, increasing the WWR from 20% to 100% results in a significant rise in summer electricity production for the case buildings: from 205.56 kWh to 1018.58 kWh in Beijing, from 156.79 kWh to 777.32 kWh in Hefei, and from 129.34 kWh to 386.59 kWh in Guangzhou.

Under a given WWR, the electricity production of the buildings in Beijing surpasses that of the buildings in Hefei and Guangzhou. This discrepancy is attributed to the greater solar irradiation on the south facade of the building due to Beijing's higher latitude. In the northern hemisphere, higher latitudes result in a lower solar altitude angle, thereby increasing the intensity of solar irradiation received by the south-facing facade of a building.

3.2 Impact of WWR on heat recovery

An increase in the WWR extends the flow distance for the supply air passing through the STPV-W. Besides, a larger STPV-W areagenerates more excess heat from the PV modules. The lengthening of the flow channel further enhances the air heating performance, increasing the outlet air temperature after preheating by the PV window. This enhancement boosts the heat recovery capability of the channel air from the PV window. For example, in Beijing, the energy recovered by the supply air increases significantly from 539.64 kWh to 1116.58 kWh as the WWR increases from 20% to 60%. When the WWR is further increased to 100%, the recoveredenergy shows a slight rise to 1127.72 kWh.

3.3 Impact of WWR on air-conditioning energy consumption

The dew-point air introduced into the channel, with its relatively low temperature, exerts a significant cooling effect on the STPV-W,maintaining the interior side glazing temperature below 26°C for most operating hours. As the WWR increases from 20% to 60%, the STPV-W area coupled with the supply air reheating process expands correspondingly. This expansion increases the cool glazing's surface area, enhancing its ability to manage indoor heat load through radiative and convective heat exchanges with the indoor environment. Consequently, the cooling energy usage of the air-conditioning system decreases, as demonstrated by a reduction from 3019.56 kWh to 2969.55 kWh in the case study conducted in Beijing. However, as the WWR increases from 60% to 100%, the cooling capacity of the introduced supply air becomes constrained. Despite extending the flow path to prolong the residence time of the supply air within the channel, the temperature of the indoor-side glass does not decrease significantly. As a result, the energy consumption of the air-conditioning system experiences a slight increase, reaching 2992.20 kWh.

In Hefei and Guangzhou, the variation in the energy use for air conditioning aligns with the trend observed in Beijing, initially decreasing and then slightly increasing. Overall, as shown in Figure 5, the air-conditioning energy consumption in Hefei decreases from 3083.67 kWh to 3040.63 kWh, while in Guangzhou, it drops from 3381.20 kWh to 3320.89 kWh. For a specific WWR, the highest energy consumption for air conditioning is observed in Guangzhou, followed by Hefei, and then Beijing. This pattern is attributed to the latitudes of these cities, with Guangzhou being the southernmost, followed by Hefei, and Beijing being the northernmost. Higher latitudes generally experience higher outdoor ambient temperatures in summer, which enhances both convective and radiative heat transfer between indoor and outdoor environments. As a result, the heat gain through the building envelope increases, leading to greater cooling energy consumption.

3.4 Impact of WWR on fan energy and lighting energy

Fan power is closely tied to the supply airflow rate of the air-conditioning system, which correlates with the variation in room coolingload. In Beijing, for instance, as the WWR increases, fan energy requirement initially decreases from 1052.29 kWh to 1029.41 kWh, before rising slightly to 1036.77 kWh. Additionally, enlarging the window area allows more daylight penetration into the interior thus reducing artificial lighting demands from 1664.02 kWh to 372.90 kWh.

3.5 Impact of WWR on overall energy performance

As illustrated in Figure 5, an increase in WWR from 20% to 100% results in a substantial decrease in the total summer NEC of the case buildings. In Beijing, this consumption drops from 4990.68 kWh to 2255.58 kWh, in Hefei from 5169.58 kWh to 2554.12 kWh, and in Guangzhou from 5602.85 kWh to 3253.11 kWh. These reductions correspond to 54.80%, 50.59%, and 41.94%, respectively. This data indicates that increasing the WWR enhances the energy efficiency of buildings utilizing this combined STPV-W system, with more pronounced effects observed in higher latitude cities in China.

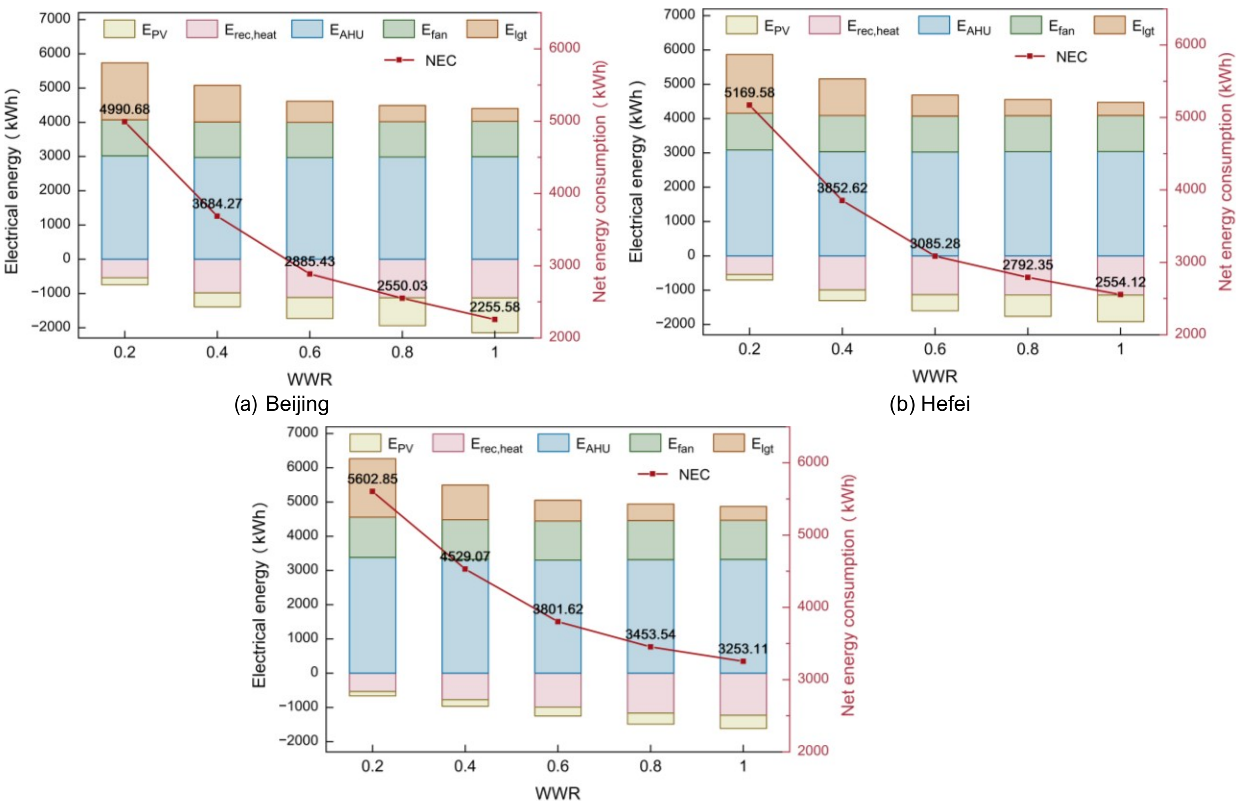

(a) Beijing (b) Hefei

(c) Guangzhou

Figure 4: Energy benefits and consumption, and NEC for different WWR

4. CONCLUSION

This study evaluated the impact of the WWR on the performance of STPV-W integrated with an air-conditioning system. An optical- thermal-electrical model was developed using Matlab, and artificial lighting energy demand was simulated with DesignBuilder.

The results indicate that increasing the WWR significantly enhances building performance, particularly in higher latitude regions of China, such as Beijing. A WWR of 60% or higher is recommended. As the WWR increases from 20% to 100%, electricity production and waste heat recovery from PV windows rise. The air-conditioning load and fan energy initially decrease before slightly increasing, while lighting energy consumption reduces due to increased natural light availability. Overall, expanding the STPV-W area reduces the NEC of the buildings in summer in Beijing, Hefei, and Guangzhou by 54.80%, 50.59%, and 41.94%, respectively. In summary, increasing the WWR is an effective approach to optimizing the architectural design of buildings that integrate STPV-W and advanced air handling processes, thereby enhancing energy-saving potential.

5. REFERENCES

QIU, C. & YANG, H. 2022. Dynamic coupling of a heat transfer model and whole building simulation for a novel cadmium telluride- based vacuum photovoltaic glazing. Energy, 250.

SKOPLAKI, E. & PALYVOS, J. A. 2009. On the temperature dependence of photovoltaic module electrical performance: A review of efficiency/power correlations. Solar Energy, 83, 614-624.

TAN, Y., PENG, J., LUO, Y., LI, H., WANG, M., ZHANG, F., JI, J. & SONG, A. 2023. Daylight-electrical-thermal coupling model forreal-time zero-energy potential analysis of vacuum-photovoltaic glazing. Renewable Energy, 205, 1040-1056.

TANG, Y., JI, J., WANG, C., XIE, H. & KE, W. 2022. Combining photovoltaic double-glazing curtain wall cooling and supply airreheating of an air-conditioning system: Energy-saving potential investigation. Energy Conversion and Management, 269.

WANG, C., UDDIN, M. M., JI, J., YU, B. & WANG, J. 2021. The performance analysis of a double-skin ventilated window integratedwith CdTe cells in typical climate regions. Energy and Buildings, 241, 110922.

WANG, M., PENG, J., LI, N., LU, L., MA, T. & YANG, H. 2016. Assessment of energy performance of semi-transparent PV insulatingglass units using a validated simulation model. Energy, 112, 538-548.

YADAV, S. & HACHEM-VERMETTE, C. 2024. Performance evaluation of semitransparent PV window systems employing periodicthermal model. Applied Energy, 353.

YOUNT, F. 2017. ASHRAE Handbook committee, ASHRAE Handbook–Fundamentals. ASHRAE.

ZHANG, C., JI, J., WANG, C. & KE, W. 2024. Annual analysis and comparison of the comprehensive performance of a CdTe PVventilated window integrated with vacuum glazing in different climate regions. Renewable Energy, 223.

#297: A Review on the R&D of heat pipe integrated photovoltaic/thermal systems

Licheng ZHOU[2],Chunlei HE[1], Mingjun LI[1],Xiaoyang ZHOU[1], Min YU [1,2,*], Jinzhi ZHOU[2],Xiaoling ZHU[2]

[1] SWJTU-LEEDS Joint School,Southwest Jiaotong University,Chengdu,Raindropmin@foxmail.com
[2] School of Mechanical Engineering,Southwest Jiaotong University,Chengdu,jinzhizhou@swjtu.edu.cn

Abstract: To overcome the possible seasonal freezing problem and thus advance the PV/T technologies and enhance their energy performance, heat pipes were brought into use. Heat pipe is a kind of passive heat transportation device that, making use of evaporation and condensation of the working fluid on different sides, can effectively remove heat away from the PV back surface and transfer it to the working fluid to create a highly efficient, safe and passive way of PV cooling and thus enable an improved overall solar efficiency. Therefore, this paper aims to present a review on the solar PV/T systems utilized heat pipe (HP-PV/Ts), identify the typical features and critical barriers of the existing HP-PV/T technologies, and thus develop the potential solutions for tackling theseidentified challenges. Firstly, the development of PV/Ts and related integrated systems are concisely introduced. Then the principle, structures, practical applications, and research progress of existing HP/LHP applicable to solar PV/T systems are outlined and analyzed. Finally, the challenges and disadvantages for the existing HP-PV/Ts including (1) high cost, (2) replying on the gravity of the working fluid owing to relatively smaller wick capillary effect; and (3) liquid film 'dry-out' occurring in the upper part of the evaporator leading to significantly reduced heat transport capacity are instructed, as well as the future development direction are clarified, which provides a reference for the further research and application of Loop Heat Pipe integrated Photovoltaic/Thermal Systems.

Keywords: Heat Pipe, Loop Heat Pipe, PV/T, Solar Energy.

1. INTRODUCTION

Climate change is now affecting every aspect of the world, causing huge numbers of environmental and social challenges today and even more tomorrow, such as extreme weather, rising sea levels and diminishing of the Arctic-sea ice (IEA, 2023). The major reason for global warming is the continuous emissions of greenhouse gases resulted from extensive fossil fuel consumption by human activities, whilst greenhouse gas emissions are reported to be now at their highest levels in history. Therefore, increasing the use of renewable energy and enhancing the efficiency of the energy systems are crucial to creating more sustainable and inclusive communities and reducing carbon emissions. Solar energy as the most abundant and free renewable energy which is available globally has been wildly concerned.

Table 1: Global installed solar capacity from 2013 to 2022(Pourasl, Barenji and Khojastehnezhad, 2023)

	Solar energy capacity (MW)				
	2018	2019	2020	2021	2022
World	489 306	592 245	720 429	861 537	1 053 115
Africa	8 150	9 493	10 819	11 628	12 641
Asia	276 406	332 854	410 326	485 413	579 573
Europe	121 603	142 272	162 795	190 143	227 799
N. America	57 664	69 656	86 493	107 172	126 443
S. America	5 512	8 562	13 164	20 795	32 773
Oceania	8 881	13 293	18 357	23 324	27 400

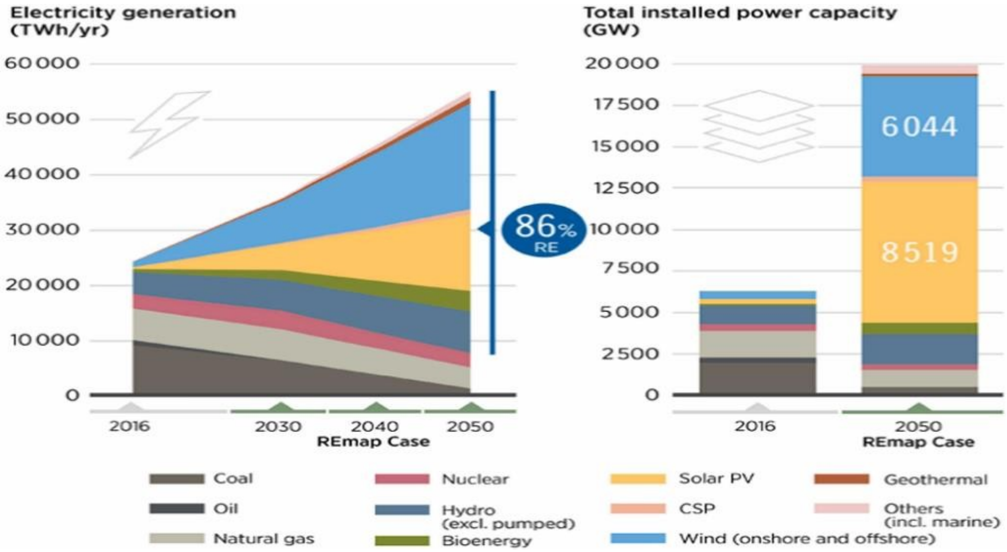

Figure 1: The contribution of energy sources in both electricity generation and total installed power capacity by 2050(Pourasl, Barenjiand Khojastehnezhad, 2023)

The two main solar energy utilization approaches are photovoltaic (PV) for electricity and photothermal (PT) for heating or hot water supply, which, however, are designed for a single function as a solar PV system for power generation or a solar thermal collector for hot water supply. At the same time, under long-term solar radiation, the accumulated heat energy of photovoltaic panels will continue to increase the panel temperature, which is an important incentive for the decrease of photoelectric conversion efficiency (Verma *et al.*, 2020). Because the increase of photovoltaic cell temperature causes a decrease of solar electrical efficiency. Furthermore, the life span of the PV cells could be shortened when the PVs are continuously operated at a higher temperature. A PV/T hybrid solar system is invented by combining photovoltaic and solar thermal system, which can produce both electricity and heat from one integrated system (Zondag *et al.*, 2005). This technology plays an important role in promoting the advancement of renewable energy technology. As the global demand for renewable energy continues to grow, technological innovation has becomea key factor driving the energy transition. The development of heat pipe solar photovoltaic technology not only improves the utilization efficiency of solar energy, but also provides a new idea for the coupling of solar energy and other renewable energy technologies, such as the combination of heat pumps, seawater desalination systems, drying systems, refrigeration systems, etc. to further improve the comprehensive utilization efficiency of energy. In addition, the heat pipe solar photovoltaic photothermal technology also has a positive significance in promoting the energy consumption revolution and the energy supply revolution. By improving energy efficiency, it promotes green and low-carbon energy consumption patterns. At the same time, as clean energy technology, it helpsto establish a diversified supply system and increase the proportion of non-fossil energy in energy supply. This paper will present the concept and advantages of HP/LHP technologies applicable to solar PV/T systems, provide a comprehensive overview on the research, development, combination and practical applications of PV/T integrated with heat pipe technologies and the relevant theories, finally assess its challenges and application potential.

2. PV/T SYSTEM

2.1. Development of PV/T System

Photovoltaic systems were first proposed by physicist Alexandre Edmund Becquerel, based on the experimental phenomenon he observed in 1839 - certain photoinduced chemical reactions generate electric currents (Chapin, Fuller and Pearson, 1954). In the following decades, the related field began to improve the PV panel in-depth research. With the development of the PV module, it is found that the system would suffer from a decline of lifetime of the solar panels and the production efficiency due to the increasing of functioning temperature (Siecker, Kusakana and Numbi, 2017). In order to enhance its performance, cooling equipment has been installed and applied in such a process. The PV/T system has combined both electricity producing and heat generating entities (Rejeb *et al.*, 2020), which not only bring heating benefits but also optimize the photovoltaic process. This concept was first proposed in 1978 by Kern and Russell, in whose experiments, the improvements of functioning process have been testified. According to its fitness to current energy situation, the investigation and research in this field is enormous and detailed. In 2002, Tripanagnostopoulos et al. (Tripanagnostopoulos, 2007) presented test results on hybrid solar systems, consisting of photovoltaic modules and thermal collectors (hybrid PV/T systems). R. Santbergen et. al. investigated the annual electrical efficiencies of the PVT systems investigated were up to 14% (relative) lower compared to pure PV systems and the annual thermal efficiencies up to 19% (relative) lower compared to pure thermal collector systems (Santbergen *et al.*, 2010).

Among them, the PV/T cooling method affects its efficiency to a large extent common cooling methods include air cooling and water cooling, different cooling methods can be selected according to the specific application needs and environmental conditions to improve the efficiency and performance of the photovoltaic system, each cooling method has its own unique advantages and application scenarios.

2.2. Air-based PV/T system

In the early exploiting process of PV/T system, air-based system---which means using air as the cooling fluid is the focus due to its low-cost and accessible features. Many novel designs have been proposed over a long period of development. In the early exploiting process of PV/T system, air-based system---which means using air as the cooling fluid is the focus due to its low-cost and accessible features. Many novel designs have been proposed over a long period of development. In the early exploiting process of PV/T system, air-based system---which means using air as the cooling fluid is the focus due to its low-cost and accessible features. Many novel designs have been proposed over a long period of development.

In 1996, Sopian proposed a double-pass air-based PV/T plate, better heat transfer performance is achieved, and capacity efficiencyis improved compared to single-pass. Ibrahim proposed a single-pass air-based system in 2009, enables air to form vortices duringthe absorption of heat, resulting in a 10% efficiency in electricity production. This technology is also widely used in the design of Building Integrated Photovoltaic Thermal (BIPVT) due to the easy handling of air.

2.3. Water-based PV/T system

Air-based PV/T system using air as a cooling material is largely limited by the natural climate. In areas with extreme temperature conditions, air cannot achieve the cooling effect. Water is better able to do this job while still maintaining its cost advantage. Garg et al. model the effect of water flow rate on heat collection capacity and calculate and analyse the optimum flow rate (Garg, Agarwal and Joshi, 1994). Ibrahim et al. analyzed the performance of different designs of water-based PV/T systems and found that the spiral design had the best performance at solar radiation of 600 w/m2 and a flow rate of 0.01 kg/s, resulting in an electrical efficiency of 11.98% (IBRAHIM *et al.*, no date). In 2007, Tripanagnostopoulosproposed a combined design which solved the limitations of water and air, acquiring better heat transfer performances (Tripanagnostopoulos, 2007).

3. HEAT PIPE: THE DEVELOPMENT, STRUCTURE

3.1. Development of heat pipe

Generally, the cooling methods of PV/T cooling methods include natural air circulation, water cooling or combination of air and water, but the shortages of them limit the translation rate. Heat pipe as cooling system was widely used in many fields such as electronic fields, mechanism field and so on, which has good cooling performance and heat translation. Meanwhile, PV/T system needs an efficient cooling way, so using heat pipe to cool PV/T system is a new way, which can provide a higher heat translation rate. The first heat pipe was invented in American Los Angeles science laboratory, then those scientists in this laboratory used heat pipe in spaceprogrammers. Gradually thereafter, heat pipes were used in the field of electronics for cooling electronics components, it was also used for machines and electric motors. In the 1970s, heat pipes were used in medical scalpels, then the new area of heat pipes applications is energy engineering.

3.2. Structure and operating principle

For heat pipes, conventional heat pipes are one of the most typical samples. Heat pipes (HPs) are the heat transfer medium owing to a high performance. Key components of HP comprise an adiabatic section, a condenser section and an evaporator section, while theheat pipe heat exchanger (HPHE) doesn’t have an extra dynamic part to provide power for working medium circulation.

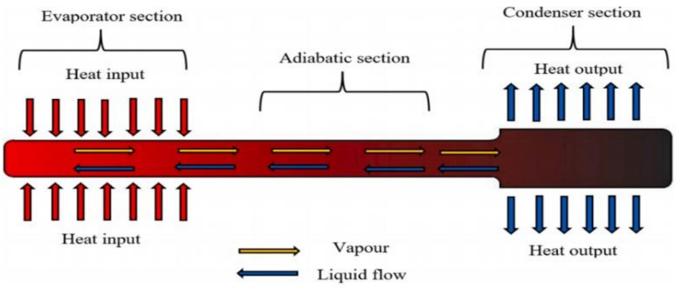

Figure 2: Heat Pipe working schematics (Senthil et al.*, 2021a)*

As Fig. 2. represents, evaporator section is exposed to heat source. In this part, the liquid inside the pipe, known as the working fluid, is heated up and turns into vapor flow (Abdelkareem *et al.*, 2022). Simultaneously, the vapor flow carries away heat, which is latent heat of evaporation, and transfers the thermal energy to another side, called the condenser section, driven by the density difference. Subsequently, the vapor condenses into liquid, emitting latent heat. Then under the action of capillary force, the condensed liquid turns back to the evaporation section, completing a closed cycle. The medium part, adiabatic section is used to insulate the working fluid from external heat condition as much as possible.

3.3. Classification of heat pipes

Senthil et al. (Senthil *et al.*, 2021b) indicated the heat pipe classification on the basis of wicks, liquid flow and features. Heat pipes can be divided into different according to the different operating temperatures: low temperature heat pipes (-273-0℃), normal temperature heat pipes (0-250℃), medium temperature heat pipes (250-450℃), high temperature heat pipes (450-1000℃), etc.

Table 2: Different operating temperature classifications

temperature	classifications
-273-0℃	low temperature heat pipes
0-250℃	normal temperature heat pipes
250-450℃	medium temperature heat pipes
450-1000℃	high temperature heat pipes

According to the reflux power of working fluid, heat pipes can be divided into heat pipes with core, two phase closed heat siphon(gravity heat pipe or heat pipe without core), magnetic fluid power heat pipe, osmotic heat pipe, etc.

Table 3: Reflow power for different working fluids

The reflux power of the fluid	classifications
Capillary force	Heat pipes with core
Gravity	Two phase closed heat siphon (gravity heat pipe or heat pipe without core)
Magnetic fluid	Magnetic fluid power heat pipe
Electrodynamic force	Osmotic heat pipe

Heat pipe is a kind of efficient heat transfer equipment, which uses the phase change process of the working medium to transfer heat. The working principle of the heat pipe is based on the working medium absorbing heat in the evaporation section and evaporating into steam, and then releasing heat in the condensing section and condensing back to the liquid state and returning tothe evaporation section through capillary action or gravity action, so as to achieve rapid heat transfer. In order to better understand the heat pipes used in solar photovoltaics and photovoltaic/thermoelectric systems, the following sections provide a brief overview of heat pipes from the perspective of classification and operation.

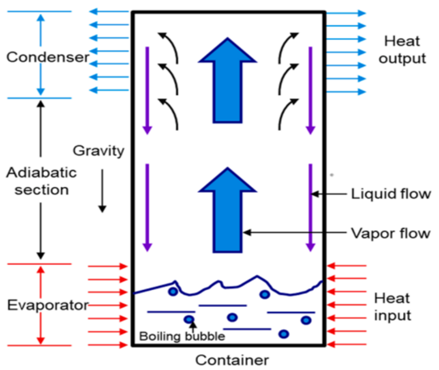

Figure 3: Schematic diagram of Gravity heat pipe

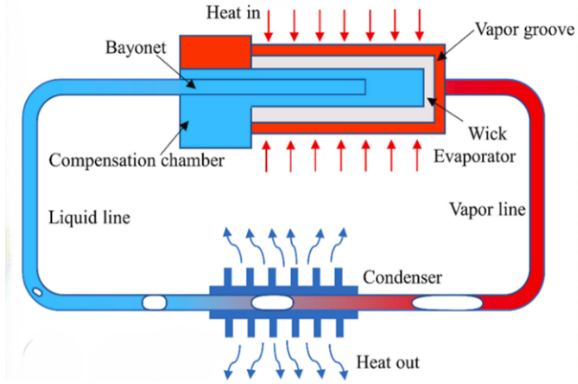

Figure 4: Schematic diagram of Loop heat pipe

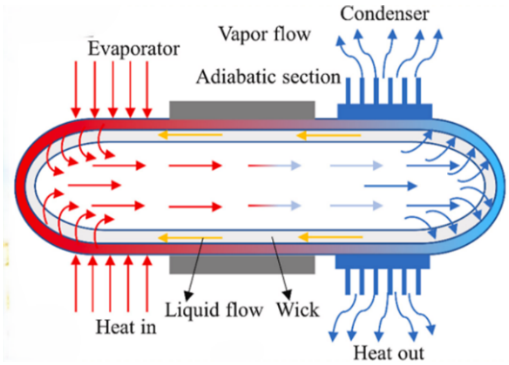

Figure 5: Schematic diagram of Conventional tubular heat pipe

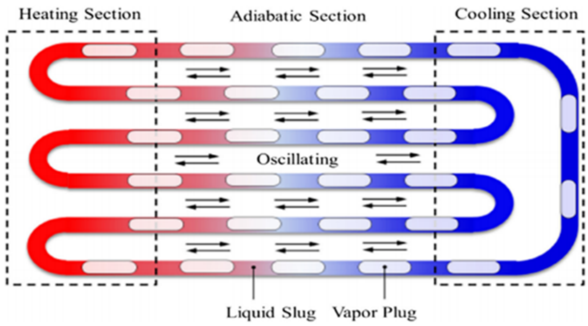

Figure 6: Schematic diagram of Pulsating heat pipe

Gravity heat pipe is a kind of high efficiency heat transfer equipment, which uses gravity to realize working fluid circulation, and is widely used in geothermal energy development, solar energy utilization and other fields. The gravity heat pipe consists of three parts: evaporator, adiabatic section and condenser section. The condenser section generates a vacuum in the sealed pipe and partially fills the pipe with heat transfer fluid. Fig.3 describes the basic structure and operation of the TPCT. The gravity heat pipe has the following advantages: the gravity heat pipe has high efficiency of heat transfer and can transmit heat stably over a long distance; The gravity heat pipe system runs stably and has low maintenance cost because of the working medium circulation by gravity. In geothermal energy development, gravity heat pipe technology has high economic benefits, can effectively reduce energy consumption and reduce environmental pollution.

A Loop Heat Pipe (LHP) is an efficient heat transfer device that is a variant of heat pipe technology. It realizes long-distance transmission and uniform distribution of heat by circulating the working medium in the closed loop. As shown in Fig.4, it consists of an evaporator, a condenser, a compensation chamber, a transmission tube, a working medium, and a liquid suction core. The evaporator is the heat source contact part, where the working medium absorbs heat and evaporates into steam. Steam condensersrelease heat and condense it back into a liquid state. The compensation chamber stores the liquid working medium and provides the buffer and recharge of the working medium. The evaporation line and liquid return line connect the evaporator and condenser to allow the flow of steam and liquid working medium. The suction core is usually located in the evaporator and compensation chamber and provides capillary force to help the liquid working fluid return to the evaporator. Loop heat pipes can efficiently transfer heat over long distances and are suitable for applications where long-distance heat dissipation is required. Through the uniform distribution and circulation of the working medium, the loop heat pipe can realize the isothermal operation of the equipment. Due to its closed circulation system, the loop heat pipe can run stably for a long time with low maintenance requirements.

The basic components of Conventional tubular heat pipes include container, working liquid and internal capillary structure. Containers are generally made of copper, stainless steel and other metal materials, with good thermal conductivity; The working liquid varies according to the temperature range of the specific application scenario, the common ones are water, ethanol, ammonia, etc. The internal capillary structure is responsible for promoting the circulation of the working fluid. This structural design allows the heat pipe to efficiently absorb heat from the heat source and transfer it quickly to the cold end, thus achieving effective heat transfer. As shown in Fig.5, in the working process, the heat pipe first absorbs heat from the heat source, so that the working liquid in the container evaporates to form steam. These vapors travel along the inner wall of the vessel towards the cold end, where they condense at lower temperatures, releasing latent heat. The condensed liquid is transported back to the hot end under the action of the capillary structure, and the above cycle is repeated. This phase change process is continuously cycled, allowing the heat pipe to continuously and efficiently transfer heat from the hot end to the cold end. With the above excellent working principle, traditional tubular heat pipes have shown excellent performance in many fields. In the field of electronic device heat dissipation, they can effectively dissipate a lot of heat generated by core components such as cpus and graphics cards to avoid overheating and affecting performance. In the field of aerospace, they are widely used in the temperature control of satellites, rockets and other airborne equipment, playing a key role in the harsh outer space environment.

Pulsating heat pipe (PHP) is divided into two types: closed loop PHP and open loop PHP. The ends of the two tubes are not connected to an open loop PHP. Instead, a closed loop system is formed by connecting the two ends of the tube to produce a closed system. Fig.6 shows the main structure and operation of the closed-loop system. PHP is a heat transfer device with an elongated inner diameter bent into a snake shape. The inside of the capillary tube is vacuumed and partially filled with working medium. The drivingforce of the circulation in the working tube is the continuous growth and rupture of the bubble in the tube, resulting in the pulsating movement of the fluid, rather than being generated by the capillary force in the wick structure of the traditional heat pipe. Pulsating heat pipe without any mechanical moving parts, simple structure, high reliability. Due to the use of latent heat of phase change, theheat transfer efficiency is extremely high, which is dozens of times higher than that of metal thermal tubes. At the same time, the pulsating heat pipe is light in weight, small in size and low in manufacturing cost, which is very suitable for applications requiring rapid and effective heat transfer. In the field of electronic equipment heat dissipation, pulsating heat pipes can effectively reduce the operating temperature of chips and circuit boards and improve the reliability and service life of equipment. In solar power generation, pulsating heat pipes can be used to absorb and transmit solar heat energy to improve the power generation efficiency of panels.

4. HEAT PIPE PV/T SYSTEM

Except for traditional PV/T system, the heat pipe solar collector has also been concerned and studied by scholars all over the world. Compared with the traditional air-cooling or water-cooling collectors, a new system based on heat pipes has better temperature control performance for photovoltaic panels when using polymerized photovoltaic panels at the same time. Specifically, compared with water-based and air-based collectors, it has the advantage that it can operate effectively in different climate conditions as long as appropriate working fluid is selected. In 2014, Moradgholi, Nowee and Abrishamchi (Moradgholi, Nowee and Abrishamchi, 2014) studied a more energy efficient collector, which can generate more electricity and recover more heat at the same time. The basic component is a two-phase closed thermal siphon (TPCT) PV/T flat with methanol as working medium. The study shows the performance of collectors in different weather conditions both in spring and summer, which results show that the surface temperature of the photovoltaic panel with the heat dissipation of working medium decreases significantly, and the maximum cooling range reaches 15℃. Compared to a conventional single PV system, the total efficiency (the sum of optical efficiency and thermal efficiency) increased by 15.3% in spring and 44.38% in summer, respectively. This finding makes HP-PV/T systems of significant application value for further commercial development.

4.1. Heat pipe PV/T: Structure

4.1.1 Gravity heat pipe PV/T system

Gravity auxiliary heat pipe (GHP) is essentially a passive two-phase heat transfer tool. So far, many researchers have used GHP as a means of heat transfer and integrated them with PV/T collectors. Zhang et al. performed sensitivity analyses on the geometryof evaporators and condensers, the wall temperature of the working fluid at the filling and operating envelope, and the thermal resistance of UDGHP under the criteria of local drying and flooding limits (Zhang *et al.*, 2022). Zhang et al. introduced gravity- assisted heat pipes (HP) to overcome the freezing and corrosion problems associated with traditional water-based photovoltaic/thermal (PV/T) solar collectors. A series of experimental studies showed that photothermal and photovoltaic efficiency increased with the increase of water mass flow rate, the diameter of the condenser section of the heat pipe and the number of heat pipes. However, when these three variables are greater than their respective specific values, the growth gradient becomes smaller. The photothermal efficiency increases first and then decreases with the increase of the cross-section length of the heat pipe condenser, indicating that the optimal length is 12 mm (Zhang *et al.*, 2019).

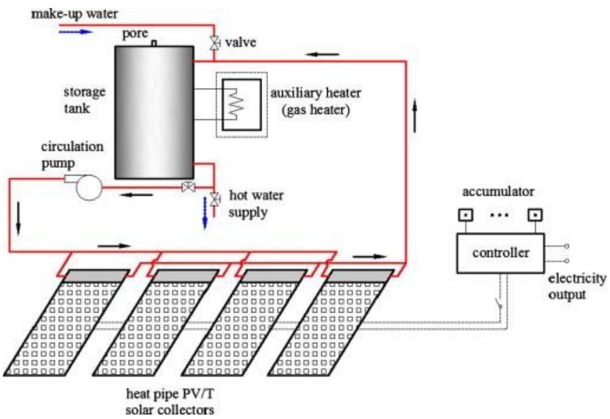

Figure 7: Graphical diagram of the GHP-PV/T system (Gang *et al.*, 2012)

4.1.2 Loop heat pipe PV/T system

Focusing on the research, the constituent parts of general LHP-PV/T are likely the one as Fig. 8 depicts, but not the same. Fig. 8 indicates the overall system by a diagram. In accordance with requirements, a controller could determine if the electricity should besupplied to consumers or to an accumulator battery. Besides, heat storage tank (with auxiliary heater) is usually the source of hot water supply for buildings or homes, whose water circulation is managed by valves and the pump.

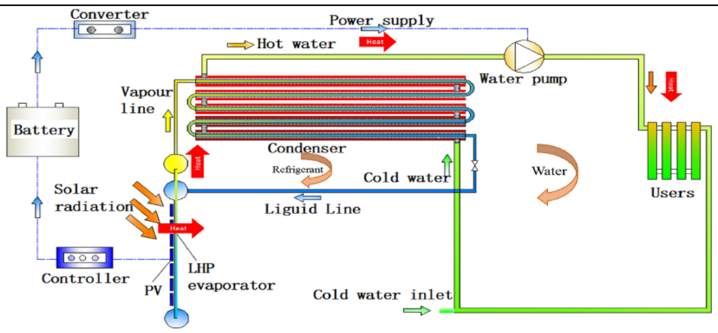

Figure 8: Graphical diagram of the LHP-PV/T system (Yu *et al.*, 2022)

The core of loop heat pipe PV/T system is to use loop heat pipe to achieve effective cooling and heat recovery of photovoltaic modules. The loop heat pipe is composed of an evaporation section, conveying section and condensing section. The heat transfer can be realized efficiently by the phase change of working medium. The photovoltaic module is installed on the evaporation section of the loop heat pipe, and the waste heat generated by absorbing solar radiation is taken away by the loop heat pipe, which reduces the working temperature of the photovoltaic module and improves the power generation efficiency. At the same time, the heat recovered by the condensing section can be used for heating, hot water and other purposes, achieving a high degree of coupling between photovoltaic power generation and heat utilization. In addition, by optimizing the design of loop heat pipes and the selection of working medium, the system can achieve efficient heat transfer and utilization under different climatic conditions.

4.1.3 Conventional tubular heat pipe PV/T system

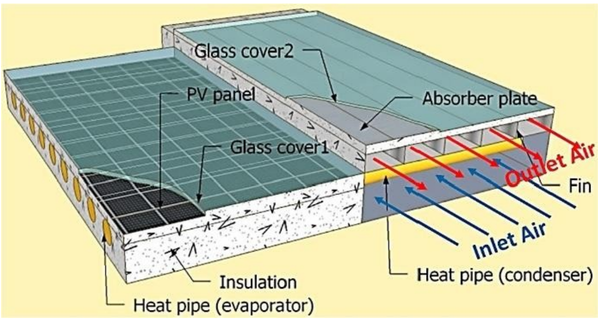

Figure 9: Graphical diagram of conventional tubular heat pipe PV/T system (Fan, Kokogiannakis and Ma, 2019)

Conventional tubular heat pipe photovoltaic/thermal (PV/T) system is an efficient energy utilization technology that integrates solarpower generation and thermal functions. As shown in Fig.9, the system is composed of photovoltaic cells, heat pipe, evaporator, condenser, working medium, liquid absorbing core, insulating material and transparent cover. Photovoltaic cells are responsible for converting sunlight into electricity, while generating heat; The heat pipe uses the phase change process of the working medium to absorb the heat generated by the photovoltaic cell through the evaporator and transfer the heat to the condenser; In the condenser, the working medium releases heat and condenses back to the evaporator, forming a closed-loop cycle. The suction core provides capillary force in the evaporator to help the liquid flow back. Insulation reduces heat loss, while transparent covers protect the photovoltaic cells and allow sunlight to penetrate. The whole system is cleverly designed to provide electricity while recycling and utilizing the heat generated by photovoltaic cells to achieve efficient and comprehensive utilization of energy.

4.2. Summary of the heat pipe PV& PV/T systems

The energy performance of the solar heat pipe mainly depends on the working efficiency of the heat pipe, the photothermal conversion efficiency of the collector, the heat storage efficiency of the heat reservoir and the heat transfer efficiency of the heat exchanger. The following is the description of the energy performance of the solar heat pipe:

1) The heat transfer efficiency of solar heat pipe refers to its ability to transfer heat received from the sun to the working fluid. High heat transfer efficiency ensures that solar heat pipes effectively convert solar radiation into heat energy. Under normal circumstances, the higher the heat transfer efficiency, the better the performance of solar heat pipes.
2) The thermal conductivity of solar heat pipes is also crucial to their overall thermal efficiency. High-quality solar heat pipes should have high thermal conductivity to ensure that heat energy can be quickly and efficiently transferred to the working fluid. The thermal conductivity will directly affect the heat transfer efficiency and the overall performance of the solar heat pipe.
3) The PV/T system using heat pipes can recover 50% of the loss of light efficiency under high intensity solar irradiation; The heat pipe cooling method can make the temperature difference between the solar cell and the working medium lower, the flat PV/T system makes the temperature difference between the working medium and the solar cell not more than 3 ° C, most of the time is kept at about 2 ° C, which helps to improve the conversion and utilization of high-grade energy; The heat pipe PV/Tsystem enhances the photothermal performance of the system due to the low night heat loss, and the annual heat gain can beincreased by 33.20% compared to the traditional PV/T system.

Comprehensive consideration of these energy performance indicators can help select solar heat pipes suitable for specific application needs, so as to improve the energy conversion efficiency and performance of solar energy systems.

Table 4: Summary of some representative structure of the heat pipe PV/T collectors.

Authors	Type of condensers (heat exchangers) and HPs	Research methods	Energy performance
Chen et al. (Chen *et al.*, 2009)	No condenser (solar water heater); Double pipe TPCT;	Long-term outdoor experiment;	After investigation on its long-term thermal performance, compared with four types of conventional solar water heater, this system reduced part of heat loss, and its efficiency increased by 18%;
Zhang et al. (Zhang *et al.*, 2013)	Condensing heat exchanger; LHP; (integrated with heat pump)	Mathematical model and controlled indoor experiment;	The actual system was modified referring to the model. Eventually, under the given condition, PV/LHP module has an electrical efficiency of 10%, thermal efficiency of 40%, overall efficiency of 50% and coefficient of 8.7 which is 2-4 times of the conventional solar/air heat pump system;
Ziapour and Khalili (Ziapour and Khalili, 2016)	Water condenser; Loop type TPCT;	Numerical modeling of the programmed system by EES, model simulation and outdoor experiment;	In the case of one and four mini loops, the thermal efficiency of collector are 11% and 60% separately, experimentally and numerically.
Diallo et al. (Diallo *et al.*, 2019)	PCM heat exchanger; MCLHP;	Numerical analysis of the overall model; evaluate the impact of parameters;	In the designed condition, the electrical, thermal efficiencies of novel PV/LHP are 12.2% and 55.6% respectively. Compared to conventional PV/LHP, the energy efficiency of new system has enhanced by 28% and COP has been 2.2 times higher;
Li and Sun (Li and Sun, 2018)	Water condenser; LHP; (heat pump)	Mathematical model, performance simulation and experimental verification;	According to the test results in Qinghuangdao, the life period cost of PV-LHP/SAHP could reduce 29.6% than the traditional ASHP;
Yu et al. (Yu *et al.*, 2019)	Coaxial tube heat exchanger; MCLHP;	Outdoor experiment and performance evaluation;	Under specific and real weather conditions, the solar thermal efficiency is 25.2%-62.2%, while electrical efficiency is 15.59%-18.34% at 10:00-15:00 of a day;
Ren et al. (Ren *et al.*, 2020)	Coaxial tube heat exchanger; MCLHP;	Dynamic distributed parameter model and indoor experiment;	To analyze the cost reduction potential, Ren et al. mainly focus on the parameter optimization. One consequence is that, when decrease the HP number from 30 to 6, decline of thermal and electrical efficiency are 4.63% and 0.12%, whereas the manufacturing cost of system reduces 28.58%;
Li et al. (Li *et al.*, 2022)	Concentric copper tube heat exchanger; LT;	Test and simulation on prototypes; case study;	Through the control variable method, under the filling ratio of 26.5%, 34.8% and 43.2%, Li rt al. obtained the exergy efficiency and thermal efficiency within the working fluid of water, ethanol and R134A.

4.3. Outlook of HP-PV/T

First of all, the solar heat pipe system has a broad application prospect in the field of construction. With the acceleration of urbanization and the development of the construction industry, the problem of traditional energy consumption such as heating and lighting has become increasingly prominent. The solar heat pipe system can use solar energy for heat collection and energy storage, provide clean and green heat energy for the building, and fundamentally solve the problem of energy consumption and environmental pollution. Secondly, the application of solar heat pipe system in industrial production also has great potential. With the acceleration of the industrialization process, the energy consumption required for industrial production continues to increase, and traditional energy consumption methods such as coal burning not only cause environmental pollution, but also cause huge waste of resources. The solar heat pipe system can use solar energy for heat collection and energy storage, provide renewable and clean heat energy for industrial production, and realize energy recycling and saving.

In general, the solar heat pipe system, as an efficient and environmentally friendly way of energy utilization, has great prospects for development. With the continuous progress and promotion of technology, solar heat pipe systems will play an important role in construction, industry and other fields, and contribute to the sustainable development of human society. It is hoped that the solar heat pipe system can be more widely used in the future and bring more benefits to our lives and the environment.

5. CONCULUSION

As a passive and efficient thermal management technology, the application of heat pipe equipment in PV/T systems offers new solutions to existing problems and has gained increasing attention in the past years, especially in the field of innovative technologies. Some shortcomings of current PVT heat pipe systems, as well as challenges and future recommendations are summarized below.

1) The combination of solar photovoltaic technology and HP system has a higher cost than the traditional solar system, which is mainly reflected in the design of the evaporation end heat pipe, the combined cost of photovoltaic panel and heat pipe and the maintenance cost in the later period.
2) Replying on the gravity of the working fluid owing to relatively smaller wick capillary effect.
3) Due to the unreasonable design of the evaporator at the time of design, such as poor capillary structure design, low internal pressure of the evaporator, high length to diameter ratio of heat pipes and other reasons, it may cause the liquid film to "dry", resulting in a significant reduction in heat transfer capacity.
4) For microchannel heat pipes, the integration with nanotechnology is an important way to improve heat transfer, and nanotechnology has not fully realized its potential in heat pipe PV/T systems, so the research potential is huge.
5) The application of solar photovoltaic solar heat pipe system integration can be expanded to a broader field, such as combiningwith the heat pump system of automobiles, especially new energy vehicles, in the winter heating system can make greater useof the heat and electricity generated by solar energy.

6. ACKNOWLEDGEMENT

The authors would acknowledge their appreciation to the financial supports from Fundamental Research Funds for the CentralUniversities (Project No. 2682023CX022) and SWJTU-Leeds Joint School “Young Talent” Scientific Research Funds.

7. REFERENCES

Abdelkareem, M.A. et al. (2022) ‘Heat pipe-based waste heat recovery systems: Background and applications’, Thermal Science and Engineering Progress, 29, p. 101221. Available at: https://doi.org/https://doi.org/10.1016/j.tsep.2022.101221.

Chapin, D.M., Fuller, C.S. and Pearson, G.L. (1954) ‘A New Silicon p-n Junction Photocell for Converting Solar Radiation into Electrical Power’, Journal of Applied Physics, 25, pp. 676–677. Available at: https://doi.org/10.1063/1.1721711.

Chen, B.R. et al. (2009) ‘Long-term thermal performance of a two-phase thermosyphon solar water heater’, Solar Energy, 83(7), pp. 1048–1055. Available at: https://doi.org/10.1016/j.solener.2009.01.007.

Diallo, T.M.O. et al. (2019) ‘Energy performance analysis of a novel solar PVT loop heat pipe employing a microchannel heat pipe evaporator and a PCM triple heat exchanger’, Energy, 167, pp. 866–888. Available at: https://doi.org/https://doi.org/10.1016/j.energy.2018.10.192.

Fan, W., Kokogiannakis, G. and Ma, Z. (2019) ‘Optimisation of life cycle performance of a double-pass photovoltaic thermal-solar air heater with heat pipes’, Renewable Energy, 138, pp. 90–105. Available at: https://doi.org/10.1016/J.RENENE.2019.01.078.

Gang, P. et al. (2012) ‘Annual analysis of heat pipe PV/T systems for domestic hot water and electricity production’, Energy Conversion and Management, 56, pp. 8–21. Available at: https://doi.org/10.1016/J.ENCONMAN.2011.11.011.

Garg, H.P., Agarwal, R.K. and Joshi, J.C. (1994) ‘Experimental study on a hybrid photovoltaic-thermal solar water heater and its performance predictions’, Energy Conversion and Management, 35(7), pp. 621–633. Available at: https://doi.org/10.1016/0196- 8904(94)90045-0.

IBRAHIM, A. et al. (no date) ‘Performance of Photovoltaic Thermal Collector (PVT) With Different Absorbers Design’, msra

[Preprint]. IEA (2023) ‘World Energy Outlook.’, pp. 23–28.

Li, H. and Sun, Y. (2018) ‘Operational performance study on a photovoltaic loop heat pipe/solar assisted heat pump water heating system’, Energy and Buildings, 158, pp. 861–872. Available at: https://doi.org/10.1016/j.enbuild.2017.10.075.

Li, Z. et al. (2022) ‘Experimental investigation and annual performance mathematical-prediction on a novel LT-PV/T system using spiral-descent concentric copper tube heat exchanger as the condenser for large-scale application’, Renewable Energy, pp. 257–270. Available at: https://doi.org/10.1016/j.renene.2022.01.079.

Moradgholi, M., Nowee, S.M. and Abrishamchi, I. (2014) ‘Application of heat pipe in an experimental investigation on a novel photovoltaic/thermal (PV/T) system', Solar Energy, 107, pp. 82–88. Available at: https://doi.org/https://doi.org/10.1016/j.solener.2014.05.018.

Pourasl, H.H., Barenji, R.V. and Khojastehnezhad, V.M. (2023) 'Solar energy status in the world: A comprehensive review', EnergyReports, 10, pp. 3474–3493. Available at: https://doi.org/10.1016/J.EGYR.2023.10.022.

Rejeb, O. et al. (2020) 'Novel solar PV/Thermal collector design for the enhancement of thermal and electrical performances', Renewable Energy, 146, pp. 610–627. Available at: https://doi.org/https://doi.org/10.1016/j.renene.2019.06.158.

Ren, X. et al. (2020) 'Assessment of the cost reduction potential of a novel loop-heat-pipe solar photovoltaic/thermal system by employing the distributed parameter model', Energy, 190, p. 116338. Available at: https://doi.org/10.1016/j.energy.2019.116338.

Santbergen, R. et al. (2010) 'Detailed analysis of the energy yield of systems with covered sheet-and-tube PVT collectors', Solar Energy, 84(5), pp. 867–878. Available at: https://doi.org/10.1016/J.SOLENER.2010.02.014.

Senthil, R. et al. (2021a) 'A holistic review on the integration of heat pipes in solar thermal and photovoltaic systems', Solar Energy,227(August), pp. 577–605. Available at: https://doi.org/10.1016/j.solener.2021.09.036.

Senthil, R. et al. (2021b) 'A holistic review on the integration of heat pipes in solar thermal and photovoltaic systems', Solar Energy.Elsevier Ltd, pp. 577–605. Available at: https://doi.org/10.1016/j.solener.2021.09.036.

Siecker, J., Kusakana, K. and Numbi, B.P. (2017) 'A review of solar photovoltaic systems cooling technologies', Renewable and Sustainable Energy Reviews, 79(July 2016), pp. 192–203. Available at: https://doi.org/10.1016/j.rser.2017.05.053.

Tripanagnostopoulos, Y. (2007) 'Aspects and improvements of hybrid photovoltaic/thermal solar energy systems', Solar Energy, 81(9), pp. 1117–1131. Available at: https://doi.org/https://doi.org/10.1016/j.solener.2007.04.002.

Verma, S. et al. (2020) 'Cooling techniques of the PV module: A review', Materials Today: Proceedings, 38, pp. 253–258. Availableat: https://doi.org/10.1016/j.matpr.2020.07.130.

Yu, M. et al. (2019) 'Experimental Investigation of a Novel Solar Micro-Channel Loop-Heat-Pipe Photovoltaic/Thermal (MC-LHP- PV/T) System for Heat and Power Generation', Applied Energy, 256. Available at: https://doi.org/10.1016/j.apenergy.2019.113929.

Yu, M. et al. (2022) 'Experimental investigation of a novel vertical loop-heat-pipe PV/T heat and power system under different height differences', Energy, 254, p. 124193. Available at: https://doi.org/10.1016/J.ENERGY.2022.124193.

Zhang, T. et al. (2019) 'Experimental, study and design sensitivity analysis of a heat pipe photovoltaic/thermal system', Applied Thermal Engineering, 162, p. 114318. Available at: https://doi.org/10.1016/J.APPLTHERMALENG.2019.114318.

Zhang, T. et al. (2022) 'Comparative and sensitive analysis on the filling, operating and performance patterns between the solar gravity heat pipe and the traditional gravity heat pipe', Energy, 238, p. 121950. Available at: https://doi.org/10.1016/J.ENERGY.2021.121950.

Zhang, X. et al. (2013) 'Characterization of a solar photovoltaic/loop-heat-pipe heat pump water heating system', Applied Energy, 102, pp. 1229–1245. Available at: https://doi.org/https://doi.org/10.1016/j.apenergy.2012.06.039.

Ziapour, B.M. and Khalili, M.B. (2016) 'PVT type of the two-phase loop mini tube thermosyphon solar water heater', Energy Conversion and Management, 129, pp. 54–61. Available at: https://doi.org/10.1016/j.enconman.2016.10.004.

Zondag, H.A. et al. (2005) PVT roadmap. A European guide for the development and market introduction of PVT technology. Netherlands. Available at: https://doi.org/https://doi.org/.

#298: Research on multi-load forecasting in regional integrated energy systems

Yuxin LIU[1], kai XUE[1], Xiaoyang HU[1], Kejie OU[1], Daotong CHONG[1], Jinshi WANG[1,2*], Junjie YAN[1]

[1] State Key Laboratory of Multiphase Flow in Power Engineering, Xi'an Jiaotong University, Xi'an, 710049, China
[2] School of Energy Engineering, Yulin University, Yulin 719000, China
* Corresponding author. E-mail: wangjinshi@mail.xjtu.edu.cn

Abstract: The Regional Integrated Energy Systems (RIES) amalgamate traditional fossil fuels with a variety of renewable energy sources such as solar and wind power. By utilizing energy in a cascading manner, these systems can efficiently meet diverse l oad demands including electricity, heat, and cooling, playing a crucial role in energy conservation and carbon reduction. Accurate load forecasting is essential for the flexible, reliable, and efficient operation of these systems. This study proposes a multi-task learning (MTL) model based on Residual Neural Networks (ResNet) and Gated Recurrent Units (GRU) for multi-load forecasting. Initially, a combination of Local Outlier Factor and K-Means++ algorithms were employed for data anomaly cleaning. Subsequently, establishing the prediction model involves using multi-layer ResNet for data feature extraction and GRU network for further exploration and prediction of the temporal features of multi-load data. Finally, employing MTL to achieve joint forecasting of multi- loads. Applying the proposed method with multi-load data from Arizona State University (ASU) Tempe campus case conducting multi-load forecasting experiments in summer, winter, and transitional seasons cases, and comparing the results with other forecasting models. The results indicate that the model in this study has the highest prediction accuracy with MAPE for electricity load at 1.67%, 1.37%, 1.44%, heat load at 2.43%, 1.22%, 1.35%, and cooling load at 0.79%, 0.99%, 1.12%. Additionally, comparing the running times of different models reveals that the model in this study has the shortest runtime, demonstrating the highest computational efficiency.

Keywords: Regional Integrated Energy System; Multi-load forecasting; Residual Network; Gated Recurrent Unit; Multi-Task Learning

1. INTRODUCTION

As global energy consumption continues to rise, traditional energy sources are no longer sufficient to meet demand, making research into renewable energy increasingly significant (Liu et al. 2023). The Regional Integrated Energy System (RIES) combines traditional fossil fuels and various renewable energy sources such as solar and wind power. Through a cascading energy utilisa tion approach, it efficiently meets the demands for electricity, heat, and cooling, making a significant contribution to energy conservation and carbon reduction (Azeem et al. 2021). Accurate load forecasting is essential for ensuring the flexibility and efficiency of regionally integrated energy systems, serving as the primary basis for energy management and optimal dispatch (Habbak et al. 2023).

Currently, research on multivariate load forecasting for RIES primarily falls into two categories: individual load forecastin g and joint load forecasting for multiple loads. In the area of individual load forecasting, studies on single load predictions for electricity, heat, and cooling have matured. Many modern intelligent forecasting methods optimise through adjustments in model structures and the incorporation of optimisation algorithms. For example, this paper (Kim et al. 2019) employed the RN N model's excellent nonlinear dynamic characteristics to achieve strong short-term electricity load forecasting results. This paper (Kong et al. 2019) utilised LSTM recurrent neural networks to develop a framework that significantly surpassed other competing algorithms in predictive performance. this paper.(Chitalia et al. 2020) analysed factors impacting load prediction outcomes, selecting nine different neural network modelsto study their robustness across different use cases, finding that models such as LSTM, A-LSTM, BiLSTM, and A-BiLSTM typically yield favourable results.For joint load forecasting, this paper (Rana et al. 2014) proposed an improved neural network based on theMarkov chain (MC-INN) which achieved excellent forecasting accuracy. This paper (Tan et al. 2020) developed the MTL-LSSVM model, which improved the average prediction accuracy by 18.60% and reduced computation time by 35.22% compared to the LSSVM model. This paper (Yuting et al 2021) combined support vector regression (SVR) with the particle swarm optimization (PSO) algorithm. this paper (Wu et al. 2021) proposed a model merging convolutional neural networks (CNN) based on attention mechanisms with long short-term memory networks (LSTM) and bidirectional long short-term memory networks (BiLSTM), enhancing prediction accuracy. This paper (Huang et al. 2023) also achieved optimal fitting accuracy with a similar CNN+LSTM+BiLSTM model.

Building upon existing research, this paper explores the strong interactions and coupling characteristics of multi-energy load data. It emphasises the multi-energy interactive coupling and temporal characteristics of load data by incorporating ResNet and GRU residual structures and introducing a multitask learning approach. The proposed ResNet-GRU-MTL multivariate load forecasting model for RIES utilises data-sharing capabilities to improve the prediction accuracy for regional integrated energy systems.

Traditional load forecasting primarily focuses on a single load, while research on regional integrated energy systems (RIES) requires the coordination of multiple energy systems and consideration of the complex coupling relationships between various energy loads to achieve accurate multivariate load forecasting. This ensures optimal system operation and supports energy conservation and carbon reduction efforts.

2. DATA PREPROCESSING AND CORRELATION ANALYSIS

To ensure the maximum performance of the model, it is necessary to consider various features that a ffect load forecasting, such ashistorical load data, historical weather data, and calendar data. This paper uses the RIES dataset from Arizona State Univers ity Tempe campus as a case study, utilizing data from 1st January 2016 to 31st December 2019, including electricity, heat, and cooling load data with a sampling period of 1 hour. Weather data is sourced from the nearest Phoenix International Airport weather station, including temperature, humidity, pressure, wind speed, and surface radiation wavelength, with a data collection time step of 1 hour.Calendar data adopts the local holiday rules of Arizona.

2.1. Load Data Preprocessing

The dataset contains numerous spurious error points which, if not cleaned, could lead to significant prediction inaccuracies. Thus, this paper opts to use a combination of the Local Outlier Factor (LOF) and an improved K-Means clustering algorithm (K-Means++)for data cleansing. The LOF algorithm, a density-based outlier detection method, operates on the principle of comparing the local density of a given data point with that of its neighboring points. Initially, the local density is calculated, defined as the number of points within a unit volume. The lower the density of the point p, the more likely it is to be classified as an outlier. For each data point p, the k-nearest neighboring points are first identified

Next, for each data point, compute the local density of each point within its neighboring points, and then calculate the *LOF* value of p, as represented in Equation 1:

Equation 11: LOF value of point p.

$$LOF(p) = \frac{1}{k} \sum_{q \in N(p)} \frac{\rho(q)}{\rho(p)}$$

Where:

- $\rho(p)$ = probability of nearest neighboring points to p

The higher the LOF value produced by this formula, such as when the density of p is greater than 1, the more likely it is that p is an outlier. Conversely, a smaller LOF value, such as when the density of p is less than 1, indicates that p is closer to oth er points in itsneighboring points and is less likely to be an outlier. By inputting the electricity, heat, and cooling data into the model for LOF calculation, the processed results are shown in Figure 1. The LOF method detected 84, 113, and 106 outliers in the electricity, heat, and cooling loads, respectively.

From the previous section, it is clear that following the use of LOF for outlier detection, most anomalous mutation data were correctly identified and processed. However, some mutated outliers still remain undetected and unprocessed. Therefore, this section continues to utilise clustering algorithms for more precise identification of data anomalies. In this study, the improved K-means++ algorithm is used instead of the traditional K-Means algorithm to enhance the selection of initial centroids, resulting in more stable clustering outcomes and higher quality clusters. Here are the specific steps:

Initially, the clustering points are initialized by randomly choosing a data point as the first cluster centre. Subsequently, the next clustering centre is selected based on a certain probability. This process continues until K initial clustering centres are selected. Then, the data points are assigned to the clusters of their nearest clustering centres. Finally, the data points within each cluster are updated and iterated until the clustering centres no longer change or the maximum number of iterations is reached.

Using the LOF-K-means++ model, the sample data in this research were clustered and outliers were identified across six categories with similar loads. The clustering results for the cooling load are illustrated in Figure 2. It is evident that post-model processing, outliers in each cluster were accurately pinpointed and labelled.

Based on the analysis, the results of identifying anomaly mutation values in the categories of electricity, heat, and cooling clusters are shown in Table 1. It can be observed from the table that the data set for this case study has the highest number of anomaly mutation values in electricity load and the lowest in heat load.

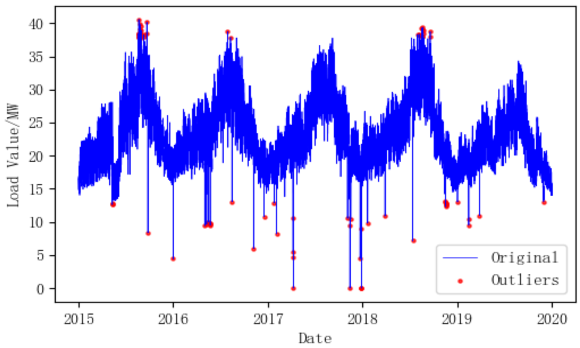

(a) Electricity load

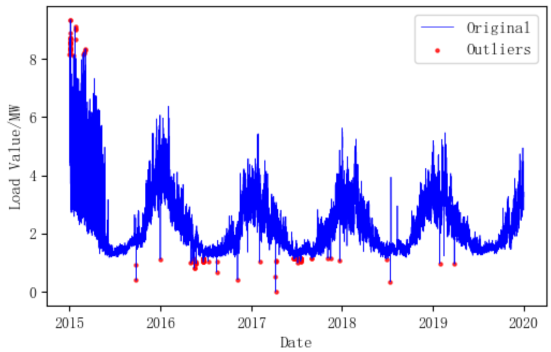

(b) Heat Load

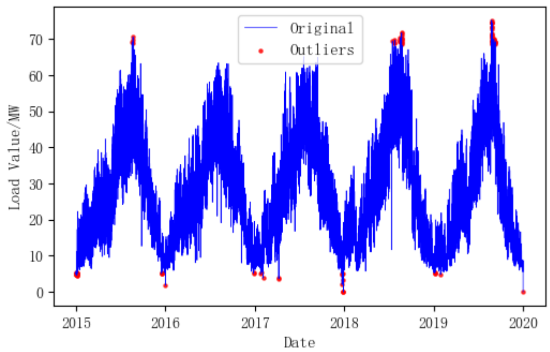

(c) Cooling Load

Figure 1: Load LOF Outlier Detection

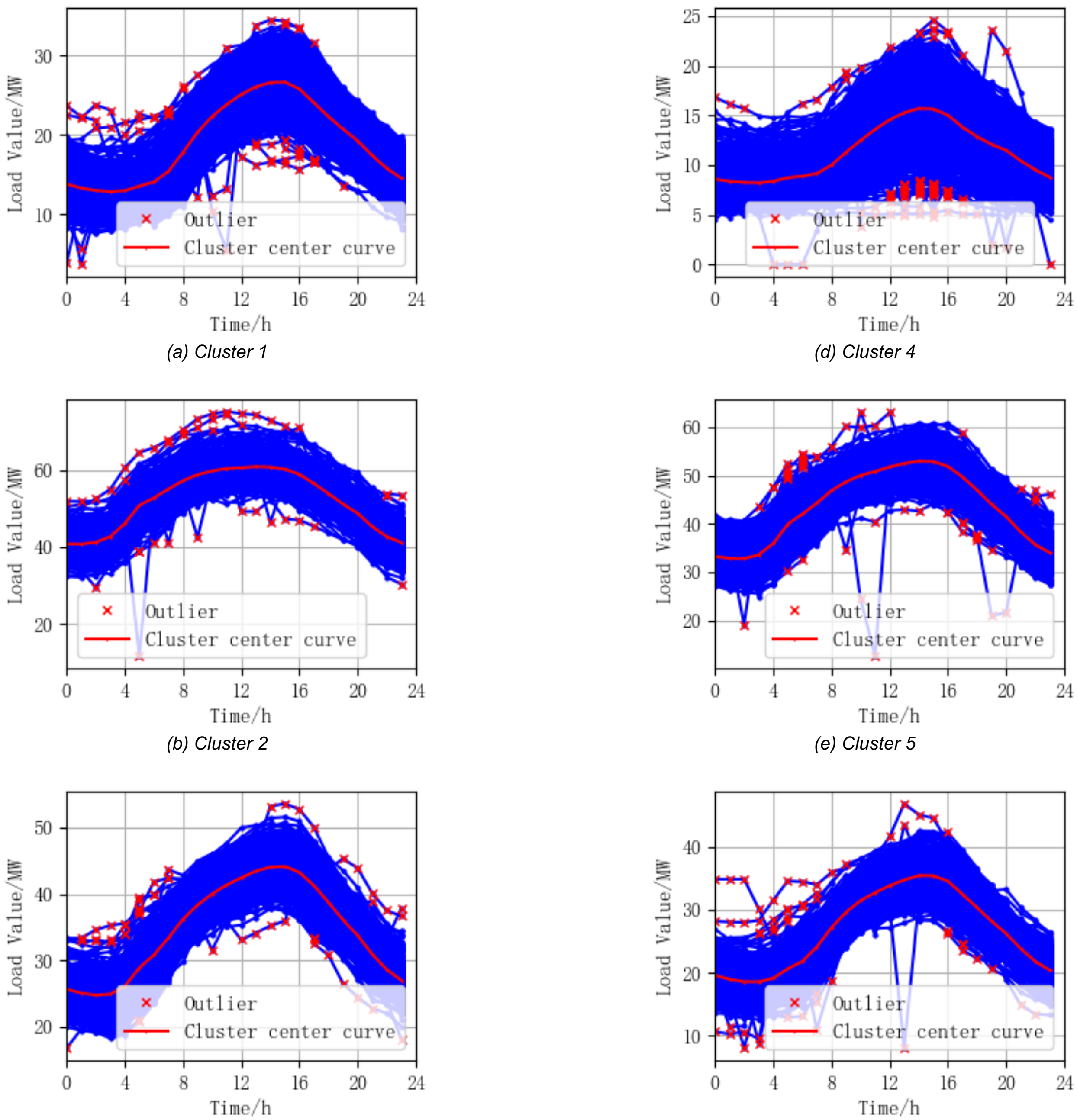

(a) Cluster 1

(d) Cluster 4

(b) Cluster 2

(e) Cluster 5

(c) Cluster 3

(f) Cluster 6

Figure 2: presents the K-means++ clustering results for the Cooling Load

Table 1: Mutation Outlier Identification Results

Data Type	Number of Sudden Anomalies					
	Cluster 2	Cluster 2	Cluster 2	Cluster 2	Cluster 2	Cluster 2
Electricity Load	56	40	85	31	70	35
Heat Load	44	5	1	17	69	20
Cooling Load	59	47	37	58	48	87

For the identified sudden load data, this paper first marks all sudden values and uniformly replaces them with 0 along with the missing values mentioned above. Then, linear interpolation is used to fill in all the "0" data in the dataset. This method is commonly used for coherent time series data, and its linear interpolation formula.

2.2. Correlation Analysis

Given the nonlinear coupling relationship between annual load data and various influencing factors, this paper employs the Spearman correlation coefficient method for correlation analysis. The principle of the Spearman correlation coefficient method is based on ranking data, where the original data values are converted into rank data values, and then the Pearson correlation coefficient between the rank data is calculated. This metric can measure the monotonic relationship between two variables. Its calculation formula is shown in Equation 2.

Equation 2: Spearman calculation formula.

$$S_p = 1 - \frac{6\sum d_i^2}{n(n^2-1)}$$

Where:

- S_p = Calculate Spearman's rank correlation coefficient.
- d_i = Calculate the difference between the corresponding positions of two sets of grade data.
- n = Sample size.

Typically, the Spearman correlation coefficient ranges from -1 to 1. When the coefficient approaches 1, it indicates a strong positivecorrelation between two variables; when it approaches -1, it indicates a strong negative correlation. A coefficient close to 0 suggests no correlation between the variables.

Based on the magnitude of these coefficients, an average correlation coefficient above 0.2 is considered the standard for sel ecting highly correlated factors for varied seasonal forecasting tasks. This approach aims to achieve more accurate predictions. The specific influencing factors chosen for different forecasting tasks are detailed in Table 2.

Table 2: Factors influencing the input for multivariate load forecasting task.

Factors	Predicting Load Types		
	Electricity Load	Heat Load	Cooling Load
Electricity Load	√	√	√
Heat Load	√	√	√
Cooling Load	√	√	√
Temperature	√	√	√
Relative Humidity	√	√	√
Pressure	√	√	×
Day Styles	√	×	×
Months	×	√	√
Hours	√	√	√

3. MULTI-LOAD FORECASTING MODEL：RESNET-GRU-MTL NEURAL NETWORK MODEL

3.1. Principles of ResNet Network

ResNet is a deep neural network structure characterized by the introduction of residual connections. This special connection method allows the network to learn complex feature representations in the data more effectively. By learning the residual mapping, it becomes easier to address issues of gradient vanishing and gradient explosion during the training process of deep neural networks. ResNet is typically composed of multiple stacked residual blocks (RB).

The ResNet used in this paper adopts a two-layer CNN structure as the basic residual unit, as illustrated in Figure 3.

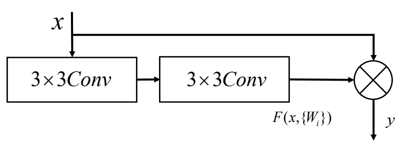

Figure 3: Basic Unit of ResNet

3.2. Principle of the GRU Network

Following feature extraction via preceding ResNet modules, this study selects the Gated Recurrent Unit (GRU) as the neural network for medium to long-term sequence prediction. GRU is a variant of the Recurrent Neural Network (RNN). Unlike traditional RNNs, theGRU uses a gating mechanism to control the flow of information, thereby addressing the issues of gradient vanishing and explosionin long sequence training tasks. Additionally, compared to the Long Short-Term Memory (LSTM) network, another RNN variant, theGRU's simpler structure—comprising only update and reset gates—reduces the number of parameters, which in turn accelerates the training process and conserves computational resources, while maintaining similar performance levels.

The internal structure of the GRU, as depicted in Figure 4, includes five key components: the input, reset gate, update gate, candidate hidden state, and output.

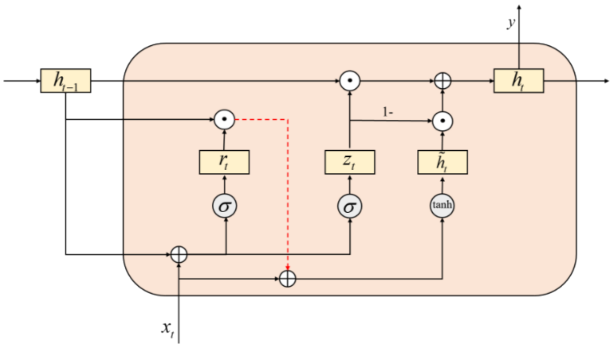

Figure 4: Schematic Diagram of GRU Neural Network

3.3. Principle of Multi-Task Learning

The principle of multi-task learning and its sharing mechanism lies in the shared model parameters among different subtasks (Caruana 1997). This allows each task to mutually learn and integrate information in the hidden layers, thereby improving the overalltask performance. The core factor is the unique sharing mechanism, which can be categorized into hard sharing and soft sharing mechanisms. Due to the strong intercorrelation between electrical, heat, and cooling prediction tasks, this paper adopts the hard sharing mechanism, as illustrated in Figure 5.

The hard sharing mechanism refers to the use of a common feature-sharing layer across different subtasks, where feature parameters are identical and not allowed to be adjusted dynamically during training. This approach is advantageous for its simplicity, ease of understanding, and reduced model parameter load, thus enhancing training efficiency.

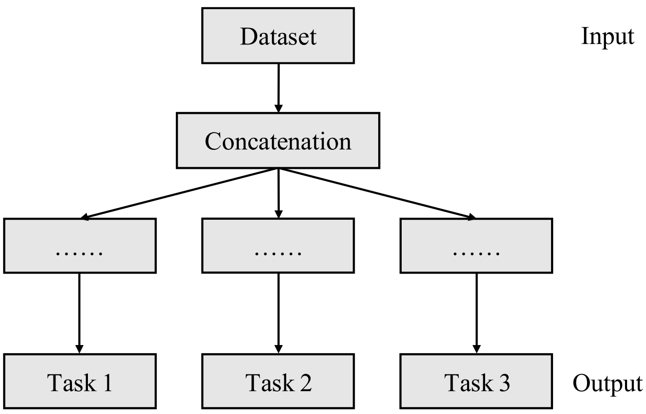

Figure 5: MTL Hard Sharing Mechanism

4. CASE STUDY

This section introduces the evaluation index and model hyperparameter settings of multivariate load forecasting and uses the ASUmulti-load dataset mentioned above as an example to test the accuracy and versatility of the prediction model.

4.1. Normalization and Evaluation Metrics

In this study, the conventional Min-Max method is employed for data normalization. This approach scales the data linearly to aspecified range, typically between [0, 1], as in Equation 3:

Equation 3: Normalization calculation method. $$X_{norm} = \frac{X - X_{\min}}{X_{\max} - X_{\min}}$$

Where:

- X_{norm} = Normalized values
- $X_{\max}$ = Maximum Value
- $X_{\min}$ = Minimum value

When forecasting the multi-load of regional integrated energy systems, it is essential to select appropriate metrics to quantify the prediction performance and effectiveness. Current load forecasting evaluation metrics are well established; therefore, we adopt thefour most commonly used metrics to quantify the performance of the prediction model. These metrics are Mean Absolute Percentage Error (MAPE), Root Mean Square Error (RMSE), Coefficient of Determination (R2), and Training Time (T). The specific formulas forthese metrics are as follows:

These evaluation metrics enable accurate assessment of the performance and accuracy of load forecasting models. They can also be used to compare the effectiveness of different models for the same forecasting task, thus allowing for the selection of theoptimal model based on practical requirements.

4.2. Model Overall Prediction Process and Hyperparameter Settings

The hardware configuration for the algorithm platform includes an Intel Core i5-10500 3.1GHz CPU, NVIDIA GeForce 1660 Super GPU, and 16GB of memory. The software environment utilizes Python, with model building and training conducted on the TensorFlow framework.

When constructing models using deep learning neural networks, the setting of hyperparameters is crucial. For the training tasks ofthe multivariate load prediction in the regional integrated energy system presented in this paper, hyperparameters were repeatedly experimented with and tuned. The following table shows the hyperparameters set for prediction tasks corresponding to summer, winter, and transitional seasons.

Table 3 ResNet-GRU-MTL Model Hyperparameters Setting

Model Location	Hyperparameters Setting	Prediction Task		
		Summer	Winter	Transition Season
MTL	Number of neurons in fully connected layers	32	32	32
ResNet	Number of residual blocks	2	2	3
	Number of CNN convolutional kernels	32	32	64
	Size of convolutional kernels	3	3	3
	Activation function	Relu	Relu	Relu
GRU	Number of neurons in the first layer	64	64	128
	Number of neurons in the second layer	32	32	32
	Activation function	tanh	tanh	tanh
Outputs	Number of neurons in fully connected layers	32	32	32
Model Compilation	Learning rate	0.01	0.01	0.01
	Decay factor	0.5	0.5	0.5
	Batch size	32	32	32
	Training iterations	300	300	300
	Optimizer	Adam	Adam	Adam

4.3. Results and Analysis

To validate the accuracy of this multi-load forecasting model, data from the test set across different seasons are selected, and various forecasting models are set up for comparison. The models involved in the prediction tasks are introduced as follows:

Model 1: Utilizes the widely used classic Gated Recurrent Unit (GRU) model. This model features a two-layer hidden structure, with64 and 32 neurons respectively as hyperparameters, a batch size of 64, 300 iterations, the Adam optimizer, an initial learning rate of 0.01, and a decay factor of 0.5. The purpose of this model is to compare the forecasting performance of the proposed advanced deep learning structure against traditional classic models.

Model 2: Uses the Random Forest (RF) regression model, which has shown effective prediction results in traditional load forecasting methods. It features 24 trees and employs bootstrap sampling during construction. The aim is to compare the performance difference between traditional shallow learning methods and the deep learning-based model in comprehensive energy multi-load forecasting.

Model 3: Employs the proposed ResNet-GRU-MTL prediction model with parameters as described in Section 3.5 of this thesis.

The comparison of different prediction tasks using the above models involves visualizing the results for selected days in the test set,displaying predictions for certain 4-day periods. The 1-48 period represents weekdays, and the 49-96 period represents weekends. For the summer prediction task, the time span is from 12:00 AM on August 22, 2019, to 12:00 AM on August 26, 2019. For the winter prediction task, the span is from 12:00 AM on January 9, 2019, to 12:00 AM on January 13, 2019. For the transition season prediction task, the period is from 12:00 AM on November 6, 2019, to 12:00 AM on November 10, 2019. The results predicted by different models are illustrated as follows:

1) Results of Electrical Load Forecasting

By observing the various electrical load forecasting results in Figures 6 and Table 4, it is evident that across different seasons and regardless of whether it is the first 48 hours of a workday or the following 48 hours of a non-workday, the proposed ResNet-GRU- MTL model consistently achieves a coefficient of determination (R^2) greater than 0.92, the highest among the three models, indicating the best fit. The model also performs well in predicting abrupt changes and peak values of electrical load, whereas Model Two shows poor prediction performance, particularly with significant fluctuations and high errors during transitional seasons. Model One fares poorly in predicting peak values at the 12th and 36th hours in winter.

Analyzing the prediction errors, the proposed model records a Mean Absolute Percentage Error (MAPE) of 1.67% in summer load forecasting, 0.57% and 0.40% lower than Model One and Model Two, respectively. In winter, the MAPE is 1.37%, similar to the summer value, with reductions of 0.32% and 1.08% compared to Model One and Model Two, respectively. During transitional seasons, the MAPE is 1.44%, 2.14% and 0.44% lower than Model One and Model Two, respectively. The Root Mean Square Error(RMSE) metrics also show corresponding decreases, representing the better fitting efficiency of the proposed method.

Overall, the ResNet-GRU-MTL model proposed in this study demonstrates the best forecasting performance with excellent stabilityacross various prediction tasks.

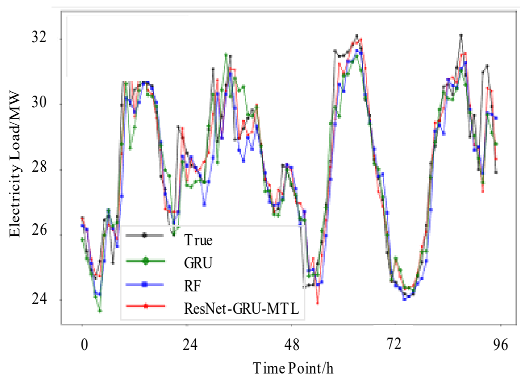

(a) Summer

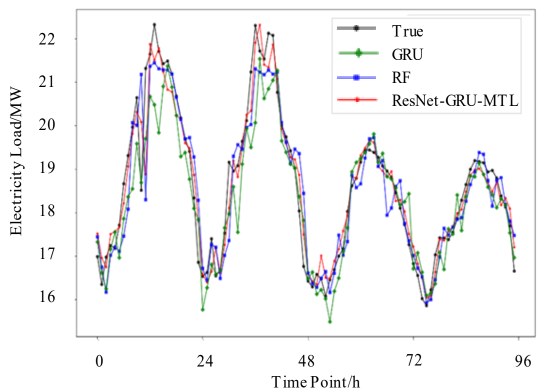

(b) Winter

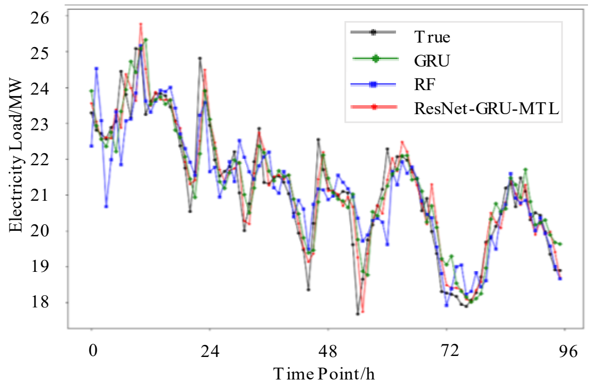

(c) Transition Season

Figure 6: Comparison of Electricity Load Prediction Results by Different Models

Table 4: Prediction Errors of Electricity Load in Different Seasons under Different Models

Model	Summer			Winter			Transition Season		
	MAPE /%	RMSE /MW	R^2	MAPE /%	RMSE /MW	R^2	MAPE /%	RMSE /MW	R^2
GRU	2.07	0.77	0.89	2.45	0.82	0.88	1.88	0.68	0.92
RF	2.24	0.84	0.87	1.69	0.79	0.90	3.58	1.02	0.85
ResNet-GRU-MTL	1.67	0.53	0.92	1.37	0.56	0.96	1.44	0.49	0.94

2) Heat Load Forecasting Results

The heat load forecasting results are shown in Figure 7. Compared to the electrical load, the heat load demand curve in winter is relatively smoother with fewer abrupt changes and more regular patterns. While all three models perform well, the model proposed in this study excels in predicting peak and valley values, as evidenced by the summer and transitional season heat load demand forecasts and Table 5. Even in summer when other models struggle to fit the heat load variations, the ResNet-GRU-MTL model proposed here achieves an R^2 value of 0.90. For winter and transitional seasons, the R^2 values are 0.94 and above, closely aligning with the actual value curves. Additionally, the Mean Absolute Percentage Error (MAPE) values are 2.43%, 1.22%, and 1.35%, and the Root Mean Squared Error (RMSE) values are 0.10MW, 0.06MW, and 0.05MW, respectively, the lowest among the three models. This indicates that the proposed model has the smallest prediction errors and highest accuracy across different seasons. Particularly in winter, due to higher load demand, the model's feature extraction capabilities are more pronounced, resulting in significantly better forecasting performance compared to the other two models.

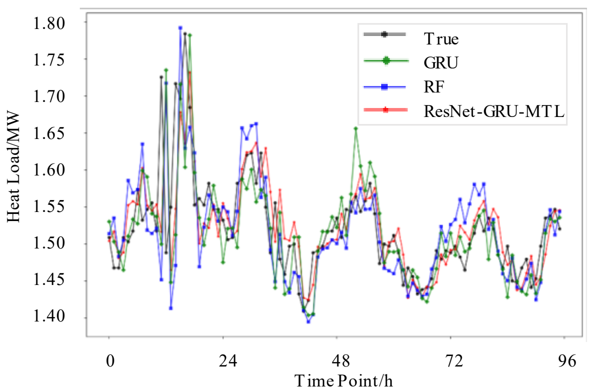

(a) Summer

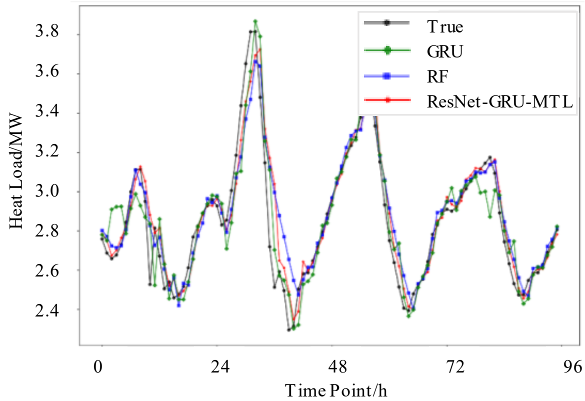

(b) Winter

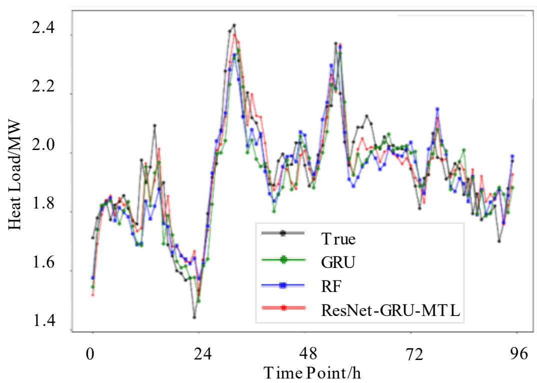

(c) Transition Season

Figure 7: Comparison of Heat Load Prediction Results by Different Models

Table 5: Prediction Errors of Heat Load in Different Seasons under Different Models

Model	Summer			Winter			Transition Season		
	MAPE /%	RMSE /MW	R^2	MAPE /%	RMSE /MW	R^2	MAPE /%	RMSE /MW	R^2
GRU	3.10	0.22	0.87	2.11	0.08	0.91	2.44	0.06	0.89
RF	4.45	0.32	0.67	1.96	0.08	0.90	1.44	0.05	0.93
ResNet-GRU-MTL	2.43	0.10	0.90	1.22	0.06	0.96	1.35	0.05	0.94

3) Cooling Load Forecast Results

The forecast results for the cooling load are shown in Figure 8. Compared to electricity and heat loads, the cooling load displays more consistent variations across different seasons and between weekdays and weekends. As a result, all models fit the data well. However, observing the demand forecast charts for summer and winter cooling loads reveal that Model 1 and Model 2 perform poorly during periods of significant load fluctuation (such as hours 71-73 in summer and hours 50-53 in winter). Additionally, Model 1 shows substantial disturbances and higher errors during transitional hours 14 and 26. According to Table 6, the ResNet-GRU-MTL model proposed in this study achieves an R2 greater than 0.98 across different seasons, indicating excellent fit. Its MAPE values are 0.79%, 0.99%, and 1.12%, and its RMSE values are 0.96MW, 0.45MW, and 0.69MW, respectively, which are the lowest among the three models, signifying the least prediction error and highest accuracy.

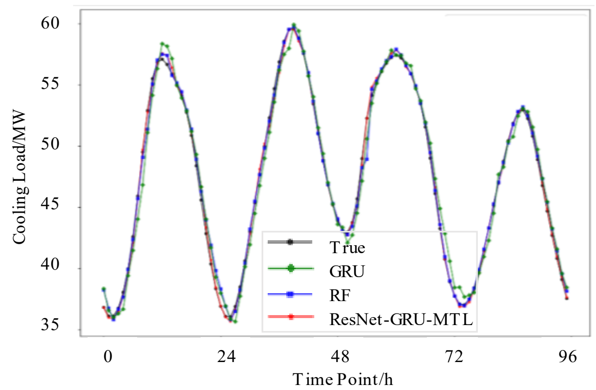

(a) Summer

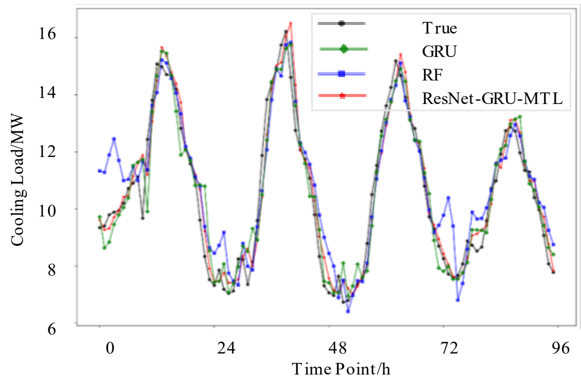

(b) Winter

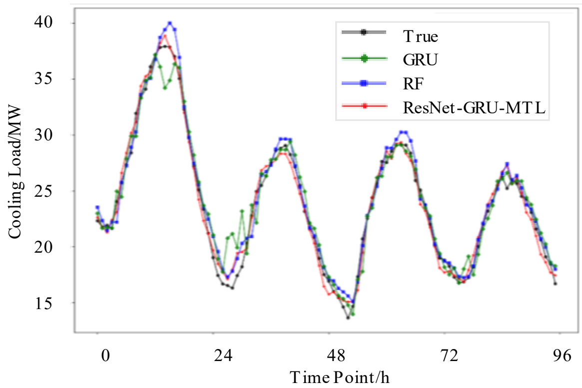

(c) Transition Season

Figure8: Comparison of Cooling Load Prediction Results by Different Models

Table 6: Prediction Errors of Cooling Load in Different Seasons under Different Models

Model	Summer			Winter			Transition Season		
	MAPE /%	RMSE /MW	R^2	MAPE /%	RMSE /MW	R^2	MAPE /%	RMSE /MW	R^2
GRU	1.12	1.44	0.96	1.24	0.59	0.94	2.25	1.33	0.92
RF	1.09	1.12	0.98	2.24	0.96	0.86	1.79	0.98	0.94
ResNet-GRU-MTL	0.79	0.96	0.99	0.99	0.45	0.98	1.12	0.69	0.98

4) Comparison of Training Time for Different Models

To examine the computational efficiency of the proposed method, we selected the traditional GRU model as a control group under identical computational resources. Using the library's time tools, we recorded the training times of various deep learning models across different training tasks. According to Table 7, the proposed ResNet-GRU-MTL load forecasting model has a significantly shorter training time compared to the cumulative time required for separate electricity, heat, and cooling load predictions using single load forecasting models. This result indicates that the shared layer mechanism of MTL effectively reduces training time and computational power, enabling quicker load forecasts for subsequent tasks such as peak shaving and frequency regulation in RIES, thereby providing greater practical value.

Table 7: Comparison of Training Times for Different Models

Model	Load Types	Train Time/s		
		Summer	Winter	Transition Season
GRU	Electricity Load	645	646	765
	Heat Load	633	638	744
	Cooling Load	641	648	759
	Total Time	1919	1932	2268
ResNet-GRU-MTL	Multi-Load	785	779	812

5. CONCLUSION

This article discusses the issue of multi-load forecasting in regional comprehensive energy systems, and the main conclusions are as follows:

(1) Preprocessing of historical load data using LOF and K-Means++ algorithms to more accurately identify anomalies in the original load data.

(2) A multi-load forecasting model ResNet-GRU-MTL for regional comprehensive energy systems was established for prediction and analysis. The model was compared with random forest regression and traditional gated recurrent unit models for load forecasting in summer, winter, and transitional seasons. The results show that the proposed model achieved an average absolute percentage (MAPE) of 1.67%, 1.37%, and 1.44% for electricity load prediction, 2.43%, 1.22%, and 1.35% for heat load, and 0.79%, 0.99%, and 1.12% for cooling load, with the highest prediction accuracy.

(3) A comparison of the running time of different models revealed that the ResNet-GRU-MTL model proposed in this article has the shortest running time and highest computational efficiency in the multi-load forecasting problem.

6. REFERENCES

Azeem, A., et al. 2021. Electrical Load Forecasting Models for Different Generation Modalities: A Review. Ieee Access, 9: 142239- 142263.

Chitalia, G., et al. 2020. Robust short-term electrical load forecasting framework for commercial buildings using deep recurrent neural networks. Applied Energy, 278.

Habbak, H., et al. 2023. Load Forecasting Techniques and Their Applications in Smart Grids. Energies, 16, (3).

Huang, X., et al. 2023. Short-Term Electric-Thermal Load Forecasting Method for Park-Level Integrated Energy System Based on Transformer Network and Multi-Task Learning. Southern Power System Technology, 17, (1): 152-160.

Kim, J., et al. 2019. Recurrent inception convolution neural network for multi short-term load forecasting. Energy and Buildings, 194: 328-341.

Kong, W. C., et al. 2019. Short-Term Residential Load Forecasting Based on LSTM Recurrent Neural Network. Ieee Transactions on Smart Grid, 10, (1): 841-851.

Liu, Y. J., et al. 2023. Review of multiple load forecasting method for integrated energy system. Frontiers in Energy Research, 11.

Rana, M., et al. (2014). Forecasting Hourly Electricity Load Profile Using Neural Networks. International Joint Conference on Neural Networks (IJCNN), Beijing, PEOPLES R CHINA.

Tan, Z. F., et al. 2020. Combined electricity-heat-cooling-gas load forecasting model for integrated energy system based on multi- task learning and least square support vector machine. Journal of Cleaner Production, 248.

Wu, K. H., et al. 2021. An attention-basedCNN-LSTM-BiLSTMmodel for short-term electric load forecasting in integrated energysystem. International Transactions on Electrical Energy Systems, 31, (1).

Yuting, Y. and Z. Zihao 2021. Cooling, Heating and Electrical Load Forecasting Method for Integrated Energy System based on SVR Model. 2021 6th Asia Conference on Power and Electrical Engineering (ACPEE): 1753-1758.

Caruana, R. 1997. Multitask learning. Machine Learning, 28, (1): 41-75.

#299: Green and sustainable cellulose-based nanocomposite for thermochemical heat storage

Shengnan SUN[1], Qiongfen YU[*2], Ming LI[3], Zhijin WANG[4], Danya ZHAN[5], Zhongfan MO[6], Zhihao SONG[7], Fen JIANG[8], Runfang MA[9]

[1] *Solar Energy Research Institute, Yunnan Normal University, Kunming, Yunnan Province, 650500, China, ssn_0606@163.com*
[2] *Solar Energy Research Institute, Yunnan Normal University, Kunming, Yunnan Province, 650500, China, qfyu@ynnu.edu.cn*
[3] *Solar Energy Research Institute, Yunnan Normal University, Kunming, Yunnan Province, 650500, China, mingli@ynnu.edu.cn*
[4] *Solar Energy Research Institute, Yunnan Normal University, Kunming, Yunnan Province, 650500, China, 981127350@qq.com*
[5] *Solar Energy Research Institute, Yunnan Normal University, Kunming, Yunnan Province, 650500, China, 1053421946@qq.com*
[6] *Solar Energy Research Institute, Yunnan Normal University, Kunming, Yunnan Province, 650500, China, 799059725@qq.com*
[7] *Solar Energy Research Institute, Yunnan Normal University, Kunming, Yunnan Province, 650500, China, 1362535946@qq.com*
[8] *Solar Energy Research Institute, Yunnan Normal University, Kunming, Yunnan Province, 650500, China, 393633602@qq.com*
[9] *Solar Energy Research Institute, Yunnan Normal University, Kunming, Yunnan Province, 650500, China, 617443329@qq.com*

Abstract: Solar energy, as the most abundant, accessible, and sustainable energy resource on the Earth, has attracted great interest in recent years due to the increasing severity of energy crisis and environmental pollution caused by fossil fuels. Furthermore, cellulose, as one of the most abundant natural polymers, is biodegradable, renewable and recyclable, and can be crosslinked into a three-dimensional network structure of cellulose gels through hydrogen bonding, covalent bonding or ionic interaction, which is alsoone of the current research hotspots. In this study, a natural composite hygroscopic gel was developed to investigate the storage and release of heat during thermochemical reactions with water vapor as the adsorption medium. We extracted cellulose from corn stalk by hydrogen peroxide assisted with alkali method. The corn stalk cellulose was dissolved in $LiBr{\cdot}3H_2O$ solution under the conditionof high temperature oil bath to obtain corn stalk cellulose/LiBr hydrogel. Then, the hydrogel was further immersed in deionized water for solvent replacement to remove excess LiBr. After that, the specimen was dried in vacuum freeze dryer to achieve corn stalk cellulose gel (CSCG). The results of water vapor adsorption experiment demonstrated that water vapor adsorption capacity of CSCG with corn stalk cellulose of 1wt% and solvent exchange time of 10 h is up to 1.58 g/g. A great energy storage density of 1189.5 J/g was measured by thermogravimetric analysis for cellulose gel. Thus, this research can provide a new idea and material for thermochemical heat storage.

Keywords: Cellulose Gel, Hygroscopic, Biocompatibility, Biodegradation

1. INTRODUCTION

At present, the world's energy consumption presents characteristics of diversification and complexity. Although the world has made remarkable progress in promoting development of renewable energy, fossil fuels are still the subject of energy consumption, accounting for 81.5% of primary energy consumption structure (2024). With continuous growth of energy consumption and demand, use of fossil energy has made environmental problems increasingly prominent (Chen and Yang, 2024), such as greenhouse effect,air pollution, water pollution and thermal pollution. At the same time, as a non-renewable limited resource, it will not be able to meetfuture energy needs. Therefore, the development of renewable clean energy is particularly important. Renewable energy sources such as solar energy, wind energy, and geothermal energy can be recycled in nature and are inexhaustible resources. However, the inherent dispersion and output instability of these energy sources make them unevenly distributed in space and time, resulting in large fluctuations in energy output and low utilization rate. As an important technology for energy storage and utilization, thermal energy storage is of great significance in solving the problem of time and space mismatch between energy supply and demand. It plays a wide and key role in solar thermal utilization, waste heat recovery, building energy conservation and other fields (Du et al., 2022,Tyagi et al., 2024, Gao et al., 2022, Moulakhnif et al., 2024). Compared with sensible heat storage materials and phase change materials, thermochemical materials (TCMs) realize energy storage and release by using the heat change between substances in chemical reactions. They have advantages of high energy storage density, long-term energy storage stability across seasons and environmental friendliness.

Thermochemical energy storage technology can be divided into chemical reaction heat storage and chemical adsorption heat storage according to the heat storage mechanism. Among them, chemical reaction heat storage has advantages of energy storage, fast release speed, non-toxic heat storage medium and low price. However, the reaction is limited to moving bed form, and active material is prone to agglomeration and sintering, which has a negative impact on heat and mass transfer. Chemical adsorption heat storageis based on reversible adsorption reaction, mainly through the adsorption, desorption, condensation and evaporation of gaseous orliquid adsorbate molecules by solid adsorbents to complete heat storage and release cycle. Its essence is to realize transformation of thermal energy and chemical energy by fracture and polymerization of intermolecular forces such as van der Waals force, electrostatic force and hydrogen bond. In the water-TCM working pair, the moisture adsorption/desorption process of water molecules on the adsorbent is often accompanied by generation, conversion and transfer of energy. The energy storage density of material depends on its hygroscopicity, which is closely related to the physical and chemical properties of the material. At present, Commonly used thermochemical materials include traditional porous materials, metal-organic frameworks (MOFs) (Makhanya et al., 2021, Padamurthy et al., 2022), covalent organic frameworks (COFs), polymer hygroscopic gels and hygroscopic salt-based adsorbents(Liu et al., 2023, Xu et al., 2024). Traditional porous materials are not suitable for energy storage due to their low adsorption performance. The hygroscopic salt-based material has the best hygroscopicity, but there are still problems of agglomeration, corrosion and solution leakage. Although this problem can be overcome by sealing the hygroscopic salt in a porousmatrix, the long-term stability and reliability in practical applications are still questionable. The difference is that polymer hygroscopicgel has attracted interest of many scholars because of its ultra-high hygroscopic properties. The adsorption mechanism of hygroscopic polymer is different from that of traditional porous materials and salt base composite materials. It uses the principle of hygroscopic swelling and desorption shrinkage to adsorb water vapor and stores the adsorbed water vapor in the three-dimensional polymer network structure (Zhu et al., 2024). This is different from other hygroscopic materials that rely on pore volume and adsorption sites for adsorption behaviour.

Currently, cellulose hydrogels, as a new type of functional heat storage and adsorption material with a three-dimensional cross-networking structure (Zhu et al., 2024), are an aggregate of cellulose polymers and water. The hydrophilic groups in the polymeric skeleton, such as -OH, -NH_2, -COOH (El Sayed, 2023), give the cellulose hydrogel network certain water absorption and water retention, and are a representative hygroscopic polymer. Hydrogels exhibit extremely high water absorption (4.20 g/g) at RH>90%, and the material can use solar energy as a heat source to achieve desorption at moderate temperatures (>55 °C) (Nandakumar et al., 2019). The excellent water absorption performance of this hydrogel at high relative humidity and desorption performance at medium temperature are expected to be used as temperature and humidity regulation materials in agricultural greenhouses (Ejeianand Wang, 2021). Among the many raw materials for preparation of hydrogels, cellulose and its derivatives become ideal materials for preparation of heat-storage adsorption hydrogels because of its wide source, renewable, biocompatibility and biodegradability, high intermolecular and intramolecular hydrogen bond and van der Waals force, hydrophilicity and solubility resistance (Zainal et al., 2021). And hydrogels prepared based on cellulose and its derivatives generally have good mechanical properties and minimal environmental impact. In summary, cellulose-based hydrogels not only have low cost, biocompatibility and biodegradability, but also meet the characteristics of high energy storage density, recyclability, economic benefit and non-toxicity of heat storage adsorbents.

Biomass gels have been widely concerned in the field of adsorptive air water intake (Li et al., 2023, Zhang et al., 2022), because of its advantages of abundant sources, biocompatibility, biodegradability, adjustable structure, temperature and humidity sensitivity, large cyclic adsorption capacity and rapid adsorption and desorption kinetics. Since the energy storage density of thermochemical materials depends on their hygroscopic properties, the biomass gels are considered as promising thermochemical materials. In thisstudy, we synthesized some heat-storage and hygroscopic natural cellulose gels based on natural cellulose and tested their hydration/dehydration properties under constant temperature and humidity. These test results lay a data foundation for exploring the thermal storage properties of materials. The results showed that the hydration/dehydration properties of corn straw cellulose gel were consistent with those of commercial cellulose gel, and both had advantages of high cyclic moisture absorption and low regeneration temperature. It is a potential thermochemical material that is a potential thermochemical material that releases heat by hydration in low temperature and high humidity environment, storages heat to dehydrate in high temperature and low humidity environment.

2. MATERIALS AND METHODS

2.1. Materials

Commercial cellulose, Lithium Bromide (LiBr) and carrageenan were purchased from Aladdin Biochemical Co., Ltd. (Shanghai, China). Corn stalks cellulose was extracted by method reported before (Zhan et al., 2024).

2.2. Synthesis of Cellulose Gels

Cellulose, LiBr·3H_2O and carrageenan were mixed at 50 °C to form a homogenization. And the homogenization was transferred to 105 °C oil bath and continued magnetic stirring for 20 min to dissolve cellulose and form transparent liquid. Then, the liquid was poured into hot mould to cool and form cellulose hydrogel. After that, cellulose hydrogel was immersed in deionized water to replace LiBr solvent, and then freeze-dried for 48 h in freeze dryer. Finally, white cellulose gel (WCG) was obtained. Black cellulose gel (BCG) was synthesized by adding 0.05 g photothermal conversion material (black TiO_2, CNT, activated carbon powder, MXene, or nano-carbon powder) into homogenization, during the synthesis process. Carbonized cellulose gel (CCG) was carbonized at 250 °C for 30 min within N_2 atmosphere. Flow chart of the composite thermochemical heat srorage material is shown in Figure 1.

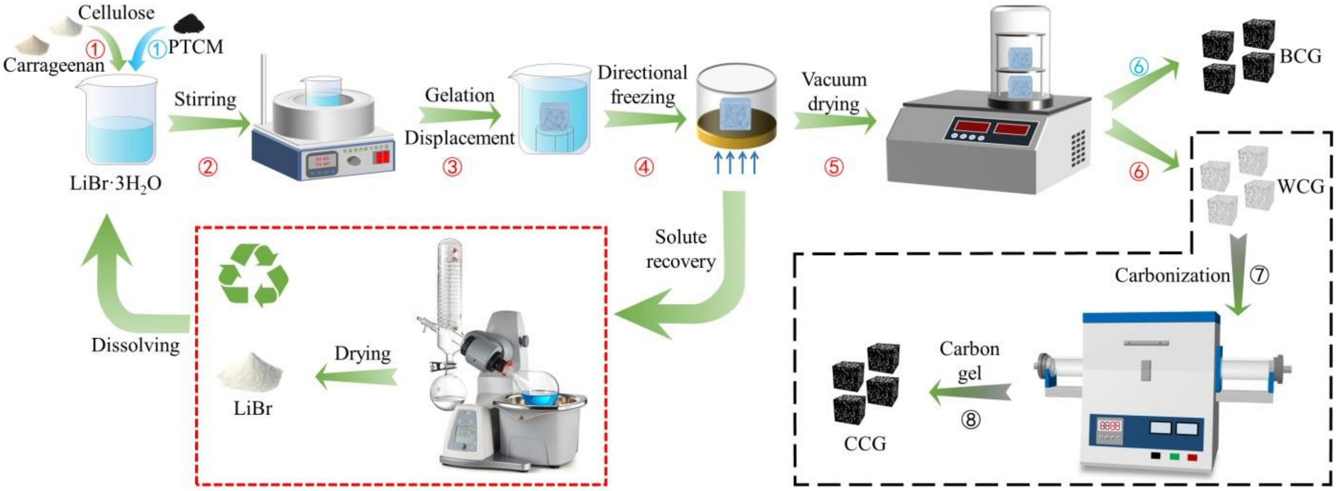

Figure 1: Synthesis methodology of composite thermochemical heat storage materia

2.3. Hygroscopicity Measurement

Cellulose gels were completely dried at 100 °C for 12 h before hygroscopicity measurement. Hygroscopicity of cellulose gels was measured in a programmable constant temperature and humidity chamber (KW-TH-225Z, Dongguan Kewen Test Equipment Co., Ltd.). Temperature and relative humidity (RH) were set as 20 °C & 80% RH for hydration and 80 °C & 20% RH for dehydration, respectively. The weight change of cellulose gels was recorded regularly using an electronic analytical balance (ME20) with 0.0001g precision during the measurement. Hygroscopic capacity of cellulose gels was calculated by the following formula：

Equation 12: hygroscopic capacity of Cellulose gel.

$$q = \frac{m_{gel-t} - m_{gel}}{m_{gel}}$$

Where:

- q = hygroscopic capacity (g/g)
- m_{gel} = weight of cellulose gel (g)
- m_{gel-t} = weight of cellulose gel at time t (g)

The WCG, water adsorbed saturated at 20 & 80% RH, was tested dehydration performance between 25~160 °C using simultaneous thermal analyzer (Mettler TGA/DSC3+). Water vapor adsorption isotherms at 20 °C were measured by automatic specific surface area and pore size analyzer (Autosorb-iQ, Anton-Paar) to obtain the equilibrium adsorption capacity under different relative humidity (relative pressure). The surface temperature change of cellulose gels under natural sunlight was recorded by an infrared thermal imager (DS-2TPH10-3AUF) every 5 min until the temperature change was dynamically stable.

2.4. Thermostability Measurement of Cellulose Gel

A small amount of cellulose gel was placed in an alumina crucible of simultaneous thermal analyzer (Mettler TGA/DSC3+) for thermostability measurement. The test conditions were as follows: flow rate of 50 mL/min nitrogen atmosphere, temperature range of 25-800 °C, and heating rate of 10 °C/min.

3. RESULTS AND DISCUSSIONS

3.1. Hygroscopicity of Cellulose Gels

The dynamic hygroscopic curves of WCGs are shown in Figure 2 and Figure 33, tested under constant temperature and humidity of 20 °C & 80% RH. Figure 2 exhibits the influence of different LiBr solvent exchange time on hygroscopicity of WCGs. It can be seenthat the hygroscopic capacity of WCGs decreases with an increase of solvent exchange time. When the solvent exchange time is extended to 8-9 h, hygroscopic capacity is no longer reduced and stable (about 1.15 g/g). And there is no LiBr solution leak. However, the hygroscopic capacities of WCGs with solvent exchange time of 6 h (1.70 g/g) and 7 h (1.52 g/g) in the first cycle are much lowerthan that in the second and third cycles (more than 1.70 g/g for 6h, 1.52 g/g for 7h). There may be two reasons for these results: onthe one hand, the first cycle of cellulose gel is not saturated; on the other hand, shorter solvent exchange time makes salt content higher and hygroscopicity stronger, but some salt leakage exists during cyclic hygroscopic process. In summary, after comprehensively considering the cyclic hygroscopic properties of WCG and salt leakage, the solvent exchange time of 8h is determined as the best preparation condition.

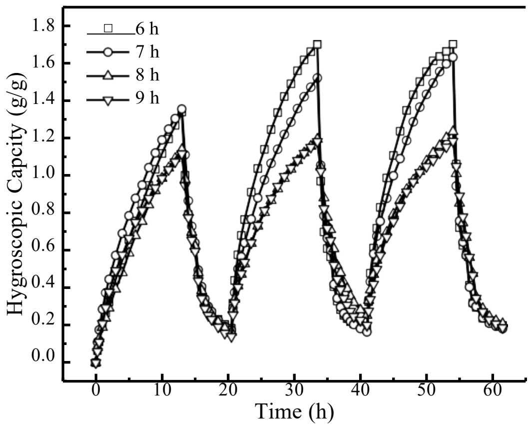

Figure 2: Dynamic hygroscopic curve of WCGs: effect of LiBr solvent exchange time on hygroscopicity

Figure 3 shows the effect of different carrageenan addition amounts on hygroscopic properties of WCGs, indicating that the addition of carrageenan reduces the hygroscopic properties of WCG. When the addition amount is $m_{cellulose}$: $m_{carrageenan}$ =5:0.5, the hygroscopic capacity of WCG is reduced from 1.14 g/g to 0.92 g/g, and cannot be completely regenerated. While the addition amount increases to 5:1.5, WCG hygroscopic capacity decreases from 1.14 g/g to 0.94 g/g, but its regeneration rate is faster, and adsorbedwater can be regenerated completely under temperature of 80 °C. In addition, although WGCs with 5:1 and 5:2 carrageenan additional amount can also achieve complete regeneration, its hygroscopic capacity is lower than that of WGCs with 5:1.5. Therefore, in the case of no salt solution leakage after water adsorption and excellent regeneration performance, the optimal of carrageenan addition amount is $m_{cellulose}$: $m_{carrageenan}$ = 5:1.5.

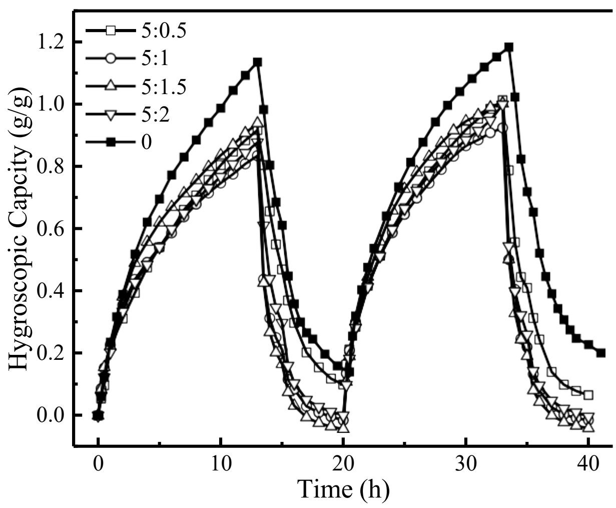

Figure 3: Dynamic moisture adsorption curve of WCGs: effect of carrageenan addition amount on hygroscopicity

3.2. Dehydration property of Cellulose Gel

Dehydration property is another important parameter which affects cyclic performance of WCG in addition to hygroscopic property. In order to determine the regeneration temperature range of WCG, dehydration performance in temperature range of 25-160 °C was measured by Mettler simultaneous thermal analyzer. Before the experiment, WCG was saturated at 20 °C & 80% RH constant temperature and humidity. Dehydration curve of WCG at 25-160 °C is shown in Figure 4. The water adsorbed by WCG can be completely regenerated under temperature below 130 °C, and the desorption rate is maximum at 82 °C. Thus, the regeneration temperature of hydration/dehydration cycle experiment is set reasonably.

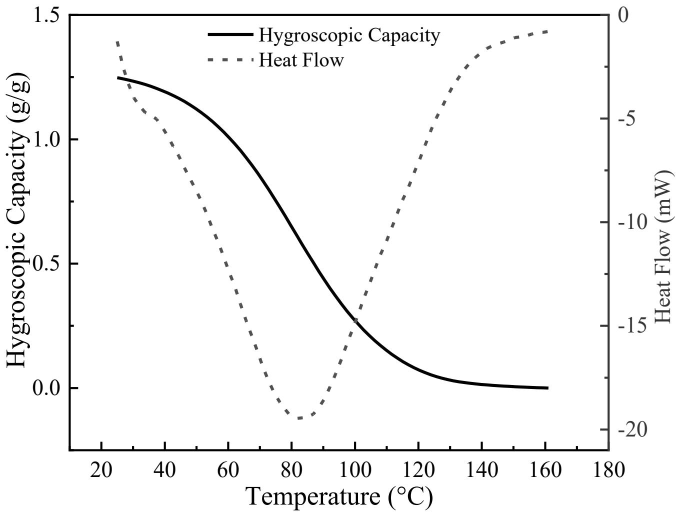

Figure 8 Dehydration curve of cellulose gel at 25-160 °C after hygroscopic saturation under 20 °C & 80% RH constant temperature and humidity

3.3. Water Vapor Adsorption Isotherm

The water vapor adsorption isotherm can describe the equilibrium adsorption amount of cellulose gel at constant adsorption temperature with different relative humidity and explore influence of relative humidity on adsorption amount. Figure 5 shows water vapor adsorption isotherm of WCG at 20 °C. It can be seen from trend in the figure that the water vapor adsorption isotherm of WCG belongs to a type II adsorption isotherm, according to IUPAC classification. At low relative pressure ($P/P_0<0.05$), hygroscopic capacity increased rapidly due to strong interaction between water molecules and cellulose gel surface. When the relative pressure is about 0.05, an inflection point appears on the isotherm, indicating completion of monolayer adsorption. With the increase of relative pressure ($0.05<P/P_0<0.8$), the second layer and more adsorption layers begin to form, and the curve gradually flattened, but still maintained an upward trend, indicating the gradual formation of multilayer adsorption. And finally saturated hygroscopic capacity of WCG is as high as 2.05 g/g.

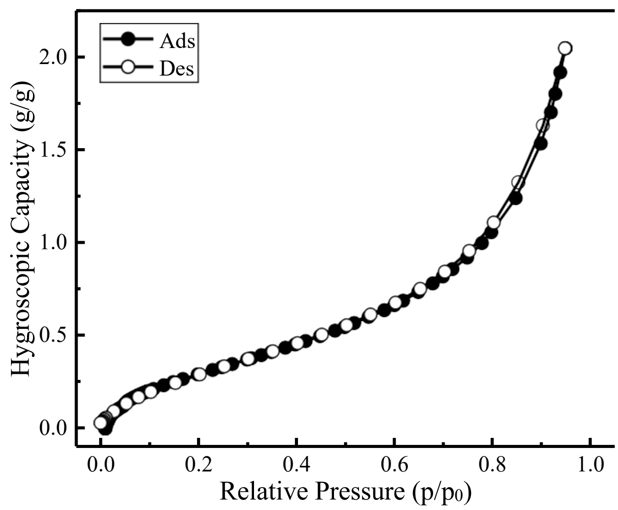

Figure 5: WCG water vapor adsorption isotherm at 20 °C

3.4. Thermostability of Cellulose Gel

Thermogravimetric analysis is a widely used technique for the thermostability of materials. This information will help to better understand the thermal property of WCG and provide a theoretical basis for carbonization temperature range of WCG. The thermostability of WCG was tested by Mettler simultaneous thermal analyzer, and the thermostability curve is shown in Figure 6. It can be seen from the TGA and DTG curves that the pyrolysis process is mainly divided into two mass loss stages in the whole temperature range: evaporation of water in WCG and thermal decomposition of cellulose and carrageenan. The first stage, which has a temperature range of 25-175 °C and is caused by water evaporation WCG, exhibits the greatest decomposition rate at 107.8 °C with a mass loss of up to 25.9%. The second stage has a larger decomposition temperature range of 175-440 °C, the mass loss is caused by simultaneous thermal decomposition of cellulose and carrageenan (Velásquez et al., 2022) and shows the largest decomposition rate at 203.2 °C with mass loss of 20.5%. Thus, it can be seen that the mass loss of WCG is about 50% at temperatures below 600 °C.

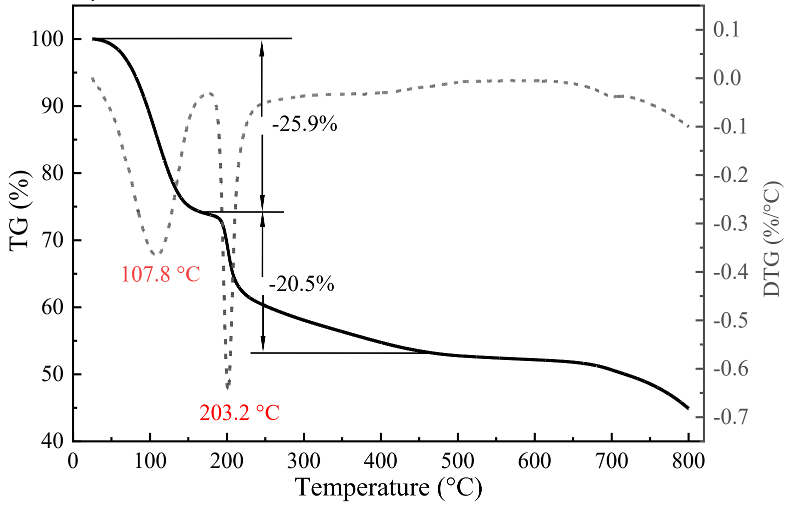

Figure 9: Thermostability curve of WCG

3.5. Photothermal Conversion Performance

Based on the above WCGs, influence of carbonization process and different photothermal conversion materials addition on BCGs hydration/dehydration properties and photothermal conversion properties were explored, as shown in Figure 7 and Figure 9. As can be seen from Figure 7, the carbonization process not only improves adsorption rate of gels, but also shorths adsorption equilibrium time without changing hygroscopic amount. Moreover, carbonized BCG has the best photothermal conversion performance, and surface temperature changes the fastest under direct sunlight. The surface temperature rises above 75 °C within15 minutes, which is better than other BCGs added with photothermal materials, in Figure 9. The results show that carbonization methods have certain advantages in the application of cellulose gel in solar dry hydrothermal recovery.

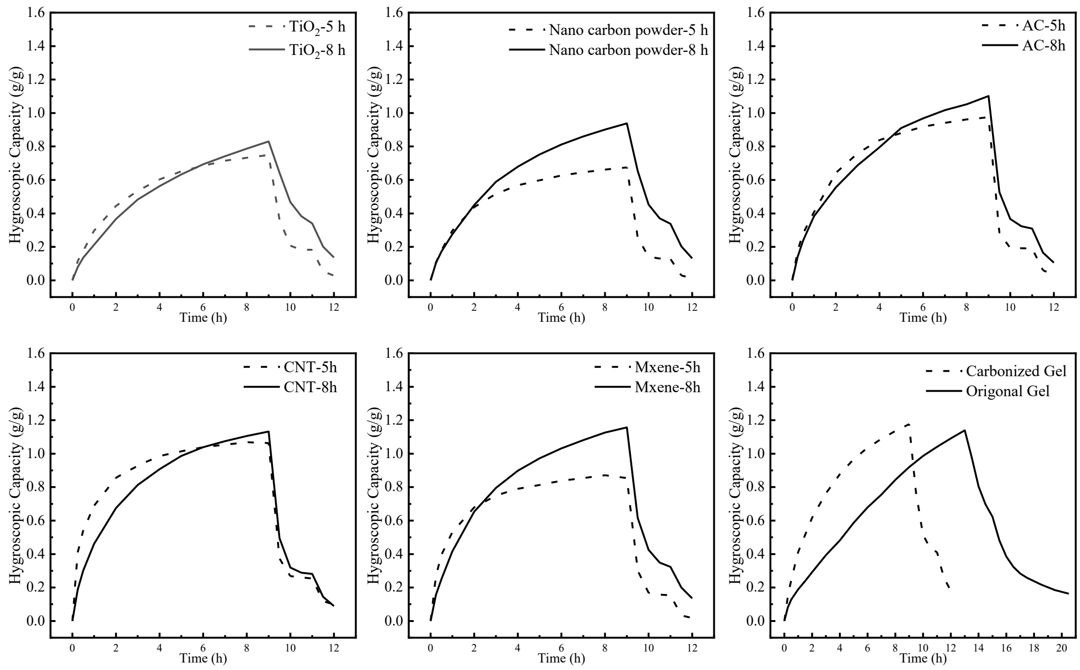

Figure 10: Dynamic moisture hydration/dehydration performance of BCGs

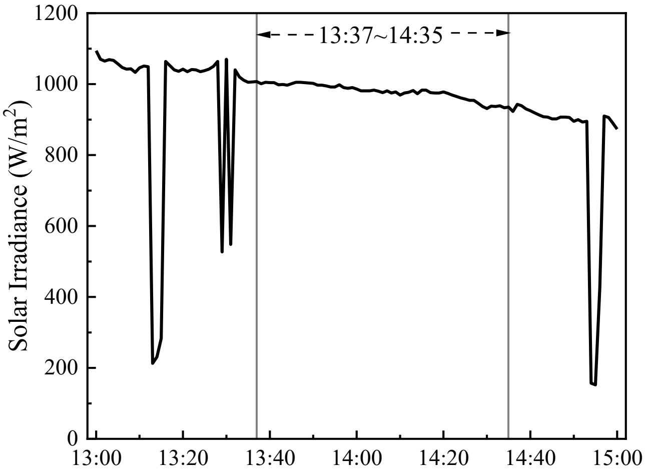

Figure 11：Natural solar irradiance on 2024.06.21

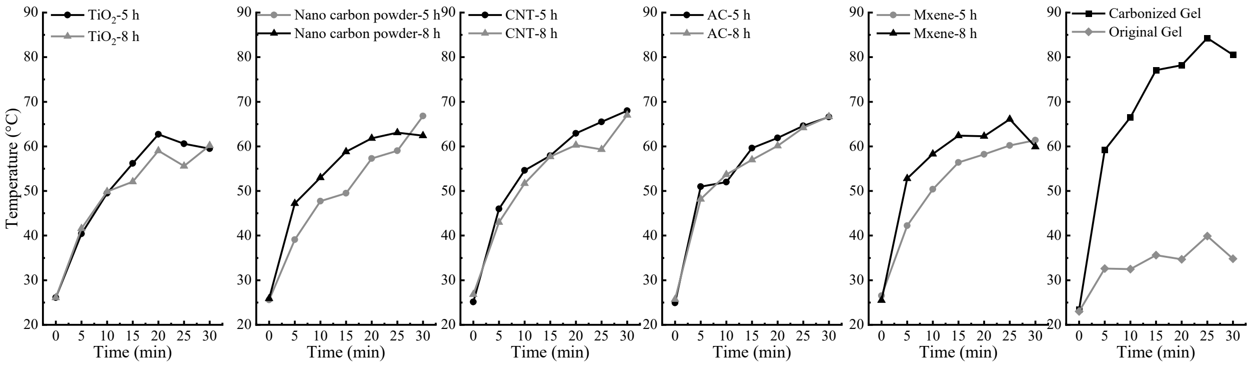

Figure 12: Surface temperature changes of different black cellulose gels under natural sunlight

3.6. Hygroscopicity of Corn Stalk Cellulose Gel

Corn stalk cellulose gels (CSCGs) were synthesized from corn stalk cellulose. Figure 10 shows the effects of different corn stalk cellulose additions on cyclic hydration/dehydration properties of CSCGs. As can be seen from the figure, the hygroscopic capacities of CSCGs decrease with an increase in the amount of corn stalk cellulose addition amount. Hygroscopic capacities of with corn stalk cellulose addition amount of 1wt%, 2wt% and 3wt% were 1.8216 g/g, 1.4463 g/g and 1.1654 g/g, respectively. However, with the progress of cyclic hydration/dehydration experiment, the hygroscopic capacities of CSCGs with cellulose addition of 1wt% and 2wt% in the second cycle adsorption process were higher than that in the first cycle. There may be two reasons for this result: on the one hand, the firstcycle is not saturated by adsorption; On the other hand, part of LiBr is leaked from the gel with adsorbed water (as shown in Figure 10). In addition, the higher the corn stalk cellulose addition amount, the less water remaining in cellulose gel after dehydration. Although the residual water desorption amount and leakage amount of cellulose gel with 1wt% added corn stalk cellulose are the most, considering that hygroscopic capacity is much higher than that of other cellulose gels, the gel with 1wt% corn stalk cellulose addition has the best cyclic hydration/dehydration performance.

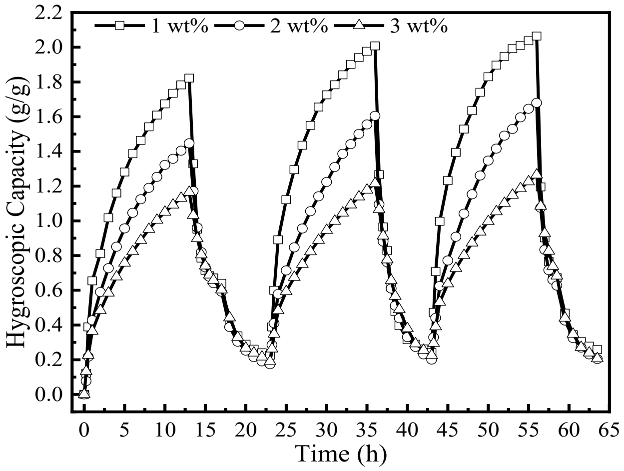

Figure 13: Dynamic hygroscopic curve of corn stalk cellulose gels: effect of corn stalk cellulose addition amount on hygroscopicity

Figure 11 shows the effect of different solvent exchange times on cyclic hydration/dehydration properties of CSCGs. As can be seen from the figure, hygroscopic capacities of CSCGs with the first cyclic solvent exchange time of 7 h, 8 h, 9h and 10 h are 1.9465 g/g,1.8216 g/g, 1.7614 g/g and 1.5869 g/g, respectively. Hygroscopic capacities of CSCGs decrease with the increase of solvent exchange time. However, with experiment of cyclic hydration/dehydration, the hygroscopic capacities of CSCGs with solvent exchange time of 7 h, 8 h and 9 h during the second cycle is higher than that of the first cycle. There may be two reasons for this result: on the one hand, the first cycle is not saturated by adsorption; On the other hand, part of LiBr is leaked from the gel with adsorbed water (as shown in Figure 11). In addition, the longer solvent exchange time, the less water remaining in cellulose gel after dehydration. Although adsorption capacity of gels with solvent exchange time of 10 h in three water vapor cycles is lower than that of gels prepared with solvent exchange time of 7 h, 8 h and 9 h, considering that residual amount of dehydration and leakage of gels with solvent exchange time of 7 h, 8 h and 9 h are more than those with solvent exchange time of 10 h. Therefore, the gel with solvent exchange time of 10 h has the best hydration/dehydration cycle performance.

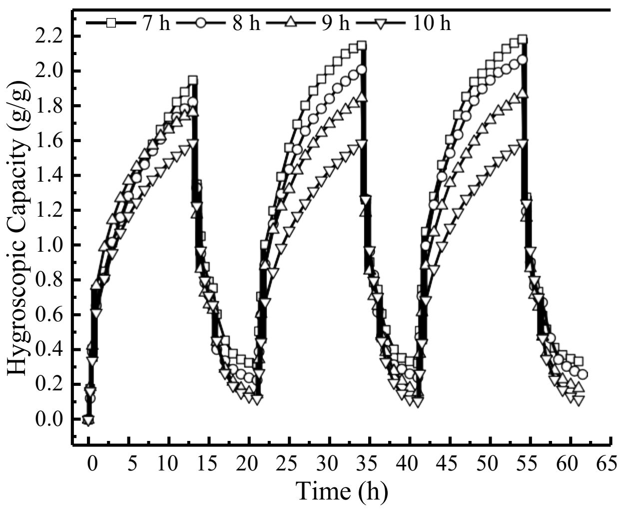

Figure 11: Dynamic hygroscopic curve of corn stalk cellulose gels: effect of LiBr solvent exchange time on hygroscopicity

3.7. Microscopic surface morphology

The microtopography of carrageenan gel, cellulose gel and composite gel was characterized by Scanning Electron Microscope (SEM, ThermoFisher). Microscopic surface morphology of the gels is shown in Figure 12. The SEM images of carrageenan gel and cellulose gel show that directional freezing during sample preparation is beneficial to formation of directional pore structure. Among them, the pore wall of single-component cellulose gel (Figure 12 c) collapsed due to sampling operation, but it still could be seen thedirectional structure formedduring preparation process. While the composite gel may be due to interaction between carrageenan and cellulose molecules that hinder the formation of longitudinal ice crystals during directional freezing, resulting in a disordered pore structure.

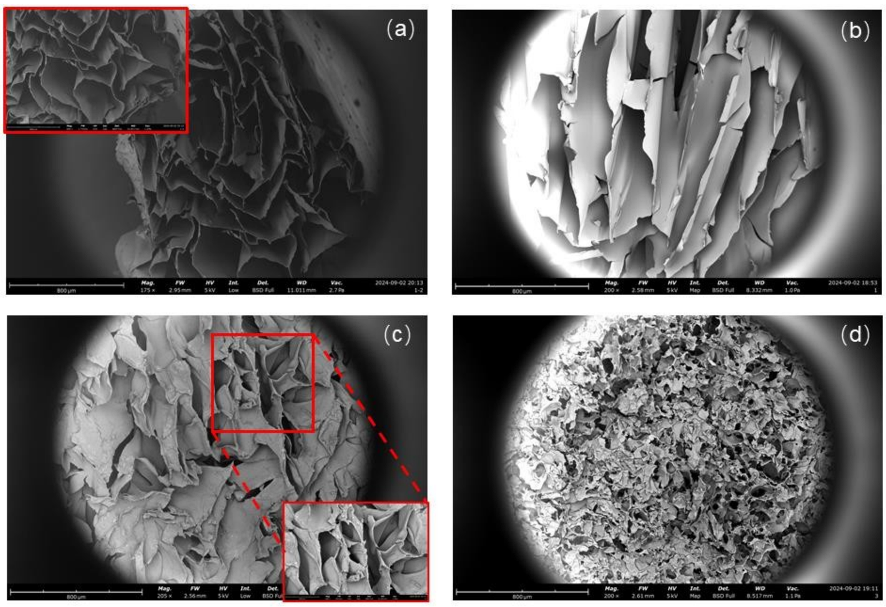

Figure 12: SEM of (a) carrageenan gel cross-section, (b) carrageenan gel longitudinal section, (c) cellulose gel and (d) composite gel

3.8. Comparative analysis of heat storage performance and cost

Material cost is one of the important indexes to evaluate feasibility and competitiveness of TCM application in practice. Since instruments involved in experiments can be used for a long time, here we only need to consider the cost of chemical raw materials for adsorbent synthesis. And we compared the heat storage performance and cost of composite TCM for thermochemical heat storage, as shown in Table 1. From the table, we can see that the existing TCMs cannot take into account both thermochemical heat storageperformance and cost. Among them, the composite TCM based on metal-organic framework, due to the fact that preparation process involves a variety of raw materials, is usually expensive, which limits its practical application, even though the energy storage density is high. On the other hand, porous material-based composite TCM has either high heat storage temperature (adsorbent regeneration temperature) and low cost and low heat storage density. The corn stalk cellulose gel obtained in this work has a low heat storage temperature, which makes the gel suitable for low temperature heat storage. From a cost point of view, the cost of cellulose gel is lower than that of other composite TCMs, although the heat storage density is slightly lower, due to low salt content.

Table 1: Comparison of composite TCMs performance and cost

TCM	Salt content	Hygroscopic capacity (g/g)	Discharge condition	Charge temperature (°C)	Energy storage density (J/g)	Price (CNY/kg) [a]	Reference
AC/$CaCl_2$	43.43% $CaCl_2$	1.07	20 °C & 80% RH	80	2981	21.99	(Zhang et al., 2024)
BNTC@$CaCl_2$	20% $CaCl_2$	20% (TWL)	30 °C & 60%RH	125	854.5	8.09	(Ait Ousaleh et al., 2022)
BNTC@LiCl	20% LiCl	14.7% (TWL)	30 °C & 60%RH	110	704.2	12.49	(Ait Ousaleh et al., 2022)
BNTC@$SrCl_2$	20% $SrCl_2$	18.9% (TWL[b])	30 °C & 60%RH	150	778.6	20.19	(Ait Ousaleh et al., 2022)
$MgSO_4$/MXene	87.6% $MgSO_4$	0.34	25 °C & 85%RH	150	1709	54.26	(Rehman et al., 2023b)
$MgCl_2$/MXene	95.3 % $MgCl_2$	1.97	25 °C & 85% RH	150	2081	33.97	(Rehman et al., 2023a)
$MgCl_2$/MXene	97.6 $MgCl_2$	2.20	25 °C & 85% RH	150	2227	36.80	(Rehman et al., 2023a)
$SrBr_2 \cdot 6H_2O$: Graphite: Cellulose	5:1:1	0.20	23 °C & 50% RH	120	764	6.07	(Salviati et al., 2020)
$CaCl_2$@GA	96% $CaCl_2$	2.89	30 °C & 90% RH	80	5688 (1580 Wh./kg[c])	33.94	(Yan et al., 2021)
EP/$CaCl_2$	15% $CaCl_2$	1.20	20 °C & 80% RH	＞100	2166	5.37	(Wei et al., 2022)
SP/$CaCl_2$	64% $CaCl_2$	0.58	20 °C & 80% RH	＞100	1026	22.40	(Wei et al., 2022)
DT/$CaCl_2$	33% $CaCl_2$	0.82	20 °C & 80% RH	＞100	1520	11.77	(Wei et al., 2022)
7.6-$MgSO_4$/BAC	7.6% $MgSO_4$	0.37	30 °C & 60% RH	150	920	14.87	(Nguyen et al., 2023)
MIL-101(Cr)−10% $Na_2S_2O_3$	61.8% $Na_2S_2O_3$	0.04	30 °C & 30% RH	100	745.9	/	(Padamurthy et al., 2022)
MIL-101(Cr)−30% $Na_2S_2O_3$	93.8% $Na_2S_2O_3$	0.05	30 °C & 30% RH	100	1099.5	/	(Padamurthy et al., 2022)
Li/ZSPCM(700)-50	50% LiOH	0.44	30 °C & 80% RH	105	1373.3	/	(Yang et al., 2021)
C1.0-SSS	21% $MgSO_4$	0.12	10 °C & 12.3 mbar	140	180 (0.18 GJ/ton[d])	1.00 (132.60 €/ton)	(Lavagna et al., 2020)
Corn stalk cellulose gel	25% LiBr	1.58	20 °C & 80% RH	80	1189.5	7.00 CNY/kg	This work

[1] Source: search on B2B platforms, e.g. Alibaba.com. [1] TWL: thermogravimetric weight loss [1] 1 Wh/kg = 3.6 J/g [1] 1GJ=10^6 kJ

4. CONCLUSION

In this article, we provide a simple and low-cost method for preparation of thermochemical heat storage materials. The results showed that the cellulose gel has a high hygroscopicity of 1.5 g/g and energy storage density of 1189.5 J/g. And this TCM can be completely regenerated under low temperature conditions. Cyclic hygroscopicity is stable and the photothermal conversion performance is excellent, which makes it possible for cellulose gels to be used as thermochemical heat-storage and hygroscopic materials for solar energy regeneration.

5. REFERENCES

73rd Statistical Review of World Energy. Energy Institute. 2024: https://www.energyinst.org/statistical-review.

AIT OUSALEH, H., SAIR, S., MANSOURI, S., ABBOUD, Y., ZAHOUILY, M., FAIK, A. & BOUARI, A. E. 2022. Enhanced inorganic salts stability using bentonite clay for high-performance and low-cost thermochemical energy storage. Journal of Energy Storage, 49**,** 104140.

CHEN, S. & YANG, Q. 2024. Renewable energy technology innovation and urban green economy efficiency. Journal of Environmental Management, 353**,** 120130.

DU, X. S., WANG, J. A., JIN, L. Z., DENG, S., DONG, Y. & LIN, S. J. 2022. Dopamine-Decorated Ti_3C_2Tx MXene/Cellulose NanofiberAerogels Supported Form-Stable Phase Change Composites with Superior Solar-Thermal Conversion Efficiency and Extremely High Thermal Storage Density. Acs Applied Materials & Interfaces, 14**,** 15225-15234.

EJEIAN, M. & WANG, R. Z. 2021. Adsorption-based atmospheric water harvesting. Joule, 5**,** 1678-1703.

EL SAYED, M. M. 2023. Production of Polymer Hydrogel Composites and Their Applications. Journal of Polymers and theEnvironment, 31**,** 2855-2879.

GAO, P., WEI, X., WANG, L. & ZHU, F. 2022. Compression-assisted decomposition thermochemical sorption energy storage systemfor deep engine exhaust waste heat recovery. Energy, 244**,** 123215.

LAVAGNA, L., BURLON, D., NISTICò, R., BRANCATO, V., FRAZZICA, A., PAVESE, M. & CHIAVAZZO, E. 2020. Cementitious composite materials for thermal energy storage applications: a preliminary characterization and theoretical analysis. Scientific Reports, 10**,** 12833.

LI, S., HERNANDEZ, S. & SALAZAR, N. 2023. Biopolymer-Based Hydrogels for Harvesting Water from Humid Air: A Review. Sustainability, 15.

LIU, Q., QIN, C., SOLOMIN, E., CHEN, Q., WU, W., ZHU, Q. & MAHIAN, O. 2023. Research progress on the development of new nano materials for solar-driven sorption-based atmospheric water harvesting and corresponding system applications. Nano Energy, 115**,** 108660.

MAKHANYA, N., OBOIRIEN, B., REN, J., MUSYOKA, N. & SCIACOVELLI, A. 2021. Recent advances on thermal energy storage using metal-organic frameworks (MOFs). Journal of Energy Storage, 34**,** 102179.

MOULAKHNIF, K., AIT OUSALEH, H., SAIR, S., BOUHAJ, Y., EL MAJD, A., GHAZOUI, M., FAIK, A. & EL BOUARI, A. 2024.
Renewable approaches to building heat: exploring cutting-edge innovations in thermochemical energy storage for building heating. Energy and Buildings, 318**,** 114421.

NANDAKUMAR, D. K., ZHANG, Y., RAVI, S. K., GUO, N., ZHANG, C. & TAN, S. C. 2019. Solar Energy Triggered Clean Water
Harvesting from Humid Air Existing above Sea Surface Enabled by a Hydrogel with Ultrahigh Hygroscopicity. 31**,** 1806730.

NGUYEN, M. H., ZBAIR, M., DUTOURNIé, P. & BENNICI, S. 2023. Thermochemical sorption heat storage: Investigate the heatreleased from activated carbon beads used as porous host matrix for $MgSO_4$ salt. Journal of Energy Storage, 59**,** 106452.

PADAMURTHY, A., NANDANAVANAM, J. & RAJAGOPALAN, P. 2022. Preparation and characterization of metal organic framework based composite materials for thermochemical energy storage applications. Applied Surface Science Advances, 11**,** 100309.

REHMAN, A. U., ZHAO, T., MUHAMMAD, I., RASHEED, S., SHAH, R., ALTAF, A. R., ZHANG, F. & YUN, S. 2023a. $MgCl_2$-MXene based nanohybrid composite for efficient thermochemical heat storage application. Journal of Energy Storage, 59**,** 106509.

REHMAN, A. U., ZHAO, T., SHAH, M. Z., KHAN, Y., HAYAT, A., DANG, C., ZHENG, M. & YUN, S. 2023b. Nanoengineering of $MgSO_4$ nanohybrid on MXene substrate for efficient thermochemical heat storage material. Applied Energy, 332**,** 120549.

SALVIATI, S., CAROSIO, F., CANTAMESSA, F., MEDINA, L., BERGLUND, L. A., SARACCO, G. & FINA, A. 2020. Ice-templated nanocellulose porous structure enhances thermochemical storage kinetics in hydrated salt/graphite composites. Renewable Energy, 160**,** 698-706.

TYAGI, V. V., PATHAK, S. K., CHOPRA, K., SAXENA, A., KALIDASAN, B., DWIVEDI, A., GOEL, V., SHARMA, R. K., AGRAWAL, R., KANDIL, A. A., AWAD, M. M., KOTHARI, R. & PANDEY, A. K. 2024. Sustainable growth of solar drying technologies: Advancing the use of thermal energy storage for domestic and industrial applications. Journal of Energy Storage, 99, 113320.

VELáSQUEZ, P., MONTENEGRO, G., VALENZUELA, L. M., GIORDANO, A., CABRERA-BARJAS, G. & MARTIN-BELLOSO, O. 2022. k-carrageenan edible films for beef: Honey and bee pollen phenolic compounds improve their antioxidant capacity. Food Hydrocolloids, 124, 107250.

WEI, S., ZHOU, W., HAN, R., GAO, J., ZHAO, G., QIN, Y. & WANG, C. 2022. Influence of minerals with different porous structureson thermochemical heat storage performance of CaCl2-based composite sorbents. Solar Energy Materials and Solar Cells, 243, 111769.

XU, J., WANG, P., BAI, Z., CHENG, H., WANG, R., QU, L. & LI, T. 2024. Sustainable moisture energy. Nature Reviews Materials.

YAN, T., LI, T., XU, J., CHAO, J., WANG, R., ARISTOV, Y. I., GORDEEVA, L. G., DUTTA, P. & MURTHY, S. S. 2021. Ultrahigh-Energy-Density Sorption Thermal Battery Enabled by Graphene Aerogel-Based Composite Sorbents for Thermal Energy Harvesting from Air. ACS Energy Letters, 6, 1795-1802.

YANG, X., LI, S., ZHAO, J., WANG, X., HUANG, H., WANG, Y. & DENG, L. 2021. Development of lithium hydroxide-metal organic framework-derived porous carbon composite materials for efficient low temperature thermal energy storage. Microporous and Mesoporous Materials, 328, 111455.

ZAINAL, S. H., MOHD, N. H., SUHAILI, N., ANUAR, F. H., LAZIM, A. M. & OTHAMAN, R. 2021. Preparation of cellulose-based hydrogel: a review. Journal of Materials Re search and Technology, 10, 935-952.

ZHAN, D., YU, Q., LI, M., GU, Z., SUN, S., LI, Y., LI, A., ZHU, R., MO, Z. & MA, R. 2024. H_2O_2-enhanced alkaline pretreatment andseparation of tobacco stems for biocellulose composite films with potential application in food preservation. Journal of Environmental Chemical Engineering, 12, 111751.

ZHANG, Q., WU, Y., DONG, S., ZHUO, J., SUN, X. & YAO, Q. 2024. Development of activated carbon/$CaCl_2$ composites for seasonalthermochemical energy storage: Effect of pore structure. Journal of Energy Storage, 97, 112697.

ZHANG, Z., FU, H., LI, Z., HUANG, J., XU, Z., LAI, Y., QIAN, X. & ZHANG, S. 2022. Hydrogel materials for sustainable water resources harvesting & treatment: Synthesis, mechanism and applications. Chemical Engineering Journal, 439.

ZHU, R., YU, Q., LI, M., LI, A., ZHAN, D., LI, Y., MO, Z., SUN, S. & ZHANG, Y. 2024. Green synthesis of natural nanocomposite with synergistically tunable sorption/desorption for solar-driven all-weather moisture harvesting. Nano Energy, 124, 109471.

#302: Analysing sustainable biomass carbon electrode materials using the scientometrics and visualisation

Menghan HE[1],Li BAI[2] *,Xinshuai GENG[3],Qi CHEN[4] ,Zhao CHEN[5]

[1] KeyLaboratory of Songliao Aquatic Environment Ministry of Education, School of Municipal and Environmental, Engineering,Jilin Jianzhu University, Changchun 130118, China,hmh1613343353@163.com
[2] * Key Laboratory of Songliao Aquatic Environment Ministry of Education, School of Municipal and Environmental, Engineering, Jilin Jianzhu University, Changchun 130118, China,baili@jlju.edu.cn
[3] Key Laboratory of Songliao Aquatic Environment Ministry of Education, School of Municipal and Environmental, Engineering,Jilin Jianzhu University, Changchun 130118, China,gengxinshuai@student.jlju.edu.cn
[4] Key Laboratory of Songliao Aquatic Environment Ministry of Education, School of Municipal and Environmental, Engineering,Jilin Jianzhu University, Changchun 130118, China;16603311877@163.com
[5]School of Municipal and Environmental Engineering,Jilin JianzhuUniversity, Changchun, 130118, China, chenzhao0703 @163.com

Abstract: Energy storage technology determines the safety, stability, and economic viability of renewable energy utilization. The utilization of carbon materials derived from biomass in energy storage batteries has garnered significant interest owing to its exceptional performance and eco-friendliness. The central research emphasis lies in the regulation of electrochemical characteristics by manipulating pores, structure, and elemental composition. In this study, a comprehensive bibliometric analysis was conducted on 500 pertinent papers obtained from the Web of Science databasespanning the years 2013 to 2023. The analysis aimed to examine research trends and the developmental trajectory of biocarbon as an electrode material. This was achieved by employing the latest dataset, keyword clustering, burst analysis, and literature visualization techniques using CiteSpace in conjunction with SATI tools. The analysis identified the most influential countries, institutions, and subject areas in this research field, and listed the top ten papers. The United States and Indonesia are noteworthy contributors to the research findings in this particular field, where the Chinese Academy ofSciences stood out for its high number of publications and citations. Research in this field has predominantly concentrated on supercapacitor preparation and biomass charcoal application. However, there has been a recent shift towards utilizing"waste biomass" in research endeavors.

Keywords: Sustainable Biomass Carbon Materials, Electrode Materials, Bibliometric Analysis

1. INTRODUCTION

In light of the significant threat that global climate change presents to human society, an increasing number of nations have adopted "carbon neutrality" as a key national strategy, envisioning a future devoid of carbon emissions. Nevertheless, the energy composition of the majority of nations continues to be predominantly reliant on fossil fuels. The consensus on the energy crisis and global warming resulting from this dependence on fossil fuels has garnered significant attention. The global energy transition has progressed from the initial accumulation phase to the current comprehensive acceleration phase, highlighting the significance of research and development in energy storage devices and materials. In recent years, there has been a growing interest in the innovative utilization of waste materials, particularly the effective utilization of waste biomass. The three northeastern provinces of China serve as the primary grain-producing regions in the country. However, a significant portion of the by-products of grain production, such as straw and rice husk, are often disposed of in the fields or incinerated. This practice leads to the generation of a substantial number of harmful substances and CO_2 through open burning, resulting in environmental pollution and resource wastage. Research investigating the utilization of carbon materials derived from biomass in energy storage batteries has revealed that biomass exhibits exceptional energy storage capabilities post-carbonization and activation. Particularly noteworthy is its performance as an electrode material in supercapacitors, where its efficiency rivals or even surpasses that of conventional energy storage materials. This discovery paves the way for a novel approach to the effective utilization of waste biomass.

Biomass-derived carbon materials possess advantageous characteristics due to their abundant sources and environmentally friendly properties, making them promise for potential use in energy storage applications. The significance of these materials is underscored by their exceptional physical and chemical attributes, including high electrical conductivity, large specific surface area, and outstanding electrochemical stability [1]. Ding et al. (2019) successfully produced camphor wood waste through the carbonization of nitrogen/phosphorus/oxygen-containing microporous carbons (CWW-N/P/O-MPCs), demonstrating outstanding capacitance characteristics. The CWW-N/P/O-MPCs-0.5 samples exhibited a specific capacitance of up to 245 Fg(-1) and a bulk capacitance of up to 208Fm(-3) at 0.5 Ag(-1), along with demonstrating long-term stability [2]. Wang et al. (2015) utilized willow catkins flocculent as the raw material to produce flaky primary activated carbon particles with three-dimensional micron-sized macropores through the KOH chemical activation method. The resulting activated carbon exhibited a moderate specific surface area, a concentrated pore size distribution, high nitrogen and oxygen content, a high degree of graphitization, as well as favorable electrical conductivity and capacitance properties [3]. Secondly, as the superior performance of biomass-derived carbon materials is increasingly recognized, their utilization has expanded to various energy storage devices. These materials are now applied in critical areas including lithium-ion batteries, supercapacitors, and fuel cells [4-7]. Li et al. (2020) conducteda study investigating the utilization of activated carbon derived from cannabis stems as anode materials for lithium-ion batteries. Their findings revealed that the pore structure of the activated carbon enhanced the electrochemical performance following low-temperature treatment, offering a novel approach for enhancing the capacity of lithium-ion batteries [8]. Despite the advantages offered by new battery technologies, such as lithium-ion batteries, in terms of energy density and lightweight properties, lead-acid batteries continue to hold a significant position in various traditional and industrial applications. This is attributed to their stability, cost-effectiveness, and high recyclability [9-11]. Lead-carbon batteries, which utilize carbon material derived from biomass as the negative electrode, represent an enhanced version of lead-acid batteries. These batteries combine the high energy density characteristic of lead-acid batteries with the high-power density advantages of supercapacitors. Moreover, the incorporation of biomass-derived carbon materials as the negative electrode further enhances the overall performance of the battery [12,13]. Lead-carbon batteries exhibit significant potential for development and broader prospects for application in specific contexts. The research team led by Lin Haibo at Jilin University specializes in the fields of electrochemistry and electrochemical engineering. They have achieved significant advancements in the technology of lead-carbon batteries by utilizing biomass carbon derived from rice husks. Significant advancements have been accomplished in critical technologies, including elucidating the mechanism of action of biomass carbon materials, understanding battery failure mechanisms, developing carbon anode additives for batteries, and producing cost-effective lead-carbon batteries. One of the innovations implemented by the team involves utilizing rice husk to create carbon-based anode additives for high-performance lead-carbon batteries [14-16]. This approach not only enhanced the battery's performance but also facilitated its commercial viability. The advanced lead-carbon battery developed has achieved a prominent position in the global arena and offers an efficient solution for enhancing the performance of super batteries. In this study, bibliometric and visualization analyses were employed to acquire a thorough comprehension of carbon materials derived from biomass. Bibliometric analyses offer researchers, policymakers, and funding agencies valuable tools to comprehend the evolving landscape of scientific research from a macroscopic viewpoint. This understanding enables more precise predictions and guidance for future research endeavors [17].

2. MATERIALS AND METHODS

2.1. Data sources

In this study, the WOS (Web of Science) database, an academic literature database operated by Clarivate Analytics, Inc., was searched for literature related to the keywords "biomass carbon materials, supercapacitors, and electrode materials." A total of 540 relevant papers, including their citation and quotation information, were retrieved from the ten-year period spanning from 2013 to 2023. After filtering out books and conference proceedings, 500 articles were obtained in plain text file format.

2.2. Data processing

Visual analytics, serving as a technique for transforming data into visual forms, significantly enhances users' comprehension, interpretation, and retrieval of data [18,19]. As a powerful communication tool, it is especially adept at elucidating intricate data to individuals without specialized knowledge [20,21]. Bibliometrics is a methodology employed to analyze a substantial volume of academic research, synthesize findings, identify focal points, and innovations within the research domain. It encompasses a diverse set of tools for the processing and interpretation of data derived from scholarly literature [22,23]. As depicted in Figure 2, subsequent to data extraction from the Web of Science (WOS) and data filtering, various network types were generated utilizing CiteSpace and SATI. These networks encompass co-citation networks, collaborative networks, and keyword co-occurrence networks. For each network, suitable time slicing and threshold parameters were established to extract the most significant and influential nodes, including papers, authors, and institutions. CiteSpace, a commonly employed software for visual analysis of literature, was employed to identify the top 10 most active researchers in biomass-derived carbon electrode materials from the Web of Science (WOS) database, along with their affiliated countries and institutions, and the number of publications within the last decade. By examining the centrality of these entities, the contributions of various countries and institutions in the field can be elucidated through keyword correlation analysis. It is possible. Moreover, CiteSpace offers keyword burst analysis and country collaboration network analysis, facilitating the exploration of research topic trajectories, identification of current hot topics, and tracking of research trends. For a more intuitive and comprehensive analysis of the literature, the top ten authors, papers, and keywords in the dataset are examined utilizing SATI software. Moreover, through the extraction of high-frequency keywords from scholarly works and the subsequent clustering of keyword co-occurrences, a deeper understanding of theorganization and evolution of the research domain can be achieved. Researchers can enhance their ability to identify and monitor significant advancements and innovations in the field more effectively through the utilization of these tools.

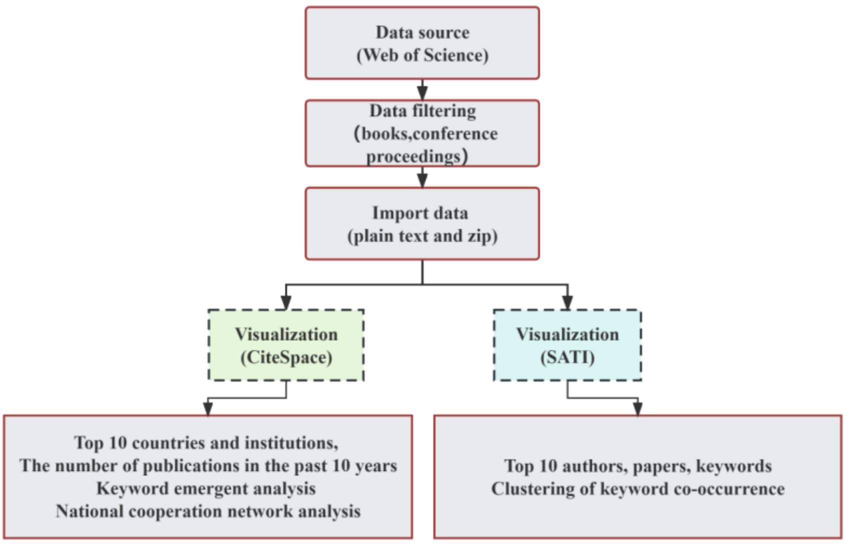

Figure 2: Bibliometric analysis. The filtered data were processed in Citespace and SATI tools respectively.

3. RESULTS

3.1. Analysis of Total Literature

Comprehensive examinations of literature is essential for academic research. By examining and analyzing an extensive volume of scientific data, researchers can gain insights into the intricacies of the evolution of a specific discipline and its emerging areas. This process also enables the identification of research activities and developmental trends within the field [24]. Through the analysis of the collective body of literature, researchers can identify related works that align with their research focus, facilitating interdisciplinary communication and collaboration.

The trend of annual publications reveals the yearly fluctuations in the field of biomass carbon electrode materials. Figure

3. provides a comprehensive overview of the research trends and advancements in the field, offering valuable insights. From the publication data spanning from 2013 to 2023, it is evident that the evolution of the research domain concerning biomass carbon electrode materials has followed a notable three-phase trajectory. Initially, there was a gradual increase in publications from 2013 to 2016, indicating the exploratory characteristics of the field and the progressive development of a research foundation. The significant surge in publications from 2017 to 2019 signifies a phase of heightened scientific productivity, reflecting the rapid advancement and increasing scholarly attention towards utilizing carbon electrode materials derived from biomass as a focal area of research. Research activity experienced a significant surge in 2021, marked by a notable increase of 30 publications compared to the previous year, reflecting a year-on-year growth rate of up to 48%. This surge indicated a new peak in research within the field. The momentum remained consistent from 2021 to 2023. While the annual publication volume exhibited fluctuations, the overall trend remained stable, suggesting a potential

gradual maturation of the field. The text highlights the swift advancement in research concerning biomass carbon electrode materials, indicating its sustained status as a prominent research area. It underscores the potential of biomass carbon electrode materials as a burgeoning field of study and the anticipated rise in market demand for such technologies, pointing towards a promising future. This outlook is further supported by the consistent growth in the annual publication output.

The global distribution of countries and organizations engaged in research on biomass carbon electrode materials over the past decade is quite extensive. As illustrated in Figure 4, the diagram depicts the density of inter-country collaborative networks within the realm of biomass carbon electrode materials, along with the progression of research emphasis over different time periods. In the lower-left corner of the figure, there is a display showing the time of emergence of each country and research theme, where darker colors represent earlier emergence in the research field. The thickness of liaison lines connecting countries serves as an indicator of the level of cooperation between them, where thicker lines symbolize closer cooperation [24]. The analysis of Figure 4 reveals that China emerges as the predominant node, signifying its leading position in terms of publications and collaborative relationships with multiple countries. This positioning underscores China's pivotal role in fostering international cooperation within this research domain. Additionally, India and the United States of America are also prominent nodes, reflecting their significant research contributions and partnerships in the field. Conversely, smaller nodes symbolize other countries like Indonesia, Canada, and Australia, which also play a role in international collaboration within this research area. Their positioning and magnitude within the network imply a relatively lower influence in the field; however, they are actively engaged in international collaborations. The right half of Figure 4. illustrates the clustering of research themes, enabling the identification of the most active and influential research themes in the field. The clusters are numbered and colored to represent various research themes or keywords. For instance, cluster #0 is associated with carbon material, whereas cluster #1 is linked to waste-derived carbon. Cluster #2 is indicative of sustainable biomass-derived porous biochar, whereas Cluster #3 pertains to sustainable energy materials. Other clusters, such as #4, focus on the activation process, and #5 is centered on the oxygen reduction reaction.

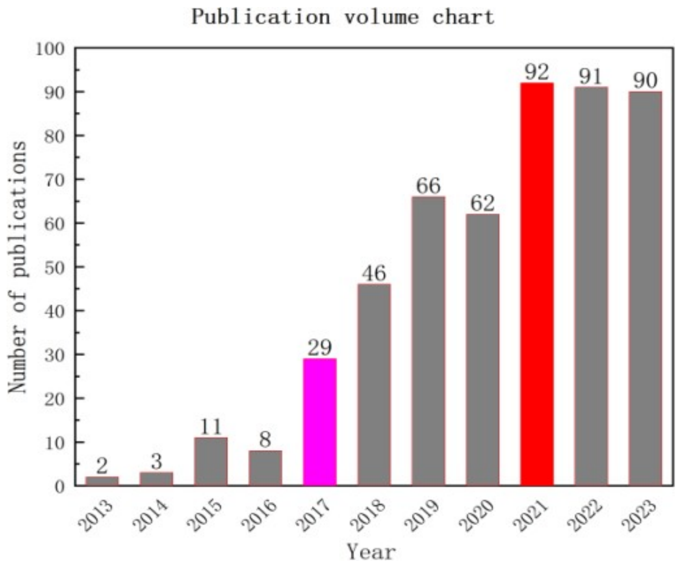

Figure 3: Number of publications in the past 10 years, 2013-2023(“Red and purple represent turning points.")

The tabulated data in Table 1. presents the country’s centrality rankings of the top 10 countries alongside their corresponding publication counts. The significance of China as the central node in the research collaboration network is evident from Table 1, highlighting its crucial role in global research collaboration. China leads with 336 publications, signifying its significant contribution to theoretical research and technological innovation in the field. India follows in second place with 64 publications, and Indonesia ranks third with 33 publications. Centrality serves as a statistical metric within a knowledge graph network, indicating the magnitude of connections. It signifies the relational status of nodes with other nodes in the graph and facilitates the linkage between nodes both preceding and following. China was ranked first with a centrality score of 0.88, while India followed closely with a score of 0.61. While certain countries exhibit a lower quantity of articles, their centrality surpasses that of other nations, indicating significant outcomes of their scientific research. For instance, the United States (0.15), Malaysia (0.12), and India, the United States, and Indonesia are noteworthy contributors to the research findings in this particular field.

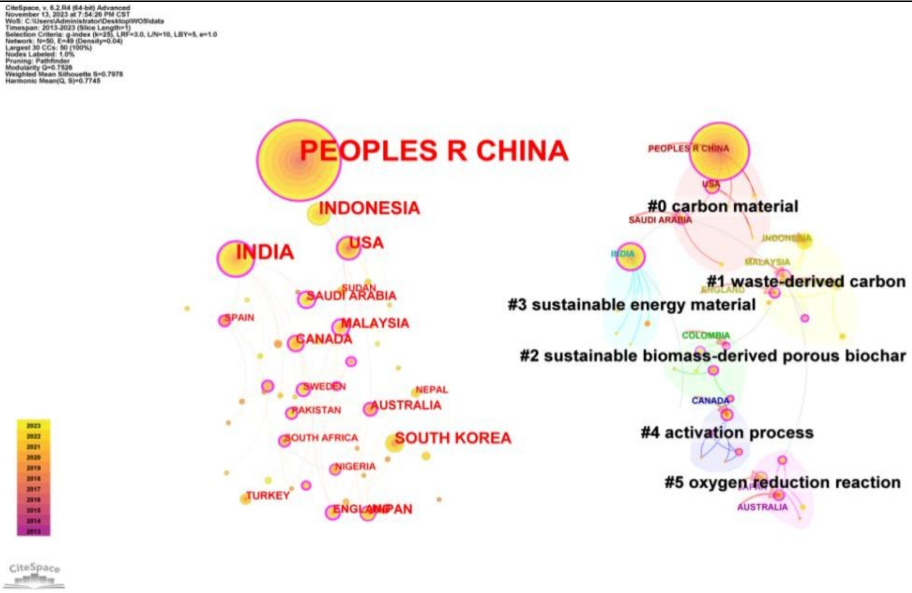

Figure 4: "National Cooperation Network and Keyword Clustering Analysis."

Table 1: Top 10 countries by number of publications.

No.	Country	Centrality	Articles
1	PEOPLES R CHINA	0.88	336
2	INDIA	0.61	64
3	INDONESIA	0.07	33
4	USA	0.15	23
5	SOUTH KOREA	0.04	20
6	MALAYSIA	0.12	12
7	JAPAN	0.11	12
8	CANADA	0.06	11
9	AUSTRALIA	0.05	9
10	SAUDI ARABIA	0.07	9

In this study, three indicators, namely the total number of articles, the total number of citations, and the average number of citations, were employed to evaluate the overall impact of institutions in the field of biomass charcoal electrode materials. Tabulating the results of the ten research institutions with the highest number of articles, citations, and average number of citations, Table 2 illustrates the dominance of Chinese research institutions in the top ten indicators. This underscores China's significant position in the field. The Chinese Academy of Sciences is particularly notable for its high volume of articles and citations, underscoring its leading position in the research field of biomass charcoal electrode materials. It is noteworthy that Beijing University of Chemical Technology, despite having a low ranking in terms of the number of articles and citations, exhibits the highest average number of citations at 12.18. After analyzing the data, the team from Beijing University of Chemical Technology published a series of influential papers on the subject. Further elaboration on these seminal articles is provided in Section 3.2.

Table 5: Ranking of publications of the top 10 research institutions in the field of biochar electrode materials. Note: The Chinese Academy of Sciences in this study is a consortium of multiple institutes/units.

No.	Name of the institution	Articles	TC	AC
1	Univ Riau	35	121	3.46
2	Chinese Acad Sci	20	159	7.95
3	Jilin Univ	16	115	7.19
4	State Islamic Univ Sultan Syarif Kasim	16	51	3.19
5	Lanzhou Univ Technol	13	23	1.77
6	Beijing Univ Chem Technol	11	134	12.18
7	Xiangtan Univ	10	106	10.6
8	Northwest Normal Univ	10	48	4.8
9	Nanjing Forestry Univ	10	31	3.1
10	Qilu Univ Technol	9	15	1.67

3.2. Analysis of the Top 10 Cited Articles

The examination of the aggregate number of articles offers a comprehensive view of the domain of carbon electrode materials for biomass, outlining an initial research framework for scholars. Nevertheless, conducting a thorough analysis of articles and authors with a high citation frequency can assist researchers in effectively and accurately focusing their research endeavors on areas that have had a substantial influence on academia [25]. Highly cited articles play a crucial role in identifying the attributes of frequently referenced papers and authors in academic research, thereby offering guidance for research strategies [26]. Biomass-derived carbon materials have emerged as a significant area of interest in the field of electrode materials, garnering considerable attention in recent research. Table 3. presents an analysis of the top 10 most cited articles in this domain, providing essential details such as the article title, author, citation frequency (FC), and year of publication. Significantly, the majority of these scholarly works were published between 2015 and 2019. This timeframe not only signifies the rapid advancement of the field but also underscores the significance of these articles in advancing the frontiers of science and shaping research agendas. The research discussed in the top ten articles centers on improving the electrochemical properties of materials to be utilized in energy storage devices, specifically supercapacitors. These studies illustrate a variety of shared methodologies and goals, while also highlighting their distinct innovations. The similarities primarily lie in the research focus, methodology, sources of material, and objectives of application. The focusof all papers is to enhance the specific capacitance, stability, and conductivity of carbon materials derived from biomass, which constitutes a fundamental goal within this research field. In methodological terms, the majority of the studies employed comparable procedures, encompassing the synthesis, characterization, and electrochemical performance evaluation of the materials. The selection of material sources relies on biomass, which serves as a prevalent renewable and cost-effective carbon source. Examples include wood, rice husk, and crop by-products. Ultimately, the primary objective of all these studies is to improve the efficiency of energy storage devices, such as supercapacitors. In the realm of innovation, the research indicates a correlation with diversity. Researchers have conducted experiments using various biomass feedstocks and pre-treatment methods to examine the impact of different biomass sources on material properties. Secondly, concerning structural design, several studies have improved material properties through the utilization of porous structures, nanostructures, or specific microstructures. Moreover, the utilization of surface modification and doping methods, such as nitrogen doping or the incorporation of other elements, proves to be efficacious in enhancing the electrochemical characteristics of materials. The optimization of synthesis methods, such as hydrothermal methods and chemical vapor deposition, represents a significant innovation highlighted in these papers. The collective findings of these studies demonstrate the significant potential of biomass carbon materials in the realm of energy storage. Each paper contributes significantly to the synthesis, structural design, and performance enhancement of materials. These innovations are evident not only in the utilization of diverse biomass feedstocks but also in the investigation of structural design and surface modification techniques. The outcomes of this study serve to advance our comprehension of the characteristics and capabilities of biomass carbon materials. Furthermore, they contribute to the improvement of energy storage devices like supercapacitors. Additionally, these findings offer abundant inspiration and avenues for future research endeavors in this domain. Li et al. (year) employed a straightforward one-step pyrolysis and activation-synthesis technique to transform willow flakes into porous carbon nanosheets, subsequently achieving successful nitrogen and sulfur co-doping. The porous carbon nanosheets, doped with nitrogen and sulfur, exhibited a notable specific capacitance of 298 F/g at 0.5 A/g and 233 F/g at 50 A/g. Additionally, they displayed exceptional rate capability and outstanding cycling stability, retaining 98% of their capacitance after 10,000 cycles [27]. The study introduced a methodology for designing green and cost-effective electrode materials to produce high-performance supercapacitors. It showcased a novel approach to regulate the pore structure of the resulting carbon by varying the mass ratio of the raw material and alkali. Gong et al. (year) conducted the synthesis of three-dimensional porous graphitized biomass carbon (PGBC) materials through a one-step process utilizing potassium ferrate. This method facilitated the simultaneous carbonization and graphitization of bamboo charcoal. The approach was noted for its high efficiency, time-saving nature, and environmentally friendly characteristics. The PGBC electrodes demonstrated a high specific capacitance of 222.0 F/g at 0.5 A/g and exhibited good energy-power output performance in both aqueous and ionic liquid electrolytes. Specifically, they achieved energy-poweroutputs of 6.68 Wh/kg at 100.2 W/kg and 20.6 Wh/kg at 12 kW/kg in aqueous and ionic liquid electrolytes, respectively. This study introduces an economical and environmentally friendly method for producing renewable biomass-derived carbon materials for advanced energy storage applications. The innovation involves efficient simultaneous carbonization and graphitization of bamboo charcoal using potassium ferrate [28]. Furthermore, these five articles, which have high citation frequencies of 4, 5, 6, 7, and 8[30-35], collectively concentrate on pioneering research concerning carbon materials derived from biomass for applications in supercapacitors. The studies emphasize the significance of heteroatom-doped porous carbon flakes obtained from diverse biomass sources as electrode materials for high-efficiencysupercapacitors. The materials significantly improve the charge storage capacity and stability in both aqueous and organic electrolytes as a result of their distinctive microporous/mesoporous structure, extensive surface area, and heteroatom doping. The pore structure and electrochemical properties of these materials can be optimized through precise adjustments in the carbonation and activation processes. This optimization can lead to a significant enhancement in their performance as supercapacitor electrodes. Three extensively cited review articles concentrate on the utilization of carbon materials derived from biomass. These materials enhance the key performance indicators of supercapacitors, including charge storage mechanisms, optimization of electrode materials, selection of electrolytes, and enhancement of system characteristics, due to their environmental and economic benefits. The article emphasizes the high-power density and rapid charging and discharging abilities of supercapacitors, characteristics that position them as a viable substitute for or addition to rechargeable batteries. The study also investigates the utilization of biomass-derived carbon materials with various dimensions, including agricultural waste, to augment the potential for capacitor applications. The results indicate that biomass carbon materials have a significant impact on improving the efficiency of supercapacitors, lowering expenses, andpromoting the development of eco-friendly technologies. In the future, these materials are expected to find broader applications in energy storage and power electronics, playing a crucial role in facilitating the achievement of a sustainable energy transition.

Table 6: Top 10 highly cited articles on bio-carbon electrode materials research.

No.	FC	Year	Authors	Articles Title	References
1	66	2016	Li YJ	Nitrogen and sulfur co-doped porous carbon nanosheets derived from willow catkin for supercapacitors	[27]
2	62	2017	Gong YN	Highly porous graphitic biomass carbon as advanced electrode materials for supercapacitors	[28]
3	53	2016	Wang YG	Electrochemical capacitors: mechanism, materials, systems, characterization and applications	[29]
4	52	2014	Qian WJ	Human hair-derived carbon flakes for electrochemical supercapacitors	[30]
5	52	2013	Sun L	From coconut shells to porous graphene-like nanosheets for high-power supercapacitorst	[31]
6	51	2013	Wang H	Interconnected Carbon Nanosheets Derived from Hemp for Ultrafast Supercapacitors with High Energy	[32]
7	50	2015	Abioye AM	Recent development in the production of activated carbon electrodes from agricultural waste biomass for supercapacitors: A review	[33]
8	46	2014	Sevilla M	Energy storage applications of activated carbons: supercapacitors and hydrogen storage	[34]
9	46	2016	Zhao YQ	Hierarchically porous and heteroatom doped carbon derived from tobacco rods for supercapacitors	[35]
10	44	2019	Bi ZH	Biomass-Derived Porous Carbon Materials with Different Dimensions for Supercapacitor Electrodes: a review	[36]

3.3. Keyword clustering and cluster analysis

Keyword analysis plays a crucial role in identifying current and significant issues within a research cycle [37]. High-frequency keywords were extracted from the literature utilizing the SATI tool and subsequently analyzed through clustering techniques. In this manner, it is possible to display correlations and temporal relationships among keywords, thereby reflecting trends in research concepts. The keywords in an article serve as the primary concepts of the study. Keyword significance denotes the sudden surge in the frequency of a specific keyword within a defined timeframe. This phenomenon aids in monitoring research focal points and emerging trends during that period. Visual analysis was conducted using the System for Automated Text Interpretation (SATI), as illustrated in Figure 5, which displays the keyword clustering graph. The density of the clusters serves as an indicator of the level of connectivity within the overall topic, where greater intensity correlates with increased topic maturity. Moreover, the frequency of keyword repetition and the extent of coverage are directly proportional to the size of the font and the intensity of the color used in the text withinthe circles. The dataset highlights keywords such as supercapacitors, biomass, composites, activation, biomass carbon preparation, electrode materials, energy storage, hydrothermal carbonization, and multilayer hierarchical porous carbon inbold font. As illustrated in Figure 6., the graph functions as a tool for trend analysis, unveiling the patterns of literature publication for keywords in the field of energy storage from 2013 to 2023. The quantity of publications related to the term "supercapacitor" has notably increased since 2017, reaching a peak in 2022. This trend underscores the significance of supercapacitor technology in current energy research. Meanwhile, there has been an increasing trend in references to the terms "porous carbon" and "activated carbon" in scholarly literature since 2017. This trend contrasts with the overall stable pattern, indicating the persistent significance of these materials in the advancement of electrodes. Research on "biomass carbon" and "biomass-derived carbon" has been steadily increasing annually since 2017. This trend could be attributed to the escalating global enthusiasm for sustainable and eco-friendly energy resources. The increasing prevalence of terms like "asymmetric supercapacitors" and "electrode materials" indicates the growing significance of these emerging technologies in the realm of energy storage solutions. In recent years, there has been a growing interest in the keywords "electrochemical properties" and "electrochemistry," underscoring the significance of electrochemical techniques in the assessment and enhancement of materials for energy storage. The trend map effectively illustrates the evolutionary trajectory of research in the field of energy storage technologies, particularly focusing on electrode materials, and highlights the promising directions for future development. By analyzing the trend of literature publication related to these keywords, researchers can pinpoint the research hotspots within the field. This analysis can help guide future research directions and inform resource allocation decisions.

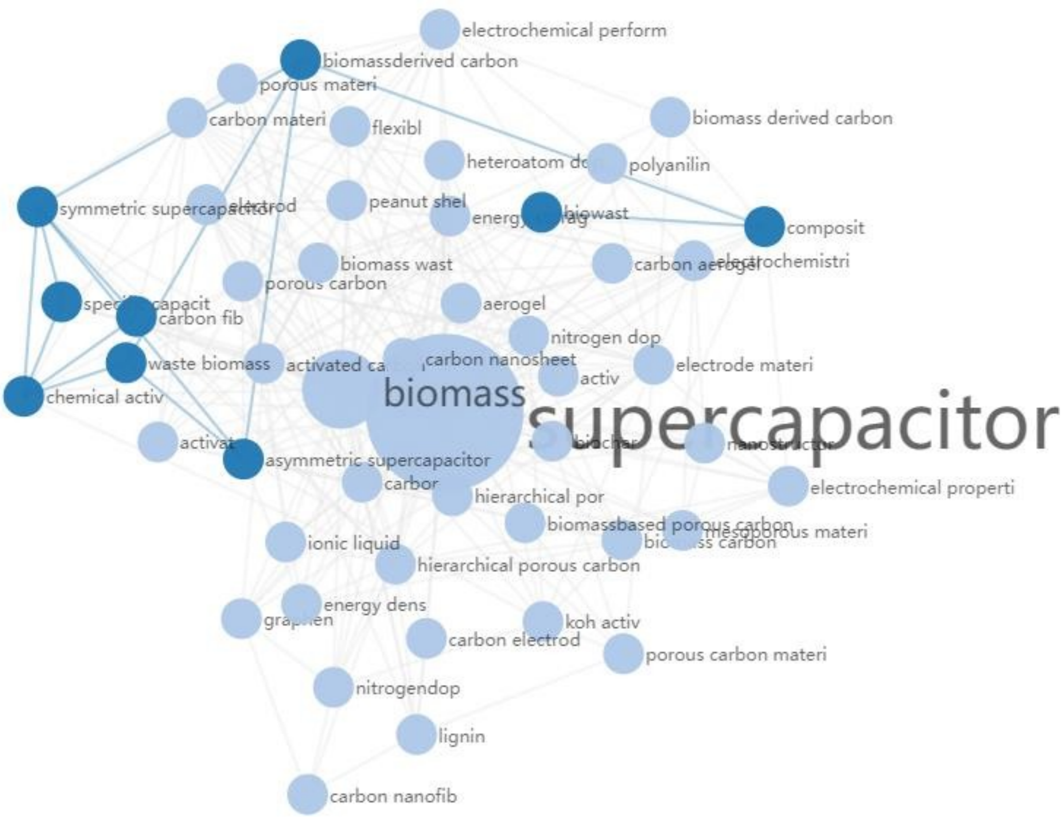

Figure 5. Keyword co-occurrence network visualization

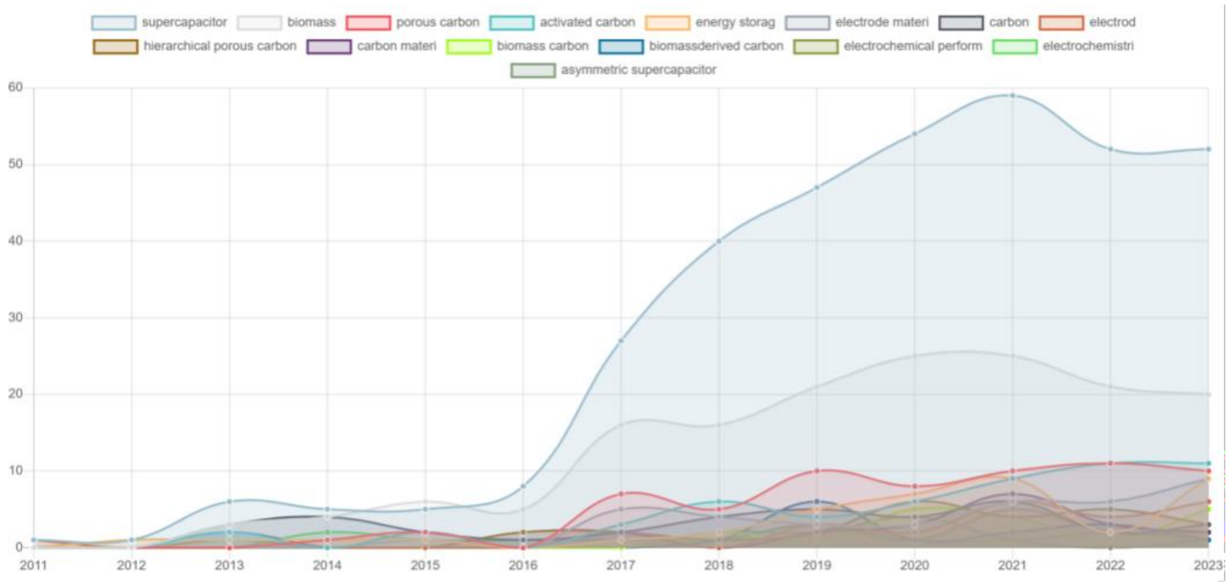

Figure 6: Dynamic analysis of keyword trends

Keyword analysis plays a crucial role in identifying current and significant issues within a research cycle [37]. High-frequency keywords were extracted from the literature utilizing the SATI tool and subsequently analyzed through clustering techniques. In this manner, it is possible to display correlations and temporal relationships among keywords, thereby reflecting trends in research concepts. The keywords in an article serve as the primary concepts of the study. Keyword significance denotes the sudden surge in the frequency of a specific keyword within a defined timeframe. This phenomenon aids in monitoring research focal points and emerging trends during that period. Visual analysis was conducted using the System for Automated Text Interpretation (SATI), as illustrated in Figure 5, which displays the keyword clustering graph. The density of the clusters serves as an indicator of the level of connectivity within the overall topic, where greater intensity correlates with increased topic maturity. Moreover, the frequency of keyword repetition and the extent of coverage are directly proportional to the size of the font and the intensity of the color used in the text within the circles. The dataset highlights keywords such as supercapacitors, biomass, composites, activation, biomass carbon preparation, electrode materials, energy storage, hydrothermal carbonization, and multilayer hierarchical porous carbon in bold font. As illustrated in Figure 6., the graph functions as a tool for trend analysis, unveiling the patterns of literature publication for keywords in the field of energy storage from 2013 to 2023. The quantity of publications related to the term "supercapacitor" has notably increased since 2017, reaching a peak in 2022. This trend underscores the significance of supercapacitor technology in current energy research. Meanwhile, there has been an increasing trend in references to the terms "porous carbon" and "activated carbon" in scholarly literature since 2017. This trend contrasts with the overall stable pattern, indicating the persistent significance of these materials in the advancement of electrodes. Research on "biomass carbon" and "biomass-derived carbon" has been steadily increasing annually since 2017. This trend could be attributed to the escalating global enthusiasm for sustainable and eco-friendly energy resources. The increasing prevalence of terms like "asymmetric supercapacitors" and "electrode materials" indicates the growing significance of these emerging technologies in the realm of energy storage solutions. In recent years, there has been a growing interest in the keywords "electrochemical properties" and "electrochemistry," underscoring the significance of electrochemical techniques in the assessment and enhancement of materials for energy storage. The trend map effectively illustrates the evolutionary trajectory of research in the field of energy storage technologies, particularly focusing on electrode materials, and highlights the promising directions for future development. By analyzing the trend of literature publication related to these keywords, researchers can pinpoint the research hotspots within the field. This analysis can help guide future research directions and inform resource allocation decisions.

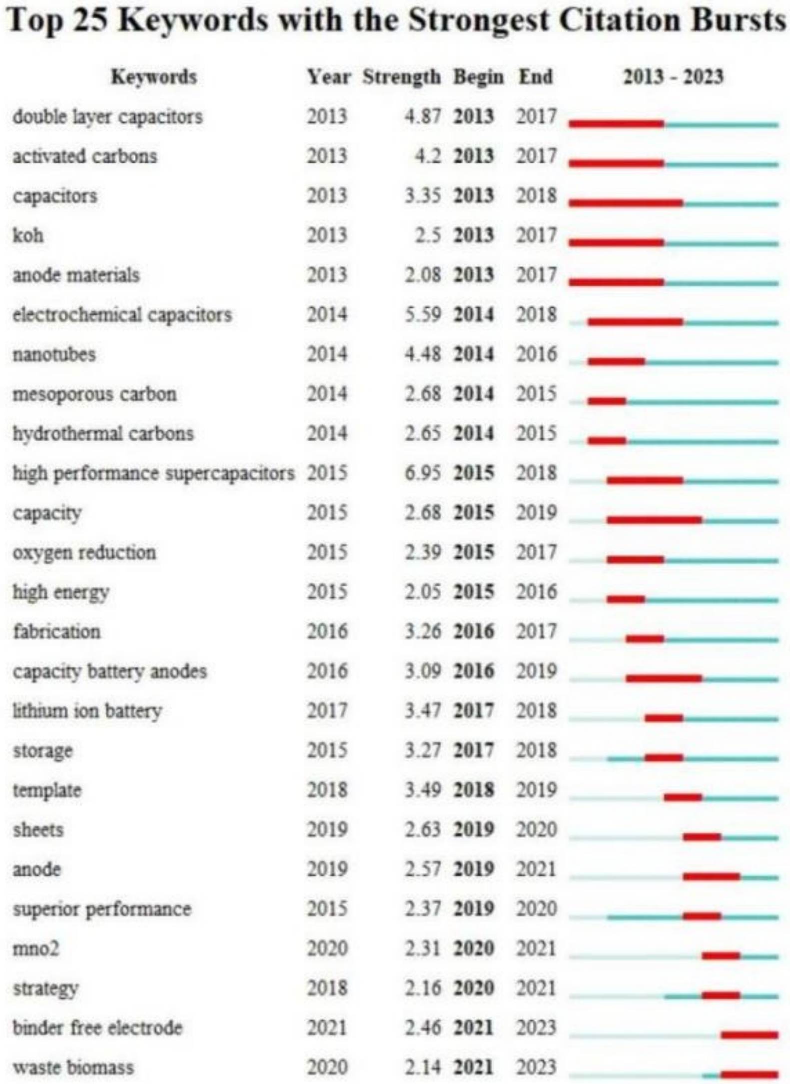

Figure 7: Top 25 Keywords with the Strongest Citation Bursts

4. CONCLUSION

Electrodes serve as fundamental components in energy storage devices, with their material characteristics playing a crucial role in shaping the overall performance of the device. Scholars have investigated biomass, transforming it into activated carbon, and enhancing its electrochemical activity through physical and chemical techniques, including doping with heteroatoms and metals. Recent research findings indicate that altered biomass carbon materials exhibit significant promise for utilization in electrochemical applications. In this study, an in-depth exploration of the preparation technology and application trends of biomass-derived carbon electrode materials was conducted using metrological and visualization analysis. China is identified as the leading country in the field of biomass-derived carbon materials research, with the Chinese Academy of Sciences emerging as the frontrunner in terms of both the quantity of published papers and the citation count. The research focus in this field has shifted towards the utilization of waste biomass. The investigation of biomass carbon electrode materials represents a current leading area of interest in the realm of energy storage.

Supercapacitor technology is increasingly emerging as a focal point in modern energy research. Biomass carbon material preparation and modification technologies are progressively advancing, characterized by the refinement of biomass feedstock selection and the optimization of preparation techniques to yield carbon materials with tailored physical and chemical attributes. These materials exhibit a broad spectrum of potential applications in various fields, including energy storage, environmental remediation, and catalysis. Considering the sustainable and environmentally friendly characteristics of biomass, it is anticipated that these materials will be utilized in a broader range of applications in the future, facilitated by additional research

5. REFERENCES

1. Tian, J.S.; Zhang, T.; Talifu, D.; Abulizi, A.; Ji, Y.J. Porous carbon materials derived from the waste cotton stalk with ultra-high surface area for high performance supercapacitors. Mater. Res. Bull. 2021, 143, 10, doi:10.1016/j.materresbull.2021.111457.

2. Ding, C.F.; Yan, X.D.; Lan, J.L.; Ryu, S.; Yu, Y.H.; Yang, X.P. Camphor wood waste-derived microporous carbons as high-performance electrode materials for supercapacitors. Carbon Lett. 2019, 29, 213-218, doi:10.1007/s42823-019-00013-3.

3. Wang, K.; Zhao, N.; Lei, S.W.; Yan, R.; Tian, X.D.; Wang, J.Z.; Song, Y.; Xu, D.F.; Guo, Q.G.; Liu, L. Promising biomass-based activated carbons derived from willow catkins for high performance supercapacitors. Electrochim. Acta 2015, 166, 1-11, doi:10.1016/j.electacta.2015.03.048.

4. Chen, Q.; Tan, X.F.; Liu, Y.G.; Liu, S.B.; Li, M.F.; Gu, Y.L.; Zhang, P.; Ye, S.J.; Yang, Z.Z.; Yang, Y.Y. Biomass-derived porous graphitic carbon materials for energy and environmental applications. J. Mater. Chem. A 2020, 8, 5773-5811, doi:10.1039/c9ta11618d.

5. Dong, W.X.; Qu, Y.F.; Liu, X.; Chen, L.F. Biomass-derived two-dimensional carbon materials: Synthetic strategies and electrochemical energy storage applications. FlatChem 2023, 37, 28, doi:10.1016/j.flatc.2022.100467.

6. Kalla, A.; Mayilswamy, N.; Kandasubramanian, B.; Mahajan-Tatpate, P. Biochar: a sustainable and an eco-friendly material for energy storage applications. Int. J. Green Energy 2023, 15, doi:10.1080/15435075.2023.2259973.

7. Liu, W.J.; Jiang, H.; Yu, H.Q. Emerging applications of biochar-based materials for energy storage and conversion. Energy Environ. Sci. 2019, 12, 1751-1779, doi:10.1039/c9ee00206e.

8. Li, Z.G.; Guan, Z.X.; Guan, Z.P.; Liang, C.; Yu, K.F. Effect of Deep Cryogenic Activated Treatment on Hemp Stem-Derived Carbon Used as Anode for Lithium-Ion Batteries. Nanoscale Res. Lett. 2020, 15, 8, doi:10.1186/s11671-020-03422-w.

9. Moseley, P.T. Lead/acid battery myths. J. Power Sources 1996, 59, 81-86, doi:10.1016/0378-7753(95)02305-4.

10. Tabaatabaai, S.M.; Rahmanifar, M.S.; Mousavi, S.A.; Shekofteh, S.; Khonsari, J.; Oweisi, A.; Hejabi, M.; Tabrizi, H.; Shirzadi, S.; Cheraghi, B. Lead-acid batteries with foam grids. J. Power Sources 2006, 158, 879-884, doi:10.1016/j.jpowsour.2005.11.017.

11. Yong, S.; Yung-Sen, S.; Shu-Hong, Z.; Yung, G.; Bin, L. Researching on the electrode for lead-acid battery. In Proceedings of the 2nd International Symposium on New Materials for Fuel Cell and Modern Battery Systems, Montreal, Canada, Jul 06-10, 1997; pp. 218-224.

12. He, P.Q.; Tu, J.; Yang, Y.; Huang, H.; Chen, B.M.; Gao, C.; He, Y.P.; Guo, Z.C. Hierarchical tubular porous carbon derived from mulberry branches for long-life lead-carbon battery. J. Energy Storage 2023, 64, 11, doi:10.1016/j.est.2023.107162.

13. Wang, M.; Yu, Q.; Li, S.T.; Chen, Z.; Zhu, W.; Han, L.; Li, H.X.; Ren, L.; Li, L.X.; Lu, X.; et al. A novel three-dimensional hierarchical porous lead-carbon composite prepared from corn stover for high-performance lead-carbon batteries. Energy 2023, 283, 13, doi:10.1016/j.energy.2023.128560.

14. Zhang, W.L.; Lin, N.; Liu, D.B.; Xu, J.H.; Sha, J.X.; Yin, J.; Tan, X.B.; Yang, H.P.; Lu, H.Y.; Lin, H.B. Direct carbonization of rice husk to prepare porous carbon for supercapacitor applications. Energy 2017, 128, 618-625, doi:10.1016/j.energy.2017.04.065.

15. Liu, D.C.; Zhang, W.L.; Lin, H.B.; Li, Y.; Lu, H.Y.; Wang, Y. A green technology for the preparation of high capacitance rice husk-based activated carbon. J. Clean Prod. 2016, 112, 1190-1198, doi:10.1016/j.jclepro.2015.07.005.

16. Bao, J.P.; Lin, N.; Lin, H.B.; Gao, W.Q.; Liu, Z.Q.; Shi, J. Sulfation on coated carbon related to lead ion and its effect on

the performance of advanced ultra-battery at high rate. Chem. Eng. J. 2021, 409, 10, doi:10.1016/j.cej.2020.128151.

17. Ellegaard, O. The application of bibliometric analysis: disciplinary and user aspects. Scientometrics 2018, 116, 181-202, doi:10.1007/s11192-018-2765-z.

18. Blazevic, M.; Sina, L.B.; Burkhardt, D.; Siegel, M.; Nazemi, K. Visual Analytics and Similarity Search - Interest-based Similarity Search in Scientific Data. In Proceedings of the 25th International Conference Information Visualisation (IV) - AI and Visual Analytics and Data Science, Electr Network, Jul 05-09, 2021; pp. 211-217.

19. Hao, M.C.; Dayal, U.; Keim, D.A.; Morent, D.; Schneidewind, J. Intelligent visual analytics queries. In Proceedings of the IEEE Symposium on Visual Analytics Science and Technology, Sacramento, CA, Oct 30-Nov 01, 2007; pp. 91-+.

20. Earnshaw, R. Visual Analytics. In Data Science and Visual Computing; Advanced Information and Knowledge Processing; Springer-Verlag London Ltd: Godalming, 2019; pp. 73-91.

21. Karolczak, P.A.; Manssour, I.H. Using Visual Analytics to Reduce Churn. In Proceedings of the 21st International Conference on Computational Science and Its Applications (ICCSA), Cagliari, ITALY, Sep 13-16, 2021; pp. 380-393.

22. Ninkov, A.; Frank, J.R.; Maggio, L.A. Bibliometrics: Methods for studying academic publishing. Perspect. Med. Educ. 2022, 11, 173-176, doi:10.1007/s40037-021-00695-4.

23. Thelwall, M. Bibliometrics to webometrics. J. Inf. Sci. 2008, 34, 605-621, doi:10.1177/0165551507087238.

24. Chen, C.M.; Assoc Comp, M. Visualizing and Exploring Scientific Literature with CiteSpace. In Proceedings of the 3rd ACM SIGIR Conference on Human Information Interaction and Retrieval (CHIIR), New Brunswick, NJ, Mar 11-15, 2018; pp. 369-370.

25. Liu, H.L.; Zhu, Y.P.; Guo, Y.Z.; Li, S.J.; Yang, J.Y. Visualization Analysis of Subject, Region, Author, and Citation on Crop Growth Model by CiteSpace II Software. In Proceedings of the 8th International Conference on Intelligent Systems and Knowledge Engineering (ISKE), Shenzhen, PEOPLES R CHINA, Nov 20-23, 2013; pp. 243-252.

26. Zhong, D.L.; Li, Y.X.; Huang, Y.J.; Hong, X.J.; Li, J.; Jin, R.J. Molecular Mechanisms of Exercise on Cancer: A Bibliometrics Study and Visualization Analysis <i>via</i> CiteSpace. Front. Mol. Biosci. 2022, 8, 12, doi:10.3389/fmolb.2021.797902.

27. Li, Y.J.; Wang, G.L.; Wei, T.; Fan, Z.J.; Yan, P. Nitrogen and sulfur co-doped porous carbon nanosheets derived from willow catkin for supercapacitors. Nano Energy 2016, 19, 165-175, doi:10.1016/j.nanoen.2015.10.038.

28. Gong, Y.N.; Li, D.L.; Luo, C.Z.; Fu, Q.; Pan, C.X. Highly porous graphitic biomass carbon as advanced electrode materials for supercapacitors. Green Chem. 2017, 19, 4132-4140, doi:10.1039/c7gc01681f.

29. Wang, Y.G.; Song, Y.F.; Xia, Y.Y. Electrochemical capacitors: mechanism, materials, systems, characterization and applications. Chem. Soc. Rev. 2016, 45, 5925-5950, doi:10.1039/c5cs00580a.

30. Qian, W.J.; Sun, F.X.; Xu, Y.H.; Qiu, L.H.; Liu, C.H.; Wang, S.D.; Yan, F. Human hair-derived carbon flakes for electrochemical supercapacitors. Energy Environ. Sci. 2014, 7, 379-386, doi:10.1039/c3ee43111h.

31. Sun, L.; Tian, C.G.; Li, M.T.; Meng, X.Y.; Wang, L.; Wang, R.H.; Yin, J.; Fu, H.G. From coconut shell to porous graphene-like nanosheets for high-power supercapacitors. J. Mater. Chem. A 2013, 1, 6462-6470, doi:10.1039/c3ta10897j.

32. Wang, H.; Xu, Z.W.; Kohandehghan, A.; Li, Z.; Cui, K.; Tan, X.H.; Stephenson, T.J.; King'ondu, C.K.; Holt, C.M.B.; Olsen, B.C.; et al. Interconnected Carbon Nanosheets Derived from Hemp for Ultrafast Supercapacitors with High Energy. ACS Nano 2013, 7, 5131-5141, doi:10.1021/nn400731g.

33. Abioye, A.M.; Ani, F.N. Recent development in the production of activated carbon electrodes from agricultural waste biomass for supercapacitors: A review. Renew. Sust. Energ. Rev. 2015, 52, 1282-1293, doi:10.1016/j.rser.2015.07.129.

34. Sevilla, M.; Mokaya, R. Energy storage applications of activated carbons: supercapacitors and hydrogen storage. Energy Environ. Sci. 2014, 7, 1250-1280, doi:10.1039/c3ee43525c.

35. Zhao, Y.Q.; Lu, M.; Tao, P.Y.; Zhang, Y.J.; Gong, X.T.; Yang, Z.; Zhang, G.Q.; Li, H.L. Hierarchically porous and heteroatom doped carbon derived from tobacco rods for supercapacitors. J. Power Sources 2016, 307, 391-400, doi:10.1016/j.jpowsour.2016.01.020.

36. Bi, Z.H.; Kong, Q.Q.; Cao, Y.F.; Sun, G.H.; Su, F.Y.; Wei, X.X.; Li, X.M.; Ahmad, A.; Xie, L.J.; Chen, C.M. Biomass-derived porous carbon materials with different dimensions for supercapacitor electrodes: a review. J. Mater. Chem. A 2019, 7, 16028-16045, doi:10.1039/c9ta04436a.

37. Yang, F.Q.; Li, X.; Ge, F.L.; Li, G. Dust prevention and control in China: A systematic analysis of research trends using bibliometric analysis and Bayesian network. Powder Technol. 2022, 411, 14, doi:10.1016/j.powtec.2022.117941.

38. Wang, J.Y.; Wang, X.; Cai, X.T.; Pan, D.K. Global trends and hotspots in IgA nephropathy: a bibliometric analysis and knowledge map visualization from 2012 to 2023. Int. Urol. Nephrol. 2023, 55, 3197-3207, doi:10.1007/s11255-023-03598-x.

#303: Biomass gasification modelling based on physics-informed neural network with hard constraints

Qihang WENG[1], Renshao JUN[2], Baoyu ZHU[3], Fengqi SI[4]

[1] *Key Laboratory of Energy Thermal Conversion and Control of Ministry of Education, School of Energy andEnvironment, Southeast University, Nanjing, PR China, qhweng@seu.edu.cn*
[2] *Key Laboratory of Energy Thermal Conversion and Control of Ministry of Education, School of Energy and Environment, Southeast University, Nanjing, PR China, rsj@seu.edu.cn*
[3] *Key Laboratory of Energy Thermal Conversion and Control of Ministry of Education, School of Energy andEnvironment, Southeast University, Nanjing, PR China, baoyuzhu@seu.edu.cn*
[4] *Key Laboratory of Energy Thermal Conversion and Control of Ministry of Education, School of Energy and Environment, Southeast University, Nanjing, PR China, fqsi@seu.edu.cn*

Abstract: In recent years, predicting biomass gasification syngas components using machine learning (ML) methods has received significant attention and interest. However, insufficient experimental data can hardly guide ML models in capturing complete knowledge of the gasification process, which can be reflected explicitly in the mismatch between ML model predictions and physical knowledge. Therefore, this study proposes a novel hard-constrained physics-informed neural network (HC-PINN) to predict biomass gasification syngas components by integrating experimental data with prior monotonicity relationships. Firstly, the monotonicity constraints between syngas components and key operating parameters are derived as inequality constraints involving solely the network parameters. Since the inequality constraints bypass the presence of model input parameters, the HC-PINN model can ensure that the model predictions in the entire input space satisfy the monotonicity relationships while avoiding the hard-to-trade-off synthetic samples. Secondly, the constrained particle swarm optimization algorithm is used to optimize the network parameters between regression losses and inequality constraints. The additional physical loss terms introduced in the soft constraints are substituted by searching for the feasible regions that satisfy the inequality constraints, avoiding the complexity associated with weight trade-offs acrossmultiple loss terms. Finally, the results show that the HC-PINN model can strictly adhere to the monotonicity relationshipseven in the no-training-sample region, reflecting better interpretability and generalization than the three state-of-the-art traditional ML methods.

Keywords: Biomass Gasification, Machine Learning, Hard-Constrained Learning, Constrained Particle Swarm Optimization, Hysics-Informed Neural Network

1. INTRODUCTION

Biomass is one of the world's most abundant and economically viable renewable resources, a promising alternative to fossil fuels. In comparison to direct combustion, gasification represents a cost-effective and environmentally beneficial method of recovering energy from biogenic wastes. Nevertheless, this potential enhancement in efficiency is accompanied by the increased complexity of the biomass gasification process, calling for the development of syngas prediction models for process design and operation optimization. First-principles models have been extensively studied in recent years, but due to the complicated reaction mechanism of the gasification process, it is challenging to satisfy simultaneous prediction accuracy and computational cost (Ajorloo et al., 2022).

Alternatively, machine learning (ML) methods can learn complex processes from actual data with superior predictive accuracy, lower modelling costs, and versatile modelling forms. Predictive modelling of biomass gasification using ML methods is of widespread concern (Umenweke et al., 2022). (Devasahayam and Albijanic, 2024) explored the performance of decision tree and ensemble methods such as random forest (RF) and gradient-boosted regression (GBR) for predicting hydrogen production from co-gasification of biomass and plastics, and the results demonstrated promising predictions. (Aslam Khan et al., 2024) presented an integrated framework of machine learning models and particle swarm optimization (PSO) to predict and optimize hydrogen production from supercritical gasification. (Kim et al., 2023) developed an RF, a support vector machine (SVM), and an artificial neural network (ANN) model to predict syngas compositions and lower heating values (LHV) from fluidized bed biomass gasifiers. Experimental data is the primary source of knowledge for ML predictive models, and the establishment of a trustworthy ML model usually requires the guidance of sufficient training data. However, biomass gasification involves many relevant factors, such as biomass feedstock characteristics and operating parameters, making it difficult to provide sufficient training data for the ML models, even though researchers have collected hundreds of experimental data from the previous literature (Wang et al., 2022). Insufficiently trained ML models exhibit poor predictive performance, including overfitting, poor extrapolation, and mismatch with physics knowledge (Di Natale et al., 2023).

Grounded in insufficient experimental data, researchers proposed supplementing the data with prior physical knowledge to guide ML modelling, namely physics-informed machine learning (PIML) (Bradley et al., 2022). Introducing prior knowledge alleviates the embarrassment of lacking knowledge and helps to improve model interpretability and generalization. (Shin and Choi, 2023) propose a physics-informed learning based on variational autoencoder (VAE) to solve data-driven stochastic differential equations with limited training data. (Xie et al., 2021) embedded physical mechanisms into a long short-term memory (LSTM) network and got better predictions than purely data-driven ML models. (Ren, Wu and Weng, 2023; Ren et al., 2024) proposed a physics-informed neural network (PINN) to introduce three syngas-produce-related monotonic knowledge into ANN training to enhance the scientific interpretability and generalization of biomass gasification prediction model, based on which disentangled representation learning was integrated to extend the knowledge coverage to a full range of feedstock types. Despite the promising results, the above PIML methods generally require synthetic samples as carriers of prior knowledge, which are often prone to the problem of the "curse of dimensionality" (CoD), especially for high-dimensional processes such as biomass gasification (Shin and Choi, 2023). In addition, the above methods usually introduce additional physical knowledge terms into the objective function, which is plagued by weight competition.

Therefore, this work proposes a novel hard-constrained physics-informed neural network (HC-PINN) that directly integrates physics knowledge into the optimized training of model parameters without employing synthetic samples, which achieves a more plausible generalization capability and interpretability in predicting the syngas components of biomass gasification. The main contributions of this work can be summarized as follows: (i) proposed a generic hard-constrained learning approach applicable to multi-layer neural network structures; (ii) employed a constrained particle swarm optimization (CPSO) algorithm to optimize network parameters between regression loss and inequality constraints; (iii) developed an HC-PINN model to predict syngas components (N_2, H_2, CO, CO_2, and CH_4) that integrate the monotonicity knowledge of syngas components with three key operating parameters (moisture content, temperature, and equivalence ratio) under full operating conditions. Finally, the validity of the HC-PINN was tested using the collected dataset and compared with three other ML methods (RF, SVM, and ANN).

2. DATA AND PRIOR KNOWLEDGE PREPARATION

In this study, the training data for the biomass gasification modelling are sourced from experimental data from previous studies, and the collected variables mainly include feedstock characteristics, operating conditions, and syngas components. After data pre-processing, including missing value cleaning, redundant variable exclusion, and categorical variable encoding (more details can be found in our previous work (Ren et al., 2024)), 200 samples were obtained, and the variable characteristics are listed in Table 1.

Table 1: Characteristics of input and output variables

Input variables	Unit	Range	Encode	Output variables	Unit	Range	Encode
C	%	[43.52,86.03]	—	H_2	%	[3.1,39]	—
H	%	[5.5,14.23]	—	CO	%	[2.2,43]	—
N	%	[0,7.32]	—	CO_2	%	[1.2,34.73]	—
O	%	[0,1.61]	—	CH_4	%	[0.25,12]	—
S	%	[0,48.9]	—	N_2	%	[0,74.9]	—
LHV	MJ/kg	[11.5,42.9]	—				
Particle size	mm	[0.25,70]	—				
Ash	%	[0.27,44]	—				
Moisture content	%	[0,27]	—				
Temperature	°C	[553,1050]	—				
Operation mode	—	{batch, continuous}	ordinally				
System scale	—	{lab, pilot}	ordinally				
Equivalence ratio	—	[0.09,0.87]	—				
Catalyst usage	—	{present, not present}	ordinally				
Gasifying agent	—	{air, steam, oxygen, air&steam, other}	one-hot				
Reactor type	—	{fixed bed, fluidized bed, other}	one-hot				
Bed material	—	{alumina, olivine, silica, other}	one-hot				

The prior knowledge adopted in this study is sourced from previous literature, including the monotonicity relationship between syngas components and equivalence ratio (ER), moisture content (MC), and temperature (T), as listed in Table 2, and more details can be found in (Silva et al., 2019).

Table 2: Characteristics of input and output variables

Input variables	Syngas components				
	$\frac{\partial \mathrm{H_2}}{\partial}$	$\frac{\partial \mathrm{CO}}{\partial}$	$\frac{\partial \mathrm{CO_2}}{\partial}$	$\frac{\partial \mathrm{CH_2}}{\partial}$	$\frac{\partial \mathrm{N_2}}{\partial}$
ER	<0	<0	>0	<0	>0
MC	>0	<0	>0	>0	<0
T	>0	>0	<0	—	—

3. HARD-CONSTRAINED PHYSICS-INFORMED NEURAL NETWORK

3.1. Basic artificial neural network

Given a measurement sample $[\boldsymbol{x},\boldsymbol{y}]^\mathrm{T}$, where $\boldsymbol{x} = [x_1, x_2, \dots, x_n] \in \mathbb{R}^n$ represents the operating parameters, $x_k \in \mathbb{R}, 1 \le k \le n$ is the k-th operating parameter, and $\boldsymbol{y} = [y_1, y_2, \dots, y_c] \in \mathbb{R}^c$ represents the prediction targets. This study uses a multi-layer ANN model that includes an input layer, N hidden layers, and an output layer. Specifically, the number of neural nodes in the i-th hidden layer is denoted by $h^{(i)}, 1 \le i \le N$. The model output can be calculated as Equation 1.

Equation 13: model output. $$\hat{\boldsymbol{y}} = \boldsymbol{\beta} g\left(\boldsymbol{w}^{(N)}\boldsymbol{x}^{(N)} + \boldsymbol{b}^{(N)}\right)$$

Where:

- $\hat{\boldsymbol{y}} \in \mathbb{R}^c$ = the model prediction of the input $\boldsymbol{x}$
- $\boldsymbol{\beta} \in \mathbb{R}^{c\times h^{(N)}}$ = the weight matrix connecting the N-th hidden layer and the output layer
- $g(\tau) = \frac{1}{1+e^{-\tau}}$ = the activation function
- $\boldsymbol{w}^{(N)} \in \mathbb{R}^{h^{(N)}\times h^{(N-1)}}$, $\boldsymbol{b}^{(N)} \in \mathbb{R}^{h^{(N)}}$ = the weight matrix and bias vector of the N-th hidden layer
- $\boldsymbol{x}^{(N)} \in \mathbb{R}^{h^{(N-1)}}$ = both the input vector of the N-th hidden layer and the output vector of the $(N-1)$-th hidden layer

$\boldsymbol{x}^{(N)}$ can be calculated as Equation 2.

Equation 2: input vector of the N-th hidden layer. $$\boldsymbol{x}^{(N)} = g\left(\boldsymbol{w}^{(N-1)}\boldsymbol{x}^{(N-1)} + \boldsymbol{b}^{(N-1)}\right)$$

Where:

- $\boldsymbol{w}^{(N-1)} \in \mathbb{R}^{h^{(N-1)}\times h^{(N-2)}}$, $\boldsymbol{b}^{(N-1)} \in \mathbb{R}^{h^{(N-1)}}$ = the weight matrix and bias vector of the $(N-1)$-th hidden layer

By analogy, the input vector of the first hidden layer is the model input $\boldsymbol{x}$. At last, the objective function of ANN is as Equation 3.

Equation 3: the objective function of ANN.

$$\underset{\boldsymbol{\beta},\boldsymbol{w}^{(i)},\boldsymbol{b}^{(i)},1\le i\le N}{argmin} \mathcal{L}_r = \underset{\boldsymbol{\beta},\boldsymbol{w}^{(i)},\boldsymbol{b}^{(i)},1\le i\le N}{argmin} \sum_{j=1}^{m} \left\| \hat{\boldsymbol{y}}_{(j)} - \boldsymbol{y}_{(j)} \right\|_2$$

Where:

- $\mathcal{L}_r$ = the regression loss
- $y_{(j)}$, $\hat{y}_{(j)}$ = are the observed NO_x concentration of j-th sample and its corresponding prediction
- m = the number of training samples

3.2. The hard-constrained learning approach

To allow the ANN model to have the ability to learn the prior monotonicity knowledge, the objective function of ANN can be expressed as Equation 4.

Equation 4: the constrained objective function.

$$\underset{\boldsymbol{\beta},\boldsymbol{w}^{(i)},\boldsymbol{b}^{(i)},1\le i\le N}{argmin} \mathcal{L}_r$$
$$s.t.\ \frac{\partial \hat{y}_l}{\partial x_k} > 0\ or\ \frac{\partial \hat{y}_l}{\partial x_k} < 0$$

Where:

- x_k = the k-th operating parameter, which has a monotonic relationship with the l-th prediction target y_l
- $\frac{\partial \hat{y}_l}{\partial x_k} > 0$ = a positive monotonicity relationship

Then, the partial derivative of the model output $\hat{y}_l$ concerning x_k can be expanded as Equation 5.

Equation 5: derivation of partial derivative.

$$\frac{\partial \hat{y}_l}{\partial x_k} = \frac{\partial\left(\boldsymbol{\beta}_l g\left(\boldsymbol{w}^{(N)}\boldsymbol{x}^{(N)} + \boldsymbol{b}^{(N)}\right)\right)}{\partial x_k} = \frac{\partial\left(\sum_{i_N=1}^{h^{(N)}} \beta_{l,i_N} g\left(\boldsymbol{w}_{i_N}^{(N)}\boldsymbol{x}^{(N)} + b_{i_N}^{(N)}\right)\right)}{\partial x_k}$$
$$= \sum_{i_N=1}^{h^{(N)}} \beta_{l,i_N} g'\left(\boldsymbol{w}_{i_N}^{(N)}\boldsymbol{x}^{(N)} + b_{i_N}^{(N)}\right) \frac{\partial\left(\sum_{i_{N-1}=1}^{h^{(N-1)}}\left(w_{i_N,i_{N-1}}^{(N)} x_{i_{N-1}}^{(N)} + b_{i_N}^{(N)}\right)\right)}{\partial x_k}$$
$$= \sum_{i_N=1}^{h^{(N)}} \beta_{l,i_N} g'\left(\boldsymbol{w}_{i_N}^{(N)}\boldsymbol{x}^{(N)} + b_{i_N}^{(N)}\right) \sum_{i_{N-1}=1}^{h^{(N-1)}} w_{i_N,i_{N-1}}^{(N)} \frac{\partial g\left(\boldsymbol{w}_{i_{N-1}}^{(N-1)}\boldsymbol{x}^{(N-1)} + b_{i_{N-1}}^{(N-1)}\right)}{\partial x_k}$$

Where:

- β_l, β_{l,i_N} = the l-th row of the matrix β and the i_N-th element of β_l.
- $b_{i_N}^{(N)}$ = the i_N-th component of the vector $b^{(N)}$
- $w_{i_N}^{(N)}$, $w_{i_N,i_{N-1}}^{(N)}$ = the i_N-th row of the matrix $w^{(N)}$ and i_{N-1}-th element of the matrix $w_{i_N}^{(N)}$
- $x_{i_{N-1}}^{(N)}$, $b_{i_{N-1}}^{(N-1)}$ = the i_{N-1}-th component of the vector $x^{(N)}$ and $b^{(N-1)}$
- $w_{i_{N-1}}^{(N-1)}$ = the i_{N-1}-th row of the matrix $w^{(N-1)}$

Equation 6: derivation of partial derivative.

$$\frac{\partial \hat{y}_l}{\partial x_k} = \sum_{i_N=1}^{h^{(N)}} \beta_{l,i_N} g^{(N)\prime} \sum_{i_{N-1}=1}^{h^{(N-1)}} w_{i_N,i_{N-1}}^{(N)} \frac{\partial g\left(\boldsymbol{w}_{i_{N-1}}^{(N-1)}\boldsymbol{x}^{(N-1)} + b_{i_{N-1}}^{(N-1)}\right)}{\partial x_k}$$
$$= \sum_{i_N=1}^{h^{(N)}} \beta_{l,i_N} g^{(N)\prime} \dots \sum_{i_2=1}^{h^{(2)}} w_{i_3,i_2}^{(2)} g^{(1)\prime} \frac{\partial\left(\sum_{i_1=1}^{h^{(1)}}\left(w_{i_2,i_1}^{(1)} x_{i_1} + b_{i_1}^{(1)}\right)\right)}{\partial x_k}$$
$$= \sum_{i_N=1}^{h^{(N)}} \beta_{l,i_N} g^{(N)\prime} \dots \sum_{i_2=1}^{h^{(2)}} w_{i_3,i_2}^{(2)} g^{(1)\prime} w_{i_2,k}^{(1)}$$

In order to simplify the representation, the derivative of the activation function corresponding to the i-th hidden layer in Equation 5 is denoted by $g^{(i)\prime}$. So, Equation 5 can be written as Equation 6.
Subsequently, for the Sigmoid function, it has $0 < g^{(i)\prime} < 1, 1 \le i \le N$. So Equation 6 can be simplified to its sufficiently

unnecessary condition as Equation 7.

Equation 7: derivation of partial derivative.

$$\frac{\partial \hat{y}_l}{\partial x_k} > 0 \rightarrow \sum_{i_N=1}^{h^{(N)}} \beta_{l,i_N} \cdots \sum_{i_2=1}^{h^{(2)}} w_{i_3,i_2}^{(2)} w_{i_2,k}^{(1)} > 0$$
$$\rightarrow \begin{cases} \beta_{l,1} w_{1,1}^{(N)} \cdots w_{1,1}^{(2)} w_{1,k}^{(1)} > 0 \\ \vdots \\ \beta_{l,h^{(N)}} w_{h^{(N)},h^{(N-1)}}^{(N)} \cdots w_{h^{(3)},h^{(2)}}^{(2)} w_{h^{(2)},k}^{(1)} > 0 \end{cases}$$

In this way, the positive monotonicity constraint, as in Equation 4, is replaced by $\widetilde{N} = \prod_{i=2}^{N} h^{(i)}$ constraints as Equation 8.

Equation 8: the positive monotonicity constraint.

$$\begin{cases} f_{1k}(\boldsymbol{\beta}, \boldsymbol{w}) = \beta_{l,1} w_{1,1}^{(N)} \cdots w_{1,1}^{(2)} w_{1,k}^{(1)} > 0 \\ \vdots \\ f_{\widetilde{N}k}(\boldsymbol{\beta}, \boldsymbol{w}) = \beta_{l,h^{(N)}} w_{h^{(N)},h^{(N-1)}}^{(N)} \cdots w_{h^{(3)},h^{(2)}}^{(2)} w_{h^{(2)},k}^{(1)} > 0 \end{cases}$$

Where:

- $f_{dk}(\boldsymbol{\beta}, \boldsymbol{w}), 1 \leq d \leq \widetilde{N}$ = the d-th constraint under the general monotonicity constraint of $\hat{y}_l$ concerning x_k

Similarly, the negative monotonicity constraint is replaced by $\widetilde{N}$ constraints as Equation 9.

Equation 9: the negative monotonicity constraint.

$$\begin{cases} f_1(\boldsymbol{\beta}, \boldsymbol{w}) = \beta_{l,1} w_{1,1}^{(N)} \cdots w_{1,1}^{(2)} w_{1,k}^{(1)} < 0 \\ \vdots \\ f_{\widetilde{N}}(\boldsymbol{\beta}, \boldsymbol{w}) = \beta_{l,h^{(N)}} w_{h^{(N)},h^{(N-1)}}^{(N)} \cdots w_{h^{(3)},h^{(2)}}^{(2)} w_{h^{(2)},k}^{(1)} < 0 \end{cases}$$

3.3. The constrained particle swarm optimization algorithm

Following the hard-constrained learning approach, the objective function of HC-PINN is as Equation 10.

Equation 10: the objective function of HC-PINN.

$$\underset{\boldsymbol{\beta}, \boldsymbol{w}^{(i)}, \boldsymbol{b}^{(i)}, 1 \leq i \leq N}{argmin} \mathcal{L}_r = \underset{\boldsymbol{\beta}, \boldsymbol{w}^{(i)}, \boldsymbol{b}^{(i)}, 1 \leq i \leq N}{argmin} \sum_{j=1}^{m} \left\| \hat{\boldsymbol{y}}_{(j)} - \boldsymbol{y}_{(j)} \right\|_2$$
$$s.t. \begin{cases} m_k f_{1k}(\boldsymbol{\beta}, \boldsymbol{w}) = m_k \beta_{l,1} w_{1,1}^{(N)} \cdots w_{1,1}^{(2)} w_{1,k}^{(1)} < 0 \\ \vdots \\ m_k f_{\widetilde{N}k}(\boldsymbol{\beta}, \boldsymbol{w}) = m_k \beta_{l,h^{(N)}} w_{h^{(N)},h^{(N-1)}}^{(N)} \cdots w_{h^{(3)},h^{(2)}}^{(2)} w_{h^{(2)},k}^{(1)} < 0 \end{cases}$$

Where:

- m_k = the monotonic factor with respect to k-th operating parameter x_k, and $m_k = -1$ if $\hat{y}$ is monotonically increasing with the x_k; $m_k = 1$ for the negative monotonicity

This paper applies the constrained particle swarm optimization (CPSO) algorithm (Perez and Behdinan, 2007) to solve the constrained optimization problem shown in Equation 10. The PSO uses a velocity vector to update the current position of each particle in the swarm until a global optimal particle within the feasible regions is identified, at which particle the search is terminated. To accommodate the inclusion of constraints, a parameter-less adaptive penalty scheme is used.

3.4. The HC-PINN training framework

Given a training sample set $[\mathbf{X}, \mathbf{Y}]^{\mathrm{T}}$ with m samples, where $\mathbf{X} \in \mathbb{R}^{m \times n}$ represents the input data and $\mathbf{Y} \in \mathbb{R}^{m \times c}$ represents the output data. Initially, the input and output data are normalized by scaling the input data to zero mean and unit variance to eliminate the effect of the variable scales. The data is normalized as Equation 11.

Equation 11: the normalized data.

$$\boldsymbol{X}_{norm} = \frac{\boldsymbol{X} - \overline{\boldsymbol{X}}}{\widetilde{\boldsymbol{X}}}$$

Where:

- $\overline{\mathbf{X}}$, $\widetilde{\mathbf{X}}$ = the vector of averages and standard deviations for each variable in the training sample set

Besides the regression loss, a regularization loss term is introduced in HC-PINN to prevent overfitting. Finally, the total loss function of HC-PINN is given by Equation 12.

Equation 12: the total loss function of HC-PINN.

$$\mathcal{L} = \mathcal{L}_r + \lambda_{reg}\mathcal{L}_{reg}$$
$$= \underbrace{\sum_{j=1}^{m} \left\| \hat{\boldsymbol{y}}_{(j)} - \boldsymbol{y}_{(j)} \right\|_2}_{regression\ loss\ term} + \underbrace{\lambda_{reg}\left[\|\boldsymbol{\beta}\|_2 + \sum_{i=1}^{N} \left(\left\|\boldsymbol{w}^{(i)}\right\|_2 + \left\|\boldsymbol{b}^{(i)}\right\|_2 \right) \right]}_{regularization\ loss\ term}$$

Where:

– $\mathcal{L}_{reg}, \lambda_{reg}$ = the regularization term in the loss function and the corresponding weight

The general training framework of HC-PINN is shown in Figure1.

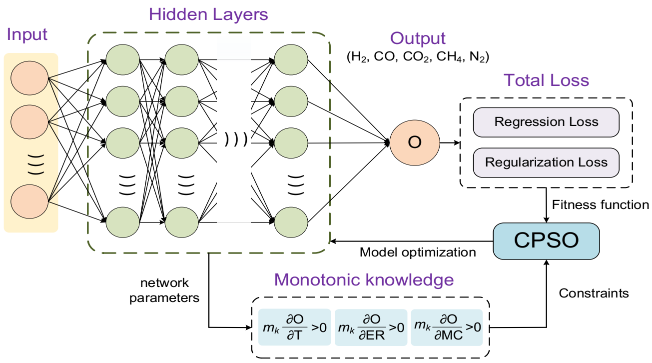

Figure 14: Schematic diagram of the HC-PINN

3.5. Model performance evaluation

Three statistical metrics are employed to assess the prediction performance of the proposed HC-PINN method.

(1) R-squared (R^2): R^2 is a unitless fraction less than one that measures how well the model explains changes in the data. The closer the R^2 value is to 1, the better the model fits the data. R^2 is defined as Equation 13.

Equation 13: R^2.

$$R^2 = 1 - \frac{\sum_{j=1}^{m} (\boldsymbol{y}_{(j)} - \hat{\boldsymbol{y}}_{(j)})^2}{\sum_{i=1}^{m} (\boldsymbol{y}_{(j)} - \bar{\boldsymbol{y}})^2}$$

Where:

– $\bar{\boldsymbol{y}}$ = the average of all observed samples

(2) Root mean square error (RMSE): The RMSE responds to the extent to which the model's predicted values differ from the actual values. The closer the RMSE is to 0, the better the model is fitted. The RMSE is expressed as Equation 14.

Equation 14: RMSE.

$$RMSE = \sqrt{\frac{1}{m} \sum_{j=1}^{m} (\boldsymbol{y}_{(j)} - \hat{\boldsymbol{y}}_{(j)})^2}$$

(3) Physical consistency degree (PCD): The PCD measures how well the model predictions agree with the prior physical monotonicity, with PCD closer to 1 representing better model interpretability. The PCD is calculated as Equation 15.

Equation 15: PCD.

$$PCD = \frac{1}{m} \sum_{j=1}^{m} ReLU(-m_k \times sgn(\frac{\partial \hat{y}_{(j)l}}{\partial x_{(j)k}}))$$

Where:

– $\mathrm{ReLU}(\tau) = \max(0, \tau)$ = the rectified linear unit

– $\mathrm{sgn}(\tau) = \begin{cases} 1, \tau > 0 \\ 0, \tau = 0 \\ -1, \tau < 0 \end{cases}$ = the sign function

- $x_{(j)k}$ = the k-th variable of the j-th input data
- $\frac{\partial \hat{y}_{(j)l}}{\partial x_{(j)k}}$ = the partial derivative of the l-th component of j-th model output $\hat{y}_{(j)l}$ concerning $x_{(j)k}$, and the finite-difference solver is used to approximate the partial derivatives for simplification

4. RESULTS AND DISCUSSION

4.1. Models Development and test methods

In this study, the HC-PINN model and three other ML models (RF, SVM, and ANN) are trained using the collected experimental data and employed to predict the five syngas components of biomass gasification. In particular, the prior monotonicity knowledge listed in Table 2 are introduced into the HC-PINN modelling.

Subsequently, the models are subjected to comparative analysis to evaluate their predictive performance, interpretability, and generalizability. Firstly, the collected experimental data are randomly divided at 85% to 15% to serve as the training and testing sets for the four models. The R^2 and RMSE of different models are compared to analyse their predictive performance. Secondly, PCD metrics and partial dependence analysis (PDA) are used to exhibit the models' monotonic behaviours and generalization capabilities.

4.2. Predictive performance analysis

Table 3 presents the prediction accuracies of the four models for the five syngas components in both the training and testing sets. For the training set, all four models showed promising prediction accuracies (R^2 greater than 0.92 and RMSE less than 3) for five syngas components. Amongst the models, HC-PINN performs slightly inferior to RF while superior to SVM and ANN. The results of the testing set indicate that the HC-PINN model significantly outperforms the other three models (with the R^2 greater than 0.93 and the RMSE less than 3.5), suggesting that HC-PINN possesses superior generalization performance as evidenced by the consistency of its prediction accuracy between the testing set and the training set. This is because the physical knowledge constraints embedded during the training of the HC-PINN model provide appropriate guidance, thereby rendering HC-PINN more closely aligned with the actual process. Generally, HC-PINN has superior predictive performance compared to the other three ML models.

Table 3: The prediction performance of different models

Syngas Components	Statistics	RF	SVM	ANN	HC-PINN
H_2	Train R^2	0.9841	0.9398	0.9536	0.9697
	Train RMSE	1.0242	1.9933	1.7511	1.4387
	Test R^2	0.9508	0.9522	0.9371	0.9650
	Test RMSE	2.2629	2.2288	2.5575	1.8240
CO	Train R^2	0.9894	0.9606	0.9633	0.9592
	Train RMSE	0.9886	1.9054	1.8402	1.9518
	Test R^2	0.9394	0.9400	0.9585	0.9616
	Test RMSE	2.4463	2.4343	2.0233	1.8918
CO_2	Train R^2	0.9886	0.9436	0.9258	0.9528
	Train RMSE	0.7088	1.5762	1.8068	1.4095
	Test R^2	0.9281	0.9376	0.8970	0.9598
	Test RMSE	1.8163	1.6918	2.1736	1.5312
CH_4	Train R^2	0.9805	0.9249	0.9304	0.9585
	Train RMSE	0.3847	0.7554	0.7271	0.5540
	Test R^2	0.8950	0.8967	0.8637	0.9372
	Test RMSE	0.8473	0.8401	0.9652	0.7087
N_2	Train R^2	0.9948	0.9819	0.9850	0.9877
	Train RMSE	1.5960	2.9843	2.7184	2.4669
	Test R^2	0.9549	0.9717	0.9763	0.9815
	Test RMSE	5.2134	4.1264	3.7771	3.3411

4.3. Interpretability and generalizability analysis

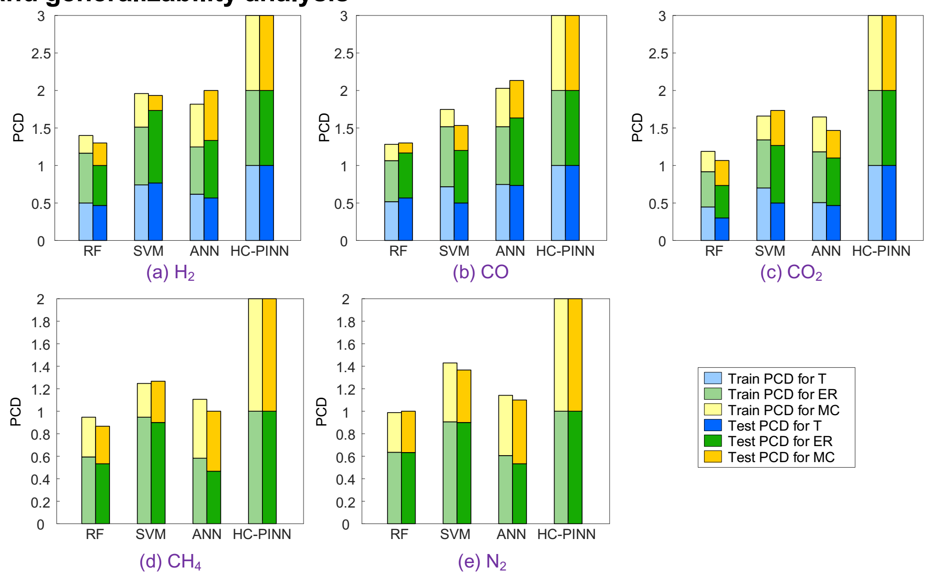

Figure 2: The PCD results of different models for five syngas components: (a) H_2, (b) CO, (c) CO_2, (d) CH_4, and (e) N_2

Interpretability and generalizability reflect the matching of the ML models to the actual processes and the feasibility of the models for operating conditions beyond the training data. Firstly, PCD statistics were employed to compare the four ML models to determine if they could correctly reflect the monotonic behaviours of actual biomass gasification processes. Figure 2 illustrates the PCD results of the four models for the monotonicity relationships associated with the five syngas components. In all cases, the PCD results of HC-PINN are equal to 1, which indicates that the HC-PINN model can strictly match the prior monotonicity knowledge and exhibits excellent interpretability. In contrast, the other three ML models exhibit varying degrees of inconsistency in first principles. As an illustration, the PCD results of RF for the monotonicity of H_2 concerning T are less than 0.5 on both the training set (0.495) and the testing set (0.467), suggesting that more than half of the predictions deviate from physical knowledge. Furthermore, the total PCDs of RF, SVM, and ANN for H_2 in both the training and testing sets do not exceed 2, which implies that at least one-third of the predictions for H_2 are inconsistent with the prior physical knowledge, indicating poor physical interpretability.

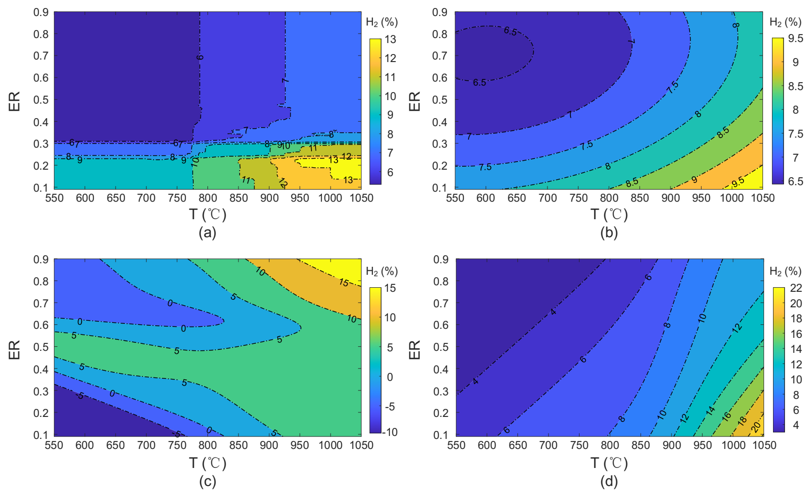

Figure 3: Two-way partial dependence plots of H_2 on T and ER for different models: (a) RF, (b) SVM, (c) ANN, and (d) HC-PINN

Then, the two-way PDA emulates the trends of the model predictions concerning the critical input variables and visualizes the interpretability and generalizability of the ML models. Initially, synthetic samples were generated with the T ranging from 550 ℃ to 1050 ℃, ER ranging from 0.09 to 0.9, and MC ranging from 0% to 30%, using one randomly selected testing sample with the other input variables held constant. Figure 3 shows four models' two-way partial dependence plots of H_2 with T and ER. The contour lines indicate the H_2 predictions, while the horizontal and vertical coordinates show the T and ER, respectively. Figure 3(a) exhibits that the contours of RF are irregularly vertical and crowd each other in individual regions, which is related to the predictive characteristics of the decision tree model and limited training data coverage. In addition, it can be discerned that RF can get the predicted trends matching the prior monotonicity in certain areas while deviating from it in a broader range. As illustrated in Figure 3(b, c), the contours of SVM and ANN exhibit a greater degree of smoothness than those of RF. However, they also lack complete alignment with the prior monotonicity, which can be attributed to insufficient training data. In contrast, the contours of HC-PINN shown in Figure 3(d) are distinctly discernible as aligning with the prior monotonicity relationships across the entire range. The incorporation of supplementary physical knowledge learning into the modelling enables the HC-PINN to provide a chain of associations connecting the regions where the training data are unevenly distributed, ultimately allowing the HC-PINN to yield credible and interpretable predictions.

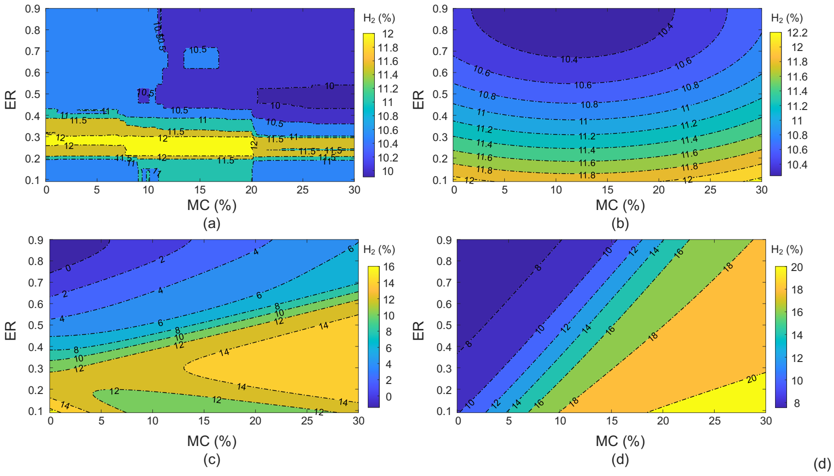

Figure 4: Two-way partial dependence plots of H_2 on MC and ER for different models: (a) RF, (b) SVM, (c) ANN, and (d) HC-PINN

Figure 4 shows four models' two-way partial dependence plots of H_2 with MC and ER. Figure 4(a-c) illustrates that RF, SVM, and ANN fail to give interpretable predictions in regions with insufficient training samples, exposing the shortcomings of poor interpretability and generalization of traditional ML models with limited data-sourced knowledge. Figure 4(d) demonstrates that the PDA results of HC-PINN can satisfy the full range of prior monotonicity relationships under the joint support of the data and the mechanism, highlighting the excellent extrapolation capability of HC-PINN. In conclusion, the GC-PINN has better interpretability and generalizability than the other three ML models.

5. CONCLUSION

This paper presents a novel HC-PINN method that employs neural network parameters as the medium of physical knowledge integration, ensuring the global consistency of model predictions and enabling concise model training. The monotonicity knowledge of the syngas components concerning three key operating parameters (T, ER, and MC) is embedded in HC-PINN for better prediction of biomass gasification processes. The testing results show that HC-PINN exhibits remarkable predictive performance, with R^2 exceeding 0.95 and 0.93 for the training and testing sets, respectively, and RMSE below 2.5 and 3.5, respectively. In addition, the PCD statistics and two-way PDA results indicate that the HC-PINN model can provide interpretable predictions with insufficient training data. In summary, HC-PINN outperforms the other three ML models (RF, SVM, and ANN) regarding predictive performance, interpretability, and generalizability.

6. REFERENCES

Ajorloo, M. et al. (2022) ‘Recent advances in thermodynamic analysis of biomass gasification: A review on numerical modelling and simulation’, Journal of the Energy Institute. Elsevier Ltd, 102(January), pp. 395–419.

Aslam Khan, M. N. et al. (2024) ‘Prediction of hydrogen yield from supercritical gasification process of sewage sludge using machine learning and particle swarm hybrid strategy’, International Journal of Hydrogen Energy. Hydrogen Energy Publications LLC, 54, pp. 512–525.

Bradley, W. et al. (2022) ‘Perspectives on the integration between first-principles and data-driven modeling’, Computers and Chemical Engineering. Elsevier Ltd, 166(May), p. 107898.

Devasahayam, S. and Albijanic, B. (2024) ‘Predicting hydrogen production from co-gasification of biomass and plastics using tree based machine learning algorithms’, Renewable Energy. Elsevier Ltd, 222(March 2023), p. 119883.

Kim, J. Y. et al. (2023) ‘Predicting and optimizing syngas production from fluidized bed biomass gasifiers: A machine learning approach’, Energy. Elsevier Ltd, 263(PC), p. 125900.

Di Natale, L. et al. (2023) ‘Towards scalable physically consistent neural networks: An application to data-driven multi-zone thermal building models’, Applied Energy. Elsevier Ltd, 340(March), p. 121071.

Perez, R. E. and Behdinan, K. (2007) ‘Particle swarm approach for structural design optimization’, Computers and Structures, 85(19–20), pp. 1579–1588.

Ren, S. et al. (2024) ‘Disentangled Representation Aided Physics-Informed Neural Network for Predicting Syngas Compositions of Biomass Gasification’, Energy and Fuels, 38(3), pp. 2033–2045.

Ren, S., Wu, S. and Weng, Q. (2023) ‘Physics-informed machine learning methods for biomass gasification modeling by considering monotonic relationships', Bioresource Technology. Elsevier Ltd, 369(November 2022), p. 128472.

Shin, H. and Choi, M. (2023) 'Physics-informed variational inference for uncertainty quantification of stochastic differential equations', Journal of Computational Physics. Elsevier Inc., 487, p. 112183.

Silva, I. P. et al. (2019) 'Thermodynamic equilibrium model based on stoichiometric method for biomass gasification: A review of model modifications', Renewable and Sustainable Energy Reviews. Elsevier Ltd, 114(August), p. 109305.

Umenweke, G. C. et al. (2022) 'Machine learning methods for modeling conventional and hydrothermal gasification of waste biomass: A review', Bioresource Technology Reports. Elsevier Ltd, 17(January), p. 100976.

Wang, Z. et al. (2022) 'The role of machine learning to boost the bioenergy and biofuels conversion', Bioresource Technology. Elsevier Ltd, 343(August 2021), p. 126099.

Xie, K. et al. (2021) 'Physics-guided deep learning for rainfall-runoff modeling by considering extreme events and monotonic relationships', Journal of Hydrology. Elsevier B.V., 603(PC), p. 127043.

#304: Study on effect of operating time for thermal storage based on building envelope

Haiying WANG [1,*], Renjie YAN[1], Zhuo CUI[1], Junli SUN[1], Hang MENG[1], Huxiang LIN[1]

[1] Qingdao University of Technology, No. 777 Jialingjiang East Road in Huangdao District
Qingdao, Shandong province, China
* Corresponding author: wanghaiying@qut.edu.cn

Abstract: Most buildings are constructed with concrete. The thermal capacity of such elements in buildings provides the possibility to store thermal energy. In this study, the character of cold storage based on building envelope was explored. The TRNSYS model was set up based on an actual office building with a floor radiant cooling system, which normally opens during 8:00-18:00 on workdays. The local peak period for electricity is 16:00-22:00, the valley tariff period is 2:00-8:00, and the parity period is 8:00-16:00 during cooling. Based on the peak-valley electricity price, four operating strategies of cold storage were proposed, namely, condition 1 (2:00-8:00), condition 2 (2:00-10:00), condition 3 (2:00-12:00), and condition 4(2:00-14:00). The simulation showed that under the cold thermal storage conditions, the indoor air temperature was lower in the morning and kept increasing during working time, which led to temperature drift in the office room. For condition 1 and 2, the indoor thermal comfort cannot be assured as indoor temperature can be higher than the comfort level in later afternoon. For condition 3 and 4, the thermal comfort was better, and the PMV index can be kept in the range of -1 to 1 all the time. Results of thermal balance showed that the cold can be stored both in the cooling floor and internalwalls by reduced the structure temperature, and the cooling loss during night was less than 10%. The running cost of both condition 3 and 4 were lower than the normal condition. Condition 3 (with same running time of the normal condition) hadbetter economic effect, in which running cost was reduced by 16.2%. The results provided information for the cost savingoperation of radiant cooling systems based on building envelope cold storage.

Keywords: Radiant Cooling, Cold Storage, Building Envelope, Thermal Environment, Running Cost

1. INTRODUCTION

In the overall energy consumption of the building, the energy consumption of the air conditioning system occupies a very significant proportion. In order to effectively reduce the energy consumption of air conditioning systems in buildings, radiant cooling systems have been used worldwide due to their advantages of energy saving and high thermal comfort level (Zhang, 2021). This type of system provides cooling mainly through radiation, which not only improves the efficiency of cooling plant, but also brings a more comfortable indoor environment for occupants. Under the background of implementing sustainable development strategy in the current society, radiant cooling undoubtedly becomes a promising technology.

The basic principle of radiation cooling is to reduce the temperature of the surrounding surfaces by using coolant circulating in the walls, ceilings, floors or panels. The coils for the coolant can be embedded in the enclosure structure. More conventionally, the radiant coil is embedded in the concrete enclosure structure. The concrete has a certain thermal storage capacity due to their thermal inertia characteristics. To avoid condensation of cooling surfaces, the temperature of coolant can be higher than that of the convective units, which provides possibility of using natural cooling resources. Therefore, the radiant cooling systems can usually be more efficient. Relevant studies have found that radiant cooling systems show significant potential in energy saving. Li et al. (2024) evaluated the differences in thermal environmental performance and energy consumption between air and radiant cooling systems in Singapore’s tropical climate. The radiant system exhibited a 33 % higher heat flux extraction than the air system and required less electrical power for the transportation of the cooling medium and ventilation air. Overall, the radiant system used 4 % less energy than the air system when controlled at 26 °C and 34 % when operated at 23 °C. Zhou et al. (2020) used CFD to study the wall performance of buried heat exchange tubes. The results show that this building structure can reduce the cooling load by 13% in summer.

For intermittent operated buildings, using cooling storage can reduce energy costs by taking full advantage of the valley price of electricity. Combining the character of thermal storage of building envelopes and the idea of reducing running costs for radiant cooling system, cold storage based on building envelopes is proposed. In this operation mode, the cooling units keep running during nighttime to store heat in the building concrete structures, and the stored cold energy can be released naturally during working time, thus taking full advantage of the low-price power during night. Therefore, the time to start the refrigeration unit during the day can be reduced and postponed, and the cooling capacity of the unit during theday can be reduced. Compared to normal cold storage systems, there is no need for extra cold storage tanks, while similar benefits, such as the reduction in maximum cooling capacity and load shifting, can be achieved. Zhang et al. (2020) discussed the thermal inertia of the floor radiation system. They found that the thermal inertia of the envelope combined with a time-division operation strategy can not only improve the indoor thermal environment effectively, but also improve the energy-saving potential of the system. Rong (2020) proposed the concept of energy storage in building entities, which stores cold energy in building structure by operating the air conditioning systems at night to make full use of natural cooling sources and peak-valley electricity prices.

In general, the research on the cold storage capacity of building envelope is not systematic and comprehensive enough. The current research shows that the thermal storage capacity and cold release process of the building envelope need to be considered when the embedded radiant cooling terminal is used. The application of the heat capacity of the envelope structure itself for cold storage has a great influence on the indoor thermal environment, energy consumption and control strategy. The cold storage capacity, cold storage loss and operation economy based on peak-valley electricity prices need to be further clarified.

Based on the peak-valley electricity price policy, this paper conducts an in-depth study on the characteristics of the building envelope during cold storage operation under the condition of embedded radiation terminal. An actual office building with the radiant floor cooling is selected as the research model. The simulation model of the building and the radiant cooling system are established. On the basis of verifying the accuracy of the model, the performance characters of the system under different cold storage operation strategies are studied, including the influence of operation control time on indoor thermal environment, cold storage capacity and loss, energy consumption and operation economy.

2. BUILDING MODELING AND VALIDATION

2.1. Introduction of the office building

An office building in the literature (Zhang, 2016) (Zhang, 2019) was selected as the typical building in this paper. In literature, the building situation, the radiant cooling system and the measured operation data were described in detail. The building located in Jinan, Shandong Province, is a five-story office building, with a total construction area of 5450 m^2, and an air conditioning area of 3815 m^2. The building has a height of 20.70 meters.

In the air-conditioning system, ground heat exchangers are used to exchange heat with the soil to provide cooling for the radiant floor. The water circulation for floors just consumes the power for the water pumps, which reduces the operating energy consumption significantly. The fresh air is handled by chilled water from an air source heat pump unit, which bears all the latent cooling load and part of the sensible load. The energy consumption of the fresh air system mainly comes from the power consumption of the heat pump unit and the water pump for the fresh air handling units. There is a cold storage tank for the heat pump to store the full load of fresh air during the low-valley electricity price stage, so as to further reduce the operating cost of the fresh air system. In general, the cooling system of the building has made full use of the natural cooling source and taken the cold storage measures, which makes the building a low energy consumption building.

The external envelope structure of the building (Zhang, 2019) consists of hybrid mortar, aerated concrete, cement mortar, and extruded polystyrene board from the inside out. The internal walls are mainly composed of brick walls and cement mortar. The roof includes reinforced concrete roof, cement mortar, extruded polystyrene board, cement mortar, and cement bricks. The windows are constructed using insulated glass with aluminium alloy. For the flooring, reinforced concrete floor slabs serve as the foundation, covered with cement mortar and granite slabs. The embedded cooling pipes have an outer diameter of 20 mm with pipe thickness of 2 mm. The pipe spacing is 220 mm. The wall heat transfer coefficient of pipe is 0.4 W/(m^2·K). Detailed parameters of the building envelope structure are listed in Table 1.

Table 1: Detailed parameters of the building envelope structure

Building Structure	Material	Thickness (mm)	Thermal Conductivity (W/m · K)	Specific Heat Capacity (kJ/(kg·℃)	Density (kg/m^3)
External Walls	Extruded Polystyrene Board	30	0.028	35	1.34
	Cement Mortar	20	0.93	1.05	1800
	Aerated Concrete	300	0.22	1.05	700
	Hybrid Mortar	20	0.93	1.05	1800
Internal Walls	Cement Mortar	20	0.93	1.05	1800
	Brick Walls	200	0.8	1.05	1800
Flooring	Granite Slabs	20	3.49	0.92	2800
	Cement Mortar	30	0.93	1.05	1800
	Reinforced Concrete Floor Slabs	100	1.74	0.92	2500
Roof	Cement Bricks	20	1.1	1.05	1900
	Cement Mortar	20	0.93	1.05	1800
	Extruded Polystyrene Board	80	0.028	35	1.38
	Cement Mortar	20	0.93	1.05	1800
	Reinforced Concrete Roof	200	1.74	0.92	2500

Figure 1 presents a sectional view of a concrete floor slab structure, detailing the ground layer, cement mortar levelling layer, concrete fill layer, and structural layer.

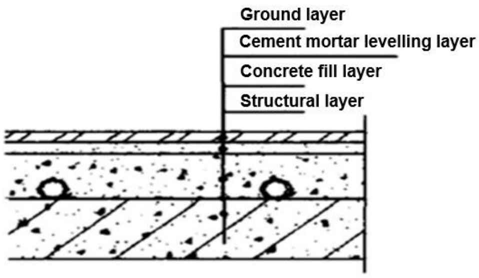

Figure 1: A sectional view of a concrete floor slab structure

In the cooling season (June 15 to September 15), the heat pump unit is used to supply the 7 ℃ chilled water during the valley power period at night (23:00 to 7:00 the next day), and the chilled water is stored in the storage tank for daytime use. At 8:00-18:00 on weekdays, the chilled water is used to handle fresh air. The cooling source of the radiant floor is the ground heat exchangers, which can provide high temperature cold water around 18 ℃ and run 24 h throughout the day. For the ground heat exchangers, the vertical single U-shaped pipes are adopted. There are 56 buried pipes with a depth of 100 m underground.

The design parameters of outdoor environment in Jinan in summer are as follows: dry bulb temperature of 34.8 ℃, wet bulb temperature of 26.7 ℃, and the enthalpy of outdoor air of 84.4 kJ/kg. The design indoor temperature is 26 ℃, the relative humidity is 60%, and the corresponding indoor air enthalpy is 59 kJ/kg. In order to meet the demand for air exchange rate in the indoor environment, the total fresh air supply volume is set to 6800 m^3/h. According to the latent cooling load and sensible heat load that the fresh air needs to take, the supply air temperature is set to 20 ℃, and the moisture content is 9.5 g/kg. The rated input power of the air source heat pump unit for fresh air handling is 23.4 kW, and the total volume of the chilled water storage tank is about 163 m^3.

2.2. Construction of simulation model

The construction of the model includes building modules and system modules based on the actual office building. The radiation floor structure layer is set in TRNBuild. The floor of the bottom layer is made of granite slab, concrete layer, cement mortar and thermal insulation layer from top to bottom. The other floors are made of granite slab, concrete layer and cement mortar from top to bottom, and the cooling coils are placed in the middle of reinforced concrete. The air-conditioning system of radiant cooling is established in TRNSYS. The radiant cooling system includes circulating water pumps, water distributor, water collector and radiant coils. The system model is shown in Figure 2.

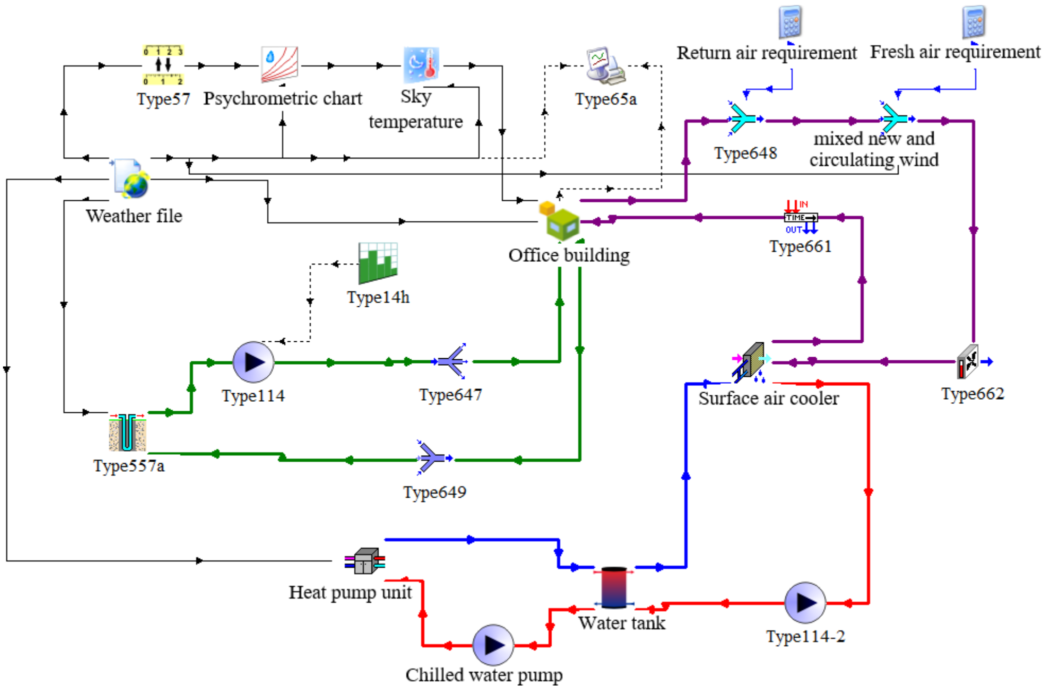

Figure 2: system model

2.3. Verification of the model

From the test conditions of literatures (Zhang, 2019) (Zhang, 2016) (Qi, 2015), the radiant cooling system runs continuously for 24 hours, and the fresh air system runs according to the actual office time (8:00-18:00). In the validation of the model, the operation time of the radiant cooling system and the fresh air system are set according to the conditions in literature. The simulation covers the whole cooling season (June 15 to September 15). In order to facilitate verification and analysis, the measured data of a typical room (32 m^2) on the third floor were selected. The maximum sensible cooling load of the typical room is 1390 W, and the latent cooling load is 452.5 W. The fresh air bears all the latent cooling load and 355.5 W sensible cooling load (accounting for 19% of the total sensible heat load of the room). The sensible cooling load taken by the radiant floor is 1564.5 W, accounting for 81%.

The conditions for model verification are consistent with the measured conditions in the literatures (Zhang, 2019) (Zhang, 2016) (Qi, 2015). The simulated data for a week from July 1 to July 8 were selected and compared with the measured data in the literature. In addition, the simulation results of the supply and return water temperature of the floor pipe in the whole cooling season are compared with the reported data in the literature, and the total energy consumption are also compared with the measured data.

The comparison between the measured air temperature and the simulated value in the typical week is shown in Figure 3. In the literature (Zhang, 2019), the measured indoor air temperature is basically in the range of 22 - 26.5 ℃. The simulated indoor temperature is between 22.5 - 26.5 ℃. The changes of measured and simulated values is basically the same, with an average deviation of 0.5 ℃. The reason for the deviation originates from a few aspects. Firstly, there were some simplifications in the simulation model. For example, in actual operation, the number of indoor personnel is dynamically changing, while in the model it is fixed. In addition, the meteorological data used in the simulation are derived from the typical meteorological year data, which inevitably has a certain deviation from the actual meteorological parameters. Generally, the deviations between the simulated and measured data are relatively small, which indicates that the model can predict the indoor temperatures accurately.

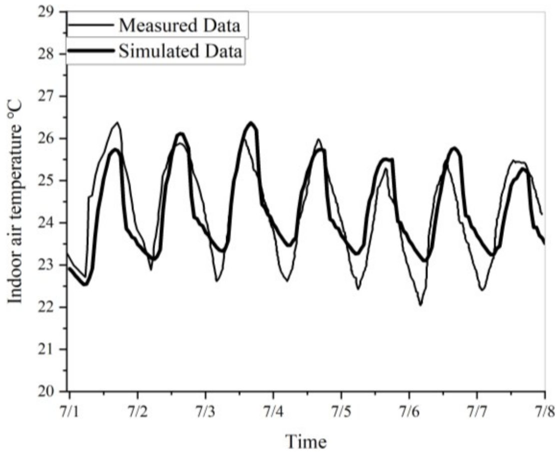

Figure 3: Comparison of measured and simulated temperature data

The calculated supply and return water temperature were compared with those in literature (Zhang, 2016), as shown in Figure 4. In the literature, the water supply temperature is in the range of 18.0 ℃ and 19.0 ℃, and the return water temperature changes between 19.0 ℃ and 20.5 ℃. The simulated supply water temperature is in the range of 18.0 ℃ and 19.0 ℃, and the return water temperature is between 19.0 ℃ and 21 ℃. The average temperature difference of supply water is 0.1 ℃, and the average temperature difference of return water is 0.2 ℃. It can be considered that the accuracy of the model built in this paper is quite acceptable.

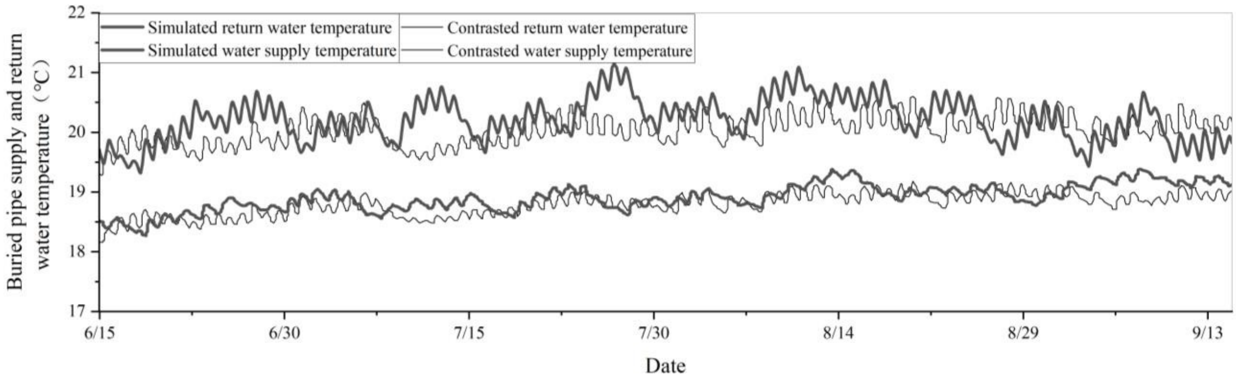

Figure 4: Comparison of supply and return water temperature of floor cooling

In addition, when the radiant cooling system operates continuously for 24h during the summer cooling season of this building in reference (Qi, 2015), the measured total power consumption during the cooling season is 19703.04 kWh, the operating cost is 11.3 million RMB, and the cost per unit area is 2.97 yuan/m^2. The power consumption from the simulation in this paper is 21073 kWh, the operating cost is 10300 RMB, and the cost per unit area is 2.73 yuan/m^2. The simulated power consumption is slightly higher than the measured value, and the deviation is about 6.5%. It can be considered that the energy consumption model is more accurate. The operating cost calculated according to the simulated energy consumption value is slightly lower than the actual operating cost in the literature. The reason is that the calculation of the cost during the simulation is based on the current peak-valley electricity price, while the actual measurement in the literature is in 2015, and the peak-valley electricity price policy used at that time is slightly different from the current electricity price.

According to the verification of the model and the comparison of the data, it is considered that the system model built in this paper can accurately predict the indoor temperatures, system supply and return water temperature, and energy consumption data.

3. SYSTEM SIMULATION RESULTS

Based on the local electricity price, the off-peak period in summer is 2:00 - 8:00, the peak period is 16:00 - 18:00, the sharp peak period is 18:00 - 22:00, and the rest of the period is shoulder period. To achieve better economic benefits during operation, the peak period and the sharp peak period should be avoided, and the off-peak period and the shoulder period should be fully considered.

Because the ground heat exchanger is used as the cooling source of the radiant floor in the building. The supply water temperature is high, and the cooling capacity of the radiant floor is limited. The actual system runs continuously for 24 hours throughout the cooling season, which is defined as the test condition. Considering the actual use time of the office building from 8:00 to 18:00, a comparative working condition operated according to the office time are proposed.

Considering the thermal inertia of the floor, the operating time is set to 7:00 - 17:00, and the total operating time is 10 h. Based on the office time and the electricity price policy, four cold storage conditions with different operating hours are also proposed. The operating time lasts from 6 h to 12 h for different reasons. The total of six conditions are shown in Table 2. The system operating schedule is configured in TRNSYS. For the office building, the system operates Monday to Friday, with shutdown from Friday night to Sunday, while cold storage starts on Sunday night.

Table 2: Six operating schemes

Conditions	Scheme	Operating time of radiant cooling system	Operating time for fresh air
Normal conditions	Test Condition	24h	8:00 - 18:00
	Comparison Condition	7:00 - 17:00	8:00 - 18:00
Cold storage conditions	Condition 1	2:00 - 8:00, operating for 6 h	8:00 - 18:00
	Condition 2	2:00 - 10:00, operating for 8 h	8:00 - 18:00
	Condition 3	2:00 - 12:00, operating for 10 h	8:00 - 18:00
	Condition 4	2:00 - 14:00, operating for 12 h	8:00 - 18:00

3.1. Indoor thermal environment

The simulation is for the whole cooling season. In analysis, the week (from August 6 to August 13) with the highest outdoor temperature is selected to show the simulation results, and August 8 is selected as a typical day to analyse the thermal environment of typical rooms.

The changes in indoor air temperature of the four cold storage conditions on the typical day are shown in Figure 5 (a). It can be seen that with the increase of cooling time, the indoor air temperature decreases, while the fluctuation range of indoor air temperature is gradually reduced. When the cooling time increases from 6 h to 12 h, the maximum temperature of indoor air decreases from 28.0 ℃ to 25.7 ℃, and the temperature difference is 2.3 ℃. It shows that the cooling time hasa great impact on the indoor air temperature level and temperature fluctuation in the cold storage condition. During cold storage during night, the temperature of the room is the lowest in the morning. Then the indoor temperature increases gradually and rises to the maximum value at the ending work hour of 18:00. From literature (Olesen, 2004), the room temperature fluctuation should be less than 2 ℃ to meet the thermal comfort requirements. As shown in Table 3, the temperature difference of indoor air temperature in typical days under the four conditions is within 2 ℃. However, with short operating time of 6 h, the indoor air temperature is higher than 27 ℃ for more than half of the working time, which means that the thermal comfort of room cannot be assured. With 8 h, the indoor temperature can be kept lower than 27 ℃. The longer the operating time, the lower the indoor temperature and the better the thermal comfort.

With radiant surfaces, thermal comfort is not only related to air temperature, but also the mean radiant temperature. The operative temperature combing the effect of both the air and mean radiant temperature are calculated. The indoor operative temperatures on the typical day are shown in Figure 5(b). The operative temperature is slightly lower than the air temperature. When the cooling time increases from 6 h to 12 h, the maximum operative temperature decreases from 27.9 ℃ to 25.5 ℃, and the difference is 2.4 ℃. The effect of operating time on operative temperature is similar to that of the air temperature.

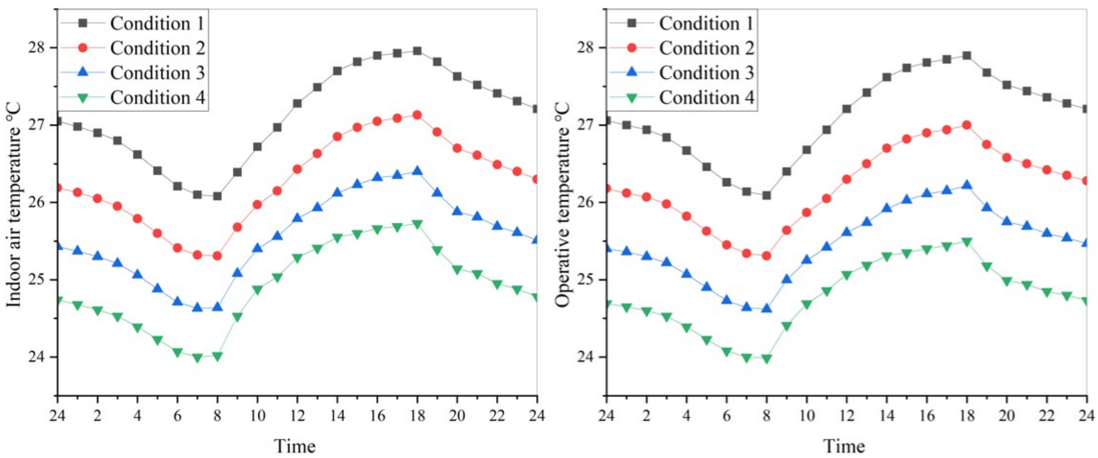

Figure 5: Indoor air temperature (a) and operative temperature (b) under different cold storage conditions on a typical day.

Table 3: Statistics of indoor air temperature and operating temperature under four conditions on typical day

Indoor Air Temperature and Operating Temperature (℃)	Condition 1	Condition 2	Condition 3	Condition 4
Maximum Value	28.0 / 27.9	27.1 / 27.0	26.4 / 26.2	25.7 / 25.5
Minimum Value	26.1 / 26.1	25.3 / 25.3	24.6 / 24.6	24.0 / 24.0
Difference	1.9 / 1.8	1.8 / 1.7	1.8 / 1.6	1.7 / 1.5

The analysis shows that the cold storage at night (2:00- 8:00) alone cannot fully meet the cooling demand during the day. Supply cooling during the daytime shoulder period can effectively reduce the indoor air temperature and improve thermal comfort. Further analysis shows that the thermal environmental parameters of the comparison condition (10 h during office time) are similar to those of condition 3 (6 h of night cold storage combined with 4 h of morning operating).

3.2. Heat balance

When the building envelope structure is used for cold storage, the cooling the supply water pipes released cooling through the floor surfaces (floor/ceiling) during night, which cool the indoor air and the envelopes. In the four cold storage conditions, condition 3 that can meet the basic comfort needs and has the same operating time as the comparison condition. Thus, it isselected for heat balance analysis, and the energy transfer at each hour of the typical day is analysed. The results are shown in Figure 6.

During the nighttime cooling storage (2:00 - 8:00), the total cooling supply from the water side can be determined based on the supply and return water temperature change and water flow rate, which is 27014 kJ. During the cold storage operation, the floor temperature, the inner wall temperature and the indoor air temperature continue to decline. The cold stored by the floor is 20724 kJ, the cold stored by the indoor air is less than 242 kJ. With large area of inner walls, the cold is stored 6297 kJ. The loss of cooling capacity through the exterior wall and window during the cold storage is 824 kJ, accounting for 3 % of the total cooling capacity. During nighttime cold storage, the outdoor temperature is relatively low and the temperature difference between indoor and outdoor air is small, so the loss of cold through the external envelope is quite small.

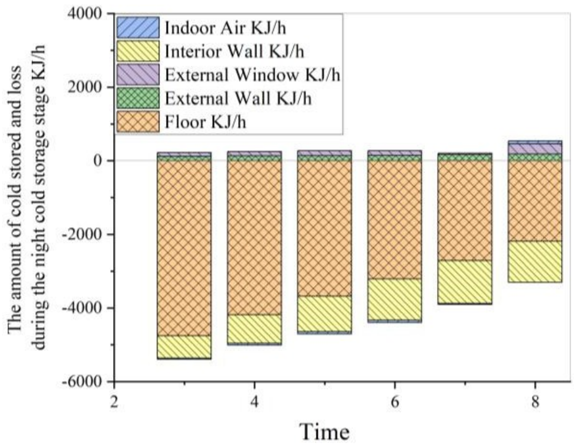

Figure 6: The amount of cold stored and loss during the night cold storage stage

Figure 7 shows the hourly heat flux of each surface on the typical day. During the operating of the radiant cooling system, the heat flux on the inner surfaces of the building envelope shows obvious dynamic changes. During the cold storage time from 2:00 - 8:00, the surface temperature of the floor and ceiling decrease slowly, which release and store cooling energy at the same time. For the interior and exterior walls, the surface heat flux is small but positive. The reason is during cold storage, both the air and surface temperature of walls are decreased, while the temperature decrease of air is larger than that of the walls. Therefore, there is net heat flux from the walls to the air. However, this heat flux is quite small. The heat flux of window changes is closely related to the outdoor temperature, showing decreasing trend first and then increasing. During the working hours operating of radiant cooling (8:00 - 12:00), the absolute value of heat flux of the floor and ceiling surface increases. It is mainly due to the increase of indoor temperature, and the increased heat transfer temperature difference leads to the increase of heat flux. When the radiant cooling stops at 12:00, there is still a heat flux on the surfaces, and the absolute value of heat flux decreases slightly. At this stage, the room temperature rises slightly, while the surface temperature of the floor/ceiling is still lower than the indoor temperature, and the stored cooling capacity will continue to be released.

Figure 8 shows the relationship between cooling capacity and hourly cooling load. During the working time from 8:00 to 18:00, the hourly cooling load is higher than cooling supplied, so that the indoor temperature continues to rise during this period. The total cooling capacity of the water side from 2:00 to 8:00 is 7.5 kWh (27000 kJ). During the period, a part of the cooling energy is stored in the floor/ceiling, others are stored in the inner envelope, the indoor air temperature, a small amount is lost. When the cooling system starts operating at 2:00, the maximum cold stored in the floor is 42 W/m^2. With thedecrease of the internal temperature of the floor/ceiling, the temperature difference between the supply and return water temperature and the surfaces decreases. Thus, the cold stored gradually decreases, and the cold released gradually increases. At 8:00, cooling released from the floor and ceiling surface is 9 W/m^2 and 6 W/m^2, respectively. After that, the office comes to the working time. With the increase of internal thermal disturbance and other factors, the room temperature increases more quickly than the inner surfaces, and the temperature difference between air and surfaces gradually increases. Under such conditions, the cooling released from the floor and ceiling also continues to increase. At 12:00, the total cooling released from the floor and ceiling is 28 W/m^2. 2 h after the cooling system stops, the heat release comesto the peak value of 29 W/m^2. Then it gradually declined to 22 W/m^2 at 18:00. Considering that the floor surface temperature is still lower than the indoor air temperature after 18:00, there is still a small part of the cooling energy released continuously before the cold storage starts again at night, which helps to reduce the indoor temperature before the cold storage operation.

According to the above analysis, the loss of cooling energy during the cold storage period at night is quite small. During the daytime office operation stage, the cooling energy released from the cooling surface and the fresh air is smaller than the required hourly cooling load, which caused the increase of room temperature. By the cold storage at night, the room temperature is low in the morning and then increases gradually. With this temperature drift, the overall room temperature can still be kept in a comfortable range.

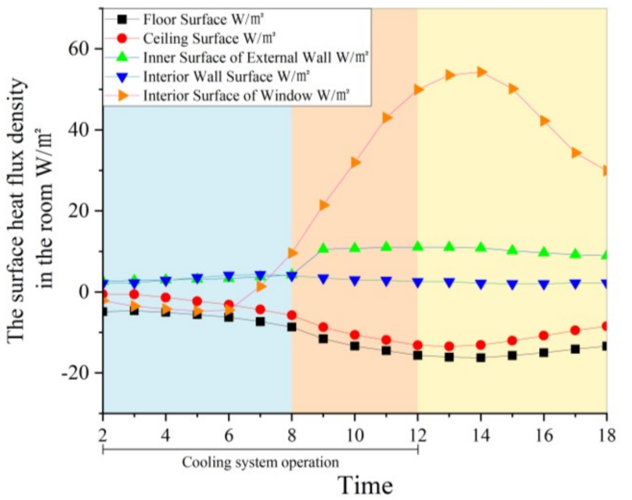

Figure 7: The surface heat flux density in the room

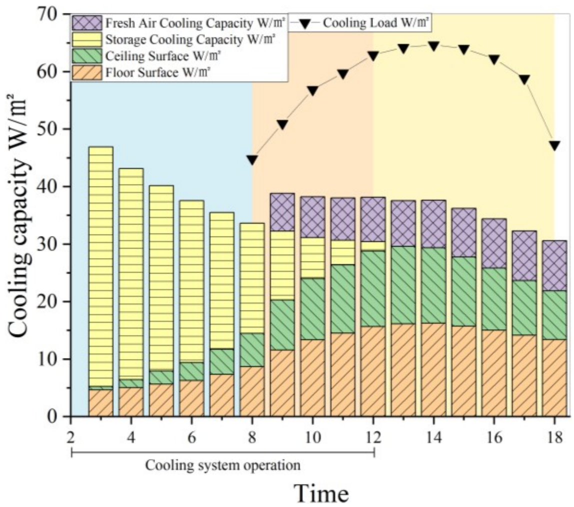

Figure 8: Relationship between cooling capacity and cooling load

3.3. Comparison of thermal comfort, energy consumption and economy

The air temperature, operating temperature and PMV index of the room under the four conditions for the whole cooling season were statistically analysed, and the results are listed in Table 4. For condition 1 and condition 2, there are 36% and 7% of the time that the PMV index is higher than 1, which means that the two conditions are difficult to meet the indoor thermal comfort requirements. For condition 3, the room thermal environment meets the requirement of comfort level Ⅱ(with PMV in the range of -1 to 1), while condition 4 can meet the requirements of comfort level Ⅰ(with PMV in the range of -0.5 to 0.5).

Table 4: Indoor thermal comfort parameters under different working conditions

Percentage	Indoor Air Temperature > 26.0 ℃	Indoor Operating Temperature > 26.0 ℃	|PMV|<0.5	|PMV|<1	|PMV|>1
Condition 1	74%	74%	26%	64%	36%
Condition 2	44%	40%	60%	93%	7%
Condition 3	17%	13%	87%	100%	0
Condition 4	3%	2%	98%	100%	0

According to the electricity price policy of Jinan, electricity tariffs are divided into sharp peak periods of 1.0394 yuan/kWh, peak periods of 0.9203 yuan/kWh, shoulder periods of 0.6226 yuan/kWh, and off-peak periods of 0.3249 yuan/kWh. The power consumption of the system mainly comes from the circulating water pump in the radiant cooling system, the heat pump and circulating water pump in the fresh air system, the draught fan and other equipment. The test condition in literature is operated 24 h continuously, the operation time of the fresh air system is from 8:00 to 18:00, and the operation time of the heat pump system as the cold source of fresh air is from 23:00 to 7:00 the next day. The statistics of the operating hours of the cooling system in each price interval under the six conditions are shown in Table 5.

Table 5: Operation hours

Condition	Sharp Peak Period	Peak Period	Shoulder Period	Off-Peak Period
Test Condition	260 h	130 h	780 h	390 h
Comparison Condition	0 h	65 h	520 h	65 h
Condition 1	0 h	0 h	0 h	390 h
Condition 2	0 h	0 h	130 h	390 h
Condition 3	0 h	0 h	260 h	390 h
Condition 4	0 h	0 h	390 h	390 h

The sub-item power consumption under the six conditions during the whole cooling season is summarized. The specific data are shown in Table 6.

Table 6: Power consumption statistics of system equipment under various working conditions

Equipment		Rated Power (kW)	Test Condition (kWh)	Comparison Condition (kWh)	Condition 1 (kWh)	Condition 2 (kWh)	Condition 3 (kWh)	Condition 4 (kWh)
Ground Heat Exchanger System	Water Pump	2.20	3432	1430	858	1144	1430	1716
Ventilation System	Heat Pump	23.4	12168	12168	12168	12168	12168	12168
	Chilled Water Pump	4.00	2080	2080	2080	2080	2080	2080
	Circulating Water Pump	0.44	286	286	286	286	286	286
	Draught Fan	2.38	1547	1547	1547	1547	1547	1547
Total Electricity Consumption (kWh)			19513	17511	16939	17225	17511	17797

The economic performance during the cooling season under the six conditions are compared and shown in Table 7. Compared with the 24 h continuous operating of the test condition, the operating time of the comparison condition is shorter, which can save 10.3 % of power consumption and 13.6% of operating cost. Condition 1 is switched on only during the off-peak power period, which saves 13.2% of electricity and 19.9% of running costs compared to the test condition. For condition 2, 3 and 4, compared with the test condition, can still reach a power saving rate of more than 8.8%, the proportion of cost savings can also be maintained at more than 14.4%. Condition 3 has the same operation time with the comparison condition, yet it operates combining the off-peak time, so it shows better economy.

In summary, through the economic analysis, it can be seen that the cold storage based on envelopes is possible to reduce energy and economic cost while keeping thermal comfort compared with test and comparison conditions.

Table 7: Comparison of power consumption and cost under different working conditions

Condition	Power Consumption (kWh)	Cost (yuan)	Unit Area Cost (yuan/m^2)	Power Saving Rate	Cost-Saving
Test Condition	19513	9675.04	2.55	/	/
Comparison Condition	17511	8360.47	2.20	10.3%	13.6%
Condition 1	16939	7748.91	2.04	13.2%	19.9%
Condition 2	17225	7926.98	2.09	11.7%	18.1%
Condition 3	17511	8105.04	2.13	10.3%	16.2%
Condition 4	17797	8283.1	2.18	8.8%	14.4%

Considering the thermal comfort requirement, condition 3 and 4 are suitable for cold storage in practice. Condition 4 has longer operated time, so it performs well to keep indoor thermal comfort. However, from the perspective of energy consumption and economy, condition 3 can be better. Condition 3 (the operating strategy from 2:00 to 12:00) can not only meet the needs of indoor thermal comfort, but also make full use of the peak-valley electricity price to achieve better economic benefits.

4. CONCLUSION

Considering the thermal characteristics of building envelopes, this study proposed the cold storage strategy for radian cooling system to make full use of the off-peak electricity hours. The indoor thermal environment parameters, thermal comfort, energy consumption, and economic aspects across different operating conditions are analysed based on simulation. The main conclusions are as follows.

(1) During cold storage modes, the room temperature gradually decreases during the night and increases during the working time. The total duration of cold storage and cooling had a great influence on the indoor thermal environment. To a certain extent, increasing the cooling time can effectively reduce the indoor air temperature and improve the thermal comfort.
(2) The cold storage and release process of condition 3 (operating from 2:00-12:00) for typical room are analysed in detail. The total cold storage capacity at night is 20724 kJ, accounting for 76% of the cooling capacity, and the cold storage loss is 824 kJ, accounting for 3%. The cold can be stored in the floor, inner walls and the indoor air. The absolute value of heat flux from the cooling surface gradually increases during the daytime. After shutting down the cooling coils, there is still cooling heat flux released from the surfaces due to the higher room temperature.
(3) Both conditions 1 and 2 are difficult to assure indoor thermal comfort during the cooling season. Condition 3 can satisfy the requirement of thermal comfort level Ⅱ, and condition 4 can meet the requirement of comfort level Ⅰ. Compared with the test and comparison conditions, condition 3 and 4 can achieve better economic effect.

5. ACKNOWLEDGEMENT

This research was supported by the Natural Science Foundation of Shandong Province (No. ZR2022ME035).

6. REFERENCES

Li, J. (2024) ‘Comparison of the environmental, energy, and thermal comfort performance of air and radiant cooling systems in a zero-energy office building in Singapore’, Energy and Buildings, 318, pp. 114487.

Olesen, B. (2004) ‘Operation and control of activated slab heating and cooling systems’, CIB World Building Congress. Canada.

Qi, Y. (2015) ‘The character of cooling-supply researching of the cooling system directly linked by buried pipes’, Shandong Jianzhu University. (in Chinese)

Rong, G. (2020) ‘Discussion on building entity energy storage’, Building Energy and Environment, 39(1), pp. 84-87. (in Chinese)

Zhang, F. (2021) ‘A critical review of the research about radiant cooling systems in China’, Energy and Buildings, 235, pp. 110756.

Zhang, L. (2016) ‘Performance analysis of thermal storage characteristic for the building envelope in a radiant floor cooling system’, Journal of Shandong Jianzhu University, 31(6), pp. 576-582. (in Chinese)

Zhang, L. (2019) ‘Research on control strategy of radiant floor cooling system in office buildings’, Shandong Jianzhu University. (in Chinese)

Zhang, L. (2020) ‘A two-dimensional numerical analysis for thermal performance of an Intermittently operated radiant floor heating system in a transient external climatic condition’, Heat Transfer Engineering, 41(9-10), pp. 825-839.

Zhou, L. (2020) ‘Study on thermal and energy-saving performances of pipe-embedded wall utilizing low-grade energy’,

Applied Thermal Engineering, 176, pp. 115477.

#305: Parametric sensitivity analysis under double-uncertainty optimization in distributed integrated energy systems

Kai XUE[1], Shuo ZHANG[2], Daotong CHONG[1], Jinshi WANG[1,3*], Junjie YAN[1]

[1] State Key Laboratory of Multiphase Flow in Power Engineering, Xi'an Jiaotong University,Xi'an, 710049, China
[2] Xi'an Thermal Power Research Institute Co., Ltd, Xi'an, 710054, China
[3] School of Energy Engineering, Yulin University, Yulin 719000, China
* Corresponding author. E-mail: wangjinshi@mail.xjtu.edu.cn

Abstract: Distributed integrated energy systems have the advantages of cleanliness and flexibility, contributing to the sustainable development of community and urban energy systems. The uncertainty of meteorology and load affects the planning and operation of the system, and it is of great significance to study the impact of key parameter fluctuations on performance indicators. Taking a regional energy system in Northwest China as a research case, the optimal configuration under certainty conditions is obtained through multi-objective optimization. Wind speed, solar irradiance, ambient temperature, and electrical load are used as uncertainty parameters of energy input and output, combined with Latin hypercube sampling and Monte Carlo simulation, to acquire the equipment capacity change when uncertainty is considered. Based on the planning results, the performance sensitivity of distributed energy systems is comparatively explored in terms of economy, environment, and energy utilization in the presence of varying degrees of stochastic fluctuations in meteorological parameters, electrical load, and electricity prices. The results show that wind speed has thegreatest impact on the environment and energy utilization, while solar irradiance has the most obvious influence on economy, and ambient temperature has the least effect on the comprehensive performance of the system. After uncertainty optimization, the system is less sensitive to load and electricity prices, and price-based demand response can effectively improve the economics of the system when electricity prices change. This work aims to improve the robustness of distributed energy systems under double uncertainties, which is of great theoretical value and practical guidance for promoting the optimal design and operation management of distributed energy systems.

Keywords: Integrated Energy System, Uncertainty Optimization, Sustainable Development, Parametric Analysis

1. INTRODUCTION

Faced with the increasingly intensifying global climate problem, countries around the world have responded one after another. As one of the largest carbon emitters, China actively participates in global climate governance and has set target timelines for carbon peaking and carbon neutrality (Si et al., 2023). In order to promote high-quality development, it is necessary to increase the utilization of renewable energy, adjust the traditional energy structure, and build a new system dominated by clean energy (Xue et al., 2023). After years of development, renewable energy power generation technologies have become mature, and the proportion of electricity sources continues to rise. By the end of December 2023, the total installed renewable energy power generation capacity in China accounted for nearly 40% of the world. However, due to the uncertainty and volatility of wind and solar output, it is difficult for a single renewable energy power generation technology to meet the needs of safe power production. Large-scale access will have a huge impact on the stability and dispatchability of the power grid, so the phenomenon of abandoned wind and light has occurred. Although the situation has improved with the deployment of energy storage, renewable energy utilization rates in some areas still hover at low levels (Kostelac et al., 2022).

Distributed integrated energy systems usually consist of energy supply equipment, energy conversion equipment, energy storage equipment and end users. Compared with traditional single energy supply or joint supply systems, the greatest advantage of distributed integrated energy systems is that they can couple various types of renewable energy, coordinate the planning and operation of multiple energy sources, and satisfy the demand of users locally. While meeting formal requirements, it can also achieve safety, low-carbon, economic purposes (Kim et al., 2023). As a typical multi-input and multi-output energy system, the distributed integrated energy system is very important to reasonably configure the capacity. During the design process, it is inevitable to be affected by various uncertain factors. These uncertainties can be defined as any deviation in the system from ideal certainty conditions. For example, the randomness of meteorological parameters, energy prices that cannot be accurately predicted, and uncertain industry prospects, etc. (Mavromatidis et al., 2018-a). Usually, systems are designed in a certainty manner, and any deviation caused by uncertainty will lead to suboptimal system performance. Although in some cases uncertainty can be reduced by obtaining additional information, it is difficult to eliminate completely and will also increase as the types of energy sources and devices coupled to the system increase. Therefore, it is crucial to consider uncertainty when optimizing capacity allocation for distributed integrated energy systems. Georgios et al. proposed a model to optimize the design of distributed integrated energy systems under uncertainty, considering the price of energy carriers, emission factors, building heating and power loads, solar irradiance, etc. as uncertain parameters, using probabilities scenarios to describe uncertainty. Two standards are adopted to limit carbon emissions, the first is based on the average emissions of the system under uncertain conditions, and the second is to set the emissions of the system individually for each possible uncertainty outcome. To illustrate the feasibility of the model, it is applied to 10 buildings in a community in Switzerland and compared with the results obtained by the certainty design model. The results show that certainty models may lead to inaccurate estimates of system costs and carbon emissions (Mavromatidis et al., 2018-b). Li et al. transformed the nonlinear two-layer robust optimization model into a single-layer mixed integer linear problem, proposed a coordination scheme with a two-layer framework to control multiple distributed integrated energy systems, and discussed the differences between the two pricing schemes, with the uncertainty of renewable energy, loads and energy prices considered (Li et al., 2021). Karmellos et al. used the annual total cost and carbon emissions as the objective function to optimize the distributed energy system, considering the uncertainty of several parameters such as energy price, interest rate, solar irradiance, and wind speed, and finally adopted four objective optimal methods including bad case, minimal regret criterion, minimal expected regret criterion and Monte Carlo simulation to explore the robustness of the scheme (Karmellos et al., 2019). Zhao et al. constructed a two-layer collaborative robust planning model for distributed integrated energy systems considering demand response (Zhao et al., 2021). In the first-level planning, the location and capacity of distributed renewable energy access are used as decision variables to minimize the operating cost of the distribution network. In the second level of planning, the uncertainty of renewable energy output is further considered. Taking the optimal operating cost of the system as the goal, robust optimization is introduced to establish a lower-layer robust optimization model. Finally, the model and method were verified through case simulation, and the impact of demand response on planning results was evaluated. The results show that considering demand response in distribution network planning can help delay investment costs, enhance power user load flexibility, and effectively avoid load reduction and other problems. Anahita et al. proposed a model-based predictive control energy scheduling framework for distributed integrated energy systems, aiming to address uncertainty in renewable energy by utilizing non-renewable resources to compensate for power shortages (Anahita et al., 2021). Kostelac et al. developed a price-responsive demand response model for distributed integrated energy systems under uncertainty by modelling uncertainty through robust optimization and two-stage stochastic optimization and applied it to an industrial scenario. The results show that savings of up to 18% can be achieved compared to passive and certainty models (Kostelac et al., 2022).

To sum up, the distributed integrated energy system is a complex system with multiple inputs and multiple outputs, and the types and capacities of equipment in the system vary widely depending on the application scenarios. At present, most of the research on uncertainty only focuses on the uncertainty of a single input or output, and there are few related studies that consider both at the same time. This paper used Monte Carlo simulation to simulate a distributed integrated energy system with double uncertainties in meteorological and load parameters, and conducted parametric sensitivity analysis, including renewable energy, load, and electricity price, which were considered to fluctuate within an interval of 50% above and below the baseline values. This study plays a positive role in more rational planning and operation of distributed integrated energy systems in engineering practice and can lead to superior overall performance. The rest of the paper is organized as follows: Section 2 shows the system model including system structure, variable and constraints. Section 3 lists the results of double-uncertainty optimization. Section 4 discusses the sensitivity of the uncertain parameters to the performance metrics. The main conclusions are enumerated in Section 5.

2. SYSTEM MODELING

The design object of the distributed integrated energy system in this work is a park located in northwest China, where there are relatively abundant solar energy and natural gas resources.

2.1. Structure

Renewable energy equipment in the energy production process uses wind turbines, photovoltaics, and solar collectors. Traditional energy supply equipment uses gas turbines and gas boilers. The power grid serves as the guarantee and supplement of electricity. Loads include electricity, heating and cooling needs, and electricit y and thermal storage equipment is provided. Electric refrigeration and absorption refrigeration are selected to jointly meet the cooling load, and the heat exchanger is used to supply the heating load. The system configuration is shown in Figure 1.

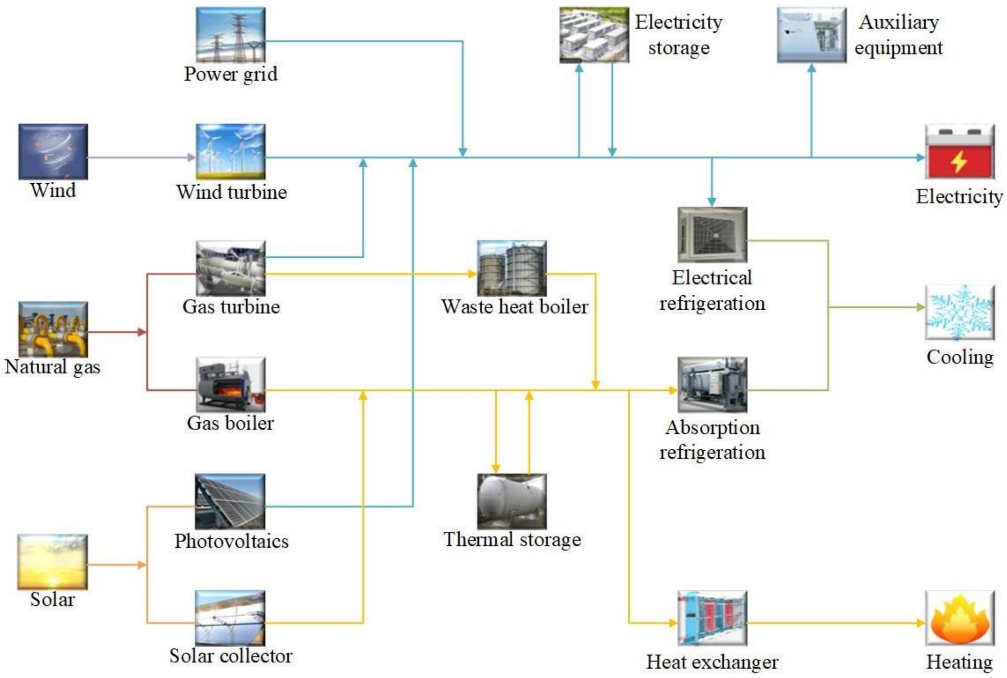

Figure 1: Structure of distributed integrated energy system

2.2. Variables and constraints

The Gas turbine and gas boiler play a fundamental role in the distributed integrated energy system. When renewable energy output fluctuates or stops, it will make up for the load vacancy. The capacity optimization range of the two is as Equation 1:

Equation 1: Capacity optimization range of gas turbine.

$$0 \leq P_{\mathrm{GT}} \leq P_{\max}$$

Where:

- P_{GT} = capacity of gas turbine (kW)
- P_{max} = maximum electrical load (kW)

The efficiency of a gas turbine operating at low load rates is very low, so it needs to be limited by specifying the minimum load rate, as shown in Equation 2:

Equation 2: Load rate constraint.

$$0.2 \leq PLR_{\min} \leq 1$$

Where:

- PLR_{min} = minimum load rate of gas turbine

The cooling load is satisfied by both electric refrigeration and absorption refrigeration. The absorption refrigeration equipment is connected to waste heat utilization equipment, gas boilers and thermal storage devices. There is a cascade utilization of energy, and its proportion in the cooling load needs to be optimized. The higher the ratio, the greater the cooling capacity of absorption refrigeration, as presented in Equation 3:

Equation 3: Constraint of absorption refrigeration. $$0 \leq \lambda_{\mathrm{AR}} \leq 1$$

Where:

- λ_{AR} = percentage of absorption refrigeration

Distributed integrated energy system has photovoltaic power generation and solar thermal collector two kinds of solar energy utilization equipment, the installed photovoltaic panels and solar collector panels of the available area is limited in the park, it is necessary to the utilization of the area share of the distribution, as in Equation 4:

Equation 4: Constraint of solar area. $$0 \leq \lambda_{\mathrm{PV}} \leq 1$$

Where:

- λ_{PV} = percentage of photovoltaic panels in the total solar available area

Wind power generation equipment is relatively independent, and its capacity optimization range is as shown in Equation 5:

Equation 5: Capacity optimization range of wind turbine. $$0 \leq P_{\mathrm{WT}} \leq P_{\mathrm{max}}$$

Where:

- P_{WT} = capacity of wind turbine (kW)

When optimizing the capacity allocation of the distributed integrated energy system, the energy balance needs to be constrained. In addition to the need to satisfy the electrical load of users, auxiliary equipment and electric refrigeration equipment will also consume electricity, and the power balance constraint is shown in Equation 6:

Equation 6: Electrical balance. $$P_{\mathrm{load}} + P_{\mathrm{ER}} + P_{\mathrm{aux}} \leq P_{\mathrm{GT}} + P_{\mathrm{PV}} + P_{\mathrm{WT}} + P_{\mathrm{grid}}$$

Where:

- P_{load} = electric load (kW)
- P_{ER} = electricity demand of electric refrigeration (kW)
- P_{aux} = electricity demand of auxiliary equipment (kW)
- P_{PV} = electricity supply of photovoltaics (kW)
- P_{grid} = electricity purchased from the power grid (kW)

The heat load of the system consists of the heat demand of users and the heat needed for absorption refrigeration, and the heating equipment includes the waste heat boiler, solar collector, and gas boiler. The heat balance constraint is as in Equation 7:

Equation 7: Heat balance. $$H_{\mathrm{load}} + H_{\mathrm{AR}} \leq H_{\mathrm{SC}} + H_{\mathrm{WHB}} + H_{\mathrm{GB}}$$

Where:

- H_{load} = heat load (kW)
- H_{AR} = heat demand of absorption refrigeration (kW)
- H_{SC} = heat supply of solar collector (kW)
- HWHB = heat supply of waste heat boiler (kW)
- H_{GB} = heat supply of gas boiler (kW)

The cooling load of the system is only the cooling demand of users, and the cooling balance constraint is as in Equation 8:

Equation 8: Cooling balance. $$C_{\mathrm{load}} \leq C_{\mathrm{AR}} + C_{\mathrm{ER}}$$

Where:

- C_{load} = cooling load (kW)
- C_{AR} = cooling supply of absorption refrigeration (kW)
- C_{ER} = cooling supply of electrical refrigeration (kW)

3. DOUBLE-UNCERTAINTY OPTIMIZATION RESULTS

Energyplus software was used for the simulation of the year-round load for the case park. Life cycle cost, life cycle primary energy saving rate, and pollutant emission reduction rate were selected as the evaluation indicators in the optimization process. The Maximum Rectangular Method, Non-dominated Sorting Genetic Algorithm II, Monte Carlo simulation, and Ideal Normalization Method were combined to optimize the capacity allocation of distributed integrated energy systems. For the distribution characteristics of the four parameters of ambient temperature, solar irradiance, wind speed and electrical load, the corresponding probability density function is selected, and the sampling value is obtained through Latin hypercube sampling, which is added to the reference value to characterize the uncertainty of the four parameters. On this basis, uncertainty optimization is carried out for the system with double uncertainties of weather and load. The simulation results show that there are some limitations in considering weather or load uncertainty alone, and it is more reasonable to consider both at the same time. Table 1 presents the results of the capacity allocation of each device after considering the double uncertainties. The primary energy saving rate of the system is reduced after considering uncertainty, and the life cycle cost and environmental friendliness are improved. Robustness can be improved by 24.6% from the certainty optimization results, and the overall index is improved to 26.9%.

Table 1: Results of equipment capacity allocation considering double uncertainties

Equipment	Unit	Value
Gas turbine	kW	1809
Gas boiler	kW	4352
Waste heat boiler	kW	3217
Photovoltaics	kW	10673
Solar collector	kW	3577
Wind turbine	kW	651
Electricity storage	kWh	142
Thermal storage	kWh	209
Heat exchanger	kW	5910
Absorption refrigeration	kW	7750
Electrical refrigeration	kW	3478

4. PARAMETRIC SENSITIVITY ANALYSIS

For the certainty optimization design and the scenarios obtained after considering the double uncertainty, the comparative analysis was carried out from the sensitivity of weather parameters, load, and time-of-use price of electricity.

4.1. Weather parameters sensitivity

The variation of life cycle cost, life cycle primary energy saving rate, and pollutant emission reduction rate for the certainty design and the optimal solution obtained after considering the double uncertainty following changes in the weather parameters are shown in Figure 2, where the input parameters are increased or decreased by 25% and 50% from the established baseline. The smaller variation indicates the lower sensitivity of the system. On the life cycle primary energy saving rate side, the uncertainty optimization results have a smaller variation whether the weather parameter decreases or increases. With respect to life cycle cost, the sensitivity of the uncertainty optimization results is lower when the weather parameters decrease by more than 25% and increase by more than 40%. In terms of pollutant emission reduction rate, the magnitude of change in the certainty optimization results is consistently greater. Taken together, the uncertainty optimization results are less sensitive to weather parameters.

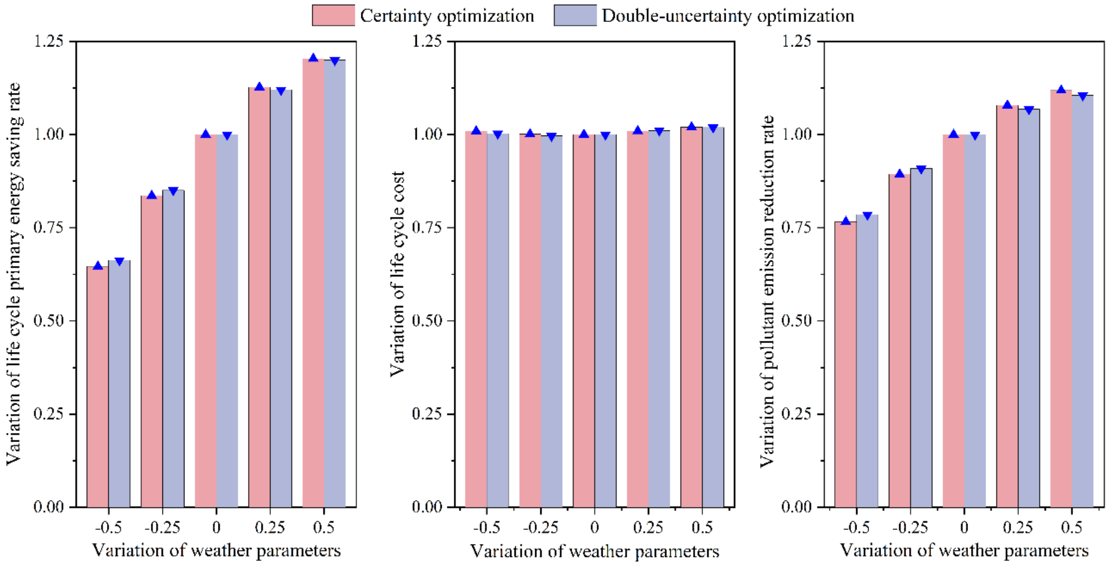

Figure 2: Impact of weather parameters on evaluation indicators

In order to compare more intuitively the effect of uncertainty in wind speed, solar irradiance, and ambient temperature on the system performance, the information entropy of the three parameters is calculated from the four perspectives of life cycle cost, primary energy saving rate, pollutant emission reduction rate, and comprehensive indicator, respectively, and the results are shown in Figure 3. Wind speed has the largest effect on primary energy saving rate, pollutant emission reduction rate, and the comprehensive indicator among the three uncertainty parameters, and has no effect on life cycle cost. Solar irradiance has the greatest effect on life cycle cost and almost no effect on primary energy saving rate and pollutant emission reduction rate. Ambient temperature has no effect on primary energy saving rate and pollutant emission reduction rate, has a low effect on life cycle cost and comprehensive indicator, and overall has the least effect on system performance among the three uncertainty parameters.

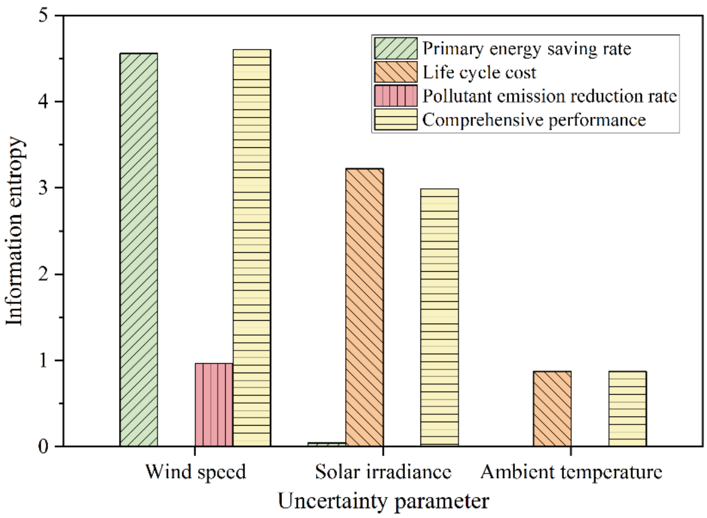

Figure 3: Information entropy of uncertainty parameters

4.2. Load sensitivity

The change in the life cycle cost, life cycle primary energy saving rate, and pollutant emission reduction rate for the certainty optimization design and the scheme after considering the double uncertainty after the change in the load input parameters are depicted in Figure 4, where the input parameters are increased or decreased by 25% and 50% from the established baseline. The sensitivity of all three metrics to load changes is lower for the uncertainty scheme, regardless of load increase or decrease. Pollutant emission reduction rate has the highest sensitivity to load, which becomes 1.39 times the original at 50% load decrease, and the rate of change decreases with load increase. Primary energy saving rate has the lowest sensitivity to load, which becomes 1.20 times the original at 50% load decrease. Life cycle cost has an approximately linear relationship with the load.

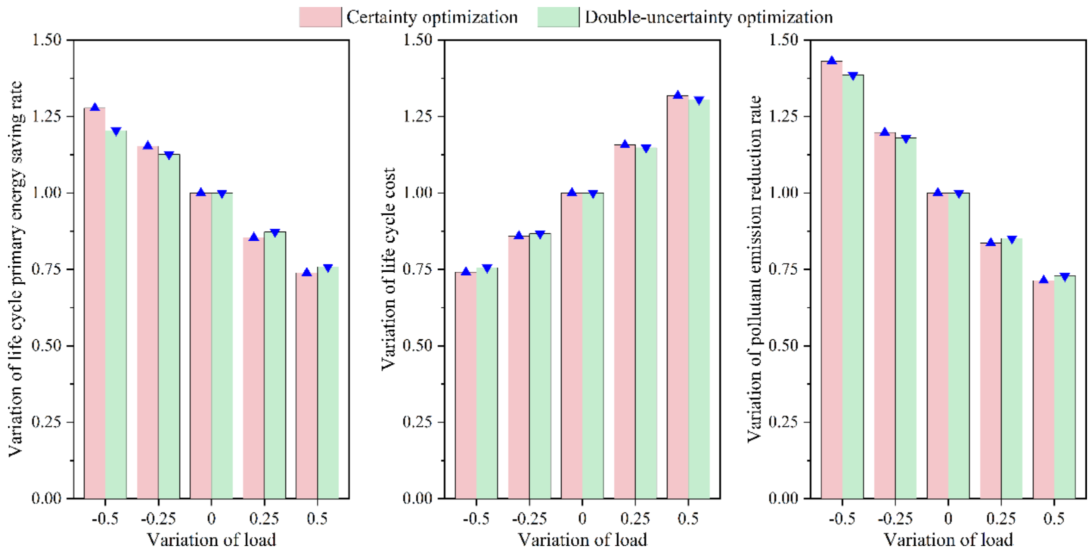

Figure 4: Impact of load on evaluation indicators

4.3. Electricity price sensitivity

The change in the life cycle cost for the certainty optimization design and the scheme after considering the double uncertainty after the change in the electricity price are presented in Figure 5, where the input parameters are increased or decreased by 25% and 50% from the established baseline. Obviously, the sensitivity of the electricity price is lower under uncertainty optimization results. There is a correlation between the price of electricity and the electric load, when the price of electricity changes, the electric load will also change accordingly. Price-based demand response can reduce the impact of load uncertainty on the economics of distributed integrated energy systems, and according to the theory of elasticity in economics can characterize the relationship between load and electricity price after the implementation of price-based demand response. The time-of-use prices of electricity for the case park are listed in Table 2.

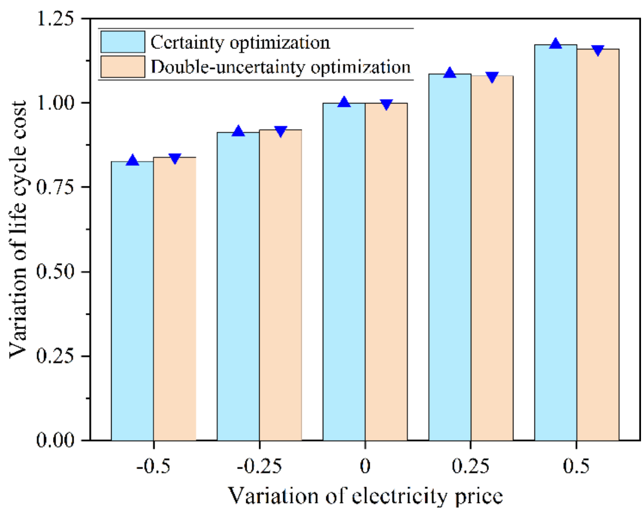

Figure 5: Impact of electricity price on evaluation indicators

Table 2: Time-of-use prices of electricity for the case park (yuan/kWh)

Period	Time	Type		
		Civilian	Business	Demand response
Normal period	8:00-9:00 ＆ 13:00-17:00	0.4271	0.4271	0.3744
Valley period	00:00-8:00	0.4271	0.2048	0.1521
Peak period	9:00-12:00 & 18:00-23:00	0.4271	0.6994	0.5967

In order to prevent the system from over-responding to alternating peak and valley loads, it is necessary to limit the amount of load change for demand response to be no higher than a set threshold. In this work, it is assumed that the self-elasticity coefficient of electric load is -0.15, i.e., the maximum load curtailment is not more than 15% of the original load, and the cross-elasticity coefficient is 0.08. Figure 6 demonstrates the changes in system metrics before and after the demand response. It can be known that the life cycle primary energy saving rate and pollutant emission reduction rate are slightly improved from the original, the life cycle cost is decreased by 42 million yuan, and the economy is significantly improved.

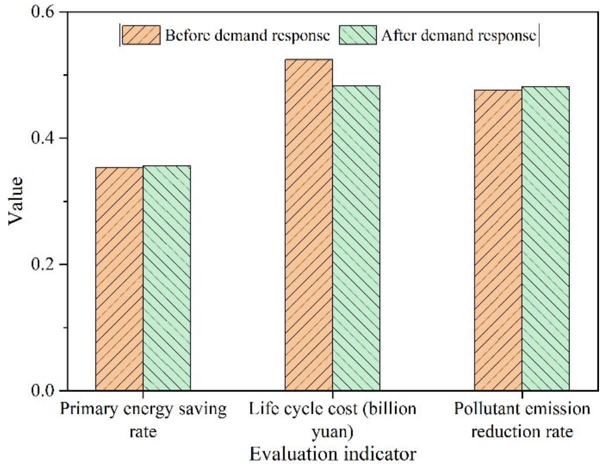

Figure 6: Comparison of evaluation indicators before and after demand response

5. CONCLUSION

A design optimization considering double uncertainties for distributed integrated energy systems is developed, and the parametric sensitivity analysis is performed. The primary energy saving rate, life cycle cost, and pollutant emission reduction rate are selected as evaluation indicators. Maximum Rectangular Method, Non-dominated Sorting Genetic Algorithm II, and Ideal Normalization Method are combined for the variable optimization. Latin hypercube sampling is used to obtain changes of uncertainty parameters, and the robustness of different schemes is obtained by Monte Carlo simulation. The main conclusions are as follows:

(1) Compared to certainty optimization, the magnitude of variation in each performance metric is smaller when double-uncertainty optimization is used. Among the three uncertain parameters, load fluctuations have a more drastic effect on system performance.
(2) The robustness of the system can be improved by 24.6% based on the certainty optimization results, and the comprehensive indicator is improved from 0.230 to 0.269. Among the meteorological uncertainty parameters, wind speed has the greatest impact on the system with an information entropy of 4.61.
(3) When the price of electricity changes, the implementation of price-based demand response can effectively improve the economics of distributed integrated energy systems.

This work discussed the impact of weather, load, and electricity price uncertainty on system performance, but distributed integrated energy systems have more uncertain factors in their actual operation. Less consideration of the parameters can lead to limitations in uncertainty optimization. Therefore, further study will encompass more uncertain aspects and obtain the laws of multiple parameters' influence on system performance, which will guide the optimal operation of the system under parameter fluctuations.

6. REFERENCES

Bhavsar S, Pitchumani R, Ortega-Vazquez M, Costilla-Enriquez N, 2023. A hybrid data-driven and model-based approach for computationally efficient stochastic unit commitment and economic dispatch under wind and solar uncertainty. International Journal of Electrical Power & Energy Systems,151, 109144.

Karmellos M, Georgiou PN, Mavrotas G, 2019. A comparison of methods for the optimal design of distributed energy systems under uncertainty. Energy, 178, 318-333.

Kim J, Park H, Kim S, Lee J, Song Y, Yi S, 2023. Optimization models for the cost-effective design and operation of renewable-integrated energy systems. Renewable and Sustainable Energy Reviews, 183, 113429.

Kostelac M, Pavic I, Zhang N, Capuder T, 2022. Uncertainty modelling of an industry facility as a multi -energy demand response provider. Applied Energy, 307, 118215.

Li L, Cao X, Wang P, 2021. Optimal coordination strategy for multiple distributed energy systems considering supply, demand, and price uncertainties. Energy, 227, 120460.

Mavromatidis G, Orehounig K, Carmeliet J, 2018-a. A review of uncertainty characterisation approaches for the optimal design of distributed energy systems. Renewable and Sustainable Energy Reviews, 88, 258-277.

Mavromatidis G, Orehounig K, Carmeliet J, 2018-b. Design of distributed energy systems under uncertainty: A two-stage stochastic programming approach. Applied Energy, 225, 932-950.

Moradmand A, Dorostian M, Shafai B, 2021. Energy scheduling for residential distributed energy resources with uncertainties using model-based predictive control. International Journal of Electrical Power & Energy Systems, 132, 107074.

Si F, Du E, Zhang N, Wang Y, Han Y, 2023. China's urban energy system transition towards carbon neutrality: Challenges and experience of Beijing and Suzhou. Renewable and Sustainable Energy Reviews, 183, 113468.

Xue K, Wang J, Hu G, Wang S, Zhao Q, Chong D, Yan J, 2023. Optimal planning for distributed energy systems with carbon capture: Towards clean, economic, independent prosumers. Journal of Cleaner Production, 414, 137776.

Zhao X, Bai Z, Xue W, Xu N, Li C, Zhao H, 2021. Research on bi-level cooperative robust planning of distributed renewable energy in distribution networks considering demand response and uncertainty. Energy Reports, 7, 1025-1037.

#307: Construction and application of multi-component molten salt component-property database (MSCPD)

Yufan YANG[1], Yuxin LUO[2], Jiale ZHOU[3], Weijun SONG[4], Ze SUN[5]

[1] East China University of Science and Technology, Shanghai 200237, China, yyufan2021@163.com
[2] East China University of Science and Technology, Shanghai 200237, China, lyxofficialwork@163.com
[3] East China University of Science and Technology, Shanghai 200237, China, zhou.jiale@ecust.edu.cn
[4] Qinghai University, Xining 810016, wjsong@mail.ecust.edu.cn
[5] East China University of Science and Technology, Shanghai 200237, China, zsun@ecust.edu.cn

Abstract: With the increasing global energy demand and the increasingly serious environmental problems, the development of sustainable energy has become an important issue in the contemporary world. Energy storage and conversion is the key issue of sustainable energy utilization, the conversion of chemical energy, heat energy, etc. into electrical energy, so that various energy sources are efficiently used, and released when needed to meet the demand for electrical energy. Molten salt energy storage is a technology that uses high-temperature molten salt to store heat energy. As a heat transfer storage medium with low melting point, high stability and low cost, mixed molten salt plays a key role in the field of Concentrated solar power (CSP) technology. It is very important to study the composition, ratio and related thermophysical properties of fused salt for promoting the development of fused salt energy storage. Most of the research focuses on the thermal properties of molten salt, but there is no database to collect the data. In this study, Molten Salt Component-Property Database (MSCPD) was established by collecting and screening samples of mixed molten salt, experimental verification and data verification. The database integrates various data on molten salts, including melting point, decomposition temperature, specific heat capacity, melting enthalpy, density, viscosity, thermal diffusivity, thermal conductivity, etc. This information enables researchers to obtain data about molten salt intuitively and quickly. At present, covering 31 elementsand 6350 sets of molten salt formulations in the MSCPD. It is currently the largest physical properties database of moltensalt used in the field of energy storage, and we will continue to pay attention to the latest research progress in the field of molten salt energy storage, and timely update the database content.

Keywords: Molten Salt; Concentrated Solar Power; Energy Storage; Database

1. INTRODUCTION

With the rapid development of energy and economy, a large number of coal, oil, natural gas and other non-renewable energy sources are exploited, which has caused the severe challenge of the increasing depletion of global energy resources and the intensification of environmental pollution (Chu et al., 2016; Steven and Arun, 2012).Vigorously developing renewable energy technology and energy storage technology is the main way to solve the current problem (Zhao et al., 2024; Zhang et al.,2024). Wind energy and photovoltaic energy are gradually being widely used as renewable and clean energy, helping the development of power networks to be more reliable and efficient. However, due to the influence of various factors such as climatic conditions, geographical location, and seasonal changes, wind and solar energy have a certain intermittency. As these intermittent renewable energy sources continue to be utilized, the stability of the grid willbe compromised. In the case of fluctuating renewables, efficient energy storage systems are essential to ensure a stable and resilient energy supply (Peter, 2015; Sun et al., 2024). Concentrated Solar Power (CSP) technology is one of the most promising new energy power generation technologies and has attracted more and more attention. CSP systems have thepotential to replace traditional power plants. CSP system uses the optical principle to convert solar radiation into heat energy through the concentrating collector, which then drives the steam turbine to do work and drives the generator to generate electricity, so as to realize the large-scale utilization of solar energy (Carbajales et al., 2024; Ong et al. 2024). Thermal Energy Storage (TES) technology is a key component of the CSP system, which is suitable for large-scale and long-term energy storage, which can achieve continuous and stable power supply and improve system efficiency (Mitin et al., 2023). In the TES system, the selection of heat transfer fluid (HTF) is crucial, and the heat transfer fluid collects heat as aheat energy carrier, and the common heat transfer fluids are water, air, molten salt, heat transfer oil and other materials (Edouard et al.,2017; Wang et al., 2023; Vignarooban et al., 2015; Yang et al., 2024). Among them, molten salt has become the first material of HTF due to its excellent physical properties such as wide operating temperature range, high stability, high specific heat capacity and low cost, and is widely used in CSP systems (Hu et al., 2023; Gunasekara et al.,2021; Ángel et al., 2019).

At present, the multi-component molten salts widely used in CSP are mainly $NaNO_3$-KNO_3 binary nitrate molten salt (60.0 wt.% -40.0 wt.%, Solar Salt), KNO_3-$NaNO_3$-$NaNO_2$ ternary mixed molten salt (53wt.%-7wt.%-40wt.%, Hitec) and KNO_3-$NaNO_3$-$Ca(NO_3)_2$ (45wt.%-7wt.%-48wt.%, Hitec XL) (Nunes et al., 2016; Zhang et al., 2022).In order to reduce the melting point of molten salt and broaden the temperature range of molten salt, researchers continue to explore and prepare a variety of new hybrid molten salt formulations by various methods to improve the efficiency of heat storage system. Zhang et al. (Zhang et al., 2018) added $LiNO_3$ and $CsNO_3$ to the composition of $NaNO_3$ and KNO_3 and designed a new polynitrate molten salt with a melting point of 95℃ by Calculation of Phase Diagram (CALPHAD). Parallel Solar Salt, $LiNO_3$-$NaNO_3$-KNO_3, $NaNO_3$-KNO_3-$CsNO_3$, $NaNO_3$-KNO_3-$Ca(NO_3)_2$, $LiNO_3$-$NaNO_3$-KNO_3-$CsNO_3$ and $LiNO_3$-$NaNO_3$-KNO_3-$CsNO_3$-$Ca(NO_3)_2$ six kinds of mixed nitrates the thermophysical properties of salt were measured and evaluated comprehensively. However, due to the high price of $LiNO_3$ and $CsNO_3$, this kind of molten salt cannot be used on a large scale. Wang et al. (Wang et al., 2024) selected $NaNO_3$, KNO_3, $Ca(NO_3)_2$, $NaNO_2$, KNO_2 with lower cost to develop a new type of quinary nitrate/nitrite mixed molten salt. The melting point of the quinary salt is 102.3℃, and the decomposition temperature is 651.2℃. The thermal properties, thermal stability and the economy of the salt are evaluated comprehensively. It is considered that the salt has good performance and can be widely used in TES system. Patange et al. (Patange et al., 2024) developed CuCl-KCl-NaCl ternary mixed chloride salts, added $CaCl_2$ to the composition of CuCl, KCl and NaCl, and conducted a detailed study on the thermophysical properties and thermal stability of these two eutectic chloride salts. The results showed that the melting point of molten salts decreased and the specific heat capacity increased after $CaCl_2$ was added. The operating temperature can reach 700℃, with excellent thermal stability.

With the rapid development of information technology and the advent of the era of big data, materials and biology have brought far-reaching influence to the research and development of their respective fields through the extensive establishment of databases. Orti et al. (Orti et al., 2023) established MLOsMetaDB (http:/mlos.leloir.org.ar) to study the function of liquid-liquid phase separation processes (LLPS) and membraneless organelles (MLOs). A comprehensive information resource on MLOs and LLPS-associated proteins, MLOsMetaDB integrates and centralizes the available information for each protein involved in MLOs, providing an interactive and user-friendly environment with modern biovisualization and easy and rapid access to proteins based on the role of LLPS, the location of MLOs, and the organism. Li et al. (Li et al., 2023) created a database of multiple principal element alloys (MPEAs) by manual extraction, which integrates the mechanical property data of multiple principal element alloys, similar to the molten salt database. Wang et al. (Wang et al., 2023) proposed a database of spectral constants of diatomic molecules (DSCDM) dedicated to the study of the spectral constants of the ground and excited states of diatomic molecules, which relies on application programming interfaces (APIs) for molecular spectral data retrieval and the ability to upload new data. Zhang et al. (Zhang et al., 2023) developed an Animal Parasitic Diseases and Drugs Database (APDDDD) specifically for the collection and analysis of animal parasitic diseases and related drugs, which provides a user-friendly and interactive website. Maria et al. (Maria et al., 2021) collected and collated the experimental data available in the field of nanofluids and developed a comprehensive database of experimental thermophysical properties of nanofluids to facilitate the understanding of the thermophysical behavior of nanofluids. Liu et al. (Liu et al., 2023) developed a biochemical methane potential database (BMP) in the form of a public platform using manual collection and collation to optimize the data information. Chellapandi et al. (Chellapandi et al., 2017) used text mining to extract the metabolic information of cyanobacterial proteins responsible for the utilization of C1 compounds and developed the Cyanobacterial C1 Metabolic Protein Structure Information Resource (CPSIR-CM) to illustrate the structural characteristics of proteins involved in the catabolism of different C1 compounds.

At the same time, with the rapid development of artificial intelligence, machine learning has gradually been adopted by various fields, and the combination of machine learning and big data technology has gradually become the mainstream (Butler et al., 2018). Machine learning has been widely used in materials science research, and machine learning methods can effectively screen the virtual space of materials to efficiently obtain new materials, and in addition, extract more information about ideal materials from predicted datasets (Wei et al., 2023; Li et al., 2020; Hu et al., 2022). As an important energy storage medium, molten salt has attracted much attention. Researchers have accumulated a lot of relevant information and data in the field of molten salt, but these data are scattered in various literatures and difficult to retrieve, which hinders the further use of molten salt in the field of energy storage. In order to make better use of molten salt, it has become a crucial task to establish an energy storage molten salt performance database to support future data-driven machine learning to predict molten salt data.

Yang et al. (Yang et al., 2023) proposed a model to predict the thermal conductivity of molten salt with temperature, and based on this, a database of molten salt thermal conductivity was established. Ard et al. (Ard et al., 2022) from Oak Ridge National Laboratory in the United States developed a Molten Salt Thermal Properties Database − Thermochemical (MSTDB−TC), in order to accurately characterize the thermochemical and phase equilibrium of molten salt components and their aggregation behavior, dedicated to molten salt nuclear reactor technology to support thermodynamic modeling of fluoride and chloride based systems for molten salt reactor (MSR). In addition, the Molten Salt Thermal Properties Database - Thermophysical (MSTDB-TP) is also being developed. Ai et al. (Ai et al., 2009) collected and sorted out the data of molten salt physical properties such as melting point, density, viscosity and surface tension recorded in the literature, and developed a Web-based database of molten salt physical properties for application in the field of biomass pyrolysis. However, due to the different application fields, the types, composition and properties of the collected molten salts are different, and it is difficult to be used in the field of energy storage. At present, there is still a lack of database dedicated to the storage of molten salt as training data.

Therefore, a Molten Salt Component-Property Database (MSCPD) dedicated to the field of energy storage is established in this paper (https://mscpd.ecust.cn). The database collected molten salt data from published literature from 1987 to 2024, experimental supplementary data, and research data accumulated in the research group over the past two decades, covering 31 elements and 6350 sets of molten salt formulations. This database will be used as a training data set for future machine learning to make accurate predictions through machine learning to get more new multi-component molten salt formulations, and comprehensively promote the research of data-driven methods to assist molten salt design.

2. METHOD

2.1. Database design

In order to satisfy the researchers to fully develop and utilize the data and information of multi-component mixed molten salt in the field of energy storage molten salt, and facilitate the query of molten salt data information, the database is mainly composed of the following parts:

1. Through literature retrieval, the data information of stored molten salt in the published literature was collected up to now;

2. Screen and sort the collected data, and standardize the data to facilitate the management and use of the data;

3. According to the database design and application requirements, build a suitable visual interface to facilitate the query of data information.

The database establishment process is shown in Figure 1.

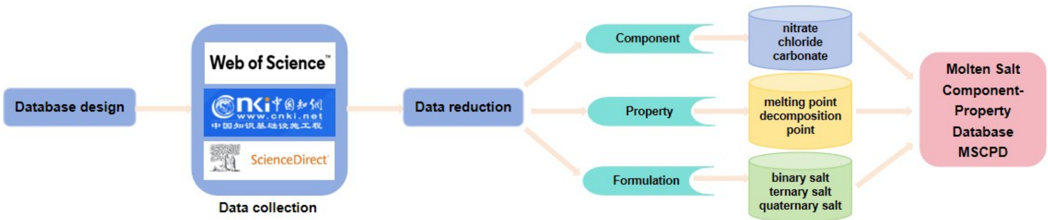

Figure 1: Database establishment process

In order to facilitate the information query and design of molten salt for energy storage, the database of salt storage materials needs to meet the following requirements: (1) including unitary~ quinary mixed molten salt materials; (2) Molten salt melting point, decomposition temperature, initial crystal temperature, density, viscosity, specific heat capacity, thermal conductivity, enthalpy and other properties; (3) provide datasets on the composition and properties of molten salts, especially temperature-related data, for data analysis and machine learning; (4) It can be easily inquired according to the composition and range of properties of molten salt; (5) Unified data units.

2.2. Data collection

At present, the database collects more than 30 years of published literature data from 1987 to 2024, and the experimental data is added when new relevant papers are published, to keep the database updated and revised, including papers from international journals and professional fields. Using Web of Science, CNKI, ScienceDirect and other search platforms, For molten salt, molten salt, nitrate, chloride, carbonate, binary salt, ternary salt, quaternary salt, Na^+, Li^+, K^+, Ca^{2+}, Zn^{2+}, Mg^{2+} and so on are searched as keywords. Through reading a large number of references, the effective data of mixed molten salts with different formulations published in the field of mixed molten salts were collected and sorted out. Finally, 593 literatures meeting the needs of the database were selected, and 5821 data information about the composition and properties of molten salts were extracted from them.

2.3. Data screening

Based on the above data collection basis, the literature content was screened according to the following conditions: (1) the full text must be provided (excluding conference abstracts and preprint abstracts); (2) Each molten salt formulation includes at least one experimentally determined thermophysical and thermochemical properties; (3) A specific and complete formula for mixing molten salts needs to be provided; (4) Experimental conditions for the preparation and testing of mixed molten salts need to be provided. According to the above screening conditions, 593 articles were finally screened out from 35694 literature that met the needs of the database, and 5821 molten salt composition and properties were extracted from them, and the mixed molten salt database MSCPD was established on this basis.

2.4. Data content

The data information of the energy storage mixed molten salt database MSCPD mainly includes the following parts:

1. Composition of mixed molten salt: type of salt;

2. The ratio of mixed molten salt: the mass fraction of different kinds of salt components;

3. Thermal physical properties of mixed molten salt: mainly including melting point, decomposition temperature, specific heat capacity, melting enthalpy, density, viscosity, thermal diffusivity, thermal conductivity, etc.;

4. The DOI number of the reference corresponds to the mixed molten salt.

First, record the molten salt recipe and identify the molten salt type. In order to facilitate query, classification and analysis, the dash character "-" is used to connect the molten salt components and ratios to facilitate the identification of the overall formula, and at the same time, it is conducive to the extraction of single salt species and their ratios for training and analysis. Cations and cations were further classified for mixed molten salts, detailing all cation and anion content contained in the formulation. In addition to the mixing of inorganic salts, in recent years, researchers have begun to improve system performance by adding nanoparticles, including multi-walled carbon nanotubes (Zhao et al., 2024), expanded graphite (Li et al., 2023), and metal oxides (Ahmad et al., 2023; Aljaerani et al., 2022; Anagnostopoulos et al., 2022). In addition to the type of nanoparticles, because the preparation method of mixed molten salt containing nanoparticles is quite different from that of pure inorganic molten salt, the database also marks the size and particle size of nanoparticles for query.

Some component information in MSCPD is shown in Table 1.

Table 1: The component information diagram in MSCPD

No.	1	2	4	5	6	7	8	9
Name	Solar Salt	/	Sandia Mix QA	/	/	/	/	/
Formula	$NaNO_3$-KNO_3	$LiNO_3$-KNO_3-EG	$LiNO_3$-$NaNO_3$-KNO_3-$Ca(NO_3)_2$	$LiNO_3$-$NaNO_3$-KNO_3-$Ca(NO_3)_2$-K_2CO_3	$NaNO_3$-KNO_3-NaCl-KCl	$CaCl_2$-NaCl	Li_2CO_3-Na_2CO_3-K_2CO_3	LiF-NaF-KF
No.	1	2	4	5	6	7	8	9
Composition（wt.%）	0.6-0.4	0.38-0.57-0.05	0.08-0.18-0.56-0.18	0.083-0.083-0.5-0.251-0.083	0.5038-0.3919-0.0533-0.051	0.67-0.33	0.2-0.7-0.1	0.2921-0.1169-0.591
Type	2	2	4	5	4	2	3	3

Li^+	0	0.38	0.08	0.083	0	0	0.4	0.2921
Na^+	0.6	0	0.18	0.083	0.5571	0.33	1.4	0.1169
K^+	0.4	0.57	0.56	0.666	0.4429	0	0.2	0.591
Ca^{2+}	0	0	0.18	0.251	0	0.67	0	0
NO_3^-	1	1	1.18	1.168	0.8957	0	0	0
Cl^-	0	0	0	0	0.1043	1.67	0	0
CO_3^{2-}	0	0	0	0	0	0	1	0
F^-	0	0	0	0	0	0	0	1
EG	0	0.05	0	0	0	0	0	0
Ref.	(Kearney et al., 2003)	(Li et al., 2023)	(Dunn et al., 2012)	(Wu et al., 2017)	(Matias et al., 2022)	(Kenisarin, 2010)	错误!未找到引用源。Wu et al., 2011)	(Matias et al., 2022)

2.5. Experimental verification

Since the experimental data of the same molten salts in different references may be different, this paper adopts the method consistent with the references to verify the thermal physical properties of each mixed molten salt.

1. In order to prevent the weighing error caused by water in the material, the drug is first dried in a drying oven at 150 ° C and stored for 48h;

2. The static mixing and melting method were used to prepare the mixed molten salt. The dried salt was evenly mixed according to the proportion, heated to 300℃ in the Muffle furnace full of protective gas, and stored for a period of time to make the sample evenly mixed, and the heating rate was set at 10min/℃, cooled and dried, and ground to obtain the experimental sample;

3. The melting point refers to that the solid state and liquid state of the mixed molten salt are in equilibrium at this temperature, and the DCS curve is obtained by differential scanning calorimetry (DCS). The melting point and melting enthalpy of the mixed molten salt can be obtained by analyzing the curve, and the temperature of the molten salt can be controlled by continuous heating or cooling, and the heat change absorbed or emitted can be measured. The melting point was determined by observing the change of peak energy;

4. The thermal gravimetric analyzer (TGA) was used to measure the TG curve of the mixed molten salt. The temperature corresponding to the mass loss of 3% or the temperature where the inflection point extension line of the TG curve was located was the decomposition temperature.

After verifying the data in the references through the above experiments and confirming that the experimental data is basically consistent with the literature, the data will be added to the physical property database of molten salt, so that researchers can effectively use the stored molten salt in the future research work.

2.6. Data query

On the database query page, you can query the database in the following ways:

1. Query by selecting the elements, cations and anions contained in the composition of the mixed molten salt to be checked;

2. Query by selecting the properties of the mixed molten salt or the numerical range of the properties data;

Finally, a query result is obtained in the form of a data table, which includes the composition of the data, the ratio of the data, the data of various thermal physical properties and the DOI of the reference of the data source.

The database query visual interface is shown in Figure 2.

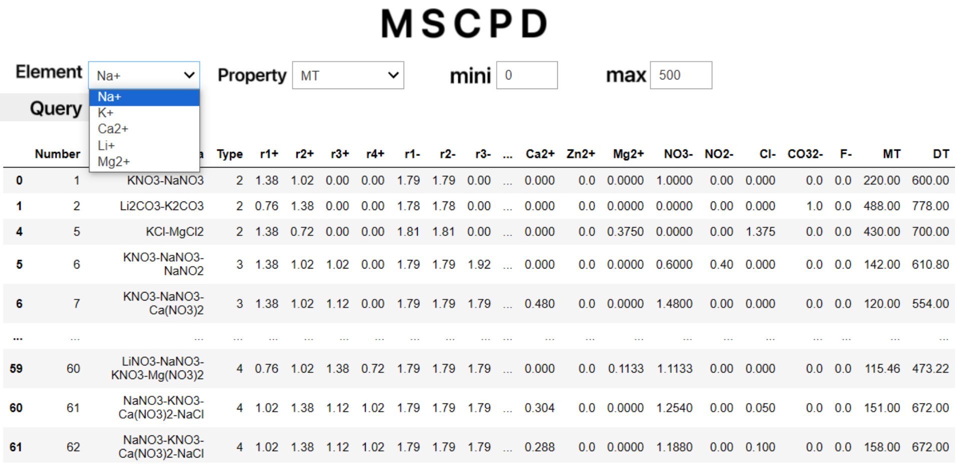

MSCPD

Element Na+ Property MT mini 0 max 500

Query

Na+
K+
Ca2+
Li+
Mg2+

	Number		Type	r1+	r2+	r3+	r4+	r1-	r2-	r3-	...	Ca2+	Zn2+	Mg2+	NO3-	NO2-	Cl-	CO32-	F-	MT	DT
0	1	KNO3-NaNO3	2	1.38	1.02	0.00	0.00	1.79	1.79	0.00	...	0.000	0.0	0.0000	1.0000	0.00	0.000	0.0	0.0	220.00	600.00
1	2	Li2CO3-K2CO3	2	0.76	1.38	0.00	0.00	1.78	1.78	0.00	...	0.000	0.0	0.0000	0.0000	0.00	0.000	1.0	0.0	488.00	778.00
4	5	KCl-MgCl2	2	1.38	0.72	0.00	0.00	1.81	1.81	0.00	...	0.000	0.0	0.3750	0.0000	0.00	1.375	0.0	0.0	430.00	700.00
5	6	KNO3-NaNO3-NaNO2	3	1.38	1.02	1.02	0.00	1.79	1.79	1.92	...	0.000	0.0	0.0000	0.6000	0.40	0.000	0.0	0.0	142.00	610.80
6	7	KNO3-NaNO3-Ca(NO3)2	3	1.38	1.02	1.12	0.00	1.79	1.79	1.79	...	0.480	0.0	0.0000	1.4800	0.00	0.000	0.0	0.0	120.00	554.00
...	...	...	...	...	...	...	...	...	...	...	...	...	...	...	...	...	...	...	...	...	...
59	60	LiNO3-NaNO3-KNO3-Mg(NO3)2	4	0.76	1.02	1.38	0.72	1.79	1.79	1.79	...	0.000	0.0	0.1133	1.1133	0.00	0.000	0.0	0.0	115.46	473.22
60	61	NaNO3-KNO3-Ca(NO3)2-NaCl	4	1.02	1.38	1.12	1.02	1.79	1.79	1.79	...	0.304	0.0	0.0000	1.2540	0.00	0.050	0.0	0.0	151.00	672.00
61	62	NaNO3-KNO3-Ca(NO3)2-NaCl	4	1.02	1.38	1.12	1.02	1.79	1.79	1.79	...	0.288	0.0	0.0000	1.1880	0.00	0.100	0.0	0.0	158.00	672.00

Figure 2: Database query visual interface

3. RESULTS AND DISCUSSION

The stored molten salt thermophysical properties database enables researchers to further utilize the research data of the mixed molten salt and have a more comprehensive understanding of the thermophysical properties of various mixed molten salts. The database contains the hot physical property database of the unitary~quinary mixed molten salts, mainly including the mixed molten salts such as chlorine salts, nitrates, carbonates, etc., which is specially used to analyze the energy storage performance of the molten salts. By searching the published data from 1987~2024, the database finally screened out 593 literatures and obtained 6350 molten salt composition and property data information. As shown in Figure 3, the literature collected were mainly concentrated from 2015~2024, reflecting the latest progress of current research.

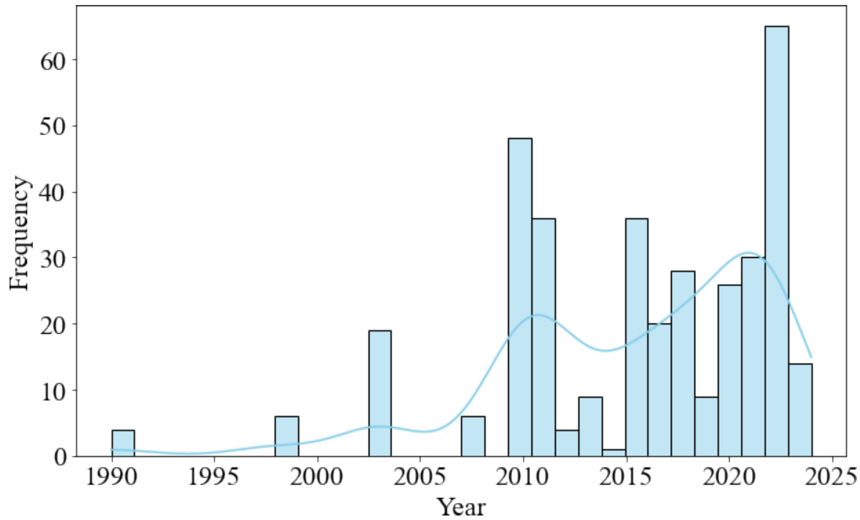

Figure 3: Statistics on the year of publication of the literature in the database and the frequency of occurrence in different years

3.1. Molten salt composition

As shown in Figure 4, the current storage molten salt data information collected in MSCPD contains 31 elements, including metals, non-metals, halogens, transition metals, alkali metals, alkaline-earth metals and metalloids.

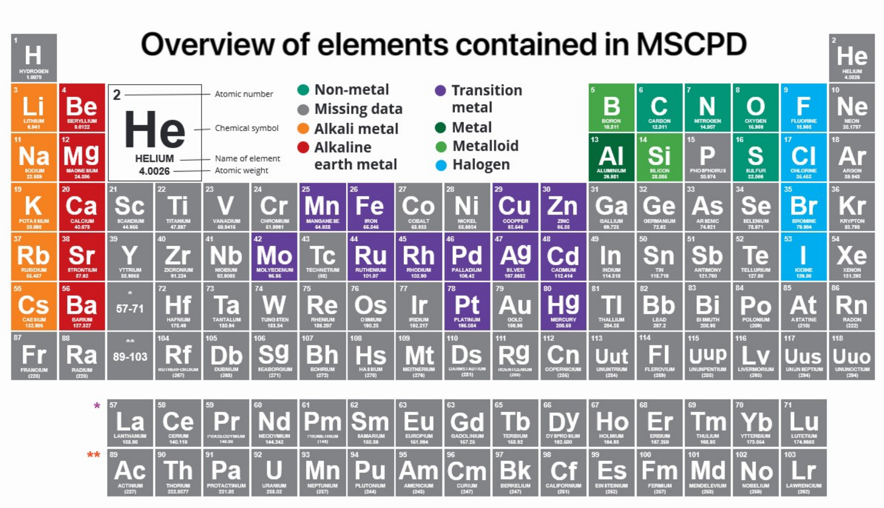

Figure 4: Schematic diagram of the elements contained in the molten salt database MSCPD

The scatter diagram of the distribution relationship between ion content and melting point in the database is drawn with Na^+, K^+, Li^+, Ca^{2+}, NO_3^-, NO_2^-, Cl^- and CO_3^{2-}, which are the most common cations in molten salt, as shown in Fig. 5. The proportion of molten Salt in MSCPD is recorded as the mass percentage of inorganic salt-inorganic salt. Taking Solar Salt as an example, its composition ratio is $NaNO_3$-KNO_3 (60wt.%-40wt.%), and the Na^+ content is recorded as 0.6 and K^+ content as 0.4 in the database. The NO3- content is recorded as 0.6+0.4=1.0 to reflect the proportional relationship between the contents of different ions.

As shown in Figure 5 (a)~(d), the distribution of the four cations is most concentrated when the melting point is below 300℃. From Figure 5 (e), it can be seen that the anions have the largest amount of nitrate data, and the nitrate content is also more evenly distributed, and Figure 5 (f) shows that the nitrite data are mainly concentrated below 0.4, and more are used as supplementary additives. Figure 5 (g) shows that chloride-containing mixed molten salts can be present in molten salts either as pure chloride salts or as supplementary additives. Figure 5 (h) shows that the carbonate content is concentrated at 1.0 and is basically in the form of pure salts, which are rarely used as additives.

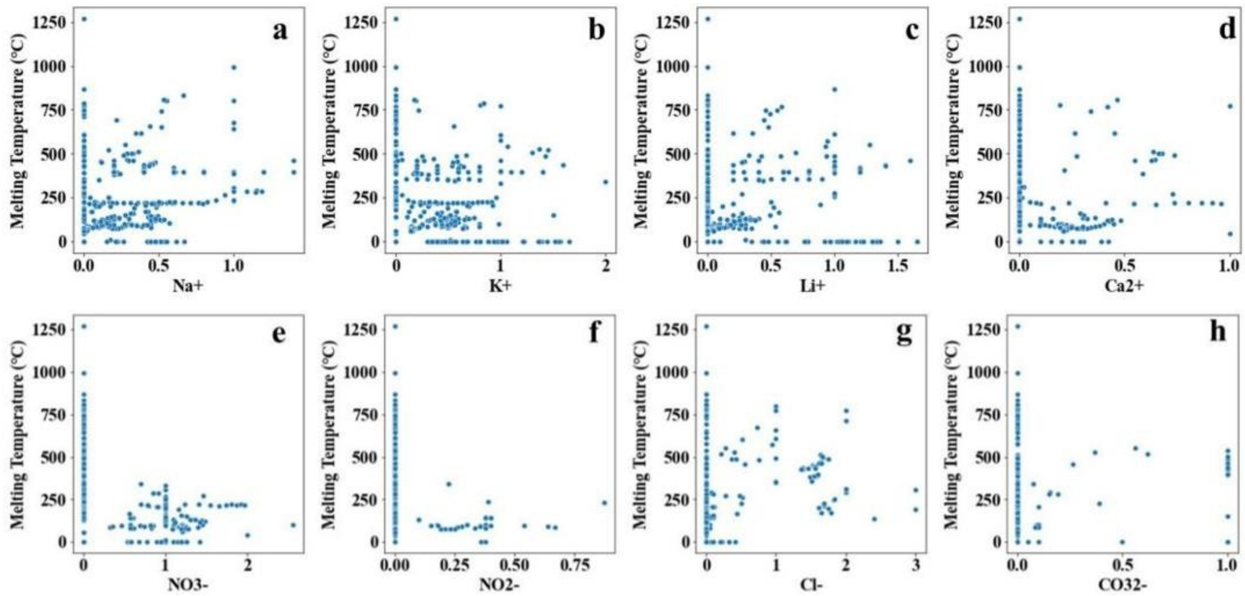

Figure 5: The scatter plots of common energy storage molten salt cations and anions content in the database and their melting point distribution are as follows: (a) Na^+; (b) K^+; (c) Li^+; (d) Ca^{2+}; (e) NO_3^-; (f) NO_2^-; (g) Cl^-; (h) CO_3^{2-}

3.2. Molten salt properties

Taking the melting point and decomposition temperature of molten salt as an example, it can be seen from Fig. 6 that the melting point of stored molten salt collected in the database ranges from 0 to 1000℃, mainly between 100 and 400℃. The decomposition temperature range is between 300 and 2000℃, mainly concentrated between 500 and 700℃.

In molten salt thermal energy storage, the melting point and decomposition temperature are in the concentration area as shown in Figure 6, which has obvious sensible heat storage characteristics compared with nuclear reactors and biomass cracking databases, which meets the design requirements. In addition, the diversity of molten salt composition and properties enables machine learning algorithms to build prediction models with high generalization, which can better promote the research process of molten salt.

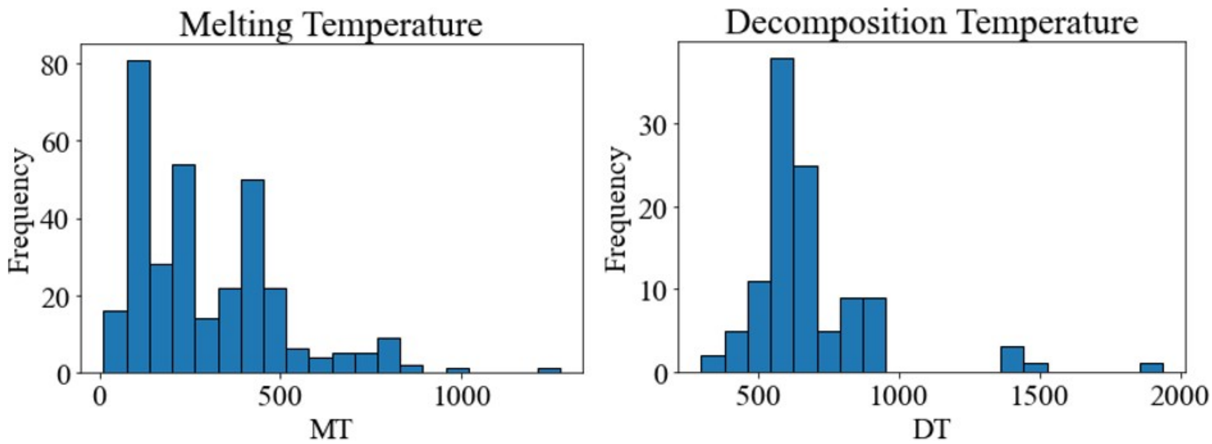

Figure 6: Histogram of frequency distribution of melting points and decomposition temperatures of molten salts in the database

4. CONCLUSION

The database provides a variety of search methods, allowing users to query the database content according to their preferences, providing users with an intuitive search interface to access the thermal physical properties of the mixed molten salt data. The user can determine the data set range of the thermal physical properties of the mixed molten salt by "selecting the elements contained in the molten salt", "selecting the thermal physical properties of the molten salt or the numerical range of the property data". The detailed information obtained from the query is displayed on the result page in the form of a table, including the composition, ratio, nature of the storage molten salt, the data of cations and ions contained in the molten salt, and the DOI of the data source literature.

The following work will strive to improve the browsing, query and other functions of MSCPD, constantly improve the accuracy of the database, effectively promote the performance of the database, provide better database services for researchers, and continue to maintain and update the mixed molten salt thermal physical properties database, making the database a valuable resource in the field of molten salt energy storage. Subsequently, the team will use machine learning methods to mine literature data, expand data in batches, reduce the time and cost of manual data collection, and improve the update efficiency of molten salt database. In addition, by using the currently known molten salt data information as a data set, machine learning method is used to predict the thermo-physical properties of other mixed molten salts, so as to obtain more data information, expand the contents of the molten salt thermo-physical properties database, and finally establish a reliable and user-friendly public database platform for researchers to find data.

5. REFERENCES

Ahmad H A, M. S, A.K. P, et al. (2023) 'Effect of TiO2 nanoparticles on the thermal energy storage of HITEC salt for concentrated solar power applications', Journal of Energy Storage, 72(PC). https://doi.org/10.1016/j.est.2023.108449.

Aljaerani H A, Samykano M, Pandey A K, et al. (2022) 'Thermophysical properties enhancement and characterization of CuO nanoparticles enhanced HITEC molten salt for concentrated solar power applications', International Communications in Heat and Mass Transfer, 132, pp. 105898. https://doi.org/10.1016/j.icheatmasstransfer.2022.105898.

Anagnostopoulos A, Navarro M E, Ding Y. (2022) 'Microstructural improvement of solar salt-based MgO composites through surface tension/wettability modification with SiO2 nanoparticles', Solar Energy Materials and Solar Cells, 238, pp. 111577. https://doi.org/10.1016/j.solmat.2022.111577.

Ángel G, Fernández, Luisa F, Cabeza. (2019) 'Molten salt corrosion mechanisms of nitrate-based thermal energy storage materials for concentrated solar power plants: A review', Solar Energy Materials and Solar Cells, 194, pp. 160-165. https://doi.org/10.1016/j.solmat.2019.02.012.

Carbajales R, Sobrino C, Alvaredo P. (2024) 'Multi-principal element alloys for concentrating solar power based on molten salt', Solar Energy Materials and Solar Cells, 271, pp. 112861-. https://doi.org/10.1016/j.solmat.2024.112861.

Chellapandi P, Hussain K M M, Prathiviraj R. (2017) 'CPSIR-CM: A database for structural properties of proteins identified in cyanobacterial C1 metabolism', Algal Research, 22, pp. 135-139. https://doi.org/10.1016/j.algal.2016.12.005.

Chu Steven, Cui Yi, Liu Nian. (2016) 'The path towards sustainable energy', Nature Materials, 16(1), pp. 16-22. https://doi.org/10.1038/NMAT4834.

C. J A, A. J Y, E. K J, et al. (2022) 'Development of the Molten Salt Thermal Properties Database − Thermochemical (MSTDB−TC), Example Applications, and LiCl−RbCl and UF3−UF4 System Assessments', Journal of Nuclear Materials, (prepublish), pp. 153631-. https://doi.org/10.1016/j.jnucmat.2022.153631.

D. K, U.H, P. N, et al. (2003) ‘Assessment of a Molten Salt Heat Transfer Fluid in a Parabolic Trough Solar Field’, Journal of Solar Energy Engineering, 125(2), pp. 170-176. https://doi.org/10.1115/1.1565087.

Dunn I R, Hearps J P, Wright N M. (2012) ‘Molten-Salt Power Towers: Newly Commercial Concentrating Solar Storage’, Proceedings of the IEEE, 100(2), pp. 504-515. https://doi.org/10.1109/JPROC.2011.2163739.

E. M M, Maria R, Joerg K, et al. (2021) ‘An open-access database of the thermophysical properties of nanouids’, Journal of Molecular Liquids, 333. https://doi.org/10.1016/j.molliq.2020.115140.

González-Roubaud E, Pérez-Osorio D, Prieto C. (2017) ‘Review of commercial thermal energy storage in concentrated solar power plants: Steam vs. molten salts’, Renewable and Sustainable Energy Reviews, 80, pp. 133-148. https://doi.org/10.1016/j.rser.2017.05.084.

Gunasekara S N, Barreneche C, Inés Fernández A, et al. (2021) ‘Thermal Energy Storage Materials (TESMs) - What Does It Take to Make Them Fly?’, Crystals, 11(11), pp. 1276. https://doi.org/10.3390/cryst11111276.

Hu T, Zhang J, Xia J, et al. (2023) ‘A Review on Recent Progress in Preparation of Medium-Temperature Solar-Thermal Nanofluids with Stable Dispersion’, Nanomaterials, 13(8), pp. 1399. https://doi.org/10.3390/nano13081399.

Huiqiang Y, Ryan G, Patrice C, et al. (2023) ‘Development of a molten salt thermal conductivity model and database for advanced energy systems’, Solar Energy, 256, pp. 158-178. https://doi.org/10.1016/j.solener.2023.04.009.

Kenisarin M M. (2010) ‘High-temperature phase change materials for thermal energy storage’, Renewable and Sustainable Energy Reviews, 14(3), pp. 955-970. https://doi.org/10.1016/j.rser.2009.11.011.

Le Z, Jingyao W, Liu C, et al. (2024) ‘Performance Design of High-Temperature Chloride Salts as Thermal Energy Storage Material’, Journal of Thermal Science, 33(2), pp. 479-490. https://doi.org/10.1007/s11630-024-1921-4.

Li J, Zhang Y, Cao X, et al. (2020) ‘Accelerated discovery of high-strength aluminum alloys by machine learning’,

Communications Materials, 1(1), pp. 73-84. https://doi.org/10.1038/s43246-020-00074-2.

Matias C, Daniel F, Rene R, et al. (2022) ‘Improving the working fluid based on a NaNO3-KNO3-NaCl-KCl molten salt mixture for concentrating solar power energy storage’, Solar Energy, 231, pp. 464-472. https://doi.org/10.1016/j.solener.2021.11.058.

Mitin M, Muhtasim M M, Talat F, et al. (2023) ‘Research Advancement and Potential Prospects of Thermal Energy Storage in Concentrated Solar Power Application’, International Journal of Thermofluids, 20. https://doi.org/10.1016/j.ijft.2023.100431.

Nunes V, Queirós C, Lourenço M, et al. (2016) ‘Molten salts as engineering fluids – A review: Part I. Molten alkali nitrates’, Applied Energy, 183, pp. 603-611. https://doi.org/10.1016/j.apenergy.2016.09.003.

Orti F, Fernández L M, Marin oBuslje C. (2023) ‘MLOsMetaDB, a meta-database to centralize the information on liquid–liquid phase separation proteins and membraneless organelles’, Protein Science, 33(1), pp. e4858-e4858. https://doi.org/10.1002/pro.4858.

Patange R S, Sutar R P, Yadav D G. (2024) ‘New frontiers in thermal energy storage: An experimental analysis of thermophysical properties and thermal stability of a novel ternary chloride molten salt’, Solar Energy Materials and Solar Cells, 271, pp. 112866-. https://doi.org/10.1016/j.solmat.2024.112866.

Peter F. (2015) ‘Energy storage: Power revolution’, Nature, 526(7575), pp. S102-4. https://doi.org/10.1038/526S102a.

Qing W, Chunlei W, Xinmin W, et al. (2023) ‘A review of eutectic salts as phase change energy storage materials in the context of concentrated solar power’, International Journal of Heat and Mass Transfer, 205. https://doi.org/10.1016/j.ijheatmasstransfer.2023.123904.

Shenxiang Z, Xian W, Xue C, et al. (2024) ‘Solar-driven membrane separation for direct lithium extraction from artificial salt-lake brine’, Nature Communications, 15(1), pp. 238-238. https://doi.org/10.1038/s41467-023-44625-w.

Steven C, Arun M. (2012) ‘Opportunities and challenges for a sustainable energy future’, Nature, 488(7411), pp. 294-303. https://doi.org/10.1038/nature11475.

Sun S, Wang K, Hong Z, et al. (2024) ‘Electrolyte Design for Low-Temperature Li-Metal Batteries: Challenges and Prospects’, Nano-Micro Letters, 16(02), pp. 371-388. https://doi

#309: Experimental and numerical study on heat transfer characteristics of supercritical CO2 in a vertical tube

Qianqian REN[1], Xiaojing ZHU[2], Qinggang QIU[3]

[1] Dalian University of Technology, 2 Ling Gong Rd. Ganjingzi District, Dalian 116024, China, 18812670581@163.com
[2] Dalian University of Technology, 2 Ling Gong Rd. Ganjingzi District, Dalian 116024, China, zhuxiaojing@dlut.edu.cn
[3] Dalian University of Technology, 2 Ling Gong Rd. Ganjingzi District, Dalian 116024, China, qqgang@dlut.edu.cn

Abstract: In order to explore the intrinsic mechanism of heat transfer deterioration (HTD) in supercritical fluids, the flow and heat transfer characteristics of supercritical CO_2 in a uniformly heated vertical circular tube were investigated by experiments and numerical simulations. The inner diameter of the circular tube was 14.5 mm, and the range of experimental parameters covered a pressure of 7.5–9.5 MPa, a mass flux of 320–940 kg/(m^2s), and a heat flux of 17–160 kW/m^2. The effects of heat flux, mass flux, and inlet temperature on the heat transfer characteristics of supercritical CO_2 were investigated. Results reveal that an increase in heat flux causes an intensification of HTD and a forward shift of the peak wall temperature towards the inlet. The increase in mass flux can weaken the HTD and enhance the overall heat transfer coefficient, but it may result in heightened localized HTD. As the inlet temperature increases, the overall heat transfer coefficient improves. The first wall temperature peak shows an increasing and then decreasing trend, while the second wall temperature peak gradually decreases with the increase in inlet temperature until it disappears completely. Numerical simulation studies were carried out using a modified variable Pr_t turbulence model to analyze the cause of HTDin supercritical CO_2. The deterioration in heat transfer was found to be closely related to the violent thermophysical changes of supercritical fluids. The drastic physical property variation results in the buoyancy force effect, which alters fluid shear stress distribution and turbulent kinetic energy generation and thus leads to HTD.

Keywords: Supercritical Pressure CO_2, Heat Transfer Deterioration, Buoyancy

1. INTRODUCTION

Transforming the traditional energy structure through advanced energy utilization technologies to achieve clean and efficient energy use has now become a new global trend in addressing climate and environmental changes. The supercritical CO_2 power cycle, as an advanced energy utilization technology, uses CO_2 as the working fluid at temperatures and pressure above its critical point (7.38 MPa, 31.10 °C). This cycle offers several advantages, including compact equipment, high thermodynamic efficiency, simple system configuration, and broad adaptability to various heat sources. Consequently, it has garnered significant attention in numerous fields, such as nuclear energy conversion, solar thermal power generation, geothermal energy systems, and fuel cells (Liao et al., 2019).

Different from subcritical fluids, supercritical fluids exhibit dramatic changes in thermosphysical properties in the near-critical region, as illustrated in Figure 1. Under supercritical pressure (7.5 MPa), the density and dynamic viscosity of CO_2 significantly decrease with increasing temperature, while the specific heat at constant pressure and thermal conductivity initially increase and then decrease, exhibiting a peak. These unique thermophysical property variations of supercritical CO_2 result in complex macroscopic heat transfer phenomena under specific flow conditions: heat transfer enhancement (HTE) and heat transfer deterioration (HTD).

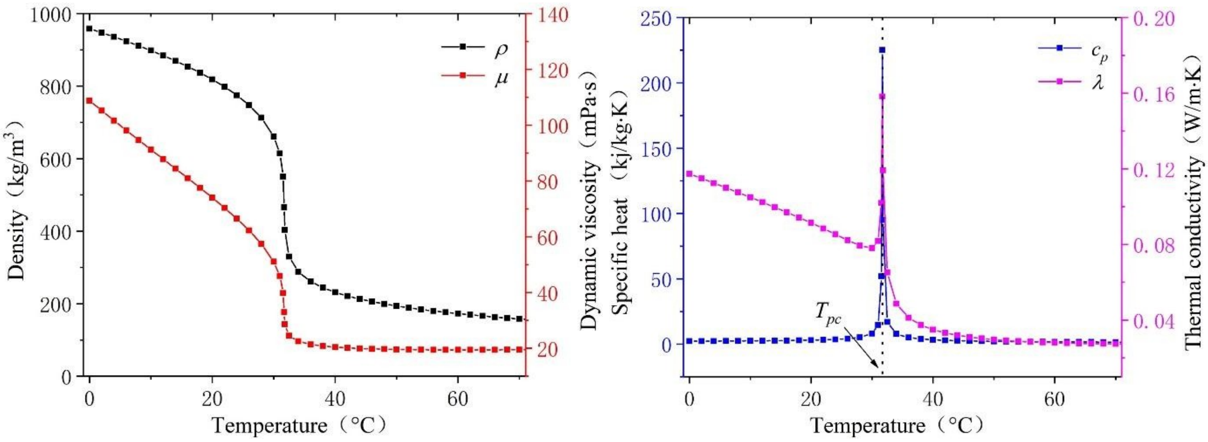

Figure 1: Physical properties of CO_2 at 7.5 MPa

The specific manifestation of the HTD in supercritical CO_2 is characterized by a sharp decrease in the heat transfer coefficient or a rapid rise in wall temperature. Compared to HTE, the negative impacts of HTD on practical engineering applications have garnered increasing attention. Jackson et al. [2-3] conducted extensive research on supercritical fluids and demonstrated that HTD results from the combined effects of buoyancy from radial density gradients and thermal acceleration from axial density gradients. Kim et al. [4-5] investigated the heat transfer characteristics of the vertically upward flow of supercritical CO_2 in heated tubes. They concluded that buoyancy and thermal acceleration effects influence heat transfer by altering the distribution of shear stress. Zhang et al. [6] conducted an experimental study to investigate the difference in the heat transfer characteristics of supercritical CO_2 under different mass flux conditions and the reason for it. Cheng et al. [7] numerically calculated the two wall temperature peaks during HTD in supercritical fluids using the SST k-ω model and analyzed the different reasons for them. Bazargan et al. [8] investigated the important role of the buffer layer in the heat transfer of supercritical fluid by means of numerical simulation, which provides a theoretical basis for understanding the mechanism of supercritical heat transfer. Although research on supercritical fluids is diverse, the causes of HTD in supercritical fluids are complex. The effects of thermophysical property changes, buoyancy forces, and thermalacceleration vary under different conditions. A unified and universally recognized theoretical explanation has yet to be established, highlighting the need for further in-depth research in this area.

The convective heat transfer characteristics of supercritical CO_2 in a vertically heated tube were studied experimentally and numerically around the pseudocritical point. By comparing the effects of heat flux, mass flux, and inlet temperatures on the heat transfer characteristics of supercritical CO_2, this study further analyzed the mechanism of HTD. The results can provide theoretical support for the industrial applications of supercritical CO_2 and its feasibility in reactor applications.

2. EXPERIMENTAL AND NUMERICAL METHODS

This section provides an overview of the supercritical CO_2 convective heat transfer experimental system and numerical method.

2.1. Experimental system

The supercritical CO_2 convective heat transfer experimental test loop is shown in Figure 2. The experiment uses a triple-plunger high-pressure pump to complete the pressurization and internal circulation. A pulsation damper is set at the outlet of the pump to minimize the fluctuation of the flow rate and pressure in the system. After being pressurized by the pump, the CO_2 passes through a turbine flow meter and an electric heater for preheating before entering the test section. Data collection is performed in the test section, followed by cooling in a shell-and-tube heat exchanger. The CO_2 then flows through a backpressure valve into a storage tank. Finally, it is pressurized again by the high-pressure pump for the next cycle.

The test section is a vertical circular tube with an outside diameter of 16 mm, an inner diameter of 14.5 mm, and a total length of 2600 mm. It is constructed of 304 stainless steels. A copper pole plate clamp is used to carry out the heating, and a heating length of 2200 mm (with an 80 mm copper pole plate) is used. Figure 3 illustrates the test section's layout and the arrangement of thermocouples on the tube wall.

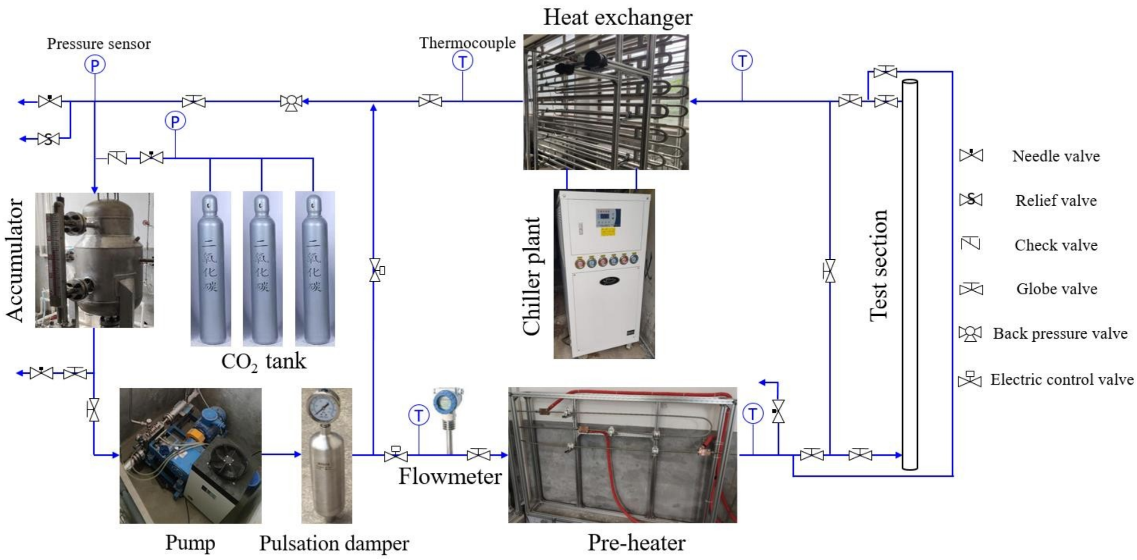

Figure 2: The schematic diagram of the designed experimental loop

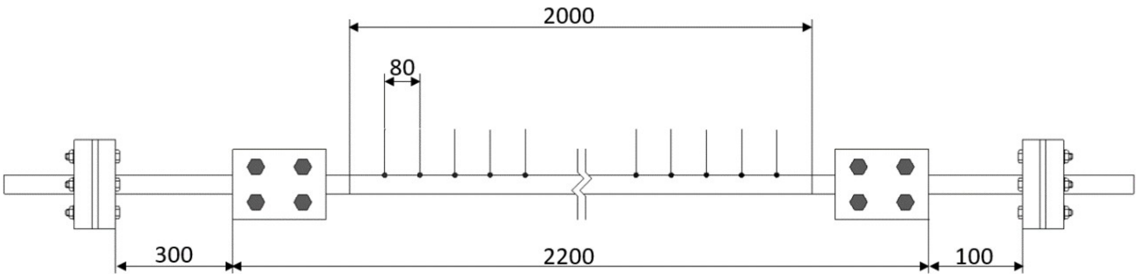

Figure 3: The schematic diagram of tube test section and arrangements of thermal couples

2.2. Numerical Methods

The geometric model used for the numerical simulation study is the same as the structure of the test section. The flow of supercritical CO2 in a uniformly heated circular tube is assumed to be steady-state and two-dimensional axisymmetric. The governing equations are as follows:

Equation 14: Continuity equation.

$$\frac{\partial(\rho u)}{\partial x}+\frac{\partial(\rho v)}{\partial y}=0$$

Equation 2: Momentum equation.

$$\frac{\partial(\rho uu)}{\partial x}+\frac{\partial(\rho uv)}{\partial y}=\frac{\partial}{\partial x}\left(\mu_{eff}\frac{\partial u}{\partial x}\right)+\frac{\partial}{\partial y}\left(\mu_{eff}\frac{\partial u}{\partial y}\right)-\frac{\partial p}{\partial x}+\rho g$$

$$\frac{\partial(\rho vu)}{\partial x}+\frac{\partial(\rho vv)}{\partial y}=\frac{\partial}{\partial x}\left(\mu_{eff}\frac{\partial v}{\partial x}\right)+\frac{\partial}{\partial y}\left(\mu_{eff}\frac{\partial v}{\partial y}\right)-\frac{\partial p}{\partial y}$$

Equation 3: Energy equation.

$$\frac{\partial(\rho uh)}{\partial x}+\frac{\partial(\rho vh)}{\partial y}=\frac{\partial}{\partial x}\left(\left(\frac{\mu}{Pr}+\frac{\mu_t}{Pr_t}\right)\frac{\partial h}{\partial x}\right)+\frac{\partial}{\partial y}\left(\left(\frac{\mu}{Pr}+\frac{\mu_t}{Pr_t}\right)\frac{\partial h}{\partial y}\right)$$

Where:

- u = velocity component in x direction
- v = velocity component in y direction
- ρ = density (kg/m^3)
- h = enthalpy (J/kg)
- μ_{eff} = effective viscosity (kg/ms)
- *Pr = molecular Prandtl number*
- *Pr_t = turbulent Prandtl number*

The expression for the turbulent Prandtl number is presented below:

Equation 4: Turbulent Prandtl number.

$$Pr_t=\frac{\mu_t/\rho}{\lambda_t/\rho c_p}=\frac{\mu_t c_p}{\lambda_t}$$

Where:

- λ_t = Turbulent thermal conductivity (W/mK)

Regarding the choice of turbulence models, among the two-equation eddy viscosity turbulence models, the $k-\varepsilon$ model performs well in solving fully developed turbulent flows away from walls, while the $k-\omega$ model accurately captures the flow parameters of the near-wall boundary layer. The SST $k-\omega$ model combines the advantages of both and has been widely used in the numerical simulation of heat transfer in supercritical fluids due to its excellent performance. Therefore, this study employs the SST $k-\omega$ model to solve the turbulent flow of supercritical CO2 in vertical tubes. The equations for turbulent kinetic energy k and specific dissipation rate ω are expressed as follows:

Equation 5: Turbulent kinetic energy.

$$\frac{\partial(\rho ku)}{\partial x}+\frac{\partial(k\rho v)}{\partial y}=\frac{\partial}{\partial x}\left(\Gamma_k\frac{\partial k}{\partial x}\right)+\frac{\partial}{\partial y}\left(\Gamma_k\frac{\partial k}{\partial y}\right)+G_k-Y_k$$

Equation 6: Specific dissipation rate.

$$\frac{\partial(\rho\omega u)}{\partial x}+\frac{\partial(\rho\omega v)}{\partial y}=\frac{\partial}{\partial x}\left(\Gamma_\omega\frac{\partial \omega}{\partial x}\right)+\frac{\partial}{\partial y}\left(\Gamma_\omega\frac{\partial \omega}{\partial y}\right)+G_\omega-Y_\omega+D_\omega$$

Where:

- G_k = turbulent kinetic energy generation term
- G_ω = specific dissipation rate generation term
- Γ_k= effective diffusion of turbulent kinetic energy
- Γ_ω = effective diffusion of specific dissipation rate
- Y_k= turbulent kinetic energy dissipation due to turbulence
- Y_ω = specific dissipation rate dissipation due to turbulence
- D_ω = *cross-diffusion term*

In the original SST $k-\omega$ model, the turbulent Prandtl number is a constant (Prt = 0.85), which is relatively insensitive to capturing the wall temperature rise associated with HTD in supercritical fluids. To address this issue, the modified model for the turbulent Prandtl number proposed by Du et al. [9] is adopted:

Equation 7: A considerate turbulent Prandtl number modification.

$$Pr_t=\begin{cases}1.0 \ ; \ \mu_t/\mu\in(0,0.1\alpha_1)\\ 0.85+\dfrac{Pr}{(f_d/f_p)\ A} \ ; \ \mu_t/\mu\in(0.1\alpha_1,10\alpha_2)\\ 0.85 \ ; \ \mu_t/\mu\in(10\alpha_2,+\infty)\end{cases}$$

Where:

- A = correction factor introduced to better fit the experimental results, with A = 1.28.

Equation 8: Correction factor for tube diameter.

$$f_d=6.2(d-4)^{0.24}$$

Equation 9: Correction factor for system pressure.

$$f_p=\left[1+0.019(\frac{P}{P_{cr}})^{29}\right]$$

Equation 10: Correction factors in the range of μ_t/μ for the tube diameter.

$$\alpha_1=0.24d-0.7$$

$$\alpha_2 = 0.05d + 0.07$$

ANSYS ICEM is used to generate the mesh for the computational domain, employing structured quadrilateral mesh throughout. The axial direction is divided using a uniform mesh with a grid size of 2 mm. To enhance computational accuracy, the mesh near the wall is refined. The radial mesh comprised 80 divisions, with the first layer of the mesh being 0.0002 mm from the wall and the mesh size growing at a rate of 1.08 along the radial direction. The total number of mesh elements in the computational domain was 110,600, with near-wall y^+ values less than 0.1.

The governing equations were discretized and solved using ANSYS FLUENT 18.0. The pressure-velocity coupling was solved with the SIMPLE method, and the momentum equation was discretized using a second-order upwind scheme. The thermophysical properties of supercritical CO_2 (density, dynamic viscosity, specific heat at constant pressure, and thermal conductivity) were taken to be functions of temperature and independent of system pressure due to the small axial pressure drop in comparison to the inlet pressure. Piecewise linear interpolation was used to enter these properties into FLUENT according to the National Institute of Standards and Technology (NIST) property demands. The convergence criterion for the residuals was set at 10^{-6}, and the computation was considered converged when the wall temperature no longer changed.

2.3. Mesh independence verification

To ensure the reliability of the computational results, a mesh independence verification is performed. Seven sets of meshes are selected, comparing the effects of axial grid height (Meshes 1, 2, 3), radial grid number (Meshes 4, 2, 5), and the height of the first near-wall grid layer (Meshes 6, 2, 7). The details of the grid sizes are shown in Table 1. The comparison of the computational results is shown in Figure 4. As seen in Figure 4(a), the results for the axial grid heights of 1 mm (Mesh 1) and 2 mm (Mesh 2) are almost identical. Figure 4(b) shows that the results for radial grid numbers of 80 (Mesh 2) and 120 (Mesh 4) are nearly the same. Figure 4(c) indicates that the results for the first near-wall grid heights of 0.0001 mm (Mesh 6) and 0.0002 mm (Mesh 2) almost overlap. Therefore, Mesh 2 was ultimately selected for the numerical simulation study.

Table 1: Test of Mesh Independence

Mesh	Axial grid height (mm)	Number of radial grids	Height of the first grid layer near the wall (mm)	Total number of grids
1	1	80	0.0002	221200
2	2	80	0.0002	110600
3	3	80	0.0002	73700
4	2	120	0.0002	54600
5	2	40	0.0002	166600
6	2	80	0.0001	110600
7	2	80	0.0003	110600

To verify the accuracy and reliability of the numerical model, the simulation results were compared with experimental results, as shown in Figure 5. In the original SST model with $Pr_t = 0.85$, it can be observed that the model is unable to capture the peak wall temperature at which supercritical CO_2 HTD occurs. The models incorporating the Prt modification by Du et al. [9] and Tang et al. [10] qualitatively capture the two wall temperature peaks of HTD. However, Du's numerical results tend to over-predict the experimental outcomes, while Tang's results tend to "under-predict," resulting in relatively larger deviations from the experimental data. Therefore, a correction factor A was added based on the Du et al. model to better fit the experimental results. The modified model successfully reproduces the experimental results more accurately.

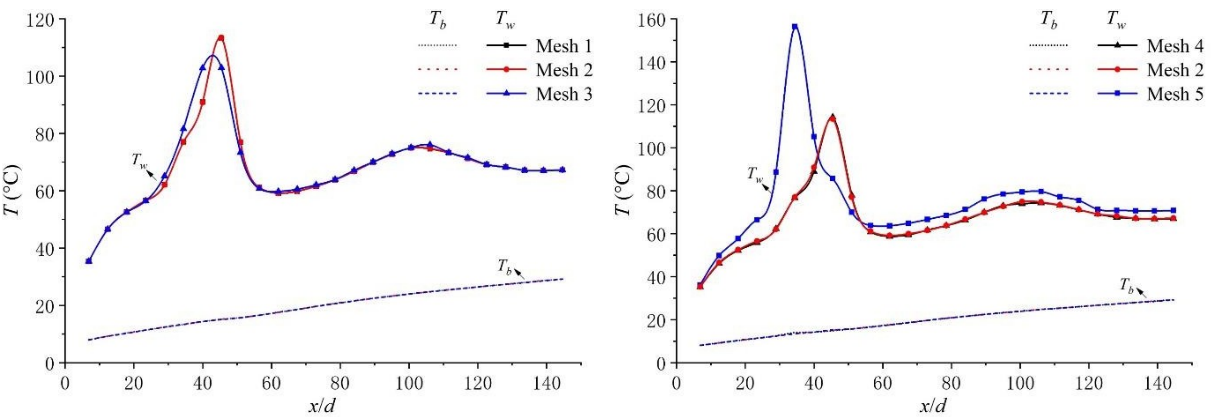

(a) Comparison of axial mesh heights

(b) Comparison of number of radial grids

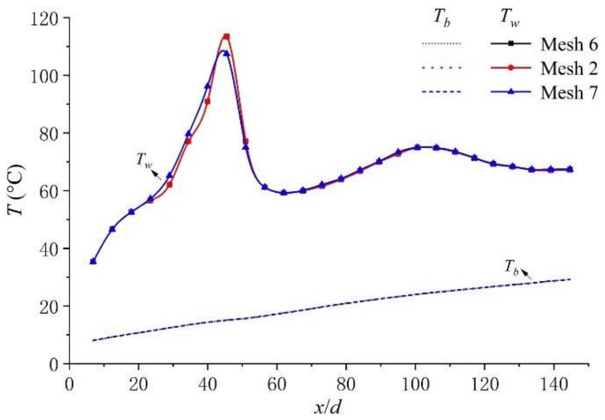

(c) Comparison of the height of near-wall first layer grids

Figure 4: The schematic diagram of tube test section and arrangements of thermal couples

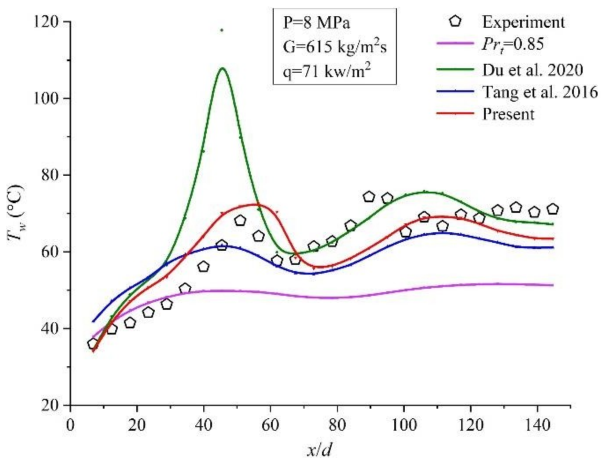

(a) Case 1

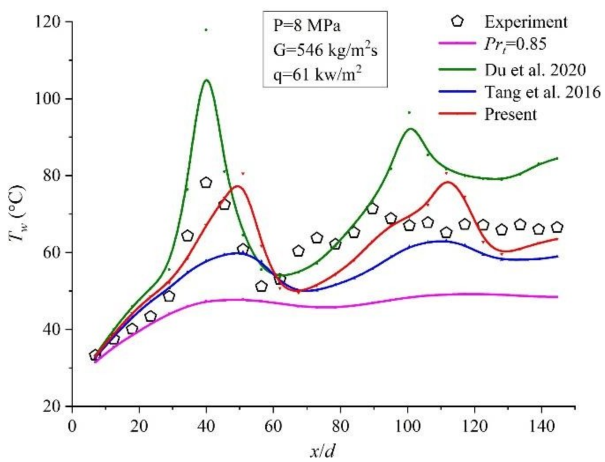

(b) Case 2

Figure 5: Validations of the numerical model

3. RESULTS AND DISCUSSIONS

3.1. Effect of heat flux

To study the effect of heat flux on the heat transfer characteristics of supercritical CO_2, numerical simulations are conducted for two conditions: one with a mass flux of 615 kg/m²s and heat flux ranging from 62.43 to 79.95 kW/m², and the other with a mass flux of 330 kg/m²s and heat flux ranging from 32.33 to 65.33 kW/m².

Figure 6 shows the axial distribution of wall temperature and heat transfer coefficient for different heat fluxes at a relatively large mass flux of 615 kg/m²s. At a relatively low heat flux density of q = 62.43 kW/m², the wall temperature shows a gradual and steady increase along the tube. When the heat flux density increases to 70.61 kW/m², the wall temperature rises and exhibits two peaks. Correspondingly, the heat transfer coefficient shows two valleys, indicating the occurrence of local HTD. As the heat flux further increases, the two wall temperature peaks rise, and the HTD intensifies. The first wall temperature peak is narrower and higher compared to the second peak, with steeper rises and falls. The peaks of wall temperature shift towards the inlet as the heat flux increases.

Figure 7 shows the distribution of wall temperature and heat transfer coefficient for a mass flux of 330 kg/m²s with a heat flux ranging from 32.33 to 65.33 kW/m². Compared to the higher mass flux condition (G = 615 kg/m²s), the temperature and heat transfer coefficient distribution curves for the lower mass flux condition exhibit some differences. Unlike Figure 6(a), the first peak in wall temperature shows a relatively milder drop-off and is positioned closer to the inlet. The second peak in the wall temperature is relatively higher, and there are instances where the second peak surpasses the first peak (q = 32.33 kW/m²). Comparing the temperature distribution profiles for a heat flux of 79.95 kW/m² in Figure 6(a) and 42.93 kW/m² in Figure 7(b), both having the same q/G ratio (0.13), shows that the wall temperature peak is significantly higher at the higher mass flux. This results in more substantial negative impacts on practical applications.

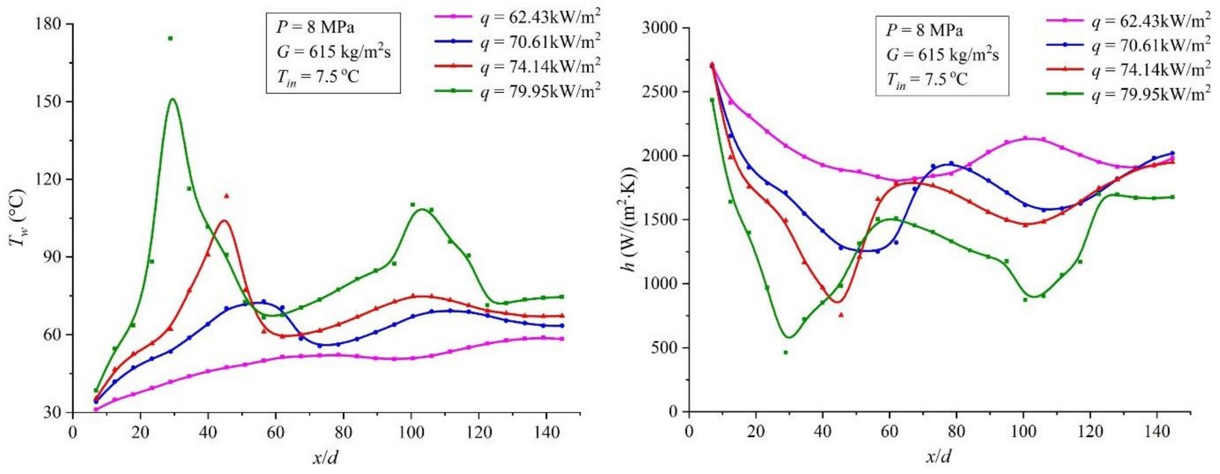

(a) Wall temperature *(b) heat transfer coefficient*

Figure 6: Effect of heat flux on wall temperature and heat transfer coefficient

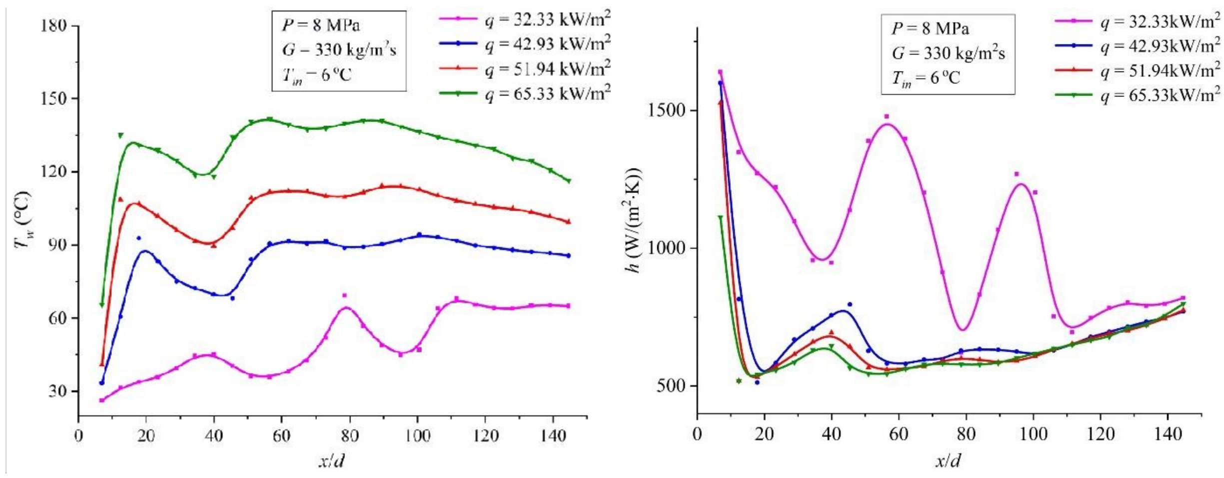

(a) Wall temperature *(b) heat transfer coefficient*

Figure 7: Effect of heat flux on wall temperature and heat transfer coefficient

3.2. Effect of mass flux

Numerical simulations are conducted for a heat flux of 61 kW/m² and mass fluxes ranging from 459 to 612 kg/m²s to study the effect of mass flux on the heat transfer characteristics of supercritical CO_2. From Figure 8(a), as the mass flux increases, the wall temperature gradually decreases. At a heat flux of 459 kg/m²s, the wall temperature exhibits two distinct peaks.

When the mass flux increases to 546 kg/m²s, the wall temperature and its peaks decrease, and the peaks shift towards the outlet. When the mass flux further increases to 612 kg/m²s, the peaks disappear, and the wall temperature linearly increases along the pipe. Figure 8(b) illustrates the axial distribution of the heat transfer coefficient, which increases with increasing mass flux. It is noteworthy that at a mass flux of 546 kg/m²s, the wall temperature exhibits two peaks, corresponding to two valleys in the heat transfer coefficient distribution. While increasing the mass flux enhances the overall heat transfer coefficient, it may exacerbate localized HTD.

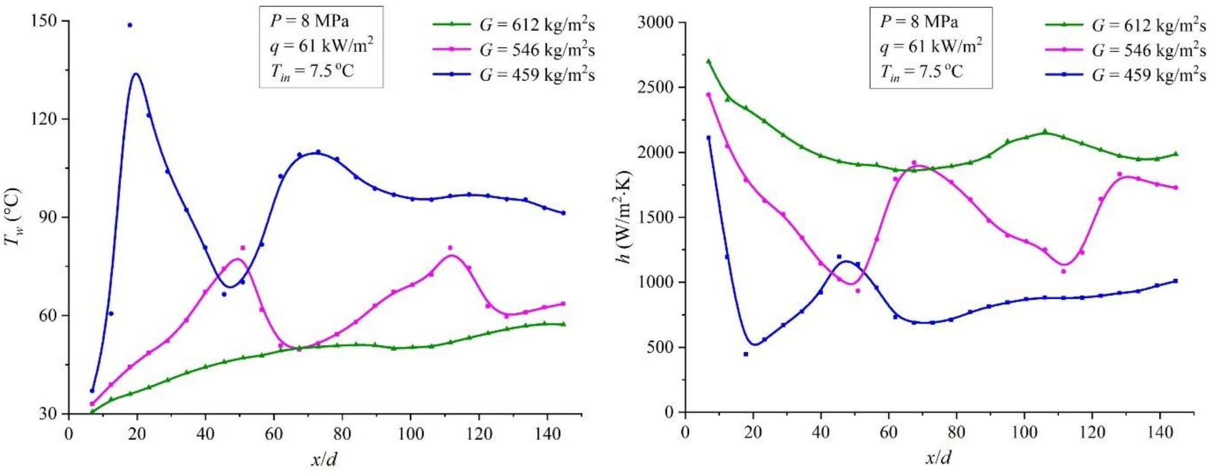

(a) Wall temperature *(b) heat transfer coefficient*

Figure 8: Effect of mass flux on wall temperature and heat transfer coefficient

3.3. Effect of inlet temperature

To investigate the effect of inlet temperature on the heat transfer characteristics of supercritical CO_2, simulations are conducted for a pressure of 8 MPa, a mass flux of 615 kg/m²s, a heat flux of 74.14 kW/m², and inlet temperatures ranging from 7.5°C to 30°C. The temperature distribution at different inlet temperatures is depicted in Figure 9 (a). As the inlet temperature increases, the peaks in the wall temperature shift towards the inlet. The first peak shows a trend of initially increasing and then decreasing, while the second peak gradually decreases and eventually disappears with an increasing inlet temperature. Figure 9 (b) shows the axial distribution of the heat transfer coefficient. As the inlet temperature increases, the overall heat transfer coefficient increases. This can be attributed to a sharp decrease in the density of the fluid near the wall, which generates upward buoyancy forces, weakening the fluid shear stress and thereby reducing turbulent production, leading to HTD. As the inlet temperature increases, the temperature difference between the bulk flow and the near-wall region decreases, along with the radial density difference, thereby weakening the buoyancy forces and alleviating HTD.

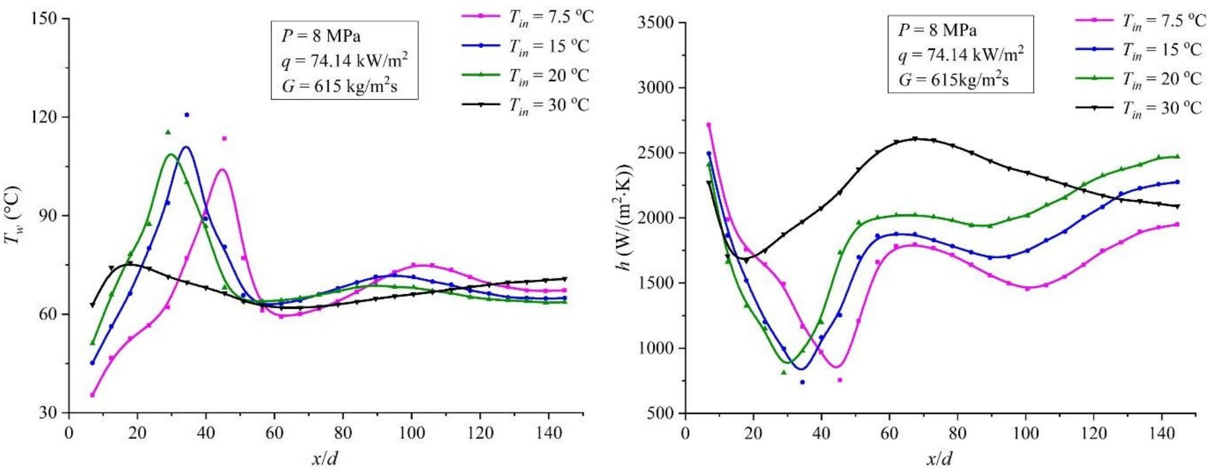

(a) Wall temperature *(b) heat transfer coefficient*

Figure 9: Effect of inlet temperature on wall temperature and heat transfer coefficient

3.4. Supercritical CO_2 heat transfer deterioration

To further analyze the HTD mechanism of supercritical CO_2, a detailed analysis is conducted for the condition with a mass flux of 615 kg/m²s and a heat flux of 74.14 kW/m². Figure 10 shows the wall temperature distribution for this condition, with annotations at five axial positions: *x*/*d* = 25, 35, 45, 52, and 62.

Figure 11 shows the radial distribution of density, velocity, and turbulent kinetic energy at five axial positions. As seen in the figure, the velocity distribution curve at *x*/*d* = 25 is similar to that of subcritical fluid during normal heat transfer. At *x*/*d* = 35, with increasing temperature, the near-wall fluid density sharply decreases, creating strong buoyancy forces that increase the near-wall fluid velocity, reduce the velocity gradient, decrease fluid shear stress, and lower turbulent kinetic energy. The reduction in turbulent kinetic energy inhibits turbulent heat diffusion, leading to a sharp rise in wall temperature. At *x*/*d* = 45, the wall temperature reaches a peak, and the near-wall fluid density hits its lowest point. The near-wall fluid velocity continues to increase and starts to exceed the mainstream velocity, forming an "M" shaped velocity curve as shown. At *x*/*d* = 52 and *x*/*d* = 62, the range of increased near-wall velocity gradually expands, the velocity gradient increases, fluid shear stress increases in the opposite direction, turbulent kinetic energy gradually recovers, turbulent heat diffusion enhances, the wall temperature decreases, and heat transfer recovers.

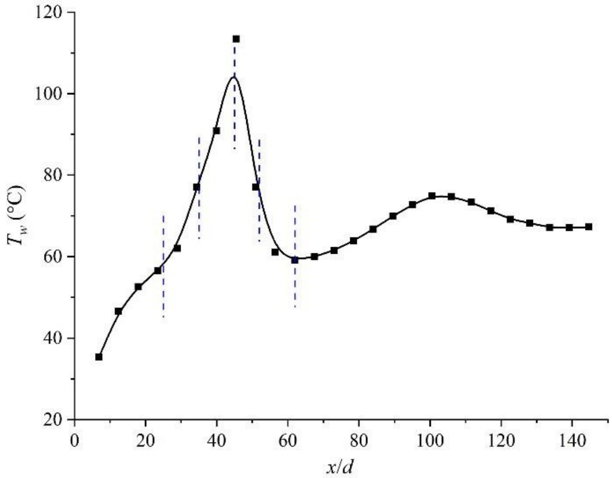

Figure 10: The distribution of wall temperature

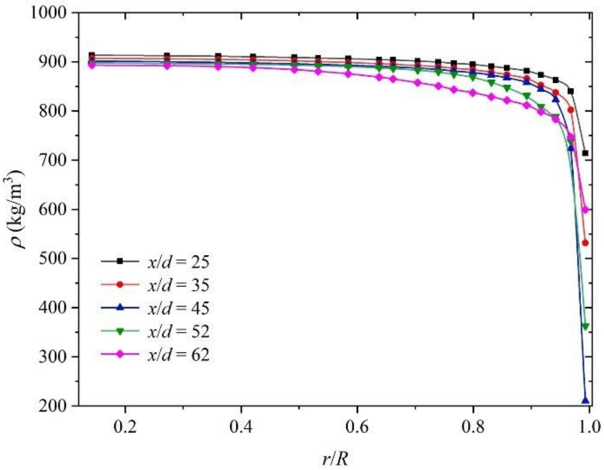

(a) Density

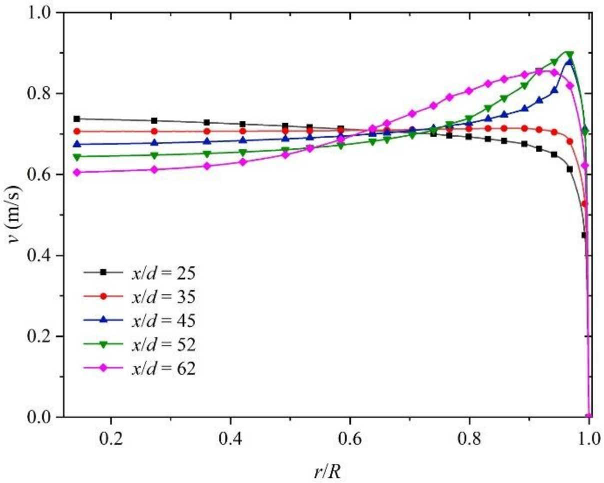

(b) Velocity

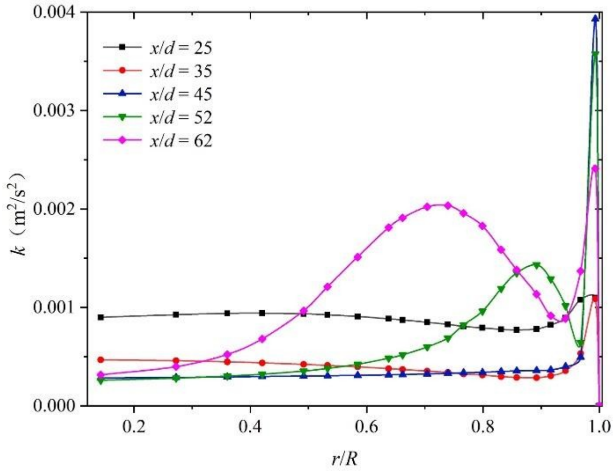

(c) Turbulent kinetic energy

Figure 11: The radial distribution of fluid density, velocity, and turbulent kinetic energy at different axial positions

4. CONCLUSION

In this study, a combination of numerical simulation and experimental methods was used to investigate the flow and heat transfer characteristics of supercritical CO_2 in a vertical circular tube. The main conclusions are as follows:

- Increasing the heat flux exacerbates HTD, causing the wall temperature peak to shift towards the inlet. Under the same *q*/*G* conditions, higher mass flux results in higher wall temperature peaks, potentially leading to more significant negative impacts in practical engineering applications.
- Increasing the mass flux mitigates HTD and enhances the overall heat transfer coefficient. However, it may also intensify localized HTD.
- As the inlet temperature increases, the first wall temperature peak initially rises and then decreases, while the second wall temperature peak gradually decreases and eventually disappears.
- The primary cause of heat transfer deterioration in supercritical CO_2 is the significant change in fluid properties, which induces buoyancy forces, alters the distribution of fluid shear stress, and the generation of turbulent kinetic energy.

5. REFERENCES

Bazargan M, Mohseni M, 2009. The significance of the buffer zone of boundary layer on convective heat transferto a vertical turbulent flow of a supercritical fluid. The Journal of Supercritical Fluids, 51(2):221-229.

Cheng H, Zhao J Y, Rowinski M K, 2017. Study on two wall temperature peaks of supercritical fluid mixedconvective heat transfer in circular tubes. International Journal of Heat and Mass Transfer, 113:257-267.

Dong E K, Kim M H, 2010. Experimental study of the effects of flow acceleration and buoyancy on heat transferin a supercritical fluid flow in a circular tube. Nuclear Engineering and Design, 240(10):3336-3349.

Dong E K, Kim M H, 2011. Two layer heat transfer model for supercritical fluid flow in a vertical tube. Journal ofSupercritical Fluids, 58(1):15-25.

Du X, Lv Z H, Yu X, et al., 2020. Heat transfer of supercritical CO2 in vertical round tube: A considerate turbulentPrandtl number modification. Energy, 192.

Jackson J D, 2013. Fluid flow and convective heat transfer to fluids at supercritical pressure. Nuclear Engineeringand Design, 264:24-40.

Jackson J D, 2017. Models of heat transfer to fluids at supercritical pressure with influences of buoyancy andacceleration. Applied Thermal Engineering, 124:1481-1491.

Liao G L, Liu L J, E J Q, et al., 2019. Effects of technical progress on performance and application of supercriticalcarbon dioxide power cycle: A review. Energy Conversion and Management, 199.

Tang G, Shi H, Wu Y, et al., 2016. A variable turbulent Prandtl number model for simulating supercritical pressure CO2 heat transfer. International Journal of Heat and Mass Tranfer, 102:1082-1092.

Zhang S J, XU X X, Liu C, et al., 2019. Experimental investigation on the heat transfer characteristics ofsupercritical CO2 at various mass flow rates in heated vertical-flow tube. Applied Thermal Engineering, 157(5).

#310: Study on anti-leakage and high thermal conductivity composite phase change material for battery thermal management system

Lei ZHANG[1], Yitian WANG[1], Qingqing WU[3], Wei HE[*], Han WANG[1], Xianghua LIU[1], Zhongting HU[1], Xiangnong LIU[3]

[1] Department of Building Environment and Equipment, Hefei University of Technology, Hefei, China, 230009
[2] Gotion High-tech Co., Ltd., Hefei, China, 230009
[3] School of Automotive and Traffic Engineering, Hefei University of Technology, Hefei, China, 230009
* Corresponding author: hwei@hfut.edu.cn

Abstract: During the study, PCM-based thermal management for lithium batteries was prevalent but faced issues like leakage and low thermal conductivity, especially in controlling high-performance battery temperatures. This paper introduced a novel composite phase change material (CPCM) with enhanced thermal conductivity and leak resistance. A mesh of expanded graphite (EG) and diatomite significantly boosted PCM's absorption. Tests showed that a CPCM blend of 90% PEG, 10% diatomite, and 6% EG maintained integrity at 50℃ for 5 hours with no surface leakage, proving effective sealing. Under the 2C mode at an initial 30℃, the battery's max temperature stayed below 40℃. CPCM also provided excellent insulation at low temperatures, increasing discharge efficiency by 16.07%, reaching 91.67% under the 1C pattern at 30℃.

Keywords: Composite Phase Change Material, Battery Thermal Management, Anti-Leakage and High Thermal Conductivity, Cell Efficiency.

1. INTRODUCTION

With the development of electric and hybrid vehicles, lithium-ion batteries have attracted attention due to their high capacity, high energy density, and low self-discharge rate (Weng et al., 2021). During the charging and discharging processes, batteries generate a significant amount of heat; if not dissipated in time, this can lead to a decline in battery performance or even thermal runaway (Huang et al., 2022). Therefore, an effective Battery Thermal Management System (BTMS) is crucial for maintaining the batteries within their normal operating temperature range.

The Phase Change Material (PCM) cooling system has gained increasing attention due to its reduced need for auxiliary equipment and its effective cooling performance (Murali et al., 2021). PCMs can be divided into two main categories based on their chemical composition: organic and inorganic. Polyethylene Glycol (PEG), as an organic material, has garnered much interest due to its high latent heat of phase transition, excellent thermochemical stability, biocompatibility, non-toxicity, and low cost. Researchers have used other functional materials to address the low thermal conductivity and poor sealing of organic PCMs. For example, a hybrid semi-interpenetrating composite material was synthesized by infiltrating 70wt.% PEG into a polyurethane network and combining it with reticulated graphite nanosheets, effectively controlling the battery temperature (Wu et al., 2022). Diatomite, when added as an adsorbent material to PEG, can enhance the absorption efficiency of PEG (Karaman et al., 2011). In most studies, expanded graphite is only considered as a heat conduction agent to enhance the heat transfer effect of composite phase change materials (CPCMs), often overlooking its own porous worm-like structure, which can efficiently absorb liquid phase change materials (Fu et al., 2018). This article describes the preparation of a PEG/diatomite/expanded graphite composite phase change material using a vacuum adsorption method, which leverages the porous structure of diatomite and expanded graphite to more effectively absorb PEG, thereby improving the mass fraction of PEG in the CPCM and its thermal conductivity.

2. MATERIAL PREPARATION

A certain mass of PEG, diatomite, and EG were weighed. Then the diatomite and EG were mixed and dispersed evenly. PEG was put into a thermostatic water bath at 80℃ for 15 minutes. After melting, it dropped into the mixed powder of diatomite and EG. This mixture was poured into a glass petri dish and stirred evenly at 80℃ for 20 minutes, then vacuum absorbed under 0.08Mpa at 80℃ for 2 hours in the vacuum drying oven. Finally, the mixture was removed and allowed to cool to the indoor temperature. The samples were shown in Table 1.

Table 7: The composition ratio of each sample

Sample number	PEG（wt.%）	diatomite（wt.%）	EG（wt.%）
1	30	70	-
2	40	60	-
3	50	50	-
4	60	40	-
5	70	30	-
6	80	20	-
7	90	10	-
8	70	30	3
9	80	20	2
10	80	20	3
11	90	10	3
12	90	10	4
13	90	10	5
14	90	10	6
15	100	-	6

3. CPCM- LITHIUM BATTERY PACK MODULE CONSTRUCTION

In this paper, we took an 18650 commercial lithium battery as the research object, which regarded lithium cobalt oxides (LiCoO2) as the anode material and graphene as the cathode material. The battery had a rated voltage of 3.7V, a rated capacity of 2600mAh, and a maximum sustained discharge current of 5A. It was 69.2mm high, 18mm in diameter, and weighed about 50g. CPCM was pressed into a honeycomb model with an aperture of 18.5mm. The battery was put into an empty hole, and four lithium batteries were connected in series. The process of preparing the CPCM-lithium battery pack composite module was shown in Figure 1.

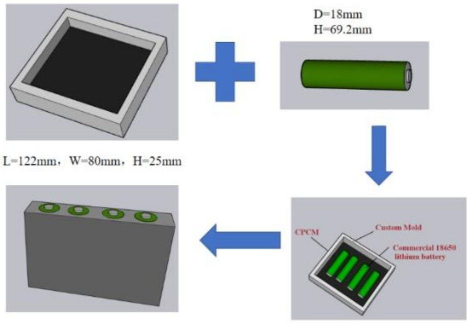

Figure 1: PCM/ battery pack model establishment

4. RESULTS AND DISCUSSION

4.1 Different characterizations of CPCM

Leak-proof test of CPCM

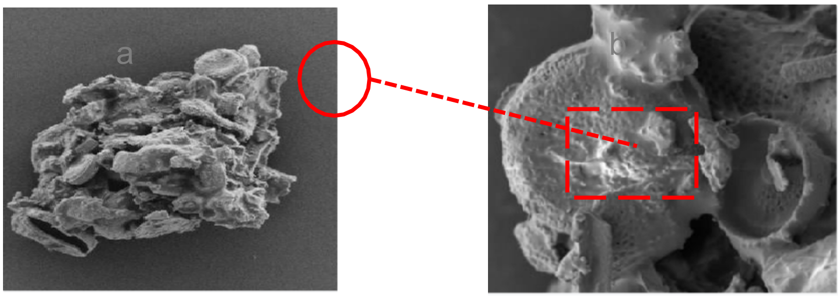

Figure 2: (a) low-multiple SEM atlas of CPCMs; (b) high-multiple SEM atlas of CPCMs.

After creating the PEG/diatomite/EG CPCM, its structure was examined using a high-resolution field emission scanning electron microscope, revealing EG's vermicular particles and diatomite micro-particles with PEG absorbed in surface pores, as depicted in Figures 2a and 2b. This microstructure confirmed effective PEG adsorption by EG and diatomite. Macroscopic tests involved heating CPCM pieces at 50℃ for 5 hours to assess leakage, with outcomes measured by dampness on qualitative filter paper and detailed in Table 2.

Table 2: Sample leakage test.

			
Sample 3	Sample 4	Sample 5	Sample 6
		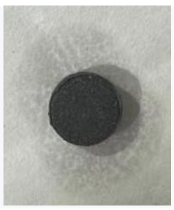	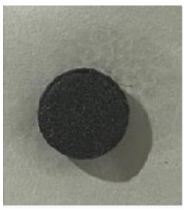
Sample 7	Sample 10	Sample 11	Sample 12
			
Sample 13	Sample 14	Sample 15	

In leakage resistance tests, combining polyethylene glycol (PEG) with diatomite worsened leakage as PEG content rose and diatomite fell. Sample 7 showed severe leakage and collapse. For compatibility with lithium batteries, no leakage under long-term high-temperature conditions is necessary. Only sample 3 met this, but its low PEG content of 50 wt.% failed to meet phase change latent heat requirements. Adding ethylene glycol (EG) was expected to increase PEG absorption and latent heat.

Further experiments with 8 composite phase change materials (CPCM) varying in EG content showed improved leakage resistance with EG addition, with a more pronounced effect at higher EG levels. At 6 wt.% EG, even with 90 wt.% PEG, no leakage occurred post long-term heating, and no liquid PEG wetted the surface. Comparisons without diatomite indicated its essential role in containment. Sample 14 excelled in the leakage test, highlighting the importance of both EGand diatomite for effective packaging.

5. TPS analysis

We selected four samples as representatives to study thermal conductivity. The thermal conductivity of the CPCMs increased with the EG content (from 1.28 W/(m•K) to 2.7 W/(m•K)). The test results well proved the theory that EG could provide an excellent three-dimensional thermal conductivity structure for the CPCM in terms of microstructure. The addition of EG gave CPCM good thermal conductivity and expanded its application range. The thermal conductivity of Sample14 could reach around 2.7W/(m•K), which was 10.4 times that of PEG1000.

5.1 Temperature test of CPCM-lithium battery model under different charge or discharge modes

In this paper, we selected a commercial 18650 lithium battery as the research object, which had a capacity of 2600mAh. The heat generated by the lithium battery during the process of charging and discharging could be divided into four parts: reaction heat, ohmic heat, polarization heat, and side reaction heat. The total reaction heat of the battery was shown in Eq (1).

–$Q = Q_O + Q_J = I^2(R_O + R_J)$ (1)

–Where:

–Q_O ——Ohmic heating, W;

–Q_J ——Joule heating, W;

–I ——Electricity, A;

–R_O ——Battery pack ohm resistance, Ω;

–R_J ——Battery pack polarization resistance, Ω.

In order to control the variable current battery, four lithium batteries were connected in series. We proposed two different charging and discharging current modes of 1C (2.6A) and 2C (5.2A). Figure 3a and Figure 3b tested the changes in battery temperature under different charging and discharging modes with two different initial temperatures of 22℃ and 30℃. When the battery was in the discharge stage, the temperature of the battery continued to rise. The range of temperature rise increased with the augmentation of current. During the battery charging stage, the temperature consistently showed a trend of rising and then falling. This occurred because the charging current in the charging mode remained unchanged at first, and the battery voltage continuously increased.

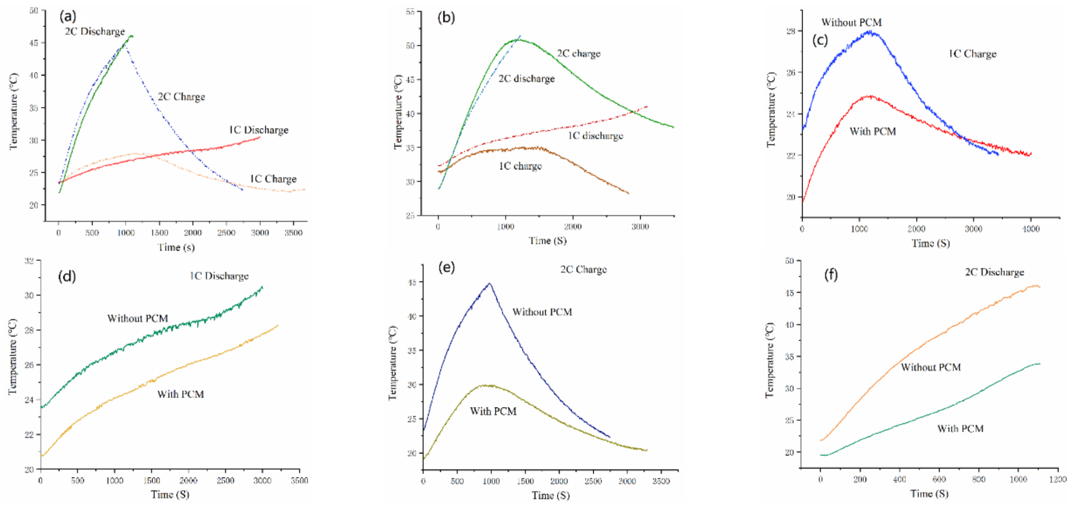

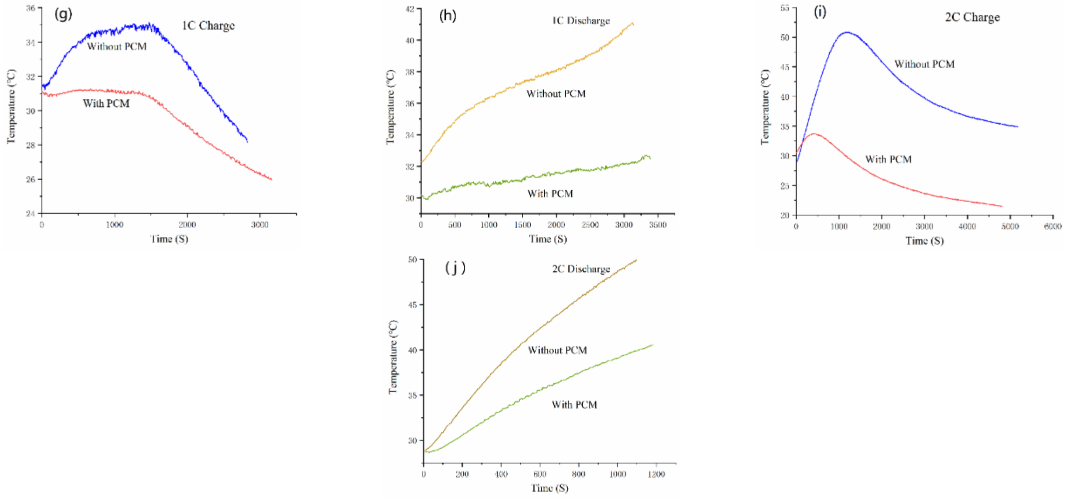

Figure 15: (a) Temperature curves of battery under different charging and discharging modes at 20℃; (b) Temperature curves of battery under different charging and discharging modes at 30℃; (c)-(j) Battery temperature change curve with or without PCM under different charging and discharging modes.

When the voltage increased to the set value (16.8V), the charging current decreased and the charging rate gradually decayed. As the current declined, the heat produced by the battery also decreased. However, the heat exchange with the surrounding environment did not stop, and the temperature of the battery gradually decreased. When the initial temperature was 20℃, it was found that the maximum temperature rise of the battery in charge/discharge mode at 1C was 5℃ and 8℃ respectively. The maximum temperature rise of the charge/discharge mode at 2C was 22℃ and 24℃ respectively. When T0 was 30℃, the maximum temperature rise of charge/discharge in 1C mode was 4℃ and 8.5℃. The maximum temperature rise of charge/discharge in 2C mode was 22.5℃ and 23℃. The initial temperature did not have a significant effect on the temperature rise of the battery under different charging and discharging modes.

Figure 3c to Figure 3j showed the curve of cell temperature variation. During the test, the ambient temperature was about 15℃. When T0 was 20℃, the presence or absence of PCM had no significant influence on the maximum temperature rise of the battery in 1C mode. This was because at 1C, the current passing through the battery pack was slight. However, in the charging mode, when the battery voltage reached the set value and the current gradually dropped, the temperature of the battery without PCM dropped rapidly. At the end of the charging period, the temperature dropped from 28℃ to 22℃, which was even lower than the initial temperature. The temperature of the battery wrapped with PCM dropped from 25℃ to 22.1℃, showing a significant decrease in the temperature drop. In 2C mode, the highest temperature of the charging and discharging stage was greatly higher than in 1C mode. After wrapping the PCM, the temperature of the battery pack dropped significantly from 45℃ to 30℃ for charging and from 47℃ to 34℃ for discharging.

When T0 was 30℃, at 1C mode, the temperature of the battery pack with PCM remained essentially unchanged during the constant current charging stage. And there was an obvious plateau in the temperature curve, which was because the temperature at this period was close to the phase transition temperature of PCM. The temperature rises in the discharge stage also changed obviously. Without PCM, the temperature of the battery increased by approximately 10℃. But with PCM wrapped, the temperature rise was just 2℃. It could be seen that the sensible heat stored energy of PCM and latent heat stored energy played a crucial role in this stage. Under 2C mode, the maximum temperature difference between the charging stage and discharge stage was extremely different. The maximum temperature dropped from 51℃ to 34℃ while charging, and from 51℃ to 39℃ in discharge mode. CPCM had a great limiting effect on the temperature rise of the battery at high temperature, especially in the 2C mode. The temperature could be controlled below 40℃.

The change in battery temperature was not only related to the intensity of the charging current and discharge current but also to the charging time and discharge time. In order to more rigorously study the temperature change of the CPCM-lithium battery model, this study proposed a new evaluation index, temperature rise rise intensity K.

– $$K = \frac{\Delta T}{t} \quad (2)$$

Where:

– ΔT—— Battery temperature difference, ℃;
– t—— Charge (discharge) time，s.

The heating intensity of the battery under eight working conditions with or without PCM was calculated respectively. The calculation results were listed in the following Table 3.

Table 3: K value of battery pack in different operating conditions

Work pattern	K（℃/s） Without PCM	With PCM
T0=22℃，1C Charge	0.0036	0.0039
T0=22℃，1C Discharge	0.0021	0.0021
T0=22℃，2C Charge	0.022	0.0106
T0=22℃，2C Discharge	0.022	0.013
T0=30℃，1C Charge	0.0025	0
T0=30℃，1C Discharge	0.0028	0.0006
T0=30℃，2C Charge	0.019	0.0065
T0=30℃，2C Discharge	0.019	0.0086

As could be seen from Table 3, except for the first and second modes, the K value of the battery with PCM was smaller than that without PCM in the remaining six operating modes. The K value of the first two modes had little change, because the battery temperature did not reach the phase transition temperature point of the composite phase change material; there was no latent heat energy storage involved in the heat transfer process. It was found that when the initial temperature of the battery was the same, the higher the working power of the battery, the more obvious the decrease of the K value of the battery after it had been wrapped by PCM.

In addition, we compared the charging stages under all conditions. After the constant current charging ended and constant voltage charging began, the temperature drops of the battery pack wrapped with PCM were considerably less than those without PCM. Taking the experimental group under the 2C charging mode as an example, when T0 was 30℃, the maximum temperature drops of the battery with PCM decreased from 16℃ to 11℃ compared with the battery without PCM during the constant voltage charging stage. In particular, under the same charging mode, the maximum temperature drop of the battery was reduced from 23℃ to 9℃ when T0 was 22℃.

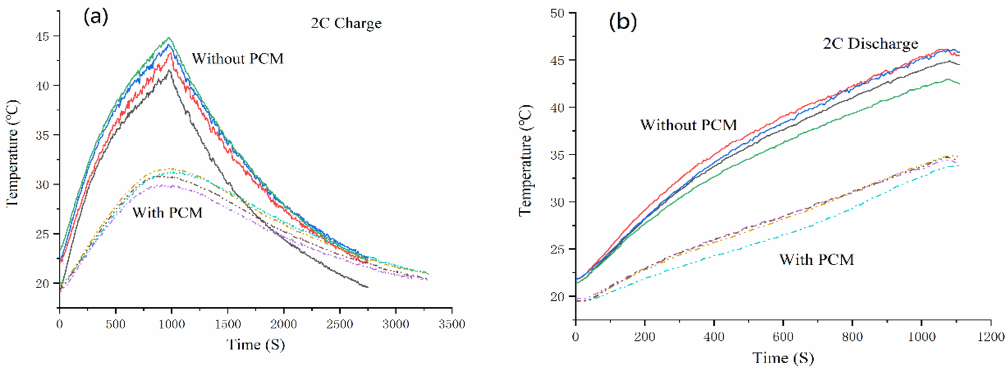

Figure 16: (a) Temperature difference between batteries during the charging stage with or without PCM; (b) Temperature difference between batteries during the discharging stage with or without PCM.

In subsequent experiments, we found that PCM could not only properly control the maximum temperature of the battery during charging and discharging but also effectively control the temperature difference between the four batteries connected in series. As shown in Figure 4a and Figure 4b, in the 2C charging mode, the maximum temperature difference between cells in the battery pack with PCM decreased from 8℃ to 3℃ compared with the battery pack without PCM. The maximum temperature difference in the 2C discharge mode had dropped from 5℃ to about 2℃.

5.2 Cell efficiency analysis

The battery discharge efficiency referred to the ratio of the actual quantity of power discharged to the terminal voltage under certain discharge conditions to the rated capacity. The calculation formula was as follows.

– $$\eta_f = \frac{I_f \cdot t_f}{W} \quad (3)$$

Where:

- I_f —— Discharge current, A;
- t_f —— Discharge time, h;
- W—— Battery rated capacity, mAh;

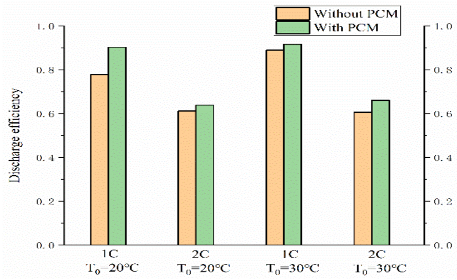

Figure 17: Histogram of battery discharge efficiency

The histogram revealed that the PCM-enhanced battery pack exhibited higher discharge efficiency across four conditions, peaking at 91.67% under the 1C condition at T0=30°C. The 1C condition's two-group discharge efficiency significantly surpassed that of the 2C condition. As depicted in Fig. 11, this was attributed to temperature control below 32℃ in both 1C scenarios, whereas the other conditions exceeded 30 ℃. This suggests an optimal operating temperature of approximately 30℃ for the commercial 18650 lithium batteries tested.

6. CONCLUSION

The preparation process of the composite phase change materials that were prepared in this paper was simple and of low cost. The main summary is as follows:

- In this experiment, 14 kinds of PEG, diatomite, and EG samples with different proportions were prepared. All samples were placed in a heating chamber and were heated at 50℃ for 5 hours to observe the leakage. After testing, it was found that Sample 14 had the best encapsulation performance. The TPS test showed that its thermal conductivity was also the highest, up to 2.7W/(m• K), which was 10.4 times that of pure PEG.
- Sample 14 was coupled with the lithium battery in full contact mode to test the temperature change of the battery pack coupled with the CPCM under different charging and discharging modes and initial battery temperatures. The maximum temperature rise of the battery was significantly reduced. In 2C mode, the maximum temperature rise of the battery was reduced by 17℃, and the maximum temperature could be controlled within 40℃.
- After coupling with Sample 14, the discharge efficiency of the battery pack was improved at four different discharge rates. When T0 was 30℃ and in the 1C discharge mode, the battery discharge efficiency reached 91.67%.

7. FUTURE RESEARCH PROSPECTS

During the experiment, only four lithium batteries were connected in series for safety reasons, but in practical applications, battery packs are usually connected in series and parallel to form a battery pack. At the same time, this paper only chooses to use an independent thermal management system for the experiment, in fact, a variety of thermal management system coupling is the best way to reduce the temperature of the battery pack.

8. REFERENCES

Fu, W., Zou, T., Liang, X., Wang, S., Gao, X., Zhang, Z., & Fang, Y., 2018, Thermal properties and thermal conductivity enhancement of composite phase change material using sodium acetate trihydrate–urea/expanded graphite for radiant floor heating system, Applied Thermal Engineering, 138, 618-626.

Huang, Q., Li, X., Zhang, G., Kan, Y., Li, C., Deng, J., & Wang, C., 2022, Flexible composite phase change material with anti-leakage and anti-vibration properties for battery thermal management, Applied Energy, 309, 118434.

Karaman, S., Karaipekli, A., Sarı, A., & Bicer, A., 2011, Polyethylene glycol (PEG)/diatomite composite as a novel form-stable phase change material for thermal energy storage, Solar Energy Materials and Solar Cells, 95(7), 1647-1653.

Murali, G., Sravya, G. S. N., Jaya, J., & Vamsi, V. N., 2021, A review on hybrid thermal management of battery packs and it's cooling performance by enhanced PCM, Renewable and Sustainable Energy Reviews, 150, 111513.

Weng, J., He, Y., Ouyang, D., Yang, X., Chen, M., Cui, S., Zhang, G., Yuen, RKK & Wang, J., 2021, Honeycomb-inspired design of a thermal management module and its mitigation effect on thermal runaway propagation, Applied Thermal Engineering, 195, 117147.

Wu, M., Li, T., Wang, P., Wu, S., Wang, R., & Lin, J., 2022, Dual-encapsulated highly conductive and liquid-free phase change composites enabled by polyurethane/graphite nanoplatelets hybrid networks for efficient energy storage and thermal management, Small, 18(9), 2105647.

#311: Study on PV performance and thermal behavior of bifacial PV Trombe wall system with reversible louvers in summer

Xiaoxiao SU[1], Chenglong LUO[2], Xinzhu CHEN[3], Ruili Peng[4], Hua ZHANG[5]

[1] School of Energy and Power Engineering, Nanjing University of Science and Technology, Nanjing 210094, China su1235210@163.com
[2] School of Energy and Power Engineering, Nanjing University of Science and Technology, Nanjing 210094, China. xxlong@ustc.edu
[3] School of Energy and Power Engineering, Nanjing University of Science and Technology, Nanjing 210094, China xzchen@njust.edu.cn
[4] School of Energy and Power Engineering, Nanjing University of Science and Technology, Nanjing 210094, China 1403625742@qq.com
[5] School of Energy and Power Engineering, Nanjing University of Science and Technology, Nanjing 210094, China 1318971827@qq.com

Abstract: This study addresses the power loss issue in traditional monofacial PV Trombe walls due to the design of PV glass plate transmittance and the thermal challenges of winter heating and summer cooling in regions with hot summers and cold winters. An innovative bifacial PV Trombe wall system with built-in reversible louvers has been proposed. An experimental platform was established in Nanjing to compare power generation performance and thermal behavior ofthe bifacial PV Trombe wall system with and without reversible louvers during the non-heating season. The results show that the system with reversible louvers improved the overall power generation efficiency from 15.40% to 16.17%, with a total power generation increase of 5.04%. Furthermore, the system not only maintains uniform vertical temperature distribution across the components but also significantly reduces the peak temperature and the rate of temperature increase in the heat-collecting wall, thereby decreasing the building's thermal load. It was also observed that the wall experienced reverse heat transfer to the photovoltaic components in the absence of louvers, negatively impacting their performance and stability. However, the integrated adjustable louvers effectively mitigated this issue. Furthermore, the investigation into the impact of PV cell coverage on the energy output of both traditional PV Trombe walls and the bifacialPV Trombe wall system revealed that both configurations experience a reduction in energy output as coverage decreases. Notably, the energy output of the bifacial PV Trombe wall system declines at a slower rate. At a coverage level of 0.5, thedifference in energy output between the two systems reaches its maximum, with the bifacial PV technology enhancing theenergy output of the traditional PV Trombe system by 17.46%.

Keywords: Bifacial PV Technology; Trombe Wall; Reversible Louvers; Building Cooling

1. INTRODUCTION

As economic development and population growth continue, global energy and resource consumption are increasing at an annual rate of 2.2% (Chen et al., 2024; Wilberforce et al., 2023). The construction industry, as a major energy-consuming sector, accounts for 36% of the world's total energy consumption and nearly 40% of CO_2 emissions (Chen; Hu, 2024; Fu et al., 2023; Fu et al., 2023; Wang et al., 2023). Under the immense pressure of global climate change, the construction industry faces significant challenges. Therefore, the development and application of efficient renewable energy technologies, particularly solar energy technologies, have become increasingly important (Wang; Zhou, 2023; Yang et al., 2023).

Solar photovoltaic (PV) technology has been widely applied in building systems, particularly through Building Integrated Photovoltaics (BIPV), which integrates PV technology into building structures to meet the local load demands of buildings or residential systems (Sarkar et al., 2020). BIPV technology can operate as standalone systems or be integrated into the grid, significantly reducing building energy consumption and enhancing energy efficiency. It is regarded as a crucial technology for achieving nearly zero-energy buildings (Ding et al., 2023; Feng et al., 2022; Sarkar; Kumar, 2020; Taşer et al., 2023). As BIPV technology continues to mature, PV modules can now be integrated into various parts of buildings, including roofs, facades, and external devices such as shading systems, blinds, windows, railings, and balconies (Abojela et al., 2023; Fu; Xu, 2023).

However, one of the challenges faced by PV systems is the high temperature of PV cells, which can reach up to 80°C (Abdalgadir et al., 2023). Since PV cells can only convert the portion of solar radiation with energy greater than the forbidden bandwidth of their material into electrical energy (Liang et al., 2022). Therefore, approximately 20% of the solar energy incident on the PV cells is converted into electricity, while 70-80% is either reflected or converted into heat, causing an increase in cell temperature and a subsequent decrease in PV conversion efficiency (Jhumka et al., 2023; Zhao et al., 2023). For PV cells with a base temperature of 25°C, efficiency decreases by approximately 0.45% for every degree increase in operating temperature (Abdalgadir; Qian, 2023). Implementing duct ventilation is often considered an ideal and cost-effective method to enhance system performance (Fu; Xu, 2023).

To address this issue, Moghaddam et al. (Ahmadi Moghaddam et al., 2023) used a three-dimensional computational fluid dynamics (CFD) model to study the effects of passive air cooling on PV modules. Their findings indicated that modifying the roof surface's emissivity could increase convective mass flow by 34% and reduce the average temperature of the PV modules by 3°C, thereby increasing efficiency by approximately 1.56% and lifespan by 21%. Kaaya et al. (Kaaya et al., 2024) conducted a simulation analysis showing that BIPV systems with ventilation features had component lifespans exceeding 25 years across all studied climate zones, whereas systems without ventilation experienced significantly shorter lifespans in hot climates. Additionally, experiments by Kaiser et al. (Kaiser et al., 2014) demonstrated that the size of the air gap and the speed of forced ventilation significantly impact the temperature and electrical efficiency of PV modules. It was found that, compared to natural ventilation at 0.5 m/s, forced ventilation at 6 m/s increased power output by 19%.

On the other hand, the solar radiation heat from BIPV arrays can increase a building's indoor thermal load, particularly during the summer (Jhumka; Yang, 2023). To address this issue, heat can be transferred from the supporting surface to the air channels of the BIPV facade and effectively dissipated through duct ventilation. This method not only enhances electrical efficiency but also increases useful air heat, facilitating heat recovery in winter and PV cooling in summer. This technology is also known as photovoltaic/photothermal comprehensive utilization integrated building (BIPV/T) technology (Abojela; Desa, 2023; Wang; Zhou, 2023; Zhao; Li, 2023). Studies have shown that modifying ventilation flow rates, air channel spacing, and integrating different cooling designs can significantly improve the overall performance of BIPV/T systems (Domjan et al., 2020; Fu; Xu, 2023; Luo et al., 2020; Shahsavar et al., 2011; Xu et al., 2020; Yang and Athienitis, 2015; Zhao; Li, 2023). Research by Zhao et al. (Zhao; Li, 2023) on an air-based BIPV/T system using copper indium gallium selenide PV modules demonstrated that increasing the airflow rate from 0.4 m/s to 2.2 m/s raised the average thermal efficiency by 28.8%, although electrical efficiency increased by only 3.5%. Comparisons across different geographical regions indicated that thermal efficiency varied by up to 8% at high flow rates, while the relative power generation showed minimal change. Fu et al. (Fu; Xu, 2023) found that increasing the air channel spacing under identicalsolar radiation conditions led to a 53.22% rise in duct heat, with thermal energy increasing by approximately 15% and electrical energy decreasing by 15%. They also proposed a new high-precision heat estimation method for heat transfer in air channels, validated to have a relative error of less than 7.49% under actual operating conditions (Fu; Xu, 2023). Shahsavar et al. (Shahsavar; Salmanzadeh, 2011) developed a BIPV/T system with an air handling unit (AHU), which increased power generation by 10.1% in summer through waste air cooling of PV modules and by 7.2% in winter throughbuilding ventilation cooling of PV modules. Additionally, winter PV module heat dissipation provided partial ventilation air heat load. Domjan et al. (Domjan; Petek, 2020) predicted solar energy utilization in different climate conditions for a semi-transparent BIPV/T glass facade with forced ventilation air gaps. Experimental results indicated that 10% of daily winter solar radiation could be used for electricity and heat supply, while air preheating utilized 75% of daily solar radiation. Yang et al. (Yang and Athienitis, 2015) proposed a dual-inlet open-loop air-based BIPV/T system that improved thermal efficiency by 5% compared to single-inlet systems. Xu (Xu; Ji, 2020) introduced a multifunctional BIPV/T solar wall system with annual average PV efficiencies of 11.2%, 10.6%, and 12.1% in Beijing, Hefei, and Xining, respectively, and heating efficiencies of 49.9%, 38.7%, and 41.3%. Luo et al. (Luo; Ji, 2020) studied a BIPV/T system combining air and water cooling channels, showing improved energy production and efficiency, with winter photovoltaic/air mode achieving an average PV efficiency of 15.3%, summer achieving 7.8%, and transitional seasons achieving 11.6% with photovoltaic/water mode.

Based on existing research, bifacial PV modules, which can convert solar radiation from both the front and back surfaces into electricity, have demonstrated higher efficiency compared to monofacial PV modules. Consequently, they can serve as a potent alternative to traditional monofacial PV modules (Abojela; Desa, 2023; Assoa et al., 2021; Li et al., 2023; Tina et al., 2021; Zhao et al., 2022; Zhao et al., 2022). However, when bifacial PV modules are integrated into building facades, their bifacial power generation advantage is often limited. To optimize their performance, various methods have been explored, such as using high-reflectivity walls or covering the walls with reflective materials to enhance rear-side power generation. In a study by Zhao et al. (Zhao; Zhang, 2022), a bifacial PV wall (BI-PVW) system was developed, integrating bifacial PV modules into building walls and utilizing the high reflectivity of the walls to boost rear-side power generation. Compared to traditional monofacial PV systems, this system increased power generation by approximately 19% in summer and 16% in winter. Demir et al. (Demir and Aktacir, 2024) improved the PV efficiency of bifacial modules by placing reflective surfaces on the walls behind the bifacial modules. Experimental results indicated that under various airflow speeds and air gap distances, the PV efficiency of bifacial PV modules significantly surpassed that of monofacial modules, with advantages ranging from 8.33% to 12.73%, and provided substantial indoor thermal load benefits in winter. Assoa et al. (Assoa; Thony, 2021) studied the thermal behavior and electrical performance of a building-integrated bifacial PV ventilated wall system considering insulation issues. The system's power generation was found to be 63.8 kWh/m², with an annual efficiency of 6.3%. Compared to similar test units with non-insulated concrete walls, this system significantly reduced indoor heat gain in summer and heat loss in winter. However, due to high site albedo, the average temperature of the PV modules reached 68.3°C. Zhao (Zhao; Zhang, 2022) found that adjusting the coverage of PV modules and installing an insulating reflective layer on the back could extend thermal comfort by approximately 8% annually.Nevertheless, Tina et al.(Tina; Scavo, 2021) conducted a simulation study revealing that while glass-to-glass bifacial PV facades with internal wall reflectors increased power generation by about 5% compared to monofacial BIPV facades, they also observed increased heat loss in winter, leading to additional heating energy consumption. Therefore, although enhancing wall reflectivity or using reflective materials can increase the power output and summer thermal comfort of bifacial BIPV/T systems, it may reduce passive heating effectiveness in regions requiring winter heating.

Trombe wall technology is a typical form of solar energy application in buildings, primarily achieving room heating by installing solar collectors on south-facing exterior walls. Due to its simple and effective application, this technology has been widely promoted globally (Li; Zhang, 2023). Combining Trombe wall technology with PV technology not only provides clean electricity but also improves the indoor thermal environment of buildings, sparking extensive research interest. Sun et al. (Sun et al., 2011) investigated the indoor thermal performance of PV Trombe walls in winter and noted that increasing the PV coverage on the glass could reduce the thermal efficiency of the Trombe wall by up to 17%. Irshad et al. and Aste et al. (Aste et al., 2012; Irshad et al., 2015) developed theoretical models for PV Trombe walls and photovoltaic/thermal (PV/T) systems, respectively. Luo et al. integrated thermoelectric modules and PV modules with Trombe walls, creating a hybrid system that achieves year-round electricity generation, winter heating, and summer cooling. Additionally, Yu et al. (Yu et al., 2022) combined thermocatalytic oxidation (TCO) technology with PV Trombe wall systems, proposing a photo-thermal-driven synergistic catalytic PV Trombe wall capable of meeting requirements for power generation, heating, and formaldehyde removal.Although Trombe wall technology demonstrates excellent performance in winter heating, it can lead to indoor overheating during the summer, thereby increasing air conditioning loads (Bruno et al., 2022; Ji et al., 2011; Luo et al., 2017; Luo et al., 2019; Yu; Fan, 2022). To address this issue, various methods have been proposed, such as using thermal insulation, shading curtains, and phase change materials to mitigate the overheating of PV Trombe walls in summer (Ji et al., 2007; Jiang et al., 2008; Luo; Xu, 2017; Luo; Zou, 2019). Additionally, PV cell coverage is a crucial factorinfluencing the performance of PV Trombe walls. However, existing research on PV cells primarily focuses on the overall performance of traditional monofacial PV Trombe walls, with limited attention given to compensating for power loss due to the light transmittance design of PV glass panels.

Based on the aforementioned literature review, it is evident that existing photovoltaic (PV) and photothermal technologies in building applications still face challenges in enhancing PV power generation and balancing thermal demands between summer and winter. To address these issues, this study innovatively combines bifacial PV technology with Trombe wall technology, creating a bifacial PV Trombe wall system with integrated reversible louvers. These louvers, featuring a highly reflective side and a highly absorptive side, can be oriented differently during non-heating and winter seasons to meet the complex requirements of electricity generation, winter heating, and summer heat gain reduction for buildings. Additionally, an experimental platform was constructed based on the initial design to test and analyze the power generation performance and thermal behavior of this system during the non-heating season.

2. EXPERIMENTAL SYSTEM AND SETUP

2.1. Bifacial PV Trombe Wall System with Reversible Louvers

The bifacial PV Trombe wall system with reversible louvers comprises the bifacial PV module, an air channel, reversible louvers with dual surfaces, outdoor upper and lower baffles, indoor upper and lower vents, a Collector wall, and a metal frame, as shown in Figure 1. The bifacial PV modules are mounted on the south façade of the experimental building using the metal frame, creating an air channel with a defined gap between the modules and the wall. Within this air channel there arereversible louvers, with one side coated with a solar reflective surface and the other with a solar selective absorptive coating, allowing orientation adjustment for summer and winter. During summer, the reflective side of the louvers faces outward, enabling the bifacial PV cells to utilize the reflected radiation for efficient PV power generation while reducing solar heat gain in the building. In winter, the absorptive side faces outward, efficiently absorbing solar radiation to provide heating for the building. During this period, the bifacial PV modules primarily absorb direct solar radiation on the front side for power generation, with the back side also generating power, albeit at a lower rate. This design enables the system to operate in two modes: "passive cooling + bifacial PV power generation" (passive cooling) during summer and "passive heating + bifacial PV power generation" (passive heating) during winter. This adaptability allows the system to meet the distinct thermal requirements for heating and cooling in buildings during different seasons.

Based on the operating principles of the system, in the passive cooling mode, the upper and lower baffles are opened, while the indoor upper and lower vents are closed. This configuration allows for a circulation loop between the air channel and the outdoor air, enabling convective heat exchange between the air in the channel, the PV modules, and the reversible louvers. The absorbed solar heat is carried away through this circulation loop, achieving solar passive cooling and efficient photovoltaic utilization for the building.

In the passive heating mode, the upper and lower baffles remain closed, and the indoor vents are open only during daytime when solar radiation is available. This setup creates a circulation loop between the air channel and the indoor air. The air within the channel can exchange heat convectively with the PV modules and the solar radiation-absorbing reversible louvers, transferring the heat indoors to provide heating. It is crucial to close the indoor vents at night or during periods without solar radiation to prevent reverse airflow, which could lead to heat loss.

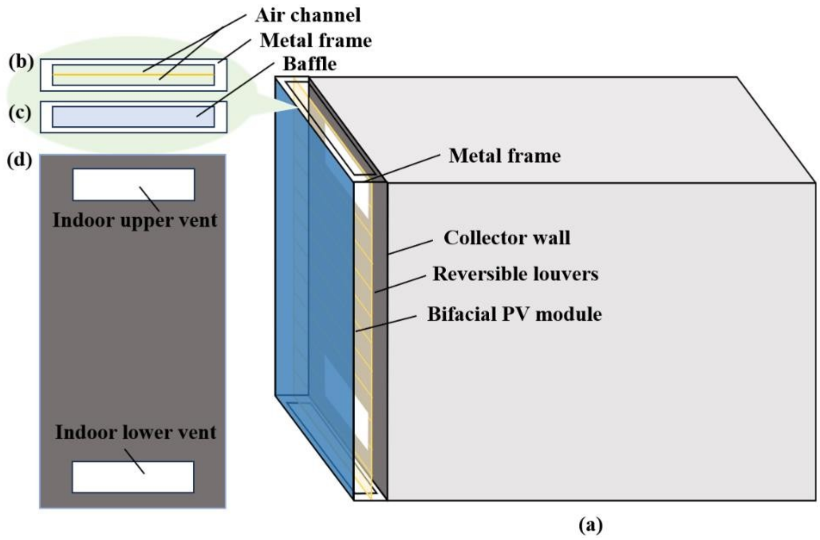

Figure 1: Structure of the Bifacial PV Trombe Wall System (a) Side view of the system (b) Outdoor baffles open (c) Outdoor baffles closed (d) Indoor vents

To investigate and analyze the photovoltaic performance and thermal behavior of the bifacial PV Trombe wall system with integrated reversible louvers in passive cooling mode, an experimental setup was established in Nanjing, China (32°3′41.6″N, 118°47′29.6″E). Two comparative experiments were conducted: one with and one without the integrated reversible louvers. Experiment 1, conducted from May 24 to June 4, 2024, involved the bifacial PV Trombe wall system without integrated louvers, allowing direct solar radiation to pass through the non-PV portions of the modules and onto the collector wall. Experiment 2, conducted from May 15 to May 23, 2024, involved the system with integrated reversible louvers. The reflective side of the louvers was oriented towards the bifacial PV modules to reflect solar radiation onto the backside of the PV modules, enhancing power generation and reducing solar heat gain in the building. In Experiment 1, the system was composed of three layers from outside to inside: the bifacial PV module layer, the air layer, and the wall. In Experiment 2, the system comprised five layers: the bifacial PV module layer, an air layer, the louvers, another air layer, and the wall. The operating principles of Experiments 1 and 2 in passive cooling mode are illustrated in Figure 2. Red dots indicate thermocouple measurement points to monitor temperature variations at various points in the system during operation.

The experimental setup comprised an experimental chamber, a bifacial PV module with a coverage rate of 64%, a micro-grid-connected inverter, a current sensor, a data acquisition device, and a pyranometer, as illustrated in Figure 3. The specifications and accuracy of each measurement instrument are detailed in Table 1. The pyranometer, installed on a plane parallel to the bifacial PV module, was used to measure the incident irradiance on the front side of the PV modules in real-time. The micro-grid-connected inverter tracked the maximum power point of the PV module to ensure optimal system performance. Current sensors converted the current signals from the PV module into measurable voltage signals for further processing and analysis. The data acquisition device, with a sampling interval of one minute, recorded various environmental and operational parameters during system operation. These parameters included the irradiance measured by the pyranometer, the temperatures recorded by the thermocouples, and the output current and voltage of the bifacial PV module, providing comprehensive data support for subsequent analysis.

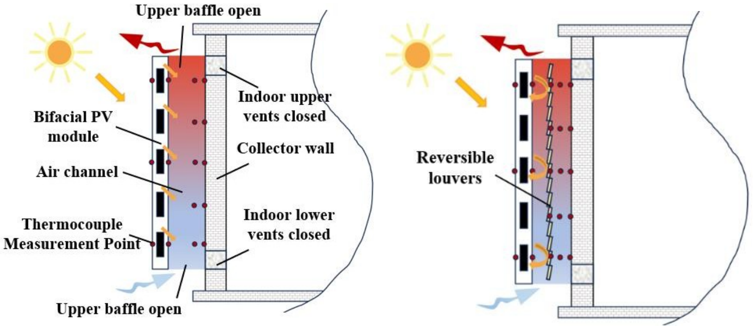

Figure 2 : Schematic of passive cooling mechanism in bifacial pv trombe wall system (a) Without internal louvers (b) With rotatable internal louvers

Figure 3: Experimental test system

Table 1: Parameters of main measuring instrument

Instrument	Parameter	Value
Micro-grid-connected inverter	Model	EZ1-M
	Peak Power Tracking Voltage	28V-45V
	Operating Voltage Range	16V-60V
	Maximum Input Voltage	60V
	Maximum Input Current	20A x 2
	Isc PV	25A x 2
	Maximum Continuous Output Power	600VA/799VA
	Nominal Output Voltage/Range	230V/184V-253V
	Nominal Output Current	2.6A/3.5A
	Default Power Factor	0.99
	Peak Efficiency	97.3%
	Nominal MPPT Efficiency	99.5%
Pyranometer	Model	HQTBQ-2-B
	sensitivity factor	7.51μV/(W•m2)
	Relative error	±2%
Current sensor	Instrument Model	SUP-DZI-20A
	Input	DC0~20A
	Output	DC0~10V
	Operating Temperature Range	-20℃~+80℃
	Relative error	±2.5%
Data acquisition device	Model	Agilent 34970A
	Relative error	±0.004 %

2.2. Theoretical Methods

Power generation performance of the bifacial PV Trombe wall system: Since both the front and rear sides of the bifacial PV modules absorb solar irradiance to generate electricity, the output power consists of the front power, Pft（W）and the rear power, Prear（W）, as shown Equation (1):

Equation 15: $$P_{\mathrm{bif}} = P_{\mathrm{ft}} + P_{\mathrm{rear}}$$

Where:

– P_{bif} = power generation of bifacial PV modules (W)

In the bifacial PV Trombe wall system, the irradiance paths for the front and rear sides of the PV modules are illustrated in Figure 4. Based on the incident irradiance on both sides of the PV modules, a power output model can be established:

Equation 2: $$P_{\mathrm{bif}} = ff \times \eta_{\mathrm{ft}} \times G_{\mathrm{ft}} + ff \times \eta_{\mathrm{rear}} \times G_{\mathrm{rear}}$$

Equation 3: $$\eta_{\mathrm{rear}} = \varphi\eta_{\mathrm{ft}};\ G_{\mathrm{rear}} = \gamma \times G_{\tau};\ G_{\tau} = \tau \times (1\text{-}ff) \times G_{\mathrm{ft}}$$

Equation 4: $$P_{\mathrm{bif}} = [1 + \varphi \times \gamma \times \tau \times (1\text{-}ff)] \times ff \times \eta_{\mathrm{ft}} \times G_{\mathrm{ft}}$$

Thus, the bifacial power generation of the PV modules, considering wall and louver reflections, can be expressed as:

Equation 5: $$P_{\mathrm{bif\_W}} = [1 + \varphi \times \gamma_{\mathrm{W}} \times \tau \times (1\text{-}ff)] \times ff \times \eta_{\mathrm{ft}} \times G_{\mathrm{ft}}$$

Equation 6: $$P_{\mathrm{bif\_Lou}} = [1 + \varphi \times \gamma_{\mathrm{Lou}} \times \tau \times (1\text{-}ff)] \times ff \times \eta_{\mathrm{ft}} \times G_{\mathrm{ft}}$$

Where:

– ff = coverage rate of the bifacial PV cells
– A = area of the PV modules (m^2)
– $P_{\mathrm{bif\_W}}$ = bifacial power generation considering wall reflections (W)
– $P_{\mathrm{bif\_Lou}}$ = bifacial power generation considering louver reflections (W)
– η_{ft} = power generation efficiencies of the front side of the PV modules
– η_{rear} = power generation efficiencies of the rear side of the PV modules
– G_{ft} = incident irradiances on the front side of the bifacial PV modules (W/m^2)
– G_{rear} = incident irradiances on the rear side of the bifacial PV modules (W/m^2)
– φ = bifacial factor of the PV modules
– γ = reflectivity (with γ_W 和 γ_{Lou} representing the reflectivity of the wall and louvers respectively)
– τ = transmittance of the bifacial PV modules

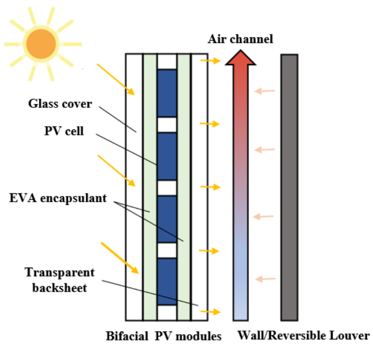

Figure 4: Incident irradiance paths on front and rear sides of PV modules in bifacial pv trombe wall system

Impact of photovoltaic cell coverage on PV Trombe wall system output: To address the power loss issues associated with the transparency design of the PV glass in PV Trombe wall systems, this study proposes a bifacial PV Trombe wall system featuring built-in adjustable louver blades. The power generation losses of both the traditional PV Trombe wall system and the bifacial PV Trombe wall system were compared across varying PV cell coverage rates. In both systems, the front-side PV performance of the utilized modules was identical, with a transparency of 0.8235 (glass cover transparency of 0.915 and backsheet transparency of 0.9). Furthermore, the bifacial PV modules used in the bifacial PV Trombe wall system exhibit a bifaciality of 0.8 and a louver reflectance of 0.53. The analysis reveals that the power output of both systems decreases with reduced PV cell coverage; however, the bifacial PV Trombe wall system experiences a slower rate of decline. When the coverage rate reaches 0.5, the power output difference between the two systems is maximized, with the bifacial PV technology enhancing the output of the traditional PV Trombe system by 17.46% (see Figure 5). This indicates that the integration of dual-sided photovoltaic technology and adjustable louvers in PV Trombe systems effectively mitigates the power losses caused by transparency design in traditional PV Trombe systems.

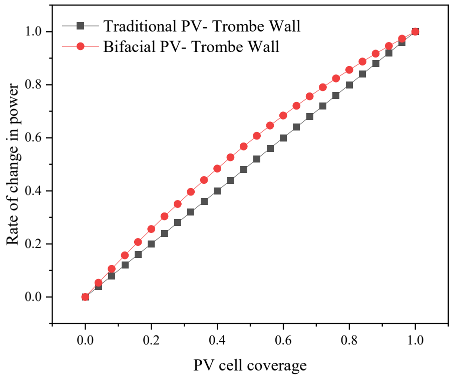

Figure 5: Impact of PV cell coverage ratio on power generation

Definition of louver gain: The effectiveness of integrated louvers in enhancing the PV performance of a bifacial photovoltaic Trombe wall system in passive cooling mode is assessed. The increase in rear-side power generation due to louver reflection compared to wall reflection under identical conditions is defined as louver gain, which can be expressed as:

Equation 7:

$$BG_{\text{Lou}} = \frac{P_{\text{bif\_Lou}} - P_{\text{bif\_W}}}{P_{\text{bif\_W}}}$$

Rearranging leads to:

Equation 8:

$$BG_{\text{Lou}} = \frac{\gamma_{\text{Lou}} - \gamma_{\text{W}}}{\frac{1}{\varphi \times \tau \times (1 - ff)} + \gamma_{\text{W}}}$$

When γw=0 the louver gain is equivalent to the bifacial gain of the bifacial PV module under louver reflection conditions, as shown below:

Equation 9:

$$BG_{\text{Lou}} = \varphi \times \tau \times \gamma_{\text{Lou}} \times (1 - ff)$$

2.3.4 Parameter Analysis of Louver Gain

For buildings with concrete exterior finishes, the reflectivity typically ranges from 0.2 to 0.35. This study analyzes the impact of the transmittance of bifacial PV modules and the reflectivity of louvers on the louver gain of the bifacial PV Trombe wall system, given a wall reflectivity of 0.3, a bifaciality of 0.8, and a PV cell coverage of 0.64. The results of the analysis are presented in Figure 6. Furthermore, according to the definition of louver gain established in Section 2.3.1, it is evident that when wall reflectivity is 0, the louver gain is equal to the bifacial gain. Therefore, under identical conditions, the influence of the transmittance of bifacial PV modules and the reflectivity of louvers on the bifacial gain of the bifacial PV Trombe wall system is illustrated in Figure 7.

The findings indicate that, within a specific range, both louver gain, and bifacial gain demonstrate a significant increasing trend with higher transmittance and reflectivity, ranging from 3.29% to 12.02% and from 8.64% to 20.74%, respectively. Additionally, under varying transmittance conditions, an increase in louver reflectivity from 0.5 to 0.8 results in louver gain and bifacial gain increasing by 1.52% to 3.81% and 4.32% to 6.91%, respectively. Conversely, when the louver reflectivity is varied, increasing the module transmittance from 0.6 to 0.9 can yield increases in louver gain and bifacial gain of 4.91% to 7.21% and 5.18% to 7.78%, respectively. A comparison reveals that the positive impact of louver reflectivity on both louver gain, and bifacial gain is significantly greater than that of module transmittance; however, the effect on the rear-side power generation of the bifacial PV module remains consistent. Given that enhancing louver reflectivity is generally more feasible than increasing module transmittance, it is recommended that efforts prioritize improving louver reflectivity to augment the energy output of the bifacial PV Trombe wall system.

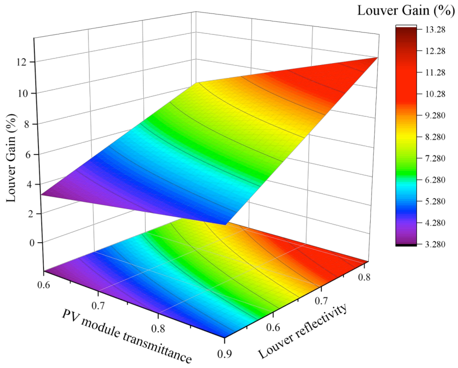

Figure 6: Influence of PV module transmittance and cell coverage on louver gain

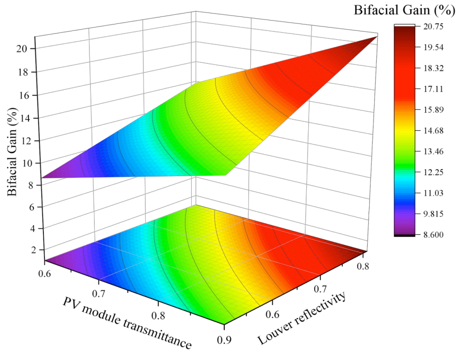

Figure 7: Influence of PV module transmittance and cell coverage on bifacial gain

Experimental analysis method for louver gain: In bifacial PV Trombe wall systems, directly measuring the incident irradiance on the rear side of the bifacial PV module is challenging, making it difficult to obtain the bifacial gain. This limitation complicates the evaluation of the effectiveness of louvers in enhancing the power generation performance of bifacial PV modules. However, the effectiveness of the louvers can be assessed through louver gain.

In the absence of integrated rotating louvers, the total power output of the bifacial PV Trombe wall system can be denoted as $P_{bif\_W\_1}$. This power is generated by both the direct irradiance incident on the front and the reflected irradiance from the wall. The overall energy conversion efficiency η_{bif_W}, based on the front irradiance G_{ft_W} of the bifacial PV module, can be expressed as:

Equation 10:
$$\eta_{\text{bif\_W}} = \frac{P_{\text{bif\_W\_1}}}{ff \times A \times G_{\text{ft\_1}}}$$

In the bifacial PV Trombe wall system equipped with integrated rotating louvers in passive cooling mode, the reflective surface of the louvers faces the bifacial PV module, allowing sunlight to be reflected onto the rear side of the module. This reflection increases the rear-side power generation, which is denoted as P_{Lou_rear}. In this case, the overall power output of the system is comprised of the bifacial power output $P_{bif\_W\_2}$ under wall reflection (without integrated louvers) and the rear power generation increase due to louver reflection P_{rear_Lou}:

Equation 11:
$$P_{\text{bif\_Lou}} = P_{\text{bif\_W\_2}} + P_{\text{rear\_Lou}}$$

The bifacial generation efficiency η_{bif_Lou}, based on the front irradiance Gft_2 of the bifacial photovoltaic module, can be represented as:

Equation 12:
$$\eta_{\text{bif\_Lou}} = \frac{P_{\text{bif\_Lou}}}{ff \times A \times G_{\text{ft\_2}}}$$

By comparing the photovoltaic performance with and without integrated rotating louvers—specifically, Experiment 2 versus Experiment 1 (which examines wall reflection under similar environmental conditions)—the increase in rear-side power generation due to louver reflection can be determined as follows:

Equation 13:
$$\frac{P_{\text{bif\_Lou}}}{P_{\text{bif\_W\_1}}} = \frac{P_{\text{bif\_W\_2}} + P_{\text{rear\_Lou}}}{P_{\text{bif\_W\_1}}}$$

Equation 14:
$$\frac{\eta_{\text{bif\_Lou}} \times G_{\text{ft\_2}}}{\eta_{\text{bif\_W}} \times G_{\text{ft\_1}}} = \frac{G_{\text{ft\_2}}}{G_{\text{ft\_1}}} + \frac{P_{\text{rear\_Lou}}}{P_{\text{bif\_1}}}$$

Rearranging yields:

Equation 15:
$$P_{\text{rear\_Lou}} = \left(\frac{\eta_{\text{bif\_Lou}}}{\eta_{\text{bif\_W}}} - 1\right) \times \frac{G_{\text{ft\_2}}}{G_{\text{ft\_1}}} \times P_{\text{bif\_W\_1}}$$

Based on the definition of louver gain, it can be expressed as:

Equation 16:
$$BG_{Lou} = P_{\text{rear\_Lou}} / (P_{\text{bif\_Lou}} - P_{\text{rear\_Lou}})$$

Further simplification leads to:

Equation 17:
$$BG_{Lou} = \frac{\eta_{\text{bif\_Lou}}}{\eta_{\text{bif\_r}}} - 1$$

3. EXPERIMENTAL RESULTS AND DISCUSSION

3.1. Experimental Conditions

To evaluate the photovoltaic and photothermal performance of the bifacial PV Trombe wall system in passive cooling mode, with and without integrated rotating louvers, two sets of experiments were conducted from May 15 to May 23, 2024, and from May 24 to June 4, 2024. Figure 8 shows the ambient temperature and solar irradiance data for May 17 and May25, 2024. Due to the sensitivity of ambient temperature to factors such as wind speed and wind direction, significant fluctuations were observed in the data collected at adjacent intervals. To improve the reliability and stability of the ambient temperature data, smoothing was applied, resulting in the smoothed ambient temperature data, denoted as T_{a_s}. The average ambient temperatures on May 17 and May 25 were 28.77°C and 28.37°C, respectively, with a difference of only 0.3°C and an absolute mean temperature difference of 1.52°C. Regarding irradiance, although cloud cover affected irradiance at certain times between 6:00 and 18:00 on both May 17 and May 25, the overall irradiance changes on these days were representative of clear, cloudless conditions. The front incident irradiance on May 17 was approximately 2.35% higher than on May 25, with values of 2356.38 Wh/m² and 2302.21 Wh/m², respectively.

These data indicate that, although there were slight differences in ambient temperature and irradiance between May 17 and May 25, the overall differences were minimal, ensuring the validity and reliability of the comparative analysis of the bifacial PV Trombe wall system under these environmental conditions. Therefore, the data from May 25, 2024, were selected to represent Experiment 1, which tested the performance of the bifacial PV system without integrated rotating louvers, while the data from May 17, 2024, were selected to represent Experiment 2, which tested the performance of the system with integrated rotating louvers.

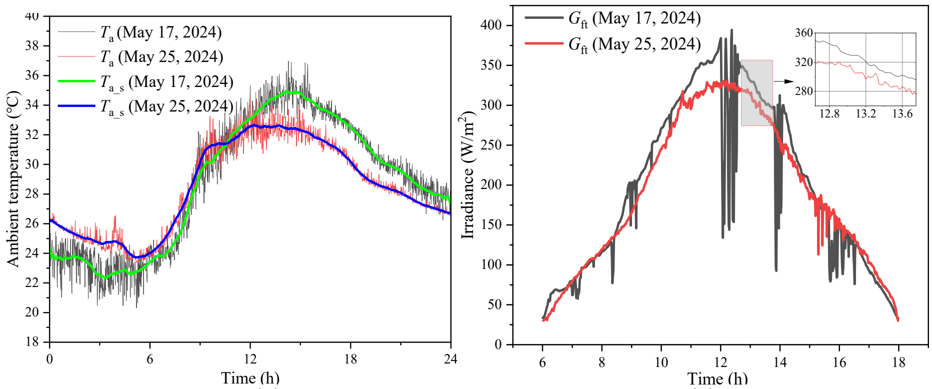

(a) (b)

Figure 8: Environmental parameters (a) Ambient temperature (b) Incident irradiance on south-facing PV module

3.2. Photovoltaic Performance of the Bifacial PV Trombe Wall System

Under similar environmental conditions, it can be approximate that efficiency changes consistently over time. Therefore, when analyzing the additional rear-side power generation due to reflective louvers in Experiment 2, the experimental results from Experiment 1 (without integrated louvers) can be utilized. Subsequently, the louver power gain defined in Section 2.3 can be used to evaluate the improvement in the photovoltaic performance of the bifacial PV Trombe wall system with integrated rotating louvers in passive cooling mode. Figure 9 presents the variations in the photovoltaic performance of the bifacial PV module during Experiments 1 and 2 (operating hours from 6:00 to 18:00). In Experiment 2, with integrated rotating louvers, the power generation was 630.14 Wh, representing a 7.52% increase compared to Experiment 1 (without integrated louvers), which generated 586.09 Wh. However, during this period, the front incident irradiance in Experiment 2 was only about 2.35% higher than in Experiment 1 (see Figure 8). Consequently, the overall power generation efficiency of the bifacial PV module increased from 15.40% to 16.17%, with efficiency gains exceeding 10% particularly in the morning and evening periods.

Further analysis reveals that the overall additional rear-side power generation due to the reflective louvers in Experiment 2 was 30.26 Wh (see Figure 10(a)), with a consistent increase in rear-side power throughout the day. This increase was especially pronounced during periods of lower solar irradiance in the morning and evening. The louver power gain curve in Figure 10(b) also indicates that the presence of reflective louvers (Experiment 1) significantly enhanced the overall power output of the bifacial PV module in the morning and evening. The overall trend shows a gradual decrease in efficiency as the sun rises, reaching a minimum at noon, and then increasing again until sunset, with an overall louver power gain of 5.04% for the entire day.

To better understand the effect of rotating louvers in passive cooling mode, data from the period of 12:64-13:75 were selected for comparative analysis. During this period, the sky was clear, solar irradiance was high, and data fluctuations were minimal. The results show that during this period, the average ambient temperatures in Experiments 1 and 2 were 32.52°C and 34.40°C, respectively, with average irradiance of 301.67 W/m² and 321.73 W/m². Despite these conditions, the power generation increased by 9.31%, with an average rear-side power increase of 2.28 W. Due to the reflective effect of the louvers, the system's average PV efficiency also increased from 15.65% to 16.04%, with a louver gain of 2.49%.

These results demonstrate that the reflectivity of the louvers not only effectively enhanced the rear-side power generation of the bifacial PV Trombe wall system but also improved the overall power generation efficiency, especially during periods of low irradiance in the morning and evening. The summarized experimental results are presented in Table 2. Therefore, installing reflective louvers in bifacial photovoltaic systems can significantly enhance the power generation performance of PV modules.

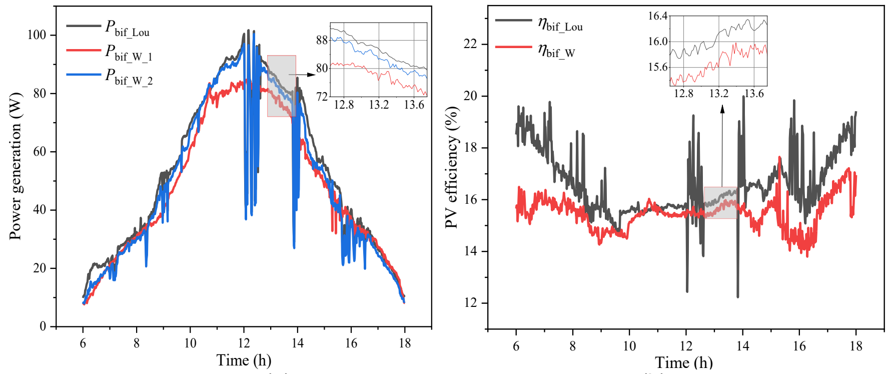

Figure 9: Bifacial PV module performance (a) Power output (b) Efficiency

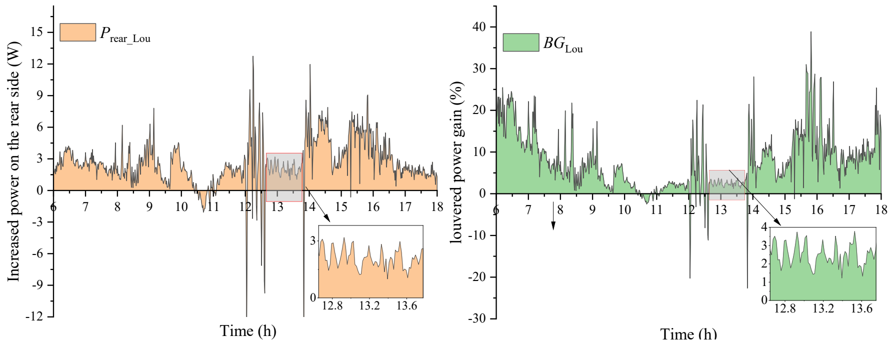

Figure 10: Impact of louvers on bifacial PV module output (a) Rear irradiance increase (b) Reflective louver power gain

Table 2: PV performance of bifacial PV trombe wall system in passive cooling mode

Experiment Name	Condition	T_a (°C)	G_{ft} (Wh/m²)	P_{bif} (Wh)	P_{rear_Lou} (Wh)	P_{bif_W} (Wh)	η_{bif} (%)	BG_{Lou} (%)
1	without integrated louvers	28.37	2302.21	586.09	-	586.09	15.40	-
2	With integrated louvers	28.77	2356.38	630.14	30.26	599.88	16.17	5.04

3.3. Analysis of Heat Transfer Processes in the System

One of the primary objectives of the dual-sided photovoltaic Trombe wall system in passive cooling mode is to cool the PV modules, thereby enhancing energy production and reducing heat gain in the building. The period from 6:00 to 18:00 represents the peak operational hours for the PV modules and the highest cooling demand for the building; thus, the following analysis is based on data collected during this timeframe.

In Experiment 1, direct sunlight passing through the transparent section of the photovoltaic components led to a rapid increase in the temperature of the Trombe wall. This resulted in a bidirectional transfer of heat, rather than a unidirectional transfer from the photovoltaic components to the Trombe wall, as illustrated in Figure 11. Specifically, around 13:22, the temperature of the Trombe wall exceeded that of the airflow within the channel, causing the heat in the airflow to derive from both the photovoltaic components and the Trombe wall. By 15:18, the temperature of the Trombe wall even surpassed the inner temperature of the PV modules, reaching 37.50°C. The heat from the Trombe wall is transferred indoors through conduction and conveyed to the airflow in the channel through convection. Additionally, heat is radiated back toward the PV modules, which can adversely affect their energy production performance and stability.

In contrast, in Experiment 2, the heat within the system was primarily concentrated in the PV modules, with some of the heat dissipating into the environment through convection and radiation, while the remaining heat gradually transferred to the collector wall, as shown in Figure 12. The experimental results indicated that the temperature of the louvers was very close to the outdoor ambient temperature, being 31.12°C and 31.19°C respectively. This similarity suggests that the reflective surface of the louvers did not absorb the solar radiation passing through the PV modules but effectively reflected this radiation back towards the rear of the PV modules and the external environment. The heat of the collector wall mainly originated from the convective heat exchange with the air in the flow channel and the radiative heat exchange from the solar-selective coating surface of the louvers. Due to the low emissivity of the solar-selective coating surface of the louvers, the radiative heat exchange with the wall was minimized, resulting in a slower temperature increase of the collector wall. Consequently, the collector wall temperature remained below the ambient temperature until 16:00. These findings demonstrate that the reflective louvers effectively reduced the temperature of the collector wall, thereby decreasing the heat gain of the building.

Furthermore, as illustrated in Figures 11(b) and 12(b), in Experiment 1, the temperature difference between the inner and outer sides of the PV modules was greater, with a maximum temperature difference of 2.13°C and an absolute average temperature difference of 0.98°C. In contrast, in Experiment 2, the inner side temperature of the PV modules was closer to the outer side temperature, with a maximum temperature difference of only 1.44°C and an absolute average temperature difference of 0.56°C. This observation further confirms that the reflective louvers effectively redirected incoming solar radiation to the rear of the PV modules. Consequently, the modules likely absorbed some of this reflected radiation, resulting in an increase in inner module temperature and a reduction in the temperature differential between the inner and outer sides. Nonetheless, the overall temperature variation of the PV modules remained within acceptable limits.

In summary, the bifacial PV Trombe wall system, under passive cooling mode, demonstrated that the integrated reflective louvers effectively redirected solar radiation to the rear of the bifacial PV modules and the external environment. This redirection facilitated increased PV energy generation from the absorbed radiation. Additionally, the louvers provided shading for the wall, significantly reducing its temperature. The low emissivity of the absorbing surface of the louvers also contributed to a decrease in radiative heat gained by the wall. Relevant experimental results are presented in Table 3.

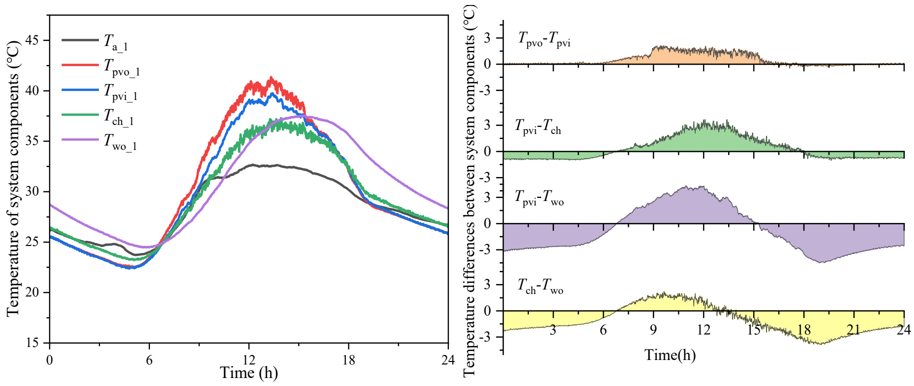

(a) (b)

Figure 11: Experimental 1: (a) Temperature characteristics of system components (b) Heat transfer process of system components

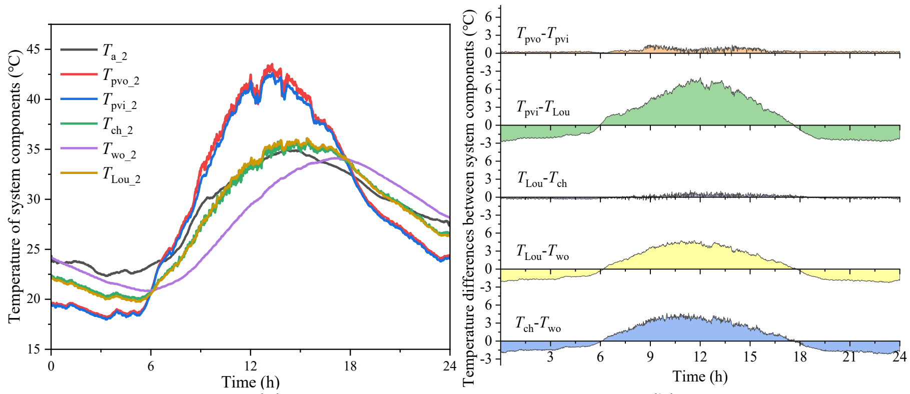

(a) (b)

Figure 12: Experimental 2: (a) Temperature characteristics of system components (b) Heat transfer process of system components

Table 3: Temperatures of components in the bifacial PV trombe wall system during passive cooling mode (6:00-18:00)

Experiment Name	Condition	T_a (℃)	T_{pvo} (℃)	T_{pvi} (℃)	T_{Lou} (℃)	T_{ch} (℃)	T_{wo} (℃)
1	without integrated louvers	30.49	34.92	33.96	-	32.59	32.67
2	With integrated louvers	31.19	35.76	35.20	31.12	30.92	28.48

4. Conclusion

The PV Trombe wall system must accommodate both heating and power generation functions, resulting in incomplete coverage of the PV cells within traditional monofacial glass. This design allows for some light transmission but often leads to a loss in power generation. To mitigate this loss, this study integrates bifacial PV technology, which offers dual-sided energy generation, with Trombe wall technology to create a bifacial PV Trombe wall system. An experimental platform was established based on preliminary designs to conduct an in-depth analysis of the system’s performance and thermal behavior under passive cooling mode. A new evaluation method called "louver gain" was introduced. The main conclusions are as follows:

(1) Both traditional PV Trombe wall systems and bifacial PV Trombe wall systems experience a reduction in energy output with decreasing PV cell coverage. However, the decline in energy output is less pronounced for the bifacial system. At a coverage rate of 0.5, the difference in energy generation between the two systems reaches its maximum, with the bifacial technology enhancing the output of the traditional PV Trombe system by 17.46%.

(2) The bifacial PV Trombe wall system, with the integration of louvers, increases overall energy efficiency from 15.40% to 16.17%, resulting in a total energy output increase of 5.04%.

(3) The system effectively reduces wall temperatures and the rate of temperature rise, demonstrating improved thermal performance and stability through the use of adjustable louvers. In contrast, without the integrated louvers, reverse heat transfer to the PV modules occurs, adversely affecting their performance and stability. The adjustable louvers effectively prevent this phenomenon.

In summary, the bifacial PV Trombe wall system with integrated adjustable louvers not only excels in energy efficiency and thermal performance but also effectively addresses the power generation losses caused by light transmission issues in traditional monofacial PV Trombe walls.

5. REFERENCES

Abdalgadir Y., Qian H., Zhao D., Adam A., Liang W., 2023. Daily and annual performance analyses of the BIPV/T system in typical cities of Sudan, Energy and Built Environment. 4, 516-529.

Abojela Z.R.K., Desa M.K.M., Sabry A.H., 2023. Current prospects of building-integrated solar PV systems and the application of bifacial PVs, Frontiers in Energy Research. 11, 1164494.

Ahmadi Moghaddam H., Tkachenko S., Yeoh G.H., Timchenko V., 2023. A newly designed BIPV system with enhanced passive cooling and ventilation. Building Simulation.

Assoa Y.B., Thony P., Messaoudi P., Schmitt E., Bizzini O., Gelibert S., Therme D., Rudy J., Chabuel F., 2021. Study of a building integrated bifacial photovoltaic facade, Solar Energy. 227, 497-515.

Aste N., Del Pero C., Leonforte F., 2012. Thermal-electrical optimization of the configuration a liquid PVT collector, Energy Procedia. 30, 1-7.

Bruno R., Bevilacqua P., Cirone D., Perrella S., Rollo A., 2022. A calibration of the solar load ratio method to determine the heat gain in PV-Trombe walls, Energies. 15, 328.

Chen L., Hu Y., Wang R., Li X., Chen Z., Hua J., Osman A.I., Farghali M., Huang L., Li J., 2024. Green building practices to integrate renewable energy in the construction sector: a review, Environmental Chemistry Letters. 22, 751-784.

Demir Y.C., Aktacir M.A., 2024. Experimental investigation of BIPV/T application in winter season under Şanlıurfa's meteorological conditions, IET Renewable Power Generation.

Ding L., Zhu Y., Zheng L., Dai Q., Zhang Z., 2023. What is the path of photovoltaic building (BIPV or BAPV) promotion?--The perspective of evolutionary games, Applied Energy. 340, 121033.

Domjan S., Petek L., Arkar C., Medved S., 2020. Experimental study on energy efficiency of multi-functional BIPV glazed façade structure during heating season, Energies. 13, 2772.

Feng C., Ma F., Wang R., Xu Z., Zhang L., Zhao M., 2022. An experimental study on the performance of new glass curtain wall system in different seasons, Building and Environment. 219, 109222.

Fu Y., Xu W., Wang Z., Zhang S., Chen X., Chu J., 2023. Experimental investigation on thermal characteristics and novel thermal estimation method of BIPV façade air channel under actual operation, Journal of Building Engineering. 72, 106489.

Fu Y., Xu W., Wang Z., Zhang S., Chen X., Zhang X., 2023. Experimental study on thermoelectric effect pattern analysis and novel thermoelectric coupling model of BIPV facade system, Renewable Energy. 217, 119055.

Irshad K., Habib K., Thirumalaiswamy N., 2015. Performance evaluation of PV-Trombe wall for sustainable building development, Procedia Cirp. 26, 624-629.

Jhumka H., Yang S., Gorse C., Wilkinson S., Yang R., He B.-J., Prasad D., Fiorito F., 2023. Assessing heat transfer characteristics of building envelope deployed BIPV and resultant building energy consumption in a tropical climate, Energy and Buildings. 298, 113540.

Ji J., Luo C., Chow T.-T., Sun W., He W., 2011. Modelling and validation of a building-integrated dual-function solar collector, Proceedings of the Institution of Mechanical Engineers, Part A: Journal of Power and Energy. 225, 259-269.

Ji J., Yi H., He W., Pei G., 2007. PV-Trombe wall design for buildings in composite climates.

Jiang B., Ji J., Yi H., 2008. The influence of PV coverage ratio on thermal and electrical performance of photovoltaic-Trombe wall, Renewable energy. 33, 2491-2498.

Kaaya I., Alzade A., Bouguerra S., Kyranaki N., Bakovasilis A., Ramesh S., Saelens D., Daenen M., Morlier A., 2024. A physics-based framework for modelling the performance and reliability of BIPV systems, Solar Energy. 277, 112730.

Kaiser A., Zamora B., Mazón R., García J., Vera F., 2014. Experimental study of cooling BIPV modules by forced convection in the air channel, Applied Energy. 135, 88-97.

Li C., Zhang W., Tan J., Liu W., Lyu Y., Tang H., 2023. Energy performance of an innovative bifacial photovoltaic sunshade (BiPVS) under hot summer and warm winter climate, Heliyon. 9.

Liang H., Su R., Huang W., Cheng Z., Wang F., Huang G., Yang D., 2022. A novel spectral beam splitting photovoltaic/thermal hybrid system based on semi-transparent solar cell with serrated groove structure for co-generation of electricity and high-grade thermal energy, Energy Conversion and Management. 252, 115049.

Luo C., Xu L., Ji J., Liao M., Sun D., 2017. Experimental study of a modified solar phase change material storage wall system, Energy. 128, 224-231.

Luo C., Zou W., Sun D., Xu L., Ji J., Liao M., 2019. Experimental Study of Thermal Effect of Lacquer Coating for PV-Trombe Wall System Combined with Phase Change Material in Summer, International Journal of Photoenergy. 2019, 7918782.

Luo K., Ji J., Xu L., Li Z., 2020. Seasonal experimental study of a hybrid photovoltaic-water/air solar wall system, Applied thermal engineering. 169, 114853.

Sarkar D., Kumar A., Sadhu P.K., 2020. A survey on development and recent trends of renewable energy generation from BIPV systems, IETE Technical Review.

Shahsavar A., Salmanzadeh M., Ameri M., Talebizadeh P., 2011. Energy saving in buildings by using the exhaust and ventilation air for cooling of photovoltaic panels, Energy and buildings. 43, 2219-2226.

Sun W., Ji J., Luo C., He W., 2011. Performance of PV-Trombe wall in winter correlated with south façade design, Applied energy. 88, 224-231.

Taşer A., Koyunbaba B.K., Kazanasmaz T., 2023. Thermal, daylight, and energy potential of building-integrated photovoltaic (BIPV) systems: A comprehensive review of effects and developments, Solar Energy. 251, 171-196.

Tina G.M., Scavo F.B., Aneli S., Gagliano A., 2021. Assessment of the electrical and thermal performances of building integrated bifacial photovoltaic modules, J Clean Prod. 313, 127906.

Wang L., Zhou J., Zhong W., Ji Y., Yuan Y., 2023. Analysis of factors affecting the performance of a novel micro-channel heat pipe PV-Trombe wall system for space heating, Sustain Energy Techn. 58, 103347.

Wilberforce T., Olabi A., Sayed E.T., Elsaid K., Maghrabie H.M., Abdelkareem M.A., 2023. A review on zero energy buildings–Pros and cons, Energy and Built Environment. 4, 25-38.

Xu L., Ji J., Luo K., Li Z., Xu R., Huang S., 2020. Annual analysis of a multi-functional BIPV/T solar wall system in typical cities of China, Energy. 197, 117098.

Yang R.J., Imalka S.T., Wijeratne W.P., Amarasinghe G., Weerasinghe N., Jayakumari S.D.S., Zhao H., Wang Z., Gunarathna C., Perrie J., 2023. Digitalizing building integrated photovoltaic (BIPV) conceptual design: A framework and an example platform, Building and Environment. 243, 110675.

Yang T., Athienitis A.K., 2015. Experimental investigation of a two-inlet air-based building integrated photovoltaic/thermal (BIPV/T) system, Applied energy. 159, 70-79.

Yu B., Fan M., Gu T., Xia X., Li N., 2022. The performance analysis of the photo-thermal driven synergetic catalytic PV-Trombe wall, Renewable Energy. 192, 264-278.

Zhao O., Zhang W., Chen M., Xie L., Li J., Li Z., Zhong J., Wu X., 2022. Experimental and numerical study on the performance of innovative bifacial photovoltaic wall system, Sustainable Cities and Society. 85, 104085.

Zhao O., Zhang W., Xie L., Wang W., Chen M., Li Z., Li J., Wu X., Zeng X., Du S., 2022. Investigation of indoor environment and thermal comfort of building installed with bifacial PV modules, Sustainable Cities and Society. 76, 103463.

Zhao Y., Li W., Zhang G., Li Y., Ge M., Wang S., 2023. Experimental performance of air-type BIPVT systems under different climate conditions, Sustain Energy Techn. 60, 103458.

#313: Response time calculation and test optimization of reactor trip system

Yongkui XIE[1], Pengcheng YANG[2], Xiliang MA[3]

[1] Suzhou Nuclear Power Research Institute, 1688 Xihuan Road, Gusu District, Suzhou City, Jiangsu Province, xieyongkui@126.com
[2] Suzhou Nuclear Power Research Institute, 1688 Xihuan Road, Gusu District, Suzhou City, Jiangsu Province, yangpengcheng207@163.com
[3] Suzhou Nuclear Power Research Institute, 1688 Xihuan Road, Gusu District, Suzhou City, Jiangsu Province, maxiliang@cgnpc.com.cn

Abstract: The article initially presents the implementation principle of a specific nuclear power Reactor Trip System and elaborates on the composition of the total response time calculation of the reactor protection system. In consideration of the requirements outlined in regular test supervision, it raises the issue of testing the total response time of the Reactor Trip System during unit overhaul in the commercial operation stage. Based on actual site conditions and combined with multi-plant and multi-equipment comparison, a representative test plan with implementable conditions is developed. The article introduces the specific implementation method and Theoretical optimization method for calculating response time.

Keywords: Safety DCS, RTS, Response Time, Calculation Method, Test Method

1. BACKGROUND

The response time is an important dynamic property of Reactor Trip System (RTS), which characterizes the response speed of the instrumentation and control system of nuclear power plants to the accident conditions. In general, according to standard for the periodic surveillance testing of nuclear power generating station safety systems, response time should be tested for all channels of RTS, of which there are about 300.

RTS can be implemented in two ways, Relay Control System (RCS) and Digital Control System (DCS). For RCS, the individual modules of each channel, such as the signal processing equipment bistables, are independent. They must perform the response time test one by one. According to statistics, the whole test process lasted for about 1.5 days, and the signal input and output terminals were disconnected and took up a lot of working hours. For DCS, a digital module can handle multiple channels. The signal conditioning, setting value judgment and decision logic processing of these channels are on the same board or microprocessor. It is only necessary to verify the response time of one channel to prove that the other channels are operable, because the signal response process is essentially implemented in the module's software. The software processing cycle of the module is fixed, and each cycle processes one acquisition signal. Therefore, it is not necessary to verify the response time of all channels. However, you need to ensure that the response time of each module of the DCS can be verified.

In previous research, the articles have generally focused on how to design site tests to verify response times across all DCS channels. There are also articles that validate the response time characteristics of the microprocessor under different load states. However, few articles study the range of response time and verify it.

The article calculates the total response time of 6 representative signals by analysing the signal transmission path of DCS. These 6 sets of signals can traverse all modules of the DCS, so that the response time of each module can be verified. Replacing all channels test with fewer channels test will save maintenance time during power plant outage. In addition, in order to verify the accuracy of the theoretical calculation, a representative test plan is designed to measure the response time of these signals.

2. STRUCTURE OF THE REACTOR TRIP SYSTEM

For a specific nuclear power plant in China, the RTS is a DCS which is supported by the TELEPERM XS (TXS). The main architecture of the DCS platform is shown in Figure 1.

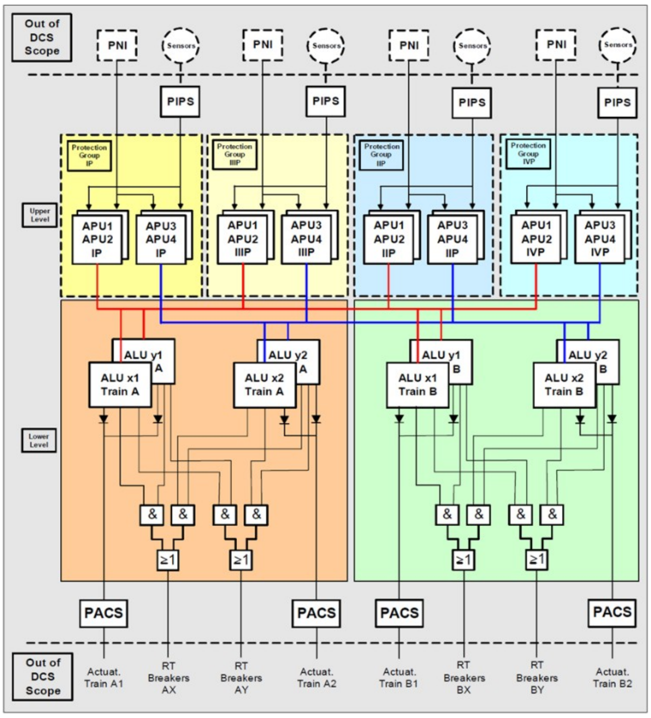

Figure 1: The architecture of the DCS

PNI (Protection Nuclear Instrumentation): these units encompass the detectors that measure the neutron flux produced by the nuclear reactor.

PIPS (Process Instrumentation Pre-processing System): this system is dedicated to the conditioning and the multiplication of the analog signals (except neutron flux) delivered by the 1E sensors. It is implemented within the four protection groups. APU (Acquisition and Processing Unit): these units specialize in the acquisition of the signals delivered by the PIPS and in the processing related to acquisition such as signal validation or threshold detection.

ALU (Actuation Logic Units): these units are dedicated to votes and actuation management (Reactor Trip). They perform logic processing of the signals delivered by the APUs and can generate an order to the reactor trip breakers.

RT Breakers：reactor trip breakers.

3. DEFINITION OF RTS RESPONSE TIME

The Reactor Trip System (RTS) initiates a unit shutdown, based on the values of selected unit parameters, to protect against violating the core fuel design limits and Reactor Coolant System (RCS) pressure boundary during anticipated operational occurrences (AOOs) and to assist the Engineered Safety Features (ESF) Systems in mitigating accidents.

The RTS Response Time shall be that time interval from when the monitored parameter exceeds its RTS trip setpoint at the channel sensor until reactor trip breakers receives the trip signal. The response time may be measured by means of any series of sequential, overlapping, or total steps so that the entire response time is measured. The RTS response time signal transmission path of a typical 4-20mA signal is shown in Figure 2.

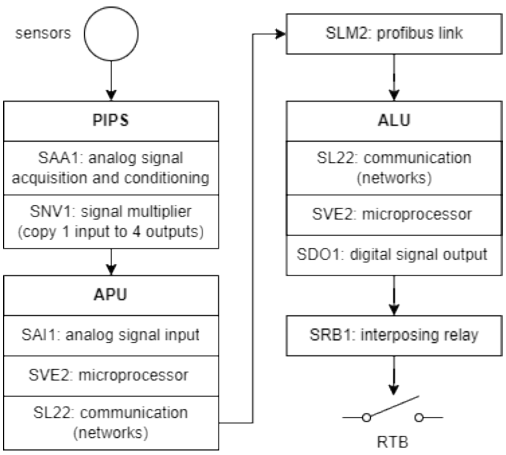

Figure 2: *The RTS response time signal transmission path*

4. CALCULATION OF RESPONSE TIME

According to the define of RTS Response Time, from the moment when an accident requiring actuation of a reactor trip occurs, to the actual actuation of reactor trip signal, the following delays should be considered: delay due to inertia of physical parameters evolution; delay due to sensors response time; delay due to RTS conditioning, acquisition, processing and actuation. This article deals with the RTS response time only.

4.1. Response time of each component

In RTS, the overall response time depends on the individual components processing time. The individual components have the following characteristics.

Table 1: Individual components response times

Component time(ms)	SAA1	SNV1	SAI1	SVE2	SL22	SLM2	SDO1	SRB1
Cycle time	NA	NA	5	50	NA	NA	5	NA
Processing time	<1	5	5	25	<1	7	5	40
Max response time	<1	5	10	75	<1	7	10	40
Min response time	<1	5	5	25	<1	7	5	40
Average response time	<1	5	7.5	50	<1	7	7.5	40

The response time calculation is done the following methods：a processing component (e.g. SAI1 and SVE2) has a cycle time (Tc) and a processing time (Tp), Tp ≤ Tc. For this context, Tc is the fixed calculation time of the processing module for a cycle, Tp is the minimum time for a processing module to react, therefore, Tp+Tc is the maximum time for a processing module to react, when the last cycle the module hasn't process trip signal. If a component does not process the signal in a cyclic manner, the max response time is equal to the min response time and is equal to the processing time.

4.2. The shortest and longest overall response time

If we consider the figure 3, the shortest time to transfer the data is Σ(Tpi), i is the individual component name. For each component that processes the signal in a cyclic manner, the signal is processed exactly in this cycle.

If we consider the figure 4, the longest time to transfer the data is Σ(Tpi+Tci), i is the individual component name. For each component that processes the signal in a cyclic manner, it happens that the signal was not processed in the last cycle, resulting in a missed cycle that can only be processed in the next cycle.

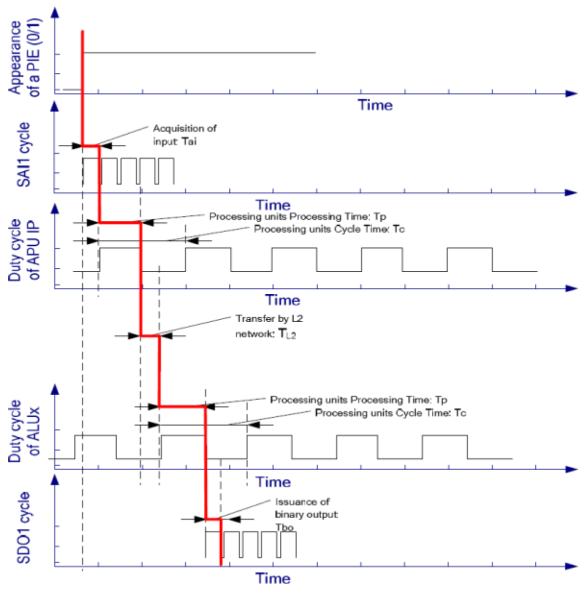

Figure 3: The shortest overall response time

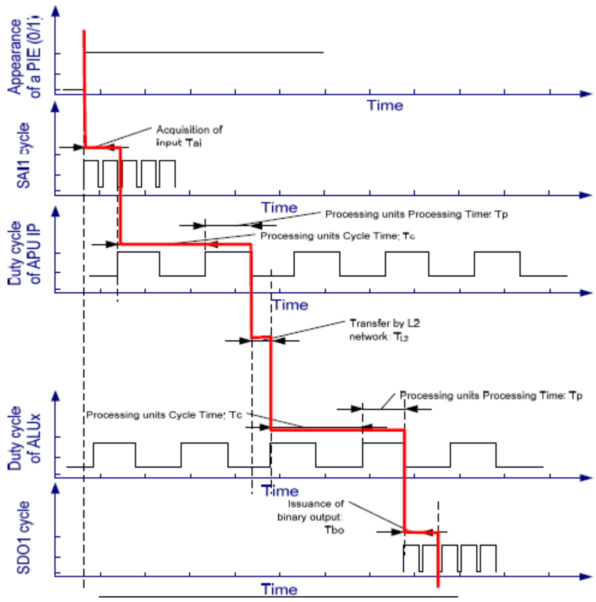

Figure 4: The longest overall response time

When a postulated initiating event (PIE) appears, the PIPS acquires and conditions accident signals， PIPS's components (SAA1 and SNV1) have a fixed response time. The shortest time of APU is min time of SA1+min time of SVE2+fixed time of SL22. The profibus link (SLM2, named L2 network) has a fixed response time too. The shortest time of ALU is like to APU, is fixed time of SL22+min time of SVE2+min time of SDO1.

For the actual Reactor Trip I&C function of the power plant, there are 6 cases:

- CASE1: For RT I&C functions using only standard sensors signals (4-20mA), the whole channel is the following: SAA1 → SNV1 → SAI1 → APU(SVE2) → SLM2 → ALU(SVE2) → SDO1 → SRB1.
- CASE2: For RT I&C functions using temperature probes, the whole channel is the following: STT1 → SNV1 → SAI1 → APU(SVE2) → SLM2 → ALU(SVE2) → SDO1 → SRB1. STT1 is a temperature transmitter, and its characteristics are listed in table 2.
- CASE3: For RT I&C functions using RCP pumps speed, the whole channel is the following: SDI1 → APU(SVE2) → SLM2 → ALU(SVE2) → SDO1 → SRB1. SDI1 is digital signal input, and its characteristics are also listed in table 2.
- CASE4: For RT I&C functions using Source Range neutron flux, the whole channel is the following: SGPIO1 → APU(SVE2) → SLM2 → ALU(SVE2) → SDO1 → SRB1. SGPIO1 is the general-purpose input for Source Range neutron flux and its characteristics are also listed in table 2.
- CASE5: For RT I&C functions using Intermediate or Power Range neutron flux, the whole channel is the following: SAI1 → APU(SVE2) → SLM2 → ALU(SVE2) → SDO1 → SRB1.
- CASE6: For RT I&C function using RCP pumps breakers status, the whole channel is the following: SDI1 → SVE2 → SLM2 → ALU → SDO1 → SRB1.

Table 2: Individual components response times (continue)

Component time(ms)	STT1	SDI1	SGPIO1
Cycle time	333	5	NA
Processing time	300	5	6
Max response time	633	10	6
Min response time	300	5	6
Average response time	466.5	7.5	6

4.3. The average overall response time

Assuming that the component processes each signal equally likely, the probability of processing the signal in one cycle is 1/2. The average response time of individual component is Tavg=Tp+Tc/2. The actual time (Tact) is between the minimum time and the maximum time. Therefore, the deviation between Tact and the Tavg is -Tc/2<(Tact-Tavg)<Tc/2. For overall response time, the average time to transfer the data is Σ(Tpi+Tci/2), i is the individual component name.

4.4. The optimum estimation overall response time

As we know the shortest and longest and average overall response time, but These times may be conservative or coincidental. The shortest and longest time is impossible because several scarce coincidences have to be met. The average time of each individual component has ± Tc/2 error. When we combinate the global error, algebraic sum of these errors is not a good method. Assume that each component is independent of each other and that each component processes signals randomly, the combination error is Root-Mean-Square (RMS) of each error. We call the overall time is optimum estimation response time (Toe). Toe=Σ(Tavgi)+RMS(Tci/2), i is the individual component name.

4.5. Summary of calculation results

So we can calculate all of 6 cases, the time is showed in table 3.

Table 3: Summary of calculation results

Case	Shortest time (ms)	Longest time (ms)	Average time (ms)	Optimum estimation time (ms)
Case 1	81	191	136	171.5
Case 2	381	824	602.5	772.8
Case 3	82	192	137	172.5
Case 4	77	187	132	167.5
Case 5	76	186	131	166.5
Case 6	76	186	131	166.5

5. RESPONSE TIME TEST

The RTS monitors a given number of operating parameters and initiates a protective safeguard action when these parameters exceed the normal range. Each parameter is measured by several redundant channels (generally 3 or 4). A protective safeguard action is only initiated if two out of three, or two out of four signals exceed the setpoint value corresponding to a fault.

5.1. Test methods

Each test is performed by simulating a fault that initiates a reactor trip or protective safeguard action. A check is then carried out to ensure that protection channel response time is well within the limits assumed in accident analyses.

Use RTS special test tool and jumper to simulate input signals of RTS. Steps are taken to ensure that parameters not being checked do not initiate a protective safeguard action. For each test, an out of limit condition is simulated or as many channels as required to initiate a protective safeguard action.

5.2. Test equipment

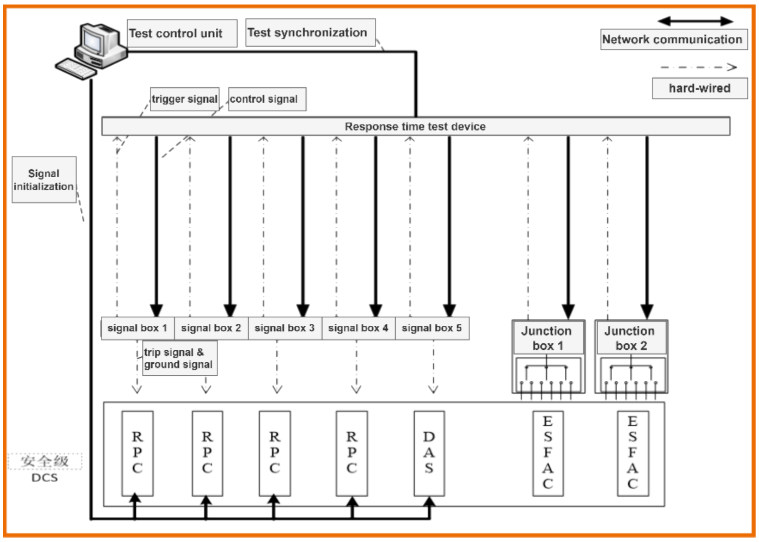

Figure 4: The schematic diagram of the test device

When the above conditions have been satisfied, sensor generated signals are simulated by means of step signals which way between 5 % below and 5 % above the setpoint. A check is carried out to ensure that the protection or safeguard channel under test is operating correctly and within the nominal time limit. If exceeding a setpoint results in several logic signals, the logic outputs are connected in series and the longest response time is recorded.

5.3. Test result

The curves showing the results of case 2 are given in figure 5. The figure shows the maximum response time between the sensors and the last output to Reactor Trip Breakers and the maximum response time between the sensors and the last output to RDU (Rod Drop Units). The response time is given from the last moment the first sensor acquisition is equal to its initial value before going to its trigger value, to the first moment the last output from ALU cabinets goes from its initial value to its trigger value. The high voltage level is normal 5V, the output voltage adds 3V bias for reading.

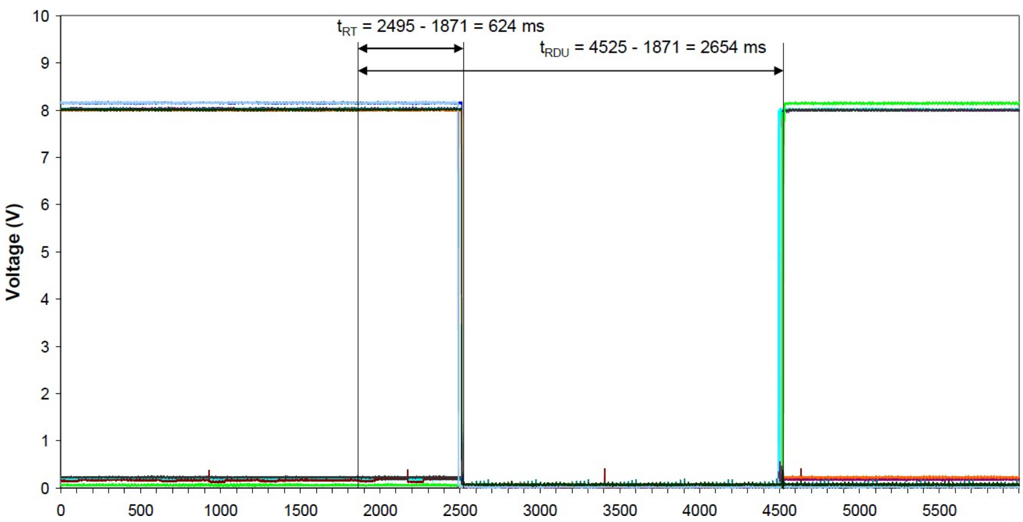

Figure 5: Response time test result of case 2

The results of all 6 cases are shown in table 4.

Table 4 the results of response time test

Case	Test time (ms)	Requirement time (ms)	Average time (ms)	Optimum estimation time (ms)
Case 1	168	200	136	171.5
Case 2	624	700	602.5	772.8
Case 3	151	200	137	172.5
Case 4	149	200	132	167.5
Case 5	138	200	131	166.5
Case 6	142	200	131	166.5

The covariance between test time and optimum estimation time is 39806.93. The covariance between test time and average time is 30925.11. The sample correlation coefficient between test time and optimum estimation time is 0.9989. The sample correlation coefficient between test time and average time is 0.9990. On the whole, optimum estimation time is more correlated with test time and is more conservative.

6. CONCLUSION

In this article, the author used 4 methods to calculate RTS response time. Practical test equipment and scheme was also used. From the actual test results of 6 cases, optimum estimation time has stronger correlation with test time and is more conservative. optimum estimation time is recommended for accident analysis.

Depending on the signal transmission path, the cycle time (Tc) and processing time (Tp) of APU and ALU's microprocessor (SVE2) have a greater impact on the overall response time. In fact, Tc is a fixed time and is equal to 50ms, but Tp is related to the microprocessor load rate. According to the design standard, the load rate is not more than 50%, and the maximum allowable limit in this paper is 50%, so Tp=1/2Tc. Therefore, the optimum estimation time of all 6 cases is greater than the test time. In order to get more accurate results, the further work is to select the actual load rate for each case.

7. REFERENCES

Heinz Prehler, 2006, TELEPERM XS system overview, AREVA NP, Inc.

Béla G. Lipták and Halit Eren, 2011, Instrument Engineers Handbook. New York: CRC Press. US

NRC, 1997, NUREG-0800.BTP7-21. Guidance on Digital Computer Real-Time Performance.

Yang LIU, 2020, A response time evaluation method of reactor protection system implemented by DCS, China Nuclear Power, Volume 13, 606-610.

Xuehui SUN, 2016, Analysis and test of response time of nuclear power plant digital control system to avalanche, Nuclear Science and Enginnering, Volume 36, 843-849.

Yong XU, 2017, Research of test scenario of T2 response time of reactor protection system, Nuclear Power Engineering, Volume 38, 116-119

Deying DONG, 2020, The design of automatic testing system for nuclear protection system response time, Nuclear Electronics & Detection Technology, Volume 40, 504-507

#314: Study on water temperature prediction and control strategy for household air source heat pump system using floor heating

Haiying WANG[1*], HANG MENG[1], Fengming ZHANG[1], Renjie YAN[1], Junli SUN[1], Huxiang LIN[1]

[1] Qingdao University of Technology, No. 777 Jialingjiang East Road in Huangdao District, Shandong province, China
*Corresponding author: Wanghaiying@qut.edu.cn

Abstract: Air source heat pump is one of the most important forms of clean heating. It is widely used in residential buildings. When heating with radiant floors, the floor's inherent heat storage exothermic properties result in a delayed thermal response to the changes of heating regulations. During the change of outdoor temperature and electricity price, how to control the indoor thermal environment and achieve operation saving is one of the issues to be studied related to air source heat pumps. This paper establishes a mathematical model for predicting the system's hour-by-hour water supply temperature based on meteorological parameters and the indoor heating temperature through buildings' heat balance relationship. A simplified model for supply water temperature controll is proposed considering the thermal inertia of floor. At the same time, a system simulation model was established using TRNSYS. Considering the influence of changes in outdoor temperature, heating load, thermal inertial characteristics of the floor, four different control strategies were proposed. According to the simulation results, with these control strategies, the indoor air room temperature can be controlled within the target range, and the maximum room temperature change was only 0.6℃on typical day. The energy use can be reduced by approximately 20% compared to the actual condition, in which overheating happens sometimes. The proposed time-shift shutdown controls can achieve energy saving, while keeping stable thermal environment during heating in residential buildings.

Keywords: Air Source Heat Pumps, Radiant Floor Heating, Supply Water Temperature Prediction, Control Strategy

1. INTRODUCTION

Air source heat pumps use electrical energy to absorb heat from a low-temperature heat source and provide heating for buildings. The flexibility in installation, use, and control makes the systems applicable in various conditions (Wang, 2020) (Zhang, 2018), especially in small residential buildings such as upscale communities and rural townships (Qu, 2016). Common heating terminals included radiators and floor radiant heating (Lin, 2016) (Sangmu, 2020). When using floor radiant heating, the indoor temperature could be 2-3 ℃ lower than that of the radiator heating while achieving the same comfort level, which reduces heat consumption during the heating season (Liu, 2003).

For small air source heat pump systems, users could set and control the heating system according to their needs. However, in practice, improper control or use could lead to poor heating performance or high energy consumption. Keeping indoor thermal comfort while adopting control strategies that enable efficient operation of the units is a crucial issue worthy of attention, which affected the energy-saving and running economic of air source heat pumps.

Previously, a detached house using an air source heat pump system in the form of radiant floor was tested, which lies in a cold climate zone. The building has two floors. The first floor includes a living room, a south-facing bedroom, a kitchen, a dining room, and a bathroom, with a small plant room under the stairwell. The second floor comprises a living room, south and north-facing bedrooms, a bathroom, and a corridor. The building has an area of approximately 300 square meters, of which about 280 square meters are heated using floor radiant heating (Li, 2023). The test was conducted during the 2021-2022 heating season, which was from 19th Nov. of 2021 to March 7th of 2022 by the use. The continuously monitored parameters included outdoor temperature and relative humidity (RH), temperature and RH in the main rooms, and the electricity consumption of the heat pump unit and water pump. Additionally, an on-site test was conducted from January 14 to January 18, 2022, focusing on parameters such as the supply and return water temperatures of the system and the system's circulation flow rate. Surface temperatures of the envelope structures in typical rooms were also tested. In the heating season, the measured outdoor temperature fluctuated between -10.8 ℃and 22.7 ℃, with an average value of 2.8 ℃. The outdoor RH fluctuated between 24.3 % and 99.9 %, with an average value of 71.4 %. The air source heat pump unit was controlled to maintain a constant outlet water temperature of 35 ℃, while the unit was equipped with variable frequency control. The room heating temperature was set to 20 ℃ and aimed to be kept in the range of 19-21 ℃. Data analysis based on the measured data showed that the room temperatures constantly exceeded the set range by 1-5 ℃ during the daytime, which led to overheating. The system could not ensure a stable indoor temperature environment, and also resulted in increased energy consumption.

To address the above issues, the heat transfer characteristics of floor heating were analysed, and the control strategies of the air source heat pump system were optimized. For the room temperature control of air source heat pump system, effective control methods include room temperature feedback control (Liu, 2022), algorithm optimization control under target constraints (Sun, 2022) (Zhang, 2021), et al. Considering the thermal inertial characteristics of the floor in radiant floor heating systems, this paper primarily aims to achieve steady room temperature by regulating supply water temperature and shut-down controls. Based on the character of floor radiant heating system, the supply water temperature control and optimized controls were proposed. By system simulation, the control strategies and effect on thermal environment and energy use were compared.

2. HEATING SYSTEM CONTROL METHODS

2.1. Transfer of radiant floor heating

The heat transfer in a radiant floor heating system includes conduction, convection, and radiation. By increasing the floor surface temperature, radiant heat exchange occurs between the floor's radiating surface and the human body as well as other interior enclosure surfaces. As the floor surface temperature rises, convective heat exchange with the indoor air also occurs and increases the indoor air temperature (Zeng, 2010).

When using radiant heating, the primary heat exchange processes within the space are illustrated in Figure 1. For floor heating, the control of air source heat pump cause temperature changes within the floor structure first. Due to the heat storage and thermal inertial of floor structure, there exist delays in heat transfer process in response to the system control. Consequently, the indoor air temperature cannot change promptly upon any control signals, resulting in control lag and potentially issues such as temperature deviations from the target one. Considering the thermal inertial of floor and response lag in control, a few concepts are proposed. The time constant (Lin, 2019) refers to the heating time required for the floor temperature to reach 63.2 % of the total temperature rise when the floor is continuously heated. The time constant can be calculated by Equation 1. The value of the time constant reflects the rate at which the floor is heated up. The floor heating time is approximately considered to be the time it takes for the floor temperature to reach 95 % of the new equilibrium temperature. At this point, the average surface temperature of the floor is considered to be the final temperature of the heating process.

The factors influencing the time constant and the heating time of the concrete floor are the same. Both are directly proportional to the density, specific heat capacity, thickness, and thermal resistance of the floor structure material, and are independent of the heating capacity and initial temperature. The final temperature of the floor is related to the ambient operating temperature during the floor heating process, the internal thermal resistance of the floor, the overall heat transfer resistance of the floor surface, and the supply water temperature, but it is independent of the initial temperature of the floor.

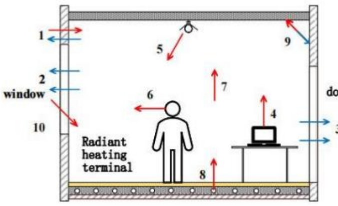

Figure 1: Thermal exchange processes within the building for floor radiant heating

Equation 1: Time constant calculation formula.

$$T = (c_p \times \rho \times V)/(A_b \times (1/R + h_z))$$

Where:

- T = time constant (s)
- c_p = specific heat capacity of floor material (J/kg℃)
- ρ = density of floor material (kg/m^3))
- V = volume of concrete floor (m^3)
- A_b = surface area of concrete floor (m^2)
- R = thermal resistance from the heating pipe wall to the floor surface (m^2℃/W)
- h_z = overall heat transfer coefficient between the floor surface and indoor air (W/m^2℃)

2.2. Building thermal balance and calcualtion of supply water temperature

Wang et al. (2022) established a heat transfer model for rooms with floor radiant heating using the thermal balance equation. They unified the influence of indoor and outdoor parameters on the overall heat transfer coefficient of the floor surface as the influence of temperature difference and verified the feasibility of the model through experiments. The literature suggests that the mathematical formula for the overall heat transfer coefficient of the floor surface should not be determined solely by the temperature difference but should also be determined by the temperature difference and the indoor air temperature.

The complex heat transfer processes within a building could be divided into two categories: heat gain and heat loss. During winter, to maintain the target room temperature, the heat loss to the outside under steady-state conditions shouldequal to the total heat gain from all indoor heat sources. By using the calculated building heat load and system heat supply as the heat loss and heat gain respectively, an ideal thermal balance equation for the building can be established.The building heat load can be calculated using energy consumption calculation software, where model parameters such as meteorological data, building information, occupancy, lighting, equipment, and indoor set heating temperature need tobe set according to measured data. The heat supply needs to be obtained through measurements of the heating system.

Taking into account the combined influence of factors such as radiation and convection on the thermal environment, the operative temperature is use to represent the target room temperature. The supply heat can be calculated based on the circulating water flow rate and the supply-return water temperature difference. The thermal balance equation is as follows:

Equation 2: The thermal balance equation where the building heat load equals the system heat supply.

$$K_w F_w (t_{op}\text{-}t_w) = \rho_w c_w V(t_{in}\text{-}t_{out})$$

Where:

- K_w = Overall heat transfer coefficient of the building envelope (W/m^{2}K)
- F_w = Surface area of the building envelope in contact with outdoor air (m^2)
- t_w = Outdoor air temperature (℃)
- t_{op} = Operative Temperature (℃)
- ρ_w = Density of circulating water (kg/m^2)
- c_w = Specific heat capacity of circulating water (J/Kg℃)

- t_{in} = Supply water temperature (℃)
- t_{out} = Return water temperature (℃)

The heat supplied by the system is equal to the radiant heat supplied by the floor under steady condition. The formula is as follows:

Equation 3: The thermal balance equation where the system heat supply equals the radiant floor heat supply.

$$K_w F_w (t_{op} - t_w) = \rho_w c_w V_w (t_{in} - t_{out}) = h_{total} F (t_f - t_{op})$$

Where:

- V_w = Volume flow rate of circulating water (m^3/h)
- F = Surface area of concrete floor in contact with indoor air (m^2)
- t_f = Average Temperature of the Floor Surface (℃)
- h_{total} = Overall Heat Transfer Coefficient of the Floor Surface (W/m^2K)

In practice, when the building envelope materials and design parameters are fixed, the variables Kw, htotal, Fw, and F are constants in the equation. Similarly, when the materials and design parameters of the heating terminal are set, there is a certain mathematical relationship between the supply water temperature and the average temperature of the floor surface. This relationship can be further derived to obtain the predictive relationship for the hourly supply water temperature corresponding to the hourly heating load under given meteorological parameters and indoor set heating temperature, as follows:

Equation 4: Equation for predicting hourly system supply water temperature.

$$t_{in} = \left[(K_w F_w / h_{total} F)\left(t_{op} - t_w\right) + t_{op} \right] + \Delta t$$

In the equation, Δt (℃) represents the mathematical fitting relationship of difference between the supply water temperature and the average temperature of the floor surface, which is determined by establishing a model for concrete floor radiant heating and further simulation calculations in this study.

3. MODEL CONSTRUCTION AND CONTROL STRATEGIES

3.1. Floor heat transfer model

The heat transfer in floor heating primarily involved complex processes such as convective heat transfer between low-temperature hot water and the inner wall of buried coils, conductive heat transfer between the inner and outer walls of buried coils, conductive heat transfer through the floor structure layers, and convective heat transfer at the floor surface. Therefore, a model was constructed by FLUENT based on the concrete floor of the measured house. The model setup is illustrated in Figure 2, which is a local model considering the symmetry of structure.

The structure of the radiant heating floor from top to bottom consists of the floor surface layer, levelling layer, filling layer, insulation layer, floating layer, and ground layer. In the model, materials were set according to those used in practice, and the physical properties of each material are as shown in Table 1. The spacing between the buried heat exchange pipes was 200 mm.

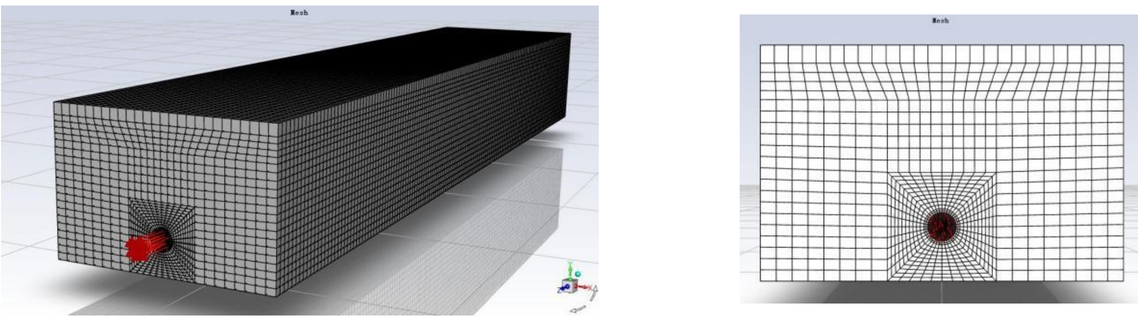

Figure 2: The model and meshing of the concrete floor

Table 1: Table of material properties

Material name	Thermal conductivity W/(m·K)	Specific heat capacity kJ/(kg·K)	Density Kg/m³
Cement mortar	0.93	1.05	1800
Expanded clay concrete	0.49	0.84	1450
Polystyrene foam	0.039	1.38	20
Marble	2.91	0.92	2800
Polyethylene pipe (PE pipe)	0.42	2.3	940

In this model, the Standard k-ε model was selected as the fluid calculation model. The model settings include velocity-inlet and pressure-outlet, with the inlet water flow velocity calculated based on the circulation water flow rate and the cross-sectional area of the buried coil, resulting in a water flow velocity of 0.21 m/s. The maximum number of iterations was set to 20, and the time step was set to 60 seconds.

To determine the time constant, final temperature, surface temperature variation, different step change conditions for the supply water temperature were set at 3°C and 5°C, respectively. And surface temperature response time of the concrete floor structure, non-steady-state simulation calculations were conducted for 14 hours of heating and cooling. The statistical simulation conditions and results are presented in Tables 2, 3 and 4.

Table 2: The simulated conditions in step temperature change

Operating conditions	Temperature variations for each operating condition (℃)				
Step temperature difference		5℃		3℃	
Step heating condition	25~30	30~35	35~40	32~35	35~38
Step cooling condition	30~25	35~30	40~35	35~32	38~35

Table 3: Results of step heating conditions

Operating conditions	Response time of the average surface temperature of the floor /min	Initial average surface temperature of the floor /℃	Final average surface temperature of the floor /℃	Final average surface temperature of the floor /℃	Time constant /h
25-30℃	21	24.29	25.65	1.36	4.08
30-35℃	19	25.74	27.10	1.36	4.07
35-40℃	20	27.19	28.55	1.36	4.07
32-35℃	24	26.32	27.12	0.8	4
35-38℃	26	27.19	28.01	0.82	4

Table 4: Results of step cooling conditions

Operating conditions	Response time of the average surface temperature of the floor /min	Initial average surface temperature of the floor /℃	Final average surface temperature of the floor /℃	Final average surface temperature of the floor /℃	Time constant /h
40-35℃	22	28.64	27.29	1.35	4.03
35-30℃	19	27.19	25.84	1.35	4.03
30-25℃	19	25.74	24.39	1.35	4.03
35-32℃	25	27.19	26.38	0.81	4.05
38-35℃	26	28.07	27.26	0.81	4.05

Analysis of the simulation data reveals that the time constants of typical concrete floor structures under different heating/cooling conditions were approximately 4 hours and were independent of the step temperature difference of the supply water. This indicates that the heating/cooling time of concrete floors is not affected by the step temperature difference of the supply water. Based on the simulation data, the mathematical fitting relationship between the supply water temperature and the average surface temperature of the floor is as follows:

Equation 5: The mathematical fitting relationship is as follows.

$$\Delta t = 36.016 \cdot e^{[-8.3/(t_f\text{-}22.375)]}$$

Considering meteorological parameters and indoor temperature target, the simplified mathematical model for predicting hourly supply water temperature corresponding to hourly building heat load can be represented by Equation 6, as follows:

Equation 6: The simplified mathematical model for predicting hourly system supply water temperature is as follows.

$$t_{in} = \left[\frac{K_w F_w}{h_{total} F}\left(t_{op}\text{-}t_w\right) + t_{op}\right] + 36.016 \cdot e^{[-8.3/(t_f\text{-}22.375)]}$$

3.2. System model of air source heat pump heating

The building model was built up by SketchUp, and the TRNSYS energy simulation software was employed to model the air source heat pump heating system. The building picture and SketchUp three-dimensional model are shown in Figure 3. The system model is shown in Figure 4.

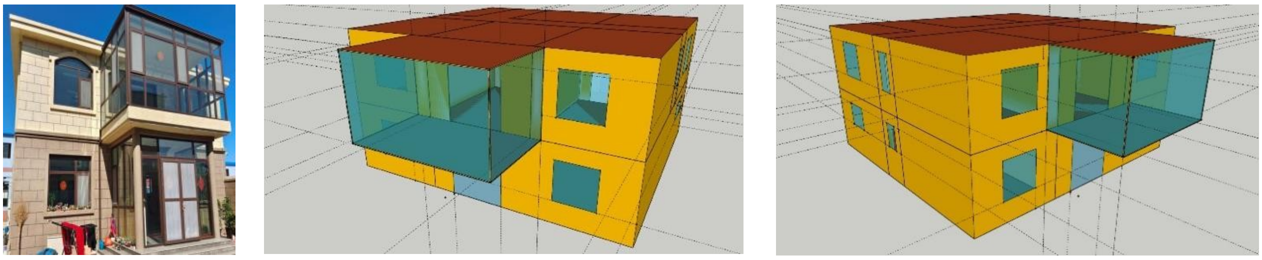

Figure 3: The building picture and SketchUp three-dimensional model

Referring to the actual building, the thermal parameters of the building envelope are set as shown in Table 5, which satisfy the requirements of the related standard (Lin, 2017) (Xu, 2012).

Table 5: Building envelope information

Structure name	Structure composition	Heat transfer coefficient [W/(㎡·K)]
Exterior wall	20mm cement mortar + 200mm reinforced concrete + 40mm polystyrene board + 20mm cement mortar	0.557
Interior wall	10mm cement mortar + 180mm brick wall + 10mm cement mortar	2.417
Roof	20mm cement mortar + 200mm reinforced concrete + 60mm extruded polystyrene foam + 20mm cement mortar	0.430
Ground floor	10mm marble + 20mm cement mortar + 80mm expanded clay concrete + 40mm polystyrene foam + 20mm cement mortar	0.710
Second floor	10mm marble + 20mm cement mortar + 120mm expanded clay concrete + (40mm polystyrene foam) + 20mm cement mortar	-
Window	6mm medium transparent heat reflection + 16mm air + 4mm transparent	2.360

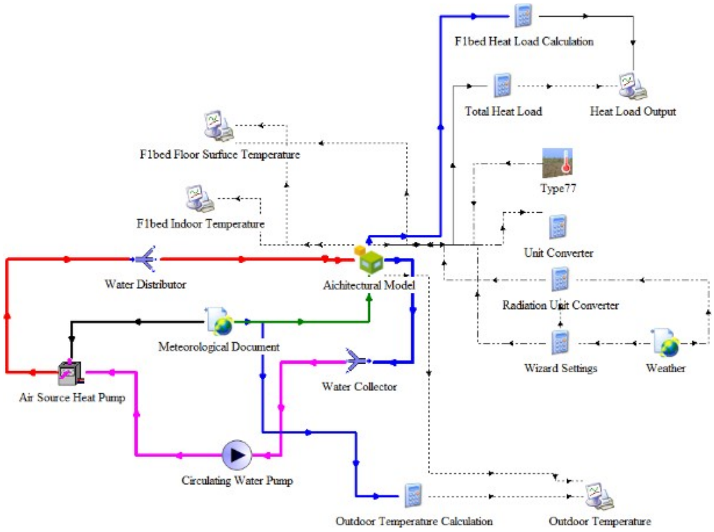

Figure 4: TRNSYS system model for air source heat pump

The indoor heating set temperature was 20 °C, the air exchange frequency was 0.6 times/hour, the equipment power density was 3.8 W/m², the lighting power density was 5 W/m². The schedules of equipment, lighting and occupancy were all set according to the daily behaviour of the house residence. The heating system consists of an air source heat pump, a heat exchanger module, a circulating water pump, a building model, a water distributor, a water collector, and a meteorological input file. The parameters of air source heat pump module are set according to the actual performance parameters. The coefficient of performance (COP) of heat pump was fitted based on the measured data during the heating season (Li, 2023). The circulating water pump module is a fixed-frequency pump with a circulating water flow rate of 2.5 m³/h, a motor power of 180 W. The measured meteorological parameters of the season are imported through the meteorological file.

Data on typical days and weeks are used to verify the model. The changes of heating load on typical day and week are basically the same in simulation to the measured values. In the typical day, the average heat supply is 0.87 kWh/㎡ in simulation, and the measured value is 0.88 kWh/㎡. The error is only 1.14 %. In the typical week, the average heat supply is 6.8 kWh/㎡ in simulation, and the measured value is 6.6 kWh/m^2, with an error of 2.41 %. For the power consumption of the heat pump system, the maximum error between the simulated and measured hour-by-hour power consumption is 9.94%, the average error was lower than 5%. Therefore, the simulation is quite accurate.

3.3. Control strategy for heating systems based on building thermal balance

Theoretically, to keep steady indoor temperature, the system's hourly supply water temperature could be calculated using Equation 6, this was named Condition one. Considering the hourly change in supply water temperature could be difficult for the heating system, control strategy two (Condition two) were proposed. For this strategy, the time when the outdoor air temperature changes by 2 °C/h was selected, and the average supply water temperature during this corresponding time period was calculated to be the target outlet water temperature for the heat pump.

Based on the average supply water temperature, when the outdoor temperature rises, the hourly supply water temperature of the unit will decrease, and in reality, the heat pump will be in an idle state. Therefore, a segmented shutdown control for the unit should be considered. The moments when the outdoor temperature reaches its maximum rate of increase and when the outdoor temperature began to rise were chosen as the moments for the system's shutdown control. By analysing the outdoor temperature data and time constant of floor, it was determined that 6:00 was the starting time of shutdown. Considering the thermal response characteristics of the floor, a shutdown time interval of 4 hours (time constant) was set. Based on this, two control strategies for segmented (start-stop) operation were defined: Condition Three (shutdown time: 8:00-12:00) and Condition Four (shutdown time: 6:00-10:00). The four controls are shown in Table 6. The corresponding TRNSYS simulation system is shown in Figure 7.

Table 6: Control strategies and simulation content

Operating conditions	Control strategy	Control mode	Input value of supply water temperature	Control content
Condition one	Continuous operation	Calculated values of supply water temperature based on building thermal balance mathematical model	Hourly supply water temperature	—
Condition two		Average supply water temperature replacing hourly supply water temperature in operating condition one	Average supply water temperature	—
Condition three	Time sharing operation	Shutdown control based on the time period with the maximum outdoor temperature rise rate		Shutdown from 8:00 to 12:00 (4 hours)
Condition four		Shutdown control based on the time period when outdoor temperature starts rising		Shutdown from 6:00 to 10:00 (4 hours)

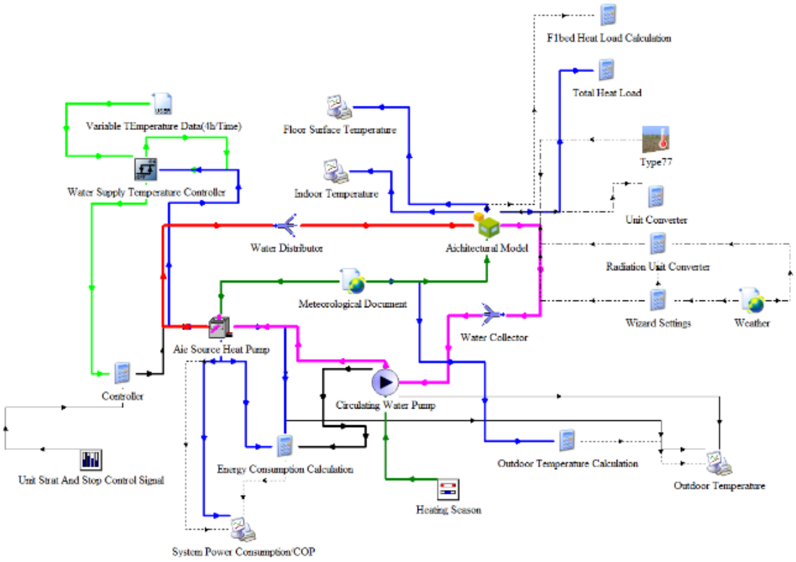

Figure 7: The corresponding TRNSYS simulation system

4. SIMULATION RESULTS

4.1. Simulation results of room temperature

In this study, the actual heating time (109 days from November 19, 2021, to March 7,2022) were chosen as the simulation time. Typical days and typical weeks were selected to analyze the temperature simulation results of each condition. The climate data used in the simulation were the measured data during the heating season. The hourly system supply water temperature or average temperature corresponding to the hourly building heat load based on meteorological parameters and indoor set heating temperature (20 °C) were calculated.

Figure 8 shows the temperature simulation results of typical days for the four operating conditions. The measured indoor temperature in the figure was the indoor air temperature of the south-facing bedroom on the first floor, which was higher than 20 °C and increased to a much higher temperature during noontime.

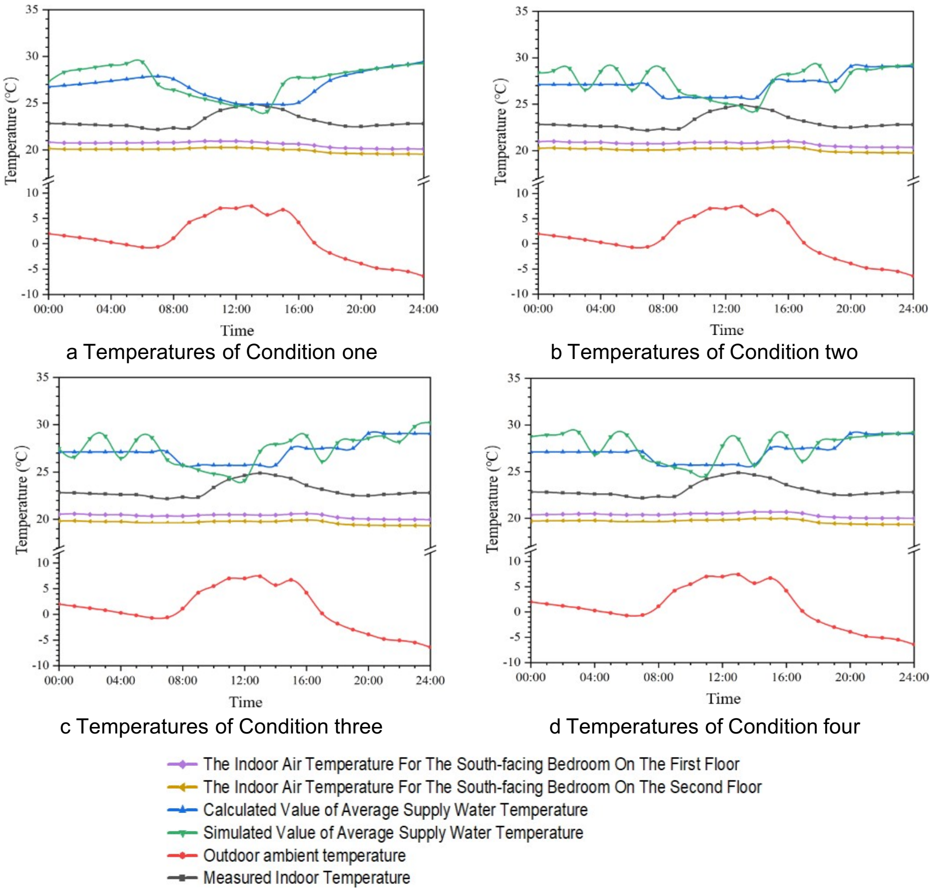

a Temperatures of Condition one
b Temperatures of Condition two
c Temperatures of Condition three
d Temperatures of Condition four

Figure 8: Simulated temperatures of the four conditions

For Condition one, the simulated supply water temperature fluctuated in the range of 24.3 °C and 30.2 °C. The indoor air temperature of the south-facing bedroom on the first floor fluctuated between 20.7 °C and 21.1 °C, with a temperature range of 0.4 °C. For the room on the second floor, the indoor air temperature fluctuated between 19.9 °C and 20.5 °C, with a temperature range of 0.6 °C. The temperature of both rooms was changed within ±1 °C from the aimed temperature of 20 °C. Compared with the temperature variation in the actual room, the daily temperature ranges from 6:00 to 18:00 was reduced from 3.4 °C to 0.3 °C. This strategy can keep indoor temperatures steady and close to the target temperature.

For Condition two, the simulated supply water temperature was in the range of 24.7 °C and 29.3 °C. The indoor air temperature in the south-facing bedroom on the first floor fluctuated between 20.6 °C and 21.2 °C, with a temperature range of 0.6 °C. In the south-facing bedroom on the second floor, the indoor air temperature fluctuated between 20 °C and 20.6 °C, with a temperature range of 0.6 °C. It could be considered that replacing the hourly supply water temperature (Condition one) with the average supply water temperature had no significant impact on the temperature control results.

In Condition three, the average simulated supply water temperature decreased from 27.7 °C to 27.3 °C. The simulated supply water temperature on a typical day fluctuated between 24.4 °C and 29.3 °C. The indoor air temperature in the south-facing bedroom on the first floor fluctuated between 20.4°C and 20.9°C, with a temperature range of 0.5 °C. In the south-facing bedroom on the second floor, the indoor air temperature fluctuated between 19.7 °C and 20.3 °C, with a temperature range of 0.6 °C. The temperature ranges for both rooms were within ±1 °C of the set heating temperature of 20 °C.

Compared to operating Condition three, in Condition four, the interval for lowering the supply water temperature was reduced from 5 h to 4 h. The average simulated supplied water temperature decreases from 27.7 °C to 27.4 °C. The simulated supply water temperature on a typical day fluctuated between 24.3 °C and 29.7 °C. The indoor air temperature in the south-facing bedroom on the first floor fluctuated between 20.5 °C and 20.9 °C, with a temperature range of 0.4 °C. In the south-facing bedroom on the second floor, the indoor air temperature fluctuated between 19.6 °C and 20.4 °C, with a temperature range of 0.8 °C. The temperature changes for both rooms were also within ±1 °C.

4.2. Energy consumption simulation results

In order to make clear the energy consumption of the system under different control strategies, the energy consumption per unit building area for each operating condition during the heating season was analysed. The simulation results are shown in Figure 9.

The measured average indoor air temperature for the first-floor room was approximately 23 °C, and for the second-floor room, it was approximately 21 °C. The tested energy consumption per unit building area was 29.68 kWh/㎡. From Figure 7, in Condition one, where the indoor heating set temperature was 20 °C for both the first and second floors, the energy consumption per unit building area was 23.56 kWh/㎡, which was 20.62 % lower than the measured energy consumption. In Condition two, using the average supply water temperature instead of the hourly supply water temperature as the system model input value, the energy consumption per unit building area was 23.48 kWh/㎡, which was 0.34 % lower than that in Condition one. For Condition three and four the consumption was 22.83 kWh/㎡ and 22.57 kWh/㎡, respectively. Compared to Condition two, energy consumption decreased by 3.11 % and 4.2 % further.

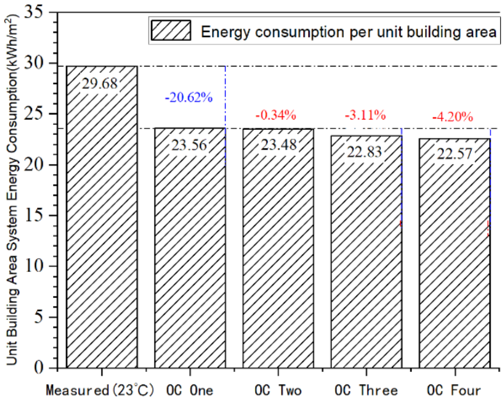

Figure 9: Simulation results of system energy consumption

The measured energy efficiency ratio (EER) of the system was in the range of 2. 36 ~ 4. 44, with a mean value of 3. 34 during the field test (Li, 2023). With the four control strategies proposed in this paper based on the time-by-time water supply temperature control and the time-sharing operation control, the simulated EER is in the range of 3.70 to 3.77, which is improved by 6.8%-12.9%. The changeable supply water temperature increases the COP and EER.

5. CONCLUSION

In this study, the floor heat transfer model was built. The simulation shows that the heating/cooling time of a concrete radiant floor is primarily related to the physical properties of the floor structure and material layers and is independent of the initial temperature and step temperature difference. The time constant for commonly used concrete floor structures is approximately 4 hours.

Based on the hourly supply water temperature of the system was established using building thermal balance equations, considering meteorological parameters and the indoor set heating temperature. A The simulation data shows that using the hourly supply water temperature and average supply water temperature calculated by the prediction model, the room temperature can be maintained within the target range (20±1 °C). The maximum room temperature variation on a typical day is 0.6 °C. With better indoor temperature control, energy consumption can be reduced by approximately 20% compared to the actual operation. When using the time-sharing operation control strategies, the operating energy consumption of the unit is further reduced by 3-4 %, and the room temperatures still remain within the target range, with amaximum room temperature variation of 0.8 °C on a typical day.

The results provide useful information about the thermal inertial for the floor heating structure. The shutdown control strategies of Condition three and four can be referred to achieving steady room thermal conditions. However, the proposed control strategies need to be verified in practice.

6. ACKNOWLEDGEMENT

This research was supported by the Natural Science Foundation of Shandong Province (No. ZR2022ME035).

7. REFERENCES

Li, J. (2023) 'Operation and Analysis of Air Source Heat Pump Floor Heating System in Cold Regions', Building Science, 39, pp. 105-112. (in Chinese)

Lin, B. (2016) 'Evaluation and comparison of thermal comfort of convective and radiant heating terminals in office buildings', Building and Environment, 106, pp. 91-102.

Lin, H. (2017) 'Code for Thermal Design of Civil Buildings of China', China Architecture & Building Press. (in Chinese)

Lin, J. (2019) ‘Stable Heating Calculation Model for Low-temperature Hot Water Radiant Floor’, Solar Energy Journal, 40, pp. 914-920. (in Chinese)

Liu, M. (2022) ‘Target temperature control strategy for air source heat pump load based on model predictive control’, Shandong Power Technology, 49, pp. 53-59. (in Chinese)

Liu, Y. (2020) ‘Analysis of Energy-saving Effects of Low-temperature Floor Radiant Heating’, Energy Engineering, 03, pp. 54-56+62. (in Chinese)

Qu, M. (2016) ‘The Impact of Different Energy Storage Defrosting Modes of Air Source Heat Pumps on Indoor Thermal Comfort’, Fluid Machinery, 44, pp. 60-65. (in Chinese)

Sangmu, B. (2020) ‘Comparative Analysis of System Performance and Thermal Comfort for an Integrated System with PVT and GSHP Considering Two Load Systems: Convective Heating and Radiant Floor Heating’, Energies, 13, pp. 5524-5524.

Sun, R. (2022) ‘Research on the operation optimization of air source heat pump heating system based on particle swarm algorithm’, Renewable Energy, 40, pp. 1465-1472. (in Chinese)

Wang, D. (2020) ‘Evaluation of Indoor Environment for Different Clean Heating Methods in Rural Residences of Tianjin’, Building Science, 36, pp. 126-132. (in Chinese)

Wang, L. (2017) ‘Experimental study of air source heat pump operation based on refrigerant capillary floor heating’, Building Science, 38, pp. 105-114. (in Chinese)

Wang, M. (2020) ‘Generic mathematical formulation of the total heat transfer coefficients between heated radiant floor surfaces and rooms’, Building and Environment, 211. (in Chinese)

Xu, W. (2012) ‘Technical Specification for Radiant Heating and Cooling of China’, China Architecture & Building Press. (in Chinese)

Zeng, Z. (2010) ‘The Efficiency of Air Source Heat Pump Direct Floor Radiant Heating and Research on Floor Heat Transfer’, Zhengzhou University. (in Chinese)

Zhang, Y. (2021) ‘Research on control strategy of domestic air source heat pump heating system’, Harbin Institute of Technology. (in Chinese)

Zhang, Z. (2018) ‘Analysis of Indoor Thermal Comfort in Floor Radiant Heating Systems’, Science, Technology and Engineering, 8, pp. 321-328. (in Chinese)

#315: Research on natural lighting design of college gymnasiums in hot summer and warm winter areas based on dynamic lighting evaluation

Shuqi WU[1], Hui JI[1]

[1] Guangdong University of Technology, Guangzhou,Guangdong Province, archwsq0130@163.com.

Abstract: As a core component of the infrastructure of colleges and universities, gymnasiums have the remarkable characteristics of large number and high frequency of use. However, the current university gymnasiums generally have problems such as roughness and obvious defects in lighting design, leading to low visual comfort and high energy consumption of artificial lighting. The research found that these problems mainly stem from the change of natural light, the shading of the building environment and the unreasonable lighting arrangement. Reasonable use of natural light not only optimizes the indoor sports environment for athletes and improves visual comfort, but also significantly reduces energy consumption, which has a positive impact on athletes' sports training and competition level. Currently, college gymnasiums in Guangzhou area overly rely on artificial lighting and neglect the application of green building technology. This study introduces the dynamic lighting evaluation index into the natural lighting design of Hangzhou university gymnasiums and explores the lighting problems of the gymnasiums and puts forward optimization suggestions through actual measurement and simulation analysis. Firstly, the problem of insufficient quantity and quality of lighting in the gymnasium is summarized through all-day dynamic lighting measurement, and improvement measures are proposed accordingly. Secondly, Ladybug software is used to simulate different lighting outlet designs, evaluate their impact on the lighting environment in the sports venues, and make suggestions for the design of lighting outlets. Once again, a lighting assistance system was added to simulate and analyze its effect on the lighting quality and to derive the optimal design parameters. Finally, the above studies are synthesized to propose the design of natural lighting in Guangzhou university gymnasiums in order to guide the actual projects and achieve sustainable development.

Keywords: Natural Daylighting Design, College Gymnasiums, Dynamic Daylighting Evaluation, Ladybug

1. INTRODUCTION

As of May 31, 2022, there were a total of 3,013 institutions of higher education in China, including 2,759 general institutions of higher education, including 1,270 undergraduate colleges and universities, 1,489 higher vocational (specialized) colleges and universities, and 254 adult institutions of higher education. In these institutions, gymnasiums, as an important sports infrastructure, play a key role in daily physical education, sports training, as well as public sports events and publicfitness activities.

With the deepening of "national fitness" activities and the popularization of the concept of "green building", the lighting design of gymnasiums has received more and more attention. Reasonable lighting designs can not only provide a good visual environment, promote the physical and mental health of athletes, but also significantly reduce the energy consumption of artificial lighting. However, the current lighting design of many gymnasiums is inadequate, often neglecting the full use of natural light, resulting in high energy consumption.

For this reason, this study is aimed at an in-depth discussion of the daylighting design of college gymnasiums. Through field research on the building spatial information and lighting indexes of the gymnasium of Guangdong University of Technology in China, combined with a parametric platform with modified typical annual meteorological parameters for simulation and analysis, it aims to explore the trend of changes in the quantity and quality of lighting under different forms of lighting openings, such as skylights and side windows.

The results of this research will provide scientific guidance for the lighting design of gymnasiums, which will help to improve the quality of lighting and realize the goal of energy-saving and environmentally friendly buildings. It also provides new ideas and methods for future research in the field of gymnasium design.

2. EVALUATION INDICATORS OF NATURAL LIGHTING

2.1. Dynamic evaluation indicators

Since the natural lighting conditions change due to the dynamic effects of the sun and weather conditions, a series of dynamic Lighting evaluation metrics. The parameters commonly used in the study are:

(1)Daylightfactor（DF）

Definition: the ratio of the illuminance at a point on the indoor reference plane, resulting from the direct or indirect reception of diffuse light from the sky from an assumed and known sky luminance distribution, to the illuminance of diffuse reflected light from the sky generated by that hemisphere of the sky at the same moment on the outdoor unobstructed horizontal plane [58]. As shown in Table 2.2, the minimum required DF value for lateral lighting in sports buildings is 2.0% and the minimum required DF value for top lighting is 1.0% [4].

(2) Daylight Autonomy (DA)

Definition: the proportion of moments in the working face when the illuminance value is greater than the threshold for turning on artificial lighting as a percentage of the total number of moments in the year.DA indicates the efficiency of a building's use of natural light, a parameter first defined in the 1989 Swiss Lighting Design Standard and later redefined by Reinhart and Walkenhorst: the total number of moments on the working surface where the illuminance value meets the minimum illuminance value required for natural lighting as a proportion of the total number of moments in the year [64]. The percentage of time during the working hours of the year when the minimum illuminance requirement can be met by natural lighting alone.

(3) DAcon (Continuous Daylight Autonomy)

Definition: The DAcon parameter was first proposed by Prof. Rogers on the basis of his research on the natural lighting environment in educational spaces. Compared with the original DA indicator, in the calculation of DAcon, the influence of lower illuminance than the minimum critical illuminance value on the effect of natural lighting in the room is also taken into account. The ratio of the lower illuminance value to the minimum critical illuminance value was calculated, and the ratio of the two was set as the degree of influence of the excessively low illuminance portion on the indoor lighting effect [41]. This parameter is proposed to show that even if there is a part of illuminance that is numerically low, it can still serve as auxiliary lighting in the room. This provides greater continuity in the evaluation of the range of illuminances for daylightingthan the DA parameter.

(4) Useful Daylight Illuminance (UDI)

Definition: the total moment when the illuminance value on the working surface conforms to a certain interval of illuminance value. In 2005, Nabil and John Mardajevic proposed the dynamic natural lighting evaluation standard UDI based on the information of reference plane illuminance [65][66]. People divided the natural light illuminance into three ranges, that is, to get three indicators: UDI <100, UDI100-2000, UDI>2000. Among them, UDI100-2000 indicators indicate that the illuminance level at this time can satisfy the workers' needs for normal visual work, and it is most widely used in the research.

(5) DAmax (Maximum Daylight Autonomy)

Definition: Percentage of the annual natural light use time that direct or excessive sunlight is present at a work surface measurement point. The DA max metric was developed to enable prediction of the probability of indoor glare. Assuming that the critical illuminance value for the occurrence of glare is related to the characteristics of the building space, the critical illuminance value for DA max is ten times the lowest critical illuminance value for that building space. For example, if a room has an interior design illuminance value of 300 lx, then the critical illuminance value for DAmax is set to 3000 lx.The main purpose of the DA max metric is to predict the probability of the occurrence of direct sunlight and other potential glares, as well as to obtain information about the extent and location of excessive illuminance contrasts in the interior of the building. Based on the DAmax daylighting index, sDAmax, 5% is the proportion of the total area in the room with DAmax>5%, which can further evaluate the range of glare generation in the room and is an important supplement to DAmax.

3. SIMULATION EXPERIMENTS

3.1. Simulation platform and experimental flow

We used Grasshopper parametric platform for natural daylighting simulation in our study, and obtained the values of daylighting parameters and visualized the simulation results through Ladybug Tools and Honeybee Tools plug-ins. The simulation experiment is divided into steps of establishing HB model, setting environmental parameters, performing lighting simulation analysis and visualizing the results, and its detailed flow is shown in Fig. 1.

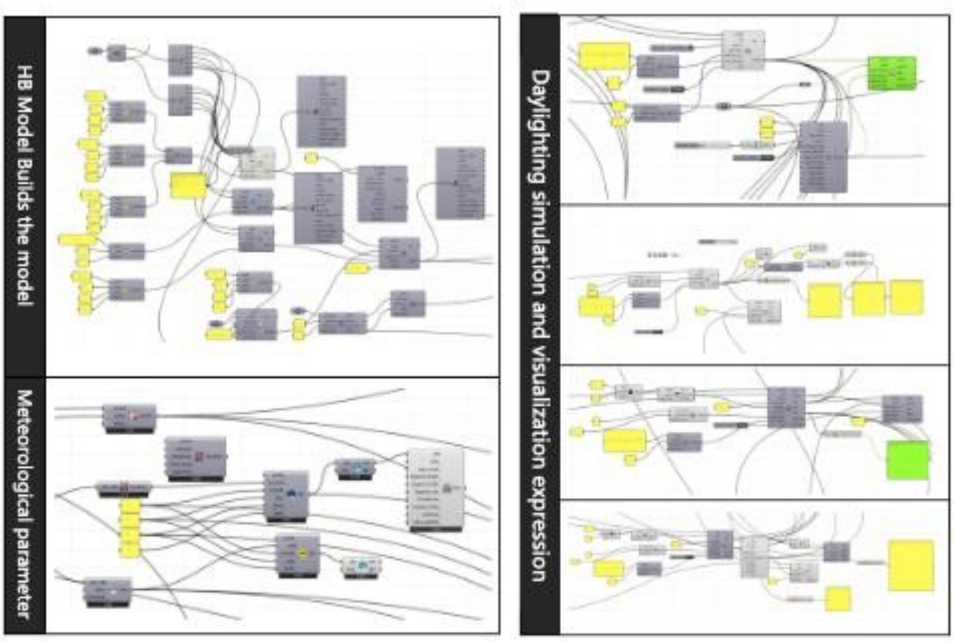

Figure 1: Flow of simulation experiment

3.2. Design parameters

We used the EPW weather data of Guangzhou citywide year to construct the simulated lighting conditions, and the lighting coefficient simulation adopted the full cloudy day model (CIE). In order to consider the operation hours of the stadium, we set the simulation time period from 7:00 a.m. to 22:00 p.m. For the analysis of the impact of glare, we chose one of the most unfavorable environmental conditions: that is, noon in summer and winter, that is, 12:00 p.m. on June 22 (summer solstice) and December 22 (winter solstice), for the use of our sky model. We set up the location of the glare impact point in the southern part of the basketball court, with a field of view at a height of 1.5 meters and a viewpoint pointing towards the entire core of the playing field.

According to the guiding principles of GB/T 5699-2017 "Lighting Measurement Methods", we chose a horizontal surface with a height of 0.8 meters above the ground as a reference point when selecting the working plane [13]. For the area of the gymnasium, we divided the working plane into appropriately sized grids, and the size of each grid was set to 1 meter × 1 meter (Figure 2) .The orientation of the building was set as due south. In the experimental setup, the material of each surface of the interior was set according to Table 1.

Table 1: Optical parameters of relevant surface materials

Component name	Materials	Roughness	Reflectance	Light transmittance
Ceiling	Steel truss	0.05	0.75	-
Intwall	Whitewash a wall	0.05	0.75	-
Intfloor	Wood floor	0.05	0. 58	-
Window	White coated glass	0.05	0.08	0.68
Intdoor	Fire door	0.05	0.10	-

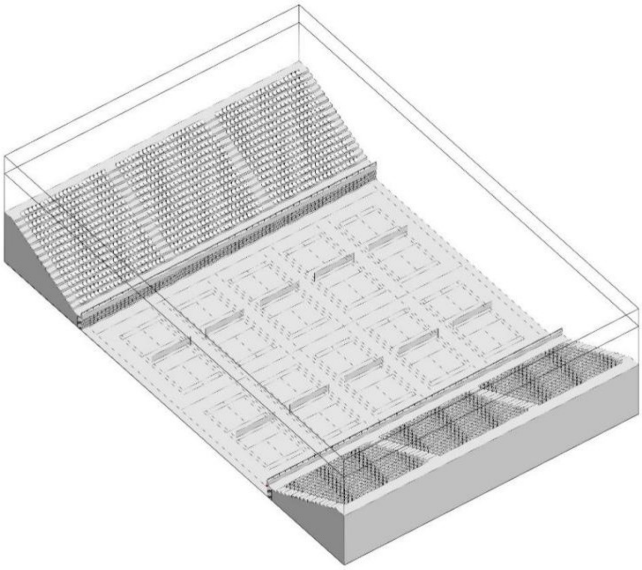

Figure 2: Site model

3.3. Simulation scheme selection

After research, gymnasium buildings open skylight whether in the light efficiency or in the light uniformity are better than the side windows, so the principle of the important gymnasium lighting to skylight as the main, side windows as a supplement. Common forms of skylights in gymnasiums are mainly flat skylights and vertical skylights. This subsection mainly compares and analyzes the impact of three different skylight forms, namely flat skylight, sawtooth and rectangularskylight (Figure 3), on the lighting environment of the playing hall under the same lighting area conditions and continues to simulate and deepen the analysis for the next subsection to select the appropriate skylight lighting outlet form.

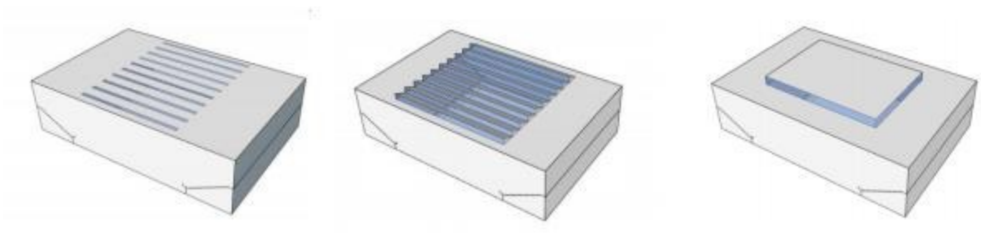

Figure 3: Skylight form scheme diagram

3.4. Program Parameter Setting

In the parameter setting of the three skylight forms, under the premise of ensuring that the total area of the skylight light opening remains unchanged, the location of the windows is kept as close as possible. Therefore, the form of flat skylight is chosen as decentralized horizontal flat skylight, each skylight is 40m long, 1m wide, 4m interval, a total of 10 skylights; serrated skylight is 40m long, 4m wide, 1m high, a total of 10 serrated skylights, skylight window facing north; rectangular skylight is 40m long, 26.7m wide, 3m high, all four sides of the window. The short axis of the competition hall is parallel to the north-south direction.

4. SOME COMMON MISTAKES YOU SHOULD AVOID

4.1. Program Parameter Setting

In this study, indoor illuminance simulations of three models were carried out, in which six different layouts of skylight forms were used, and the skylight area ratios were set to 0.1 and 0.2. The skylight forms were selected as the six forms in typical [9]. The specific simulation results and values are shown in Table 2.

Table 2: Optical parameters of relevant surface materials

Skylight form	DF(%)	DA300lx	UDI<100(%)	100<UDI<2000	UDI>2000	DAmax（%）
Flat skylight	8.56	75.98	16.63	51. 34	31. 97	21.34
Serrated skylight	1.59	45.55	31.80	61.55	6.47	4.50
Rectangular skylight	2.55	60.71	24.52	68.50	6.56	4.70

Comparison of the above lighting evaluation index data. In the case of the same total area of skylight lighting, the average annual DF of flat skylight is much larger than the other two forms, which is 5.4 times more than that of the serrated skylight and 3.4 times more than that of the rectangular skylight. The average DF of the rectangular skylight is 1.6 times higher than that of the serrated skylight, and the average DF of the serrated skylight is lower than 2%, only 1.59%, which does not satisfy the minimum daylighting design requirements. As a result, when the sawtooth skylight opening faces north, it tends to result in lower illuminance levels in the playing field.

Flat skylights have the highest ability to increase DA300lx in sports fields among the three skylight forms, with a value of 75.98%, which is 1.7 times higher than that of serrated skylights. Rectangular skylight DA300lx mean value is 1.3 times higher than serrated skylight. The average value of DA300lx for the serrated skylight does not reach 50% and is only 45.55%, which does not meet the minimum standard requirements. The average DA300lx value of rectangular skylight reaches 60.71%, which is at a better level. According to the analysis of the cloud maps obtained from the simulation of the three types of skylights, the distribution of the percentage of autonomous lighting in the sports ground of the competition hall is similar for the flat skylight and the rectangular skylight, and both of them are more uniform. The distribution of the percentage of autonomous lighting in the sports field of the serrated skylight is concentrated in the north of the field, and the value gradually decreases from north to south. Therefore, for the sawtooth skylight, it is possible to raise the side windows on the south wall, which can help to increase the percentage of autonomous lighting on the south side of the playing field.

By analyzing the average value of UDI (effective illuminance) ratio under the three working conditions, the comfortable illuminance (100lx-2000lx) ratio of rectangular sunroof is the highest and reaches a superior level of 68.50% (Table 3). The average value of comfortable illuminance ratio of serrated skylight also exceeds 60% to 61.55%, while the average value of comfortable illuminance ratio of flat skylight is the lowest, only 51.34%, although it has obvious advantages in the lighting coefficient and the percentage of autonomous lighting. The average value of the percentage of excessive illuminance (2000lx) of the flat skylight reaches 31.97%, which is 5 times more than that of the sawtooth skylight and rectangular skylight, and the average value of DAmax is also 5 times more than that of the other two forms. It can be seen that the probability of glare is greatly increased by the flat skylight while the lighting efficiency is high, which is 5 times the probability of glare of the other two forms. The average values of the percentage of over-illumination and the average value of DAmax for the serrated skylight and the rectangular skylight are comparable, and both are at a low level of about 6.5%and 4.5%, respectively. The serrated skylight is slightly lower than the rectangular skylight, and the probability of glare in the sports venue is very low for both skylight forms.

Table 3: Simulated cloud image of different lighting evaluation indexes under different skylight forms

	Flat skylight	Serrated skylight	Rectangular skylight
DA	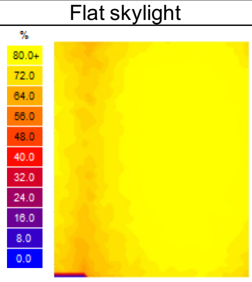	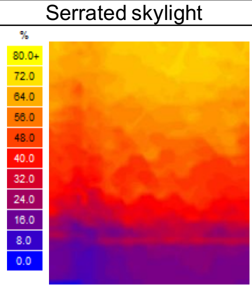	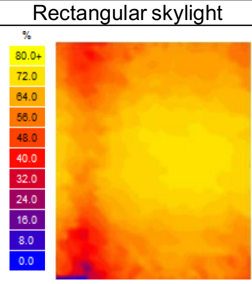

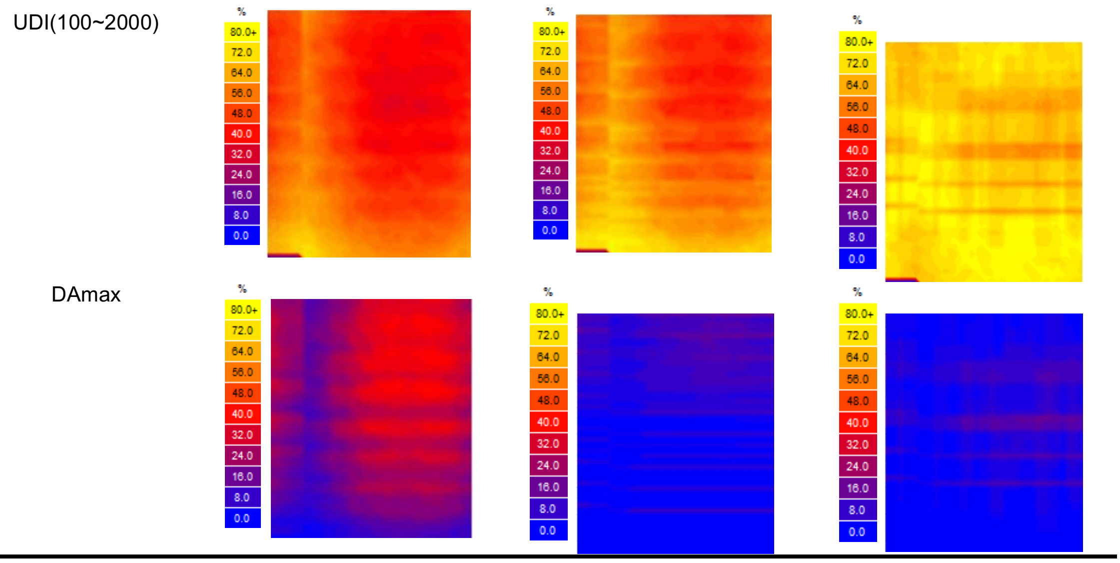

5. CONCLUSION

Comprehensive lighting evaluation indexes above, it can be seen that the flat skylight lighting efficiency is the highest, but if the opening area exceeds a certain range is likely to lead to a lower percentage of comfortable illuminance, too high illuminance accounted for a higher percentage, increasing the probability of glare. Serrated skylight light opening to the north, although it can make the sports venue almost no glare generation, but the lighting efficiency is very low, the percentage of autonomous lighting in the sports venue is unevenly distributed, the south side of the venue is smaller percentage of autonomous lighting. Therefore, the sawtooth skylight can increase the high side window synergistic lighting on the south side to make up for the shortcomings of insufficient lighting on the south side, while the probability of glare can also be maintained at a low level. Reasonable rectangular skylight design can not only ensure sufficient percentage of autonomous lighting in the sports venue, but a comfortable illumination ratio of more than 60%, and the venue is almost no glare interference. Vertical skylight applied to the stadium competition hall basically does not produce glare, but it is easy to lead to a low level of illumination in the sports venue, and the design of vertical skylight is generally combined with the design of the building structure, subject to structural constraints, in the structural allowances can be appropriately enlarged vertical light port to improve the level of illumination in the sports venue.

Skylight form: In terms of the quantity and quality of light, it is recommended that the order of skylight form be rectangular skylight with four windows > sawtooth skylight > flat skylight. Vertical skylights are less efficient but can greatly reduce the probability of glare. Flat skylights have higher lighting efficiency, but at the same time the probability of glare is greater. Rectangular skylights with windows on all four sides allow the minimum requirements for the amount of light in a sports venue to be met while being essentially glare free. Rectangular skylights with north-facing windows do not produce glare, but the amount of light easily fails to meet the standard requirements, while the percentage of autonomous light is unevenly distributed in the sports field, and the area that does not meet the requirements for the percentage of autonomous light is concentrated on the south side, which can be improved by opening side windows on the south side to increase the percentage of autonomous light on the south side.

6. ACKNOWLEDGEMENT

This research was supported by the National Natural Science Foundation of China (No. 52078140), the Reform of Degree and Postgraduate Education in Guangdong Province (No. 2022JGXM049), and the Undergraduate Teaching Engineering Project of Guangdong University of Technology (No. 2023-51).

7. REFERENCES

[1] Reinhart C F, Wienold J.The daylighting dashboard-A simulation-based design analysis for daylit spaces ［J］. Building and Environment, 2011, 46 (2) : 386-396.

[2] Bellia L, Pedace A, Fragliasso F. The impact of the software ' s choice on dynamic daylight simulations ' results: A comparison between Daysim and 3ds Max Design ［J］. Solar Energy, 2015, 122: 249-263.

[3] Mardaljevic J.Examples of climate-based daylight modelling ［C. CIBSE National Conference 2006: Engineering the Future,London,UK (2006) .

[4] Reinhart C F, Mardaljevic J, Rogers Z. Dynamic Daylight Performance Metrics for Sustainable Building Design [J]. LEUKOS, 2006, 3 (1) : 7-31.

[5] Nabil A,Mardaljevic J.Useful daylight illuminance: a new paradigm for assessing daylight in buildings ［J］. Lighting Research＆Technology, 2016, 37 (1) : 41-57.

[6] Nabil A, Mardaljevic J. Useful daylight illuminances: A replacement for daylight factors［J］. Energy and Buildings, 2006, 38 (7) : 905-913.

[7] Azza Nabil, John Mardaljevic. Useful daylight illuminance a new paradigm for assessing daylight in buildings, Lighting.Research and Technology. 37(1)(2005).

[8] Galatioto A,Beccali M. Aspects and issues of daylighting assessment: A review study ［J］.Renewable and Sustainable Energy Reviews,2016,66: 852-860.

[9] Korsavi S S, Zomorodian Z S, Tahsildoost M.Visual comfort assessment of daylit and sunlit areas: Alongitudinal field survey in classrooms in Kashan, Iran ［J］. Energy and Buildings, 2016,128: 305-318.

[10] Zomorodian Z S, Tahsildoost M. Assessing the effectiveness of dynamic metrics in predicting daylight availability and visual comfort in classrooms［J］. Renewable Energy, 2019, 134: 669-680.

[11] Zhao Y, Hongyuan M. Dynamic Simulation and Analysis of Daylighting Factors for Gymnasiums in Mid-Latitude China. Building and Environment 2013(63), 56-68.

[12] Acosta I, Navarro, J Sendra. Daylighting Design with Lightscoop Skylights: Towards an Optimization of Shape under Overcast Sky Conditions. Energy and Buildings 2013, 60, 232–238.

[13] Anastasios I. Stamou, Ioannis Katsiris,AloisSchaelin. Evaluation of thermal comfort in Galatsi Arena of the Olympics “Athens 2004” using a CFD model. Applied Thermal Engineering, 2008:1206-1215.

[14] J. Bouyer, J. Vinet, P. Delpech, S. Carre. Thermal comfort assessment in semioutdoor environments: Application to comfort study in stadia. Journal of Wind Engineering and Industrial Aerodynamics, 2007: 963~976.

[15] Agota Szucs, Sophie Moreau, Francis Allard. Spectators’aerothermal comfort assessment method in stadia. Building and Environment, Volume 42, Issue 6, June 2007: 2227-2240.

[16] G. B. Smith, A. Earp, J. Stevens, P. Swift, G. McCredie, J. Franklin. Materials Properties for Advanced Daylighting in Buildings. World Renewable Energy Congress VI, 2000: 201-206.

[17] L. Serres,A. Trombe, J. H.Conilh. Study of coupled energy saving systems sensitivity factor analysis. Building and Environment,Volume32,Issue2,March 1997 :137-148.

#317: Machine learning enabled prediction in the thermophysical properties of molten salt

Sikai GENG[1], Yuxin LUO[2], Jiale ZHOU[3], Xiaobo YANG[4], Ping SONG[5], Weijun SONG[6], Ze SUN[7]

[1] East China University of Science and Technology, Shanghai 200237, China, skgeng@mail.ecust.edu.cn
[2] East China University of Science and Technology, Shanghai 200237, lyxofficialwork@163.com
[3] East China University of Science and Technology, Shanghai 200237, zhou.jiale@ecust.edu.cn
[4] Qinghai Minzu University, Xining 810007, yang_1101979@163.com
[5] Qinghai University, Xining 810016, songpingd@126.com
[6] Qinghai University, Xining 810016, wjsong@mail.ecust.edu.cn
[7] East China University of Science and Technology, Shanghai 200237, China, zsun@ecust.edu.cn

Abstract: The growing demand for environment protection in modern society requires us to increase the proportion and efficiency of renewable energy. In the pursuit of sustainable energy solutions, molten salts have emerged as vital for energy storage due to their unique thermophysical properties. In particular, the property of melting point determines the minimum operating temperature of molten salt as a fluid heat storage medium. However, it's a challenge to meet the need with the traditional trial-and-error method in materials engineering which is costly and repetitively inefficient as well. The absence of predictive models has been a roadblock in the design and optimization of these systems. In this paper, we found that the Gradient Boosting Regression (GBR) algorithm is one of the best algorithms for prediction of the melting point. A machine learning (ML) model with GBR algorithm developed from scratch was reported to predict the melting point of molten salts. This achievement was made possible through the compilation of a dataset and the application of sophisticated ML techniques including feature engineering and hyperparameter tuning. The melting point was accurately predicted by our ML model which enabling rapid evaluation of salt mixtures for energy storage applications. It has been verified that machine learning is feasible for measuring the melting points of molten salts. This work accelerated the discovery of new high-performance, low-cost molten salt formulations, pioneering a new direction in data-driven molten salt design, paving the way for tailored innovation in high-temperature energy storage materials. Furthermore, we envisage that this ML-driven approach would inspire analogous methodologies across diverse fields, fostering innovation and accelerating the transition towards more sustainable and efficient energy systems.

Keywords: Machine Learning; Molten Salt; Energy Storage; Melting Point; Gradient Boosting Regression

1. INTRODUCTION

Molten salts were considered to play a role in molten salt reactors and solar thermal electric (STE) plants, for the advantages of high heat capacity, good thermal conductivity, low viscosity at high temperatures, low vapor pressure, high decomposition temperature, and wide working range of temperature (Porter *et al.*, 2022). In solar thermal electric plants, molten salts play a very important role as thermal energy storage (TES). It is precisely for these advantages that energy storage technology of molten salts had been applied in STE and has achieved significant results (Gil *et al.*, 2010). According to the International Energy Agency (IEA), if sufficient research, development and economic support are provided, STE could account for 11.3% of global electricity generation. In high renewable energy scenarios, STE would contribute to a reduction of 2.1 $GtCO_2$ in emissions, which is approximately 16% of the emissions from the electricity generation sector, and 9% in the overall high renewable energy scenario (Jayathunga *et al.*, 2024).

Melting point (MP) is a significant property of molten salts. It is related to the low boundary of the operating temperature range of molten salts. For example, Solar Salt, one of the most commonly used molten salts for industry, melts at 496 K(A. G. Fernández *et al.*, 2014), with its lower limit of operating temperature being 563 K. Consequently, one of the major challenges of molten salts is their high MP. Lower melting point of energy storage molten salts could decrease the probability of pipeline freezing, increase the heat exchange temperature difference, enhance the heat storage capacity, and even reduce the corrosion of molten salts on the tank under some conditions (Kearney *et al.*, 2003). Therefore, lowering the MP is very important for molten salts design. However, the rational design of MP for molten salts currently is limited by the lack of generalized physicochemical insights with wide chemical space coverage, as well as reliable data resources to guarantee the reproducibility (Chen *et al.*, 2024). Many researchers obtained new low-MP molten salts by adding other substances to Solar salt to improve its properties. Roget et al. lowered the MP by adding $LiNO_3$ to Solar Salt, and the ternary eutectic nitrate mixture ($LiNO_3$-KNO_3-$NaNO_3$) they prepared had a MP of 396.5 K(Roget, Favotto and Rogez, 2013). Zhao et al. added $Ca(NO_3)_2$ to Solar Salt, and obtained the ternary eutectic nitrate mixture ($Ca(NO_3)_2$-KNO_3-$NaNO_3$), which melts at 353 K. Zhong et al. added $Mg(NO_3)_2$ to Solar salt, successfully made a ternary eutectic salt ($Mg(NO_3)_2$-KNO_3-$NaNO_3$), which melts at 395.56 K(Zhong *et al.*, 2021). Ren et al. put both $LiNO_3$ and $Ca(NO_3)_2$ into the Solar Salt, and prepared a quaternary nitrate mixture ($LiNO_3$-$Ca(NO_3)_2$-KNO_3-$NaNO_3$) with a MP lower than 363K.

There were other researchers who had taken a different approach as well. Li et al. designed and investigated a novel ternary molten nitrate salt of KNO_3-$NaNO_2$-KNO_2 (KNK), which melts at 417.1 K(Li *et al.*, 2021). Zhong et al. studied the effects of KNO_3 and $Mg(NO_3)_2$ on melting points and discovered a ternary eutectic mixture with a melting point at 363 K(Zhong *et al.*, 2020). Fernandes et al. used phase diagram combined with experimental methods to investigate the effects of lithiumnitrate on the melting point, thermal stability, heat capacity, and viscosity of mixed molten salts and newly designed a mixed molten salt of $LiNO_3$-KNO_3-$Ca(NO_3)_2$, with a MP of 405.3 K(A.G. Fernández *et al.*, 2014). Wang et al. applied the asymmetric Toop model to predict the phase diagram of the ternary system $LiNO_3$-$NaNO_3$-$Ca(NO_3)_2$, they successfully predicted the melting point of a mixed eutectic salt with an error of about 2%(Wang *et al.*, 2015). The dilemma of the traditional experimental method is that it requires a large number of repetitive and tedious experimental tests. Just for ternary data, hundreds of repeated thermal experiments are needed, which is time-consuming and labor-intensive.

Since 2010, the development and prosperity of data science had enabled artificial intelligence to guide scientific research by analysing relevant data from large datasets. It optimized parameters and functions, automates data collection, processes data through visualization, and generates hypotheses along with estimates of their uncertainties to propose relevant experiments (Wang *et al.*, 2023) (Thakkar *et al.*, 2024) (Porter *et al.*, 2022). Therefore, machine learning could be an excellent method to assist the design of molten salts. To use machine learning methods, one first needs to establish a suitable molten salt database. The earliest research on a molten salt database came from the Oak Ridge National Laboratory (from the US), where they studied molten salt primarily for nuclear reactors. And two databases, MSTDB-TB and MSTDB-TC, were released by them (Besmann and Schorne-Pinto, 2021) (Ard *et al.*, 2022) (Termini *et al.*, 2023). Serrano-López et al. published a compilation of molten salt data based on the literature collected at that time, but their database mainly consisted of chloride and fluoride salts, both of which are unsuitable for thermal energy storage (Serrano-López, Fradera and Cuesta-López, 2013).

According to the survey of literature, there is currently no publicly available literature that utilizes machine learning methods to analyse the MP of molten salts. However, some successful cases of machine learning-assisted research in other fields can serve as references for us. Hong built a machine learning model to predict melting temperature from chemical formula, and the root-mean-square errors (RMSE) of melting temperature were 75 and 135 K for the training and testing sets, respectively (Hong *et al.*, 2022). But the model of Hong could not perform well in the prediction of mixed salts. Yang et al. studied a HCNN (hybrid convolutional neural network) method which is proposed to make battery cycle life early prediction and RUL prediction for lithium-ion batteries (Yang, 2021). Li et al. constructed a deep neural network model called DeepTM, using graph convolutional neural networks and self-attention networks, with the aim of directly predicting the MP values of proteins from their sequence information (Li *et al.*, 2023). Gu et al. built a quantitative Support Vector Regression (SVR) model for predicting the band gaps and melting points of some semiconductors (Gu *et al.*, 2006).

In this paper, a machine learning model utilizing the gradient boosting regression algorithm had been developed, which was planned to be used for the design of new energy storage molten salts. A high-quality MP dataset comprising 141 nitrates mixtures was obtained by strict data collection with criteria of the species of molten salts included the accuracy of instrument detection and the consistency of the same data in different literatures. After data processing, algorithm selection, and hyperparameter optimization, this model demonstrated excellent performance in predicting the melting points of a limited range of nitrate mixtures. This work has verified that machine learning is feasible for measuring the melting points of molten salts and could significantly reduce experimental costs and improve design efficiency in energy storage moltensalts design. Furthermore, it might be expected to make new breakthroughs in the structure activity relationship of moltensalts.

2. METHOD

2.1. Construction of high-quality dataset

The properties data of molten salts was extracted from published literature. These data were measured via thermogravimetric (TG) or differential scanning calorimetry (DSC). In order to improve the quality of the properties data, the species of molten salts included the accuracy of instrument detection and the consistency of the same data in different literatures are all included in the criteria for screening data. (1) nitrate was only contained in the chemical formula; (2) precious metals were not included (such as Sc); (3) TG and DSC instrument must be calibrated before thermal analysis. (4) heating rate of DSC must be between 5 and 10 $K \cdot min^{-1}$, (5) mean values were calculated for multiple properties records, (6) the error between different literatures must not exceed 5%.Among them, criterion (1) is defined because the nitrates mixture is considered to possess better corrosion control and lower melting point(Vignarooban *et al.*, 2015); the criteria (2) were used to manage the cost of molten salt; the settings of criteria (3)-(6) were designed to regulate the possible measurement deviations in TG and DSC analysis. As a result, a high-quality molten salt dataset of 141 nitrates mixtures was obtained for further study.

2.2. Feature selection and representation

There are many target parameters for the design of energy storage molten salt, such as melting point, decomposition point, and specific heat capacity. After collecting data, more literature on the melting point were found, while less data on the decomposition temperature; The specific heat capacity of energy storage molten salt can be enhanced by doping additives such as nanomaterials (Angayarkanni and Philip, 2015), which is difficult to predict via machine learning models. Therefore, this article chooses the melting point as the target parameter of the machine learning model. In terms of molten salt formulations, due to the high melting point of carbonates, the corrosion problem of chloride salts has not been resolved yet, and both the cost and corrosion issues of fluoride salts are significant, this article chooses to use nitrates as the input parameter for the machine learning model. For composite molten salts, the mass of each single salt involved in the composite affects phenomena such as eutectics, thus also affecting the melting point to some extent. However, adding the molecular weight of each molten salt to the parameters would be redundant. Therefore, this article chooses to incorporate the molecular weight of composite molten salts into the parameters through a custom function.

In this work, melting points were reported in Kelvin (K), and the proportions of various single salts were described as decimal fractions.

2.3. Data processing

The data preprocessing has been completed during the dataset constructing step because this work is not a large volume of data research. The work of preprocessing includes data screening, data classification, data labeling, and data validation steps.

For numerical feature types, we often use normalization method (or feature scaling) to process them, which can make all numbers approximately uniform within a similar interval, avoiding that some numbers are dominant just because they are large rather than important in the model, occupying more weights. In addition, normalization can improve efficiency during gradient descent. The most commonly used normalization methods include Min-Max normalization, mean normalization, and Z-score normalization.

Min-Max normalization transforms a column of data to a specific fixed interval is commonly done, with the interval usually being between [0, 1]. This is primarily for the convenience of data processing, as mapping data within the range of 0 to 1 facilitates more efficient and rapid handling. The calculation of Min-Max normalization is performed using Equation 1:

Equation 1 Min-Max normalization calculation formula $$x = \frac{X - X_{min}}{X_{max} - X_{min}}$$

Where:

- x is the normalized value (K)
- X is the original data (K)
- X_{min} is the minimum value in the original data (K)
- X_{max} is the maximum value in the original data (K)

Mean normalization can normalize the data distribution to (-1,1), and was calculated using Equation 2:

Equation 2 Mean normalization calculation formula $$x = \frac{X - X_{mean}}{X_{max} - X_{min}}$$

Where:

- X is the original data (K)
- X_{min} is the minimum value in the original data (K)
- X_{max} is the maximum value in the original data (K)
- X_{mean} is the mean of the original data (K)

Z-score normalization (Standardization) can translate the data into a distribution with a mean of 0 and a standard deviation of 1. As a result, the mean of the centralized data is 0, with no specific requirements for the standard deviation. The calculation method is shown in Equation 3:

Equation 3 Z-score normalization calculation formula $$x = \frac{X - X_{mean}}{\sigma}$$

Where:

- X is the original data (K)
- X_{mean} is the mean of the original data (K)
- σ is the standard deviation of the original data

2.4. Machine learning algorithms for molten salts

In supervised learning, a training set typically consists of a group of inputs and corresponding outputs. The goal of the algorithm is to train a function that, when given a specific set of inputs, can produce acceptable data outputs. If the available dataset contains only input values, unsupervised learning can be used to attempt to identify trends, patterns, or clusters within the data. If there is a large amount of input data but only limited corresponding output data, semi-supervised learning may be valuable.

An important aspect of machine learning data is whether it is labeled or not. For labeled data, supervised learning methods are commonly used to train machine models to achieve objectives such as regression. In the field of molten salt design, because each piece of data has a corresponding physical significance, it is considered labeled data. Additionally, since the goal is to use given data to predict an unknown outcome, regression methods are required.

In this study, six algorithms were selected Table 1.

Table 1: Machine learning models explored in this work

No.	Abbreviation	Full title
1	GBR	Gradient Boosting Regression(Velthoen *et al.*, 2023)
2	LR	Linear Regression(Moscarelli, 2023)
3	DT	Decision Tree(Li, 2024a)
4	RF	Random Forest(Breiman, 2001)
5	SVM	Support Vector Machines(Shmilovici, 2023)
6	KNN	K-Nearest Neighbor(Li, 2024b)

2.5. Model evaluation index

MRE and RMSE are commonly used model evaluation data in machine learning. These two parameters were used in this work, and the calculation methods are listed as follows:

Mean Relative Error (MRE) is defined as Equation 4:

Equation 16 Mean Relative Error calculation formula $$MRE = \frac{1}{n} \cdot \frac{\sum(y_{pred} - y_{test})}{100 \cdot y_{test}}$$

Where:

- y_{pred} presents the predicted melting point by model (K)
- y_{test} is the actual melting point in the dataset (K)
- n is the number of data points in the training set

Root Mean Square Error (RMSE) is defined as Equation 5:

Equation 17 Root Mean Square Error calculation formula $$RMSE = \sqrt{\frac{\Sigma\left(y_{pred} - y_{test}\right)^2}{n}}$$

where:

- y_{pred} represents the predicted melting point by the model (K)
- y_{test} is the actual melting point in the dataset (K)
- n is the number of data points in the training set

2.6. Optimization of hyperparameters

In this study, six hyperparameters were selected:

Table 8: Hyperparameters of GBR algorithms explored in this work

Hyperparameters	Description	Default
learning_rate	the learning rate, a common concept in machine learning, used to describe the impact of each iteration on the model	0.1
max_depth	the maximum computation depth	3
max_features	the maximum number of features, i.e., the number of features considered when searching for the best split, with two options: 'sqrt', 'log2'	none
min_samples_leaf	the minimum number of samples for leaf nodes	1
min_samples_split	the minimum number of samples for node splitting	2
n_estimators	represents the number of steps in the boosting stage	100

3. RESULTS AND DISCUSSION

3.1. Data processing result

This work uses the StandardScaler class in the sklearn.preprocessing module to implement Z-score normalization, which is more stable and less affected by outliers in use. The processing results are shown in Figure 1, where only the results of 35 data points are plotted for demonstration purposes. Figure 1a showed the unprocessed dataset, while Figure 1b illustrated the normalized data.

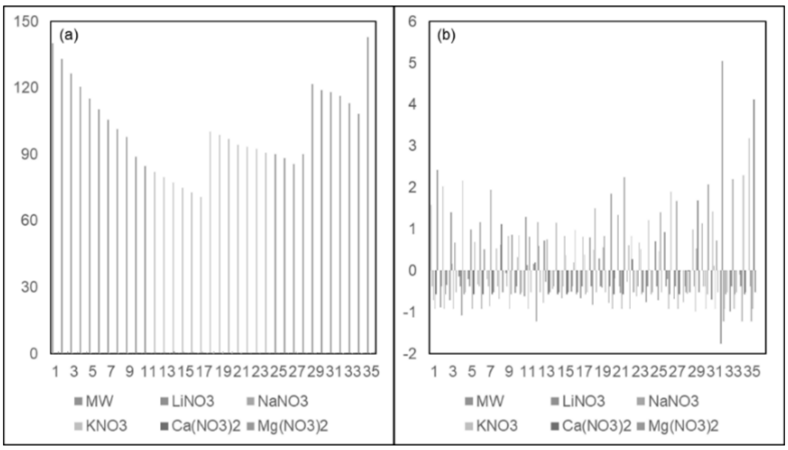

Figure 1: Normalized Data Processing Results. a) The partial dataset before normalization. b) The partial dataset after normalization

From the left graph, it illustrated that the MW values in the unprocessed data are significantly higher than the composition of the molten salt, making them almost invisible in the histogram. From the right image, it can be seen that the data after normalization is evenly distributed around the 0 axis (note the scale of the vertical axis). Therefore, the goal of normalization processing was achieved.

3.2. Comparison of algorithms

With MRE as the target parameter (the closer MRE is to 0, the better), ten rounds of cyclic tests were conducted on six models, and the experimental results are shown in Figure 2. It is not difficult to see that the GBR algorithm and the RF algorithm performed the best. However, it is impossible to determine the superiority of the two models based solely on MRE, so further analysis of the models is required.

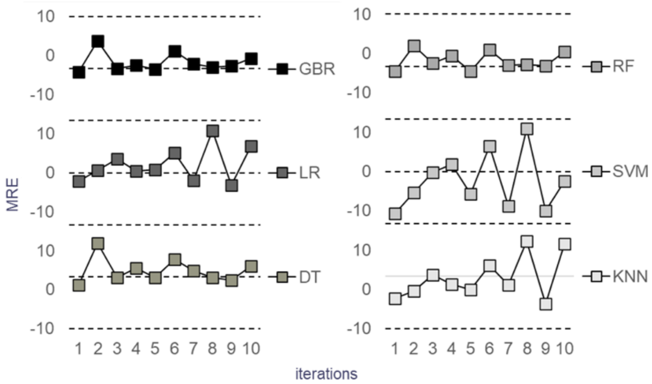

Figure 2: Ten Rounds of Experimental MRE Index Results of 6 algorithms

The GBR algorithm and the RF algorithm were used for twenty rounds of cyclic testing, and the RMSE data were recorded, with the results shown in Figure 3. By combining the line chart and the box plot, it can be seen that the GBR algorithm is slightly superior to the RF algorithm. Therefore, this work chooses the GBR algorithm for modelling and melting point prediction.

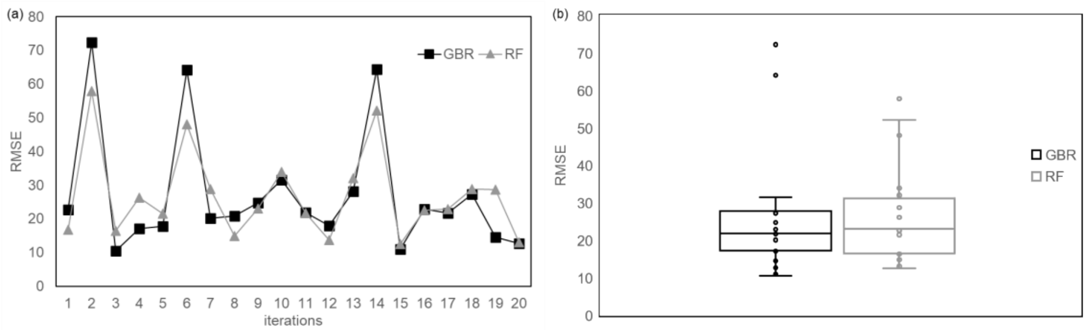

Figure 3: Twenty Rounds of Experimental RMSE Index Results of GBR and RF algorithms. a) line chart. b) box plot.

3.3. Optimization of Sample Rate

By changing different parameters "test_size" to alter the ratio of the test set to the training set, the RMSE results are calculated as shown in Figure 4.

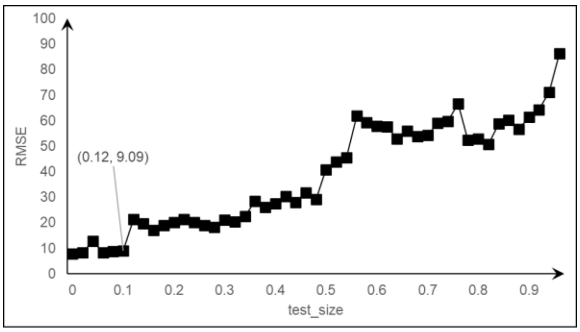

Figure 4: Different training set proportions' impact on the model

It is evident that as the proportion of the training set increases, leading to a larger number of training samples, MRSE of the model decreases. This aligns with our expectations. However, if the training ratio is too high, it implies that there are too few samples in the test set, potentially resulting in inaccurate test outcomes. Therefore, setting parameter "test_size" as indicated by the marked point in Figure 4 is more reasonable.

3.4. Optimization of hyperparameters

The GridSearchCV() function was used for hyperparameter optimization. The optimization results are shown in Table 3:

Table 3: Result of hyperparameters optimizing

hyperparameters	optimization
learning_rate	1
max_depth	5
max_features	0.5
min_samples_leaf	2
min_samples_split	5
n_estimators	200

After conducting hyperparameter optimization, both the accuracy and stability of the model were improved. These two aspects could be identified from Figure 5a and Figure 5b, respectively, indicated that the hyperparameter optimization was effective.

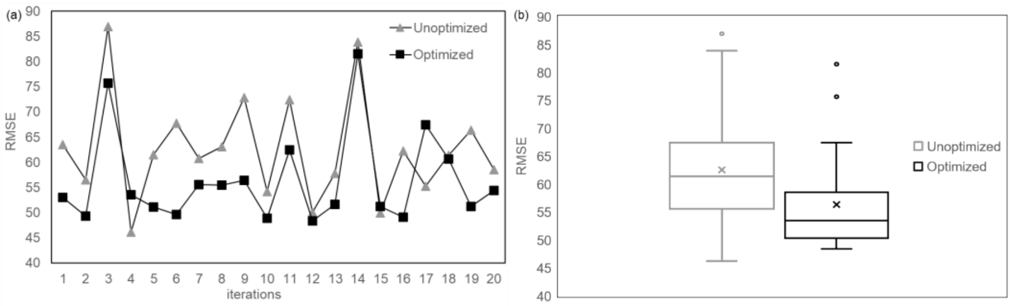

Figure 5: Effectiveness of hyperparameter optimization. a) Line chart. b) Box plot.

3.5. The GBR algorithms for the prediction of melting point

In this study, 141 experimental datasets were used to train the GBR machine learning model. representative experimental datasets.

10 rounds of melting point predictions were conducted via using the trained model. The data from the first 2 rounds are displayed (with a test_size of 0.12, there are 17 tests per round), as shown in Table 4. The MRE and RMSE of the 10 rounds of melting point predictions are shown in Table 5, and all data points are illustrated in Figure 6.

Table 9: The prediction result of the GBR model (the first 2 rounds)

Iterations	Experiment data [K]	Prediction data [K]	Iterations	Experiment data [K]	Prediction data [K]
1	422.24	408.66	18	476.00	469.74
2	471.39	466.33	19	741.83	484.19
3	419.12	435.29	20	447.71	447.42
4	609.18	607.68	21	443.84	369.80
5	496.00	503.01	22	424.47	575.01
6	456.80	456.8	23	472.60	456.59
7	608.94	624.11	24	668.81	683.5
8	400.60	407.10	25	461.71	496
9	447.01	447.42	26	423.97	416.08
10	522.28	518.41	27	413.61	393

11	673.24	670.76	28	467.84	469.56
12	404.37	406.49	29	412.39	408.79
13	473.88	491.25	30	432.67	433.25
14	474.03	477.33	31	555.31	528.99
15	498.70	498.01	32	461.71	503.02
16	433.51	433.41	33	560.93	545.94
17	428.78	455.53	34	461.12	498.01

Table 10: The MRE and RMSE index of prediction result

Iterations	MRE [%]	RMSE [K]
1	1.12	9.30
2	7.80	69.93
3	2.51	25.14
4	8.43	76.18
5	2.23	23.11
6	2.44	23.57
7	5.31	35.49
8	2.10	15.64
9	4.37	36.07
10	3.54	28.86

The mean of the above data shows that the 20-round average MRE of this model is 3.99%, and the RMSE is 34.33 K.

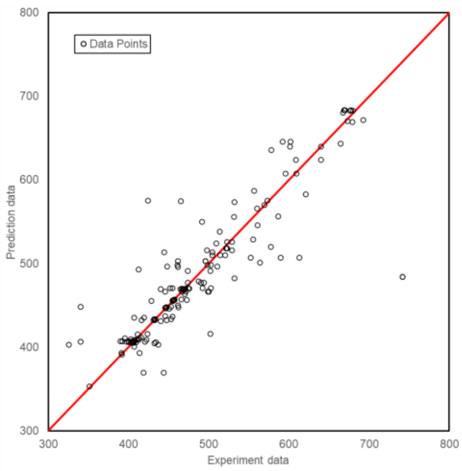

Figure 6: Comparison of the experienced and predicted performance of the GBR model.

Figure 6 shows a comparison between the experienced and predicted performance of the GBR model. It is evident that there is no significant difference between the predicted values of GBR model and the actual measured values, and only a few data points deviated seriously from the linear regression line. It illustrated that the GBR model trained in this work owned good melting point prediction performance.

4. CONCLUSION

It has been verified that machine learning is feasible for measuring the melting points of molten salts. A machine learning model had been developed that could be used to predict the melting point of mixed molten salts composed of lithium nitrate ($LiNO_3$), sodium nitrate ($NaNO_3$), potassium nitrate (KNO_3), calcium nitrate ($Ca(NO_3)_2$), magnesium nitrate ($Mg(NO_3)_2$). A high-quality MP dataset was constructed, including the mass fraction of the constituent salts and the molecular weight of salt mixture. These data inside were under explicit criteria and well processed. The data processing involves data preprocessing and data normalization. A total of 6 machine learning models were investigated to realize the accurate MP prediction of the molten salts. Through our research, a GBR model that achieved a MRE of just 3.99 % was trained. This level of accuracy is highly encouraging and indicates that our model can reliably assist in predicting the melting points of molten salts. The model we've developed will undoubtedly support and enhance our ongoing research efforts in this field, helping us to further understand and work with these materials more effectively.

Due to data source limitations, only five types of nitrates could be inputted: lithium nitrate ($LiNO_3$), sodium nitrate ($NaNO_3$), potassium nitrate (KNO_3), calcium nitrate ($Ca(NO_3)_2$), magnesium nitrate ($Mg(NO_3)_2$), and magnesium nitrate (Mg(NO3)2). The predictions of this model regarding molten salt performance had certain limitations and could not fully reflect the thermal storage performance of molten salts. The target parameter of this machine learning model is only the MP, but there were some impacts among the physical properties of molten salts. For example, between the MP and decomposition temperature, when the MP decreases, the decomposition temperature also decreases, and vice versa. From the perspective of feature engineering, the current model lacks sufficient features, such as spatial structure parameters and parameters related to eutectics.

In the future, sodium nitrite ($NaNO_2$) and potassium nitrite (KNO_2) should be added as input data. Additionally, data sources can be expanded beyond publicly available papers by attempting to obtain data through simulation calculations, experimental characterization, and other methods. We can continue to construct a more complete parameter description in hopes of improving model performance.

5. REFERENCES

Angayarkanni, S.A. and Philip, J. (2015) ‘Review on thermal properties of nanofluids: Recent developments’, Advances in Colloid and Interface Science, 225, pp. 146–176. Available at: https://doi.org/10.1016/j.cis.2015.08.014.

Ard, J.C. et al. (2022) ‘Development of the Molten Salt Thermal Properties Database − Thermochemical (MSTDB−TC), example applications, and LiCl−RbCl and UF3−UF4 system assessments’, Journal of Nuclear Materials, 563, p. 153631. Available at: https://doi.org/10.1016/j.jnucmat.2022.153631.

Besmann, T.M. and Schorne-Pinto, J. (2021) ‘Developing Practical Models of Complex Salts for Molten Salt Reactors’, Thermo, 1(2), pp. 168–178. Available at: https://doi.org/10.3390/thermo1020012.

Breiman, L. (2001) ‘Random Forests’, Machine Learning, 45(1), pp. 5–32. Available at: https://doi.org/10.1023/A:1010933404324.

Chen, P. et al. (2024) ‘Deciphering melting behaviors of energetic compounds using interpretable Machine learning for melt-castable applications’, Chemical Engineering Journal, 479, p. 147392. Available at: https://doi.org/10.1016/j.cej.2023.147392.

Fernández, A. G. et al. (2014) ‘Corrosion of alumina-forming austenitic steel in molten nitrate salts by gravimetric analysis and impedance spectroscopy’, Materials and Corrosion, 65(3), pp. 267–275. Available at: https://doi.org/10.1002/maco.201307422.

Fernández, A.G. et al. (2014) ‘Development of new molten salts with LiNO3 and Ca(NO3)2 for energy storage in CSP plants’, Applied Energy, 119, pp. 131–140. Available at: https://doi.org/10.1016/j.apenergy.2013.12.061.

Gil, A. et al. (2010) ‘State of the art on high temperature thermal energy storage for power generation. Part 1—Concepts, materials and modellization’, Renewable and Sustainable Energy Reviews, 14(1), pp. 31–55. Available at: https://doi.org/10.1016/j.rser.2009.07.035.

Gu, T. et al. (2006) ‘Using support vector regression for the prediction of the band gap and melting point of binary and ternary compound semiconductors’, Solid State Sciences, 8(2), pp. 129–136. Available at: https://doi.org/10.1016/j.solidstatesciences.2005.10.011.

Hong, Q.-J. et al. (2022) ‘Melting temperature prediction using a graph neural network model: From ancient minerals to new materials’, Proceedings of the National Academy of Sciences, 119(36), p. e2209630119. Available at: https://doi.org/10.1073/pnas.2209630119.

Jayathunga, D.S. et al. (2024) ‘Phase change material (PCM) candidates for latent heat thermal energy storage (LHTES) in concentrated solar power (CSP) based thermal applications - A review’, Renewable and Sustainable Energy Reviews, 189, p. 113904. Available at: https://doi.org/10.1016/j.rser.2023.113904.

Kearney, D. et al. (2003) ‘Assessment of a Molten Salt Heat Transfer Fluid in a Parabolic Trough Solar Field’, Journal of Solar Energy Engineering, 125(2), pp. 170–176. Available at: https://doi.org/10.1115/1.1565087.

Li, H. (2024a) ‘Decision Tree’, in H. Li (ed.) Machine Learning Methods. Singapore: Springer Nature, pp. 77–102. Available at: https://doi.org/10.1007/978-981-99-3917-6_5.

Li, H. (2024b) ‘K-Nearest Neighbor’, in H. Li (ed.) Machine Learning Methods. Singapore: Springer Nature, pp. 55–66. Available at: https://doi.org/10.1007/978-981-99-3917-6_3.

Li, J. et al. (2021) ‘Novel high specific heat capacity ternary nitrate/nitrite eutectic salt for solar thermal energy storage’, Solar Energy Materials and Solar Cells, 227, p. 111075. Available at: https://doi.org/10.1016/j.solmat.2021.111075.

Li, M. et al. (2023) 'DeepTM: A deep learning algorithm for prediction of melting temperature of thermophilic proteins directly from sequences', Computational and Structural Biotechnology Journal, 21, pp. 5544–5560. Available at: https://doi.org/10.1016/j.csbj.2023.11.006.

Moscarelli, M. (2023) 'Linear Regression', in M. Moscarelli (ed.) Biostatistics With 'R': A Guide for Medical Doctors. Cham: Springer International Publishing, pp. 137–179. Available at: https://doi.org/10.1007/978-3-031-33073-5_9.

Porter, T. et al. (2022) 'Computational methods to simulate molten salt thermophysical properties', Communications Chemistry, 5(1), p. 69. Available at: https://doi.org/10.1038/s42004-022-00684-6.

Roget, F., Favotto, C. and Rogez, J. (2013) 'Study of the KNO3–LiNO3 and KNO3–NaNO3–LiNO3 eutectics as phase change materials for thermal storage in a low-temperature solar power plant', Solar Energy, 95, pp. 155–169. Available at: https://doi.org/10.1016/j.solener.2013.06.008.

Serrano-López, R., Fradera, J. and Cuesta-López, S. (2013) 'Molten salts database for energy applications', Chemical Engineering and Processing: Process Intensification, 73, pp. 87–102. Available at: https://doi.org/10.1016/j.cep.2013.07.008.

Shmilovici, A. (2023) 'Support Vector Machines', in L. Rokach, O. Maimon, and E. Shmueli (eds) Machine Learning for Data Science Handbook: Data Mining and Knowledge Discovery Handbook. Cham: Springer International Publishing, pp. 93–110. Available at: https://doi.org/10.1007/978-3-031-24628-9_6.

Termini, N. et al. (2023) An Overview of the Molten Salt Thermal Properties Database–Thermophysical, Version 2.1.1 (MSTDB-TP v.2.1.1). ORNL/TM-2023/2955. Oak Ridge National Laboratory (ORNL), Oak Ridge, TN (United States). Available at: https://doi.org/10.2172/1988348.

Thakkar, P. et al. (2024) 'Advances in materials and machine learning techniques for energy storage devices: A comprehensive review', Journal of Energy Storage, 81, p. 110452. Available at: https://doi.org/10.1016/j.est.2024.110452.

Velthoen, J. et al. (2023) 'Gradient boosting for extreme quantile regression', Extremes, 26(4), pp. 639–667. Available at: https://doi.org/10.1007/s10687-023-00473-x.

Vignarooban, K. et al. (2015) 'Heat transfer fluids for concentrating solar power systems – A review', Applied Energy, 146, pp. 383–396. Available at: https://doi.org/10.1016/j.apenergy.2015.01.125.

Wang, H. et al. (2023) 'Scientific discovery in the age of artificial intelligence', Nature, 620(7972), pp. 47–60. Available at: https://doi.org/10.1038/s41586-023-06221-2.

Wang, J. et al. (2015) 'Thermodynamic Modeling and Experimental Verification of Eutectic Point in the LiNO3-NaNO3-Ca(NO3)2 Ternary System', Journal of Phase Equilibria and Diffusion, 36(6), pp. 606–612. Available at: https://doi.org/10.1007/s11669-015-0412-4.

Yang, Y. (2021) 'A machine-learning prediction method of lithium-ion battery life based on charge process for different applications', Applied Energy, 292, p. 116897. Available at: https://doi.org/10.1016/j.apenergy.2021.116897.

Zhong, Y. et al. (2020) 'Phase Diagrams of Binary Systems Mg(NO3)2-KNO3, Mg(NO3)2-LiNO3 and ternary system Mg(NO3)2-LiNO3-NaNO3', Journal of Chemical & Engineering Data, 65(7), pp. 3420–3427. Available at: https://doi.org/10.1021/acs.jced.9b01091.

Zhong, Y. et al. (2021) 'Thermodynamic description of the quaternary Mg(NO3)2–KNO3–NaNO3–LiNO3 system and investigation on the novel Mg(NO3)2 based nitrate salts with low temperature', Solar Energy Materials and Solar Cells, 230, p. 111148. Available at: https://doi.org/10.1016/j.solmat.2021.111148.

#318: Multi-Step building temperature prediction using GRU neural network based on temporal feature engineering

Case study of rooms dominated by natural indoor temperature

Wanlin ZHANG[1], Zhi ZHUANG[2]

[1] Sino-German Applied Science College, Tongji University, Shanghai, China, wanlinzhang0728@yahoo.com
[2] College of Architecture and Urban Planning, Tongji University, Shanghai, China, zhuangzhi@tongji.edu.cn

Abstract: The energy consumption of buildings' Heating, Ventilation, and Air Conditioning (HVAC) systems accounts for approximately 15%-20% of the total societal energy consumption, indicating significant potential for energy-saving design. Accurate indoor temperature prediction in buildings is crucial for the pre-planning, coordinated control, and energy management of HVAC systems. However, building indoor temperature is influenced by spatial variability due to weather conditions and building structure, as well as by seasonal changes, occupant activities, and equipment usage patterns, which exhibit both long and short cycles, making long-term precise prediction challenging. This paper proposes a multi-step indoor temperature prediction model based on Gated Recurrent Unit (GRU) neural networks, leveraging correlation analysis of relative parameters and temporal feature construction. By employing data resampling and moving window averaging methods, historical cycle features of related variables and indoor temperature sequences are constructed. Additionally, a multi-step synchronous prediction neural network output structure is established, effectively enhancing the model's robustness. The performance of the optimized model is validated on the smart building open-source dataset PLEIAData. Multi-model comparative experiments and ablation experiments demonstrate that the proposed GRU-F1-F2-M model improves MAE by 16.15% and 38.03% and RMSE by 15.36% and 57.89% compared to the optimized single-step GRU model and commonly used statistical model SARIMA, respectively.

Keywords: Indoor Temperature Prediction, Gated Recurrent Unit, Time Series, Feature Engineering, Multi-Step Forecasting

1. INTRODUCTION

1.1. Background

In the sector of energy consumption, buildings constitute approximately 40%, with HVAC (Heating, Ventilation, and Air Conditioning) systems accounting for almost 50% of this, equivalent to 15-20% of total energy consumption (Ibarra et al., 2023) and offering significant potential for energy-saving designs. The primary objective of HVAC system operation is to create specific indoor thermal environments, with indoor temperature serving as a core parameter for regulation. Accurately predicting indoor temperatures is crucial for HVAC systems: for residential or office buildings, minimizing temperature fluctuations enhances indoor thermal comfort, and early access to temperature distribution information aids in optimizing overall heating and cooling loads for flexible energy management. For functional buildings like factories and warehouses, rigorous monitoring of indoor temperatures can prevent anomalies and ensure production efficiency (Shi et al., 2021).

Indoor temperatures in buildings exhibit various temporal and spatial characteristics. Apart from mutual interactions between building regions, temperature variations are coupled with environmental parameters such as humidity and light exposure. Additionally, the operational status of HVAC systems and human activities introduce different long and short-term periodic features in temperature across zones (Wang, 2023). Predicting temperatures using physical models or numerical simulations often fails to meet the requirements for precise long-term, multi-zone indoor temperature forecasting needed for flexible HVAC system control.

1.2. Current research and organisation of the paper

With advancements in sensor technology enabling extensive data collection in buildings and rapid theoretical developments in various time-series prediction models, researchers are increasingly exploring deep learning methods for predicting building temperatures. (Attoue et al., 2018) employed artificial neural networks to stepwise forecast room facade and centre temperatures, achieving excellent predictive performance for the next two hours. (Afroz et al., 2018) used stepwise modelling to select relevant parameters and achieved high accuracy in single-zone temperature forecasts over the next month using Nonlinear Autoregressive with External Inputs (NARX) networks. (Xu et al., 2019) optimized an LSTM model with an Error Correction Model (ECM) for predicting indoor temperatures 30 minutes in advance, demonstrating its performance superiority over Back Propagation Neural Network (BPNN), Support Vector Regression (SVR), and Decision Tree (DT). (Shi et al., 2021) simplified Computational Fluid Dynamics (CFD) simulation grids based on sensor accuracy ranges and used a hybrid model of LightGBM and LSTM to predict global building temperatures for the next 60 hours with sparse sensor data nodes. (Wang, 2023) integrated multi-layer LSTM networks to extract temporal features of various related parameters and fused them with spatial correlation features of inter-zonal temperatures obtained from Graph Convolutional Networks (GCN), achieving high-precision multi-zone building temperature forecasts for the next week. (Alawadi et al., 2022) comprehensively considered HVAC system operation status, solar radiation, and other parameters, comparing 36 machine learning algorithms including General Regression Neural Network (GRNN) and Extreme Learning Machine (ELM) for indoor temperature forecasting accuracy over the next three hours, demonstrating performance variations with increasing prediction horizons. Current studies collectively focus on selecting relevant parameters for temperature prediction and analysing spatiotemporal characteristics of temperature variations, differing in algorithm selection and prediction duration settings.

Currently, research primarily focuses on predicting room temperatures during air conditioning operation, with less attention given to predicting room temperatures under natural room conditions. Accurate prediction of room temperatures in natural conditions is crucial for forecasting the need to activate the air conditioning system. This enables intelligent management of system start-ups and shutdowns, as well as effective off-peak regulation of energy consumption for future periods.

The structure of this paper includes algorithm introduction, data analysis, feature engineering, model optimization, and comparative experiments. The goal is to achieve high-accuracy prediction of indoor building temperatures for the upcoming week, with a prediction interval of 4 hours.

2. ALGORITHMS AND PRINCIPLES

The ARIMA model is one of the most classic models in time series analysis, and SARIMA extends it by enhancing the model's ability to fit seasonal data (Cao et al., 2024). Among various machine learning models, LSTM has proven to offer higher accuracy in temperature prediction compared to NARX, BPNN, SVR (Xu et al., 2019). Further, The GRU model, similar to LSTM, reduces computational complexity and improves calculation efficiency. Therefore, SARIMA and GRU are chosen as two baseline models in this paper.

2.1. SARIMA Model

The Seasonal Autoregressive Integrated Moving Average (SARIMA) model assumes that a time series becomes stationary after applying regular and seasonal differencing, which means that the periodic components of the series have consistent statistical properties, such as mean and variance, across each cycle. The model then performs the analysis on this stationary time series. The basic form of the model's hyperparameters is SARIMA (p, d, q) (P, D, Q, S), in which p and q represent non-seasonal autoregressive (AR) and moving average (MA) orders, P and Q represent seasonal autoregressive and moving average orders, d represents the order of non-seasonal differencing, and D represents the order of seasonal differencing. The mathematical expressions for differencing and model fitting are as follows (Equation 1):

Equation 18: The sequence differencing calculation formula for the SARIMA model.

$$y_t = (1-B)^d(1-B_s)^D x_t$$

$$y_t = \sum_{i=1}^{p} \varphi_i x_{t-i} + \sum_{j=1}^{P} \emptyset_j x_{t-j*s} + \sum_{k=1}^{q} \vartheta_k \epsilon_{t-k} + \sum_{l=1}^{Q} \theta_l \epsilon_{t-l*s} + \epsilon_t$$

Where:

- x_t: initial sequence
- y_t: stationary sequence after differencing
- B, B_s: Lag Operators, $x_{t-p} = B^p x_t$, $x_{t-s*P} = B_s^P x_t$
- φ, $\emptyset$, P, θ: fitting parameters in SARIMA
- ϵ: random disturbances

2.2. GRU Neural Network Model

GRU (Gated Recurrent Unit) neural network is a classic variant of recurrent neural networks, specifically developed to address the issues of memory and gradient vanishing in time-series data. The structure of a recurrent neural network with GRU is illustrated in (Figure 1). Here, Input and Output denote the network inputs and outputs, which can be single-dimensional or multi-dimensional data. The computation performed in each GRU unit is described by (Equation 2), in which r and z represent the reset gate and update gate respectively. The detailed structure of the GRU unit is depicted in (Figure 2).

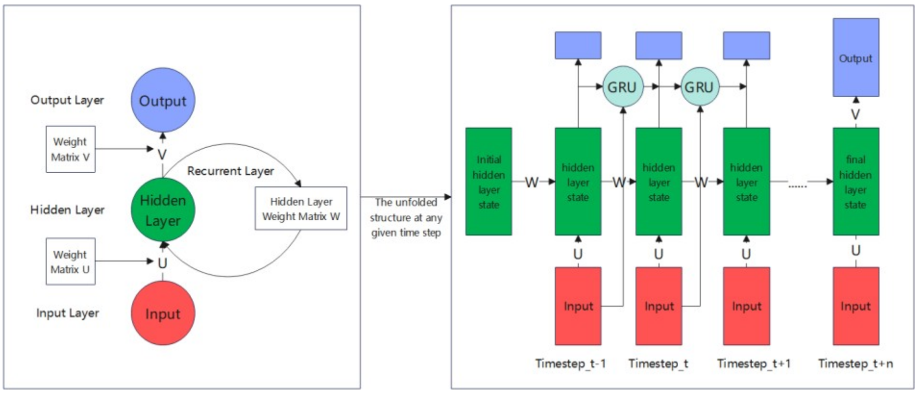

Figure 1: The structure of a recurrent neural network with Gated Recurrent Unit

Equation 2: The computation performed in each GRU unit.

$$r_t = \sigma(x_t W_{xr} + h_{t-1} W_{hr} + b_r)$$

$$z_t = \sigma(x_t W_{xz} + h_{t-1} W_{hz} + b_z)$$

$$\tilde{h_t} = \tanh\,[x_t W_{xh} + (r_t * h_{t-1}) W_{hh} + b_h]$$

$$h_t = z_t * h_{t-1} + (1-z_t) * \tilde{h_t}$$

Where:

- σ: Activation Function
- x_t: sequence value at time t
- h_t: hidden state at time t
- W, b: weight matrix and bias matrix of the network
- h̃t: candidate hidden state before memory update in GRU
- *：Hadamard Product Operator

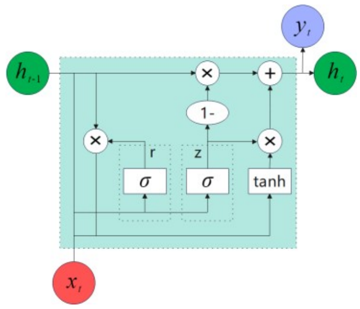

Figure 2: The inside structure of a Gated Recurrent Unit

3. DATA PREPARATION

3.1. The open-source dataset PLEIAData

The number of open-source datasets suitable for studying data-driven approaches to predict building indoor temperatures is increasing globally, providing a foundational basis for training and validating temperature prediction models. (Schweiker et al., 2019) focused on a naturally ventilated, low-energy passive office building in Frankfurt, Germany, collecting four years of historical data on CO2 levels, temperature, and humidity across 17 key areas of the building at 10-minute intervals. (Langevin, 2019) considered the impact of human behaviour patterns on building thermal environments, gathering temperature, humidity, illumination, room occupancy, and behavioural data at 15-minute intervals from an office building in Philadelphia, USA, throughout the year. (Pipattanasomporn et al., 2020) collected temperature, humidity, and visible spectrum radiation data every minute for two years from all 33 zones of a large public building in Bangkok, Thailand. Other studies have focused on parameters such as air flow velocity, building ventilation status, and various electrical consumption metrics (Shin et al., 2019).

The experimental data used in this paper is sourced from PLEIAData (Ibarra et al., 2023), an open-source smart building dataset published in Nature in 2023. This dataset captures building operation data at 10-minute intervals from January 1, 2021, to December 18, 2021, for the Pleiades building located at the University of Murcia in Spain. The building consists of three main areas spanning from five floors. PLEIAData stands out for its comprehensive coverage of meteorological data, indoor environmental conditions, HVAC system operations, building energy consumption, and other parameters across multiple sampling frequencies. Additionally, the dataset includes floor plans and other relevant information, providing a solid foundation for multi-parameter analysis and spatiotemporal feature analysis in indoor temperature prediction.

3.2. Data Preprocessing

The author selected data from 10 rooms out of 50 rooms equipped with various sensors provided by the dataset. These rooms have similar schedules for HVAC system operations and are equipped with a full range of sensors. The figure below (Figure 3) illustrates the average percentages of natural ventilation, cooling, and heating hours throughout the year, as well as the deviations between rooms. These selected rooms rely primarily on natural ventilation throughout the year, with some percentage of cooling and heating during autumn and winter, ensuring comparability.

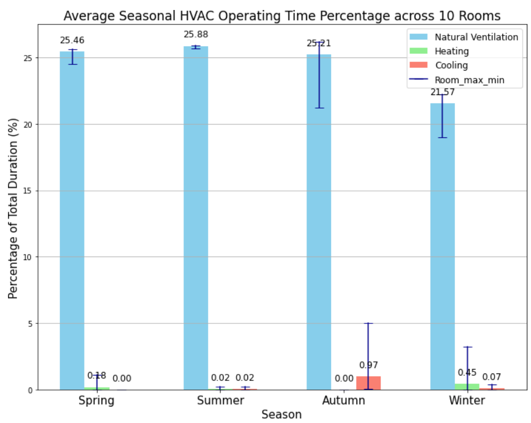

Figure 3: Average seasonal HVAC operating time percentage across 10 rooms

Room temperature prediction is primarily used for managing the startup and shutdown of air conditioning and heating systems. The HVAC system in the case building allows temperature adjustments in increments of 0.5 ℃. Excessive data sampling can lead to data redundancy, significantly increasing the length of time series and the complexity of learning. The author summarized temperature data from these 10 representative rooms using first-order differences to reflect temperature changes under different sampling intervals, illustrated through box plots (Figure 4) where T represents minutes and H represents hours. In the box plots, the box represents the interquartile range (IQR), covering the middle 50% of the data, with the upper and lower boundaries being the third quartile (Q3) and the first quartile (Q1), respectively. The whiskers extend to the maximum and minimum values within 1.5 times the IQR from Q3 and Q1.

As shown in the figure, temperature variations generally reach 0.5 ℃ when sampled every 4 hours (4H). As the sampling interval is further reduced, the time step for temperature prediction increases, leading to more coarse-grained control of HVAC equipment management. Therefore, this study chose a historical data resampling frequency of every 4 hours, corresponding to the prediction time step.

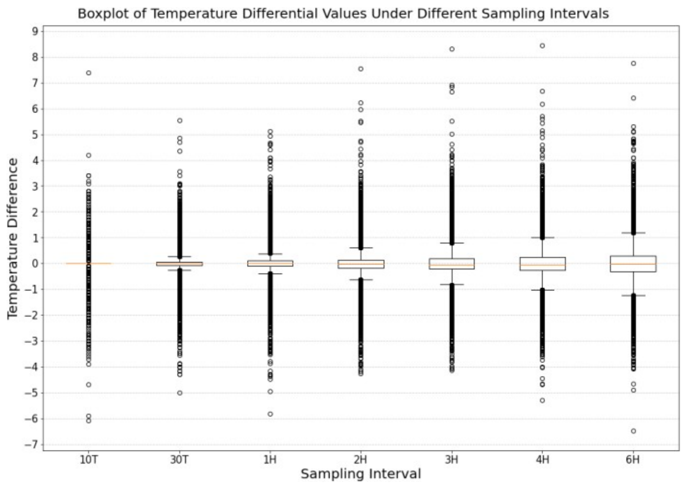

Figure 4: Boxplot of temperature differential values under different sampling intervals

Due to the natural room temperature conditions, variations in room temperature do not exhibit significant long or short-term cyclic patterns influenced by HVAC system on-off cycles, resulting in low autocorrelation in the data. Room temperature changes follow an annual cycle. The author analysed correlations among temperature data from 10 representative rooms. The Pearson correlation coefficients between pairwise room temperature sequences are presented in (Table 1). The letters denote the building areas where the rooms are located, and numbers represent the room identifiers. Rooms with highly correlated temperatures were integrated into a composite training set to broaden sample coverage. The results, depicted in (Figure 5), show that rooms with high correlation exhibit similar annual temperature variation curves, albeit with variations among different integrated datasets.

Table 1: The correlation among the temperatures of the 10 representative rooms

	A37	A38	A43	B9	B10	B11	B15	VB16	B17	B18
A37	1	0,99	0,98	0,94	0,95	0,91	0,96	0,95	0,96	0,94
A38	0,99	1	0,99	0,94	0,96	0,92	0,96	0,95	0,96	0,95
A43	0,98	0,99	1	0,92	0,94	0,91	0,94	0,93	0,94	0,93
B9	0,94	0,94	0,92	1	0,96	0,92	0,97	0,97	0,97	0,95
B10	0,95	0,96	0,94	0,96	1	0,94	0,97	0,97	0,97	0,95
B11	0,91	0,92	0,91	0,92	0,94	1	0,91	0,92	0,92	0,90
B15	0,96	0,96	0,94	0,97	0,97	0,91	1	0,99	0,99	0,98
B16	0,95	0,95	0,93	0,97	0,97	0,92	0,99	1	0,99	0,97
B17	0,96	0,96	0,94	0,97	0,97	0,92	0,99	0,99	1	0,98
B18	0,94	0,95	0,93	0,95	0,95	0,90	0,98	0,97	0,98	1

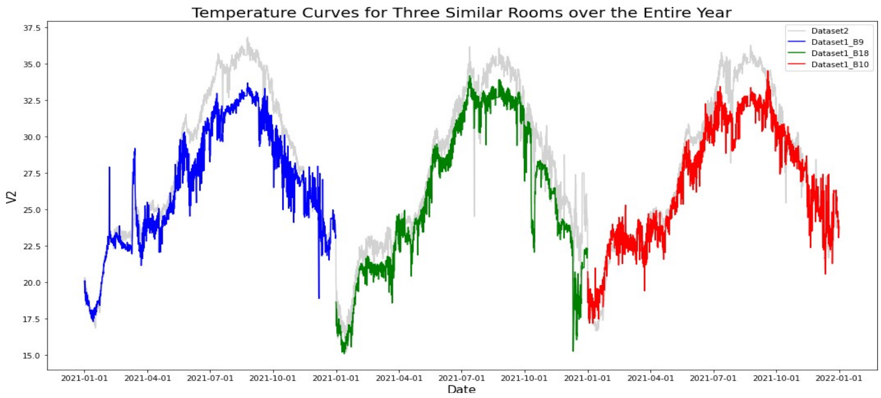

Figure 5: Temperature curves for three similar rooms over the entire year

3.3. The selection of relevant parameters

In terms of temperature prediction problems, there are various types of parameters involved, and different methods are needed to calculate their correlations. The Pearson correlation coefficient is a statistical measure that assesses the strength and direction of the linear relationship between two continuous variables. Its expression is as follows (Equation 4). Point-biserial correlation coefficient is a statistical measure that assesses the relationship between a binary variable and a continuous variable. Its expression is as follows (Equation 5).

Equation 4: Quantity of energy stored in water.

$$r_{xy} = \frac{\sum_{i=1}^{n}(x_i - \bar{x})(y_i - \bar{y})}{\sqrt{\sum_{i=1}^{n}(x_i - \bar{x})^2 \sum_{i=1}^{n}(y_i - \bar{y})^2}}$$

Where:

- x_i, y_i: the observed values of two variables
- $\bar{x}, \bar{y}$ the means of the two variables
- n: the sample size

Equation 5: Quantity of energy stored in water.

$$r_{pb} = \frac{\overline{X_1} - \overline{X_0}}{\sqrt{\frac{N_1 N_0}{N(N-1)}}(\frac{S_1^2}{N_1} + \frac{S_0^2}{N_0})}$$

Where:

- $\overline{X_1}$, $\overline{X_0}$: the mean of the continuous variable when the Boolean variable is 1 and when it is 0
- N_1, N_0: the sample size of the Boolean variable when it is 1 and when it is 0
- S_1^2, S_0^2: the variance of the continuous variable when the Boolean variable is 1 and when it is 0
- N: the total sample size

Both correlation coefficients range between -1 and 1. r_{xy}=1 indicates a strong positive correlation, r_{xy}=-1 indicates a strong negative correlation, and absolute values greater than or equal to 0.5 indicate significant correlation between variables. r_{pb}=1 or close to 1 indicates that the mean of the continuous variable is significantly higher when the binary variable is 1 compared to when it is 0. r_{pb}=0 or close to 0 indicates no significant difference in the continuous variable across the two categories of the binary variable.

The author conducted correlation analysis between temperatures from 10 representative rooms and a diverse set of parameters and calculated the differences among the rooms. The results are presented in （Table 2）. In the table, "mean" represents the average correlation coefficient of room temperature (V2) with each parameter across the 10 rooms, and "std" indicates the standard deviation of these 10 coefficients. Specific parameters include: tmed (average outdoor temperature), dewpt (outdoor dew point temperature), dpv (outdoor vapor pressure difference), cons_total (cumulative electricity consumption within each area), dif_cons (first-order difference in electricity consumption), pred (precipitation), V27 (indoor occupancy status of each room), hrmed (average outdoor relative humidity), dvmed (outdoor wind direction), and V17 (carbon dioxide concentration in each room). During calculations, V27 was treated as a boolean variable using the point-biserial correlation coefficient, while Pearson correlation coefficients were used for continuous variables. The results indicate that, apart from significant variations in the impact of carbon dioxide concentration on room temperature, the selected parameters exhibit high similarity across the ten rooms. Particularly, tmed, dewpt, dpv, and cons_total show

pronounced correlations.
To reduce redundancy in the input features for the GRU network, correlations among these parameters were analysed and visualized using a heatmap (Figure 6). The analysis revealed a strong linear correlation between dpv and tmed among outdoor meteorological parameters, leading to the decision to remove dpv as a redundant parameter. Given the significant fluctuations in correlation coefficients between carbon dioxide concentration and temperature, suggesting a potentially complex non-linear relationship, this parameter was retained for further analytical study due to the GRU network's powerful capabilities in non-linear fitting and feature extraction.

Table 2: Correlation Analysis of Room Temperature and Various Parameters in 10 Representative Rooms

	mean	std
tmed	0.804	0.020
dewpt	0.779	0.019
dpv	0.499	0.022
cons_total	0.467	0.061
radmed	0.187	0.017
vvmed	0.147	0.022
dif_cons	0.000	0.066
pred	-0.026	0.005
V27	-0.045	0.016
hrmed	-0.171	0.038
dvmed	-0.178	0.010
V17	-0.196	0.304

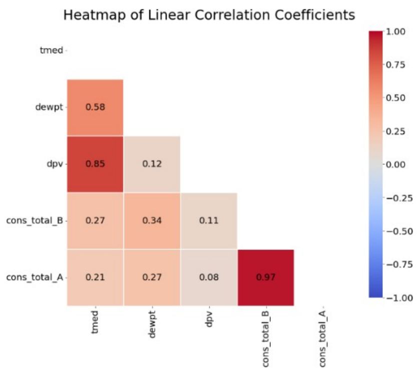

Figure 6: Linear correlation coefficients between selected parameters

4. MODEL CONSTRUCTION

The SARIMA model construction process is as follows: First, the optimal seasonal differencing period of 6 time steps (equivalent to one day) was determined through time series trend decomposition. Next, the author conducted Augmented Dickey-Fuller (ADF) and white noise tests on the series after regular differencing and seasonal differencing to confirm its stationarity and non-white noise characteristics. Using the Akaike Information Criterion (AIC) as the optimization objective, the optimal SARIMA hyperparameters (4, 1, 1) (1, 1, 4, 6) were identified through grid search. Subsequently, the SARIMA model was fitted, providing dynamic predictions of 42 future time steps (equivalent to one week) of temperature values for each current time step.

The input parameters of the GRU neural network include tmed, dewpt, cons_total, V12, and the current time step V2 value. The output is the future time step's V2 value. The author performed three types of temporal feature constructions for the network:

1. The original data is sampled at 10-minute intervals. During the resampling at 4-hour intervals, the mean, maximum, minimum, median, and mode of each input parameter are retained and added to the network input, referred to as F1.

2. Using the sliding window averaging method, sliding window offsets are set at 6, 12, 18, 24, 30, 36, and 42 time steps, with a window size of 6 time steps and a sliding step of 1 time step. The average daily temperature values for the past one week at each current time step are added to the network input, allowing the network to capture coarser-grained temperature cycle features, referred to as F2.

3. The temperature values for all 42 time steps over the next week are added to the network output, allowing the model to

simultaneously consider prediction errors across all time steps during backpropagation to update model parameters, referred to as M. Correspondingly, the model with only the temperature value at the 42nd time step as the network output is referred to as the S-type construction. The optimized model is named GRU-F1-F2-M.

5. EXPERIMENTAL ANALYSIS

5.1. Multi-model comparative experiments

The GRU model training employs mini-batch training with the Adam optimizer. Subsequence random indexing is set up. The ratio of training, testing, and validation sets is 8:1:1. The model has 5 hidden layers with 400 units each. Each batch includes 10 subsequences. One subsequence consists of 20 time steps. The initial learning rate is 0.001, and the initial number of iterations is set to 400. To prevent overfitting, a threshold for the best training and validation set loss functions is established; training stops early if the loss falls below this threshold. Details of the experimental environment parameters are listed in (Table 3).

Table 3: Experimental environmental parameters

Device	Version
CPU Model	Intel(R) Core (TM) i5-1035G1 CPU @ 1.00GHz 1.19 GHz
GPU Model	NVIDIA GeForce MX350
RAM	16.0 GB
Deep Learning Framework	Pytorch 2.2.2 +CUDA 12.1
Programming Language	Python 3.11.5
Operating System	Windows 10

Model evaluation metrics include Mean Absolute Error (MAE, Equation 6), Mean Squared Error (MSE, Equation 7) and Root Mean Squared Error (RMSE) for prediction assessment.

Equation 6: Mean Absolute Error.

$$MAE = \frac{1}{N}\sum_{i=1}^{N}\left|Y_i - \widehat{Y_i}\right|$$

Equation 7: Mean Squared Error.

$$MSE = \frac{1}{N}\sum_{i=1}^{N}\left(Y_i - \widehat{Y_i}\right)^2$$

Where:

- Y_i, $\widehat{Y_i}$: actual values and predicted values
- i: time steps
- N: sample size

In the testing set of the integrated dataset, using a sliding window with a size of 42 time steps and a stride of 42 time steps, predictions were made with three models. As shown in the figure (Figure 7) below, the SARIMA model can perform short-term predictions and follow trend changes. However, due to cumulative errors from dynamic predictions, significant deviations from the actual values occur after multiple time steps. After dataset integration and relative parameter selection, the GRU-S model accurately predicts data at short time intervals and captures long-term temperature trends, but it can exhibit significant localized errors, as demonstrated at the beginning of the prediction curve, indicating weaker model robustness. The overall prediction error evaluation metrics for the testing set sequences are shown in (Table 4), indicating that compared to the two baseline models, the optimized GRU-F1-F2-M model increased MAE by 16.15% and 38.03%, and RMSE by 15.36% and 57.89%, respectively.

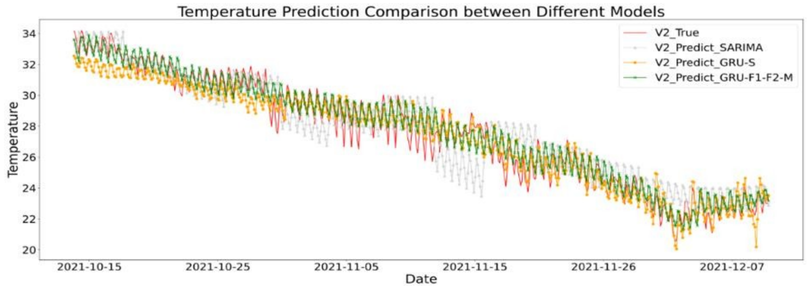

Figure 7: Temperature prediction comparison between different models on test set

Table 4: The overall prediction error of three models on test set

Model	MAE	RMSE	MSE
SARIMA	0.744	1.080	1.167
GRU-S	0.626	0.789	0.623
GRU-F1-F2-M	0.539	0.684	0.469

The author further analysed the average prediction errors of the three models at different time steps on the test set, and the results are shown in the figure below (Figure 8). It can be observed that prediction errors increase with the number of forecasted time steps. However, compared to the SARIMA model, the GRU multi-time step prediction model shows a significantly reduced growth rate in prediction errors. Compared to single-step predictions, the GRU neural network, after optimizing relevant parameters and constructing temporal features, achieves synchronized multi-step temperature predictions while maintaining lower long-term prediction error levels. It also significantly improves the issue of error accumulation caused by dynamic predictions.

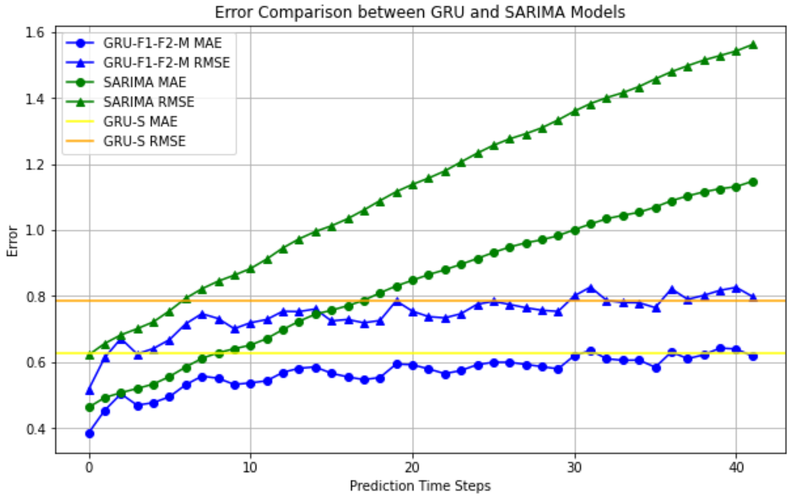

Figure 18: Error comparison between GRU and SARIMA models

5.2. Ablation experiments

To evaluate the actual impact of the three temporal feature constructions on improving the performance of the GRU neural network, the author conducted ablation experiments. These experiments tested different models on the integrated dataset from three rooms in Area A, focusing on the prediction accuracy at the farthest time step (time step 42). To minimize the impact of random initialization on the model training results, each model was trained multiple times, and the average error of the five best-converging training runs was used. The results of the ablation experiment are shown in (Table 5).

The experimental results indicate that applying the three temporal feature constructions significantly improves model accuracy on the condition that the model structure remains unchanged. Specifically, compared to GRU-S, GRU-M reduces fluctuations in the loss function convergence and reliance on random initialization. However, due to the considerable increase in network output dimensions, the model's expressive capability is insufficient, leading to higher error. The F1 construction enhances network complexity and improves the model's fitting capability, while the F2 construction boosts model generalization ability, with notable improvements in the validation set loss function after employing F2. Additionally, the early stopping training strategy also notably enhanced the model's performance on the test set.

Table 5: Average prediction error at the farthest time step on the test set

Model	MAE	RMSE	MSE
GRU-F1-F2-M	0.668	0.853	0.728
GRU-F1-M	0.729	0.920	0.846
GRU-M	0.735	0.958	0.925

6. CONCLUSION

Based on the open-source smart building dataset PLEIAData, the author selected 10 representative rooms equipped with air conditioning and heating systems and with similar HVAC operating schedules. Through detailed correlation analysis and various temporal feature constructions, the optimized GRU neural network model accurately predicts indoor building temperatures for the upcoming week at 4-hour intervals. The results showed improvements in MAE by 16.15% and 38.03%, and RMSE by 15.36% and 57.89%, compared to two baseline models.

The author analysed the temperature variation of rooms under natural ventilation conditions throughout the year in the case building. It was found that with a 4-hour sampling interval, the temperature variation reached 0.5 degrees Celsius. This sampling frequency is practically significant for HVAC system start-stop management and temperature settings. Additionally, the spatial correlation of room temperatures dominated by natural indoor temperatures was analysed, revealing that while the overall temperature trends of the building are similar, there are differences. Neighbouring rooms showed a high linear correlation in temperature. Based on these findings, the author proposed expanding the sample coverage through dataset integration.

Within the scope of 10 representative rooms, the author explored the relevant parameters for predicting natural indoor temperatures and found that outdoor average temperature, outdoor dew point temperature, and total electrical consumption within the area are generally related to indoor temperature changes. Furthermore, the correlation degree of carbon dioxide concentration varies among rooms.

Discussion: The dataset used in this study employs PIR sensors to monitor indoor occupancy. These sensors operate by triggering a high signal when movement is detected, which then returns to a low signal after 3 to 5 minutes. The data collected are binary. Analysis revealed that this type of sensor suffers from significant data loss in each room, which may be the reason for the lack of a linear correlation between occupancy and temperature predictions. More accurate indoor occupancy data would be beneficial for further analysing this correlation.

7. REFERENCES

Afroz, Z., Urmee, T., Shafiullah, G. M. & Higgins, G, 2018. Real-time prediction model for indoor temperature in a commercial building. Applied Energy231, 29–53.

Alawadi S, Mera D, Fernández-Delgado M, Alkhabbas F, Olsson CM, Davidsson P, 2022. A comparison of machine learning algorithms for forecasting indoor temperature in smart buildings. Energy Systems, 13, 689–705.

Attoue, N., Shahrour, I. & Younes, R, 2018. Smart Building: Use of the Artificial Neural Network Approach for Indoor Temperature Forecasting. Energies, 11, 395.

Cao, H., Chen, J., & Li, X., 2024. Water level prediction using SARIMA-GRU combined model. Journal of Nanchang Engineering College, 43(03), 8-12.

Ibarra, A.M., González-Vidal, A. & Skarmeta, A, 2023. PLEIAData: consumption, HVAC, temperature, weather and motion sensor data for smart buildings applications. Sci Data, 10, 118.

Langevin, J, 2019. Longitudinal dataset of human-building interactions in U.S. offices. Sci Data, 6, 288.

Pipattanasomporn, M., Chitalia, G., Songsiri, J. et al, 2020. CU-BEMS, smart building electricity consumption and indoor environmental sensor datasets. Sci Data 7, 241.

Schweiker, M., Kleber, M. & Wagner, A, 2019. Long-term monitoring data from a naturally ventilated office building. Sci Data, 6, 293.

Shi, X., Tian, W. B., Leng, Z. L., Lu, H., 2021. A global prediction model of indoor temperature in buildings based on CFD and LightGBM algorithms. Journal of Instrumentation and Measurement, 2021(01), 237-247.

Shin, C., Lee, E., Han, J. et al, 2019. The ENERTALK dataset, 15 Hz electricity consumption data from 22 houses in Korea. Sci Data, 6, 193.

Wang, X. W., 2023. Prediction of Indoor Temperature in Large Public Buildings Based on Deep Learning [D]. Shandong University. DOI: 10.27272/d.cnki.gshdu.2023.001599.

Xu, C., Chen, H., Wang, J., Guo, Y. & Yuan, Y, 2019. Improving prediction performance for indoor temperature in public buildings based on a novel deep learning method. Building and Environment, 148, 128–135.

#323: Thermal insulation and flame retardancy properties of konjac glucomannan/sodium alginate aerogel for building application

Kao WU, Zijian YE, Junjie CHENG, Zihan YU, Fatang JIANG*

Cooperative Innovation Center of Industrial Fermentation (Ministry of Education & Hubei Province), School of Life and Health Sciences, Hubei University of Technology, Wuhan 430068, China
Corresponding author: Fatang JIANG, email: jiangft@mail.hbut.edu.cn

Abstract: This study presented the preparation and property characterization of polysaccharide aerogel as a kind of thermal insulation and flame-retardant biomass material. For safe and sustainable thermal insulation applications in buildings, a polysaccharide aerogel with both low flammability and thermal conductivity is of great importance. Therefore, the konjac glucomannan (KGM) /sodium alginate (SA) aerogels prepared by the sol-gel and freeze-drying method were investigatedin this study. KGM was used as the skeleton material of aerogel and SA was selected due to its inherent flame retardancy properties, which easily formed a dense carbon layer barrier to prevent the fire. Results showed that the pore characteristics were impacted by both total solid mass and KGM/SA ratios. The mechanical properties were significantly enhanced by the formation of hydrogen bonding interactions between KGM and SA. Finally, the KGM/SA aerogel with the optimized formula had a peak heat release of 33.12 W/g, mechanical properties of 161.5 kPa, density of 0.0348 g/cm3, porosity of 95.67±0.11%, and thermal conductivity of 0.0385 W/(mK). These results revealed the great application potential of KGM/SA aerogel to be used in building fire protection and thermal insulation and guided the formulae design of polysaccharide aerogels.

Keywords: Biomass Aerogel; Mechanical Strength; Thermal Conductivity; Combustion Property; Sustainable Architecture

1. INTRODUCTION

There is a wide variety of available insulation materials (Abu-Jdayil, Mourad, Hittini, Hassan, & Hameedi, 2019), such as polystyrene foam (G. de Moraes, Sangiacomo, P. Stochero, Arcaro, R. Barbosa, Lenzi, et al., 2019; M.-E. Li, Zhao, Cheng, Wang, Fu, Zhang, et al., 2022), polyurethane (Andersons, Kirpluks, Cabulis, Kalnins, & Cabulis, 2020; Uram, Prociak, Vevere, Pomilovskis, Cabulis, & Kirpluks, 2021) and biomass insulation (Sen, Singh, Bera, Roy, & Kailasam, 2022; Yan, Ge, Qin, Ruan, Guo, He, et al., 2020). Most organic materials showed better thermal insulation performance than inorganic materials. Moreover, inorganic materials were mostly derived from non-renewable fossil resources and could cause serious damage to the environment after discarded. Therefore, increasing research focused on natural polymer-based organic materials in recent years like aerogels. Aerogel is a kind of porous solid material with the structural characteristics of low density, high specific surface area, and high porosity, which has excellent thermal insulation and adsorption properties and is widely used in aerospace, construction industry, and ecological environments.

However, most biomass aerogels were flammable (Dorez, Taguet, Ferry, & Lopez-Cuesta, 2013), which hindered their application. To enhance the flame retardancy performance of biomass aerogel, usually the addition of flame retardant materials containing phosphorus, nitrogen, and halogen was adopted, which could reduce the reaction heat during combustion by trapping free radicals (P. Wang, Chen, Xiao, & Zhan, 2020; Zou, Duan, Chen, Ji, Cao, & Ma, 2020) and/or release the flame-retardant gases or forming a dense carbon barrier layer through condensed phase and gas phase flame retardant mechanisms. However, traditional flame retardants produced toxic and carcinogenic substances during combustion, causing harm to people's health (Levchik & Weil, 2006; L. Li, Wang, Hua, Wang, Zhang, Xi, et al., 2021; W. Zhang, He, Song, Jiao, & Yang, 2014). It was reported that starch (Zhu, 2019), cellulose (Q. Zhang, Chen, Li, Sun, Ren, Cheng, et al., 2023) and cyclodextrin (Zeng, Xing, Chen, Xu, Li, & Zhang, 2020; X. Zhang, Yang, Li, Wu, Zhu, Bi, et al., 2023), and lignin (Cen, Chen, Yang, Zheng, & Qiu, 2023; M. Zhang, Wang, Li, Jiang, Bai, Wang, et al., 2023) were natural carbon sources that can replace conventional traditional flame retardants to form new environmentally friendly intumescent flame retardant systems due to the excellent char formation ability. In addition, alginate (Cen, Chen, Yang, Zheng, & Qiu, 2023; Han, Ding, Zhu, & Wang, 2023) and chitosan (Chen, Zhou, Miao, Liu, Huang, Chen, et al., 2023; Tang, Liang, Wang, Yuan, Dessie, Liu, et al., 2023) showed good flame retardant properties and can reduce the heat release rate of insulation materials.

Natural polysaccharides are widely used because of their non-toxicity, sustainability, and biodegradability. Konjac glucomannan (KGM) is a kind of natural renewable polymer, mainly composed of glucose and mannose units connected by β-1,4-glycosidic bonds and containing small amounts of acetyl groups. The highly linear and flexible KGM chains can easily interact with other biopolymers through hydrogen bonds and can be an excellent backbone material for aerogel preparation, according to our previous research on the KGM-based thermal insulation aerogels (Kuang, Liu, Yang, Wang, Liu, Wang, et al., 2023; Qian, Fang, Wu, Wang, Li, & Jiang, 2021; Y. Wang, Wu, Xiao, Riffat, Su, & Jiang, 2018; Wu, Wu, Wang, Yan, Sun, Liu, et al., 2022). Sodium alginate (SA), a natural polysaccharide extracted from brown algae, is widely used as one kind of natural flame retardant. Xu, Qu, Liu, and Zhu (2021) reviewed the progress of alginate in the field of flame retardancy and its pyrolytic behavior and indicated that alginate was an "ideal" future "promising material for flame retardants. However, SA aerogel has poor mechanical property which seriously hinders its application. Therefore, in this work, composite KGM/SA aerogels were prepared, and their thermal insulation and flame retardancy-related properties were investigated compared with pure SA aerogels. The present study was of good significance in improving the flame retardancy property of polysaccharide thermal insulation aerogels.

2. MATERIALS AND EXPERIMENTAL METHODS

2.1. Materials preparation

KGM (Mw = 9.67 × 10^5 Da) was supplied by Hubei Konson Konjac Technology Co., Ltd. (Wuhan, China). Sodium alginate (Food grade) was purchased from Maclin Biochemical Co., Ltd. (Shanghai, China).

2.2. Preparation of the KGM-Based Aerogels

Firstly, SA was dissolved in 100 mL of distilled water in a water bath at 60°C for half an hour under constant stirring at 600 rpm, then KGM was added with a stirring speed of 800 rpm for 1h. Subsequently, the obtained sol was poured into the mold and immediately pre-cooled in a refrigerator at 4 °C for 2h, before being placed in a freeze dryer at - 55°C for 24 h under 1 Pa vacuum to obtain aerogels. All samples are coded as shown in Table 1.

Table 1. Aerogels formulae and corresponding porosity and density of the samples

Sample codes	KGM (g/100mL)	SA (g/100mL)	Porosity (%)	Density(g/cm^3)
SA1	0	1	97.85± 0.03	0.0148± 0.0002
SA2	0	2	96.60± 0.03	0.0345± 0.0006
SA3	0	3	95.21± 0.08	0.0372± 0.0007

K0.5SA1	0.5	1	97.65± 0.06	0.0201± 0.0005
K0.5SA2	0.5	2	95.72± 0.14	0.0337± 0.0004
K0.5SA3	0.5	3	94.19± 0.09	0.0471± 0.0004
K1SA1	1	1	97.16± 0.02	0.0242± 0.0006
K1SA2	1	2	95.67± 0.04	0.0348± 0.0004
K1SA3	1	3	91.97± 0.11	0.0516± 0.0010

2.3. Dry density

An analytical balance and vernier calipers were used to measure the prepared aerogels. All tests were repeated three times, and the dry density (ρ) was calculated using the following equation (1),

$$\rho = \frac{m}{V} \quad (1)$$

where *m* is the weight of the biomass aerogel, and *V* is the volume of the biomass aerogel sample.

2.4. Porosity estimation

Porosity is an important indicator for determining the structure of aerogels (Wu, et al., 2022). First, the dried biomass aerogel weighed with mass m0 and then completely immersed in a beaker containing ethanol, and the total mass was recorded as m1. The beaker containing the aerogel and ethanol was placed in a vacuum desiccator and evacuated until no air bubbles emerged from the aerogel. After evacuation, the aerogel was removed and the beaker with residual ethanol was weighed, and the mass was recorded as m2. Four parallel experiments were performed for each test. The porosity of the aerogels was calculated as equation (2):

$$P = \frac{m_1 - m_2 - m_0}{m_1 - m_2} \times 100\% \quad (2)$$

2.5. Pore microstructure

Scanning electron microscopy (SEM) was used to observe the aerogel pore microstructure. Before SEM, the aerogel was cut into 5.0 mm × 5.0mm × 1.0 mm small cubes. Then the samples were subjected to gold spraying (Bio-Rad type SC 502, JEOL Ltd, Japan). The microstructure of the aerogel was observed at a magnification of ×50 using an accelerating voltage of 50kv.

2.6. Mechanical properties

The mechanical properties of aerogels were tested by compression using a texture analyzer (TA, XT Plus, Stable Micro Systems, Surrey, UK) equipped with a 30 kg load cell and a discoidal probe (P/36R, No. 14631). The test parameters were as follows: compression ratio: 60 mm/min; compression strain: 60%; trigger force: 1.00 N. The compressive strength of the samples was defined as the maximum stress during the test. The stress (σ) is calculated from the following standard equation (3):

$$\sigma = \frac{F}{S_0} \quad (3)$$

where F is the force on the surface of samples.

2.7. Thermal conductivity

The steady-state plate method was used to determine the thermal conductivity according to a thermal conductivity tester (DRPL-2A, Xiangtan Instrument Co., Ltd., China) following the previous method (Wu, et al., 2022). The samples were mounted between two metal plates with thermal sensors and were wrapped in an insulation gasket with a weatherproof cover on the outside. For all samples, the air contact side of the aerogel was in contact with the hot plate and the mold support side of the aerogel was in contact with the cold plate. The temperature of the hot side of the metal plate was controlled at 50 °C and the heat was transferred through the sample to the cold side (20 °C). The thermal conductivity was automatically calculated based on the heat transfer value as well as the thickness and area of the sample.

2.8. Microscale combustion calorimeter measurement

The flame retardancy property of KGM-based aerogels was determined by an FAA microscale combustion calorimeter (MCC, FTT0001, FTT Ltd., West Sussex, UK). About 3.0–4.0 mg of samples was placed in an alumina ceramic crucible and heated between 100 and 500 °C at a heating rate of 1°C/s in an inert nitrogen atmosphere. The decomposition products flowed from the pyrolyzer to a 900 ° C combustion furnace at the 80 cm^3/min gas stream of nitrogen and 20 cm^3/min of oxygen, where the decomposition products were completely oxidized.

2.9. Thermogravimetric analysis

The thermogravimetric test was measured using a Netzsch TG 209 (Thermogravimetric Analyzer, Nexi, Germany). The freeze-dried composite biomass aerogel sample was pulverized before testing. The sample was heated from 40 to 700 °C at a heating rate of 20°C/min under a nitrogen flow rate of 20 ml/min.

2.10. Statistical analysis

SPSS (version 22, Endicott, NY, USA) was used for the analysis of variance by Tukey's multiple range test at $p < 0.05$. Origin 2019 (OriginLab, MA, USA) was used for figure drawing.

3. RESULTS AND DISCUSSION

3.1 Density and porosity

Density and porosity are important properties of aerogel (Table 1 and Figure 1). The density and porosity of the samples ranged from 0.02-0.05g/cm^3, and 91.97 to 97.85%, respectively, supporting aerogel pore characteristics. With increased solid concentration, the density of aerogel became higher with reduced porosity for all the samples. A similar phenomenon was observed for KGM/starch/gelatin/wheat straw composite aerogel and was used to control the pore size distribution (Wu, Fang, Wu, Wan, Qian, Jiang, et al., 2021).

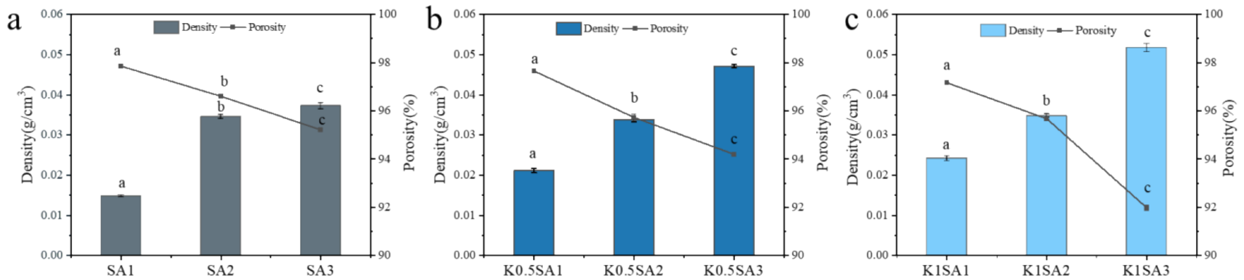

Figure 1: Aerogels formulae and porosity, density. (The data points with the same letter did not have a significant difference)

3.2 Pore microstructure

The microstructure of the aerogel samples showed significant differences (Figure 2 a-c). The pore structure of SA aerogel was small and polygonal in shape (SA1, SA2, and SA3), and the pore size appeared to be a few larger for SA1 due to the relative SA low concentration in the sol, agreeing the porosity result. With 0.5% KGM addition, the pore microstructure appeared to have an irregular shape. With further higher KGM addition, K1SA1 and K1SA2 showed smaller pores. This was probably due to the strong water combination capability of KGM contributing to restricting water movement, which resulted in smaller ice crystals and therefore benefited the small pore formation. On the other hand, the pore size of K1SA3 appeared to be similar to SA3 and K0.5SA3, and their pore structure might be more influenced by the high SA content rather than KGM.

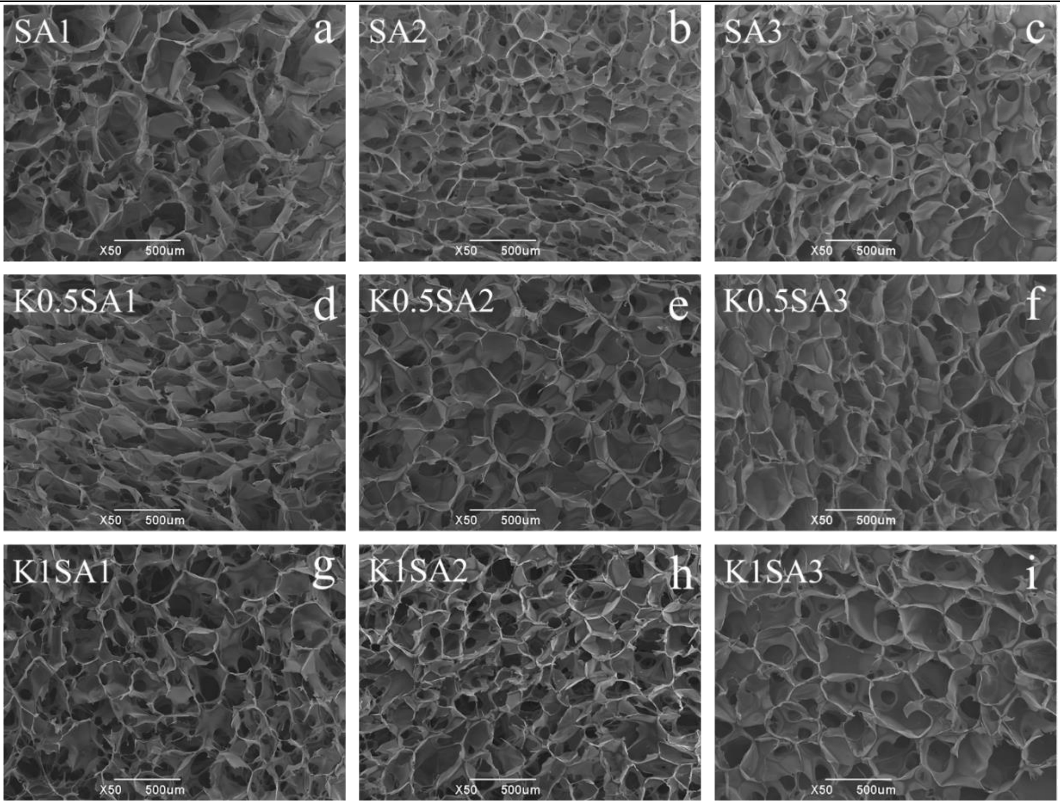

Figure 2: SEM images of SA aerogels and KGM/SA aerogels

3.3 Mechanical property

Mechanical properties are important parameters of material properties that reflect the strength of the material. According to the stress-strain curve of the composite aerogel (Figure 3a-c), the mechanical strength of the aerogels showed significant differences with a strain of 60%. For SA aerogels, their compressive strength was very weak, and the compressive strength at of SA1, SA2, and SA3 were 21.6 kPa, 64.8 kPa, and 139.0 kPa, respectively. With KGM addition, the increased sol solid concentration led to the higher density of aerogels (Table 1), and therefore, the compressive strength was enhanced. Clearly, the addition of KGM contributed more to the mechanical strength, agreeing previous study that KGM was a good skeleton material for biomass aerogel preparation. The highest compressive strength (313.4 kPa) was reached for K1SA3, indicating the most solid pore wall structure.

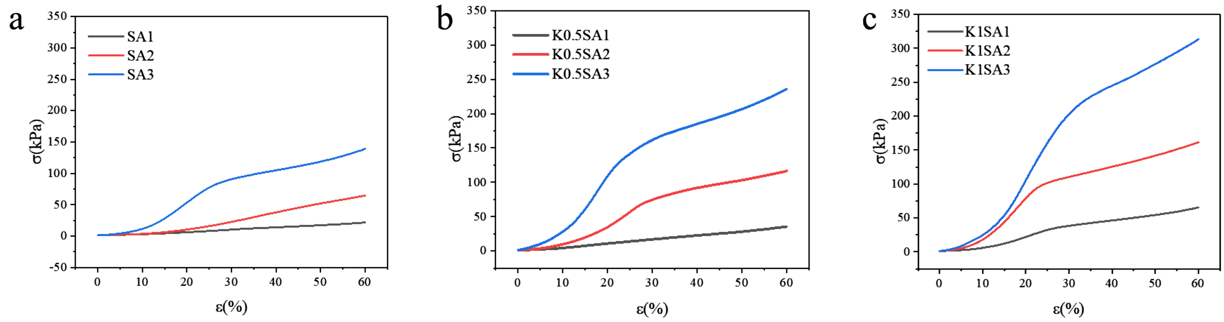

Figure 3: Stress-strain curves of SA aerogels and KGM/SA aerogels

3.4 Thermal conductivity

To evaluate the thermal insulation property of aerogels, thermal conductivity is often determined, and a lower thermal conductivity is preferred. According to Figure 4, the thermal conductivity of SA aerogels was all around 0.0375W/(mK) and was relatively low compared with KGM/starch/gelatin/wheat straw aerogel (Y. Wang, Wu, Xiao, Riffat, Su, & Jiang, 2018).

Usually, higher solid content leads to higher thermal conductivity as the heat conduction is enhanced. But for SA aerogel, the pore size was also decreased with higher SA content, which hindered the air convection, and therefore the thermal conductivity remained unchanged. With KGM addition, the thermal conductivity would remain as low if the SA addition was 1%. However, if the SA addition reached 2.0% or above, the thermal conductivity started to increase, and this impact was more significant at the SA addition of 3.0%. This was caused probably by the reduced porosity and higher density of the aerogels (Table 1) which benefited the heat transfer.

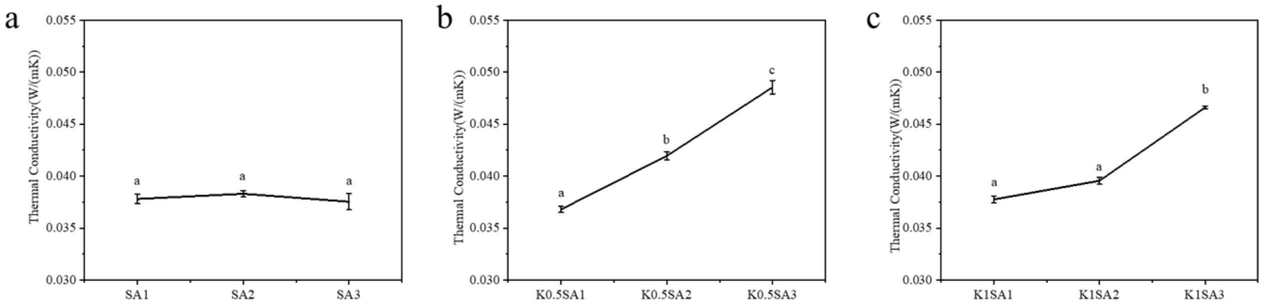

Figure 4: Thermal conductivity of SA aerogels and KGM/SA aerogels. (The data points with the same letter did not have a significant difference)

3.4 Combustion behavior

The combustion properties of SA aerogels and KGM-based aerogels were investigated using a microcalorimeter. Their heat release rate (HRR) and total heat release amount (THR) are presented in Figure 5, and the peak heat release rate (PHRR), the corresponding temperature (TPHRR), and the total heat release amount (THR) are shown in Table 2. It can be seen that all SA aerogels exhibited low HRR and THR, confirming that they had good flame retardancy properties and could be used as a natural flame retardant. The mechanism was that during combustion, SA could form more carbon expansion layer which hindered the oxygen transfer to the interior of the aerogel and therefore prevented the combustion (Jiang, Pang, Deng, Sun, Zhao, Xu, et al., 2019; Kabir, Sorrell, Mofarah, Yang, Yuen, Nazir, et al., 2021). With a constant KGM addition of 0.5%, the increased SA addition from 1.0% to 3.0% did not show a significant impact on the flame retardancy property, but with a constant KGM addition of 1.0%, the increased SA addition appeared to significantly lower the heat release. Their difference might be accredited to the irregular pore structure of K0.1SA aerogels. Therefore, for the composite KGM/SA aerogel, the KGM addition of 1.0% was preferred.

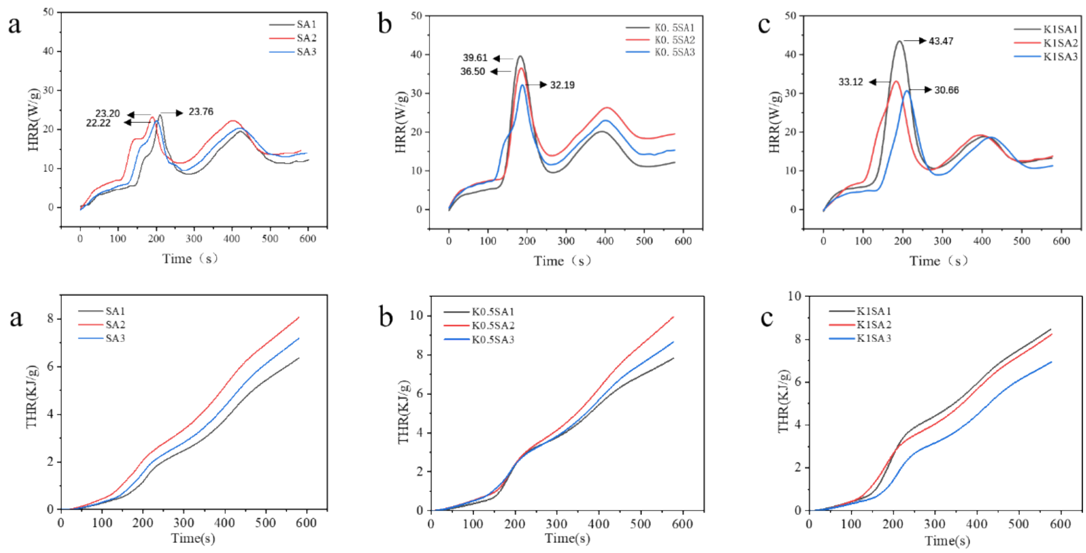

Figure 5: The heat release rate and total heat release of KGM/SA aerogels with different contents

Table 2: Heat release rate, maximum heat release temperature, and heat release amount of composite aerogels

Sample	PHRR (W/g)	TPHRR (℃)	THR（kJ/g）
SA1	23.76	227.31	6.61
SA2	23.20	242.23	8.07
SA3	22.22	243.28	7.41
K0.5SA1	39.61	239.83	7.82
K0.5SA2	36.50	237.19	9.95
K0.5SA3	32.19	240.86	8.66
K1SA1	43.47	252.177	8.47
K1SA2	33.12	238.34	8.22
K1SA3	30.66	240.75	6.94

4. CONCLUSION

The thermal insulation and flame retardancy-related properties of pure KGM, pure SA, and KGM/SA aerogel were compared and analyzed. All aerogels showed high porosity (91.97-97.85%) and low density (0.0148-0.0516 g/cm^3). According to the results, the SA aerogel had a relatively small and polygonal pore shape, and the KGM/SA aerogel showed an irregular shape with varied pore size distribution, which was impacted by the solid concentration and KGM/SA ratio. Compared with SA, KGM contributed more to the improvement of the mechanical strength. The SA addition appeared to contribute to the flame retardancy and thermal insulation but the impact was also affected by the pore structure. Considering all the properties, the optimal biomass aerogel was considered to be K1SA2 and showed potential to be used in sustainable buildings, with a mechanical strength of 161.5 kPa, thermal conductivity of 0.0385 W/(mK), PHRR of 33.12 W/g, and THR of 8.22 kJ/g

5. REFERENCES

Abu-Jdayil, B., Mourad, A.-H., Hittini, W., Hassan, M., & Hameedi, S. (2019). Traditional, state-of-the-art and renewable thermal building insulation materials: An overview. Construction and Building Materials, 214, 709-735.

Andersons, J., Kirpluks, M., Cabulis, P., Kalnins, K., & Cabulis, U. (2020). Bio-based rigid high-density polyurethane foams as a structural thermal break material. Construction and Building Materials, 260, 120471.

Cen, Q., Chen, S., Yang, D., Zheng, D., & Qiu, X. (2023). Full Bio-Based Aerogel Incorporating Lignin for Excellent Flame Retardancy, Mechanical Resistance, and Thermal Insulation. ACS Sustainable Chemistry & Engineering, 11(11), 4473-4484.

Chen, J., Zhou, Z., Miao, Y., Liu, H., Huang, W., Chen, Y., Jia, L., Zhang, W., & Huang, J. (2023). Preparation of CS@BAC composite aerogel with excellent flame-retardant performance, good filtration for PM2.5 and strong adsorption for formaldehyde. Process Safety and Environmental Protection, 173, 354-365.

Dorez, G., Taguet, A., Ferry, L., & Lopez-Cuesta, J. M. (2013). Thermal and fire behavior of natural fibers/PBS biocomposites. Polymer Degradation and Stability, 98(1), 87-95.

G. de Moraes, E., Sangiacomo, L., P. Stochero, N., Arcaro, S., R. Barbosa, L., Lenzi, A., Siligardi, C., & Novaes de Oliveira, A. P. (2019). Innovative thermal and acoustic insulation foam by using recycled ceramic shell and expandable styrofoam (EPS) wastes. Waste Management, 89, 336-344.

Han, X., Ding, S., Zhu, L., & Wang, S. (2023). Preparation and characterization of flame-retardant and thermal insulating bio-based composite aerogels. Energy and Buildings, 278, 112656.

Jiang, Y., Pang, X., Deng, Y., Sun, X., Zhao, X., Xu, P., Shao, P., Zhang, L., Li, Q., & Li, Z. (2019). An Alginate Hybrid Sponge with High Thermal Stability: Its Flame Retardant Properties and Mechanism. Polymers, 11(12), 1973.

Kabir, I. I., Sorrell, C. C., Mofarah, S. S., Yang, W., Yuen, A. C. Y., Nazir, M. T., & Yeoh, G. H. (2021). Alginate/Polymer-Based Materials for Fire Retardancy: Synthesis, Structure, Properties, and Applications. Polymer Reviews, 61(2), 357-414.

Kuang, Y., Liu, P., Yang, Y., Wang, X., Liu, M., Wang, W., Guo, T., Xiao, M., Chen, K., Jiang, F., & Li, C. (2023). Study on the Influence of the Preparation Method of Konjac Glucomannan-Silica Aerogels on the Microstructure, Thermal Insulation, and Flame-Retardant Properties. In Molecules, vol. 28).

Levchik, S. V., & Weil, E. D. (2006). A Review of Recent Progress in Phosphorus-based Flame Retardants. Journal of Fire Sciences, 24(5), 345-364.

Li, L., Wang, H., Hua, F., Wang, M., Zhang, Y., Xi, H., Yang, J., Yang, Z., & Lei, Z. (2021). Flame Retardancy of Epoxy Resin Improved by Graphene Hybrid Containing Phosphorous, Boron, Nitrogen and Silicon Elements. Macromolecular Research, 29(9), 625-635.

Li, M.-E., Zhao, H.-B., Cheng, J.-B., Wang, T., Fu, T., Zhang, A.-N., & Wang, Y.-Z. (2022). An Effective Green Porous Structural Adhesive for Thermal Insulating, Flame-Retardant, and Smoke-Suppressant Expandable Polystyrene Foam. Engineering, 17, 151-160.

Qian, H., Fang, Y., Wu, K., Wang, H., Li, B., & Jiang, F. (2021). Air filtration improvement of konjac glucomannan-based aerogel air filters through physical structure design. International Journal of Low-Carbon Technologies, 16(3), 867-872.

Sen, S., Singh, A., Bera, C., Roy, S., & Kailasam, K. (2022). Recent developments in biomass derived cellulose aerogel materials for thermal insulation application: a review. Cellulose, 29(9), 4805-4833.

Tang, W., Liang, G., Wang, L., Yuan, Y., Dessie, W., Liu, F., Qin, Z., Wang, Y., Xiao, A., & Jin, X. (2023). Multi-functional flame retardant coatings comprising chitosan/ gelatin and sodium phytate for rigid polyurethane foams. Journal of Cleaner Production, 394, 136371.

Uram, K., Prociak, A., Vevere, L., Pomilovskis, R., Cabulis, U., & Kirpluks, M. (2021). Natural Oil-Based Rigid Polyurethane Foam Thermal Insulation Applicable at Cryogenic Temperatures. In Polymers, vol. 13).

Wang, P., Chen, L., Xiao, H., & Zhan, T. (2020). Nitrogen/sulfur-containing DOPO based oligomer for highly efficient flame-retardant epoxy resin. Polymer Degradation and Stability, 171, 109023.

Wang, Y., Wu, K., Xiao, M., Riffat, S. B., Su, Y., & Jiang, F. (2018). Thermal conductivity, structure and mechanical properties of konjac glucomannan/starch based aerogel strengthened by wheat straw. Carbohydrate Polymers, 197, 284-291.

Wu, K., Fang, Y., Wu, H., Wan, Y., Qian, H., Jiang, F., & Chen, S. (2021). Improving konjac glucomannan-based aerogels filtration properties by combining aerogel pieces in series with different pore size distributions. International Journal of Biological Macromolecules, 166 1499-1507.

Wu, K., Wu, H., Wang, R., Yan, X., Sun, W., Liu, Y., Kuang, Y., Jiang, F., & Chen, S. (2022). The use of cellulose fiber from office waste paper to improve the thermal insulation-related property of konjac glucomannan/starch aerogel. Industrial Crops and Products, 177, 114424.

Xu, Y. J., Qu, L. Y., Liu, Y., & Zhu, P. (2021). An overview of alginates as flame-retardant materials: Pyrolysis behaviors, flame retardancy, and applications. Carbohydrate Polymers, 260(1), 117827.

Yan, Y., Ge, F., Qin, Y., Ruan, M., Guo, Z., He, C., & Wang, Z. (2020). Ultralight and robust aerogels based on nanochitin towards water-resistant thermal insulators. Carbohydrate Polymers, 248, 116755.

Zeng, S.-L., Xing, C.-Y., Chen, L., Xu, L., Li, B.-J., & Zhang, S. (2020). Green flame-retardant flexible polyurethane foam based on cyclodextrin. Polymer Degradation and Stability, 178, 109171.

Zhang, M., Wang, D., Li, T., Jiang, J., Bai, H., Wang, S., Wang, Y., & Dong, W. (2023). Multifunctional Flame-Retardant, Thermal Insulation, and Antimicrobial Wood-Based Composites. Biomacromolecules, 24(2), 957-966.

Zhang, Q., Chen, J., Li, D., Sun, L., Ren, Y., Cheng, C., & Liu, X. (2023). Simultaneous enhancement of mechanical strength and flame retardancy of lyocell fiber via filling fire-resistant cellulose-based derivative. Industrial Crops and Products, 199, 116757.

Zhang, W., He, X., Song, T., Jiao, Q., & Yang, R. (2014). The influence of the phosphorus-based flame retardant on the flame retardancy of the epoxy resins. Polymer Degradation and Stability, 109, 209-217.

Zhang, X., Yang, Y., Li, M., Wu, J., Zhu, Z., Bi, C., Xie, Y., Wang, T., Sun, Y., Yin, J., Xie, Z., Liu, F., Wang, J., & Yang, J. (2023). Modified β-cyclodextrin microspheres towards the application in intumescent fire resistance and smoke-suppressing of bio-based poly(L-lactic acid). International Journal of Biological Macromolecules, 234, 123666.

Zhu, F. (2019). Starch based aerogels: Production, properties and applications. Trends in Food Science & Technology, 89, 1-10.

Zou, J., Duan, H., Chen, Y., Ji, S., Cao, J., & Ma, H. (2020). A P/N/S-containing high-efficiency flame retardant endowing epoxy resin with excellent flame retardance, mechanical properties and heat resistance. Composites Part B: Engineering, 199, 108228.

#324: A heat pipe-based radiant floor system designed for passive heating in well-insulated low-rise building

Menglei ZHONG[2], Xiaoni GAO[3], Pengyuan SHEN* [1]

[1]Shenzhen International Graduate School, Tsinghua University, Shenzhen, China, pengyuan_pub@163.com
[2] School of Architecture, Harbin Institute of Technology, Shenzhen, China, zhongmenglei@hit.edu.cn
[2] School of Architecture, Harbin Institute of Technology, Shenzhen, China, hathaway886@gmail.com

Abstract: This study introduces a passive heating system for well-insulated low-rise buildings, utilizing a heat pipe-driven radiant floor system directly connected to the earth. Distinguished from conventional radiant floor systems, this approach eliminates moving parts and functions passively during winter, offering enhanced energy efficiency and sustainability. Simulations in Shanghai's hot summer and cold winter climate zone reveal that the system's energy-saving potential is influenced by indoor temperature setpoints and the water temperature in horizontal heat pipes. Further evaluations in Beijing (cool summer and cold winter climate) and Guangzhou (hot summer and warm winter climate) demonstrate different performances. In colder climates, the system's effectiveness reduces, while milder winters see significant energy savings. The study concludes that this passive heating system can be highly effective in regions with mild winters, but less so in colder climates. The importance of climatic considerations in the heat pipe driven passive heating system design is highlighted, contributing to sustainable building practices and energy conservation.

Keywords: Heat Pipe, Passive Heating, Radiant Floor, Building Simulation.

1. INTRODUCTION

The development of passive heating and cooling systems in low-rise buildings has gained significant attention in recent years, driven by the urgent need for energy-efficient and sustainable building solutions (Tejero-González et al. 2016). In this context, heat pipe systems have emerged as a promising technology due to their high thermal conductivity and ability to transfer heat over considerable distances with minimal energy input (Zohuri,2008). Traditional ground heat pump systems, while effective, often come with the drawback of requiring active components, such as compressors and pumps, leading to higher energy consumption and maintenance requirements (Mustafa,2008). Recent advancements in passive heating and cooling systems have focused on integrating these systems more directly with building structures for enhanced efficiency. For instance, studies on radiative floor heating using heat pipes have shown considerable potential for energy savings and maintaining indoor thermal comfort (Hassan and Abdelaziz, 2020). The application of heat pipes in building structures, especially in low-rise buildings, offers a unique approach to harnessing the thermal stability of the ground for heating and cooling purposes (Yao et al. 2023).

This research introduces an innovative system that incorporates heat pipes directly linking building structures with the earth side, marking a novel approach in the field. This system stands out for its passive operation, eliminating the need for mechanical moving parts, which is an advantage over traditional ground heat pump systems. The passive nature of this system not only reduces energy consumption but also minimizes maintenance requirements and increases the system's lifespan. Furthermore, the feasibility and application value of this system across different climate zones are explored using building simulation, which is crucial for evaluating its adaptability and efficiency under varying environmental conditions (Shen and Lior, 2016). The potential advantages of this system, including its simplicity, energy efficiency, and reduced environmental impact, position it as an alternative to conventional heating systems in low-rise buildings.

2. SYSTEM DESIGN

Mechanical heating and cooling use a large portion of energy in buildings (Xu et al. 2012). Advanced passive heating and cooling technology is an important step of reaching zero energy building goals. In order to achieve the goal of realizing zero energy building, a new type of passive heating and cooling system with heat pipes and water wells linking buildings structures with the earth soil is proposed in this paper (see Fig. 1). This time, heat pipes connect earth and building structures through casing wells and heat exchangers. The system has advantages over the traditional ground heat pump systems. It has no moving parts and is 100% passive in heating seasons. In summer, only a small pump is needed to circulate the water in wells, and no compression circling is needed.

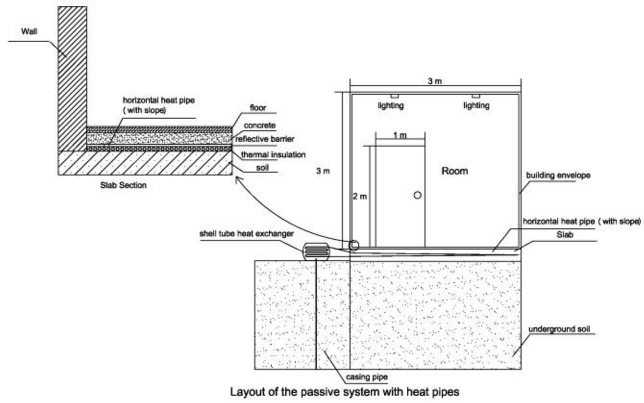

(a)

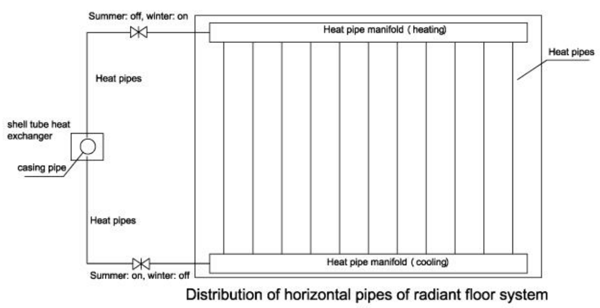

(b)

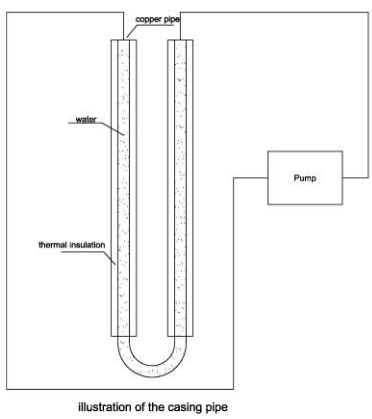

(c)

Figure 1: Diagrams of the proposed passive heating system

A system similar to traditional radiant heating floor system is used as the terminals to release the heat to the interior space. Radiant floor technology has been used for a long time and if it can maintain a warm floor, the space heating load canbe reduced drastically (Jin et al. 2010). Heat pipes are embedded in the slab and connected to a U-form casing pipe through a heat exchanger (Holopainen et al. 2007). The casing pipes are buried underground to serve as heat source. Water is injected into the casing pipes and exchange heat with the deep ground soil. The internal core pipe is the heat pipe embedded in the slab. In winter, since the water at the lower end is warmer than that in the upper end, natural convectionwill move underground heat up to the ground level through the U-shape pipes. Then the heat pipe will transfer the heat from the casing pipe to the slab with heat pipes buried in. The heat pipe can also be called thermosyphon. It only works when the upper end of the pipe is serving as condenser while the low end is evaporator.

The design of the horizontal pipe system of the radiant floor is also different from traditional radiant floor. In traditional radiant floor system, hot water heated by boilers or other heat sources is forced circulating inside the slab. In this design, water pumps are not necessary anymore and the heat pipes will be able to maintain the slab temperature only a few degrees lower than the deep underground soil temperature in wintertime. The horizontal heat pipes are put at an angle (about 2°) to allow fluid to flow back. The distribution style of the horizontal pipes is indicated in Fig. 1. The heat pipes inside of the slab will have two ends at different heights to switch around between summer and winter. In winter, heat exchange will connect to the low end of the manifold, so that the fluid inside of the pipe can always flow back by gravity force. In summer, heat pipes will connect to the upper end of the slab, so that the condensed fluid inside of heat pipe can flow back through gravity force to the low temperature side. With little modification, the casing wells will work in summer as well. In summer, the natural convection inside of the casing well will disappear because the heat pipe is warmer on top and cold in bottom. Therefore, a pump is needed to circulate the water inside of the U-shaped casing pipe.

3. SYSTEM APPLICATION FEASIBILITY

In order to study the feasibility of installing such a system in real building, a room model, which is $3\mathrm{m} \times 5\mathrm{m} \times 3\mathrm{m}$ in scale, isproposed to evaluate the effect of the system. Indoor temperature and radiant floor temperature can have significant influence on thermal comfort. The thermal balance inside the chamber in its steady state is analyzed. It is also assumed that the chamber is empty, without human activity, mechanical equipment and lighting. The purpose is to verify if the heat-pipe-driving radiant floor system can provide low rise buildings with comfortable indoor environment in winter even without much internal load. As previous research focusing on radiant floor system has indicated, the temperature field of radiant floor is usually obtained by finite difference, finite volume or finite element method in simulation models, and then the floor surface average temperature is calculated. In this paper, the authors used an analytical method to determine the indoor air temperature and floor surface temperature to study the feasibility of directly applying ground heat source to radiant floor system. In the following analysis, it is supposed that the small chamber is located in a cold winter and hot summer climate condition (Shanghai in this case).

3.1. The calculation of heat transfer inside the radiant floor

In the case of heating in winter, the heat transfer rate between the floor surface and horizontal heat pipe system can be calculated by the following equation.

Equation 19: The heat transfer rate between the floor surface and horizontal pipe system.

$$q_{w,s} = \frac{t_w - t_s}{R_{w,s}}$$

Equation 2: The thermal resistance between the horizontal pipe system and the floor surface.

$$R_{w,s}=R_{upper}+R_{lower}$$

Where:

- $q_{w,s}$= the heat transfer rate between the floor surface and horizontal pipe system
- $R_{w,s}$ = the thermal resistance between the horizontal pipe system and the floor surface
- R_{upper} = the thermal resistance of the upper layer above the horizontal pipe system (m^2K/W)
- R_{lower} = the thermal resistance of the lower layer surrounding the horizontal pipes (m^2K)/W

$R_{w,s}$ is made up of R_{upper} (m^2K/W) (the thermal resistance of the upper layer above the horizontal pipe system) and R_{lower} (m^2K)/W (the thermal resistance of the lower layer surrounding the horizontal pipes). The structure of the layers is shown in Fig. 2, where the floor construction adopted a homogenous floor design. t_w (℃) and t_s (℃) are the water temperature in the horizontal pipes and the floor surface temperature, respectively.

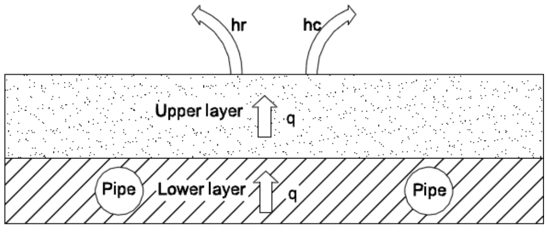

Figure 2: Structure layout of the radiant floor

A horizontal heat pipe system is designed according to Technical Regulations of Radiant Floor Heating in China (Research, 2004). A pipe diameter of 20mm and a pipe spacing of 300mm are chosen. The effect of thermal resistance of lower layer on the floor surface temperature is very little because the thermal resistance of the lower layer is much smaller than that of the upper layer (Jin X et al. 2010). Moreover, in the research conducted by Sattari and Farhanieh (Sattari and Farhanieh, 2006), it is concluded that pipe type, diameter and the number of pipes have minimum effects on the thermal performance of the heating floor system. Thus, the design process of the horizontal pipe system is not further illustrated here since it is not the focus of the research and the R_{lower} can be omitted because of its relative insignificance in this case. It is assumed that the water temperature in the horizontal pipe system is the same as the underground soil temperature at 100m below the ground (tiny difference in temperature in two ends of the heat pipe can trigger the heat transfer process inside the heat pipe) and there is almost no heat loss in this process.

According to the thermal physical test of the underground soil at the lab site, we can find that the initial soil temperature is about 19.8℃ at the depth of 100m in Shanghai. Because of the high heat transfer capability, we ideally assume that the water temperature in the horizontal pipe system (t_w) is also 19.8℃. The floor materials such as marble and cement for the test cell of a single room are preferred since they have higher conductive heat transfer coefficients. The same floor surface and the indoor air temperatures may be reached in shorter heating time (Bozkır and Canbazoğlu, 2004). Cement is chosen as the floor and upper layer material. The thermal Ku is 15W/(m^{2}K). Therefore, the thermal resistance of the upper layer is:

Equation 3: The thermal resistance of the upper layer above the horizontal pipe system.

$$R_{upper} = \frac{1}{K_{upper}}$$

Where:

- K_{upper} = the heat conduction coefficient of upper layer which is made up of concrete

K_{upper} is 15W/(m^2 ℃) (Jin X et al. 2010). After calculation, the R_{upper} can be achieved, which is 0.067 (m^2 ℃/W).

3.2. The calculation of heat transfer between floor surface and indoor air

Since the room temperature and the heat transfer coefficient between the floor and the walls almost both keep the same during heating or cooling, the floor surface temperature is the most important parameter which affects the heating capacity of the system (Jin X et al. 2010). Thus, the floor surface temperature and indoor air temperature can be determined when the whole system reaches steady-state heat transfer conditions through calculation. In the case of heating, the natural convective heat transfer coefficient for heated floor can be calculated by the following equation (Awbi and Hatton, 1999):

Equation 4: The heat transfer coefficient of natural convection.

$$h_c = \frac{2.175}{H^{0.076}}(t_s - t_a)^{0.308}$$

$$\mathrm{H} = \frac{4\mathrm{ab}}{2(\mathrm{a}+\mathrm{b})}$$

Where:

- h_c= the heat transfer coefficient of natural convection (W/(m^2· ℃))
- t_s= the floor surface temperature (℃)
- t_a= the indoor air temperature (℃)
- a = the length the room
- b= the width of the room

While the radiant heat transfer rate of the radiant heating floor (q_r) can be calculated by the following equation (Hui, 2007),

Equation 5: The radiant heat transfer rate of the radiant heating floor.

$$q_r = 4.98\{\left(\frac{t_s + 273}{100}\right)^4 - \left(\frac{t_a + 273}{100}\right)^4\}$$

The steady heat transfer between the floor surface and the indoor environment can be achieved by adding together radiant heat transfer rate and natural convective heat transfer rate, which is as follows:

Equation 6: The steady heat transfer between the floor surface and the indoor environment.

$$Q_{i,s} = h_c A_f (t_s - t_a) + q_r A_f$$

Where:

- $Q_{i,s}$= the steady heat transfer between the floor surface and the indoor environment
- A_f= the floor surface area

3.3. The calculation of heat loss to the outdoor environment

In winter, the heating load of the room can be determined by the heat gain and heat loss of the room. Generally, the heating load in winter involves two important factors: the heat loss from the building envelope and the heat loading for heating the outdoor air penetrated from windows and doors. In this study, the heat transferred through windows is omitted since there are no windows installed and the door. Only heat transferred through door is considered. The heat loss rate from the building envelope can be calculated as the following method:

Equation 7: The heat loss rate from the building envelope.

$$Q_{l.e} = K_e A_e (t_a - t_R)$$

Where:

- $Q_{l,e}$= the heat loss from the building envelope (W)
- A_e= the area of the building envelope of the room (m^2)
- K_e= the heat transfer coefficient of the room envelope (W/(m^2·℃))

In this case, the heat transfer coefficient of the building envelope of 0.6 W/(m^2· ℃) is used to stand for a high level of insulation. t_R and t_a are the mean outdoor temperature in Shanghai (3℃) (according to GB 50736-2012 in China) and the indoor air temperature of the chamber, respectively. Thus, the heat loss from the room envelope can be determined. The heat loss rate from the gap of the door can be determined by the following equation:

Equation 8: The heat loss rate from the gap of the door.

$$Q_{l.d} = 0.278 L \rho_a c_p (t_a - t_R)$$

Where:

- $Q_{l.d}$= heat loss rate from the gap of the door
- L= the cold air permeability (m^3/h)
- ρ_a= the density of air
- c_p= the specific heat at constant pressure

In a room with one window, the air change rate is about 1 h^{-1}, the cold air permeability L can be calculated by multiplying the air change rate by the volume of the room (45m^3), which is 22.5 m^3/h; ρ_a is 1.29kg/m^3; c_p is 1kJ/kg· ℃. Then the heat loss rate from the aperture of the door can be calculated.

After that, the total heat loss from the chamber can be calculated by adding together the heat loss rate from building envelope and heat loss rate from air permeability, which is:

Equation 9: The total heat loss from the chamber.

$$Q_l = 0.278 L \rho_a c_p (t_a - t_R) + A_e K_e (t_a - t_R)$$

3.4.Indoor Heat Balance

In the case of steady heat transfer, the heat transfer rate between the floor surface and horizontal pipe system, the heat transfer rate between floor surface and indoor environment, and the heat loss of the chamber should be the same. Thus, the indoor air temperature and floor surface temperature in steady state can be determined by establishing a system of simultaneous equations including equations (1), (6) and (9) as the following:

Equation 10: the indoor air temperature and floor surface temperature in steady state.

$$0.278 L \rho_a c_p (t_a - t_R) + A_e K_e (t_a - t_R) = \frac{t_w - t_s}{R_{w,s}} A_f$$

$$\frac{t_w - t_s}{R_{w,s}} A_f = h_c A_f (t_s - t_a) + q_r A_f$$

After solving the above equations, the two unknown variables of indoor air temperature and floor surface temperature can be determined. Hence, the heat transfer rate in a steady state can be further achieved. The result shows that in the typical heating days in Shanghai (outdoor temperature at around 3℃), indoor temperature can be kept at around 17℃. Thus, it shows that the radiant floor system with heat pipes getting heat directly from underground can be used as a passive heating method in buildings in Shanghai. Further analysis of the energy saving potential of the system in various climates is conducted in the following sections.

4. SEASONAL ENERGY SAVING POTENTIAL

In this study, EnergyPlus is used to evaluate the energy saving potential of the system. EnergyPlus is an energy analysis and thermal load simulation program. It is capable of calculate the heating loads necessary to maintain thermal control set points, conditions throughout a secondary HVAC system and coil loads, and the energy consumption of primary plant equipment as well as many other simulation details that are necessary to verify that the simulation is performing as the actual building would (Abd and Mohamed, 2007) The EnergyPlus model of the low-rise building in this research is composed of a low temperature radiant floor system and a packaged terminal heat pump (PTHP). The two systems are installed in a chamber 3 meters in width, 5 meters in length and 3 meters in height. Two faces of the chamber are exposed to the outside environment. Internal heat gains of people, lighting and electric equipment are considered. The setting of the zone infiltration rate of the chamber is that the house has 1 air change per hour. The building envelop of the chamber is supposed to be thermally insulated well to have limited heat loss under steady state. The set point of the water temperature inside the horizontal heat pipes of the radiant floor system and the set point of the indoor temperature can be manually set to meet the need of simulating different scenarios.

It is crucial to understand the energy saving potential of the supposed radiant floor system and what the most important factors affect the energy saving rate of the system. In the first place, the computer model for simulating heating energy saving potential in winter is built and the simulation period of the simulation is from November to March. When the indoor air temperature is set, the system will meet the internal heating load by launching the radiant floor system. When the indoor temperature demand is not satisfied, then the PTHP will be launched to satisfy the internal heating load of the chamber. Hence the radiant floor system is considered as the basic air conditioning system in the house. After comparing the simulation result between the heating energy consumption of the chamber with and without the low temperature radiant floor system, the energy saving potential of the proposed system can be achieved. A detailed building energy performance simulation is run in hourly granularity to compare the heating energy use in three representative cities having distinct climate conditions in China, namely Beijing, Shanghai, and Guangzhou. Beijing, Shanghai, and Guangzhou represent distinct climate zones in China, each characterized by unique TMY conditions. Beijing experiences a cool summer and cold winter climate, with significant temperature variations between seasons. Winters are particularly harsh, with frequent sub-zero temperatures. Shanghai, located in the hot summer and cold winter zone, has hot and humid summers and mild winters with occasional cold spells. Guangzhou, in contrast, features a hot summer and warm winter climate, characterized by high temperatures and humidity levels throughout the year, with winters being mild and rarely experiencing temperatures below 10°C. These diverse climatic conditions significantly influence the performance and energy-saving potential of the proposed passive heating system, as demonstrated in the detailed hourly simulation results.

The seasonal energy saving rate is calculated to evaluate the performance of the proposed passive heating system compared to a conventional heating system. The formula for the seasonal energy saving rate (ESR) is defined as follows:

Equation 11: seasonal energy saving rate calculation

$$\mathrm{ESR} = \frac{E_{\text{only PTHP}} - E_{\text{w/ heat pipe}}}{E_{\text{only PTHP}}} \times 100\%$$

where $E_{\text{only PTHP}}$ represents the seasonal energy consumption of the scenario with only the PTHP system, and $E_{\text{w/heat pipe}}$ represents the total seasonal energy consumption of the scenario with the proposed passive heating system using heat pipes. The energy consumption values are obtained through detailed simulations using EnergyPlus, considering various indoor temperature setpoints and water temperatures in the horizontal heat pipes. The resulting ESR provides a percentage measure of the energy savings achieved by the passive heating system relative to the conventional system, highlighting its efficiency and sustainability benefits.

5. RESULTS AND DISCUSSIONS

We run the simulation by inputting the typical meteorological year (TMY) weather data of Shanghai first because the climate in Shanghai is one of the most typical ones representing the hot summer and cold winter zone in China. After several simulations, it is found that the energy saving potential of the proposed system correlates with the set point of indoor temperature and the temperature of water in horizontal heat pipes. It is reasonable that when the setpoint of indoor temperature rises, the energy consumption of the PTHP rises accordingly and when the temperature of the water in horizontal pipes changes, the energy saved by the radiant floor system changes in the same way as shown in Figure 1.

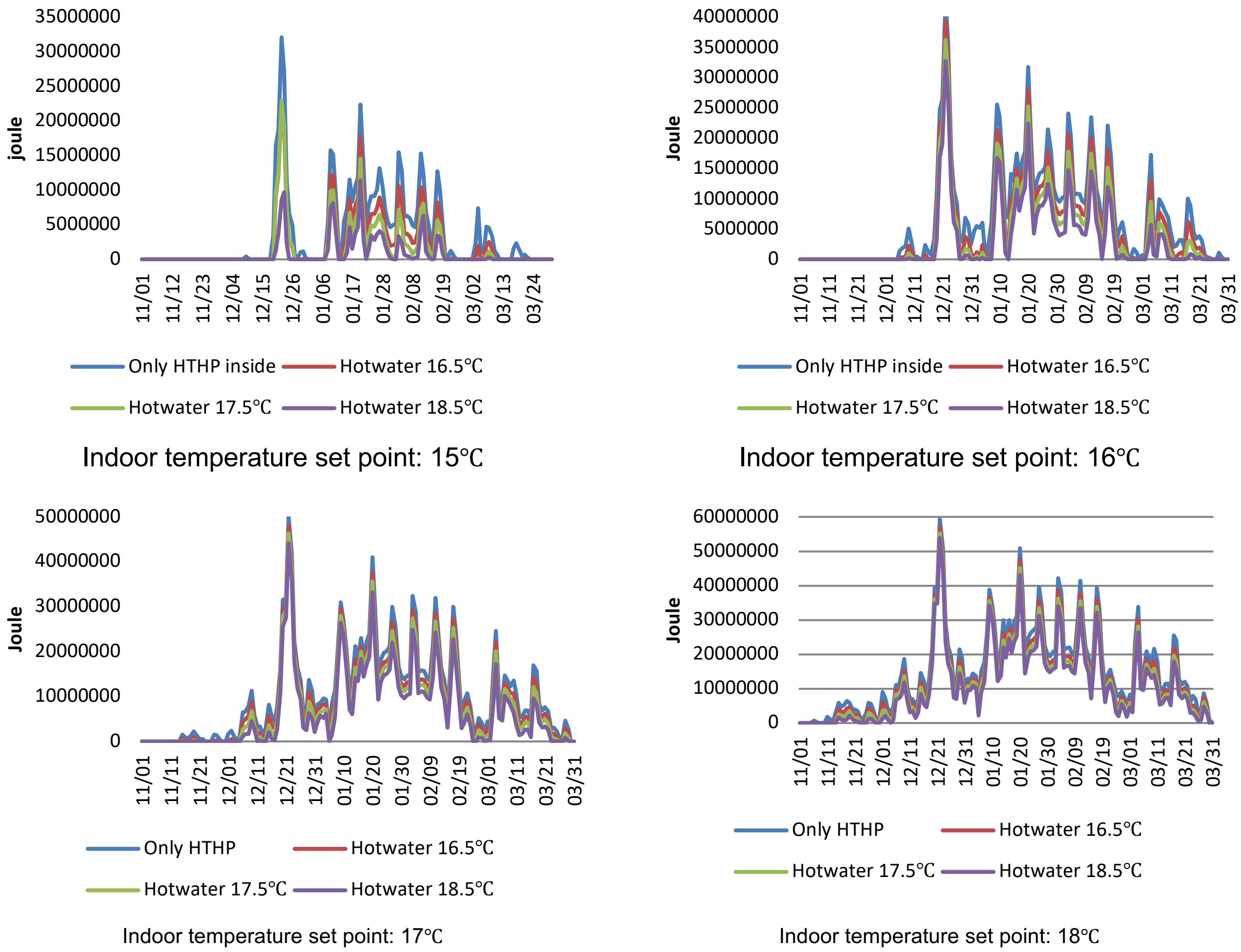

Figure 1: Hourly simulation results under different indoor temperature setpoint scenarios in Shanghai (Unit: Joule)

Simulations are further conducted by setting up four scenarios according to different indoor temperature set points (15℃~18℃). The temperature set point of water in the horizontal pipe system is also divided into three temperature categories based on different scenarios of what temperature the water inside the horizontal pipe is (water temperature between 16℃~18℃). In addition, we insert the scenario in which there is no radiant floor system inside the house as reference for comparison. In each group, the highest energy saving potential is achieved when the temperature of water inside the horizontal pipes reaches the highest (18℃). As the set point of indoor temperature rises, the energy consumption of the PTHP rises accordingly and the gaps among energy consumption of PTHP in different water temperature scenarios narrow, which means when indoor temperature is set higher, the energy saving potential of the passive heating system gets lower. It is due to the fact that there is more time that the building heating load cannot be satisfied by the mere working of the radiant heating floor system. More energy is needed to be consumed by the PTHP to satisfy the desired indoor thermal environment set by user. In other words, the simulation results reveal that the energy saving potential of the passive heating system cannot be significant if the building occupant set the indoor temperature too high. However, this system would be of great importance to those residential building occupants in Yangtze River Basin Region of China, who seldom used air-conditioners in the past and now do have a demanding requirement on building heating quality (Xu et al. 2013). The simulation result is compiled in Table I to show the overall evaluation of the energy saving potential of the proposed passive heating system according to different scenarios. The scenario of “only PTHP” scenario serves as the baseline for comparing the energy saved by the system by each group.

Table 1: Seasonal Energy saving rate compared with the scenarios of different set point of indoor temperature (Shanghai)

	Only PTHP	16℃	17℃	18℃
Indoor 15℃	Ref	38.5%	53.5%	76.1%
Indoor 16℃	Ref	24.5%	38.8%	51.9%
Indoor 17℃	Ref	14.4%	24.4%	35.3%
Indoor 18℃	Ref	12.9%	21.1%	28.2%

In Table I, the highest seasonal energy saving rate of the proposed passive heating system reaches 76.1% compared with the scenario in which only PTHP system is available. The highest saving rate occurs when water temperature in the horizontal pipe is at 18℃ and the set point of indoor temperature is at 15℃. However, because the indoor temperature is set too low to make most people feel thermally neutral, the energy saving in real condition cannot be that high. Research conducted by Cao et al. concluded the thermal comfort level of occupants at different indoor operative temperature by using the methodology of TSV (Thermal Sensation Vote) (Cao et al. 2011). In our research, we do not refer to PMV, but rather to TSV because people could endure the comparatively low indoor temperature, and their real thermal sensation was not as cold as PMV predicted (Cao et al. 2011). The result of the research shows that when the indoor operative temperature is lower than 16℃, people will feel cold (TSV index is lower than -1). Thus, the energy saving rate of the passive heating system in scenario where indoor temperature is set at 16℃, 17℃ and 18℃ is more meaningful.

According to the result, the proposed passive heating system is still capable of providing energy saving potential when the indoor temperature is set almost the same as the water temperature in the horizontal pipe because of the variation in outdoor temperature. The passive system can purvey the PTHP system with pre-heating and better thermal inertia after it stops work. In this research, occupant behavior is not considered as a factor influencing the energy saving potential of the passive heating system. In order to better study the energy saving potential of the system in different climate zones in China, the city of Beijing (cool summer and cold winter climate) and Guangzhou (hot summer and warm winter climate) are also included to demonstrate the energy saving potential of the system. Results are shown in Table II and Table III. The simulation result of scenario where indoor temperature set point is at 15℃ are removed considering thermal comfort.

Table 2: Energy saving rate compared with the scenarios of different Set point of indoor temperature (Beijing)

	Only PTHP	16℃	17℃	18℃
Indoor 16℃	Ref	9.5%	16.0%	22.7%
Indoor 17℃	Ref	7.2%	12.0%	17.4%
Indoor 18℃	Ref	6.3%	10.4%	14.2%

Table 3. Energy saving rate compared with the scenarios of different set point of indoor temperature (Guangzhou)

	Only PTHP	16℃	17℃	18℃
Indoor 16℃	/	/	/	/
Indoor 17℃	Ref	47.3%	74.9%	92.5%
Indoor 18℃	Ref	37.6%	58.0%	72.3%

Since Beijing has a lower average outdoor temperature in winter, the energy saving potential of the passive heating system is much lower than that of Shanghai. While Guangzhou is in southern China and possesses a warm winter (the average outdoor temperature in Guangzhou is above 10℃), the energy saving potential of the system rises drastically. This is due to the reason that the purchased heated air provided by the passive heating system has a limitation. When the outdoor temperature drops significantly, leading to a substantial increase in the building's heating load, the proportion of the heating load met by the passive heating system decreases. Consequently, a larger portion of the heating demand must be fulfilled by an active mechanical heating system, such as the PTHP in this instance. Comparing the simulation results in three types of climates--- Shanghai, Beijing, and Guangzhou, it is indicated that the passive heating system can provide potential energy saving for low-rise building heating energy consumption in place where a warm climate is available in winter.

6. CONCLUSION

In this paper, a conceptual design and simulation analysis of a heat pipe driven radiant floor system are carried out. A new type of passive heating system with heat pipes directly linking buildings structures with the earth side is proposed. The feasibility and application value of the system in different climate zones by using computer models is evaluated. The system has many advantages over the traditional ground heat pump systems. The primary advantage of using heat pipes in the proposed passive heating system is their ability to operate without moving parts, significantly reducing maintenance requirements and energy consumption compared to traditional ground source heat pumps. Heat pipes leverage natural convection to transfer heat from the ground to the radiant floor system, eliminating the need for pumps and compressors inherent in ground source heat pumps. This passive operation enhances system reliability and longevity, while also promoting sustainability by minimizing energy inputs, particularly in regions with mild winters where the system can operate more efficiently.

This research investigates the energy-saving potential of a passive heating system with horizontal heat pipes in different climatic zones of China. Initial simulations in Shanghai, representing the hot summer and cold winter zone in China, reveal that energy savings correlate with indoor temperature setpoints and water temperatures in the horizontal heat pipes. Results indicate that as the indoor temperature setpoint increases, so does the energy consumption of the Packaged Terminal Heat Pump (PTHP), reducing the energy-saving potential of the passive system. Simulations across four indoor temperature scenarios (15°C to 18°C) and various water temperature ranges (16°C to 18°C) show that the highest energy savings occur at the highest water temperature. However, energy savings diminish with higher indoor setpoints, as the passive system cannot satisfy the increased heating load, necessitating more energy from the PTHP. In scenarios of Beijing (cool summer and cold winter climate) and Guangzhou (hot summer and warm winter climate), the passive system's performance varied significantly. In Beijing's colder climate, the system's energy-saving potential is limited, while in Guangzhou’s milder winters, substantial energy savings are observed. This variation is attributed to the system's ability to pre-heat and provide thermal inertia, aiding the PTHP. The study concludes that the passive heating system, with its reliance on outdoor temperatures and setpoint conditions, can offer significant energy savings in regions with milder winters. However, in colder climates, its effectiveness is reduced, necessitating supplementary active heating systems. This research underscores the importance of climatic considerations in the design and application of passive heating systems for well-insulated low-rise buildings.

7. ACKNOWLEDGEMENT

This research is supported by National Natural Science Foundation of China (NSFC) (Grant No. 52008132).

8. REFERENCES

Abd El-Baky MA, Mohamed MM, 2007. Heat pipe heat exchanger for heat recovery in air conditioning. Applied Thermal Engineering. 27:795-801.

Awbi HB, Hatton A, 1999. Natural convection from heated room surfaces. Energy and Buildings. 30:233-44.

Bozkır O, Canbazoğlu S, 2004. Unsteady thermal performance analysis of a room with serial and parallel duct radiant floor heating system using hot airflow. Energy and Buildings.36:579-86.

Cao B, Zhu Y, Ouyang Q, Zhou X, Huang L, 2011. Field study of human thermal comfort and thermal adaptability during the summer and winter in Beijing. Energy and Buildings. 43:1051-6.

Hassan MA, Abdelaziz O, 2020. Best practices and recent advances in hydronic radiant cooling systems – Part II: Simulation, control, and integration. Energy and Buildings. 224:110263.

Hui X, 2007. Thermal Performance of Thermosyphon-Embedded Floor Heating. Journal of Tianjin University.

Holopainen R, Tuomaala P, Piippo J, 2007. Uneven gridding of thermal nodal networks in floor heating simulations. Energy and Buildings. 39:1107-14.

Jin X, Zhang X, Luo Y, 2010. A calculation method for the floor surface temperature in radiant floor system. Energy and Buildings. 42:1753-8.

Mustafa Omer A, 2008. Ground-source heat pumps systems and applications. Renewable and Sustainable Energy Reviews. 12:344-71.

Cao B, 2004. Technical Regulations of Radiant Floor Heating. Ministry of Housing and Urban-Rural Development of China.

Sattari S, Farhanieh B, 2006. A parametric study on radiant floor heating system performance. Renewable Energy. 31:1617-26.

Shen P, Lior N, 2016. Vulnerability to climate change impacts of present renewable energy systems designed for achieving net-zero energy buildings. Energy. 114:1288-305.

Tejero-González A, Andrés-Chicote M, García-Ibáñez P, Velasco-Gómez E, Rey-Martínez FJ, 2016. Assessing the applicability of passive cooling and heating techniques through climate factors: An overview. Renewable and Sustainable Energy Reviews. 65:727-42.

Xu P, Xu T, Shen P, 2012. Advancing evaporative rooftop packaged air conditioning: A new design and performance model development. Applied Thermal Engineering. 40:8-17.

Xu P, Xu T, Shen P, 2013. Energy and behavioral impacts of integrative retrofits for residential buildings: What is at stake for building energy policy reforms in northern China? Energy Policy. 52:667-76.

Yao W, Liu C, Kong X, Zhang Z, Wang Y, Gao W, 2023. A systematic review of heat pipe applications in buildings. Journal of Building Engineering. 76:107287.

Zohuri B, 2016. Heat pipe design and technology: Modern applications for practical thermal management: Springer.

#326: New waste to energy (WtE) alternative: fuel gas production and power generation via gas engine

Shaoheng GE[1,2], Dezhen CHEN[1,2*]

[1] Thermal & Environmental Engineering Institute, Tongji University, Shanghai 200092, China
[2] Shanghai Engineering Research Center of Multi-source Solid Wastes Co-processing and Energy Utilization, Tongji University, Shanghai 200092, China
*chendezhen@tongji.edu.cn

Abstract: Management and disposal of municipal solid waste (MSW) is an important issue in waste-free cities. Although waste of energy (WtE) via incineration is widely adopted in the world, the emissions of pollutants from the MSW incinerators, especially the dioxin emissions in gaseous and solid phases are a serious problem. In addition, for MSW management in towns or small counties, the conventional WtE via incineration is not applicable due to the economic limitation. For years we have developed an alternative WtE technology, which is characterized by thermochemical processes including pyrolysis and reforming of volatiles afterwards, and finally fuel gas is obtained and cleaned to feed a gas engine for power generation. In the developed system all of the oil or tar from MSW pyrolysis is converted into gas bycatalytic cracking over the char. The char acted as a catalyst, but it was also partially or entirely gasified simultaneously. The obtained fuel gas is cleaned before feeding the gas engine and also was used to warm the pyrolysis reactor. The dioxin emissions from the flue gas and partially gasified char were checked. The lower heat value (LHV) of the fuel gas as well as the energy recovering efficiency changes from waste to power were also investigated. The results supported the soundness of this newly developed technology.

Keywords: MSW, Pyrolysis, Gasification, Gas Purificaion, Gas Engine

1. INTRODUCTION

During the "14th Five-Year Plan" period, there is an urgent need for efficient and hygienic disposal of small-scale municipal solid waste (MSW) in towns and counties. In response to this, in July 2020, the National Development and Reform Commission, along with two other ministries, jointly issued the "Implementation plan for strengthening the weaknesses in urban household waste sorting and treatment facilities". It encourages small-scale MSW thermal treatment facilities in areas where daily waste collection and transportation is less than 300 tons. However, extensive engineering practices have demonstrated that, from the perspectives of technical reliability and economic feasibility, it is not advisable to adopt traditional grate furnace incinerator for scales below 300 tons per day. In the absence of mature alternative technologies to grate furnace incineration, pyrolysis and gasification involved incineration facilities have been emerged as an important measure to dispose MSW of small-scale.

Although waste incineration technology is well-developed, the emission of pollutants, particularly dioxins, from incineration plants remains a significant concern. Compared to direct incineration, pyrolysis generates lower levels of dioxins and flue gas, making it more suitable for small-scale waste treatment facilities and decentralized MSW management schemes (Chen et al., 2014; Yin et al., 2017). The gas products derived from pyrolysis generally have a higher calorific value than the syngas produced by gasification (Wang et al., 2017). However, due to the unfavourable characteristics of pyrolysis oil derived from waste, such as high viscosity, acidity, and corrosiveness, it is challenging to find suitable end users in the market (Yang et al., 2015). In contrast, pyrolysis gas, especially purified pyrolysis gas, can serve as an excellent fuel or chemical feedstock. By gasifying both the char and the oil into combustible gas, gas becomes a single energy carrier, enhancing the quality and cleanliness of energy utilization from waste. The simultaneous gasification of char and volatiles can employ pyrolytic char as a catalyst for reforming the pyrolysis volatiles. The advantages of this process include: (1) the use of in-situ generated pyrolytic char as a catalyst, eliminating the need for external catalysts; and (2) the direct use of pyrolytic char for catalytic reforming without heat loss, as the interaction between volatiles and char can utilize the latent heat of steam and the sensible heat of both volatile and char.

This paper will systematically introduce the newly developed pyrolysis-gasification combination system with gas purification process involved, focusing on the following aspects: (1) the gasification efficiency of the pyrolysis-gasification system and the calorific value of the produced combustible gas; (2) the purification effect of the gas purification system; and (3) the flue gas emissions. The study aims to verify the feasibility of this process and provide a reference to energy recovery from small-scale MSW management.

2. DESCRIPTION OF PYROLYSIS-GASIFICATION AND POWER GENERAATION SYSTEM

The project (shown in Figure 1) processes 80 tons of MSW per day, located in Sichuan Province, China, at an altitude of approximately 3,500 meters. The system comprises a waste storage pit, a pretreatment system using a shredder, a waste conveyance system and the main processing facility consisting of a waste drying section, a pyrolysis reactor, a gasification furnace and a gas purification unit. The energy recovery system includes a gas engine for power generation system and a boiler to recover the waste heat in the flue gas discharged from the gas engine. The cleaned syngas is stored in a gas tank and it also provides heat for the pyrolysis reactor and the drying section. The flue gas emitted from the drying section is discharged from the stack. Figure 2 shows the diagram of the whole system.

The waste storage pit receives the raw MSW, and the pretreatment system crushes the MSW to reduce the size to less than 200 mm. The shredded material is then conveyed to the drying section before the pyrolysis reactor via a sealed feeding system. The drying section, with a kiln structure, heats the MSW through indirect heating with the flue gas of 250-600°C via a jacketed heat exchanger. The moisture in the MSW evaporates, and the moisture content of the MSW at the outlet of the drying section is reduced to below 18 %. This drying method minimizes odour emission and reduces the dust carried by exhaust gases.

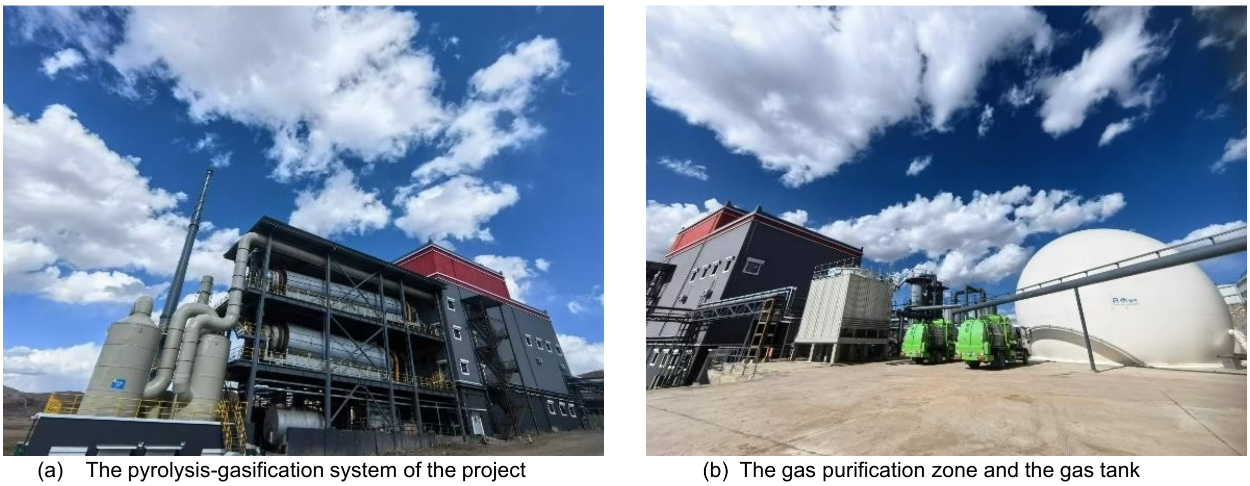

(a) The pyrolysis-gasification system of the project (b) The gas purification zone and the gas tank

Figure 1: The picture of the 80 tpd MSW processing system for power generation

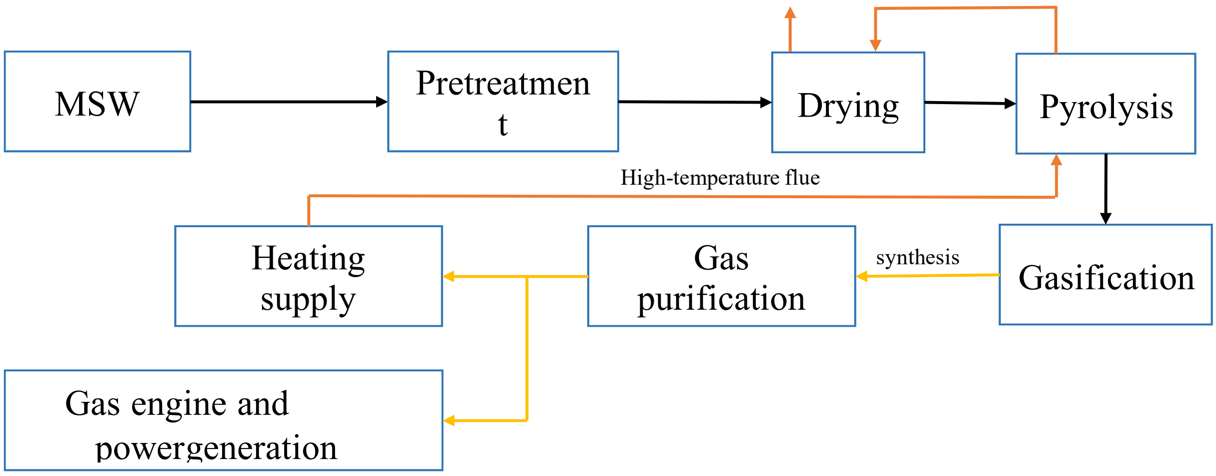

Figure 2: The flow diagram of the WtE system

The exhaust gas from the drying furnace, containing a large amount of water vapor, is directed into a condenser, where the water vapor is condensed. The uncondensed gas is routed to the gasification furnace as a gasifying agent, while the condensate is used to replenish water in the slag cooling machine. After drying the MSW is discharged into the pyrolysis reactor, where the combustible components undergo pyrolysis under heating (600°C–650°C) under an inert condition. The pyrolysis process converts the MSW into combustible gas, oil, and char, all of them are then fed into the reforming and gasification reactor. The pyrolysis reactor is a rotary kiln, and the heat source is provided indirectly by high-temperature flue gas produced from the combustion of the cleaned synthetic gas in the combustion chamber (hot blast furnace). In the gasification reactor, the char generated from pyrolysis is further gasified, and the tar is reformed and gasified. At the inlet, a special designed structure ensures that the tar-containing volatiles pass through the char layer, where the tar is catalysed by the char and undergoes reforming and gasification. The char residue yield reduces and is pushed forward by the grate, while air and steam are supplied from below. The amount of air is controlled by the furnace temperature, which is maintained below 1000°C to ensure the quality of the produced gas and avoid the loss of too much sensible heat. The steam used in this process originates from the drying section.

The synthetic gas emitted from the gasification reactor is fed to the purification system, which employs a process of "cyclone dust removal + primary scrubbing tower + electrostatic tar precipitator + wet acid gas removal + dry desulfurization". The cyclone dust separator separates coarse particles, and the primary scrubbing tower cooling the synthetic gas and remove most of the particulates, then the electrostatic precipitator removes the tar and small particulates in the gas, the poles are cleaned with the steam from the boiler. The wet acid gas removal is carried out in a secondary scrubbing tower, where alkaline solution is used to remove acid gases, to ensure the effect of scrubbing, a dry desulfurization tower is used with a demister on the front. The process flow is illustrated in Figure 3.

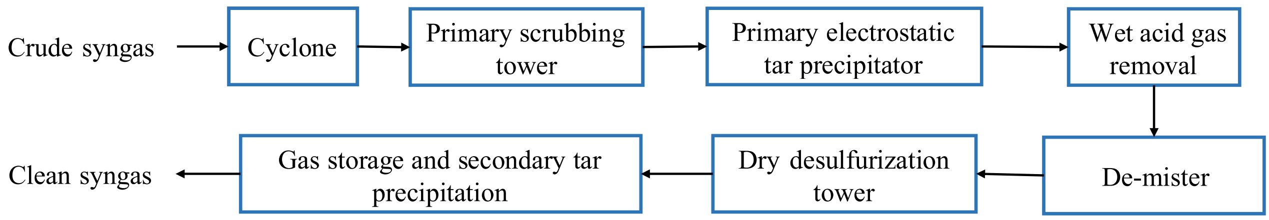

Figure 3: The gas purification system

The gas power generation system in this project primarily consists of two internal combustion gas engine generator units of 600 kW, equipped with an SCR (Selective Catalytic Reduction) system for NOx reduction, equipped with a 1 t/h waste heat boiler. To improve the energy recovery efficiency of the internal combustion generator units, the air-fuel ratio is relatively low. Consequently, in the oxygen-deficient zone of the gas engine, incomplete combustion of carbon compounds happens, which leads to a certain level of CO emission. As a result, the CO content in the exhaust gas from the gas engine units is relatively high. According to the operation data, the CO concentration in the exhaust gas is around 500 mg/m³.

3. RESULTS AND DISCUSSION

3.1. Calorific value of the synthetic gas and power generation efficiency

The calorific value of MSW exhibits some fluctuations, with the average HHV measured from three tests being around 14.57 MJ/kg in Jan.2024. The moisture contents varied between 38-50%. The calorific value of the pyrolysis gas was monitored in real time, and the 5-hour average value was recorded as shown in Table 1. The gas components included

O_2, CH_4, CO, CO_2, H_2, and C_nH_m (C_2 and higher hydrocarbons), with a lower heating value of 12.28 MJ/Nm³, which is significantly higher than that of typical gasification gases (Ge et al., 2022). This is primarily due to the high content of C_nH_m, which has a relatively high calorific value, whereas typical gasification gases mainly consist of H_2 and CO (Wang et al., 2023). The high LHV of the synthetic gas makes it more valuable and versatile in applications and results in higher power generation efficiency in gas engines, enabling the achievement of higher power output. The O_2 content is below 1%, meeting the design specifications, indicating good system sealing and enhanced operational safety.

Table 11: Gas composition, calorific value and cold gas efficiency

Item	CH_4 (%)	CO (%)	CO_2 (%)	H_2 (%)	C_nH_m (%)	O_2 (%)	LHV (MJ/Nm^3)	Yield (Nm^3/$_{\text{ton MSW}}$)	Cold gas efficiency (%)
Value	9.35	3.92	11.28	12.61	10.98	0.39	12.28	859	72.5%

At a processing capacity of 80 tons per day (3.33 t/h), the gas production rate is 2860 Nm³/h, corresponding to a cold gas efficiency of 72.5%. The heating supply furnace consumes about half of the gas (around 1420 Nm³/h), while the other 1440 Nm³/h of the gas was fed to the gas engine. The engine can operate at full load, with an average output of 1375 kW and an efficiency of 28%. The relatively low efficiency of the gas engine is primarily due to the high-altitude location of the project, as altitude has a significant impact on the efficiency of gas engines (Martínez et al., 2022). However, even with this limitation, the efficiency is still considerably higher than the averaged 22-25% which is typical for MSW incineration plants for power generation (Ou and Long, 2015).

3.2. Gas purification effect

The gas engine has stringent requirements for its feeding fuel gas, with specific limits for contaminants such as tar (<100 mg/m³)(Asadullah, 2014), particulates (<20 mg/m³), H_2S (<20 mg/m³), and NH_3 (<10 mg/m³). These limitations are critical for ensuring long-term stable operation. Additionally, since the project does not include a flue gas purification system, the compliance of heating supply furnace emissions with regulatory standards depends on the cleanliness of the synthetic gas. The raw syngas from the gasifier contains high concentrations of pollutants, as shown in Table 2, with significant levels of NH_3, H_2S, and HCl, particularly NH_3. After purification, the cleaned gas was tested to check the pollutants, with results shown in Table 3. The H_2S content was measured at 5 mg/m³, while tar and dust levels were found to be less than 21 mg/m³, quite below the intake requirements of the gas engine. NH_3 and HCl are highly soluble in water, and since the purification process includes two scrubbing stages, their removal efficiency is very high. Given the high concentration of NH_3 in the raw gas, the tar separator and second scrubbing stage all operate under alkaline conditions, with pH values of 8.8 and 8.15, respectively. These stages also contribute to the removal of H_2S, which explains its very low concentration in the final gas. Additionally, the concentrations of heavy metals in the gas are extremely low. Since the project handles municipal solid waste (MSW), valuable materials, such as metals, are typically sorted out manually before waste collection, leading to low heavy metal content in the incoming waste. Consequently, the feedstock's heavy metal concentration is low, which helps reduce the heavy metal content in the syngas. Furthermore, the pyrolysis and gasification processes trap most of the residual heavy metals in the slag. Any remaining gaseous heavy metals that rise with the syngas are adsorbed by the porous carbonaceous material formed from the gasified waste, resulting in minimal heavy metal content in the finalgas output. Two main strategies are used to mitigate heavy metal emissions: "low-temperature control" and "particulate collection." In this project, the temperature of the syngas is rapidly reduced to around 80°C in the first scrubber, which causes most gaseous heavy metals to condense into solid or liquid particles that are easier to capture and are partially attached to dust particles. The syngas then passes through electrostatic tar precipitator, which further remove the heavy metals that are attached to dust and tar. Therefore, the combustible gas purification process implemented in this project is feasible and effective at ensuring that the syngas meets the required cleanliness standards, contributing to stable gas engine operation and emissions compliance.

Table 2: Gaseous pollutant concentrations before purification

Item	H_2S (mg/m^3)	HCl (mg/m^3)	NH_3 (mg/m^3)
Value	450	650	2200

Table 3: Gaseous pollutant concentration after purification

Item	H_2S (mg/m^3)	Tar and dust (mg/m^3)	Chloride ion(mg/m^3)	Hg (ng/m^3)	Cd+Tl (mg/m^3)	Sb+As+Pb+Cr+Co+Cu+Mn+Ni (mg/m^3)
Value	5	21	<1	<10	<0.1	<1

3.3. Flying ash collection and testing

In this project, a cyclone separator is employed to capture larger particulate matter during the gas purification process. The presence of dioxins and heavy metals has been analysed, as shown in Table 4 and Table 5, with the toxicity equivalent of dioxins measured at 0.0048 μg TEQ/kg, which is significantly lower than the regulatory standards. Through process control, the magnetic separation equipment was adopted to reduce the heavy metal content in MSW prior to incineration, thereby contributing to the control of dioxin formation. During the operation of the pyrolysis furnace, the MSW is rapidly heated, resulting in hydrogen-induced milliseconds cracking and gasification reactions. Throughout the heating process, nearly all organic chlorine and some inorganic chlorine in the waste are released in the form of HCl. Due to the lack of oxygen, HCl cannot generate molecular chlorine or chlorine free radicals, which are essential for the high-temperature gaseous formation of dioxins. This significantly inhibits the formation of dioxins. The gasification process operates under a hypoxic atmosphere (with oxygen content <1%), where only a small amount of inorganic chlorine is present, lacking the necessary conditions for dioxin formation. Therefore, the generation of dioxins is effectively suppressed under the conditions of pyrolysis and gasifcation atmosphere. According to the study by Ma and Jin (2022), who conducted an investigation on a county in Sichuan on the dioxin toxicity equivalent emissions from a new village town waste pyrolysis gasification furnace (gasification chamber + secondary combustion chamber), similar results were obtained and dioxin emissions from gasification reactors are lower. The analysis showed that the original dioxin emission concentration in the gasification chamber was relatively low, with the dioxin toxicity equivalent concentration at the outlet of the gasification chamber measured at 0.027 ng TEQ/m³, which can be attributed to the oxygen-deficient conditions during gasification.

Table 4: Dioxins of fly ash

Serial number	PCDDs & PCDFs	Value (μg /kg)	Toxic equivalent (μg TEQ /kg)	Toxic equivalent factor (I-TEF)
1	2,3,7,8-TCDD	N.D.(<0.2902ng/kg)	0.0001451	1
2	1,2,3,7,8-PeCDD	0.0007	0.00035	0.5
3	1,2,3,4,7,8-HxCDD	0.0007	0.00007	0.1
4	1,2,3,6,7,8-HxCDD	0.0009	0.00009	0.1
5	1,2,3,7,8,9-HxCDD HxCDD	0.0011	0.00011	0.1
6	1,2,3,4,6,7,8-HpCDD	0.0077	0.000077	0.01
7	OCDD	0.0459	0.0000459	0.001
8	2,3,7,8-TCDF	0.0046	0.00046	0.1
9	1,2,3,7,8-PeCDF	0.0034	0.00017	0.05
10	2,3,4,7,8- PeCDF	0.0036	0.0018	0.5
11	1,2,3,4,7,8-HxCDF	0.0043	0.00043	0.1
12	1,2,3,6,7,8- HxCDF	0.0044	0.00044	0.1
13	1,2.3,7,8,9-HxCDF	0.0007	0.00007	0.1
14	2,3,4,6,7,8- HxCDF	0.0025	0.00025	0.1
15	1,2,3,4,6,7,8-HpCDF	0.0199	0.000199	0.01
16	1,2,3,4,7,8,9- HpCDF	0.0035	0.000035	0.01
17	OCDF	0.0501	0.0000501	0.001
	SUM	-	0.0048	-

Table 5 indicates that heavy metal concentrations are also significantly below the GB16899-2024 standards. Unlike traditional waste incineration fly ash, the ash collected by the cyclone separator in this project consists of general solid waste. In municipal waste, heavy metals and their compounds can be differentiated based on their boiling points and volatility. Heavy metals such as Hg, As, and Cd have boiling points lower than the outlet temperature of the furnace (700–800°C), making them more likely to evaporate into the combustible gas during thermal treatment, where they are effectively captured during gas purification. In contrast, heavy metals like lead, which have higher boiling points, remain predominantly in the slag. The temperature at the cyclone separator does not significantly decrease, remaining around 650°C; therefore, other heavy metal vapors do not condense at this stage but are carried to subsequent purification processes. Consequently, dust contains heavy metal levels that do not exceed regulatory limits.

Table 5: Heavy metals of the fly ash

Analyte	Method	Unit	Detection limit	Value
Fluoride	F GB5085.3-2007	mg/L	0.2	0.3
Cyanide	G GB5085.3-2007	mg/L	0.005	<0.005
Hexavalent Chromium (Cr)	GB/T 15555.4-1995	mg/L	0.05	<0.05
Mercury (Hg)	HJ 702-2014	mg/L	0.00002	0.00045
Silver (Ag)	HJ 766-2015	mg/L	0.01	<0.01
Arsenic (As)	HJ 766-2015	mg/L	0.05	<0.05
Barium (Ba)	HJ 766-2015	mg/L	0.01	1.86
Beryllium (Be)	HJ 766-2015	mg/L	0.01	<0.01
Cadmium (Cd)	HJ 766-2015	mg/L	0.001	<0.001
Chromium (Cr)	HJ 766-2015	mg/L	0.01	<0.01

Copper (Cu)	HJ 766-2015	mg/L	0.01	<0.01
Nickel (Ni)	HJ 766-2015	mg/L	0.01	<0.01
Lead (Pb)	HJ 766-2015	mg/L	0.01	<0.01
Selenium (Se)	HJ 766-2015	mg/L	0.05	<0.05
Zinc (Zn)	HJ 766-2015	mg/L	0.05	<0.05
Methyl Mercury	GB/T 14204-1993	ng/L	10	<10
Ethyl Mercury	GB/T 14204-1993	ng/L	20	<20
Alkyl-Mercury	GB/T 14204-1993	ng/L	20	<20

3.4. Flue gas emissions test

The results of the flue gas pollutants are presented in Table 6, which is measured in the exit of the drying section. It demonstrates that the concentrations of various pollutants are well below the limitations set by GB18485-2014. The flue gas discharged from the drying section, following direct combustion of the purified synthetic gas, meets the standard without any prior purification, and the concentrations are significantly lower than required. This is primarily attributed to the high purity of the synthetic gas, which exhibits low concentrations of H_2S and HCl; consequently, the emission levels of SO_2 and HCl in the flue gas are correspondingly low. Regarding CO emissions, the combustion of gas is more easily controlled compared to the direct incineration of MSW, allowing for more complete combustion of the gas. As a result, theCO concentrations are very low. Moreover, this project does not employ any de-NOx measures; instead, it utilizes De-NOx combustion technology, which ensures that NOx emissions are within acceptable limits. This approach significantly reduces the costs associated with flue gas purification, thereby demonstrating the superiority of this process.

Table 6: Pollutant concentration of flue gas

Item	Concentration	unit
NO_X	102	mg/m^3
SO_2	23	mg/m^3
CO	13	mg/m^3
HCl	23	mg/m^3
Cd+Tl	0.00012	mg/m^3
Sb+As+Pb+Cr+Co+Cu+Mn+Ni	<0.001	mg/m^3

4. CONCLUSION

This paper presents a novel waste treatment method involving pyrolysis, reforming gasification and gas purification, exemplified by a specific engineering project. In this technology, thermochemical processes, including pyrolysis and reforming, serve as the core components. The pyrolysis process converts MSW into gas, oil, and char. Subsequently, the char and volatiles (including gas and oil) undergo reforming in a reformer to produce high-quality syngas. The purified syngas can be utilized in mature gas engines or turbines for power generation. The project operates effectively, yielding a combustible gas with a heating value exceeding 10 MJ/Nm^3 and a gasification efficiency of approximately 72.5%. Moreover, the quality of the purified combustible gas meets the intake requirements for internal combustion gas engines, and the flue gas emissions are significantly below China's National standards incineration.

5. REFERENCES

Asadullah, M. (2014). Barriers of commercial power generation using biomass gasification gas: A review. Renewable and Sustainable Energy Reviews 29, 201–215. https://doi.org/10.1016/j.rser.2013.08.074

Chen, D. (2014). Pyrolysis technologies for municipal solid waste: A review. Waste Management 34, 2466–2486. https://doi.org/10.1016/j.wasman.2014.08.004

Ge, S. (2022). Municipal solid wastes pyro-gasification using high-temperature flue gas as heating resource and gasifying agent. Waste Management 149, 114–123. https://doi.org/10.1016/j.wasman.2022.06.010

Martínez, J. (2022). Effects of altitude in the performance of a spark ignition internal combustion engine. Materials Today: Proceedings 49, 72–78. https://doi.org/10.1016/j.matpr.2021.07.475

Ma J. and Jin Y. (2022). Dioxin emssion characteristics of a novel 30 t/d village and town-scale solid wastes gasification system. Environmental Engineering, Vol 40 No.10

Ou Y. (2015). New appUcation technology for increasing generating efficiency of waste incineration plants. Environmental

Sanitation Engineerin，February 2015，V0l．23，No.1

Wang, B. (2023). A review on gasification of municipal solid waste (MSW): Syngas production, tar formation, mineral transformation and industrial challenges. International Journal of Hydrogen Energy S036031992301128X. https://doi.org/10.1016/j.ijhydene.2023.03.086

Wang, N. (2017). Hot char-catalytic reforming of volatiles from MSW pyrolysis. Applied Energy 191, 111–124. https://doi.org/10.1016/j.apenergy.2017.01.051

Yang, Z. (2015). Review of recent developments to improve storage and transportation stability of bio-oil. Renewable and Sustainable Energy Reviews 50, 859–870. https://doi.org/10.1016/j.rser.2015.05.025

Yin, L.-J. (2017). AHP-based approach for optimization of waste disposal method in urban functional zone. Environmental Technology 38, 1689–1695. https://doi.org/10.1080/09593330.2016.1244565

#330: Plant operation states analysis for low power and shutdown PSA on EPR

Wang WEIJIN[1,2], Wang YONGXIANG[1,2]

[1] Suzhou Nuclear Power Research Institute Co.,ltd, Suzhou in China,215004
[2] National Engineering Research Center for Nuclear Power Plant Safety & Reliability, 215004

Abstract: This paper outlines the analysis method of plant operation states (POSs) under low power and shutdown (LPSD) operations, with a focus on the key steps. Using this analysis method, a set of LPSD POSs, the statistical analysis method and results of each POS duration, and a sensitivity analysis have been determined in this paper. According to the sensitivity, it is reasonable to calculate each POS duration based on existing outage records and in conjunction with the medium and long-term outage plans. This paper could provide a reference for the probabilistic safety assessment (PSA) on EPR.

Keywords: Plant Operational States; Low Power and Shutdown; PSA

Throughout the entire cycle of a nuclear power plant, the plant operation state is subject to complex and variable conditions, such as the temperature and pressure of the primary loop, core decay heat, operational conditions, and maintenance configurations. These states will directly impact the accident progression and the PSA results. Therefore, they are necessary to identify and define the operating conditions and plant operational states.

POS is the primary task in developing a PSA model and is also a key step in comprehensively sorting out the characteristic parameters of various plant conditions. By properly identifying, grouping, and categorizing POS, the entire cycle of the plant can be divided into several configurations, which facilitate the management and application of PSA. Due to the complexity of the systems and the multitude of unit states on EPR, POS poses a challenge in PSA.

This article describes the POS analysis method, defines the plant configurations that cover low power and shutdown conditions, and provides boundary conditions of each POS for the core damage (CD) assessment.

1. OVERVIEW

1.1. Current technical standards related to LPSD

Since 1980s, China has begun to conduct research on PSA. Currently, PSA evaluations have been carried out in both operating and under-construction nuclear power plants in China, gradually applying PSA technology to risk assessmentand management work. Based on the ANSI/ANS 58.22 and ASME RA-Sb-2005 capability categoriy II requirements, theNational Energy Administration issued NB/T 20073.2-2012, which puts forward relevant requirements of nine elements (including POS) in the level 1 PSA for internal events at-low power and shutdown.

To ensure the quality of PSA analysis, the China Nuclear Energy Association has established the implementation Measures of Level 1 PSA Peer Review and guidelines of Level 1 PSA Peer Review for Internal Events at low power and shutdown. The latter provides methods for evaluating the technical quality and adequacy of PSA and standardizes the criteria for assessing whether the PSA meets technical requirements.

In 2018, Suzhou Thermal Power Research Institute Co., Ltd. took the lead in revising the reference 2, then in 2021, NB/T 20037.2-2021 was released.

As one of the elements of PSA, POS is analyzed in accordance with reference 3 and reference 4 to ensure its quality.

1.2. POS analysis process

POS typically **involves six steps.**

1) collect information

Each POS is one configuration closely related to the states of primary loop temperature, pressure, decay heat, operation,and maintenance configuration. The information includes but is not limited to the following documents:

(1) operating technical specifications;

(2) procedures for normal star-tup / shutdown and records (such as recent shutdown plans and records, maintenance plans and records, operational data, etc);

(3) Safety analysis reports;

(4) Other operational procedures (such as system operation procedures, control point procedures, test and maintenance procedures, accident procedures, etc);

(5) System manuals, etc.

2) Select the outage type

Based on the operational experience of EPR nuclear power units, the conditions、operating times of the power plant in operation modes may vary under different outage types. Therefore, it is necessary to clarify the outage types to be analyzed. EPR adopt an 18-month refueling cycle, and within the 60-year design life, three outage types are defined: simple refueling outage, partial maintenance refueling outage, and Ten Year outage. Considering that the refueling outage can encompass the operational states of the power plant during low power and shutdown conditions, as well as the historical records of plant shutdown activities, the refueling outage is selected as the outage type for the “average outage PSA” [2] maintenance process analysis, while also considering the planned LPSD evolutions.

3) POS classification criteria

4)

The POS classification criteria is derived from HLR-POS-A in reference 4, which includes the following content:

(1) Reactor coolant system operation modes in operating technical specifications;

(2) Reactor coolant system configuration;

(3) Reactor coolant system parameters;

(4) Activities changing RCP configuration and parameters used to define POS;

(5) Containment status, etc.

5) Define and classify POS

Based on the classification criteria, in conjunction with the operation modes、procedures for normal start-up / shutdown and records, It can preliminarily determinate a set of POS. It is necessary to consider the different outage type processesto refine the POS. The process should cover the entire LPSD evolutions, and take into account potential POS that may be encountered in the future or scenarios where entry into a certain POS might occur earlier.

6) POS grouping

Grouping POS in accordance with both criteria.

(1) POSs can be considered similar in terms of plant response, success criteria, timing, and the effect on the functionalityand performance of operators and relevant mitigation systems;

(2) POSs subsumed into a group are bounded by the worst-case impacts within the “new” group provided that this doesnot mask the key contributors. It should be ensured that “new” group does not mask the important contribution to plant risk, the core damage frequency (CDF) and the large early release frequency (LERF).

Create separate POSs for time periods involving significant activities (operational or maintenance) that could lead to initiating events that are "demand-based”. For example, draining to the 3/4 loop level.

7) POS duration

Determine the average duration associated with each POS and its share in one year, as well as the typical decay heat level or the time to reach the POS. For the former, shutdown records can be dealt out. In the absence of conditions (such as during the design or construction phase of a nuclear power plant, where there is no outage experience), analysis can be conducted based on the reference nuclear power plant or nuclear power plants with the most similar design. The latter is mainly used for defining success criteria and the time window for operator intervention.

The following text will focus on three key steps on EPR：Preliminary POS classification， grouping and POS duration.

2. POS CLASSIFICATION

EPR operating technical specifications has six operation modes or several standard states. The six operation modes are defined: Reactor in Power (RP)、Normal Shutdown on Steam Generators(NS/SG)、Normal Shutdown on RIS-RHR(NS/RIS-RHR), Maintenance Cold Shutdown (MCS)、Refueling Cold Shutdown (RCS)、Reactor CompletelyDischarged (RCD), see figure 1.The boundaries between different operation modes are based on plant operations such as the core divergence, the connection to the RIS system in RHR mode, the loss of primary integrity, the opening of the reactor pressure vessel or the unloading of the core.

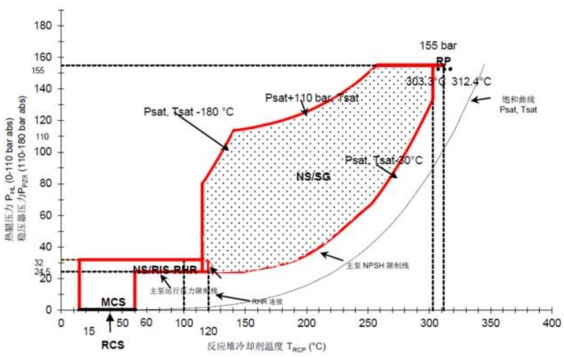

Figure 1: Operating limits of pressure and temperature in primary loop

Based on EPR operation modes, outage experience and subsequent potential outage evolutions, preliminary POS classification has been made, see table 1. It shows the preliminary classification results at shutdown process.

3. POS GROUPING

Based on the following methods, POSs are grouped into nine groups.1） Grouping POSs for shutdown and start-up operation shutdown operation and start-up operation are symmetrical, with the main difference being the level of decay heat and the activities. After grouping, the decay heat level is taken as the worst-case decay heat level among the two POS before grouping. This approach is conservative.

1) Creating 3/4 loop level POS

When the primary loop is drained to 3/4 loop level, the water level is very low, the operation conditions for the RIS-RHR pumps are severe, and the risk of loss of RHR function is very high. Therefore, separate POS should be created.

Table 1: classification and grouping of POSs

POS classification	Standard states	RCP state	POS（group）	Decay heat removal path	Boundaries between different POS
1	Reactor in power	closed	POS A1	SG，APA	-
2	Reactor at low power				
3	Hot standby and in criticality search		POS A2	SG，AAD	AAD supply water for SG
4	Hot shutdown		POS B	SG，AAD	Reactor is critical or not
5	Intermediate shutdown on SG P_{RCP}≥130bar.a				
6	Intermediate shutdown on SG P_{RCP} ＜130bar.a		POS C	SG，AAD	P12 locks some protection signals, which affects the engagement of the mitigation system.
	Intermediate shutdown on RIS-RHR connection conditions				
7	Two-phase intermediate shutdown on RIS-RHR		POS D1	RIS-RHR（SG backup）	Different decay heat removal path
8	Solid intermediate shutdown on RIS-RHR		POS D2	RIS-RHR	the primary loop is two-phase or not
10	Normal cold shutdown (RCP pressurizable)	Non-closed	POS D3	RIS-RHR	the primary loop is closed or not, as well as the primary loop water level
11	Normal cold shutdown for maintenance (RCP not pressurizable)		POS E	RIS-RHR	RCP not pressurizable
12	Normal cold shutdown for refueling		POS F	RIS-RHR	The primary loop is fully open and filled with water
13	Core totally unloaded	-	-		-

4. POS DURATION

4.1 Methods of POS duration

The duration of POS directly affects the core risk results. With the accumulation of outage experience, improvement in management capabilities, and optimization of outage schedules, the duration of each outage varies, and there is an overall trend of decreasing duration. The more outage samples collected that closely reflect current outage duration levels, the more effectively the statistically obtained POS durations can predict the actual average risk. Therefore, how to obtain POS durations is particularly important. Depending on the scenarios of outage experience, it is recommended to adopt different methods for obtaining POS durations.

Case 1) Power plants with rich outage experience

Usually, experience from at least six outages is used as the source. Through collecting the duration of each POS, then the annualized duration of each POS is obtained by averaging them.

Case 2) Power plants without rich outage experience

Due to the lack of experience for carrying out outages, there may be a number of occasional factors at every outage, each outage duration may be very different. In order to reflect the current and future average risk levels as accurately as possible, it is recommended to obtain POS durations on existing outage experience, and in conjunction with medium and long-term outage planning.

Case 3) Power plants without outage experience

For nuclear power plants in the design or construction stage, it can reference other nuclear power plants with similar design, and the POS durations can be updated in the future by tracking the outage experience itself.

By the end of 2023, EPR has conducted three outages（T101、T201 and T202）, which represents a situation without rich outage experience. Therefore, Case 3 is suitable for obtaining POS durations on EPR.

There are 7 outages over 10 years with 18 month-long cycles on EPR. It is assumed that, over 10 years, the following planned outage occur: 1 ten-year outage, 6 outages for refueling. Limited by the outage experience for refueling, it is roughly assumed that the remaining five outages duration will be same to the T202 outage duration. The calculation formulas for each POS time can be seen in Equation 1.

Equation 20: $\mathrm{POS^i} = \left(POS_{ten}^{i} \times 1 + \sum_{j=1}^{6} POS_{j}^{i}\right)/T$

Where:

POS_{ten}^{i} = POS i duration at the ten-year outage （hour/per year)

- POS_{j}^{i}= POS i duration at the j-th outage between consecutive ten-year outage（hour/per year）;
- T =Interval between consecutive ten-year outage (approximately 10.5 years).

4.2 Sensitivity analysis of POS duration

To analyse the impact of different methods of obtaining POS duration on EPR, the POS duration is calculated through another method, referred to as method 2. it is thought that there are three outages（T101、T201 and T202）in 4.5 years.

Using Equation 1 and method 2 to obtain POS duration, we find that it has very small change on total CDF, but has significant differences on CDF of each POS. It is not recommended to use method 2 on EPR, as it only reflects the POS duration within past time in a short period and cannot effectively represent the future POS duration levels.

5. CONCLUSION

Analysis is conducted about the POS element in the average outage PSA on EPR, offering a reference for the effective implementation of subsequent PSA work. At the current stage, the operational and outage experience of EPR is not yet abundant. When applying for PSA in the future, it is recommended to pay attention to the impact of the POS duration.

6. REFERENCES

China Nuclear Energy Association, 2014. Level 1 PSA Peer Review guideline for Internal Events at-low Power and Shutdown, Beijing: China Atomic Energy Press.

National Energy Administration, 2021. level 1 Probability Safety Assessment for nuclear power plant applications- Part 2: Internal events at low power and shutdown, NB/T 20073.2-2021，Beijing: China Atomic Energy Press.

#335: Numerical study on enhanced heating of a novel solar chimney and soil-air heat exchanger combined system

Wuyan LI [1], Yuanxiu GONG [2], Linfeng WANG [3], Qinyao LI [4], Yongcai LI*[,5]

[1] *Faculty of Civil Engineering and Mechanics, Kunming University of Science and Technology, Kunming, 650500, China, wuyanlee@foxmail.com*
[2] *Faculty of Civil Engineering and Mechanics, Kunming University of Science and Technology, Kunming, 650500, China, 3223992364@qq.com*
[3] *Department of Civil Engineering, Faculty of Engineering, Universitiy Malaya, Lembah Pantai, 50603 Kuala Lumpur, Malaysia; linfeng wang@outlook.com*
[4] *Faculty of Civil Engineering and Mechanics, Kunming University of Science and Technology, Kunming, 650500, China, 865851573@qq.com*
[5] *School of Civil Engineering, Chongqing University, Chongqing, 400045, China, yongcail85@163.com*

Abstract: The combination of a Solar Chimney and Soil-Air Heat Exchanger (SCEAHE) system for passive ventilation in buildings is an effective method for improving indoor air quality and enhancing thermal comfort. However, Soil-Air Heat Exchangers often fail to meet the heating demands indoors. To address this issue, this study proposes a new SCEAHE system that enhances its winter heating capacity based on the conventional SCEAHE design. Using a validated numerical model (MATLAB+TRNSYS), the annual performance of the system is simulated and analyzed. The results indicated that the average indoor temperature can be increased by 6 °C in winter compared to the conventional ventilation model. In addition, the innovative system saves 32.27% of energy during the heating season. This demonstrates that the system, while ensuring the original ventilation capability, makes more effective use of solar energy, significantly improving its winter heating performance.

Keywords: Solar Chimney, Soil-Air Heat Exchanger, Natural Ventilation, Heating.

1. INTRODUCTION

Energy consumption in buildings accounts for about 40% of the total global energy consumption [1]. The energy consumption of the building industry accounts for about 20-25% of China's total energy consumption and more than 1/3 of the total carbon emissions, of which the energy consumption of air conditioning equipment in buildings accounts for about 60% of the total energy consumption of buildings [2][3]. Reducing building energy consumption can be achieved through passive technology with conscious design and effective utilization of natural energy, and the development of energy-efficient buildings provides an effective solution for building energy efficiency [4][5]. Passive ventilation technology has the function of reducing heat gain from buildings, enhancing heat dissipation from buildings and providingfresh air to buildings [6][7]. Solar chimney (SC) and earth air heat exchanger (EAHE) have attracted a lot of attention dueto their method of achieving natural ventilation by utilizing two renewable energy sources, solar and geothermal energy [8].

Solar chimneys (SC) are utilized to promote natural air circulation based on the buoyancy generated by solar radiation [9]. Solar chimneys utilize solar energy economically and environmentally friendly, and are now mostly used for building ventilation, which also reduces the cost of the building ventilation system [10], and scholars have also concluded from their studies that the cooling potential and airflow rate of SC systems are lower in hot summers and cold winters when the ambient air temperature deviates significantly from the thermal comfort limit, but the average ventilation rate of the indoor environment of a building is higher in hot climates [11]. However, solar chimney ventilation is greatly affected by outdoor temperature, and the ventilation is unstable solar chimney ventilation performance process found that the area ofthe solar collector affects the airflow induction rate of the SC system [12], when the solar intensity is higher than 400W/m^2, the use of 15m^2 solar collector and a chimney with a height of 5m can achieve a better ventilation effect [13]; the ventilation performance of the SC system is also affected by latitude, operating season and collector inclination [14][15]. Some scholars have studied the thermal behavior of solar chimneys under different heat fluxes and concluded that the performance of solar chimney systems is more affected by solar radiation, Yang and Clements-Croome [16] found that the temperature of the air entering the indoor space must be lower than the indoor temperature in order to efficiently cool and carry away the heat from the interior space, and found that the solar chimney (SC) system's ability to regulate indoor thermal comfort is insufficient, to enhance the SC system's ability to regulate indoor thermal comfort can be coupled with other systems that can regulate indoor thermal comfort.

Earth-air heat exchanger (EAHE, buried pipe) is a kind of renewable energy to realize heating and cooling to regulate the indoor thermal comfort environment, the system uses the fan as a power device, the outdoor fresh air is transported to the indoor through the buried pipe, and the air supply air is heat exchanged through convective heat transfer and thermal conductivity in the buried pipe, which makes the soil and the soil and the horizontal buried pipe heat exchanger to meet the requirements of the building. The fresh air in the buried tube exchanges heat between the soil and the fresh air in the horizontal buried tube through convection heat transfer and heat conduction to meet the thermal comfort requirements of the building indoor [17], and the EAHE system can be used as an auxiliary device for heating and cooling in the hot-summer and cold-winter regions [18]. Integrating EAHE systems with buildings can reduce costs and provide more significant energy savings than conventional air conditioning systems [19]. In the study of EAHE systems, it was found that the performance of the system is affected by the geometry and arrangement of the EAHE ducts, where the smaller the diameter and the longer the ducts, the more favourable it is to improve the heat transfer performance of the EAHE [20]. In hot and dry climates, it was found that the heating potential of an EAHE system would be lower than the cooling potential [21], but deeply buried EAHE piping could reduce indoor air temperatures by up to 7℃ in summer [22][23]. During further evaluation of the performance of the EAHE system in a hospital in India, it was found that the systemcould meet the cooling requirements of the building but struggled to meet the heating requirements [24], and also because the EAHE system uses a fan as a power unit, it also generates mechanical noise during operation, which affects the activities of the people in the building.

In order to enhance the SC system's ability to regulate the indoor thermal comfort environment, and at the same time to improve the EAHE system's problems of mechanical noise and power consumption, it is considered that the two are coupled to obtain the SCEAHE system, which utilizes the SC system instead of the fan in the EAHE system to provide the driving force, and the EAHE system can provide the coupled system with the ability to provide heating or cooling to enhance the ability to regulate the indoor thermal comfort environment regulation[25]. The solar chimney is efficient enough to passively provide drive for the EAHE cooling system without any electrical power energy savings are better [26]. In order to investigate the feasibility of SCEAHE system Li and Yu et al. [27] carried out an experimental study and found that the coupled system can create a better thermal comfort environment for the indoor, keeping the indoor temperature in the range of 21.3-25.1℃. The performance of SCEAHE system was further investigated and it was found that the SCEAHE system can naturally ventilate the building for 24h with the combined effect of building thermal mass and SC, these show the advantages of SCEAHE system application, but it was also found that SCEAHE system can be affected by chimney inclination, length, width, gap range, pipe length and pipe diameter of the coupled system [28][29], and these influences need to be fully considered when designing the use of SCEAHE systems. In applied research, it was found that the use of SCEAHE system in Egyptian region can make the indoor temperature in summer 5-6℃ lower than the ambient temperature, and the indoor temperature in winter 10℃higher than the ambient temperature [29]. Bai et al.[30] experimentally evaluated the performance of SCEAHE system for natural ventilation in summer and winter, and found that indoor temperatures in summer were lower than 29oC for a total of 168h 78.6% in summer and 77.4% of the total 168h with indoor air temperature higher than 5℃in winter; in the same period Long et al. [31] found that the use of a SCEAHE system could reduce the average indoor air temperature by 4.4℃in summer and increase it by 6.4℃ in winter; there are also some literatures[32] that show that the use of a SCEAHE system can improve the indoor thermal comfort environment, but after studying other sources [33] it was found that in summer the average indoor temperature was reduced by 4.4℃ almost reaching the thermal comfort temperature of 24-28℃ in summer, with better ventilation performance, but in winter the average indoor temperature was only increased by 6.4℃, still in the difficulty of reaching the thermal comfort temperature of 16-20℃ in winter [34], and heating equipment is still needed, and the use of heating equipment makes the building's energy consumption increase; at the same time, the night-time ventilation of SCEAHE systems drive is generated in summer by the thermal mass collected by the solar chimney in conjunction with the subsoil, while in winter it is provided only by the subsoil and the heat collected by the solar chimney is wasted. From the above literature, it can be seen that the SCEAHE system can undertake building ventilation and the SCEAHE systemhas good ventilation performance in summer, but there is still room for further research to improve the ventilation performance of this system in winter.

In order to fully utilize the solar energy, and further improve the heating performance of the SCEAHE system in winter, a new configuration of the SCEAHE system is designed for winter heating. This is critical for the SCEAHE system, as the energy consumed by active heating system can be reduced significantly if it is ascertained that the new configuration of the SCEAHE system could operate efficiently in winter. This study aims to investigate the heating effect of a newly designed SCEAHE system numerically. The induced ventilation rate, indoor air temperatures, were comprehensively discussed in this paper. The obtained data were quantitatively evaluated and have been comparatively analysed with those of the conventional SCEAHE system and heating SCEAHE system, offering quantitative evidence to demonstrate the superiority of the new proposed system over the conventional passive heating systems.

2. MODELS OF DIFFERENT CONFIGURATIONS OF SCEAHE SYSTEMS

To fully and passively utilize solar energy for heating buildings, a solar-assisted heating model is proposed in this study. In this study, the improved SCEAHE system can automatically switch to heating or ventilation mode according to the change in the outdoor environment to better regulate the indoor environment. Since the conventional SCEAHE system delivers limited fresh air temperature to the room during the daytime in winter, switching the SCEAHE system to heating mode during the daytime was considered to provide higher fresh air temperature to the room. The decision to switch the SCEAHE system from ventilation mode to heating mode depends on the intensity of solar radiation and the indoor and outdoor temperatures. When the solar radiation intensity is greater than 50 W/m^2 and the indoor and outdoor temperature is below 20℃, this means that heating is required. In this case, the system will switch from ventilation mode to heating mode. The system configuration for the different modes is as follows.

Ventilation (Typical) mode: As shown in Figure. 1(a), the SC consists of two parts: a solar collector and a vertical chimney. During the day, the air inside the solar collector is heated by solar energy, and then due to the superposition effect, the heated air flows upward along the vertical chimney. The buoyancy force generated by the SC drives the outdoor air into the building through the EAHE, where the air is heated by the subsoil. Due to the buoyancy generated by the subsoil heating effect, the system can work continuously at night.

Heating mode: Outdoor air is first heated by the EAHE ducts and then flows upwards into the solar collectors. The flowing air is further heated by the solar collectors and the hot air is sent into the indoor space through the lower openings for displacement flow. As shown in Figure. 1(b), the indoor air is drawn into the vertical chimney through the higher opening due to the temperature difference between the inside and outside of the building.

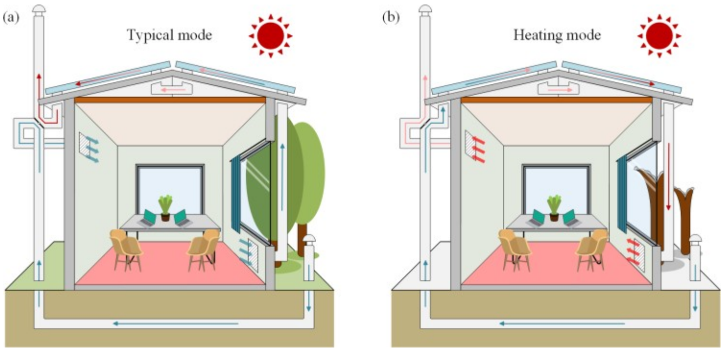

Figure 1: Schematic diagram of SCEAHE system in different models: (a) Ventilation mode, (b) Heating mode

The differences between the two systems of this study species are as follows.

- Conventional SCEAHE system： The system has only ventilation mode without a mode switcher.
- Innovative SCEAHE system: In this system there is a mode switcher that directly switches between ventilation mode and heating mode. The mode switcher switches modes according to changes in the external environment, e.g. heating mode during the day in winter to heat the room and ventilation mode during the day in summer to ventilate the room.

In practice, the innovative SCEAHE can be easily retrofitted from a conventional SCEAHE by adding a four-way valve and a certain amount of ductwork. This modification incurs a minimal cost compared to the overall system investment butcan yield significant benefits during the heating season.

The key components of both SCEAHE systems are the solar collector, the vertical chimney and the EAHE duct. The numerical modelling of the relevant components follows the conventional SCEAHE system in the published article [35~39]. This is an experimental study involving a comprehensive SCEAHE system. The experimental test setup, system component dimensions, test methodology and setup, and test results are described in detail in reference [34].Tables 1 and 2 summarise the important information used in this TRNSYS-MATLAB model.

Table 12: Important information about the SCEAHE system

items	Material	Geometry
Building	Perforated brick	Internal dimensions 4m(l) × 4m(w) ×3 m (h)
Solar collector	Stainless steel and glass	7m(l) × 1.5m(w) × 0.3m(h)
Solar chimney	Stainless steel	6m high with 0.3m diameter
EAHE pipe	PVC	30m long horizontal effective pipe with 0.3m diameter

To solve the numerical simulation problem for the three developed systems, numerical models of EAHE, solar collector and vertical chimney were developed using MATLAB, while the model of the building was generated using TRNSYS software as TRNSYS can accurately simulate the heat transfer process in buildings.

3. RESULTS AND DISCUSSION

The hypothetical building for the simulation is assumed to be located in a cold region ⅡA of China (Beijing) and a typical heating week is simulated for system performance analysis. The parameters of the simulated building are listed in Table 2, and the year-round climate performance of the Beijing area is shown in Fig. 2(a). As shown in the figures, the temperature in Beijing remains below 20°C for most of the year. From November to March, the average temperature is below 10°C. Consequently, the centralized heating period in Beijing spans from November 15 to March 15. A schematic diagram of a typical rural building selected for the simulation is shown in Fig. 2(b).

Table 2: Physical parameters of the exterior envelope of the room.

Envelop	Material layers: Name	Material layers: Thickness (mm)	Convective heat transfer coefficient ($w/(m^2 \cdot k)$): Interior	Convective heat transfer coefficient ($w/(m^2 \cdot k)$): Lateral	U-value ($w/(m^2 \cdot k)$)
External Wall	Plaster	2.5	3.06	17.78	ⅡA:0.6, ⅡB:0.5 错误!未找到引用源。 Ⅲ(A-C): 1.5 错误!未找到引用源。
	Brick	Ⅱ(A/B): 370 Ⅲ(A-C): 240			
	Insulation	ⅡA:48, ⅡB:60 Ⅲ(A-C): 9			
Floor & Interior walls	Insulation	Ⅱ(A/B): 30 Ⅲ(A-C): 10	3.06	3.06	Ⅱ(A/B):1.0 错误!未找到引用源。 Ⅲ(A-C): 2.0 错误!未找到引用源。
	Concrete	120			
External window	Glass	4	3.06	17.78	ⅡA:2.8, ⅡB:3.2 错误!未找到引用源。 Ⅲ(A-C): 3.2 错误!未找到引用源。
	Air	ⅡA:16 ⅡB, Ⅲ(A-C): 3.2			
	Glass	4			

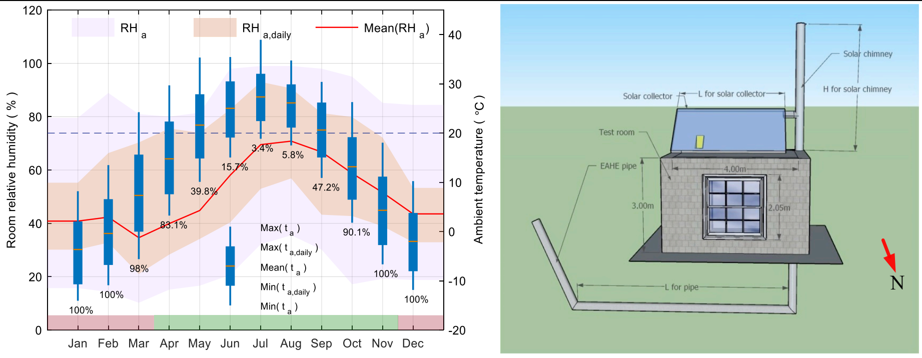

(a) Climate performance in Beijing (b) Architectural schematic

Figure 2: Pre-simulation preparation: (a) Climate performance in Beijing (b) Architectural schematic

3.1. Comparison of energy-saving efficiency

Figure. 3(a) illustrates the comparison of indoor temperatures between the conventional SCEAHE system and the innovative SCEAHE system when they are operated throughout the heating season, from which it can be more clearly demonstrated that the adoption of the innovative SCEAHE system can lead to a significant increase in indoor temperatures in winter. In order to further analyze the performance of the different systems, the time of the red coil in Figure. 3(a) (January 15-January 21) was chosen as a typical heating week for the simulation study.

Figure 3(b) compares the heat demand of two different SCEAHE systems to achieve an indoor temperature of 20°C during the heating season. It is clear from the figure that the innovative SCEAHE system has a lower average daily indoor heat load throughout the heating season. This is due to the fact that the innovative SCEAHE system utilizes solar collectors to heat fresh air during daytime operation in winter. As a result, the air entering the room is warmer than in a conventional SCEAHE system, which reduces the indoor heat demand.

The calculated indoor loads for the whole heating season are 8682.3 kW·h for the conventional SCEAHE system and 6600.18 kW·h for the innovative SCEAHE system. Compared to the conventional system, the innovative SCEAHE system saves 2082.12 kW·h of electricity during the heating season, which is a significant reduction of 32.27%.

Comparative simulations show that the innovative SCEAHE system can not only satisfy indoor ventilation needs in winter but also provide relatively high indoor air temperatures. The innovative SCEAHE system effectively utilises the untapped solar energy in the conventional SCEAHE system and achieves substantial building energy savings while providing heat.

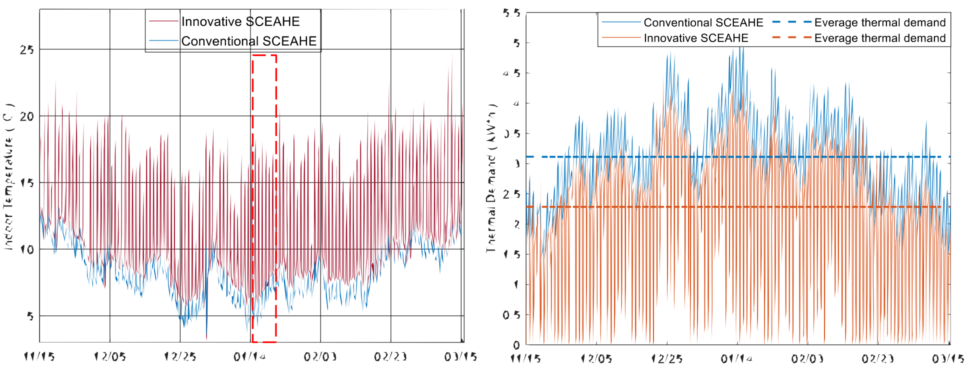

(a) Comparison of indoor temperatures (b) Comparison of heating demind

Figure3: Simulation of the heating season:(a) Comparison of indoor temperature, (b) Comparison of heating demind

3.2. Comparison of different systems

To thoroughly analyse the operational characteristics of the system, the study first examined the simulation results for a typical heating week, from January 15 to January 21. Figure. 4 shows the comparison of room temperatures (a), ventilation (b), fresh air heating (c), and room heating (d) for a typical heating week with two different SCEAHE systemsin operation. It is clear from Figure. 4(a) that the innovative SCEAHE system can provide higher temperature fresh air to the room in winter compared to the other two systems.

Unlike conventional SCEAHE systems, the air in the novel SCEAHE system is preheated by solar collectors before it is brought into the room. As a result, the system's air supply temperature and indoor temperature are higher during the day. Specifically, the average indoor air temperatures in winter were 12.65°C and 6.96°C for the novel SCEAHE system and the conventional SCEAHE system, respectively. Overall, the daily maximum temperature in rooms with the novel SCEAHE system exceeds 15°C, while rooms with the conventional system only reach 8°C, showing a significant improvement.

Additionally, due to the building's heat storage capacity, rooms equipped with the novel system also maintain higher indoor temperatures at night compared to those with the conventional system. The average nigh-time indoor air temperatures for the novel SCEAHE system and the conventional SCEAHE system are 7.24°C and 6.06°C, respectively.

Figure. 4 illustrates the airflow variations under the operation of two different SCEAHE systems. The conventional SCEAHE system exhibits the highest ventilation rate. This difference arises from the varying driving forces in each system. In the heating mode, the driving force is generated by the thermal pressure difference between the solar chimney and the room. Conversely, in the conventional ventilation mode, the driving force is provided by the thermal pressure difference between the buried pipe and the room. Figure. 4(c) shows a comparison of the amount of heat addedto the fresh air and room by the different systems. It is found that the average heating capacity of the conventional SCEAHE system is 22.22 kW·h for fresh air and 15.34 kW·h for the room, the innovative SCEAHE system has a heating capacity of 28.62 kW·h for fresh air and 19.37 kW·h for the room. 22% more fresh air heating and 21% more room heating is achieved with the innovative system compared to the conventional SCEAHE system. This provides warmer fresh air for the room in winter.

This is due to the fact that with the innovative system, the fresh air passes through the solar collectors during the day before entering the room, providing a heat exchange with the solar collectors to gain heat from the solar collectors and thus be preheated; at night, the building walls have a certain heat storage capacity that allows the room temperature to be higher at night compared the conventional SCEAHE system.

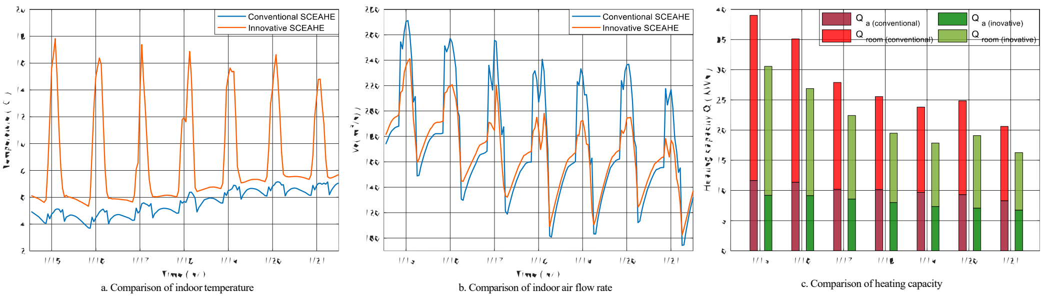

Figure 4: Comparison of different systems on (a) indoor temperature, (b)air flow rat, (c) heating capacity

3.3. Parameters analysis of the innovative SCEAHE system

Effect of Solar Collector Length

Figure. 5 illustrates a comparison of the performance of the innovative SCEAHE system as affected by the length of the solar collector. The effect of solar collector length on indoor temperature is shown in Figure. 5 (a) and the effect of collector length on system airflow is shown in Figure. 5 (b). It is found that the indoor temperature and airflow increase with the increase in solar collector length. This is because longer solar collectors favour increased solar heat gain and higher buoyancy differential pressure. However, it is also found from the graph that the increase in indoor temperature and airflow is decreasing. Specifically, when the length of the collector increases from 5m to 7m, the average indoor temperature increases from 8.62 °C to 9.29 °C, which is an increase of 0.67 °C; the average air flow increases from 150.25m^3/h to 155.56m^3/h, which is only an increase of 5.56 m^3/h. The increase in the length of the solar collector from 11m to 13m only increases the average temperature by 0.4oC. This indicates that the length of the solar collector has a significant effect on the average indoor temperature and airflow. This indicates that the length of the solar collector has a greater degree of influence on the indoor temperature and a smaller effect on the airflow.

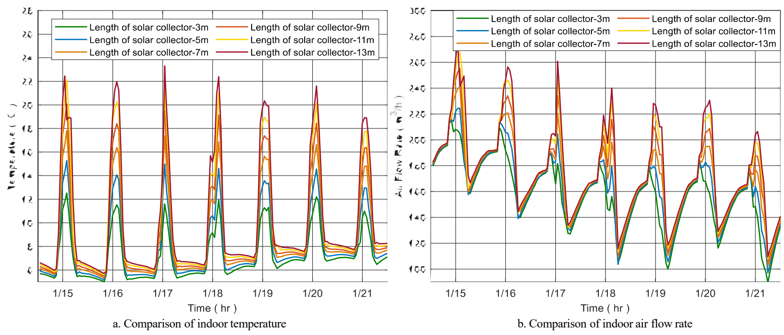

Figure 5: Effects of length of solar collectors on (a) indoor air temperature, (b) air flow rate

Effect of Pipe Length

Figure.6 illustrates the effect of the length of the buried pipe on the indoor temperature and fresh air volum e. From Figure.6 (a), it can be seen that the indoor temperature increases as the length of the buried pipe increases. However, it is obvious that the temperature rise is larger at the beginning, and the increase in temperature is smaller after the length is increased to 50m. At the same time, it is found in Fig.6 (a) that the effect of pipe length on the indoor temperature is not as large as the effect on the night temperature. This is because the heating mode is turned on during the daytime of the heating season, and the supply air enters the room through the solar collector, and the supply air is heated by the solar collector. Specifically, the increase in buried pipe length from 20m to 30m increased the average indoor temperature by 1.62 ºC. In comparison, the rise in buried pipe length from 60m to 70m only increased the average indoortemperature by 0.22 ºC.

Figure. 6 (b) illustrates that the airflow increases and then decreases with the increase in the length of the buried pipe. After calculation, it is found that the average airflow gradually increases from 165.76m^3/h to 172.65m^3/h and then decreases to 165.17m^3/h as the length of the buried pipe increases. This result is due to the fact that the pressure drop inside the buried pipe increases as the length of the pipe increases and the airflow is suppressed.

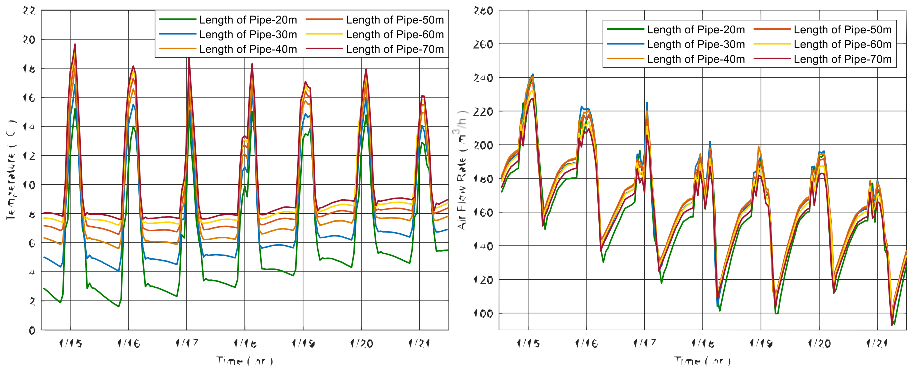

a. Comparison of indoor temperature

b. Comparison of indoor air flow rate

Figure 6: Effects of length of pipe on (a) indoor air temperature, (b) air flow rate

Effect of Pipe Diameter

Figure. 7(a) illustrates the effect of buried pipe diameter on indoor temperature and fresh air volume. From Figure. 7(a), it can be seen that the indoor temperature first increases and then decreases as the diameter of the buried pipe increases. When the diameter of the buried pipe increases from 0.2 m to 0.7 m, the average indoor temperature of the buried pipe increases from 6.2°C to 8.62°C, then decreases to 7.03°C. The highest average indoor temperature was observed when the diameter of the pipe was 0.3 m.

Figure. 7 (b) illustrates that the airflow has been increasing with the increase of the pipe diameter, but the magnitude of the increase is decreasing. The average airflow is calculated to increase from 63.60 m^3/h at 0.2 m to 409.02 m^3/h at 0.7 m. This result is due to the fact that the increase in diameter of the pipe increases the ventilation capacity, but the increase in diameter increases the pressure loss of the buried pipe too much.

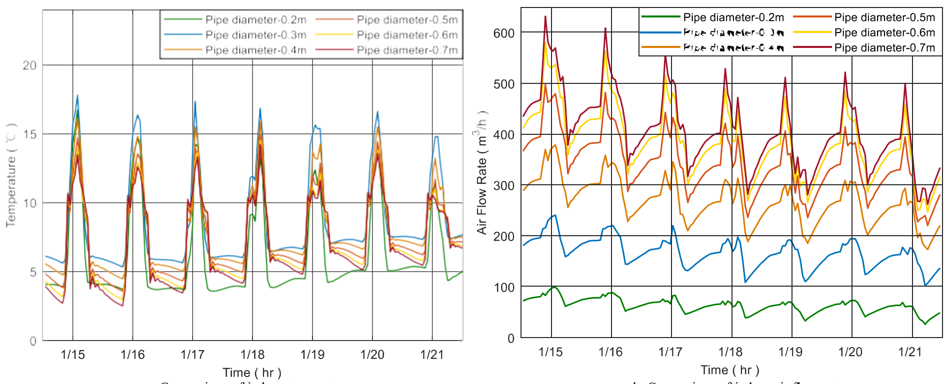

a. Comparison of indoor temperature

b. Comparison of indoor air flow rate

Figure 7: Effects of the diameter of the pipe on (a) indoor air temperature, (b) air flow rate

Effect of Solar Chimney Length

Figure.8 illustrates the effect of the length of the solar chimney on the indoor temperature and the amount of fresh air. The effect of chimney length on indoor temperature is shown in Figure. 8 (a), which shows that the indoor temperature does not change much with increase in chimney length. After calculation it is found that the change in average indoor temperature with increase in chimney length is only within 1 ^{o}C.

Figure. 8 (b) illustrates the effect of chimney length on airflow, as the chimney length increases from 6m to 16m with an increase of 2m, it is found that the average airflow increases from 149.03m^3/h to 241.61m^3/h. It is also found that the average airflow has a large increase at the beginning, and an increase in chimney height by 2m increases the airflow to 23.63m^3/h. At the end, an increase of 2m only increases the airflow to 23.63 m^3/h, and at the end, an increase of 2m only increases the airflow by 1m. Increasing the chimney height by 2m can only increase the average airflow by 14.87m^3/h. Figure. 8 shows that the chimney length has a small effect on the indoor temperature, but a relatively large effect on the airflow. This sample result is due to the fact that the chimney is used in the system to provide differential pressure and thus ventilation to the room.

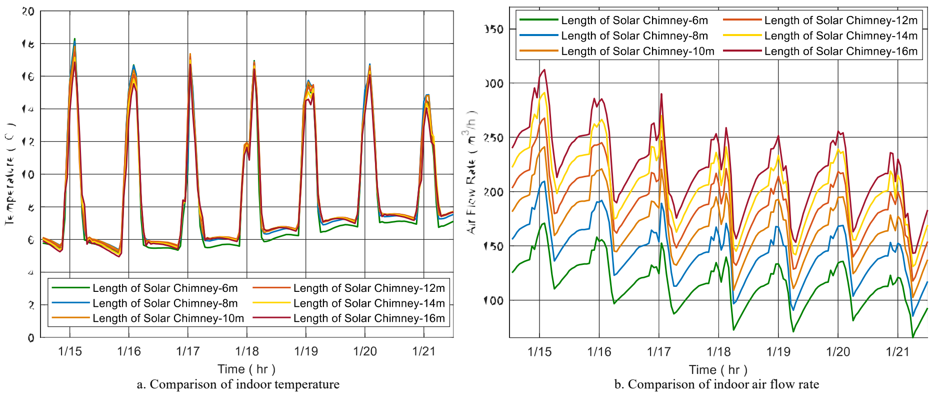

Figure 8: Effects of the length of solar chimney on (a) indoor air temperature, (b) air flow rate

Effect of Solar Chimney Diameter

Figure. 9 illustrates the effect of the diameter of the solar chimney on the indoor temperature and the amount of fresh air. The effect of chimney diameter on indoor temperature is shown in Figure. 9 (a), which shows that the indoor temperature hardly changes as the length of the chimney increases. The average indoor temperature is maintained at 9.26 to 9.26 ^{o}C. Figure. 9 (b) shows the effect of chimney diameter on airflow, which also changes relatively little. It is found that as the diameter of the chimney increases, the magnitude of the average airflow increases only from 160.03 m^3/h to 178.61 m^3/h. This indicates that the diameter of the solar chimney has a relatively small degree of influence on the indoor temperature and airflow. This is due to the fact that the solar chimney mainly performs the function of providing differential pressure to the system and thus ventilation. The simulation comparison reveals that the indoor temperature is less sensitive to the diameter of the chimney.

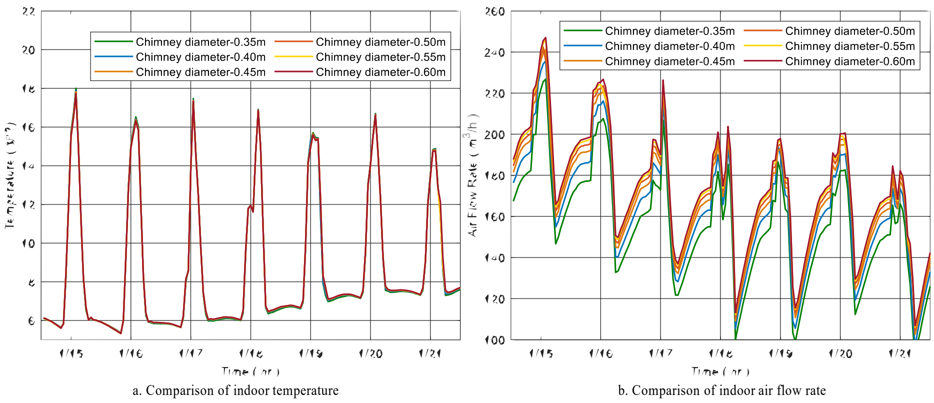

Figure 9: Effects of the diameter of solar chimney on (a) indoor air temperature, (b) air flow rate

By simulating the different parameters that affect the performance of the system, it was found that the greater influence on the indoor temperature is the length of the collector and the length of the buried pipe; the greater influence on the ventilation is the diameter of the buried pipe. However, as the length of the equipment increases, the effect on the indoor temperature and ventilation gradually becomes smaller. Therefore, when choosing the length of the collector and the length of the buried pipe, should consider the economic factors and performance effects.

4. CONCLUSION AND FUTURE WORK

This study improves the conventional SCEAHE system in that it enables the system to utilize solar energy for heating in winter in order to achieve a win-win situation for both heating and energy saving. The system airflow and indoor air temperature were used as the evaluation indexes of system performance. The performance and energy savings of three different SCEAHE systems were compared during a typical heating week in winter; the effects of some geometrical parameters affecting the innovative SCEAHE system on these two evaluation indexes were investigated. The main conclusions and future work are presented below.

4.1. Main conclusions

(1) Comparing the system performance of the conventional SCEAHE system, the fully-heated SCEAHE system and the innovative SCEAHE system during the heating season, the innovative SCEAHE system operates better and can raise the indoor temperature to 16~20ºC during the daytime of the heating season.

(2) The innovative SCEAHE system is more energy efficient. Compared with the conventional SCEAHE system, at a heating temperature of 20ºC, the use of the innovative SCEAHE system can save 32.27% of energy in winter.

(3) The length of the collector and the length of the buried pipe have a greater impact on the indoor temperature. Larger collector lengths and buried pipe lengths result in higher indoor air temperatures and larger air volumes. Buried pipe diameter and chimney length have a greater effect on system ventilation. However, indoor temperature is not sensitive to solar chimney length.

4.2. Future work

The current study of the innovative SCEAHE system is only through theoretical calculations and numerical simulations, this study explores some of the performance of the innovative system for heating in winter, but does not address the performance of the system in summer, and it is hoped that the later study will explore how the innovative system should be switched to system modes to regulate the indoor ventilation and thermal environments in the summer.

5. ACKNOWLEDGEMENT

The work described in this paper was supported by Chongqing Science and Technology Commission of China (No. CSTB2022NSCQ-MSX1019) and supported by Yunnan Fundamental Research Projects (grant NO. 202401CF070134).

6. REFERENCES

[1] Singh R ,Sawhney R ,Lazarus I , Et Al.Recent Advancements In Earth Air Tunnel Heat Exchanger (Eathe) System For Indoor Thermal Comfort Application: A Review[J].Renewable And Sustainable Energy Reviews,2018,82(P3):2162-2185.

[2] Jihong P ,Chao S ,Shaoxin Y , Et Al.Feasibility Investigation On Using Silver Nanorods In Energy Saving Windows For Light/Heat Decoupling[J].Energy,2022,245.

[3] Building Energy Efficiency Research Center, Tsinghua University. China Building Energy Efficiency Annual Development Research Report 2023 (Urban Energy System Topic) [M]. Beijing: China Construction Industry Press, 2023.

[4] Tabbi W ,A.G. O ,Taha E S , Et Al.A Review On Zero Energy Buildings – Pros And Cons[J].Energy And Built Environment,2023,4(1):25-38.

[5] M. H M ,Ali M A ,Khaled E , Et Al.A Review Of Solar Chimney For Natural Ventilation Of Residential And Non-Residential Buildings[J].Sustainable Energy Technologies And Assessments,2022,52(Pb):

[6] Bagiorgas S H ,Chaideftou E ,Assimakopoulos N M , Et Al.The Use Of Wind Energy For Passive Cooling Applications In Western Greece[J].Intelligent Buildings International,2009,1(3):209-221.

[7] Mohammed A ,Mehdi M ,Zabetian M T , Et Al.An Innovative Hybrid System Consists Of A Photovoltaic Solar Chimney And An Earth-Air Heat Exchanger For Thermal Comfort In Buildings[J].Case Studies In Thermal Engineering,2022,40.

[8] V ,J.M.A. N ,J.F. H , Et Al.Effect Of The Solar Roof Chimney Position On Heat Transfer In A Room[J].International Journal Of Mechanical Sciences,2021,209.

[9] Youbo H ,Bin W ,Long S , Et Al.Performance Evaluation Of Solar Chimney In Tunnel For Passive Ventilation And

Smoke Exhaustion: A Numerical Approach[J].Applied Thermal Engineering,2024,238122227-.

[10] N.K. Bansal, Rajesh Mathur, M.S. Bhandari,Solar Chimney For Enhanced Stack Ventilation,Building And Environment,Volume 28, Issue 3,1993, 373-377.

[11] Khedari J ,Boonsri B ,Hirunlabh J .Ventilation Impact Of A Solar Chimney On Indoor Temperature Fluctuation And Air Change In A School Building[J].Energy Buildings,2000,32(1):89-93.

[12] Hussain H. Al-Kayiem, Sreejaya K.V., Syed Ihtsham Ul-Haq Gilani,Mathematical Analysis Of The Influence Of The Chimney Height And Collector Area On The Performance Of A Roof Top Solar Chimney,Energy And Buildings,Volume 68, Part A,2014, 305-311,

[13] Kong J ,Niu J ,Lei C .A Cfd Based Approach For Determining The Optimum Inclination Angle Of A Roof-Top Solar Chimney For Building Ventilation[J].Solar Energy,2020,198555-569.

[14] Yongcai Li, Shuli Liu,Numerical Study On Thermal Behaviors Of A Solar Chimney Incorporated With Pcm,Energy And Buildings,Volume 80,2014, 406-414.

[15] Yang T, D.J. Clements-Croome .Natural Ventilation In Built Environment[J].Sustainable Built Environments, 2020,Pp :431-464.

[16] Yang D., Wei H. Theory Of Coupled Soil-Air Heat Exchangers And Building Thermal Storage [M]. Beijing:Science Publishing House,2023,2-4.

[17] Jinxin X ,Qiang W ,Xiaoyan W , Et Al.An Earth-Air Heat Exchanger Integrated With A Greenhouse In Cold-Winter And Hot-Summer Regions Of Northern China: Modeling And Experimental Analysis[J].Applied Thermal Engineering,2023,232.

[18] Montaser Mahmoud, Mohammad Ali Abdelkareem, Abdul Ghani Olabi,Chapter 2.4 - Earth Air Heat Exchangers,Editor(S): Abdul Ghani Olabi[J].Renewable Energy - Volume 2: Wave, Geothermal, And Bioenergy,Academic Press, 2024, 163-179,

[19] Ruth S.Brum,Jairo V.A.Ramalho,Michel K.Rodrigues,Et Al.Design Evaluation Of Earth-Air Heat Exchangers With Multiple Ducts[J].Renewable Energy,2018,135:1371-1385.

[20] Jilani H N M ,Yadav S ,Panda S , Et Al.Assessment Of Annual Performance Of Quonset Gipvt System Combined With An Earth-Air Heat Exchanger (Eahe) For Hot And Dry Climatic Conditions[J].Renewable Energy,2024,223119990-.

[21] Yang D ,Zhang J .Analysis And Experiments On The Periodically Fluctuating Air Temperature In A Building With Earth-Air Tube Ventilation[J].Building And Environment,2015,85:29-39.

[22] Yongcai L ,Tianhe L ,Xi B , Et Al.An Experimental Investigation On The Passive Ventilation And Cooling Performance Of An Integrated Solar Chimney And Earth–Air Heat Exchanger[J].Renewable Energy,2021,175:486- 500.

[23] M.S. Sodha, A.K. Sharma, S.P. Singh, N.K. Bansal, Ashvini Kumar, Evaluation Of An Earth—Air Tunnel System For Cooling/Heating Of A Hospital Complex[J].Building And Environment,1985,115-122.

[24] Xiao J ,Li J .Influence Of Different Types Of Pipes On The Heat Exchange Performance Of An Earth-Air Heat Exchanger[J].Case Studies In Thermal Engineering,2024,55104116-.

[25] Maerefat M ,Haghighi A .Passive Cooling Of Buildings By Using Integrated Earth To Air Heat Exchanger And Solar Chimney[J].Renewable Energy,2010,35(10):2316-2324.

[26] Li H ,Yu Y ,Niu F , Et Al.Performance Of A Coupled Cooling System With Earth-To-Air Heat Exchanger And Solar Chimney[J].Renewable Energy,2014,62468-477.

[27] Serageldin A A ,Abdelrahman K A ,Ookawara S .Parametric Study And Optimization Of A Solar Chimney Passive Ventilation System Coupled With An Earth-To-Air Heat Exchanger[J].Sustainable Energy Technologies And Assessments,2018,30,263-278.

[28] Long, T, Et Al., Numerical Investigation Of The Working Mechanisms Of Solar Chimney Coupled With Earth-To-Air Heat Exchanger (Sceahe). Solar Energy, 2021. 230: 109-121.

[29] Serageldin A A ,Abdeen A ,Ahmed M M , Et Al.Solar Chimney Combined With Earth To-Air Heat Exchanger For Passive Cooling Of Residential Buildings In Hot Areas[J].Solar Energy,2020,206:145-162.

[30] Bai, Y., Et Al., Experimental Investigation Of Natural Ventilation Characteristics Of A Solar Chimney Coupled With

Earth-Air Heat Exchanger (Sceahe) System In Summer And Winter. Renewable Energy, 2022. 193: 1001-1018.

[31] Tianhe L ,Ningjing Z ,Wuyan L , Et Al.Numerical Simulation Of Diurnal And Annual Performance Of Coupled Solar Chimney With Earth-To-Air Heat Exchanger System[J].Applied Thermal Engineering,2022,214.

[32] Tianhe L ,Ningjing Z ,Wuyan L , Et Al.Natural Ventilation Performance Of Solar Chimney With And Without Earth-Air Heat Exchanger During Transition Seasons[J].Energy,2022,250

[33] Lu Y J, Ma T L, Zou P H. Hvac [M]. Beijing:China Construction Industry Press,2007,9-10.

[34] Gb 50019-2003, Design Code For Heating, Ventilation And Air Conditioning. [M] Beijing: China Planning Press.

[35] T.L. Bergman, A.S. Lavine, F.P. Incropera, D.P. Dewitt, Fundamentals Of Heat Andmass Transfer, Wiley Press, 2011.

[36] W.H. Mcadams, Heat Transmission. 3rd Ed, New York: Mcgraw-Hill, 1994.

[37] K.S. Ong, A Mathematical Model Of A Solar Chimney, Renew Energ 28 (2003) 1047–1060.

[38] J. Mathur, S. Mathur, Anupma, Summer-Performance Of Inclined Roof Solar Chimney For Natural Ventilation, Energy & Buildings 38(10) (2006) 1156-1163.

[39] K.S. Ong, C.C. Chow, Performance Of Solar Chimney, Sol. Energy 7 (2003) 41–117.

[40] National Civil Building Engineering Design Technical Measures Of China. 07jscs-Jj, Ministry Of Housing AndUrban-Rural Development Of China, 2007.

[41] Design Standard For Energy Efficiency Of Residential Buildings In Hot Summer And Cold Winter Zone. Jgj134-2010, Ministry Of Housing And Urban-Rural Development Of China, 2010.

#338: Investigation of solar assisted dual function heat pump for application in low energy buildings

Osamah ALANAZI[1], Rabah BOUKHANOUF[2], Xiaofeng ZHENG[3]

[1] University of Nottingham, Nottingham, osamah.alanazi@nottingham.ac.uk
[2] University of Nottingham, Nottingham, lazrb@exmail.nottingham.ac.uk
[3] University of Nottingham, Nottingham, Xiaofeng.Zheng@nottingham.ac.uk

Abstract: This review paper investigates energy consumption in Saudi Arabia with a focus on the residential sector and compares it to the global scale. Furthermore, the paper looks at cooling consumption and looks at recent literature that reports the integration of renewable systems into residential buildings to increase air conditioning efficiency as well as reduce conventional consumption. It focuses on solar and geothermal energy for residential buildings. Due to its abundant sunshine, Saudi Arabia is well-positioned to harness solar energy through photovoltaic (PV) technology. Studies have shown that integrating PV panels into buildings alongside energy-efficient materials offers promising energy savings. Geothermal energy, another renewable resource, can be utilized through ground source heat pumps (GSHPs) that extract heat from the shallow ground source. These systems leverage the Earth's stable temperature for heating and cooling purposes, offering a potentially self-sufficient solution for single houses. Overall, the paper highlights the significant potential of solar and geothermal energy to contribute to a more sustainable energy mix in the residential sector for Saudi Arabia. Further research and development are crucial to optimize these technologies and maximize their benefits for the country.

Keywords: Cooling, Renewable Energy, Solar Energy, Buildings, Heat Pumps

1. INTRODUCTION

On Earth, living organisms have relied on the sun's energy since its beginning. However, the Industrial Revolution marked a shift towards the extensive use of fossil fuels like coal, oil, and natural gas (Ritchie, 2021). This progress, while leading to a modern era, has unfortunately accelerated climate change due to increased greenhouse gas emissions. The G20 nations, including Saudi Arabia, are significant contributors, responsible for roughly 76% of global emissions (UN). In 2020, Saudi Arabia ranked fourth globally in oil consumption (3.5 million barrels daily) and sixth in natural gas consumption (112.1 billion cubic meters) (BP, 2021). Recognizing the need for sustainable solutions, Saudi Arabia's Vision 2030 prioritizes energy efficiency and aims to achieve net zero emissions by 2060 through strategies like a circular carbon economy and increasing renewable energy use to 50% (Vision2030). The Saudi Energy Efficiency Center (SEEC) was established to optimize energy use across different sectors, with industry being the primary consumer, followed by buildings at nearly one-third of the national total. The industrial sector leads in energy consumption, while buildings account for nearly one-third of the country's energy use. Figure 1 shows the main consumers of the Kingdom by sector (Center, 2021).

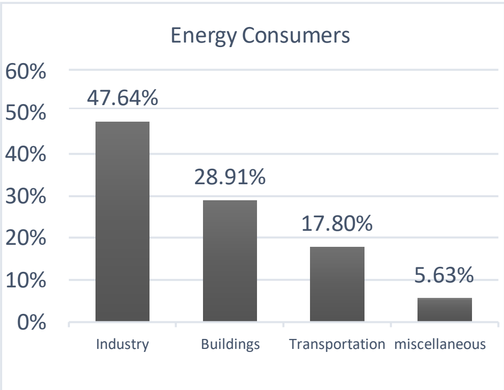

Figure 1: Saudi Arabia's main energy consumers

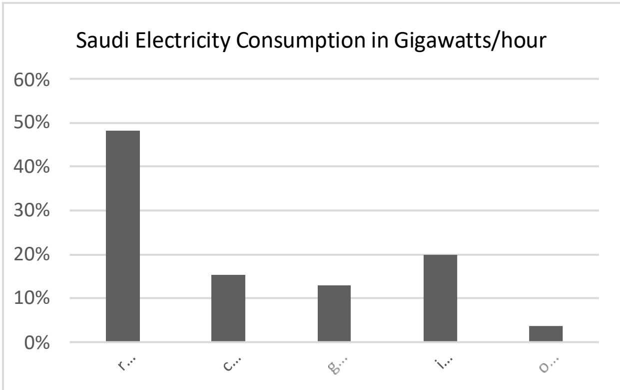

Figure 2: Saudi electricity consumers by sector

Even though the data shows that buildings in the Kingdom consume a bit less than a third of energy, other reports indicate that the residential sector consumes almost half of the country’s electricity generation. This clearly indicates that the kingdom must lower the residential’s large consumption to meet its net zero energy goals. Figure 2 reports how electricity is consumed in the country (Saleh, 2023) (SAMA).

1.1. KSA PROFILE AND CLIMATE

Located in Southwest Asia, Saudi Arabia covers a large portion of the Arabian Peninsula. Its diverse landscape ranges from mountains to coastlines, creating a variety of climates across the country. This geographical complexity requires specific considerations when designing buildings for both comfort and energy efficiency. The country's young and growing population will further impact its future energy demands (CIA, 2024) (Statistics, 2023). To ensure accurate and effective energy consumption predictions, local climatic conditions must be factored into the modelling process (Rashid et al., 2020). Figure 2 reports how electricity is consumed in the country (Saleh, 2023). The Kingdom has established different approaches to energy efficiency, the residential sector is still the largest electricity consumer, and heating and cooling demand accounts for more than 70% of that electricity consumption (SAMA).

As depicted in Figure 2.2 (Alrashed and Asif, 2015), Saudi Arabia's extensive coastline, stretching for 3,800 kilometers, contributes to its diverse climatic regions. Despite past classifications grouping the entire country as a single arid desert zone, more assessments have begun to recognize the differences between the continental desert, the humid coastal regions, and the cooler, higher-altitude areas with high summer and winter temperatures. This climatic diversity has found its way into the Saudi Buildings Energy Conservation Code 602, which divides the country into three distinct climatic zones and reports wider data on different cities in those zones, acknowledging the varying thermal demands of each region as shown in Figure **3** (Albogami and Boukhanouf, 2019).

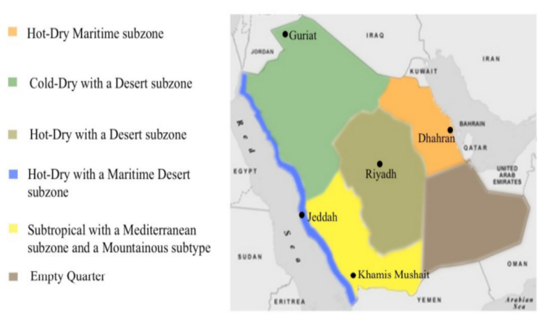

Figure 19: Climatic zones of Saudi Arabia

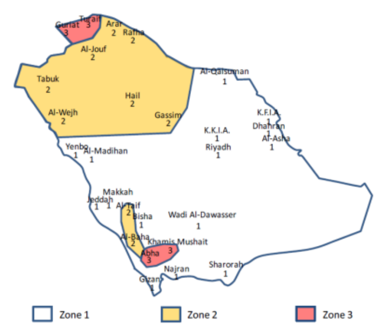

Figure 20: Climatic zones based on the Saudi Building Code

1.2. BUILDINGS IN KSA

Electricity generation in Saudi Arabia, similar to other Gulf Cooperation Council member countries, it relies significantly on the consumption of fossil fuels. (Administration, 2019). Regardless, it stands out as the country that burns the crudestoil for power generation globally. In 2018, Saudi Arabia ranked 11th globally in electricity generation, producing 384 TWh, equivalent to 55% of the GCC region's total. The country boasted a peak load of 61 GW and a near-85 GW total generation capacity (bp, 2022). Its rapid 7% annual growth is projected to continue, but with summer peak demand soaring 121% between 2004 and 2016, the 290 TWh consumed annually puts pressure on the national grid (Bank, 2019, Nachet and Aoun, 2015). Several factors contribute to this growth, including population growth, high demand for air conditioning during the summer, expansion of the industrial sector, and a low electricity tariff. In fact, during the transition from winter to summer, it was estimated that the growth in electricity demand could exceed 100% (Alyami, 2022). A study investigateshow Saudi Arabia's electricity needs will evolve between 2018 and 2040. The peak load already reached more than 61 GW in2018, but researchers predict it will jump to 74 GW by 2025 and hit 83.8 GW by 2030. The most dramatic rise is peak load potentially reaching 103.2 GW by 2040 (Harbi and Csala, 2019). Figure 5 and Figure 6 show those predictions for both peak loads and electric consumption.

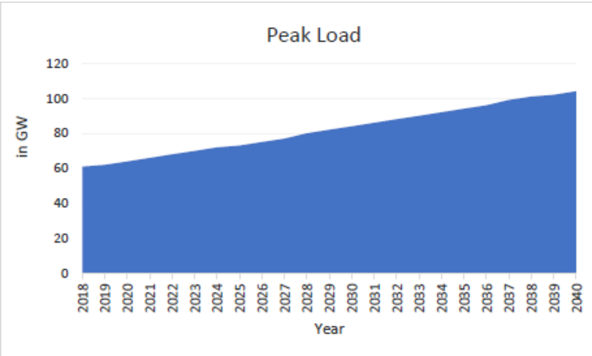

Figure 5: Projection of peak loads in the Kingdom

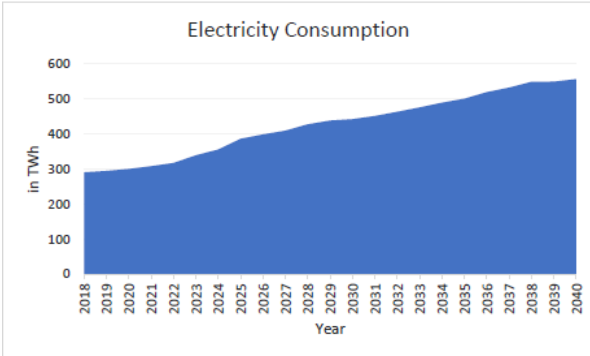

Figure 6: Projection of electricity consumption in KSA

Prior to 2007, sustainable building practices weren't a major focus in Saudi Arabia's construction industry. However, a turning point came in March 2007 with the establishment of the Green Building Council (SGBC) and subsequent regulations and codes (Surf & Saied, 2014). The Saudi Energy Efficiency Centre (SEEC) introduced the Saudi Energy Conservation Code (SBC602), which sets benchmarks for energy efficiency in new residential buildings nationwide. This code leverages international standards like the 2003 International Energy Efficiency Code and those from the American Society of Heating, Refrigerating and Air-Conditioning Engineers (ASHRAE). It applies to new single-family homes up to three floors and residential apartments, excluding buildings with four or more stories (considered commercial). SBC602 also mandates thermal performance standards for building envelopes in low-rise residential structures. These envelopes encompass exterior walls, roofs, and floors that separate temperature-controlled spaces from the outside environment or unconditioned areas within the building. While mandatory for new constructions, existing buildings can achieve recognition through the voluntary Estidama Green Building Rating System (GBRS), which rewards buildings that meet or exceed SBC602 requirements. The Saudi government actively supports SBC602 implementation by funding training programs for architects, engineers, and builders, and establishing an inspector network for code enforcement. Notably, Saudi Arabia's national building code, SBC602, divides the country into three climate zones based on cooling degree-days (CDD), a metric reflecting air conditioning demand. Zone 1, encompassing areas with extreme heat (CDD exceeding 5,000), covers a significant portion of the nation, including major cities like Riyadh. Zone 2 experiences high temperatures (CDD over 3,500), while Zone 3 is classified as simply hot. SBC602 establishes reference levels for indoor conditions: 23.9°C and 50% humidity in summer, and 21.1°C with 30% humidity in winter (Committee, 2021, Al-Homoud and Krarti, 2021, Committee,2023).

1.3. Residential Buildings in KSA

The Saudi General Authority for Statistics conducted a comprehensive housing survey in 2019 (Statistics, 2019b). The survey utilized two primary data sources: household field surveys and administrative records from the Ministry of Housing. This data collection effort examined housing units and their occupants, including both Saudi and non-Saudi families. It covered aspects like dwelling type, age, construction materials, number of floors, water and electricity access, and other housing-related indicators. This information is crucial for understanding typical housing characteristics in Saudi Arabia. The survey revealed that apartments were the most common dwelling type for Saudi families, accounting for 43.74% of occupied units, followed by villas (29.75%) and public housing (18.06%). Notably, the data lacked details on housing size and specific construction materials. However, the Saudi Real Estate General's comparison tool offers valuable data for further analysis (Authority, 2023). This tool allows users to explore rental and purchase trends across the Kingdom from 2019 to 2022, including transaction volume and price per square meter. This Data can be utilized to find average residential land sizes in Saudi Arabia (Times, 2021).

Table 13: Number of deals for Saudi lands

Number of Deals				
Year	2019	2020	2021	2022
Riyadh	12700	17800	21600	17100
Dammam	4681	6584	7577	6224
Jeddah	4184	3229	3488	3864
Madinah	476	490	598	1749
Mecca	472	459	569	1508
Taif	156	118	99	355
Hufuf	13	0	0	114
Buraydah	6	43	76	421
Tabuk	37	57	53	204
Khamis Mushayt	20	18	7	307
Khubar	324	107	102	71

Table 14 Cost of deals for Saudi lands

Cost of Deals (Billions of SAR)				
Year	2019	2020	2021	2022
Riyadh	24,540	25,540	33,010	28,930
Dammam	10,090	3,830	3,520	4,280
Jeddah	8,720	10,490	12,530	11,870
Madinah	711	527	710	1,890
Mecca	808	805	844	2,410
Taif	133	113	94	394
Hufuf	7	-	-	67
Buraydah	3	29	52	273
Tabuk	25	44	46	163
Khamis Mushayt	13	12	5	243
Khubar	285	95	63	53

Based on available data from official government reports and from Table 1, Table 2, and Table 3, the average plot of land purchased by Saudis for residential housing is approximately 388 square meters as shown in Figure 7. This land size translates to an average gross floor area of 640.2 square meters for a typical Saudi house with two and a half floors (Ministry of Municipal, Rural Affairs, and Housing, 2023). These houses typically house around 7 occupant s. While government data clarifies the size and occupancy of these houses, construction materials remain unclear. Research by Esmaeil et al. (2019) suggests two main housing types in Saudi Arabia: spacious villas with private courtyards and individual apartments in multi-unit buildings. Reinforced concrete is the most common material for both types, offering durability. However, traditional houses often use bricks, blocks, and adobe. Apartments cater to those seeking a more compact and affordable living space, while houses are generally older with an average of 3 or fewer bedrooms for most families. Larger houses with 4 to 6 bedrooms exist but are less common. These findings align with Alrashed and Asif's study (2015) which indicates that the average Saudi household resides in a single-family villa with 6 members. Notably, 62.1% of Saudi households own their homes, while 35.5% rent. As renters are typically responsible for utility costs, their houses tend to prioritize lower upfront costs over energy-saving features. While regulations require obtaining approval for electricity connection, this doesn't guarantee adherence to engineering plans or building codes (Aldossary et al., 2017). Data from (Center, 2021) reveals that over 70% of buildings lack insulation, highlighting a gap between mandatory building codes and their implementation within the construction industry.

Table 3: Average price for Saudi lands [40]

Average price of land m2 (SAR)				
Year	2019	2020	2021	2022
Riyadh	3,444	3,697	4,113	4,642
Dammam	3,227	3,020	2,969	3,411
Jeddah	3,880	3,277	3,398	4,066
Madinah	2,600	2,399	2,723	2,950
Mecca	3,419	4,857	3,192	2,839
Taif	2,853	2,916	3,048	3,116
Hufuf	1,536	-	-	2,619
Buraydah	1,841	2,238	2,184	2,571
Tabuk	2,022	2,649	2,869	2,743
Khamis Mushayt	2,082	1,984	2,372	2,782
Khubar	3,097	4,644	2,976	3,508

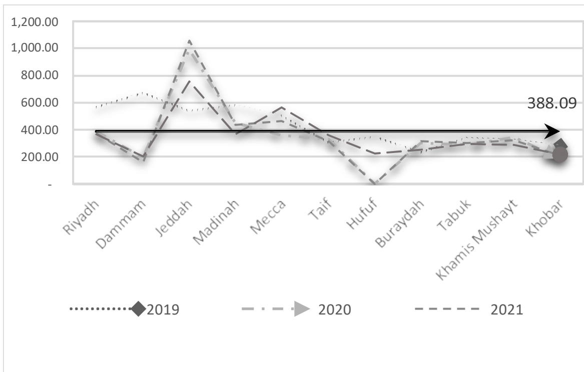

Figure 7: Average size of Lands

A survey by the Saudi Electricity Company (SEC) found that only about less than 1% of new buildings (580 out of 15,000) complied with mandatory thermal insulation regulations. Jeddah is one of the worst cities when it comes to compliance, where compliance in 2014 was a mere .01% (52 out of 5,200 buildings) (Asif, 2016). Al-Homoud and Krarti explain that new house owners don't comply with the rules due to two factors: weak energy-efficiency regulations and low energy costs (Al-Homoud and Krarti, 2021). This results in a dependence on window air conditioners with more than (71%) and split systems for about (25.8%) for heating and cooling, with window units dominating older buildings. However, split systems are gaining popularity in new construction and renovations, promising better energy efficiency through reduced air leaks (Statistics, 2019). Although the adoption of smart thermostats for managing energy use remains limited (Al-Homoud and Krarti, 2021). There is a positive shift towards energy-saving lighting. The use of CFL and LED lamps is rising (35.1%), although incandescent bulbs remain more common (48.7%). Unfortunately, only a small percentage of households (1.6%) utilize solar energy, despite its potential benefits. Additionally, power savers, devices that reduce overall consumption, are still not widely adopted, with only 36.3% of households owning them (Statistics, 2019).

2. COOLING TECHNOLOGIES

The global future projections for building energy consumption under the implementation of zero-carbon energy codes and the widespread adoption of highly efficient equipment, space heating demand is expected to reduce by nearly 70% before 2050, despite a simultaneous 30% increase in heated floor area. However, without positive changes, space cooling energy consumption is projected to more than double in the same timeframe (IEA, 2023). Space cooling, the fastest-growing energy demand in buildings, has tripled globally since 1990. The global presence of air conditioning (AC) units has surpassed 6 billion, with China and the United States accounting for half of this total. Sales figures indicate that approximately 135 million new AC units enter the market each year, consuming over 2,000 terawatt-hours (TWh) of electricity (IEA, 2018). Saudi Arabia, with its hot summers, has the highest AC penetration rate in homes, leading to a significant summer spike in electricity consumption. Thus, AC use has become ubiquitous, ensuring thermal comfort in all buildings, but at the cost of increased electricity demand and peak loads during summer months. (Goetzler et al., 2016, Khalfallah et al., 2016)

Krarti and Howarth have done a study on the economic benefits of transitioning to high efficiency air conditioning in the Kingdom of Saudi Arabia (Krarti and Howarth, 2020). The authors report that the current AC systems in the kingdom are less efficient and by moving towards higher efficient systems the country could save great money. This is because of low energy prices because of the subsidies thus making residents lack care of efficiency measures and look for cheaper AC systems to install. The same study offers a comprehensive analysis of the prevalence and varieties of air conditioning (AC) systems currently utilized within residential buildings throughout the various regions of the Kingdom of Saudi Arabia (KSA). Figure 8 below reveals a strong preference for window AC units, particularly in the Western and Middle regions, where they represent the dominant method of maintaining thermal comfort within residential buildings. Split AC systems and fan coils follow in terms of popularity, while evaporative coolers and central AC systems are relatively uncommon. This preference for window ACs can be attributed, in part, to the hot and dry climates prevalent in many KSA regions, which do not readily lend themselves to the efficient operation of evaporative coolers.

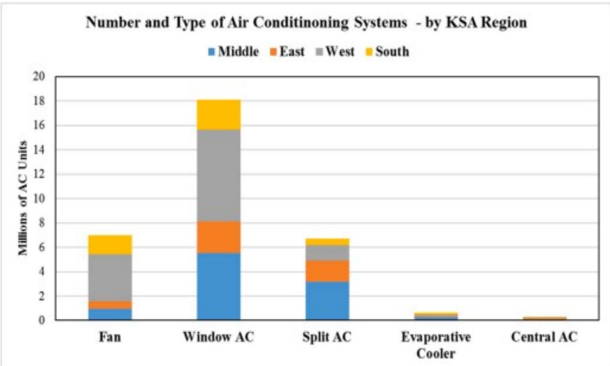

Figure 8: Types of AC systems and their numbers

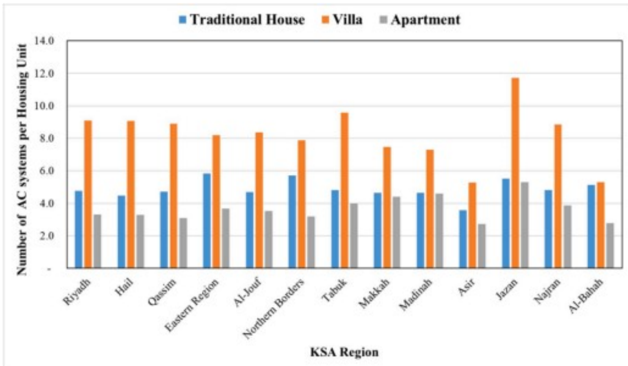

Figure 9: Number of AC units per house in different regions

Figure 9 further illuminates this trend by showcasing the number of AC units per housing unit type across all KSA provinces (Krarti and Howarth, 2020). The data clearly demonstrates that villas boast the highest average number of AC units, followed by traditional houses and then apartments. Interestingly, in most KSA provinces, the average number of AC units in villas exceeds 7, while traditional houses and apartments average 4 and 3 units respectively. This disparity suggests that the larger living spaces associated with villas necessitate a higher number of cooling systems for adequate thermal comfort. The typical Saudi household employs approximately five air conditioning units to ensure comfortable temperatures inside their dwellings. Window ACs reign supreme across all regions, representing between 83% (Western region) and 58% (Eastern region) of the total AC stock. Split ACs come in second, ranging from 39% (Eastern region) to just 14% (Western region). Evaporative coolers, though well-suited to the dry climate of Riyadh (Middle region), constitute only 2.4% of the total AC stock in KSA (Krarti and Howarth, 2020).

2.1. Window air conditioning systems

The indoor unit houses an evaporator coil and air filter. The coil absorbs heat from indoor air, lowering its temperature. A fan then circulates this cooled air throughout the room. Users can control temperature and fan speed through a control panel. A thermostat monitors temperature and a filter drier removes moisture from the refrigerant to prevent system issues. Condensed water is collected in a drain pan. The outdoor unit contains a compressor and condenser coil. The compressor pressurizes a refrigerant, which absorbs heat indoors. This heated refrigerant travels outside to the condenser coil, where it releases the heat into the surrounding air. A fan helps dissipate this heat efficiently. Both the indoor and outdoor units have fans that work together to circulate air through the system. This process cools the air, which is then distributed back into the room, reducing both temperature and humidity. Users can control the introduction of fresh air for further adjustments. Additionally, a filter prevents dust buildup, maintaining optimal cooling performance (Club, 2007). Studies have explored replacing window AC units with split systems through incentives and restrictions (Essam Al Ammar, 2022; Alshehri et al., 2020). The government's High Efficiency Air Conditioning (HEAC) program offers subsidies for split-system purchases with high energy efficiency ratings. Research suggests that restricting window AC sales could be beneficial despite the higher upfront cost of split systems. Window AC units, while common (almost 73% of all home AC units), are less energy-efficient as shown in Figure 10. Replacing them with split systems could save over 215 GWh of energy annually, reducing pressure on oil resources and saving the government an estimated 1.2 billion dollars per year.

2.2. Split Systems

Split-system air conditioners are the most popular choice for cooling in Saudi Arabia, with over 70% of recent installations being this type (Krarti & Howarth, 2020). Their affordability and ease of use make them a preferred option. These systems have two main units: an indoor unit mounted on a wall or window and an outdoor unit. Split systems are well-suited for single-story buildings and residences were disposing of condensation is a challenge. They offer greater efficiency and year-round climate control compared to window units. An indoor unit manages air distribution, temperature control, and heat exchange, while the outdoor unit houses the compressor and condenser coils. The indoor unit typically goes near the conditioned space, and the outdoor unit is placed on the roof or nearby. Both units connect with refrigerant lines. While split systems offer advantages, they come with some drawbacks. The initial cost can be higher than window units, and they require more space due to multiple units and equipment closets. Additionally, maintaining these systems may be more complex because of the various components. Despite these considerations, split-system air conditioners remain a versatile and efficient solution for many situations, especially where window units are not suitable (N/A). Studies by King Abdullah Petroleum Studies and Research Center (KAPSARC) (Alshehri et al., 2020) support this conclusion. Replacing inefficient window units with high-efficiency split systems could significantly reduce Saudi Arabia's energy consumption and environmental impact as it can be seen from Figure 11. This shift could save substantial electricity (20-35 terawatt-hours annually) and decrease carbon emissions (14-24 million tonnes per year).

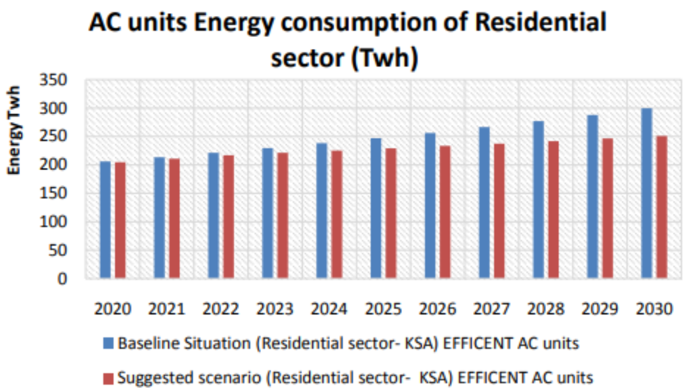

Figure 21 : Forecasted energy saving by switching to efficient split systems

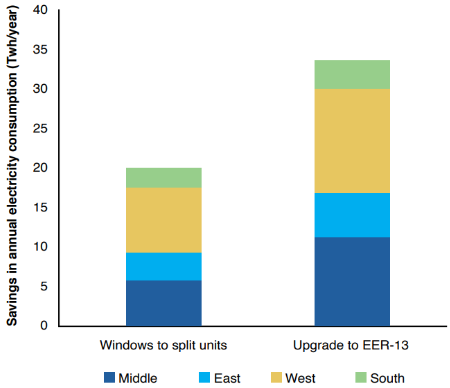

Figure 22 : Savings in Twh from switching to split systems with higher efficiency

3. RENEWABLE ENERGY IN BUILDINGS

3.1. Solar energy in Buildings

Saudi Arabia has great potential for solar energy due to its abundant sunshine. Photovoltaic (PV) technology is a promising solution, especially when integrated into buildings alongside energy-efficient materials. There are two main types of solar energy systems: solar thermal and photovoltaic. PV systems convert sunlight directly into electricity, but their efficiency can be reduced by high temperatures. Hybrid photovoltaic-thermal (PV/T) systems address this issue by using a solar thermal absorber to capture heat from the PV cells, keeping them cool and improving overall efficiency. Studies have shown that solar PV panels are the most cost-effective option in Saudi Arabia compared to other solar thermal technologies. Grid-connected PV systems, without batteries, are also found to be most feasible. Research has also been conducted to identify the best locations and types of PV panels within the country. Another area of exploration is using solar energy for cooling buildings. A techno-economic analysis suggests that solar absorption systems may be more cost- effective than solar PV systems for large buildings with high daytime cooling needs, under current electricity rates. Building- integrated photovoltaics (BIPV) and building-integrated photovoltaic/thermal (BIPV/T) systems are gaining traction. BIPV systems focus on cooling PV panels, while BIPV/T systems can also capture heat for other uses. These systems can be especially beneficial in hot climates, where they can improve panel efficiency and reduce solar absorption. However, theirpayback period can be long due to high upfront costs.

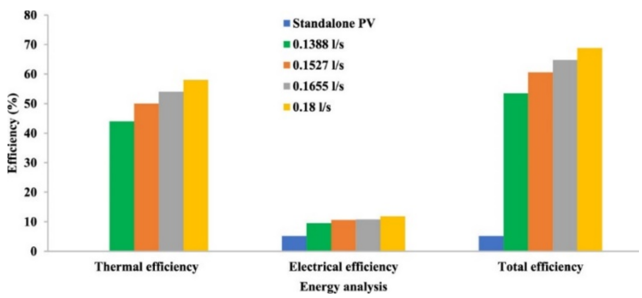

Figure 23: Average PVT system's efficiencies with different flow rates

Table 15: Design parameters for GSHP of the building

Parameters	Value
Average Thermal Conductivity for soil, W/m×K	2.6
The underground temperature at 60m of depth, ℃	29
Outside Temperature, ℃	45
Average Annual Temperature (ASHRAE Handbook 2013), ℃	26.5
Liquid Temperature at the heat pump inlet, ℃	32.8
Liquid Temperature at the heat pump outlet, ℃	39.5
Thermal diffusivity, m2/day	0.54
Total cooling load (Actual Data), KW	196
Total heating load (Actual Data), KW	38

3.2. Geothermal energy in Buildings

Geothermal energy is a clean and efficient renewable resource that taps into the Earth's internal heat. This heat comes from various sources, including molten rock, radioactive elements, and even solar radiation absorbed by the planet (2016). Geothermal energy can manifest in various ways, from hot springs used for bathing to powering entire buildings with heating, cooling, and even agricultural applications (Rosen and Koohi-Fayegh, 2017). One way to utilize geothermal energy is through ground source heat pumps (GSHPs), developed in the 1940s. These pumps extract and store heat from the shallow ground using shallow geothermal energy systems (SGES), reducing greenhouse gas emissions in the process.

While the concept originated earlier, widespread adoption only began after the 1973 oil crisis. Government support through subsidies, research funding, or renewable energy initiatives can be crucial for wider use of GSHPs. SGES encompass various technologies like geothermal piles, borehole heat exchangers, and even underground wall exchangers. These systems leverage the Earth's stable temperature for heating and cooling buildings, offering a potentially self-sufficient and renewable solution (Cunha and Bourne-Webb, 2022). GSHPs exploit the temperature difference between the Earth's surface and its interior. Below a certain depth (around 10-15 meters), the ground temperature remains stable and increases with depth (typically 3°C every 100 meters). This makes the ground a natural reservoir of warmth in winter and coolness in summer, providing a reliable source of energy for GSHPs (Rosen and Koohi-Fayegh, 2017). GSHPs can use different configurations, including closed loops (with dedicated fluid), open loops (using groundwater), and vertical or horizontal layouts depending on available space and soil conditions. Alfadhil (2019) developed a software tool called "GCV Tool" to aid in designing ground-coupled ventilation systems. This tool helps streamline the design process by estimating energy consumption for heating and cooling throughout the year. The tool's accuracy was validated by comparing its output with existing systems and other simulation programs. Alfadhil further applied the tool to a case study in Riyadh, demonstrating its practical application.

4. CONCLUSION

This comprehensive review has examined the energy consumption landscape of Saudi Arabia, with a particular emphasis on the residential sector and its comparison to global trends. The paper has delved into the significant role of cooling systems in residential energy consumption and has surveyed recent literature exploring the integration of renewable energy technologies, such as solar and geothermal, to enhance energy efficiency and reduce reliance on conventional energy sources.

Given Saudi Arabia's abundant sunshine, photovoltaic (PV) technology presents a promising avenue for harnessing solar energy. Research has consistently demonstrated the potential of integrating PV panels into residential buildings, in conjunction with energy-efficient materials, to achieve substantial energy savings. Additionally, geothermal energy, as harnessed through ground source heat pumps (GSHPs), offers a viable alternative for both heating and cooling purposes. By leveraging the Earth's stable temperature, GSHPs can provide a potentially self-sufficient energy solution for individual homes.

In conclusion, this review underscores the significant potential of solar and geothermal energy to contribute to a more sustainable energy mix within the residential sector of Saudi Arabia. Further research and development efforts are imperative to optimize these technologies, maximize their benefits, and position Saudi Arabia as a leader in renewable energy adoption.

5. REFERENCES

ADMINISTRATION, U. S. E. I. 2019. Saudi Arabia used less crude oil for power generation in 2018. https://www.eia.gov/todayinenergy/detail.php?id=39693.

AL-HOMOUD, M. S. & KRARTI, M. 2021. Energy efficiency of residential buildings in the kingdom of Saudi Arabia: Review of status and future roadmap. Journal of Building Engineering, 36, 102143.

ALBOGAMI, S. & BOUKHANOUF, R. 2019. Residential building energy performance evaluation for different climate zones. IOP Conference Series: Earth and Environmental Science, 329, 012026.

ALYAMI, M. 2022. An approach to enhancing energy performance in residential buildings in hot climate regions (The case of Saudi Arabia).

ASIF, M. 2016. Growth and sustainability trends in the buildings sector in the GCC region with particular reference to the KSA and UAE. Renewable and Sustainable Energy Reviews, 55, 1267-1273.

BANK, S. C. 2019. Yearly statistics. http://www.sama.gov.sa/en-US/EconomicReports/Pages/YearlyStatistics.aspx.

BP 2021. Statistical Review of World Energy. 70 ed. https://www.bp.com/content/dam/bp/business-sites/en/global/corporate/pdfs/energy-economics/statistical-review/bp-stats-review-2021-full-report.pdf

BP. 2022 bp Statistical Review of World Energy. Available: https://www.bp.com/en/global/corporate/energy-economics/statistical-review-of-world-energy.html.

CENTER, S. E. E. 2021. Annual Report.

CIA 2024. The World Factbook: Saudi Arabia.

COMMITTEE, S. B. C. N. 2021. Code Updates.

COMMITTEE, S. B. C. N. 2023. Saudi Building Codes.

GOETZLER, W ., GUERNSEY, M., YOUNG, J., FUJRMAN, J. & ABDELAZIZ, A. 2016. The future of air conditioning for buildings. Navigant Consulting, Burlington, MA (United States).

HARBI, F. A. & CSALA, D. Saudi Arabia's Electricity: Energy Supply and Demand Future Challenges. 2019 1st Global Power, Energy and Communication Conference (GPECOM), 12-15 June 2019 2019. 467-472.

IEA. 2018. The Future of Cooling, IEA, Paris Available: https://www.iea.org/reports/the-future-of-cooling.

IEA, T. I. E. A. 2023. Roadmap A Global Pathway to Keep the1.5°C Goal in Reach. https://iea.blob.core.windows.net/assets/9a698da4-4002-4e53-8ef3-631d8971bf84/NetZeroRoadmap_AGlobalPathwaytoKeepthe1.5CGoalinReach-2023Update.pdf [Online]. Available: https://iea.blob.core.windows.net/assets/9a698da4-4002-4e53-8ef3-631d8971bf84/NetZeroRoadmap_AGlobalPathwaytoKeepthe1.5CGoalinReach-2023Update.pdf.

KHALFALLAH, E., MISSAOUI, R., EL KHAMLICHI, S., BEN HASSINE, H. & AFRICA, N. 2016. Energy-efficient air conditioning: a case study of the Maghreb: Opportunities for a more efficient market. Disclosure.

KRARTI, M. & HOWARTH, N. 2020. Transitioning to high efficiency air conditioning in Saudi Arabia: A benefit cost analysis for residential buildings. Journal of Building Engineering, 31, 101457.

NACHET, S. & AOUN, M.-C. 2015. The Saudi electricity sector: pressing issues and challenges. France.

RASHID, I. U., ALMAZROUI, M., SAEED, S. & ATIF, R. M. 2020. Analysis of extreme summer temperatures in Saudi Arabia and the association with large-scale atmospheric circulation. Atmospheric Research, 231, 104659.

RITCHIE, H. 2021. How have the world’s energy sources changed over the last two centuries? Our World in Data.

SALEH, S. 2023. Electricity consumption in Saudi Arabia 2021, by sector. www.statista.com: statista.

SAMA, S. C. B. In: (SAMA), S. C. B. (ed.) Electricity Consumption by Sectors. https://www.sama.gov.sa/en-US/EconomicReports/Pages/report.aspx?cid=126.

STATISTICS, G. A. F. 2023. Latest Statistical Releases. In: STATISTICS, G. A. F. (ed.).

STATISTICS, S. G. A. F. 2019. Bulletin of Household Energy Survey 2019. Saudi General Authority for Statistics.

TIMES, S. 2021. Population of Cities in Saudi Arabia. In: TIMES, S. (ed.). https://statisticstimes.com/demographics/country/saudi-arabia-cities-population.php.

UN. For a livable climate: Net-zero commitments must be backed by credible action. Available: https://www.un.org/en/climatechange/net-zero-coalition#:~:text=Yes%2C%20a%20growing%20coalition%20of,about%2088%25%20of%20global%20emissions

VISION2030. ENVIRONMENT & NATURE [Online]. Available: https://www.vision2030.gov.sa/en/progress/environment-nature/ [Accessed 30/11 2023].

#344: Analysis of heat transfer characteristics of capillary heat exchanger in shield tunnel under typical working conditions

Xinru WANG[1], Yongming JI[1], Shouheng SHEN[1], Hui ZHANG[1], Songtao HU[1]

[1]School of Environmental and Municipal Engineering, Qingdao University of Technology, Qingdao, China, wx1326561@163.com

Abstract: With the extended operation of subway systems, waste heat generated by train operations and lighting systems accumulates within tunnels, leading to significant thermal pollution. Compared to traditional buried pipes, capillary tubes are smaller in size and offer superior heat transfer performance, making them a promising candidate for mitigating waste heat accumulation in subway tunnels. However, existing research primarily focuses on tunnels utilizing conventional buried pipes, with a notable lack of studies on the application of capillary networks as front-end heat exchangers in tunnels. To address this research gap, this study proposes a novel design methodology for energy tube units based on empirical data from Qingdao's metro system and investigates the heat transfer performance of Capillary Heat Exchangers (CHEs) within these units. The research reveals significant variations in CHE heat transfer characteristics under different operational conditions. Temperature emerges as a critical factor influencing CHE performance: reducing inlet water temperature enhances heat transfer efficiency during heating seasons; while increasing it is beneficial in cooling seasons.Additionally, increasing flow velocity enhances CHE unit-area heat transfer, with lower velocities showing more pronouncedimprovements, albeit caution is warranted against excessive flow rates due to potential energy wastage. Thus, pump adjustments are recommended to achieve optimal flow velocities. Variations in branch pipe spacing and length directly impact CHE heat transfer area, necessitating thoughtful configuration in engineering applications to maximize heat transferefficiency. This study provides valuable insights into the design and operational strategies of metro energy tunnels.

Keywords: Energy Tunnels, Heat Pumps, Energy Segment, Capillary Heat Exchangers, Heat Transfer Characteristics.

1. INTRODUCTION

With economic development and technological advancements, urban rail transit has grown rapidly. By the endof 2022, 55 cities in mainland China had operational urban rail transit systems, with a total route length of 10,287.45 kilometers. Subways, characterized by their high capacity, convenience, and punctuality, accountedfor 8,008.17 kilometers, which is 77.84% of the total. In 2022, an additional 754.44 kilometers of subway lineswere added (China Urban Rail Transit Association, 2023: 13-15).

However, with the rapid expansion of subway construction, the accumulation of heat generated during operation has increasingly exacerbated the thermal environment within subway tunnels, exhibiting a worseningtrend over time. This not only decreases the efficiency of onboard air conditioning systems, resulting in higherenergy consumption for the subway environmental control system, but also significantly impacts the safe operation of subways and the stability of tunnel linings (Wu, 2022: 6-10).

To address these challenges, researchers both domestically and internationally have proposed the integrationof heat exchangers within tunnel linings to function as front-end heat exchangers in energy tunnels. Current research on front-end heat exchangers in energy tunnels primarily focuses on traditional buried pipes and capillary networks. A schematic diagram of the energy tunnel system is presented in Figure 1 (Loria, A. F. R.,2020: page 13).

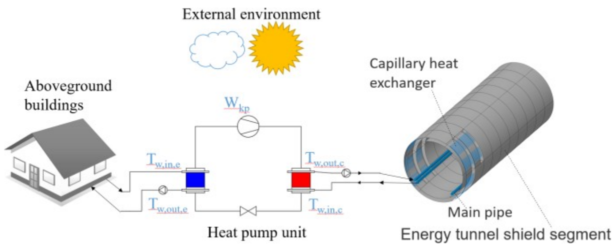

Figure 1: Schematic Diagram of the Energy Tunnel System

Barla et al. explored the feasibility of using buried pipes as front-end heat exchangers in tunnel linings, using the Turin subway tunnel as an example (Wu, 2022: 3-7) (Barla, M. & Insana, A., 2022: 10-14). DiDonna et al.investigated the impact of tunnel environment on the performance of energy tunnels, analyzing two influencingfactors: convective heat transfer coefficients between tunnel air and lining, and temperature difference between tunnel air and circulating fluid (Cui, 2022: 17-20). RottaLoria et al. studied the influence of changes in internalairflow characteristics on the heat exchange potential of energy tunnels (A, A. B. , & B, G. A. N., 2018: 83- 95). Hu et al. proposed a novel energy tunnel system utilizing capillary tubes as front-end heat exchangers and conducted experimental studies on its heat transfer performance (Li, 2019: 683-685). Ji et al. establisheda rapid prediction model for CHE heat flux using multivariate linear regression under typical conditions of practical engineering (Ji, 2023: 23-27) (Wu, 2023: 17-25).

Capillary heat exchangers offer large heat exchange areas, excellent heat transfer performance, compact volumes, and flexible structures, allowing for disassembly and assembly according to practical application needs. Compared to traditional buried pipes, capillary heat exchangers emerge as potent candidates for addressing the accumulation of waste heat in subway systems due to their unique advantages. However, current research predominantly focuses on energy tunnels utilizing traditional buried pipe methods, lacking in-depth studies on the design methodologies and heat transfer characteristics of capillary heat exchangers as front-end heat exchangers.

This study integrates engineering practicality and numerical simulation as the primary research approach, focusing on investigating the heat transfer performance of capillary heat exchangers (CHE) within energy shield tunnels.

2. MODEL FOUNDATION

2.1. Geometric model

Continuing the assumptions from previous studies, the horseshoe-shaped subway tunnel is simplified to a circular shape (Ji, 2022: 246). In response to subway sections using shield tunneling, a novel design proposal for energypipe segments featuring CHE as the front-end heat exchanger is introduced. The CHE units are positioned on the rebar cage and integrated into the shield tunnel segments through concrete casting, forming a unified structure. Recognizing that non-uniform pipe layouts result in higher heat exchange rates per unit area compared to uniform layouts (Zhu, 2019:11-15), to enhance heat transfer efficiency, each subway tunnel ring comprises four energy pipe segments, one standard shield block, and one top block arranged symmetrically. Within eachpair of energy pipe segments on the same side, CHE units are connected in series to create two independent supply and return water circuits.

The specifications for the energy pipe segments are 350mm thick and 1.5m wide, with a front-end heat exchanger utilizing a U-shaped capillary network. The specific arrangement is as follows: capillary headers are radially arranged with dimensions of Φ20×2mm; U-shaped capillary branch pipes are arranged in parallelwith dimensions of Φ4.3×0.85mm; two capillaries form a single group with a 5mm gap between pipes and a 44mm gapbetween groups; CHE units are installed 30mm from the outer edge of the pipe segment. To streamline production processes, the capillary heat exchanger adopts identical layout methods in adjacent and standard blocks. The specific layout is depicted in Figure 2.

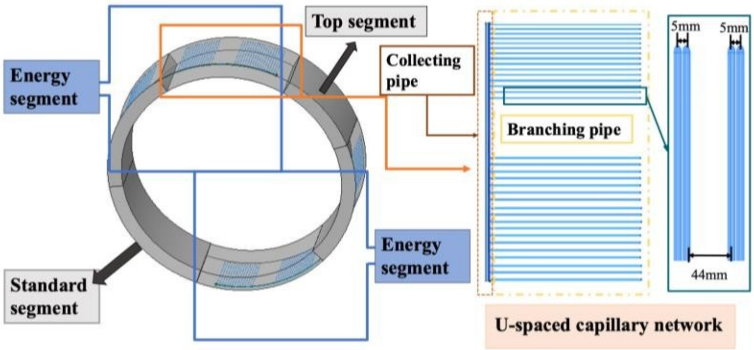

Figure 2: Layout of Energy Segments within the Shield Tunnel

2.2. Governing equation

Equation 21: continuity. $$\frac{\partial}{\partial x_j}(\rho u_j) = 0$$

Where:
- ρ = Fluid density (kg/m^3)
- u_j= Instantaneous velocity components in three vertical coordinates (m/s)
-

Equation 2: momentum. $$\frac{\partial}{\partial t}(\rho u_i) + \frac{\partial}{\partial x_j}(\rho u_j u_i) = -\frac{\partial p}{\partial x_i} + \frac{\partial t_{ji}}{\partial x_j} + \rho F_i$$

Where:
- u_i , u_j= The instantaneous velocity component in the direction i ,j (m/s)
- p = Instantaneous pressure (Pa)
- t_{ji} = Viscous stress tensor component (N)
- F_i = Volume force acting on a fluid (m/s^2)

Equation 3: energy. $$\frac{\partial}{\partial t}[\rho(e + \frac{u_i u_i}{2})] + \frac{\partial}{\partial x_j}[\rho u_j(e + \frac{u_i u_i}{2}) = \frac{\partial}{\partial x_j}(u_i t_{ij}) - \frac{\partial}{\partial x_j}(p u_j) + \rho F_i u_i - \frac{\partial q_i}{\partial x_i} + \rho q_{source}$$

Where:
- e= The internal energy of a fluid (J)
- q_i= Heat flow of fluid in the x_i direction (W/m^2)
- q_{source} = Energy source in fluid (W)

Equation 4: heat conduction. $$\int_s \lambda gradt \cdot \vec{n} ds + \int_v q_v dv = \int_v \frac{\partial}{\partial \tau}(\rho c t) dv$$

Where:
- λ = Heat conductivity coefficient (J/(m·K))
- s = The length along the direction of the temperature gradient (m)

Equation 5: heat exchange amount. $$Q = M_f C_p \Delta t$$

Where:
- Q= Total heat transfer (W)
- M_f= Mass flow of heat exchanger in tube (kg/s)
- C_p = Specific heat capacity of heat exchanger in tube (J/(kg·℃))
- Δt = Temperature difference between inlet and outlet of heat exchange medium in tube (℃)

2.3. Simulation model

This study establishes a numerical simulation model based on the physical model of the CHE. To simplify thecalculations due to the large cross-sectional dimensions of the tunnel, the following assumptions are made: there is no groundwater flow around the subway tunnel; the composite medium is isotropic, and the heat exchange conditions for each CHE group are identical. Based on these assumptions, the neutral planes of twoadjacent CHE groups are considered adiabatic surfaces. Consequently, the numerical simulation model selects the segment between two adiabatic surfaces, taking a 1.1-degree sector of the tunnel cross-section asthe simulation area to analyze the heat transfer characteristics of a single CHE group.

Due to the long-term operation of the subway system, the temperature of the tunnel strata increases, forminga "thermal envelope" extending 20 meters from the tunnel (Wang, 2022: 257). To ensure the accuracy of the simulation results, the surrounding rock is set to have a thickness of 50 meters, with the assumption that the far end of the surrounding rock is adiabatic.

In the model, the heat transfer process includes convective heat transfer between the tunnel air and the tunnelwall, convective heat transfer between the water inside the CHE and its inner walls, and conductive heat transfer through the CHE tube walls, energy segments, and surrounding rock. Due to the involvement of gas-liquid-solid three-state heat transfer, the following simplifications are made:All objects within the subway tunnelare assumed to have constant physical properties and to be isotropic.The initial temperature of objects surrounding the tunnel is assumed to be the local annual average soil temperature.The contact thermal resistance between adjacent objects is neglected.The tunnel air temperature and flow rate are constant duringsubway operation. The mesh division of the model is in Figure 3.

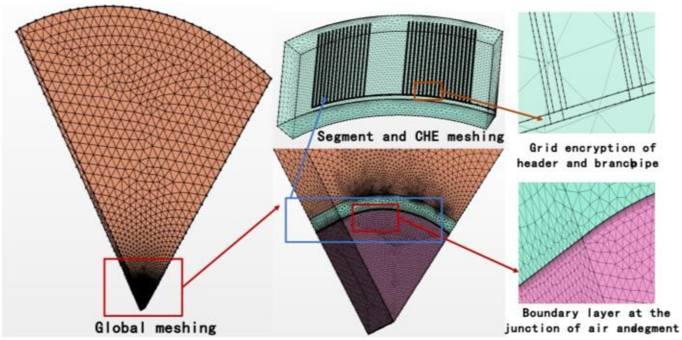

Figure 3: Mesh Division of the Model

The subway tunnel is located within the constant temperature layer 20 meters underground, where the annualtemperature is maintained at 14.6°C (Hu, 2019: 6-10). The far end of the surrounding rock is set to a constanttemperature boundary condition of 14.6°C. By calculating the air speed in the tunnel during various conditions—such as no train movement, constant train speed, peak times, and parallel segments—the average wind speedat the tunnel wall during subway operation is determined to be 4.61 m/s (Ji, 2022: 246). Since the temperaturevariation inside the subway tunnel is smaller than the variation in outdoor temperatures (Fan, 2021: 33-37) (Liu, 2021: 22-40), the tunnel air temperature is assumed to be the seasonal average tunnel air temperature, set at 12°C in winter and 25°C in summer (Wang, 2018: 35-40).

Heat within the tunnel primarily comes from train operation and related infrastructure designed to support normal train operation. Typical daily heat production in the tunnel during heating and cooling seasons is estimated at 80 W/m and 90 W/m respectively (Qi, 2023: 23-24). The subway tunnel is situated within a constant temperature layer 20 meters underground, maintaining a yearly average temperature of 14.6°C (Qi, 2023: 24-25).. The far-end boundary condition of the surrounding rock is set as a constant temperature of 14.6°C to simulate an infinite boundary.

The thermal physical parameters required for the model include the thermal conductivity, density, and heat capacity of the surrounding rock, concrete lining, water, and air, as well as the viscosity coefficients of water and air. The thermal physical parameters of water and air are obtained from the Fluent Software User Guide (Fluent User's Guide, 2022 edition), while the thermal physical parameters of the surrounding rock are sourcedfrom the geological survey report of Qingdao. The segments are cast from C55 concrete, with all parameters set according to the concrete structure design specifications. The specific values are detailed in Table 1.

Table 1: Boundary condition settings.

Model materials	Density (kg/m3)	Thermal conductivity (W/(m·℃))	Specific heat capacity (J/(kg·℃))
Concrete lining	2400	2.95	960
Surrounding rock	2800	3.49	920
CHE pipe wall	900	0.24	2000.0
Water	998.2	0.60	4182
Air	1.225	0.24	1006.43

2.4. Simulation model

At a distance of 3 meters from the tunnel axis, a temperature monitoring curve approximately 3261 mm long was plotted. Steady-state simulations were conducted on models with different numbers of grids, yielding temperature values at various points along the heating season curve, as shown in Figure 4. When the grid count increased from 4,495,798 to 5,219,404, the maximum relative error in temperature at each monitoring point was only 0.05%. To minimize simulation time, the final grid count was determined to be 4,495,798.

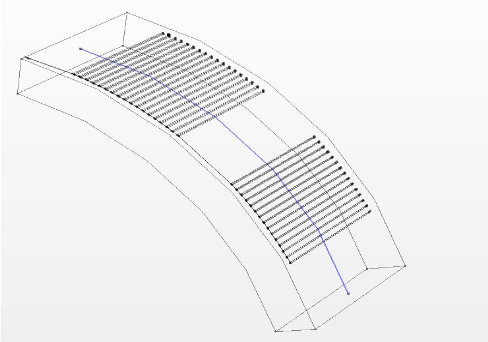

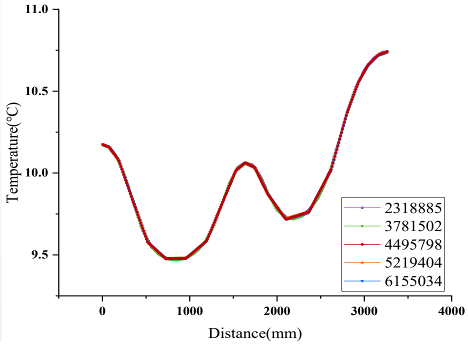

(a) Temperature Monitoring Curve Schematic Diagram (b) Temperature Curve at Different Grid Counts
Figure 4: Temperature Monitoring Curve and Corresponding Temperature Values

3. RESULTS AND DISCUSSI

3.1. Operation setting

The thermal exchange pipes within the energy tunnel play a crucial role in the heat exchange between the heat transfer medium and the segment liner. According to heat transfer theory, under steady-state conditions,the total heat absorbed or released by the heat transfer medium flowing through the heat exchanger can be expressed using the following formula .

Equation 2: heat transfer calculation. $$Q = M_f C_p \Delta t = kFT_m$$

Where:
- Q = The total heat exchange (W)
- M_f= The mass flow rate of the heat transfer medium inside the pipe (kg/s)
- C_p = Specific heat capacity of the heat transfer medium inside the pipe (J/(kg·℃))
- Δt = Temperature difference between the inlet and outlet (℃)
- k = Heat transfer coefficient (W/(m²·℃))
- F = Heat exchange area (m²)
- T_m= Logarithmic mean temperature difference (℃)

Due to the differing sizes of adjacent and standard blocks within the shield tunnel, for comparative analysis ofthe heat transfer efficiency of the Compact Heat Exchanger (CHE), this study conducts heat exchange analysisbased on the projected area of the microchannel profile per unit heat exchanger.

Equation 2: heat transfer calculation per unit area. $$q = \frac{Q}{S}$$

Where:
- q = Heat exchange per unit area of the microchannel profile projection of the heat exchanger (W)
- Q = The total heat exchange (W)
- S = Area of the microchannel profile projection of the heat exchanger (m²)

Research has shown that variations in design parameters of heat exchange pipes significantly impact the performance of heat exchangers. This study conducts simulation analyses on the inlet water temperature, flow rate of the heat transfer medium, CHE branch spacing, and pipe length of the heat exchanger. The ranges of each influencing factor are presented in Table 3.

Table 3: The ranges of each influencing factor are presented

Factor	Range of Values	Other Parameter Values
Inlet water temperature t_{in}/℃	6、8、10、12、14（Heating season） 20、22、24、26、28、30、32、34、36、38、40（Cooling season）	v=0.1m/s、d=44mm、l=2600mm
Flow velocity inside the pipe v/（m/s）	0.02、0.04、0.06、0.08、0.1、0.12、0.14	tin=8/35℃、d=44mm、l=2600mm
Distance between branch pipes d/(mm)	44、52、60、68、76、84、92	tin=8/35℃、v=0.12m/s、l=2600mm
Length of branch pipes l/(mm)	2000、2100、2200、2300、2400、2500、2600	tin=8/35℃、v=0.12m/s、d=44mm

3.2. Effects of inlet water temperatures

Different heat transfer rates per unit area of CHE at various inlet water temperatures are shown in Figure 5.

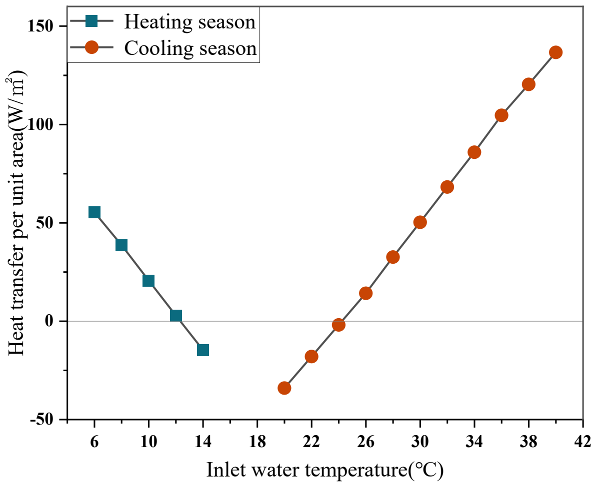

Figure 5: Influence of inlet water temperature on heat transfer per unit area

Figure 5 illustrates that during the heating season, the unit heat transfer rate of the CHE decreases linearly with an increase inlet water temperature. Specifically, as the inlet water temperature rises from 6°C to 12°C, theheat transfer per unit area decreases from 82.87 W/m² to 1.54 W/m². Furthermore, as the inlet water temperature increases from 12°C to 14°C, the water inside the CHE transitions from absorbing heat to releasing heat, emitting 14.68 W/m² into the subway tunnel at 14°C. Additionally, as depicted in Figure 6.a, when the temperature is 12°C, the proportion of heat transfer from the CHE surface to the wall is less than 0 W/m, indicating the CHE is primarily absorbing heat. Conversely, as shown in Figure 6.b, at 14°C, the proportion of heat transfer from the CHE surface to the wall exceeds 0 W/m, indicating the CHE is primarily releasing heat.

In contrast, during the cooling season, the heat transfer rate of the CHE shows a linear increasing trend with rising inlet water temperature. Specifically, as the inlet water temperature decreases from 40°C to 26°C, the heat transfer per unit area decreases from 121.38 W/m² to 14.16 W/m². As the inlet water temperature furtherdecreases from 26°C to 20°C, the water inside the CHE transitions from releasing heat to absorbing heat, absorbing 34.04 W/m² from the subway tunnel at 20°C. Additionally, as shown in Figure 6.c, at 26°C, the proportion of heat transfer from the CHE surface to the wall exceeds 0 W/m, indicating the CHE is primarily releasing heat; whereas as shown in Figure 6.d, at 24°C, the proportion of heat transfer from the CHE surfaceto the wall is less than 0 W/m, indicating the CHE is primarily absorbing heat.

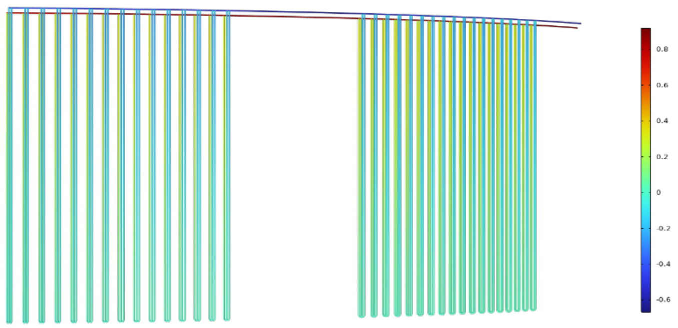

(a). Wall heat transfer cloud map of CHE at 12℃ (unit: W/m)

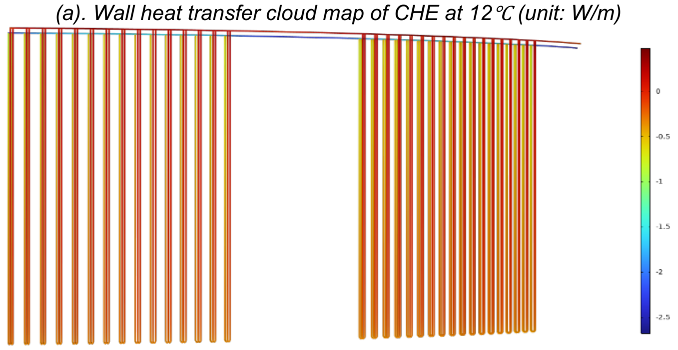

(b). Wall heat transfer cloud map of CHE at 14℃ (unit: W/m)

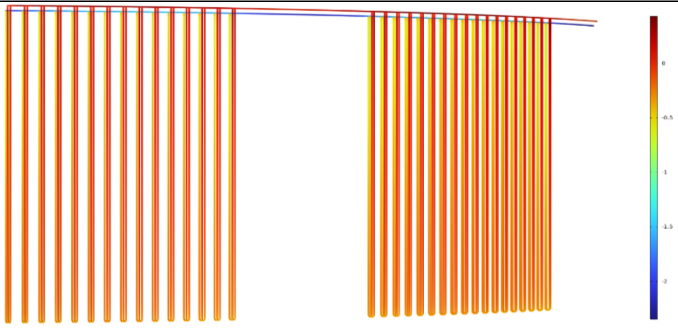

(c). Wall heat transfer cloud map of CHE at 26℃ (unit: W/m)

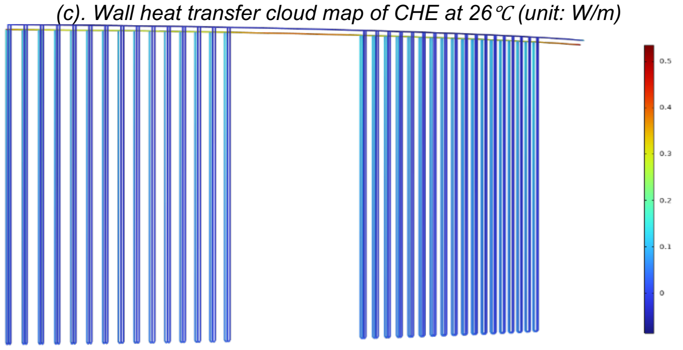

(d). Wall heat transfer cloud map of CHE at 24℃ (unit: W/m)

Figure 6: Clouds of CHE wall heat transfer at different temperatures

During the heating season, when the inlet water temperature to the Combined Heat Exchanger (CHE) is at 12°C (equal to the tunnel air temperature), the surrounding rock acts as a heat source supplying heat to the CHE, resulting in the outlet water temperature from CHE being higher than the tunnel air temperature. When the tunnel air temperature is between the inlet water temperature (14°C) and the rock temperature, the convective heat transfer intensity between the energy pipes and the tunnel air exceeds the conductive heat transfer intensity with the rock. Therefore, during this period, the rock and the energy pipes release heat to theair.

Conversely, during the cooling season, when the rock temperature is lower than the inlet water temperature (20°C/22°C) but higher than the tunnel air temperature, the heat transfer fluid absorbs heat from the subway tunnel, causing the water temperature to rise.

To optimize the heat exchange efficiency of CHE, in practical engineering, the inlet water temperature shouldbe controlled at lower levels during the heating season and as high as possible during the cooling season. Additionally, due to the existence of a critical temperature threshold, which causes CHE's heat exchange statusto transition from heating to cooling or from heat release to heat absorption, engineering practice should pay special attention to this critical point to avoid unnecessary energy loss or affecting tunnel temperature control.

3.3. Effects of flow rates

Heat transfer per unit area of CHE under different flow rates is shown in Figure 7.

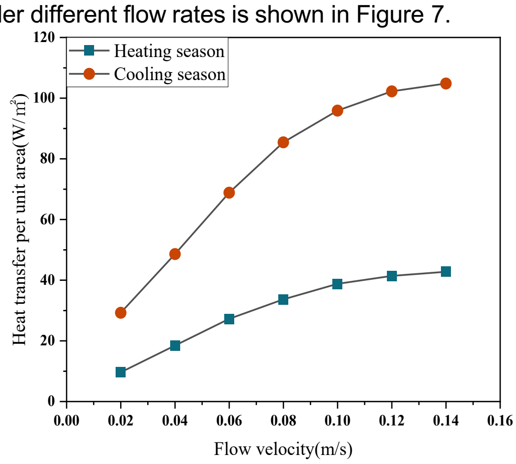

Figure 7: Influence of flow velocity on heat transfer per unit area of CHE

Figure 7 illustrates that the unit area heat transfer coefficient of the CHE increases with flow velocity, and therate of increase in the unit area heat transfer coefficient gradually diminishes with higher flow velocities, a trendobserved during both heating and cooling seasons. When the flow velocity increases from 0.02 m/s to 0.14 m/s, the unit area heat transfer coefficient rises from 9.61 W/m² to 42.74 W/m² during heating season, and from 29.23 W/m² to 104.81 W/m² during cooling season.

As shown in Figure 8, at lower flow velocities, the fluid undergoes extensive heat exchange within the capillarytubes, resulting in maximum inlet-outlet temperature differences for the CHE at a flow velocity of 0.02 m/s. With increasing flow velocity, the residence time of the fluid in the heat exchanger decreases, thereby reducingthe inlet-outlet temperature difference of the CHE. However, higher flow velocities enhance the convective heat transfer coefficient, leading to an increase in unit area heat transfer coefficient, albeit with diminishing growth rates. In practical applications, adjusting the pump to increase flow velocity at lower speeds can effectively enhance heat transfer.

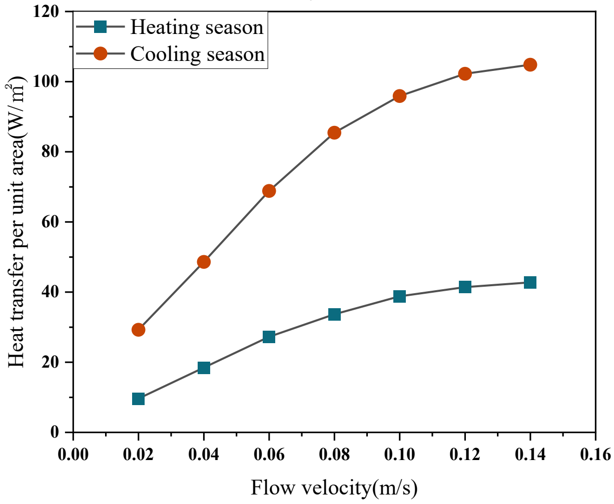

Figure 8: Influence of flow velocity on temperature difference between inlet and outlet

3.4. Effects of branch tube spacing

When the spacing between supports pipes increases, in order to maintain minimal changes in the projected area of the capillary tube profiles, the number of capillary tubes is correspondingly reduced. Based on this principle, heat transfer models with varying support pipe spacings were designed. As shown in Figure 8, whenthe support pipe spacing is 44 mm, the projected area reaches its maximum value at 2.42 m². However, increasing the support pipe spacing to 84 mm reduces the projected area to 2.36 m². The arrangement of different tube spacing is shown in Figure 9.

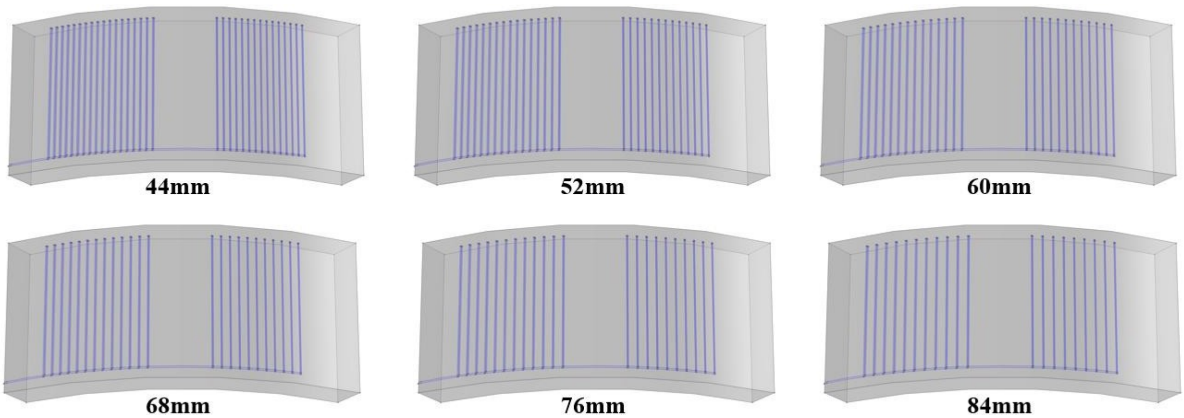

Figure 9: CHE layout of different branch pipe spacing

Heat transfer per unit area of CHE under different branch tube spacing is shown in Figure 10.

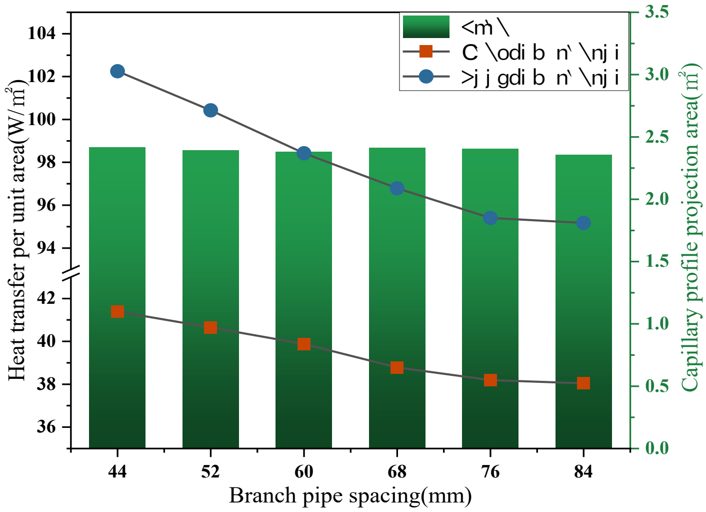

Figure 10: Influence of branch tube spacing on heat transfer per unit area of CHE

Figure 10 illustrates the influence of tube spacing on the unit area heat transfer coefficient (CHE) during bothheating and cooling seasons. During heating season, as the spacing increases from 44 mm to 84 mm, the heat transfer coefficient decreases from 40.9 W/m² to 38.04 W/m². Similarly, during the cooling season, the heat transfer coefficient decreases from 102.25 W/m² to 95.17 W/m² with the same increase in spacing. Additionally, the number of capillary tubes within a single energy transfer tube decreases from 33 to 20, resulting in a decrease in capillary heat transfer area from 2.44 m² to 1.68 m². Due to the positive correlation between heat transfer coefficient and heat transfer area, an increase in tube spacing inevitably leads to a reduction in the unit area heat transfer coefficient of CHE. In practical engineering applications, tube spacing should be carefully chosen to balance cost and heat transfer effectiveness. The optimal tube spacing for achieving maximum unit area heat transfer coefficient and overall heat transfer efficiency is observed at 44 mm, as shown in the figure. Therefore, in engineering design, a tube spacing of 44 mm is recommended to achieve optimal heat transfer performance.

3.5. Effects of branch pipe lengths

Heat transfer per unit area of CHE under different branch pipe lengths is shown in Figure 11. Temperaturedistribution in capillary tubes of different lengths is shown in Figure 12.

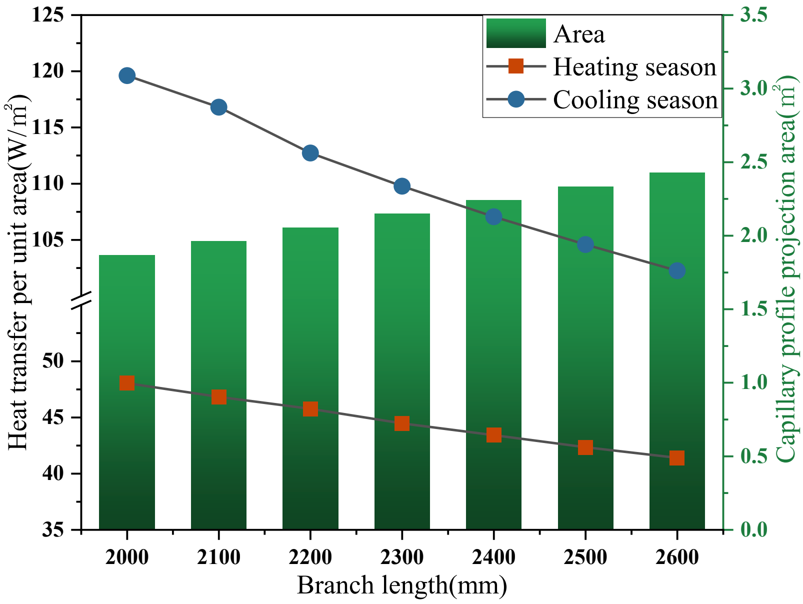

Figure 11: Influence of pipe length on heat transfer per unit area of CHE

Figure 11 illustrates that as the length of the branch pipe increases, the unit area heat transfer coefficient (CHE) decreases accordingly. During the heating season, when the capillary tube length increases from 2000mm to 2600 mm, the unit area heat transfer coefficient decreases from 48.03 W/m² to 41.39 W/m². Similarly, during the cooling season, the unit area heat transfer coefficient decreases from 119.61 W/m² to 101.86 W/m².

Taking the heating season as an example, the capillary tube closest to the return water inlet of the manifold was selected for analysis. As depicted in Figure 12, along the flow direction, the temperature variation trends are similar for capillary tubes of different lengths: in the first half of the branch pipe, the water temperature rises rapidly. In the latter half, the temperature reaches its peak and remains relatively stable, with a slight decrease observed towards the outlet, indicating a short-circuit phenomenon. Therefore, for capillary tubes ofvarying lengths, the unit length heat transfer efficiency decreases as the tube length increases.

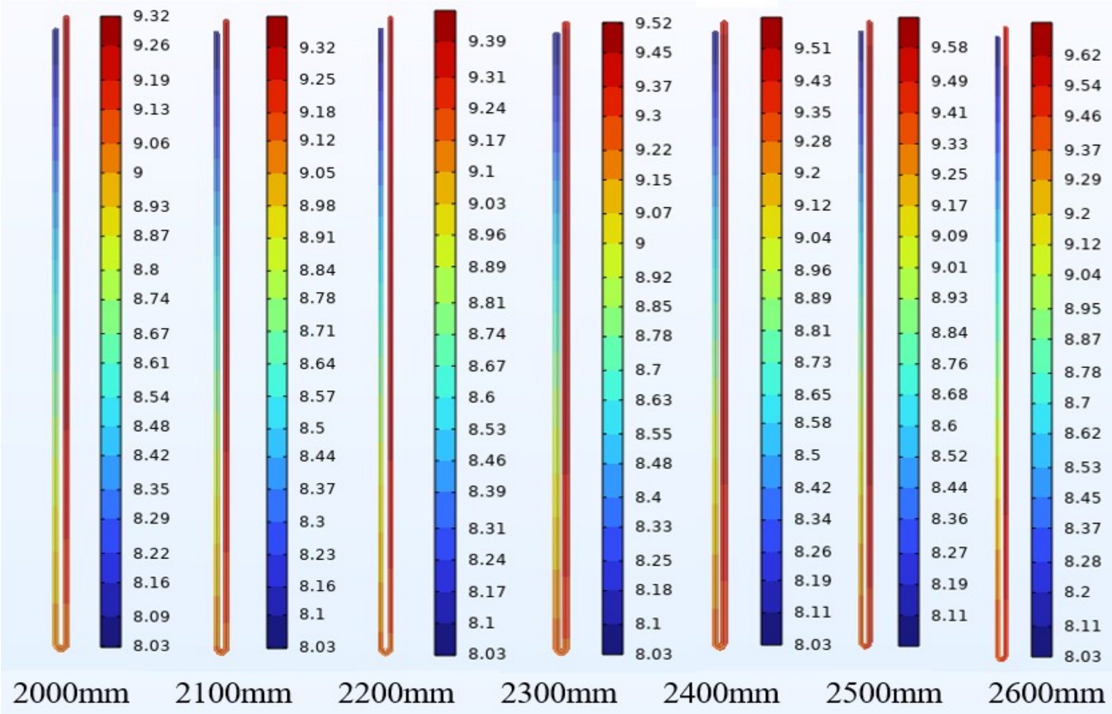

Figure 12: Temperature distribution in capillary tubes of different lengths

4. CONCLUSION

Based on actual metro data from Qingdao, this study proposes a novel design approach for energy tube unitsand investigates the heat transfer performance of the Capillary Heat Exchanger (CHE) within a single energytube unit. The results demonstrate significant variations in CHE heat transfer characteristics under different operating conditions. Specifically, temperature exerts a pronounced influence on CHE heat transfer performance. During the heating season, lowering the inlet water temperature enhances CHE heat transfer efficiency, whereas during the cooling season, increasing the inlet water temperature is advisable. In practicalapplications, adjusting the inlet water temperature according to seasonal changes optimizes heat transfer efficiency. Increasing flow velocity appropriately can elevate the unit-area heat transfer rate of CHE, with lowervelocities showing more substantial gains in heat transfer efficiency. However, excessive flow rates may leadto energy wastage; hence, pump adjustments should be tailored to achieve suitable flow velocities based on specific conditions. Variations in branch pipe spacing and length directly impact the heat transfer area of CHEunits. Therefore, in practical engineering, rational configurations of branch pipe spacing and length are crucialfor achieving optimal heat transfer effects. This study offers insights into the design and operation of metro energy tunnels.

5. ACKNOWLEDGEMENT

The authors are indebted to the National Natural Science Foundationof China (Grant no.52108079).

6. REFERENCES

China Urban Rail Transit Association. (2023). Urban Rail Transit 2022 Annual Statistics and Analysis Report.Urban Rail Transit (4), 13-15.

Wu Wenze.(2022). Research on Multi-frequency Response Heat Transfer Characteristics of Source Side Heatexchangers in Metro Source Heat pump System. Master's Thesis, Qingdao University of Technology)

Loria, A. F. R. . (2020). Energy geostructures: theory and application. E3S Web of Conferences, 205(13),01004.

Barla, M. , & Perino, A. . (2014). Energy from geo-structures: a topic of growing interest. EnvironmentalGeotechnics, 2(1), 3-7.

Barla, M. , & Insana, A. . (2023). Energy tunnels as an opportunity for sustainable development of urban areas.Tunnelling and underground space technology.

Chunjing, M. A. , Donna, A. D. , Zhang, J. , & Dias, D. . (2021). Numerical investigations of the tunnelenvironment effect on the performance of energy tunnels. Renewable Energy.

A, S. C. D. , B, A. F. R. L. , B, M. Z. , B, L. B. , A, J. L. E. , & C, P. T. . (2020). Heat exchange potential of energy tunnels for different internal airflow characteristics. Geomechanics for Energy and the Environment.

Cui H, Li Y, Bao X .. (2022)Thermal performance and parameter study of steel fiber-reinforced concretesegment lining in energy subway tunnels. Tunnelling and Underground Space Technology.

A, A. B. , & B, G. A. N. . (2018). Heat exchange mechanisms in energy tunnel systems. Geomechanics forEnergy and the Environment, 16, 83-95.

Li, Tong, SongtaoHu, ShanLu, Yimei, & Wang. (2019). Study on heat transfer performance of metro tunnelcapillary heat exchanger - sciencedirect. Sustainable Cities and Society, 45, 683-685.

Ji, Y. , Yin, Z. , Jiao, J. , Hu, S. , Kalogirou, S. A. , & Christodoulides, P. . (2023). Long-term performanceof a subway source heat pump system with two types of front-end heat exchangers. SSRN Electronic Journal.

Ji Yongming, Jiao Jiachen, Yin Zhenfeng, Ji Chengfan & Hu Songtao.(2023).Rapid performance predictionmodel for capillary heat exchangers in subway tunnel linings. Applied Thermal Engineering.

Ji, Y. , Wu, W. , Qi, H. , Wang, W. , Hu, S. , & Lund, H. , et al. (2022). Heat transfer performance analysisof front-end capillary heat exchanger of a subway source heat pump system. Energy, 246.

Zhu Z N, & Guo H X. (2019). Exploration of shield tunnel construction using geothermal energy: A case studyof Qinghuayuan Tunnel energy segment design, fabrication and installation. Tunnel construction (English andChinese).

Wang, L. , Zuo, H. , Kong, M. , Ma, C. , Mao, Z. , & Zeng, X. M. , et al. (2022). Study on the evolution characteristics of temperature and heat storage of the soil surrounding the tunnel with years. Energy and buildings(Feb.), 257.

Hu S T, Xu W P, Tong Z, & Cheng Y. (2019). Simulation of cooling effect of capillary heat exchangers in subway tunnels. Journal of Qingdao University of Technology.

Ji, Y. , Wu, W. , Qi, H. , Wang, W. , Hu, S. , & Lund, H. , et al. (2022). Heat transfer performance analysis of front-end capillary heat exchanger of a subway source heat pump system. Energy, 246.

Fan Yujing.(2021). Research on Heat transfer Model of Capillary Front heat exchanger of Subway Source heatpump and Collaborative characteristics of thermal process of system. Master’s Thesis, Qingdao University ofTechnology)

Liu Nan.(2021). Research on thermal pollution law and Treatment Strategy of Subway Tunnel. Master's Thesis,Qingdao University of Technology.

Wang Y. M. (2018). Research on Performance of Waste Heat Source heat pump System in subway. Master'sThesis, Qingdao University of Technology.

QI Haoyu. (2023). Influence of groundwater seepage on heat transfer characteristics of capillary front heat exchanger of Metro Source heat pump.

#347: A Comprehensive study on the effects of urban vegetation configuration on $PM_{2.5}$ and outdoor thermal comfort

Yang LINA[1], Gao SHUO[2], Xie MINGZHAO[3], Liu JIYING[4*]

[1] BinZhou Polytechnic, Binzhou, linaya1996@163.com
[2] Northeastern University, Shenyang, gaoshuo@stumail.neu.edu.cn
[3] Northeastern University, Shenyang, xiemingzhao@stumail.neu.edu.cn
[4] Shandong Jianzhu University, Jinan, jxl83@sdjzu.edu.cn

Abstract: Despite the process of urbanization accelerating, the outdoor environmental quality is gradually declining. Greenery is generally considered an effective measure for improving environmental quality, it not only can reduce the dispersion and deposition of pollutants in the environment but can improve the outdoor thermal environment in the summer by regulating microclimate. The goal of our work is to optimize the types and layout of vegetation in specific spaces to maximize the creation of comfortable and safe outdoor environments. In our work, we selected a densely populated typical residential area in Jinan city and used ENVI-met software to simulate the impact of different vegetation configurations on pollutants and microclimate. According to the simulation results, we found that altering the canopy shape, vegetation type, tree spacing, and leaf area density (LAD) of vegetation have significant impacts on air quality and outdoor thermal environment, even exhibiting conflicting factors. Based on the comprehensive analysis, we suggested that planting trees on the outer row and shrubs on the inner row, and in this way, the reduction efficiency of $PM_{2.5}$ was 65.34%, and the physiological equivalent temperature (PET) decreased by 8.24 °C, which achieved the better performance. The research will provide important recommendations for urban planners, contributing to promoting sustainable urban development and improving the physical and mental health of urban residents.

Keywords: Outdoor Air Quality, Outdoor Thermal Environment, Vegetation Configurations, ENVI-Met

1. INTRODUCTION

Outdoor environment serves as an important space for human activities, and individuals engaged in outdoor pursuits increasingly seek a high-quality environment for their comfort. Factors such as outdoor thermal conditions, air quality, lighting, and sound environment all influence human perception of the outdoor environment. Among the most concerning influencing factors are environmental pollution and high temperatures, which have a direct impact on people's health and public property (Zhong et al., 2023, Fu et al., 2024). For instance, air pollution has been linked to an increased risk of heart disease, lung cancer, as well as chronic and acute respiratory diseases including asthma (Jia et al., 2024, An et al., 2021). Besides, according to the study of The World Health Organization's Ambient (outdoor) air pollution, air pollution cause millions of premature deaths annually(WH, 2024). Simultaneously, Extreme high temperatures have a severe impact on the physical and mental health of urban residents. For instance, Chen's research reveals that heat waves increased the risk of mortality, particularly in relation to cardiovascular and respiratory diseases (Cheng et al., 2024). Therefore, controlling outdoor particulate pollution and outdoor thermal environments play a crucial role in improving outdoor environment.

Greening is commonly seen as an effective measure for improving environmental quality (Qin et al., 2023). In urban areas, the environment is often enhanced by adding street trees, green screens, lawns and green roofs. These green infrastructures release oxygen, absorb carbon dioxide and harmful gases, aiding in the deposition and removal of air pollutants (Kandelan et al., 2022, Liu et al., 2024). Furthermore, the vegetation's photosynthesis and transpiration processes lower summer air temperatures, increase humidity (Abdi et al., 2020), and can alleviate the urban heat island effect (Tomson et al., 2021, Yang et al., 2022). However, the presence of trees alters the wind field within street canyons, decreasing turbulent kinetic energy within the canyons, particularly dense tree canopies at the top, impacting the dispersion of pollutants upward and leading to negative effect of outdoor environment (Abhijith et al., 2017, Gromke and Blocken, 2015). Green infrastructure in street canyons leads to an increase in pollutant concentration in hotspots, and green roofs also contribute to elevated pollutant levels in specific areas (Rafael et al., 2018). Besides, hedges as green barriers can reduce wind speed, affect the dispersion of pollutants, causing an increase in pollutant concentration in street canyons (Taleghani et al., 2020). In contrast, tall trees with only trunks at the bottom and no branches allow pollutants to disperse well, leading to reduced concentrations. Therefore, it is evident that vegetation has both positive and negative impacts on environmental quality, depending on the type of vegetation and the surrounding environment.

Urban vegetation improves air quality through two main mechanisms: deposition and dispersion (Janhäll, 2015). The impact of vegetation on outdoor thermal environments is complex (Fei et al., 2023, Li et al., 2023). Previous works (Chen et al., 2015, Dong et al., 2023) have tended to examine the effects of greening on outdoor environmental factors yet neglecting the different vegetation's impact on air quality and outdoor thermal environments. Therefore, in our work, we designed 10 different green scenarios tailored to specific outdoor environments and regions. These scenarios included four variables: tree crown shape, vegetation type, spacing between trees, and LAD. We conducted a comprehensive analysis of how varying vegetation configurations impact outdoor pollutants and the outdoor thermal environment.

In our work, we selected a typical residential area along the street in Jinan City and conducted field measurements of meteorological parameters and $PM_{2.5}$ concentrations. The ENVI-met program was used to establish a model of the community, and different greenery configurations were implemented to investigate the optimal greenery layout for improving outdoor environmental quality in the residential area. The specific objectives include: (i) exploring the positive and negative effects of different greening configurations on residential areas and surrounding streets in specific areas and environments; (ii) examining the impact of greening configurations on outdoor thermal comfort under the same environmental conditions; (iii) summarizing the optimal types and layouts of greening in residential areas along the street. According to our experimental results, we find that optimizing outdoor green facilities can significantly enhance the physical and mental well-being as well as comfort of outdoor individuals. Additionally, our study offers valuable recommendations for urban planners and landscape designers in terms of effective outdoor green arrangements, thereby contributing to the sustainability of cities.

2. METHODS

2.1. Study area

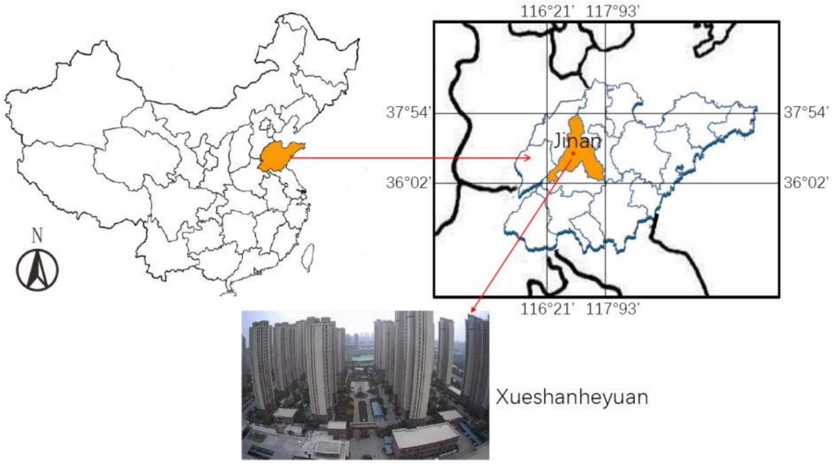

Figure 1: Location and layout of the study area

As shown in Figure 1, Jinan, the capital of Shandong Province, is located at 36°40' north latitude and 117°00' east longitude. Jinan belongs to a cold region, according to the meteorological data, Jinan has the highest temperature in July with daily average highs reaching 35°C, while it has the lowest temperatures in January, with daily average lows of -8°C. In winter, the prevailing wind is from the north, with average wind speeds ranging from 1.5 to 2.2 m/s. In summer, the prevailing wind is from the southeast, with average wind speeds between 1.8 and 2.6 m/s. Jinan is classified as a large city with a dense population and heavy traffic congestion, significantly impacted by traffic-related pollutants.

In our study, we selected a residential area which consists of high-rise buildings with an average height of around 90 m in Jinan for our research. The area is arranged densely with a regular layout of buildings. And spans approximately 360 m in the east-west direction and 320 m in the north-south direction. Century Avenue on the south and Fengming Road on the east are main roads with four lanes in each direction, while the west and north sides have collector streets with single lanes in each direction, as shown in Figure 1. There are no industrial pollution sources near the residential area, making automobile exhaust the primary source of atmospheric particulate matter.

2.2. Field measurement

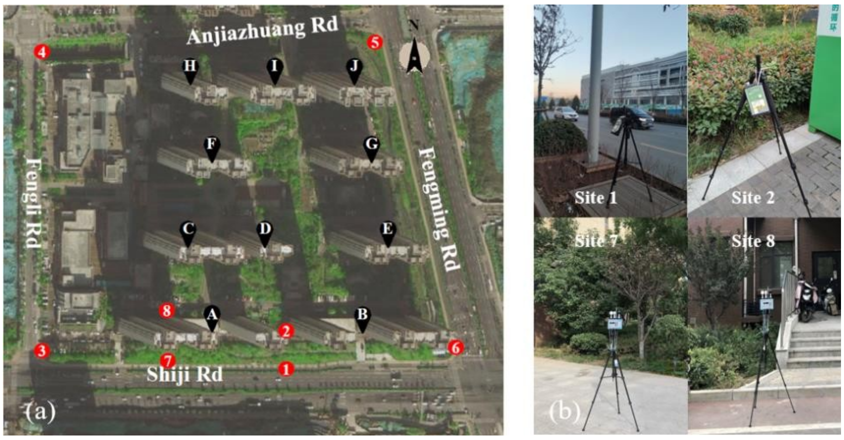

Figure 2: Photos of study area and measuring points: (a) study area; (b) measured photos

The on-site measurements were conducted on September 30 and October 27-28, from 7:00 to 19:00, on weekdays. As shown in Figure 2, considering the variations in pollutants, outdoor thermal environment and building layout, we established 8 measurement points. We selected measurement point 1 within the green belt between the motorized lane and the pedestrian walkway, with point 2 placed vertically between two buildings, 40 m apart. Points 3, 4, 5, and 6 were set at different azimuth angles within the neighborhood for subsequent outdoor environment analysis. Two measurement points, 7 and 8, were positioned on the windward and leeward sides of building A. The $PM_{2.5}$ concentrations were measured using MetOne 804 laser particle counters. Air temperature and relative humidity were recorded with a JA-IAQ-50 multifunctional tester. The measurement height was fixed at 1.5 m. These points primarily experienced vehicle exhaust pollution from

Century Avenue. Hourly traffic flow was documented by capturing videos at different time intervals on the road, and the traffic volume data is presented in Table 1. Relevant road parameters were determined using online Baidu satellite images (https://map.baidu.com/).

Table 1: Hourly traffic flow statistics

Hour	q (Veh/h)	PC(Veh/h)	LDV(Veh/h)	Bus(Veh/h)	Tatal(Veh/h)
6-7	887	860	50	48	958
7-8	957	989	52	75	1116
8-9	867	1002	58	70	1130
9-10	906	865	56	68	989
10-11	948	820	53	55	928
11-12	917	825	54	58	937
12-13	879	886	53	54	993
13-14	877	921	56	53	1030
14-15	914	844	54	50	948
15-16	1033	864	55	53	972
16-17	1067	978	58	63	1099
17-18	978	1167	58	70	1295
18-19	924	1032	48	65	1145
19-20	721	760	45	50	855

Note: Total, PC, LDV and bus represent total vehicles passenger cars, light-duty vehicles and public transport, respectively.

2.3. Simulation methodology

Simulation Model

In our study, we utilized ENVI-met 5.1.1 to simulate the outdoor environment of a high-rise residential area. The ENVI-met model, proposed by the Bruse and Fleer team in 1998, is a CFD model designed to simulate outdoor microenvironments. This model requires detailed input of building structures, vegetation, pollutants, and surface characteristics to output weather conditions, pollutant dispersion, and human thermal comfort indices. The model employs standard advection-diffusion equation to calculate the mass, momentum, energy budgets and dispersion of gases and particles in the atmosphere, introducing source and sink terms in pollutant dispersion, such as representing traffic pollution sources with linear sources and calculating particle concentrations through emission rates. Numerous previous studies have validated the accuracy of ENVI-met in simulating outdoor environments (Viecco et al., 2021, Hofman and Samson, 2014). Additionally, it includes a separate vegetation model that allows for the selection of common vegetation types or the specification of vegetation parameters (i.e., LAD, Height, Width, Tree Calendar, Leaf Type) to simulate the interactions of different vegetation types with the atmosphere, making it suitable for simulating the impact of vegetation configuration on outdoor environments.

Modeling setting

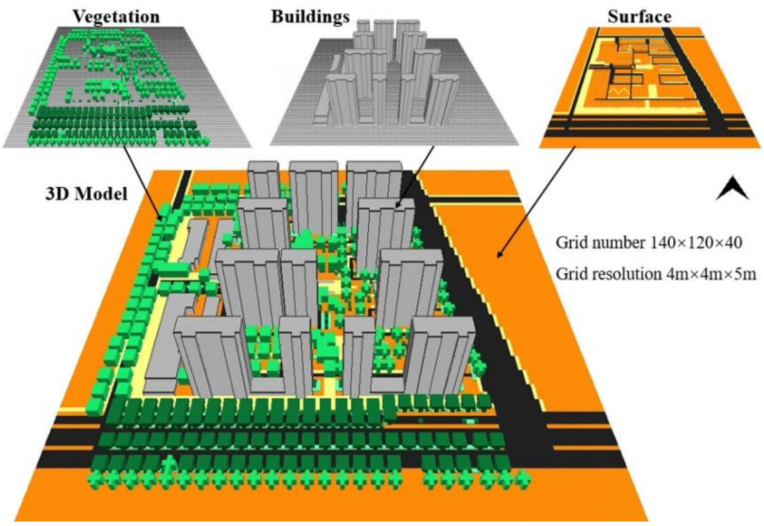

Figure 3: Simulation area model

Based on the actual conditions of the study area, the 3D view of the model is depicted in Figure 3. The model grid was set at 140 × 120 × 40, with a grid resolution of 4 m × 4 m × 5 m, and the lowermost 5 grids were 0.5 m × 2 = 1 m. The simulation time of the model was set for 24 h, encompassing daily peak and off-peak traffic flow periods, with data output intervals of 1 h. Typical meteorological year data was utilized for meteorological parameters. Vegetation, surfaces, pollutants, and buildings within the model were configured based on the actual conditions of the study area. The tree species were selected from albero based on common tree species in Jinan City. The height of shrubs was set at 1.5 m, while grass height was0.25 m. Pollution concentrations were determined according to traffic flow detection and placed on each street. The pollutant height was 0.3 m, the linear source emission rate was 12.7 μg/s/m, and the background concentration was set at 60 μg/m3.

2.4. Vegetation layout

The objective of the study is to examine how different vegetation parameters affect the outdoor environment. There are four varying parameters: tree crown shape, vegetation type, spacing between street trees, and LAD. Tree crown shapes were set as Spherical and Cylindric based on common tree species in Jinan City, corresponding to conditions A2 and A3 in Table 2. The vegetation types include shrubs (A4), trees (A5), and a combination of trees and shrubs further divided into three conditions: alternate planting of trees and shrubs (A3), inner rows of trees and outer rows of shrubs (A6), and inner rows of shrubs and outer rows of trees (A7). The spacing between street trees was set at 4 m and 8 m, corresponding to A5 and A8. The LAD values for vegetation were set at 0.5, 1.0, 1.5, and 2.0, corresponding to conditions A9, A10, A11, and A3, respectively. These vegetation configurations were designed in two different orientations with respect to the prevailing wind. The south and east sides of the neighbourhood are both congested main roads, so the model includes both vertical and horizontal orientations with respect to the wind direction.

Table 2: Cases considered in this study

Cases	Crown shape	Type	Tree spacing (m)	LAD
A1	-	-	-	-
A2	Spherical	Trees and Shrubs	8	2
A3	Cylindric	Trees and Shrubs	8	2
A4	Cylindric	Shrubs	4	2
A5	Cylindric	Trees	4	2
A6	Cylindric	tall trees on the inner row	8	2
A7	Cylindric	tall trees on the outer row	8	2
A8	Cylindric	Trees	8	2
A9	Cylindric	Trees and Shrubs	8	0.5
A10	Cylindric	Trees and Shrubs	8	1.0
A11	Cylindric	Trees and Shrubs	8	1.5

2.5. Evaluation indices

Reduction efficiency

The study employed percentage reduction to evaluate the impact of different vegetation configurations on pollutant concentrations.

Equation 1: Reduction rate of $PM_{2.5}$. $$P = \frac{(C_s - C_m)}{C_m} \times 100\%$$

Where:

- P = Reduction efficiency
- C_s = the $PM_{2.5}$ concentration value at the roadside (μg/m^3)
- C_m = the $PM_{2.5}$ concentration value at various distances from the street (μg/m^3)

Physiological Equivalent Temperature

PET is a common index for evaluating outdoor thermal environments and is suitable for assessing thermal environments with large seasonal temperature variations (Miao et al., 2023, Lai et al., 2019). PET is defined as the temperature of a given environment at which the core and skin temperatures of a person in that environment are equivalent to those in a standard space (air temperature of 20°C, relative humidity of 50%, air velocity of 0.1 m/s) (Höppe, 1999).

3. RESULTS

3.1. Simulation verification

To determine the accuracy of the model, we employed two validation metrics: Root Mean Square Error (RMSE) and correlation coefficient (R^2). RMSE is commonly used to assess the degree to which ENVI-met simulation results deviate from actual values, with smaller values indicating better performance. R^2 represents the assessment of this goodness between measured and simulated values, varying between 0 and 1, with values closer to 1 indicating a better fit.

The study utilized meteorological parameters such as T_a, relative humidity (RH), and pollutant $PM_{2.5}$ to validate the model's accuracy. The RMSE and R^2 between the measured and simulated values were calculated, as shown in Table 3. According to Lu et al.'s research, an effective model should have an RMSE value less than 4.83(Lu et al., 2017). The RMSE values in Table 4 range from 0.64 to 0.93, indicating the model's effectiveness. The R^2 values range from 0.86 to 0.97, demonstrating a high level of agreement between simulated and measured values. Therefore, the model's simulations can accurately represent measured values.

Table 3: Model validation results in each site based on T_a, RH and $PM_{2.5}$ concentration

	RMSE			R^2		
	T_a	RH	$PM_{2.5}$	T_a	RH	$PM_{2.5}$
Site 1	0.64	1.24	1.08	0.97	0.93	0.93
Site 2	0.93	2.43	2.42	0.95	0.89	0.86

3.2 The impact of different vegetation configurations on air quality

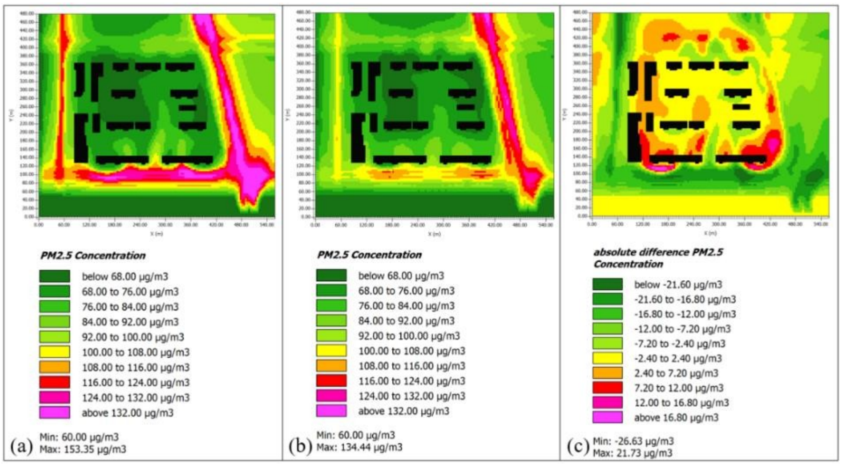

Figure 4: $PM_{2.5}$ distribution map at 1.5 m during peak hours: (a) A1; (b) A3; (c) difference between A1 and A2

Figure 4 depicts the distribution and differences in $PM_{2.5}$ concentrations between scenarios with and without vegetation. Figure 4(a) illustrates the condition without vegetation (A1), with the highest $PM_{2.5}$ concentration reaching 153.35 μg/m^3. When the $PM_{2.5}$ concentration exceeds 35 μg/m^3, it can impact human life expectancy, with a 10-year reduction in life expectancy for every additional 10 μg/m^3(Martins and Carrilho da Graça, 2020, He et al., 2023). Therefore, the $PM_{2.5}$ concentration in the figure significantly impacts human health and longevity. Figure 4(b) shows the scenario with added greenery (A3), where the $PM_{2.5}$ concentration notably decreases. The specific concentration changes are shown in Figure 4(c). Figure 4(c) compares the differences in $PM_{2.5}$ concentrations between scenarios with vegetation (A3) and without vegetation (A1). The green areas indicate a decrease in $PM_{2.5}$ concentration with the addition of vegetation, signifying improved air quality. The orange and red areas indicate worsened air quality after adding vegetation, while the yellow areas indicate minimal impact of vegetation on pollutant levels. With increased vegetation, pollutant concentrations on roads and sidewalks decrease significantly, up to 26.63 μg/m^3, suggesting the vegetation's adsorption role aids in pollutant deposition. However, pollutant concentrations between buildings and streets increase, with an increment ranging from $_{2.5}$ to 17.5 μg/m^3, possibly due to the influence of buildings on the wind environment, hindering pollutant dispersion. Therefore, adding vegetation has both positive and negative effects on air quality, necessitating different choices based on specific locations. Additionally, it is observed that pollutants from the main road on the southern side have a greater impact within the residential area due to prevailing summer winds. Traffic pollutants on the east and west sides have a minor impact within the residential area, emphasizing the need for studying the impact of streets perpendicular to the prevailing wind direction on pollutants within residential areas.

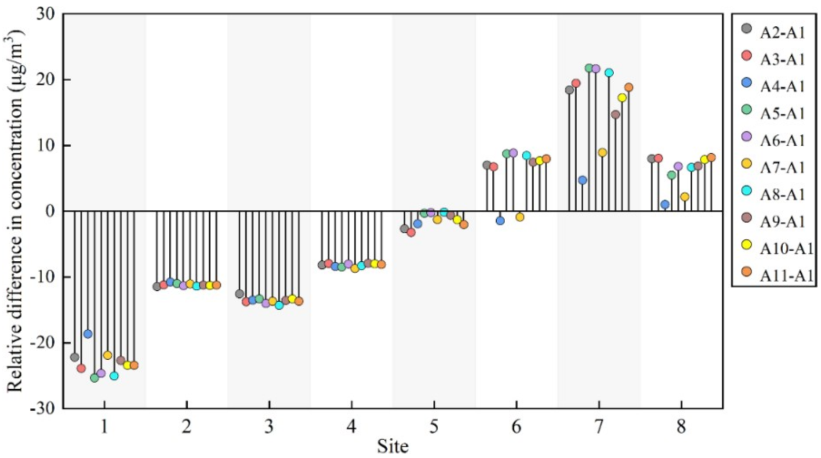

Figure 5: The relative concentration difference between all green cases at a pedestrian height of 1.5 m and case without vegetation

The article discusses the differences in average $PM_{2.5}$ concentrations between all green conditions and the A1 condition, focusing on six selected measurement points from Figure 1 and the windward face of buildings (recorded as Measurement Point 7) and the leeward face (recorded as Measurement Point 8). These differences are presented in Figure 5. Positive values in the figure indicate an increase in pollutant concentration after vegetation is added, while negative values signify a decrease in pollutant concentration. Overall, $PM_{2.5}$ concentrations at Measurement Points 1, 2, and 3 decreased by over 10 μg/m^3. This is primarily because the measurement points are located on the south side of the main road, where the deposition effect of vegetation is significant. Measurement Point 5 showed a slight decrease in $PM_{2.5}$ concentration within the range of 0.21 to 3.2 μg/m^3 because of its distance from the main road, indicating minimal impact from added vegetation. Measurement Points 6, 7, and 8 experienced an increase in $PM_{2.5}$ concentration due to the influence of buildings and wind direction, with Measurement Point 7 reaching up to 21.75 μg/m^3, exacerbating environmental pollution from $PM_{2.5}$. A detailed analysis of individual measurement points revealed no significant differences between the A2 and A3 conditions and the condition without vegetation, indicating that the shape of the canopy has minimal impact on $PM_{2.5}$. In comparison among the A3, A4, A5, A6, and A7 conditions, significant variations in pollutant concentration were observed in the region where $PM_{2.5}$ concentration decreased, with Measurement Point 1 showing the most significant change (A5 > A6 > A3 > A7 > A4), while Measurement Points 2, 3, 4, and 5 exhibited similar differences across all conditions. In the region where $PM_{2.5}$ concentration increased, the pollutant elevation under the A4 condition was notably lower compared to other conditions. Particularly at the prominent Measurement Point 7, the increase in $PM_{2.5}$ concentration under other conditions ranged from 19.46 to 21.75 μg/m^3, while under the A4 condition, the increase was only 4.73 μg/m^3. Thus, planting shrubs alone is the most beneficial for outdoor air quality improvement. A comparison between the A6 and A7 conditions revealed that planting shrubs on the inner were better air quality improvement than planting trees. $PM_{2.5}$ concentration under the A7 condition being 0.3 to 12.7 μg/m^3 lower than under the A6 condition. No significant differences were observed between the A5 and A8 conditions, indicating that the row spacing of trees has an insignificant impact on $PM_{2.5}$. Comparing the differences between A9, A10, A11, A3, and A1, it was found that with an increase in LAD, the increase in pollutants is greater, while the decrease is not significantly affected, suggesting that increasing the vegetation's LAD will exacerbate environmental pollution.

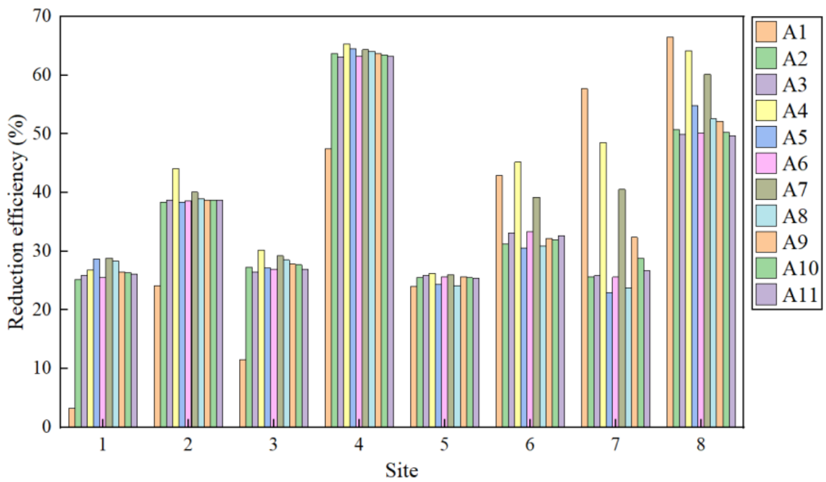

Figure 6: The reduction efficiency of $PM_{2.5}$ in all cases where the pedestrian height is 1.5 m

The attenuation rate of $PM_{2.5}$ at various monitoring points was calculated using Equation 1 with the edge of the motor lane set as 0 m, as shown in Figure 6. In conditions with vegetation, the attenuation rates of $PM_{2.5}$ at monitoring points 1, 2, 3, and 4 were higher than A1, with monitoring point 1 showing the most significant improvement. Monitoring point 1, located closest to the motor lane, had an attenuation rate of only 3.27% without vegetation. After adding vegetation, the attenuation rate increased to 25.12-28.85%, indicating an improvement in outdoor air quality due to greening. For monitoring points 6, 7, and 8, the $PM_{2.5}$ attenuation rates after greening were lower than in the non-greening condition (A1), suggesting increased pollution levels after greening. Among all monitoring points, condition 4 consistently exhibited higher attenuation rates, reaching 65.34% at monitoring point 4 and 64.19% at monitoring point 8. The vegetation in condition 4,consisting of shrubs, facilitated the diffusion of pollutants upwards. It was also observed that the shape of the canopies and the spacing between trees had little impact on $PM_{2.5}$ concentrations. Comparing conditions A9, A10, A11, and A3, it was found that with an increase in LAD of vegetation, the attenuation rates of $PM_{2.5}$ gradually decreased, but not significantly, consistent with the previous findings.

3.3. The impact of different vegetation configurations on outdoor thermal environment

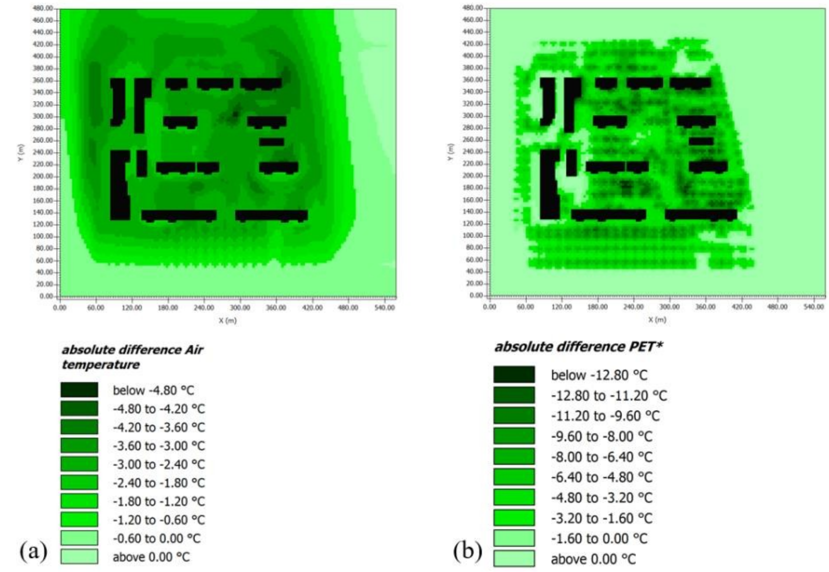

Figure 7: Differences in T_a and PET based on the presence or absence of vegetation: (a) T_a; (b) PET

In the study of outdoor thermal environment, we analysed the differences in meteorological parameters (T_a) and the human thermal comfort index (PET) under different vegetation configurations. Figure 7 depicts the comparison of T_a and PET between conditions A3 and A1 at 14:00 at a pedestrian height of 1.5 m. In Figure 7, both T_a and PET decreased, indicating that increasing vegetation is beneficial for improving the outdoor thermal environment. A comparison with the vegetation layout in Figure 3 revealed a significant improvement in the thermal environment in the vegetation-covered area, with T_a decreasing by 3 to 4.8°C and PET decreasing by 8 to 12.8°C, while other areas experienced a cooling effect of less than 3% and PET values decreased by less than 8°C. Due to the influence of the southern wind, the temperature drop on the north side of the area was higher than on the south side. PET values seemed to be minimally affected by wind direction.

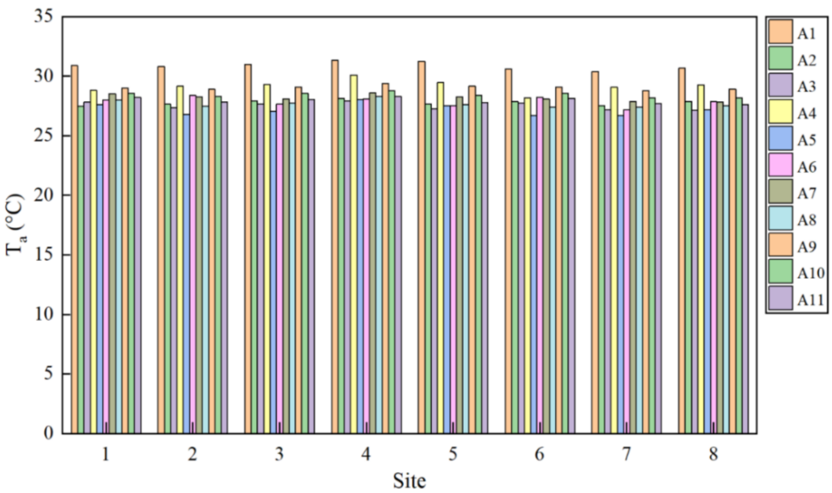

Figure 8: The T_a at a height of 1.5 m under all cases

Figure 8 displays the temperatures at different measuring points under various conditions. After greening, the temperatures at all points decreased. Among the conditions, A4 showed the least noticeable cooling effect with an average temperature decrease of 1.7°C, possibly due to the presence of low shrubs leading to higher solar radiation and thus a poorer cooling effect. In comparison to A2, the cooling effect of A3 was better, indicating the advantage of a Cylindric tree canopy in reducing summer temperatures. Further comparisons among A3, A4, A5, A6, and A7 conditions revealed that A3 had the best cooling effect, followed by A5, A6, and A7, with A4 showing the least improvement. This suggests that a combination of trees and shrubs is more effective in reducing temperatures than having only trees or shrubs. Additionally, the influence of trees on either the inner or outer row had minimal impact on the temperature. Condition A5 had an average temperature decrease of 3.67°C, while A8 had an average decrease of 3.18°C, indicating that reducing the distance between trees benefits the improvement of T_a. Furthermore, comparisons with A9, A10, A11, and A3 conditions revealed a significant increase in cooling effects with an increase in LAD, opposite to the trend of $PM_{2.5}$ concentration change.

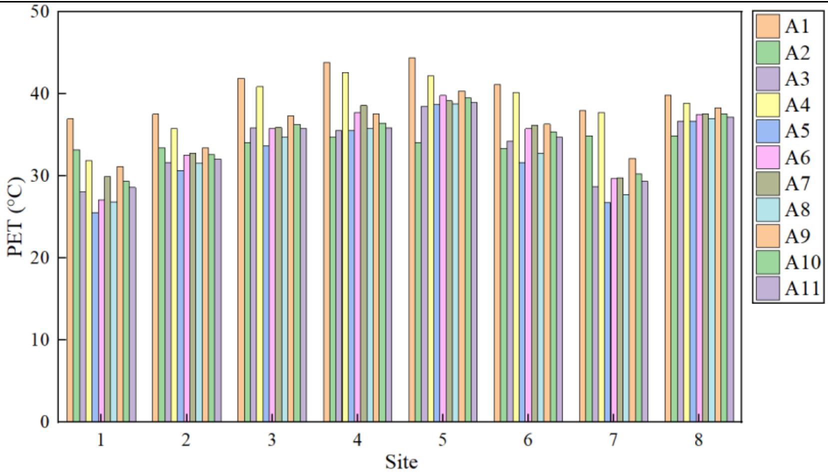

Figure 9: The PET at a height of 1.5 m under all cases

Figure 9 illustrates the PET values at different measurement points for each scenario. The increase in greenery contributes to a reduction in PET, thereby enhancing the outdoor thermal environment. In scenarios without greenery (A1), the PET at measurement point 4 reaches 44.5°C. Previous studies have shown that in cold regions, a PET exceeding 40°C can make individuals feel extremely hot, significantly impacting the health of outdoor personnel. Following the introduction of vegetation, the PET values noticeably decrease at various measurement points for all scenarios, with only A4 showing PET values exceeding 40°C in certain areas, indicating that shrubbery has limited effectiveness in improving the outdoor thermal environment (Matzarakis et al., 1999, Lai et al., 2014). The PET range for A5 falls between 25.58°C and 38.72°C, with a notable decrease in PET values, suggesting that dense planting of tall trees is most beneficial for improving the outdoor thermal environment. Increasing the LAD is beneficial for reducing PET, making individuals feel more comfortable in outdoor environments, aligning with the trend of environmental temperature fluctuations.

4. DISCUSSION

Previous studies have commonly segregated discussions on outdoor air quality and thermal environment, although both are crucial factors in influencing the outdoor environment, there always exists some degree of correlation and even conflicting elements between them. In this study, we aim to investigate the optimal vegetation configuration based on both air quality and outdoor thermal environment, so as to foster a more comfortable and healthy outdoor setting. According to our experimental results, we find that increasing vegetation has simultaneous positive and negative impacts on air quality. Besides, the results also demonstrate that enhancing vegetation is advantageous for improving the outdoor thermal environment, even if enhancing outdoor thermal environment often leads to increased pollutant concentrations. Therefore, urban planning should carefully consider the interplay between the outdoor air quality and thermal environment in future.

It is worth noting that in our work, we mainly focus on exploring how various vegetation parameters affect the outdoor environment. Although our experiments were conducted in a typical residential area of Jinan during a typical summer weather day, the street layout and meteorological parameters remain relatively consistent. Vegetation configurations have indeed some impacts on the outdoor environment, however, it is widely recognized that various factors such as meteorological parameters (Heshani and Winijkul, 2022) and urban form (Jareemit et al., 2023) also influence outdoor pollutants and thermal conditions. Therefore, in our future research, we need to enhance the generalization ability of greening configurations to adapt outdoor environments of different characteristics and scales.

5. CONCLUSION

(1) Increasing vegetation has both positive and negative impacts on air quality. Vegetation cover on urban main roads and sidewalks can improve air quality, with the potential to reduce $PM_{2.5}$ concentration by up to 26.63 μg/m^3. Conversely, air quality around buildings may deteriorate, leading to an increase in $PM_{2.5}$ concentration up to 17.5 μg/m^3. Vegetation has a minimal impact on pollutant concentration within residential areas.

(2) Tree crown shape and spacing have a minimal impact on $PM_{2.5}$ concentration. Different types of vegetation significantly affect local $PM_{2.5}$ concentrations, with shrubs having the most favorable impact on air quality. In areas with higher $PM_{2.5}$ concentrations, trees can cause an increase of 21.75 μg/m^3, while shrubs only increase by 4.73 μg/m^3. Moreover, Condition 4 shows the highest reduction rate, reaching 65.34%. Additionally, planting shrubs on the inner row was better air quality improvement than planting trees. As $PM_{2.5}$ concentration increases with LAD, it is not advisable to plant vegetation with high LAD for the sake of air quality.

(3) Increasing vegetation is beneficial for improving the outdoor thermal environment in summer. Under all cases of increased vegetation, both Ta and PET decrease, with cooling effects reaching up to 4.8°C and a decrease in PET of 12.8°C. Among different tree crown types, columnar shapes are more advantageous for improving the outdoor thermal environment. Decreasing the spacing between trees contributes to better outdoor thermal conditions. Regarding vegetation

types, the combination of trees and shrubs has the most significant effect, followed by trees alone, while the effect is weakest with only shrubs, contradicting their favorable impact on air quality. Planting trees on the inner row or outer row does not have a significant impact on the outdoor thermal environment. Increasing LAD helps reduce air temperature and PET, contrary to the change in PM2.5 concentration.

(4) Vegetation has a complex impact on the outdoor environment. To balance outdoor air quality and thermal conditions, it is recommended to plant shrubs on the inner row and trees on the outer row. Furthermore, choosing appropriate planting methods according to different regions and environmental needs is necessary.

6. REFERENCES

ABDI, B., HAMI, A. & ZAREHAGHI, D. 2020. Impact of small-scale tree planting patterns on outdoor cooling and thermal comfort. Sustainable Cities and Society, 56, 102085.

ABHIJITH, K. V., KUMAR, P., GALLAGHER, J., MCNABOLA, A., BALDAUF, R., PILLA, F., BRODERICK, B., DI SABATINO, S. & PULVIRENTI, B. 2017. Air pollution abatement performances of green infrastructure in openroad and built-up street canyon environments – A review. Atmospheric Environment, 162, 71-86.

AN, F., LIU, J., LU, W. & JAREEMIT, D. 2021. A review of the effect of traffic-related air pollution around schools on student health and its mitigation. Journal of Transport & Health, 23, 101249.

CHEN, X., PEI, T., ZHOU, Z., TENG, M., HE, L., LUO, M. & LIU, X. 2015. Efficiency differences of roadside greenbelts with three configurations in removing coarse particles (PM_{10}): A street scale investigation in Wuhan, China. Urban Forestry & Urban Greening, 14, 354-360.

CHENG, C., LIU, Y., HAN, C., FANG, Q., CUI, F. & LI, X. 2024. Effects of extreme temperature events on deaths and its interaction with air pollution. Science of The Total Environment, 915, 170212.

DONG, S., REN, G., XUE, Y. & LIU, K. 2023. How does green innovation affect air pollution? An analysis of 282 Chinese cities. Atmospheric Pollution Research, 14, 101863.

FEI, F., WANG, Y., WANG, L., FUKUDA, H. & YAO, W. 2023. Influence of greenery configuration on summer thermal environment of outdoor recreational space in elderly care centers. Building and Environment, 245, 110857.

FU, N., KIM, M. K., HUANG, L., LIU, J., CHEN, B. & SHARPLES, S. 2024. Investigating the reliability of estimating real-time air exchange rates in a building by using airborne particles, including $PM_{1.0}$, $PM_{2.5}$, and PM_{10}: A case study in Suzhou, China. Atmospheric Pollution Research, 15, 101955.

GROMKE, C. & BLOCKEN, B. 2015. Influence of avenue-trees on air quality at the urban neighborhood scale. Part II: Traffic pollutant concentrations at pedestrian level. Environmental Pollution, 196, 176-184.

HE, S., YANG, L., LIU, J. & JAREEMIT, D. 2023. Spatial distribution of $PM_{2.5}$ concentration around high-rise residential buildings during peak traffic hours in autumn and winter seasons. Indoor and Built Environment, 33, 757-778.

HESHANI, A. L. S. & WINIJKUL, E. 2022. Numerical simulations of the effects of green infrastructure on $PM_{2.5}$ dispersion in an urban park in Bangkok, Thailand. Heliyon, 8, e10475.

HOFMAN, J. & SAMSON, R. 2014. Biomagnetic monitoring as a validation tool for local air quality models: A case study for an urban street canyon. Environment International, 70, 50-61.

HöPPE, P. 1999. The physiological equivalent temperature – a universal index for the biometeorological assessment of the thermal environment. International Journal of Biometeorology, 43, 71-75.

JANHäLL, S. 2015. Review on urban vegetation and particle air pollution – Deposition and dispersion. Atmospheric Environment, 105, 130-137.

JAREEMIT, D., LIU, J. & SRIVANIT, M. 2023. Modeling the effects of urban form on ventilation patterns and traffic-related $PM_{2.5}$ pollution in a central business area of Bangkok. Building and Environment, 244, 110756.

JIA, X., ZHANG, B., YU, Y., XIA, W., LU, Z., GUO, X. & XUE, F. 2024. Greenness mitigate cause-specific mortality associated with air pollutants in ischemic and hemorrhagic stroke patients: An ecological health cohort study. Environmental Research, 251, 118512.

KANDELAN, S. N., YEGANEH, M., PEYMAN, S., PANCHABIKESAN, K. & EICKER, U. 2022. Environmental study on greenery planning scenarios to improve the air quality in urban canyons. Sustainable Cities and Society, 83,103993.

LAI, D., GUO, D., HOU, Y., LIN, C. & CHEN, Q. 2014. Studies of outdoor thermal comfort in northern China. Building and Environment, 77, 110-118.

LAI, D., LIU, W., GAN, T., LIU, K. & CHEN, Q. 2019. A review of mitigating strategies to improve the thermal environment and thermal comfort in urban outdoor spaces. Science of The Total Environment, 661, 337-353.

LI, J., ZHAI, Z., DING, Y., LI, H., DENG, Y., CHEN, S. & YE, L. 2023. Effect of optimal allocation of urban trees on the outdoor thermal environment in hot and humid areas: A case study of a university campus in Guangzhou, China.Energy and Buildings, 300, 113640.

LIU, C., DAI, A., SHENG, Q. & ZHU, Z. 2024. Study on the changes in concentration of air pollutants and influencing factors in road green spaces in Nanjing City during autumn and winter. Atmospheric Pollution Research, 15, 102003.

LU, J., LI, Q., ZENG, L., CHEN, J., LIU, G., LI, Y., LI, W. & HUANG, K. 2017. A micro-climatic study on cooling effect of an urban park in a hot and humid climate. Sustainable Cities and Society, 32, 513-522.

MARTINS, N. R. & CARRILHO DA GRAçA, G. 2020. A simulation study of decreased life expectancy from exposure to ambient particulate air pollution ($PM_{2.5}$) in naturally ventilated workspaces. Journal of Building Engineering, 30, 101268.

MATZARAKIS, A., MAYER, H. & IZIOMON, M. G. 1999. Applications of a universal thermal index: physiological equivalent temperature. International Journal of Biometeorology, 43, 76-84.

MIAO, C., HE, X., GAO, Z., CHEN, W. & HE, B.-J. 2023. Assessing the vertical synergies between outdoor thermal comfort and air quality in an urban street canyon based on field measurements. Building and Environment, 227, 109810.

QIN, Y., SUN, C., LI, D., ZHANG, H., WANG, H. & DUAN, Y. 2023. Does urban air pollution have an impact on public health? Empirical evidence from 288 prefecture-level cities in China. Urban Climate, 51, 101660.

RAFAEL, S., VICENTE, B., RODRIGUES, V., MIRANDA, A. I., BORREGO, C. & LOPES, M. 2018. Impacts of green infrastructures on aerodynamic flow and air quality in Porto's urban area. Atmospheric Environment, 190, 317-330.

TALEGHANI, M., CLARK, A., SWAN, W. & MOHEGH, A. 2020. Air pollution in a microclimate; the impact of different green barriers on the dispersion. Science of The Total Environment, 711, 134649.

TOMSON, M., KUMAR, P., BARWISE, Y., PEREZ, P., FOREHEAD, H., FRENCH, K., MORAWSKA, L. & WATTS, J. F. 2021. Green infrastructure for air quality improvement in street canyons. Environment International, 146, 106288.

VIECCO, M., JORQUERA, H., SHARMA, A., BUSTAMANTE, W., FERNANDO, H. J. S. & VERA, S. 2021. Green roofs and green walls layouts for improved urban air quality by mitigating particulate matter. Building and Environment, 204, 108120.

WH, O. 2024. Ambient (outdoor) air pollution [Online]. Available: https://www.who.int/news-room/fact-sheets/detail/ambient-(outdoor)-air-quality-and-health [Accessed 2 August 2024].

YANG, L., LIU, J. & ZHU, S. 2022. Evaluating the Effects of Different Improvement Strategies for the Outdoor Thermal Environment at a University Campus in the Summer: A Case Study in Northern China. Buildings, 12, 2254.

ZHONG, H., FENG, J., LAM, C. K. C., HANG, J., HUA, J. & GU, Z. 2023. The impact of semi-open street roofs on urban pollutant exposure and pedestrian-level thermal comfort in 2-D street canyons. Building and Environment, 239, 110387.

#351: Comparative analysis of the thermal stability from binary to quaternary nitrate molten salt systems

Li Bingyao[1,2], Liu Jiawei[1,2], Song Weijun[3], Yang Xiaobo[4], Sun Ze[1,4]

[1] National Engineering Research Center for Integrated Utilization of Salt Lake Resource, East China University ofScience and Technology, Shanghai 200237, China, yaofriday@163.com, zsun@ecust.edu.cn
[2] School of Chemical Engineering, East China University of Science and Technology, Shanghai 200237, China, 18321626552@163.com
[3] School of Chemical Engineering, Qinghai University, Xining, Qinghai 810007, China, wjsong@mail.ecust.edu.cn
[4] School of Chemistry and Chemical Engineering, Qinghai Minzu University,Xining, Qinghai 810007, China, yang_1101979@163.com

Abstract: The high-temperature thermal stability of molten salts determines their upper limit of use. In this paper, two high thermal stability tetragonal molten salts (S1 and S2) were developed independently and the high temperature thermal stability of nitrate molten salts with components ranging from binary to tetragonal was systematically studied. High- temperature cycling experiments and constant-temperature thermal weight loss experiments were conducted on a series of nitrate molten salts in the corresponding operating temperature ranges. The thermal stability of these salts at elevated temperatures was assessed in terms of mass loss, cycling performance, composition, structure, and morphology before and after high-temperature treatment. The results showed that after the high temperature cycling experiment and high temperature heat loss of weight experiment, all the component molten salts showed mass loss, but compared with the binary and ternary molten salts, the developed ones showed lower mass loss and better high temperature thermal stability, and the DSC-TG test indicated that the two tetrameric molten salts developed had a low melting point (~110 ℃) and a high decomposition temperature (~610 ℃).The XRD study indicated that after a long-term high-temperature treatment, the composition of the molten salts remained unchanged, and the relative contents of the components did not change. Meanwhile, the crystallinity and solubility of the mixture increased after high temperature treatment, and the liquid phase composition became more homogeneous. Based on comparative analysis, compared with the binary and ternary mixed salts, the S1 and S2 tetrameric mixed salts have good application value in practical engineering applications.

Keywords: Thermal Storage Medium, Thermal Stability, Nitrate Molten Salt

1. INTRODUCTION

As we all know, fossil fuels have been the main source of energy worldwide, driving economic and technological development (Höök and Tang, 2013; Jones et al., 2023). However, as reliance on them has deepened, their negative impact on the environment and health has become more evident. Issues such as air pollution, global warming and resource constraints are too pressing to be ignored (Basavapattan, n.d 2021.; Ofremu et al., 2024; Wang and Azam, 2024). The global pursuit of efficient and sustainable energy solutions is driven by the need to reduce carbon emissions and mitigate climate change (Holmes et al., 2022; Kallio, n.d.). In response, there is an increasing tendency for the whole world to make a transition toward the renewable energy sources (Lucas et al., 2021; Zhang and Chen, 2022). Renewable energy sources such as solar, wind, and hydroelectric power have gained significant traction (Ang et al., 2022; Wörman et al., 2024). However, one of the major challenges with these sources is their intermittency, which necessitates effective energy storage systems to ensure a reliable and continuous energy supply (Wu et al., 2022a, 2022b). Thermal energy storage (TES) has emerged as a critical component in enhancing the reliability and efficiency of renewable energy systems (Ali et al., 2024; Rahnama et al., 2024). TES systems store excess thermal energy for later use, helping to bridge the gap between energy supply and demand. Among various TES technologies, molten salts have garnered considerable attention due to their high thermal stability, low vapor pressure, and capability to operate at high temperatures (Faizan et al., 2024).

Molten salts, particularly nitrate-based salts, are widely used in TES applications for concentrated solar power (CSP) plants and other high-temperature industrial processes (Ma et al., 2024). These salts, including sodium nitrate ($NaNO_3$), potassium nitrate (KNO_3), etc, offer favorable thermal properties and cost-effectiveness (Zhao et al., 2017). Molten salts can be used individually (single-component systems) or in mixtures (binary, ternary, and quaternary systems) to optimize their thermal performance (Roper et al., 2022). The addition of multiple components in molten salt mixtures aims to lower the melting point, enhance thermal stability, and improve heat transfer properties, which are critical for efficient energy storage and transfer (Starke et al., 2024). The thermal stability of molten salt systems is a key factor that determines their viability for long-term use in TES applications (Wang et al., 2023). Thermal stability refers to the ability of salt to withstand high temperatures without undergoing significant decomposition or phase changes. This property is crucial for maintaining the efficiency and safety of the TES system over extended periods of operation (Patange et al., 2024).

Concerning the thermal stability analysis of binary nitrate molten salt system, Pyoungchung Kim et al. (Kim et al., 2024) investigated the effect of pretreatment on the thermal stability of solar salts. The results showed that the pretreated solar salts were more stable than the unpretreated solar salts because they had lower daily mass loss rates than the unpretreated solar salts at conventional operating temperatures of 480°C and 510°C. Julian Steinbrecher et al (Steinbrecher et al., 2023) found that solar salts have significantly lower oxide ion generation rates and NOx release rates compared to salt films. The oxide generation rate was about $10^{-8}s^{-1}$ in the temperature range of 560°C to 650°C, suggesting that solar saltsare more stable than previous findings. By combining classical molecular dynamics and differential scanning calorimetry experiments, B. D'Aguanno et al (D'Aguanno et al., 2018) present a systematic study of all thermostatic, high temperatureproperties of pure KNO_3 and $NaNO_3$ salts and "solar salt" mixtures, then analyze the cP and cV specific heats of the pure salts and of the liquid phase of the mixtures. The results allow us to resolve a long-standing experimental uncertainty about the cP(T) thermal behavior of these systems.

The multi-component nitrate molten salt formed by multi-component melt mixing of single-component nitrate molten salt will significantly lower the melting point, increase the decomposition temperature, and have a higher improvement for thermal stability, for this reason, many scholars have investigated about the thermal stability performance of multi-component mixed nitrate/nitrite molten salt. Yan Han et al. (Han et al., 2021) studied the maximum difference of decomposition temperature between quaternary nitrate-nitrite mixed salt and Solar salt after 500 thermal shock cycles. Zhao Baicen et al (Zhao et al., 2019). analyzed the short-term 25 h and long-term 500 h stability of the ternary mixed nitrate salt $LiNO_3$-$NaNO_3$-KNO_3 and obtained the optimal working temperature range of 118.3-587.2°C. Alexander Bonk et al (Bonk et al., 2022). determined the thermal stability of nitrate salt containing four alkali metals, namely, Ca, Li, Na, and K, and found that the thermal stability of Solar Salt was much lower than that of Solar Salt, and it was much lower than that of Solar Salt. Solar Salt thermal stability is not significantly improved, but the working temperature range is 90°C higher than Solar Salt. Zhang Cancan et al (Zhang et al., 2021). carried out the development and thermal stability study of tetrameric mixed nitrate/nitrite molten salt, mainly and compared with Solar Salt, and pointed out that the mass ratio of NO_2^-/NO_3^- plays an important role in the thermophysical properties of nitrite/nitrate molten salt through the constant temperature experiments on tetrameric salt at three temperatures, namely, 500 ℃, 565 °C and 600 °C, for 1008 h. The thermal stability of tetrameric mixed nitrate/nitrite molten salt was also compared with that of Solar Salt. Wang Yuanyuan et al (Wang et al., 2024). developed a new type of penta-nitrate molten salt and tested and evaluated its stability by carrying out long-term high-temperature test and several heating-cooling cycle tests, which showed that the change rate of various thermophysical properties of penta-nitrate molten salt was less than 10%, and it exhibited excellent thermal stability.

Despite the many advantages of using nitrate molten salts, understanding the thermal stability mechanisms of binary to quaternary systems is still an area that requires in-depth research. Previous studies have provided insight into the thermal behavior of individual salts and some binary mixtures, but comprehensive analyses covering the range from lesser compositions to quaternary systems are limited. The present study aims to fill this gap by providing a detailed comparative analysis of the thermal stability of nitrate molten salt systems, ranging from binary components to quaternary mixtures. By systematically evaluating the thermal stability of these systems, the study attempts to identify more stable and efficient components for practical applications. The results of the study will help optimize molten salt formulations and improve the performance and reliability of TES technology.

2. EXPERIMENTS

2.1. Materials

The specific sources and purities of the basic nitric acid molten salts used in this study are shown in the following table. Solar salt, Hitec, and quaternary salts S1 and S2 were prepared by static fusion method according to their respective ratios. All samples were pre-treated in a muffle furnace at a constant temperature of 300°C for 12 h and set aside. Table 1 presents the materials used.

Table 1: Sample detailed information

Basic salt	Source	Purity
$NaNO_3$	Sinopharm Chemical Reagent Co	99.7%
KNO_3	Sinopharm Chemical Reagent Co	99.7%
$NaNO_2$	Sinopharm Chemical Reagent Co	99.7%
KNO_2	Sinopharm Chemical Reagent Co	99.7%

2.2. Preparation

In this paper, the thermal stability of molten salt from two aspects of the experiments carried out: (1) cyclic hot and cold cycle experiments: 20g of molten salt in a muffle furnace from 400 ° C program heating up to 650 °C in 120 min and then after 120 min down to 400 ° C for many times to repeat the cycle. The mass of the sample was recorded before and after each cycle, and after 20 cycles, the temperature was plotted against the cycling time of the molten salt to obtain the hot and cold cycling curves of the molten salt. Stable molten salt should keep the melting temperature and solidification temperature basically unchanged in the process of multiple temperature rises and falls; (2) short cycle thermostatic heat loss experiment. Put the alumina crucible with cover containing 20g of molten salt into muffle furnace, heat it at constant temperature for 48h, take it out for cooling and weighing in 6h intervals, and use the mass loss to graph the time to get the mass loss rate of molten salt at this temperature. Repeat the experiment by changing the constant temperature and the length of the constant temperature, and the mass loss rate curves at different temperatures can be obtained. According to the decline in the mass loss rate curve can determine the maximum temperature for the use of multi-volume samples. This temperature is generally higher than that obtained by microanalysis.

2.3. Characterization

In this paper, firstly, the mass of the molten salt was recorded before and after thermal cycling and weight loss at constant temperature, and the mass loss is more intuitive to reflect the effect of thermal stability of the molten salt, and secondly, the DSC-TG analysis was carried out on the trace molten salt, and the temperature at which the mass of the thermogravimetric curve decreased by 3% of the molten salt from 5 to 10 mg was the decomposition temperature of the molten salt, which was measured by using the Q600 synchronous thermal analyzer produced by the U.S. TA Company, and also by using the UV spectrophotometer. The mass ratio of NO_2^-/NO_3^- before and after the experiment was measured by photometric method to measure its effect on the thermal stability of the molten salt of the system, in addition to the XRD measurements before and after the sustained high temperature and thermal cycling to compare the structural changes of the molten salt before and after the experiment. The XRD plots of the stabilized molten salts before and after the sustained high temperature and thermal cycling were basically unchanged, and no diffraction peaks characterizing new substances appeared.

3. RESULTS AND DISCUSSION

3.1. Heating-cooling cycle thermal stability

Mass loss analysis

Figure 1 show the mass loss of four different molten salt samples (Solar Salt, Hitec, S1 and S2) over 20 heating and cooling cycles. Figure 1.a corresponds to the cycling experiment at 400 °C and Figure 1.b corresponds to the cycling experiment at 565 °C.

At 400 °C (Fig. a), all the samples showed large mass loss in the initial cycling, especially the S1 and S2 samples, whose initial mass loss was close to 0.10 g. As the number of cycling increased, the mass loss of all the samples decreased rapidly and stabilized. The S1 and S2 samples showed relatively small fluctuations in the subsequent cycling, which demonstrated better thermal stability. In contrast, Solar Salt and Hitec samples showed larger fluctuations in mass loss and poorer stability.

At 565 °C (Fig. b), all the samples showed large mass loss during the initial cycling, especially the S1 and S2 samples, whose initial mass loss was close to 0.10 g. As the number of cycling increased, the mass loss of all the samples tended to stabilize, and the S1 and S2 samples showed small fluctuations throughout the cycling process, displaying better thermal stability. While Solar Salt and Hitec samples showed larger fluctuations in mass loss and poorer stability.

Combining the results of the two sets of experiments, it can be seen that both S1 and S2 samples showed better thermal stability at 400 °C and 565 °C, and the mass loss stabilized and fluctuated less in the subsequent cycles. On the other hand, the Solar Salt and Hitec samples showed relatively poor stability at high temperatures with large fluctuations in mass loss. This suggests that S1 and S2 have superior thermal stability for high temperature applications (>600℃) and are suitable for prolonged use under high temperature conditions.

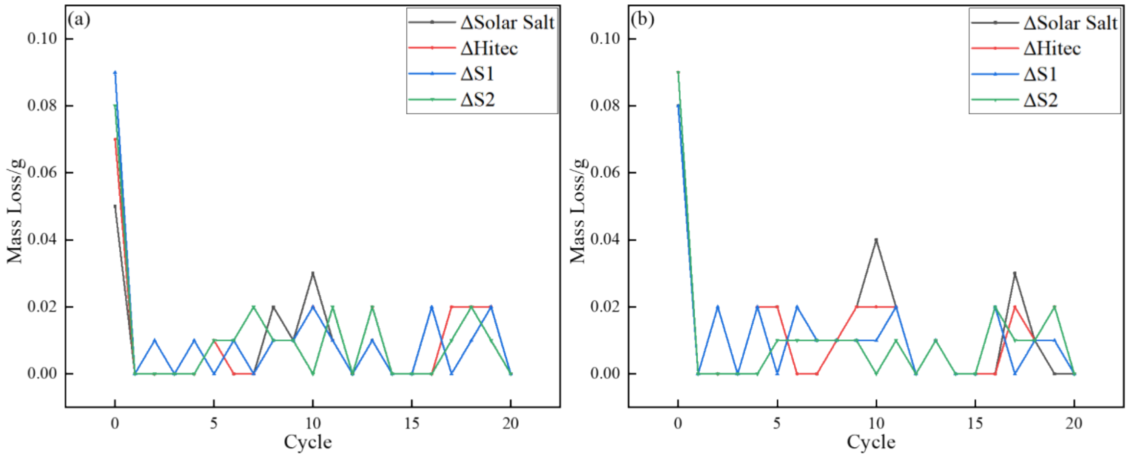

Figure 1: Cyclic mass loss of 20 heating and cooling cycles : a) 400°C b) 565°C

Components analysis

Figure 2 demonstrates the compositional changes of the S1 (Fig. a) and S2 (Fig. b) samples over 20 heating and cooling cycles at 600 °C for four compositions, including potassium (K), sodium (Na), nitrite nitrogen (N-NO_2^-) and nitrate nitrogen (N- NO_3^-), respectively. The results showed that the compositional changes of both S1 and S2 at 600 °C were relatively stable. Specifically, the compositional changes of potassium and sodium in the S1 sample remained relatively stable, and the content of nitrite nitrogen and nitrate nitrogen changed very little, with insignificant compositional fluctuations. The S2 sample also showed the same stability in the composition of potassium and sodium, and the fluctuations of nitrite nitrogen and nitrate nitrogen were small, showing a similar stabilization trend as that of S1.

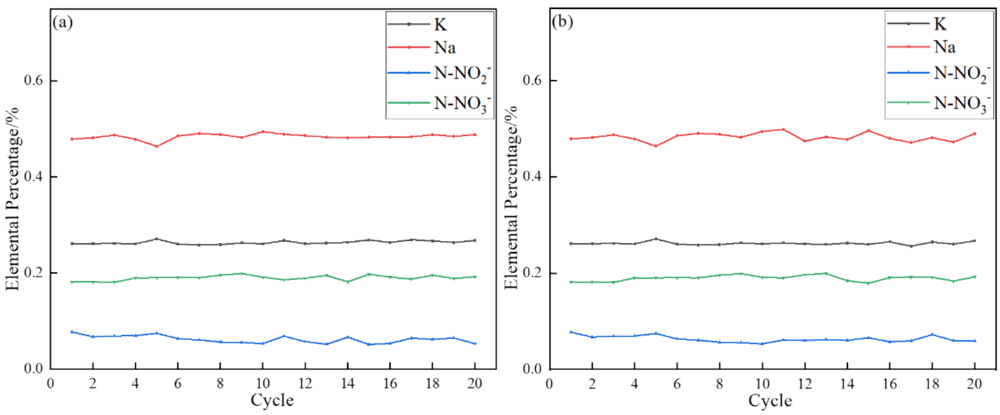

Figure 2: Components changes over 20 heating and cooling cycles at 600°C: a)S1, b)S2

By comparison, it can be seen that although the two samples showed slight differences in different cycling processes, the overall composition fluctuations were small and showed good stability. In particular, the compositional changes of the S1 and S2 samples showed almost no significant fluctuations under the high temperature 600 °C condition, indicating that they are chemically more stable in high temperature cycling. In summary, both samples, S1 and S2, showed excellent compositional stability at a high temperature of 600 °C, and were able to adapt to repeated heating and cooling cycles.

DSC-TG analysis

Figure 3 shows the DSC-TG curves of three different states (initial state, 400°C hot and cold cycling, and 565°C hot and cold cycling) for four samples (Solar Salt, Hitec, S1, and S2). As can be seen from Figs. a and b, the melting points and decomposition temperatures of Solar Salt and Hitec in the initial state are not much different from the literature values, and the tetrameric salts, S1 and S2, both have lower melting points (~110 °C) and higher decomposition temperatures (~610°C), which indicates that the physical properties of polymerized molten salts have been improved compared to those ofsolar salt, and the working temperature range has been broadened.

From Figures c and d, after 20 times of hot and cold cycling at 400°C, the DSC and TG curves of the four samples did not change significantly, indicating that they can be used stably at this temperature. In Figures e and f, after 20 times of hot and cold cycling at 565°C, it can be seen that, except for Hitec, which had a large loss of weight, and Solar Salt, which had a slight loss of weight, the stability of S1 and S2 was not changed significantly, indicating that the stability of both of them was improved. The large changes indicate that S1 and S2, which have higher decomposition temperatures, have higher stability.

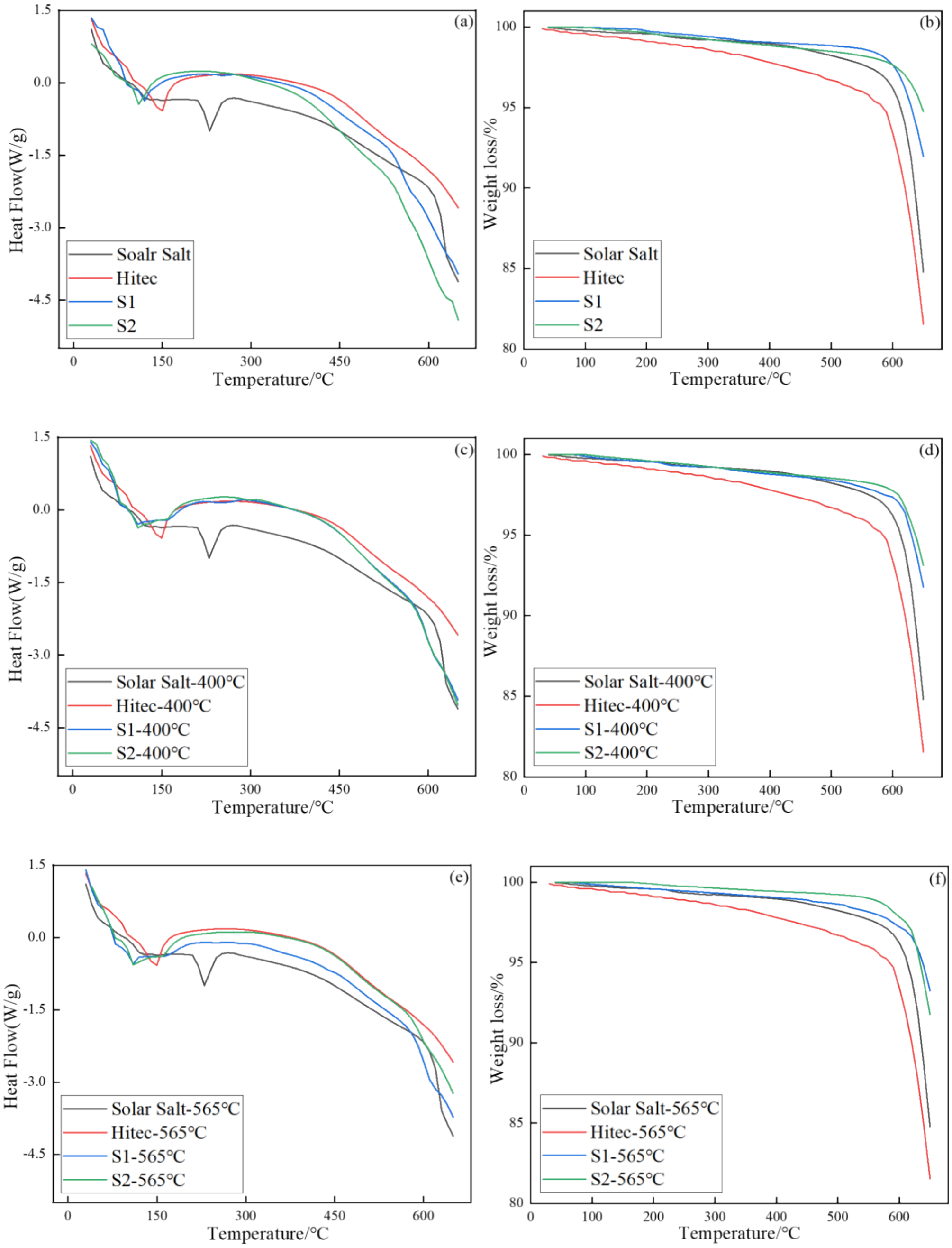

Figure 3: DSC-TG of each molten salt before and after heating and cooling cycles

3.2. Constant temperature thermal weight loss.

Mass loss analysis

Figure 4 demonstrates the mass loss of four molten salt samples (Solar Salt, Hitec, S1, and S2) at 400 °C and 565 °C for 48 h at constant temperature. The left graph corresponds to the experimental results at 400 °C and the right graph corresponds to the experimental results at 565 °C.

The mass loss of all four molten salt samples at 400 °C increased with time. Among them, the Solar Salt (SS) sample had the largest mass loss, which gradually increased from the initial 0.1 g to nearly 0.35 g, showing poor thermal stability. The Hitec sample had the second largest mass loss, which eventually reached about 0.25 g. The S1 and S2 samples had relatively small mass losses, which increased to about 0.20 g and 0.15 g, respectively, showing good thermal stability.

The experimental results at 565 °C showed a similar trend in mass loss for the four samples as at 400 °C, but with a greater overall mass loss. The Solar Salt sample still showed the greatest mass loss, increasing from 0.1 g to ~0.40 g. The Hitec sample showed an equally significant mass loss, eventually reaching ~0.30 g. In contrast, the S1 and S2 samples showed better thermal stability at high temperatures, with mass loss increasing to ~0.30 g, respectively. stability, with mass loss increasing to ~0.25g and 0.20g, respectively.

Taken together, the experimental results at the two temperature conditions showed that the thermal stability of the S1 and S2 samples was superior to that of Solar Salt and Hitec at high temperatures. In particular, the mass loss of the S1 and S2 samples was significantly lower than that of the other two samples at a high temperature of 565 °C, showing their superior performance in high-temperature applications. Therefore, the S1 and S2 molten salt samples have greater potential and advantages in the application of high-temperature energy storage materials.

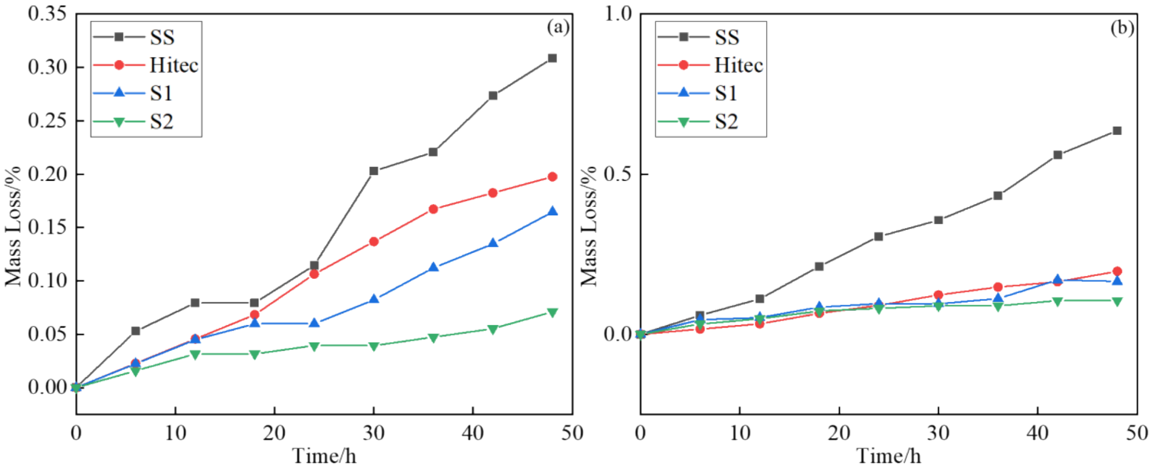

Figure 4: Loss of mass at constant temperature for 48h at different temperatures: a)400°C, b)565°C.

DSC-TG analysis

Figure 5 shows the differential scanning calorimetry (DSC) and thermogravimetric analysis (TG) curves of the S1 and S2 samples after 20 cold and hot cycle experiments at 400 °C and 565 °C. The left figure shows the experimental results at 400 °C, while the right figure shows the experimental results at 565 °C.

As can be seen from the figures, the DSC curves of both S1 and S2 samples at different temperatures show multiple heat absorption peaks, indicating that the two samples underwent a phase transition during the heating process. Specifically, the positions of the heat absorption peaks of S1 and S2 at 400 °C and 565 °C are different, reflecting the influence of different temperature conditions on the phase transition behavior of the samples. The TG curves show the mass change of the samples during the heating process. It can be observed that at 400 °C, the mass loss of the S1 and S2 samples is relatively small, indicating that they have better thermal stability at this temperature. In contrast, at 565 °C, the mass loss of both samples increased significantly, showing a decrease in their thermal stability at higher temperatures.

Based on the analytical method of 3% mass loss as decomposition temperature (T3 method), the decomposition temperatures of S1 and S2 samples at 400 °C and 565 °C can be determined as follows: at 400 °C, the decomposition temperatures of both samples are higher, which show good high-temperature stability; at 565 °C, the decomposition temperatures of the samples are significantly lower, reflecting the effect of higher temperatures on the thermal stability of the samples. Overall, the thermal stability of S1 and S2 at 400 °C is better than their performance at 565 °C, especially after multiple heating and cooling cycles, and this trend is more significant.

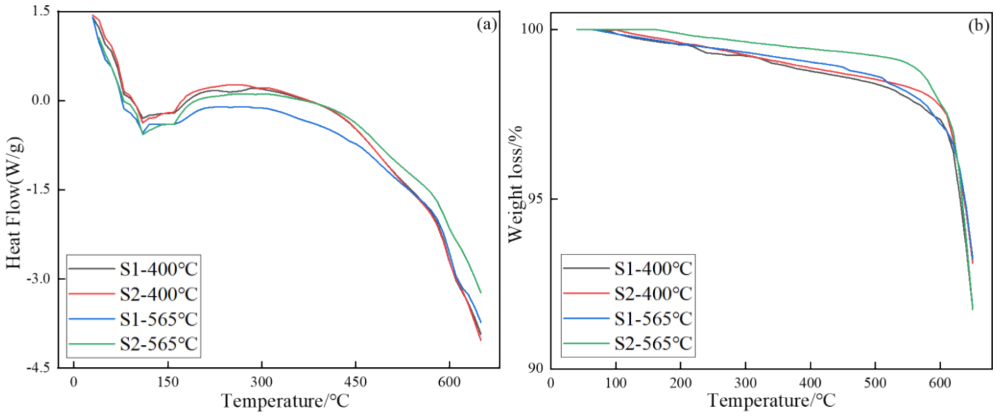

Figure 5: DSC-TG before and after heat loss of weight of various nitric acid molten salts

XRD analysis

Figure 6 presents the X-ray diffraction (XRD) patterns of four samples (Solar Salt, Hitec, S1, and S2) under different temperature conditions, including the initial state, and after 20 hot and cold cycles at 400 °C and 565 °C, respectively. By comparing the XRD patterns under different conditions, the crystal structure changes of each sample and its stability can be analyzed.

The XRD patterns of the four samples in the initial state are shown in Fig. a. The patterns of the Solar Salt and Hitec samples show several obvious diffraction peaks, indicating that they have more complex crystal structures. samples S1 and S2 have fewer diffraction peaks, indicating that their crystal structures are relatively simple and stable.

Fig. b shows the XRD patterns of the samples after 20 hot and cold cycles at 400 °C. Compared with the initial state, the intensities of the diffraction peaks of Solar Salt and Hitec have changed, indicating that their crystal structures have been partially transformed during the high-temperature cycling process, while the diffraction peaks of the S1 and S2 samples have not changed much, showing that their crystal structures are relatively stable at 400 °C. The right panel shows the XRD patterns of the samples after 20 cycles of hot and cold cycling.

Figure c shows the XRD patterns of the samples after 20 hot and cold cycles at 565 °C. It can be seen that the diffraction peaks of the Solar Salt and Hitec samples changed significantly, with the peak positions and intensities altered, indicating that their crystal structures were significantly transformed at high temperatures, while the diffraction peaks of the S1 and S2 samples at 565 ˚C showed relatively small changes and still maintained a better stability of their crystal structures.

In summary, by comparing the XRD patterns under different temperature conditions, it is found that the crystal structure stability of S1 and S2 samples is better than that of Solar Salt and Hitec after many hot and cold cycles at high temperatures, especially at a high temperature of 565 ˚C, S1 and S2 show better thermal stability. In contrast, the crystal structures of Solar Salt and Hitec changed significantly during high-temperature cycling, showing their poorer stability. These results indicate that S1 and S2 have potentially superior stability in high-temperature applications and are suitable for use under more severe temperature conditions.

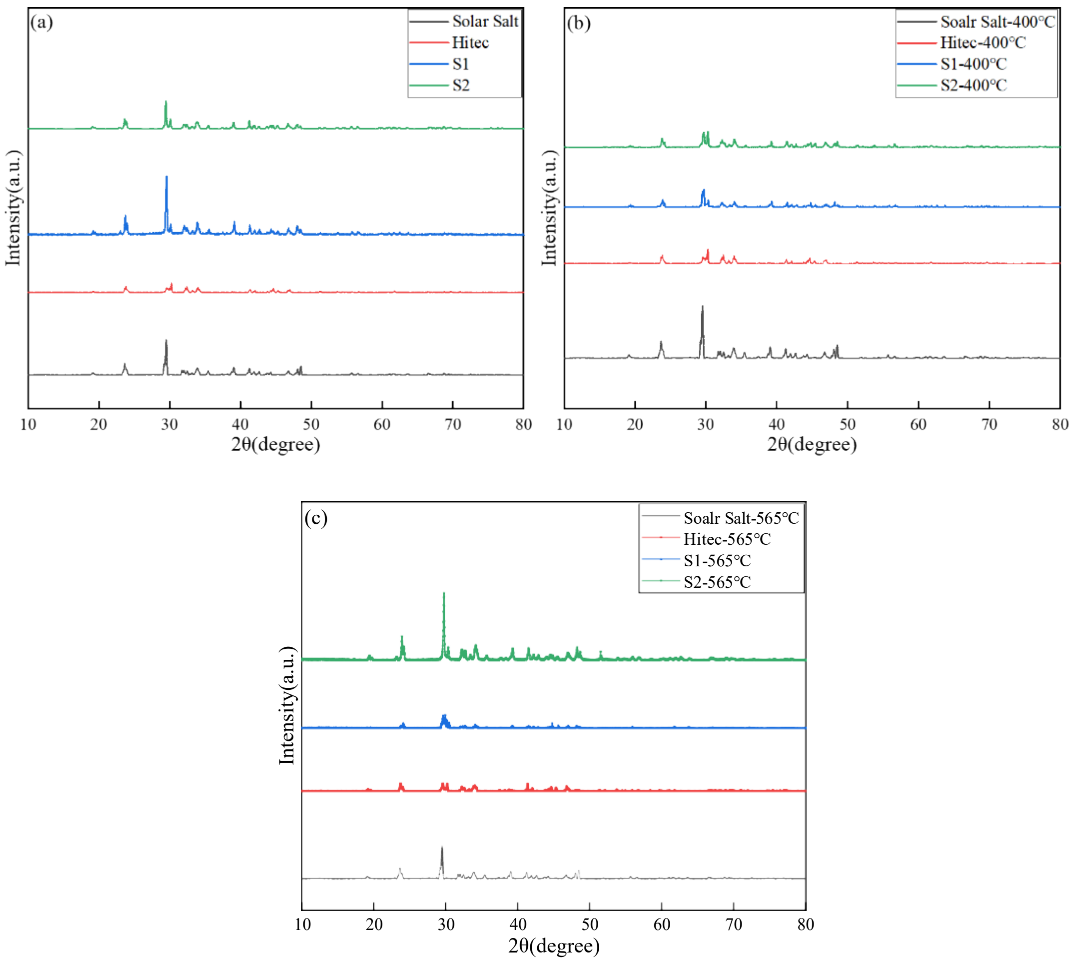

Figure 6: XRD of Solar Salt、Hitec、S1 and S2 in different constant conditions：a)25℃、b)400℃、c)565℃

4. CONCLUSION

In this study, the thermal stability of binary to quaternary nitrate molten salt systems was systematically investigated through a series of cyclic cold-heat cycle experiments and constant temperature thermal weight loss experiments. The samples, including Solar Salt, Hitec, S1, and S2, were comprehensively characterized using differential scanning calorimetry-thermogravimetric analysis (DSC-TG), X-ray diffraction (XRD), inductively coupled plasma emission spectroscopy (ICP-OES).

The DSC-TG analysis revealed that both S1 and S2 samples maintained their structural integrity better than Solar Salt and Hitec after multiple heating and cooling cycles at both 400°C and 565°C. The XRD patterns indicated that S1 and S2 experienced minimal structural changes, showcasing their superior thermal stability, especially at higher temperatures. The mass loss experiments demonstrated that S2 had the least thermal weight loss at 565°C, further confirming its excellent high-temperature stability.

Overall, the study concluded that the quaternary nitrate molten salts, particularly S1 and S2, exhibited enhanced thermal stability compared to binary and ternary systems. The reasonable matching and synergistic effects of multiple components effectively inhibited ion migration and decomposition, thereby providing outstanding thermal stability under high-temperature conditions. These findings suggest that multi-component nitrate molten salts, especially quaternary systems like S1 and S2, are promising candidates for use in high-temperature thermal energy storage applications, offering improved performance and reliability.

5. REFERENCE

Ali, H.M., Rehman, T., Arıcı, M., Said, Z., Duraković, B., Mohammed, H.I., Kumar, R., Rathod, M.K., Buyukdagli, O., Teggar, M., 2024. Advances in thermal energy storage: Fundamentals and applications. Prog. Energy Combust. Sci. 100, 101109. https://doi.org/10.1016/j.pecs.2023.101109

Ang, T.-Z., Salem, M., Kamarol, M., Das, H.S., Nazari, M.A., Prabaharan, N., 2022. A comprehensive study of renewable energy sources: Classifications, challenges and suggestions. Energy Strategy Rev. 43, 100939. https://doi.org/10.1016/j.esr.2022.100939

Basavapattan, D.R., n.d. Causes, Effects and Solutions for Depletion of Natural Resources: Theoretical Perspective.

Bonk, A., Braun, M., Bauer, T., 2022. Phase diagram, thermodynamic properties and long-term isothermal stability of quaternary molten nitrate salts for thermal energy storage. Sol. Energy 231, 1061–1071. https://doi.org/10.1016/j.solener.2021.12.020

D'Aguanno, B., Karthik, M., Grace, A.N., Floris, A., 2018. Thermostatic properties of nitrate molten salts and their solar and eutectic mixtures. Sci. Rep. 8, 10485. https://doi.org/10.1038/s41598-018-28641-1

Faizan, M., Alkaabi, A.K., Nie, B., Afgan, I., 2024. Thermal energy storage integration with nuclear power: A critical review. J. Energy Storage 96, 112577. https://doi.org/10.1016/j.est.2024.112577

Han, Y., Zhang, C., Wu, Y., Lu, Y., 2021. Investigation on thermal performance of quaternary nitrate-nitrite mixed salt and solar salt under thermal shock condition. Renew. Energy 175, 1041–1051. https://doi.org/10.1016/j.renene.2021.05.002

Holmes, G., Clemoes, J., Marriot, K., Wynne-Jones, S., 2022. The politics of the rural and relational values: Contested discourses of rural change and landscape futures in west wales. Geoforum 133, 153–164. https://doi.org/10.1016/j.geoforum.2022.05.014

Höök, M., Tang, X., 2013. Depletion of fossil fuels and anthropogenic climate change—A review. Energy Policy 52, 797–809. https://doi.org/10.1016/j.enpol.2012.10.046

Jones, M.W., Peters, G.P., Gasser, T., Andrew, R.M., Schwingshackl, C., Gütschow, J., Houghton, R.A., Friedlingstein, P., Pongratz, J., Le Quéré, C., 2023. National contributions to climate change due to historical emissions of carbondioxide, methane, and nitrous oxide since 1850. Sci. Data 10, 155. https://doi.org/10.1038/s41597-023-02041-1

Kallio, M.K.Y., n.d. Energy Security in the EU Solar Energy Strategy: Solar PV Supply Chain Vulnerability and China.

Kim, P., Eichel, D., Stuart, J., Graves, S., Berz, M., Zimmer, B., Reynolds, G., 2024. Effect of pre-heating on thermal stability of molten nitrate salt. J. Energy Storage 84, 110858. https://doi.org/10.1016/j.est.2024.110858

Lucas, H., Carbajo, R., Machiba, T., Zhukov, E., Cabeza, L.F., 2021. Improving Public Attitude towards Renewable Energy. Energies 14, 4521. https://doi.org/10.3390/en14154521

Ma, S., Yang, Q., Li, Y., Yan, C., Wang, X., 2024. A review on preparation, thermal transport properties, phase-change characteristics, and thermal stability of molten salts. J. Clean. Prod. 444, 141272. https://doi.org/10.1016/j.jclepro.2024.141272

Ofremu, G.O., Raimi, B.Y., Yusuf, S.O., Dziwornu, B.A., Nnabuife, S.G., Eze, A.M., Nnajiofor, C.A., 2024. Exploring the Relationship between Climate Change, Air Pollutants and Human Health: Impacts, Adaptation, and Mitigation Strategies. Green Energy Resour. 100074. https://doi.org/10.1016/j.gerr.2024.100074

Patange, S.R., Sutar, P.R., Yadav, G.D., 2024. New frontiers in thermal energy storage: An experimental analysis of thermophysical properties and thermal stability of a novel ternary chloride molten salt. Sol. Energy Mater. Sol. Cells 271, 112866. https://doi.org/10.1016/j.solmat.2024.112866

Rahnama, S., Khatibi, M., Maccarini, A., Farouq, M.M., Ahranjani, P.M., Fabrizio, E., Ferrara, M., Bogatu, D., Shinoda, J., Olesen, B.W., Kazanci, O.B., Bazdar, E., Nasiri, F., Zeng, C., Wei, X., Haghighat, F., Afshari, A., 2024. A methodical approach for the design of thermal energy storage systems in buildings: An eight-step methodology. Energy Storage 6, e600. https://doi.org/10.1002/est2.600

Roper, R., Harkema, M., Sabharwall, P., Riddle, C., Chisholm, B., Day, B., Marotta, P., 2022. Molten salt for advanced energy applications: A review. Ann. Nucl. Energy 169, 108924. https://doi.org/10.1016/j.anucene.2021.108924

Starke, A.R., Cardemil, J.M., Bonini, V.R.B., Escobar, R., Castro-Quijada, M., Videla, Á., 2024. Assessing the performance of novel molten salt mixtures on CSP applications. Appl. Energy 359, 122689. https://doi.org/10.1016/j.apenergy.2024.122689

Steinbrecher, J., Hanke, A., Braun, M., Bauer, T., Bonk, A., 2023. Stabilization of Solar Salt at 650 °C – Thermodynamics and practical implications for thermal energy storage systems. Sol. Energy Mater. Sol. Cells 258, 112411. https://doi.org/10.1016/j.solmat.2023.112411

Wang, J., Azam, W., 2024. Natural resource scarcity, fossil fuel energy consumption, and total greenhouse gas emissions in top emitting countries. Geosci. Front. 15, 101757. https://doi.org/10.1016/j.gsf.2023.101757

Wang, Q., Wu, C., Wang, X., Sun, S., Cui, D., Pan, S., Sheng, H., 2023. A review of eutectic salts as phase change energy storage materials in the context of concentrated solar power. Int. J. Heat Mass Transf. 205, 123904. https://doi.org/10.1016/j.ijheatmasstransfer.2023.123904

Wang, Yuanyuan, Lu, Y., Wang, Yanquan, Wu, Y., Gao, Q., Zhang, C., 2024. Investigation on thermal performance of quinary nitrate/nitrite mixed molten salts with low melting point for thermal energy storage. Sol. Energy Mater. Sol. Cells 270, 112803. https://doi.org/10.1016/j.solmat.2024.112803

Wörman, A., Pechlivanidis, I., Mewes, D., Riml, J., Bertacchi Uvo, C., 2024. Spatiotemporal management of solar, wind and hydropower across continental Europe. Commun. Eng. 3, 3. https://doi.org/10.1038/s44172-023-00155-3

Wu, C., Zhang, X.-P., Sterling, M., 2022a. Solar power generation intermittency and aggregation. Sci. Rep. 12, 1363. https://doi.org/10.1038/s41598-022-05247-2

Wu, C., Zhang, X.-P., Sterling, M., 2022b. Solar power generation intermittency and aggregation. Sci. Rep. 12, 1363. https://doi.org/10.1038/s41598-022-05247-2

Zhang, C., Han, Y., Wu, Y., Lu, Y., 2021. Comparative study on high temperature thermal stability of quaternary nitrate-nitrite mixed salt and Solar salt. Sol. Energy Mater. Sol. Cells 230, 111197. https://doi.org/10.1016/j.solmat.2021.111197

Zhang, S., Chen, W., 2022. China's Energy Transition Pathway in a Carbon Neutral Vision. Engineering 14, 64–76. https://doi.org/10.1016/j.eng.2021.09.004

Zhao, Q.-G., Hu, C.-X., Liu, S.-J., Guo, H., Wu, Y.-T., 2017. The thermal conductivity of molten NaNO3, KNO3, and their mixtures. Energy Procedia 143, 774–779. https://doi.org/10.1016/j.egypro.2017.12.761

ZHAO Bozen, DING Jing, WEI Xiaolan, LIU Bin, LU Jianfeng, WANG Weilong. 2019. LiNO3-NaNO3-KNO3.Design and thermal stability study of ternary molten salt materials. Journal of Chemical Engineering.70, 2083–2091.

#357: Comprehensive energy utilization study of novel air-cooled BIPVT Modules in low-carbon buildings

A case study of a laboratory building in Tianjin

Chang LI[1], Zhenhua QUAN[1], Yuechao DENG[3], Yubo WANG[1], Yuchen ZHANG[1], Yaohua ZHAO[1,2]

[1] Beijing Key Laboratory of Green Built Environment and Energy Efficient Technology, Beijing University of Technology, Beijing 100124, China
[2] Zibo Boienergy Science and Technology Co., Ltd., Zibo 255200, Shandong Province, China
[3] China Academy of Building Research, Beijing 100013, China

Abstract: Building integrated photovoltaic thermal (BIPVT) technology combines solar photovoltaic modules with the building envelope, which can enable the modules to generate electricity and heat, providing an effective technical way to reduce building energy consumption, and it is a very promising low-carbon energy-saving technology for application. In this article, the author proposed to apply air-cooled BIPVT modules based on micro-heat pipe arrays to the building envelope. Taking a certain experimental building in Tianjin as a demonstration application object, a mathematical model of the module and an energy consumption simulation model of the experimental building were established. The surface temperature, power generation, and heat collection power of the module under different conditions were analysed. The results show that, under typical winter conditions, the total solar energy utilization efficiency is 35.7%, and the comprehensive performance efficiency is 55.28%. The maximum heat collection of the module can meet 24.81% of the fresh air heating demand. Under typical summer conditions, the presence of cooling fans significantly increases the power generation capacity of BIPVT modules, with a total increase of 6.33 W/m² of power generation on that day compared to the case without the cooling fan (natural convection). The air-cooled BIPV/T module has a significantly higher instantaneous power generation efficiency compared to conventional PVT modules, with an average daily solar power generation efficiency of 10.7%. An analysis of the energy-saving and emission reduction benefits of the BIPV/T building indicates that the annual power generation of the module is 7679.32kWh, reducing the consumption of standard coal by 5648.14kg. In the whole winter, the heat collection of the BIPVT module bears a fresh air load of 8866.48kW, which means that the modules can reduce carbon dioxide emissions by 6521.3kg compared to electric heating. Consequently, the building diminishes its CO_2 emissions by a collective 12,169.44 kg over the span of a year. The results showed that applying air-cooled BIPVT modules based on micro-heat pipe arrays to a building can not only satisfy the building's multiple energy demands, but also reduce the building's consumption of conventional energy, which has good energy-saving, environmental protection and economic benefits.

Keywords: Building Integrated Photovoltaic-Thermal; Low-Carbon Buildings; Heating Supply; Simulation Models; Solar Utilization

1. INTRODUCTION

In developed countries, buildings consume 30%-40% of primary energy annually, compared to about 15%-25% in developing countries. Energy demand in buildings continues to grow worldwide but fossil fuels are finite reserves. Impacts of peak oil will be perceived soon or later in the next decades. The scale of the challenge in reducing fossil fuel dependency in the built environment is vast and will require a dramatic development in green low-carbon building technology. The application of green low-carbon building technology in the construction industry has gradually been promoted in recent years.

As one of the common renewable energy sources, solar energy has been widely utilised in recent years. Building-integrated photovoltaic-thermal (BIPVT) technology can well combine solar energy with buildings. The use of BIPVT modules as part of the building wall structure not only makes efficient use of the heat and electricity produced by the modules, but also reduces the consumption of building materials for the building envelope, making it a very promising low-carbon and energy-saving technology.

An increase in temperature dramatically decreases the performance of the photovoltaic (PV) panel, therefore, the heat pipe is used to reduce the PV temperature and extract heat from PV back surface. Various researchers have worked on different types of heat pipes based PVT systems. In order to solve the non-uniform cooling of solar PV cells and control the operating temperature of solar PV cells conveniently, Wu et al. (2011) proposed a heat pipe photovoltaic/thermal (PV/T) hybrid system, which is described by selecting a wick heat pipe to absorb isothermally the excessive heat from solar PV cells. Results show that the overall thermal, electrical and exergy efficiencies of the heat pipe PV/T hybrid system corresponding to 63.65%, 8.45% and 10.26%, respectively can be achieved under the operating conditions presented in this paper. Pei et al. (2011) designed and constructed a novel heat-pipe photovoltaic/thermal system, which can simultaneously supply electrical and thermal energy. In addition, when compared with the traditional water-type photovoltaic/thermal system, this system can be used in cold regions without freezing. Results indicated that the daily thermal and electrical efficiencies of the heat-pipe photovoltaic/thermal system were 41.9% and 9.4%, respectively, whilethe average heat and electrical gains were 276.9 and 62.3 W/m^2, respectively. Deng at al. (2015) presented a novel method of dissipating solar photovoltaic heat based on the technology of micro-heat-pipe array and the utilization of photovoltaic- cell waste heat. Test results showed that the system met the demand of power supply on sunny days and the demand of hot water between March and November, except in cloudy days. Hou et al. (2016) developed a micro heat pipe array (MHPA) technology to regulate the working temperature by retrofitting the PV panel into the PV-thermal (MHPA-PV/T) collector. Results showed that the electrical efficiency was relatively stable at approximately 13% and the total efficiency of the MHPA-PV/T collector for the entire year fluctuated between 30% and 50%. These experimental results can providebasis and reference for practical applications of the system.

Plenty of experimental and numerical studies have been performed on BIPVT. Yang, Burnett and Ji (2000) compared the cooling load of buildings with PV-walls in Beijing, Shanghai and Hong Kong, and found that the cooling load in the case of BIPV wall was decreased by 33–55% compared with that of a conventional building. Also, PV area with stronger solar radiation had a greater impact in reducing cooling loads. Jeong et al. (2012) evaluated the heating performance of heating system combined with PVT collectors that on integrated building roof. From the experimental results, the solar fraction of the heating system with BIPVT was 15% for the lab room. It was also found that the heating energy for the house can be reduced by 47%, as the heat gained from BIPVT system pre-heated the water used for heating system. Annamaria et al. (2016) developed dynamic simulations models of different BIPVT system layouts. By varying the weather location and the building-plant configuration, the adoption of BIPVT panels produces a decrease in the primary energy demands from 67% to 89%. Piratheepan and Anderson (2017) developed a combined optical and thermal model to describe the performance of a façade integrated BIPVT solar concentrator system and subsequently was validated with a physical prototype. Using the validated model, it was shown that key parameters such as tube spacing, and thermal conductivity between the solar cell and the absorber have a significant effect on overall efficiency. It is suggested that façade integrated BIPVT solar concentrator systems would serve as a complement to roof mounted photovoltaic systems, and that this may be a step towards net zero energy buildings. Ma et al. (2021) used the heat generated by BIPVT system to preheat incoming fresh air in HRV (heat recovery ventilation) in order to reduce it defrost cycle for a 120m^2 house located in Iqaluit, NU, Canada through simulations. The results showed that the outlet air of a BIPVT façade installation could be 14.8 ◦C higher than outdoor air on a clear sky winter day and that the defrost cycle could be reduced by 13%.

The aforementioned research content fully demonstrates that the application of BIPVT technology to buildings can, to some extent, meet the thermal, cooling, and electrical needs of buildings, thereby significantly improving energy utilization and carbon reduction performance. However, current research is still lacking in significantly enhancing the power generation performance of the modules, reducing carbon emissions, and increasing the proportion of fresh air load handled by the system in winter.

Based on the previous work, the authors applied the MHPA, a highly efficient heat conductive element, to the BIPVT module, serving as the building envelope. Utilizing air cooling, the waste heat generated by the photovoltaic power generation of solar modules is efficiently utilized in winter and dissipated in summer, thereby enhancing power generation efficiency. This novel PVT building-integrated module was applied to an experimental building in Tianjin as part of the building envelope. A mathematical model of the module was established, and a simulation model of the experimental building was constructed. The study examined the backboard temperature, power generation, heat collection and dissipation power, and their influencing factors of the BIPVT module under winter and summer conditions. The low-carbon energy-saving characteristics of the building were analysed. This research provides theoretical support and practical guidance for the application of air-cooled PVT building-integrated modules in the field of low-carbon buildings.

2. BUILDING-INTEGRATED PHOTOVOLTAIC-THERMAL MODULES AND LOW-CARBON BUILDINGS

2.1. Building-integrated photovoltaic-thermal Modules

The air-cooled building-integrated photovoltaic-thermal (BIPVT) module can be used as a building facade enclosure. It consists of a cadmium telluride PV module, a micro heat pipe array, a finned air duct, and an insulation layer, as shown in Figure 1.

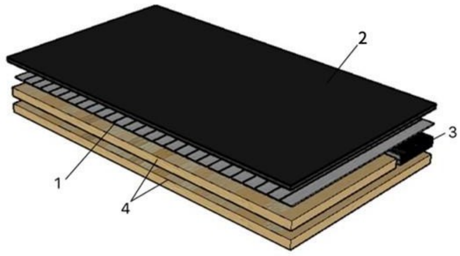

1. Micro heat pipe array; 2. Photovoltaic module; 3. Finned duct; 4. Insulation layer.

Figure 1: Air-Cooled BIPVT modules structure

In this study, the cadmium telluride PV module model used is ASP-S1-100, with a peak power output of 100W. The dimensions of a single photovoltaic module are 1200mm × 600mm (width × height), with an open-circuit voltage of 123.5V and a short-circuit current of 1.24A. Several micro heat pipe arrays are attached to the back of the PV module using thermally conductive silicone. These arrays consist of micro-channel heat pipes with micro-fin structures. The micro heat pipe array is a highly efficient flat heat pipe with a flat shape and large surface area, allowing it to adhere closely to the heat exchange surface and reduce contact thermal resistance. While the photovoltaic module generates electricity during the day, solar radiation heat is rapidly transferred from the evaporator section at the bottom of the high-efficiency micro heat pipe array to the condenser section. At the bottom of the condenser section, thermally conductive silicone attaches a finned heat collection air duct to collect the heat dissipated by the photovoltaic module. Phenolic insulation boards are laid on the back of the heat pipe evaporator section and the heat collection air duct to reduce heat loss while ensuring structural flatness.

The heat flow direction in the air-cooled BIPVT modules is as follows: a portion of the solar radiation incident on the PV modules is used for power generation, while another portion generates heat. A small amount of this heat is conducted upwards to the outer surface of the tempered glass, where it is dissipated by convection with the outdoor air and by radiation to the sky. The majority of the heat is conducted downwards to the micro-heat pipe array on the back of the module. The working fluid in the heat pipe transfers the absorbed heat from the evaporation section to the condensation section via evaporation and condensation. The heat at the condensation end of the heat pipe is conducted to the outer wall of the finned air duct and the first layer of fins inside, where it is transferred to the first layer of air by convection. The heat from the first layer of air and fins is then transferred to the wall of the middle layer, which in turn transfers the heat tothe second layer of fins and air. Finally, the heat from the second layer of air and fins is transferred to the bottom layer of the metal air duct wall, which conducts the heat to the adjacent insulation layer. Some heat is still conducted to the insulation layer while the heat pipe's evaporation section absorbs heat. The outer surface of the insulation layer exchanges heat with the indoor air through convection.

2.2. Overview of the Low-Carbon Building

The air-cooled BIPVT modules were applied to an experimental building in Tianjin, China, as shown in Figure 2. The building has a total footprint of approximately 5,800m^2, and an air-conditioned and heated area of about 12,000m^2. The building comprises 3 floors with a south-facing facade divided into east and west sections. On the southern façade of the building, each air-cooled BIPVT unit consists of three air-cooled BIPVT modules. Each floor on both sides of the building houses 5 air-cooled BIPVT units, totalling 30 such units on the south facade and 90 modules overall. Fifteen air-cooled BIPVT modules on each side of the south facade are connected in series per floor, resulting in a total of 6 parallel groups throughout the building.

Figure 24: Aerial view of the experimental building

Each side of the south facade features a horizontal fresh air supply duct per floor, and there are vertical fresh air mains on both east and west sides. The fresh air supply ducts on both sides pass through the air passages of each air-cooled BIPVT module, collecting the fresh air treated by these modules into the two fresh air mains on the east and west sides. These mains enter the building at the top of the second floor and merge into a single main duct, which finally connects to the HVAC room on the second floor, integrating with the laboratory's fresh air pipeline. In winter, the modules use air cooling to preheat the fresh air with the waste heat generated by the photovoltaic power generation, thereby reducing the building's primary energy consumption. In summer, the modules dissipate heat through air cooling to improve power generation efficiency and extend the lifespan of the solar panels. The electricity generated throughout the year is used to meet the building's energy needs, thus reducing its carbon emissions.

3. MATHEMATICAL MODEL OF THE MODULES AND BUILDING SIMULATION MODEL

3.1. Module Model Assumptions and Simplifications

Based on the specific characteristics of each layer, the following assumptions are made:

(1) The heat storage effect of the PV module cannot be ignored; thus, transient terms are added to each solid layer.

(2) Each layer is considered to have a uniform distribution due to its small thickness, and the temperature within each layer is calculated uniformly. Therefore, each layer is modelled as a one-dimensional heat transfer model.

(3) The surface area of the BIPVT modules is much larger than their side area, so lateral heat loss is neglected.

(4) Contact thermal resistance between layers and heat loss in the pipes are ignored.

The BIPVT modules on the facade wall are connected in series in groups of three, with thirty groups in parallel. Therefore, in the calculations, the outlet temperature of the first module is used as the inlet temperature for the second module to determine the series-connected modules' heat collection temperature. Each parallel branch has the same thermal process, so individual calculations for each branch are not necessary.

The mathematical model of the main part of the BIPVT module is as follows:

Equation 22: Front Glass Cover Layer. $C_{pg}M_g\frac{(T_{g1}-T_{g1s})}{dt}=Ga_{bg}A_g+h_{ga}(T-T_{g1})A_g+h_{gsky}(T_{sky}-T_{g1})A_g+h_{gp}(T_p-T_{g1})A_g$

Where:

- M_g = the mass of the glass cover plate (kg)
- C_{pg}= specific heat capacity of glass covers (J/(kg·K))
- T_{g1}= temperature of the front glass cover layer (K)
- T_{g1s}= temperature of the front glass cover layer at the last moment (K)
- G = solar intensity (W/m^2)
- a_{bg} = absorption rate of glass cover
- A_g = surface area of glass cover layer (m^2)
- h_{ga} = convective heat transfer coefficient between the glass cover layer and the surrounding environment (W/m^2·K)
- T = the ambient temperature (K)
- h_{gsky} = the radiative heat transfer coefficient between the glass cover layer and the sky (W/m^2·K)
- T_{sky} = the sky temperature (K)
- h_{gp} = heat transfer coefficient between the glass cover layer and the PV layer (W/m^2·K)
- T_p = temperature of the PV layer (K)

Equation 2: PV Layer. $C_{pp}M_p\frac{(T_p-T_{ps})}{dt}=Gt_{rg}a_{bp}A_p+h_{gp}(T_{g1}-T_p)A_p+h_{gp}(T_{g2}-T_p)A_p-P$

Where:

- M_p =the mass of the PV layer (kg)
- C_{pp}= specific heat capacity of the PV layer (J/(kg·K))
- T_{ps}= temperature of the PV layer at the last moment (K)
- t_{rg} = transmittance of the glass cover layer
- a_{bp} = absorption rate of the PV layer
- A_p = surface area of the PV layer (m^2)
- T_{g2}= temperature of the back glass cover layer (K)
- P = PV module power generation (W)

Equation 3: Flat plate micro heat pipe layer.

$$C_{php}M_{hpe}\frac{(T_{hpe}-T_{hpes})}{dt}=h_{ghpe}(T_{g2}-T_{hpe})A_{hpe}+h_{bhpe}(T_{b1}-T_{hpe})A_{hpe}+h_{ce}(T_{hpc}-T_{hpe})A_{ec}$$

Where:

- C_{php}= specific heat capacity of the flat plate micro heat pipe layer (J/(kg·K))
- M_{hpe} = the mass of the evaporating section of the flat plate micro heat pipe layer (kg)
- h_{bhpe} = heat transfer coefficient between the evaporating section of the flat plate micro heat pipe layer and the insulation layer (W/(m^2·K))
- T_{hpe}= temperature of the evaporating section of the flat plate micro heat pipe layer (K)
- T_{hpes}= temperature of the evaporating section of the flat plate micro heat pipe layer at the last moment (K)
- h_{ghpe} = heat transfer coefficient between the evaporating section of the flat plate micro heat pipe layer and the back glass cover layer (W/(m^2·K))
- A_{hpe} = surface area of the evaporating section of the flat plate micro heat pipe layer (m^2)
- T_{hpc}= temperature of the condensing section of the flat plate micro heat pipe layer (K)
- T_{b1} = temperature of the insulation layer at the back of the evaporation section (K)
- h_{ce} = heat transfer coefficient between the evaporating and condensing sections of the microtubular layer (W/(m^2·K))
- A_{ec} = cross-sectional area of heat pipe layer (m^2)

Equation 4: Finned air ducts.

$$C_{pc}M_F\frac{(T_{F1}-T_{F1s})}{dt}=h_{F1hpc}(T_{hpc}-T_{F1})A_{hpc}+h_a((T_{in1}+T_{out1})/2-T_{F1})A_F+h_{Ff}(T_{fin1}-T_{F1})A_{Ff}$$

Where:

- C_{pc} = specific heat capacity of aluminium metal (J/(kg·K))
- M_F = the mass of the finned duct substrate (kg)
- T_{F1} = temperature of the upper substrate layer of the duct (K)
- T_{F1s}= temperature of the upper substrate layer of the duct (K)
- h_{F1hpc} =heat transfer coefficient between the condensing section of the flat plate micro heat pipe layer and the upper substrate layer of the duct (W/(m^2·K))
- A_{hpc} = surface area of the condensing section of the flat plate micro heat pipe layer (m^2)
- h_a =heat transfer coefficient between finned duct substrate and duct air (W/(m^2·K))
- T_{in1} = inlet temperature of duct air (K)
- T_{out1} = outlet temperature of duct air (K)
- T_{fin1} = temperature of the fin (K)
- A_F = heat exchange area between air and duct substrate (m^2)
- h_{Ff} = heat transfer coefficient between finned duct substrate and fins (W/(m^2·K))

3.2. Building Trnsys Simulation Model

Trnsys is a transient system simulation program notable for its modular analysis approach. When modelling a system, it is divided into several modules, each performing a specific function. Trnsys has a substantial number of functional modules available for direct use, and special modules can be added by rewriting code or using MATLAB, making it highly suitable for the energy system modelling proposed in this study.

Elements needed in the building simulation system include local meteorological parameters, BIPVT modules based on micro-heat pipe arrays, fans, time control modules, temperature difference control modules, and the building itself. Table 1 presents the corresponding modules in Trnsys.

Table 1: Corresponding Moules in Trnsys

Module	Function
Type 56	Simulates building thermal behaviours, including convective and radiative heat transfer on the inner wall surfaces, indoor ventilation, HVAC energy consumption, and load simulation.
Type 155	Simulates the thermal and electrical performance of BIPVT walls and can read MATLAB-written BIPVT module model files.
Type 15	Reads typical meteorological year data, including ambient temperature, wind speed, and irradiation intensity.
Type 77	Simulates underground soil temperature, providing ground boundary conditions for the building.
Type 65	Plots output result curves.
Type 117	Air heater.
Type 165	Control module for start-stop control.
Type 146	Duct fan.
Equation	Unit conversion.

The above modules are combined to establish the BIPVT system model shown in the Figure 3. The parameters for the BIPVT modules, fans, and buildings are consistent with those used in the experiments. Figure 4 shows the system connection diagram.

The operation of the fan is controlled by the time module Type14, starting from 6:00 to 18:00 each day, and shutting down at other times. The number of series and parallel connections in the BIPVT modules is set, and the total heat and power output under multiple series-parallel configurations is obtained through calculations. During the operating period from 6:00 to 18:00, the outlet temperature of the BIPVT modules is further checked to determine if it meets the air supply requirements. If the outlet temperature is below 18°C, a start signal is output; if it exceeds 20°C, a stop signal is output. This model can calculate the cooling load, heating load, and fresh air load of a building under different outdoor temperature and solar radiation conditions. It also determines the back panel temperature, outlet temperature of the modules, heat dissipation in summer, heat collection in winter, supplemental heat for fresh air, and the electricity generation of the modules.

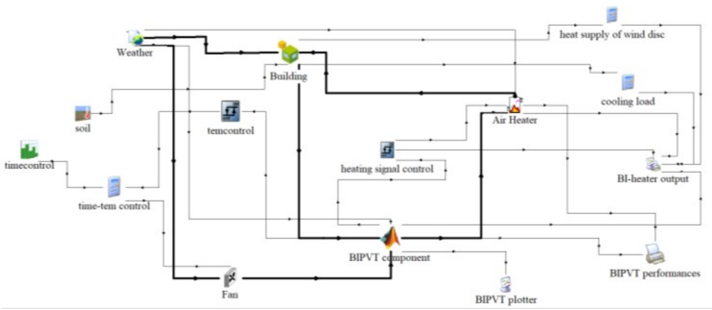

Figure 3: Trnsys simulation model

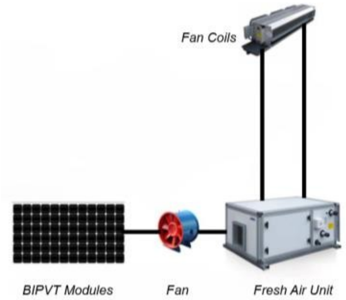

Figure 4: System connection diagram

4. EVALUATION METRICS

Equation 5: Instantaneous Power Generation of Solar Modules.

$$P = UI$$

Where:

- P = instantaneous power generation of the photovoltaic system (W)
- U = instantaneous voltage (V)
- I = instantaneous current (A)

Equation 6: Instantaneous Solar Power Generation Efficiency.

$$\eta_e = \frac{P}{AG} \times 100\%$$

Where:

- η_e = instantaneous power generation efficiency
- A = total illuminated area of the module (m^2)
- G = solar radiation intensity (W/m^2)

Equation 7: Instantaneous Heat Collection of Solar Collectors or Instantaneous Dissipation of Heat.

$$Q = c_p m_s \Delta T$$

Where:

- Q = instantaneous heat collection(winter) or dissipation of heat(summer) (W)
- c_p = specific heat capacity of the working fluid (J/(kg•℃))
- m_s = mass flow rate (kg/s)
- ΔT = temperature difference between the inlet and outlet of the working fluid (℃)

Equation 8: Instantaneous Solar Heat Collection Efficiency.

$$\eta_{th} = \frac{Q}{AG} \times 100\%$$

Where:

- η_{th} = instantaneous solar heat collection efficiency

The total solar utilization efficiency, as one of the evaluation metrics for solar power generation and heat collection modules, can be expressed as the sum of power generation efficiency and heat collection efficiency:

Equation 9: Total Solar Utilization Efficiency. $$\eta_{tot} = \eta_e + \eta_{th}$$

Where:

- η_{tot} = total solar utilization efficiency

The comprehensive performance efficiency, as another evaluation metric for solar power generation and heat collection modules, reflects both the quantity and quality of solar energy conversion:

Equation 10: Comprehensive Performance Efficiency. $$\eta_f = \frac{\eta_e}{\eta_p} + \eta_{th}$$

Where:

- η_f = comprehensive performance efficiency
- η_p = conventional power plant efficiency, typically taken as 38%

5. ANALYSIS AND DISCUSSION

5.1. Performance Analysis of Modules on a Typical Winter Day

The performance of the BIPVT system was analysed on February 10, 2024, during the winter.

Meteorological parameters on the simulated day are shown in the Figure 5. The simulated period was from 10:00 to 17:00. During this period, the average solar irradiance on the south wall was 274.29 W/m^2, the average outdoor temperature was -0.13℃, and the average wind speed was 1.23 m/s.

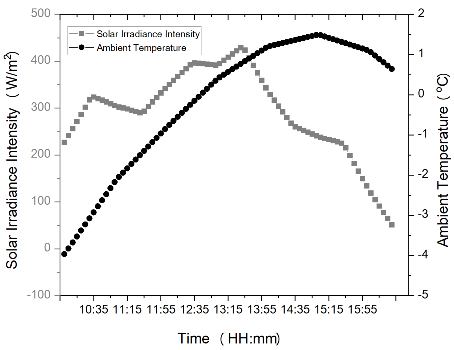

Figure 25: Solar irradiance intensity and ambient temperature on a winter day

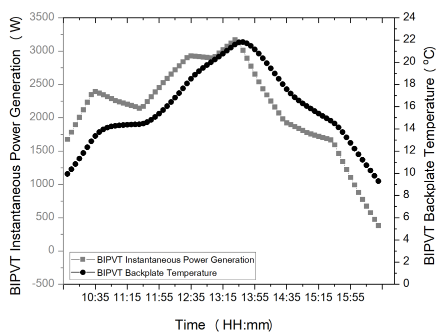

Figure 26: BIPVT instantaneous power generation and backplate temperature on a winter day

The instantaneous power generation and backplate temperature of the BIPVT modules during the simulation period are shown in Figure 6. The power output curve of the air-cooled cadmium telluride BIPVT modules follows a trend similar to the solar irradiance curve. However, due to the influences of backplate temperature, ambient temperature, and other factors, the efficiency curve does not exactly match the solar irradiance. During the simulation period, the maximum system power output was 3172.37 W, and the total power generation of the BIPVT modules was 16.76 kWh.

Between 10:00 and 13:55, the backplate temperature of the modules increased with the rise in solar irradiance and ambient temperature. Since the cooling medium for the modules is ambient air, the backplate temperature is also affected by the ambient temperature. The average backplate temperature of the BIPVT modules during the entire simulation period was 15.42℃.

The instantaneous heat collection efficiency of the air-cooled cadmium telluride BIPVT modules during the simulation period is shown in Figure 7.The heat collection efficiency of the modules is influenced by solar irradiance, ambient temperature, and wind speed. Throughout the period, the daily average solar heat collection efficiency of the air-cooled cadmium telluride BIPVT modules was 23.7%, the maximum heat collection efficiency was 32.19%, the total solar utilization efficiency was 35.7%, and the comprehensive performance efficiency was 55.28%.

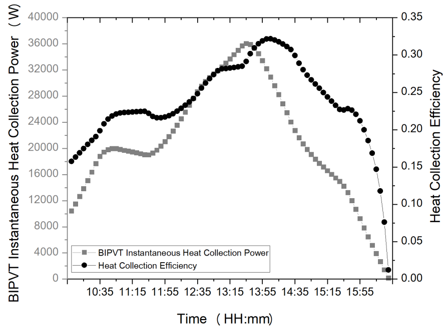

Figure 27: BIPVT instantaneous heat collection power and heat collection efficiency on a winter day

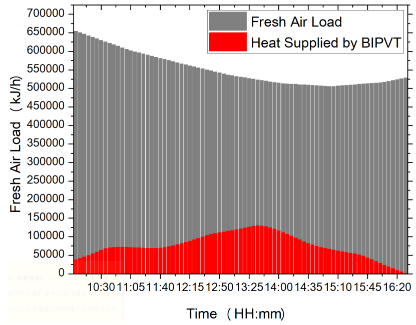

Figure 28: BIPVT modules in supporting fresh air heating load on a winter day

Figure 8 shows the fresh air load borne by the heat collected by the BIPVT module during the typical day of the winter operating condition. The results demonstrate that during the test period, the heat collected by the module can satisfy up to 24.81% of the fresh air load, which at this moment in time is 523250kJ. In the whole winter, the heat collection of the BIPVT module bears a fresh air load of 8866.48kW. The main output period of the BIPVT system is during midday when solar radiation is the strongest, which also has a certain effect on improving the indoor temperature of the room.

5.2. Performance Analysis of Modules on a Typical Summer Day

The performance of the BIPVT system was analysed on July 22, 2024, during the summer. The simulated period was from 10:00 to 17:00. The solar irradiance and the ambient temperature are shown in Figure 9. The average solar horizontal irradiance was 321.92 W/m^2, the average ambient temperature was 32.25℃, and the average wind speed was 6.26 m/s.

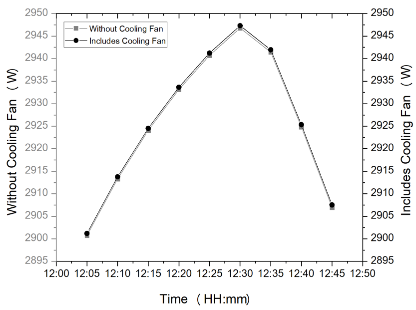

Figure 29: Comparison of instantaneous power generation of bipvt modules with and without cooling fans under summer operating conditions

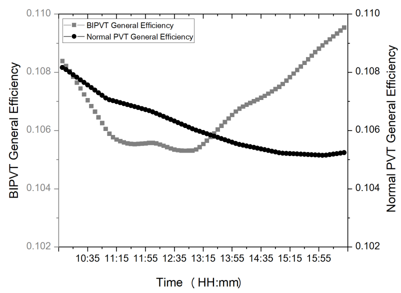

Figure 30: Comparison of instantaneous electrical generation efficiency between bipvt and conventional pvt modules under summer conditions

To compare the performance advantages of the air-cooled BIPVT module, the author replaced the air-cooled BIPVT module in the model with conventional module (type 563). The module is used to model an unglazed solar collector that serves a dual purpose: to generate electricity from embedded photovoltaic (PV) cells and to provide heat to the fluid that is connected via a pipe to an absorber plate located below the PV cells. The waste heat removed from the fluid flow serves two purposes: 1) to cool the PV cells to improve power conversion efficiency, and 2) to provide a heat source for many possible low temperature applications.

Through simulation, the instantaneous power generation efficiency of the air-cooled BIPV/T module was compared with that of a conventional PVT module, as shown in Figure 12. The power generation efficiency of the modules is influenced by both solar irradiance intensity and the temperature of the back plate. The air-cooled BIPV/T module exhibits greater sensitivity compared to the conventional PVT module, but its overall power generation efficiency is significantly higher. The daily average solar power generation efficiency of the air-cooled BIPV/T module is 10.7%.

5.3. Carbon Reduction Performance Analysis

According to *Design Standard for New Energy Application of Buildings*, the provincial average carbon dioxide emission factor for electricity of Tianjin is 0.7355kgCO_2/kWh in 2024. According to the above simulation analysis, the annual power generation of this BIPVT building is 7679.32 kWh, thus reducing the consumption of standard coal by 5648.14kg. In winter, the heat collection of the BIPVT module bears a fresh air load of 8866.48kW, which means that the modules can reduce carbon dioxide emissions by 6521.3kg compared to electric heating. Consequently, the building diminishes its CO_2 emissions by a collective 12,169.44 kg over the span of a year.

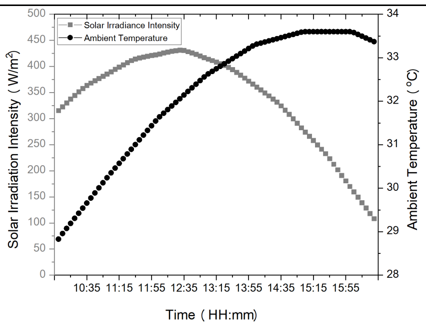

Figure 31: Solar irradiation intensity and ambient temperature on a summer day

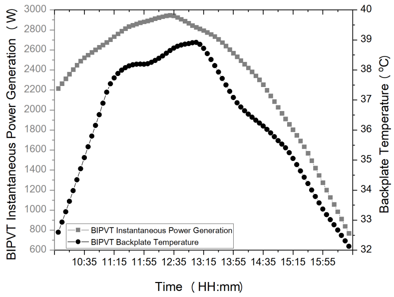

Figure 32: BIPVT instantaneous power generation and backplate temperature on a summer day

The instantaneous power generation and backplate temperature of the air-cooled cadmium telluride BIPVT modules during the simulation period are shown in Figure 10. During the simulation, the instantaneous power generation curve of the modules followed a trend similar to the solar irradiance at the respective angle. Before 12:35, the backplate temperature of the modules increased with the rise in solar irradiance; afterward, as solar irradiance decreased, both the power output and backplate temperature of the modules declined. In this case, the reduction in backplate temperature of the module is occurring at a slower rate than anticipated, which can be attributed to the thermal inertia of the material. Throughout the simulation period, the average backplate temperature of the BIPVT modules was 35.98℃, and the total power generation was 21.12 kWh.

By simulating the power generation of air-cooled BIPV/T modules with and without cooling fans (natural convection), a comparison was made, and the results are shown in Figure 11. From the figure, it can be seen that in summer, the presence of cooling fans increased the power generation of the BIPV/T modules to a certain extent. During the typical summer day, the total power generation without a cooling fan was 20.71 kWh, compared to 21.12 kWh with the cooling fan. This equates to a total increase of 6.33 W/m² of power generation on that day. This is because the fans reduced the back panel temperature of the BIPV/T modules through cooling, thereby enhancing their power generation capability.

6. CONCLUSION

In this article, the author discussed the application of air-cooled BIPVT modules based on micro heat pipe arrays in actual buildings. The panel surface temperature, power generation, and heat collection under different operating conditions are analysed. Finally, the author assessed the energy-saving and emission-reduction characteristics of the building based on the power generation of the modules and the fresh air load borne by the heat collection in winter. The author has provided theoretical support and practical guidance for the application of air-cooled photovoltaic-thermal integrated building modules in the field of low-carbon buildings. The conclusions of this study are as follows:

(1) During a typical winter day, the daily average solar heat collection efficiency of the air-cooled cadmium telluride BIPVT modules was 23.7%, the maximum heat collection efficiency was 32.19%, the total solar energy utilization efficiency is 35.7%, and the comprehensive performance efficiency is 55.28%. In the winter months, the BIPVT modules have a heat gain of up to 24.81% of the fresh air heat requirement.

(2) On a typical summer day, simulations comparing the power generation of air-cooled cadmium telluride BIPV/T modules with and without cooling fans (natural convection) show that the presence of cooling fans significantly increases the power generation capacity of BIPVT modules, with a total increase of 6.33 W/m² of power generation on that day. Furthermore, simulations comparing the instantaneous power generation efficiency of air-cooled cadmium telluride BIPV/T modules and ordinary PVT modules indicate that the air-cooled cadmium telluride BIPV/T modules are more sensitive but have a significantly higher overall power generation efficiency than ordinary PVT modules. The daily average solar power generation efficiency of the air-cooled cadmium telluride BIPV/T is 10.7%.

(3) Taking this building as an example, the annual power generation is 7679.32 kWh, thus reducing the consumption of standard coal by 5648.14kg. In the whole winter, the heat collection of the BIPVT module bears a fresh air load of 8866.48kW, which means that the modules can reduce carbon dioxide emissions by 6521.3kg compared to elec tric heating. Consequently, the building diminishes its CO_2 emissions by a collective 12,169.44 kg over the span of a year.

7. ACKNOWLEDGEMENT

This study was supported by a grant from the National Key R&D Program of China (No. 2022YFE0118500).

8. REFERENCES

Buonomano, A., Calise, F., Palombo, A. and Vicidomini, M. (2016) ‘BIPVT systems for residential applications: An energy and economic analysis for European climates’, Applied Energy, 184, pp. 1411-1431.

Deng, Y.C., Quan, Z.H., Zhao, Y.H., Wang, L.C. and Liu, Z.L. (2015) ‘Experimental research on the performance of household-type photovoltaic–thermal system based on micro-heat-pipe array in Beijing’, Energy Conversion and Management, 106, pp. 1039-1047.

Pei, G., Fu, H.D., Zhang, T. and Ji, J. (2011) 'A numerical and experimental study on a heat pipe PV/T system', Solar Energy, (5), pp. 911-921.

Hou, L.S., Quan, Z.H., Zhao, Y.H., Wang, L.C. and Wang, G. (2016) 'An experimental and simulative study on a novel photovoltaic-thermal collector with micro heat pipe array (MHPA-PV/T)', Energy Buildings, 124, pp. 60-69.

Ibrahim, A., Fudholi, A., Sopian, K., Othman, M.Y. and Ruslan, M.H. (2014) 'Efficiencies and improvement potential of building integrated photovoltaic thermal (BIPVT) system', Energy Conversion and Management, 77, pp. 527-534.

Jeong, Seon-Ok, Kim, Jin-Hee, Kim, Ji-Seong... and Jun-Tae (2012) 'The Heating Performance Evaluation of Heating System with Building-Integrated Photovoltaic/Thermal Collectors', Journal of the Korean Solar Energy Society, (6), pp. 113-119.

Li, X.T., Wu, W. and Chuck, W.F.Yu. (2015) 'Energy demand for hot water supply for indoor environments: Problems and perspectives', Indoor and Built Environment, (1), pp. 5-10.

Ma, L., Ge, H., Wang, L. and Wang, L.Z. (2021) 'Optimization of passive solar design and integration of building integrated photovoltaic/thermal (BIPV/T) system in northern housing', Building Simulation, (5), pp. 1-20.

Piratheepan, M. and Anderson, T.N. (2017) 'Performance of a building integrated photovoltaic/thermal concentrator for facade applications', Solar Energy, 153, pp. 562-573.

Wu, S.Y., Zhang, Q.L., Xiao, L. and Guo, F.H. (2011) 'A heat pipe photovoltaic/thermal (PV/T) hybrid system and its performance evaluation', Energy Buildings, (12), pp. 3558-3567.

Yang, H.X., Burnett, J. and Ji, J. (2000) 'Simple approach to cooling load module calculation through PV walls', Energy Buildings, (3), pp. 285-290.

#360: Safety analysis and quantitative risk assessment of hydrogen releases accident in a highway hydrogen refueling station

Qingnan MU[1], Jiaxin ZHANG[1], Hao CHEN[1], Dianji WANG[1], Qingxin BA[2], Xuefang LI[1,*]

[1] Institute of Thermal Science and Technology (Institute for Advanced Technology), Shandong University, Jinan 250061, China.
[2] School of Mechanical Engineering, Shandong University, Jinan 250061, China
Corresponding author email: lixf@email.sdu.edu.cn

Abstract: Hydrogen is a clean energy that has the advantage of a wide variety of sources. Hydrogen energy is one of the important means to replace traditional fossil energy and achieve the goal of "carbon peak and carbon neutrality". Ensuring the safe use of hydrogen is critical for the large-scale commercialization and success of hydrogen energy initiatives. Hydrogen refueling stations are essential nodes in the development and commercialization of hydrogen energy, especially those located in highway service areas, which are characterized by high pedestrian flow and frequent traffic. Therefore, conducting a post-incident consequence analysis and quantitative risk assessment for this highway hydrogen refueling station is vital to inform their safe design and operational practices. This study uses the FLACS software to simulate potential hydrogen leakage and explosion scenarios within a hydrogen refueling station situated in a highway service area. To mitigate the potential harm from hydrogen accidents, the study assesses the protective efficacy of safety barriers against hydrogen leaks and explosions. Finally, a quantitative risk assessment is performed on the refueling station, calculating risk values for typical accident conditions and comparing these values against acceptable criteria to determine the acceptability of the risks associated with such incidents. The findings show that the strategic placement of safety barriers can significantly reduce the lateral spread of hydrogen clouds, lessening the potential harm from combustion or explosion to both humans and structures in open spaces, and consequently narrowing the required safety distances between various facilities within the station. However, due to the potential for shock wave reflection by safety barriers, leading to increased overpressure within their vicinity, it is advisableto maintain an adequate distance between these barriers and hydrogen-related equipment. For the conditions analyzed in this study, the hazard radius resulting from diffusion, fire, and explosion in the event of a hydrogen leak is relatively small,and the overall risk of such incidents is considered acceptable. The research presented in this paper offers valuable insights into the design and safety precautions of hydrogen refueling stations along highways.

Keywords: Hydrogen Safety, Highway Hydrogen Refueling Station, Hydrogen Leakage, Hydrogen Explosion, Quantitative Risk Assessment

1. INTRODUCTION

Hydrogen energy is a clean, flexible and efficient renewable energy that can reduce reliance on fossil fuels. With the rapid development of hydrogen industry, high-speed hydrogen refueling stations are dedicated to serving hydrogen vehicles on expressways, providing fast and convenient hydrogenation services, which can effectively promote the development of "hydrogen high-speed" and become a key factor in promoting the rapid development of hydrogen economy. Hydrogen gas has the smallest molecular mass, a high diffusion coefficient, and low ignition energy (Metzler, 1952). Its static flammable concentration limit ranges from 4% to 75% (Coward, 1952)[0]. At normal conditions, small, sudden hydrogen leaks dissipate quickly without posing a threat. However, ignition of large, continuous leaks can result in accidents like combustion and explosions, causing varying degrees of harm to personnel, buildings, and the station's surroundings. Thus, safety concerns regarding hydrogen must be cafefully addressed. Hydrogenation stations built in the service areas of expressways have the characteristics of large flow of people, many vehicles, hydrogen leakage and explosion accidents may cause more serious consequences than common urban hydrogenation stations. Thus, erecting protective walls near hydrogen zones is an effective safety measure. This can minimize the impact of leaks and explosions on equipment at refueling stations.

Numerous studies have demonstrated that protective walls are effective in safeguarding personnel and equipment in proximity to refueling stations. They mitigate the spread of hydrogen leakage in the direction of the leak and impede the longitudinal propagation of hydrogen (Schefer, 2011) (Li, 2017) (Wang, 2018). Additionally, researchers have examined how protective walls of varying shapes (Tchouvelev, 2007), positions (Schefer, 2009), heights (Kang, 2022), and materials (Chiquito, 2021) influence explosions, including their impact on the excitation effects of the explosion cycle near the walls. Findings suggest that taller protective walls are more effective in attenuating stronger pressure waves and hydrogen jet flames. However, an increase in the height of protective walls leads to a rise in the flame radiation score. Beyond a height difference of 1-meter, further increments in wall height yield marginal enhancements in fire protection efficacy (Yu, 2022). Some researchers use DNV SAFETI or HYRAM quantitative risk assessment software to establish historical accident databases and mathematical models of related accidents, carry out quantitative risk assessment on related hydrogen-related equipment, and calculate the risk value of each equipment in the hydrogen refueling station, which provides a reliable basis for the setting of the safety distance of the hydrogen refueling station (Li, 2010) (Su, 2016).

The existing accident site research of hydrogen refueling stations mainly focuses on small and medium-sized stations such as highway hydrogen refueling stations(Kim, 2013) (Qian, 2020), skid-mounted hydrogen refueling station (Zhao, 2023) (Zhao, 2023), seaport hydrogen refueling stations(Cui, 2023) (Pua, 2023), renewable hydrogen refueling station (Pan,2016) (Liang, 2019), liquid hydrogen refueling stations(Yoo, 2021) (Yuan, 2022) and mobile hydrogen refueling stations (Sun, 2014)(Kim, 2022) (Li, 2023). There is a lack of research on highway hydrogen refueling stations and evaluation of the effectiveness of protective walls in large open Spaces. In view of the fact that the quantitative risk assessment of highway hydrogen refueling station has not been involved at present, and the highway hydrogen refueling station has the characteristics of large passenger flow, many vehicles and high public safety demand of highway. Therefore, the Computational Fluid Dynamics method is used to simulate the leakage, explosion and other accidents of hydrogen equipment in a high-speed hydrogen-fueling station in China. DNV SAFETI software was used to conduct quantitative risk assessment of the accident, evaluate the protective effect of the protective wall on hydrogen leakage and explosion in a large open space, and obtain the personal risk and social risk caused by hydrogen leakage accident. The findings of this study can serve as a guide for designing protective wall structures at highway refueling stations.

2. NUMERICAL SIMULATIONS

High-pressure hydrogen leakage will generate underexpanded air flow at the outlet of the leak and form a complex shock wave structure for a short distance outside the outlet. In order to simplify the calculation, this study calculated the equivalent outlet conditions based on the virtual nozzle model established by Birch et al. 1987(Birch, 1987). The flow between the real nozzle outlet and the virtual nozzle outlet could be regarded as one-dimensional flow, as shown in Figure 1.

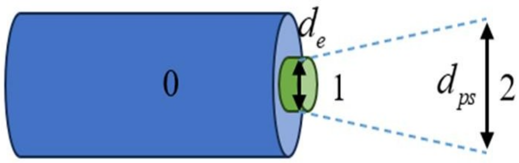

Figure 1: Notional nozzle model

The momentum conservation and mass conservation equations are as follows:

$$\rho_1 V_1^2 A_1 - \rho_2 V_2^2 A_2 = A_1 \left(P_1 - P_2 \right) \tag{1}$$

$$\rho_1 V_1 A_1 = \rho_2 V_2 A_2 \tag{2}$$

Combined dimensions (1) and (2) obtain:

$$V_2 = V_1 + \frac{P_1 - P_2}{\rho_1 V_1} \tag{3}$$

The outlet area and diameter of the virtual nozzle can be calculated by the following formula:

$$A_e = A_2 = \frac{\rho_1 V_1^2 A_1}{\rho_2 \left(P_1 - P_{amb} + \rho_1 V_1^2\right)} \qquad (4)$$

$$d_e = d_2 = 2\sqrt{\frac{V_1 \rho_1 A_1}{\pi V_2 \rho_2}} \qquad (5)$$

This study used the FLACS software to conduct numerical simulations of hydrogen leakage and explosion accidents occurring at a hydrogen refueling station. FLACS, an acronym for FLame Acceleration Simulator, is an advanced software tool developed by GexCon, designed for detailed modeling of fluid dynamics and explosion phenomena. It is particularly used in the domain of safety and risk assessment, providing comprehensive simulations to help understand and mitigate potential hazards (Vyazmina, 2016). Numerous prior studies have validated the accuracy of FLACS for simulating hydrogen leakage and explosions in complex building and industrial environments (Launder, 1975) (Middha, 2011) (Ichard, 2012).

FLACS uses the finite volume method to solve compressible conservation equations on a three-dimensional structured Cartesian grid. Its numerical solver utilizes the SIMPLE pressure correction algorithm, while the standard k-epsilon (k-ε) model is used to solve the equations governing turbulent kinetic energy transport and dissipation rates. The general conservation equation solved in the physical model has the following form:

$$\frac{\partial}{\partial t}(\rho\phi) + \frac{\partial}{\partial x_j}(\rho\mu_i\phi) - \frac{\partial}{\partial x_j}\left(\rho\Gamma_\phi \frac{\partial}{\partial x_j}(\phi)\right) = S_\phi \qquad (6)$$

$$\Gamma_\phi = \frac{\mu_{eff}}{\sigma_\phi} \qquad (7)$$

$$\mu_{eff} = \mu + \rho C_\mu \frac{k^2}{\varepsilon} \qquad (8)$$

where ϕ represents the variable under consideration for solving, ρ is the density, μ is the dynamic viscosity, μ_{eff} is the effective viscosity, σ_ϕ is the turbulent Prandtl-Schmidt number, S_ϕ is the source term, k is the turbulent kinetic energy, and ε is the turbulent dissipation kinetic energy.

The FLACS software performs combustion simulations employing the β-flame model. The β factor intensifies the flameby augmenting diffusion and diminishing reaction rates. The governing equations for this model are formulated as follows:

$$\frac{\partial}{\partial t}(\beta_v \rho Y_F) + \frac{\partial}{\partial x_j}(\beta_j \rho \mu_j Y_F) = \frac{\partial}{\partial x_j}\left(\beta_j \rho D \frac{\partial Y_F}{\partial x_j}\right) + R_F \qquad (9)$$

$$D = \frac{\mu_{eff}}{\sigma_{fuel}} \qquad (10)$$

$$R_F = C_{\beta R_F} \frac{S}{\Delta} \rho \min\left[c, 9(1-c)\right] \qquad (11)$$

$$c = 1 - \frac{Y_F}{Y_{F0}} \qquad (12)$$

where D is the diffusion coefficient, R_F is the reaction rate, $C_{\beta R}$ is the model constant, S is the combustion rate, Δ is a constant comparable to the grid scale, c is the process variable, Y_F mass fraction the fuel mass fraction, and Y_{F0} is the initial fuel mass fraction.

3. GEOMETRIC MODELS AND SIMULATION SETTINGS

This study used a geometric model of a practical hydrogen refueling station situated in China, encompassing hydrogen storage tanks, hydrogen refueling units, compressors, buffer tanks, and hydrogen production units. The total domain dimensions were 58 m × 33 m × 8 m (length × width × height). The diameter of A hydrogen storage tank is 1.5 m and the length is 5.0 m. The diameter of B hydrogen storage tank is 1.0 m and the length is 10.0 m. In order to evaluate the protective effect of the protective wall, a protective wall with a height of 4.5 m is set up at the vertical leakage direction of 1.5 m. The simplified satellite and geometric model are shown in Figure 2.

(a) A highway hydrogen refueling station satellite imagery

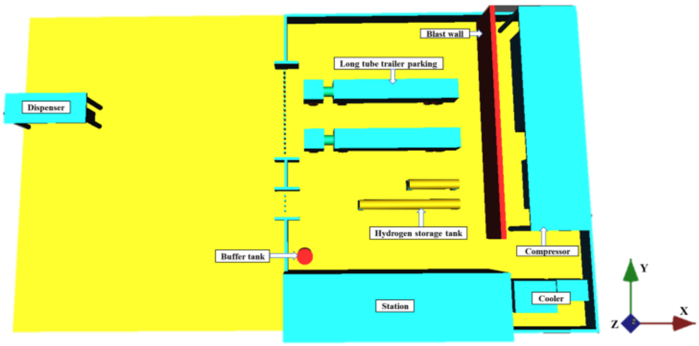

(b) Without protective wall

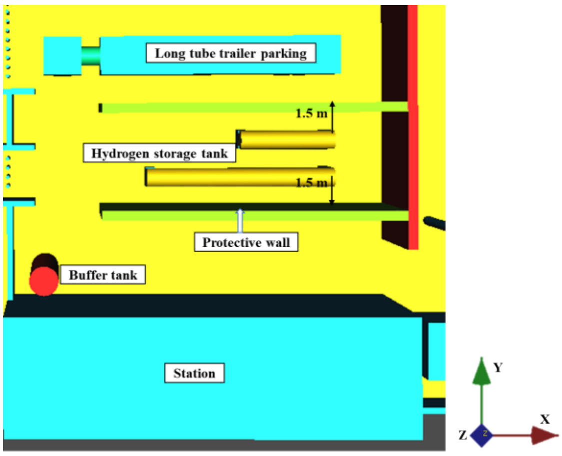

(c) With protective wall

Figure 2: Geometric model of a practical hydrogen refueling station

The A hydrogen storage pressure in the hydrogen storage tanks was 20 MPa at the hydrogen refueling station, with a total storage capacity of 37.7 kg. The B hydrogen storage pressure in the hydrogen storage tanks was 45 MPa at the hydrogen refueling station, with a total storage capacity of 72.3 kg. The leakage point was located at the center of the leftmost hydrogen storage tank, at a height of 1.5 m. The coordinates of the leakage point were (17.5, 12.5, 1.5) and (17.5, 14.5, 1.5), with the leakage occurring in the +X direction.

Unlike most CFD software, FLACS uses the concept of distributed porosity to handle sub-grid scale objects. This approach enables accurate simulation of diffusion processes in complex geometrical structures while reducing computational expenses. Structured mesh was used with specialized cell refinement along the direction of hydrogen leak and jet, as shown in Figure 3. The smallest gird cells measured 0.05 m. Grid sizes increased smoothly from the jet core region towards the boundaries of the computational domain, with the largest cells being 1.00 m. The grid comprised a total of 1,110,000 cells. Operating parameters were set with hydrogen and ambient temperatures at 20 ℃, environmental pressure at standard atmospheric levels (101325 Pa), and gravitational acceleration at 9.8 m/s² acting vertically downward.

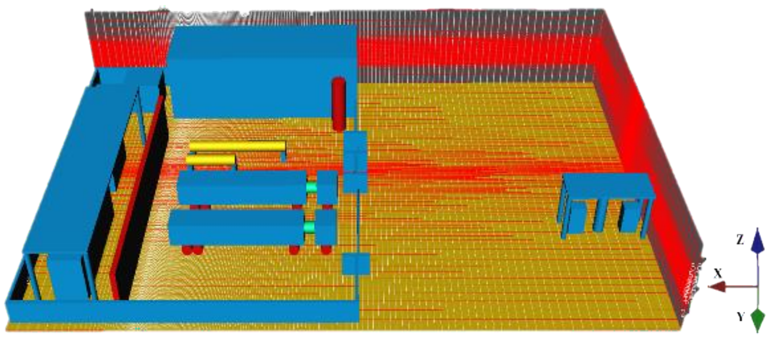

Figure 3: Grid

In the quantitative risk assessment of this paper, DNV SAFETI software is used to assume that the following accidents may occur at hydrogen refueling stations: Small aperture leakage accidents occurred in high-pressure and low-pressure hydrogen storage cylinders, the leakage aperture was 10 mm, and the accident frequency was 8.76×10^{-4}/AvgeYear. The high and low pressure hydrogen storage cylinders were completely ruptured, with a frequency of 1×10^{-6}/AvgeYear. There are ignition sources in the hydrogen refueling station building, compressor and nearby gas stations. According to the main facilities of the hydrogen refueling station and combined with TNO Purple book (Book, 1999), the ignition probability of this ignition source is 0.5 within 60 s.

Meteorological factors are an important factor affecting quantitative risk assessment. By summarizing meteorological data over the years and in accordance with the international unified classification standard of meteorological conditions (Yu, 2000), the annual average meteorological conditions of a city in China are obtained, as shown in Table 1.

Table 16: Annual average meteorological conditions in Zibo

Predominant wind direction	Average wind velocity(m/s)	Annual mean temperature	Relative humidity	Atmospheric stability
east wind、south wind	3.4	13.8	0.61	A/B

The process of quantitative risk calculation also needs to consider the population density of the area involved in the accident. According to the Bulletin of the Seventh National Population Census of Shandong Province released by ShandongProvince in 2021, the rural population density near the hydrogen refuelling station is 3,751 people /km^2.

4. RESULTS AND DISCUSSION

4.1. Hydrogen Leakage Diffusion

The evolution of the hydrogen cloud within 2.3 seconds following a hydrogen storage tank leak in an open environment is shown in Figure 4 and Figure 5. Without protective barriers, the hydrogen jet forms a cloud that reaches the compressor area outside wall and subsequently disperses outward along its surface within 0.4 seconds. At 1.0 seconds, the hydrogen jet has reached the top of the long tube trailer and station house and continues to spread to both sides. At 2.3 seconds, the hydrogen jet stabilizes, with its maximum extension reaching 15.7 meters. With protective barriers, the hydrogen cloud reaches within 0.4 seconds the outer wall of the compressor and begins to disperse around the wall. As hydrogen continues to leak, the cloud reaching the protective wall disperses to both sides, gradually expanding laterally. At 1.0 seconds, protective walls limit hydrogen diffusion. At 2.3 seconds, the extension distance of hydrogen in the vertical jet direction of the jet is reduced by 68% due to the influence of the protective wall. This reduction significantly decreases the hydrogen concentration near potential ignition sources such as compressors, thereby lowering the risk of more severe explosion accidents.

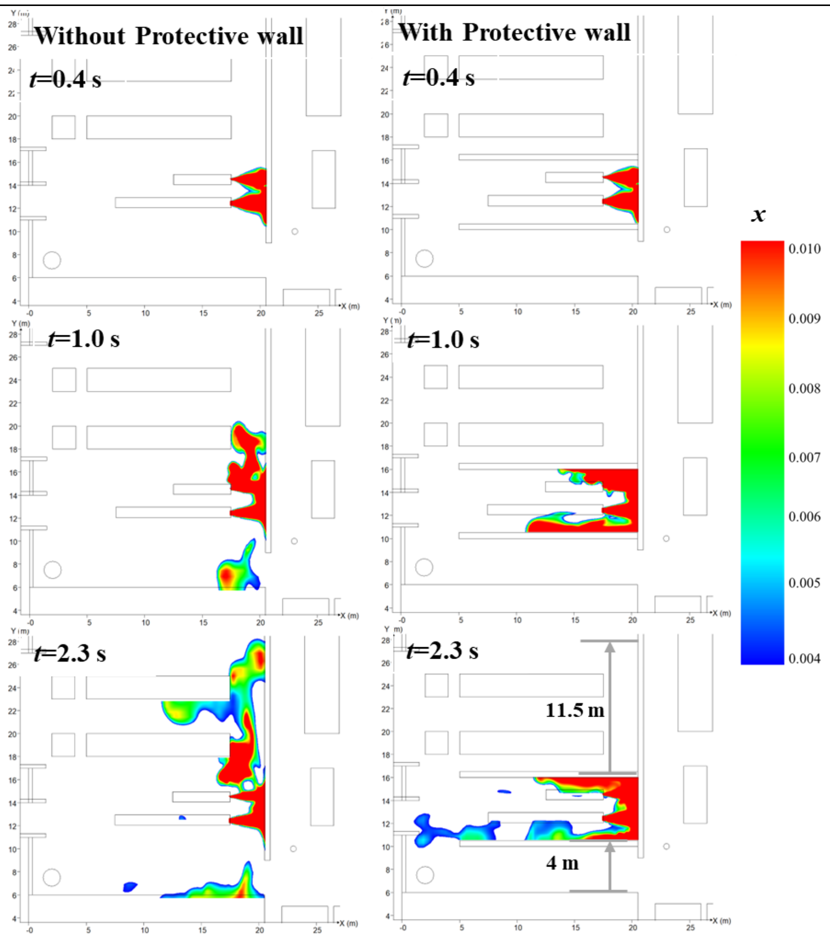

Figure 4: Hydrogen concentration distributions after leakage with/without protective wall (XY plane)

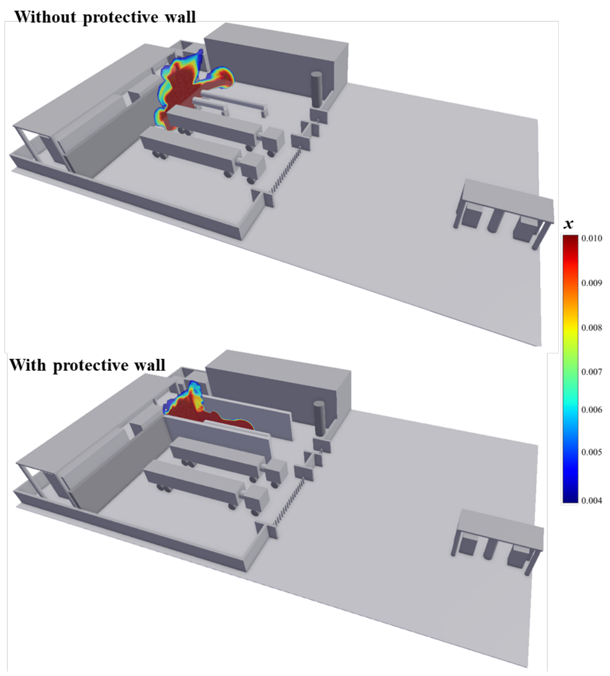

Figure 5: Hydrogen concentration distributions after leakage with/without protective wall

4.2. Hydrogen Combustion

The temperature and overpressure distributions were calculated for ignited hydrogen and air mixture in the hydrogen storage tank area. Hydrogen premix-combustion was simulated using a 30% hydrogen volume fraction.

The overpressure distribution after 0.25 s of ignition is shown in Figure 6. Without a protective wall, overpressure impacts the station structure within 0.25 seconds after combustion, the maximum overpressure is greater than 0.2 bar. Based on the overpressure injury criteria (Wei, 2014), personnel within the station building are at risk of fatal injuries and structural damage due to overpressure. The installation of a protective wall decreases the propagation of overpressure in the y-direction by 37%, thereby mitigating damage to the station building. However, the impact on overpressure propagation at the x-direction is minor.

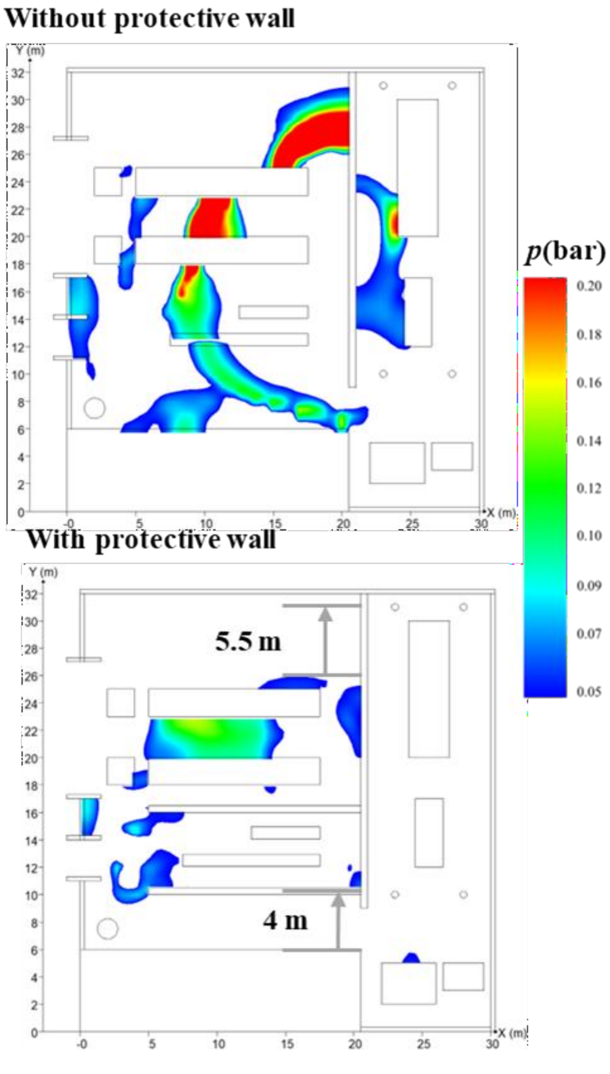

Figure 6: Overpressure distributions at 0.25 s after combustion without and with protective wall

The temperature distribution after 0.25 s of ignition is shown in Figure 7. A high-temperature accumulation zone is formed in the compressor and station building, reaching a peak temperature of 2353 K. According to the high-temperature injury criteria (Fu, 2009), high temperatures exceeding 873 K can lead to severe human injuries and complete structural failure of the building's steel components. The installation of a protective wall significantly reduces the high-temperature zone in the y-direction, cutting down the area impacted by high-temperatures by over 64%. The high temperature area is limited in the protective wall, thus protecting the life safety of the long tube trailer area and station house staff, and effectivel y avoiding the damage of equipment such as long tube trailer and station house caused by high temperature.

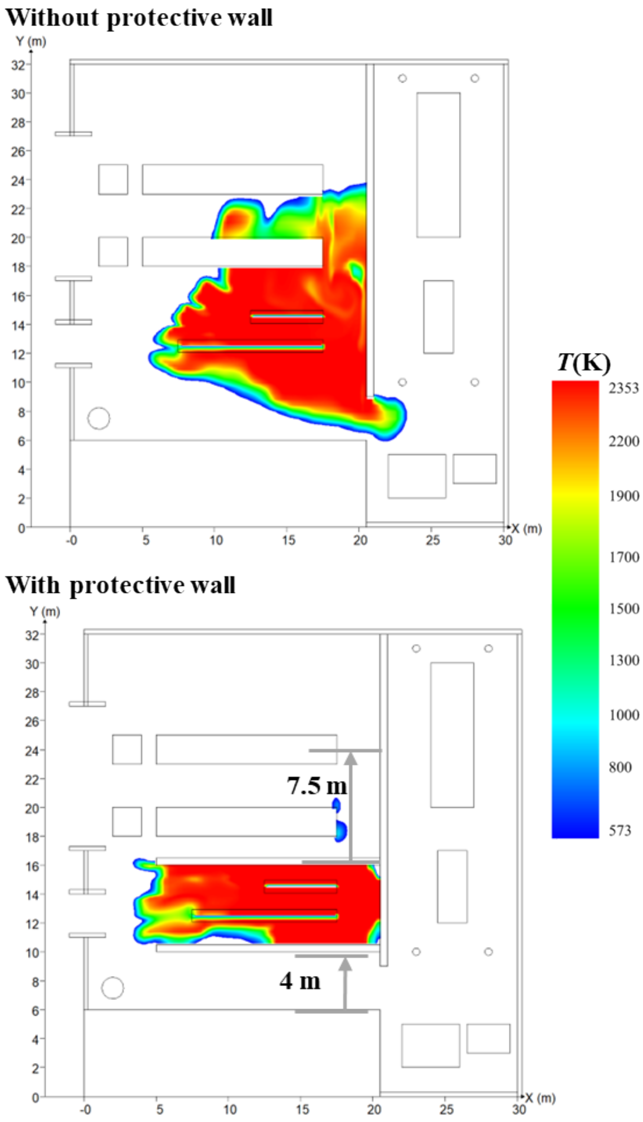

Figure 7: Temperature distributions at 0.25 s after combustion without and with protective wall

4.3. Risk Assessment of Leakage Accidents in Hydrogen Storage System

After the leakage of harmful substances, the personnel exposed to the dangerous range have a certain personal risk, and the accident will also cause a certain social risk. The process of risk assessment is mainly analyzed from two aspects: individual risk and social risk. According to the acceptable standards of personal risk and social risk of the State Administration of Work Safety and other regions (Ke, 2005), the acceptable frequency range of general personal risk is less than 1×10^{-6}, while the acceptable range of social risk is judged according to the relationship curve between cumulative frequency and the number of deaths (F-N curve).

4.3.1. Individual risk assessment

Individual risk refers to the individual death probability of personnel at a fixed position in the region caused by various potential fires, explosions and toxic gas leakage accidents of hazardous chemical production and storage equipment, that is, the individual death rate within a unit time, which is usually expressed by the individual risk contour line (Chen, 2007).

The calculated individual risk contour lines are shown in Figure 8. Different contour lines represent the individual death frequency caused by leakage of 10 mm of hydrogen storage cylinder, and the individual death frequency shows a decreasing relationship from inside to outside. Therefore, when hydrogen leakage occurs in highway hydrogenation, the personal risk caused is within the acceptable range.

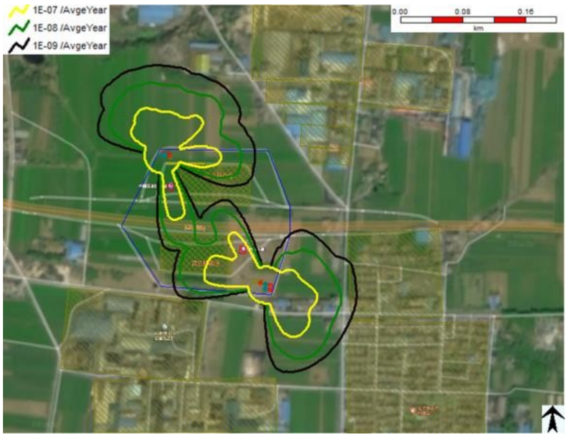

Figure 8: Individual risk isoclines of hydrogen leak accident

4.3.2. Social risk assessment

Social risk is a supplement to personal risk, which means that on the basis of personal risk, taking into account the population density of the surrounding area of the danger source, so as to avoid the probability of casualties exceeding the acceptable range of the public, usually expressed by F-N curve, in which the upper limit, lower limit and middle area between the upper and lower limits are determined. The evaluation results of social risk are shown in Figure 9. The ordinate represents the annual fatality probability of accidents, and the abscissa represents the number of deaths caused by accidents. The results show that the social risk curve is below the upper limit of the risk standard, and the part of the curve falls in the completely acceptable range, so the social risk of the hydrogen leakage accident of the highway hydrogen refueling station is in the acceptable range.

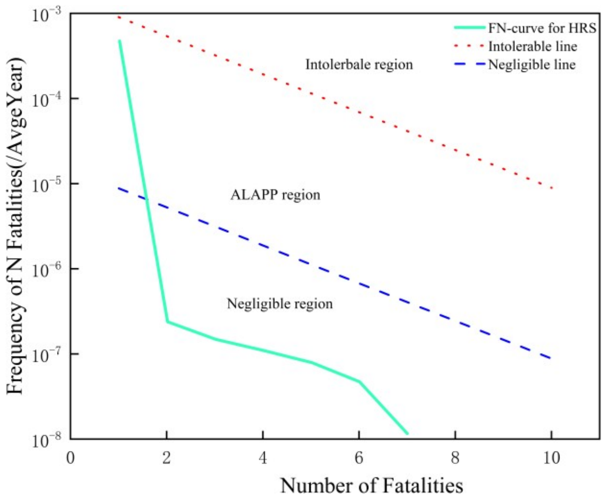

Figure 9: Social risk F-N curves of hydrogen leak accident

5. CONCLUSION

By using FLACS software and DNV SAFFTI software, this paper conducts quantitative risk assessment simulation analysis on the protective effect of hydrogen leakage and explosion and protective wall of a domestic highway hydrogenation station, analyzes the protective effect of protective wall on hydrogen leakage and explosion, judges whether the accident risk is acceptable, and draws the following conclusions:

(a) In the open space area of highway hydrogen refueling stations, the installation of protective walls can effectively prevent the diffusion of hydrogen clouds to equipment areas such as long tube trailers and station buildings, thus significantly reducing the safety distance of hydrogen leakage accidents.

(b) Placing a protective wall will cause hydrogen clouds to accumulate on the inside of the protective wall. Therefore, electrical components should be avoided near the inside of the protective wall to avoid accidental fire. After hydrogen combustion, the protective wall will reduce the overpressure and temperature behind the wall, reducing the damage of hydrogen-related equipment by high temperature overpressure.

(c) There is a large flow of people and vehicles in the hydrogen refueling station on the highway, and once the hydrogen leakage accident occurs, it will cause huge losses to life and property, so it is very important to rationally arrange the hydrogen refueling station and set up protective walls.

(d) Through quantitative risk evaluation, the accident risk of expressway hydrogen refueling station is acceptable.

This paper provides a basis for the scientific and reasonable design of the protective wall structure of the hydrogen refueling station and provides a reference for the safety distance and accident risk control of the hydrogen refueling station.

6. ACKNOWLEDGEMENT

This work is supported by the National Key Research and Development Program of China (2023YFB4004501). The scientific calculation of this paper is supported by the high performance computing cloud platform of Shandong University.

7. REFERENCES

Birch A D, Hughes D J, Swaffield F, 1987. Velocity decay of high pressure jets. Combustion science and technology, 52(1-3), 161-171.

Book P, 1999. Guidelines for quantitative risk assessment[J]. Committee for the Prevention of Disasters, The Netherlands.

Chen G, 2007. Risk Engineering [M]. National Defense Industry Press.

Chiquito M, Castedo R, Santos A, López L, Caldentey A, 2021. Numerical modelling and experimental validation of the behaviour of brick masonry walls subjected to blast loading. International Journal of Impact Engineering, 148, 103760–103774.

Coward H, Jones G, 1952. Limits of flammability of gases and vapors. Washington D.C: University of North Texas Libraries.

Cui W, Yuan Y, Tong L, et al. Numerical simulation of hydrogen leakage diffusion in seaport hydrogen refueling station. International Journal of Hydrogen Energy, 48(63), 24521-24535.

Fu Z, Huang J, Zang N, 2009. Quantitative analysis for consequence of explosion shock wave[J]. Fire Science and Technology, 28(6), 390-395.

Ichard M, Hansen O R, Middha P, Willoughby D, 2012. CFD computations of liquid hydrogen releases. International Journal of Hydrogen Energy, 37(22), 17380-17389.

Kang H, Kim S, Kim J, 2022. Safety issues of a hydrogen refueling station and a prediction for an overpressure reduction by a barrier using OpenFOAM software for an SRI explosion test in an open space. Energies, 15(20), 7556.

Ke J, Li C, 2005. Study on the coordinated development of regional resources, environment and economy in China based on DEA cluster analysis[J]. China Soft Science, (2), 144-148.

Kim D, Lim J, Park W, Joe C, 2022. Quantitative risk assessment of a mobile hydrogen refueling station in Korea. International Journal of Hydrogen Energy, 47(78), 33541-33549.

Kim E, Park J, Cho J, Moon I, 2013. Simulation of hydrogen leak and explosion for the safety design of hydrogen fueling station in Korea. International Journal of Hydrogen Energy, 38(3), 1737-1743.

Launder B, Reece G, Rodi W, 1975. Progress in the development of a Reynolds-stress turbulence closure. Journal of Fluid Mechanics, 68(3), 537-566.

Li J, Ma G, Hao H, Huang Y, 2017. Optimal blast wall layout design to mitigate gas dispersion and explosion on a cylindrical FLNG platform. Journal of Loss Prevention in the Process Industries, 49, 481–492.

Li Y, Wang Z, Shi X, Fan R, 2023. Safety analysis of hydrogen leakage accident with a mobile hydrogen refueling station. Process Safety and Environmental Protection, 171, 619-629.

Li Z, Pan X, Ma J, 2010. Quantitative risk assessment on a gaseous hydrogen refueling station in Shanghai. International Journal of Hydrogen Energy, 35(13), 6822-6829.

Liang Y, Pan X, Zhang C, Xie B, Liu S, 2019. The simulation and analysis of leakage and explosion at a renewable hydrogen refueling station. International Journal of Hydrogen Energy, 44(40), 22608-22619.

Metzler A, 1952. Minimum ignition of six pure hydrocarbon fuels of the C_2 and C_6 series. NACA.

Middha P, Ichard M, Arntzen B, 2011. Validation of CFD modelling of LH_2 spread and evaporation against large-scale spill experiments. International Journal of Hydrogen Energy, 36(3), 2620-2627.

Pan X, Li Z, Zhang C, Lv H, Liu S, Ma J, 2016. Safety study of a wind-solar hybrid renewable hydrogen refueling station in China. International Journal of Hydrogen Energy, 41(30), 13315-13321.

Pua C, Hu P, Ji C, Zhu Z, Zheng B, Zhai S, 2023. Simulation analysis of protective wall against hydrogen combustion from liquified hydrogen storage tank on the offshore launching platform. International Journal of Hydrogen Energy, 48(33), 12501-12518.

Qian J, Li X, Gao Z, Jin Z, 2020. A numerical study of unintended hydrogen release in a hydrogen refueling station. International Journal of Hydrogen Energy, 45(38), 20142-20152.

Schefer R, Groethe M, Houf W, Evans G, 2009. Experimental Evaluation of Barrier Walls for Risk Reduction of Unintended Hydrogen Releases. International Journal of Hydrogen Energy, 34(3), 1590-1606.

Schefer R, Mcrilo E, Groethe M, Houl W, 2011. Experimental investigation of hydrogen jet fire mitigation by barrier walls. International Journal of Hydrogen Energy, 36(3), 2530–2537.

Sun K, Pan X, Li Z, Ma J, 2014. Risk analysis on mobile hydrogen refueling stations in Shanghai. International Journal of Hydrogen Energy, 39(35), 20411-20419.

Sun Y, 2016. Research on safe distance in design code for hydrogen fueling station[J]. Shanghai Gas, 2, 1-5.

Tchouvelev A, Cheng Z, Agranat V, Zhubrin S, 2007. Effectiveness of Small Barriers as Means to Reduce Clearance Distances. International Journal of Hydrogen Energy, 32(10-11), 1409-1415.

Vyazmina E, Jallais S, 2016. Validation and recommendations for FLACS CFD and engineering approaches to model hydrogen vented explosions: effects of concentration, obstruction vent area and ignition position. International Journal of Hydrogen Energy, 41(33), 15101-15109.

Wang J, Jin G, Yang F, Zhang J, Lu S, 2018. Effects of hydrogen concentration on the vented deflagration of hydrogen-air mixtures in a 1-m^3 vessel. International Journal of Hydrogen Energy, 43(45), 21161–21168.

Wei C, Chen G, Liu K, 2014. Leakage gas deflagration characteristics and safety area of FPSO[J]. Acta Petrolei Sinica, 35(4), 786-794.

Yoo B, Wilailak S, Bae S, Gye H, Lee C, 2021. Comparative risk assessment of liquefied and hydrogen refueling stations. International Journal of Hydrogen Energy, 46(71), 35511-35524.

Yu D, 2000. Quantitative risk assessment of flammable, explosive and toxic dangerous goods during storage and transportation [M]. China Railway Publishing House.

Yu X, Yan W, Liu Y, Zhou P, Li B, Wang C, 2022. The flame mitigation effect of vertical barrier wall in hydrogen refueling stations. Fuel, 315, 123265.

Yuan W, Li J, Zhang R, Li X, Xie J, Chen J, 2022. Numerical investigation of the leakage and explosion scenarios in China's first liquid hydrogen refueling station. International Journal of Hydrogen Energy, 47(43), 18786-18798.

Zhao Z, Liu M, Xiao G, Cui T, Ba Q, Li X, 2023. Numerical study on protective measures for a skid-mounted hydrogen refueling station. Energies, 16(2), 910.

Zhao Z, Xiao G, Zhang X, Ba Q, Wang J, Li X, 2023. Numerical study of hydrogen releases and explosions in a skid-mounted hydrogen refueling station. SAE Int, 4(1), 137-148.

#361: The technical progress and application prospect of aluminum-silicon alloys as high-temperature phase change heat storage materials are reviewed

Yutian YANG[1], Jianfegn LIU[1,2], Tao ZHANG[1,2], Zhengrong SHI[1,2]

[1] College of energy and mechanical engineering, Shanghai University of Electric Power, Shanghai 201306, China
[2] Shanghai Non-carbon energy conversion and utilization institute, Shanghai 200240, China

Abstract: With the progressive depletion of traditional fossil energy and the adjustment of the global energy structure, the development and utilization of new energy have emerged as a research focus. Al-Si alloy exhibits significant potential in phase change heat storage materials due to its high heat storage density, outstanding thermal cycle stability, and favorable cost performance. Nevertheless, the oxidation and corrosion of aluminum-silicon alloy at elevated temperatures still impose constraints on the development of its related industries in the high-temperature direction. In this paper, the preparation method, performance optimization approach, and packaging method of Al-Si alloy are comprehensively presented. The choice of material preparation methods is of great significance for controlling the quality and production cost of materials. Sorting out the development process of related preparation technologies also indirectly supports the upgrading and transformation of related industries. The crux for the application of phase change materials in practice lies in whether the properties of the materials themselves and the packaging methods can meet the requirements. In this paper, the mechanical and thermal properties of Al-Si alloy are presented from macroscopic and microscopic perspectives. Through high-temperature treatment, chemical modification, and element addition, not only can the mechanical properties of the material be enhanced, but also the heat storage density, phase transition temperature, corrosion properties, and thermal stability can be optimized. The packaging of PCM can ensure safety and enhance heat transfer, and by analyzing the advantages and disadvantages of various packaging methods and application scenarios, it can further promote the commercial application of aluminum-silicon alloy in the field of high-temperature phase transformation.

Keywords: Aluminum-Silicon Alloy; Phase Transition; Performance Optimization; Encapsulation

1. INTRODUCTION

With the depletion of traditional fossil energy and the adjustment of the global energy structure, the installed capacity of new energy, primarily represented by wind and solar energy, keeps developing rapidly. Owing to the distinctive instability and intermittency of wind power and solar power, the grid-connection of wind power and photovoltaic power is poor. If integrated on a large scale into the power grid, it will threaten the safe and stable operation of the power grid, as energy storage devices are required as buffers to guarantee the effective utilization of energy. Aluminium-silicon alloy has a high energy storage density, is non-toxic, cost-effective, and has a phase change temperature up to 577℃, making it a highly ideal high-temperature phase change heat storage material, which is of great significance for alleviating the current predicament of new energy.

The most prevalently employed process in the production of aluminium-silicon alloy is casting. From traditional casting through semi-solid metal casting to additive manufacturing, the production approach of aluminium-silicon alloy keeps evolving, yet it still fails to fulfill the increasingly intricate demands. Aluminum-silicon alloy boasts outstanding thermal properties but has low mechanical properties and is prone to oxidize and corrode containers upon melting. Hence, the mechanical and thermal properties can be further enhanced through high-temperature treatment, chemical modification and addition of elements. Oxidation and corrosion can be minimized by choosing the appropriate packaging materials and methods. In this paper, the current packaging methods of Al-Si phase change alloys are systematically reviewed from three aspects: macro packaging, microcapsule packaging and nano packaging.

2. THE PREPARATION PROCESS OF ALUMINUM-SILICON ALLOY

Aluminum-silicon alloy possesses the merits of lightweight, excellent thermal conductivity, strength, hardness, and corrosion resistance, among others. Its manufacturing encompasses mold casting, sand casting, high pressure die casting, and other conventional manufacturing procedures. Semi-solid metal processing, additive manufacturing, and the recycling of aluminum-silicon alloys are also significant preparation approaches of aluminum-silicon alloy.

2.1. Conventional casting

The presence of silicon enables aluminum-silicon alloy to possess outstanding casting properties, and casting is the most prevalently employed process route in the production of aluminum-silicon alloy. Once the aluminum-silicon alloy is molten, the molten liquid will be poured into a mold of the desired geometry during its solidification. The conventional casting approaches of aluminum-silicon alloy encompass mold casting, sand casting, gravity casting, permanent mold casting, and so on. The selection of the casting process encompasses numerous factors, primarily the economic benefits of the casting process. For instance, approximately 80% of metal castings in the current automotive market are dominated by the high-pressure die casting (HPDC) process since the high-pressure die casting process is more cost-efficient and has a high cycle rate. Table 1 summarizes the advantages and disadvantages of various conventional casting methods.

Table 17: A summary of advantages and disadvantages of various casting methods

Casting Methods	Advantages	Disadvantages	Ref
Permanent mold/ gravity die casting	- Low set up cost - Can be highly automated - Mechanical strength can be improved by performing heat treatment	- Low production rate and casting quality compared to pressurized die casting - the turbulent filling of the mold cavity, which causes oxidation of the melt, leading to poor mechanical properties	[1]
Sand Casting/ Precision Sand Casting	- Low initial set up cost - High uniformity through automation	- Poor surface finish and dimension accuracy. - Need extra cost for secondary machining - poor complexity and low integrity of the castings - a slower rate of solidification leading to oxidation	[2]
Die Casting/ High Pressure Die Casting	- Refined microstructure - Minimum achievable wall thickness of 1 mm - Excellence surface finish - have a higher productivity and volume of manufacturing with near-net-shaped products - Less porosity	- Initial set up cost is too high - Demanding for high production rates - Formation of pores and voids following the rapid filling and solidification - Need draft angle	[3]
Low Pressure Die casting	- Lower set up cost than high pressure die casting - Long die life - High yield	- Lower production rates with poorer casting details, surface finishing, minimum wall thickness and quality soundness compared to high pressure die casting	[4]
Permanent mold/ gravity die casting	- Low set up cost - Can be highly automated - Mechanical strength can be improved by performing heat treatment	- Low production rate and casting quality compared to pressurized die casting - the turbulent filling of the mold cavity, which causes oxidation of the melt, leading to poor mechanical properties	[5]
Centrifugal	- Denser, finer microstructure and	- Limited to small parts	[6]

	improved mechanical strength - Solidification shrinkage is minimal - Can separate inclusions and gas bubbles - No feeders and gates - Able to produce hollow, asymmetrical parts or functional graded material	- Non-uniform composition throughout the casting - High cost -Require skill worker	
Squeeze Casting	- Lesser porosity and solidification shrinkage than high pressure die casting - Mechanical properties improvement - High Yield - have high integrity and improved heat-treatability	- Incurred extra machining cost for post trimming work and reduced cycle time due to slow melt filling process.	[7]

2.2. Semi-solid metal processing

Semi-solid metal (SSM) casting encompasses a diverse range of solidification procedures that operate by injecting a partially solidified alloy into a mold cavity to fabricate a near-net-shaped component. Certain metal alloys exhibit the characteristics of thixotropic media or non-Newtonian fluids, which can impede turbulence in semi-solid metals, thereby minimizing the formation of entrapped air or oxides. Semi-solid forming technology represents a processing technology bridging casting and plastic processing. It constitutes a highly effective near-net forming processing technology and holds promising development prospects. The crux of semi-solid forming technology lies in the preparation of fine semi-solid billets with non-dendritic structures. The approaches for billet preparation encompass mechanical stirring, electromagnetic stirring, liquidus casting, and solid-liquid mixed casting. A diagram of the three most prevalently utilized semi-solid metal casting methods is presented in Figure 1.

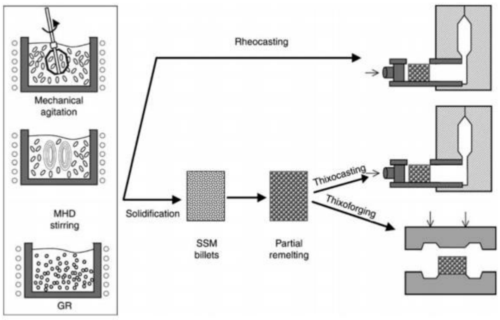

Figure 1: Schematic illustration of semisolid metal processing routes: Thixocasting, Thixoforging and Rheocasting. MHD: magnetohydrodynamic; GR: grain refinement [8]

2.3. Additive manufacturing

Additive manufacturing, also known as 3D printing, commences with the modeling of three-dimensional objects. It can be accomplished through various processes, adding material layer by layer under computer control. The drawbacks of traditional manufacturing include the delayed production process, high cost, and the formation of thin walls and irregular shapes when fabricating complex geometric structures. In contrast, additive manufacturing designs are flexible and enable rapid prototyping and are currently transitioning from producing prototypes to creating highly complex parts that can be manufactured in small batches to better manage costs. The disadvantage of metal additive manufacturing is that the part size is constrained by the size of the machine cavity, and there exist some processing defects, such as lack of fusion holes, cracks, impurities, poor surface finish, etc., and the product exhibits anisotropy and high powder cost. Aluminum alloys assist in reducing the tendency to crack during the printing process, for instance, the rapid solidification of additive manufacturing Al-Si-Mg enhances the static strength of the alloy but makes the cycling properties unpredictable. Additionally, additive manufacturing can be utilized to manufacture high-precision loss or investment casting.

2.4. Regenerated aluminum-silicon alloy

Aluminum alloy boasts a high recovery rate, and the energy consumption of recycling is less than 5% of that of primary aluminum extracted from bauxite, which can enhance energy efficiency and mitigate greenhouse gas emissions. Iron is a prevalent impurity element in aluminum alloys; it is typically present in scrap and secondary aluminum alloys. The content of iron in recycled alloys is restricted to 1%, yet reuse demands that the iron content be reduced to less than 0.2%. Iron exerts an influence on the mechanical properties, casting properties, machining properties and corrosion resistance of aluminum alloys. Furthermore, it tends to accumulate in the recycling process, leading to a significant reduction in the economic benefits of recycling waste aluminum and restricting industrial production. It was discovered that the addition of Mn and Sr could lower the content of Fe. Cinkilic et al. [9] proposed an Fe/Mn ratio model based on calphad to prevent the formation of iron-rich intermetallic compounds by regulating the cooling rate of Al-Si alloy in castings.

3. OPTIMIZATION OF THE PERFORMANCE OF ALUMINUM-SILICON ALLOYS

The basic production technology of Al-Si alloy has been highly developed; however, the comprehensive mechanical properties remain relatively low. Therefore, enhancing the performance of cast aluminum-silicon alloys to fulfill the diverse requirements of industrial production has emerged as one of the key focuses in the current research of the aluminum alloy industry. High-temperature treatment, chemical modification, and element addition are the most frequently employed approaches for optimizing aluminum-silicon alloys.

3.1. Aluminum-silicon alloy

The microstructure of Al-Si alloy consists of α-Al solid solution and various forms of silicon phase. The refinement of the as-cast microstructure of aluminum alloy is not only beneficial to the solidification process itself and the enhancement of the mechanical properties of cast aluminum alloy, but also the small anisotropy of uniform and fine equiaxial crystals is conducive to the improvement of the plastic forming ability and mechanical properties of deformed aluminum alloy. The Al-Si eutectic structure in sub-eutectic or eutectic alloys is long, acicular, and acicular particles, which enhances the mechanical properties of Al-Si alloys. In hyper-eutectic alloys, different casting processes result in the diversity of silicon morphology. According to the different morphology, primary silicon is classified into six basic shapes, and the relevant information is shown in Table 2.

Table 2: A Summary of morphology of hypereutectic silicon [10]

Hypereutectic silicon form	Formation condition	Reinforcement method
Star-like (Fivefold Branched)	Low subcooling or slow growth rate	Maintain low subcooling
Feathery Silicon	Superheat 100-850℃	Maintain low superheat
Polyhedral (Octahedral) Primary Silicon	Inoculate the alloy with P	Maintain the Si-Si clusters formed by small primary silicon nuclei
Dendritic Primary Silicon	The alloy is treated with Sr	Maintain low growth rate of Sr
Spheroidal Primary Silicon	The alloy is treated with Na	Increase the content of Na
Plate-like Silicon	Low cooling rate and low undercooling state with high silicon content	Increase the silicon content in the alloy

The precise characteristics of pure Al-Si alloys are contingent upon whether the composition of the alloy lies above, near, or below the eutectic point. When the silicon content is low (such as 0.7), the ductility of the Al-Si alloy is excellent, and it is typically utilized as a deformation alloy; When the Si content is less than 6%, the tendency of thermal cracking is lower. When the Si content is between 6% and 8%, the propensity for cavity formation is the lowest. When the silicon content is high (such as 7%), the fillability of the aluminum-silicon alloy melt is favorable, and it is commonly employed as a casting alloy; The mechanical properties are optimal when the Si content is within the range of 6% to 12%. When the Si content is 12%, the mold filling capacity attains the maximum, and it is also satisfactory for other contents; The alloy with a silicon content of 11% to 13% is one of the most superior piston materials due to its light weight, low expansion coefficient, and high corrosion resistance. When the Si content is 12.6%, aluminum and silicon form eutectic, and the solubility of siliconin silicon reaches 1.65% at this temperature, after which the solubility decreases rapidly with the increase in temperature. When the silicon content surpasses the Al-Si eutectic point and the silicon particle content amounts to 14.5% to 25%, the comprehensive mechanical properties of Al-Si alloys can be enhanced by adding a certain quantity of Ni, Cu, Mg, and other elements. The casting property is the most favorable when the Si content is approximately 17%. Hypereutectic alloys with a silicon content ranging from 16% to 19% can be applied in high wear scenarios.

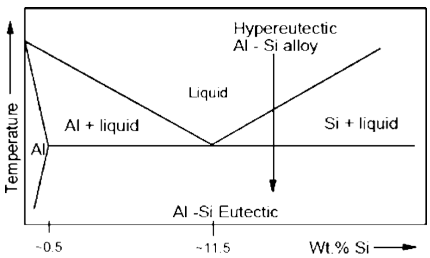

Figure 2: Binary phase diagram of Al–Si alloy system [11]

The latent heat of phase change of the Al-Si-based phase change heat storage material is approximately 500 $kJ \cdot kg^{-1}$, and the eutectic temperature is around 577℃. In comparison with salt change heat storage materials, Al-Si alloy has less corrosion to the container, lower undercooling, a moderate price, and a suitable working temperature up to 627℃. It is an extremely ideal high-temperature phase change heat storage material. Generally, the higher the Si content, the lower the solid specific heat of the aluminum-silicon alloy, the higher the initial melting point, the smaller the linear expansion coefficient, and the thermal conductivity also shows a downward trend. The Al-Si alloy near the eutectic composition not only possesses high thermal conductivity, a high latent heat of phase transition, a moderate price, but also has excellent high-temperature oxidation resistance and thermal cycle stability. It is discovered that with the increase of cycle times, the initial melting point of the Al-Si alloy rises and the thermal conductivity declines. The latent heat of melting and the coefficient of linear expansion will decrease only marginally. In general, the thermal properties of aluminum-silicon alloys are relatively stable and decay slowly.

3.2. High temperature treatment

There are three main purposes for the solid solution heat treatment of Al-Si cast alloy: (1) The soluble phase rich in Cu and Mg formed during the dissolution and solidification process; (2) Homogenize the alloying elements; (3) Spheroidize the eutectic Si phase. After cooling, a supersaturated solid solution with a uniform structure and composition can be formed, enabling a better subsequent aging treatment effect. However, it should be noted that when the solution temperature and solution time are excessively high, overburning will occur, which will reduce the effect of the subsequent aging treatment and adversely affect the properties of the alloy.

Quenching is a heat treatment process whereby castings are rapidly cooled to a lower temperature in water, oil, air, or other appropriate quenching medium. The objective of quenching is to prevent the precipitation of equilibrium phases such as Al2Cu and Mg2Si during the cooling process of castings, while retaining a considerable number of solute atoms and vacancies in the supersaturated solid solution to enhance the precipitation strengthening effect of the subsequent aging treatment. The quenching duration and rate are the primary influencing factors at this stage, and the cooling rate is dependent on the initial temperature of the quenching alloy, the requisite microstructure, mechanical properties, and alloy composition. Excessively rapid quenching rate will lead to deformation or even cracks in the castings, and an overly slow quenching rate will diminish the optimal mechanical properties after aging.

The aging treatment of Al-Si cast aluminum alloy is typically conducted at a temperature ranging from 90 to 210℃. The objective of aging is to acquire a uniformly distributed fine dispersed precipitated phase, thereby obtaining a high-strength alloy. It exhibits excellent cost performance in industrial production and is currently one of the most commonly employed heat treatment methods for aluminum alloys. The current research on aging treatment mainly centers on the addition of alloying elements such as Mg, Zn, Cu, single-stage aging, double-stage aging, and regression re-aging. The strengthening effect of the age-hardened alloy is achieved through the age-precipitated phase impeding the movement of dislocations. The strength of the alloy is dependent on the size and distribution of the precipitated phase as well as its ability to hinder the movement of dislocations. Dislocations can pass through the precipitated phase in two distinct manners, as depicted in Figure 3. One is to shear the overprecipitated phase, known as the Friedel effect (shear mechanism), and the other is to form a ring around the precipitated phase and proceed to move, referred to as the Orowan mechanism (bypass mechanism).

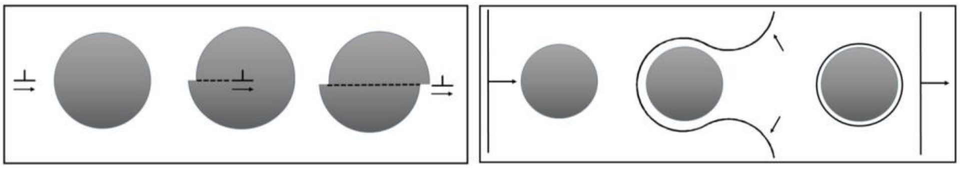

Figure 3: Schematic representation of dislocation movement according to Friedel effect and Orowan mechanism [12]

3.3. Chemical modification

The Pacz [13] invention patent indicated that introducing the Na element into the aluminum-silicon alloy melt could refine the eutectic Si, and subsequently, the modification treatment emerged. Research has discovered that adding modifiers is more effective and economical compared to any other processes. The modification of commercial aluminum-silicon alloys is typically accomplished by adding P, S, Na, Sr, rare earths, or a combination of them to the melt. The modificationof aluminum-silicon alloys encompasses the modification of the Al phase and the Si phase (eutectic Si and primary Si). The significance of the modification treatment for aluminum-silicon alloys lies in refining the aluminum phase, the silicon phase, or improving the form of the silicon phase, and ultimately enhancing the comprehensive mechanical properties of the alloy.

For the Al phase (primary α-Al and eutectic Al), the metamorphic elements are Ti, B, Zr, etc. The reason is that the related compounds (TiAl3, AlB2, TiB2, TiC, ZrAl3) of these elements and Al have similar crystal structures and comparable lattice constants, which enable them to serve as the heterogeneous nucleation cores of Al. Al-5Ti-1B intermediate alloy is the most prevalently utilized grain refiner for aluminum alloys. Nevertheless, the Al-Ti-B alloy has the drawback that TiB2 particles tend to aggregate, and deterioration and toxicity occur during the application of some aluminum alloys, thus giving rise to the emergence of the Al-Ti-C intermediate alloy. Kumar et al. [14] discovered that adding 0.2% Al-5Ti-0.8C or Al-5Ti-1.2C can effectively refine Al-7Si alloys.

There exists Na, Sr, Ca, Ba, RE and other elements exerting a metamorphic effect on eutectic Si, capable of altering the morphology of eutectic Si from coarse flake to fine fiber, thereby enhancing the strength and plasticity of Al-Si alloy. The nature of Na is overly active; even when using NAF-containing metamorphic agents, it is prone to react with oxygen, water vapor, etc., leading to deterioration, porosity and other issues; The effective period of Sr deterioration is long, the remelting effect is favorable, it does not corrode the furnace lining and tools, causes no pollution, and gradually substitutes for Na. Nevertheless, the long incubation period of Sr deterioration intensifies the getter tendency of the melt and readily causes the microstructure of the alloy to loosen. The recovery rate of Ca as a modifier is high, and the effect can still be maintained after repeated remelting. However, it demands a large cooling rate and increases the porosity. Rao et Al. [15] discovered that when 0.15wt.% Ba is added to Al-7Si alloy, the tensile strength and elongation of the alloy are significantly increased, and if the content exceeds this level, the plasticity will be adversely affected. Xing et al. [16] found that rare earth elements have the same metamorphic effect on eutectic Si, causing it to change from coarse lamellar to fine fibrous, and the mechanical properties of the alloy are significantly improved.

The main element exerting a metamorphic effect on primary Si P. Due to their similar crystal structures and lattice constants, AlP and Si can serve as the heterogeneous nucleation core of primary Si. It is challenging to add pure P, and it is typically fabricated into a composite modifier and added in the forms of red phosphorus, phosphorus salt, or phosphorus- containing intermediate alloy. The direct utilization of red phosphorus has a low recovery rate and brings about environmental and safety issues. The addition of salt is substantial, generating a large quantity of reaction slag, which leads to the corrosion of the furnace lining and an unstable refining effect along with a high scrap rate. Hence, it is frequently added in the form of intermediate alloys containing phosphorus, such as Cu-P, Si-P, Ni-P, Al-Cu-P, Al-Fe-P, Al-P, Al-Si-P, and Al-Zr-P. Cu-P and Al-Cu-P intermediate alloys are more stable but demand higher temperatures to be effective. Al- Fe-P intermediate alloys are abandoned because of the presence of Fe content, which is regarded as an impurity. This gave rise to the development of the Al-P series of intermediate alloys, free of any impurities, as ideal refiners for hypereutectic Al-Si alloys.

3.4. Add element

Different elements are incorporated into the aluminum-silicon alloy, which can be classified into several categories. Elements such as Mg, Cu, Ni, and Mn are regarded as the primary alloying elements, while transition metals like Sr, Ti, P, B, and rare earth elements are considered as minor additions. The primary alloying elements offer much-needed solid solution strengthening and precipitation strengthening to the alloy. The minor additions of alloying elements enhance the mechanical integrity, overall wear resistance, robustness, and porosity of the alloy. Impurities like Fe, Pb, Sb, and Sn are of major concern for the industry as they are the causes of poor physical, mechanical, and service characteristics in various applications.

The addition of Mg can notably enhance the yield strength and age hardening properties of Al-Si alloy yet reduce the ductility of the alloy. For the Al-Si-Mg ternary alloy, the escalation of Si content results in the decline of phase transition temperature and the augmentation of latent heat. When Si and Mg increase simultaneously, the latent heat of phase transition will ascend, and the latent heat of phase transition per unit mass attains 545kJ/kg at Al-36Si-30Mg. The introduction of Cu enhances the casting strength and high-temperature strength of Al-Si alloy but gives rise to high porosity and low ductility. For the Al-Si-Cu ternary alloy, with the increment of Cu content, the phase transition temperature, latent heat per unit mass, and latent heat per unit volume initially increase and then decrease. The incorporation of Zn does not significantly enhance the properties of the alloy unless Mg and/or Cu are present in the alloy. For the Al-Si-Zn ternary alloy, the phase transition temperature, latent heat per unit mass, and latent heat per unit volume decrease as the zinc content rises. Other elements, such as Ni, can boost the high-temperature strength of Al-Si alloy within the range of 250-375℃, but diminish the elongation at room temperature. According to the design requirements of the components, secondary alloying elements like Sr, Na, Sc, transition metals, and rare earth elements can also be added to the alloy. Nevertheless, the content needs to be restricted to <1% to prevent the formation of other defects in the alloy, such as porosity and shrinkage.

Iron and manganese are both regarded as common impurity elements. When the iron content in the alloy surpasses a certain critical value, the hard needle/sheet iron phase will precipitate in the aluminum alloy, causing the deterioration of the performance of the aluminum alloy. Additionally, the formation of the β-Fe phase during the solidification process makes it difficult for liquid aluminum to fill the dendrite void, which will result in poor casting performance. Manganese is also a common neutral element in the iron phase, and the addition of manganese inhibits the precipitation of the β-Fe phase. Although it has some beneficial effects in the manufacturing process, the presence of Mn is considered an impurity due to the excessive formation of dendritic and blocky intermetallic compounds in the Al-Fe-Mn-Si system.

4. ENCAPSULATION MODE

The crux of PCM applications lies in material selection and packaging. Based on the varying size, the packaged PCM can be classified into macro packaging, micro packaging, and nano packaging. The merits of encapsulated PCM can be generalized as follows: prevent PCM leakage, enhance the heat transfer area, control the volume variation during the PCM phase transition, and prevent PCM from reacting with the environment.

4.1. Macroencapsulation

The crux of macroscopic packaging lies in selecting the suitable shell shape and shell material based on the traits of PCM. It is also indispensable to reserve some space during the packaging process. The prevalent shapes of macroscopic packaged PCM are tubular and spherical, as depicted in Figure 4. The straightforward geometry of tubular packages, the simplicity of assembly and disassembly, and the low cost render them conducive to practical applications. The spherical package conserves materials, has a large heat transfer coefficient, a stable geometric and chemical structure, and is mainly utilized in heat storage systems such as the packed bed and the fluidized bed. Common packaging materials include ceramic and metal. Ceramics like Al_2O_3, AlN, and Si_3N_4, etc., can fulfill the requirements of strength, toughness, and corrosion resistance. Metals like Cu, Al, and stainless steel possess excellent thermal conductivity but exhibit poor corrosion resistance.

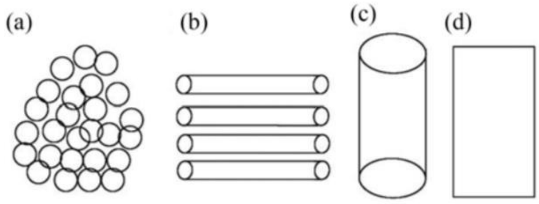

Figure 4: Encapsulation PCM of (a) spherical encapsulation, (b) tubular encapsulation, (c) cylindrical encapsulation and (d) rectangular encapsulation [17]

The mixed sintering approach involves combining aluminum alloy powder, utilized as a phase change material, with another type of high melting point material powder serving as a substrate after thorough mixing and compression, followed by sintering, thereby achieving the macroscopic phase change of the material. Under the mixed pressing procedure, the phase change material is dispersed within the matrix phase, enabling the encapsulation of the phase change material without altering the outstanding thermal properties inherent to the phase change material itself. Besides being immiscible with PCM and having favorable compatibility, it also demands good thermal conductivity and certain mechanical attributes. In addition to ceramic substances such as zirconia and aluminum nitride, matrix materials like carbon powder, kaolin, and fly ash can also undergo mixed sintering with aluminum base powder. Miscible gap alloy (MGA) is a typical mixed sintering method, and its structure is depicted in Figure 5. However, due to the random distribution of phase change materials within the matrix during the mixing and pressing process, a certain quantity of aluminum alloys will be distributed on the surface, prone to leakage during multiple thermal cycles, thereby posing the risk of container corrosion. The detriment caused by aluminum is more pronounced than that of other materials, so this issue must be given due attention in the design of material applications.

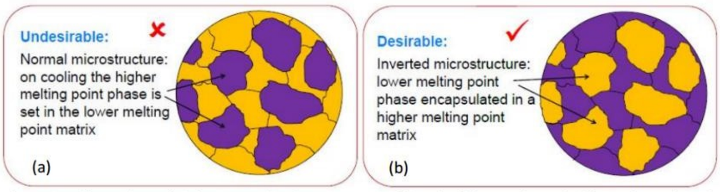

Figure 5: Illustration of a) the 'natural' microstructure of immiscible metals cooled from the melt and b) the inverted microstructure produced using powder metallurgy [18]

Silicon can be purified through high-frequency electromagnetic directional solidification. During the solidification of hypereutectic Al-Si alloy under the influence of RMF, segregation of the primary Si phase takes place. Based on this, by regulating the cooling conditions and the flow field induced by RMF, a silicon-rich layer with a high silicon content is acquired, which can be utilized as a self-encapsulation strategy for containerless eutectic Al-Si PCM. Due to the insufficient strength of the silicon-rich layer, it is necessary to incorporate supporting materials within the silicon-rich layer. Zou et al. [19, 20] constructed [SiC&Si-rich] Al-Si and [Cf&Si-rich] Al-Si, and its three-dimensional structure is depicted in Figure 6. The addition of supporting materials can address the issue of leakage of eutectic Al-Si PCM from the package housing and significantly enhance the limit damage temperature of PCM. Both structures exhibit outstanding structural stability at various heating/cooling rates and can effectively encapsulate the Al-Si region. The thermal conductivity of this encapsulation method is 2 to 8 times that of traditional encapsulation shell materials, and it also demonstrates excellent cyclic performance.

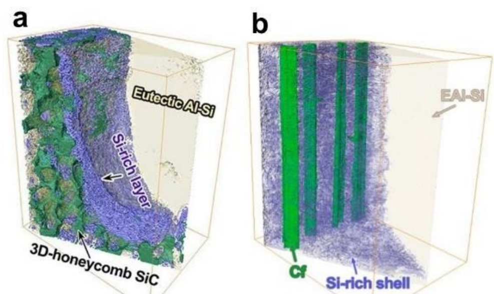

Figure 6: (a) 3D reconstruction images of the [SiC&Si-rich]◎EAl-Si30 cPCM. [19] (b)3D reconstruction images of the [Cf&Si-rich]◎EAl-Si30 cPCM. [20]

Porous materials characterized by low density, high strength, large specific surface area, stable shape, and high porosity are frequently employed as PCM support materials for the synthesis of porous shaped composite PCM. Pore structure, chemical compatibility, carrier surface properties, and cost constitute significant factors in the selection of porous materials. The prevalently utilized porous carrier materials primarily encompass metal-based porous materials, mineral-based porous materials, carbon-based porous materials, and other types of materials. Metal foam bases exhibit high thermal conductivity: the mineral-based porous material can tightly adsorb PCM within the pores under the interplay of capillary force, surface tension, and other forces. Carbon-based porous materials possess a large specific surface area and high thermal conductivity. Mesoporous SiO_2 has a large specific surface area and controllable pore size. Additionally, with the assistance of external forces such as the temperature field, electric field, and magnetic field, the packing is oriented or a three-dimensional network is constructed to form a highly ordered directional structure, which can further enhance heat conduction [21]. The thermal conductivity can also be augmented by adding high thermal conductivity additives. Table 3 delineates the additives for carbon-based materials and metal-based materials, along with their respective approaches for further enhancing heat transfer.

Table 3: High thermal conductivity additive to enhance heat transfer [22,23]

additive	peculiarity	Increase thermal conductivity
expended graphite (EG)	possesses a porous structure	Increase packing density
Carbon fiber (CF)	possesses excellent corrosion resistance and chemical attack resistance	Increase the aspect ratio of carbon fiber
graphene	distinctive chemical and physical nature, large aspect ratio, and outstanding thermal conductivity	Reduced specific surface area
carbon nanotube (CNT)	high thermal conductivity, low density and large surface area–to–volume ratios, and easy to form stable mixture with organic–based matrix	Use columnar structures whenever possible
Metal foam	includes a great volume fraction of gas–charged pores	Porosity reduction
Metal particles	It has strong mixing properties	Make the operating temperature close to the particle melting temperature
metal oxides.	Thermal conductivity of metal oxide is lower than that of metal, but much higher than that of most PCMs	Increase oxide content

4.2. Microencapsulation

Microcapsules employ phase change materials as the core and utilize inorganic or organic materials as the shell to encapsulate the phase change materials, forming a core-shell structure, with a general size of microns. The shell is typically a ceramic material featuring oxidation resistance, high-temperature resistance, and a certain degree of strength. It has a higher heat transfer rate than macro encapsulated phase change materials but is also more challenging to fabricate. Microencapsulated PCM possesses an extremely high specific surface area, which can endure the volume change during the phase transition. The high heat transfer rate enables microencapsulated PCM to melt and solidify rapidly. In terms of thermal and chemical stability, microencapsulated PCM is more dependable than macroscopic packaging. Since the aluminum base is prone to oxidation to form a corrosion-resistant alumina shell, a superior metal is generally plated on the alumina shell. Additionally, AlN and other ceramics can also serve as the shell of aluminum microcapsules. Although microcapsules may reduce the energy storage density, the packaging effect is favorable, and it is also the most commonly utilized packaging method for aluminum-based phase change materials. Wei et al. [24] discovered a method that can adjust the thickness of the Al_2O_3 shell and the melting temperature, and the prepared composite phase change material has a certain self-healing ability. The diagram of the preparation process is presented in Figure 8.

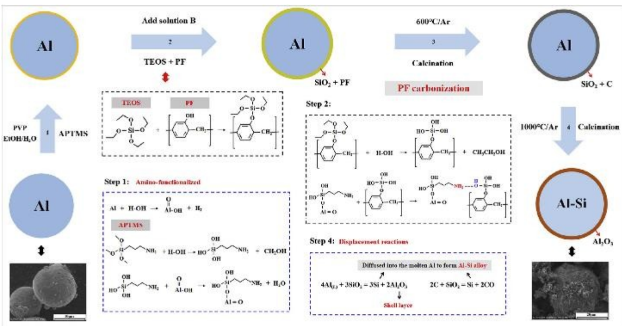

Figure 7: Schematic diagram of the preparation process of Al-Si/Al_2O_3 composite PCM, Steps 1 and 2 correspond to the formation of precursor shell on the surface of mino-functionalized Al microspheres, Steps 3 and 4 represent the calcination process in an argon atmosphere. [24]

4.3. Nanoencapsulation

Once the material size is diminished to less than 1000nm upon encapsulation, nanocapsulated phase change materials are acquired. Nanocapsule shells are typically constituted by polymers as they achieve an optimal equilibrium between strength and flexibility. Inorganic shells can also be employed, which possess higher thermal conductivity but are more fragile. It is also feasible to form a composite polymer/no case combining their respective advantages. In contrast to macro and micro packages, nanocapsules are structurally more stable and hold great potential in thermal energy storage applications. Moreover, smaller capsules imply a larger surface-area-to-volume ratio, which enhances heat transfer. Nevertheless, constrained by the preparation technology, the research of nanocapsulated phase change materials still remains in the laboratory stage, while microcapsules and macroscopic encapsulation phase change materials have been successfully commercialized.

There have been numerous reports concerning the techniques for manufacturing microcapsules and nanocapsules. These methods encompass spray drying, microemulsion polymerization, precipitation of pre-formed polymers, layer-by-layer assembly (LbL), or other more sophisticated polymerization reactions such as radical addition-cleavage chain transfer (RAFT), and tree polymer production. While the deposition of preformed materials constitutes a straightforward process, polymerization reactions are typically more adaptable. The pros and cons of commonly utilized polymerization reactions are presented in Table 4. Excellent nanocapsules ought not only to possess a single-layer shell with a sole function but also be capable of assembling multiple layers of shells and endowing each layer with a distinct function. The nanocapsules are capable of gradually adsorbing diverse components (polyelectrolytes, nanoparticles, proteins, enzymes, etc.) and forming a multilayer shell with nanometer-level precision. This also points out a direction for the future development of nano-encapsulation technology.

Table 4: The advantages and disadvantages of various encapsulation techniques.

<table>
<tr><th>Encapsulation techniques</th><th>Advantages</th><th>Disadvantages</th><th>ref</th></tr>
<tr><td>In situ polymerization</td><td rowspan="4">- Small size of the microcapsules
- Uniform distribution of the microcapsules
- Tight shell of the microcapsules
- Good stability of the microcapsules</td><td>- Reasonable mass ratio of the monomer
- Temperature control of the reaction
- pH value regulation of the reaction
- Use of formaldehyde</td><td>[25]</td></tr>
<tr><td>Interfacial polymerization</td><td>- Reasonable mass ratio of the monomer
- Temperature control of the reaction
- Suitable emulsor</td><td>[26]</td></tr>
<tr><td>Suspension polymerization</td><td>- Reasonable mass ratio of the monomer
- Temperature control of the reaction
- Suitable emulsor</td><td>[27]</td></tr>
<tr><td>Sol–gel polymerization</td><td>- Reasonable mass ratio of the monomer
- pH value regulation of the reaction</td><td>[28]</td></tr>
<tr><td>Complex coacervation</td><td>- pH value regulation of the reaction.
- Temperature control of the reaction.</td><td>- Big size of the microcapsules.
- Loose shell of the microcapsules.
- Poor stability of the microcapsules.</td><td>[29]</td></tr>
</table>

The selection of cladding material and cladding structure also exerts a significant impact on the stability and performance of cladding. One intriguing potential solution for enhancing stability is the application of self-healing capsules. There are numerous instances in the literature regarding self-healing capsules that contain shell monomers in the core (e.g., diisocyanate in the core of a polyurethane capsule [20]). Additionally, the combination of polymerization and the LbL assembly method to form the PCM capsule shell can attain the self-healing effect.

5. CONCLUSION

This paper offers a systematic concept for the commercial application of Al-Si phase change alloy from three aspects: preparation, performance optimization, and packaging. Regarding the preparation methods, the casting approaches currently employed are mainly high-pressure casting, which is more cost-efficient and has a high cycle rate. The properties of aluminum-silicon alloys are largely dependent on the casting process, composition, and melt treatment of the alloys. The mechanical and thermal properties of Al-Si alloy can be optimized through high-temperature treatment, addition of modifiers, and addition of elements. The packaging methods of Al-Si phase change alloy have their own advantages and disadvantages, and flexible consideration should be given to the packaging methods of Al-Si alloy based on the actual requirements.

6. REFERENCES

[1] Gursoy O, Timelli G. 2020. Lanthanides: A Focused Review of Eutectic Modification in Hypoeutectic Al–Si Alloys. J. Mater. Res. Technol. 2020, 9, 8652–8666.

[2] Sobhan S D, Daolun C. 2023. A Review on Processing–Microstructure–Property Relationships of Al-Si Alloys: Recent Advances in Deformation Behavior[J].Metals,2023,13(3):609-609.

[3] Grosselle F, Timelli G, Bonollo F, Molina R. 2009. "Correlation between microstructure and mechanical properties of Al-Si diecast engine blocks," Metallurgical Science and Technology, vol. 27, no. 2, pp. 2-10.

[4] Swift K G, Booker J D. 2013. Manufacturing Process Selection Handbook: From design to manufacture, United Kingdom: Butterworth-Heinemann.

[5] Vinarcik E G. 2002. High Integrity Die Casting Processes, USA: John Wiley & Sons.

[6] Garg S K. 2009. Comprehensive Workshop Technology, India: Laxmi Publications.

[7] Luo A A, Sachdev A K, Apelian D. 2022. Alloy Development and Process Innovations for Light Metals Casting. J. Mater. Process. Technol. 2022, 306, 117606.

[8] Kenneth P Y. 1995. SSM casting process.18th International Die Casting Congres Transactions,Indianapolis Indiana.

[9] Cinkilic E, Ridgeway C D, Yan X, Luo A A. 2019. A Formation Map of Iron-Containing Intermetallic Phases in Recycled Cast Aluminum Alloys. Metall. Mater. Trans. A 2019, 50, 5945–5956.

[10] V V,Prabhu N K. 2013. Review of Microstructure Evolution in Hypereutectic Al–Si Alloys and its Effect on Wear Properties[J].Transactions of the Indian Institute of Metals,2013,67(1):1-18.

[11] Alloy phase diagrams, ASM Handbook, Vol. 3, ASM International, Materials Park, OH (1992).

[12] Xiong J J, Li Y, Feng Z Z, et al. Research progress of heat treatment technology of Al-Si series casting alloy [J]. Foundry,2022,71(05):544-550.

[13] Pacz A. 1921. Alloy: US, 1387900[P].

[14] Vinod Kumar G S, Murty B S, Chakraborty M. 2005. Development of Al–Ti–C grain refiners and study of their grain refining efficiency on Al and Al–7Si alloy[J]. Journal of Alloys and Compounds, 2005, 396(1): 143-150.

[15] Rao J, Zhang J, Liu R, et al. 2018. Modification of eutectic Si and the microstructure in an Al-7Si alloy with barium addition[J]. Materials Science and Engineering: A, 2018, 728: 72-79.

[16] Xing P, Gao B, Zhuang Y, et al. 2010. Effect of erbium on properties and microstructure of Al-Si eutectic alloy[J]. Journal of Rare Earths, 2010, 28(6): 927-930.

[17] Salunkhe P B, Shembekar P S. 2012. A review on effect of phase change material encapsulation on the thermal performance of a system[J]. Renewable and sustainable energy reviews, 2012, 16(8): 5603-5616.

[18] Kisi E, Sugo H, Cuskelly D, et al. 2017. Miscibility Gap alloys: a new thermal energy storage solution[C]//Transition Towards 100% Renewable Energy: Selected Papers from the World Renewable Energy Congress WREC 2017. Springer International Publishing, 2018: 523-532.

[19] Zou Q C, Dong Z H, Yang X H, et al. 2021. Electromagnetic self-encapsulation strategy to develop Al-matrix composite phase change material for thermal energy storage[J].Chemical Engineering Journal,2021,425

[20] Zou Q C, Dong Z H, Yang X H, et al. 2022. Electromagnetic self-encapsulation of carbon fiber reinforced Al matrix composite phase change material for high-temperature thermal energy storage[J].Journal of Alloys and Compounds,2022,901

[21] Wu S, Li T X, Wu M Q, et al. 2021. Dual-functional aligned and interconnected graphite nanoplatelet networks for accelerating solar thermal energy harvesting and storage within phase change materials [J]. ACS Applied Materials & In terfaces, 2021, 13(16): 19200-19210.

[22]Fang G, Tang F, Cao L. 2014. Preparation, thermal properties and applications of shape-stabilized thermal energy storage materials[J].Renewable and Sustainable Energy Reviews,2014,40237-259.

[23] Lin Y, Jia Y, Alva G, et al. 2018. Review on thermal conductivity enhancement, thermal properties and applications of phase change materials in thermal energy storage[J].Renewable and Sustainable Energy Reviews,2018,82(P3):2730-2742.

[24] Wei H, Wang C, Yang S, et al. 2019. A strategy for designing microencapsulated composite phase change thermal storage materials with tunable melting temperature[J]. Solar Energy Materials and Solar Cells, 2019, 203: 110166.

[25] Mason T G, 2000. Ultrason. Sonochem., 2000, 7, 145–149.

[26] Shukla A, Buddhi D, Sawhney R L. 2008. Renewable Energy, 2008, 33, 2606–2614.

[27] Xu H, Zeiger B W, Suslick K S, Chem. 2013. Soc. Rev., 2013, 42, 2555–2567.

[28] Sathishkumar P, Mangalaraja R V, Anandan S. 2016. Renewable Sustainable Energy Rev., 2016, 55, 426–454.

[29] Price G J. 2003. Ultrason. Sonochem, 2003, 10, 277–283.

[30] Yang J, Keller M W, Moore J S, White S R, Sottos N R. 2008. Macromolecules, 2008, 41, 9650–9655.

#365: A novel biomass wood fiber-based composite phase change material for building envelope

Aizheng LI[1], Yingying YANG[1*], Zhonghua SHEN[1], Vogt-Wu TINGTING[2,3], Bouzouidja RYAD[2,3], Bossu JULIE[4], Weidong WU[1], Hua ZHANG[1]

[1] *University of Shanghai for Science and Technology, 516 Jun Gong Road, Shanghai, China, liaizheng0826@163.com, yingyingyang@usst.edu.cn, 497172688@qq.com, usstwwd@usst.edu.cn, zhanghua3000@163.com*
[2] *Univ. Bordeaux, CNRS, Bordeaux INP, I2M, UMR 5295, F-33400, Talence, France, tingting.vogt-wu@u-brodeaux.fr, ryad.bouzouidja@u-bordeaux.fr*
[3] *Arts et Metiers Institute of Technology, CNRS, Bordeaux INP, Hesam Universite, I2M, UMR 5295, F-33400 Talence, France,*
[4] *CNRS, UMR EcoFoG, Kourou, Guyane Française ,France, julie.bossu@cnrs.fr*

Abstract: The thermal performance of the building envelope significantly affects indoor thermal comfort and operational energy consumption. Biomass envelopes are attracting more attention due to their eco-friendly properties, renewability, and other notable benefits. In this paper, a novel wood fiber-based biomass composite phase change material (PCM) (A-WF/LASA/h-BN) with high thermal storage performance was developed. It encapsulates lauryl alcohol-stearic acid PCM into acetylated wood fibers by vacuum adsorption, with hexagonal boron nitride added to reinforce its thermal conductivity. SEM, DSC, FT-IR, and TG were used to characterize its thermal and chemical properties, and thermal storage experiments were carried out to evaluate its thermoregulation performance. Results show that A-WF/LASA/h-BN is structurally, chemically, and thermally stable as well as having excellent thermoregulation performance. No significant leakage was observed during the experiment. Within the range of 0 to 100°C, the leakage rate was only 1.66%. After 400 thermal cycles, the latent heat of phase change decreased by only 2.63 $J \cdot g^{-1}$. The appropriate temperature range of the phase change and the high enthalpy of the phase change make it suitable for building envelope applications. Compared with acetylated wood fibers, the peak temperature of A-WF/LASA/h-BN was reduced by 3.09°C, and the peak time was delayed by 7.78 min. Infrared thermal imaging shows the temperature distribution of the A-WF/LASA/h-BN sample is more uniform during the heating up and cooling down process, which indicates a superior ability to suppress temperature fluctuations. The superior composite PCM applied in the envelope can reduce building energy consumption while enhancing indoor thermalcomfort.

Keywords: Biomass Materials; Phase Change Materials; Wood Fiber; Building Energy Efficiency

1. INTRODUCTION

Building energy consumption accounts for 40% of global final energy consumption and 35% of total emissions from the energy field (Liu et al., 2023). It is crucial to reduce energy consumption in the building field in the background of the energy crisis as well as in the perspective of sustainable development. Developing zero-energy buildings is one of the key technologies for addressing energy conservation and emission reduction in the building field (Alqaed et al., 2024). On the one hand, passive thermal energy storage technology can be utilized to enhance the thermal performance of building envelopes and reduce indoor heat loads, thus lowering energy consumption and carbon emissions during building operations. On theother hand, employing building products with minimal environmental impact can facilitate the provision of green buildings more effectively, thereby reducing energy demand and carbon emissions during both the construction phase and the lifecycle of the building.

Bio-based composite phase change material (PCM) is a composite PCM with bio-based porous material as a carrier and bio-based PCM as a core material (Barbieri et al., 2020; Kallavus et al., 2017). Due to its high energy storage density, thermal stability, long cycle life, and environmentally friendly nature, bio-based composite PCM has become the mainstream choice for enhancing the self-regulating temperature performance of building envelopes, garnering widespread attention in the pursuit of low-energy buildings. However, for bio-based composite phase change core materials, their thermal conductivity is relatively low, with values such as 0.25 W·(m^{-1}·K^{-1}) for paraffin (Zhao et al., 2021) and 0.22 W· (m^{-1}·K^{-1}) for palm oil (Wang et al., 2010). It greatly affects the rate of energy storage and release. Phase change core materials change phase when releasing or storing heat (Wei et al., 2017). Although biobased porous materials possess a higher specific surface area and good adsorption capacity, allowing for the encapsulation and restriction of the transition from solid to liquid phase after heat absorption, their adsorption capacity remains limited. Moreover, there is potential for further enhancement.

Currently, scholars have conducted preliminary research on bio-based adsorption materials and bio-based PCMs. Li et al. (Li et al., 2016) attempted to encapsulate polyethylene glycol in unmodified fir wood, resulting in energy storage wood with a melting temperature of 26.74 °C and a phase change latent heat of 73.59 J·g^{-1}. Meanwhile, it was noted that due to the water permeability of wood, coating treatment is necessary to achieve better encapsulation properties. Boussaba et al. (Boussaba et al., 2019) utilized natural clay and cellulose fibers as supporting materials, coconut oil as a biomass PCM, and graphite for enhancing thermal conductivity. They fabricated composite materials by physically adsorbing PCM onto the supporting material through a direct impregnation method. This material melts at 27.33 °C, with a phase change enthalpy of 40.27 J·g^{-1} and good thermal stability, making it suitable for building envelopes. Sari et al. (Sarı et al., 2020) used waste wood fibers to adsorb 52 wt% fatty acid phase change material, achieving a phase change enthalpy of 92.1 J·g^{-1} in the leak-proof shaped PCM. Thermal performance tests on the composite board showed that, compared to pure wood fiberboard, the composite PCM board reduced the central cavity temperature by 2.67 °C. Ma et al. (Ma et al., 2018) investigated various modification conditions for wood flour. They found that treatment with composite salt solutions (sodium chloride, potassium nitrate, and lithium chloride) maximized the pore size and impregnation ratio of wood flour. This treatment allowed for the preparation of composites PCM with an encapsulation capacity of up to 60%. Additionally, the wood flour-based PCMs demonstrated good thermal reliability. Gökhan et al. (Hekimoğlu et al., 2023) developed a leakproof composite with enhanced properties by blending bio-based PCMs, specifically lauric and capric acid, as the phase change core material impregnated in an activated carbon framework derived from almond shells. The composites PCM, with a melting temperature of 21.58 °C and a latent heat capacity of 126.8 J/g, were ultimately incorporated into cement mortar in suitable proportions. Overall, research on bio-based composite phase change materials with high heat storage performance is still in its early stages. It still faces challenges such as low adsorption efficiency and poor heat transfer efficiency (Low thermal conductivity), making it difficult to achieve efficient regulation of indoor thermal comfort.

In this study, a binary phase change core with an ideal phase change temperature zone, high latent heat, and stable characteristics was prepared through binary compounding using a bio-based phase change material: lauryl alcohol-stearic acid (LASA). Its thermal conductivity is enhanced by incorporating metal nanoparticles, specifically hexagonal boron nitride (h-BN). Wood fiber (WF) is used as a porous scaffold, and its adsorption performance and stability are enhanced through acetylation modification. Finally, utilizing the vacuum adsorption method, the thermally reinforcing binary PCM was absorbed into the modified wood fibers. A novel biomass wood fiber-based composite PCM (A-WF/LASA/h-BN) was developed. The novel biomass wood fiber-based composite PCM exhibits good physical and chemical stability, excellent thermal stability, and superior heat storage and thermal conductivity properties. Experimental results on heat storage performance indicate that this material effectively regulates temperature and suppresses unstable fluctuations. The application of this composite PCM in the building field can improve the thermal performance of building envelopes, extend indoor thermal comfort, and reduce building energy consumption and carbon emissions.

2. PREPARATION OF BIOMASS WOOD FIBER-BASED COMPOSITE PCMS

Firstly, acetylation modification of wood fibers is performed to address the issues of strong hydrophilicity leading to moisture susceptibility and mold growth, as well as their poor compatibility with non-polar polymer matrices. Acetylation modification can enhance the hydrophobic and oleophilic properties of wood fibers and improve their compatibility with PCMs. To overcome the issues of low enthalpy in phase change materials and the mismatch of phase change temperature ranges, the binary composite phase change material LASA (LA: SA=0.82: 0.18) was prepared using lauryl alcohol and stearic acid as raw materials. Metal nanoparticles with high thermal conductivity and small size were incorporated into the PCMs for their thermal conductivity directly influences the rates of energy storage and release. Finally, the thermally reinforcing PCM was embedded into the pore structure of the acetylated wood fibers using the vacuum adsorption method. This embedding process utilized the internal and external pressure difference, along with the combined effect of capillary force and the surface adsorption effect of wood fibers. After drying, a novel biomass wood fiber-based composite PCMwas prepared. The process of preparation of biomass wood fiber-based composite PCM is given in Figure 1.

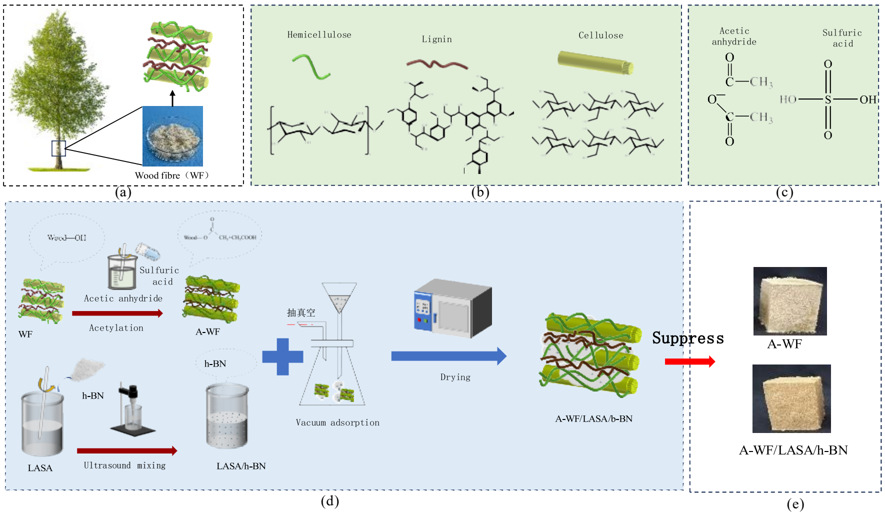

Figure 1: A schematic of the preparation process of biomass wood fiber-based composite PCMs (a) Components of wood fibers (b) Structural composition of wood fibers (c) Structures of acetic anhydride and sulfuric acid (d)preparation process of biomass wood fiber-based composite PCM (e) A-WF *and* A-WF/LASA/h-BN samples *(30×30×30 mm)*

3. EVALUATION OF BIOMASS WOOD FIBER-BASED COMPOSITE PCMS

3.1. Properties and characterization of modified wood fibers

WFs were acetylated using acetic anhydride under the following conditions: 5 g of dried wood fibers, 100 mL of acetic anhydride, sulfuric acid concentration of 2 mol·L^{-1}, reaction temperature of 60 ℃, reaction time of 4 h, and 3 mL of sulfuric acid added. The modified wood fiber was named A-WF. A-WF was characterized by the water droplet contact angle and leakage test. The results indicate that the modified wood fibers exhibit excellent oil repellency and water resistance. The optimal incorporation ratio of PCM without significant leakage is 45 wt%.

Figure 2 shows the static contact angle images of WF and A-WF. Within 5s of contacting the WF surface, water quickly penetrates the gaps between the WF. However, for A-WF, there is no significant penetration of water within 30 s. The left contact angle is 116.9°, the right contact angle is 117.0°. This demonstrates excellent hydrophobic performance, indicating the successful acetylation modification of the WF for improved hydrophobicity.

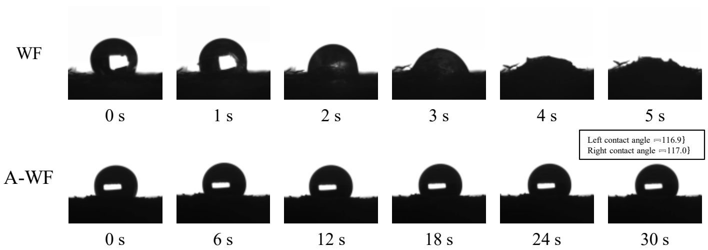

Figure 2: The static contact angle images of WF and A-WF.

Table 1 shows the leakage rates of biomass wood fiber-based composite PCMs with different mass mixing ratios of LASA after heating. The leakage rate of the composite PCMs was below 1 % at 15.6 wt%, 25.3 wt%, 35.3 wt% and 45.2wt%. The leakage rate is three times higher when the mass mixing rate exceeds 45.2 wt% compared to when it is at 45.2%. Thus, 45 wt% can be identified as the critical threshold for A-WF capillary forces to stabilize the adsorption of PCMs.

Table 1: The leakage rates of biomass wood fiber-based composite PCMs with different LASA mass addition ratios before and after heating.

Addition ratio/wt%	Initial mass/g	Mass after heating/g	Leakage rate/%
15.6	1.4637	1.4603	0.23
25.3	1.5140	1.5089	0.34
35.3	1.5622	1.5562	0.38
45.2	1.6137	1.6029	0.67
50.2	1.6786	1.6419	2.19

3.2. Properties and Characterization of PCMs

To enhance the thermal conductivity of the phase change material LASA, various concentrations of thermally conductive reinforcing particles, including Al_2O_3, CuO, and h-BN were added. After considering the effects of thermally conductive reinforcing particles on the thermal conductivity and energy storage density of phase change materials, h-BN was selected as the thermally conductive reinforcing particle for LASA. The mass addition ratio was 1.5 wt% and named LASA/h-BN. The melting temperature of LASA/h-BN was 20.9 °C, the latent heat of phase change was 198.6 J·g^{-1}, the thermal conductivity was 0.2513 W·(m^{-1}·K^{-1}), and the enhancement was 19.6%.

Figure 2 illustrates the variation in the thermal conductivity of LASA with the addition of different types and concentrations of thermally conductive reinforcing nanoparticles. It can be observed that the thermal conductivity of the composite phase change materials increases with the increase in the addition of thermally conductive reinforcing particles. When Al_2O_3, CuO, and h-BN reached the planned maximum addition of 2 wt%, the thermal conductivity was improved by 21.66%, 14.90%, and 25.56%, respectively, compared to LASA. Among them, the thermal conductivity enhancement of h-BN is superior to that of Al_2O_3 and CuO.

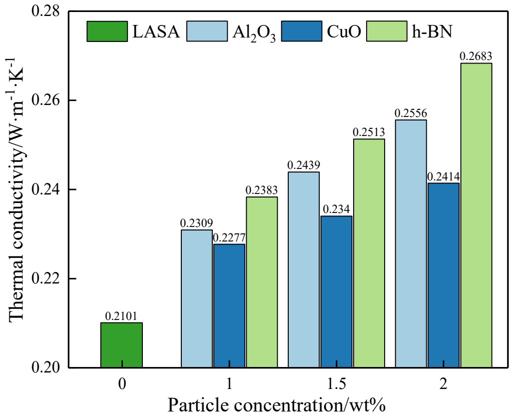

Figure 2: The variation in thermal conductivity of LASA with the addition of different types and concentrations of thermally conductive reinforcing nanoparticles.

Figure 3 shows the Differential Scanning Calorimetry (DSC) thermograms of LASA with varying concentrations of thermally conductive reinforcing nanoparticles h-BN added. From the figure, it can be observed that with the increasing proportion of h-BN addition, the peak area of the phase change material gradually decreases. This indicates that the addition of thermally conductive reinforcing particles h-BN leads to a gradual reduction in the latent heat of the thermally enhanced composite phase change material LASA/h-BN. Compared to the melting temperature of LASA (21.3 °C), the melting temperature of LASA/h-BN remains essentially unchanged. This indicates that the addition of thermally conductive reinforcing particles does not alter the melting temperature of the phase change material. Meanwhile, the endothermic curves of LASA/h-BN exhibit only one endothermic peak, consistent with the endothermic process of LASA. This indicates that the addition of h-BN does not alter the phase transition of the phase change material.

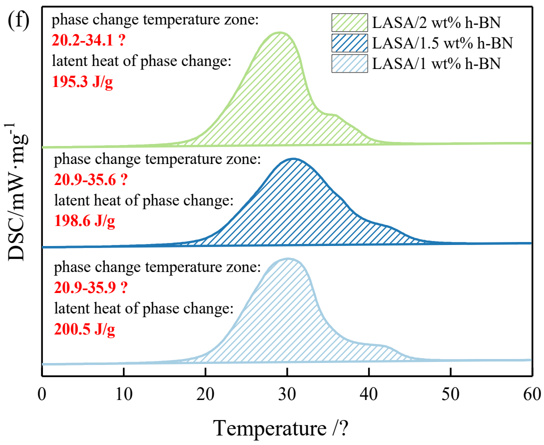

Figure 3: The DSC thermograms of LASA with varying concentrations of thermally conductive reinforcing nanoparticles h-BN were added

3.3. Properties and characterization of A-WF/LASA/h-BN

According to the above analysis, LASA/h-BN (with an h-BN addition ratio of 1.5 wt%) was chosen as the phase change core material, with A-WF serving as the porous support material. The modified wood fiber-based composite phase change material was prepared using the vacuum adsorption method. It was named A-WF/LASA/h-BN. SEM (Scanning electron microscope), DSC, FT-IR (Fourier-transform infrared), and TG (Thermogravimetric) were used to characterize it. The results indicate that LASA/h-BN was successfully adsorbed into A-WF. The compounding process of A-WF/LASA/h-BN does not affect the phase behavior of the phase change materials employed, and no other chemical changes have occurred. No phase change material volatilizes within the temperature range of 0 to 100 °C. It has good thermal stability with 400 cycles. The thermal properties of A-WF/LASA/h-BN are presented in Table 2. The heat storage coefficients in the solid and liquid temperature ranges are 5.41 and 5.13 W·m^{-2}·K^{-1}, respectively, which are more than double those of A-WF (1.87 and 1.75 W·m^{-2}·K^{-1}).

Table 2: The thermal properties of A-WF/LA-SA/h-BN

Material	A-WF/LA-SA/h-BN
Density /kg·m^{-3}	547.28
Melting temperature /℃	19.30
Latent heat of phase change /J·g^{-1}	87.01
Thermal conductivity /W·m^{-1}·K^{-1}	0.13
Specific heat capacity /J·g^{-1}·K^{-1} (solid/liquid)	5.36 /4.83
Heat storage capacity /W·m^{-2}·K^{-1} (solid/liquid)	5.41/5.13

Figures 4(a) and (b) respectively show the SEM images of A-WF and A-WF/LASA/h-BN. In comparison to the rough surface of A-WF, the surface of A-WF/LASA/h-BN appears smoother, with the phase change material evenly distributed on the surface. Fewer visible pores were observed on the surface of A-WF/LASA/h-BN, indicating that most of the pore space of A-WF was occupied by LASA/h-BN, and the phase change material was successfully adsorbed into A-WF. Due to the rough and irregular fiber structure on the surface of A-WF, the phase change material tends to be trapped within it even in its molten state, making serious leakage less likely to occur. As a result, the composite phase change material exhibits good stability.

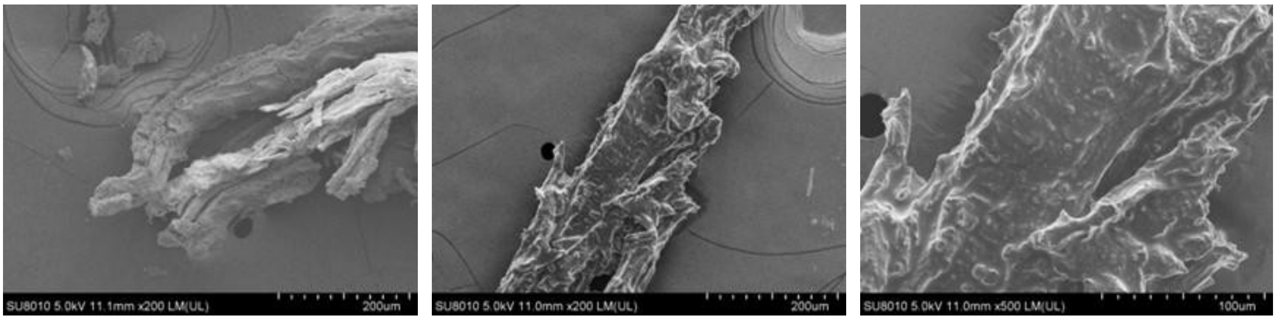

(a) (b) (c)

Figures 4: SEM images of A-WF and A-WF/LASA/h-BN (a)A-WF×200(b)A-WF/LASA/h-BN×200(c)A-WF/LASA/h-BN×500

Figure 5 shows the DSC thermograms of LASA and A-WF/LASA/h-BN. From the figure, it can be observed that the DSC thermogram of A-WF/LASA/h-BN exhibits only one endothermic peak, consistent with the single peak endothermic process observed in LASA. This indicates that A-WF does not alter the phase state of the phase change material used in the compounding process.

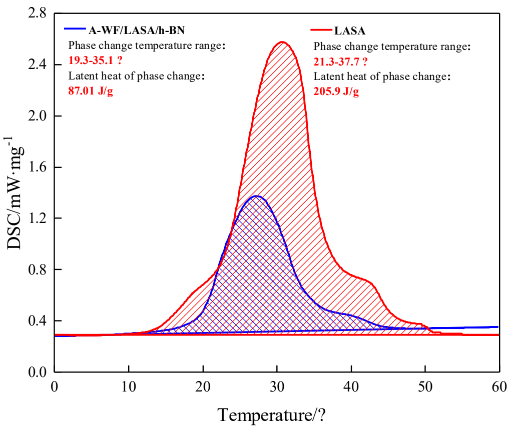

Figure 5: DSC thermograms of LASA and A-WF/LASA/h-BN

Figure 6 shows the characteristic absorption peaks in the FT-IR spectra of A-WF/LASA/h-BN. From the figure, it can be observed that all characteristic absorption peaks of LASA and h-BN are visible in the prepared LASA/h-BN, with no new characteristic peaks appearing.

The characteristic absorption peak of A-WF/LASA/h-BN in the infrared spectrum appears at 717.44cm^{-1},808.3cm^{-1},909.38 cm^{-1},1026.41cm^{-1},1051.41cm^{-1},1218.81cm^{-1},1372.93cm^{-1},1409.03cm^{-1},1435.26cm^{-1},1472.29cm^{-1},1597.25cm^{-1},1704.01cm^{-1}, 1740.32 cm^{-1}, 2846.8cm^{-1}, 2915.58cm^{-1} and 3263.26cm^{-1}. In the characteristic absorption peaks of A-

WF/LASA/h-BN, the absorption peak attributed to lignin in A-WF (around 1504 cm⁻¹) is not observed, mainly due to the strong absorption peak at 1464.67 cm⁻¹ in LASA/h-BN overshadowing it. The FT-IR absorption peaks of A-WF/LASA/h-BN incorporate all the characteristics of both the phase change material LASA/h-BN and A-WF. The intensity of the characteristic absorption peaks shows only minor variations or slight shifts in position, with no new characteristic peaks emerging. This indicates that LASA and h-BN, as well as LASA/h-BN and A-WF, have successfully compounded without any other chemical changes occurring during the compounding process.

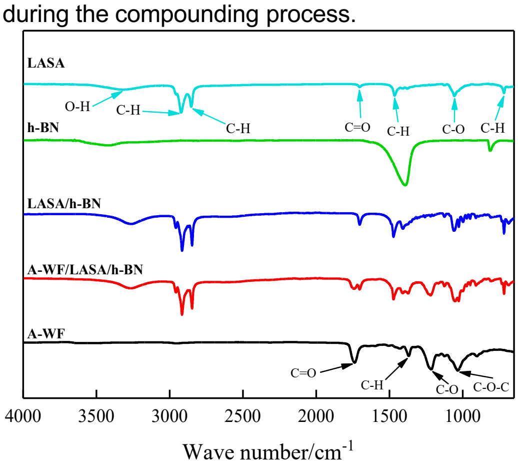

Figure 1: The FT-IR spectra of A-WF/LASA/h-BN

Figure 7 shows the TG analysis curves of A-WF, LASA/h-BN, and A-WF/LASA/h-BN. The mass loss rates of A-WF, LASA/h-BN, and A-WF/LASA/h-BN at 100°C were shown to be 1.3%, 0.94%, and 1.66%, respectively. It can be observed that within the range of 100°C, the TG curves of all three samples remain relatively stable, with the mass loss rates of all materials being less than 2%. This indicates that A-WF/LASA/h-BN possesses excellent thermal stability.

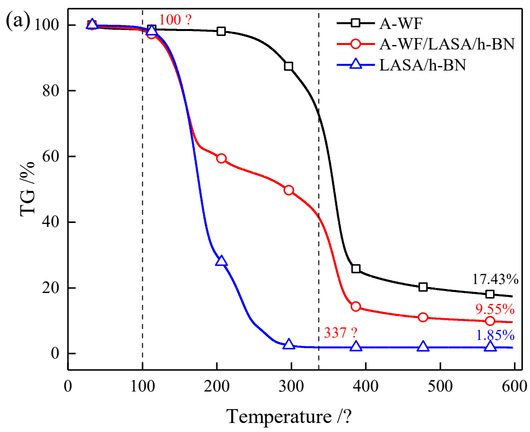

Figure 7: The TG analysis curves of A-WF, LASA/h-BN, and A-WF/LASA/h-BN.

Figure 8 shows the DSC thermograms of A-WF/LASA/h-BN after 0, 100, 200, 300, and 400 thermal cycles of heating and cooling. From the figure, it can be observed that after 400 cycles, the DSC curves of A-WF/LASA/h-BN show no significant changes in shape, only slight variations in melting temperature and peak area. After 400 cycles, the melting temperature of A-WF/LASA/h-BN decreases to 19.1 °C, a reduction of 0.3 °C, and the latent heat decreases to 84.38 J·g^{-1}, a reduction of 2.63 J·g^{-1}. The thermal storage performance of A-WF/LASA/h-BN has not undergone significant changes, demonstrating the good thermal cycle stability of the synthesized shaped composite phase change material.

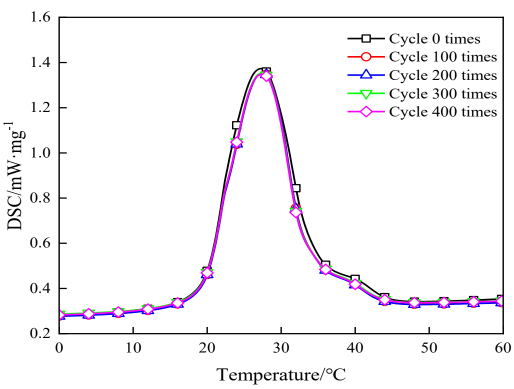

Figure 8: DSC Thermal Analysis Curves of A-WF/LASA/h-BN at Different Cycle Numbers

4. THERMAL STORAGE PERFORMANCE OF A-WF/LASA/H-BN

A- WF and A-WF/LASA/h-BN samples were used for the study, with A-WF serving as the comparison sample. The experimental testing system is shown in Figure 9. The testing conditions are as follows: initial temperature is 15 °C, the heating temperature of the water-cooled plate is 60 °C, the heating duration is 30 min, and the natural cooling duration is 240 min. A cycle of this is in progress. The sample is shown in Figure 1(e). The perimeter of the sample was enveloped with an XPS insulation board to minimize heat exchange with the surroundings, leaving only one surface exposed for infrared testing. The temperature variations on the exposed surface of the sample were recorded using an infrared thermal imager. Captec heat flux sensors were placed on the upper and lower surfaces of the sample to measure the heat flux density and temperature at the hot and cold ends of the sample. The experimental components were positioned inside a constant temperature and humidity chamber to maintain a stable experimental environment. Each sample underwent three cycles of constant temperature heating and natural cooling. The experimental system is given in Figure 9.

B-

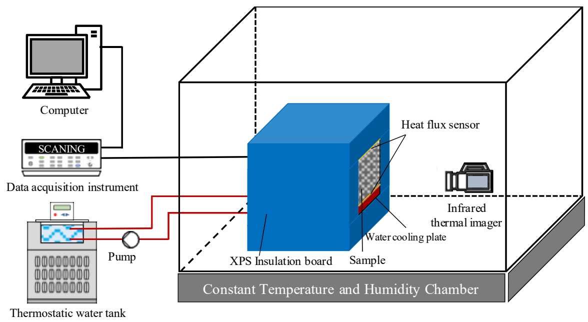

Figure 9: Schematic of thermal storage performance experiment system

Figure 10 depicts the temperature variation curves of the hot and cold ends of the samples A-WF and A-WF/LASA/h-BN under the thermal storage performance test conditions. The temperature variation trends of the hot ends of A-WF and A-WF/LASA/h-BN are essentially the same. The temperature of the cold end of the A-WF/LASA/h-BN is lower compared to that of the A-WF. After 30 min of heating, the temperature at the cold end of the A-WF/LASA/h-BN specimen reaches 17.98 °C, while the temperature at the cold end of the A-WF specimen is 21.26 °C, resulting in a difference of 3.28 °C. In addition, the peak temperature of 21.34 °C reached only 2.39 min after heating was stopped for A-WF, whereas it took 10.17 min to reach the peak temperature of 18.25 °C for A-WF/LASA/h-BN. During the three cycles of "constant heating - natural cooling" tests, the peak temperature difference between the cold end temperatures of A-WF/LASA/h-BNand A-WF reached an average of 3.09 °C. Due to its high thermal conductivity and excellent phase-change heat storage capability, A-WF/LASA/h-BN can efficiently store heat in a short time and release it promptly after the heat source is removed. It indicates that A-WF/LASA/h-BN has a good effect on suppressing temperature fluctuation and delaying temperature rise.

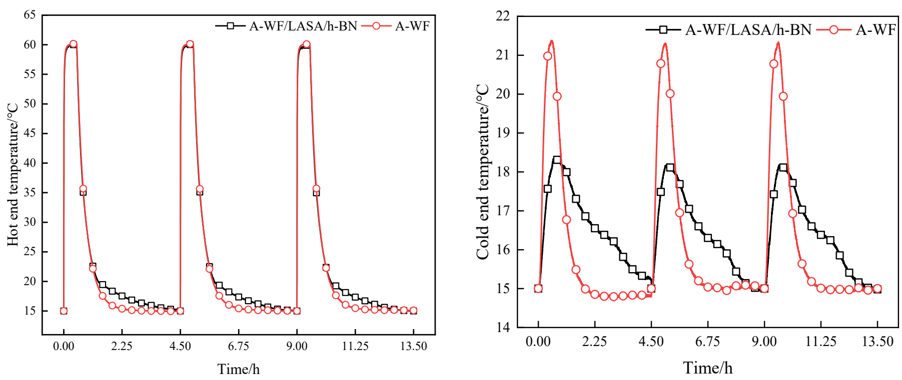

Figure 10: The temperature variation curves of the A-WF sample and the A-WF/LASA/h-BN sample during the heating-cooling tests

(a) hot end(b) cold end

Figure 11 shows the infrared thermal images of the A-WF sample and the A-WF/LASA/h-BN sample at different time points when they are heated at a constant temperature of 60 °C with an initial temperature of 10 °C. From the thermal images, it can be observed that the cold end temperature of the A-WF/LASA/h-BN sample is lower at each time point from 5 to 30 min compared to the cold end temperature of the A-WF sample. Additionally, the temperature variation of the A-WF/LASA/h-BN specimen is slower, with high-temperature blocks mainly concentrated near the heat source. The cold end temperature of the A-WF sample rises to 21.0 °C after heating for 30 min, while that of the A-WF/LASA/h-BN sample is 18.1°C, resulting in a difference of 2.9 °C. This is primarily due to the phase change of LASA during the heating process, which stores the heat transferred from the heating plate in the form of latent heat, thereby slowing down the transfer of heat to the cold end. As a result, the specimen exhibits a more uniform temperature distribution at different points in time.

As the heating time increases, the isotherms of the A-WF specimens become inclined with a "convex" shape, while the isotherms of the A-WF/LASA/h-BN specimens remain relatively straight. Firstly, the XPS insulation board is not completely adiabatic and perfectly flat, leading to heat leakage from the sample during the experiment. Secondly, due to the superior thermal storage performance and thermal conductivity of the A-WF/LASA/h-BN sample compared to A-WF, it can partially regulate the temperature when transferring heat to the surrounding area, resulting in a more uniform temperature distribution of the test block.

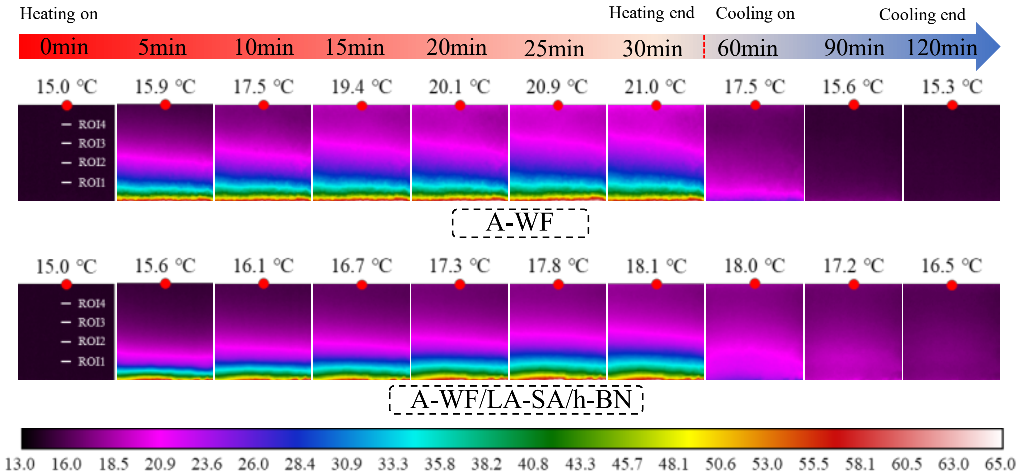

Figure 11: Infrared thermal images of A-WF Sample and A-WF/LASA/h-BN Sample

5. CONCLUSION

In this study, A novel biomass wood fiber-based composite PCM (A-WF/LASA/h-BN), was prepared. The modified wood fiber (A-WF) was used as a porous adsorbent carrier, lauryl alcohol-stearic acid (LASA) as the raw material for the phase change, and h-BN as the thermally conductive reinforcing particles. SEM, DSC, FT-IR, and TG were used to characterize its thermal and chemical properties, and experiments were carried out to evaluate its thermoregulation performance. The main conclusions are as follows:

1. The acetylation modification did not affect the phase change performance of the WF. Additionally, A-WF exhibits good hydrophobic and oleophilic properties. Its capillary forces can stably adsorb PCMs up to a critical mass ratio of 45 wt%.

2. A 1.5 wt% concentration of h-BN was chosen as the thermally conductive reinforcement material. LASA/h-BN exhibited a melting temperature of 20.9 °C, a latent heat of phase change of 198.6 $J \cdot g^{-1}$, and a thermal conductivity of 0.2513 $W \cdot (m^{-1} \cdot K^{-1})$, representing a 19.6% enhancement.

3. A-WF/LASA/h-BN, with 45 wt% LASA/h-BN addition, demonstrated excellent thermal stability and cycling stability. Under constant heating at 60 °C for 30 min, compared to A-WF, it exhibits a delay in peak time by 7.78 min and an average decrease of 3.09 °C in cold end temperature, indicating superior thermal storage and thermal conductivity performance. This composite PCM applied in the envelope can reduce building energy consumption while enhancing indoor thermal comfort.

6. REFERENCES

Alqaed, S., Mustafa, J., Sajadi, S.M., Aybar, H.Ş., 2024. Enhancing energy efficiency in zero energy buildings: Analyzing the impacts of phase change material-filled enclosures and outlet air distance on solar wall performance. Case Studies in Thermal Engineering 58, 104342. https://doi.org/10.1016/j.csite.2024.104342

Barbieri, V., Lassinantti Gualtieri, M., Siligardi, C., 2020. Wheat husk: A renewable resource for bio-based building materials. Construction and Building Materials 251, 118909. https://doi.org/10.1016/j.conbuildmat.2020.118909

Boussaba, L., Makhlouf, S., Foufa, A., Lefebvre, G., Royon, L., 2019. vegetable fat: A low-cost bio-based phase change material for thermal energy storage in buildings. Journal of Building Engineering 21, 222–229. https://doi.org/10.1016/j.jobe.2018.10.022

Hekimoğlu, G., Sarı, A., Gencel, O., Önal, Y., Ustaoğlu, A., Erdogmus, E., Harja, M., Tyagi, V.V., 2023. Thermal energy storage performance evaluation of bio-based phase change material/apricot kernel shell derived activated carbonin lightweight mortar. Journal of Energy Storage 73, 109122. https://doi.org/10.1016/j.est.2023.109122

Kallavus, U., Järv, H., Kalamees, T., Kurik, L., 2017. Assessment of durability of environmentally friendly wood-based panels.

Energy Procedia 132, 207–212. https://doi.org/10.1016/j.egypro.2017.09.756

Li, Y., Li, Xianjun, Liu, D., Cheng, X., He, X., Wu, Y., Li, Xingong, Huang, Q., 2016. Fabrication and Properties of Polyethylene Glycol-Modified Wood Composite for Energy Storage and Conversion. BioResources 11, 7790– 7802. https://doi.org/10.15376/biores.11.3.7790-7802

Liu, L., Tam, V.W.Y., Almeida, L., Le, K.N., 2023. Dynamically assessing life cycle energy consumption of buildings at a national scale by 2020: An empirical study in China. Energy and Buildings 296, 113354. https://doi.org/10.1016/j.enbuild.2023.113354

Ma, L., Guo, C., Ou, R., Sun, L., Wang, Q., Li, L., 2018. Preparation and Characterization of Modified Porous Wood Flour/Lauric-Myristic Acid Eutectic Mixture as a Form-Stable Phase Change Material. Energy Fuels 32, 5453– 5461. https://doi.org/10.1021/acs.energyfuels.7b03933

Sarı, A., Hekimoğlu, G., Tyagi, V.V., 2020. Low cost and eco-friendly wood fiber-based composite phase change material: Development, characterization and lab-scale thermoregulation performance for thermal energy storage. Energy 195, 116983. https://doi.org/10.1016/j.energy.2020.116983

Wang, J., Xie, H., Xin, Z., Li, Y., Chen, L., 2010. Enhancing thermal conductivity of palmitic acid based phase change materials with carbon nanotubes as fillers. Solar Energy 84, 339–344. https://doi.org/10.1016/j.solener.2009.12.004

Wei, K., Ma, B., Wang, H., Liu, Y., Luo, Y., 2017. Synthesis and thermal properties of novel microencapsulated phase-change materials with binary cores and epoxy polymer shells. Polym. Bull. 74, 359–367. https://doi.org/10.1007/s00289-016-1718-z

Zhao, B., Wang, Y., Wang, C., Zhu, R., Sheng, N., Zhu, C., Rao, Z., 2021. Thermal conductivity enhancement and shape stabilization of phase change thermal storage material reinforced by combustion synthesized porous Al2O3. Journal of Energy Storage 42, 103028. https://doi.org/10.1016/j.est.2021.103028

#368: The impact of optimizing thermal interface conditions on thermal concentration

Enhancing efficiency and output voltage through innovative thermal interface optimization

Yangyang WU[1], Mengqi FENG[2], Yin GUO[3], SONG LV[4*]

[1] Wuhan University of Technology, Wuhan, 331699@whut.edu.cn
[2] Wuhan University of Technology, Wuhan, 2807647773@qq.com
[3] Wuhan University of Technology, Wuhan, 525236111@qq.com
[4] Wuhan University of Technology, Wuhan, lvsong@whut.edu.cn

Abstract: Passive electricity generation via radiative cooling, combined with thermoelectric generators, is garnering global attention for its potential to mitigate environmental pollution and greenhouse gas emissions associated with fossil fuel-based power generation. However, optimizing radiative cooling and thermoelectric generator systems often encounter challenges of increased costs and complexity when employing novel materials and structures, with marginal improvements in efficiency. Recently, researchers have proposed a novel optimization approach by focusing on the thermal interface of radiative cooling and thermoelectric generator systems to achieve enhanced thermal concentration, yielding remarkable progress. To elucidate the specific impact of altering thermal interface conditions on system performance, we employed a controlled variable approach and conducted simulations using COMSOL Multiphysics software, investigating various thermal boundary conditions, including dimensions and thermal conductivity, on the temperature differential and output voltage of the system. Following optimization of the thermal interface conditions, the radiative cooling-thermoelectric generator system (RC-TE) generated an output voltage of 0.36082V. This represents a 2.23-fold increase in output voltage compared to the unoptimized RC-TE system, which yielded 0.1618V, providing compelling evidence for significant enhancement in system performance.

Keywords: Thermoelectric Generators; Radiative Cooling; Power Generation Optimization; Transversal Heat Conduction

1. INTRODUCTION

Currently, electricity is predominantly generated through the combustion of fossil fuels, leading to a significant increase in global energy demand and causing environmental pollution, greenhouse gas emissions, and other severe environmental issues (Aili et al., 2019). Therefore, there is an urgent need to find a green, energy-efficient, and environmentally friendly alternative solution for power generation worldwide. Radiative cooling (RC) emerges as a novel passive cooling technology that channels the infrared radiation generated by a heat source through the atmospheric window into outer space (8~13μm), aligning with the blackbody radiation near 300K. The thermal emitter surface absorbs solar energy and atmospheric radiation, emitting infrared radiation. The advent of RC technology holds promise in addressing the energy consumption and environmental pollution issues caused by traditional cooling methods, garnering widespread attention from scholars worldwide. Thermoelectric generators (TE) operate on the principle of Seebeck effect, converting temperature differentials into electrical energy. This device boasts several advantages including simple structure, absence of mechanical components, power generation solely dependent on temperature differentials, among others. Such design brings forth multiple operational benefits such as noiseless operation, leak-free operation, portability, scalability, and longer lifespan. This technology finds widespread application across various domains including solar energy, aerospace, automotive, among others, and holds significant promise as a promising field in the realm of new clean energy sources. Moreover, recent research endeavors have combined RC technology with thermoelectric generators. Utilizing the cooling energy generated by the radiative cooling film, a continuous passive cooling source is provided for the thermoelectric generator, facilitating passive and environmentally clean power generation (Bao et al., 2017). In previous studies, researchers have aimed to maximize the power output and output voltage of the RC-TE system by enhancing the cooling power of the radiative cooling film through the selection of superior materials and optimized structural designs(Z. Chen, Zhu, Raman, & Fan, 2016; Mandal, Yang, Yu, & Raman, 2020; Raman, Anoma, Zhu, Rephaeli, & Fan, 2014; Zhai et al., 2017), thereby increasing the reflectivity and thermal radiation rate of the atmospheric window (Aili et al., 2019; Bao et al., 2017; Berdahl & Fromberg, 1982; Chae et al., 2020; M. Chen, Pang, Chen, & Yan, 2021; Gentle & Smith, 2015; Hu et al., 2016; Z. Li, Chen, Song, Zhu, & Zhu, 2020; Liu, Son, Chae, Jung, & Lee, 2020; Ma et al., 2020; Peng et al., 2018; Rephaeli, Raman, & Fan, 2013; Son et al., 2021; T. Wang et al., 2021), or by employing thermoelectric generators with higher ZT values to enhance the temperature gradient and output voltage ofthe RC-TE system (Z. Chen et al., 2016; Khalil et al., 2021; Luo, Li, Chen, & Kim, 2022; Raman et al., 2014). Significant progress has been made in research on the structural optimization of radiative cooling film and the development of high- performance materials both domestically and internationally, achieving daytime radiative cooling (PDRC) and radiative cooling power density ≥100W/m^2.

Lv et al. (Lv et al., 2021) devised a simple and cost-effective Radiative Sky Cooling Thermoelectric Generator (RSC-TEG) system for passive power generation around the clock. Their research encompassed a comprehensive exploration of various parameters, including wind speed, ambient temperature, relative humidity, load resistance, area ratio, TEG leg structural parameters, and the natural logarithm of TEG leg. Khan et al. (Khan, Cheema, Abbas, Ullah, & Park, 2023) [23] studied the feasibility of TEG power generation facilitated by radiative sky cooling, employing a combination of experimental and numerical methods. They conducted an in-depth analysis of morphological features, including material composition (aluminum and copper), plate thickness, number of thermocouples, and TEG leg length, to evaluate their impact on open-circuit voltage. These studies provided multifaceted analysis and research on the optimization and enhancement of RC-TE experimental setups, making significant contributions to the performance optimization of RC-TE systems. Yu et al. (Yu et al., 2022) integrated TEG with Selective Solar Absorber (SSA) to capture thermal energy from the heat source (sun) and combined it with Passive Daytime Radiative Cooling (PDRC) coatings to release heat to the cold source (also the sun). Through this novel approach combining solar heating and outer space cooling, uninterrupted power supply for small-scale devices and remote areas is provided around the clock. Zhang et al. (G. N. Li, Zhang, Zheng, Zhu, & Guo, 2018) successfully designed and manufactured a groundbreaking Self-Heating Radiative Cooling Thermoelectric Generator (SA-RCE-TEG), achieving continuous daytime power generation utilizing photothermal and RC effects. Their innovative approach introduced a revolutionary concept of utilizing sustainable and renewable resources simultaneously harnessing solar radiation and outer space cooling. They utilized structural optimization and introduced solar energy or PCM to significantly enhance the temperature gradient of the system, effectively increasing the system's power generation and output voltage. However, the introduction of new structures and components significantly increases the complexity and cost of the system.

Lee et al. (Lee et al., 2021) proposed an economically efficient inorganic-polymer nanocomposite material, SiO_2-PMMA, as an effective passive radiative cooling device. By stacking the cooling device on the cold end of TEG devices, it was demonstrated that the output current of the TEG could increase from 6 mA to 10 mA when the hot end temperature was 50 ℃. Wang, CH et al. (C. H. Wang, Chen, Jiang, & Zhang, 2023) significantly enhanced the cooling power of radiative cooling films by using different mixtures of silica particles and liquid acrylic resin, achieving passive continuous power generation of 90.74 mW m^2 throughout the day when coupled with thermoelectric generators. Xie, HL et al.(Xie, Yin, Xia, & Fan, 2024) designed a dual-diamond radiative cooling metamaterial with net cooling powers of 213.80 and 165.09 W/m^2 at room temperature during night and day, respectively. The maximum temperature difference during the day was 8.28 K, and the maximum power generation reached 0.44 W/m^2. Developing novel radiative cooling films can achieve excellent cooling power, directly enhancing the power generation performance of RC-TE systems. However, the development difficulty and cost of novel radiative cooling films are also extremely high.

Recently, researchers have been focusing on increasing the cooling power density of radiative cooling films by concentrating and managing heat within films, aiming to achieve extraordinary cooling power densities through suitable heat concentration methods. Wang et al. (Poredoš et al., 2024) achieved significant cooling power density by capitalizing on the geometric asymmetry between a centralized heat source per unit area and a large area of radiatively cooled film. Exploiting the substantial area difference between the radiatively cooled film and the centralized heat source led to a breakthrough in the radiant cooling power density per unit area, reaching an astonishing 1554 W/m^2. This serves as a compelling demonstration of the considerable potential of alternative heat management methods, such as heat concentration, to enhance the cooling power density of radiatively cooled films. While this method is confined to cooling relatively small area heat sources (e.g., precision electronic components like CPUs) with large area radiative cooling films due to the constraints of the heat concentration method's conditions, it presents a novel avenue for augmenting the power density of radiative cooling films. This approach leverages heat management and heat concentration methods at alow cost, with high feasibility and evident enhancement effects. In RC-TE systems, we can similarly consider the TE module as a unit heat source for the radiative cooling film. By enhancing the cooling power density of the radiative cooling film through thermal management, we can increase the temperature gradient on both sides of the RC-TE system,thereby achieving the goal of improving the system's output power.

In order to enhance the radiative cooling power density and output power of the RC-TE system through enhanced heat concentration and management methods, it is necessary to modify the thermal interface conditions between the RC and TE components. Different thermal interface conditions will inevitably have multidimensional effects on the temperature distribution and temperature gradients of the RC-TE system. To comprehensively analyze the specific effects of changing thermal interface conditions to achieve heat concentration on the system and to select the optimal thermal interface conditions, we utilized the thermal-electric simulation module of COMSOL Multiphysics software. We conducted a comprehensive analysis of the specific trends of different thermal interface conditions on the temperature gradient and output voltage of the RC-TE system. Additionally, we investigated the specific parameters of the optimal thermal interface conditions for the RC-TE system, providing thermal interface references for future research aimed at enhancing the power generation of RC-TE systems. Against the backdrop of increasing environmental pollution and greenhouse gas emissions due to the heavy reliance on fossil fuels for electricity generation, altering the thermal interface conditions of RC-TE systems to achieve heat management and concentration holds significant importance in improving the system's output power.

2. SYSTEM MODELING

We first simplified the construction of a PN junction RC-TE system, as shown in Figure 1. The radiative cooling membrane is coupled to the cold side of the TE module by attaching it to a heat-conducting plate. The environment is chosen as the continuous heat source for the TE module. Heat is primarily extracted from the ambient air into the RC-TE system through convection and conduction between the ambient air and the thermal surface of the TE module, and then emitted into the distant space through the radiative cooling membrane facing the sky. The temperature difference between the cold and hot sides serves as the driving force for electricity generation in the TE module. Several assumptions are proposed to simplify the mathematical description of the thermal and electrical analysis of the device: 1)Heat transfer is modeled under steady-state conditions, 2) Convective heat transfer from the air to the surface of the radiative cooling film is neglected, as in experiments the radiative cooling film is typically encapsulated with a polyethylene (PE) film, 3) Only thermal conduction of the P and N elements is considered, 4) Radiative heat transfer between the cooler and the hot surface is assumed negligible, and 5) The Seebeck coefficient, internal resistance, and thermal conductivity of the P and N elements are assumed to be temperature-independent, given the minimal temperature difference between the hot and cold sides of the TEG in this study.

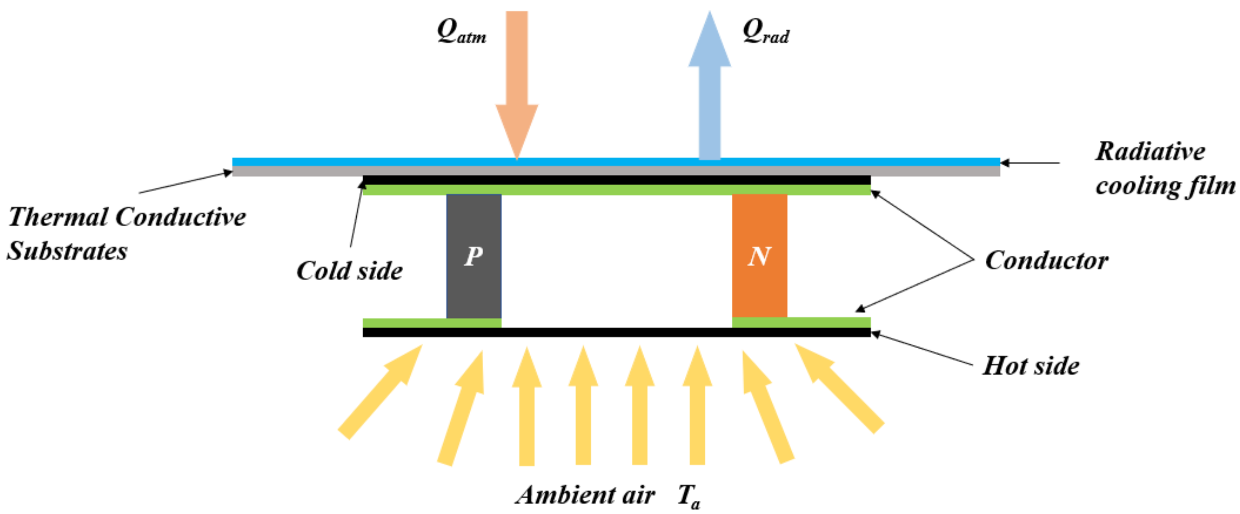

Figure 1: Schematic diagram of the unit cell of the RC-TE unit. The environment is selected as the heat source for the TEG cell. Q_{rad} is the thermal radiant power of the cooler, Q_{atm} is the absorbed atmospheric thermal radiant power

2.1. Energy flux of the system

According to the energy balance analysis of TE, the energy fluxes at the hot surface and cooler of the RC-TE device are established by：

$$Q_h = S_{PN}T_I + K_{PN}(T_h - T_c) - \frac{1}{2}I^2R_{PN}$$

Equation 1: Hot surface receives heat flux

$$Q_c = S_{PN}T_I + K_{PN}(T_h - T_c) + \frac{1}{2}I^2R_{PN}$$

Equation2: cold surface receives heat flux

Where ***Q*** represents heat energy, ***I*** denotes current, ***T*** signifies temperature, ***S*** stands for Seebeck coefficient, ***K*** represents thermal conductance, and ***R*** indicates electrical resistance. Subscripts ***h*** and ***c*** denote the hot and cold surfaces respectively, while subscript PN denotes a single PN thermocouple. Typically, S_{PN}, K_{PN}, and R_{PN} are closely associated with the geometry of PN thermocouples and the material properties of the P and N elements. TEG data in the simulation is from commercial Bi_2Te_3 module which was manufactured by Hubei Segalong New Energy Technology Co. Manufactured by New Energy Technology Co., Ltd. (Product No. TEG-12708) 3. physical model (Ji & Lv, 2023).

The output power of the TE cell can be obtained by incorporating the load resistor R_{load} through equation (3). The output power is determined by R_{load}. Power Pe. input heat flux Q_h.

Equation3: The output power of the TE device

$$P_e = I^2R_{load} = \frac{S_{PN}^2(T_h - T_c)^2}{(R_{PN} + R_{load})^2}R_{load}$$

Here, two area ratios are defined as $\gamma_{hot}= A_{hot}/A$ and $\gamma_{cold}= A_{cold}/A$, describing the relationship between the areas of the hot (or cold) surface and the cross-section of the P or N element. According to the first law of thermodynamics, the heat energy obtained by the hot surface, Q_h, can be determined through the heat transfer process between the hot surface and the ambient air. Likewise, the heat energy dissipated by the cooler, Q_c, can be represented by the net cooling power of the cooler.

$$Q_h = \gamma_{hot}Ah_{hot}(T_a - T_h)$$

$$Q_c = Q_{rad} - Q_{atm}$$

Equation4: The thermal energy gained by the hot surfaceEquation5: The cold surface gains cooling energy.

In this context, h_{hot} represents the effective heat transfer coefficient between the hot surface and the local ambient air, T_a denotes the ambient temperature, Q_{rad} stands for the thermal radiation power of the cooler, and Q_{atm} indicates the absorbed atmospheric thermal radiation power. Typically, Q_{rad} and Q_{atm} can be obtained through the following formulas:

Equation6: The cooling power of radiative cooling.

$$Q_{rad} = \gamma_{cold}A\varepsilon_{cooler}\sigma T_h^4$$

Equation7: The radiative heat exchange between the cold surface and the environment.

$$Q_{atm} = \gamma_{cold}A\varepsilon_{cooler}\varepsilon_{atm}\sigma T_c^4$$

Where σ represents the Stefan-Boltzmann constant, ε_{cooler} signifies the emissivity of the cooler, and ε_{atm} denotes the effective emissivity of the atmosphere, which has been experimentally determined (Berdahl & Fromberg, 1982) previously to fit the following model: $\varepsilon_{atm}=0.741 +0.0062\times(T_{dew}-273.15)$, where T_{dew} represents the dew point temperature in Kelvin.

2.2. Grid validation

Before conducting simulations, it is crucial to perform a grid independence test to ensure the accuracy of computational results. The simulation temperatures on both the hot and cold sides of the TEG were compared using various grid cell counts, namely 14299, 19844, 29233, 54974, 116722, and 229433. The results of calculations with different grid counts are depicted in Figure 2.

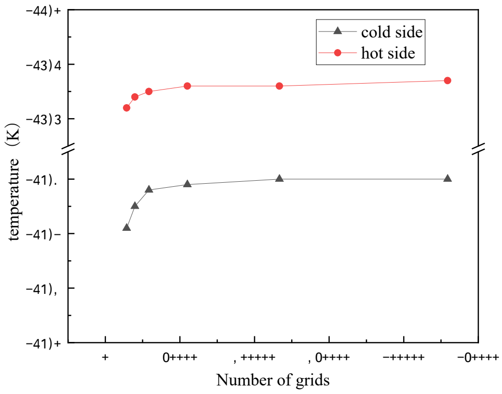

Figure 2: Comparison of hot and cold measured temperatures for different number of grids

From Figure 2, it can be observed that the temperature data from both groups show minimal variation across different numbers of grid cells. As the number of grid cells increases from 14299 to 229433, the temperature variation on both the hot and cold sides of the TEG is less than 0.02%. Increasing the number of grid cells leads to longer computation times without significant computational benefit. Therefore, to reduce computational costs, we have decided to set the subsequent grid count for the model to 111003.

2.3. Model validation

We employed the finite element method (FEM) embedded in COMSOL Multiphysics software for computer simulations to model the thermal and electrical behavior of the RC-TE system. The physical model of the RC-TE system is depicted in Figure 3. We utilized a model from our previous work, and to enhance its accuracy, we compared the model with previous experiments (Ji & Lv, 2023), adjusting environmental parameters as well as the dimensions and details of the RC-TE system to simulate the specific conditions of our experiments. Subsequently, we compared the model data with both previous experimental data and simulated data and conducted a comparison of the final steady-state temperatures of the cold and hot sides as well as the output voltage of the model.

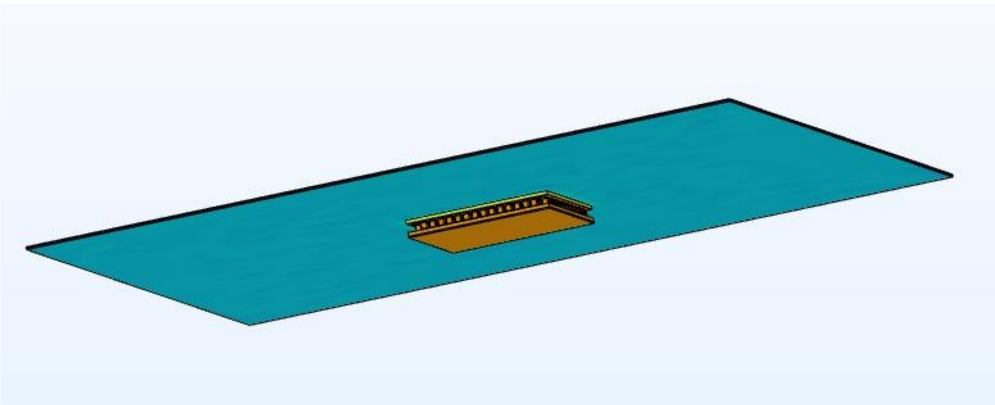

Figure 3: RC-TE physical model construction

Table 18: Comparison of hot-side temperature, cold-side temperature, and temperature difference between the two sides, and generating voltage between the previous work and our current work.

	Hot side(K)	Cold side(K)	Temperature different(K)	Voltge(mV)
Previous work	298.4	295.93	2.47	92
Content of this article	298.85	296.28	2.57	95

Here, the temperature difference between the cold and hot ends is only 0.15%, and the difference in output voltage is only 3.3%. This indicates that our model is reliable and accurate. Validating the accuracy of the model is crucial for our subsequent discussions on optimizing the design under different thermal interface conditions affecting the system's thermal concentration performance.

3. RESULTS AND DISCUSSION

3.1. RC and thermally conductive homogenizing plates of different areas

In general, the larger the area of the radiative cooler, the greater the radiative cooling power, and consequently, the stronger the cooling capability of the radiative cooling membrane. However, due to the limited heat concentration ability of the RC-TE system's thermal boundary, the power generation of the RC-TE system does not exhibit linear growth with increasing RC area in practical experiments and simulations. Therefore, our study aims to explore the optimal thermal boundary conditions regarding the ratio of RC membrane area to TE module area to maximize the power generation and cooling capacity of the RC-TE system, while also seeking the optimal thermal boundary conditions for heat concentration effects in the RC-TE system. In COMSOL Multiphysics software, utilizing a validated model, we conducted thermal and electrical simulations by varying the size of the radiative cooling membrane while keeping the dimensions of the thermoelectric module constant. The simulated dimensions of the radiative cooling membrane ranged from 0.2 meters to 0.9 meters, with an increment of 0.1 meters. The simulation results are depicted in Figures 4 and 5.

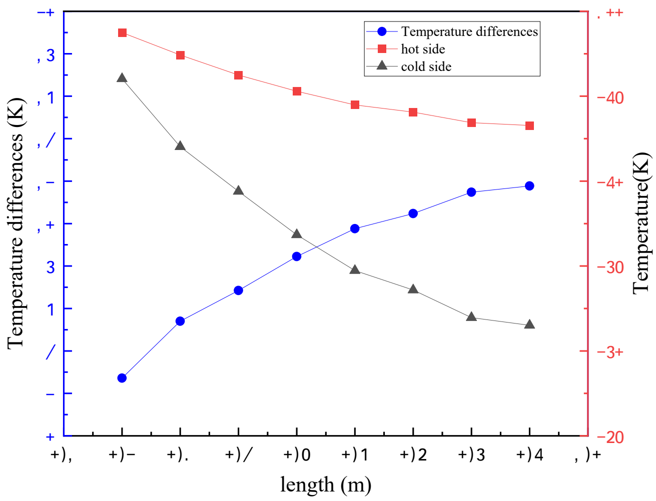

Figure 4: The effect of different sizes of the RC film and heat-conducting substrate on the temperatures at both sides of the RC-TE system

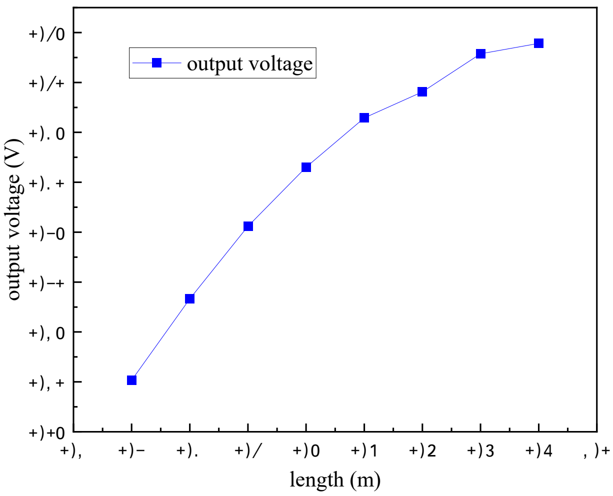

Figure 5: The impact of varying sizes of the RC film and heat-conducting substrate on the output voltage of the RC-TE system

The observed trends from Figures 3 and 4 indicate that as the area of the RC membrane increases, the temperature difference between the two ends of the RC-TE system gradually increases, leading to a corresponding increase in the system's output voltage. Prior to a side length of 0.6 meters, both the temperature difference and output voltage increase rapidly with the increase in side length. However, beyond 0.6 meters, this growth trend becomes sluggish, primarily due to the limited heat concentration capability of the thermal boundary. With increasing area, the cold energy surrounding the radiative cooling membrane cannot be efficiently concentrated onto the cold side of the TE module. Furthermore, RC membranes larger than 0.6 meters in side length would escalate the cost and difficulty of experimental assembly, significantly affecting the experimental process. Therefore, we chose to set the side length of the TE module in the RC- TE system to 0.2 meters, and the optimal side length of the RC membrane and heat-conducting substrate to 0.6 meters. Through our simulations, we verified that at these dimensions, the thermal boundary conditions of the RC-TE system exhibit optimal heat concentration performance, resulting in maximum output power.

3.2. Investigation into the Influence of Thermally Conductive Substrate Thermal Conductivity on RC-TE Systems

The thermal boundary conditions of the RC-TE system influence the efficiency of transferring cooling generated by the radiative cooler to the cold side of the TE module. Increasing the thermal conductivity of the thermal boundary reasonably can enhance its temperature uniformity and strengthen its heat concentration ability, thereby reducing the temperature at the cold side of the TE module. This, in turn, increases the temperature difference between the two sides of the TE module, consequently boosting the output power of the TE module. However, excessively high thermal conductivity of the thermal boundary may, in turn, impede the transfer of cold from the edge of the RC membrane to the cold end of the TE module. To determine the optimal thermal conductivity of the thermal boundary for the RC-TE system, we utilized COMSOL Multiphysics software. Employing a controlled variable approach, we fixed the area of the RC membrane at 0.6 meters. We gradually increased the thermal conductivity from 200 to 10000 W/(m·K) to replace the previously validated aluminum plate heat-conducting substrate (thermal conductivity of 238 W/(m·K)). This allowed us to simulate the impact trends of different thermal conductive materials on the temperature difference between the two sides of the TE module and the output voltage of the RC-TE system. To enhance the credibility of the trends displayed by the model with a side length of 0.6 meters, we also employed a model with a side length of 0.3 meters as a control group. The simulation results are shown in Figures 6 to 9. Additionally, we provided a comparison of the surface temperature distribution between the RC-TE model using a 0.3 m aluminum plate as the thermal boundary and the RC-TE model using a 0.6 m thermal boundary with a thermal conductivity of 4000 W/(m·K), as shown in Figure 10.

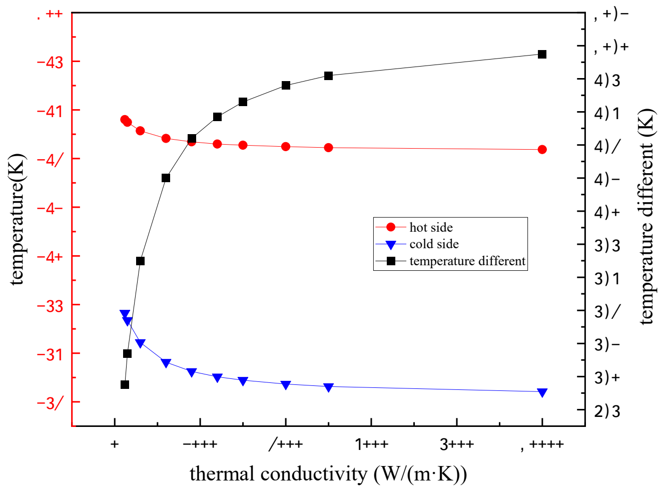

Figure 6: Effect of thermal conductivity of 0.6m side length RC-TE model on temperature difference between two sides of TE

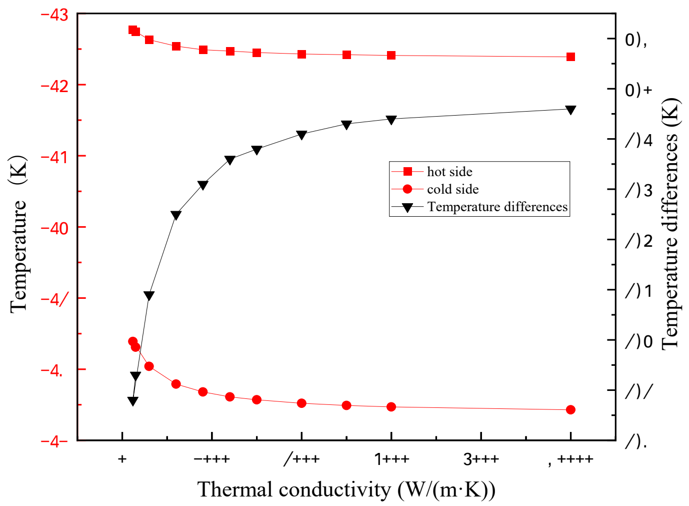

Figure 7: Effect of thermal conductivity of 0.3m side length RC-TE model on temperature difference between two sides of TE

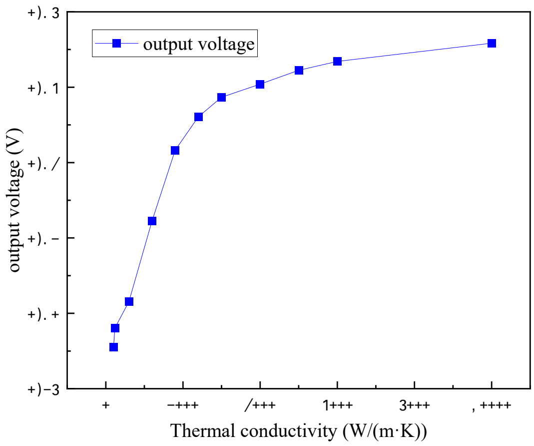

Figure 8: Thermal conductivity of 0.6 m side length RC-TE model on system output voltage

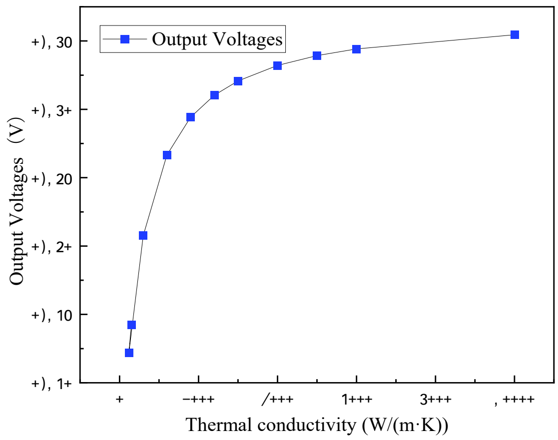

Figure 9: Thermal conductivity of 0.3 m side length RC-TE model on system output voltage

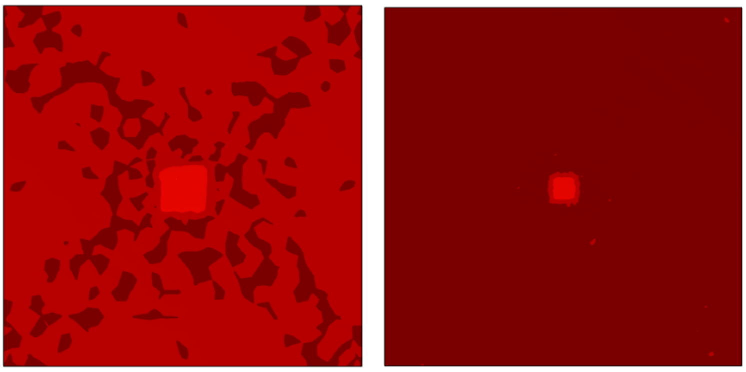

Figure 10: (a) Surface temperature distribution of the RC-TE model with an aluminum plate with a side length of 0.3 m serving as a thermally conductive substrate. (b) Surface temperature distribution of the RC-TE system with a side length of 0.6m and thermal conductivity of 4000 W/(m·K)

From the simulation results, it is evident that regardless of whether the side length of the thermally conductive substrate is 0.3 meters or 0.6 meters, the trends in temperature difference and output voltage remain largely consistent. As the thermal conductivity approaches approximately 4000 W/(m·K), both parameters demonstrate an upward trend with increasing thermal conductivity. This phenomenon is elucidated by the surface temperature distribution depicted in Figure 10, where low thermal conductivity impedes the efficient transfer of coldness from the surrounding boundaries to the cold side of the TE, resulting in suboptimal utilization of coldness. Augmenting the thermal conductivity effectively enhances the uniformity of the radiative cooling film and the thermally conductive substrate, thereby elevating temperature differences and output voltages. However, beyond this threshold value, the incremental improvements in thermal conductivity exert limited influence on the performance of the RC-TE system. For instance, comparing models with thermal conductivities of 4000 and 10000 W/(m·K), the temperature difference shows only a 0.2°C disparity, while the output voltage differs by just

0.02 V. This phenomenon may stem from the limited temperature difference across the heat-conducting substrate's two sides, where excessively high thermal conductivity weakens the substrate's ability to concentrate on heat. Additionally, the cooling power of the radiative cooling film is limited, capable of reducing temperatures only to a certain extent. Therefore, once the thermal conductivity surpasses a certain threshold, its further increase has minimal impact on the entire RC-TE system. This comparative analysis not only validates the reliability of the model data for a side length of 0.6m but also elucidates the trend in the influence of thermal conductivity on the overall performance of the RC-TE system when employing a 0.6m side length for both the radiative cooling film and the heat-conducting substrate.

4. CONCLUSION

Taking a TE module with dimensions of 0.04 meters and 127 PN junctions, along with an RC membrane with a reflectance of 93%, as an example, we utilized a validated model to investigate the influence of different thermal boundary conditions on heat management and concentration in the RC-TE coupled system. By varying the size of the RC membrane and the thermal conductivity of the thermal boundary, we aimed to explore the impact trends of different thermal boundary conditions on the heat concentration performance and output voltage of the RC-TE system. Our goal was to determine the optimal thermal boundary conditions for the RC-TE system to achieve the best heat concentration effect and enhance the overall output power of the system.

1. Using a controlled variable approach, we identified the maximum response point of the RC-TE system's performance concerning the system length when using an aluminum plate as the heat-conducting substrate (thermal conductivity of 238 W/(m·K)), with a TE module of 127 PN junctions and a side length of 0.04 meters. At this point, the side length of the RC membrane was determined to be 0.6 meters. Beyond 0.6 meters, the system encounters several issues due to the disproportionate ratio of the radiative cooling membrane to the TE module, where cold energy around the RC membrane cannot be effectively transferred to the cold side of the TE module, resulting in an incomplete concentration of cooling effects. Moreover, oversized radiative cooling membranes increase the cost and difficulty of assembling the experimental framework. When the side length is less than 0.6 meters, the RC membrane cannot transfer sufficient cooling to the cold side of the TE module through the thermal boundary, which is necessary to generate significant temperature gradients and enhance the output voltage of thermoelectric power generation.

2. After setting the side length of the RC membrane to 0.6 meters, we used a controlled variable approach to change the thermal conductivity of the thermal boundary in the RC-TE system. Using models with side lengths of 0.3 meters and 0.6 meters, we determined that the optimal thermal conductivity of the thermal boundary for the RC membrane with a side length of 0.6 meters is approximately 4000 W/(m·K). Beyond this value, a significant increase in thermal conductivity diminishes the heat concentration capability of the RC membrane boundary in the RC-TE system, reducing the rate of temperature difference and output voltage growth at both ends of the system. Conversely, if the thermal conductivity of the substrate is lower than 4000 W/(m·K), the heat transferred from the RC membrane to the cold side of the TE module through the thermal boundary would be insufficient due to the low thermal conductivity, leading to a decrease in the output voltage of thermoelectric power generation.

3. In our RC-TE power generation system model, when the side lengths of the RC membrane are both 0.6 meters and the thermal conductivity of the substrate is 4000 W/(m·K), the system's power generation capacity is significantly enhanced. Compared to the previous scenario where the side length of the RC membrane was 0.3 meters but using the same TE and RC membrane materials, the output voltage of the RC-TE system increased from 0.16218 V to 0.36082 V, an increase of 2.23 times. It is worth noting that by simply changing the thermal boundary conditions of the system to enhance the heat concentration and management capabilities of the thermal boundary, such a significant improvement in the system's output voltage can be achieved without adopting new materials or structures. This proposed improvement method is of great significance for the development of RC-TE systems, indicating how to enhance the performance of RC-TE systems without adopting new materials or structures. Moreover, research on heat concentration and thermal management improvements in RC-TE systems provides meaningful insights for the utilization of new energy sources and addressing environmental pollution, greenhouse gas emissions, and related issues through the utilization of RC cooling energy.

5. REFERENCES

Aili, A., Wei, Z., Chen, Y., Zhao, D., Yang, R., & Yin, X. (2019). Selection of polymers with functional groups for daytime radiative cooling. Materials Today Physics, 10, 100127.

Bao, H., Yan, C., Wang, B., Fang, X., Zhao, C., & Ruan, X. (2017). Double-layer nanoparticle-based coatings for efficient terrestrial radiative cooling. Solar Energy Materials and Solar Cells, 168, 78-84.

Berdahl, P., & Fromberg, R. (1982). The thermal radiance of clear skies. Solar Energy, 29(4), 299-314.

Chae, D., Kim, M., Jung, P.-H., Son, S., Seo, J., Liu, Y., . . . Lee, H. (2020). Spectrally selective inorganic-based multilayer emitter for daytime radiative cooling. ACS applied materials & interfaces, 12(7), 8073-8081.

Chen, M., Pang, D., Chen, X., & Yan, H. (2021). Enhancing infrared emission behavior of polymer coatings for radiative cooling applications. Journal of Physics D: Applied Physics, 54(29), 295501.

Chen, Z., Zhu, L., Raman, A., & Fan, S. (2016). Radiative cooling to deep sub-freezing temperatures through a 24-hday–night cycle. Nature Communications, 7(1), 13729.

Gentle, A. R., & Smith, G. B. (2015). A subambient open roof surface under the Mid‐Summer sun. Advanced Science, 2(9).

Hu, M., Pei, G., Wang, Q., Li, J., Wang, Y., & Ji, J. (2016). Field test and preliminary analysis of a combined diurnal solar heating and nocturnal radiative cooling system. Applied Energy, 179, 899-908.

Ji, Y. S., & Lv, S. (2023). Experimental and numerical investigation on a radiative cooling driving thermoelectric generator system. Energy, 268. Retrieved from <Go to ISI>://WOS:000923972000001. doi:10.1016/j.energy.2023.126734

Khalil, A., Elhassnaoui, A., Yadir, S., Abdellatif, O., Errami, Y., & Sahnoun, S. (2021). Performance comparison of TEGs for diverse variable leg geometry with the same leg volume. Energy, 224, 119967.

Khan, S., Cheema, T. A., Abbas, A., Ullah, R., & Park, C. W. (2023). Impact of environmental factors on night-time electricity generation using thermoelectric generator. Sustainable Energy Technologies and Assessments, 56, 103000.

Lee, J. Y., Wang, C. M., Chi, C. L., Wu, S. R., Lin, Y. X., Wei, M. K., & Lin, C. H. (2021). Enhanced Heat-Electric Conversion via Photonic-Assisted Radiative Cooling. Nanomaterials, 11(4), 10. Retrieved from <Go to ISI>://WOS:000643362100001. doi:10.3390/nano11040983

Li, G. N., Zhang, S., Zheng, Y. Q., Zhu, L. Y., & Guo, W. W. (2018). Experimental study on a stove-powered thermoelectric generator (STEG) with self starting fan cooling. Renewable Energy, 121, 502-512. Retrieved from <Go to ISI>://WOS:000426413600045. doi:10.1016/j.renene.2018.01.075

Li, Z., Chen, Q., Song, Y., Zhu, B., & Zhu, J. (2020). Fundamentals, materials, and applications for daytime radiative cooling. Advanced Materials Technologies, 5(5), 1901007.

Liu, Y., Son, S., Chae, D., Jung, P.-H., & Lee, H. (2020). Acrylic membrane doped with Al2O3 nanoparticle resonators for zero-energy consuming radiative cooling. Solar Energy Materials and Solar Cells, 213, 110561.

Luo, Y., Li, L., Chen, Y., & Kim, C. N. (2022). Influence of geometric parameter and contact resistances on the thermal-electric behavior of a segmented TEG. Energy, 254, 124487.

Lv, S., Ji, Y., Qian, Z., He, W., Hu, Z., & Liu, M. (2021). A novel strategy of enhancing sky radiative cooling by solar photovoltaic-thermoelectric cooler. Energy, 219, 119625.

Ma, H., Yao, K., Dou, S., Xiao, M., Dai, M., Wang, L., . . . Zhan, Y. (2020). Multilayered SiO2/Si3N4 photonic emitter to achieve high-performance all-day radiative cooling. Solar Energy Materials and Solar Cells, 212, 110584.

Mandal, J., Yang, Y., Yu, N., & Raman, A. P. (2020). Paints as a scalable and effective radiative cooling technology for buildings. Joule, 4(7), 1350-1356.

Peng, Y., Chen, J., Song, A. Y., Catrysse, P. B., Hsu, P.-C., Cai, L., . . . Wu, D. S. (2018). Nanoporous polyethylene microfibres for large-scale radiative cooling fabric. Nature sustainability, 1(2), 105-112.

Poredoš, P., Shan, H., Wang, C., Chen, Z., Shao, Z., Deng, F., . . . Wang, R. (2024). Radiative Sky Cooling Thermal Concentration with Cooling Power Exceeding One kW Per Square Meter. Energy & environmental science.

Raman, A. P., Anoma, M. A., Zhu, L., Rephaeli, E., & Fan, S. (2014). Passive radiative cooling below ambient air temperature under direct sunlight. Nature, 515(7528), 540-544.

Rephaeli, E., Raman, A., & Fan, S. (2013). Ultrabroadband photonic structures to achieve high-performance daytime radiative cooling. Nano letters, 13(4), 1457-1461.

Son, S., Jeon, S., Chae, D., Lee, S. Y., Liu, Y., Lim, H., . . . Lee, H. (2021). Colored emitters with silica-embedded perovskite nanocrystals for efficient daytime radiative cooling. Nano Energy, 79, 105461.

Wang, C. H., Chen, H., Jiang, Z. Y., & Zhang, X. X. (2023). Design and experimental validation of an all-day passive thermoelectric system via radiative cooling and greenhouse effects. Energy, 263. Retrieved from <Go to ISI>://WOS:000878826300006. doi:10.1016/j.energy.2022.125735

Wang, T., Wu, Y., Shi, L., Hu, X., Chen, M., & Wu, L. (2021). A structural polymer for highly efficient all-day passive radiative cooling. Nature Communications, 12(1), 365.

Xie, H. L., Yin, H. Y., Xia, H., & Fan, C. Z. (2024). Efficient radiative cooling with bi-rhombic metamaterial and its application in thermoelectric power generation. International Journal of Heat and Mass Transfer, 222. Retrieved from <Go to ISI>://WOS:001155517400001. doi:10.1016/j.ijheatmasstransfer.2024.125176

Yu, L., Xi, Z., Li, S., Pang, D., Yan, H., & Chen, M. (2022). All-day continuous electrical power generator by solar heating and radiative cooling from the sky. Applied Energy, 322, 119403.

Zhai, Y., Ma, Y., David, S. N., Zhao, D., Lou, R., Tan, G., . . . Yin, X. (2017). Scalable-manufactured randomized glass-polymer hybrid metamaterial for daytime radiative cooling. Science, 355(6329), 1062-1066.

#371: Improvement of ventilation and cooling technology for industrial buildings with high waste heat

Lin LIU[1], Yunpeng SHEN[2], Jianlin LIU[3], Henggen SHEN[4], Guanghui WANG[5]

[1] Shanghai Institute of Technology, No.100 Haiquan Road Fengxian District Shanghai P.R. China, linda_rabbit@126.com
[2] Donghua University, No.2999 North Renmin Road Songjiang District Shanghai P.R. China, shenypbird@qq.com
[3] Donghua University, No.2999 North Renmin Road Songjiang District Shanghai P.R. China, jianlin.liu@dhu.edu.cn
[4] Donghua University, No.2999 North Renmin Road Songjiang District Shanghai P.R. China, shenhg@126.com
[5] Shanghai Institute of Technology, No.100 Haiquan Road Fengxian District Shanghai P.R. China, 1614837448@qq.com

Abstract: The traditional design scheme of ventilation system of high waste heat industrial building is full fresh air scheme, that is, outdoor ambient air will ventilate indoor heat. Fresh air evaporation cooling scheme, which carries out evaporative cooling for outdoor ambient air based on the full fresh air scheme, and another scheme, which carries out evaporative cooling for indoor ambient air on basis of fresh air evaporation cooling scheme, are discussed to improve the technical methods.By calculating, analyzing and comparing the advantages and disadvantages of the three design schemes, and comparedwith the air volume of actual engineering case by using these three schemes, the recommended air treatment methods are as follows: indoor and outdoor ambient air evaporative cooling scheme, by which the inlet air volume decreased by about 40%, followed by full fresh air evaporative cooling scheme, by which the inlet air volume decreased by about 23%. These two schemes have significant energy saving potential compared with the full fresh air scheme and can be providedin use for practical engineering.

Keywords: Evaporation Cooling, Industrial Building, High Waste Heat, Energy Saving

1. INTRODUCTION

This paper took a pump house as the object, carried on the application analysis of the pump house environment purification and energy saving technology. The heat dissipation of pump equipment in pump houses is the main problem to be solved in the ventilation of pump houses. The heat dissipation of pump equipment has the following characteristics: the heat dissipation is the sensible heat which causes the temperature rise and causes the decrease of indoor relative humidity. Therefore, under the condition that the relative humidity of the control house does not exceed the maximum allowable value of the equipment operation, the indoor heat value Q can be reduced by transforming sensible heat into latent heat, so to reduce the ventilation volume of the pump house and realize the ventilation and energy saving of the pump house.

Three feasible schemes involved in high waste heat ventilation system engineering: full fresh air scheme, fresh air evaporative cooling scheme and indoor and outdoor ambient air evaporative cooling scheme were discussed in this paper. The three schemes involved were calculated and analyzed and the advantages and disadvantages of each design scheme were compared.

2. METHODOLOGY

Reducing the ventilation volume of pump room can be solved by increasing the supply air temperature difference and reducing the residual heat. Direct evaporative cooling technology can be used to deal with outdoor air supply and indoor ambient air.

The calculation formula of ventilation volume for heat load conversion using evaporative cooling technology is as follows:

Equation 23: Ventilation volume for heat load conversion

$$G = \frac{Q}{C_P(t_P - t_j)}$$

Where:

- G = the amount of ventilation required (kg/s)
- Q = residual heat (kJ/s)
- c_p = specific heat of air (kJ/kg°C) (1.01 kJ/kg°C for water)
- t_p = exhaust air temperature, and also the indoor temperature limit (°C))
- t_j = Intake air temperature (°C))

The heat generated by the operation of the pump is distributed in the pump room, and the indoor heat can be efficiently eliminated by using reasonable air flow organization, and the heat accumulation in the dead corner can be avoided. CFD software can be used to simulate and analyze air flow organization, and the established physical model was shown in Figure 1. There were 5 pumps in the pump station, 6 air intakes and 5 air exhausts of the same size.

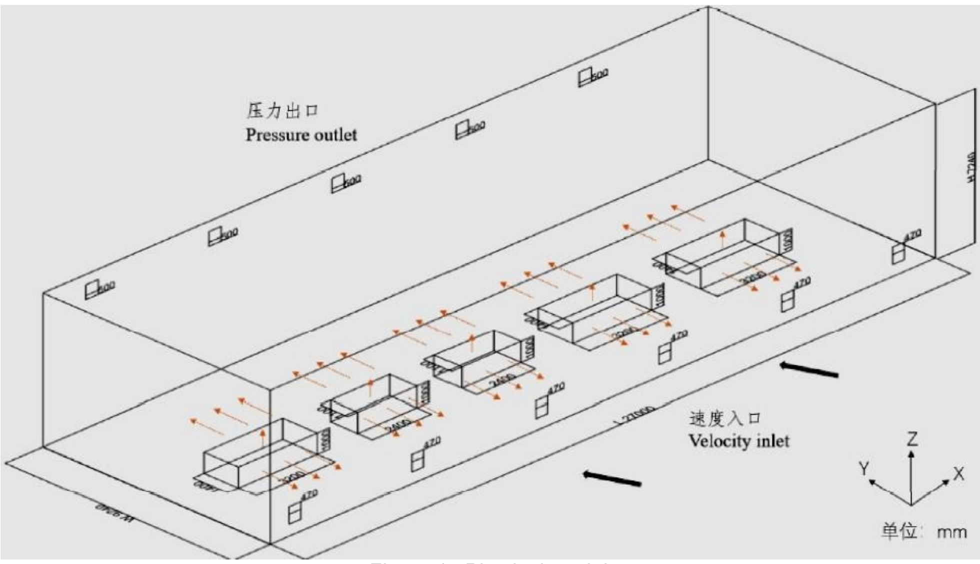

Figure 1: Physical model

The initial boundary conditions were wall conditions, air intake and air exhaust.

The fixed wall mainly included the ground, the wall and the surface of the pump unit. Defined floor insulation, heat flux 0W/m; Heat flux of wall 4.5W/m; The heat flux of the pump heat dissipation was simulated in the daytime peak condition (maximum heat load condition). A 1750m/h pipeline booster pump, a 1200m/h pipeline booster pump and a 1000m/h reservoir booster pump were started, and the calculated heat dissipation was 44.5kW, 25.28kW and 30.34kW respectively. The heat flux was 2800.5W/m, 2013.16W/m and 2195.36W/m, respectively.

The air inlet of the pump room: the air supply parameter was the calculated outdoor ventilation temperature of 31.2℃ and the relative humidity of 69%. The white blade took 1.0m/s into the air. Outdoor units were used for evaporation cooling and purification of outdoor wind. After evaporation cooling treatment, the air supply temperature was 27.1℃, the humidity was 95%, and the air supply speed was 4.0m/s.

Pump room exhaust outlet: The fresh air-cooling scheme and heat load conversion scheme adopted positive pressure ventilation, and the exhaust outlet was set as the white outlet.

The classical SIMPLE algorithm was used to simulate the flow structure and the thermal and humid environment in the high waste heat water supply pumping station.

Computing environment setting: atmospheric pressure was set to Shanghai atmospheric pressure value :100500Pa; The coordinate origin position was defined as (0,0,0), which was the pressure reference position; g is opposite to the Z axis and had a magnitude of $g=-9.8m/s^2$.

3. FINDINGS

3.1. Air volume calculation of different design schemes

Table1： Comparison of air volume

Scheme	Ventilation rate G kg/h	Inlet air temperature t_j ℃	Waste heat Q kW/h	**Ventilation volume** L m^3/h
1	$G=Q/C_p(t_p-t_j)$	31.2	100.12	25859
2	$G'=Q/C_p(t_p-t_j')$	27.1	100.12	19917
3	$G''=(Q-Q_p)/C_p(t_p-t_j')$	27.1	80.12	15953

The comparison of the data of the residual heat removal design schemes of the three pump houses was shown in Table 1. After adopting the "indoor and outdoor ambient air-evaporative cooling" technical solution, the theoretical design air volume decreased to 60.3% of the original value; The implementation of positive pressure ventilation could keep the existing pump house building without major changes.

The outdoor unit system of "purification and dust removal + direct evaporative cooling + fan + air supply pipeline + low opening and closing shutter air supply port" was set; Indoor evaporative cooling machine; Original building structure unchanged, doors and Windows could be unchanged; The original exhaust fan could continue to be used; All power equipment and air outlet opening and closing into the intelligent control, indoor and outdoor environment set temperature and humidity, particulate matter concentration (PM10, PM2.5) monitoring.

3.2. Simulation analysis of temperature distribution

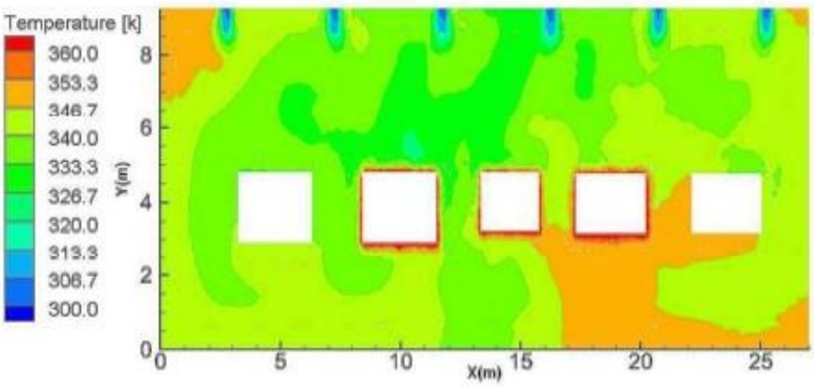

(a) Scheme 1

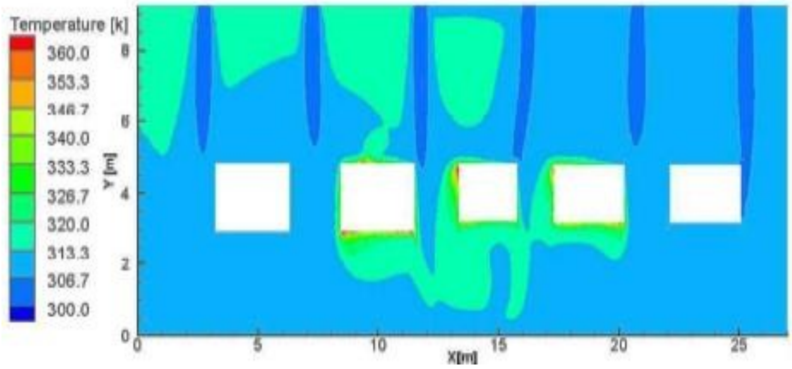

(b) Scheme2

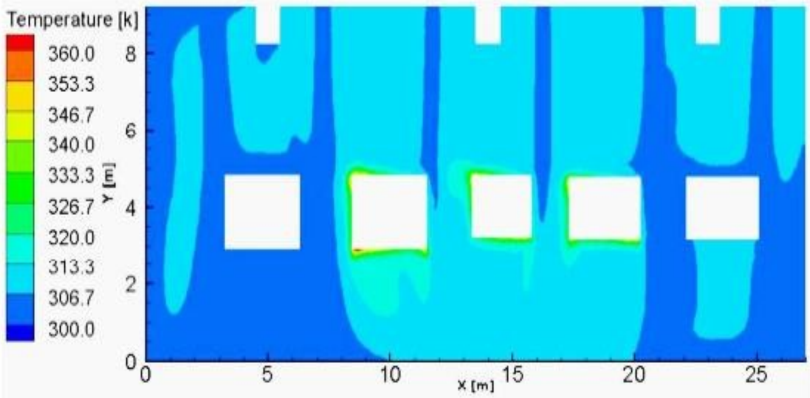

(c) Scheme3

Figure 2: Temperature distribution at the height of 0.6m

CFD simulation software Fluent was used to analyze three different schemes (all fresh air schemes; Full fresh air evaporative cooling scheme; Indoor and outdoor evaporative cooling scheme) to predict and analyze the space temperature field. Figure 2 showed the temperature distribution of the horizontal section Z=0.60m in the pump house under the three schemes.

In scheme 1, the use of natural air supply had a very limited cooling effect on the pump room, and the temperature range between the air supply outlet and the pump was between 45 and 50℃. The temperature between the pump and the exhaust fan was close to 60~65℃. Although the temperature of the upwind side of the pump was about 55℃, it could be found that the cooling effect of natural air supply was not significant; The suction effect of exhaust air was limited to the periphery of the suction port, and the affected area was small. This airflow organization method caused many dead spots of indoor heat accumulation, and the ventilation airflow played a limited role.

In scheme 2, the temperature on the windward side of the pump was lower than that on the leeward side of the pump. The temperature on the leeward side was about 45 °C, and the temperature in other areas was about 40 °C. Compared with the all-fresh air scheme, the ventilation cooling effect was significantly improved, and the maximum temperature was not higher than 45℃.

In scheme 3, the temperature between the air supply port and the water pump did not exceed 35 ° C, and the temperature at the rear of the water pump did not exceed 45 ° C. The operating temperature was below 45 ° C. The temperature in the area between the two air supply outlets and the area far away from the pump did not exceed 35℃. It could be seen that due to the increase of indoor evaporative cooling, the environmental cooling effect could achieve the environmental temperature and humidity control to meet the design requirements.

3.3. Numerical simulation analysis of air flow organization

As the mechanism of temperature and humidity evolution in the pump room, it was necessary to further study the velocity field and flow line of air flow in the pump room.

Scheme 1

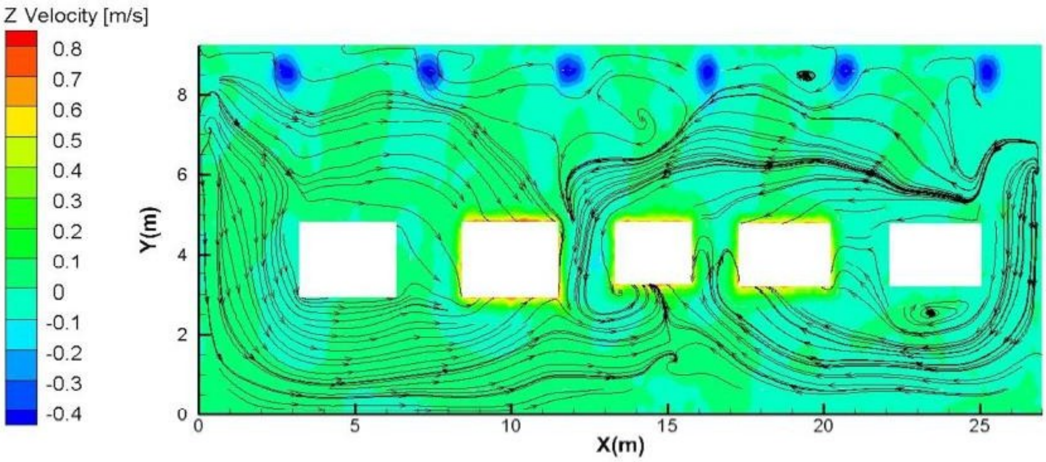

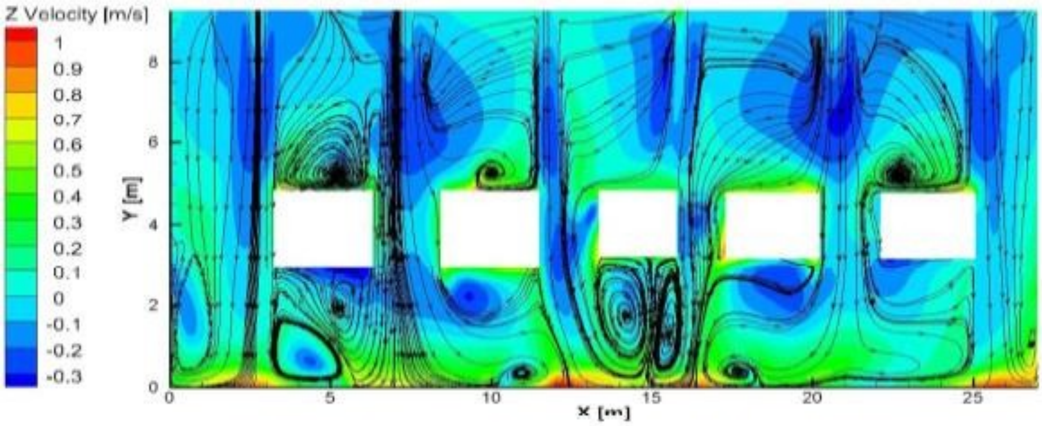

(d) Scheme2

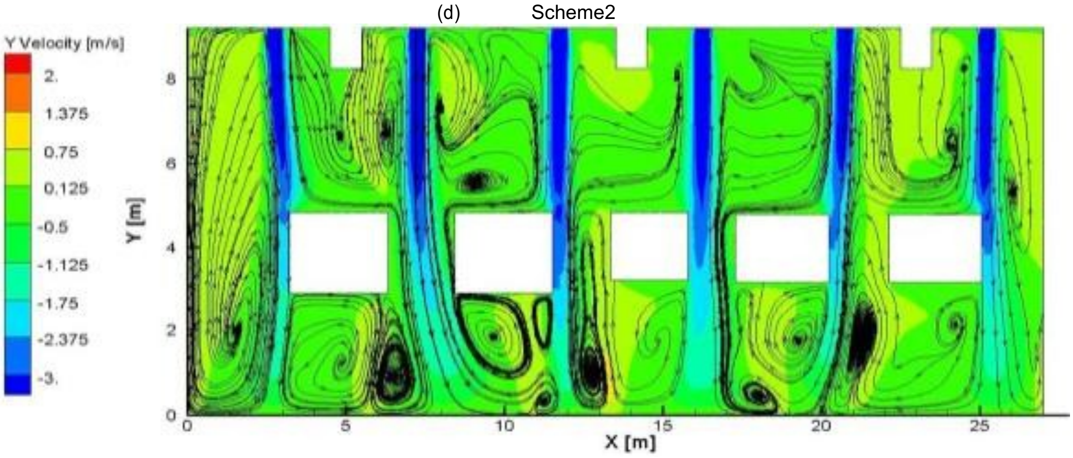

(e) Scheme3

Figure 3: Temperature distribution at the height of 0.6m

For scheme 1, the airflow velocity field and flow line distribution in the horizontal section of Z=0.60m at the height of pump house in all fresh air schemes. It could be seen that when natural air supply was used, the air velocity of the air inlet ended into the pump room environment was 0.30m/s, and that of the exhaust end was about -0.35m/s. The large amount of heat emitted by the pump made the surrounding ambient air move around the pump and played a heated rising movement.

As for scheme 2, the air on both sides was absorbed by the mechanical air supply, so that the air flow in the spring room was in a turbulent state. The forward and backward movement of the air flow was conducive to the mixing of the low-temperature air supply and the high-temperature air in the indoor environment, so to achieve the effect of ventilation and cooling.

For scheme 3, the ventilation and cooling design scheme had higher wind speed than the fresh air design scheme, and the mechanical air supply could stabilize and maintain the ventilation and cooling of the pump in the pump house of the supply air temperature. Through the observation of the change of the flow field diagram, the mechanical supply air could be more turbulent, which could disturb the heat accumulation to achieve the cooling effect of the pump station.

3.4. Relative humidity simulation analysis

Figure 4 showed the relative humidity of the pump position in the pump room with the change of height for the three design schemes. It could be seen that the relative humidity of the pump room in the three design schemes was lower than 70%. In the working area from 0.00m to 1.2m (pump height 0.60 to 1.0m), the relative humidity decreased rapidly, and the fresh air decreased from 16% to 7%; Fresh air cooling decreased from 60% to 33%; Indoor and outdoor air cooling decreased from 67% to 48%. In space above 1.0m, the relative humidity of the whole fresh air scheme changed in 7% to 5%, and the humidity decreased slightly with the increase of height. The relative humidity rised from 33% to 43% when the fresh air cooled from 1.2m to 3.0m, and then the humidity droped slightly to about 40% as the height increased. In the indoor and outdoor air cooling scheme, the relative humidity was 47% at 1.50m, and then the relative humidity rised to 53% withthe increase of 3.0m in height, and decreased to about 50% with the increase of height above 6.0m.

Overall, the relative humidity of the whole fresh air scheme was 7~16% at the whole height, the relative humidity of the space above 1.0m in the pump room was very dry, less than 8%, and the personnel inspection environment was poor. The relative humidity of the other two schemes after evaporation cooling was 69% lower than that of outdoor ventilation in summer, which meet the ambient air conditions of equipment and personnel inspection.

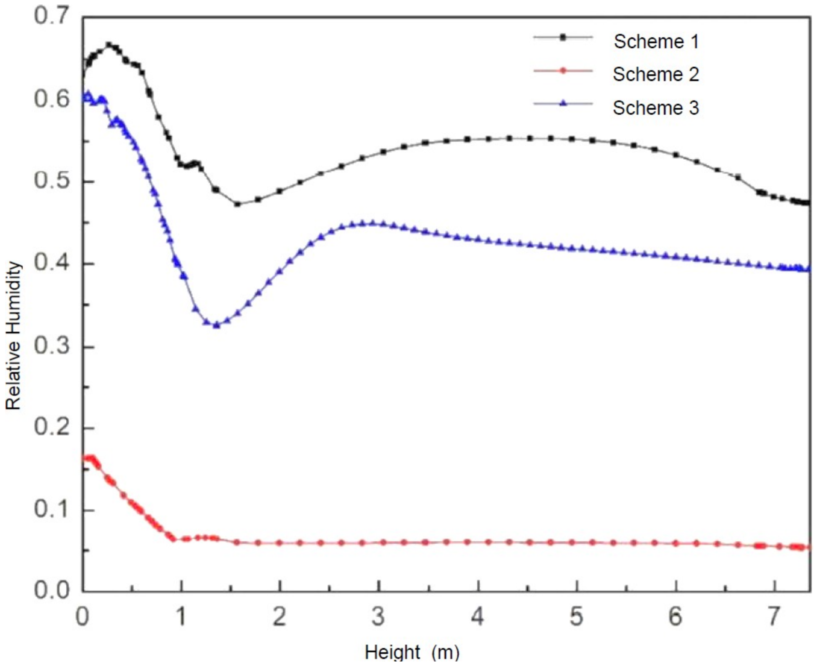

Figure 4: Physical model

4. CONCLUSION

From the above three schemes, we can find that:

- The full fresh air scheme did not meet the design requirements.
- The full fresh air evaporative cooling scheme, by which the inlet air volume decreased by about 23%, had remarkable energy-saving effect.
- The indoor and outdoor ambient air evaporative cooling scheme, which meets the design requirements and could reduce the air volume by about 40 %, had very significant energy saving effect compared with the full fresh air scheme,

#372: Experimental study of the photoelectric performance and mismatch loss phenomenon of curved photovoltaic modules

WANG JUN[1,2], Xinyi TIAN[3], Qiansheng FANG[1,2], Jie JI[3*]

[1] Anhui Province Key Laboratory of Intelligent Building and Building Energy-saving, Anhui Jianzhu University, Hefei, Anhui, China
[2] Anhui Institute of Strategic Study on Carbon Emissions Peak and Carbon Neutrality in Urban-rural Development, Anhui Jianzhu University, Hefei, Anhui,China, wj0412@mail.ustc.edu.cn
[3] Department of Thermal Science and Energy Engineering, University of Science and Technology of China, Hefei, Anhui,China, txy0818 @mail.ustc.edu.cn
[1] Anhui Province Key Laboratory of Intelligent Building and Building Energy-saving, Anhui Jianzhu University, Hefei, China
[2] Anhui Institute of Strategic Study on Carbon Emissions Peak and Carbon Neutrality in Urban-rural Development, Anhui Jianzhu University, Hefei, Anhui,China, fqs@ahjzu.edu.cn
[3] Department of Thermal Science and Energy Engineering, University of Science and Technology of China, Hefei, Anhui,China, jijie@.ustc.edu.cn

Abstract: Flexible photovoltaic technology not only has high power generation efficiency, but also is thin and light, which can be well adapted to the surface form of curved buildings. In this paper, the power output of different curved photovoltaic modules under outdoor dynamic conditions were investigated experimentally. Six same flexible CIGS modules were used to test all-day electrical power and temperature data in different bending forms, including length-oriented concave(lgcav) and convex(lgcvx) bending, width-oriented concave(wdcav) and convex(wdcvx) bending, length-oriented corrugated(lgcg) bending, and flat mounting. The experimental results showed that the circumferential irradiance distribution of the PV is seriously uneven in the curved types, and there are multiple peaks in the current-voltage curve of the modules. In one typical sunny day during the heating season in Hefei city of China, the experiment results showed that, the width-oriented forms showed the worst mismatch effect than the flat type, the concave bending forms showed more electrical loss than the convex bending forms. In the experiment day, the average power output of different bending forms decreased by 75.46% of width-oriented convex, 42.27% of length-oriented concave, 8.75% of length-oriented convex. The research can preference and data support for curved photovoltaic buildings.

Keywords: Curved Photovoltaic Building; Flexible Photovoltaic; Concave and Convex Bending Forms; Mismatch Loss; Copper Indium Gallium Selenium (CIGS)

1. INTRODUCTION

With the development of social economy and urbanization, energy consumption has become a global problem. Among them, the building sector will be the largest segment in 2022 with a share of 34% of total global energy consumption and 37% of associated CO2 emissions [1]. According to China association of building energy efficiency (CABEE), in 2020, the carbon emissions caused by the building and construction were 5.08 billion tce, accounting for more than half of the country's total carbon emissions. At present, China has proposed to reach the peak of carbon emissions by 2030 and achieve carbon neutrality by 2060. Exploring building energy efficiency and renewable energy technologies are considered two of the most important ways to address the growing energy needs of the building industry and achieve the dual-carbon goal.

Building integrated photovoltaic (abbreviate as BIPV) is the most widely used technology of solar photovoltaic in buildings, mainly in the form of BIPV roofs [2, 3], walls [4], windows [5] and shadings [6]. At present, the widely used planar c-Si PV modules are large weight, easy to crack, and the structural load requirements of the building are higher. It can seriously damage the original architectural style if it is directly attached to the surface of the curved building envelope. In addition, the area of the south building facade is limited, and the flat modules can only have a maximum of 1:1 installation area. In contrast, flexible PV modules not only have high photoelectric efficiency, light weight, good flexibility and strength, but also well adapted to non-plane, especially curved building skin. Besides, in the same projection area, the surface area and installation amount of the PV module are increased by the curved PV compared with the flat, and the power generation per unit area is higher than that of the conventional module. Alpuerto et al. [7] compared PV modules with three shapes of plane, sine curve and ellipse, and the results showed that under the same two-dimensional projection area, the irradiance obtained by the curved surface increased by 50%, and its power curve would produce multiple peaks in a day. Therefore, it is of great significance to explore the application of flexible PV in curved BIPV buildings.

For curved BIPV, the shape of the surface can cause the irradiance to be distributed unevenly, thereby affecting the electricity yield. Because of the shading cast by curved PV itself, it will lead to mismatch effect. In flexible PV modules, the current and voltage characteristics of the cell are usually nonlinear, that is, non-equivalent circuit models. Therefore, the mismatch effect causes the equivalent circuit to change, which decreases the electrical efficiency. Li et al. [8] did the typical performance prediction of BIPV under no-shading, shading and masking conditions based on a multi-physics model. The result showed that of great necessary to explore the electricity yield prediction by comparing PV modules with or without shading. Saoud et al. [9] studied the partial shading effect on one complexly shaped BIPV roof, optimising maximum yield to determine the optimal configuration and number of modules for each string by genetic algorithm. Walker et al. [10] presented a novel workflow of BIPV system losses in combination with system optimizations. Based on a parametric 3D model, one bending type CIGS module has been numerically and experimentally studied. The result showed that the longitude orientation outperforms the orthogonal one by 5-8%. Wang et al. [11] proposed a flexible c-Si based curved PVT structure, which could produce both electricity and hot water. The experimental results showed that the structure has an electrical efficiency of 14.71% and thermal efficiency of 56.79% at a flow rate of 0.9L/min. Bugaj et al. [12] proposed a semi-flexible PVT system based on c-Si PV cells, which is used to develop the testing methodology of different bendable conditions. The results revealed that when the BAM (bending angel modifier) varied from 1 to 1.1, the thermal power in deflection of 30° was lower by about 18% compared to flat type, and the electrical power was close to 14%. Tian et al. [13] compared the electrical performance of a serious of curved/flat PV modules under different meteorological conditions and with various inclination angles. The result indicated that in 30° angle, the flat module performs better while the difference getting smaller since the inclination comes to 75°. The curved module shows superiority in annual electricity generation with a high inclination angle in summer.

However, according to the literature review above, no research has been conducted on flexible PVs based on comparing different bending forms which are suitable to vary shapes of BIPV technologies. In this work, considering the flexible CIGS PV modules can be bent in different directions, we proposed various forms including length-oriented concave and convex bending, width-oriented concave and convex bending, length-oriented corrugated bending and flat mounting, which represent typical types of building sector that used in curved building integrated photovoltaic (abbreviate as C-BIPV). In terms of flexible CIGS PV, comparing the traditional flat types, the curved types may cause inevitable voltage mismatch loss and power loss in some conditions. Besides, the different operating curved CIGS modules can cause noticeable thermal distribution. An outdoor test rig that consists of six types of flexible CIGS modules was constructed in Hefei city of China, and a series s of experiments were conducted. Electrical performance and temperature distribution of the curved PV modules were analyzed and discussed in this present work.

2. TESTING SYSTEM DESCRIPTIONS AND EXPERIMENT EQUIPEMENT

In this section, the fabrication of the curved CIGS PV module and the system structure in different bending forms was described. Specific working principles and flow of the electrical system as well as experiment equipment which operating in field were explained.

2.1. Objective of testing

Due to the complexity of the curved photovoltaic geometry, uneven irradiance and temperature distribution will be formed when combined with the building envelope, resulting in mismatch phenomenon and partial overheating in PV modules. The inhomogeneous distribution of the irradiance on curved PV surface will make the photogenerated current, voltage and power output different from the flat type. Electrical loss will cause a part of the current cannot be output, and voltage mismatch will cause the operating point deviate from the maximum power point (MPP), which will affect the output power. Besides, the gradient of the PV temperature will lead to overheating in part of the PV, which causes uneven thermal stress. Thus, the service life and operation safety of PV modules are affected.

Considering the CIGS PV module is light weight, good flexible and easy to be bent in different shapes. Thereby, as shown in Fig.1, we chose to bend it in length-oriented convex, width-oriented concave, length-oriented corrugate bending forms. Among them, the two convex and two concave systems are distinguished by the length and width orientation, the two length and two widths are distinguished by the concave and convex shapes, and the irradiance, temperature and infrared thermal distribution will show difference. The length-oriented corrugate would show special changes when it has waved shapes. The curved shapes will compare with the flat one, and they can represent typical shapes of curved PV building envelopes.

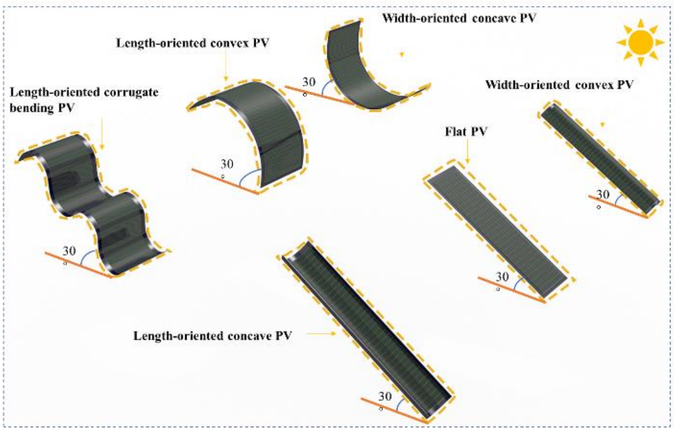

Figure 1: Schematic drawing of the experiment

2.2. Fabrication of the curved CIGS PV modules

Considering the more convincible contrast between the length-orient bending and width-orient bending forms, the module with a large aspect ratio is selected. As shown in Fig.2a, the main key components of the flexible CIGS PV cell are the chipset string. The module has a length of 1.72m and the width of 0.35m, but the actual photoelectric area was 1.58m(length) *0.31(width) because of the necessary sealing part. Every single chip has a dimension of 312mm length and 43.75mm width, and every 4 chips are connected in series to form a chipset and connected with a silicon diode in parallel. Then 9 groups of chipsets consist the whole PV which means it has 36 pieces of chips in total. The flexible CIGSmodule has the rated power (Pmpp) of 80W, photoelectrical efficiency (η) of 16.3%, maximum voltage (Vmpp) of 20.0V, maximum current (Impp) of 4.01A, open circuit voltage (Voc) of 24.70V, short circuit current (Isc) of 4.54A. Besides, the rated operating temperature is 48°C at STC. As shown in Fig.2b, the IV curve of the flat type was presented, there were no peak or though points. As shown in Fig. 1c, considering that the irradiance is circumferential changing, every curved module is a semicircle of 180°。That means the experimental data can be simplified and obtained more accurately.

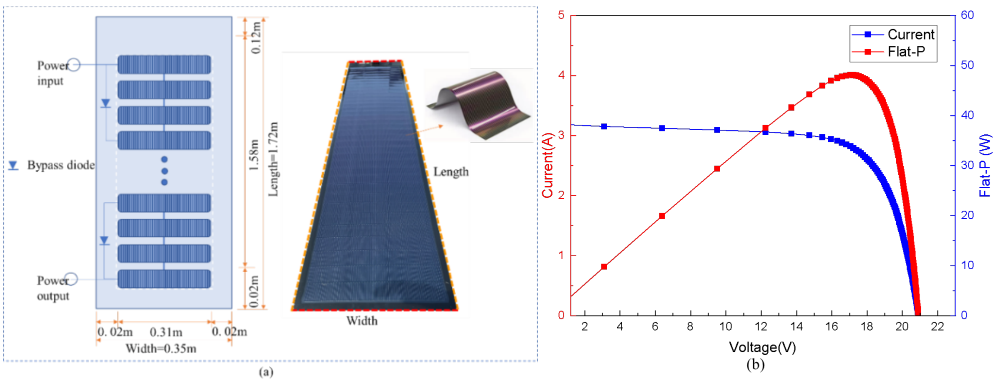

Figure 2: (a) The structure dimension of the flexible CIGS PV module;(b) PV structure composition;(c) Curvature of the PV module

For the construction process of the curved CIGS PV module, the detailed flow chart is shown in Fig.3a. Firs of all, the thin film CIGS plane combined with the flat/curved aluminum plate by thermal silica gel, so the metal plate can be heat dissipation. Then, the sizes and shapes of different aluminum plates are customized to each PV panel by precise calculation. Every part that is related to the curved shape is bent into half cylinder by CNC press bending machine and fixed with rivets. Finally, under six groups of CIGS PV modules with different shapes, stainless steel frames are fixed to adapt to outdoor experiments with different angles, orientations, weather conditions in future, ensuring the stability and strength of the components. As shown in Fig.3b, the current-voltage characteristic curve of the flat typed PV module has been displayed. The curve line is smooth as the change of voltage.

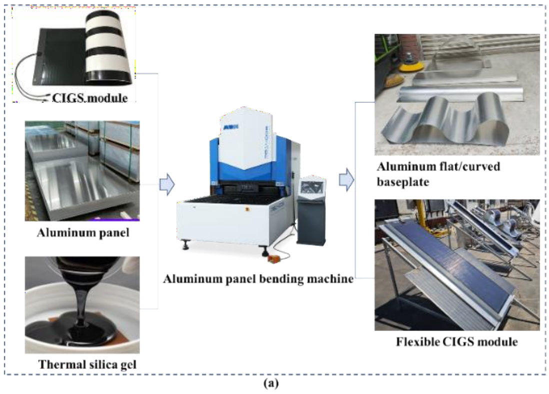

Figure 3: Detailed construction process of the curved CIGS PV modules

2.3. Description of the test rigs on flexible CIGS PV module

A series of curved CIGS PV systems were built on the rooftop of a building in the campus of University of Science and Technology of China, Hefei (32° N, 117° E), for the comparative experimental tests. The systems are completely identical except for the bending forms, and everyone has the same testing method for error reduction.

In the first stage, the test rig was placed parallel along north-south direction with the inclination of 30°, facing due south. The tilt angel and the facing direction will change in the requirements of experimental research. There are five modules be bent in nonplanar forms to compare with the flat one. In addition, sufficient placing will ensure there is no shading from each other but only itself. As shown in Fig.4, the photo of the experiment was displayed.

*Figure 4: P*hoto of the experiment

2.4. Equipment for the test experiments

As shown in Fig.4, the flow of the PV system was presented. The test comprises the following factors: ambient conditions, electrical performance, temperature and infrared thermal image distribution. The ambient conditions consist of solar irradiation, ambient temperature, and wind velocity. The electrical performance is exemplified by the PV voltage, current, output power at mpp (Vmpp, Impp,Pmpp), filling factor(FF), electrical efficiency(η). The temperature and infrared thermal image distribution described the various thermal distribution of different forms of PV modules.

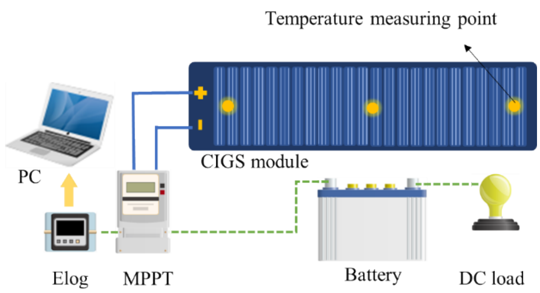

Figure 5: Flow of the PV system

As shown in Fig.6, experimental instruments were presented. During the experiments, the temperature measurements are all measured by T-type thermocouples. The solar irradiance is monitored by a pyranometer that is placed parallel to the baseplate at the same incident angle. The wind velocity is collected by a three-cup wind speed sensor. These three sections are recorded by a data logger at an interval of 10 seconds. Each PV module is linked to the maximum power point tracking (MPPT) along with storage batteries and loads to form a closed circuit. eLOG01 captures the power output every5 minutes. In every system, the temperature measurements of PV modules are symmetrically dispersed at 3 points on the rear of PV cells, from air inlet to air outlet. For heat distribution, a high-resolution infrared thermal imager was used to testat noon, when the sun was at its strongest.

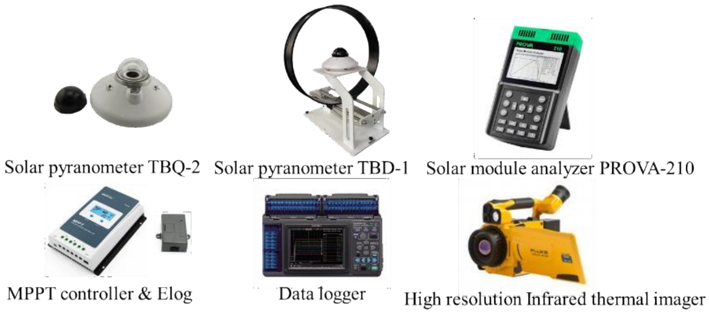

Figure 6: Key equipment of the test rig

3. PERFORMANCE EVALUATION PARAMETERS

For a flat-type PV module, it is simple to collect the solar irradiance that reaches the surface. However, the solar irradiance arriving at the curved PV surfaces is inhomogeneous and cannot be measured directly by the pyranometer. Considering the curved surfaces are welded on a flat baseplate, it is necessary to define efficiency to evaluate the performance of the system reasonably.

For the electrical performance evaluation, electrical efficiency (η_{pv}) is introduced to evaluate the photoelectrical conversion efficiency and is defined as:

Equation 1: Electrical efficiency

$$\eta_{pv} = \frac{P_{max}}{GA_{pv}} = \frac{UI}{GA_{pv}}$$

Where:

- P_{max}=instantaneous maximum power output of the PV module
- U = output voltage of the PV module (V)
- I= output current of the PV module(A)
- G= solar irradiation intensity in the corresponding tilt angel (W/m^2)
- A_{pv}= total orthographic projection area of the curved PV module on the inclined surface area (m^2)

As a semiconductor device, the I-V curve of the flexible PV module conforms to the features of semiconductor device. The filling factor is an inevitable parameter to characterize the performance of PV modules. The higher the value, the higher the photoelectric conversion efficiency. The filling factor defined as:

Equation 2: Filling Factor (FF)

$$FF = \frac{P_{mpp}}{V_{oc} \times I_{sc}} = \frac{V_{mpp}I_{mpp}}{V_{oc} \times I_{sc}}$$

Where:

- V_{oc} = the open circuit voltage (V)
- I_{sc} = the short circuit current (A)

4. RESULTS AND DISCUSSIONS

Based on the established operating principles, an experiment was conducted in July 5th 2024. The tests lasted from the initial low irradiance to the highest irradiance, then till the irradiance become decrease, which describing convincible results. The ambient condition is shown in Fig.6. The temperature was in the range of 33.21°C -38.26 °C and the total solar irradiance during the period that received by the PV module was 12.43MJ. This is a typical sunny day in heating season of Hefei.

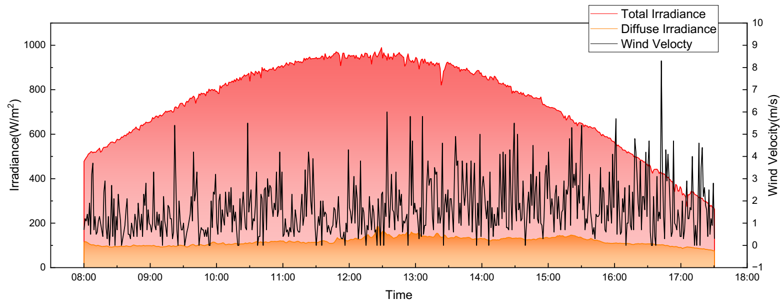

Figure 6: Ambient conditions of the experiments 5th July 2024

4.1. Electrical performance

For the PV system, electrical power generation is one of the most significant indexes. The electrical power output (P), current(I), and voltage(V) of the PV system were shown in Fig.7. During the field experimental test, the electrical power output of the flat type performed best than others, the width-oriented convex bending form (wdcvx) became the worst, and the second one was the length-oriented convex bending form (lgcvx), then was length-oriented concave bending form (lgcav). The electric changes followed by irradiance, which means the highest point was at noon. The total power output was 413.91W·h for flat type, 347.74W·h for lgcvx form, 259.76 W·h for lgcav form and 75.14 W·h for wdcvx form. The PV voltage showed the relatively stable data, they were around 17.36V for flat type, around 15.02V for lgcvx form, 16.76V for lgcav form, 13.78V for wdcvx form. The width-oriented form lost more electricity than others, because the big shape changes made inhomogeneous distribution of the irradiance on curved PV surface, which lead to electricity mismatch phenomenon. Thereby, the current output was decreased and the power output lost. For both length-oriented systems, the concave form lost more electricity than the convex form. That is because complementary to the convex form, the two sides of the concave surface have curved parts higher than the plane part, which cast their shadow in the projection of their own during test period. For both convex systems, the width-oriented form lost more than the length-oriented form. That is because the width-orient form changes more part of the curved surface casted in shadow, which become a significant resistance in the electrical circuit. Hence, the photogenerated current, voltage and power output were all decreased.

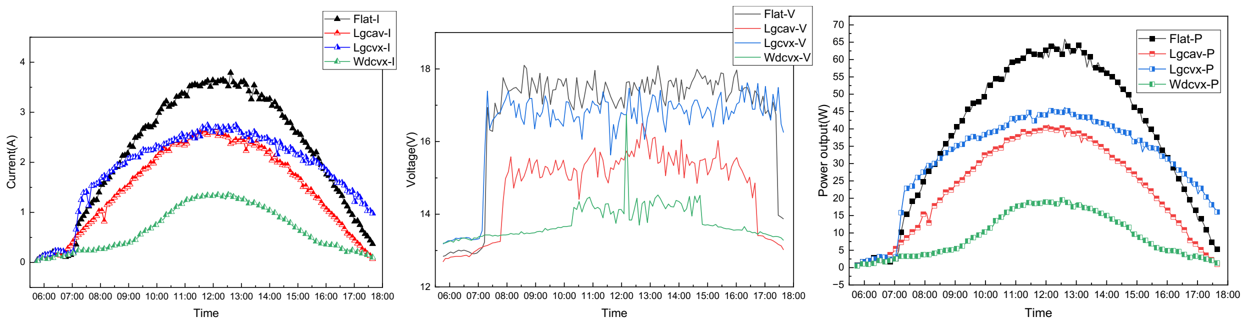

Figure 7: Electrical performance of the curved PV modules

As shown in Fig.8, for the current-voltage characteristic curve image of the different forms of PV modules, it reflected the relationship among the PV voltage, current, and power output. The typical flat type of flexible CIGS PV module was shown in Fig.2a, the curves were very smoothy while the bending forms showed the abnormal fluctuation in different ways. As the PV voltage changes, the corresponding changes in PV current and power output. They all showed noteworthy behaviour but deviated from the maximum power point. The tests were conducted on 7th July, a sunny day. As shown in Table1, the ambient conditions were presented. Three test period were chosen that is 8:00 in the morning when the solar irradiance just began, to 12:00 in the noon when the solar irradiance strongest, till 15:00 in the afternoon when the solar irradiance become decrease. All of them showed multiple peaks and troughs.

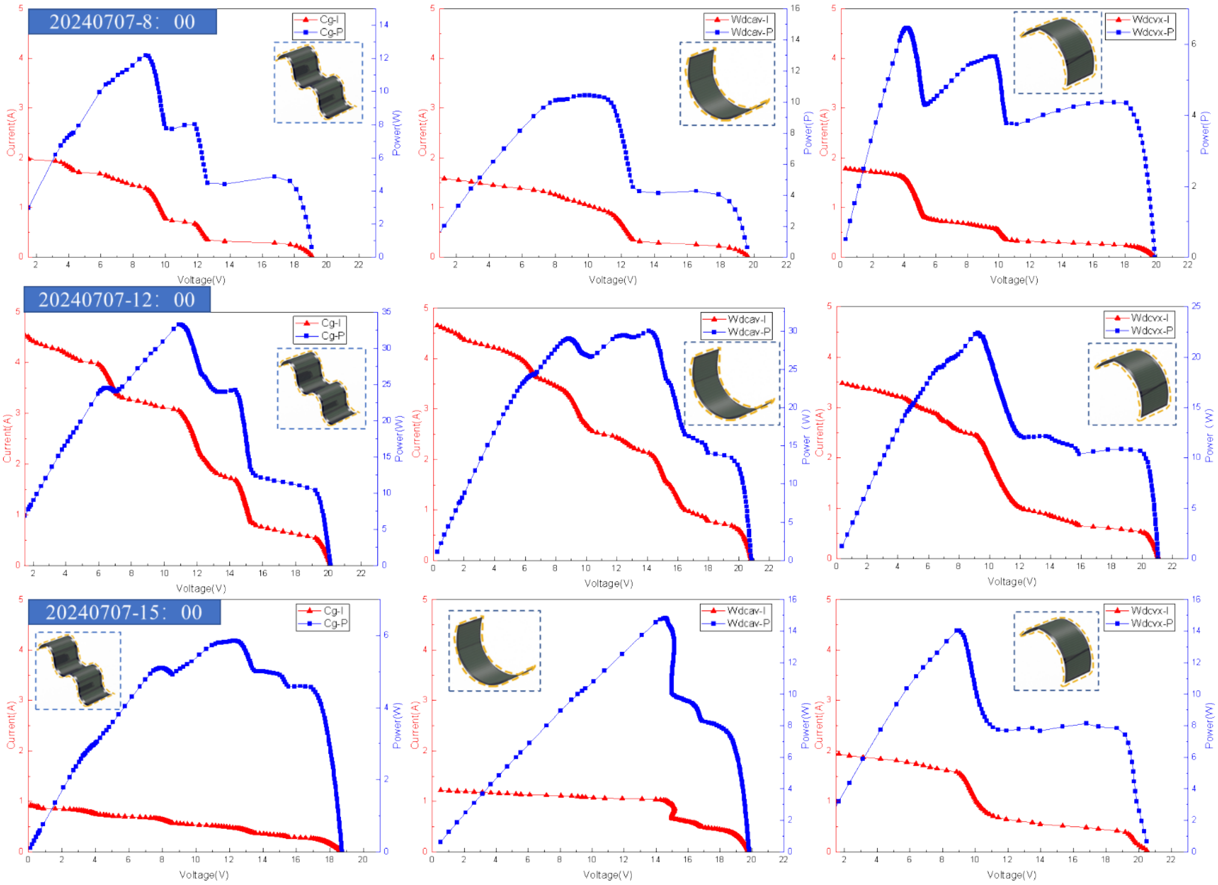

Figure 8: The I-V characteristic curve of the mismatch effect systems

Table 1: The ambient condition of IV curve measuring on 7th July 2024

Time	Tam (℃)	T-flat (℃)	T-lgcav (℃)	T-lgcvx (℃)	T-Stcvx (℃)	Tilt angel (°)	Total-irrad(W/m^2)	Diffuse-irrad(W/m^2)	Wind velociy(m/s)
08:00	33.65	47.02	36.27	47.07	43.44	30°	382.316	79.8823	1.53
12:00	36.4	53.35	48.77	54.95	53.51	30°	1051.35	154.674	12.03
15:00	36.9	42.36	41.89	44.43	38.86	30°	723.676	133	4.2

As shown in Fig9., the filling factor (FF) difference was described. Compared to the best performance of flat type module, the two length-oriented bending forms had higher FF than the width-oriented bending form. For two length-oriented forms, the convex bending one changes followed by the flat one, while the concave one showed great change suddenly at around 9:10 am and exceeded the convex one in the afternoon. The width-oriented bending form behaved steadily at the lowest level and showed a centra symmetric distribution.

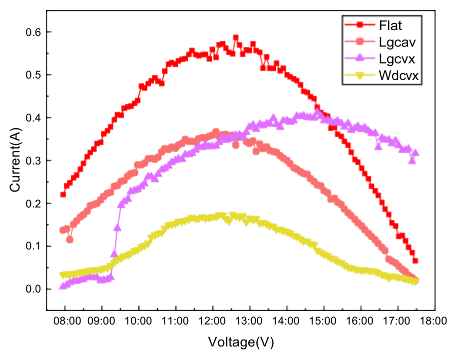

Figure 9: The filling factor of the curved PV modules

4.2. Temperature field

For temperature distribution, the average temperature of the PV modules from north to south were measured and displayed in Fig.10. Compared with the flat type of module, the length-oriented convex bending form showed higher temperature in themorning and decreased from around 13:00 pm. That is because with the circumferential variation of solar irradiance, the photoelectric changes, which would increase the PV temperature. The length-oriented concave bending form showed thelowest temperature in the morning but kept increasing during the experiment period. That is because the concave cylindrical surfaces received more solar irradiance than the convex surfaces during the experimental period. The width-oriented convex bending forms showed a relatively steady change between 36.11°C-54.53°C.

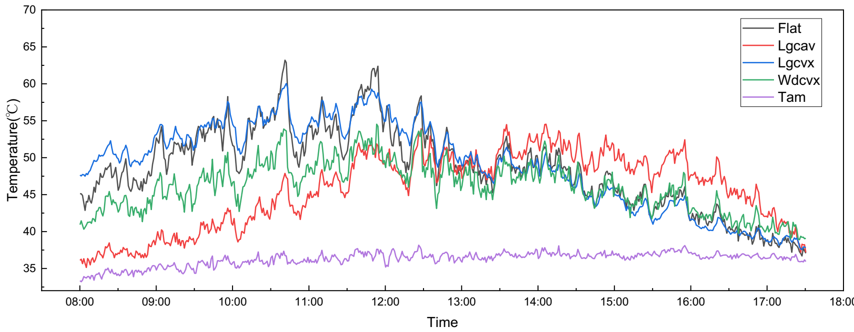

Figure 10: The temperature distribution of the curved PV modules

As shown in Fig.11, the infrared thermal distribution of each PV module was displayed. The high-definition resolution of the image was recorded from the distance of 2.35m, and direct to the orthographic projection of the curved PV surfaces. Each of them has a part of highest temperature, that because the back of that sheet doesn't adhesive thermal gel. Apart from that, the flat type presented evenly temperature distribution the whole module, which means it receives the uniformly solar irradiance during the test period.

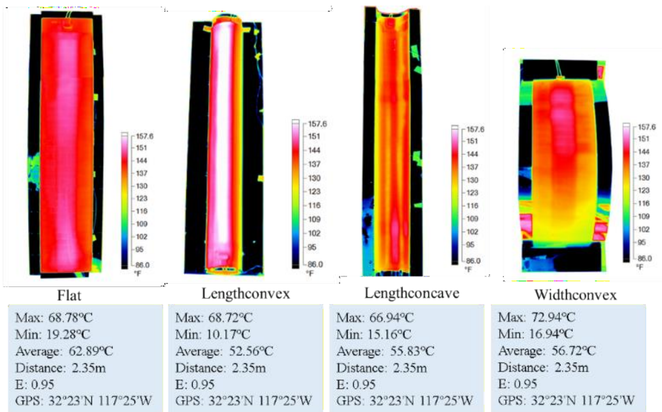

Figure 11: The infare thermal image of the curved PV modules

5. CONCLUSION

It is worth noting that the curved module has great potential in the application of the curved BIPV buildings with different bending forms. In this current work, a series of curved CIGS PV modules with different bending forms were proposed and constructed. Six comparable outdoor test rigs were established to evaluate the system's comprehensive electrical performance and temperature distribution. Main conclusions are shown as follows:

- For the electrical performance, the width-oriented bending forms showed the worst mismatch effect than the flat type, the concave bending forms showed more electrical loss than the convex type. In the test of one typical sunny day during heating season in Hefei, China, the average power output of different bending forms decreased by 75.46% of width-oriented convex, 42.27% of length-oriented concave, 8.75% of length-oriented convex.
- For flexible PV modules, the mismatch effect always happens in either length or width orientation bending forms. Then, it's of great importance to carefully design the series parallel arrangements to minimize electrical loss.
- For curved PV modules, the different bending forms with changing inclination will lead to various inhomogeneous irradiance distribution, which lead to varying degrees of power loss. They need to be designed by specific geometrics, optimizing PV installation and their electrical layout.

Nevertheless, several problems might be faced in future. The electrical performance of the curved PV module with changing inclination needed more outdoor experiments. Besides, considering the chipset string distributed in 9 groups that set parallel to length-oriented direction, the comprehensive direction that parallel to east-west direction are worthy to study. In addition, there are some other kinds of flexible PV modules that can be compared with. Anyhow, this research still provides an effective way to explore the mismatch phenomenon of curved PV modules with different bending forms.

6. REFERENCES

[1] GlobalABC U(2024)2023 Global Status Report for Buildings and Construction.

[2] Tian X et al.(2023)A multifunctional curved CIGS photovoltaic/thermal roof system: A numerical and experimental investigation. Energy,273,

[3] Wang C et al.(2021)A novel solar spectrum-splitting utilization photocatalytic CdTe double-skin façade: Concept, design and performance investigation. Building and Environment,195,

[4] Hu Z et al.(2017)Design, construction and performance testing of a PV blind-integrated Trombe wall module. Applied Energy,203,643-56.

[5] Zhang C et al.(2022)Experimental and numerical studies on the thermal and electrical performance of a CdTe ventilated window integrated with vacuum glazing. Energy,244,

[6] Lu HYL(2007)The Optimum Tilt Angles and Orientations of PV Claddings for Building-Integrated Photovoltaic (BIPV) Applications.pdf>. Journal of Solar Energy Engineering,,129,2,253-55.

[7] Lance Alpuerto RSB(2019)Energy harvest potential of flexible photovoltaics on curved surfaces. 2019 IEEE Texas Power and Energy Conference (TPEC).1-6.

[8] Li Q et al.(2020)Performance prediction of Building Integrated Photovoltaics under no-shading, shading and masking conditions using a multi-physics model. Energy,213,

[9] Al-Janahi SA et al.(2020)A Novel BIPV Reconfiguration Algorithm for Maximum Power Generation under Partial Shading. Energies,13,17,

[10] Walker L et al.(2019)High-resolution, parametric BIPV and electrical systems modeling and design. Applied Energy,238,164-79.

[11] Wang J et al.(2024)Design and experimental study of a novel flexible PV/T structure. Energy,296,

[12] Bugaj MA and K Mik(2023)Can PVT bend?: The elaboration of flexible hybrid photovoltaic thermal solar collector structure and testing methodology. Renewable Energy,215,

[13] Tian X et al.(2022)Comparative performance analysis of the flexible flat/curved PV modules with changing inclination angles. Energy Conversion and Management,274,

#375: Performance evaluation of a novel high drop composite power/storage system for low-temperature thermal energy utilization and storage

Zixuan WANG[1,2], Yuze CHEN[1], Peipei MA[1,2], Yanfei DENG[1,*], Weikang LI[2], Shuang LENG[2], Wansheng LI[3], Feng CHEN[3], Yu FENG[3]

[1] Institute of Intelligent Ocean Engineering, Harbin Institute of Technology (Shenzhen), Shenzhen, 518055, China
[2] School of Energy Science and Engineering, Harbin Institute of Technology, Harbin 150001, China
[3] School of Mechanical Engineering and Automation, Harbin Institute of Technology (Shenzhen), Shenzhen 518055, China

Abstract: With the increasingly severe global climate issues and high targets for carbon emissions, the efficient and rational utilization, as well as storage, of low-temperature thermal energy such as solar energy, geothermal energy and industrial waste heat is crucial for achieving energy conservation and emission reduction targets. In order to solve the problems of high additional energy consumption, limited geographical environment, and significant transmission losses in traditional gravity energy storage systems, this paper first proposes a high drop composite power/storage (HD-CPS) system, which can achieve efficient utilization of low-temperature thermal energy for power generation while further storing the utilized thermal energy by thermal-to-gravitational energy potential conversion. In this paper, a series of performance evaluation indicators for the "energy charging-power generation" stage and the "energy discharging-power generation" stage were established. And the carbon reduction benefit, working fluid selection, and system performance were analyzed. The results indicated that the carbon reduction benefit of this system was 1.22, approximately 8 times that of conventional large-scale pumped storage systems (a typical gravity energy storage system), reflecting the superiority of this system in carbon reduction. To select the optimal working fluid, the defined total energy storage efficiency was taken as the optimization objective, which concluded that R1234ze(Z) was superior to others. The total energy storage efficiency of R1234ze(Z) was about 28%-86% higher than other working fluids such as R236ea and R141b at the cold source temperature of 10°C. And the maximum thermal efficiency of the R1234ze(Z) system can reach 13.77% during the "energy charging-power generation" stage. In conclusion, the proposed HD-CPS system has a positive effect on broadening the utilization and storage forms of low-temperature thermal energy, which has great application potential in high drop buildings located in industrial parks or large giant mining ships that contain low-temperature heat sources and high drop building structures, and the low-temperature heat sources can come from industrial waste heat, solar energy, geothermal energy, etc.

Keywords: Low-Temperature Thermal Energy; High Drop; Power Generation; Energy Storage; Carbon Emission Reduction

1. INTRODUCTION

With the increasing cost of coal, oil, and other raw fuels and the increasingly severe global climate issues (Frolicher, Fischer and Gruber 2018; Rogelj et al. 2019). “Carbon peak” and “carbon neutral” have attracted much attention in China and worldwide (Pan et al. 2023; Wang et al. 2024). The research and popular application of energy conservation and carbon reduction are important approaches to achieve the carbon emission reduction goal (Wang et al. 2024; Wu et al. 2024). At the present stage of production and life, huge quantities of low-temperature thermal energy such as solar energy, geothermal energy, and industrial waste heat (Li et al. 2024; Wang et al. 2024) usually cannot be fully and reasonably recycled due to their low grade, which causes a large amount of wasted energy. According to statistics, China's energy utilization rate is only about 33%, which is lower than developed countries about 10%. At least 50% of industrial energy consumption is directly abandoned in various forms of waste heat. The efficient and rational utilization and storage of low-temperature waste heat is crucial to achieving the carbon reduction objective.

In the past decade, domestic and international research on gravity energy storage has received widespread attention (Rastler et al. 2010; Rehman, Al-Hadhrami and Alam 2015). Among them, pumped storage is currently the most researched and put into use worldwide, which is especially suitable for long-term large-scale energy storage (Lott et al. 2014; Berrada, Loudiyi and Zorkani 2016). Wind power and solar power combined with pumped storage were proposed. Kapsali, Anagnostopoulos and Kaldellis (2012) proposed the pumped storage system combining wind power to store 65% of the surplus wind energy in a specific facility on the Greek island of Lesbos. Katsaprakakis et al. (2012) optimised a combined wind and water pumped storage system whose electricity production can produce more than 23% of the annual local electricity consumption. Margeta and Glasnovic (2012) proposed a hybrid power system, which combined photovoltaic power with a pumped storage system and provided a continuous energy supply. Gu et al. (2007) proposed the concept of gravity storage solar aircraft, which uses extra solar radiation energy to make the aircraft climb upwards thereby increasing endurance. The above gravity energy storage technologies still consume high-grade electrical energy as the main power source.

On the other hand, to efficiently utilize low-temperature thermal energy from solar thermal energy, industrial waste heat, geothermal heat, ocean temperature difference, et al., low-temperature thermal driven power generation technology is achieved by thermodynamic cycles such as the organic Rankine cycle (ORC), absorption power cycle (APC), organic flash cycle (OFC), triangular loop cycle (TLC), and transcritical cycle (TC). Among them, numerous studies of ORC were proposed (Miao et al. 2014; Wang et al. 2021), mainly focused on the application of waste heat power generation. Clemente et al. (2012) investigated the performance of the vortex expander in automotive ORC by using exhaust gases from the internal combustion engine as a heat source. Koppauer, Kemmetmuller and Kugi (2017) proposed an ORC system employing runoff turbo and using ethanol as the working fluid, whose output power can reach up to 0.6 kW and use the exhaust gas of a diesel engine as the heat source. Wang et al. (2013) analyzed the influence of three working fluids R123, R245fa, and R600 on the ORC system based on thermodynamics, and the results showed that R245fa had the greatest performance. Peng et al. (2022) found that the thermal efficiency of the ORC system is 17% and the net output power reaches 8 kW at 120~140 °C evaporation temperature and 20~30 °C condensation temperature. Yang et al. (2020) designed a new exhaust gas compression and recirculation ORC system (CR-ORC) by improving the condenser to recover and reuse the exhaust gas of the expander.

In summary, new gravity energy storage methods and low-temperature waste heat power generation technologies have been investigated separately. However, the existing forms of gravity energy storage mainly use electric energy as the main energy source, and the system operation has demanding requirements on the geographical environment, which cannot satisfy the requirements of energy storage and local consumption in the load central area. And the current research on low-temperature thermal power generation technologies mainly focuses on cycle optimization, component optimization, and working fluid selection (Gholizadeh et al. 2024; Ling et al. 2024). Therefore, the combination of power generation and gravity energy storage is severely under-researched.

To solve the limitations of high additional electric energy consumption, restricted geographical environment, and large transmission loss of traditional gravity energy storage system. A novel high-drop composite power/storage (HD-CPS) system through the cooperative action of low-temperature thermal energy and gravitational potential energy is proposed in this study. The gravity energy storage is achieved by the phase transition of the liquid working fluid by using industrial waste heat as the heat source. The mathematical models of the “energy charging-power generation” stage and the “energy discharging-power generation” stage of the HD-CPS system are established. The evaluation indicators of the composite power/storage system are further constructed. And the performance of different factors such as cold and heat source parameters and working fluid on the energy storage and power stages of the system are investigated. The proposed HD-CPS has great application potential in high drop buildings located in industrial parks or large giant mining ships that contain low-temperature heat sources and high drop building structures, and the low-temperature heat sources can be obtained from industrial waste heat, solar energy, geothermal energy, etc.

2. SYSTEM DESCRIPTION

For the HD-CPS cycle system shown in Figure 1, it is composed of evaporator, gas expander, liquid expander, high drop anti-condensation reflux device, condensers (Condenser I and Condenser II), reservoirs (Reservoir I and Reservoir II), pump, preheater, electronic control system and several valves. The working modes of this system include the “energy charging-power generation” stage and the “energy discharging-power generation” stage, and the switching operation of both stages can be controlled by the valves. The detailed description of these two stages is as follows.

"Energy charging-power generation" stage: Open the valves V1, V2, V3, V4/V6, V10/V11, V12, V13, V15 and close the valves V5/V7, V8/V9, V14 ("/" means that the two valves cannot be opened and closed at the same time). The working fluid from the reservoir (Reservoir I) and preheater is evaporated to a high-temperature and high-pressure vapor by the low-temperature thermal energy, and then flows through the gas expander. During the isentropic expansion process in the expander, working fluid changes from the high-temperature and high-pressure state to the low-temperature and low-pressure state, and simultaneously drives the expander to output shaft work, thereby generating electricity. After that, the exhaust gas from the expander outlet passes through the high-drop anti-condensation reflux device (HD-ACRD), as is shown in the right and upper corners of Figure 1, and enters the condenser (Condenser I). By natural cooling, the energy is ultimately stored in the condenser (Condenser I) in the form of a low-temperature and low-pressure liquid working fluid with high potential energy.

"Energy discharging-power generation" stage: Open the valves V5/V7, V8/V9, close the valves V1, V2, V3, V4, V5, V10, V11, V12, V13, V14, V15. By the effect of gravity, the low-temperature and low-pressure working fluid stored in the condenser (Condenser II) flows from the high position to the low position. The working fluid flows through the liquid expander at a low position, drives the expander to output shaft work, thereby generating electricity. Finally, the working fluid is stored in the reservoir (Reservoir II) in the form of low-temperature and low-pressure state with low potential energy.

In this case, two condensers (Condenser I and Condenser II) work alternately to achieve continuous circulation, as well as the two reservoirs (Reservoir I and Reservoir II).

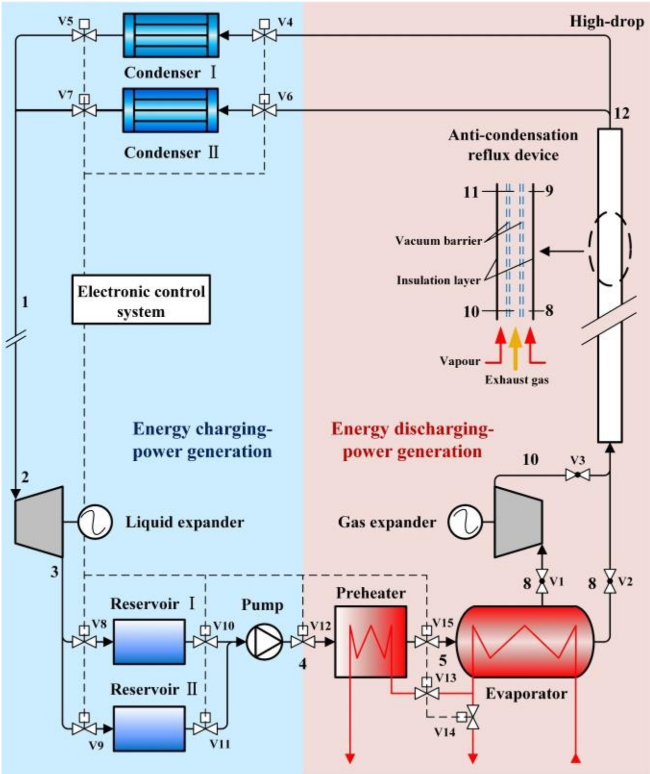

Figure 1: High drop composite power/storage system structure diagram

3. MODELING AND SYSTEM ANALYSIS

3.1. Model assumptions

Assumptions proposed regarding the HD-CPS system analysis are as follows:

(1) The thermal loss of the heat exchanger is ignored, and the convection form of the heat exchanger is counter-current.

(2) The expansion and pump processes are isentropic, and the isentropic efficiency of the expander and working fluid pump is a constant value. The process of exhaust gas inside the HD-ACRD performs as an adiabatic expansion process, which is isenthalpic. And the energy of the branch vapor from the evaporator is consumed to resist the heat exchange effects of the environment on the inside exhaust gas.

(3) The waste heat energy source is simplified to the hot water (with 2 Mpa pressure), and the exchange temperature difference of the heat source is determined according to the return water temperature requirements of the waste heat source.

(4) The system mainly considers the pressure loss in the rising section of the pipe and equates it to the height head loss.

(5) 5-10 K superheat/subcooling at the evaporator/condenser outlet separately is considered to prevent working fluid from causing damage to the expander.

3.2. Model establishment and system analysis

Nomenclature		m_1'	Working fluid flow after pumping, $[kg/s]$
		h_2	Expander inlet specific enthalpy, $[J/kg]$
		h_{3s}	Isentropic outlet specific enthalpy, $[J/kg]$
Abbreviations		h_3	Actual outlet specific enthalpy, $[J/kg]$
ORC	Organic Rankine Cycle	R	Total thermal resistance, $[m^2 \cdot K/W]$
APC	Absorption Power Cycle	m_x	Pumping flow, $[kg/s]$
OFC	Organic Flash Cycle	ΔT	Working fluid temperature drop in insulation, $[K]$
TLC	Triangular Loop Cycle	ΔT_m	Average temperature difference, $[K]$
TC	Transcritical Cycle	ΔZ	Net height of energy storage, $[m]$
CR-ORC	Compression and Recirculation ORC	g	Gravitational acceleration, $[m/s^2]$
HD-ACRD	High-Drop Anti-Condensation Reflux Device	h_1	Energy storage outlet specific enthalpy, $[J/kg]$
HD-CPS	High-Drop Composite Power/Storage	W_{elc}	Gas expander power, $[W]$
		W_{pump}	Pump energy consumption, $[J/kg]$
Symbols		Q_{totle}	Total heat absorption, $[W]$
Q_i	Heat exchange, $[W]$	E_{in}	Heat source exergy drop, $[W]$
m_h	Heat source flow, $[kg/s]$	Z_1	Height of energy storage, $[m]$
m_1	Working fluid flow, $[kg/s]$	Z_2	Height of expansion machine, $[m]$
c_{p_i}	Specific heat capacity, $[J/(kg \cdot K)]$		
T_{hi}	Heat source inlet temperature, $[K]$	*Greek symbols*	
T_{ci}	Heat source outlet temperature, $[K]$	α_1	Thermal convection coefficient on working fluid side, $[W/(m^2 \cdot K)]$
h_{ai}	Heat exchanger inlet specific enthalpy, $[J/kg]$	α_3	Thermal convection coefficient on Airside, $[W/(m^2 \cdot K)]$
h_{bi}	Heat exchanger outlet specific enthalpy, $[J/kg]$	λ_2	Thermal conductivity of insulation materials, $[W/(m \cdot K)]$
W_i	Expander power, $[W]$	η_i	Efficiency indicators

In Table 1, the mathematical models of the components in the HD-CPS system are proposed, and the performance evaluation indicators of the HD-CPS system are established from six aspects. In addition, Figure 2 shows the modeling calculation flow chart of the HD-CPS system.

Table 19: Mathematical models of the components in the system

	Component	Equations
System modeling	Heat exchanger model	$Q_i = m_h c_{p_i}(T_{hi} - T_{ci}) = m_1(h_{ai} - h_{bi})$
	Expander model	$W_i = m_1'(h_2 - h_{3s})$
		$\eta_i = \frac{h_2 - h_3}{h_2 - h_{3s}}$
	Anti-condensation reflux device model	$R = \frac{1}{\alpha_1} + \frac{D_3}{2\lambda_2} ln \frac{D_3}{D_2} + \frac{1}{\alpha_3}$
		$L = \frac{c_p m_x \Delta T}{\frac{\Delta T_m}{R} \pi D_3}$
	Falling pipe model	$h_2 = \Delta Z \times g + h_1$
System evaluation indicators	Thermal efficiency in the "Energy charging-power generation" stage	$\eta_1 = (W_{elc} - m_1 \times W_{pump})/Q_{totle}$
	Exergy efficiency in the "Energy charging-power generation" stage	$\eta_2 = (W_{elc} - m_1 \times W_{pump})/E_{in}$
	Storage efficiency in the "Energy charging-power generation" stage	$\eta_3 = m_1 \times g \times (Z_1 - Z_2)/Q_{totle}$
	Net storage efficiency in the "Energy charging-power generation" stage	$\eta_4 = m_1 \times g \times (Z_1 - Z_2)/(Q_{totle} - W_{elc})$
	Power efficiency in the "Energy discharging-power generation" stage	$\eta_5 = (h_2 - h_3)/(g \times (Z_1 - Z_2))$
	Total efficiency in the energy storage section	$\eta_6 = \eta_3 \times \eta_5$

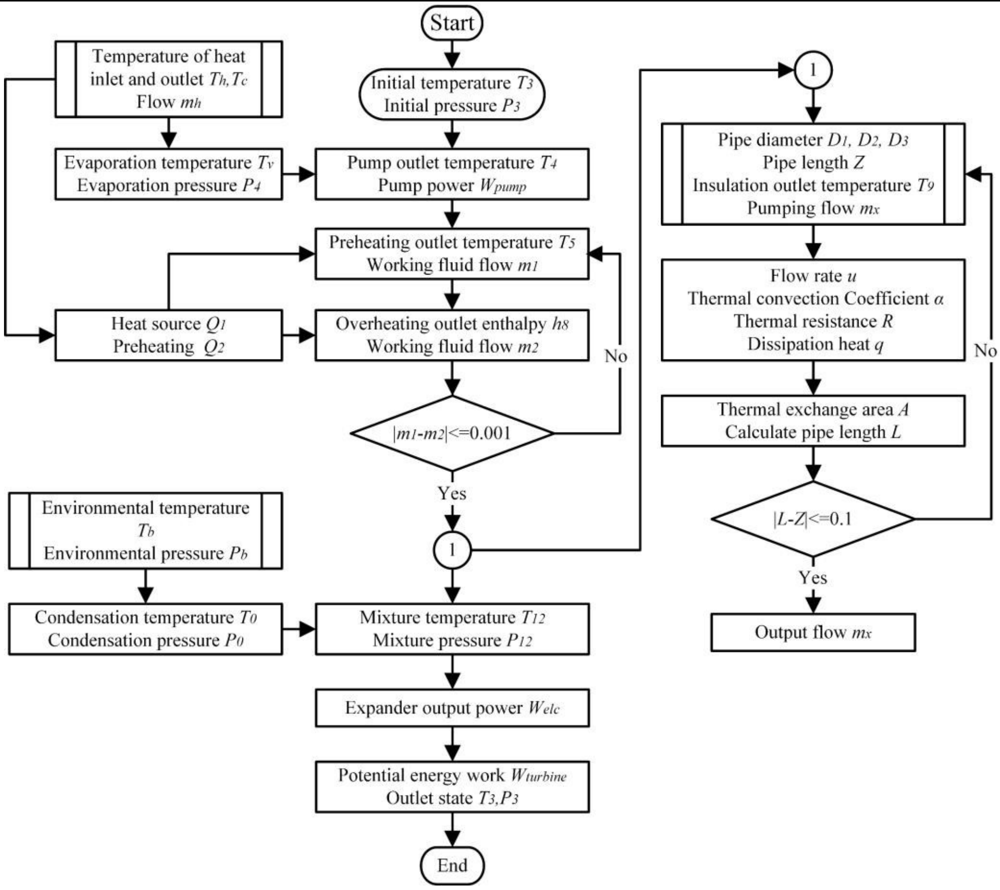

Figure 2: System modeling calculation flow chart

According to the above assumptions and models, the thermodynamic analysis is proposed in the *T-s* diagram of the HD-CPS cycle (Figure 3). The numbers in Figure 3 correspond to the numbers in Figure 1. And the working process of this cycle is as follows.

1. Isobaric endothermic process in preheater and evaporator: In the preheater, the supercooled working fluid (state 4) absorbs the heat from the heat source, the state parameter of which rises along the isobar of the working fluid at evaporating pressure to state 5. In the evaporator, the supercooled working fluid (state 5) ulteriorly absorbs the heat from the heat source, the state parameter of which rises along the isobar of the working fluid at evaporating pressure firstly to the saturated liquid state 6, then to the saturated vapor state 7 and finally to the superheated vapor state 8.

2. Isentropic expansion process in gas expander and liquid expander: Gaseous working fluid is isentropic expanded to state 10s (ideal state), and state 10 represents the real state. Liquid working fluid is isentropic expanded to state 3s (ideal state), and state 3 represents the real state.

3. Complex process in the HD-ACRD: There are two flows (the exhaust gas from the gas expander outlet and the working fluid vapor from the evaporator outlet) flowing through the HD-ACRD under the differential pressure to overcome frictional resistance and gravity, the former passing through the center channel (state 10-11, change along the isoenthalpy line to the condensation pressure), and the latter passing through the outer channel (state 8-9, temperature and pressure dropping process). The end of the HD-ACRD is a mixture (state 12) of two flows (state 9 and state 11).

4. Isobaric exothermic process in condensers: The superheated vapor (state 12) is condensed in condensers at the high location to supercooled liquid working fluid (state 1), the state parameter of which falls along the isobar of the working fluid at condensation pressure, performing as process 12-13-0-1.

5. Isentropic compression process in the high drop pipeline connecting the condenser and the liquid expander: The pressure of the liquid gradually rises as it passes through the downward pipeline under the gravity effect, and develops from state 1 to state, achieving the temperature and pressure rise of the liquid working fluid.

6. Isentropic compression process in the working fluid pump: The working fluid is pressurized to evaporation pressure by the working fluid pump, performing as process 3-4.

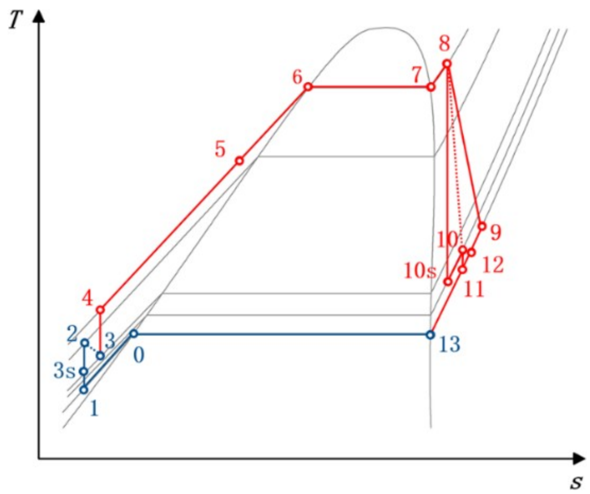

Figure 3: Composite power/storage cycle T-s chart

4. RESULTS AND DISCUSSION

4.1. Analysis of carbon reduction

At present, there are two main methods to calculate the economic value of CO_2 indirectly. One is the “carbon tax method”, and the other is the “afforestation cost method”, which is used for calculation of carbon reduction benefits in this study (Li 2024).

Burning 1 ton of standard coal will produce 2.496 tons of CO_2. The cultivation cost of wood is 240 RMB/m, which can balance the CO_2 produced by carbon combustion. Therefore, the carbon reduction value of wood can be calculated as 71.09 RMB/t. The economic benefit of CO_2 reduction of this system is calculated as follows:

$$I_{CO_2} = R_{CO_2} \times 2.496 \times 71.09 \quad \text{Equation 1}$$

Where

- I_{CO_2} = economic benefit of carbon reduction
- R_{CO_2} = amount of standard coal saved by the system (t)

According to the common calculation method of carbon reduction benefits of pumped storage. A new indicator with dimensions for analyzing carbon reduction is proposed to compare the carbon reduction capacities of different systems.

$$\eta_{CO_2} = E_m / I_n \quad \text{Equation 2}$$

Where:

- E_m = emission reduction of CO_2 (kg)
- I_n = installed capacity (W)

Assuming the factory's waste heat has a stable output of 10 h per day, approximately 3650 h per year. Under the same working conditions as Zhou, Yang and Li (2022), the standard coals saved by energy storage are 10.33 t/year and the economic benefits of carbon reduction are about 1800 RMB/year. Under the same working conditions as Zhou, Huang and Ding (2022), the standard coals saved by energy storage are 13.16 t/year and the economic benefits of carbon reduction are about 2300 RMB/year. Under the same working conditions as Gong (2018), the standard coals saved by energy storage are 0.32 t/year and the economic benefits of carbon reduction are about 60 RMB/year. Based on the above case data, it can be calculated that the system's η_{CO_2} is about 1.22. This indicator is about 8 times higher than typical large pumped storage systems, which shows the superiority of this system on carbon reduction.

The economic benefit of the system’s carbon reduction is significant, which can be calculated by using the afforestation cost method with different parameters. When the heat source is 130 ºC and its flow rate is 130 t/h, the saved standard coals are 1047.6 t/year and the economic benefits of carbon reduction are about 186,000 RMB/year.

4.2. Working fluids selection

The working fluids used in this study include R245fa, R123, R1234ze (Z), R141b, R365mfc, R236ea and R1233zd(E). The basic properties of working fluids are shown in Table 2. Figure 4~Figure 7 illustrate the efficiency variation of different working fluids at various cold and heat source temperatures.

Table 2: Basic properties of working fluids

Working fluid	GWP	ODP	Safety Class	P_{cr}	T_{cr}	Freezing point
R245fa	790	0	B1	3.651MPa	154 °C	<-160 °C
R123	120	0.012	B1	3.67MPa	183.7 °C	-107 °C
R1234ze(Z)	6	0	A2L	3.5MPa	150 °C	-104.53 °C
R141b	0.09	0.11	A1	4.25MPa	204.5 °C	-103.5 °C
R365mfc	850	0	B2L	3.266MPa	186.85 °C	-93.6 °C
R236ea	1200	0	/	3.5MPa	139.25 °C	-111 °C
R1233zd(E)	1	0	A1	3.57MPa	165.6 °C	-107 °C

Figure 4 shows the variations of thermal efficiency within the 80~140 °C heat source during the "Energy charging-power generation" stage. With the increase in heat source temperature and evaporation temperature, the pressure difference between the inlet and outlet of the expander increases, resulting in an increase in output power and thermal efficiency. The thermal efficiency difference of each working fluid is smaller at lower temperatures. At 80°C, the thermal efficiency of R1234ze(Z), R236ea, and R365mfc is below 11.5%, while the thermal efficiency of other working fluids is above 11.5%. The thermal efficiency of each working fluid gradually increases with rising temperature, R141b working fluid has the highest thermal efficiency, reaching 17.6% at 138 °C. Since the critical temperature of R1234ze(Z) is low, its efficiency curve ends at about 120 °C for the heat source.

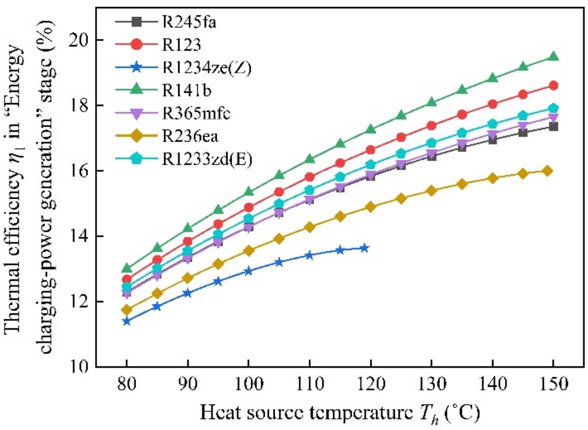

Figure 33: Variations of thermal efficiency with heat source in the "Energy charging-power generation" stage

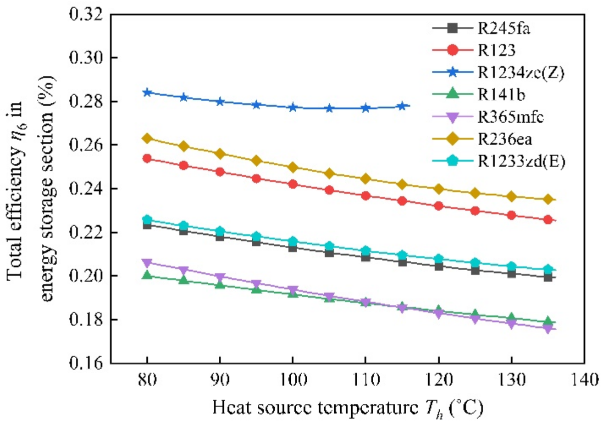

Figure 34: Variations of total efficiency with heat source in the energy storage section

Figure 5 shows the variations of total efficiency within the 80~140 °C heat source (the cold source temperature is -20 °C) in the energy storage section. The energy storage efficiency of the system decreases with the increase of heat source temperature, all overall efficiencies are below 0.5%. The reason is that this indicator takes into account the thermal input energy of the whole system but doesn't calculate the output power of the "Energy charging-power generation" stage. On the other hand, the output power of the liquid potential energy depends mainly on the height difference. The temperature of the heat source increases, and the total heat absorption of the system increases, but the output of the potential energy remains almost unchanged, thus the total efficiency of the energy storage section decreases as the temperature of the heat source increases. R1234ze (Z) has the highest efficiency of 0.284%, which is less affected by temperature changes.

Figure 6 shows the variations of thermal efficiency within -20~10 °C cold source in the "Energy charging-power generation" stage. The thermal efficiency of each working fluid decreases gradually as the temperature increases. As a result of the increase in the cold source temperature, the pressure of the exhaust gas rises, which causes a decrease in the pressure difference between the inlet and outlet of the expander, subsequently decreasing the thermal efficiency. It's observed that the highest efficiency of R141b is 14.3% at -20 °C and 9.0% at 10 °C.

Figure 7 shows the variations of total efficiency with -20~10 °C cold source (the heat source temperature is 100 °C) in the energy storage section. As the temperature increases the efficiency of each working fluid gradually increases. The reason is that the heat source parameters will affect the gravitational potential energy generation stage of the system, the increase of the cold source temperature will make the enthalpy of both sides of the liquid expander increase. Due to the increasing rate of enthalpy in front of the expander is faster, the enthalpy difference is gradually increased, which directly affects the potential output work. In Fig. 7, the efficiency of R1234ze (Z) is significantly greater than the other working fluids, has a maximum efficiency of 0.4% at 10 °C and 0.277% at -20 °C. The remaining working fluids, such as R236ea, have a maximum efficiency of 0.327% at 10 °C.

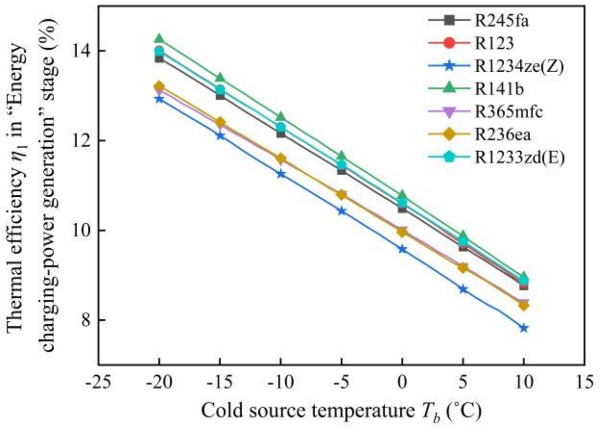

Figure 35: Variations of thermal efficiency with cold source in the "Energy charging-power generation" stage

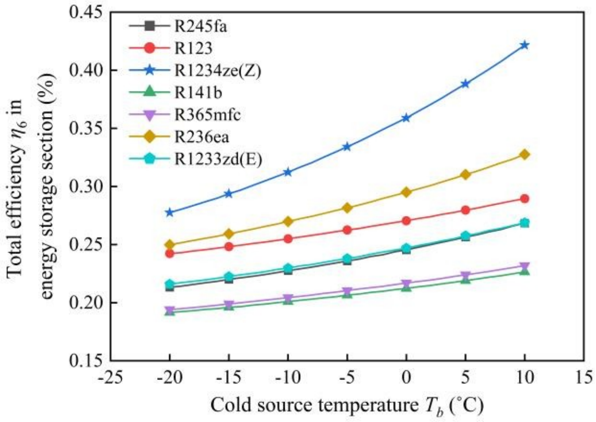

Figure 36: Variations of total efficiency with cold source in the energy storage section

In summary, the R141b demonstrates excellent performance in thermal efficiency during the "Energy charging-power generation" stage, with efficiency reaching up to 17.6%, especially at higher heat source temperatures. However, R1234ze(Z) performs better than other working fluids during the whole energy storage stage. R1234ze(Z) can still achieve high storage efficiency even at low heat source temperatures. And its "total efficiency in the energy storage section" is less affected by the temperature change of the heat source, showing better stability within a certain range of heat sources. Because this system aims to effectively utilize low-temperature waste heat and pay more attention to the effect of energy storage, R1234ze (Z) is selected as the working fluid of the system.

4.3. Performance Analysis of the R1234ze(Z) system

Figure 8~Figure 12 show the variation of system evaluation indicators of the optimal working fluid R1234ze (Z) at different heat source and cold source temperatures.

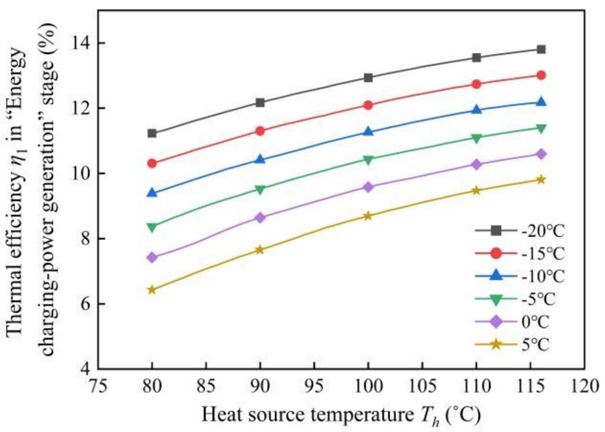

Figure 37: Variations of thermal efficiency with heat source in the "Energy charging-power generation" stage

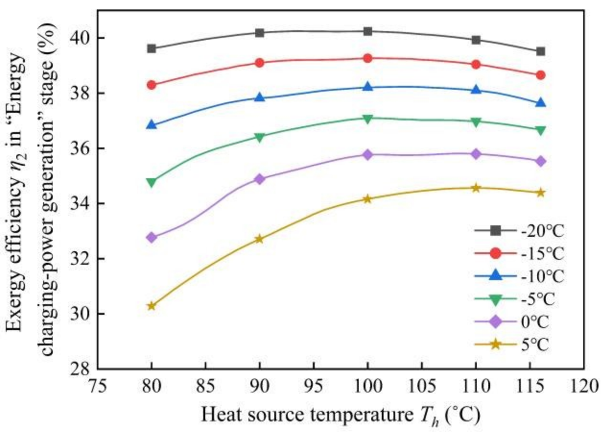

Figure 38: Variations of exergy efficiency with heat source in the "Energy charging-power generation" stage

Figure 8 shows the variation curve of thermal efficiency in the "Energy charging-power generation" stage. The thermal efficiency improves as the temperature of the heat source rises and as the temperature of the cold source drops. When the cold source temperature remains fixed and the heat source temperature increases, or vice versa, the pressure difference between two sides of the expander increases while the system's heat absorption remains relatively unchanged. This results in higher expander power and improved system thermal efficiency, with the highest efficiency is 13.77% at 115 °C for the heat source and -20 °C for the cold source, while the lowest efficiency is 5.66% at 0 °C for the heat source and 5 °C for the cold source.

Figure 9 shows the variation curve of exergy efficiency in the "Energy charging-power generation" stage. Exergy efficiency increases with the decrease of the cold source temperature when the heat source temperature is constant.

However, the exergy efficiency increases with the heat source temperature to the maximum value and then decreases when the cold source temperature is steady. The reason is that a rise in the evaporation temperature leads to the expander power increasing as the heat source temperature rises. When the system's heat transfer temperature difference is constant, meaning the exergy delivered to the system does fluctuate only slightly, higher expander work causes an increase in exergy efficiency with the increasing heat source temperature. However, a higher heat source temperature will raise the evaporation temperature, indirectly improve the requirement of the evaporation pressure, and significantly increase the working fluid pump power consumption. Overall, the exergy efficiency requires considering the trade-off between the rising expander power and the rising power consumption as the heat source temperature rises. When the heat source temperature increases to a certain degree, the rising power consumption of the working fluid pump will cause a decreasein the exergy efficiency. Therefore, each cold source temperature corresponds to an optimal heat source temperature, making the system's exergy highest. The lowest exergy efficiency is 30.27% when the heat source temperature is 80 °C and the cold source temperature is 5 °C. In contrast, the maximum exergy efficiency is 40.18% when the heat source temperature is 90 °C and the cold source temperature is -20 °C.

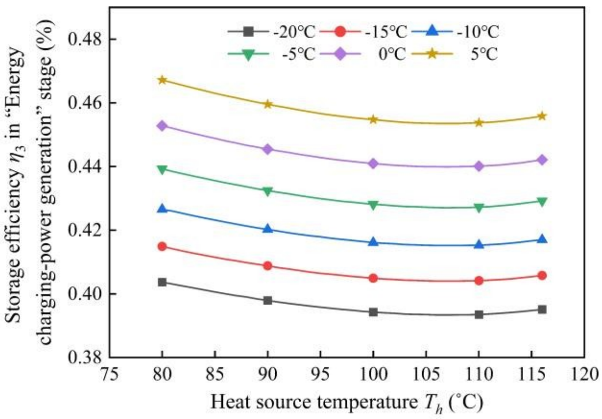

Figure 39: Variations of storage efficiency with heat source in the "Energy charging-power generation" stage

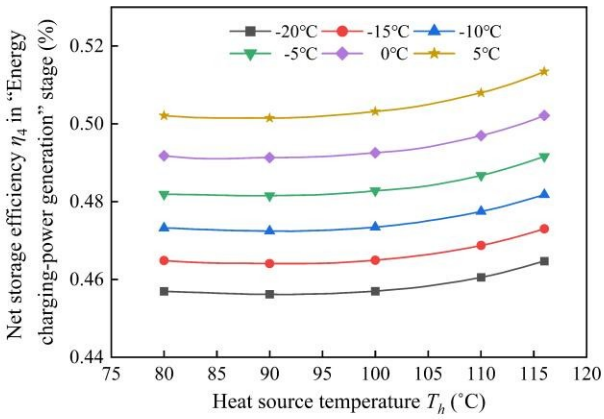

Figure 40: Variations of net storage efficiency with heat source in the "Energy charging-power generation" stage

Figure 10 shows the variation curve of storage efficiency in the "Energy charging-power generation" stage. When the cold source temperature remains constant, the efficiency doesn't change significantly with increasing heat source temperature (variation range < 0.02%). The reason is that the height of the system is fixed, and the total heat absorption does not change much when the heat transfer temperature difference is constant, resulting in the storage efficiency changing less with the increase in the heat source temperature. Besides, the variation curve shows a small downward trend before a slight upward trend, indicating an optimal heat source temperature exists when the cold source temperature is fixed. The reason is that increasing the exergy difference between the two sides of the expander reduces the working fluid mass flow rate as the heat source and evaporation temperatures rise. At low heat source temperatures, the impact of the preheater is negligible. However, at high heat source temperatures where the preheater's impact is significant, the working fluid mass flow rate slightly increases because the preheater reduces the enthalpy difference of the evaporator. When the heat source temperature is constant and the cold source temperature decreases, the total heat absorption remains constant, and the pressure difference between the two sides of the expander rises, leading to a decrease in the working fluid mass flow rate, resulting in a decrease in the efficiency of energy storage during the "storage + power generation" phase. The lowest efficiency is 0.39% when the heat source temperature is 105 °C and the cold source temperature is -20 °C, the highest efficiency is 0.47% when the heat source temperature is 80 °C and the cold source temperature is 5 °C.

Figure 11 shows the variation curve of net storage efficiency in the "Energy charging-power generation" stage. Compared to the efficiency of energy storage in the "Energy charging-power generation" stage, it subtracts the effect of expander power on energy storage. With the increase of the heat source temperature or the decrease of the cold source temperature, the output work of the expander increases, causing the gradual increase of the net energy storage efficiency in the "Energy charging-power generation" stage. The lowest efficiency is 0.46% when the heat source temperature is 80 °C and the cold source temperature is -20 °C. The highest efficiency is 0.51% when the heat source temperature is 115 °C and the cold source temperature is 5 °C.

Figure 12 shows the variation curve of the total efficiency in the energy storage section. η_6 is the ratio of the actual amount which is produced by the release of the stored gravitational potential energy to the total energy consumed in the energy storage. This is the result of the combined effect of the variation of energy storage efficiency in the "Energy charging-power generation" stage and the variation of power efficiency in the "Energy discharging-power generation" stage.

Through the analysis of the efficiency change of the R1234ze(Z) at different cold and heat source temperatures, the larger the temperature difference between the cold and heat source, the higher the thermal efficiency. Meanwhile, there exists a great value of exergy efficiency under different cold source temperatures. In summary, the higher the temperature of the cold source, the higher the total efficiency of the energy storage section. According to energy storage consideration, the system installation is suitable for environments with higher cold source temperatures.

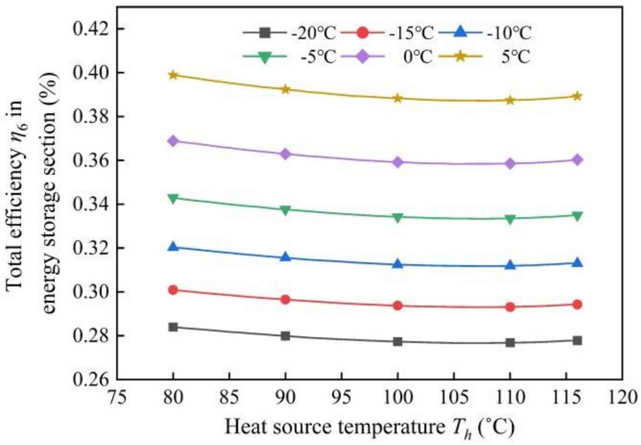

Figure 12: Variations of total efficiency in the energy storage section

5. CONCLUSION

In this study, a novel high-drop composite power/storage (HD-CPS) system through the cooperative action of low-temperature thermal energy and gravitational potential energy is proposed, which achieves the transportation of gravitational potential energy from a low position to a high position by using low-temperature thermal energy to drive the phase transition of the stored working fluid. In this case, the dual function of “Energy charging-power generation” and “Energy discharging-power generation” is achieved, which can significantly reduce the electricity consumption during the storage process of liquid potential energy compared with the traditional gravity energy storage system. A mathematical model of the HD-CPS system is established. Performance evaluation from the aspect of carbon reduction, thermal efficiency, exergy efficiency, storage efficiency, net storage efficiency, power efficiency and total efficiency is carried out in this study. The main conclusions extracted from the research are summarized as:

(1) The carbon reduction benefit of the system is calculated to be approximately eight times greater than that of large-scale pumped storage systems, indicating the superiority of the system in terms of carbon reduction.

(2) In the “Energy charging-power generation” stage, the maximum thermal efficiency of R141b is 17.60% and R1234ze(Z) has a thermal efficiency of 13.77%. The total energy storage efficiency of R1234ze(Z) is about 28%-86% higher than that of other working fluids, such as R141b and R236ea, at 10 °C cold source temperature. Taking the energy storage efficiency into account, R1234ze(Z) is superior to other working fluids.

(3) For the R1234ze(Z) working fluid, the total efficiency of the energy storage section increases as the temperature of the cold source increases, indicating that the system installation is suitable for environments with higher cold source temperatures.

In conclusion, the proposed HD-CPS system has a positive effect on broadening the utilization and storage forms of low-temperature thermal energy, which has great application potential in high drop buildings located in industrial parks or large giant mining ships that contain low-temperature heat sources and high drop building structures, and the low-temperature heat sources can come from industrial waste heat, solar energy, geothermal energy, etc.

6. ACKNOWLEDGEMENT

This work was supported by the Guangdong Provincial Natural Science Foundation General Program under contract NO. 2024A1515011319 and Guangdong Provincial Basic and Applied Basic Research Foundation Joint Fund-Youth Fund Program under contract NO. 2023A1515110653.

7. REFERENCES

Berrada, A., Loudiyi, K., and Zorkani, I. (2016) 'Sizing and economic analysis of gravity storage', Journal of Renewable and Sustainable Energy, 8, pp. 024101. Available at: https://doi.org/10.1063/1.4943119

Clemente, S. et al. (2012) 'Energy efficiency analysis of Organic Rankine Cycles with scroll expanders for cogenerative applications', Applied Energy, 97, pp. 792-801. Available at: https://doi.org/10.1016/j.apenergy.2012.01.029

Frolicher, T.L., Fischer, E.M., and Gruber, N. (2018) 'Marine heatwaves under global warming', Nature, 560, pp. 360-364. Available at: https://doi.org/10.1038/s41586-018-0383-9

Gholizadeh, T. et al. (2024) 'Techno-economic optimization and working fluid selection of a biogas-based dual-loop bi-evaporator ejector cooling cycle involving power-to-hydrogen and water facilities', International Journal of Hydrogen Energy, 76, pp. 247-262. Available at: https://doi.org/10.1016/j.ijhydene.2024.04.104

Gong Z. (2018) Performance analysis and application simulation of small ORC system, Master's thesis, Tianjin University.

Gu, W. et al. (2007) 'The latest research findings concerning low-temperature heat energy based power generation and its development trend', Journal of Engineering for Thermal Energy and Power, 22(2), pp. 115-119.

Kapsali, M., Anagnostopoulos, J.S., and Kaldellis, J.K. (2012) 'Wind powered pumped-hydro storage systems for remote islands: a complete sensitivity analysis based on economic perspectives', Applied energy, 99, pp. 430-444. Available at: https://doi.org/10.1016/j.apenergy.2012.05.054

Katsaprakakis, D.A. et al. (2012) 'Introduction of a wind powered pumped storage system in the isolated insular power system of Karpathos-Kasos'. Applied Energy, 97, pp. 38-48. Available at: https://doi.org/10.1016/j.apenergy.2011.11.069

Koppauer, H., Kemmetmuller, W., and Kugi, A. (2017) 'Modeling and optimal steady-state operating points of an ORC waste heat recovery system for diesel engines', Applied Energy, 206, pp. 329-345. Available at: https://doi.org/10.1016/j.apenergy.2017.08.151

Li, C. et al. (2023) 'Preparation and characterization of quinary nitrate salt based composite phase change material with low melting point for low and medium temperature thermal energy storage', Journal of Energy Storage, 74, pp. 109277. Available at: https://doi.org/10.1016/j.est.2023.109277

Li, C. (2021) 'Study on Carbon Reduction Benefit of Pumped Storage Power Station', Hydropower and Pumped Storage, 7(6), pp. 45-48. Available at: https://link.cnki.net/doi/10.3969/j.issn.2096-093X.2021.06.013

Ling, W. et al. (2024) 'Modeling of geothermal tailored CCHP system with heat recovery centered thermal design/analysis; ANN-based optimization and economic study', Case Studies in Thermal Engineering, 59, pp. 104511. Available at: https://doi.org/10.1016/j.csite.2024.104511

Lott M. et al. (2014) Technology roadmap: Energy storage. France Paris: International Energy Agency.

Margeta, J. and Glasnovic, Z. (2012) 'Theoretical settings of photovoltaic-hydro energy system for sustainable energy production', Solar energy, 86(3), pp. 972-982. Available at: https://doi.org/10.1016/j.solener.2012.01.007

Miao, Z. et al. (2014) 'Development and dynamic characteristics of an organic Rankine cycle', Chinese Science Bulletin, 59, pp. 4367-4378. Available at: https://doi.org/10.1007/s11434-014-0567-0

Pan, H. et al. (2023) 'Contribution of prioritized urban nature-based solutions allocation to carbon neutrality', Nature Climate Change, 13, pp. 862-870. Available at: https://doi.org/10.1038/s41558-023-01737-x

Peng, B. et al. (2022) 'Influence of different working fluids on performance of organic Rankine cycle low temperature waste heat power generation system', Thermal Power Generation, 51(2), pp. 43-48. Available at: https://link.cnki.net/doi/10.19666/j.rlfd.202106119

Rastler, D.D. (2010) Electricity energy storage technology options: A white paper primer on applications, costs and benefits. Palo Alto, CA: Electric Power Research Institute.

Rehman, S., Al-Hadhrami, L.M., and Alam, M.M. (2015) 'Pumped hydro energy storage system: A technological review', Renewable and Sustainable Energy Reviews, 44, pp. 586-598. Available at: https://doi.org/10.1016/j.rser.2014.12.040

Rogelj, J. et al. (2019) 'A new scenario logic for the Paris Agreement long-term temperature goal', Nature, 573, pp. 357-363. Available at: https://doi.org/10.1038/s41586-019-1541-4

Wang, L. et al. (2024) 'Carbon emissions and reduction performance of photovoltaic systems in China', Renewable and Sustainable Energy Reviews, 200, pp. 114603. Available at: https://doi.org/10.1016/j.rser.2024.114603

Wang, L. et al. (2023) 'Full-scale utilization of geothermal energy: A high-efficiency CO2 hybrid cogeneration system with low-temperature waste heat', Journal of Cleaner Production, 403, pp.136866. Available at: https://doi.org/10.1016/j.jclepro.2023.136866

Wang, J. et al. (2013) 'Thermodynamic analysis and optimization of an (organic ra nkine cycle) ORC using low grade heat source', Energy, 49, pp. 356-365. Available at: https://doi.org/10.1016/j.energy.2012.11.009

Wang, W. et al. (2024) 'Self-powered carbon-neutral system', Cell Reports Physical Science, 5(3), pp. 101871. https://doi.org/10.1016/j.xcrp.2024.101871

Wang, Z. et al. (2021) 'Experimental investigation on a small-scale ORC system with a pump driven by internal multi-potential', Science China Technological Sciences, 64, pp. 1599-1610. Available at: https://doi.org/10.1007/s11431-020-1832-x

Wu, X. et al. (2024) 'Multi-stage planning of integrated electricity-gas-heating system in the context of carbon emission reduction', Applied Energy, 358, pp. 122584. Available at: https://doi.org/10.1016/j.apenergy.2023.122584

Yang, X. et al. (2020) 'Thermodynamic characteristics analysis for an ORC system with exhaust gas compression recycling', Proceedings of the CSEE, 40(3), pp. 886-897. Available at: https://link.cnki.net/doi/10.13334/j.0258- 8013.pcsee.190990

Zhou, G., Yang, Z., and Li, Y. (2022) 'Development of 315 kW Organic Rankine Cycle Test Prototype', Dongfang Turbine, (3), pp. 9-13. Available at: https://doi.org/10.13808/j.cnki.issn1674-9987.2022.03.003

Zhou, T., Huang, Z., and Ding, X. (2022) 'Research and industrial application of ORC power generation system with waste heat of high pressure temperature-regulating water', Thermal Power Generation, 51(2), pp. 27-34. Available at: https://link.cnki.net/doi/10.19666/j.rlfd.202108159

#376: Optimization of photovoltaic supplementary lighting system in strawberry greenhouse

Yilian TANG[1], Yunfeng WANG [2*], Jing LI[3*], Jingyu HE[3], Youwen ZHAI[1]

[1] School of Mechanical and Electrical Engineering, Kunming University, Kunming, Yunnan, China, 650214, candy1806@163.com

[2*] Solor Energy Research Institute, Yunnan Normal University, Kunming, Yunnan, China, 650500, wangyf@ynnu.edu.cn

[3*]School of Agriculture and Life Science，Kunming University，Kunming, Yunnan,China,650214, lijingkmu@163.com

Abstract: Greenhouse planting can effectively control indoor environmental parameters, thereby improving the quality of greenhouse crops. Photovoltaic (PV) greenhouses not only provide clean energy, but also control the lightingenvironment. In order to improve the quality of strawberries, the off-grid PV supplementary lighting system was designed. The monocrystalline silicon PV module and the LED lights were used to supplement light for 2 hours every night on the 'Miaoxiang 7' strawberries on a 5-layer cultivation shelf, then their fruit quality was measured. The results showed that the maximum single fruit weight of strawberries without supplementary light was 19.3 g, the maximum soluble solid content of strawberries was 13.0%, while the maximum weight of strawberries optimized with supplementary light was 33.7 g, the optimized soluble solid content of strawberries was 15.5%. The PV module had been tested to generate 10.08 kW·h per day. In order to improve the operating speed of the supplementary light control system, particle swarm optimization (PSO) algorithm was used to optimize the control parameters, and the adjustment parameters K_p, K_i, and K_d in Proportional-Integral-Derivative (PID) controller were obtained to be 0.36,0.35, and 0.3, respectively. The average intensity of LED lamps was 19530 Lux at night. In this study, PSO algorithm was used to optimize the parameters of the supplemental lighting system to ensure that the system control output had no oscillation or overshoot. Thereby reducing the theoretical power consumption of 40 LED lamps running for 2 hours from 1.2 kW·h to the actual power consumption of 0.97 kW·h. This paper provides optimization ideas for light control in photovoltaic greenhouses, while also optimizing the quality parameters of strawberries.

Keywords: Photovoltaic Supplementary Lighting System；Particle Swarm Optimization；Proportional–Integral–Derivative Controller；Strawberry Quality Optimization

1 INTRODUCTION

Controlled greenhouse cultivation is a solution to overcome climate diversity (Fernandeza and Villar-Fernandez et al., 2022). Especially in the case of strawberries, which are sensitive to the growing environment, changes in environmental parameters such as temperature, light and photoperiod have a significant effect on plant growth, strawberry yield and quality (De Lima Nechet and Heck et al., 2015; Cervantes and Ariza et al., 2019). Greenhouse cultivation not only provides a suitable growing environment, but also prevents damage to strawberry plants from extreme environments (Khoshnevisan and Rafiee et al., 2013). The results of many studies have shown that photosynthesis has a more significant effect on the quality of berry crops (Khammayom and Maruyama et al., 2022), and artificial supplemental lighting can promote photosynthesis in the plant, thus improving the quality of the fruit (Valiante and Sirtori et al., 2019). A study found that excessive or insufficient light intensity negatively affects photochemical efficiency and growth (Cervantes and Ariza et al., 2019). Supplemental light promoted significant increases in lettuce growth and yield, with at least 32% improvement (Zhang and Whitman et al., 2019). It has been shown that by utilising LED technology and prolonging photosynthesis in crops during dusk and dawn, crop yields increased by 51.29% in a complete 96-day tomato crop cycle compared to conventional greenhouses with no additional photosynthesis (Tomar, 2024). LED lamps also regulate the ratio of red to blue light according to the crop needs, matching the light source required by the plant through light regulation and spectral composition, thus promoting plant growth, morphology, flowering and photosynthetic efficiency (Choi and Moon et al., 2015). In one study, strawberries were supplemented with light using LED and fluorescent lamps, and their growth and yield were improved (Hidaka and Dan et al., 2013).

In recent years, many studies have centred around the coexistence model of photovoltaic (PV) power generation and greenhouse cultivation (Tang and Li et al., 2019; Peng and Ma et al., 2023). Typically, PV modules are placed on the roof of a greenhouse to shade some of the sunlight while generating electricity for cultivation in deliberately shaded conditions in areas of excessive sunlight (Kumar and Haillot et al., 2022). The use of PV modules as a shading materialis beneficial in this case (Yano and Cossu, 2019). The authors have studied the growth, quality and yield of strawberries in greenhouses in Kunming, China, when the roof covered 25.9% by PV modules, but the study was limited to greenhouses with high light intensity and long sunlight hours (Tang and Ma et al., 2020). Although partial coverage of photovoltaic roofs has a positive impact on crop growth in conditions of sufficient or excessive light, shading has a negative effect on crops in greenhouses with insufficient light (H. Marrou, 2013). Therefore, changing the PV location andusing an off-grid PV system to provide supplemental energy becomes a viable solution for greenhouses with insufficient light.

The use of LED lamps in greenhouses has lower energy consumption than other fill lights [14, 15], moreover, LED lamps can be easily integrated into digital control systems, allowing complex lighting schemes to change brightness or spectral composition as plants grow (Choi and Moon et al., 2015; Pengfei and Lijuan et al., 2017). For precise control of LED lamps, proportional-integral-derivative (PID) controllers can be used to optimise the control parameters of the PID, making the supplemental lighting system consume less power (Copot and Thi et al., 2018). A study was conducted to compare five meta-heuristic algorithms for optimization of PIDs, including Equilibrium Optimizer (EO), Particle Swarm Optimization (PSO), Teaching Based Optimization (TLBO), Differential Evolution (DE) and Genetic Algorithm (GA) (Manuel and İnanç et al., 2023). Among them, PSO algorithm is to simulate cooperation and competition in the process of searching for food in a flock of birds to produce group intelligence to guide the optimization of search, which has the advantages of simple structure, fewer setup parameters, fast convergence, and easy to implement. It can be an effective solution to the parameter optimization problem (Shuai and Yuyou et al., 2023). The PSO algorithm can select the optimal control parameters to optimize the PID controller. In addition, it has been proven that PID controllers optimized with POS algorithms for speed control of brushless DC motors can reduce energy consumption by approximately 3.1% (from 1.015 kWh to 0.984 kWh) (Naqvi and Jamil et al., 2024).

In summary, this paper proposes an off-grid photovoltaic supplementary lighting (PVSL) system with optimally controllable LED lamps for replenishing strawberry plants in greenhouses to continuously promote photosynthesis during the strawberry fruiting season. The PSO algorithm is used to iterate and optimize the parameters of the PID controller to precisely control the replenishment system and reduce energy consumption. The quality assessment of strawberriessignificantly improved compared to strawberry plants without supplemental light. The photovoltaic supplementary lighting system proposed in this paper was validated in field experiments during a full strawberry fruiting period of 90 days, and the results were compared with strawberry fruits without supplementary lighting in the same greenhouse. The optimization method proposed in this paper can effectively improve the quality of strawberry fruits and save energy consumption by controlling the greenhouse. The method may also provide a new optimization concept for other berry crops and greenhouses with different light resources.

2 METHOD AND MATERIALS METHOD AND MATERIALS

The main aim of this study is to optimize the quality of strawberries by controlling the light environment inside the PV greenhouse, using PSO to optimize the parameters of the PID controller, thereby effectively saving photovoltaic energy. This greenhouse was built at Kunming University in Kunming City, Yunnan Province (102°47′38″ E, 24°58′35″ N). A greenhouse equipped with off grid PV system and supplementary lighting system, as shown in Figure 1. The greenhouse lighting system consists of a controller and LED lamps. The off grid photovoltaic system consists of five parts. When sunlight shines on the PV modules, the monocrystalline silicon solar panels start generating electricity, and after being judged by the control and detection circuit, they charge the battery; When there is no sunlight or the sunlight is relatively weak, the current emitted by the photovoltaic module is too small to reach the charging current of the battery. The controlwill detect the circuit and disconnect the circuit, while preventing the battery from charging the photovoltaic module in reverse. By welding stainless steel square tubes on the cultivation frame, the LED lamps were fixed 20 cm above the strawberry, powered by a battery and inverter, and controlled by a PID controller for supplementary lighting. During the 90 days full fruiting period after successful strawberry planting, when the evening light intensity decreases, continuous supplementary light was applied for 2 hours in this study.

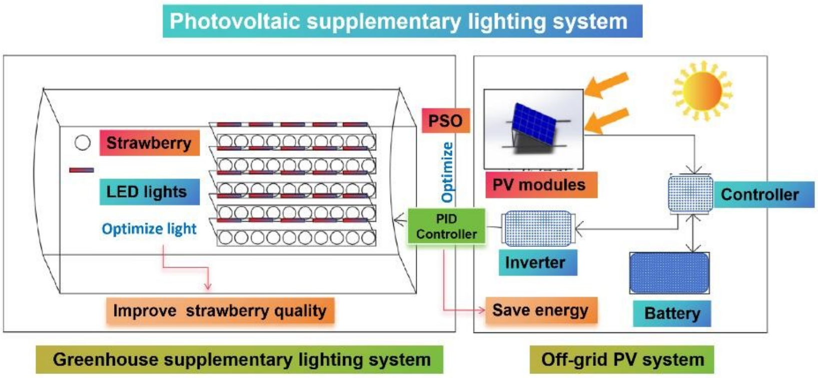

Figure 1: Schematic diagram of PV greenhouse lighting supplementary system

2.1 DESIGN AND CONSTRUCTION OF GREENHOUSE

The experimental greenhouse is an east-west arched greenhouse covering an area of 98.01 m^2 (8.1m × 12.1m), with a maximum height of 4.9 m. The greenhouse covering material is polyethylene film. Based on the greenhouse space design, 5-layer cultivation shelves were constructed, measuring 5.3 m in length, 1.5 m in width, and 1.4 m in height. Each layer has a height of 0.2 m and a width of 0.3 m, as shown in Figure 2.

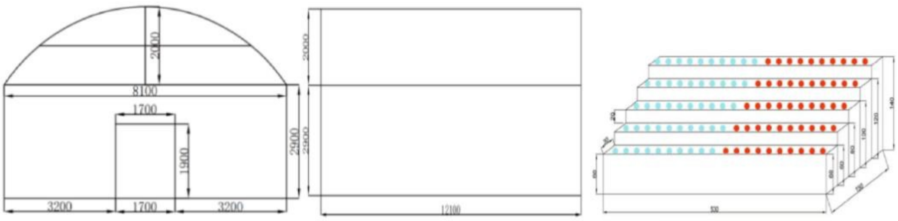

Figure 2 Design of experimental greenhouse and internal cultivation shelf

As shown in Figure 3(a). Two 5-layer cultivation shelves were set up inside the greenhouse, which were treated with 2 hours of supplementary light and no supplementary light, respectively, as shown in Figure 1(b).

Figure 3: Photos of experimental greenhouse (a) and cultivation shelf(b)

2.2 CONSTRUCTION OF PVSL SYSTEM

The PVSL system in this study used monocrystalline silicon photovoltaic cells, with electrical parameters shown in Table 1, and a photovoltaic conversion efficiency Module efficiency of 21%. When installing photovoltaic modules, in order to obtain more solar energy, taking into account the latitude, longitude, solar altitude, and azimuth of the experimental site, the tilt angle of the photovoltaic modules is determined to be 30 °, facing south.
According to the lighting conditions inside the greenhouse, strawberries need to be supplemented with light. Using LED lamps with a red to blue ratio of 5:1, there are a total of 40 lamps with a power of 15W, and each LED lamp contains 72 beads. The PVSL system ran for 2 hours in the evening and lasted for 90 days. The supplementary lighting effect is shown in Figure 4.

Table 1: Monocrystalline silicon photovoltaic modules parameter

Project	Value	Unit
Peak power	505	W
Voltage	0~+5	W
Current	43	V
Open circuit	11.75	A
Short circuit	51.9	V
Weight	12.35	A
Dimensions	26.3	Kg
Peak power	2187*1102*35	mm

Figure 4: Photos of PVSL system

2.3 ENERGY SUPPLY AND CONSUMPTION

The experimental greenhouse is limited by the obstruction of nearby buildings, and the PV modules placed next to the greenhouse can only receive solar radiation for 6 hours a day. The conversion efficiency of PV modules is 21%. The energy provided can be calculated by the following equation (Anding and Quanya, 2018).

Equation 24 PV module power generation

$$E_P = P_{AS}(H_A/G_S)K$$

Where:

- E_P = PV module power generation during a period of time (kW • h)
- P_{AS} = power of a solar panel under standard conditions (kW)
- H_A = solar radiation received by solar panels during a certain period (kW • h/m^2)
- G_S = solar irradiation intensity in standard state (kW/m^2)
- K=output power coefficient of PV system

The theoretical energy consumption of LED lights can be calculated by measuring the current and voltage, which can be compared with the

Equation 2 Power consumption of LED lamps

$$W_L = \sum_{n=1}^{i} U_L I_L t$$

Where:

- W_L = power consumption of LED lamps (kW • h)
- U_L = voltage of LED lamp (V)
- I_L = current of LED lamp (A)
- i = otal number of LED lamps
- t=running time of PVSL system (h)

2.4 CONTROL SYSTEM OPTIMIZATION

To reduce the oscillation or overshoot caused by various parameters in the control process, PSO algorithm can be used to optimize the control parameters of PID and improve the overall stability performance of the control system. PSO algorithm is a group iteration algorithm with fewer parameters to consider, which can achieve nesting of non-convex models, nesting of logical models, and optimization calculation of experiments. The application of PSO algorithm is based on the assumption that the search space is N-dimensional, representing that the original optimization problem has N optimization variables. There exists a population consisting of S particles, each particle's spatial position represented by vector X, and the direction and position of movement within the feasible domain represented by V. It can be simulated by the following equation (Issa, 2023).

Equation 3 Optimal position of particles

$$gbest(t) = min\{pbest_1(t), pbest_2(t), pbest_3(t), \cdots pbest_N(t),\}$$

Where:

- $gbest(t)$ = best position experienced by particles in historical iterations
- $pbest(t)$ = best position experienced by each particle in the current population that can be known

Captions may be done automatically if you right-click on the table or figure and select ‘insert caption’. If captions

As the algorithm progresses to the next generation, particles in space will update their velocity and position based on the information from the previous generation and the current generation. Particles update their position through continuous iteration until they find the optimal position, which is the optimal solution. This article uses the particle swarm optimization algorithm in optimization algorithms to implement the optimization process. The PID control flow of PSO optimization is shown in Figure 5. Block diagram of PID controller based on particle swarm optimization algorithm, PSO algorithm assigns ar bit values of Kp, Ki, Kd, calculates the objective function and continuously updates the controller parameters until the objective function is optimized. The simulation process should be implemented in the MATLAB software.

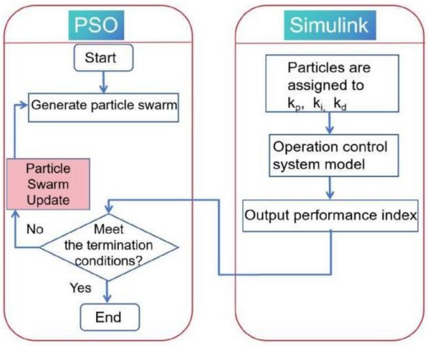

Figure 5 PSO optimized PID control

2.5 STRAWBERRY SAMPLES AND MEASURING EQUIPMENT

The ‘Miaoxiang 7’ strawberry selected in this study is a strawberry variety bred by Shandong Agricultural University through hybridization of ‘Red Face’ × ‘Sweet Charlie’ (Jiayu and Yuxuan et al., 2023). Each plant was planted in a separate pot and placed on 5-layer cultivation shelves, with 20 strawberry plants placed on each layer, for a total of 100 samples. As a control group, 100 strawberry plant samples were also placed on the 5-layer cultivation shelves without supplementary light. As shown in Figure 6.

The main test values for PV systems include solar radiation intensity and actual power generation of PV modules; The supplementary lighting system mainly tests the light intensity and actual energy consumption of LED lamps; The quality assessment of strawberries includes maximum single fruit weight, soluble solids content, and vitamin C content The testing equipment and parameters required for this experiment are shown in Table 2.

Figure 6: Planting layout of strawberry samples

Table 2: Testing instruments and parameters

Instrument name	Specification and Model	Scope and accuracy
Illumination photometer	AS823	1-200.000LUX/±5%rdg±10
Electronic balance	BSA2202S	0.5g-500g/0.1g
Digital refractometer	WZ-118/ATC	0-80%/0.5%
Solar radiation meter	TRT-2	0-2000 W/m2/±2% W/m2
Data acquisition recorder	FSR-4	1-60 min/1 min

3 RESULTS AND DISCUSSION

After successful strawberry planting, a supplementary light control experiment was conducted during its full period (December to February).

3.1 PV SYSTEM DATA

In January, when Kunming had almost no rainy days, two weather conditions, sunny and cloudy, were selected to test the solar radiation intensity. Record and analyze the measured data every half hour from 9:00-15:00, as shown in Figure 7. The maximum value of solar radiation was 1086 W/m^2 on sunny days and 1045 W/m^2 on cloudy days, with little difference, which can be used as an input value reference for simulation.

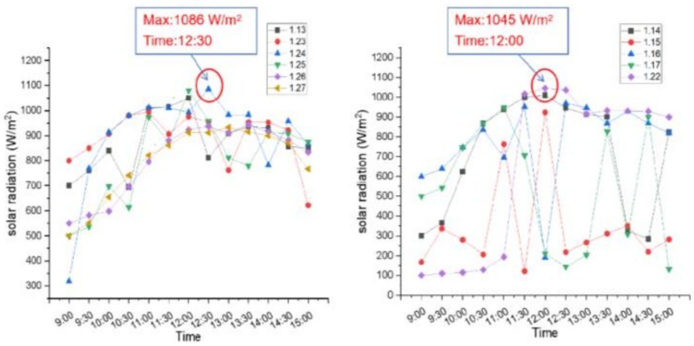

Figure 7: Comparison of solar radiation in different weather conditions

Considering the fluctuation of solar radiation, this experiment also measured the current and voltage of PV modules during the optimal period of sunny days, and drew a power generation graph for analysis, as shown in Figure 8. According to actual measurements, the average power generation was 424.65W, and the average daily power generation of a single photovoltaic module was 2.55 kW•h.

3.2 SUPPLEMENTARY LIGHT SYSTEM DATA

Before optimizing the system, to determine the simulation input values, it is necessary to measure the light intensity in the greenhouse during the evening (18:00-19:00). Conduct light testing on strawberry plants on each cultivation shelf, summarize all data according to different layers, and calculated the average light intensity. Finally, the light intensity between natural light and the LED lamps in the greenhouse were compared, as shown in Figure 9.

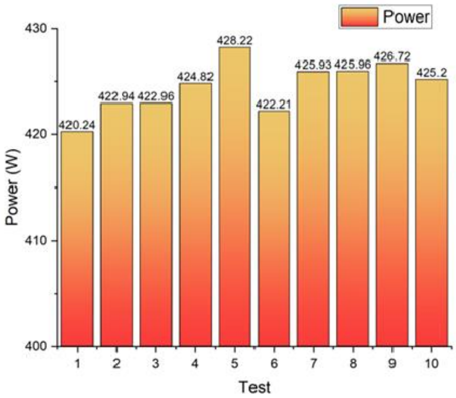

Figure 8: Power generation of PV modules

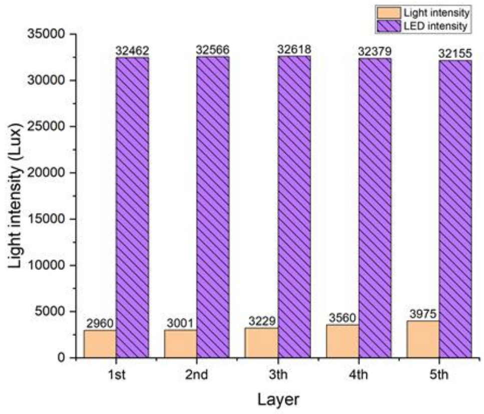

Figure 9: Comparison of light intensity

In the evening, the average natural light in the greenhouse was 3345 Lux, which could no longer meet the conditions for strawberry photosynthesis, and the received light was uneven, gradually weakening from top to bottom cultivation shelves. The measured light intensity on each layer of the cultivation shelf was relatively uniform, with an average value of 32436 Lux, which was within the range of 31900-39100 Lux for strawberry photosynthesis (Tang and Li et al., 2019).

3.3 SIMULATION AND OPTIMIZATION OF CONTROL SYSTEMS

In order to obtain the numerical values of the control parameters required for PSO optimization, it is necessary to use the Simulink toolbox in MATLAB software model and simulate the fill light system. The signal input to the control system is analyzed and tuned by the PID control algorithm, which sets three main parameters: proportional, integral, and derivative. The PID control simulation is shown in Figure 10.

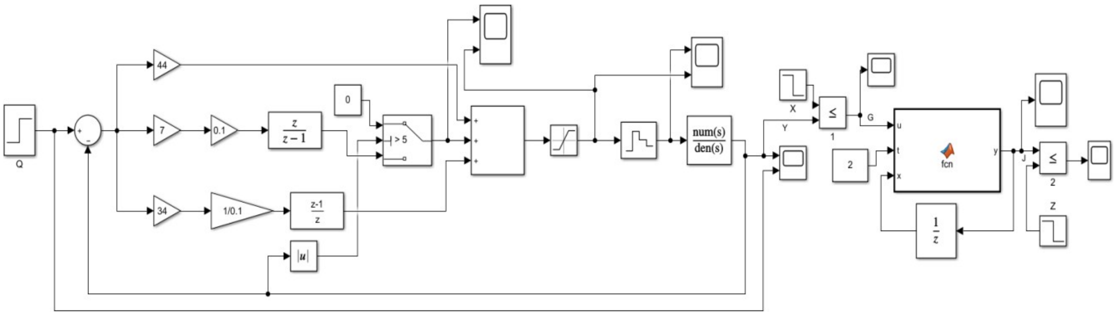

Figure 10: Simulation of supplementary lighting control system

The parameter Q is input into the PID control system, and then the PID control system performs parameter analysis and tuning before outputting signal Y. The output signal Y is compared with the input signal X of another comparator 1. If the output signal Y of the PID control system is less than or equal to the signal X of another comparator 1, the output is 1, and a voltage is applied to the Simulink timer to start timing. The output J of the Simulink timer is transmitted to another comparator and compared with the signal Z of another comparator 2. If the signal J output from the Simulink timer is less than or equal to the signal Z, the output continues to be 1. Otherwise, the output is zero. According to actual measurements, the average light intensity in the greenhouse is 3345 Lux in the evening. Therefore, when the light intensity is less than this average value, strawberries in the greenhouse need to be supplemented with light for simulation purposes. The system parameters are rounded to 3000 Lux, and then a simulated light parameter of 2000 Lux is input into the supplementary light control system for testing, as shown in Figure 11. After the simulation test of the control system, code the PSO algorithm in MATLAB to optimize the various adjustments and setting coefficients in the PIDcontrol system. A part of the PSO algorithm code is shown in Figure 12.

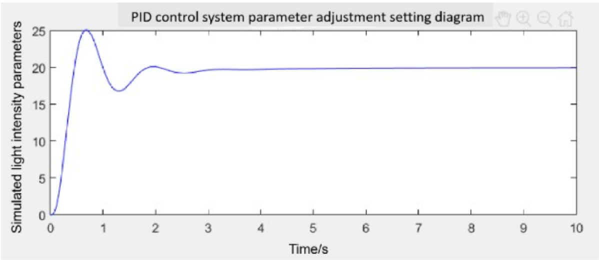

Figure 11: PID control parameter setting diagram

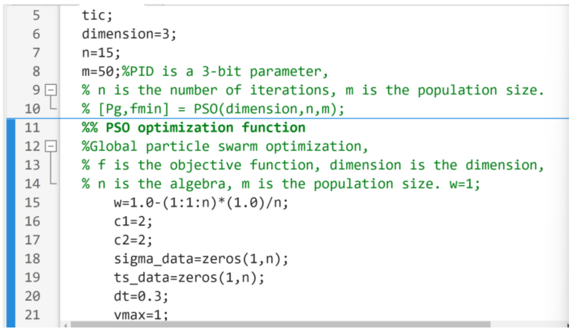

```
tic;
dimension=3;
n=15;
m=50;%PID is a 3-bit parameter,
% n is the number of iterations, m is the population size.
% [Pg,fmin] = PSO(dimension,n,m);
%% PSO optimization function
%Global particle swarm optimization,
% f is the objective function, dimension is the dimension,
% n is the algebra, m is the population size. w=1;
    w=1.0-(1:1:n)*(1.0)/n;
    c1=2;
    c2=2;
    sigma_data=zeros(1,n);
    ts_data=zeros(1,n);
    dt=0.3;
    vmax=1;
```

Figure 12: A part of the PSO algorithm code

In this study, the PSO algorithm was used to optimize and adjust from 0-50 iterations, and the optimal adjustment result was obtained at 15 iterations. Therefore, the iteration number n selected for this optimization was 15. When the optimization program starts running, the first input is the simulated input lighting parameter value, as shown in Figure 13 (a). As the number of iterations increases, the tuning curve in the figure basically overlaps, indicating that the value has stabilized at 2000Lux and conforms to the input parameter tuning curve in the PID control system. The second step of optimization is to adjust the fitness function of the algorithm, as shown in Figure 13 (b). The selection of the fitness function is related to whether the entire algorithm can find the optimal value. Through program debugging, the oscillation of the fitness function is ultimately reduced and stabilized. The third step of optimization is to optimize the adjustment time, as shown in Figure 13 (c). The figure shows that the PID control adjustment time of the control system is too long during operation. After optimization, the system adjustment time is significantly shortened and stable without overshoot. The fourth step of optimization is to optimize the overshoot of the system control, as shown in Figure 13 (d). The figure shows that the system will generate overshoots when it starts running. After optimization algorithm optimization, the overshoot is reduced and finally optimized to zero.

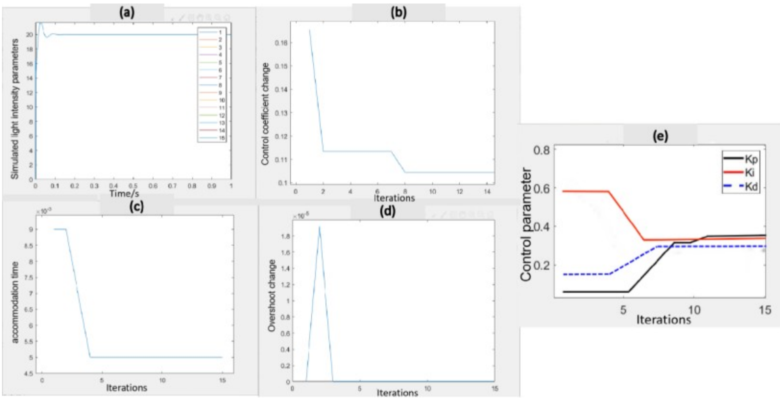

Figure 13: PSO algorithm optimization process

After the first four steps of optimization are completed, the overshoot of the system is zero. When the adjustment time is stable, the optimization program then optimizes and adjusts the proportional coefficient K_p, integral velocity K_i, and differential coefficient K_d in the PID, as shown in Figure 13 (e). The PSO algorithm improves the overall performance of the control system by increasing the proportional coefficient and differential coefficient, while reducing the integral velocity of the control system and minimizing the oscillation of system regulation, making the system more stable. Finally, the optimal parameters obtained by PSO algorithm optimization are: K_p =0.36, K_i=0.35, K_d=0.3.

3.3 ENERGY CONSUMPTION OF PVSL SYSTEM AFTER OPTIMIZATION

In the PVSL system, the DC power of the battery is converted into AC power through an inverter and supplied to 40 LED lights. In this experiment, the voltage and current of the battery during operation were measured to calculate the energy consumption and obtain the actual power consumption of the LED light. In this study, the PVSL system was supplemented with light for 2 hours per day, and the energy consumed by continuous illumination for different periods was summarized in Table 3.

Table 3: Energy consumption before and after optimization of PVSL system

Supplementary light cycle	Measurement value (W • h)	Theoretical value (W • h)	Energy savings (W • h)
1 hour	485	600	115
2 hours	970	1200	230
30 Days	29100	36000	6900
90 Days	87300	108000	20700

The measured value showed that the PVSL system consumed 485 W of electricity per hour, and the actual power consumption after 2 hours of supplementary lighting was 0.97 kW•h, which was less than the theoretical power consumption of 1.2 kW•h, effectively saving 19.17% of electricity. If continuous light supplementation is carried out during the 90 day peak fruiting period of strawberries, the PVSL system can save 20.7 kW•h.

3.5 EVALUATION OF STRAWBERRY FRUIT QUALITY

The strawberry plants were planted on September 1st, and after entering the peak fruiting period, the PVSL system was used for 90 days starting from December 1st. Nine strawberry samples were selected from each of the first to fifth layers of two cultivation shelves, total 90 strawberry plants. The quality of the strawberry fruits harvested within 90 days was tested and analysed, including single fruit weight, soluble solids content, and vitamin C content. The average quality of each layer of strawberry fruit was taken as the sample. 45 samples without light supplementation were named as "Original", and the other 45 samples with light supplementation were named as "Treatment". The results are shown in Figure 14(a) Single fruit weight; (b) Soluble solids content; (c) Vitamin C content; (d) Comparison photo of strawberries.

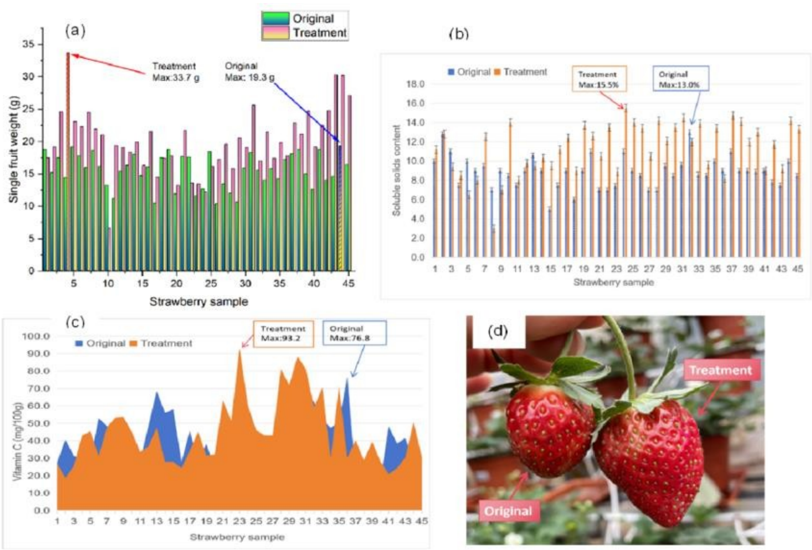

Figure 14: Data analysis of strawberry fruits

4 CONCLUSION

The PVSL system and PSO algorithm optimization proposed in this study can not only improve the quality of berry crops, but also save greenhouse energy consumption. The conclusion drawn is as follows:

-Through a comparative experiment of greenhouse supplementary lighting during the full fruiting period of strawberries, the PVSL system has demonstrated its effectiveness in improving the quality of berries.

-Compared with strawberries without LED lamps in the greenhouse, the PVSL system significantly improved fruit quality, with an average maximum weight gain of 74.61% per fruit; The content of soluble solids increased by 2.5%; The content of vitamin C increased by 21.35%, demonstrating the potential of this system to optimize fruit quality.

- By using the PSO algorithm, the PID controller of the PVSL system was optimized, and the optimal control parameters K_p, K_i, and K_d were obtained to be 0.36, 0.35, and 0.3, respectively.

-The optimized PVSL system effectively saved 19.17% of electricity while extending crop photosynthesis by 2 hours of supplementary light per day and has the ability for sustainable optimization improvement.

This study represents progress in the field of photovoltaic agriculture integration. The proposed PVSL system and optimization method can also provide a new optimization concept for greenhouses in other berry crops and regions with different light resources, with the potential to promote a new model of sustainable photovoltaic agriculture.

5 ACKNOWLEDGEMENT

This study was supported by Science and Technology Plan Project of Yunnan Province (Grant No.202301BA070001-006), Scientific Research Fund Project of Kunming University (Grant No.YJL20022), Reserve Talents Of Young And Middle-Aged Academic And Technical Leaders In Yunnan Province (Grant No.ZX20220143), Spring City Plan Youth Top notch Talent Project (Grant No.C201914005).

6 REFERENCES

Anding, L. and L. Quanya (2018). Solar photovoltaic power generation system engineering. Beijing, Chemical Industry Publisher.

Cervantes, L. and M. T. Ariza, et al. (2019). "Light exposure affects fruit quality in different strawberry cultivars under f ield conditions." Scientia Horticulturae 252: 291-297.

Choi, H. G. and B. Y. Moon, et al. (2015). "Effects of LED light on the production of strawberry during cultivation in a plastic greenhouse and in a growth chamber." Scientia Horticulturae 189: 22-31.

Copot, C. and T. M. Thi, et al. (2018). "PID based particle swarm optimization in offices light control." Science Direct 51

(4): 382-387.

De Lima Nechet, K. and D. W. Heck, et al. (2015). "Effect of the increase of UV-B radiation on strawberry fruit quality." Scientia Horticulturae 193: 7-12.

Fernandeza, E. F. and A. Villar-Fernandez, et al. (2022). "Global energy assessment of the potential of photovoltaics for greenhouse farming." Applied Energy 309: 118474.

H. Marrou, L. G. L. D. (2013). "Microclimate under agrivoltaic systems: Is crop growth rate affectedin the partial shade of solar panels?" Agricultural and Forest Meteorology(177): 117– 132.

Hidaka, K. and K. Dan, et al. (2013). "Investigation of supplemental lighting with different light source for high yield of strawberry." IFAC Proceedings Volumes 46 (4): 115-119.

Issa, M. (2023). "Enhanced Arithmetic Optimization Algorithm for Parameter Estimation of PID Controller." Arab J Sci Eng 48 (2): 2191-2205.

Jiayu, H. and L. Yuxuan, et al. (2023). "Comparative experiments in introduced 10 v arieties of strawberry in the chongqing suburb greenhouse cultivation." Journal of Anhui Agricultural Sciences 51 (7): 46-49.

Khammayom, N. and N. Maruyama, et al. (2022). "Impact of environmental factors on energy balance of greenhouse for strawberry cultivation." Case Studies in Thermal Engineering 33: 101945.

Khoshnevisan, B. and S. Rafiee, et al. (2013). "Environmental impact assessment of open field and greenhouse strawberry production." European Journal of Agronomy 50: 29-37.

Kumar, M. and D. Haillot, et al. (2022). "Survey and evaluation of solar technologies for agricultural greenhouse application." Solar Energy 232: 18-34.

Manuel, N. L. and N. İnanç, et al. (2023). "Control and performance analyses of a DC motor using optimized PIDs and fuzzy logic controller." Results in control and optimization 13: 100306.

Mingxin, Z. and W. Yuping, et al. (2024). "Introduction performance and the main cultivation techniques of strawberry new superiority characteristic cultivars in Yuzhong alpine area." Journal of Fruit Resources 5 (4):114-118.

Naqvi, S. S. A. and H. Jamil, et al. (2024). "Multi-objective optimization of PI controller for BLDC motor speed control and energy saving in Electric Vehicles: A constrained swarm-based approach." Energy Reports 12: 402-417.

Peng, Y. and X. Ma, et al. (2023). "Energy performance assessment of photovoltaic greenhouses in summer based on coupled optical-electrical-thermal models and plant growth requirements." Energy Conversion and Management 287: 117086.

Pengfei, W. and W. Lijuan, et al. (2017). "Effects of different light quality of led on tissue culture of fragaria ananassa." Hubei Agricultural Sciences 56 (10): 1895-1897.

Shuai, M. and W. Yuyou, et al. (2023). "Control strategy of mine electromechanical equipment based on improved particle swarm optimization PID." Industrial Instrumentation & Automation(5): 115-119.

Tang, Y. and M. Li, et al. (2019). "Study On Photovoltaic Modules On Greenhouse Roof For Energy And Strawberry Production." E3S Web of Conferences 118: 03049.

Tang, Y. and X. Ma, et al. (2020). "The effect of temperature and light on strawberry production in a solar greenhouse." Solar Energy 195: 318-328.

Tomar, A. (2024). "Enhancing crop productivity in photovoltaic greenhouses using extended PAR-based photosynthesis." Solar Energy 276: 112689.

Valiante, D. and I. Sirtori, et al. (2019). "Environmental impact of strawberry production in Italy and Switzerland with different cultivation practices." Science of The Total Environment 664: 249-261.

Yano, A. and M. Cossu (2019). "Energy sustainable greenhouse crop cultivation using photovoltaic technologies." Renewable and Sustainable Energy Reviews 109: 116-137.

Zhang, M. and C. M. Whitman, et al. (2019). "Manipulating growth, color, and taste attributes of fresh cut lettuce by greenhouse supplemental lighting." Scientia Horticulturae 252: 274-282.

#377: High-efficiency and coloured solar photovoltaic modules enabled by interference pearlescent pigments

Yuning CHEN[1], Jingyi LIU[2], Xiting DAI[3], Tao MA[4,*]

[1] Shanghai Jiao Tong University, Shanghai, China, chenyuning@sjtu.edu.cn
[2] Shanghai Jiao Tong University, Shanghai, China, ljycarrie@sjtu.edu.cn
[3] Shanghai Jiao Tong University, Shanghai, China, daisy2021@sjtu.edu.cn
[4] Shanghai Jiao Tong University, Shanghai, China, tao.ma@sjtu.edu.cn
* Corresponding author

Abstract: Building-integrated photovoltaic (BIPV) has emerged from the inspiration of sustainability strategies and the need for zero-carbon buildings, while the monotonous appearance of PV modules hinders the development of BIPV. Nevertheless, it is challenging to colorize PV modules while meeting their high-power conversion efficiency (PCE). In practical application, pearlescent pigments were widely applied to colorize the PV modules for an aesthetic appearance due to their vivid interference colour and low absorption in the visible region. However, a high reflection of pearlescent pigments in the near-infrared (NIR) region will reduce the PCE, indicating that there is room for further improvement. In this study, an interference pigment with a mica/titanium dioxide/silica (M/T/S) structure suitable for PV modules was proposed. The feasibility of the interference pigment with high reflection in the visible region and low reflection in other wavelength bands can be proved through a multi-layer films theory and different colours can be obtained by varying the thickness of the interference layer. Compared with commercial pearlescent pigments, the average reflectance of the interference pigments decreased from 17.1% to 11.9% in the NIR band, and its average transmittance can be increased by 12.0%. Then interference pigments were easily fixed to glass by screen printing and ultra-violet (UV) curing, and high-efficiency PVs with structured colours were obtained by lamination. The suitability and practicality of interference pigments for PV modules have been demonstrated by efficiency tests under a standard condition, and the PCE loss of yellow PVs coated with M/T/S interference pigments was limited to 3.77%.

Keywords: Building-integrated photovoltaic (BIPV), Coloured photovoltaic modules, Interference pigments, Optica regulation

1. INTRODUCTION

The energy demand is increasing due to social development needs, while greenhouse gases, such as methane and carbon dioxide, produced by the combustion of fossil fuels will drive up the global average temperature, which will lead to a variety of global climate problems (Olabi and Abdelkareem, 2022). The twenty-eighth United Nations Climate Change Conference proposed that to maintain a liveable planet global renewable energy capacity, including wind and solar, would need to triple by 2030 to limit temperature rise to 1.5°C above pre-industrial levels (González-Torres et al., 2022). The International Energy Agency (IEA) report stated that the building sector accounted for a third of energy consumption and contributed a quarter of final CO_2 emissions (IEA, 2021). In this context, promoting distributed photovoltaic (PV) applications and combining PV modules with buildings not only save land resources but also reduce building costs and energy consumption (Hirsch et al., 2018).

However, the monotonous appearance of PV modules, usually black and blue, limits the integration of the PVs with buildings and is often installed as an accessory on the roof of the building, namely BAPV. Introducing a colourful and adjustable appearance to PVs can deepen the combination between PV modules and buildings, whereby the PV modules can be used as a part of the building materials such as the facade and roofing structure, namely BIPV (Martin-Chivelet et al., 2022).

In some studies, an attractive appearance of coloured PV modules was obtained by inserting additional colouring layers containing structural or pigmented colours into the PV modules (Eder et al., 2019). However, structural colours, which exhibit characteristics such as little light absorption, bright colours, and resistance to fading, have become a dominant force in the field of coloured PV technology. The application of structural colours in PV modules can be divided into two principal categories in accordance with the stage of colour formation. One category encompasses the deposition of colourless raw materials directly onto glass or cells, whereby the formation of colours occurs. Xu et al.(Xu et al., 2022) deposited alternating multilayer stacked films of TiO_2/SiO_2 with varying high and low refractive indices on a rugged glass surface by a multi-target radio-frequency magnetron sputtering system. The power conversion efficiency (PCE) of coloured PV modules was 18.2% (cyan), representing a relative decline of 11.7%. In the study conducted by Li et al. (Li et al., 2022), a suspension of alcohol and ZnS nanoparticles was sprayed onto silicon cells to form purple, green, and blue photonic glass (PG) layers. The PCE of a 5 cm × 5 cm coloured PV module was found to decrease to 20.9%, representing a relative decline of 1.4%. The alternative approach is to apply the structural colour units to the glass surface via inks or to incorporate them into an adhesive film, and pearlescent pigments are the primary pigments. Masuda et al. (Masuda et al., 2018) applied a coating of 10 wt% blue pearlescent pigments on the inner face of the front glass, relatively maintaining the PCE of the PV module at 80%. Lim et al. (Lim et al., 2022) employed the spin-coating method to apply a coloured EVA emulsion containing pearlescent pigments to glass, resulting in coloured PV modules with a relative PCE from 85.4% to 91.4%.

The structured colour of the stacking films in the first method allows for precise colour control, however, the use of expensive deposition equipment increases the cost of the coloured PV modules. Despite the high PCE performance of the use of the PG layer, the fabrication has low single-batch yields and poor colour repeatability, which in turn prolongs the preparation process for PV modules. In the second method, although the principle of colour formation is the same as that of layer-stacked structural colours, pearlescent pigments are often prepared by the chemical liquid deposition (CLD) method (Wang et al., 2017). The pre-synthesized structural colour unit effectively separates the colour formation process of the structural colours from the PV module preparation process, furthermore, it allows for seamless integration with the deep processing technology of glass, ultimately reducing the production time and costs of coloured PV modules. Nevertheless, our previous study (Chen et al., 2024) has revealed that the current commercial pearlescent pigments exhibit high reflection peaks in the near-infrared wavelength band (700-1200 nm), which are unable to generate colours or electricity and account for approximately 50% of the total loss, indicating that there is still scope for improvement.

In this study, interference pigments suitable for PV modules were prepared via the CLD method. The spectral regulation was achieved by modifying the structure of the interference pigments to restrict the reflection peak to the visible wavelength band while maintaining the transmission in the remaining wavelength bands, thus allowing for maintaining high PCE while generating an aesthetic appearance of PV modules.

2. MATERIALS AND METHODS

In this study, layer-stacked interference pigments were synthesized by the CLD method, employing highly transparent synthetic mica powder as the substrate and selected TiO_2 and SiO_2 as coating materials. The pigments can be divided into two main structural categories. The first comprises a three-layer structure of TiO_2/Mica/TiO_2, with mica as the substrate and TiO_2 as the coating material. This structure will be designated as M/T-X, where X represents the serial number of the samples obtained with varying reaction times. The second is a five-layer structure of SiO_2/TiO_2/Mica/TiO_2/SiO_2 fabricated by further coating SiO_2 around M/T-X samples, which will be designated as M/T/S-X. The serial number X will correspond to the serial number of the M/T sample.

2.1. The fabrication of TiO_2/Mica/TiO_2

TiO_2 was deposited on a mica substrate by hydrolysis of $TiCl_4$. After sieving and acid washing, mica powder was added to an acidic solution, regulated by HCl. The solution was then warmed up and maintained at 80°C, followed by dropping a certain concentration of aqueous $TiCl_4$ at a constant rate, meanwhile, a NaOH solution was titrated to keep a stable pH of the solution throughout the process of hydrolysis. When the addition of the aqueous $TiCl_4$ was finished, the solution continued to react for different times and the solution was then decanted into a centrifuge tube. The turbid liquid was then subjected to a centrifuge and ultrasonic cleaner, whereby it was washed three times in deionized water and subsequently placed in an oven at 95°C for drying. The resulting powder was then calcined in a muffle furnace at 850°C for 45 minutes, finally obtaining the mica-based TiO_2-coated interference pigments M/T-X with varying colours.

2.2. The fabrication of SiO_2/TiO_2/Mica/TiO_2/SiO_2

A layer of SiO_2 was deposited on the M/T-X samples via hydrolysis of tetraethyl orthosilicate (TEOS). The dried powder of M/T samples from the previous step was then subjected to a round-bottom flask for further coating of SiO_2. The initial step involved the preparation of the solution environment. A modest quantity of KCl and deionized water was introduced to the flask for ample dissolution. Then, a substantial quantity of anhydrous ethanol and a modest amount of ammonia were introduced and thoroughly stirred by a magnetic rotor. Furthermore, the heating was activated to maintain a constant temperature of 40℃. In the meantime, the reaction solution was configured by mixing TEOS with an anhydrous ethanol solution using ultrasonic mixing for 10 minutes. The solution was then added to the syringe and dropped into the flask at a uniform rate of 0.15 mL/min. After an addition of 9 mL, the solution was allowed to react for another 30 minutes. The material was washed three times by a centrifuge and an ultrasonic cleaner through anhydrous ethanol and deionized water, respectively. Subsequently, the centrifuged powder was put in an oven at 95℃ for thorough drying, after which it was calcined in a muffle furnace at 850℃ for 45 minutes, finally obtaining an interference pigment with a five-layer structure of SiO_2/TiO_2/Mica/TiO_2/SiO_2.

2.3. The fabrication of coloured PVs

The production of coloured UV inks involved the mixing of 4 wt% interference pigments with highly transparent UV curable inks, which contained prepolymers, monomers, defoamers, adhesion enhancers, and photo initiators. The mixed colour ink was screen printed on a 55mm x 55mm glass sheet using a 150-mesh screen-printing plate. Subsequently, the colouring layer was cured on the glass by a UV lamp, resulting in the formation of a coloured glass sheet. The coloured glass sheet was stacked facing inwards with the adhesive film, the 52mm x 52mm cell, and the backsheet layer by layer. Subsequently, the laminate was subjected to a vacuum environment at 140°C for 10 minutes through a photovoltaic module laminator, thereby obtaining the coloured PV modules.

3. CHARACTERISTICS OF INTERFERENCE PIGMENTS

In the course of the solution reaction, after the addition of the aqueous $TiCl_4$, the powder presented initially a blue hue, which then transitioned through a series of alternating tonal variations, including yellow, orange, purple, blue, and green. Following the completion of the reaction and calcination, the overall appearance of the interference pigments was white, which is due to the light scattering by the powder in a loose and disordered state, which in turn diluted the main interference colours. However, when little pigments are applied to a black substrate, the majority of the pigment lies flat on the substrate, thereby revealing the main interference colour.

A minimal quantity of pigments was smeared directly to a black acrylic substrate and observed beneath an optical microscope. As shown in Figure 1, the dimensions of the interference pigments exhibit a lack of uniformity, which is attributable to the quality of the mica. The mesh number of the mica, 250 mesh employed in this investigation, merely guaranteed the majority of the powder exhibiting a diameter of approximately 58 μm. Furthermore, throughout the solution reaction process, the solution was maintained in a state of rotation and agitation. The mutual collision between the powders may also result in the fragmentation of the mica powder with a high aspect ratio, leading to the production of tiny mica particles and ultimately forming unevenly sized pigments. While the interference pigments exhibit a lack of uniformity in size, a majority of pigments display a relatively consistent interference color. However, on some of the larger particles, there is evidence of colour variation, with the simultaneous appearance of stepped yellow, red, and green variations on some particles in the M/T-1 sample. This phenomenon can be attributed to the non-uniform thickness of the mica substrate. The simultaneous appearance of multiple interference colours may result in a reduction in the overall saturation of the interference colours.

M/T-1 and M/T-2 are interference pigments taken at different reaction times. The colours of the calcined powders match the colours in the reaction solution and both follow the yellow-violet-blue-green colour change rule. When spraying with alcohol, the saturation and brightness of the interference colour increased and were closer to the colours in the next colour stage. For example, M/T-1 changed from pale yellow to yellow, M/T-2 changed from yellow to orange, and M/T/S-2 changed from orange to purple. After the alcohol evaporates, the colour returns to the colour it was in the air. The overall colour is related to the refractive index of the surrounding medium, so different components of the carrier ink may create different colour appearances in practice.

M/T/S-1 and M/T/S-2 are the results of further coating of the same amount of SiO_2 around M/T-1 and M/T-2 respectively. Compared to the interference pigment coated only with TiO_2, the colour change continues according to the above variation principle, and the colours are more vivid and saturated, for example, M/T/S-1 goes from pale yellow to yellow compared to M/T-1, and M/T/S-2 goes from orange-red to reddish-purple compared to M/T-2.

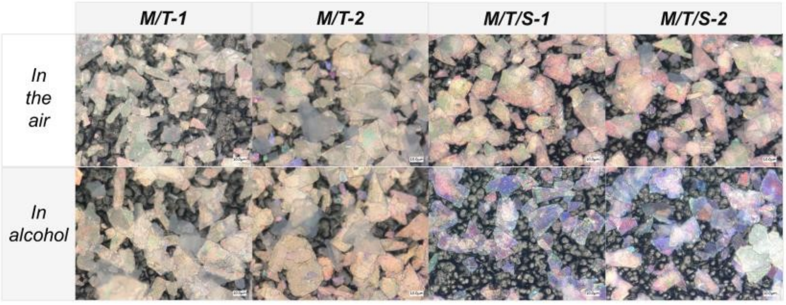

Figure 1: The microphotographs of interference pigments of M/T-X and M/T/S-X immersed in the air and alcohol taken by the optical microscope under the coaxial side light mode

4. OPTICAL CHARACTERISTICS OF COLORED GLASS

The UV light curing ink containing 4wt% interference pigment was fixed on the glass by screen printing and UV curing and the obtained glass sheets were tested for transmittance and reflectance using a UV-visible-near infrared (NIR) spectrophotometer and the results are shown in Figure 2. The black lines are the transmittance and reflectance of the glass without colouring layers. For different interfering pigment structures, the transmittance and reflectance curves are generally smoother, with the transmittance of the M/T structure ranging from 65% to 85% and the reflectance from 10% to 22%, and the transmittance further increasing and the reflectance further decreases after further coated with SiO_2. The transmittance and reflectance of commercial yellow pearlescent pigments are shown in Figure 3, which exhibits a high reflectance of about 17.1% in the NIR band. In contrast, the reflectance of M/T and M/T/S structural interference pigments in the NIR wavelength band is lower than that of commercial yellow pearlescent pigments, in which the average reflectance of M/T/S-1 is 11.9%, with a relative decrease of 29.1%.

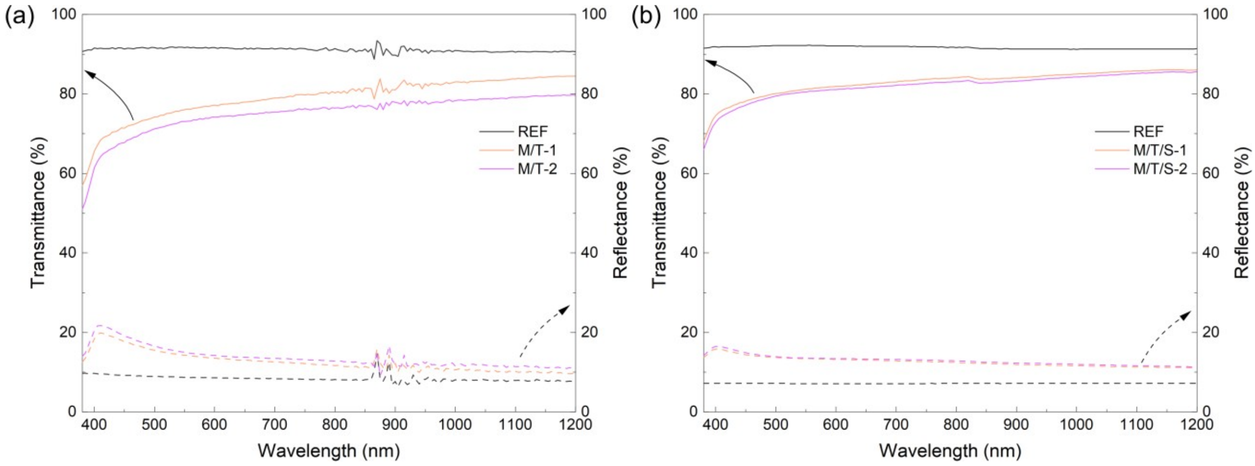

Figure 2: The optical characteristics of coloured glasses coated with UV curable inks, which contained: (a) M/T and (b) M/T/S interference pigments

The average transmittance of the coloured glass flakes was calculated with reference to the IQE of high-efficiency passivated emitter and rear cell (PERC) PV cells (Balaji et al., 2021). The transmittance of the glass sheet without a colouring layer was 90.8% and the average transmittance of the commercial pearlescent pigments was 73.4%, whereas the average transmittance of the M/T three-layer structured interference pigments prepared in this study was 78.0% and 74.2%, and the transmittance of the M/T/S five-layer structured interference pigments was 82.2% and 81.3%, respectively, which is an increase of 12.0% compared to the commercial pearlescent pigments, meaning that more photons can pass through the colouring layer to reach the battery layer to generate electricity.

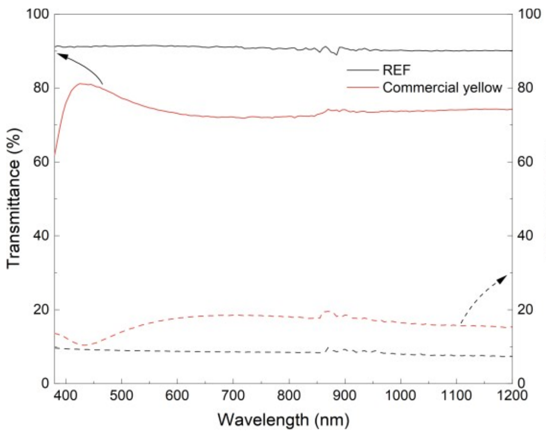

Figure 3: The transmittance and reflectance of commercial yellow pearlescent pigments

5. CHARACTERISTICS OF COLORED PVS

Coloured PV modules were produced by laminating the above glass sheets with the PV cells and their appearance pictures are shown in Figure 4. The coloured PV modules laminated with M/T-X, the three-layer structured interference pigmented glass sheets, were coloured pale yellow and purple respectively. When the pigment structure changed to five layers of M/T/S, the colours changed to yellow and orange, respectively. The colours of PV modules are different from the microscopic pictures of the powder, which is due to the change of refractive index when the medium around the powder is changed from air to UV curable inks after lamination into PV modules. In the physical view, when the pigment changes from a three-layer structure to a five-layer structure, the colours of the modules become bright and pure.

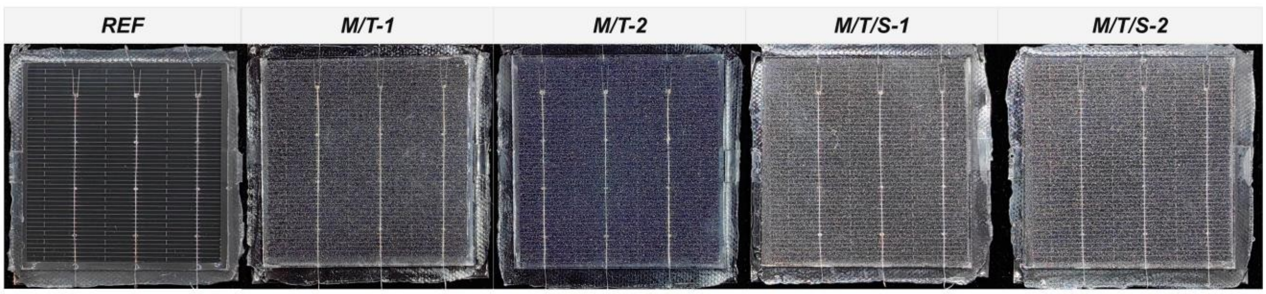

Figure 4: The photograph of coloured PVs coated with M/T-X and M/T/S-X interference pigments

The I-V characteristics of PV modules were measured in the standard test condition (STC): AM1.5G, 25℃, 1000 W/m^2, as shown in Figure 5. The PV modules using the commercial yellow pearlescent pigments and the interference pigments had their control groups due to different preparation batches and welding materials. The efficiency loss of the PV modules using commercial pearlescent pigments is 11.30%, while the efficiency loss of the PV modules using M/T-X interference pigments is all within 7.55%. The five-layer interference pigments achieved a lower efficiency loss with a purer colour, only 3.77% and 2.29% for M/T/S-1 and M/T/S-2 respectively.

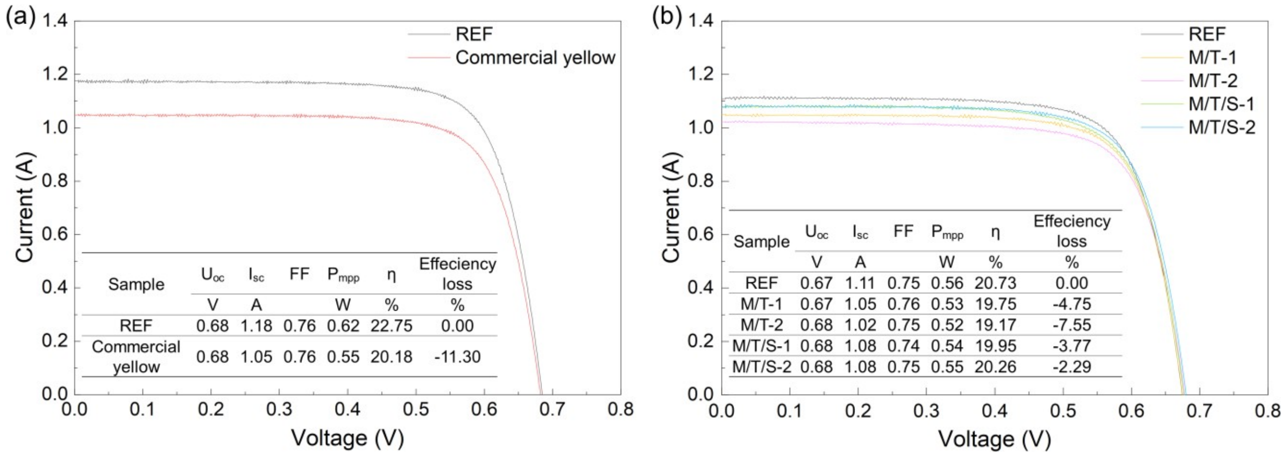

Figure 5: The I-V characteristics of the commercial yellow pearlescent pigment, M/T-X, and M/T/S-X interference pigments

6. CONCLUSION

In this study, interference pigments suitable for PV modules were prepared and the visual colour of such interference pigments was correlated with the type of medium surrounding the pigments. The reflectance of the M/T three-layer and M/T/S five-layer interference pigments in the NIR band was significantly reduced to about 11.9% compared to that of the commercial pigments, which was about 17.1%. Furthermore, the average transmittance of the prepared interference pigments is 12.0% higher than that of the commercial pearlescent pigment, thus achieving a higher PCE. Compared with the efficiency loss of 11.30% of PV modules using commercial pearlescent pigments, the modules using M/T/S five-layer structured interference pigments control the efficiency loss within 3.77%, achieving an aesthetic appearance with less efficiency cost, which helps to promote the integration of PV module and architecture.

7. REFERENCES

BALAJI, N., LAI, D., SHANMUGAM, V., BASU, P. K., KHANNA, A., DUTTAGUPTA, S. & ABERLE, A. G. 2021. Pathways for efficiency improvements of industrial PERC silicon solar cells. Solar Energy, 214**,** 101-109.

CHEN, Y., LI, Z., LI, S., LIU, J., DAI, X., MA LU, S. & MA, T. 2024. Colored and patterned silicon photovoltaic modules through highly transparent pearlescent pigments. Solar Energy Materials and Solar Cells, 275**,** 113033.

EDER, G., PEHARZ, G., TRATTNIG, R., BONOMO, P., SARETTA, E. & FRONTINI, F. 2019. Coloured BIPV : Market, research and development, https://iea-pvps.org/key-topics/iea-pvps-15-r07-coloured-bipv-report/, Report IEA-PVPS T15-07: 2019.

GONZ LEZ-TORRES, M., P REZ-LOMBARD, L., CORONEL, J. F., MAESTRE, I. R. & YAN, D. 2022. A review on buildings energy information: Trends, end-uses, fuels and drivers. Energy Reports, 8**,** 626-637.

HIRSCH, A., PARAG, Y. & GUERRERO, J. 2018. Microgrids: A review of technologies, key drivers, and outstanding issues. Renewable & Sustainable Energy Reviews, 90**,** 402-411.

IEA 2021. Greenhouse Gas Emissions from Energy. IEA, Paris.

LI, Z. P., MA, T., LI, S. J., GU, W. B., LU, L., YANG, H. X., DAI, Y. J. & WANG, R. Z. 2022. High-efficiency, mass-producible, and colored solar photovoltaics enabled by self- assembled photonic glass. Acs Nano, 16**,** 11473-11482.

LIM, S., AHN, H. S., GASONOO, A., LEE, J. H. & CHOI, Y. 2022. Fabrication of color glass by pearlescent pigments and dissolved EVA film. Materials, 15**,** 11.

MARTIN-CHIVELET, N., KAPSIS, K., WILSON, H. R., DELISLE, V., YANG, R. B. C., OLIVIERI, L., POLO, J., EISENLOHR, J., ROY, B., MATURI, L., OTNES, G., DALLAPICCOLA, M. & WIJERATNE, W. 2022. Building-Integrated Photovoltaic (BIPV) products and systems: A review of energy-related behavior. Energy And Buildings, 262**,** 18.

MASUDA, T., KUDO, Y. & BANERJEE, D. 2018. Visually attractive and high-power-retention solar modules by coloring with automotive paints. Coatings, 8**,** 7.

OLABI, A. G. & ABDELKAREEM, M. A. 2022. Renewable energy and climate change. Renewable & Sustainable Energy Reviews, 158**,** 7.

WANG, Y., LIU, M. M., LIU, Y. Q., LUO, J. Q., LU, X. Y. & SUN, J. 2017. A novel mica-titania@graphene core-shell structured antistatic composite pearlescent pigment. Dyes And Pigments, 136**,** 197-204.

XU, Z. H., MATSUI, T., MATSUBARA, K. & SAI, H. 2022. Tunable and angle-insensitive structural coloring of solar cell modules for high performance building-integrated photovoltaic application. Solar Energy Materials And Solar Cells, 247**,** 10.

#379: Lime-plaster enhanced with phase change materials: Results of an experimental monitoring campaign

Eleonora BACCEGA[1*], Michele BOTTARELLI[1]

[1] Department of Architecture, University of Ferrara, via Quartieri 8, 44121 Ferrara, Italy
*eleonora.baccega@unife.it

Abstract: The building sector strongly affects the energy required, especially for heating and cooling. The need to limit the energy demand and the impact on the environment has to deal, however, with an ever-increasing energy demand inside buildings and with an obsolete building stock. The design and construction of new and energy efficient buildings is not enough to tackle the problem, which can be really addressed only by working on the improvement of existing buildings. Considering that a consistent number of these existing buildings are individually protected or are inserted in wider protected contexts, interventions may be challenging due to several limitations that reduce the number of possible strategies that can be adopted. Therefore, possible strategies for the energy refurbishment of historical buildings to be integrated within the building envelope are crucial to reach the ambitious aim of reducing the impact of the building sector. The efficacy of phase change materials (PCMs) was investigated in case of integration within lime-based plasters for the application on walls' outermost layer. Experimental tests under real outdoor conditions were carried out initially to estimate whether and how much the addition of PCM affected the thermal behaviour of walls and the building energy demand for cooling. Plasters with different PCMs were realized and arranged in a customized set up realized at the TekneHub Laboratory of the University of Ferrara and were then tested for several months. Results showed good performance in terms of attenuationof the daily temperature fluctuations and reduction of the energy required.

Keywords: Phase Change Materials, Lime Plaster, Energy Refurbishment, Historical Buildings

1. INTRODUCTION

The greatest energy consuming sector is the building and construction one (Sinka, 2019), which accounts for more than 30% of the global consumption and almost 40% of the total related CO2 emissions (Asadi, 2012). The major responsible are residential buildings, whose energy demand is about three times higher than non-residential buildings (Global Status Report, 2020). The impact of the urban heat island effect, the ever-increasing living standards and the decrease of the cost of cooling equipment further aggravate the energy requirement for HVAC systems, especially during summer (Pandey, 2021; Pavlik, 2014). In addition to this, a consistent share of the building stock is made of old and obsolete buildings whose energy performance is not up to the standards. As an example, in Italy about 70% of the buildings were built before the release of the first law that established the limits for the energy consumption, in 1976 (Coppola, 2016; Milone, 2015). At the same time, the rate of new buildings is only about 1% per year (European Parliament, 2015). Based on these assumptions, interventions on existing buildings aimed at their energy refurbishment seem of utmost importance. This, however, is not so easily feasible in case of particular buildings protected by regulatory restrictions due to aesthetic qualities, cultural relevance or as part of sensitive areas, such as city centres. In these contexts, the so-called passive design strategies emerge as a valid possibility to improve buildings' performance and indoor comfort at the same time without additionally stressing the energy demand (Pajek, 2022). Song et al. (Song, 2021) divided the conventional passivecooling methods into three main groups, namely solar and heat control, heat removal and heat exchange reduction. As regards the solar control, strategies usually consist of shadings and are aimed at limiting the heat transmission into the buildings. For what concerns heat removal, adopted strategies are aimed at removing the heat entered into the building and can be achieved, for instance, through natural ventilation. Lastly, heat exchange reduction mainly consists of intervention on the building envelope that can be achieved with or without thermal mass. Strategies with thermal mass include, for instance, the application of phase change materials (PCMs), through which the building envelope's thermal inertia is increased, and the indoor thermal comfort is improved by reducing indoor temperature fluctuations (Akeiber, 2016; Sà, 2012). The research here presented is focused on the evaluation of the addition of granular PCM into a lime-based plaster as a possible strategy for the refurbishment of existing and historical buildings, even the protected ones. The research consisted of preliminary experimental tests carried out at lab scale at the TekneHub Laboratory of the Universityof Ferrara that were aimed at the thermo-physical characterisation of the plaster enhanced with PCM, previously reportedin (Baccega, 2022; Baccega, 2024). The research was then brought to a bigger scale. Plaster samples with different concentrations of PCM were prepared and then tested under real outdoor conditions for several weeks, and the results here reported represent a selection of some of the data acquired. These data were then used in further developments to validate a numerical model through which they carry out additional investigations, in which different boundary conditions, different wall configurations and different PCM properties could be defined.

2. METHODOLOGY

The tests carried out at lab scale aimed at preliminarily investigating the effect of PCM when mixed into plasters. The interesting results obtained brought the research to a further step, which consisted in a monitoring activity under real conditions. This part of the research was conducted in collaboration with Fassa S.r.l. (Fassa), an Italian industry leader in the production of mortars, premixed plasters, paints and thermal insulation. An experimental set up was designed and realized to simultaneously monitor different wall samples. The installation of the set up was done exploiting an already mock up facility at the TekneHub Laboratory at the University of Ferrara, which was built in 2016 within the European project LIFE Climate Change Adaptation - HEROTILE (High Energy savings in building cooling by ROof TILE shape optimization toward a better above sheathing ventilation) (Herotile). The building has a rectangular 10 m x 8 m plan and is made of five adjacent independent test rooms and two guard rooms, one on each side, that ensures identical boundary conditions in each test room. For this research, one of these test rooms was used and part of the southern façade was removed to allow the installation of the wooden set up, as represented in Figure 1.

Figure 1: South façade of the mock up with the wooden set up installed

2.1. Experimental set up

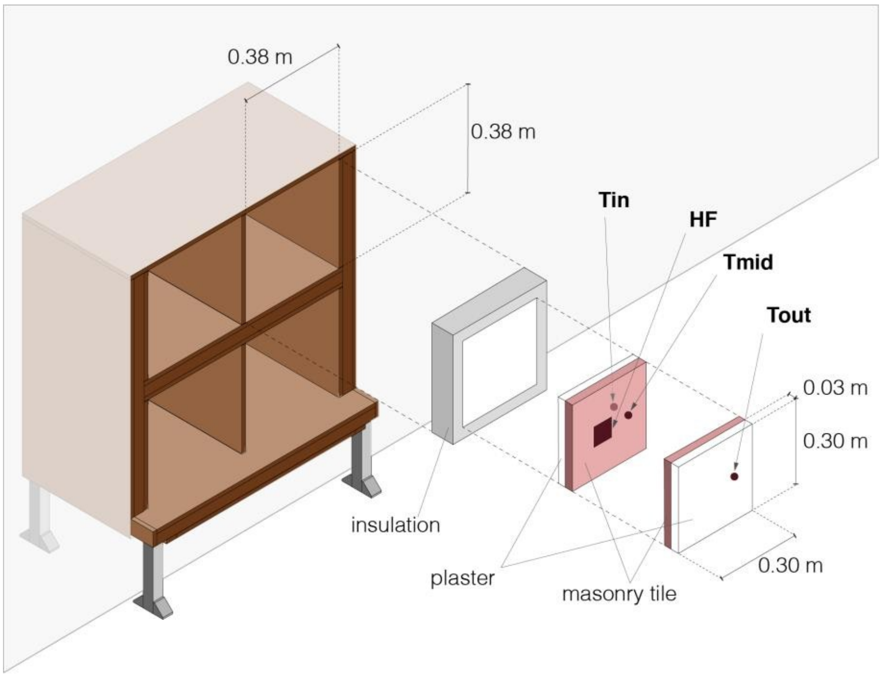

Figure 2: Schematic representation of the set up: materials and sensors' position

The set up realized has an aluminium structure covered by OSB panels and was designed to test up to four wall samples at the same time. The set-up is approximately 0.90 m x 0.90 m x 0.50 m, while each available slot, containing the wall samples, is 0.38 m x 0.38 m x 0.50 m. Each wall sample realized consists of a brick layer covered with plaster both on exterior as well as on the interior side. However, in order to ensure the maximum flexibility and the possibility of changing the configurations to be tested, the wall samples are made of two identical parts, consisting in a 0.03 m masonry tile layer covered by 0.03 m of plaster, which were kept together by means of wooden frames and metal profiles, as depicted in Figure 2. The wall samples were 0.30 m x 0.30 m and had a 0.04 m insulation frame to limit the heat transfer on the edges, thus establishing a mono-dimensional heat transfer through the walls and preventing them from influencing each other. Pictures of the realization of the set up and the installation of the plaster samples are reported in Figure 3.

Figure 3: Plaster samples installation and view of the complete installation

2.2. Monitoring system

A monitoring system was also implemented in order to collect data regarding temperatures and heat fluxes for each configuration. T-type thermocouples (accuracy: 0.5 K) were positioned on the surface of the exterior and the interior plasters, as well as inside the mock up room to monitor air temperature. Heat flux meters with integrated temperature sensor (heat flux accuracy: 5%, temperature accuracy: 2% of value in °C) (Hukseflux, FHF04) were positioned between the two brick layers, in the middle of each wall sample. These sensors were connected to a datalogger, a DataTaker DT85 series 3 (DataTaker), which acquired data with a timestep of 1 minute. As regards the boundary conditions, data in terms of air temperature, solar radiation, wind speed and wind direction were acquired by means of a weather station (Davis), already installed close to the mock up facility. An additional pyranometer (Hukseflux SR20) was vertically installed close to the mock up in order to acquire data in terms of vertical hemispherical irradiance that were later used for the validation of the numerical model implemented.

2.3. Realized samples

During the monitoring campaign different plaster samples and wall configurations were tested. A selection of the collected data was made and data hereafter reported are referred to the monitoring that took place in August, in which a reference plaster, used as benchmark, was compared to three plasters containing 10%, 20% and 30% of the same PCM, purchased from Smart Advanced Systems GmbH (Smart Advanced System GmbH). This PCM consisted in granules of paraffin with melting temperature around 28°C and an active PCM content indicated between 70% and 80%. From now on, the plaster sample without PCM will be indicated as Reference, while those containing 10%, 20% and 30% of PCM will be indicated as 10AS28, 20AS28 and 30AS28, respectively.

The thermo-physical properties of the reference and enhanced plasters were estimated during the tests at lab scale as reported in (Baccega, 2022; Baccega 2024) and values are summarized in Table 1.

Table 1: Estimated thermo-physical properties of the plasters tested

	ρ *[kg/m³]*	λ *[W/(m·K)]*	c_p *[J/(kg·K)]*	L_h [kJ/kg]	T (range) [°C]	
					melting	solidification
Reference	1646	0.31	895	-	-	-
10AS28	1522	0.28	1100	9.2	28 (6)	24 (6)
20AS28	1402	0.26	1200	18.4	28 (6)	24 (6)
30AS28	1170	0.24	1300	27.6	28 (6)	24 (6)

3. RESULTS

The monitoring campaign here reported was carried out between August 4th and August 31st. The boundary conditions that characterized that period are reported in Table 2. A representative interval of six consecutive days, between August 9th and August 14th, was chosen. In terms of boundary conditions, depicted in Figure 4, outdoor temperature fluctuated between 20°C and 35°C with lower values on August 12th and 13th. As regards solar irradiance, values reached peaks between 750 W/m² and 850 W/m² with clear sky only on August 9th and 11th. Temperatures on the outer plaster surfaces are depicted in Figure 5. In general, temperatures on the outer surfaces are quite similar among the different wall samples, with differences slightly clearer during nights.

Table 2: Average boundary conditions

	day (9-20)	night (20-9)	interval 12-15
Average outdoor temperature [°C]	29.3	22.6	30.5
Maximum outdoor temperature [°C]	39.6	30.7	38.7
Minimum outdoor temperature [°C]	17.4	16.4	19.8
Average indoor temperature [°C]	25.2	23.3	25.8
Average solar irradiance [W/m²]	433	24	662
Maximum solar irradiance [W/m²]	884	434	884
Solar gain [kWh/(m²·day)]	5.19	0.28	2.65

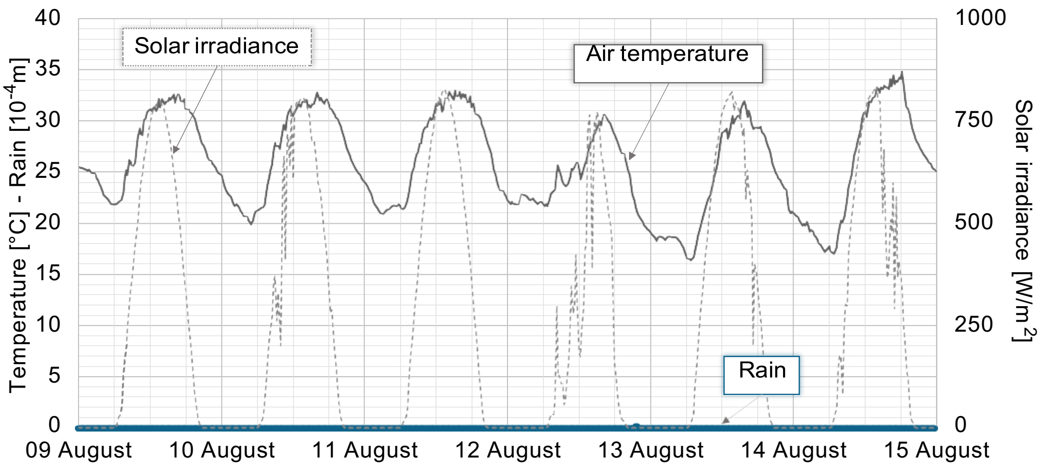

Figure 4:. Boundary conditions in the selected interval

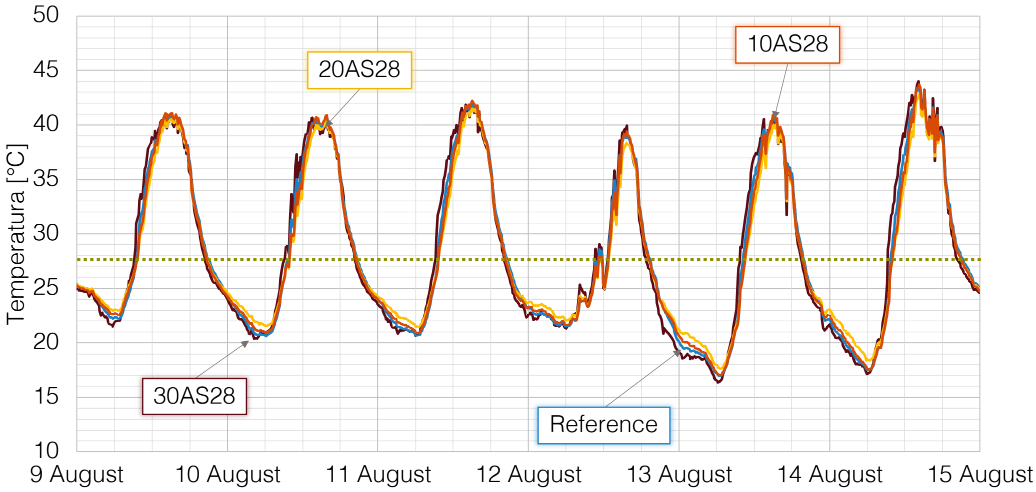

Figure 41: Outer surface temperatures (Tout)

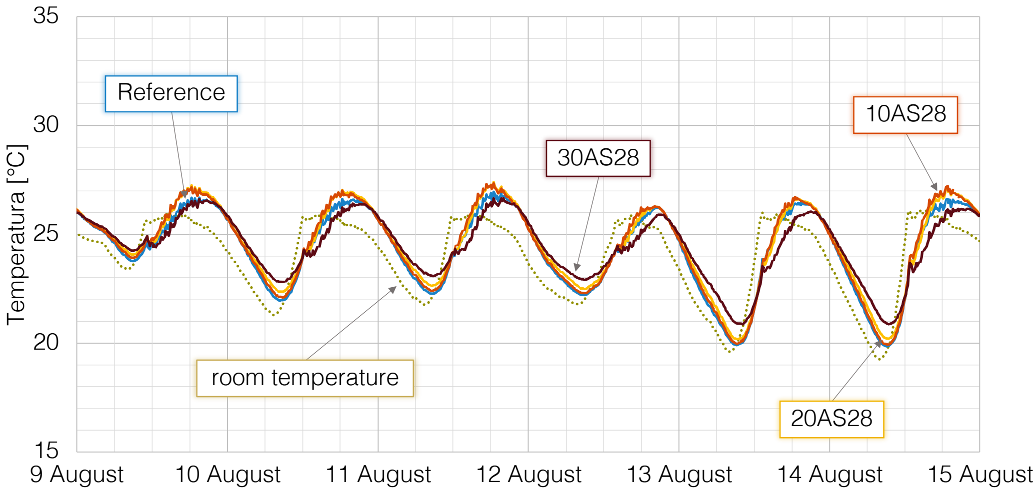

Figure 42: Inner surface temperatures (Tin)

Temperatures on the inner plaster surfaces are depicted in Figure 6. The fluctuation between minimum and maximum temperatures is limited and less than 6 K, hence differences between the wall samples are minimal. Temperatures on 10AS28 and 20AS28 are almost identical and differ from the Reference for less than 0.5 K while in case of 30AS28 maximum values are about 1 K lower and minimum values about 1 K higher than Reference.

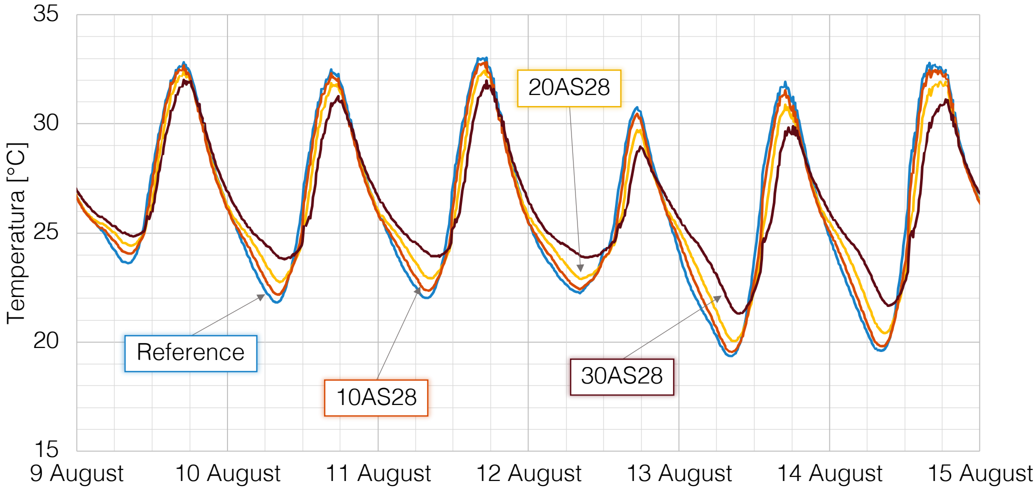

Figure 43: Temperatures in the middle (Tmid) of the wall samples

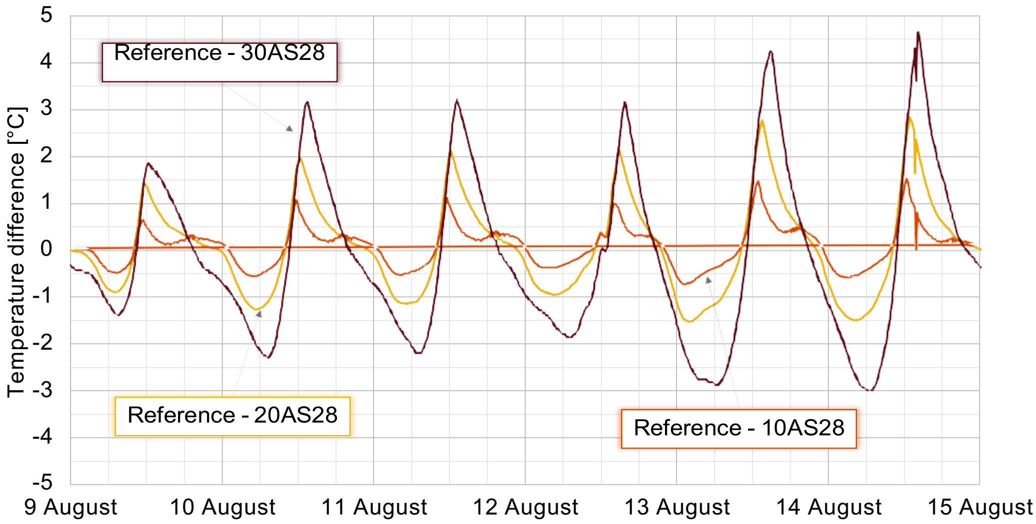

Figure 8: Temperature differences in the middle of the wall samples compared to the Reference

Temperatures in the middle of the wall samples are depicted in Figure 7 and their differences from the Reference are depicted in Figure 8. In this case the higher amount of PCM inside the plaster corresponded to an increase in the difference between the temperatures monitored to those of the Reference. During the day, 10% of PCM corresponded to temperatures 1 K lower, 20% to temperatures 2-2.5 K lower while 30% to temperatures between 3 K and 4 K lower. During the night the temperature on Reference was the lowest, with differences of about 0.5 K with 10AS28, 1 K with 20AS28 and 2-3 K with 30AS28.

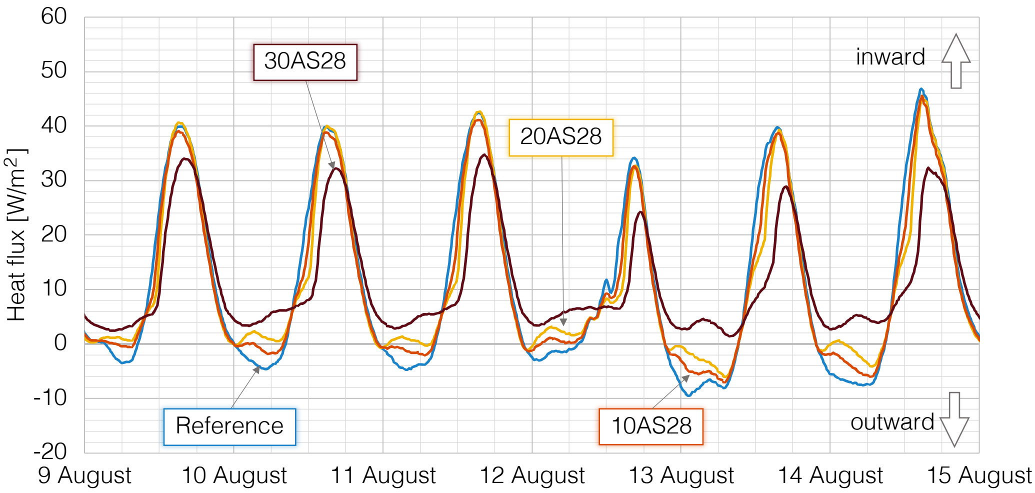

Figure 44: Heat fluxes (HF) in the middle of the wall samples

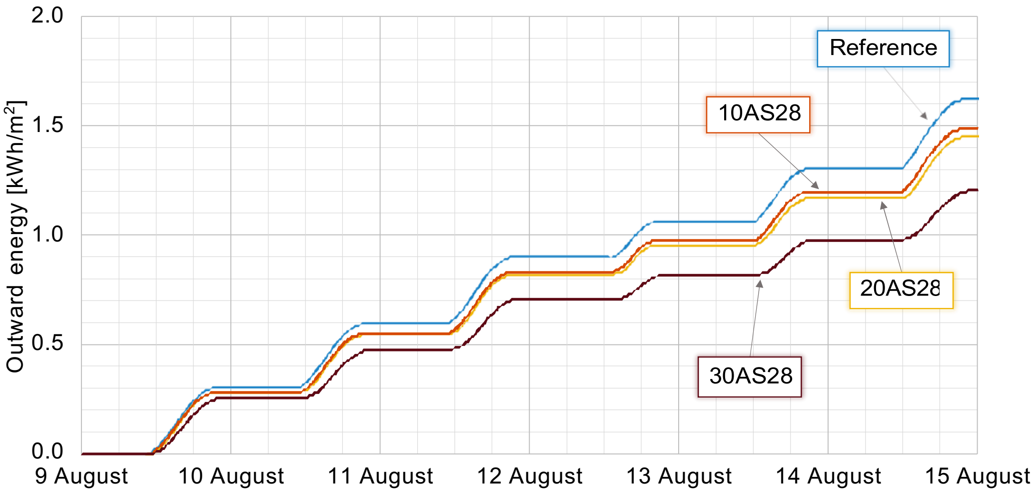

Figure 10: Inward energy for each of the wall samples

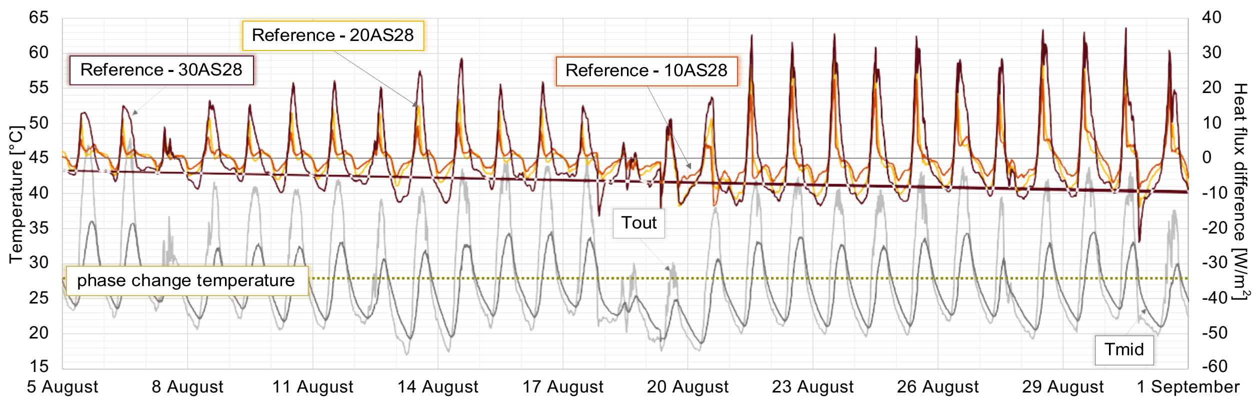

Figure 11: Comparison between heat fluxes

Monitored heat fluxes are depicted in Figure 9. During the day, maximum values of Reference, 10AS28 and 20AS28 were almost identical, while in 30AS28 peaks were 6-8 W/m^2 lower. In all samples containing PCM, however, the phase change could be seen both during melting as well as during solidification through the change of the curves' slope. The total inward energy through each wall sample was then calculated considering the working period of the fan-coil and results are depicted in Figure 10. The total inward energy was 1.63 kWh/m^2 through the Reference, 1.50 kWh/m^2 through 10AS28, 1.46 kWh/m^2 through 20AS28 and 1.21 kWh/m^2 through 30AS28. This means that reductions were, in order, of 7.9%,10.4% and 25.8%.

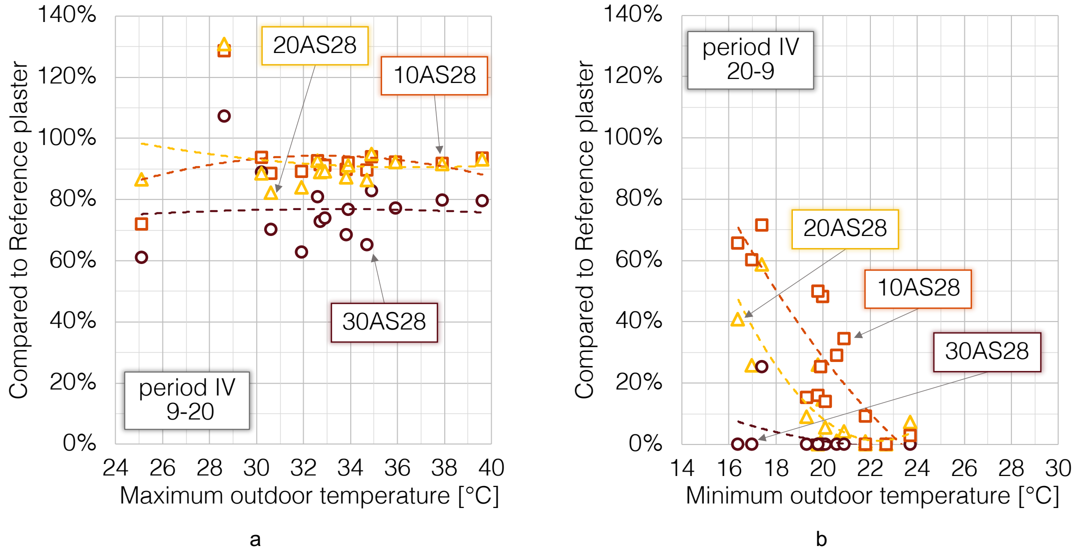

Figure 45: (a) reductions of inward energy if compared to the Reference according to the maximum outdoor temperature, (b) reductions of outward energy if compared to the Reference according to the minimum outdoor temperature

In Figure 11 the differences between the heat flux through the Reference and that of each of the other wall samples are depicted together with temperatures monitored on the Reference outer plaster surface and in the middle of the wall. In this case the three curves, referred to plasters containing different quantities of the same PCM, had the same trend and the differences from the Reference seemed to be proportional to the PCM quantities. On the basis of all data acquired during the period, the energy through each wall sample was calculated differentiating between the inward (time interval 9:00-20:00) and the outward one (20:00-9:00) and then comparing it to the Reference. The reductions were then related to the outdoor temperature and in Figure 12(a) and Figure 12(b) are depicted on the basis of the maximum and minimum temperature, respectively. During the day, almost no difference could be observed between the various maximum temperatures, with average reductions of 8-10% for 10AS28, 12-15% for 20AS28 and 25-30% for 30AS28. During the night, on the other side, values were quite different since the solidification of the PCM involved the release of part of the absorbed heat which led to incoming heat fluxes, contrarily to the Reference in which night heat fluxes were always outward. The percentage differences with respect to the Reference were calculated both during the day (9:00-20:00) and during the critical interval (12:00-15:00) and values are reported. In the former case, reductions were 7.6% for 10AS28, 10.6% for 20AS28 and 24.6% for 30AS28, while in the latter one reduction were about 5.2% for 10AS28, 12.1% for 20AS28 and 39.2% for 30AS28. Lastly, as regards outgoing energy, reductions were of 91.8% for 10AS28, 91.6% for 20AS28 and 100% for 30AS28, which, as previously mentioned, were due to the incoming heat fluxes during the during the night.

Table 3: Percentage comparison of the energy through each wall sample compared to the Reference

	compared to Reference		
	inward		outward
	9:00-20:00	12:00-15:00	20:00-9:00
10AS28	-7.6%	-5.2%	-91.8%
20AS28	-10.6%	-12.1%	-91.6%
30AS28	-24.6%	-39.2%	-100.0%

However, despite the interesting results in terms of temperatures and heat flux of the plaster with 30% of PCM, during the monitoring campaign a progressive deterioration of the plaster was observed, as depicted in. This was most probably due to the volumetric expansion of the PCM during the phase change, which was exacerbated by the high mass ratio of the PCM inside the plaster. It was estimated, in fact, that 30% by mass of PCM corresponded to about 44% by volume. For this reason, further developments of the research will only consider 10% and 20% by mass of PCM, respectively.

Figure 13: Deterioration of 30AS28

4. CONCLUSION

The focus of this research was the realization of plaster samples with different concentrations of PCM which were then tested under real outdoor conditions for several weeks. This research was carried out with the collaboration of Fassa S.r.l., an Italian industry leader in the production of mortars, premixed plasters, paints and thermal insulation. A dedicated set up was built to monitor up to four wall samples simultaneously, each of which was made of a thin masonry layer covered with plaster on both sides. One of these samples was a reference one, hence no PCM was added, while the others had exterior plaster containing different amounts of PCM, namely 10%, 20% and 30% by mass.

The monitoring activity was carried out between August 4th and 31st, and for all three plasters data acquired confirmed that the PCM greatly contributed to the reduction of the incoming heat flux and hence to a reduction of the temperature fluctuations on the inner surface. In terms of energy through the wall sample, 10% by mass of PCM corresponded to a reduction of nearly 8% of the incoming energy during the day, while with 20% and 30% by mass the reductions were of more than 10% and almost 25%, respectively. Focusing on a narrower time period, between noon and 3 pm, in reductions were, in order, of 5.2%, 12.1% and 39.2%. The lower reduction with 10% of PCM was most likely due to the fact that the small amount of PCM had already completely melt, hence the effect was less visible. However, despite the interesting results in terms of temperatures and heat fluxes, only 10% and 20% by mass of PCM could be considered a feasible solution for the energy refurbishment of buildings, since the plaster containing 30% by mass of PCM suffered from excessive deterioration due to the volumetric expansion of the PCM between solid and liquid state.

5. ACKNOWLEDGEMENT

The results here presented are part of wider research carried out with the financial support of Fassa s.r.l. which is thanked for allowing the publication.

6. REFERENCES

Akeiber H., Nejat P., Majid M.Z.A., Wahid M.A., Jomehzadeh F., Famileh I.Z., Calautit J.K., Hughes B.R., Zaki S.A., 2016. A review on phase change material (PCM) for sustainable passive cooling in building envelopes, Renewable and Sustainable Energy Reviews, vol. 60, pp. 1470-1497. DOI: 10.1016/j.rser.2016.03.036.

Asadi E., da Silva M.G., Antunes C.H., Dias L., 2012. Multi-objective optimization for building retrofit strategies: A model and an application, Energy and Buildings, vol. 44, pp. 81-87. DOI: dx.doi.org/10.1016/j.enbuild.2011.10.016.

Baccega E., Bottarelli M., Su Y., 2022. Alternative experimental characterization of phase change material plasterboard using two-step temperature ramping technique, Energy and Buildings, vol. 267. DOI: 10.1016/j.enbuild.2022.112153.

Baccega E., 2024. Thermo-physical characterisation of plasters containing phase change materials (PCMs), International Journal of Thermophysics, vol. 45. DOI: 10.1007/s10765-023-03327-7.

Coppola L., Coffetti D., Lorenzi S., 2016. Cement-Based Renders Manufactured with Phase-Change Materials: Applications and Feasibility, Advances in Materials Science and Engineering. DOI: 10.1155/2016/7254823.

Davis Vantage Pro2. https://www.davisinstruments.com/pages/vantage-pro2. Accessed January 2023.

European Parliament, Boosting Building Renovation: What potential and value for Europe?, 2016. Available: https://www.europarl.europa.eu/RegData/etudes/STUD/2016/587326/IPOL_STU(2016)587326_EN.pdf. Accessed: March 2022.

Fassa S.r.l.' https://www.fassabortolo.it/it/. Accessed: January 2022.

Global Status Report for Buildings and Construction, 2020. Available: https://globalabc.org/resources/publications/2020-global-status-report-buildings-and-construction. Accessed: March 2022.

HEROTILE - High Energy savings in building cooling by ROof TILEs shape optimization toward a better above sheathing ventilation. https://www.lifeherotile.eu/it/. Accessed: January 2021.

Hukseflux FHF04. https://www.hukseflux.com/products/heat-flux-sensors/heat-flux-sensors/fhf04-heat-flux-sensor. Accessed January 2023.

Hukseflux SR20. https://www.hukseflux.com/products/pyranometers-solar-radiation-sensors/pyranometers/sr20-pyranometer Accessed January 2023.

Milone D., Peri G., Pitruzzella S., Rizzo G., 2015. Are the Best Available Technologies the only viable for energy interventions in historical buildings?, Energy and Buildings, vol. 95, pp. 39-46. DOI: 10.1016/j.enbuild.2014.11.004.

Pajek L., Potočnik J., Košir M., 2022. The effect of a warming climate on the relevance of passive design measures for heating and cooling of European single-family detached buildings, Energy and Buildings, vol 251. DOI: 10.1016/j.enbuild.2022.111947.

Pandey B., Banerjee R., Sharma A., 2021. Coupled EnergyPlus and CFD analysis of PCM for thermal management of buildings, Energy and Buildings, vol. 231. DOI: https://doi.org/10.1016/j.enbuild.2020.110598.

Pavlik Z., Trnik A., Keppert M., Pavlikova M., Zumar J., Cerny R., 2014. Experimental investigation of the properties of lime-based plaster-containing PCM for enhancing the heat storage capacity of building envelope, International Journal of Thermophysics, vol. 195, pp. 205-215. DOI: 10.1007/s10765-013-1550-8.

Sá A. V., Azenha M., de Sousa H., Samagaio A., 2012. Thermal enhancement of plastering mortars with Phase Change Materials: Experimental and numerical approach, Energy and Buildings, vol. 49. pp. 16–27. DOI: 10.1016/j.enbuild.2012.02.031.

Sinka M., Bajare D., Jakovics A., Ratnieks J., Gendelis S., Tihana J., 2019. Experimental testing of phase change materials in a warm-summer humid continental climate, Energy and Buildings, vol. 195, pp. 205-215. DOI: 10.1016/j.enbuild.2019.04.030.

Smart Advanced Systems GmbH. https://www.smart-advanced-systems.de. Accessed July 2021.

Song Y., Darani K.S., Khdair A.I., Abu-Rumman G., Kalbasi R., 2021. A review on conventional passive cooling methods applicable to arid and warm climates considering economic cost and efficiency analysis in resource-based cities, Energy reports, vol. 7, pp. 2784-2820. DOI: 10.1016/j.egyr.2021.04.056.

#383: Investigation of the air conditioning regulation behaviours and sleep characteristics during sleeping in summer for Chinese

Xiaohui TIAN[1], Shimin LIANG[1], Hui ZHU[1], Jinfu ZHENG[1], Songtao HU[1]

[1] School of Environmental and Municipal Engineering, Qingdao University of Technology, Qingdao, China, liangshimin@qut.edu.cn

Abstract: The sleep environment has an impact on the quality of one's sleep, which is an important stage in the body's recovery of physical and mental energy. Since the body temperature changes during sleep, whether a constant temperature and humid environment can ensure thermal comfort during night sleep has become a major research issue. At the same time, during the summer night sleeping, the bedding microclimate can be adjusted to a lower degree, and thedemand for room temperature is higher. Therefore, in this paper, a questionnaire survey was conducted in China to address the ways of regulating nighttime sleeping in summer and the subjective sleep quality of the occupants. The results showed that 75% of the respondents used air conditioning to regulate the thermal environment while sleeping at night during the summer months. There were differences in subjective sleep quality among respondents in different climate regions, but more than 50% of respondents in all regions woke up during the night due to thermal discomfort. Additionally, 68% of respondents had a need for dynamic temperature change while sleeping at night during the summer months. These results suggested that air conditioning played a very important role in the summer nighttime sleeping process. Therefore, we canavoid the discomfort of constant temperature by considering dynamic adjustment within the desired temperature range ofthe respondents.

Keywords: Summer; Sleep Environment; Thermal Comfort; Air Conditioner

1. INTRODUCTION

People spend a third of their lives sleeping. However, the quality of sleep was closely related to people's health. A report mentioned that sleep problems impaired the quality of life of up to 45% of the world's population (2017). And the thermal environment had a significant impact on sleep quality (Cao et al., 2021a). The using of air conditioning at night while sleeping could provide a comfortable indoor thermal environment (Srisuwan and Shoichi, 2017). It had been documented that air conditioning was installed in bedrooms in all climatic regions except in moderate areas. The proportion of air-conditioning used in cold regions, hot summer and warm winter regions, and hot summer and cold winter regions could reach up to 100 percent (Liu et al., 2019).Wang et al (Wang et al., 2023) showed that most of the interviewed households in hot summer and warm winter regions concentrated their air conditioning use at night (23:00~9:00). Hot and humid environments in the summer could also increase the time spent waking up in the middle of the night, thus impairing sleep efficiency (Tsuzuki et al., 2015). The results of the above studies had shown that air conditioning had become an essential part of indoor thermal environment regulation. Especially during the summer night's sleeping, people chose air conditioning to maintain a comfortable indoor thermal environment and improved the quality of sleep.

The ambient temperature of the bedroom affected the quality of sleep of the occupants. A comfortable thermal environment was important to maintain the quality of sleep, health and productivity of the occupants (Tsuzuki et al., 2015). As a result, the concept of thermally thermo-neutral temperatures had been introduced. Thermo-neutral temperature was the ambient temperature at which the human body theoretically felt neither cold nor hot. Studies had shown that the physiological response of a person during sleeping due to changes in room temperature was not exactly the same as when the person was awake (Muzet et al., 1984, Lavie, 1996, Candas et al., 1982). Chris Leung et al (Leung and Ge, 2013) concluded that the thermoneutral temperature of the human body in the waking state was different from that of the sleeping state. They believed that people could adapt to lower temperatures while sleeping in winter than while awake, and higher temperatures in summer. Lan et al (Lan et al., 2014) conducted sleep experiments at night at 23°C, 26°C, and 30°C. Their results indicated that subjects felt 23°C as a thermo-neutral temperature in the waking state, however, they felt cooler when they slept. These findings suggested that occupants had higher thermoneutral temperatures during sleeping than during wakefulness. Different climate regions had different temperature characteristics and differences in the thermo-neutral temperatures at which occupants sleeping at night. Lin (Lin and Deng, 2006) conducted a survey on the nocturnal sleep of high-rise residential residents in Hong Kong. The results showed that 60% of the residents who used air conditioning woke up at night because of uncomfortable ambient temperatures. And more than 80% of the respondents were comfortable with indoor temperatures below 24°C. Cheng (Cheng and Liu, 2015) conducted a survey study on college dormitories in summer in Harbin City. The results of the experiment indicated that the student's thermo-neutral temperature was 23.2°C and the thermal expectation temperature was 25.2°C. Zhang et al (Zhang et al., 2018) tested dormitories in Beijing. The results of the study indicated that the most satisfactory operating temperature was 24.2°C. However, the results of many studies had indicated (Lan et al., 2014, Lan et al., 2016a, Lan et al., 2016b) that thermal sensation, thermal comfort of subjects in a thermo-neutral environment at constant temperature varies across sleep stages. That is, thermally neutral environments did not necessarily satisfy subjects' thermal comfort throughout the night. Meanwhile, Cao et al andZhu et al suggested that human comfort decreased with increasing time in a steady-state environment. And due to the lack of appropriate hot and cold stimulation, it would reduce the body's immunity, leading to a decline in the body's thermoregulatory capacity and resistance, affecting human health (Cao et al., 2013, Zhu et al., 2016). Therefore, it is necessary to consider dynamic temperature change within the thermal comfort range.

Regulatory behaviour of air conditioning users was variable and diverse (Gu et al., 2023). Therein, the values of the air conditioner's set temperature were significant differences. Wang et al investigated the living environment, thermal comfort, and behavioural regulation of the elderly in residential buildings in Beijing, China. The results of the study indicated that the air conditioning setting temperature for older people in summer was 28.7°C (Wang et al., 2020). Chen et al conducted a questionnaire survey and real-time measurements in a dormitory at a university in China, and the results showed that air conditioning settings between 25°C and 28°C (Chen et al., 2017). However, the thermo-neutral temperatures proposed by existing studies were generally 26°C (Cao et al., 2021b, Tsuzuki et al., 2004, Okamoto-Mizuno and Mizuno, 2012). It could be seen that the occupants' actual air conditioning temperature settings might differ from the thermo-neutral temperatures. However, there was a lack of further research on whether the air-conditioning temperatures set by occupants in different climate regions could satisfy their sleep quality. At the same time, the occupants' dynamic temperature change demands for indoor ambient temperatures and the desired range of changes were still unclear.

Therefore, in this paper, a questionnaire study was conducted to investigate the air conditioning regulation behaviour and subjective sleep quality during the summer night sleeping. The aim of the study was to analyse the subjective sleep quality of people in different climate regions and at comfortable setting temperatures. It also determined the range of sleeping room temperatures desired by the occupants while they slept and the need for dynamic temperature change. This paper can provide data support for the air conditioning regulation mode and dynamic temperature change range during the summer night sleeping. And further satisfy the sleep thermal comfort needs of occupants in different climate regions.

2. QUESTIONNAIRE STUDY CONTENT

2.1. Research Methods

In this paper, the method of questionnaire survey was used, and the air conditioning modes of the bedroom environment and the dynamic temperature change demands during summer sleep were investigated. The questionnaire had a total of 21 questions, most of which were single choices. Among them, air-conditioning habits and the way to regulate waking up from sleep were multiple choice questions.

2.2. Questionnaire contents

The questionnaire was designed according to the purpose of the study and was divided into three sections:

(1) Background questions: Age, sex, and place of residence of respondents.

(2) Air conditioning uses behaviours and sleep characteristics: Respondents' air conditioning usage patterns, temperature settings, whether they had concerns about waking up from cold or heat during sleep, the actual situation of waking up from cold or heat during sleeping, whether they thought the room temperature reached the set temperature, and the measures taken to regulate the temperature.

(3) Dynamic temperature change demand: Whether the respondent expected dynamic changes in indoor temperature, and the desired change profile.

2.3. Research population

The questionnaire was distributed from January 1, 2023 and a total of 571 samples were received, with a male to female ratio of 1:1. Respondents were asked to recall sleep air conditioning use in past summer time periods and to answer the questionnaire.

Respondents were distributed across four climate regions and all age groups were surveyed. The age composition of the respondents and the climatic zone of their residence were shown in Figure 1.

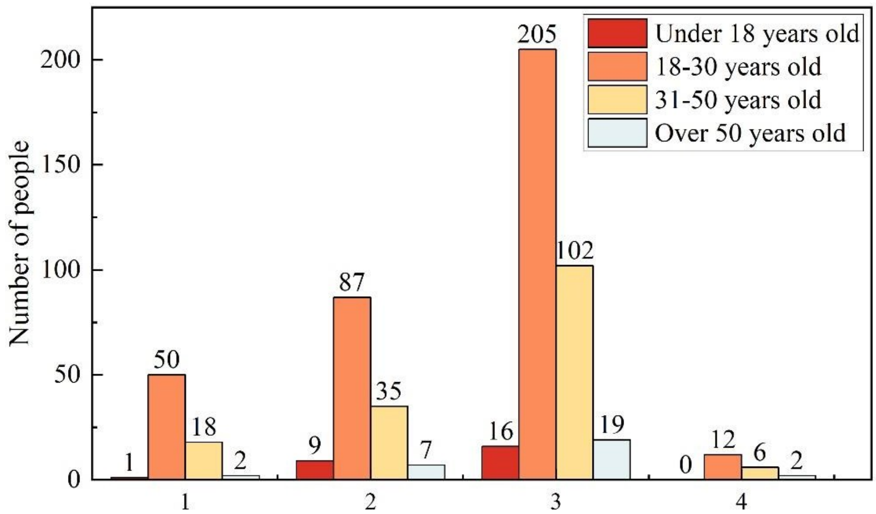

Figure 1: Distribution of respondents by age and place of residence

Abscissa:1-Hot summer and warm winter regions,2- Hot summer and cold winter regions,3-Cold regions,4- Severely cold regions

3. QUESTIONNAIRE RESULTS AND DISCUSSION

3.1. Behaviours of environmental regulation during sleeping at night in summer

There were differences in summer climate characteristics as respondents came from different climate zones. It is therefore assumed that during nighttime sleeping, respondents took different measures to regulate their thermal environment. This study investigated the measures taken to regulate the thermal environment during summer nighttime sleeping. However, due to the changing climatic conditions, respondents would not use only one way to regulate, so this question was set as a multiple-choice question and the results were shown in Figure 2. Figure 2 indicated that 75% of respondents used air conditioners to regulate their thermal environment while sleeping at night during the summer months, 54% used fans to regulate their thermal environment, and only 6% did not take any measures. This result indicated that under the development of today's society, people were more in pursuit of sleep comfort and health and were more concerned about the environment in which they sleep. Air conditioning was widely favoured by occupants in regulating the thermal environment during nighttime sleeping. And it had become the main way to regulate the indoor thermal environment.

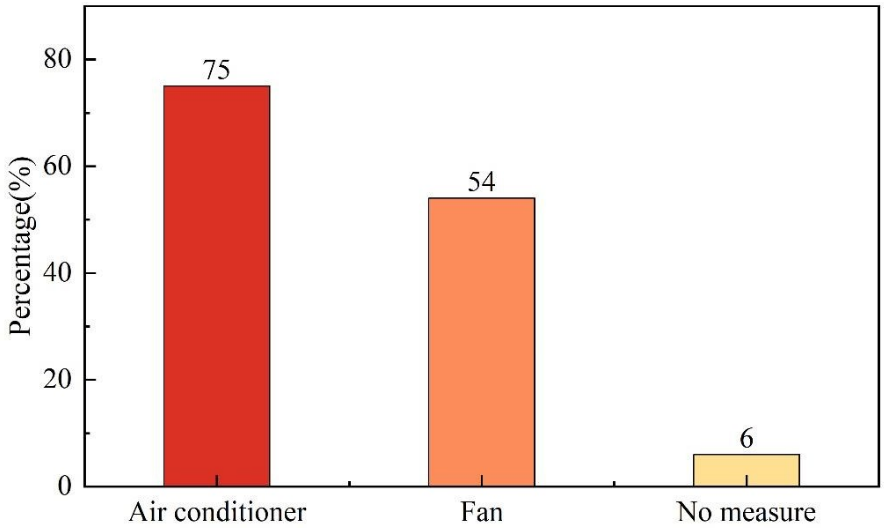

Figure 2: Environmental regulation during nighttime sleeping in summer

When respondents woke up during the night, they tended to take some conditioning measures to fall asleep as quickly as possible. An analysis of the different regulation measures was shown in Figure 3. Figure 3 indicated that during summer nighttime sleeping, when respondents woke up, more than half of them chose to adjust the air conditioner or fan in order to rebalance the thermal environment. Nearly half of the respondents adjusted their bedding coverings or adjusted their clothing, these two measures that were more related to the subjects' sleeping habits. And only 73 of the respondents would choose the measures of opening or closing windows to regulate the thermal environment. From the above data analysis, it could be seen that respondents preferred to use convenient ways to regulate the thermal environment of their sleep, with air conditioning or fans being the primary choices.

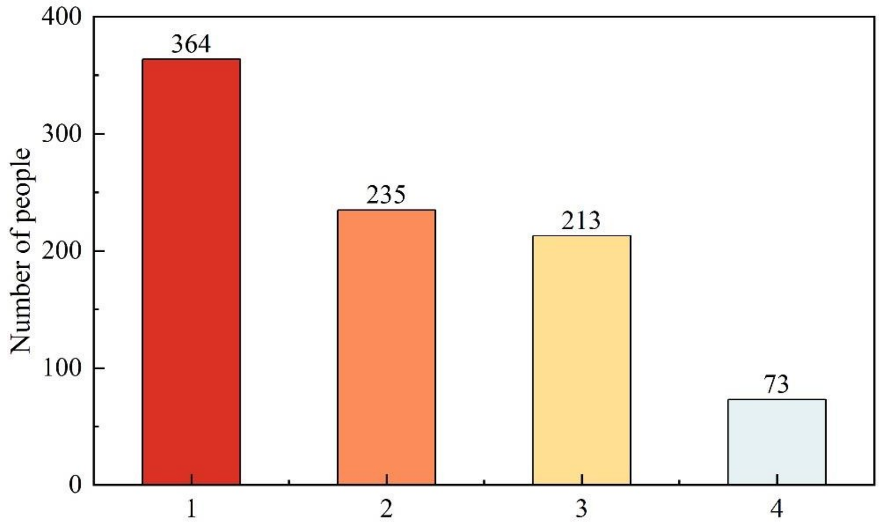

Figure 3: The way people adjust when they wake up from cold or heatAbscissa:1-Adjust the air conditioner or fan,2-Add or subtract bedding,3-Add or subtract clothes,4-Open or close the window

3.2. Subjective sleep quality during nighttime sleeping in summer

Subjective sleep quality in different climate regions

The scope of this survey was for people living in different parts of the country, due to the fact that respondents lived in different cities and therefore in different climatic regions. The summer months were characterized by different climates with differences in indoor and outdoor temperature and humidity, so this paper examined the air conditioning setting temperatures and subjective sleep quality of respondents from different climatic regions. As seen in Figure 4, the average air conditioning setting temperature was highest in hot summer and warm winter regions at 24.2°C, hot summer and cold winter regions at 23.6°C, cold regions had the lowest air conditioning setting temperature at 22.7°C, and severely cold regions had a setting temperature of 23.2°C. It could be seen that there were differences in the subjective temperature settings of the respondents between different climate regions, which might be related to humidity and the effect of bedding on the body's thermal sensation.

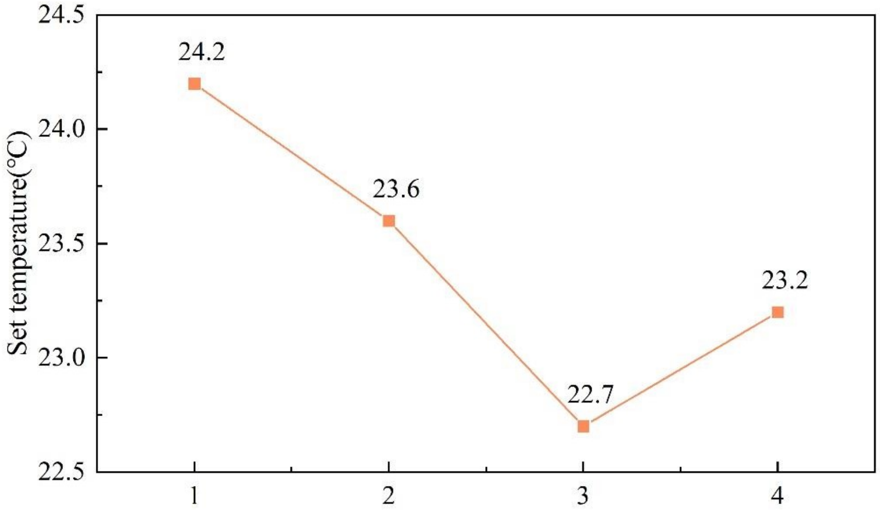

Figure 4: Air conditioner set temperature of respondents in different climate regions

Abscissa: 1-Hot summer and warm winter regions,2- Hot summer and cold winter regions,3-Cold regions,4- Severely cold regions

From Figure 5, it could be seen that 64% of the respondents in hot summer and warm winter regions woke up from cold or heat during summer night sleeping, 65% of the respondents in hot summer and cold winter regions woke up from cold or heat during summer night sleeping, 71% of the respondents in cold regions woke up from cold or heat during summer night sleeping, and 75% of the respondents in severely cold regions woke up from cold or heat during summer night sleeping. It could be seen that the subjective quality of sleep was worst for respondents in the severely cold regions in different climatic regions and best for respondents in the hot summer and warm winter regions.

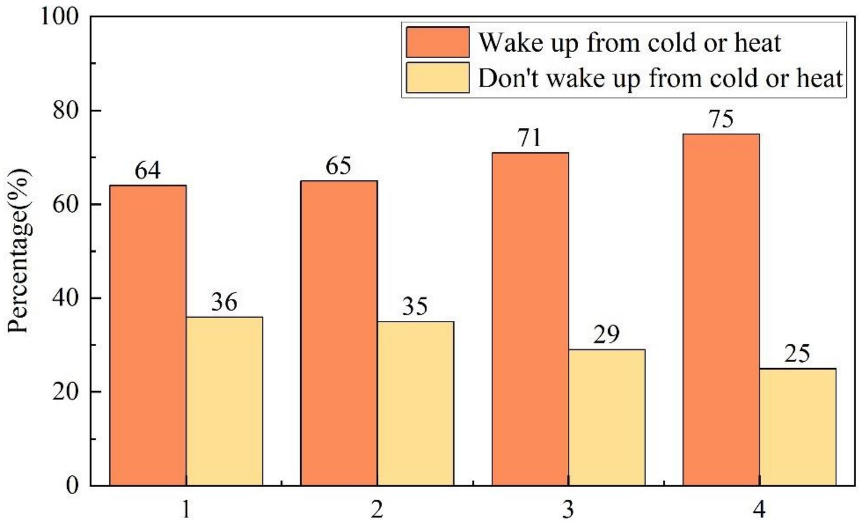

Figure 5: Comparison of waking up from cold or heat among respondents from different climate regions

Abscissa:1-Hot summer and warm winter regions,2- Hot summer and cold winter regions,3-Cold regions,4- Severely cold regions

Subjective sleep quality when reaching the set temperature

Respondents' air-conditioning turn-on temperatures during nighttime sleeping were mostly set when they were awake. However, thermo-neutral temperatures were different in waking and sleeping states, so air conditioning temperature settings before bed would affect sleep. This paper therefore analysed the subjective quality of sleep when the respondents perceived that the set temperature was reached during sleep. As could be seen from Figure 6, even when respondents thought that the temperature reached the set temperature during summer night sleeping, 64% of respondents woke up from cold or heat during sleeping. Meanwhile, from Figure 7, it could be seen that the most cases of waking up from cold or heat were found when the set temperature was 21-22°C, and the least cases of woke up from cold or heat were found when the set temperature was 25-26°C. As a result, sleep quality was slightly better at 25-26°C. However, since the respondents were awake at the time of setting the air conditioning temperature, there were differences in the assessment of the thermo-neutral temperature of the sleep state, which could lead to waking up at night due to thermal discomfort.

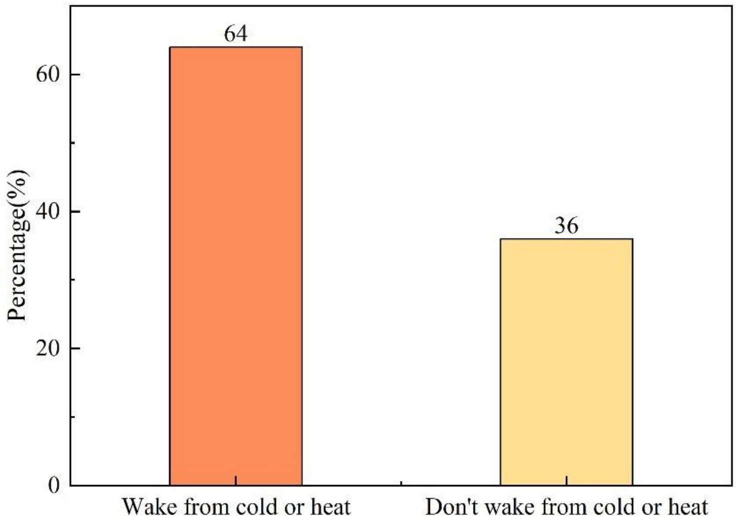

Figure 6: Respondents' perception of waking up from cold or heat when setting temperature was reached

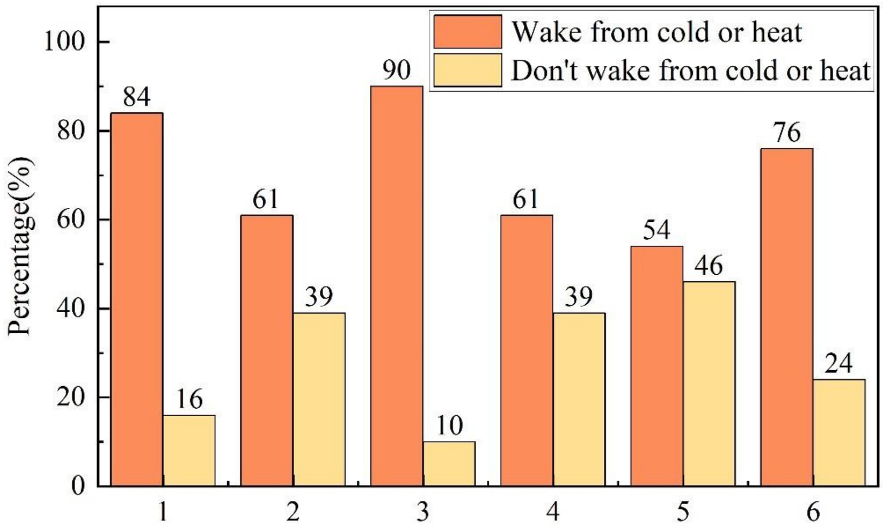

Figure 7: Respondents' perception of waking up from cold or heat at different set temperatures

Abscissa:1-[16°C,18°C],2-[19°C,20°C],3-[21°C,22°C],4-[23°C,24°C],5-[25°C,26°C],6-[27°C,29°C]

In addition, some respondents believed that the temperature required during sleeping was different from that at bedtime, so they adjusted the temperature up or down when setting the temperature at bedtime to accommodate the sleep state. However, as could be seen from Figure 8, 83% of the respondents would wake up from cold or heat when the temperature was turned up, and 86% of the respondents would wake up from cold or heat when the temperature was turned down. Therefore, turning the temperature up or down would still result in most of these respondents woken up from cold or heat. So, a temperature change at night could be considered to avoid the effects of setting a thermo-neutral temperature at bedtime on sleep state.

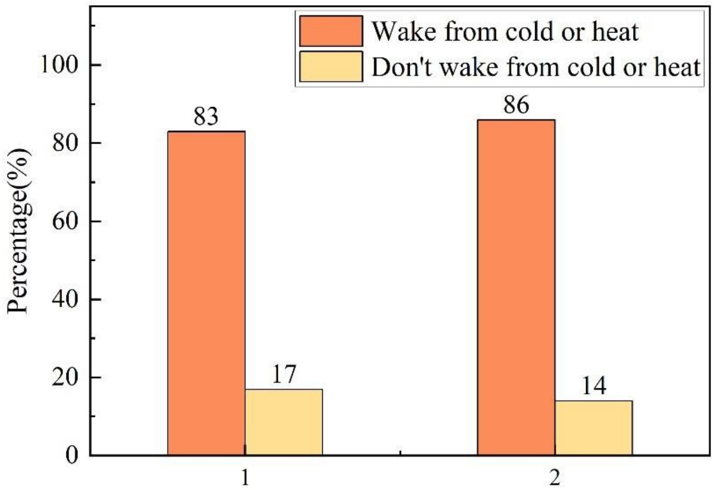

Figure 8: After taking temperature control measures, the situation of waking up from cold or heat

Abscissa:1- Turn up the temperature before bedtime,2- Turn down the temperature before bedtime

3.3. Desired indoor temperature range for sleeping at night in summer

According to section 3.2, it could be seen that there was a difference between the air conditioning temperature set by the respondents before going to bed and the temperature they needed to sleep. This difference could cause respondents to wake up during the night due to thermal discomfort. Therefore, this paper addressed the range of indoor temperatures that respondents expected during the summer nighttime sleeping period. From Figure 9, 49% of the respondents expected the indoor temperature to be 20-24°C, 42% of the respondents expected the indoor temperature to be 24-28°C, and only 6% and 3% of the respondents expected the indoor temperature to be below 20°C and above 28°C.

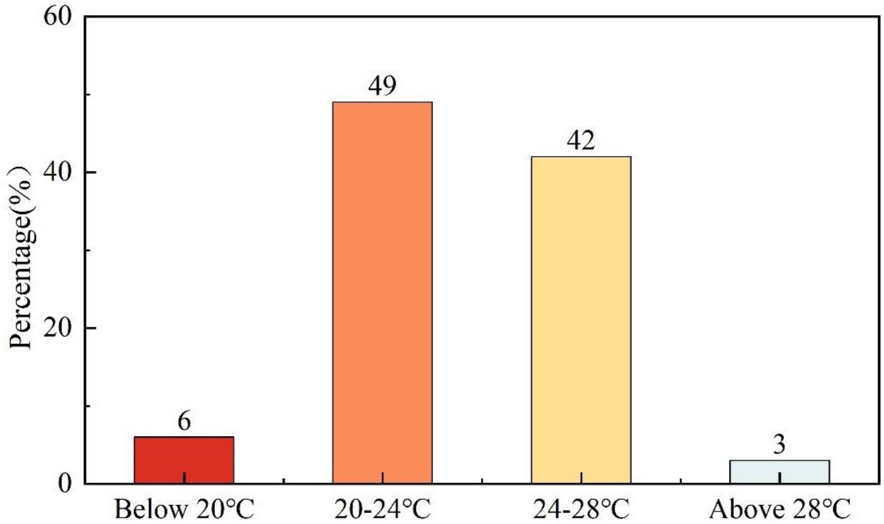

Figure 9: Respondents' desired indoor temperatures

There were circadian rhythms in people's sleep mechanisms and thermoregulatory mechanisms. Therefore, this paper analysed the dynamic thermoregulatory needs of respondents during summer night sleeping. As could be seen from Figure 10, 68% of respondents expected dynamic temperature change during summer night sleeping, reflecting the demand for dynamic temperature change. In conjunction with Figure 9, it could be seen that variable temperatures within 20-24°C could be considered to adapt to the occupant's sleep stage during the summer night sleeping to meet the occupant's thermal comfort throughout the night.

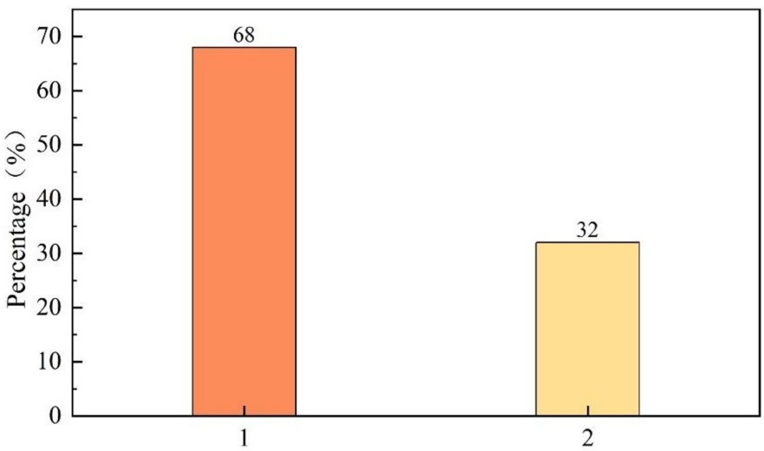

Figure 10: Dynamic temperature change demand during nighttime sleeping in summer

Abscissa:1- Expect dynamic indoor temperature change,2- Do not expect dynamic indoor temperature change

4. CONCLUSION

This paper analysed the way in which respondents regulated their sleep environment and their subjective sleep quality during summer night sleeping, and the conclusions were as follows:

1. Respondents tend to use air conditioning to regulate their sleep at night during the summer. Yet only 6% of respondents did not take any measures. And among the different climate regions, respondents in severely cold regions had the worst nighttime sleeping quality and respondents in hot summer and warm winter regions had the best nighttime sleeping quality.

2. 64% of respondents would set the temperature on the high or low side of the comfort temperature during nighttime sleeping. This was because they were concerned about waking up at night due to uncomfortable temperatures. However, more than 80% of respondents woke up during the night, and more woke up due to turning down the temperature. In addition, even though respondents believed that the temperature was at the set temperature during sleep, 64% of respondents woke up from cold or heat. In addition, 21-22°C was the temperature at which respondents were most likely to wake up at night.

3. Through the survey on the respondents' desired temperature and dynamic temperature change demand, 49% of the respondents preferred the indoor temperature of 20-24°C for sleeping at night in the summer, and 42% of the respondents preferred the indoor temperature of 24-28°C for sleeping at night in the summer. At the same time, 68% of the respondents had the need for dynamic temperature change.

The findings of this paper indicated that occupants tended to use air conditioning to regulate their thermal environments while sleeping at night during the summer. The subjective quality of sleep and air conditioning set temperature varied among respondents in different climate regions due to the influence of climate. At the same time, the majority of respondents woke up when they slept at different comfortable temperatures, and the majority of respondents had dynamic temperature change needs. Therefore, more research is needed to determine the different needs of occupants for thermal environments during nighttime sleeping and the dynamic thermoregulation curves.

5. ACKNOWLEDGEMENT

This work was supported by the National Natural Science Foundation of China the granted number 52078257 and the Shandong Provincial Natural Science Foundation the granted number ZR2022ME148.

6. REFERENCES

2017. World sleep day，http://worldsleepday.org/toolkit [Online]. [Accessed].

CANDAS, V., LIBERT, J. P. and MUZET, A. 1982. Heating and cooling stimulations during SWS and REM sleep in man. Journal of Thermal Biology, 7, 155-158.

CAO, B., SHANG, Q., DAI, Z. and ZHU, Y. 2013. The Impact of Air-conditioning Usage on Sick Building Syndrome during Summer in China. Indoor and Built Environment, 22, 490-497.

CAO, T., LIAN, Z., MA, S. and BAO, J. 2021a. Thermal comfort and sleep quality under temperature, relative humidity and illuminance in sleep environment. Journal of Building Engineering, 43, 102575.

CAO, T., LIAN, Z., ZHU, J., XU, X., DU, H. and ZHAO, Q. 2021b. Parametric study on the sleep thermal environment. Building Simulation, 15.

CHEN, S., ZHUANG, Y., ZHANG, J., FU, Y. and ZHANG, H. 2017. Statistical Characteristics of Usage Behavior of Air Conditioners in The University Students' Dormitories. Procedia Engineering, 205, 3593-3598.

CHENG, W. and LIU, Y. 2015. Research on the indoors thermal environment of university student dormitory in Harbin during summer. Fluid Machinery, 43, 79-82.

GU, X., LIU, M., LI, Z., LIU, H., CHEN, X. and DAI, L. 2023. Dynamic thermal demand analysis of residential buildings based on IoT air conditioner. Building and Environment, 243, 110593.

LAN, L., LIAN, Z. W. and LIN, Y. B. 2016a. Comfortably cool bedroom environment during the initial phase of the sleeping period delays the onset of sleep in summer. Building and Environment, 103, 36-43.

LAN, L., LIAN, Z. W., QIAN, X. L. and DAI, C. Z. 2016b. The effects of programmed air temperature changes on sleep quality and energy saving in bedroom. Energy and Buildings, 129, 207-214.

LAN, L., PAN, L., LIAN, Z., HUANG, H. and LIN, Y. 2014. Experimental study on thermal comfort of sleeping people at different air temperatures. Building and Environment, 73, 24-31.

LAVIE, P. The enchanted world of sleep. 1996.

LEUNG, C. and GE, H. 2013. Sleep thermal comfort and the energy saving potential due to reduced indoor operative temperature during sleep. Building and Environment, 59, 91-98.

LIN, Z. and DENG, S. 2006. A questionnaire survey on sleeping thermal environment and bedroom air conditioning in high-rise residences in Hong Kong. Energy and Buildings, 38, 1302-1307.

LIU, J., HONG, W. and LAI, D. 2019. Long-term monitoring of subjective sleep thermal comfort and adaptive behavior in ninecities of China. HVAC, 49, 8.

MUZET, A., LIBERT, J. P. and CANDAS, V. 1984. Ambient temperature and human sleep. Experientia, 40, 425-9.

OKAMOTO-MIZUNO, K. and MIZUNO, K. 2012. Effects of thermal environment on sleep and circadian rhythm. J Physiol Anthropol, 31, 14.

SRISUWAN, P. and SHOICHI, K. 2017. Field Investigation on Indoor Thermal Environment of a High-rise Condominium in Hot-humid Climate of Bangkok, Thailand. Procedia Engineering, 180, 1754-1762.

TSUZUKI, K., MORI, I., SAKOI, T. and KUROKAWA, Y. 2015. Effects of seasonal illumination and thermal environments on sleep in elderly men. Building and Environment, 88, 82-88.

TSUZUKI, K., OKAMOTO-MIZUNO, K. and MIZUNO, K. 2004. Effects of humid heat exposure on sleep, thermoregulation, melatonin, and microclimate. Journal of Thermal Biology, 29, 31-36.

WANG, M., LI, Q., WANG, F., YUAN, Z., WANG, L. and ZHOU, X. 2023. Residential indoor thermal environment investigation and analysis on energy saving of air conditioning in hot summer and warm winter zone in China. Urban Climate, 47, 101369.

WANG, Z., CAO, B., LIN, B. and ZHU, Y. 2020. Investigation of thermal comfort and behavioral adjustments of older people in residential environments in Beijing. Energy and Buildings, 217, 110001.

ZHANG, N., CAO, B. and ZHU, Y. 2018. Indoor environment and sleep quality: A research based on online survey and field study. Building and Environment, 137, 198-207.

ZHU, Y., OUYANG, Q., CAO, B., ZHOU, X. and YU, J. 2016. Dynamic thermal environment and thermal comfort. Indoor Air, 26, 125-37.

#393: Introducing PV grid-parity to Yemen power system

Experimental and feasibility studies

Ali M. AL-ASHWAL[1], Osamah Eskandar SHERHAN[2], Omar Omer Ahmed OBAD[3], Mazen Mofadl ALMASHWALI[4]

[1] Lebanese International University, Sana'a Campus, Yemen, amashwal48@gmail.com
[2] Lebanese International University, Sana'a Campus, Yemen, osamaheskander@gmail.com
[3] Lebanese International University, Sana'a Campus, Yemen, omar.o.abbad@gmail.com
[4] Lebanese International University, Sana'a Campus, Yemen, mazen_mofadl@hotmail.com

Abstract: The imposition of a blockade on Yemen by the coalition led by Saudi Arabia resulted in severe fuel scarcity, leading to a lack of electricity from fossil fuel-based sources like diesel-based generation. In response, households and other energy consumers sought alternative power supply options. Accordingly, PV Systems emerged as the most economically viable, commercially available, and sustainable solution. Consequently, a rapid diffusion of PV Solar Home Systems (SHS) led to sudden dissemination and significant growth of the PV SHS market. Numerous traders, including ordinary shops, entered the business of selling PV SHS, creating a thriving market during the blockade period. Eventually, the Yemen power system will not only return to its initial state but should also grow further to meet the increasing demand from households and other customers. Consequently, a substantial amount of installed PV power of SHS which might reach hundreds of Mega Watts (MW), could go into power demand side trading. In this case, technically adapting the Grid-Parity practice becomes economically feasible and environmentally beneficial. This study is a pilot project to examine various aspects of Grid-Parity application: technical, viable, and environmental. This paper presents an experimental demonstration of the high potential of the Grid-Parity application and an essential initiative for its future diffusion in Yemen. In addition, an economic assessment is performed, showing the viability of Grid- Parity in Sana'a. Thus, it irrefutably covers the technical, financial, and environmental aspects.

Keywords: Photovoltaic (PV), Solar Home System, Grid-Parity, Experiment, Feasibility, Environmental Impact

1. INTRODUCTION

The imposition of a blockade on Yemen by the coalition led by Saudi Arabia resulted in a severe scarcity of fuel, leading to a lack of electricity from fossil fuel-based sources like diesel-based generation. In response, households and other energy consumers sought alternative power supply options. Accordingly, the use of PV Systems emerged as the most economically viable, commercially available, and sustainable solution. Consequently, a rapid diffusion of PV Solar Home Systems (SHS) led to sudden dissemination and significant growth of the PV SHS market. Numerous traders, including ordinary shops, entered the business of selling PV SHS, creating a thriving market during the blockade period. According to (Al-Ashwal, 2019, pp. 382-389) the estimated installed peak power in Sana'a may reach 120 MWp.

Eventually, the Yemen power system will not only return to its initial state but should also grow further to meet the increasing demand from households and other customers. Consequently, a substantial amount of installed PV power of SHS which might reach hundreds of Mega Watts (MW), could go into power demand side trading. This Project is concerned with Photo Voltaic (PV) technology application as an energy source for different purposes, particularly for household electrification which could be connected to Grid, i.e. Grid-Parity. The Grid-Parity practice has gained in recent decades special importance as stated by (Breyer, 2013), who said that the Grid-Parity is a tipping point for solar dominance in the energy market. This Paper presents Experimental and Feasibility Studies, and the Environmental Impact of Grid-Parity in Sana'a, Yemen. The Experiment Setup consists of experiment objectives, setup components, site conditions, measurements, and calculations. Further experimental results were obtained in the form of daily records presented here. Then, graphs reflecting system performance are presented and calculations are carried out. Finally, a Feasibility evaluation and environmental impact based on local conditions are performed. Finally, necessary conclusions are derived.

2. EXPERIMENTAL SETUP AND EXPERIMENT

2.1. Experimental Objectives

The objectives are to measure all parameters concerning the generated energy of the PV system, and the conversion of this energy from DC into AC, hence transmitting it to the grid during the daytime starting at 09:05 and ending at 16:30. The measured parameters include irradiance, array voltage, and current as an input to the Inverter, the output voltage and current of the inverter, inverter frequency, generated electric energy, and the harmonics injected into the grid.

2.2. Ownership

The sponsor and project owner are the Lebanese International University (LIU), Sana'a Campus. The location is on the roof of the Educational Building of LIU, Sana'a Campus. The output of the PV System is connected to the Power System of LIU representing the Grid. The Campus has two sources of supply, namely National Grid and LIU local diesel generation.

2.3. Setup Components

As shown in Figure 1, the components consist of (a) 12 PV panels of 12 V and 260 Wp (yields 3.12 kWp.); (b) a Well-known on-grid MPPT interactive Inverter and Controller; (c) Power Quality Analyser SA2100 (6000 sample/second). (d) Solar Radiation Meter. (e) Energy meter (f) Clamp Ammeters and Voltmeters.

2.4. Site Conditions

Site Conditions are: Solar declination angle (α) = -21.3°, latitude angle(ϕ) = 15.3694° North, Tilted angle (β) = 15°, Solar azimuth(ɣ) = 15°, longitude = 44.19, Altitude = 2200 m. Minimum ambient temperature could reach -3 C°. Maximum ambient temperature could reach +35 C°.

2.5. Measurements

The measurements were taken every 5 minutes and covered the following parameters: Irradiance, Inverter Input and Output Voltage, Current, and Powe, Transmitted Energy to the Grid, output Frequency, and Third and Fifth Harmonic content for Inverter Voltage and Current. These measurements were taken for 7 months. However, five days were selected as samples to demonstrate the system's performance. Figures 2 to 9 show samples of parameter waveforms.

2.6. Calculations

The calculation includes the daily average of Inverter Input and Output voltages, current, and Powers. In addition, the Efficiency of PV Panels, overall System Efficiency, daily generated panel energy, and daily generated transmitted energy to the grid. Finally, daily average powers and harmonic content were also calculated.

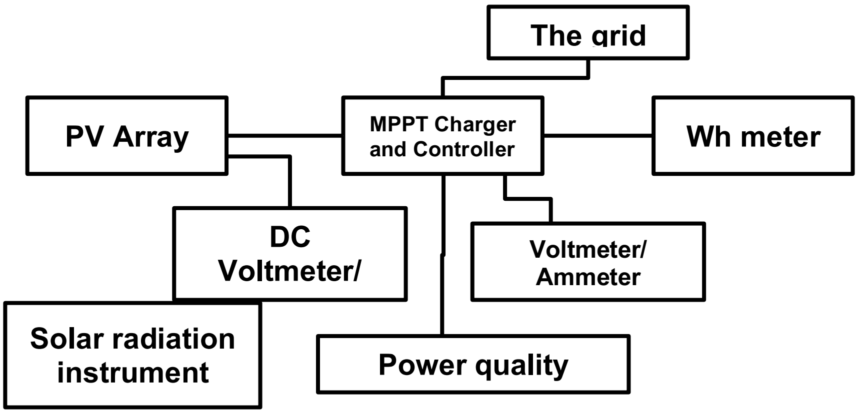

Figure 46: Experiment set-up block diagram

3. EXPERIMENTAL RESULTS AND RESULT DISCUSSION

3.1. Experimental Results

- Two days were selected to demonstrate PV Grid-Parity performance, namely two measurements taken on July 14 and August 4. The measurements include Irradiance, Panel Voltage and Inverter Voltage, Panel Currents and Inverter Current, Panel Power, and Inverter Power. These charts are shown in Figures 2 to 9.
- The reading of the kWh meter, included in the experimental setup, showed 3009 kWh after 215 days of recording. This number of days can be assumed sufficient to calculate the daily average energy generated by the system because the average deviation of monthly solar radiation is around 1.1% (HelioClim-3 Archive Database of Solar Irradiance v5). This result gives a daily PV-generated energy average of 13.995 kWh.
- At the same time, the theoretical calculation for the daily average of yield energy was performed, resulting in E_{sys} = 14.368 kWh (Krauter, 2006), (Wenham, 2006). The Appendix depicts the average insolation calculation for a year assuming the peak sun hours (PSH) equals 7.44 for the site conditions. It is interesting to notice that the difference between calculated and measured is less than 2.6%. The small difference between experimental and theoretical calculations proves the correctness and preciseness of both methods.

3.2. Calculation Results

The power source is solar radiation which falls to the PV panel surface. As shown in Fig. 1 an instrument to measure the irradiance (W/m^2) is fitted to the system, as the irradiance is the fundamental component of PV energy generation. The calculated parameters, based on section 2.5 of the paper are the following daily average values:

Irradiance intensity (I_{ri}) (W/m^2), PV array output values (Power (P_{ar}), current (I_{ar}), voltage (V_{ar})), and Inverter output values (current (I_{inv}), voltage (V_{inv}), power (P_{inv}), frequency (f)). Further parameters are calculated too, namely: current third harmonics (THD), array efficiency (η_{ar}), Inversion efficiency (η_{inv}), and daily solar radiation (S_{rd} [kWh], PV array generated Energy (E_{PV}), transmitted Energy to the grid (E_{trans}). The calculation is carried out for two sample days, namely July 14 and August 4.

The following table shows the calculation results:

Table 1: Calculation Results

No	Measurement date / Parameter	July 14	Aug. 4	No	Measurement date / Parameter	July 14		Aug. 4	
1	I_{ri} [W/m^2]	752	383	8	f [Hz]	50.19		50.68	
2	Par [kW]	1.908	1.06	9	THD [%]	THDi	THDv	THDi	THDv
						12.9* 27.7**	4* 5.3**	10.3* 18.7**	4* 5.2**
3	I_{ar} [A]	16.842	9.68	10	η_{ar} [%]	13.1		14.52	
4	V_{ar} [V]	113.444	110.3	11	η_{inv} [%]	89.89		93.46	
5	I_{inv} [A]	8.102	4.576	12	E_{irr} [kWh]	9963.077		1201.431	
6	V_{inv} [V]	221	220.3	13	E_{PV} [kWh]	14.30693		7.949496	
7	P_{inv} [kW]	1.781	0.991	14	E_{trans} [kWh]	13.3		7.4	

*Minimum value; **maximum value

3.3. Result Discussion

Calculations

- It is worth noticing that the obtained maximum output power is around 80% of array rated peak power (P_{ar}), i.e. P_{ar} =3120 Wp, as the actual at-site measured P_{max} = 2472.8 W. The obtained result differs from the rated because thesite conditions do not satisfy the standard test conditions. The ratio of P_{max} (at site) to P_{max} (rated) = 0.7926 for a clear day (July 14). However, for August 4, P_{max} = 2198.85 W. The ratio of P_{max} (at site) to P_{max} (rated) = 0.705. Theseresults show that the user should expect a reduction at the site in Sana'a, Yemen 20% to 30% of the selected PV peak power.
- The efficiency of higher output power is less than the lower output power. This is due to temperature increases with higher power, which leads to a reduction in efficiency.
- Harmonic distortion of the Third Harmonic is shown for both voltage and current in both measurement samples. THDi content reached around 28% in the July 14 measurement, which is unacceptable. However, (Ahsan, 2021, p. 3709) has shown the dependency of harmonic distortion on the load type, where a very high level occurs withelectronic loads, e.g. computers, mobile chargers, LED light, and fluorescent lamps, etc. cause very high harmonic distortion. It is worth mentioning that the PV system is connected to the LIU distribution network in the daytime when the load consists mostly of the appliances mentioned above. This fact is behind the abnormal level of harmonic distortion. To mitigate high harmonic levels (Ahsan, 2021, p. 3709) proposes a simple treatment calleda distributed filtering scheme for residential networks.

Measurements (Plots)

Measurements for July 14th and August 4th are provided in this section.

A. Charts related to July 14 records

July 14 was a clear day. The irradiance curve is shown in Figure 2 which reflects this situation, where the maximum value reached around 1000 W/m^2.

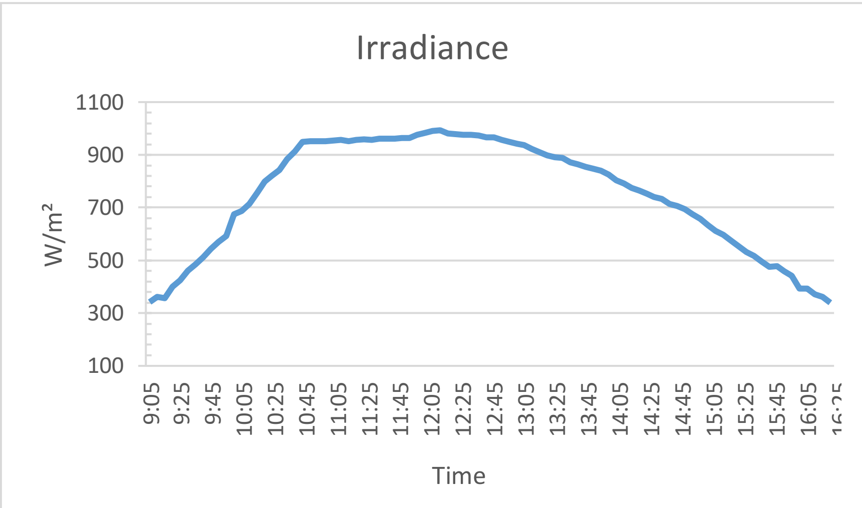

Figure 2: Irradiance measurement on 14th July

Figure 3 shows the array voltage (DC) and output voltage of the Inverter (AC). As the array voltage has slight calibration the inverter voltage is practically constant, which reflects the high quality of the used MPPT interactive inverter. Figure 4 shows the waveform of the array current (DC) and output current of the Inverter, due to variation of irradiance the current varies. Due to the inherent existence of the energy storage elements in the PMMT controller, the inverter current goes smoother than the array current.

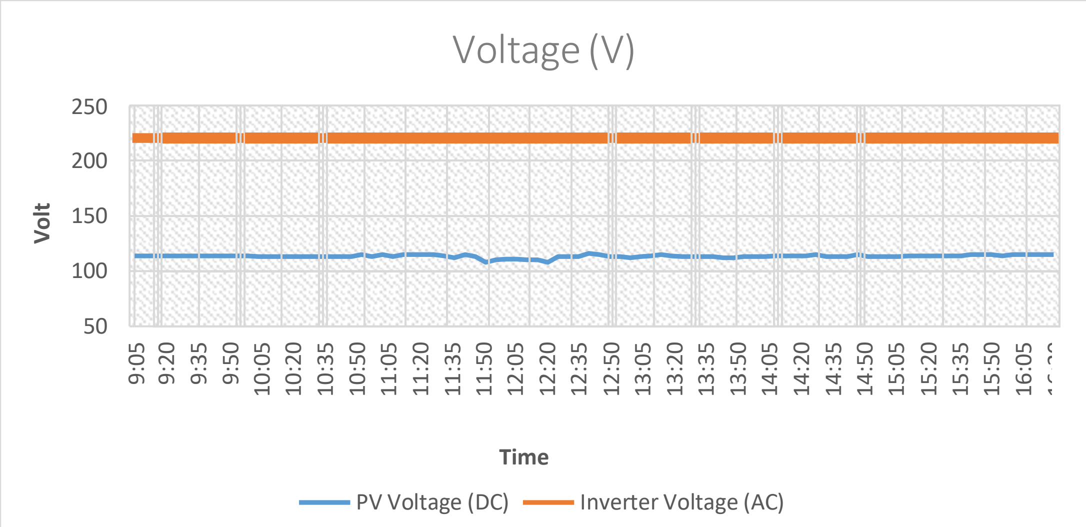

Figure 3: Voltage measurement on 14th July

Figure 5 is related to the powers generated by the PV array and sent to the Grid. The sent power is less than the generated power due to losses associated with the inversion process and produced heat. The losses are bigger with higher power generation.

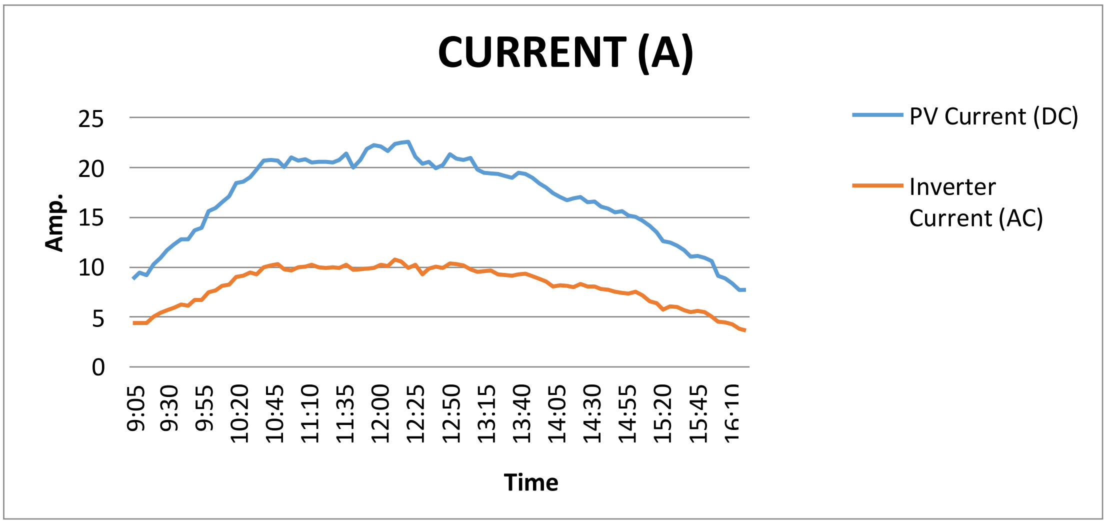

Figure 4: Current measurement on 14th July

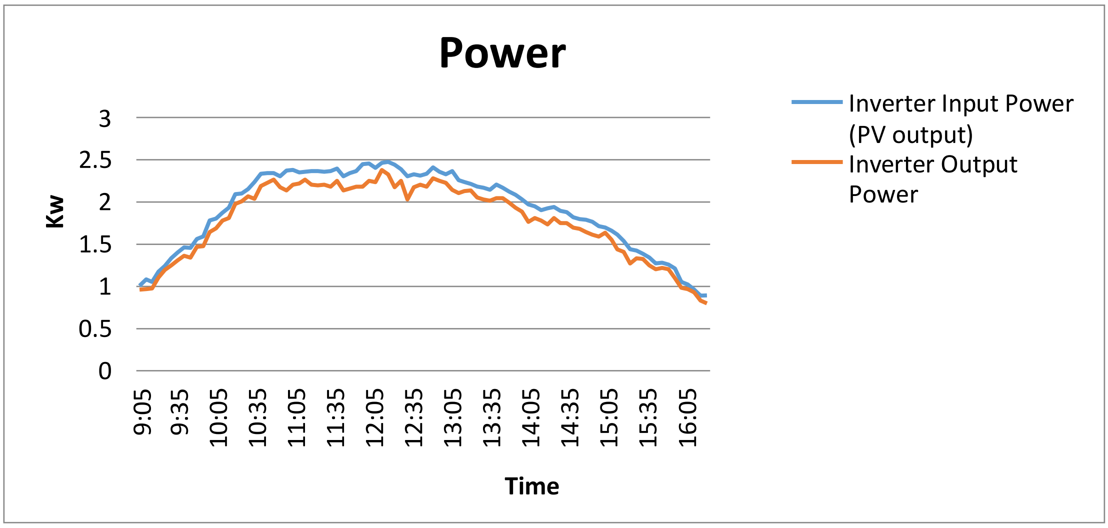

Figure 5: Power measurement on 14th July

B. Charts related to August 4 records

On the 4th of August, the weather was mostly cloudy. Therefore, the irradiance is significantly variable and has less magnitude than July 14 records as shown in Figure 6. In addition, there is a big difference between the peak and trough values. However, the waveform of the array voltage (DC) and output voltage of the Inverter (AC) is verysimilar to July 14 records. The array voltage has slight calibration as the inverter voltage (AC) is practically constant (see Figure 7). Figure 8 shows the waveform of the array current (DC) and output current of the Inverter, due to variation of irradiance the array current sharply varies. However, the inverter current goes much smoother than the array current, due to the inherent existence of energy storage elements in the PMMT controller. It can also be seen that the array current is lagging the irradiance in 5 minutes. Figure 9 is related to the power generated by the PV array and the power sent to the Grid of August 4th records. The sent power is close to the generated power due to lower losses associated with this case, which was cloudy, hence the generated heat is less, and the losses are small with lower power generation.

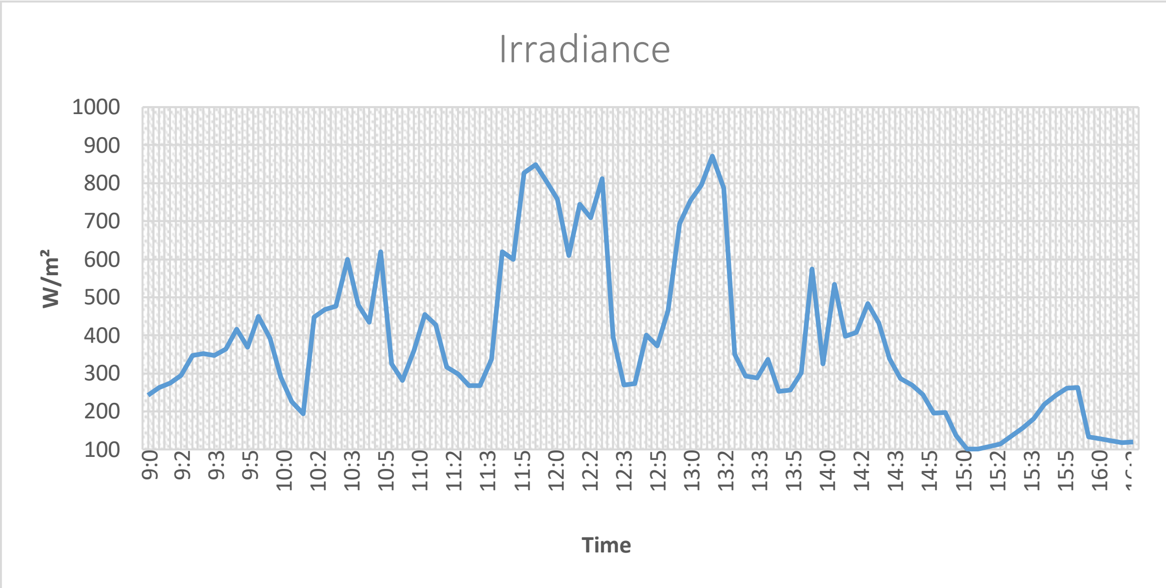

Figure 6: Irradiance measurement on 4th August

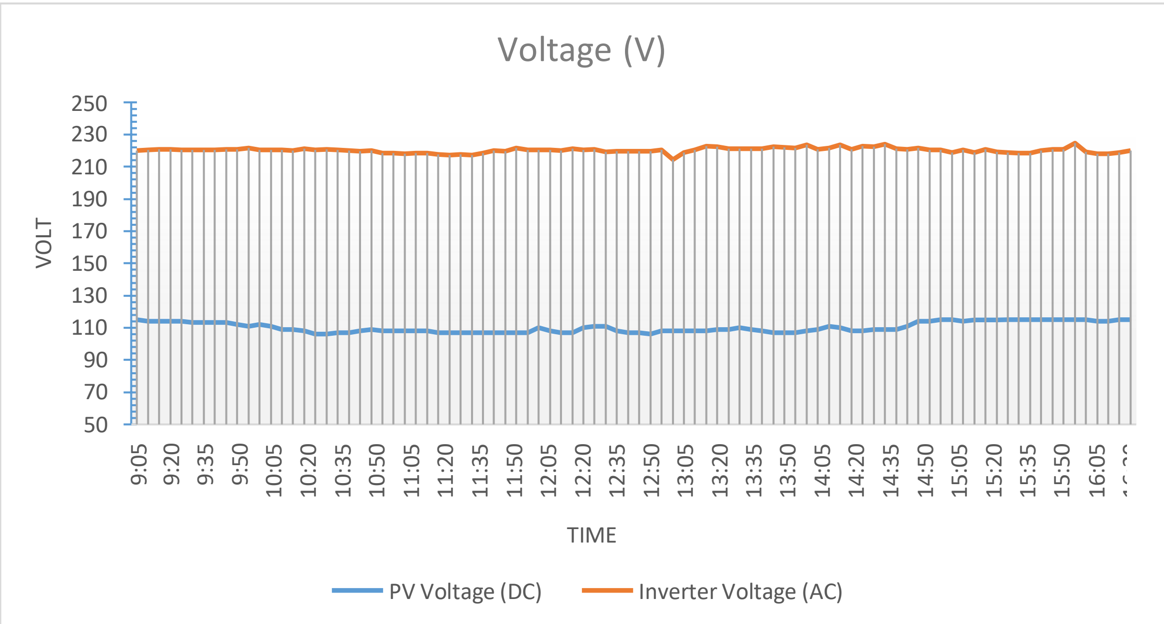

Figure 7: Voltage measurement on 4th August

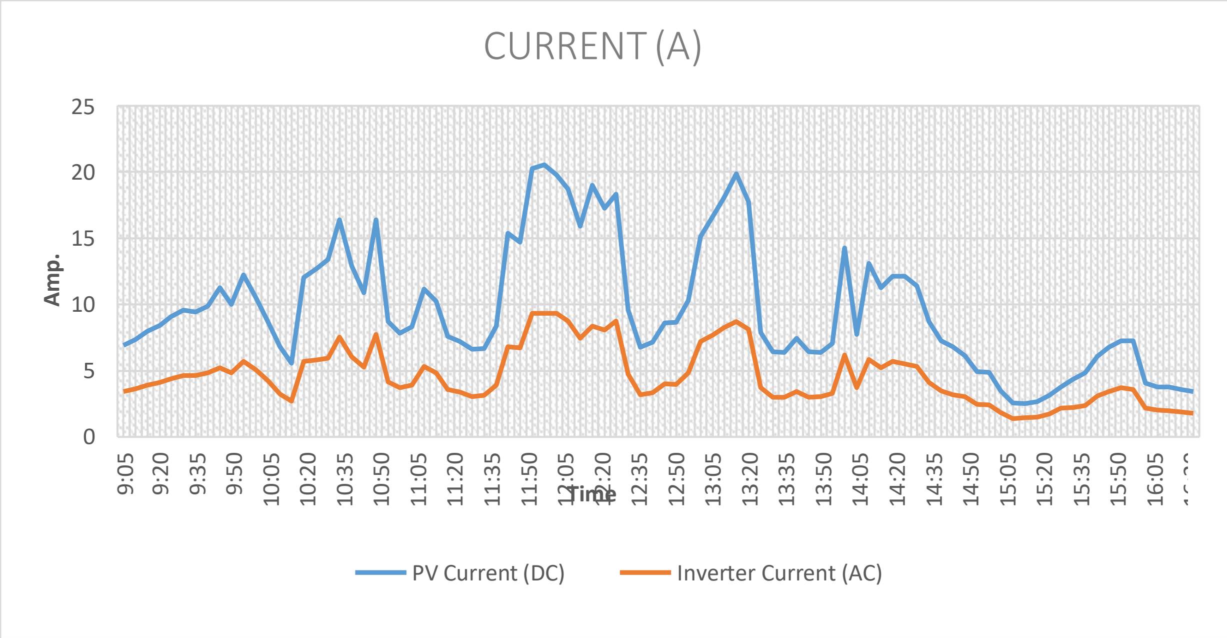

Figure 8: Current measurement on 4th August

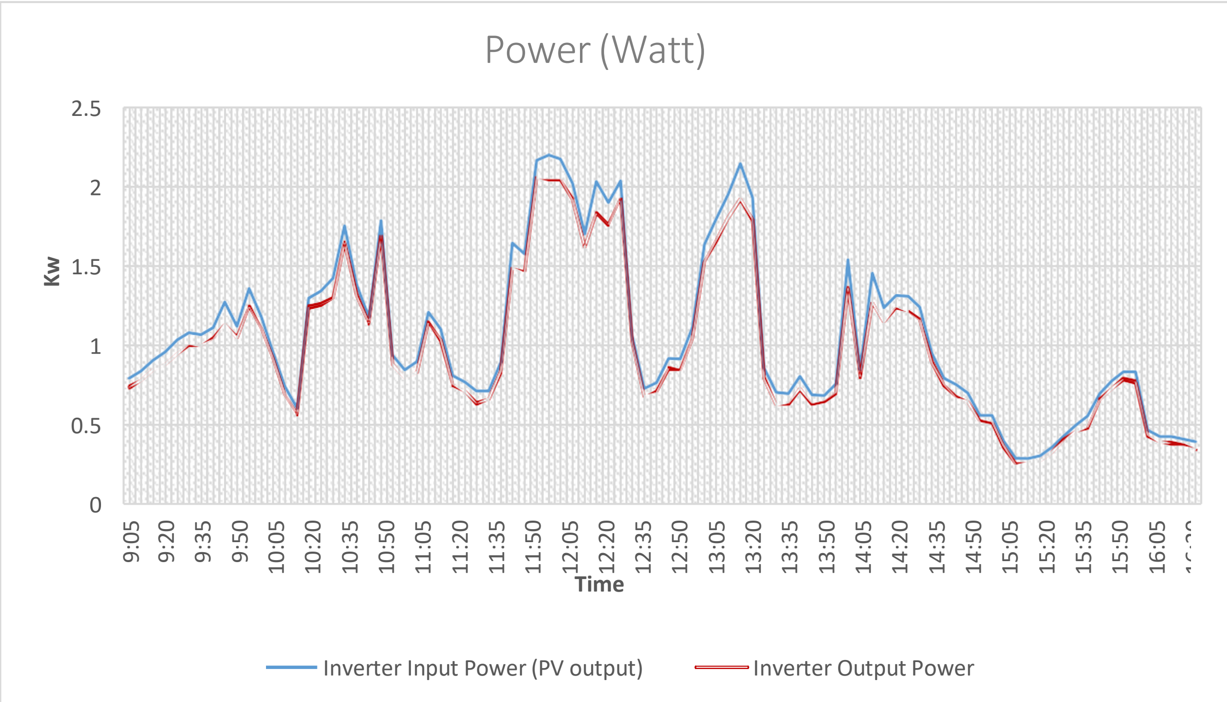

Figure 9: Power measurement on 4th August

4. GRID-PARITY FEASIBILITY

The concept of Grid-Parity is influenced by several factors (Kamran M. et al., 2019, p. 244). In the case of Sana'a, Yemen, a significant factor is the high penetration of Solar Home Systems (SHS), having a penetration rate of 87.37% among households (Al-Ashwal, 2019, Vol. 1, p. 44). This high diffusion rate enhances the country's feasibility of implementing Grid-Parity solutions because the low diffusion rate is considered a challenging factor for project implementation of the Grid-Parity dissemination.

Grid-Parity is generally deemed achievable when the cost of electricity from a Photovoltaic (PV) system equals or is less than that from the other conventional sources. The Levelized Cost of Energy (LCOE) serves as a crucial tool for quantitatively assessing Grid-Parity (Adeyemi-Kayode et al., 2023, p. 16) (Kamran M. et al., 2019, p. 244).

The LCOE represents the lifetime cost of electricity generated by a PV system, compared against current retail electricity prices from other sources. This comparison is vital because while grid electricity prices are subject to change, the LCOE for PV remains fixed once the system is purchased.

When evaluating PV Grid-Parity viability LCOE should ideally be compared against current electricity prices and adjusted for estimated future increases in these prices.

Calculating LCOE involves two key variables:

1. All-in cost for the system (capital costs): This includes initial investment, financing costs, and subtracting any incentives received (e.g., tax credits).

2. Lifetime energy production of the solar array, which determines how much energy the system will produce over its operational lifespan.

Equation 1 is the interpretation of these points

Equation 1

$$LCOE = \frac{Life\ cycle\ cost\ of\ solar\ project}{Lifetime\ energy\ production\ of\ solar\ project}$$

The mathematical expression of LCOE is Equation 2

Equation 2

$$\sum_{t=1}^{T}\left(\frac{LCOE_{\ t}}{(1+r)^{\ t}} \times E_t\right) = I + \sum_{t=1}^{T}\frac{C_{\ t}}{(1+r)^{\ t}}$$

Assuming a constant value per year, LCOE can be derived by rearranging Equation 2, as follows:

Equation 3

$$LCOE = \frac{I + \sum_{t=1}^{T}\frac{C_t}{(1+r)^t}}{\sum_{t=1}^{T}\frac{E_t}{(1+r)^t}}$$

Where:

- T = the average PV system lifespan
- I = the initial investment
- C_t = the Operation and Maintenance (Running) costs
- E_t = the PV-generated electricity over the system's lifespan
- r = the discount rate

To apply Equation 3 to the case using measured data the following assumptions and data are introduced:

- The average PV system lifespan is 25 Years reduced to 22 years when taking into account the discount rate of efficiency.
- Initial investment is US$3200.
- Operation and Maintenance costs are assumed 1% of the investment cost per year.
- Average produced energy per day is taken from the actual reading of the kWh meter installed within the experimental setup for 215 days where the meter showed 3009 kWh. Thus, the daily average generated energy is 13.995 kWh. Then PV-generated electricity per year will be 5,108.3 kWh, and over the system's lifespan shall be 5108.3×22 = 112.379 MWh.
- Thus, the PV system shall produce 5.108 MWh per year.
- Discount rate is assumed 2%.

Substituting these values in Equation 3 gives LCOE = 0.047 $/kWh

- Current average electricity prices can be found on the website of the Ministry of Electricity operating in Sana'a.

  a) Average private sector electricity price = US$0.486/kWh

  b) Average government electricity price = US$0.428/kWh

Both prices are much higher than LCOE, confirming the feasibility of the PV system and its higher economy.

5. ENVIRONMENTAL IMPACT ASSESSMENT

The yearly energy produced by the PV system is 5108 kWh. In electricity generation, the diesel Consumption rate is 3.9 kWh per liter (3.9 kWh/L) (Al-Ashwal, 2006). Then the diesel saving shall reach 1310 L per year. The diesel emission rate is 2.68 kg of CO_2 per liter (2.68 kg/L) of diesel burned according to the Intergovernmental Panel on Climate Change (IPCC). This means emission reduction according to IPCC, 2006. (2006 IPCC Guidelines) will be: CO2 = 3,510 kg/year. This amount represents the environmental impact of the installed peak power of the experimental setup. Let's assume the possibility of initiating a pilot project in Sana'a to cover 20% to 25% of households using SHS. Based on Sana'a's estimated peak power, the project could include more than 100,000 SHS units. The peak power of these units could reach 25 MWp, but this work's measurement has shown that the daily generated energy is 13.995 kWh. Accordingly, 25 MWp shall give an average output energy of 112.14 MWh. This amount will cause a CO2 emission of 28,126.9 Tons/year. Recently, the World Bank issued a report titled "State and Trends of Carbon Pricing" (World Bank, 2024), which showed a significant increase in Carbon Pricing exceeding US$100 billion in 2023. Furthermore, many implementation mechanisms have been developed to promote the reduction of Carbon emissions. This condition upgrades the potential of initiating a Grid-Parity pilot project in Yemen based on Carbon Price Instruments and International Community support.

6. CONCLUSIONS

Having finalized this study, the following conclusions can be drawn:

1. The paper can be considered a milestone of the Grid-Parity application in Yemen.
2. This work has completely ascertained the well-known Grid-Parity practices, for example, the high content of THD injected by the current into the grid from residential loads and lower efficiency when higher power is transmitted.
3. The Paper has shown the high viability of the Grid_Parity implementation in Sana'a, Yemen with the following important advantages:
   - LCOE is so low that the price of 1 kWh equals around 11 times the LCOE produced by the private sector and around 10 times that produced by the public utility.
   - Positive environmental impact as the CO2 saving could be more than 28 Ton/year, for installed power of 25 MWp
4. The paper has also shown mutual verification of both experimental and theoretical calculation methods, as can be seen, the difference between the two methods is 5.734% (theoretical is greater).
5. This work opens up opportunities for further research fields like harmonic impact on Grid-Parity, harmonic mitigation, assessment of installed SHS, temperature effect on PV efficiency in Yemen, etc.
6. This work could be the first step in initiating a Grid-Parity pilot project in Yemen.

7. REFERENCES

Al-Ashwal, A M, 2019, "Market Development of PV Solar Home System (SHS) and PV Pumping in Yemen", Modern Environmental Science and Engineering (ISSN 2333-2581), July 2022, Volume 8, No. 7, pp. 382-389.

Al-Ashwal. A M, Hazza, G, Al-Ashwal, N, 2006, "Environmental Impact Assessment of Using Solar Heaters Instead of Electrical Heaters in The Highlands of Yemen", World Renewable Energy IX, Florence 2006.

Ahsan, S M, Khan, H A, Hussain, A,Tariq, S, Zaffar, N A, 2021, "Harmonic Analysis of Grid-Connected Solar PV Systems with Nonlinear Household Loads in Low-Voltage Distribution Networks", Sustainability 2021, 13(7).

Adeyemi-Kayode, T M, Misra, S, Maskeliunas, R, Damasevicius, R, "A bibliometric review of grid parity, energy transition and electricity cost research for sustainable development", 2023, Heliyon, Volume 9, Issue 5.

Breyer Christian, Gerlach Alexander "Global overview on grid-parity", Progress in Photovoltaics: Research andApplications: Volume 21, Issue 1 January 2013 Pages 121-136

HelioClim-3 Archive Database of Solar Irradiance v5 (derived from satellite data) and meteorological data (MERRA-2/NASA and GFS/NCEP), MINES ParisTech / Armines / Vaisala / National Aeronautics and Space Administration (NASA) / National Centers for Environmental Prediction (NCEP)
http://www.soda-pro.com, http://gmao.gsfc.nasa.gov/reanalysis/MERRA-2 and https://www.emc.ncep.noaa.gov/emc/pages/numerical_forecast_systems/gfs/documentation.php

Kamran, M, Fazal, M R, Mudassar, M, Ahmed, S R, Adnan, M, Abid, I, Randhawa, F J S, Shams, H, 2019, " Solar Photovoltaic Grid Parity: A Review of Issues, Challenges and Status of Different PV Markets", International Journal of Renewable Energy Research, Vol 9, No 1.

Krauter, S C W, 2006, "Solar Electric Power Generation – Photovoltaic Energy Systems", Rio de Janeiro RJ Brazil, by Springer.

Wenham, SR, Green, MA, Watt, M E, Corkish, R, 2006, "Applied photovoltaics", 2nd edition, University of New South Wales Centre for Photovoltaic Engineering, Australia.

World Bank, 2024, "States and Trends of Carbon Pricing".

8. APPENDIX

According to (Stefan C.W. Krauter) electrical energy generated by a PV array over an entire year isknown as the system "Energy Yield"; can be calculated as follows:

$\mathbf{E}_{sys} = (P_{array\ STC} \times F_{temp} \times F_{man} \times F_{dirt} \times H_{tilt} \times \eta_{subsystem} \times \eta_{inv})$

Where: E_{sys} - Energy Yields; P_{array} – peak power of the array; F_{temp} is temperature factor; $\mathbf{F}_{man}$ is the de-rating factor for manufacturing tolerance

H_{tilt} = daily peak Sun hours (PSH) for the selected site; $\eta_{sub\text{-}system}$ is the efficiency of sub-system (cables, connectors, etc.); η_{inv} Inverter efficiency. Thus, daily produced energy, transmitted to the grid will be:

E_{sys} = 14.8465 kW/m^2 when PSH is 7.44 as daily average. The yearly yield energy will be: $\mathbf{E}_{sys}$ = 5419 kWh per year

#394: Multi-objective optimization on sustainable retrofit of historical buildings using NSGA-II Algorithm

A case study of Suzhou

Shihao ZHANG[1], Qi XU[2], Saffa RIFFAT[3]

[1] School of Architecture and Urban Planning, Suzhou University of Science and Technology, Suzhou,215011, China, Email: shihaozhang@usts.edu.cn
[2]College of Architecture, Nanjing Tech University, Nanjing, 210044, China, Email: xuqi@njtech.edu.cn
[3] Department of Architecture and Built Environment, University of Nottingham, Nottingham NG7 2RD, UK, Email: saffa.riffat@nottingham.ac.uk

Abstract: In order to promote the revitalization of historical buildings, it is essential to preserve their historical character while addressing issues such as poor thermal performance and low environmental comfort, making historical buildings more suitable for modern needs. Using historical buildings in Suzhou as a case study, the study explores comprehensive renovation strategies that simultaneously meet objectives such as historical preservation, energy consumption, cost reduction, and enhancement of environment comfort. The theoretical aspect of the research involves clarifying the potential for renovation of Suzhou's historical buildings from perspective of sustainable retrofit. It aims to uncover the intrinsic connections among historical preservation, sustainable goals, and retrofit strategies, thus proposing a set of strategies that cope with multiple objectives, providing a more holistic decision-making framework for historical building green renovation. Overall, this research is poised to offer comprehensive solutions for green renovation of historical buildings, thereby promoting environmental sustainability and maximizing the benefits of urban historical and cultural heritage preservation.

Keywords: Multi-Objective Optimization, Heritage Building, Sustainable Retrofit

1. INTRODUCTION

Suzhou, often referred to as the "Venice of the East," is renowned for its classical gardens, canals, and traditional Chinese architecture. The city has a history that dates back over 2,500 years, making it one of the oldest cities in China. Historically, Suzhou was a major center for silk production and trade, contributing to its economic prosperity and the development of a unique architectural style. These buildings are not only valuable cultural assets but also serve as a testament to the city's architectural legacy. Traditional buildings in Suzhou reflect the Jiangnan style, characterized by whitewashed walls, black-tiled roofs, and intricate wooden carvings. This style emphasizes simplicity, elegance, and a deep connection with nature.

However, many of these historical structures suffer from poor thermal performance and low environmental comfort, making them less suitable for modern occupancy and use. Addressing these issues is essential for the sustainable revitalization of these buildings, ensuring they remain functional and valuable parts of urban fabric. Apart from the modern building retrofit, the primary challenge in retrofitting historical buildings lies in balancing the need for modernization with the imperative of preserving their distinguish features. Conventional buildings often have outdated construction methods and materials, leading to inefficiencies in energy use and comfort levels (Chae & Kim, 2022; Silvero et al., 2018a). Strict protection regulations limit the scope and nature of modifications to these buildings, making this issue even more complicated. Therefore, finding retrofit strategies that can improve energy efficiency, reduce operational costs, and enhance environmental comfort, all while maintaining the historical character of these buildings, is a complex and trade-off needed task.

The main aim of this study is to find suitable retrofit strategies focusing not only on the common retrofit objective, such as energy consumption and initial cost reduction, thermal comfort improvement, but also the historical preservation. On the basis of the maintaining the architectural significance of the building, identity the retrofit strategies to improve energy efficiency and thermal comfort of the heritage buildings in Suzhou. Hence, this study would be divided into two parts. The first part is to evaluate the suitability of the retrofit strategies on the heritage building and extract compatible strategies. And the second part is to analyze the various retrofit scenarios comprised by the above strategies with multi-criteria decision analysis (MCDA) method to identify the most trade-off scenarios.

The scope of this research includes a detailed analysis of selected historical buildings located in the Shuitan Street, Gusu District, Suzhou. The study involves assessing the current conditions of the building, identifying potential retrofit measures, and evaluating the effectiveness of these measures in achieving the stated objectives. The research also aims to develop a set of guidelines and recommendations that can be applied to similar buildings in Suzhou and other regions with comparable heritage contexts. This research is significant for providing valuable insights for policymakers and other stakeholders of heritage building preservation and utilization. The findings and recommendations of this study can support in the broader efforts of urban revitalization, making historical districts more vibrant and liveable, responding to the call on preservation and actively utilization on heritage buildings from President Xi (Jiang et al., 2022a; Wang, 2014).

2. LITERATURE REVIEW

2.1. Overview of Historical Preservation Principles

The retrofit of historical buildings requires thorough research and engineering plans to achieve the goal of not altering their authenticity and integrity. It is necessary to use the principle of minimum disturbance as a guideline and use appropriate technologies to achieve the goal of reusing historic buildings (Jiang et al., 2022b). However, in practical engineering, the complexity of engineering decisions and the weak performance of historical buildings have become the biggest obstacles to their reuse (Paul & Taylor, 2008). Therefore, it is necessary to scientifically and rationally analyze the transformation of historical buildings and help them to burst out new vitality while inheriting the special cultural value of heritage buildings.

In the context of urban renewal and the carbon peaking and carbon neutrality goals, the retrofit of existing buildings has increasingly become a hot topic in academic research. Due to the diverse needs of the user population, the objectives of the renovation and optimization of existing buildings have also evolved from facade renewal, functional transformation to deep objectives such as environmental comfort, energy conservation (Jiang et al., 2022b), carbon emissions (Kadrić et al., 2023), and cost optimization (Kadrić et al., 2023; Lou et al., 2022). As for the retrofit of heritage building, the preservation of architectural integrity is also of vital importance during decision-making process.

In order to evaluate the impact of retrofit strategies on historical buildings, existing research mainly evaluates alternative strategies and selects strategies that meet adaptive needs as the research boundary, ensuring minimal impact on the current status of historical buildings. (Ge et al., 2022a) taking the old house of the Luo family in Hangzhou as an example, a comprehensive evaluation system was established based on the three sub objectives of adaptability, economy, and energy efficiency of retrofit strategies, and the non-dominated genetic algorithm (NSGA-II) was used to find suitable renovation strategies. In the sustainable historical building behavior guidance proposed by the UK government, the energy-saving efficiency, environmental comfort, and historical value protection of renovation strategies are taken as the behavioral guidelines for building heritage protection. In summary, the optimization goals generally include the protection of historical value, cost, energy-saving effect, lifecycle carbon emissions, environmental comfort, and so on. Under the constraint of multiple optimization objectives, the decision-making process for the renovation of historical buildings is quite complex.

2.2. Reviews on Sustainable Retrofits

The applicability of heritage building renovation strategies depends on various factors, including the historical significance, architectural style, structural conditions, and specific objectives of the renovation (e.g., improving thermal comfort, reducing energy consumption, preserving cultural heritage). Table 1 shows a series of preferred renovation strategies that canbe considered for heritage buildings mentioned in previous publications.

Table 20: Extraction of common retrofit strategies from previous publication

Components	Strategies	(Şahin et al., 2015)	(Mingkai, 2016)	(Roberti et al., 2017)	(Silvero et al., 2018b)	(Lu et al., 2021)	(He et al., 2021)	(Gupta & Deb, 2022)	(Ge et al., 2022b)	(Marzouk et al., 2023)	(Choi et al., 2023)
Exterior wall	Inner insulation	✓		✓	✓		✓	✓	✓		✓
	Outer insulation		✓			✓			✓		
Roof	Thermal mortar	✓	✓			✓					✓
	Thermal slab			✓	✓			✓	✓	✓	
Windows	Window frame										
	Glazing replace	✓	✓	✓	✓	✓	✓		✓	✓	
Air permeability	Air tightness	✓				✓					
Foundation	Insulation layer	✓									
Floor	Insulation layer	✓	✓		✓						
Interior wall	Insulation layer	✓	✓								
Device	Green energy					✓	✓				✓
	HVAC					✓	✓			✓	
	Light					✓	✓			✓	

It's worth noting that the majority of previously published papers have predominantly focused on passive design or building envelope improvements. These measures encompass actions like adding insulation, upgrading windows, and reducing air leakage, all of which have the potential to enhance thermal comfort and curtail energy consumption. Notably, the replacement of glazing was the second most frequently discussed strategy due to its high energy efficiency and cost-effectiveness. Some papers also introduce additional strategies, such as HVAC system upgrades, the integration of renewable energy sources, and the adoption of LED lighting.

This summary highlights the practical experiences regarding the prioritization of retrofitting strategies. However, it's essential to recognize that the choice of strategies can vary depending on the specific heritage building in question. Consequently, a more comprehensive evaluation is warranted. This evaluation should encompass historical and architectural considerations, energy audits, and economic calculations, as elaborated below.

2.3. Challenges in Retrofitting Heritage Buildings

Heritage buildings are often protected by local, national, or international laws that impose strict guidelines on any modifications. These regulations aim to preserve the historical and architectural integrity of the buildings, often limiting the scope of retrofit interventions. The limit retrofit practice is always focusing on the structural repair. Actually, any retrofit project on a heritage building typically requires approval from multiple administration organization, which can be time-consuming, complicated and not friendly to nonspecialist.

The regulation or codes on the heritage building often insist that the exterior appearance of heritage buildings remain unchanged, which can limit the use of modern materials and technologies that are visible from the outside. Normally, the use of traditional materials and construction techniques, which can be more expensive and less efficient than modern alternatives. Thus, the practice of sustainable retrofit on heritage building is very limited. The occupants of heritage building often suffer from high energy consumption and poor thermal comfort but are unable to improve the current situation.

Most of heritage buildings with conservation value in China are already well protected and renovate to museum. But there are also a great number of buildings with relatively less value but also the important constituent part of Chinese historical architecture. In order to utilization and promote the protection of those buildings, the governments in China have encouraged the retrofit and utilization to satisfy the modern requirement with minimal intervention, which would provide generous potential retrofit case.

Under the policy of carbon peak and carbon neutrality, it is essential to reduce the energy consumption of the heritage building. But many heritage buildings have little to no insulation, leading to significant heat loss in the winter and heat gain in the summer. Adding insulation and devices without affecting the building's appearance and structure is a major challenge. Furthermore, while there are grants and funding available for heritage preservation, they may not cover all retrofit costs, leaving building owners to bear a significant financial burden. The study on the sustainable retrofit on heritage building is necessary to balance preservation and modernization.

3. METHODOLOGY

In this study, the summarized retrofit strategies from previously published paper should be evaluated the suitability on the historical building to identify the potential options as the research boundary. Then, the parametric model of the sample building would be established in Rhinoceros and evaluated the correctness via comparation between result of simulation and measured. The final part of this study is to identify the retrofit scenarios that can achieve energy consumption, cost reduction and better thermal comfort simultaneously within research boundary. The Wallacei and Ladybug Tools components would be implemented in this section to identify the priority strategies.

According to the investigation on the 120 buildings, it can be seen that the heritage buildings in 3 standard widths is most common, accounting for 67% of the surveyed buildings. In terms of building depth, buildings in 3 standards depth account for a relatively high proportion. The building has high floors, with single and two-story buildings dominating. Other parameters are also selected as benchmarks based on the parameters that have an absolute advantage. The sample building is selected based on the above field investigation. It has representativeness within the surrounding traditional residential areas, and the test results can reflect the thermal performance of local residential buildings. During the period of investigation, the questionnaire on the willingness to retrofit the building is also undertaken. It is worth mentioning that themain barrier of retrofit is the initial cost. Occupants or landlords always have limit budget on the retrofit. As for them, the preservation on the historical value of building is not that necessary. Therefore, the recommendation on the retrofit should be proposed according to the various budget.

4. DESCRIPTION OF THE SAMPLE BUILDING

The sample building is located at No. 29, Shuitan Street, Gusu District, Suzhou City. It has two floors with a total area of about 167 m^2, as shown in Figure 1. It is one of the well-preserved residential buildings with residents living in the lane. The house is east-west oriented, with two rooms about 5.5 meters wide and a depth of about 13 meters. The house has brick-concrete structure for the wall and wooden structure for the roof. Some rooms have suspended ceilings with a net height of about 2.5 meters. The main functional rooms include bedrooms and living rooms. The exterior wall materials of the residential building are mainly brick, with some additions on the second floor. The wall materials are red clay bricks, and the roof is covered with tiles. The windows still retain wooden frames with single-layer glass. The use of doors is mainly wooden doors. Currently, there are three permanent residents in the residential building, including two elderly people and one rental tenant.

Figure 1: The Plan of the sample building (a) Ground floor; (b) First floor

Detailed architectural plans and data of sample building were collected to create an accurate parametric model, which serves as the basis for simulation and analysis. A series of detailed measurements were conducted. These measurements encompass various aspects of thermal comfort and energy consumption, providing critical data for subsequent simulations and optimization.

The following parameters were measured:

1) Thermal property of the building envelops

- Measurement Tools: K-type thermocouples, Centertek 309 thermometer, and Hukesflux heat flux sensor were implemented to capture thermal transmittance of building envelopes.
- Data Collected: Heat flux sensors and thermocouples readings were taken to calculate the U-value of building envelopes.

2) Energy Consumption

- Measurement Tools: The records of energy meters were collected to monitor heating/cooling energy consumption.
- Data Collected: Data on energy consumption patterns were collected over summer to capture variations in usage

and identify opportunities for energy efficiency improvements.

The summary of the measured thermal property of sample building has been listed in Table 2.

Table 21: Summary of thermal property of sample building

Component	Structure	Indicators
Exterior wall	Plastering 10mm + Cement mortar 15mm + 280 Brick wall + Cement mortar 15mm	1.49 W/(m^2*K)
Interior Wall	Mortar 10mm + Brick 190mm + mortar 10mm	1.44 W/(m^2*K)
Window	Wooden frame with single glazing in 6mm	4.4 W/(m^2*K)
Roof	Grey tile 10 mm + Waterproofing membrane 2mm + Fir board 12mm	3.64 W/(m^2*K)
Infiltration	Poor	0.0006 m^3/s per m^2 facade
Door	Wooden door in 25mm	2.98 W/(m^2*K)
HVAC	Split air conditioner	$T_{cooling}$=26, $T_{heating}$=18
Shades	No	

5. RETROFIT STRATEGIES

5.1. Suitability of Retrofitting Strategies in the Context of Historical Building

AHP-Based Fuzzy Evaluation, also named as FAHP (Fuzzy Analytic Hierarchy Process), is a decision-making method based on fuzzy mathematics and hierarchy analysis (Li et al., 2022).

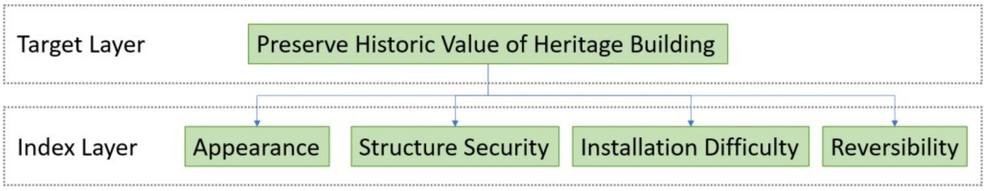

Figure 2: The hierarchy structure with main evaluation criteria

It combines the advantages of AHP and fuzzy comprehensive evaluation, while avoiding their disadvantages. It integrates hierarchical structure, weight analysis, consistency testing, and fuzzy evaluation. The evaluation process of FAHP generally involves determining the weight and factor set using the analytic hierarchy process, determining the evaluation set based on the actual situation, and then using fuzzy comprehensive evaluation to make a comprehensive evaluation.

As shown in Figure 2, an AHP was first implemented to establish a hierarchy structure with main evaluation criteria. The criteria that were collected from previous studies such as (Yuk et al., 22023) (arzouk et al., 2023) (Ge et al., 2022b)(Zhang et al., 2021), are identified to compare and rank based on questionnaire retrieve from expert with rich project experience. All experts were invited to compare the impacts of various application components on the unique values of the historic building. There were 15 questionnaires sent out and 12 valid questionnaires were returned. Then, the pairwise comparison matrix was developed shown in Table 1. The consistency test of the current AHP showed a consistency ratio CR = 0.011 < 0.1, which meant the judgement matrix is acceptance. Table 3 shows impact weight of four indexes on the preservation of historic value, ranging from 0.095 to 0.397. The appearance and structure security had the highest impact weights, which suggests the retrofit solutions on the ventilation should be considered carefully in the view of the historic protection.

Table 3: Impact weights of various indicators

Index	Appearance	Structure Security	Installation difficulty	Reversibility
Impact weight	0.397	0.346	0.162	0.095

Appearance: The components have been carefully selected to blend in with the building's aesthetics, minimizing any visual disruption. **Structure Security**: Showcase how the research considers building’s structural safety to ensure that the proposed retrofitting solution is compatible with the existing structure. **Installation difficulty**: The installation is labour intensive and invasive on the structure, such as inaccessible components. **Reversibility**: The location is easy to install and capable of being reversed so that the original states of heritage are restored easily.

After the impact weight identified in the AHP, the fuzzy evaluation method which transfers the qualitative results to the quantitively indicators is implemented to identify the most suitable components for ventilator application. The indicators for various index are divided into 5 ranks and range from 0-10. Grade 1 means the ‘the invasive impacts on historic value; grade 9 represents the ‘the least impact on the historic value’; the other level shoes the intermediate impacts on the historic value. The results of the evaluation can be calculated by membership functions. The components for ventilator application have been prioritized by the distribution of fuzzy evaluation. The results of LED replacement and airtightness belonged tothe high adaptability, which means the greater potential on preservation of historic value. The fenestration, smart control and HP were relatively suitable for application. The inner insulation had advantages on appearance preservation. As for other potential strategies, the score of evaluation demonstrated unsuitability in perspective of all four indexes. Thus, the potential strategies for heritage building in Suzhou would be LED, seal strips, fenestration replacement, thermostat, high performance heating/cooling device and inner envelope insulation.

5.2. The Potential Retrofit Options

The potential retrofit options in this study cover insulation material for envelopes, the thickness of insulation, air seal strips, glazing type, and the depth of the shades. Table 4 summarized the retrofit options in this study.

Table 4: The summary of the potential retrofit strategies.

	Name	Conductivity	Density	Specific heat	Price CNY/m^3
Inner insulation material for floor, exterior wall, and roof	EPS	0.037	18	1300	600
	SEPS	0.033	18	1300	700
	XPS	0.032	22	1450	800
	SXPS	0.024	30	1450	900
	PU	0.024	35	1400	1200
	MPF	0.024	35	1450	2500
	Rock Wool	0.04	140	840	500
	Glass Wool	0.036	32	840	400
	Foam Glass	0.058	140	800	1000
	Perlite	0.085	400	800	300
Insulation thickness (m)					
0	0.05	0.1	0.15	0.2	0.25
Glazing	Name	U-value	SHGC	transmittance	Cost CNY/m^2
	Original metal frame 6mm	5.15	0.85	0.9	60
	Low-e 6mm	3.72	0.63	0.73	200
	6G+12A+6G	2.59	0.75	0.81	150
	6Low-e+12A+6G	1.63	0.46	0.68	300
	6Low-e+12Ar+6G	1.44	0.45	0.623	350
	6G+12A+6G+12A+6G	1.71	0.67	0.74	300
	6Low-e+12A+6G+12A+6G	1.23	0.42	0.62	500
	6low-e+12Ar+6G+12A+6G	1.01	0.42	0.62	550
Air seal strips m^3/s per m^2 facade					
0.0006	0.0003	0.0001			

6. CASE STUDY ANALYSIS

6.1. Simulation Setup

As shown in Figure 3 (a), the parametric model is established in Rhino and the analysis is undertaken in Grasshopper with help of Ladybug Tools and Wallacei component. The setup of simulation is crucial to assure the correctness of the simulation. In this study, the setup not only covers the thermal property of the building components, but also includes setup for the loads from occupants, lights, ventilation and setpoints of HVAC system. Overall, the sample building has been divided into 5 types of function space. Every kind of space accounts for the specific building program in Ladybug tools. The program in this study is based on filed questionnaire and related codes in China. The HVAC system is an ideal air system without consideration of COP (Coefficient of Performance). In another words, the cooling and heating energy consumption are the cooling and heating loads. The infiltration of the current building is poor, and the application of air seal strips would help to improve the air tightness.

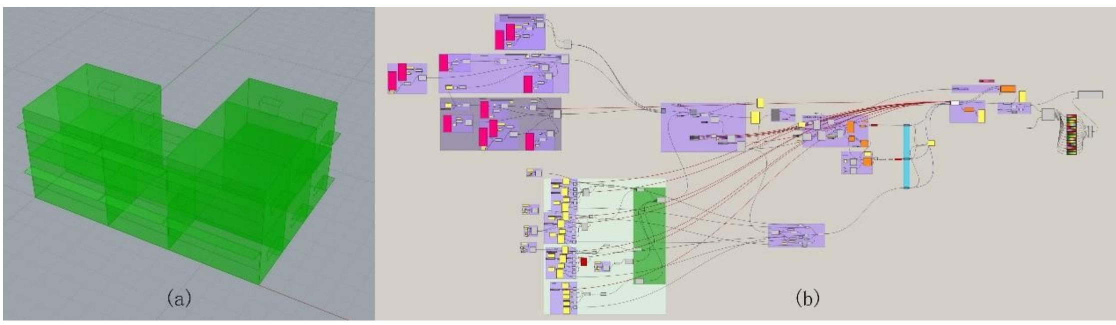

Figure 3: (a) The screenshot of the parametric model in Rhino; (b) The screenshot of the Grasshopper

The optimization objectives include thermal comfort, energy consumption, and initial cost in CNY. The PMV-PPD model is selected as the thermal comfort model. Normally, the PMV model evaluates the thermal comfort of a conditioned space during whole year. However, during the transition season, spring and autumn, the thermal comfort of exterior environment is acceptable for most people. The average UTCI indicator in Suzhou during summer and winter is about 0.587409 and -0.963889, respectively. Thus, this study would like to specially optimize the thermal comfort during summer and winter. In Grasshopper, Ladybug tools can be implemented to evaluate the PMV of interior room. In PMV model, the indicator ranges from -3 to +3, indicating the cold, neutral and hot feelings. In Wallacei component, the objective of thermal comfort has been set up to minimize the sum of absolute number of PMV indicators during summer and winter. The less of the sum, the thermal comforts during summer and winter are more acceptable. It is worth to mention the energy consumption in this study only covers the energy consumed by HVAC system. In the Wallacei component, the total number of generations is 40 and there are 35 solutions per generation. Overall, there are 1,400 potential solutions that have been generated. The crossover probability and random seed is set as 0.9 and 1, respectively.

6.2. Baseline Simulation

In this section, the heating/cooling loads, thermal comfort and have been simulated. The heating/cooling loads are 12,474 kWh in total and 86.7 kWh/m^2. As shown in Figure 4, the average PMV indicator for all rooms during summer and winter is 1.74 and -2.74, respectively. It can be seen that the PMVs of rooms facing north are worse than the rooms facing south, especially during winter. As Suzhou located in a region of hot summer and cold winter, it the demand for heat preservation is even more urgent. The analyzed UTCI index for Suzhou during summer and winter is about 0.587409 and -0.963889, respectively. Thus, this study would like to specially optimize the thermal comfort during summer and winter.

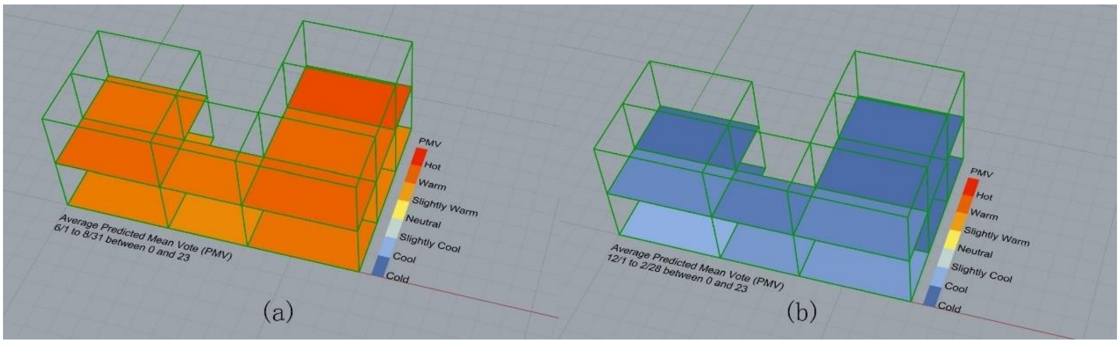

Figure 4: The PMV during (a) Summer; (b) Winter

6.3. Performance Evaluation

The optimization process yielded about 1,400 renovation strategies that balance environmental comfort, initial cost and energy efficiency. These strategies include specific recommendations on insulation improvements, window upgrades, shades design and the air seal stripes. The results demonstrate significant potential improvements in both comfort levels for residents and overall energy performance of the building. As shown in Figure 4 (a), the potential retrofit option includes 14 genes in the NSGA-II algorithm, with 99 potential gene options.

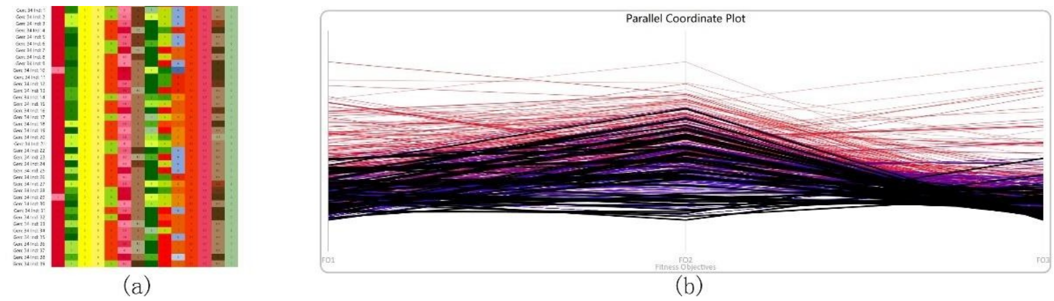

Figure 5: (a) The gene graph; (b) The parallel coordinate plot.

There are 74 solutions that constitute the pareto front. The most balanced option is generation 30, solution 4, ranking 362nd, 3rd, 845th in three objectives of all generated solutions. The most balanced state that can be achieved by above individual. Thecooling and heating loads are about 6,574 kWh, with total cost 46,401 CNY. The thermal comfort during winter and summer is about -1.71 and 1.25, which are improved over original condition. The insulation for exterior wall is PU in 0.05m. As for the roof, the suggested insulation option is PU in 0.3m. The proposed glazing is 6mm single glazing and air seal strips is recommended. The depth of the louvre is about 0.1m.

As shown in Figure 5 (a), based on the simulation result of pareto front, there is no need for extra insulation material on floor, and the suggested insulation material for exterior wall is glass wool in 0.1 thickness. As for the roof, the suggested material is glass wool and in 0.2m thickness. The louvre depth is suggested to be about 0.3m. The glazing type suggested is low-e 6mm single glazing and triple glazing. The aperture ratio is about 0.2 and 0.4 for north and south, respectively.

6.4. Cluster on Result

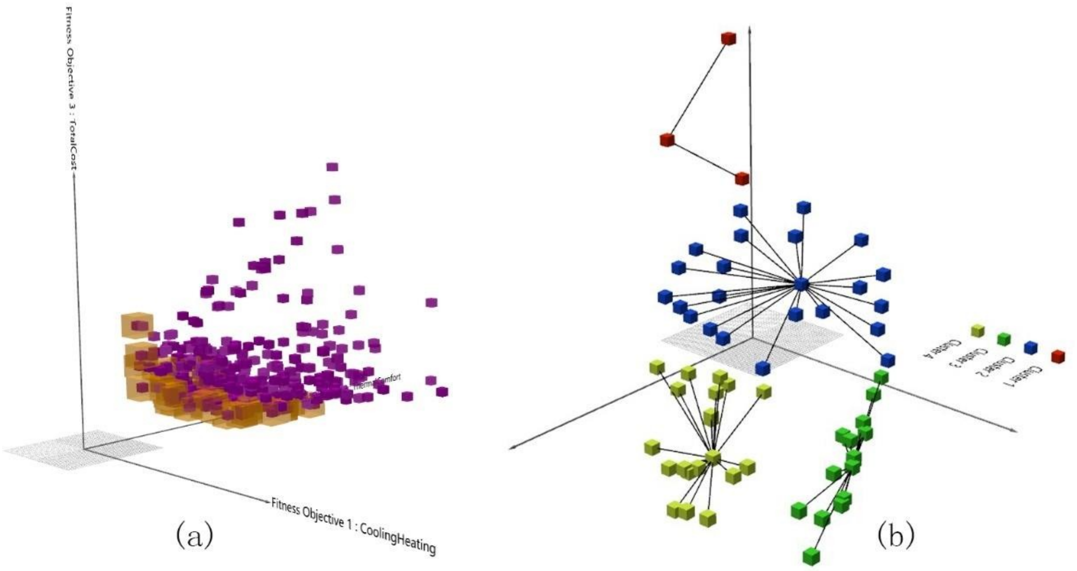

Figure 6: (a) The pareto front; (b) The k-means cluster algorithm on the solutions.

As stated above, the main limiting factors on the retrofit in the perspective of tenants is the initial cost. Hence, the solutions on the pareto front have been clustered via K-means algorithm. K-means is one of the most popular and widely used clustering algorithms in data mining and machine learning, used to group similar data points into clusters based on their features. In this study the solutions have been separated into 4 groups. The cluster 1, the red individuals shown in Figure 6 (a), has the tendency to minimum the heating/cooling loads and better thermal comfort, but no consideration on the budget. The Gen. 30 Solution 3 represent this cluster, the total loads are about 5418 kWh, and the PMV during summer and winter is about -1.55 and 0.9 with initial cost about 112,797 CNY. Cluster 2 is the most balanced among the three objectives. Cluster 3 and 4 are focusing on limiting costs. The core solution for cluster 3 is Gen. 33 Solution 14. The total cost of this scenario is only 8,984 CNY. The total loads are about 8,119 kWh with 0.84 and -2.48 for PMV during summer and winter. The Gen.23 solution 7 is the core scenario for cluster 4, with total cost 13,149 CNY, loads 9395 kWh and PMV 1.01 for summer and -2.0 for winter. It can be seen that total costs of Cluster 3 and 4 are much lower than previous scenarios. It would be recommended to the stakeholder with limit budgets.

7. CONCLUSION

The sustainable retrofit of heritage buildings in Suzhou presents a complex challenge that requires balancing historical preservation with the need for modern energy efficiency and environmental comfort. Through this study, retrofit strategies have been identified that can address these challenges while maintaining the architectural and cultural integrityof Suzhou's historical buildings. The research highlights the following key points:

1) Historical Preservation: The importance of preserving the unique architectural features and cultural significance of Suzhou's heritage buildings cannot be overstated. Retrofit strategies must be carefully designed to ensure that they do not compromise these aspects.
2) Priority the strategies: Based on the simulation result of pareto front, there is no need for extra insulation material on floor, and the suggested insulation material for exterior wall is glass wool in 0.1 thickness. As for the roof, the suggested material is glass wool and in 0.2m thickness. The louvre depth is suggested to be about 0.3m. The glazing type suggested is low-e 6mm single glazing and triple glazing. The aperture ratio is about 0.2 and 0.4 for north and south, respectively.
3) Cost-Effectiveness: While the initial costs of retrofitting can be high, the long-term benefits in terms of energy savings, enhanced building lifespan, and improved occupant comfort justify the investment.

The sustainable retrofit of Suzhou's heritage buildings requires a multidisciplinary approach that respects the past while embracing the future. By incorporating advanced analytical tools such as space syntax and machine learning, alongside a deep understanding of historical preservation principles, we can develop comprehensive retrofit strategies that enhance energy efficiency, environmental comfort, and cost-effectiveness. This research provides a foundation for future efforts, offering a roadmap for achieving sustainable urban development that honors and preserves the rich cultural heritage of Suzhou.

8. REFERENCES

Chae, Y., & Kim, S. H. (2022). Selection of retrofit measures for reasonable energy and hygrothermal performances of modern heritage building under dry cold and hot humid climate:A case of modern heritage school in Korea. Case Studies in Thermal Engineering, 36, 102243. https://doi.org/https://doi.org/10.1016/j.csite.2022.102243

Choi, J. Y., Nam, J., Yuk, H., Yun, B. Y., Lee, S., Lee, J. K., & Kim, S. (2023). Proposal of retrofit of historic buildings as cafes in Korea: Recycling biomaterials to improve building energy and acoustic performance. Energy and Buildings, 287, 112988. https://doi.org/https://doi.org/10.1016/j.enbuild.2023.112988

Ge, J., Lu, J., Wu, J., Luo, X., & Shen, F. (2022a). Suitable and energy-saving retrofit technology research in traditional wooden houses in Jiangnan, South China. Journal of Building Engineering, 45, 103550. https://doi.org/https://doi.org/10.1016/j.jobe.2021.103550

Ge, J., Lu, J., Wu, J., Luo, X., & Shen, F. (2022b). Suitable and energy-saving retrofit technology research in traditional wooden houses in Jiangnan, South China. Journal of Building Engineering, 45, 103550. https://doi.org/https://doi.org/10.1016/j.jobe.2021.103550

Gupta, V., & Deb, C. (2022). Energy retrofit analysis for an educational building in Mumbai. Sustainable Futures, 4, 100096. https://doi.org/https://doi.org/10.1016/j.sftr.2022.100096

He, Q., Hossain, Md. U., Ng, S. T., Skitmore, M., & Augenbroe, G. (2021). A cost-effective building retrofit decision-making model – Example of China's temperate and mixed climate zones. Journal of Cleaner Production, 280, 124370. https://doi.org/https://doi.org/10.1016/j.jclepro.2020.124370

Jiang, W., Hu, H., Tang, X., Liu, G., Guo, W., Jin, Y., & Li, D. (2022a). Protective energy-saving retrofits of rammed earth heritage buildings using multi-objective optimization. Case Studies in Thermal Engineering, 38, 102343. https://doi.org/https://doi.org/10.1016/j.csite.2022.102343

Jiang, W., Hu, H., Tang, X., Liu, G., Guo, W., Jin, Y., & Li, D. (2022b). Protective energy-saving retrofits of rammed earth heritage buildings using multi-objective optimization. Case Studies in Thermal Engineering, 38, 102343. https://doi.org/https://doi.org/10.1016/j.csite.2022.102343

Kadrić, D., Aganović, A., & Kadrić, E. (2023). Multi-objective optimization of energy-efficient retrofitting strategies for single-family residential homes: Minimizing energy consumption, CO2 emissions and retrofit costs. Energy Reports, 10, 1968–1981. https://doi.org/https://doi.org/10.1016/j.egyr.2023.08.086

Li, Y., Zhou, T., Wang, Z., Li, W., Zhou, L., Cao, Y., & Shen, Q. (2022). Environment improvement and energy saving in Chinese rural housing based on the field study of thermal adaptability. Energy for Sustainable Development, 71, 315–329. https://doi.org/https://doi.org/10.1016/j.esd.2022.10.006

Lou, Y., Yang, Y., Ye, Y., He, C., & Zuo, W. (2022). The economic impacts of carbon emission trading scheme on building retrofits: A case study with U.S. medium office buildings. Building and Environment, 221, 109311. https://doi.org/https://doi.org/10.1016/j.buildenv.2022.109311

Lu, Y., Li, P., Lee, Y. P., & Song, X. (2021). An integrated decision-making framework for existing building retrofits based on energy simulation and cost-benefit analysis. Journal of Building Engineering, 43, 103200. https://doi.org/https://doi.org/10.1016/j.jobe.2021.103200

Marzouk, M., El-Maraghy, M., & Metawie, M. (2023). Assessing retrofit strategies for mosque buildings using TOPSIS. Energy Reports, 9, 1397–1414. https://doi.org/https://doi.org/10.1016/j.egyr.2022.12.073

Mingkai, L. (2016). Indoor thermal environment technology research of the ancient residential houses In the ancient city areas of Suzhou. Suzhou University of Science and Technology.

Paul, W. L., & Taylor, P. A. (2008). A comparison of occupant comfort and satisfaction between a green building and a conventional building. Building and Environment, 43(11), 1858–1870. https://doi.org/https://doi.org/10.1016/j.buildenv.2007.11.006

Roberti, F., Oberegger, U. F., Lucchi, E., & Troi, A. (2017). Energy retrofit and conservation of a historic building using multi-objective optimization and an analytic hierarchy process. Energy and Buildings, 138, 1–10. https://doi.org/https://doi.org/10.1016/j.enbuild.2016.12.028

Şahin, C. D., Arsan, Z. D., Tunçoku, S. S., Broström, T., & Akkurt, G. G. (2015). A transdisciplinary approach on the energy efficient retrofitting of a historic building in the Aegean Region of Turkey. Energy and Buildings, 96, 128–139. https://doi.org/https://doi.org/10.1016/j.enbuild.2015.03.018

Silvero, F., Montelpare, S., Rodrigues, F., Spacone, E., & Varum, H. (2018a). Energy retrofit solutions for heritage buildings located in hot-humid climates. Procedia Structural Integrity, 11, 52–59. https://doi.org/https://doi.org/10.1016/j.prostr.2018.11.008

Silvero, F., Montelpare, S., Rodrigues, F., Spacone, E., & Varum, H. (2018b). Energy retrofit solutions for heritage buildings located in hot-humid climates. Procedia Structural Integrity, 11, 52–59. https://doi.org/https://doi.org/10.1016/j.prostr.2018.11.008

Wang, Y. (2014). Suzhou | Creative Cities Network - UNESCO. Suzhou Intangible Cultural Heritage Conservation and Management Office. https://en.unesco.org/creative-cities/suzhou

Yuk, H., Jo, H. H., Choi, J. Y., Nam, J., Chang, S. J., & Kim, S. (2023). Evaluation of suitability for passive retrofit of wooden roof considering the specificity of historic buildings. Building and Environment, 242, 110608. https://doi.org/https://doi.org/10.1016/j.buildenv.2023.110608

Zhang, F., Ju, Y., Santibanez Gonzalez, E. D. R., Wang, A., Dong, P., & Giannakis, M. (2021). A new framework to select energy-efficient retrofit schemes of external walls: A case study. Journal of Cleaner Production, 289, 125718. https://doi.org/https://doi.org/10.1016/j.jclepro.2020.125718

#395: Multi-objective optimization for environmental retrofits of elderly care buildings

A case study of Suzhou

Qi XU[1], Shihao ZHANG[2], Saffa RIFFAT[3]

[1] College of Architecture, Nanjing Tech University, Nanjing, 210044, China, Email: xuqi@njtech.edu.cn
[2] School of Architecture and Urban Planning, Suzhou University of Science and Technology, Suzhou,215011, China, Email: shihaozhang@usts.edu.cn
[3] Department of Architecture and Built Environment, University of Nottingham, Nottingham NG7 2RD, UK, Email: saffa.riffat@nottingham.ac.uk

Abstract: With the increasing aging population, the environmental comfort of the elderly has garnered significant attention, raising societal expectations for eldercare buildings. However, there remains a lack of systematic research on effective environmental retrofits to improve the living quality of the elderly. This study aims to propose comprehensive renovation strategies for eldercare buildings, utilizing an interdisciplinary approach integrating architecture and evolutionary algorithms to enhance the environmental comfort of elderly residents. Initially, an elderly care building in Suzhou, named as the Gusu District Shuangta Street Jinfan Community Health Service center, has been selected, measured and parametrically modeled as the case study for this research. Subsequently, a plugin called Wallacei for Grasshopper, based on the NSGA-II algorithm, has been implemented to evaluate performance under multiple objectives. Ultimately, trade-off retrofit strategies among environmental comfort and energy consumption will be developed for the case building, offering tailored decision support for various elderly individuals and eldercare facilities. This study aims to provide a scientific basis and practical guidance for eldercare facility renovations, ultimately enhancing the quality of life for the elderly and promoting societal sustainability. Additionally, it serves as a model for interdisciplinary research, expanding research methodologies and application prospects in related fields.

Keywords: Eldercare Building, NSGA-II Algorithm, Thermal Comfort

1. INTRODUCTION

The global demographic landscape is undergoing a significant transformation, characterized by a rapidly increasing aging population (Wang et al., 2019). According to the World Health Organization (WHO), the number of people aged 60 and over is expected to double by 2050, reaching approximately 2.1 billion. This demographic shift stimulates the requirements for various societal systems, particularly healthcare facilities. As eldercare facilities that can provide a comfortable and supportive living environment tailored to the unique needs of older adults.

In order to actively address the issue of aging, Chinese government has proposed a comprehensive elderly care service system to promote the social eldercare service, including nursing homes, assisted living centers, community health care center, and senior housing complexes (Gui et al., 2024). Nowadays, elderly people in China still face the problem of insufficient nursing facilities per capita (Feng et al., 2020). Therefore, the government encourages other abandoned or unoccupied buildings to be renovated and retrofitted to the eldercare building as eldercare building, which quickly and efficiently supplement the insufficient elderly care facilities. However, many of these buildings were constructed decades ago and are not designed for the eldercare purpose and hardly meet contemporary standards for environmental comfort and energy efficiency. Common issues involve the retrofits include inadequate thermal comfort, high initial cost and high energy consumption. These factors can adversely affect the physical and mental health of elderly residents, and relative to the social participation enthusiasm in eldercare industry, leading to increased susceptibility to illnesses, and lower overall quality of eldercare service.

Thermal comfort is particularly crucial for elderly individuals (Mendes et al., 2015). The elder people have various physiological responses to environment change away from younger people. They would be more sensitive to the temperature variation and require higher thermal comfort levels. Therefore, the built building used for other purposes should be retrofitted to ensure a high level of environmental comfort before the application as the eldercare building.

Actually, there are some published papers related to the retrofit of the eldercare building. (Zhou et al., 2023) stated that there are various evaluation models for occupancy thermal comfort. The PMV and adaptive comfort model are the most recognized by the academic researchers. However, there is no systematic and widely admitted thermal comfort model specially for elder people (Zhou et al., 2023). As for this research, the Gusu District Shuangta Street Jinfan Community Health Service center with central air conditioning has been selected as the research sample. Thus, the PMV model is implemented to estimate the thermal comfort of elder people. The Predicted Mean Vote (PMV) model is an approach to assessing and managing thermal comfort in buildings proposed by Pro. Fanger in the 1970s. The model assumes there are six parameters related to the thermal comfort, including air temperature, mean radiant temperature, air velocity, relative humidity, clothing insulation, and metabolic rate (Roelofsen et al., 2022).

Despite there are several research on the retrofit of building, most of the current research focuses on the isolated aspect of building performance, such as energy consumption or cost, rather than consider the building from various perspectives simultaneously. This fragmented approach can result in suboptimal outcomes and missed opportunities for synergistic improvements (Li et al., 2024). There is a lack of systematic research on effective environmental retrofits for eldercare buildings. The difference between utilization mode of eldercare building and other building results in the inability to directly appliance of existing retrofit experience mentioned in previous paper (Kadrić et al., 2023; Lou et al., 2022; Xu et al., 2023).

To address these gaps, this study proposes an interdisciplinary approach that integrates architectural design principles with advanced optimization algorithms to develop comprehensive renovation strategies for eldercare buildings. This research aims to identify and evaluate multiple renovation scenarios that balance requirement from environmental comfort, initial cost and energy efficiency. The sample building will be parametrically modeled to simulate various retrofit scenarios, and the Wallacei plugin for Grasshopper, based on the Non-dominated Sorting Genetic Algorithm II (NSGA-II), will be used to optimize the renovation strategies. This multi-objective optimization process will consider diverse factors such as thermal comfort, initial cost, and energy consumption, ultimately developing trade-off strategies that can be tailored to different eldercare facilities and individual needs. This study aims to offer a model for future research in related fields, demonstrating the potential of integrating architectural design with computational optimization techniques to assist the retrofit decision making.

2. DESCRIPTION OF THE SAMPLE BUILDING

The selected case study for this research is a former government administration office located in Suzhou, now named as the Gusu District Shuangta Street Jinfan Community Health Service centre. This building has recently been retrofitted to serve as a community health centre specifically designed for neighbour residents, as shown in Figure 1 (a). The transformation from an office building to an eldercare facility presents unique challenges and opportunities for optimizing environmental comfort and energy efficiency. The building's original design, intended for administrative functions, did not prioritize the specific needs of elderly occupants, necessitating comprehensive retrofit strategies to create a comfortable and supportive living environment. Furthermore, the location of the sample building, Suzhou, with its hot summers and cold winters, presents a challenging climatic context for achieving optimal indoor environmental conditions.

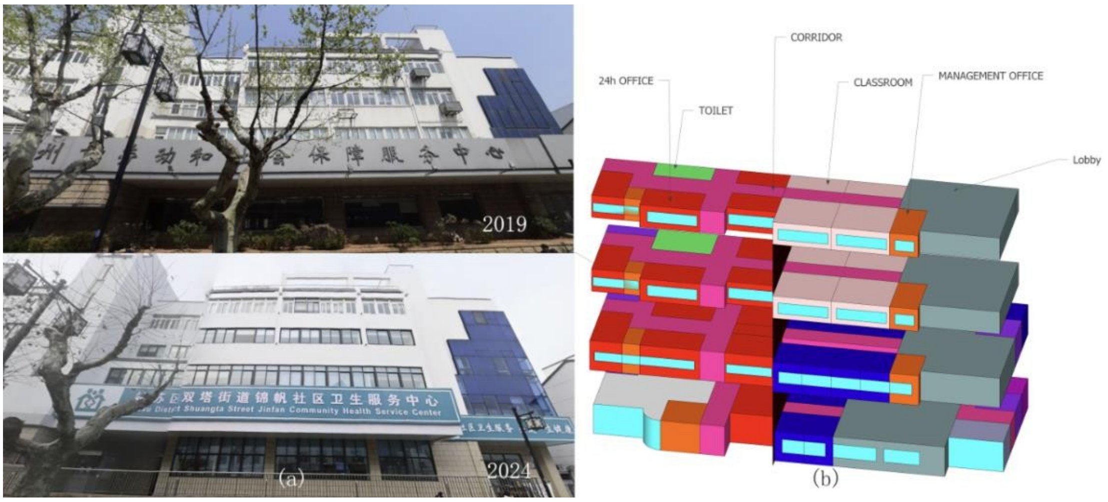

Figure 1: (a) the sample building in 2019 and now; (b) the distribution of the room functions.

Currently, the building consists of two main room groups. The first is for health care, shown on the right side of the building on Figure 1 (b), and the other one is for Shuangta community administration office, shown in left side of the building on Figure 1 (b). The healthcare part mainly includes reception, office, pharmacist, lobbies, nursing unit and outpatient department. The building currently served as the largest and most comprehensive community health service center in the Gusu District, with a total area of 3000 m^2. The community administration part includes a reception, 24h office, offices, and storage room. Thetwo parts are independent to each other. There is a partition wall in the middle for separation, as shown in Figure 1 (b).

3. MEASUREMENT ON THE BUILDING

Detailed architectural plans and data of sample building were collected to create an accurate parametric model, which serves as the basis for simulation and analysis. A series of detailed measurements were conducted. These measurements encompass various aspects of thermal comfort and energy consumption, providing critical data for subsequent simulations and optimization.

The following parameters were measured:

1) Indoor Temperature
- Measurement Tools: K-type thermocouples and Centertek 309 thermometer were deployed throughout the building to capture temperature variations across different rooms and floors.
- Data Collected: Indoor temperature readings were taken at multiple points during the day and night to account for diurnal variations.

2) Thermal property of the building envelops
- Measurement Tools: K-type thermocouples, Centertek 309 thermometer, and Hukesflux heat flux sensor were implemented to capture thermal transmittance of building envelopes.
- Data Collected: Heat flux sensors and thermocouples readings were taken to calculate the U-value of building envelopes.

3) Energy Consumption
- Measurement Tools: The records of energy meters were collected to monitor heating/cooling energy consumption.
- Data Collected: Data on energy consumption patterns were collected over summer to capture variations in usage and identify opportunities for energy efficiency improvements.

The summary of the measured thermal property of sample building has been listed in Table 1.

Table 1: Current situation and characteristics of building structure

Component	Structure	Indicators
Exterior wall	Colid brick wall without insulation layer in 240mm	1.49 W/(m^2*K)
Window	Single glazing in 6mm with aluminum frame	5.3 W/(m^2*K)
Roof	20mm concrete panel with 10mm insulation layer	1.21 W/(m^2*K)
Infiltration	Average	0.0003 m^3/s per m^2 facade
HVAC	Central air conditioner	$T_{cooling}$=26, $T_{heating}$=18
Shades	No	

4. SIMULATION

The parametric model of the building was simulated using Rhinoceros and Grasshopper to assess different retrofit scenarios. Key variables, such as insulation materials, window designs, HVAC systems, and available insulation options, were adjusted to explore their impact on environmental comfort, cost and energy efficiency.

4.1. Setup of the simulation

The setup is crucial to assure the correctness of the simulation. In this study, the setup not only covers the thermal property of the building components, but also includes setup for the loads from occupants, lights, ventilation and setpoints of HVAC system. Overall, the sample building has been divided into 10 types of function space. Every kind of space accounts for the specific building program in Ladybug tools. The program in this study is based on filed questionnaire and related codes in China. The HVAC system is an ideal air system without consideration of COP (Coefficient of Performance). The cooling and heating energy consumption are the cooling and heating loads. The table below summarizes the program for each kind of space.

Table 22: Setup of the simulation

People	Spare OFFICE	CLASS ROOM	CORRIDOR	GATE	Biohazard	OFFICE	PATIENT	RECEPTION	STORAGE	TOILET
ppl/area	0.1	0.215	0.0107	0.322	0	0.1	0.215	0.1076	0.1615	0
0	1	0	0.4	0	0	0	0	0	0	0
1	1	0	0.4	0	0	0	0	0	0	0
2	1	0	0.4	0	0	0	0	0	0	0
3	1	0	0.4	0	0	0	0	0	0	0
4	1	0	0.4	0	0	0	0	0	0	0
5	1	0	0.4	0	0	0	0	0	0	0
6	1	0	0.4	0	0	0	0	0	0	0
7	0	0.37	0.4	0	0	1	0	0	0	0
8	0	0.37	0.6	0.005	0	1	0.05	0.05	0.05	0
9	0	0.37	0.6	0.005	0	1	0.05	0.05	0.05	0
10	0	0.19	0.6	0.005	0	1	0.05	0.05	0.05	0
11	0	0.19	0.6	0.005	0	1	0.05	0.05	0.05	0
12	0	0.37	0.6	0.005	0	1	0.05	0.05	0.05	0
13	0	0.37	0.6	0.005	0	1	0.05	0.05	0.05	0
14	0	0.37	0.6	0	0	1	0.05	0.05	0.05	0
15	0	0.37	0.6	0	0	1	0.05	0.05	0.05	0
16	0	0.37	0.4	0	0	1	0.05	0.05	0.05	0
17	0	0.19	0.4	0	0	1	0	0	0	0
18	0	0.19	0.4	0	0	0.5	0	0	0	0
19	0.5	0.19	0.4	0	0	0	0	0	0	0
20	0.5	0	0.4	0	0	0	0	0	0	0
21	0.5	0	0.4	0	0	0	0	0	0	0

22	1	0	0.4	0	0	0	0	0	0	0
23	1	0	0.4	0	0	0	0	0	0	0
Lighting	7.965	7.64	7.64	9.04	4.09	7.96	9.79	9.04	4.52	6.78
Equipment	11.84	10	0	11.84	1.07	11.84	16.1485	11.84	32.29	4.3
Ventilation	0.00236	0	0	0.0024	0	0.0024	0.00708	0.00236	0.00236	0
setpoint	18/26	18/26	18/26	0/0	18/25	18/26	18/26	18/26	18/26	0/0

4.2. Verification of the simulation

Verification of the simulation process is a crucial step to ensure that the computational models accurately represent the real-world conditions of the sample building. In this study, the verification process involves comparing the simulated results of the current situation of the eldercare facility with the actual measured data. This comparison helps validate the reliability and accuracy of the simulation models used in developing renovation strategies.

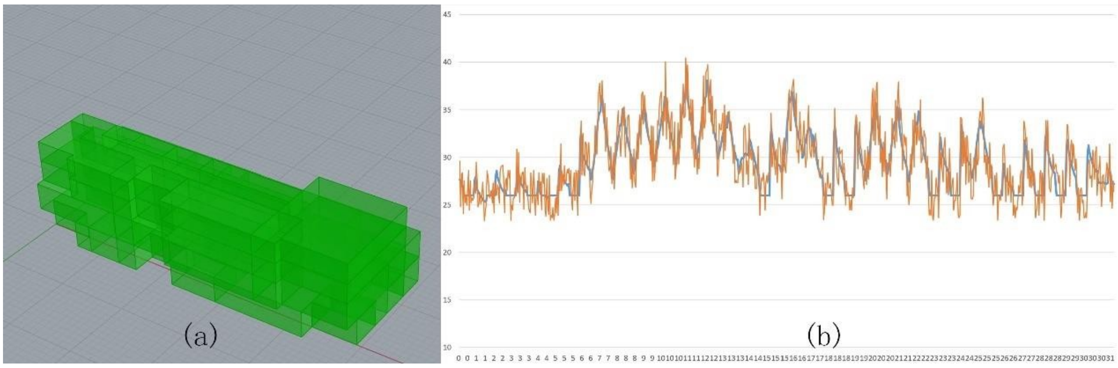

Figure 2: (a) The screenshot of the building model; (b) The comparisons of the temperature（Orange line：Field measurement, blue line: Simulated result）

The correlation number between the measured and simulated results is about 0.86. The verification results demonstrate that the simulation models accurately represent the real-world conditions of the sample building. The discrepancies between the simulated and measured data were minimal. This validation confirms the reliability of the simulation process and supports the use of these models for developing and evaluating renovation strategies.

4.3. NSGA-II with Wallacei

The potential retrofit options in this study cover insulation material for envelopes, the thickness of insulation, air seal strips, glazing type, and the depth of the shades. Table 3 summarizes the retrofit options in this study.

Table 3: Summary of retrofit options

	Name	Conductivity	Density	Specific heat	Price CNY/m^3
Insulation material for floor, exterior wall, and roof	EPS	0.037	18	1300	600
	SEPS	0.033	18	1300	700
	XPS	0.032	22	1450	800
	SXPS	0.024	30	1450	900
	PU	0.024	35	1400	1200
	MPF	0.024	35	1450	2500
	Rock Wool	0.04	140	840	500
	Glass Wool	0.036	32	840	400
	Foam Glass	0.058	140	800	1000
	Perlite	0.085	400	800	300

Insulation thickness (m)					
0	0.05	0.1	0.15	0.2	0.25
	Name	U-value	SHGC	transmittance	Cost CNY/m^2
Glazing	Original metal frame 6mm	5.15	0.85	0.9	60
	Low-e 6mm	3.72	0.63	0.73	200
	6G+12A+6G	2.59	0.75	0.81	150
	6Low-e+12A+6G	1.63	0.46	0.68	300
	6Low-e+12Ar+6G	1.44	0.45	0.623	350
	6G+12A+6G+12A+6G	1.71	0.67	0.74	300
	6Low-e+12A+6G+12A+6G	1.23	0.42	0.62	500
	6low-e+12Ar+6G+12A+6G	1.01	0.42	0.62	550
Depth of Shades (m)					
0	0.15	0.3	0.45	0.6	

The total number of potential retrofit scenarios are over 840,000. If they adjust the parameter with every potential scenario, the estimated simulation period would up to 291 days. In order to save time to get the optimization suggestions on the retrofit. The Non-dominated Sorting Genetic Algorithm II (NSGA-II) is introduced to this study. NSGA-II is a multi-objective optimization algorithm widely used for solving complex problems with conflicting objectives. In this study, NSGA-II algorithm is implemented through the Wallacei plugin for Grasshopper to optimize the renovation strategies. The algorithm evaluates multiple objectives, such as maximizing thermal comfort and minimizing energy consumption and initial cost and identifies optimal trade-offs among them.

In this study, the optimization objectives include thermal comfort, energy consumption, and initial cost in CNY. The PMV-PPD model is selected as the thermal comfort model. Normally, the PMV model evaluates the thermal comfort of a conditioned space during whole year. However, during the transition season, spring and autumn, the thermal comfort of exterior environment is acceptable for most people. The average UTCI indicator in Suzhou during summer and winter is about 0.587409 and -0.963889, respectively. Thus, this study would like to specially optimize the thermal comfort during summer and winter. In Grasshopper, Ladybug tools can be implemented to evaluate the PMV of interior room. In PMV model, the indicator ranges from -3 to +3, indicating the cold, neutral and hot feelings. In Wallacei component, the objective of thermal comfort has been set up to minimize the sum of absolute number of PMV indicator during summer and winter. The less of the sum, the thermal comforts during summer and winter are more acceptable. It is worth to mention the energy consumption in this study only covers the energy consumed by HVAC system.

In the Wallacei component, the total number of generations is 32 and there are 32 solutions per generation. Overall, there are over 1000 potential solutions been generated. The crossover probability and random seed are set as 0.9 and 1, respectively. The optimization process lasts for over 15 hours. Figure 3 (b) shows the distribution of all the generated solutions on the three objective dimensions.

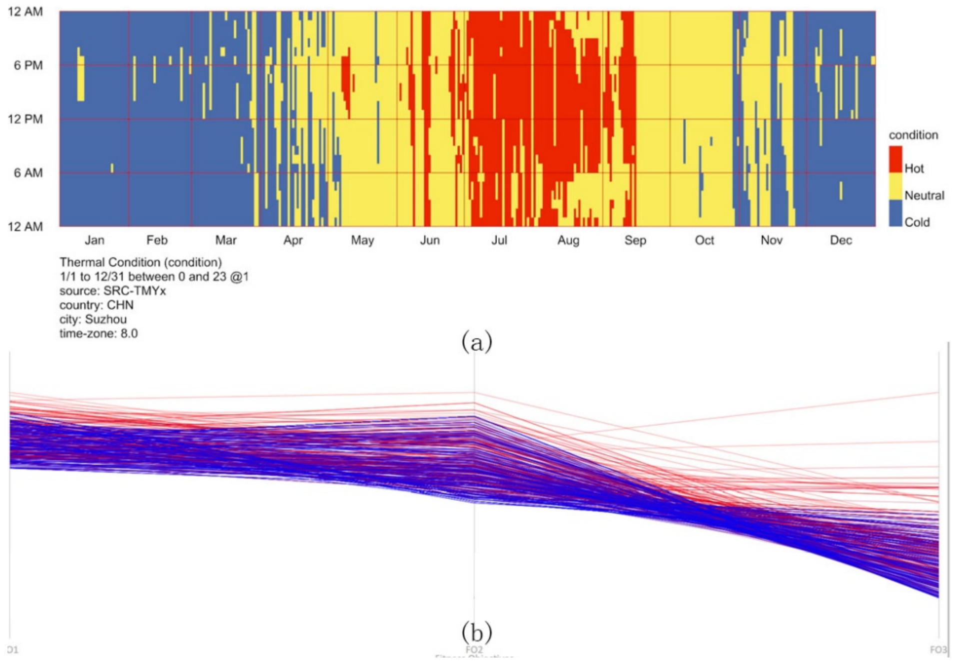

Figure 47: (a)The UTCI indicator for the whole year; (b)The Parallel Coordinate Plot

4.4. Result of the Optimization

The optimization process yielded about 1,000 renovation strategies that balance environmental comfort, initial cost and energy efficiency. These strategies include specific recommendations on insulation improvements, window upgrades, shades design and air seal stripes. The results demonstrate significant potential improvements in both comfort levels for residents and the overall energy performance of the building. As shown in Figure 4 (a), the potential retrofit option includes 10 genes in the NSGA-II algorithm, with 71 potential gene numbers.

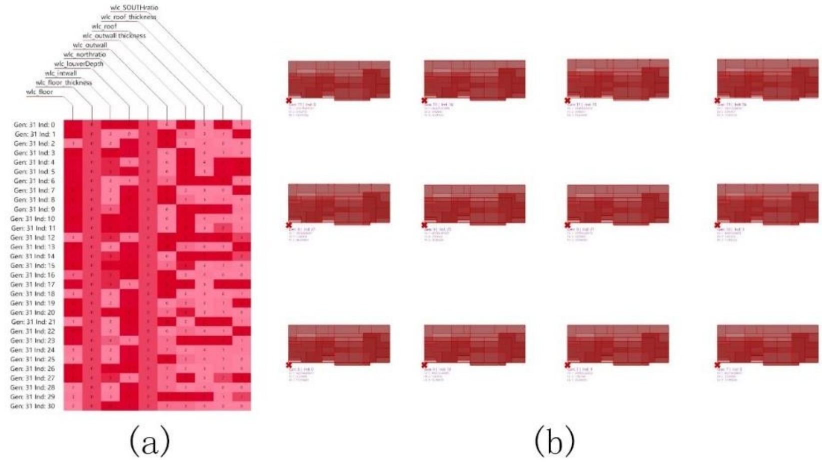

Figure 4: (a) Gene graph of the last generation; (b) the phenotype of part optimized solutions.

In the perspective of NSGA-II, a Pareto solution is one where no other solution is better in all objectives. Instead, each Pareto solution represents a trade-off among the different objectives. The set of all Pareto optimal solutions forms the Pareto front. This front provides decision-makers with a range of optimal solutions, each balancing the objectives differently. In this study, the Wallacei component has generated 114 solutions to form the Pareto front, as shown in Figure 5 (a). The solutions on the pareto front are the purple cubes enclosed with a yellow envelope.

The solution with best performance on the cooling and heating loads is the generation 24, solution 4, with 337,412 kWh, with the thermal comfort value about 1.92 and the total cost about 817,133 CNY. The individual in Gen.26 and solution 4 ranked 1st place in thermal comfort, with fitness value 1.82. The option of least cost is generation 5, solution 5 with cost about 120,000 CNY, cooling and heating loads about 422,194 kWh and thermal comfort about 2.28.

The most balanced option is generation 16, solution 23, ranking 126th, 469th, 397th in three objectives of all generated solutions. The most balanced state that can be achieved by above individual. The cooling and heating loads are about 359,410kWh, with thermal comfort about 2.01 and total cost 381,377 CNY. Based on the simulation result, there is no need for extra insulation material on floor, and the suggested insulation material for exterior wall is rock wool in 0.1 thickness. As for the roof, the suggested material is glass wool and in 0.2m thickness. The louvre depth is suggested to be about 0.45m. The glazing type suggested is 6Low-e+12Ar+6G. The aperture ratio is about 0.3 and 0.4 for north and south, respectively.

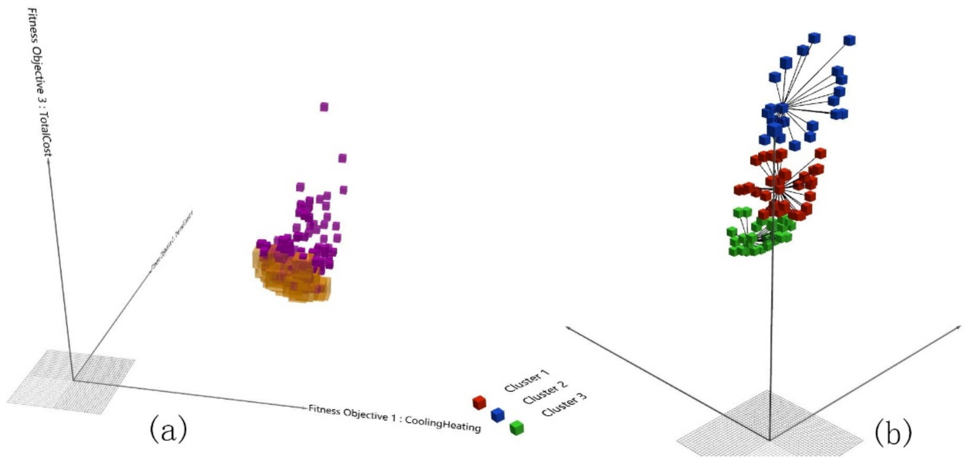

Figure 48: (a) The pareto front; (b) The k-means cluster algorithm on the solutions.

As shown in Figure 5 (b), the generated solutions have been divided into 3 clusters with K-means cluster algorithm. According to the previous questionnaire with staff in healthcare center, the main obstacle for the building retrofit is the high initial cost. With cluster algorithms, three solutions can be selected to present different tendencies. The Cluster 2 Gen.20 Solution 28 presents options with low cost, relatively high energy consumption, and low thermal comfort, which is more suitable when the budget is limited. The suggested insulation material for roof and exterior wall are glass wool in 0.05m thickness and glass wool in 0.1m thickness. The suggested glazing type is low-e single glazing. The aperture ratio for both north and south are 0.3, with louver depth in 0.45m. Another option, Cluster 3 Gen.9 Solution 21, presents high initial cost but in better thermal comfort and low heating and cooling loads, which is more suitable with no budget restrictions. Cluster 1 presents the neutral performance on all three objectives.

5. CONCLUSION

This study presents a comprehensive approach to eldercare building renovations, integrating architectural design with advanced optimization algorithms. The proposed strategies provide practical guidance for enhancing the living quality of elderly residents while promoting energy efficiency and sustainability. The findings underscore the importance of interdisciplinary research in addressing complex challenges in eldercare and building retrofits. The key findings in this study are listed below,

- The most balanced solution suggested from Wallacei is the generation 16, solution 23.
- If consider the budget limit, the cluster algorithm would be helpful to find suitable solutions. In this study, the Cluster 2 Gen.20 Solution 28 presents tendencies with low cost, relatively high energy consumption.
- From the gene graph of last generation, the most suggested glazing type is 6mm low-e glazing, and the suggested louver depth should range from 0.45 to 0.6m. There is no need for extra insulation material on the floor. The suggested insulation material for roof and exterior wall are SXPS and rockwool, respectively.

Future work will focus on implementing the recommended strategies in the case study building and evaluating their real-world effectiveness. Additionally, this research framework can be adapted to other building types and regions, further expanding its applicability and impact.

6. REFERENCES

Feng, Z., Glinskaya, E., Chen, H., Gong, S., Qiu, Y., Xu, J., & Yip, W. (2020). Long-term care system for older adults in China: policy landscape, challenges, and future prospects. The Lancet, 396(10259), 1362–1372. https://doi.org/https://doi.org/10.1016/S0140-6736(20)32136-X

Gui, Z., Ji, W., Wang, Y., Li, J., Cheng, Y., Li, L., Dong, G., Yang, B., & Zhou, Y. (2024). Severer air pollution, poorer cognitive function: Findings from 176,345 elders in Northwestern China. Ecotoxicology and Environmental Safety, 271, 116008. https://doi.org/https://doi.org/10.1016/j.ecoenv.2024.116008

Kadrić, D., Aganović, A., & Kadrić, E. (2023). Multi-objective optimization of energy-efficient retrofitting strategies for single-family residential homes: Minimizing energy consumption, CO2 emissions and retrofit costs. Energy Reports, 10, 1968–1981. https://doi.org/https://doi.org/10.1016/j.egyr.2023.08.086

Li, Y., Du, H., & Kumaraswamy, S. B. (2024). Case-based reasoning approach for decision-making in building retrofit: A review. Building and Environment, 248, 111030. https://doi.org/https://doi.org/10.1016/j.buildenv.2023.111030

Lou, Y., Yang, Y., Ye, Y., He, C., & Zuo, W. (2022). The economic impacts of carbon emission trading scheme on building retrofits: A case study with U.S. medium office buildings. Building and Environment, 221, 109311. https://doi.org/https://doi.org/10.1016/j.buildenv.2022.109311

Mendes, A., Bonassi, S., Aguiar, L., Pereira, C., Neves, P., Silva, S., Mendes, D., Guimarães, L., Moroni, R., & Teixeira, J. P. (2015). Indoor air quality and thermal comfort in elderly care centers. Urban Climate, 14, 486–501. https://doi.org/https://doi.org/10.1016/j.uclim.2014.07.005

Roelofsen, P., Jansen, K., & Vink, P. (2022). A larger statistical basis and a wider application area of the PMV equation in the Fanger model: application area of the PMV equation. In Intelligent Buildings International (Vol. 14, Issue 4). https://doi.org/10.1080/17508975.2021.1928595

Wang, R., Lu, Y., Zhang, J., Liu, P., Yao, Y., & Liu, Y. (2019). The relationship between visual enclosure for neighbourhood street walkability and elders' mental health in China: Using street view images. Journal of Transport and Health, 13. https://doi.org/10.1016/j.jth.2019.02.009

Xu, Y., Yan, C., Wang, G., Shi, J., Sheng, K., Li, J., & Jiang, Y. (2023). Optimization research on energy-saving and life-cycle decarbonization retrofitting of existing school buildings: A case study of a school in Nanjing. Solar Energy, 254, 54–66. https://doi.org/https://doi.org/10.1016/j.solener.2023.03.006

Zhou, S., Li, B., Du, C., Liu, H., Wu, Y., Hodder, S., Chen, M., Kosonen, R., Ming, R., Ouyang, L., & Yao, R. (2023). Opportunities and challenges of using thermal comfort models for building design and operation for the elderly: A literature review. Renewable and Sustainable Energy Reviews, 183, 113504. https://doi.org/https://doi.org/10.1016/j.rser.2023.113504

#396: Characteristics of pyrolysis products of biomass under cryogenic pretreatment using liquid nitrogen

Tao XU[1], Lingyun ChEN[1], Jie CHEn[1], Yurui LEI[1]

[1] School of Energy Engineering，Xi'an University of Science and Technology，Xi'an 710054

Abstract: Biomass is a valuable and sustainable energy source that can be converted into bio-oil and combustible gases through pyrolysis. Despite being a widely used method for biomass conversion, pyrolysis has been plagued by the issue of low yield and poor quality of pyrolysis products. To address these challenges, a novel approach involving cryogenic pretreatment with liquid nitrogen was explored for wheat straw and corn straw. This method, which combines cryogenic pretreatment with fast pyrolysis, aims to enhance product yield and quality. Results from the study show that compared to traditional pyrolysis, this method increased bio-oil yields by 14.16~23.73 wt%. The highest bio-oil yield of 22.3~26.3 wt% was achieved at a pretreatment temperature of -90 °C, with a direct relationship observed between cryogenic temperature and bio-oil yield. Cryogenic pretreatment with liquid nitrogen has a significant transformation effect on the composition distribution of bio-oil, and there is a significant increase in BTEX and phenolic substances in the bio-oil composition. Cryogenic pretreatment with liquid nitrogen inhibits the release of CO_2 and CO in the biomass pyrolysis gas,and the content ratio of the components decreases by 7.2% to 29.7%; it promotes the generation of CH_4 and H_2, and the content ratio of the components increases by 0.2% to 14.7%. In addition, cryogenic pretreatment increases the content ratio of C elements in the elemental composition of the solid product by 0.2% to 2.98%, while reducing the content ratio of O elements by 0.28% to 2.52%, which is beneficial to improving the combustibility of bio-char and reducing its risk of spontaneous combustion. Thus, cryogenic pretreatment significantly enhances both the yield and composition of bio-oil, providing a promising pathway for efficient biomass conversion into liquid fuels.

Keywords: Biomass; Fast Pyrolysis; Cryogenic Pretreatment; Bio-Oil Yield and Composition; Gas Composition

1. INTRODUCTION

In the context of the escalating energy crisis and environmental pollution nowadays, the development of renewable energy sources to substitute traditional fossil fuels has become an urgent global demand. Biomass is a clean and renewable energy source, referring to all organic substances directly or indirectly produced by plants through photosynthesis, characterized by extensive occurrence, balanced carbon cycling, and low sulfur and nitrogen content. Hence, the high-value utilization of biomass is one of the crucial approaches to reduce reliance on fossil energy [1].

Pyrolysis technology is an effective bio-chemical thermochemical conversion method, denoting the process in which biomass is heated and pyrolyzed into three different forms of energy products: gas, liquid (bio-oil), and solid (biochar), in an oxygen-free environment. However, the complexity of the biomass pyrolysis conversion process and the instability of the products have limited its pace of industrial application. The different components of biomass raw materials, such as cellulose, hemicellulose, and lignin, have varying reaction activities during the pyrolysis process, resulting in significant differences in the yield and quality of the final pyrolysis products. Therefore, optimizing the biomass pyrolysis processand increasing the yield of related energy products is a current research hotspot in the field of biomass energy [2-3].

In recent years, there have been numerous studies on improving the biomass pyrolysis process, such as catalytic pyrolysis, fast pyrolysis, and low-temperature pyrolysis. Among them, pretreatment technology has been proven to be an effective method to improve the distribution of pyrolysis products and increase the product yield. Traditional pretreatment methods include mechanical grinding, drying, chemical treatment, etc. These methods optimize the biomass pyrolysis technology by modifying the composition and physicochemical characteristics of biomass, thereby improving the distribution and quality of pyrolysis products. MA [4] et al. used ionic aqueous solutions to pretreat rice husk and achieved the highest bio-oil yield at a lower temperature, with the liquid yield increasing by 20.28%. KUMSAR [5] et al. pretreated rice husk with acids and alkalis respectively to study the effect of activation energy of biomass before and after pretreatment on the pyrolysis process. The results showed that both acid and alkali pretreatment increased the activation energy of biomass raw materials and improved the pyrolysis process. However, although these methods can improve the pyrolysis process and product characteristics to a certain extent, they still have problems such as high energy consumption, low treatment efficiency, and the use of chemicals.

Liquid nitrogen low-temperature pretreatment is a technique that can reduce the temperature of a material below its freezing point, which can improve the structural characteristics of the material. Freezing causes the internal moisture in the substance to freeze, forming ice crystals. These ice crystals can reduce the interparticle connection, thereby loosening their structure and changing the pore characteristics of the material [6]. MENG et al. [7] conducted low- temperature pretreatment on biomass and found that the pretreated biomass had a more complete porous surface structure, and the biomass carbon obtained by pyrolysis had more micropores. YANG et al. [8] utilized the low- temperature freezing technology to conduct experiments and simulations on biomass simultaneously. The common feature of the simulation and experimental results was that the total volume of mesopores and macropores increased with the low-temperature treatment, but the growth rate of pore volume decreased significantly with the repetition of freeze-thaw. The pores of different diameters had varying degrees of degradation, indicating that the low-temperature technology had a significant effect on the pore structure of biomass. For biomass, low-temperature freeze pretreatment may change the physical structure of biomass at the microscopic level, disrupting its fibrous tissue, thereby affecting its pyrolysis kinetics and product distribution. In addition, low-temperature pretreatment may affect the state of water molecules and other volatile components in biomass, thereby changing the pyrolysis atmosphere and the composition of products [9]. However, currently, there are relatively few research reports on the effect of liquid nitrogen low-temperature pretreatment on the characteristics of biomass pyrolysis products, especially the lack of systematic studies on the influence of freezing temperature on the distribution and composition of pyrolysis products.

Therefore, this study proposes a new method of combining liquid nitrogen low-temperature pretreatment with fast pyrolysis for the production of oil from biomass, aiming to address the core problems of low bio-oil yield and poor quality in the pyrolysis of biomass. Corn stover and wheat stover were selected as research objects, and the liquid nitrogen rapid freezing pretreatment method was adopted to study the effect of low-temperature freezing pretreatment temperature on the distribution and yield of pyrolysis products of these two different biomasses. Furthermore, this study particularly focused on the evolution mechanism of gas composition at different freezing temperatures and explored the mechanism of action of different freezing temperatures on the distribution and composition of bio-oil, with the aim of providing new ideas for the efficient conversion of biomass.

2. SAMPLES AND EXPERIMENTAL METHODS

2.1. Biomass sample

The experimental samples were wheat straw and corn straw. The wheat straw was produced in Gou Long Village, Xuezhen Town, Fuping County, Shaanxi Province, and the variety was Xiaoyan 22, with a harvest time of June 2023. The corn straw was produced in Hantai District, Ankang City, Shaanxi Province, and the variety was Zhengdan 958, with a harvest time of October 2023. According to the GB/T 1341-2007 standard, the yield of bio-oil was determined by aluminium retort; based on the GB/T 28731-2012 standard, the industrial analysis of the samples was carried out using amoisture analyzer and an intelligent muffle furnace; the C, H, and N elements in the samples were quantitatively analyzed using a Vario EL III elemental analyzer, and the S element in the samples was quantitatively analyzed using ICP-OES. The relevant data are shown in Table 1. It can be seen from Table 1 that the yields of bio-oil from corn straw and wheat straw were 20.7 wt% and 22.3 wt%, respectively.

The air-dried basis sample was crushed using a crusher, and then sieved through a 200-mesh (74 μm) sieve. The sample was then placed in a 105 ℃ constant-temperature drying oven for 12 h. The samples after sufficient drying (M < 0.5 wt%) were used for the experiment.

Table 1: Proximate analysis, Ultimate analysis and bio-oil yield of biomass samples

samples	Proximate analysis（ad, wt%）				Ultimate analysis（daf, wt%）					Bio-oil yield Y
	M	A	V	FC	C	H	N	S	O*	（d, wt%）
corn	5.59	6.00	17.25	71.16	56.97	7.29	1.79	0.15	33.8	20.70
wheat	3.97	12.00	25.81	58.22	53.66	6.62	1.23	0.25	38.24	22.30

2.2. Pretreatment

The experiment used liquid nitrogen for cryogenic pretreatment of biomass, and a T-type ultra-fine thermocouple was used to measure the sample temperature in real time. During low-temperature freezing treatment, put about 0.4 L of liquid nitrogen into the Dewar flask first, then take 3 g of biomass sample and fill it into a porcelain boat, connect the T- type ultra-fine cryogenic thermocouple (0.1mm in diameter) to detect the surface temperature of the central particle of thesample in real time. The thermocouple has a temperature measurement range of -200~200 ℃ and a response time of 0.01 s. Then, the filled porcelain boat was sealed in a plastic sealed bag and placed in the Dewar flask for about 10 minutes of low-temperature freezing pretreatment, and the sample temperature dropped to about -178 ℃. Subsequently, the sample was taken out of the liquid nitrogen and quickly placed at the right end of the pyrolysis tubular furnace. When the sample temperature rose to the target temperature (0~-90 ℃), the sample was quickly pushed into the furnace for pyrolysis reaction.

The cooling rate of the sample in liquid nitrogen and the heating rate of the cryogenic sample in the 450 ℃ pyrolysis environment are shown in Figure 1. During liquid nitrogen immersion, the maximum cooling rate Vmax of biomass reached 291℃/min and 345℃/min, respectively. In the 450 ℃ pyrolysis environment, the initial maximum heating rate of biomass is positively related to the sample freezing temperature, that is, the lower the cryogenic pretreatment temperature of the sample, the faster the heating rate, up to 369℃/min (pretreatment at -90 ℃).

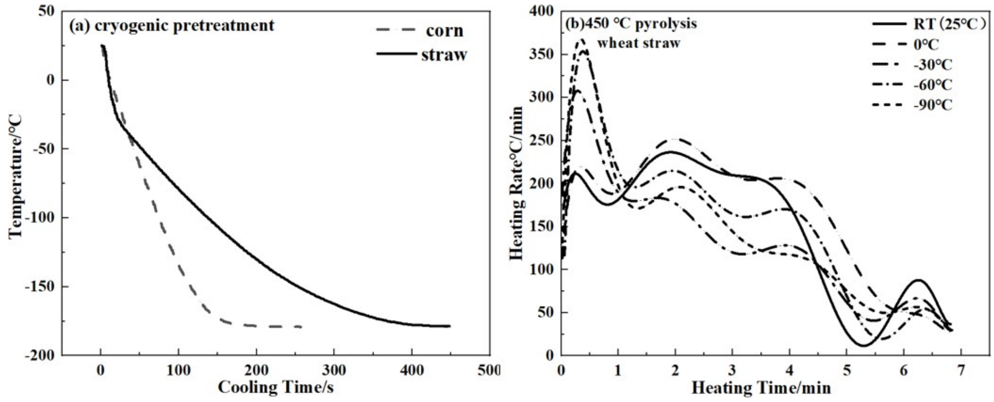

Figure 1: Freezing rate of biomass under liquid nitrogen and heating rate of biomass samples under pyrolysis environment of 450 ℃

2.3. Experimental procedure

Employing the TL1500 tubular furnace for the pyrolysis experimental study of biomass, Figure 2 presents a schematic diagram of the pyrolysis experimental process. Placing the porcelain boat containing 3 g of dry biomass at the extreme right of the tubular furnace. Inserting a T-type ultrafine thermocouple into the center of the sample and affixing it with the porcelain boat to detect the heating rate during the pyrolysis process of the sample. Configuring the temperature rise program of the tubular furnace. Once the temperature reaches the target temperature range of 300 to 600 degrees Celsius, introduce nitrogen gas at a rate of 0.15 L/min to purge the air within the furnace, ensuring an inert environment within the experimental furnace. Subsequently, promptly push the sample into the middle reaction zone of the tubular furnace to conduct a rapid pyrolysis reaction. Activate the gas collection bag to gather the gaseous products. The pyrolysis duration lasts for 30 minutes. Upon completion of the reaction, shut off both the N2 and the gas collection bag. Collect the solid product, bio-char, and seal it for dry storage. Utilizing isopropanol as the bio-oil organic solvent, collect the bio-oil on the condensation bottle and the tube wall of the tubular furnace. Employ a needle-type filter (filter diameter: 0.22 μm) to filter the solution, eliminating particulate impurities. Record the weight and data. Finally, seal the bio-oil solution for refrigerated storage and reserve it for subsequent detection.

The mass of the pyrolysis solid product is obtained by weighing the mass of the bio-char within the porcelain boat, the mass of the liquid product is acquired by calculating the mass difference before and after the bio-oil collection, and the volume of the gaseous product is determined by measuring the gas volume within the gas collection bag using a syringe aspiration method. To minimize experimental errors and obtain stable experimental data, the entire pyrolysis experiment process is replicated thrice under identical conditions, and the average of the experimental results is taken to ensure excellent experimental reproducibility.

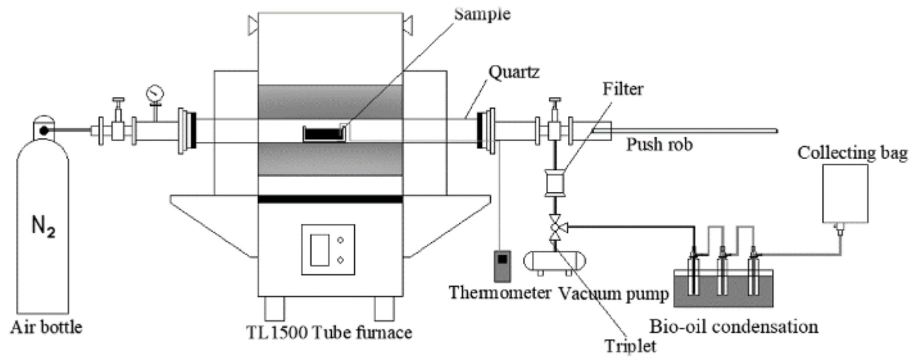

Figure 2: The schematic of biomass pyrolysis experiments

2.4. Analytical methods

The distribution of pyrolysis products is calculated based on the solid-phase method. The yield of solid products is obtained by weighing the mass of bio-char, the yield of liquid products is acquired by weighing and calculating the mass of bio-oil, and the yield of gas products is obtained by the subtraction method.

Using a gas chromatograph (GC-2014, Shimadzu, Japan), the composition of H_2, CO, CO_2, and CH_4 in the gas product was quantitatively analyzed, with a detection limit of 0.01%. The composition of the liquid product was detected and analyzed using GCMS (19091S-433, Agilent, US), and the composition distribution of the liquid product was quantitatively analyzed based on the peak area normalization method.

The carbon conversion rate ηC can reflect the energy utilization efficiency during the biomass pyrolysis process, which is calculated by Equation.

$$\eta_c = 1 - \frac{m_2 c_2}{m_1 c_1}$$

- m_1 = the mass of biomass (g)
- c_1 = the carbon content of biomass (%)
- m_2 = the mass of bio-char (g)
- c_2 = the carbon content of bio-char (%)

3. RESULTS AND DISCUSSION

3.1. Yield of pyrolysis product

The relationships between the yields of conventional pyrolysis products and carbon conversion rates of the two biomass samples with temperature are shown in Figure 3. As can be seen from Figure 3, with the increase in pyrolysis temperature, the yield of gas products of biomass gradually increases, while the yield of solid products gradually decreases. The yield of liquid products first increases with the increase in temperature, and the highest yield of corn straw and wheat straw is at 450 °C, and the maximum bio-oil yields are 22.3 wt% and 19.3 wt% respectively. This is because the increase in temperature in the early stage is beneficial to the primary pyrolysis reaction of biomass, promoting the generation of volatile components. However, when the temperature exceeds the optimal temperature, the secondary pyrolysis reaction intensifies, further forming the primary volatiles into gaseous and solid forms of biochar, thereby promoting the release of gaseous products and inhibiting the generation of liquid products [10].

The carbon conversion rate of biomass is directly proportional to the pyrolysis temperature. The carbon conversion rates of corn and wheat reach the maximum values at the highest temperature of 600 °C, which are 58.3% and 54.7% respectively. Experiments show that high temperatures are conducive to the pyrolysis reaction, thereby increasing the carbon conversion rate.

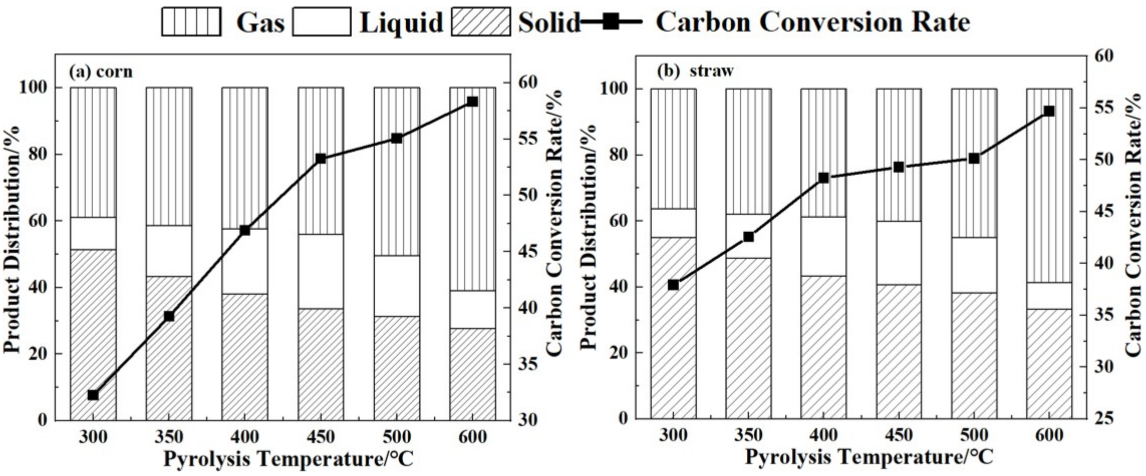

Figure 3: Product yield and carbon conversion of conventional pyrolysis products of biomass

Employing the temperature point that yields the maximum bio-oil as the pyrolysis temperature, a comparison was conducted on the bio-oil yields under conditions of low-temperature pretreatment (-90 to 0 °C), conventional pyrolysis, and low-temperature dry distillation in an aluminum retort.

As can be seen from Figure 4, compared to conventional pyrolysis, the bio-oil yield of wheat pyrolysis after low- temperature pretreatment can increase by up to 18.31%, and the bio-oil yield of corn stover can increase by up to 14.16%. Compared with the bio-oil yield in the aluminum retort method, the bio-oil yield can increase by up to 8.5% for wheat and up to 22.71% for corn stover. It can be concluded from Figure 4 that there is a proportional relationship between the low-temperature pretreatment temperature and the bio-oil yield of pyrolysis, meaning the lower the freezing temperature, the higher the bio-oil yield of pyrolysis. When pre-treated at -90 °C, the bio-oil yields of the two types of biomasses reach the maximum values (21.9-25.4 wt%). Compared with the bio-oil yield in the aluminum retort method, low-temperature pretreatment increases the bio-oil yield by 1.9-4.7 wt%, with an increase ranging from 8.5 to 22.71%. The experimental results demonstrate that low-temperature pretreatment can effectively enhance the bio-oil yield, and there is a positive correlation between the freezing temperature and the bio-oil yield. This is because during low-temperature pretreatment, the temperature of the biomass is significantly lower than the pyrolysis temperature, and the temperature gradient between the biomass and the environment increases, resulting in an increased heating rate of the biomass, thereby enhancing the bio-oil production. Additionally, low-temperature pretreatment can increase the number of micropores on the surface and inside of the biomass, which is also conducive to the precipitation of bio-oil [11].

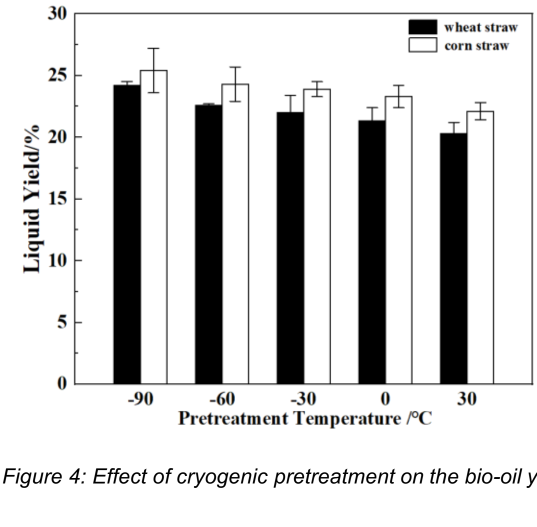

Figure 4: Effect of cryogenic pretreatment on the bio-oil yield

3.2. Pyrolysis gas products

Biomass pyrolysis gas can serve as a gaseous fuel or be converted into feedstock gas for the production of substitute natural gas or liquid fuels, possessing high industrial value [12]. The composition of pyrolysis gas from conventional pyrolysis and biomass after cryogenic pretreatment is depicted in Figure 5. Within the temperature range of 300 to 600 °C, as the pyrolysis temperature increases, the proportion of CO_2 in the pyrolysis gas of both biomass straws undergoes a substantial decrease, with a reduction range of 46.6 to 50.1%. In contrast, the proportions of H_2, CH_4, and CO all exhibit varying degrees of increase, with the increment ranges for corn and wheat straw reaching 121.4 to 233% and 244.4 to 336.1%, respectively. As the pyrolysis temperature elevates, the content of CO_2 in the pyrolysis gas of both agricultural biomass straws declines significantly, while the contents of CH_4, CO, and H_2 increase. This is because under cryogenic pyrolysis conditions, the three major components of biomass straw tend to generate a large amount of CO_2 through reactions such as carboxyl decarboxylation. However, as the pyrolysis temperature rises, the probability of decarboxylation reactions decreases, and other reaction pathways become more dominant. Additionally, high temperatures facilitate the cleavage of chemical bonds such as carbon-hydrogen bonds and hydroxyl groups, promoting methane reforming and water-gas shift reactions. These reactions can consume CO_2 to generate CH_4, CO, and H_2, thereby reducing the concentration of CO_2 [13].

After cryogenic pretreatment, the proportions of various gas components of both biomasses remain essentially constant, indicating that the cryogenic pretreatment temperature has a relatively small impact on the composition of biomass pyrolysis gas. In comparison to conventional pyrolysis, after cryogenic pretreatment, the content of CO_2 in the gas components of both biomasses shows a marked reduction, with a reduction range of 7.2 to 29.7%. The contents of CH_4 and H_2 increase to a certain extent, with increments ranging from 0.2% to 6.5% and 2.7% to 14.7%, respectively. However, there is no obvious regular change in the CO content after cryogenic pretreatment. Evidently, cryogenic pretreatment inhibits the generation of CO_2 during biomass pyrolysis and promotes the release of CH_4 and H_2.

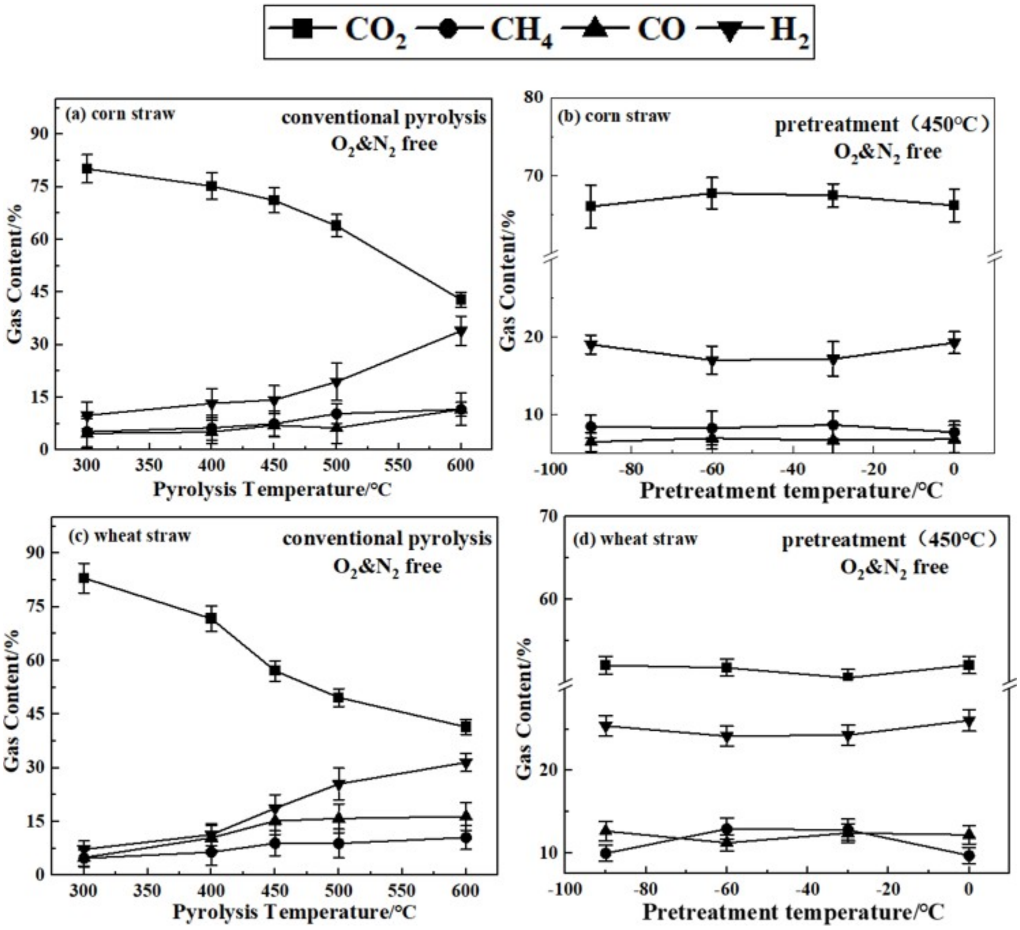

Figure 5: Gas composition of biomass under conventional pyrolysis and cryogenic pretreatment

3.3. Pyrolysis liquid products

The composition of pyrolysis liquid products under conventional pyrolysis and cryogenic pretreatment is shown in Table 2. It can be known from Table 2 that, with the increase of the conventional pyrolysis temperature the BTEX content of corn stalk decreases with the increase in pyrolysis temperature. The BTEX content decreases from 47.39 wt% (300 °C) to 29.08 wt% (600 °C); while phenols show a trend of first increasing and then decreasing. The aromatic derivatives showed a decreasing trend with the increase in pyrolysis temperature, decreasing from 26.09 wt% (300 °C) to 0.93 wt% (600 °C); the results indicate that the increase in the pyrolysis temperature of corn stalk is beneficial to the formation of alcohols, and inhibits the formation of phenols and aliphatic compound aromatic derivatives. Compared to conventional pyrolysis, there is no significant change in the BTEX content in the corn bio-oil after cryogenic pretreatment, while the phenolic content increases relatively, with the maximum increase of 12.45 wt%. cryogenic pretreatment has a significant inhibitory effect on the formation of alcohol, with the maximum decrease of 24.65 wt%. However, the cryogenic pretreatment temperature has no significant effect on the acids, esters, ketones, and sugars in the corn stalk bio-oil components, and the content of each component does not show a significant change pattern with temperature.

Table 2: Bio-oil composition of corn straw under cryogenic pretreatment and conventional pyrolysis

Temperature/℃ Content/%	Conventional pyrolysis			Pretreatment			
	300	450	600	0	-30	-60	-90
Corn straw							
BTEX	47.39	22.55	29.08	44.89	25.05	21.31	22.42
Phenols	11.81	35.96	12.20	32.45	44.64	48.41	45.16
PAHs	-	-	-	0.63	0.30	-	0.09
Aromatic	26.09	5.02	0.93	4.82	4.70	2.86	6.35
Acids	2.29	3.50	0.77	3.01	3.10	4.52	5.11
Alcohols	9.07	27.8	53.06	3.15	9.53	8.67	6.10
Esters	1.49	1.04	1.50	2.58	4.38	3.19	4.03
Ketones	1.88	2.84	-	4.91	4.88	8.37	8.89
Sugars	-	-	-	1.58	2.25	1.10	0.92
Others	0.55	0.89	1.14	1.79	0.7	1.25	0.78

The BTEX content of wheat straw shows a trend of first decreasing and then increasing with the increase in pyrolysis temperature. The BTEX content decreases from 32.71 wt% (300 °C) to 20.26 wt% (400 °C) and then increases to 68.92 wt%; while phenols show a trend of first increasing and then decreasing, increasing from 24.93 wt% (300 °C) to 38.45 wt% (450 °C) and then decreasing to 15.73 wt%; the results indicate that a higher pyrolysis temperature of wheat straw is conducive to the generation of BTEX, while a relatively moderate temperature promotes the formation of phenolic substances. Compared to conventional pyrolysis, the BTEX content in wheat bio-oil after cryogenic pretreatment shows a significant increase, with the maximum increase of 43.61 wt%. The phenolic content decreases relatively, with the maximum decrease of 19.81 wt%. Similarly, the cryogenic pretreatment temperature has no significant effect on the acids, alcohols, esters, ketones, and sugars in the wheat straw bio-oil components, and the content of each component does not show a significant change pattern with temperature.

Table 3: Bio-oil composition of wheat straw under cryogenic pretreatment and conventional pyrolysis

Temperature/℃ Content/%	Conventional pyrolysis			Pretreatment			
	300	450	600	0	-30	-60	-90
Wheat straw							
BTEX	32.71	20.26	68.92	59.20	63.87	36.89	49.57
Phenols	24.93	38.45	15.73	19.55	18.64	30.06	24.34
PAHs	-	-	0.37	-	0.02	-	0.05
Aromatic	14.19	2.60	3.96	0.86	3.20	8.59	1.96
Acids	7.68	1.79	-	1.58	2.09	3.50	3.03
Alcohols	2.57	13.01	1.69	6.06	1.43	2.19	5.01
Esters	5.12	5.25	3.03	1.47	1.19	3.19	2.27
Ketones	5.66	10.20	4.26	4.75	5.19	9.14	6.46
Sugars	3.99	3.90	-	1.55	2.31	3.15	3.49
Others	3.13	3.80	2.04	3.73	1.68	2.81	3.59

In conclusion, compared to conventional pyrolysis, cryogenic pretreatment has a certain promoting effect on high-value substances such as BTEX and phenols. It also has a significant transformational effect on the distribution of bio-oil. Cryogenic pretreatment improves the yield of bio-oil from biomass pyrolysis, enhances the quality of bio-oil, and is conducive to reducing the cost of subsequent deep processing. This has great significance for the efficient utilization of biomass.

3.4. Pyrolysis solids products

The contents of C and O elements in the solid products obtained from pyrolysis under both conventional pyrolysis and cryogenic pretreatment are shown in Figures 6 and 7. As depicted in Figure 6, within the temperature range of 300°C to 600°C, the proportion of C element content in both types of biomass bio-char increases with the increase in pyrolysis temperature. Specifically, the proportions of corn and wheat increase by 13.30% and 12.79%, respectively. This can be attributed to the fact that as the pyrolysis temperature rises, a large number of lighter and easily volatile components (primarily functional groups rich in H and O) in the biomass undergo thermal decomposition and are converted into gaseous forms and released. Additionally, the remaining solid undergoes aromatization, resulting in an increase in the proportion of relatively carbon-rich components in the bio-char product.

As indicated in Figure 7, the proportion of O element content shows a decreasing trend as the pyrolysis temperature increases. This is because the increase in temperature promotes the evaporation of moisture in the biomass and the removal of water from the chemical structure, thereby reducing the proportion of O element content. In addition, the increase in pyrolysis temperature leads to the breakage of chemical bonds in the biomass, and functional groups such as carboxyl, hydroxyl, and ether bonds decompose at high temperatures. Consequently, the O element is released in gaseous forms such as CO and CO2, further reducing the proportion of O element content.

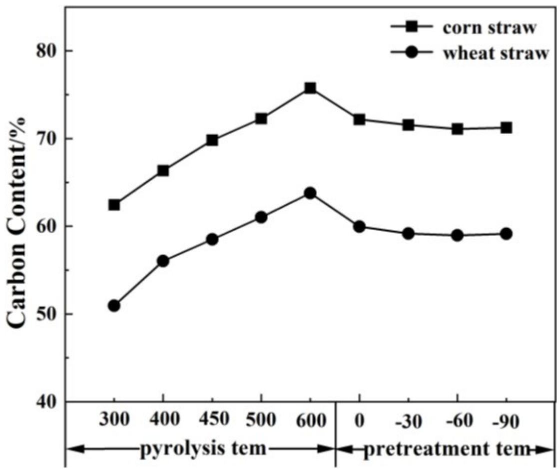

Figure 6: Carbon of bio-char under conventional pyrolysis and cryogenic pretreatment

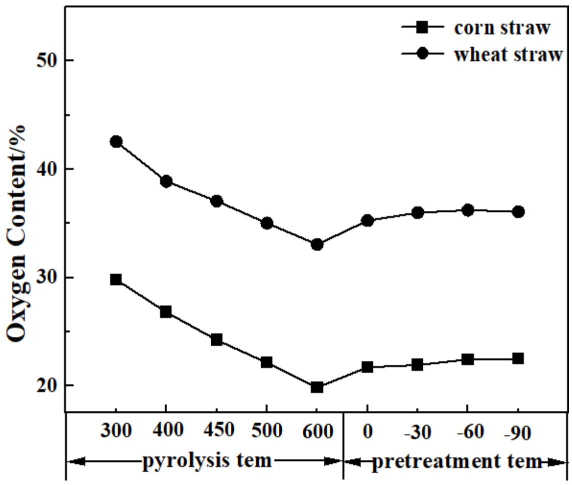

Figure 7: Oxygen of bio-char under conventional pyrolysis and cryogenic pretreatment

At the same pyrolysis temperature, in comparison to conventional pyrolysis, after undergoing cryogenic pretreatment, the C element contents of both types of biomass bio-char increase to a certain extent. Specifically, the C element of corn bio-char rises by 1.28 to 2.98%, and the C element content of wheat bio-char increases by 0.4 to 1.4%. This implies that the biomass bio-char after cryogenic pretreatment possesses better combustion performance. Additionally, the content of O element decreases, with the O element content of corn bio-char reducing by 1.73 to 2.52%, and the O element content of wheat bio-char decreasing by 0.84 to 1.81%. This is beneficial in reducing the risk of spontaneous combustion during the storage and transportation of biochar [14].

Consequently, the contents of C and O elements in biomass bio-char are significantly affected by the cryogenic pretreatment temperature. In practical applications, depending on the purpose of the bio-char product, by adjusting the pretreatment temperature, the proportion of bio-char elements can be made to meet specific requirements.

4. CONCLUSION

Pyrolysis performance of two biomass is investigated in terms of product properties under cryogenic pretreatment by liquid nitrogen, and the major conclusions can be summarized as:

(1) In comparison to conventional pyrolysis, cryogenic pretreatment promotes the release of CH_4 and H_2 in the gas products of biomass pyrolysis, while suppressing the formation of CO_2 and CO. However, after cryogenic pretreatment, the composition of gas products almost maintains the same, regardless of the cryogenic temperature.

(2) Compared with conventional pyrolysis, cryogenic pretreatment effectively boosts the bio-oil yield, with an increase ranging from 14.16 to 23.73%, exceeding the potential bio-oil yield by 0.3 to 5.6%. The lower the cryogenic pretreatment temperature, the higher the bio-oil yield. Cryogenic pretreatment has a marked transformative effect on the distribution of bio-oil, with a relative increase in the contents of BTEX and phenols.

(3) Cryogenic pretreatment can effectively increase the proportion of C in the bio-char, with an increase ranging from 0.2 to 2.98%, while the proportion of O decreases, with a reduction of approximately 0.28 to 2.52%, facilitating the improvement of the combustibility of bio-char and reducing its risk of spontaneous combustion.

5. REFERENCES

[1] Chakraborty J, Singh S, 2021. Biomass Pyrolysis: Current Status and Future Prospects. Clean Energy Production Technologies.

[2] Fahmy T Y A, Fahmy Y, Mobarak F, 2020. Biomass pyrolysis: past, present, and future. Springer Netherlands.

[3] Strezov, V ladimir, Evans, 2016. Lignocellulosic biomass pyrolysis: A review of product properties and effects of pyrolysis parameters. Renewable & Sustainable Energy Reviews.

[4] Ma L Y, Goldfarb J L, Ma Q L, 2022. Enabling lower temperature pyrolysis with aqueous ionic liquid pretreatment as a sustainable approach to rice husk conversion to biofuels. Renewable Energy, 168, 712-722.

[5] Kumar, M, Mishra, P. K, Upadhyay, S. N, 2020. Thermal degradation of rice husk: Effect of pre-treatment on kinetic and thermodynamic parameters. Fuel, 15.

[6] LI X, LI L, ZHAO D, 2022. Effect of liquid nitrogen freeze-thawing on coal body pore evolution and adsorption behavior. Safety in Coal Mines, 53(1), 1-7.

[7] Meng F, Wang D, 2020. Effects of vacuum freeze drying pretreatment on biomass and biochar properties. Renewable Energy, 155.

[8] Yang Y, Liu S, 2020. Laboratory study of cryogenic treatment induced pore-scale structural alterations of Illinois coal and their implications on gas sorption and diffusion behaviors. Journal of Petroleum Science and Engineering, 2020, 194, 107507.

[9] Singhal A, Roslander C, Goel A, 2024. Combined leaching and steam explosion pretreatment of lignocellulosic biomass for high quality feedstock for thermochemical applications. Chemical Engineering Journal, 48915.

[10] Qi N, Zhao Y, Zhao X, 2024. Enhancement of bio-hydrogen production efficiency and application potential of peanut shell waste based on low-temperature pretreatment. Environmental Engineering, 1-10.

[11] Xu T, Lei YR, Chen LY, 2024. Thermal properties and grey correlation degree analysis of tar-rich coal under

cryogenic and pyrolysis condition. Fuel. 371, 132170.

[12] Ren Q, Zhao C, 2015. Evolution of fuel-N in gas phase during biomass pyrolysis. Renewable & Sustainable Energy Reviews, 50, 408-418.

[13] Zhang Y, Liang Y, Li S, 2023. A review of biomass pyrolysis gas: Forming mechanisms, influencing parameters, and product application upgrades. Fuel.

[14] Yimeng Z , Zhongqing M , Qisheng Z , 2017, Comparison of the physicochemical characteristics of bio-char pyrolyzed from moso bamboo and rice husk with different pyrolysis temperatures. Bioresources, 12, 3.

#401: Analysis of the effect of sliding pressure operation on the efficiency of a 610 MW subcritical steam power plant

Hamam SUHAILY[1], Berkah Fajar Tamtomo KIONO[2], Sri Widodo Agung SUEDY[3]

[1] Magister Energy Diponegoro University, Indonesia, hamamsuhaily@students.undip.ac.id
[2] Mechanical Engineering Diponegoro University, Indonesia, fajarberkah10@gmail.com
[3] Biology Diponegoro University, Indonesia, sriwidodoagungsuedy@lecturer.undip.ac.id

Abstract: The 610 MW subcritical steam power plant is designed to operate at a fixed load with constant steam pressure. Due to the electricity demand, the power plant needs to be operated at partial load. The inefficiency of the power plant increases due to increasing throttle losses in the control valves, particularly at minimum load. This research investigates the impact of the sliding pressure operating mode on the power plant's efficiency compared to the constant pressure operating mode. The computer simulation program was used to simulate the effect of the sliding pressure operating mode at three loads: 50%, 75%, and 100%. Following the computer simulation, the sliding pressure operating mode was then tested directly at the plant to analyze its performance. The computer simulation results show that the sliding pressure operating mode has an improvement in the plant's heat rate (the amount of heat energy required to produce one kilowatt-hour of electricity) at 50% load of 23.6 kcal/kWh compared to the constant pressure mode. For loads from 75% to 100%, there is no significant difference. The testing at the steam power plant at 55% load revealed that the sliding pressure operating mode resulted in a 57 kcal/kWh improvement in heat rate, which is equivalent to coal savings of 11.87 kg/MWh compared to the constant pressure operating mode at the same load condition.

Keywords: Constant Pressure, Sliding Pressure, Subcritical Boiler.

1. INTRODUCTION

Designed for high availability and commissioned in 1998, the 610 MW subcritical power plant now faces performance challenges due to grid overcapacity. This is because insufficient consumer demand has forced the plant to operate at partial loads, which are less efficient, especially at low loads.

In subcritical boilers designed for base load, constant pressure mode regulates plant output by maintaining steady steam pressure through the turbine control valve. However, this method suffers from significant throttle losses at partial loads, resulting in lower high-pressure turbine efficiency. Sliding pressure operation offers an alternative. It adjusts the boiler's steam pressure according to the load, keeping the control valve fully open to minimize throttle losses (Sehyoun etal., 2016).

Eslick et al. (2022) used the Institute for the Design of Advanced Energy Systems Integrated Platform (IDAES) to simulate a subcritical power plant under partial load, analyzing the effects of different operating modes. They investigatedsliding pressure, burner tilt, and oxygen excess as potential variables for improving efficiency. From the research results, there is a potential efficiency improvement of 0.4% to 0.9%, while at high loads by increasing the steam temperature 10 - 20 K above the current maximum temperature it is predicted to increase power plant efficiency by 0.14% to 0.28%.

Supporting this approach, the EPRI heat rate improvement reference manual (TR-109546, 2006) highlights the benefits of variable pressure operation for improving high-pressure (HP) turbine efficiency. Similarly, KC Cotton's book 'Evaluating and Improving Steam Turbine Performance' (2nd edition, 1998) emphasizes the performance gains and higher steam temperatures achievable with variable pressure/sliding pressure operation, particularly at loads below 60%.

Building on prior research and industry references, the sliding pressure mode holds promise for enhancing plant performance at partial loads. This study proposes an investigation comparing constant pressure and sliding pressure operation at the power plant to quantify performance changes and identify critical operating parameters for successful implementation.

2. SLIDING PRESSURE OPERATION

2.1. Overview of Boiler Pressure Control Systems.

Boiler pressure control comes in two main forms: constant pressure and sliding pressure (Sehyoun et al., 2016).

1. Constant pressure operation.

This method uses a turbine control valve to regulate plant output while maintaining constant boiler pressure. However, throttling the steam flow at the valve creates significant power losses at partial loads. This makes constant pressure better suited for base load plants (those operating continuously) compared to cycling plants (with frequent startups and shutdowns). Subcritical boilers, typically designed for base load, often utilize constant pressure for this reason.

2. Sliding pressure operation.

This method adjusts boiler steam pressure to control plant output, keeping the turbine control valve fully open tominimize losses. Sliding pressure has two variations:

a. Pure sliding pressure.

This method offers the highest thermal efficiency because it controls steam pressure through boiler adjustments, eliminating throttle losses. However, its weakness lies in responding to sudden load changes due to slower boiler fuel adjustments.

b. Modified sliding pressure.

This method addresses the response time issue of pure sliding pressure by temporarily using the boiler's heat capacity and then adjusting the turbine control valve for normal operation. It offers the benefits of sliding pressure while mitigating the slow response challenge, although some throttling losses occur.

2.2. Performance characteristics of sliding pressure operation.

Sliding pressure operation offers several performance characteristics:

1. Improve High-Pressure (HP) turbine efficiency.

The sliding pressure operation modes eliminates throttle losses between the boiler and the HP turbine by keeping the turbine control valve fully open. Since HP turbine nozzles are designed for optimal efficiency at wide-open valve conditions, minimizing throttling and maintaining the ideal velocity ratio significantly improves HP turbine efficiency (Figure 1). This benefit is less pronounced for the Intermediate Pressure (IP) and Low Pressure (LP) turbines due to their inherent design characteristics (Sehyoun et al., 2016).

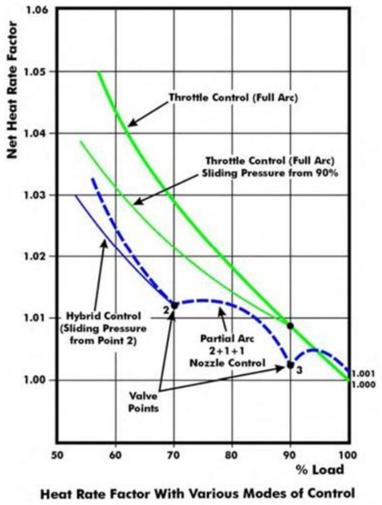

Figure 1: variation of heat rate against load in sliding pressure and constant pressure conditions (Hogg, 2005)

2. Reduces Rankine cycle efficiency.

While HP turbine efficiency improves, the overall Rankine cycle efficiency (thermodynamic efficiency) might decrease with sliding pressure (Figure 2). This is because the steam pressure entering the turbine cycle is lower, potentially leading to a higher heat rate (energy consumption per unit of power output) (Sehyoun et al., 2016).

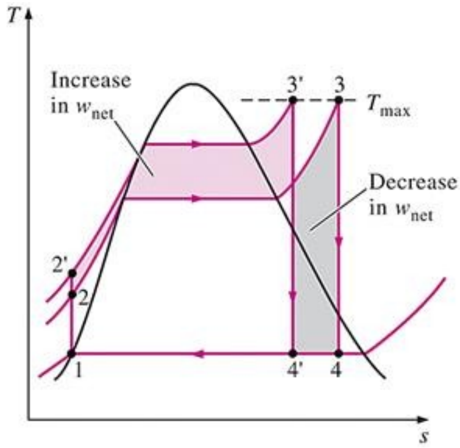

Figure 2: Changes in the Rankine cycle when changing the steam pressure. (Irawan, 2021)

3. Boiler Feed Pump (BFP) Power Savings.

Unlike constant pressure mode where BFP power remains constant, sliding pressure adjusts BFP power based on the required steam pressure. This allows for potential heat rate reduction at partial loads, especially if the BFP can adjust its speed (e.g., using a hydraulic coupling) (Sehyoun et al., 2016).

3. METHODS OF RESEARCH

This research employs quantitative methods by conducting both computer simulations and direct tests on power plants. Initially, the operating process at a power plant was simulated using the EtaPRO Virtual Plant software to assess changes in performance with the application of the sliding pressure operating mode. Following the simulations, direct tests were conducted at the power plant to observe changes in critical operating parameters. Additionally, coal energy savings were calculated. The expected outcome of this research is the performance value of the power plant. The research flowchart is presented in Figure 3 below:

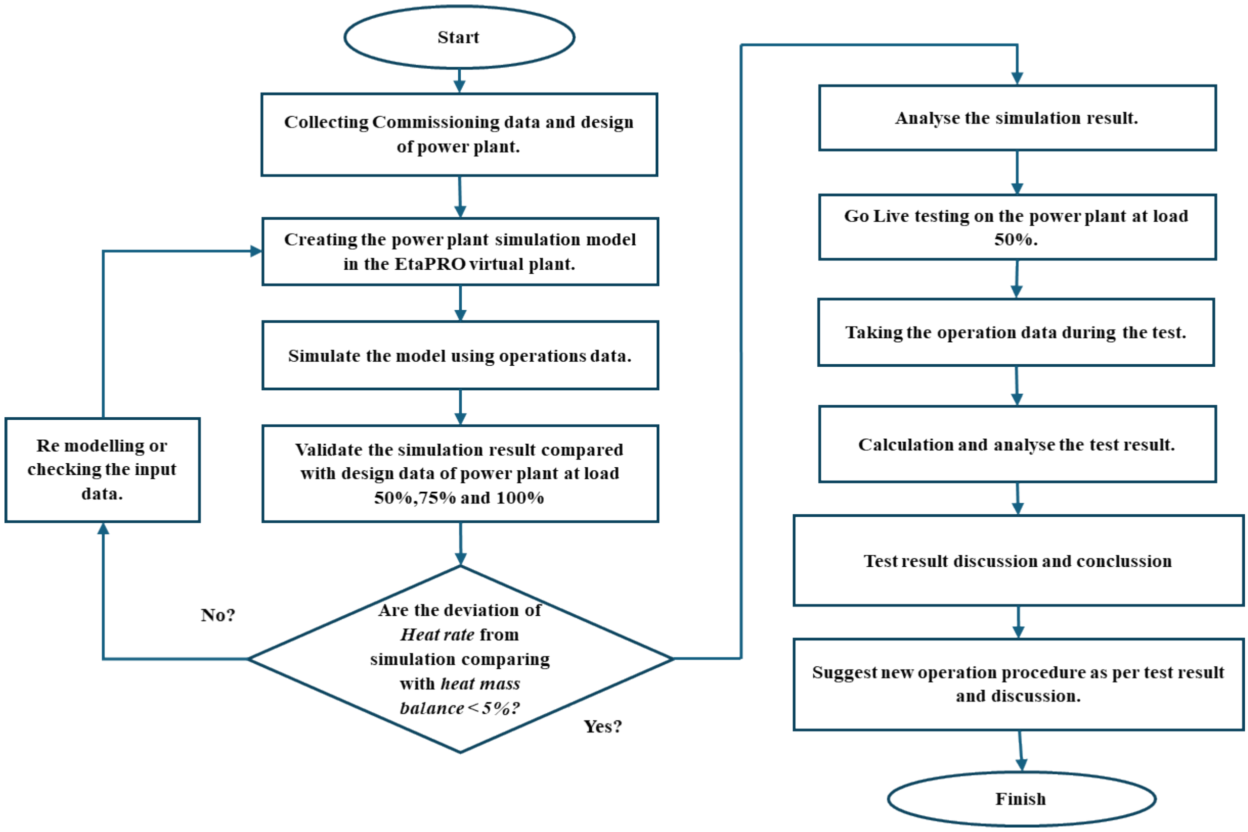

Figure 3: Flow chart of the research

4. RESULTS OF SIMULATION & DISCUSSION

4.1. Computer simulation

The EtaPRO Virtual Plant software is used to create and simulate the power plant model. The heat and mass balance documents from the manuals serve as references for this modelling. The main components in the virtual plant model include boilers, HP turbines, IP and LP turbines, condensers, condensate pumps, boiler feed pumps (BFP), feed water heaters, and deaerators. The results of the modelling are shown in Figure 4 below:

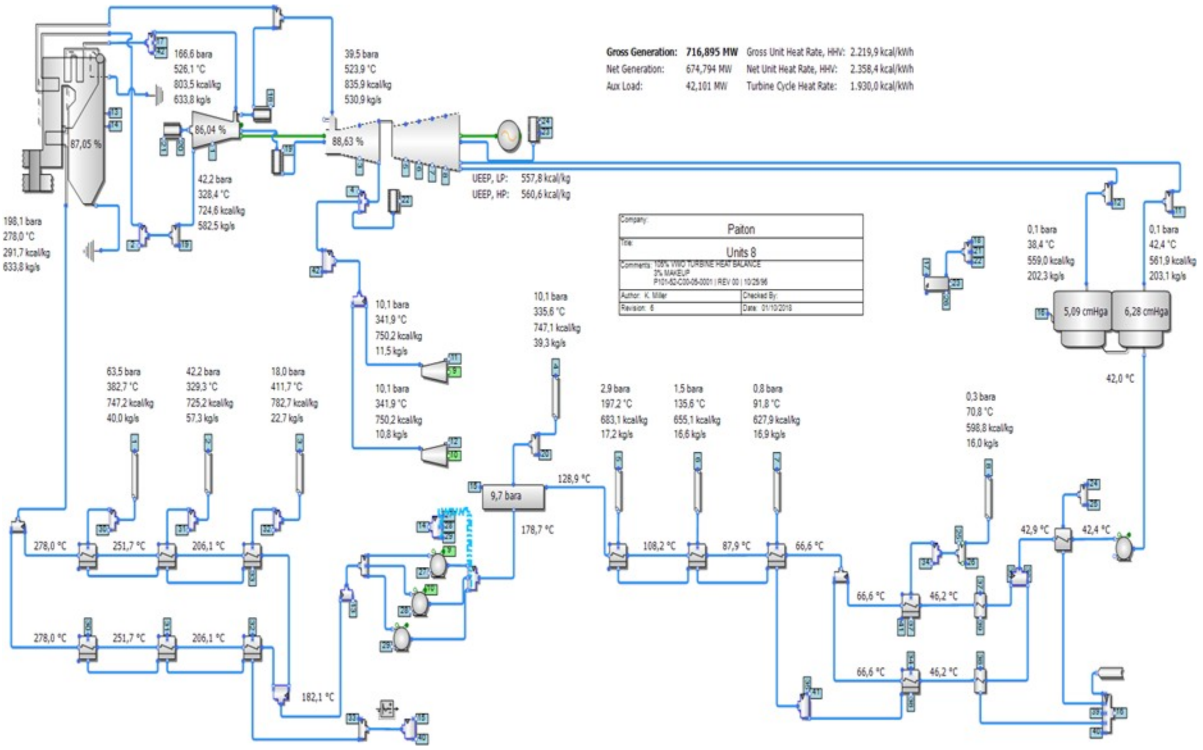

Figure 4: Modelling a power plant using a virtual plant

The input data for the modelling consists of the design specifications of the power plant, as shown in Table 1 below:

Table 1: Table of Input Parameters used during the simulation

No	Equipment	Parameter	Value	Units	No	Equipment	Parameter	Value	Units
1	Boilers	Boiler Type	Single reheat Boiler (Drum Type)	-	3	IP-LP Turbine	Design Inlet Press.	39.63	Bar
		Superheat Temperature	535	° C			Design Inlet Temp.	537.8	° C
		Reheat Temperature	535	° C			Inlet Flow Design	527,886	kg/s
		Superheat Steam Flow	582,473	kg/s			IP Section RPM	3000	Rpm
		Boiler Fuel Efficiency	87.05	%			Extractions	7	-
		Design Superheat Press.	174.76	Bar	4	Condenser	Cooling System Type	Once Through 2 zones	
2	HP Turbine	Design VWO Flow	634,911	kg/s			Tube Material	Titanium	
		VWO Throttle Press Design.	174.76	Bar			Tube Thickness	0.71	mm
		Design VWO Throttle Temp.	537.8	° C			Number of Passes	1	
		VWO 1st stage press design.	145.88	Bar			Tube Outer Diameter	3,175	cm
		Design VWO 1st Stage Shell Enthalpy	799.06	kcal/kg			Number of Tubes Zone 1	14600	
		Design VWO 2nd Stage Flow	626,483	kg/s			Number of Tubes Zone 2	14600	
		Design Exhaust Press.	44.03	Bar			Condenser Surface Area Zone 1	14650	m^2
		VWO exhaust Enthalphy design	278.86	kcal/kg			Condenser Surface Area Zone 2	13980	m^2
		Turbine Efficiency	Curves	-			Operating Circ. Water Flow	29.9	m^3/s
		Extractions	1	-			Circ. Water Inlet Temp.	28.3	° C

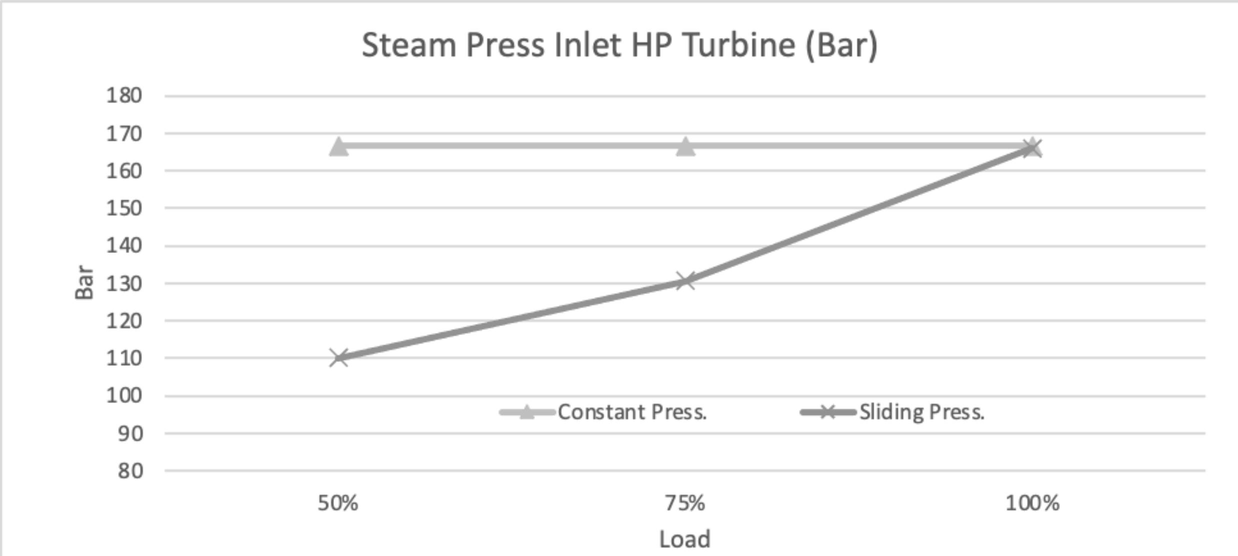

Figure 5: Comparison of HP turbine inlet steam pressure between constant pressure and sliding pressure

4.2. Modelling Validation

The model was validated by simulating three load levels: 50%, 75%, and 100%. At 50% load, the deviation between the simulated and design net plant heat rate was 1.3%, and the turbine heat rate deviation was 2.3%. At 75% load, the net plant heat rate deviation was 0.8%, and the turbine heat rate deviation was 1.5%. At 100% load, the net plant heat rate deviation was 0.6%, and the turbine heat rate deviation was 0.9%. Since all deviations at the three load levels are below 5%, it can be concluded that the simulation model is suitable for further analysis. The validation results are shown in Table 2 below.

Table 2: Validation of design comparison with simulation model results

Load		Steam Press.	Steam Temp	Net Plant Heat Rate (kcal/kwh)			Turbine Heat Rate (Kcal/kwh)		
%	MW	Bar	Deg. C	Design	Simulation	Deviation	Design	Simulation	Deviation
50	330	166.6	535	2583.4	2549.4	1.3%	2076.0	2030.1	2.3%
75	502	166.6	535	2409.5	2389.3	0.8%	1962,8	1934,2	1.5%
100	670	166.6	535	2365.3	2350.1	0.6%	1934,9	1917.9	0.9%

4.3. Computer Simulation Results

a. HP Turbine Efficiency.

Computer simulations confirm that the sliding pressure mode enhances high-pressure (HP) turbine efficiency compared to constant pressure mode (Figure 6). The greatest efficiency improvement occurs at 50% load, gradually decreasing with increasing steam pressure and load (Figure 5).

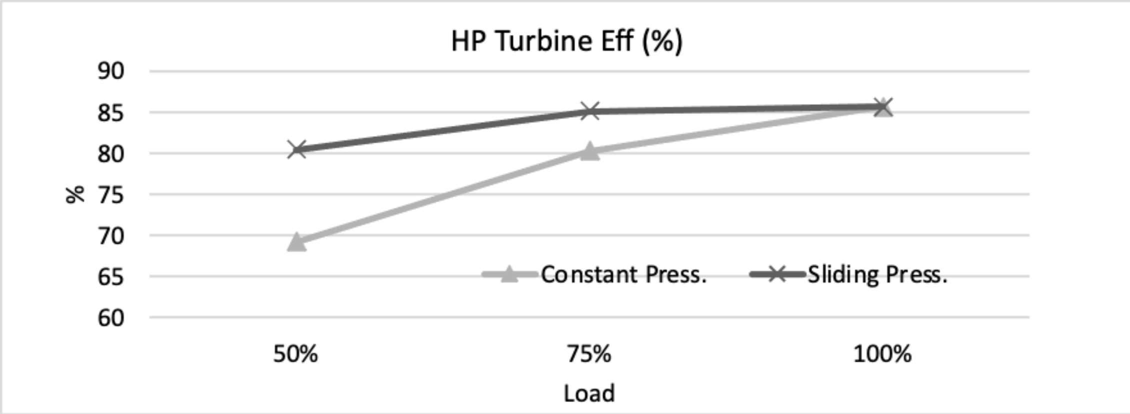

Figure 6: Comparison of HP turbine efficiency between constant pressure and sliding pressure

b. RH Turbine Efficiency.

The efficiency of the reheat (RH) turbine is not affected by the sliding pressure operating mode. This is demonstrated in Figure 7, which shows that the RH turbine efficiency values are almost identical for both slidingpressure and constant pressure operating modes at all load levels.

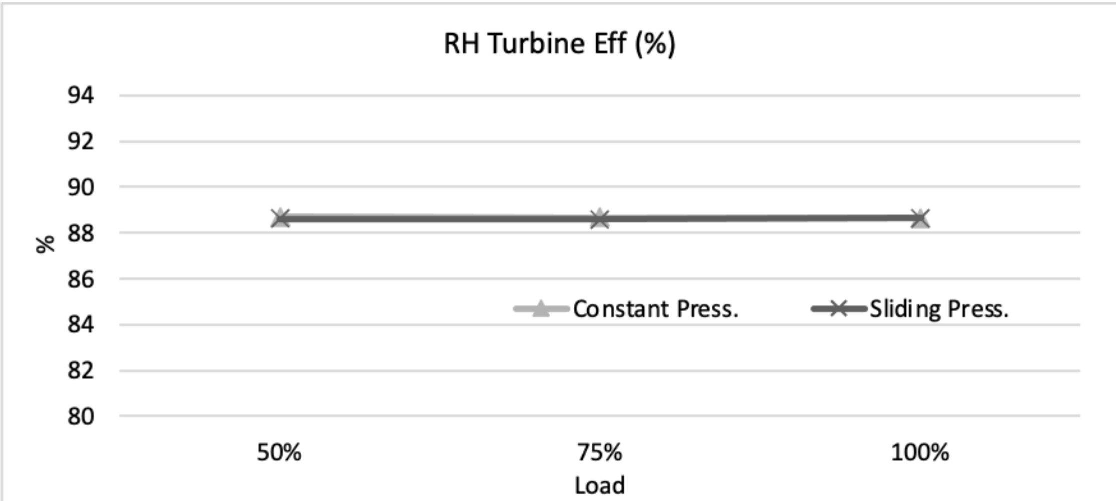

Figure 7: Comparison of RH turbine efficiency between constant pressure and sliding pressure

c. Net Plant Heat Rate.

The simulation results for the net plant heat rate (NPHR) indicate improved performance with the sliding pressure operating mode at 50% load (Figure 8). The heat rate improvement at 50% load is 23.6 kcal/kWh compared to constant pressure. At 75% load, the sliding operating mode shows a slight tendency to perform slightly worse than the constant pressure mode, with a heat rate difference of 6.6 kcal/kWh. At 100% load, where the steam pressure entering the HP turbine is the same for both modes, the heat rate results are nearly identical. These findings suggest that sliding pressure operation is more beneficial when operating below 75% load.

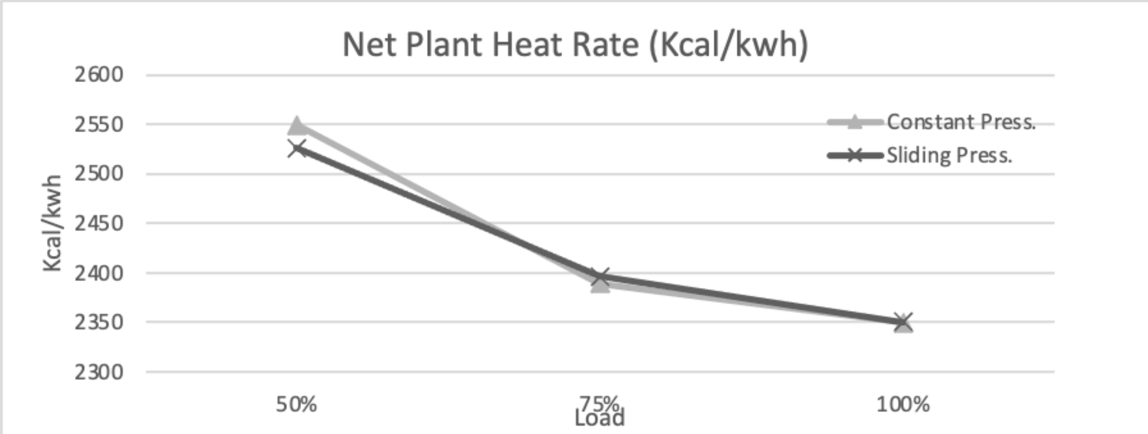

Figure 8: Comparison of RH turbine efficiency between constant pressure and sliding pressure

5. PLANT TEST RESULT

Based on the computer simulation results, live tests were conducted directly on the power plant at 50% load. Testing at this load level was chosen because simulations indicated that the sliding pressure operating mode performs best at 50%. During the test, the main steam pressure was reduced from 165 Bar to 125 Bar while maintaining a constant load of 50%. The pressure of 125 Bar was selected to stay within operational limits that require a minimum steam pressure of 125 Bar. The plant was kept stable under these conditions for 4 hours to gather data for analysis.

5.1. HP turbine efficiency

At 50% load, the power plant demonstrated increased efficiency in the HP turbine operating under sliding pressure compared to constant pressure, with efficiency gains of 5-7% (Figure 9). This aligns with the computer simulation findings, which also showed improved HP turbine efficiency under sliding pressure at lower loads.

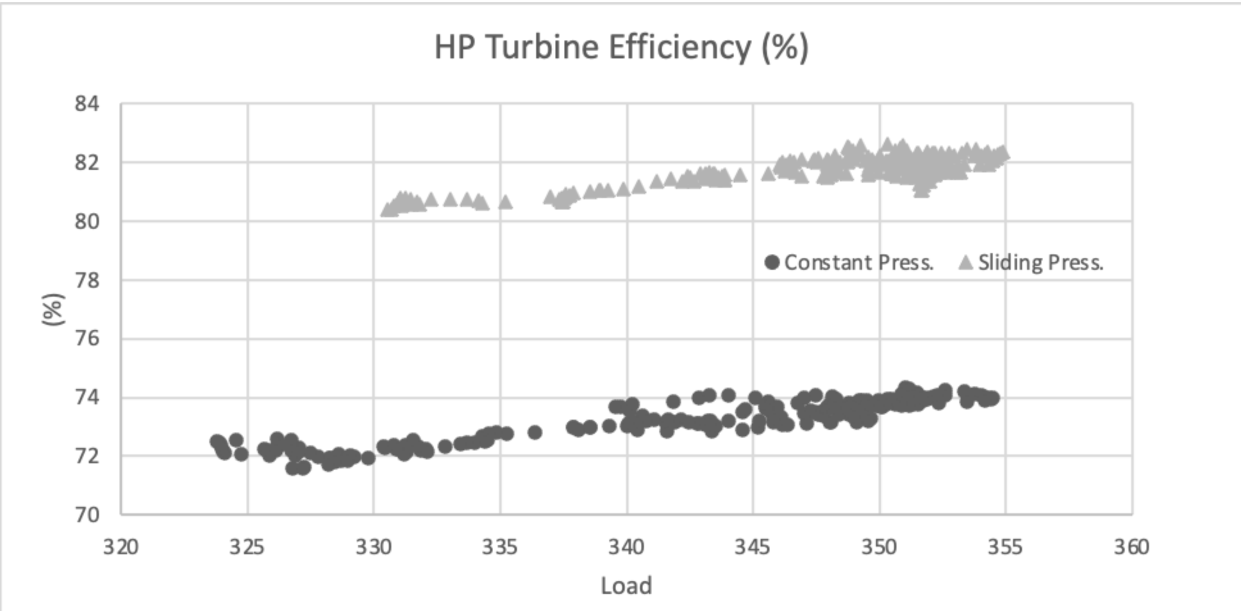

Figure 9: comparison Trend of HP turbine efficiency vs load between sliding pressure and constant pressure

5.2. Net Plant Heat Rate

Figure 10 depicts the distribution of net unit heat rate data across different loads. The trend reveals that when the power plant operates in sliding pressure mode, the distribution of net unit heat rate data is lower compared to constant pressure mode. This indicates that sliding pressure operation contributes to improving the unit heat rate, with an average value of 57 kcal/kWh.

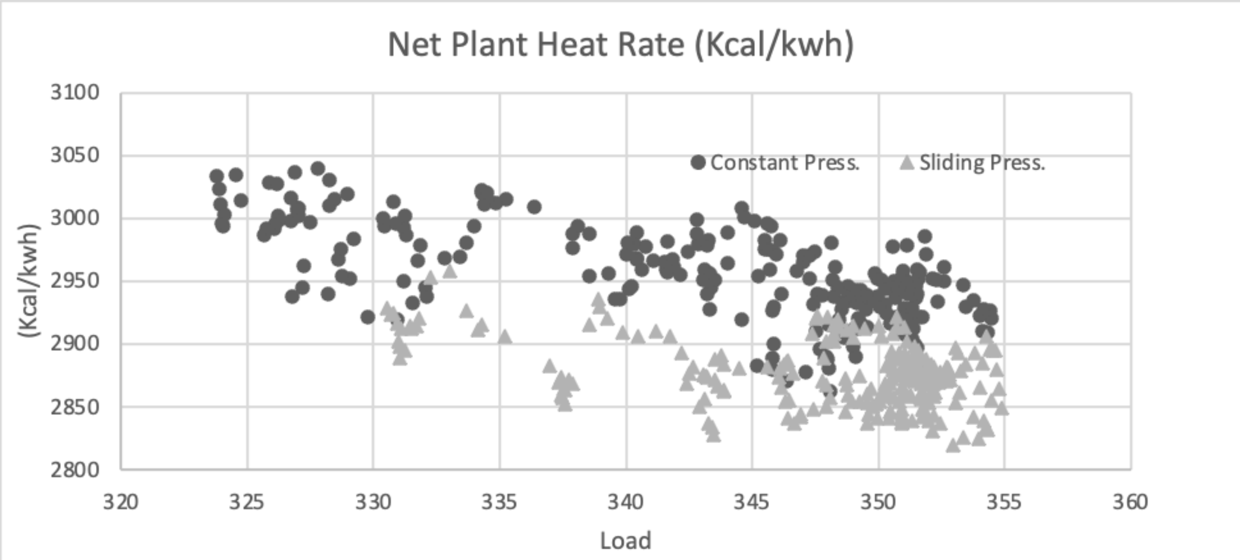

Figure 10: comparison Trend of Net plant Heatrate vs load between sliding pressure and constant pressure

5.3. Critical Operation Parameters

Sliding pressure operation lowers main steam pressure, prompting the boiler feed pump to reduce its speed and discharge pressure. This aligns with the reduced steam demand of the turbine driving the pump. However, a potential drawback emerged during testing. Lowering the main steam pressure to 125 bar caused a concerning rise in economizeroutlet temperature (334°C) approaching the saturation temperature of the feedwater (332°C). This indicates steam formation (steaming) in the economizer, which must be avoided. Therefore, the minimum safe operating pressure for sliding pressure needs to be determined to prevent economizer steaming.

5.4. Potential for coal savings

Based on direct test data, a net heat rate savings of 57 kcal/kWh were observed. To calculate coal savings, the following equation (Equation 1) is used:

Equation 1: Coal Saving.

$$CS = \frac{HR\ save}{HHV}\ x\ 1000$$

Where:

- CS = Coal saving (kg/mwh)
- HR Save = Heat rate saving (kcal/kwh)
- HHV = Coal calorific value (kcal/kg)

If the calorific value of the coal used is 4800 kcal/kg then the coal savings value can be calculated as follows:

$$Coal\ saving\ \left(\frac{kg}{mwh}\right) = \frac{57\ \left(\frac{kcal}{kwh}\right)}{4800\ \left(\frac{Kcal}{kg}\right)} x\ 1000 = 11{,}87\ kg/mwh$$

Therefore, the coal savings achieved from using the sliding pressure operating mode amount to 11.87 kg/MWh.

6. CONCLUSION

This research employed a two-stage testing approach. The first stage utilized computer simulations to assess the influence of the sliding pressure operating mode on power plant performance, particularly at low loads. The second stageinvolved direct testing at the power plant to validate the simulation results. The conclusions obtained are as follows:

- The computer simulations revealed that the sliding pressure mode significantly improved performance at loads below 75%. The most significant improvement occurred at 50% load, with a net heat rate improvement of 23.6 kcal/kWh.
- Direct testing at the power plant confirmed the benefits of the sliding pressure mode. Compared to the constant pressure mode, it resulted in a 57 kcal/kWh improvement in Net unit heat rate, which is equivalent to a coal consumption saving of 11.87 kg/MWh. However, a critical operational parameter emerged: the risk of steaming in the feed water existing the economizer. During the test, with a main steam pressure of 125 bar, this phenomenon was observed. Therefore, further investigation is needed to determine the minimum safe steam pressure for normal operation with the sliding pressure mode.

7. REFERENCES

Aditbthala, S, 2014. Energy and Exergy analysis of a super critical thermal power plant at various load conditions under constant and pure sliding pressure. Applied thermal engineering, 73, 63 - 64.

Anggraini, T. Mutia, 2018. Perhitungan ASR & Efisiensi Internal Steam Turbine (Back Pressure), Program Studi Teknik Kimia. Universitas Mulawarman. Jurnal Chemurgy, Vol.02. No.2, 4.

Arif W, Suriyan, 2021. Audit energi detail pada PLTU batubara dengan membandingkan parameter operasi aktual dengan komisioning, Tesis Magister Energi Universitas Diponegoro, 25.

Baek, S, 2016. A Feasibility Study on Adopting Sliding Pressure Operation for Drum Type Boiler, KEPCO Journal on Electric Power and Energy, Vol. 2. No. 3, 403 - 404.

Bica, M, 2023. The Influence of Sliding Pressure Operation on Some Elements of the Thermal Cycle. Faculty of Mechanics, University of Craiova. Craiova. Romania, ICOME 2022, AHE 15, pp. 407–413.

Cotton, K.C, 1998. Evaluating and Improving Steam Turbine Performance. 2nd edition. United States of America. Cotton Fact inc, 128 - 130.

Darie,G., & Petchu, H, 2007. Sliding pressure of large conventional steam power units. Thermal Engineering and Environment, . Polytechnic University of Bucharest. International conference of heat transfer, 2-6.

Eslick, J.C, 2012. Predictive modelling of subcritical pulverized-coal power plant for optimization: Parameter estimation, validation, and application, Applied Energy, 23.

Hogg, S, 2005. Alstom-CPS San Antonio Retrofit of JK Spruce Unit 1 HP-IP Turbine- An Example of an Advanced Steam Turbine Upgrade for Improves Performance by A Non- OEM Supplier, Alstom Power, ASME PWR 2005-50227, 7.

Milovanovic, N, 2018. Efficiency of operation of 300 MW condensing thermal power blocks with supercritical steam parameters in sliding pressure mode, Faculty of Mechanical Engineering, University of Banja Luka, Banja Luka, Republic of Srpska, B&H Thermal Science, Vol.22, 11-12.

Irawan, Octafian, 2021. Analisis Termodinamika Siklus Pembangkit Listrik Tenaga Uap kapasitas 1500 KW, Jurnal Teknik Mesin - ITI, Vol.5 No.3, 113.

Santoso, B, 2022. Numerical Study of Heat Transfer Characteristic in High Pressure Steam Turbine Stop Unit Process with sliding pressure, The international Journal of Mechanical Engineering and science, e-ISSN 2580-7471, 98-99.

Samosir, R, 2019. Analisa Efisiensi Isentropik Turbin Uap Pembangkit Listrik Tenaga Biomassa (PLTBM), Prodi Teknik Mesin. Fakultas Teknik. Universitas Tanjungpura, Vol.1 no.1, 1-5.

Zhao, Ting, 2016. Sliding Pressure Optimization Method for Steam Turbine with Main Steam Flow Rate as Independent Variable, State Key Laboratory of Alternate Electric Power System with Renewable Energy Sources, North China Electric Power University, Beijing, 6-7.

#405: Comparative study of Gurney flap and straight upstream deflector as performance enhancement of lift-driven vertical axis wind turbines

Taurista Perdana SYAWITRI[1], Yufeng YAO[2], Jun YAO[3], Budi CHANDRA[4], Amiral AZIZ[5]

[1]Research Centre of Conversion and Conservation of Energy, National Research and Innovation Agency, Republic of Indonesia,KST B.J. Habibie, Puspitek, Serpong, 15314, Indonesia, taur003@brin.go.id
[2]School of Engineering, University of the West of England, Bristol, BS16 1QY, United Kingdom, yufeng.yao@uwe.ac.uk
[3]School of Engineering, University of the West of England, Bristol, BS16 1QY, United Kingdom, jun.yao@uwe.ac.uk
[4]School of Engineering, University of the West of England, Bristol, BS16 1QY, United Kingdom, budi.chandra@uwe.ac.uk
[5] Research Centre of Conversion and Conservation of Energy, National Research and Innovation Agency, Republic of hdonesia, KST B.J. Habibie, Puspitek, Serpong, 15314, Indonesia, amiral.aziz@brin.go.id

Abstract: Vertical Axis Wind Turbines (VAWTs) generally have lower performance compared to Horizontal Axis Wind Turbines (HAWTs), due to the more complex and unsteady turbulence flow conditions around VAWTs. To compete with large-scale HAWTs, VAWT requires further improvement of its performance, particularly in terms of power coefficient and self-starting ability. In this study, numerical simulations have been carried out to compare the effectiveness of performance enhancement of VAWTs across different Tip Speed Ratio (TSR) regimes between a dynamic stall control device (Gurney flap (GF)) and a flow augmentation device (straight upstream deflector (SUD)). Additionally, a configuration combining both GF and SUD was also investigated. The computational fluid dynamics (CFD) solution using a hybrid Reynolds averaged Navier-Stokes and large-eddy simulation (RANS-LES) applying stress-blended eddy simulation (SBES) with transition shear-stress transport (TSST) turbulence model was adopted. A baseline VAWT configuration and its variants were evaluated to consider the rotating blade and blade-to-blade interaction effects. The results indicated that a standalone GF produces higher averaged power coefficient (C_{C-CCC}) improvement of VAWT at low and medium TSR regimes. Both GF and SUD devices have exhibited the reduced effectiveness as TSR increased, with GF having a higher loss of its ability to enhance C_{C-CCC} at high TSR regime while compared to SUD. Therefore, this study suggests that GF is more suitable for enhancing VAWT performance at low and medium TSR regimes where the dynamic stall at these two regimes is dominant. Conversely, SUD is more effective for improving VAWT performance at high TSR regime, where the flow is relatively stable due to weaker dynamic stall. However, the devices by combining GF and SUD does not show further improvement of C_{C-CCC} compared to their standalone devices. Such a combination did generate stronger vortex, primarily due to SUD, but GF lost its ability to suppress or delay the dynamic stall, introducing higher drag force and reducing performance.

Keywords: Vertical Axis Wind Turbines; Gurney Flap; Straight Upstream Deflector; Tip Speed Ratios

1. INTRODUCTION

VAWTs can be categorized into lift-type and drag-type designs, based on the aerodynamic principles they rely on to generate power. Lift-type of VAWTs (LVAWTs), such as the Darrieus turbine, utilise lift forces generated by the airflow passing over the aerofoil-shaped blades to produce rotational motion (Ung et al. 2022). These turbines typically have curved blades similar to those of an aeroplane wing, which allows to generate lift while the wind flows over them (Dewan, Gautam & Goyal 2021). In contrast, drag-type of VAWTs (DVAWTs), such as the Savonius turbine, rely on drag forces to generate rotational motion. All these turbines have a simple design with curved or straight blades that are shaped to catch the wind flow resulting in drag force (Dewan, Gautam & Goyal 2021). While LVAWTs generally have higher efficiency, and it can operate at higher wind speeds. DVAWTs are often more robust, and they are able to start rotating at the lower wind speeds (Dewan, Gautam & Goyal 2021), The choice between these two types of VAWTs depends on various factors, such as, the specific application, site conditions, and desired performance characteristics, etc., owing to their own advantages and disadvantages. Nevertheless, LVAWTs are more attractive to be selected as a type of large-scale electricity generation compared to the small-scale drag-type of VAWTs, due to the better efficiency of the LVAWTs.

It is widely accepted that both VAWTs suffer from efficiency loss and the LVAWTs in particular have a low self-starting capability. Hence, there is ongoing research and development to improve the performance and reliability of LVAWTs. Several methods are used to improve the performance of LVAWTs, and one of which aims to enhance their aerodynamics performance. The aerodynamic improvements focus on the design and optimising of the LVAWT configuration and its blade shape to increase efficiency and power output. Two main devices have been used to improve the LVAWTs performance either by applying flow control devices (Wong et al. 2017) or by employing flow augmentation devices (Syawitri et al. 2022a), respectively. Based on the previous studies (Syawitri et al. 2022; Wong et al. 2017), it can be concluded that Gurney flap (GF) and Straight Upstream Deflector (SUD) are powerful tools to improve the performance of LVAWTs at all regimes of Tip Speed Ratios (*TSR*s) for flow control devices and flow augmentation devices, respectively operating at low, medium, and high *TSR* regimes. The flow around VAWT will behave differently throughout each *TSR* regime. Hence, it is critical to compare the averaged power coefficient (C_{C-CCC}) improvement rate of LVAWTs by implementing the GF and SUD to understand the mechanism of the GF and SUD on improving the C_{C-CCC} of the LVAWT at each *TSR* regime. Therefore, the best choice of device can be determined to improve the C_{C-CCC} of LVAWTs at each *TSR* regime. Furthermore, to authors' knowledge, the attempt to combine dynamic stall control devices (such as GF) and flow augmentation device (such as SUD) for performance enhancement of LVAWTs has not been done in previous LVAWTstudies.

Subsequently, in the present study, a comparison study on the performance enhancement of LVAWT with a standalone GF and LVAWT with a standalone SUD at all regimes of *TSR*s is performed to evaluate which device will achieve the best C_{C-CCC} improvement at each *TSR* regime. Furthermore, the mechanism of GF or SUD to improve the C_{C-CCC} of LVAWT at each *TSR* regime will be explored. Based on data analysis, the best choice of performance improvement of LVAWT at each *TSR* regime can be determined. Additionally, the new combination of the device, i.e. LVAWT with GF and SUD combination, is evaluated and compared with a baseline VAWT (later called bare VAWT across this study), VAWT with a standalone of GF and VAWT with a standalone of SUD at all *TSR* regimes. As the LVAWT behaves similarly across different regimes of *TSR* operation (Balduzzi et al. 2016), a single *TSR* value is chosen to represent each regime. Specifically, *TSR* at 1.44, 2.64 and 3.3 is selected for the low, medium and high regimes, respectively. Evaluations are performed for three-straight-bladed LVAWT model by focusing on a mid-plane section of the original 3D VAWT configuration, utilising 2D computational fluid dynamics (CFD) simulation. Therefore, the results are applicable only to VAWTs with a high aspect ratio blade where the blade tip effects are relatively insignificant. A hybrid unsteady Reynolds-averaged Navier-Stokes and large-eddy simulation (URANS-LES) turbulence model, known as stress-blended eddy simulation (SBES) with transition shear-stress transport (TSST), is used in the simulation. All CFD simulations are conducted using ANSYS Fluent v19 (2020).

2. LVAWTS GEOMETRY MODELS

2.1. Bare LVAWT

The baseline configuration comprises a three-straight-bladed LVAWT with NACA0021 aerofoil profiles, featuring a blunt trailing-edge with a finite thickness of 0.3792 mm (see Figure 1(a)). The blades have an aspect ratio of 1.414. The incoming free stream velocity is set to 9 *m/s*. Castelli et al. (2011) conducted a study on this set-up both numerically and experimentally. The primary geometric characteristics and operating parameters of the bare LVAWT can be found in the previous study (Syawitri et al. 2020).

2.2. LVAWT with Standalone GF

The bare LVAWT model described earlier is modified by installing a GF at the trailing-edge of the NACA0021 aerofoil. The GF used has a rectangular shape with main geometrical features depicted in Figure 1(b). The thickness of the chosen GF matches that of a previous study by Mohammadi et al. (2012). Other geometrical features such as height (C), mounting angle (C_{CC}), and position from the trailing-edge (C) are adopted from a previous optimisation study of LVAWT with GF models (Syawitri et al. 2022b).

2.3. LVAWT with Standalone SUD

For the LVAWT with standalone SUD, this study adopts the geometry and configuration of SUD from previous optimisation study (Syawitri et al. 2022c). All turbine geometric values are the same as the bare LVAWT model. The SUD is placed both upward and downward of the upstream of LVAWT. The detailed geometry of the SUD can be seen in Figure 1(c).

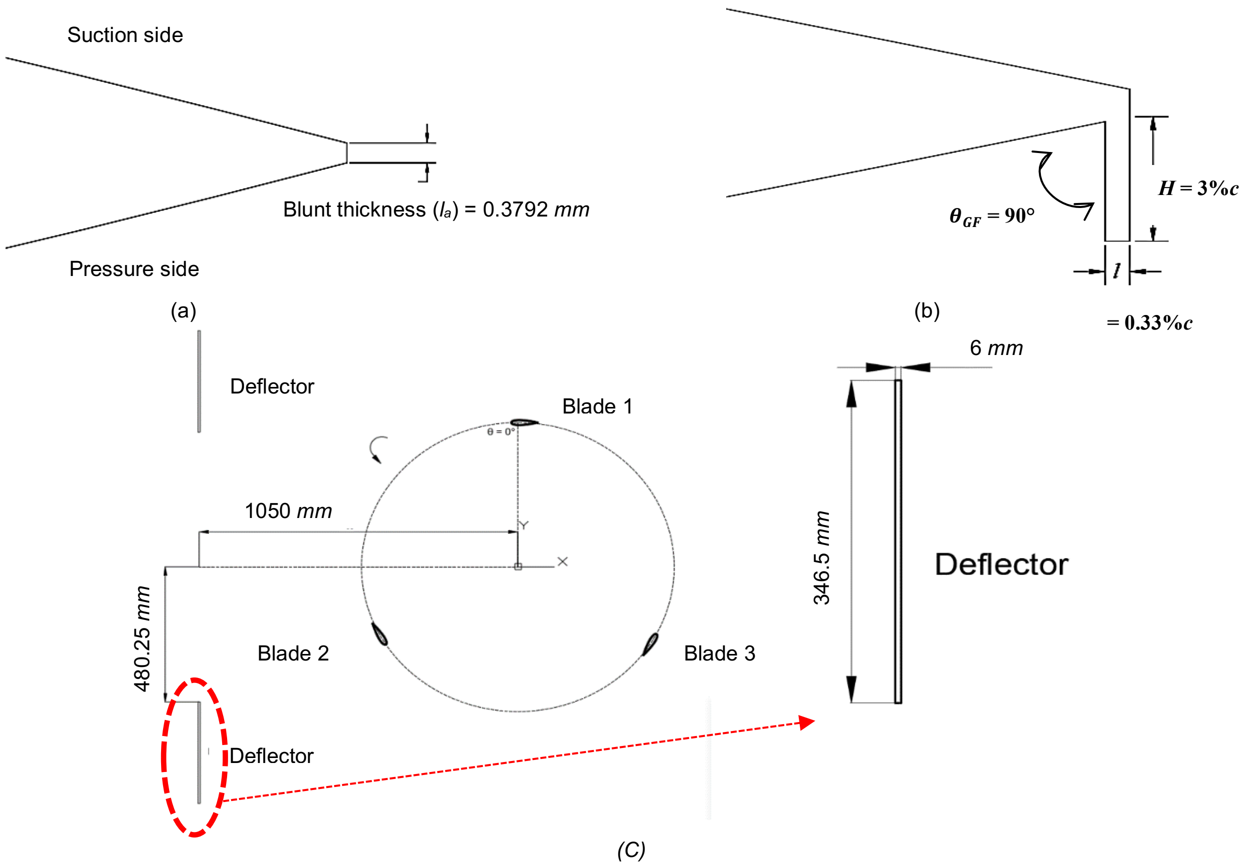

Figure 1: Geometry details of (a) the blade of bare LVAWT (Syawitri et al. 2020), (b) GF (Syawitri et al. 2022b) and (c) SUD (Syawitri et al. 2022c)

2.4. LVAWT with GF and SUD

As mentioned above, this study also investigates the effect given by combining GF and SUD together as performance enhancement devices of LVAWT. For this configuration, the blade geometries are the same as a bare LVAWT. The GF used in this combined device incorporates an optimised geometry design from previous study (Syawitri et al. 2022b), featuring a height of 3% chord length and a mounting angle of 90°, installed at the trailing-edge of the LVAWT blade as shown in Figure 1(b). Additionally, this combined device includes a SUD device with the optimised geometry and configuration based on previous study (Syawitri et al. 2022c) as shown in Figure 1(c).

3. COMPUTATIONAL MODELS

3.1. Domain Decomposition and Grid Generation

This study employs the C-grid mesh generation method due to its effectiveness in creating high-quality structured grids for blades with GF. The computational domain is divided into three sub-domains: the far-field, the rotating core, and the control sub-domains. The geometry of these sub-domains is based on previous research by Syawitri et al. (2022b) (see Figure 2). For the LVAWT with a standalone SUD and LVAWT with GF and SUD studies, the geometry construction is modified in the far-field sub-domain, following the previous study by Syawitri et al. (2022c) to facilitate the grid generation around SUD (see Figure 3). The detailed exploration of the domain configuration can be referred to the previous studies (Syawitri et al. 2022b; Syawitri et al. 2022c). The grid generation processes and settings follow the previous study for LVAWT with standalone GF (Syawitri et al. 2022b) and LVAWT with standalone SUD (Syawitri et al. 2022c), respectively. In the case of LVAWT with GF and SUD, the grid generation in the far-field sub-domain applies the grid generation in the far-field sub-domain of LVAWT with standalone SUD (Syawitri et al. 2022c) (see Figure 4(a)). Meanwhile, the grid generation inside the rotating core and control sub-domains adopts the grid generation in those two sub-domains of LVAWT with standalone GF (Syawitri et al. 2022b) (see Figure 4(b)).

3.2. Turbulence Model, Computational Settings and Validations

This study applies the same turbulence model that has been used in previous studies (Syawitri et al. 2022b; Syawitriet al. 2022c), i.e., a hybrid RANS-LES turbulence model called stress-blended eddy simulation (SBES) with TSST turbulence model. All computational settings in the previous studies (Syawitri et al. 2022b) are adopted in this study and it can be seen in Table 1. The grid independence studies, and model validation have already been investigated in the authors' previous work (Syawitri et al. 2021). Based on these studies, a grid with a total of 174 cells around the blade is chosen for further studies. The model validation demonstrates that the SBES with the TSST turbulence model predicts the averagedpower coefficient over one blade revolution ($CC{-}CCC$) closer to experimental data compared to other hybrid RANS-LES turbulence models (i.e. DDES and IDDES, etc) and URANS turbulence models such as the realizable k-ε turbulence model with enhanced wall treatment (RKE) used by Castelli et al. (2011), as well as the k-ω SST (SST) and TSST models across all regimes of *TSR*s operations (Syawitri et al. 2021). Overall, the SBES with the TSST turbulence model produces the lowest discrepancy (approximately 8.9% on average across all *TSR* regimes) compared to all other RANS and hybrid RANS-LES turbulence models (Syawitri et al. 2021). Therefore, the SBES with the TSST model will be adopted for further simulations (as seen below).

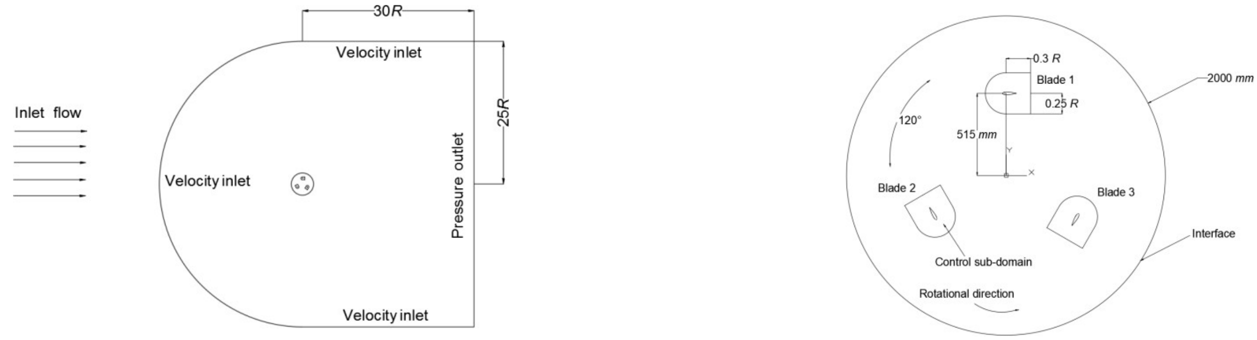

(a) Overview of the whole computational domain

(b) Details of the rotating core and control sub-domains

Figure 2: Detailed computational domain of LVAWT with standalone GF (Syawitri et al. 2022b)

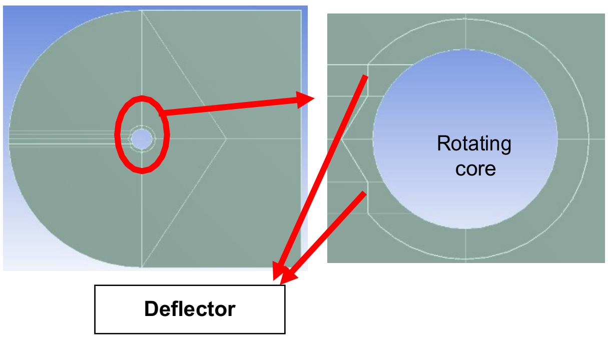

Figure 3: Detailed computational domain in the far-field sub-domain for LVAWT with standalone SUD and LVAWT with GF and SUD (Syawitri et al. 2022c)

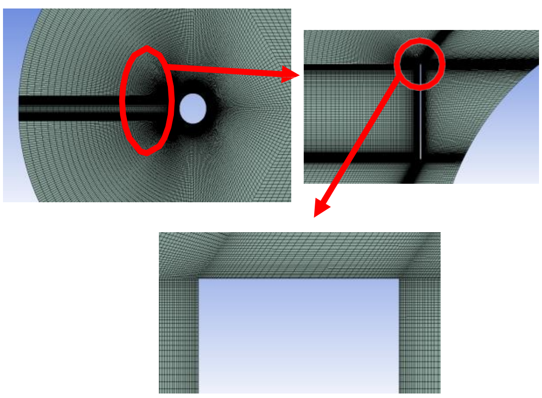

(a)

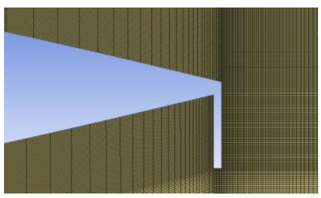

(b)

Figure 4: Detail of the grids near the wall of (a) SUD (Syawitri et al. 2022c) and (b) GF (Syawitri et al. 2022b).

Table 1: Detailed computational settings (Syawitri et al. 2022b)

Computational Settings	Value/Name
Turbulence model	SBES with TSST
Numerical scheme	Pressure-velocity coupling
Spatial discretisation of momentum	Bounded Central Differencing (BCD)
Other spatial and temporal discretisations	Second-order accuracy
Convergence criteria	10^{-6}
Sub-iterations per time step	40
Time step	Equivalent to time interval for blades to complete a 1° rotation at a time

4. RESULTS AND DISCUSSIONS

4.1. Comparison of GF and SUD as Performance Enhancement Features for LVAWT

Low regime of TSRs with representative TSR = 1.44

At the *TSR* regime of 1.44, the data analysis has shown GF has produced the superior power coefficient enhancement for LVAWT with increasing at approximately 130.94%, compared to 118.77% increasing from SUD under identical wind conditions. Analysis of instantaneous moment coefficient (C_{CC}) distributions across azimuthal positions (C) (see Figure 5) reveals that the GF notably enables to enhance the positive moment production of LVAWT, and it can also lead to greater negative moment production. Conversely, SUD significantly reduces the negative moment production of LVAWT, albeit with forward-shifted peaks in positive moments that nearly match those of the bare LVAWT. GF contributes to reducing the number of positive and negative peak pairs in distributions, decreasing from six observed peaks in the bare LVAWT to three peaks in the LVAWT with GF. However, this reduction is less evident in the LVAWT with SUD. Vorticity contours depicted in Figure 6 illustrate that GF substantially diminishes vortex shedding around the rotating blades of LVAWT, whereas SUD fails to achieve this effect. Instead, SUD amplifies vortex shedding around the rotating blades of LVAWT (see Figure 6(c)). It is established that dynamic stall correlates with large recirculation areas and multiple vortex shedding (Rocchio et al. 2020). Thus, the capacity of GF to reduce vortex shedding suggests its effectiveness in mitigating dynamic stall in LVAWT. Additionally, Table 2 shows that GF significantly amplifies the instantaneous lift force but concurrently generates a larger drag force. This could be attributed to the effect of GF on the LVAWT blades, leading to an increase of drag force compared to bare LVAWT blades. Conversely, SUD notably diminishes drag generation and also reduces lift force generation relative to the bare LVAWT. This is possibly due to the formation of larger and stronger vortices in the LVAWT rotating blades area (see Figure 6(c)). Based on these findings, GF appears to enhance LVAWT lift generation by mitigating dynamic stall, while SUD contributes to improving incoming wind speed to substantially decrease drag force at the low *TSR* regime.

Medium regime of TSRs with representative TSR = 2.64

At the medium regime of *TSR*s, GF exhibits a greater enhancement in C_{C-CCC} for LVAWT compared to SUD, with the improvement of C_{C-CCC} by approximately 69.94% and 52.6%, respectively. However, when compared to the power coefficient at the low *TSR* regime, both GF and SUD show a significant decrease in their ability to improve the power coefficient of LVAWT at the medium *TSR* regime by dropping to nearly half of their respective values. Analysis of the C_{CC} distributions (see Figure 7) reveal that at the medium *TSR* regime, both GF and SUD effectively eliminate the negative moment production of LVAWT. However, the maximum positive moment production also diminishes with the presence of GF or SUD. Moreover, the illustration given by Figure 6 has shown that there are no significant disparities in distributions between the modified LVAWTs equipped with GF or SUD. This observation confirms that GF's ability at the medium *TSR* regime to mitigate LVAWT's dynamic stall is not as pronounced as that observed at the low *TSR* regime (for instance, GF can reduce the number of pairs of positive/negative peaks of fluctuation by a half at the low *TSR* regime, as depicted in Figure 5). The incorporation of SUD into the LVAWT set-up introduces minor secondary peaks in distributions, suggesting that the presence of SUD enhances flow unsteadiness upstream of blades. This phenomenon may be attributed to SUD's potential to induce robust wake vortices traversing through the LVAWT blades area, a behaviour that is not exhibited by GF (see Figure 8). The ratio of averaged lift coefficient (C_{C-CCC})/averaged drag coefficient (C_{C-CCC}) in Table 3 shows that GF produces a slightly higher ratio than SUD, indicating that LVAWT with GF can generate more power than LVAWT with SUD. GF can reduce the amplitude of instantaneous lift coefficient (C_{CC}) and instantaneous drag coefficient (C_{CC}) variations of bare LVAWT (see Figure 9), indicating that GF can ease the dynamic stall of LVAWT at medium regime of *TSR*s. The C_{CC} distributions shown in Figure 9(b) and the C_{C-CCC} value in Table 3 confirm that both GF and SUD increase the drag force generation compared to bare LVAWT, indicating that SUD no longer can decrease the drag force as it does at low regime of *TSR*s. At medium *TSR* regime, as the rotational speed is already sufficiently high, further wind speed increment due to SUD will have a negligible effect on the higher rotational blade speed. Conversely, this can cause the blockage effect (e.g., the blade can act as an obstructed solid wall due to its high rotational speed) to the flow with higher vibrations and drag losses (Bakırcı & Yılmaz, 2018). Nevertheless, there are considerable improvements of lift force by both standalone GF and standalone SUD (see Figure 9(a)) compared to bare LVAWT, which will suppress the adverse effects from the increment of drag force. Therefore, GF and SUD can still achieve higher ratios of C_{C-CCC}/C_{C-CCC} (see Table 3), resulting in the improvement of the C_{C-CCC} of LVAWT.

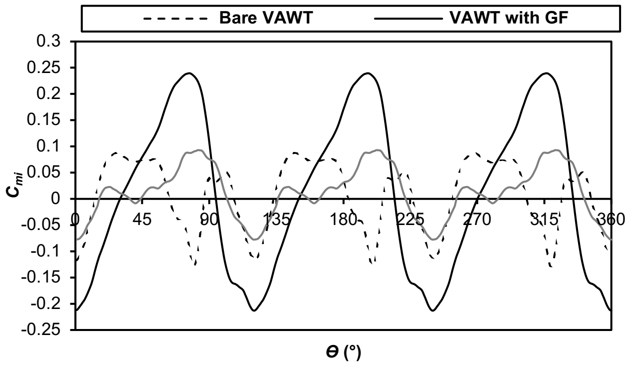

Figure 5: Comparison of C_{mi} among the bare LVAWT, LVAWT with standalone GF, and LVAWT with standalone SUD at TSR = 1.44

Table 2: Comparison of C_{l-ave}, C_{d-ave} and C_{l-ave}/C_{d-ave} over one blade revolution between bare LVAWT, LVAWT with GF and LVAWT with SUD at TSR = 1.44

Case	C_{l-ave}	C_{d-ave}	C_{l-ave}/C_{d-ave}
Bare LVAWT	0.2373	0.2314	1.0255
LVAWT with GF	0.3220	0.3006	1.0713
LVAWT with SUD	0.1960	0.1877	1.0442

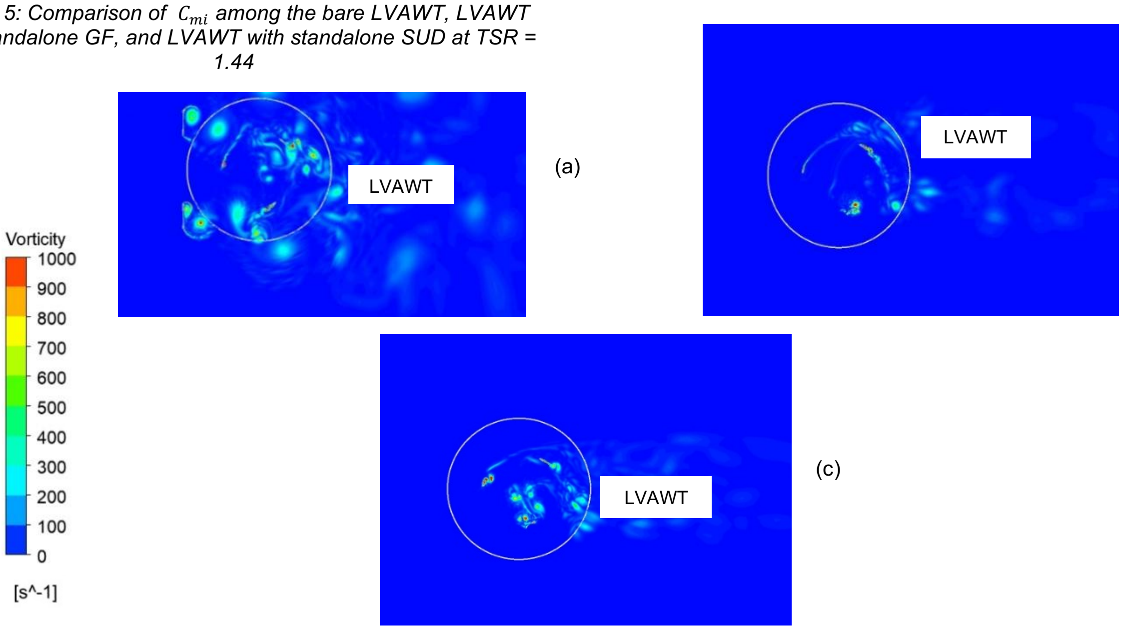

Figure 6: The z-vorticity (ξ) contours for (a) the bare LVAWT, (b) the LVAWT with standalone GF, and (c) the LVAWT with standalone SUD at TSR = 1.44 (θ = 90°). The solid white circles indicate the rotating core sub-domain.

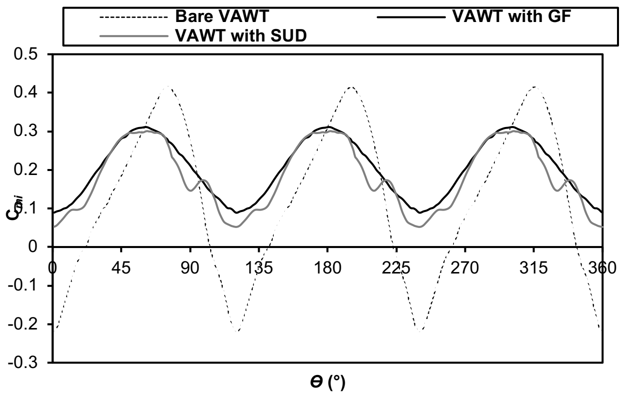

Figure 7: Comparison of the bare LVAWT, LVAWT with standalone GF and LVAWT with standalone SUD at TSR = 2.64

Table 3: Comparison of C_{l-ave}, C_{d-ave} and C_{l-ave}/C_{d-ave} over one blade revolution between bare LVAWT, LVAWT with GF and LVAWT with SUD at TSR = 2.64

Case	C_{l-ave}	C_{d-ave}	C_{l-ave}/C_{d-ave}
Bare LVAWT	0.2175	0.0973	2.2360
LVAWT with GF	0.3657	0.1614	2.2663
LVAWT with SUD	0.3829	0.1697	2.2563

High regime of TSRs with representative TSR = 3.3

When it comes to improving the power generation of LVAWT at the high regime of *TSR*s, GF's performance has been greatly diminished in comparison to the medium regime of *TSR*s (e.g. the C_{C-CCC} improvement has decreased to 31.66%). However, this does not apply to SUD, which continues to provide a comparable level of C_{C-CCC} improvement to that of *TSR*s at the medium regime of *TSR*s (e.g., 52.5%). A comparison of C_{CC} distributions is shown in Figure 10 to evidence that the GF can remove the negative moment production while maintaining a positive moment production that is rather close to that of bare LVAWT. On the other hand, compared to bare LVAWT, LVAWT with SUD exhibits the distinct behaviour with respect to its C_{CC} distributions, which considerably enhances the production of positive moments and marginally enhances the negative moments. As a result, at higher *TSR* regimes, the LVAWT with SUD has a higher C_{C-CCC} since its averaged moment output is larger than that of the LVAWT with GF and bare LVAWT. Both SUD and GF have the potential to greatly boost the drag output of LVAWT, as evidenced by the C_{CC} distributions in Figure 11(b) and the C_{C-CCC} in Table 4. According to Bakırcı & Yılmaz (2018), SUD produces more drag generation at the high regime of *TSR*s due to the increased blade rotating speed and obstruction effects. This is comparable to the medium regime of *TSR*s that was previously mentioned. At the high *TSR* regime, SUD generates the highest C_{C-CCC}/C_{C-CCC} ratio, and its distributions over one blade revolution (see Figure 11(a) and Table 4, respectively) show that SUD produces the highest lift generation when compared to LVAWT with GF and bare LVAWT. It demonstrates that the optimising of wind speed at high *TSR* regime by guiding the wind flow towards the frontal blade's region via SUD is a more efficient way to increase LVAWT power generation than using GF to regulate the blade's dynamic stall. The reason for this could be that the flow surrounding LVAWT has weak flow unsteadiness when *TSR*s are high. This is mostly because the angle of attack (CCC) at the high *TSR* regime is often below the static stalls of CCC. According to Malael, Dumitrescu & Cardos (2014), this indicates that the dynamic stall is not as important as it is at the low and medium regimes of *TSR*s. The potential of GF to lessen the dynamic stall of LVAWT will therefore not be entirely beneficial in this regard. Furthermore, the power coefficient enhancement at the high regime of *TSR*s is not as good as at the low and medium *TSR* regimes due to the additional drag generation induced by the addition of GF.

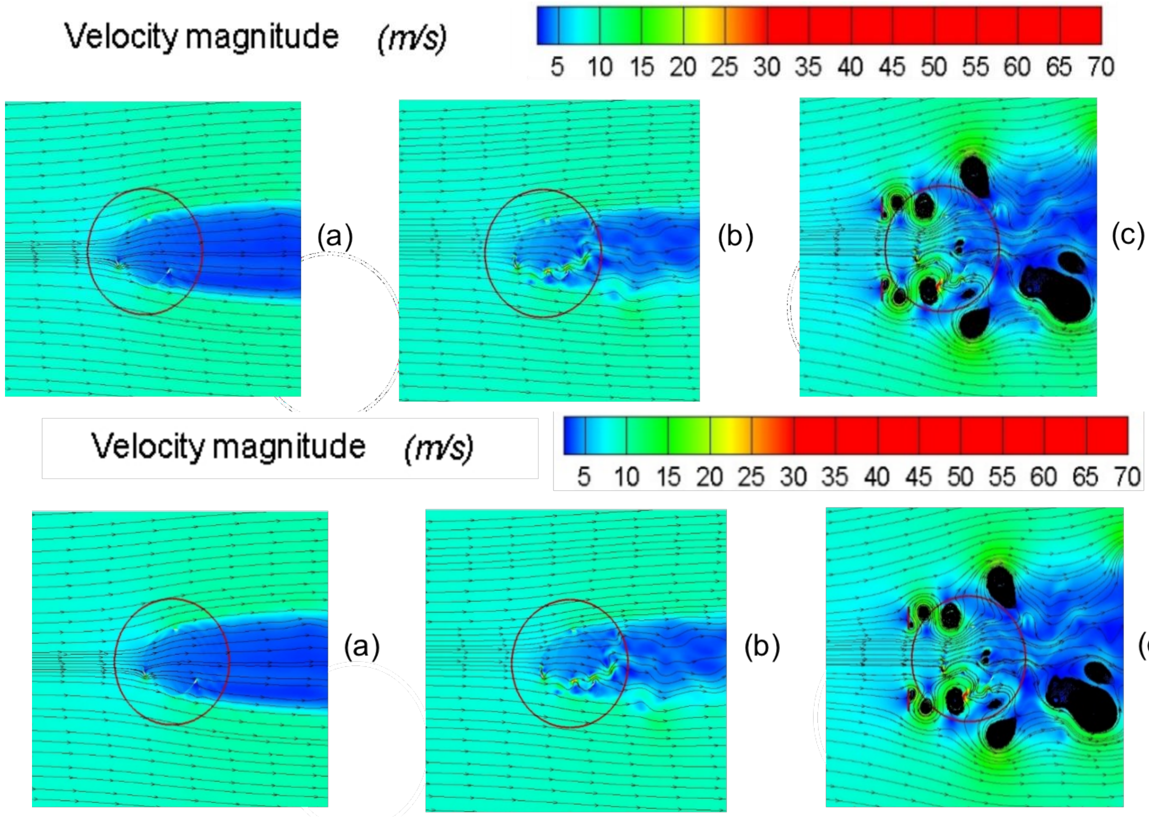

Figure 8: Streamlines coloured by the velocity magnitude (m/s) of the flow around (a) bare LVAWT, (b) LVAWT with standalone GF, and (c) LVAWT with standalone SUD (TSR = 2.64, θ = 360°). The circles in dark solid lines represent the rotating core sub-domain

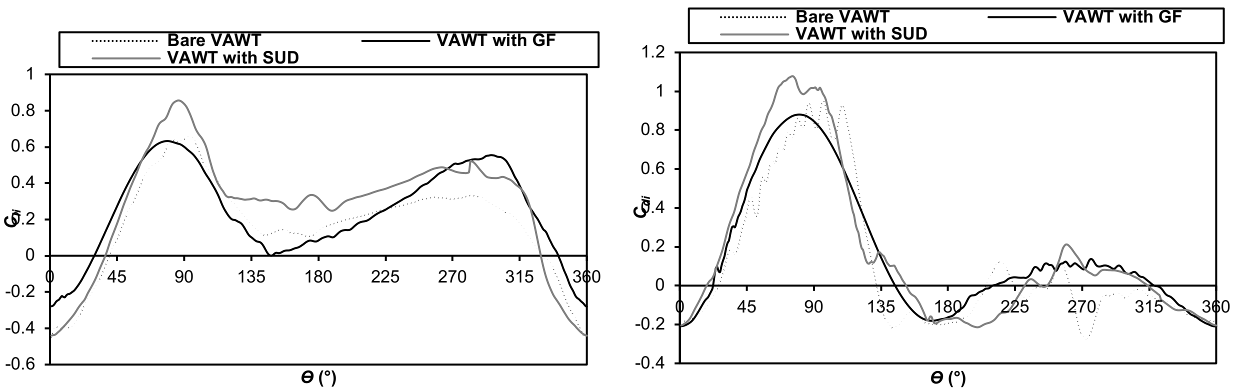

(a) (b)

Figure 9. (a) C_{li} and (b) C_{di} comparison between bare LVAWT, LVAWT with standalone GF and LVAWT with standalone SUD at TSR = 2.64

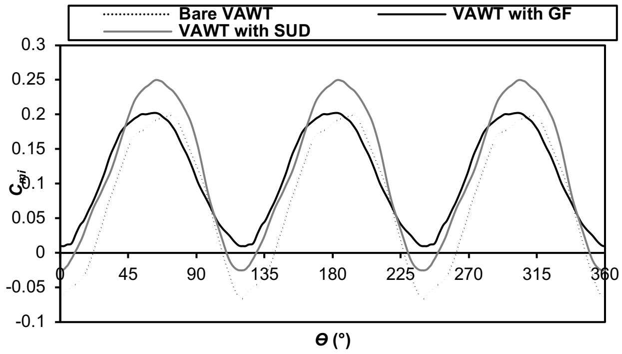

Figure 10: Comparison of C_{mi} for the bare LVAWT, LVAWT with standalone GF, and LVAWT with standalone SUD at TSR = 3.3

Table 4: Comparison of C_{l-ave}, C_{d-ave} and C_{l-ave}/C_{d-ave} over one blade revolution between bare LVAWT, LVAWT with GF and LVAWT with SUD at TSR = 3.3

Case	C_{l-ave}	C_{d-ave}	C_{l-ave}/C_{d-ave}
Bare LVAWT	0.1730	0.0937	1.8460
LVAWT with GF	0.2430	0.1309	1.8561
LVAWT with SUD	0.2802	0.1507	1.8597

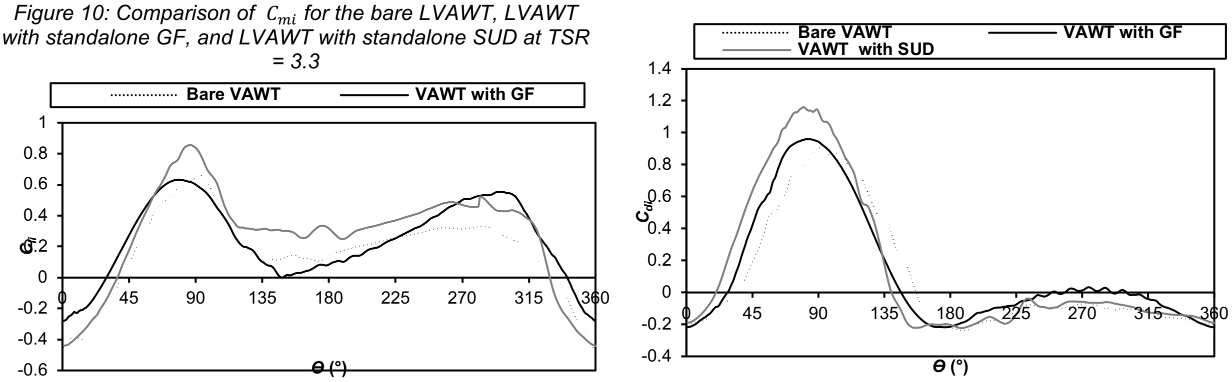

(a) (b)

Figure 11: (a) C_{li} and (b) C_{di} comparison between bare LVAWT, LVAWT with standalone GF and LVAWT with standalone SUD at TSR = 3.3

4.2. Impact of the GF and SUD Combination on LVAWT Performance

Based on the discussions above, it is evident that deploying flow augmentation devices (e.g., an SUD) and/or dynamic stall control devices (e.g., a GF) at all *TSR* regimes can improve the LVAWT's power generation performance. SUD can specifically speed-up the incoming wind speed and direct it towards the front of blade to increase the power generation of LVAWT. Meanwhile, GF can reduce the dynamic stall of LVAWT, increasing its power generating potentially. Since SUD creates stronger wake vortices than bare LVAWT and LVAWT with GF, it will cause increased flow unsteadiness at all *TSR* regimes. Additionally, GF will enhance the drag output of LVAWT in comparison to bare LVAWT. As a result, it is worthwhile investigating the combined effect of a flow augmentation device SUD and a dynamic stall control device GF in improving LVAWT performance, particularly at the high *TSR* regime. According to the findings of a standalone device investigation, SUD can increase LVAWT lift generation to improve the lift-to-drag ratio, whilst GF can diminish the induced flow unsteadiness by SUD. Therefore, in this section, a study is conducted to investigate the combined effort of GF and SUD, leading to increase LVAWT performance, and the findings are compared to those produced by LVAWT with a standalone GF and standalone SUD. The current study has determined the best performance enhancement at the low, medium, and high *TSR* regimes of 1.44, 2.64, and 3.3, respectively. The data in table 5 are utilised to compare the predicted C_{C-CCC} of LVAWT via four different scenarios: bare LVAWT, LVAWT with standalone SUD, LVAWT with standalone GF and LVAWT with both GF and SUD. Surprisingly, employing both a GF and an SUD to improve the performance of the LVAWT across all *TSR* regimes does not result in a higher C_{C-CCC} than utilising just one of the two devices. Nevertheless, the GF and SUD combination improves the C_{C-CCC} of the bare LVAWT at all *TSR* regimes. Figure 12 has illustrated the C_{CC} distributions fue to the effect given by LVAWT with GF and SUD combination in comparison of LVAWT with standalone GF and LVAWT with standalone SUD at all *TSR* regimes, respectively. In general, the results indicate that SUD exerts a greater influence on the alteration of flow characteristics than GF, since the distributions of C_{CC}LVAWT with GF and SUD bear similarities to those of LVAWT with standalone SUD. In comparison of LVAWT with standalone SUD, the vorticity contours displayed in Figure 13 further demonstrate that LVAWT with GF and SUD enablesto generate equal or even greater vortices. As a result, combining flow augmentation devices like SUD with dynamic stall control devices like GF will not increase LVAWT performance when compared to LVAWT with standalone GF or standalone SUD. The C_{C-CCC} of can be improved by 84.49% at low regime of *TSR*s when a bare LVAWT installed with both GF and SUD, whilst C_{C-CCC} has an approximately 35.31% and 28.68% decrease, when GF and SUD are used separately. The reason is likely due to the fact that a GF and SUD combination produces the largest reduction in negative moment outputin comparison to a standalone GF or SUD (see Figure 12(a)). It suggests that adding GF can reduce the negative moment output of LVAWT or over. However, GF will result in a strong drag force of LVAWT, as mentioned previously. As a result of SUD location positioned upstream of LVAWT, the increased blade rotation speed brought on by the increased incoming wind speed will exert more drag force on the GF. As a result, adding GF will greatly increase drag and somehow improve lift force at the same time. Furthermore, in comparison with a standalone SUD, the combined effort of GF and SUD can result in greater vortices induced at upstream and propagating downstream around LVAWT blades (see Figure 13(a)). Subsquently, the LVAWT with GF and SUD has the lowest peak values of positive moment generation, resulting in less improvement of C_{C-CCC}.

Meanwhile, a combination of GF and SUD at the medium *TSR* regime produces the least C_{C-CCC} improvement compared to those at both low and high TSR regimes. The $CC-CCC$ of a bare LVAWT can be only raised roughly by 19.43%, which is far less than that of VAWT with standalone SUD or GF to the $CC-CCC$ by 52.6% and 69.94%, respectively, in comparison of a bare LVAWT. LVAWT, with GF and SUD combination produces a similar peak value for positive moment production (about 0.3) as LVAWT with standalone GF or VAWT with standalone SUD. However, this combination can reinstate LVAWT's negative moment production at the medium TSR regime (see Figure 12(b)).

Additionally, when compared to LVAWT with standalone SUD, the distributions of C_{CC} by LVAWT with GF and SUD combination exhibit greater vibrancy. GF addition produces a greater drag force at the low and medium regimes of *TSR*s, and the drag generation likewise rises when blade rotational speed increases. The vortex generation of the LVAWT with GF and SUD is also greater than LVAWT with a standalone SUD (see Figure 13(b)). Since the blade is already spinning At a high speed, the lift force improvement is not shown noticeably at this condition. Therefore, the mean value of drag force only slightly improves, leading to a low improvement of C_{C-CCC}.

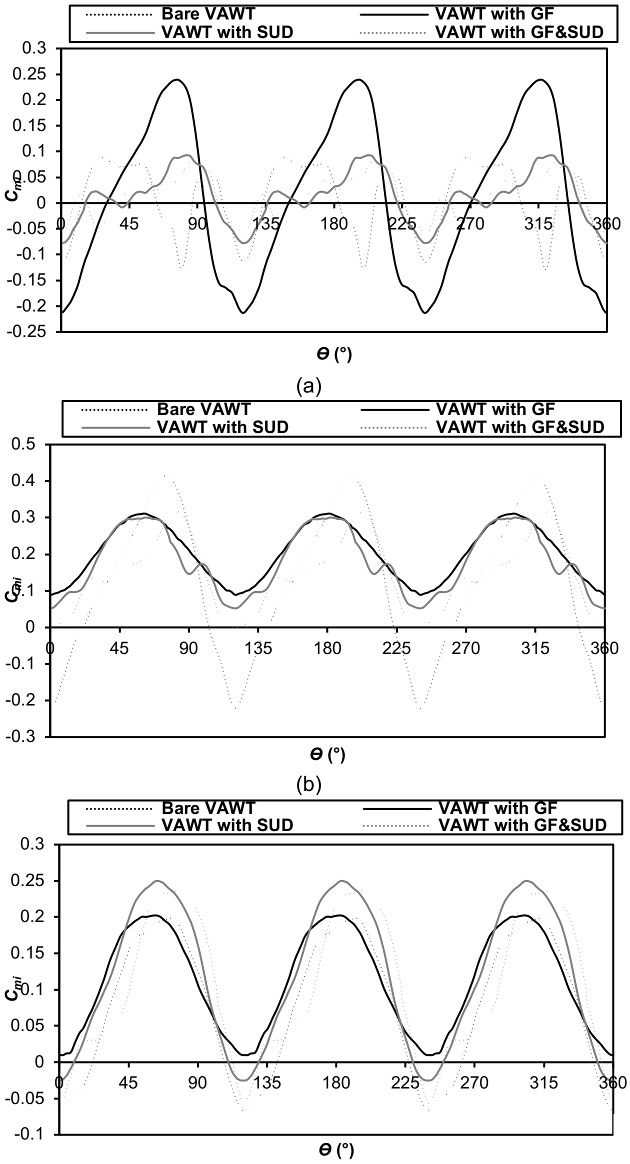

Figure 12: Comparison of C_{mi} between bare LVAWT, LVAWT with standalone GF, LVAWT with standalone SUD and VAWT equipped with GF and SUD at (a) TSR = 1.44, (b) TSR = 2.64 and (c) TSR = 3.3

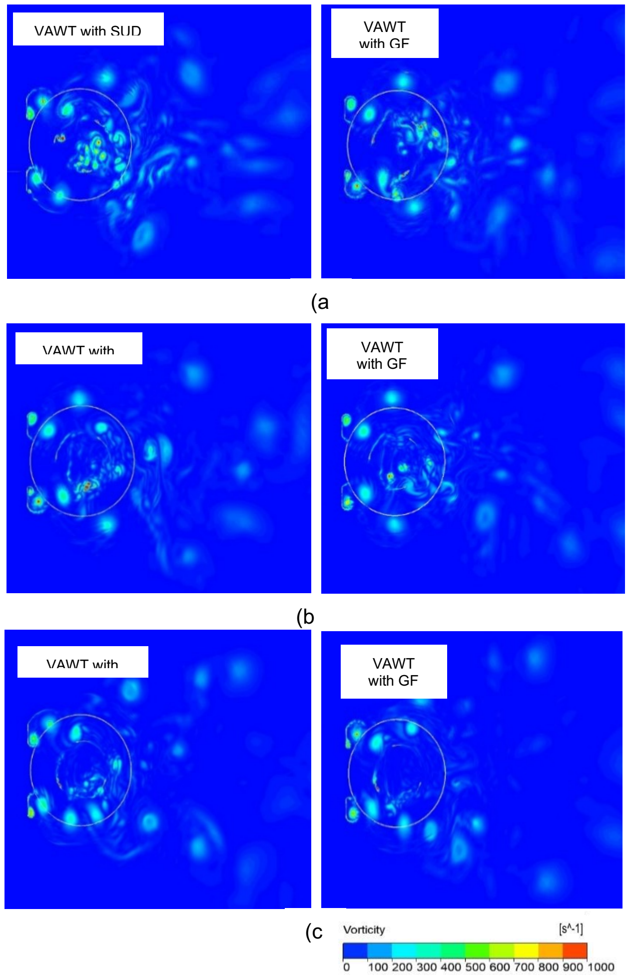

Figure 13: z-vorticity (ξ) contours comparison between LVAWT with SUD and VAWT with GF and SUD at (a) TSR = 1.44, θ = 90° (b) TSR = 2.64, θ = 90° and (c) TSR = 3.3, θ = 135°. The circles in white solid lines represent the rotating core sub-domain

Table 5: Comparison of C_{p-ave} between bare LVAWT, LVAWT with standalone GF, LVAWT with standalone SUD and LVAWT with GF and SUD

TSR	Bare LVAWT	GF	SUD	GF & SUD
1.44	0.0085	0.0196	0.0193	0.0157
2.64	0.3174	0.5394	0.4846	0.3791
3.3	0.2617	0.3699	0.3991	0.3461

In comparison of LVAWT with a standalone GF and LVAWT with a standalone SUD, the C_{C-CCC} improvement of LVAWT with GF and SUD decreases at high regimes of *TSR*s. In contrast to those at the low and medium *TSR* regimes, the reduction of C_{C-CCC} at high *TSR* regime is the least significant. The LVAWT equipped with GF and SUD can nevertheless produce a C_{C-CCC} improvement of 32.29% at high *TSR* regime, that is about 30% or 9% less than those improvements by LVAWT with standalone SUD or LVAWT with standalone GF, respectively. The C_{CC} distributions (see Figure 12(c)) show that the employing of GF and SUD together can still improve bare LVAWT's positive moment generation. Even though, the positive moment generation enhancement is not as great as LVAWT with standalone SUD. Moreover, the negative moment output of bare LVAWT can only be marginally decreased by employing both GF and SUD. In comparison with a standalone GF and a standalone SUD, it produces the least reduction of negative moment production. Therefore, the LVAWT with GF and SUD combination does not favourably influence the improvement of LVAWT, similar to those cases at low and medium regimes of *TSR*s. The C_{CC} distributions in Figure 12 (c) shows that the combination of GF and SUD causes a slight amplitude fluctuation in the C_{CC} distributions, which do not appear at standalone GF and standalone SUD. Furthermore, the vorticity contours (see in Figure 13(c)) plot indicates that employing both GF and SUD can generate greater vortices than a standalone SUD. In this instance, GF can no longer alleviate the dynamic stall of LVAWT as effectively as it has behaved in a standalone GF case, and its capacity to ease the dynamic stall of LVAWT is likewise less effective at the high *TSR* regime. Additionally, because of the increased incoming wind speed brought on by SUD, GF will introduce greater drag force while blade rotating speed increases (compare to bare LVAWT). Consequently, the use of both GF andSUD at the high regime of *TSR*s will result in the least improvement of LVAWT when compared to a standalone GF and a standalone SUD.

5. CONCLUSION

A comparative study has been conducted using CFD simulations to assess the effectiveness of a dynamic stall control device (GF) and a flow augmentation device (SUD) on enhancing the performance of LVAWTs across low, medium and high *TSR* regimes. Additionally, the effect of employing both GF and SUD to increase the performance of LVAWT is also investigated. The results reveal that standalone GF yields better improvement of the C_{C-CCC} of LVAWT at low and medium *TSR* regimes, while standalone SUD shows superior performance at the high *TSR* regime. Both standalone GF and standalone SUD demonstrate the reduced capability to enhance C_{C-CCC} of LVAWT with the increase of *TSR*. GF experiences a higher loss of effectiveness to improve the C_{C-CCC} of LVAWT at the high *TSR* regime compared to SUD (e.g., compared to medium regime of *TSR*s, LVAWT with standalone GF loses the ability by about 28% whilst VAWT with standalone SUD only loses around 0.3%). This study suggests that GF is more suitable for improving LVAWT performance at low and medium *TSR* regimes due to stronger dynamic stalls at these regimes than at high *TSR* regime. Therefore, the ability of GF to control dynamic stalls can be utilised more effectively at low and medium regimes of *TSR*s. Conversely, SUD is more effective for enhancing LVAWT performance at the high *TSR* regime, where the flow is relatively stable (i.e., exhibits less dynamic stall and much lower flow unsteadiness than the other two *TSR* regimes). Hence, the dynamic stall control mechanism is not entirely functional at this regime. To improve the performance of LVAWT, it is more important toenhance the incoming wind speed and direct it towards the front of LVAWT to increase the blade rotating speed at high regime of *TSR*s. Additionally, the use of both GF and SUD together did not lead to the higher value of C_{C-CCC} compared to the LVAWT with a standalone device of GF or SUD. In fact, the combination of GF and SUD introduces stronger vortex generation, primarily due to SUD, while GF loses its ability to control dynamic stall and introduces higher drag force. This confirms that GF is more suitable for low and medium regimes of *TSR*s, while SUD is better used for high regime of *TSR*sto improve LVAWT performance.

6. REFERENCES

"Ansys Fluent User's Guide," ANSYS Inc, [Online]. Available: https://ansyshelp.ansys.com/account/secured?returnurl=/Views/Secured/corp/v194/flu_ug/flu_ug.html. [Accessed 02 11 2020].

Bakırcı, N and Yılmaz, S 2018, 'Theoretical and computational investigations of the optimal tip-speed ratio of horizontal-axis wind turbines', Engineering Science and Technology, an International Journal, vol. 21, no. 6, pp. 1128-1142.

Balduzzi, F, Bianchini, A, Maleci, R, Ferrara, G & Ferrari, L 2016, 'Critical issues in the CFD simulation of Darrieus wind turbines', Renewable Energy, vol. 85, pp. 419-435.

Castelli, M R, Englaro, A & Benini, E 2011, 'The Darrieus wind turbine: Proposal for a new performance prediction model based on CFD', Energy, vol. 36, pp. 4919-4934.

Dewan, A, Gautam, A & Goyal, R. 2021, 'Savonius wind turbines: A review of recent advances in design and performance enhancements', Mater. Today Proc., vol. 47, pp. 2976–2983.

Malael, I, Dumitrescu, H & Cardos, V 2014, 'Numerical simulation of vertical axis wind turbine at low speed ratios', Global Journal of Researches in Engineering: I Numerical Methods, vol. 14, no. 1, pp. 9-20.

Mohammadi, M, Doosttalab, A & Doosttalab, M 2012, 'The effect of various Gurney Flap shapes on the performance of wind turbine airfoils', in ASME Early Career Technical Conference (ASME ECTC), Georgia, USA, 2012.

Syawitri, TP, Yao, YF, Chandra, B & Yao, J 2021, 'Comparison study of URANS and hybrid RANS-LES models on predicting vertical axis wind turbine performance at low, medium and high tip speed ratio ranges', Renewable Energy, vol.168, pp. 247-269.

Syawitri, TP, Yao, YF, Chandra, B & Yao, J 2022, 'Geometry optimisation of vertical axis wind turbine with Gurney flap for performance enhancement at low, medium and high ranges of tip speed ratios', Sustainable Energy Technologies and Assessments, vol. 49, Paper ID 101779.

Syawitri, TP, Yao, YF, Yao J & Chandra B 2022, 'A review on the use of passive flow control devices as performance enhancement of lift-type vertical axis wind turbines', Wiley Interdisciplinary Reviews: Energy and Environment, vol. 11, no. 4, Paper ID e435.

Syawitri, TP, Yao, YF, Yao J & Chandra B 2020, 'Assessment of stress-blended eddy simulation model for accurate performance prediction of vertical axis wind turbine', International Journal of Numerical Methods for Heat & Fluid Flow, vol. 31, no. 2, pp. 655-673.

Syawitri, TP, Yao, YF, Yao J & Chandra B 2022, 'Optimisation of straight plate upstream deflector for the performance enhancement of vertical axis wind turbine at low, medium and high regimes of tip speed ratios', Wind Engineering, vol. 46, no. 5, pp. 1487-1510.

Ung, S-K, Chong, W-T, Mat, S, Ng, J-H, Kok, Y-H & Wong, K-H 2021, 'Investigation into the aerodynamic performance of a vertical axis wind turbine with endplate design,' vol. 15, no. 19, Paper ID 6925.

Wong, KH, Chong WT, Sukiman NL, Poh, SC, Shiah Y-C & Wang, CT 2017, 'Performance enhancements on vertical axis wind turbines using flow augmentation systems: A review', Renewable and Sustainable Energy Reviews, vol. 73, pp. 904-921.